NBS SPECIAL PUBLICATION 425

Volume I

U.S. DEPARTMENT OF COMMERCE / National Bureau of Standards

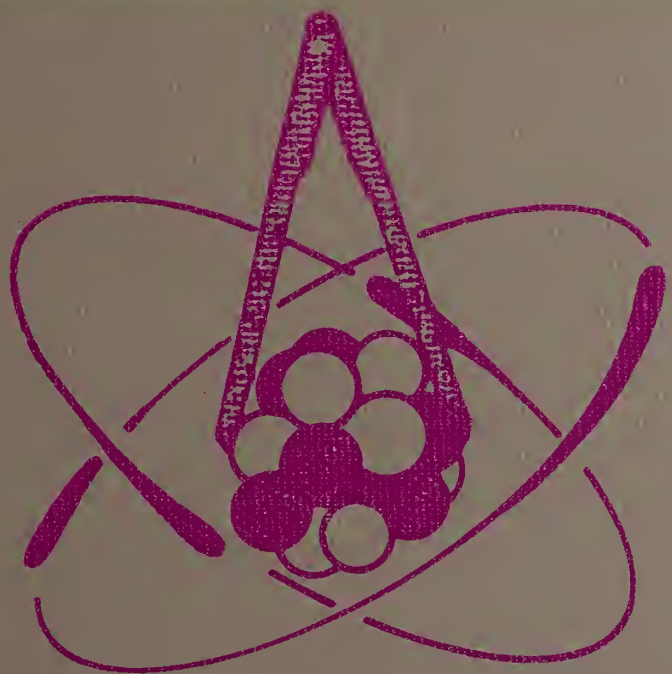

NUCLEAR CROSS SECTIONS AND TECHNOLOGY

PROCEEDINGS OF A CONFERENCE

Nuclear Cross Sections and Technology
Volume I

Proceedings of a Conference
Washington, D.C.
March 3-7, 1975

Edited by

R. A. Schrack and C. D. Bowman

Center for Radiation Research
National Bureau of Standards
Washington, D.C. 20234

U.S. DEPARTMENT OF COMMERCE, Rogers C. B. Morton, *Secretary*

U.S. NATIONAL BUREAU OF STANDARDS, Ernest Ambler, *Acting Director*

Issued October 1975

Library of Congress Cataloging in Publication Data

Conference on Nuclear Cross Sections and Technology, Washington, D.C., 1975
Nuclear Cross Sections and Technology.
(NBS Special Publication; 425)
Conference sponsored by the Reactor and Shielding Division of the American Nuclear Society and others.
Includes Indexes.
Supt. of Docs. No.: C 13.10:425
1. Cross Sections (Nuclear physics)—Congresses.
2. Cross Sections (Nuclear physics)—Standards—Congresses.
I. Schrack, Roald A. II. Bowman, Charles E., 1935- III. American Nuclear Society. Reactor and Shielding Division. IV. Title. V. Series: United States. National Bureau of Standards. Special publication; 425.
QC100.U57 no. 425 [QC794.6.C7] 389'.08s [539.7'5] 75-619216

National Bureau of Standards Special Publication 425

Nat. Bur. Stand. (U.S.), Spec. Publ. 425, 487 pages (Oct. 1975)

CODEN: XNBSAV

U.S. GOVERNMENT PRINTING OFFICE
WASHINGTON: 1975

For sale by the Superintendent of Documents, U.S. Government Printing Office
Washington, D.C. 20402 - Price $19.45 per 2 vol. set sold in sets only
Stock Number 003-003-01461-3

FOREWORD

The development of new energy sources is one of the critical problems facing our society, and the use of nuclear energy is expected to grow rapidly in the coming decades. Thus, the recent Conference on Nuclear Cross Sections and Technology was a most timely event. I think that the Conference successfully met its goal of summarizing the present status of nuclear cross sections and technology, discussing future cross section needs and exchanging information between nuclear scientists and engineers. The National Bureau of Standards has long been involved in the development of nuclear science and technology. While the generation of measurement techniques and the publication of nuclear data are important activities, so is the sponsorship of and participation in conferences such as this one. It is through the publication of these conference proceedings that we will continue widening the forum of interchange.

Ernest Ambler
Acting Director

PREFACE

These are the proceedings of the Nuclear Cross Sections and Technology Conference held at the Shoreham Americana Hotel in Washington, D.C., March 3-7, 1975. It might be considered as the fourth in a series of conferences formerly entitled "Neutron Cross Sections and Technology" or as the first of a new series of conferences of a broader scope. The list of participants and the table of contents indicate the success of the conference in attracting representatives of many disciplines and countries.

The conference was sponsored by the Reactor and Shielding Division of the American Nuclear Society, the Nuclear Physics Division of the American Physical Society, the International Union of Pure and Applied Physics, the National Bureau of Standards, and the United States Energy Research and Development Administration. The purpose of the conference was to provide a forum for the exchange of information related to the use by technology of nuclear data and techniques. The great majority of technological contributions reflects the current needs and interests of the fields of reactor technology and biomedicine. Scientific contributions to the conference deal with the development of nuclear standards and the measurement of cross sections. Included are papers on measurement techniques and experimental results, as well as data evaluation and analysis. The reader is directed to the summary paper in session JA for a more detailed evaluation of the conference.

The papers are printed in the proceedings as they were received from the authors and in the order in which they were presented in the sessions and in the Bulletin of the American Physical Society, Series II Volume 20, pp. 132-177 (1975). For convenience we have preserved the conference notation for the sessions. In a few cases manuscripts were not submitted by the authors. The following papers for which abstracts appeared in the Bulletin were not submitted: BA-3, BB-17, CB-8, CB-9, EB-12, HB-1, HB-18, and HB-24. Several papers have been added at the end of some sessions that arrived after the deadline for the Bulletin.

To speed the publication of the proceedings, all papers were submitted by the authors in camera-ready form. We are greatly indebted to the authors and all those who assisted in the preparation of the manuscripts. Their efforts have made it possible to get the proceedings in print much more rapidly than would otherwise be the case. To make the proceedings more useful we include, as well as a table of contents, an author index, a list of participants, and a CINDA index of subject matter. We would like to thank Dr. Norman Holden of Brookhaven National Laboratory for the preparation of the CINDA index.

When commercial equipment, instruments and materials are mentioned or identified in this proceedings it is intended only to adequately specify experimental procedure. In no case does such identification imply recommendation or endorsement by the National Bureau of Standards, nor does it imply that the material or equipment identified is necessarily the best available for the purpose.

We wish to express our appreciation for the financial support from the U. S. Energy Research and Development Administration and the National Bureau of Standards which made the publication possible.

The Editors gratefully acknowledge the assistance of the National Bureau of Standards Office of Technical Information and Publications and the extensive secretarial assistance of Mrs. Julia Marks, Mrs. Lois Gallahan, and Mrs. Linda Cline.

R. A. Schrack

C. D. Bowman

ABSTRACT

These proceedings are the compilation of 221 papers presented at the Conference on Nuclear Cross Sections and Technology held in Washington, D.C. on March 3-7, 1975. The Conference summarized the present status of nuclear cross sections and technology and discussed future cross section needs. Special emphasis is placed on reactor technology and biomedical applications of nuclear science and the measurement of standard cross sections.

Key words: Biomedical; Conference; cross section; nuclear; standards; technology.

TABLE OF CONTENTS

Contents, Volume I

SESSION CB (Continued)

SESSION DA: MANAGEMENT OF THE ACTINIDES

SESSION DB: CROSS SECTIONS AND FLUX STANDARDS

Contents, Volume II

Papers from Sessions FB through JA — Pages 469 through 970

SESSION FB: VARIOUS APPLICATIONS OF NUCLEAR DATA

SESSION GA: VARIOUS APPLICATIONS OF NUCLEAR DATA

SESSION GB: CROSS SECTIONS MEASUREMENTS ON FISSIONABLE ISOTOPES

SESSION HB (Continued) Page

SESSION IB (Continued) Page

SESSION JA: ROUNDTABLE DISCUSSION OF THE SIGNIFICANCE AND ACCOMPLISHMENTS OF THE CONFERENCE

PROGRAM COMMITTEE

W. W. Havens, Jr., Chairman -- Columbia University
R. S. Caswell -- National Bureau of Standards
F. Feiner -- General Electric Corporation
H. Goldstein -- Columbia University
D. Harris -- Los Alamos Scientific Laboratory
D. J. Horen -- Oak Ridge National Laboratory
H. Jackson -- Argonne National Laboratory
D. A. Lind -- University of Colorado
S. Pearlstein -- Brookhaven National Laboratory
F. Perey -- Oak Ridge National Laboratory
C. Preskitt -- Intelcom Radiation Technology
J. S. Robertson -- Brookhaven National Laboratory
A. B. Smith -- Argonne National Laboratory
D. Steiner -- Oak Ridge National Laboratory

INTERNATIONAL ADVISORS TO THE PROGRAM COMMITTEE

S. W. Cierjacks -- Karlsruhe
W. G. Cross -- Atomic Energy of Canada, Ltd.
A. S. Divatia -- Bhabha Atomic Research Centre
R. Joly -- Saclay
B. Rose -- Harwell
J. J. Schmidt -- IAEA
K. Tsukada -- Japan Atomic Energy Research Institute
L. N. Usachev -- Obninsk

ARRANGEMENTS

E. H. Eisenhower, National Bureau of Standards

SESSION CHAIRMEN

SESSION AA: OPENING SESSION, FISSION REACTORS I
W. W. Havens, Jr.

SESSION BA: FISSION REACTORS II
F. Feiner

SESSION BB: INSTRUMENTS AND TECHNIQUES
A. B. Smith

SESSION CA: MICROSCOPIC DATA AND TECHNIQUES
H. Jackson

SESSION CB: BENCHMARKS AND SENSITIVITIES
D. Harris

SESSION DA: MANAGEMENT OF THE ACTINIDES
D. J. Horen

SESSION DB: CROSS SECTIONS AND FLUX STANDARDS
L. Stewart

SESSION EA: CROSS SECTIONS AND FLUX STANDARDS
R. S. Caswell

SESSION EB: EVALUATION AND CALCULATION OF CROSS SECTIONS OF NONFISSIONABLE MATERIALS
F. Perey

SESSION FA: REACTOR PHYSICS; TRANSPORT AND SENSITIVITY
H. Goldstein

SESSION FB: VARIOUS APPLICATIONS OF NUCLEAR DATA
J. I. Trombka

SESSION GA: VARIOUS APPLICATIONS OF NUCLEAR DATA
J. S. Robertson

SESSION GB: CROSS SECTIONS MEASUREMENTS ON FISSIONABLE ISOTOPES
M. Moore

SESSION HA: FUSION
J. M. Williams

SESSION HB: NEUTRON CROSS SECTION MEASUREMENTS ON NONFISSIONABLE MATERIALS
V. Orphan

SESSION IA: BENCHMARKS AND SENSITIVITIES
S. Pearlstein

SESSION IB: MEASUREMENTS OF NEUTRON CROSS SECTIONS OF NONFISSIONABLE MATERIALS
R. Lane

SESSION JA: CRITIQUE AND SUMMARY LESSON
H. Jackson

OPENING REMARKS FOR THE NUCLEAR CROSS SECTIONS AND TECHNOLOGY CONFERENCE

W. W. Havens, Jr.

Columbia University

This is the opening of the first Conference on Nuclear Cross Sections and Technology which would be known more familiarly to most of you as the fourth of the Conferences on Neutron Cross Sections and Technology. These conferences were so successful in bringing together those who measured, evaluated, and used neutron cross sections that it was felt desirable to do the same for those who measured, evaluated, and used a broader variety of nuclear data. The title of the conference has therefore been changed to suit those who now participate. The conference is sponsored by the Atomic Energy Commission, the National Bureau of Standards, The American Physical Society, the American Nuclear Society, and the International Union of Pure and Applied Physics.

The Conferences on Nuclear Cross Sections and Technology grew out of the old AEC information meetings which regularly took place at national laboratories while much of the atomic energy program was still classified. In the early days of the Manhattan Project, those who measured, evaluated, and used nuclear cross sections were the same people, so no problems in communications arose. If a man designing a reactor found he didn't have a necessary piece of information, he would go to the laboratory and measure it. He usually did not have to worry about whether or not it agreed with previously existing data because there was none. If the cross section was unknown, and could not be measured, then he asked Fermi for the necessary information and Fermi produced an answer which was used whether it was correct or not.

Several public conferences preceded the Neutron Cross Sections and Technology Conferences. The first public conference on data exchange after the extensive declassification of information at the Atoms for Peace Conference in Geneva in 1955 was probably the Time of Flight Conference in Gatlinburg, Tennessee in the fall of 1956. This was followed by the Columbia Conference on the Neutron Interactions with Neutrons in September of 1957, the Saclay Symposium on Neutron Time of Flight in July 1961, and the International Conference on the Study of Nuclear Structure with Neutrons in Antwerp in July 1965. The first conference in this series on Nuclear Cross Sections and Technology was held at this hotel in March 1966 and was originally organized for the Nuclear Cross Sections Advisory Committee, an advisory committee to the Research Division of the United States Atomic Energy Commission. This 1975 conference was organized by its successor the United States Nuclear Data Committee. The International Atomic Energy Agency has also sponsored conferences on nuclear data, Paris in 1966, Helsinki in 1970, and Paris in 1973, which have been loosely coordinated with our series of conferences on Neutron Cross Sections and Technology.

As nuclear technology has developed, the scientists find it more difficult to master all aspects of the science and technology and they have become separated into groups of specialists who no longer understand each other's problems. We hope that this conference will give the specialist in one aspect of nuclear technology a better understanding of the problems which arise in the other specialties.

The purpose of these topical conferences on Nuclear Cross Sections and Technology and "topical conferences" in general is to facilitate communications in a specialized field. This purpose is accomplished through formal presentation of invited and contributed papers, corridor communications, and the publication of the Proceedings. The Program Committee attempts to determine what new, most interesting and stimulating information should be presented at the conference. It then selects invited speakers to discuss this material. These discussions constitute the subject matter of the conference. The members of the Program Committee generate a lot of correspondence even before the tentative program of the conference is set. Once the tentative program of the topical conference is announced, the individual scientists and engineers must determine whether or not the subject on which they are working is appropriate for presentation at the topical conference. Each does a great deal of work and very little communicating until the abstracts of papers to be submitted to the conference are prepared. The first flood of communications occurs when the abstracts of the invited and contributed papers are printed in the program.

The conference finally starts with the presentation of the invited and contributed papers. Some are extremely interesting and stimulating; others, unfortunately, are dull and contain little information. However, one of the outstanding benefits of the topical conference is that many experts in the various aspects of the subject matter of the conference gather together in one place and can talk with their colleagues about mutual problems. A great deal of information is transmitted in the formal sessions and probably even more in the informal discussions which take place in the corridors at the conference.

Of particular interest to the old timers in the nuclear cross sections and technology field is the present status of the perennial competition between the measurers of nuclear cross sections and those who develop the theory which uses microscopic nuclear data. In the early days of the Atomic Energy Commission it was clear that the data required to design nuclear energy systems did not exist and an extensive experimental research program was undertaken to obtain this information. When large amounts of nuclear cross sections data became available, the theory was not

sufficiently well developed to make use of this excellent data. Extensive developments in the theory then took place aided extensively by the introduction of large scale computers. A few years ago the theory was better than the measurements and a new measurement program was again developed. It will be interesting to see at this conference who is ahead in this horse race: the experimentalists or the theorists. I think this competition will continue indefinitely because a symbiotic relationship exists between theory and experiment. If one progresses much further than the other, it languishes, until it is stimulated by an advance by its competitor, and the contest continues as it must.

Finally, the manuscripts must be prepared for the permanent record of the conference: the Proceedings which contain the full text of all invited and contributed papers. I personally find the Proceedings of these conferences extremely valuable documents, both for research and for teaching. They gather together in one place the latest status reports on a large fraction of the research in progress on a particular topic and keep me abreast of the field.

The large number of papers contributed to this conference demonstrates the great interest and vigor of this field. The Program Committee expected between 75 and 100 contributed papers and the number contributed was 181. The number would have been much larger had it not been for the French mail strike. There are over 300 scientists registered for the conference with about 25 percent coming from overseas. There should be adequate opportunity to discuss all aspects of nuclear cross sections and technology with your colleagues from all parts of the world. I am delighted to see so many old friends present and look forward to meeting the many younger scientists and others who have recently entered this field and have contributed papers to this conference. I am certain you will have a stimulating, interesting and informative week.

NEUTRON CROSS SECTION NEEDS

Herbert J. C. Kouts, Director, RES
U. S. Nuclear Regulatory Commission
Washington, D. C. 20555

When Bill Havens called me to ask if I would give the keynote address to this Fission Reactors session of this International Conference on Cross Section Technology, I was surprised. I have been away from any real contact with cross section needs for over ten years. But Bill pointed out that I had given the corresponding talk a number of years ago, and so it would be reasonable that I give another. As I think back to that conversation, I am now kind of surprised that this piece of logic convinced me. But I have been confronted by and defeated with much less adequate chains of logic since I came to Washington nearly two years ago. So maybe I was just overcome by the relative weight of argument in this particular case.

There is still a question as to what I in my present incarnation can tell you about cross sections and their needs in connection with fission reactors. Certainly in asking me to talk you did not believe I would tell you anything new about the field. I have thought very hard about what I could in fact contribute, and I made a number of notes, and then I found that all my thoughts ran along the common line of relating what I did in the past on cross section needs to what I perceive to be some real issues now. So in addressing you, I shall act as a Rip Van Winkle returned after many years to view again the land I once inhabited, and the many friends here.

I was once heavily involved in putting together the cross sections request list. This duty fell on me almost by accident. Up until the middle 1950's, the list of cross section measurement requests was kept by the Neutron Cross Sections Advisory Group. The NCSAG was the ancestor of all cross section committees. It advised the AEC on the research program and on the compilation of cross sections issued in those days by Don Hughes' group as the Barn Book. NCSAG at one point had become deluged with requests that various cross sections be measured or that they be measured better. They did not really feel able to guess why requests were made, or what priorities they should have. So they asked the Advisory Committee on Reactor Physics to take a look at the requests, to screen them. I had just replaced Irving Kaplan on the ACRP as the Brookhaven member, and since the Barn Book was put together at Brookhaven, I was asked to do the job. In fact, at various times, several other members of ACRP joined in the work. I recall sessions including Jack Crandall, Fred Mainschein, Gerhard Dessauer, John Morphett, and others.

We faced some peculiar problems at the outset, and I see that some of these problems have never been solved. Some of the requests were simply for thermal cross sections, without specifying what that meant. What was a thermal cross section, one averaged over a Maxwellian energy distribution at 300^{o} K, perhaps, or a point value at 2200 m/sec? In many cases, the requester had not thought out what the difference meant. But the answer had a definite effect on the kind of experiment that might be needed to satisfy the request. And in those days, we knew far too little about the dependence of cross sections on energy to be able to relate the two kinds of meaning of thermal cross-section. In discussions on this difference, we first met a problem that has proved bothersome ever since. This is, how do we assess the value of integral experiments in providing microscopic cross section data? I shall have some more to say about this later.

Another question that arose quite early was that of attaching statements of required accuracy to cross section requests. Many requestors did not know what had been measured and how well, so they simply asked that a certain cross section be measured. It was hard to tell how much of the stated need was an expression of a real gap in knowledge, and how much represented ignorance of the state of knowledge. Some requesters simply asked for better measurements of something: better values of the fission cross section of uranium 235 in the thermal energy region, for instance. We began an educational campaign directed at the cross section requesters. We told them all that no request would be reviewed unless it included a statement of the accuracy needed. We got back a number of strange clarifications. One of the most astonishing was a request for the total, scattering, and absorption cross sections of all the separate fission product isotopes, from 0 to 10 Mev, to 1% accuracy. Clearly, more education was needed than we realized at first. The theorists who used neutron cross sections as vital input data for their calculations did not understand what is feasible or practical in the measurement of these quantities, nor did they understand the sensitivity of their own results to the precise values of the input data. So we found that the difficulty in communication between cross section producers and cross section consumers was almost complete.

Part of the problem is not so bad as it once was. The space between the producers and the consumers is now filled by an army of

evaluators who have pretty well learned to communicate with their two sets of neighbors. The activities of the Cross Section Evaluation Working Group, and the National Neutron Cross Section Center have been of particular value. It is difficult to see how the bridge could be made between supply and demand without these two groups.

But the part of the problem dealing with the propagation of data uncertainties into uncertainties in integral calculations has never really been solved, at least to my satisfaction. The hardest part of the problem is to state the question in a useful way. The reactor theorist deals with group equations in which the cross sections are averaged over energy intervals through use of approximate spectral weighing functions, and then only a relatively small number of such averaged cross sections is used in the real calculations. The cross section measurer has almost the opposite approach. He measures with an apparatus that has a certain resolution function, which he tries to get rid of in his search for data that represent point functions. What does it mean to ask how the output of the reactor theorist depends on his input from the cross section measurer?

We have learned through long discussion and much clearing-up of misunderstanding that the answer is not unique. It depends on the kind of cross section and the kind of application. Some cross sections are slowly varying over broad energy spans, for instance those for light nuclei and those in the unresolved resonance region. For these it makes sense to ask how the values of calculated parameters of interest depend on the uncertainty of the cross section over that region. We can even ask what is the derivative of a calculated parameter with respect to a multiplicative factor applied to the cross section input, and this derivative will supply the answer to the question of accuracy needed.

If there are resonances or appreciable variations of other kinds in the cross section, there are several possibilities, non perfect. Why not just specify an absoluate accuracy need over the range, in these cases, too? Well, for one thing, it does not make sense to ask for a uniform accuracy in a measured cross section that varies by, say, a factor of 100 over the interval. Accuracy in the measurements is more complicated than that. Even where there is a practice of fixed counting statistics point-to-point, a rarity in these days of multi-dimensional channel analyzers, the other counting corrections lead to different accuracies at the peaks and valleys of the cross sections. The requester may be asking for one percent accuracy where the value is high and important, and he may be leading the experimenter to try to measure to one percent where the value is low, where it does not really matter, but the experimenter is strained to do almost the impossible.

For another thing, there is the problem of error in energy scale in experiments. Where the cross section varies rapidly with energy, an error in energy scale can cause large localized errors in measured values. These are seldom of importance to the reactor theorist unless they are really bad. How do we get this point over in a statement of required accuracy?

In a few very important cases, resonances are spaced well enough apart for the single level Breit-Wigner expression to be adequate. In these cases, the accuracy requirement can be reexpressed in terms of resonance parameters. But then new questions come up. Why should we ask for the same accuracy for small resonances as for large ones? If we do, we impose a real penalty on the cross section measurer. Furthermore, how good are the resonance parameters themselves? Estimates of their experimental accuracy depend on a detailed understanding of the instrument resolution and sources systematic of experimental error,. and these are very hard to evaluate.

In the most important cases, where resonances are close together and multi-level resonance formulae are needed to fit nature, the problem of how to specify accuracy needs may never be solved. We may just have to go back to hard spectrum reactors where the problem is not so intractable.

Our first solutions to what I call the accuracy problem were much easier. In the middle 1950's we still had no real good-sized computers, and many calculations were still limited to what could be done by hand or by desk calculator methods. In those days we profited a lot by intuitive methods that I doubt many people use these days. These methods, based on the old four-factor formula, have nearly vanished from sight as the reactors to which they can be applied diminish in interest to research and design groups. I remember one working session that Herb Goldstein attended, where he got a little mad at some of the offhand statements being made, about accuracy needs. "Ten percent should be o.k. here, but five percent is probably needed there." I guess we may have been a little cavalier about some of our statements, but relatively crude semi-analytical formulae that can be manipulated mentally are good enough for many such estimates of cross section accuracy requirements. We would probably be better off if Bernie Spinrad and Irving Kaplan had continued their exploration of semi-analytical methods of analysis as they might be used for fast reactors.

As I thought about what I might say to you today, I remembered papers that had once been in my possession, that can tell us something about how we got where we are. These are old Manhattan District reports containing the compilations of cross sections used in that period. I once had these in my possession, when the reports

were still all classified and were carefully indexed and filed sequentially. Declassification set in about 1955, and slowly the old reports disappeared from the files. I mentioned to Charles Kelber that I was interested in resurrecting certain ones for this meeting, and he set off a search that was in fact rewarding. We find that in late 1942, the progress reports reflected an intense effort to account for the exponential experiments at Columbia University in terms of fundamental quantities, so that the Hanford reactors could be designed properly. In the progress report for September 15, 1942, Anderson reported the fission and absorption cross sections of uranium for thermal neutrons as 4.6 and 3.2 barns respectively. In the report a month later, more data were added. A fast fission cross section of 0.5 barns had been measured by the Princeton group under Wigner. The value of ν was now believed to be 2.2 neutrons per fission. Some other integral data were also given, pertaining to graphite lattices. Additional data were added in November, and by December 1972 the cross sections had settled into a set deemed suitable to explain the Columbia and Chicago data. In particular, the value of ν for natural uranium was set at 1.31.

It is interesting to speculate on the data, though we can only guess now at some of the why's and wherefore's. The value of ν was too low by 10%. This was almost exactly compensated by a value of $1 + \alpha$ which was also too low by just over 10%. The result was that the value of the integral parameter η, which is neutrons produced per neutron absorbed, was correct to within 0.4% (here I am using as the basis for comparison an evaluation of η I made in 1955 for natural uranium, based on some measurements with slightly enriched uranium lattices). This all made the criticality of graphite-natural uranium reactors come out on the nose. We have had eigenvalues good to 1% ever since, with a few notable exceptions.

How did the compensating errors occur? One is inclined to believe that the existence of the integral experiments turned the trick. Score one for integral experiments as against microscopic measurements. Except that the integral experiments did not lead to modifying the value of $1 + \alpha$, where the principal error in microscopic data existed. The lesson is that one can indeed test cross section sets against good clean experiments and get guidance that will help to modify the cross section sets to fit the data. But the cross section may end up wrong.

These were the first evaluated nuclear data sets for use in reactor analysis. They were compiled in CP-333, November 5, 1942, by Ibser. They led in a progression of more and more sophisticated publications to today's computer-based data compilations and evaluated data files.

But it is time to turn from the past to discuss cross sections today. I have been going over some of the current literature to find what impels the experiments of today. I see much that is familiar. I find a few upsetting points, and one outright scandal.

Of course, the primary motivation for interest in cross sections now is the correct design of fast breeder reactors. The present request list, which Al Smith kindly sent me a copy of, is full of data requests of this kind. It is in fact somewhat overwhelming at first to see the detail required, especially for the fissile and fertile materials, and the coolant and structural materials.

It is appropriate to ask why the detail is required. In 1967, Phil Palmedo and I did a review of the status of criticality experiments for fast reactors. We turned up several points that we felt should be improved, some of which had bearing on cross section matters. One of these was a perplexing inability of any of the current calculations to match the reactivity worths of materials placed in the center of the reactor. This has continued until now, and is now called the "central worth discrepancy." Another was an apparent inability to fit values of the neutron lifetime measured in fast critical experiments. So far as I am aware, this discrepancy has not been followed up or resolved. A third was a discrepancy between measured and calculated values of the internal breeding ratio. I am not aware that this has been resolved. A fourth was a channeling effect in the platelets used in ZPR experiments, with results that might show up only in higher order Sn calculations. The reality and size of this effect may be clarified in the pin-geometry ZPPR loadings.

Recent studies of the origin of the central worth discrepancy indicate that this effect may simply be the result of a number of separate causes. Bohn finds that broad group cross sections adjusted to match integral reaction rate data lead to a noticeable improvement in reducing the magnitude of the discrepancy. The central worth comparison is important as an integral test of fast reactor theory, and also it has inherent importance as a differential datum for the calculation of core disassembly accidents. In the absence of assured ability to match calculated central reactivity worths to measured ones, it may turn out necessary to design the reactors more conservatively to meet safety standards. It is still too early to know if the discrepancy is related principally to experimental methods, calculational methods, or cross sections. Detailed cross sections including energy and angular dependence will be needed to ensure the innocence of the input data.

The use of the integral reaction rates to improve the agreement between experiment and analysis is interesting, but perhaps we should bear in mind the wartime experience with the η of natural uranium. And we should perhaps review the implication that the reaction rates themselves are not properly predicted by the analysis, although they probably should be more reliably calculated than the central worth.

The second point I would like to bring out with respect to the review that Palmedo and I did is related to the breeding ratio. Unfortunately, there is no good way to measure true conversion ratio or breeding ratio by activation in a critical experiment. It will be absolutely necessary to depend on calculations starting from cross sections to conduct economic analyses. But an error of 1% in relative normalization of fission and absorption cross sections can mean an error of order of magnitude of 10% in the doubling time calculated. My impression from the current cross section request list is that what is being asked for may not be good enough for economic studies.

Now for the scandal. Herb Goldstein has recently done a check list of discrepancies in nuclear data, for review by the International Nuclear Data Committee. He lists many familiar landmarks, discrepancies that refuse to go away, such as the medium energy capture cross section of U-238, and the possible existence of structure in the energy dependence of ν. But the one item which leaps to my eye in his list is the discrepancy in the value of neutrons per fission for Cf-252. He comments, "Data divides into two groups (according to method of measurement) about 2.5% apart." He further says, "Vital standard; especially important for thermal constants of fissile nuclei." Well, that is an understatement, indeed. Considering that the value of ν is used to balance the neutron economy in all reactor theory, so that an error in ν is reflected as a corresponding error in the eigenvalue, and considering that all values of ν for fissile nuclei are referred to the value of ν for spontaneous fission of Cf-252, we would conclude that there is an uncertainty of 2.5% in all comparisons of criticality calcualtions with experiments.

Of course, we don't really believe the discrepancy is that bad, or the matter might have even hit the newspapers. But a discrepancy of this magnitude is unsettling for so fundamental a quantity, and my feeling is that this must absolutely be cleared up.

I have gone over the cross section request list to see if there are instances where additional data should be requested for reasons of safety interest. By and large, I conclude that the data requested for design purposes would suit the safety needs also. There is one area in which we have started new work because of a safety need, and others are welcome to join in. This is the remeasurement of the beta ray and gamma ray heating from fission products as a function of time after the fission. We find that present data are uncertain by up to 15% for a period of up to 1000 seconds after fission, and we need to reduce this uncertainty by a substantial factor. I feel we shall not have succeeded until several measurements exist, done by different methods.

It is a pleasure to be back among my friends at this meeting. I am sure it will be a very successful meeting.

THE LIGHT WATER REACTOR INDUSTRY-NUCLEAR DATA NEEDS

V. O. Uotinen, J. D. Robertson and J. S. Tulenko
Nuclear Power Generation Division
Babcock & Wilcox Company
Lynchburg, Virginia 24505

Introduction

Nuclear data play a fundamental role in the design of power reactors. Therefore, the light water reactor industry continues to have a keen interest in the activities going on in the acquisition, evaluation and reporting of nuclear data. A conference such as this provides a forum for experimenters, evaluators and users of nuclear data to discuss their work and to gain an insight into each other's current activities and needs.

A number of papers have been presented in the past which have addressed the impact of nuclear data uncertainties on the calculation of reactor parameters. In particular we would like to mention a series of papers[1,2,3], which presented results of calculational studies of the sensitivity of light water lattice parameters to experimental uncertainties in neutron cross sections. This approach led to rather large error estimates of $\pm 1.5\%$ for k_{eff} of tight UO_2 lattices, and $\pm 2\%$ for k_{eff} of tight UO_2-PuC_2 lattices.

A somewhat different view was taken in a paper[4] presented by French at the second conference of this series. His paper discussed the status of PWR design (as of 1968) and showed that the agreement achieved between calculated and measured parameters, using standard industrial calculational tools, was routinely much better than one would expect purely on the basis of quoted uncertainties in the basic cross section data. This is even more true today. The LWR industry has further refined its calculational tools in the intervening years, and is developing standards[5] (ANS-19) which will assure a high quality of reactor design calculations in the future.

In this paper we discuss the current state-of-the-art of core calculations. A discussion is presented of the role of basic cross section data in the overall design effort of LWRs. Illustrations are then given of current calculation-experiment comparisons for a number of reactor parameters. Finally, several areas are identified in which more accurate basic data can possibly further improve the accuracy of core calculations, and thereby improve the economic operation of LWRs.

The Role of Basic Data in the Design Effort

The physics behavior of a power reactor represents a highly complex, three-dimensional problem. The analysis is complicated by non-uniformities such as control rods, water gaps, burnable poisons, fuel assemblies of different enrichments, and thermal-hydraulic effects. An exact solution of the space-and-energy-dependent three-dimensional problem is not feasible. Thus, various simplifications are made to reduce both the spatial and energy detail. The spatial details of the problem are simplified by homogenization of regions of the reactor. The energy detail is simplified by condensation of the total energy range into just a few broad groups. These simplified methods, together with various other approximations and assumptions are used in conjunction with a library of basic cross section data. This combination of cross sections and approximate methods collectively form a calculational "package" which is used as the design "tool."

The goal of the reactor designer is to be able to use this tool to accurately predict the behavior of the reactor. Thus, the overall goal is to achieve reliable predictive capability. The reliability of the predictive capability can be tested by comparing calculated parameters with measured parameters.

As long as the reactor behavior can be predicted to within acceptable accuracies using a particular combination of cross sections and approximate models, there is no real incentive to change the cross sections, or any other aspect of the tool. It is only when the differences between predicted and actual parameters lead to unacceptably large conservatisms that one considers changes that could result in improving the predictions. (The criteria used to judge whether a conservatism is "unacceptably large" are mainly economic.) However, it is not always easy, and often it is essentially impossible to determine what portion of a discrepancy is attributable to the cross section data and what portion is attributable to theoretical methods and models. In any event, when looking for the best way to improve the accuracy of some given calculated reactors parameters, the reactor designer most often takes the pragmatic engineering approach of semi-empirical adjustments based on measured reactor parameters. From an engineering point of view, this is a perfectly valid and acceptable course of action. What happens then, in most practical situations, is that one's predictive capability is improved -- not by the use of more recently evaluated cross section data -- but by the application of semi-empirical adjustments to calculational models. This pragmatic, engineering approach is especially useful in that the adjusted tools can then be used with well-established confidence to predict the behavior of later, similar reactors. This becomes even more significant as the industry moves towards standardized plants.

Nevertheless, there certainly are areas that we can identify in which more accurate basic cross section data can lead to future improvements in our predictive capability. Some such areas will be discussed in later sections of the paper.

The Testing of Calculational Methods Using Critical Experiments

Critical experiments have provided data that have been useful in testing calculational tools. Two levels of complexity can be identified with regard to critical experiments: (1) critical experiments with uniform lattices of rods; and

(2) critical experiments with non-uniform lattices (which may contain several types of rod, or perturbations like water holes or control rods).

Uniform Lattices

Critical experiments with uniform lattices of rods in water provide useful data for the testing of any calculational tool used in nuclear design. The first goal in a typical methods verification effort is to demonstrate that the particular methods being tested can adequately predict the effective multiplication factor, k_{eff}, for a number of uniform critical assemblies. For example, the design model that is used at Babcock & Wilcox has been verified by calculating k_{eff} for 17 selected UO_2 critical experiments. These calculations resulted in an average value of 0.9983 ± 0.0047 for k_{eff}[6]. The quoted uncertainty corresponds to one standard deviation of a sample about the mean. In addition, 14 selected UO_2 - PuO_2 critical experiments have been calculated, resulting in an average k_{eff} of 1.0001 ± 0.0048.[6]

Non-Uniform Lattices

Lattices that contain non-uniformitites such as water holes, control rods, or several types of rods, form the next higher level of complexity. Examples of this type of experiment are provided by a series of large (more than 4950 rods) critical experiments[7] conducted by Babcock & Wilcox with full and part length poison pin clusters. Three poison pin clusters mocked up control rods in a typical PWR. Axial power distributions were measured on selected fuel rods within the core to provide a measure of the core power distribution in three dimensions. Results of three-dimensional diffusion theory calculations were compared with measured values.

The calculated average eigenvalue for 25 critical assemblies was 0.9977 with a standard deviation of 0.00095. Considering a total of 22,000 power data points in 26 cores, the average deviation between calculation and experiment is 3.66%, indicating a standard deviation of 4.57%. These points include many near the top, bottom, and periphery of the core, where diffusion theory loses accuracy near boundaries of dissimilar materials. The deviations at these locations are larger than average, but the power values are low and of less concern to the reactor designer. As far as the peak power is concerned, the average deviation in the 26 cores is 1.20%, and the standard deviation is 1.44%. Thus, the accuracy of the methods used by Babcock & Wilcox has been demonstrated quantitatively for these non-uniform critical experiments.

Babcock & Wilcox has also obtained a large amount of data from a series of non-uniform critical experiments which mocked up PWR mixed-oxide assemblies surrounded by UO_2 assemblies. A preliminary evaluation of these experiments indicates that k_{eff} and power peaking can be calculated with essentially the same degreee of accuracy in mixed-oxide assemblies as they are for UO_2 assemblies.

Current Predictive Capability in Power Reactors

The ultimate goal of the reactor designer is to be able to predict accurately the behavior of power reactors. Thus, the ultimate test of the usefulness of calculational tools is provided by comparisons with physics data obtained from operating power reactors. Illustrations of current predictive capability are given below, based on recent B&W experience.[8,9]

Consider the capability to predict the reactivity of reactor cores. An important indicator of reactivity is the boron concentration with the reactor critical with all control rods withdrawn from the core. The all rods out (ARO) critical boron concentration, along with inverse multiplication plots, provide early assurance that a particular core is performing as designed. The measured and calculated values of critical boron concentration shown in Table 1 are indicative of current capability with regard to prediction of initial PWR core reactivities. The calculated values are the reference values published in the startup testing reports prior to reactor operation. The largest difference between measured and calculated ARO critical boron concentration, 32 ppm, is equivalent to approximately 0.32% $\Delta k/k$.

Measured and calculated critical boron concentrations from throughout fuel cycle 1 of Duke Power Company's Oconee Unit 1 are compared in Figure 1. The comparison demonstrates the ability to accurately predict reactivity changes during the PWR fuel cycle.

Another parameter of importance in the operation of PWR's is control rod worth. Experience with control rod worth calculations at B&W has been, in general, good. Typical results obtained with our current best control rod calculated model are shown in Table 2. Values for rod groups 1, 2 and in one case, group 3, are not shown because of large uncertainties associated with the measured worths, which were obtained by "rod drop" techniques. The measured values shown were obtained using a "boron swap" method for which the uncertainty is $\pm 5\%$. Excellent agreement between measured and calculated rod worths was obtained at 250 and 400°F. The results at 532°F, while acceptable, indicate a slight bias in the calculational model. The control rod model utilized is based on zero power (70°F) critical experiments and is therefore semi-empirical. Small deviations at higher temperatures were therefore not unexpected. Refinements in the model are currently being developed in order to improve the rod worth calculations at higher temperatures.

The final reactor parameters which will be considered are the core power and burnup distributions. Again, experience at B&W has been quite good. The calculated maximum relative assembly powers have always been within 5% of the highest measured values and core burnup distributions have been within a few per cent of predicted values. Typical relative radial power distributions are shown in figures 2 and 3. Measured and calculated batch average burnup values for cycle 1 of Oconee Unit 1 are shown in Table 3.

Economic Incentives for Improving Predictive Capability

There are very real economic incentives for continually improving our predictive capability. This can be illustrated by looking at two areas, one of which relates to the ability to calculate core lifetime, and another which relates to the ability to predict power peaking.

Consider the monetary consequences of an uncertainty in the lifetime calculation. For a typical modern light water reactor, an uncertainty of 1% in neutron multiplication at the end of life requires a compensating enrichment adjustment of 0.15 wt% ^{235}U. This extra enrichment costs more than $2,000,000 at today's prices.

Additionally, the potential monetary consequences of an uncertainty in calculated power peaks can be equally large. Each 1% of uncertainty in power peaking that limits plant operation 1% in power costs the utility ~$1,000,000 or more annually in replacement power costs.

An example which illustrates the improvement in predictive capability in the industry over the past six or seven years, is provided by the critical boron concentration at beginning of life. As shown in Table 1, the maximum difference between measured and calculated values using current methods is 2.0%, and the average difference is 0.9%. By contrast, the situation as it stood in 1968 is illustrated by the values reported in Reference 4. There the maximum difference was 8.2% and the average difference was 4.7%. This kind of improvement allows unnecessarily large conservatisms to be reduced and results in reduced costs.

Areas of Basic Data Needs

In light of our experience, we discuss some areas of basic data in which we feel improvements can result in improved predictive capability. The items that are discussed are not new, for after all, the commercial light water reactor industry is twenty years old. The basic data needs of the industry today are essentially the same as they were five years ago, or even ten years ago. Nevertheless, it is beneficial to discuss them in light of the status of the industry in 1975. It is realized that all of these areas will be covered in more detail by other speakers at this conference.

Cross Sections of Heavy Isotopes

The continuing buildup of high-exposure plutonium inventories acts as an increasing incentive to have available to us more accurate cross section information for the higher plutonium isotopes and neptunium, americium and curium isotopes, which are produced in appreciable quantities in plutonium recycle. A self-generated recycle core contains about three times the amount of plutonium and about thirty times the amount of transplutonium elements contained in a uranium-fueled LWR.

In a uranium reactor these isotopes are present in relatively small quantities, and their effects can be accounted for adequately with present data. However, in the case of plutonium recycle one needs to be able to calculate their production more accurately because of their potential effects on the reprocessing and fabrication industries. Existing uncertainties in this area can lead to rather large uncertainties in estimates of the production and depletion of these heavy isotopes. Additionally, some of these isotopes have large absorption cross sections, and affect the reactivity significantly. Such uncertainties in the reactivity, as discussed in the preceeding section, have a significant impact on fuel costs. It is also important to be able to estimate the amount of these isotopes because of their potential use for other applications.

Thus, there is a need for good evaluated cross sections in both the thermal and epithermal energy ranges, especially for the isotopes ^{241}Pu, ^{242}Pu, ^{237}Np, ^{241}Am, ^{243}Am, ^{242}Cm and ^{244}Cm. There is also a continuing need for improved radioactive decay data for the heavy isotopes.

Fission Product Cross Sections

An error of 1% in the fission product cross sections results in an error of ~0.09% in the neutron multiplication. Such an error in neutron multiplication is equivalent to ~0.014 wt% in 235U enrichment, which is worth close to $200,000.

It was pointed out in Reference 5 that without any normalization of the fission product cross section, one would expect an uncertainty of about 3.5% in the final fission product cross section in a three-cycle core. Normalization of the fission product cross section at intermediate burnup values can reduce this uncertainty by as much as a factor of five. Nevertheless, there is a continuing need for improved cross section data for the fission products, which will allow us to refine our calculations of fission product poisoning. In particular one should emphasize those isotopes which are the major sources of uncertainty in the total fission product absorption, such as ^{131}Xe, ^{147}Pm, ^{148}Pm, (metastable state), and ^{148}Nd.

Fission Product Yields

In calculating the reactivity effects of fission products it is important to know their yields as well as their cross sections. Yield uncertainties also affect calculations of ^{135}Xe oscillations in large reactors, as well as the transient behavior of isotopes like ^{135}Xe, ^{105}Rh, ^{149}Sm, and ^{151}Sm following reactor shutdown.

In addition to their effects on reactivity and their effects on reactor dynamics, fission product yields are of growing importance in the experimental field of burnup monitoring. Gamma-spectrometric measurements of isotopes such as ^{135}Cs, ^{134}Cs, ^{144}Ce, ^{144}Pr, ^{106}Ru, ^{106}Rh, ^{95}Zr and ^{95}Nb have been used to determine the burnup of irradiated fuel rods. The reliability of such measurements depends on the accuracy of the basic data used to interpret the results. Improved accuracies in basic data can lead to improved accuracy in experimental burnup determinations, which in turn can lead to better evaluations of theory-experiment discrepancy in this area.

There is a continuing need for improved data concerning fission product yields in general. Of particular importance we would point out the yields from ^{239}Pu and ^{241}Pu thermal fissions, where the existing uncertainties seem to be appreciably larger than those for ^{235}U.

Fission Product Decay Data

Fission product radioactive decay data are of primary importance for estimating the decay heat following a potential loss-of-coolant accident in a LWR. There is widespread agreement that more and better data are needed, particularly for times <100 sec after shutdown, so that current large conservatisms can be reduced on the basis of more accurate data. The USAEC, through the Cross Section Evaluation Working Group, has sponsored the generation of a library of radioactive decay data.[10,11] It is intended that

these data will be included in ENDF/B-version IV. The American Nuclear Society has generated a proposed standard on decay energy release rates following a shutdown of uranium fuel thermal reactors. The light water reactor industry should welcome and encourage activity in this area.

Improved decay data are of importance also in the application of gamma-spectrometry to acquire burnup information on irradiated fuels. Accurate decay data, as well as accurate yield data, are needed to assure accurate burnup information by this method.

Shapes of Cross Section Curves

It was pointed out a number of years ago[2] that the shapes of the ^{239}Pu thermal cross section curves affect calculated temperature coefficients significantly. In reference 1 it was shown that the calculated temperature coefficient of a plutonium critical assembly changed by 20% between two cases in which two separate evaluated cross section shapes were used. The need to evaluate the shapes, as well as the 2200 m/s values of fissile isotopes was pointed out. Publication of the results of this kind of an evaluation would be a useful contribution to the industry.

Conclusion

The light water reactor industry has improved its predictive capability through experience gained over the past twenty years. Nevertheless, basic nuclear data continue to play a fundamental role in the design effort. We encourage the experimenters to continue to measure basic data, especially in the areas that we have discussed. Likewise, we encourage the evaluators to continue to evaluate the new data that are produced. We need their constructive criticism applied in this area to differentiate between good and bad data. And finally, we encourage the compilers to continue to compile and make available to the LWR community, data compilations that reflect the latest and best knowledge of the basic nuclear data. As this is done, we can expect to continue to make progress in our ability to predict the performance of light water power reactors.

Acknowledgment

We gratefully acknowledge the significant contributions made by H. A. Hassan, W. A. Wittkopf, W. T. Brunson, J. J. Woods, and many others.

References

1. U. P. Jenquin, V. O. Uotinen and C. M. Heeb, Proc. of Conf. on Neutron Cross Sections and Technology, p. 273, National Bureau of Standards, Washington, D.C., (1968).

2. F. G. Dawson, D. E. Deonigi, R. C. Liikala and U. P. Jenquin, Plutonium as a Reactor Fuel, Proc. of Conf., p. 3, IAEA, Vienna (1967).

3. R. C. Liikala, V. O. Uotinen and U. P. Jenquin, Nucl. Technol., 15, 272 (1972).

4. R. J. French, Proc. of Conf. on Neutron Cross Sections and Technology, p. 259, National Bureau of Standards, Washington, D.C. (1968).

5. P. Greebler, Trans. Am. Nucl. Soc., 19, 387 (1974).

6. J. M. Tilford and H. A. Hassan, "Verification of LIFET Nuclear Design Model," BAW-382, Babcock & Wilcox, Lynchburg, Va., June, 1970.

7. H. A. Hassan and W. A. Wittkopf, "Three-Dimensional Power Distribution Analysis," NPGD-TM-198, Babcock & Wilcox, Lynchburg, Va., November, 1972.

8. J. D. Robertson, Trans. Am. Nucl. Soc., 19, 219, October, 1974.

9. W. Morris Sample and J. J. Woods, to be published in Transactions of American Nuclear Society, June, 1975.

10. C. W. Reich and R. G. Helmer, Proc. of Conf. on Nuclear Cross Sections and Technology, National Bureau of Standards, Washington, D.C. (1975).

11. R. E. Schenter and F. Schmittroth, Proc. of Conf. on Nuclear Cross Sections and Technology, National Bureau of Standards, Washington, D.C. (1975).

Table I

Initial All Rods Out Critical Boron Concentrations, ppm.

Unit	Temp.°F	Meas.	Calc.	Meas.-Calc.
Oconee I	250	1329	1334	-5
	400	1403	1378	25
	532	1476	1477	-1
Oconee II	300	1555	1571	-16
	532	1630	1634	-4
Oconee III	532	1570	1582	-12
Three Mile Island I	532	1617	1634	-17
Arkansas Nuclear One	532	1602	1634	-32
Rancho Seco	300	1493	1506	-13
	532	1553	1566	-13

Table II

Control Rod Worths at Zero Power

CR Group	Temp. °F	Worth,%Δk/k Meas.	Calc.	% Difference
3	250	2.28	2.27	0.4
4	250	.52	.52	0.0
5	250	.63	.63	0.0
6	250	.74	.73	1.4
7	250	.87	.86	1.1
		5.04	5.01	0.6
4	400	.58	.58	0.0
5	400	.67	.67	0.0
6	400	.83	.82	1.2
7	400	.96	.97	-1.0
		3.04	3.04	0.0
3	532	2.60	2.73	-5.0
4	532	.62	.67	-8.1
5	532	.68	.72	-5.9
6	532	.93	.96	-3.2
7	532	1.09	1.10	-0.9
		5.92	6.18	-4.4

Table III

Burnup at 310 EFPD, MWD/MTU
(Oconee Unit I, Cycle 1)

Batch	Measured	Calculated	% Difference
1	11,560	11,783	-1.9
2	11,377	11,417	-0.35
3	7,312	7,176	1.9

FIGURE 1

OCONEE 1, CYCLE 1

CRITICAL BORON CONCENTRATION

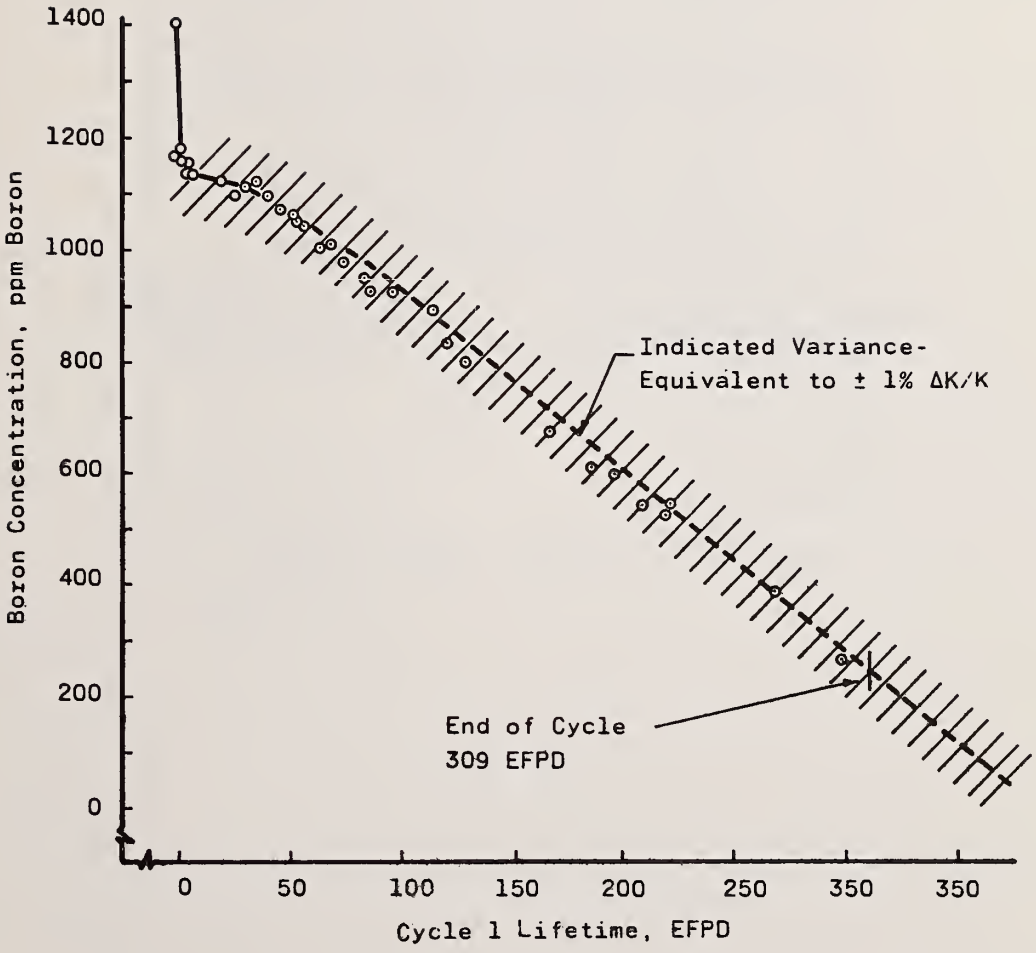

FIGURE 2

OCONEE 1, CYCLE 1

RELATIVE RADIAL POWER DISTRIBUTION

(48.4 EFPD)

	8	9	10	11	12	13	14	15
N	1.46 1.42	1.42 1.40	1.38 1.41	1.52 1.47	1.52 1.49	1.40 1.41	1.13 1.06 (6)	.66 .60
O		1.24 1.28 (6)	1.33 1.26	1.37 1.37	1.35 1.44	1.36 1.35	1.05 1.08	.59 .58
P			.79 .77 (7)	1.20 1.20	1.18 1.19 (8)	1.18 1.17	.89 .91	.43 .42
R				1.14 1.15	1.07 1.03	.94 .93	* .62	
					.56 .54 (7)	.66 .61	.36 .35	
						.35 .34 (n)		

MEASURED (OLC)

CORE FOLLOW CALCULATION

CONTROL ROD GROUP

* MEASURED VALUE NOT AVAILABLE - INOPERATIVE DETECTOR

FIGURE 3

OCONEE 1, CYCLE 1

RELATIVE RADIAL POWER DISTRIBUTION

(200 EFPD)

	8	9	10	11	12	13	14	16
	1.20 1.16	1.10 1.06	.75 .76 (7)	1.20 1.13	1.30 1.25	1.23 1.27	1.16 1.12 (6)	.74 .70
		1.11 1.09 (6)	1.17 1.12	1.22 1.21	1.19 1.26	1.28 1.24	1.07 1.09	.68 .67
			1.33 1.30	1.33 1.32	1.22 1.18 (8)	1.21 1.16	.96 .96	.49 .51
				1.28 1.35	1.17 1.14	1.04 1.04	* .73	
N					.72 .73 (7)	.80 .77	.47 .46	
O						.48 .48 (n)	MEASURED (OLC) CORE FOLLOW CALCULATION	
P							CONTROL ROD GROUP	
R								

* INOPERATIVE DETECTOR

RADIOACTIVE-NUCLIDE DECAY DATA IN SCIENCE AND TECHNOLOGY†

C. W. Reich and R. G. Helmer
Idaho National Engineering Laboratory
Aerojet Nuclear Company
Idaho Falls, Idaho 83401

The scope of ENDF/B has recently been expanded to include radioactive-nuclide decay data. In this paper, the content and organization of the decay data which are included in ENDF/B are presented and discussed. The application of decay data in a wide variety of nuclear-related activities is illustrated by a number of examples. Two items pointed up by the ENDF/B decay-data compilation effort are treated: the identification of deficiencies in the data; and the importance of a radioactive-nuclide metrology effort oriented toward supplying these needs in a systematic fashion.

(ENDF/B-IV decay-data file; applications of decay data)

Introduction

Historically, the study of the radiation emitted in the decay of radioactive nuclei has been a highly productive source of important information in many basic scientific disciplines as well as in many areas of applied technology. In basic nuclear physics, for example, such studies have provided much of the experimental basis for our present understanding of the nucleus, as embodied in current models of nuclear structure. In their impact in other areas, radioactive-nuclide decay data are directly relevant to and of vital importance in a wider range of disciplines and areas of applied technology than is perhaps any other category of nuclear data.

Major advances in the study and application of the decay of radioactive nuclides have been made in the past 5-10 years as the result of a number of developments. In the area of data acquisition and analysis, the impact of the Ge(Li) γ-ray detector has been especially significant. With its excellent energy-resolution characteristics, it has provided great improvements in the quality of γ-ray spectral data over that which was previously available from NaI(Tl) scintillation spectrometers. The potential of these solid-state devices as radiation detectors has been enhanced as a result of developments which have taken place in the associated low-noise electronic circuitry and multichannel pulse-height analyzers as well as in the use of computer-based systems for data acquisition and analysis.[1] Another facet of the effort related to these detectors is the large amount of work which has been directed toward making them capable of intensity and energy measurements of high precision. At present, for example, γ-ray intensity measurements with a precision of $\sim$ 1-2% have been reported for some cases, and γ-ray energy values suitable for use as energy-calibration standards have been measured with precisions of a few tens of eV at $\sim$ 1 MeV.

Improvements in the capabilities of particle accelerators have also had a significant impact on the field of radioactive-nuclide decay studies. The increasing energies and intensities of the particle beams which can be obtained from these machines, together with the increasingly wide range of nuclei (e.g., heavy ions) which are being used as projectiles, provide an ever expanding number of radioactive nuclides which can be produced for detailed study. The continuing development of techniques for fast radiochemical separations and the increasing use of isotope separators to produce samples of high chemical and isotopic purity have materially increased the wealth of detail which can be extracted from the experiments. The development which represents perhaps the most significant tool for future work in this field is the use of isotope separators "on-line" at accelerators and nuclear reactors. This combination makes feasible the extension of the conventional techniques for studying decay schemes to nuclides whose half-lives are as short as 1 sec or so. This capability constitutes a significant extension of the "off-line" studies, which were effectively limited to the half-life range $\gtrsim$ 1 h. The importance of this technique in basic nuclear-physics studies has been discussed at a number of international conferences.[2-4] Of particular relevance to the subject matter of this conference is the fact that, through the use of "on-line" isotope separation, a varied and ever increasing body of decay data on the short-lived fission products is being generated.

The use of radioactivity is continuing to increase in a number of areas such as, e.g., nuclear medicine, industrial applications and all aspects of the nuclear industry. This has necessitated development of techniques for isotopic analysis and a more detailed characterization of the radiation emitted by radioactive nuclides. There presently exists a large and varied "community" of radioactive-nuclide users, with a number of different requirements for nuclear decay data. This has created a need for re-examining the status of decay data in the light of the needs of these users. Involved in this re-examination are not only the quality of the data and how they are to be used but also improved access to these data and the necessity for having them available in a form useful for special needs.

Nuclear Data Derived from Radioactive-Decay Studies

The category of "Nuclear-Decay Data" is a broad one and is perhaps most simply discussed by reference to a specific case. As an example, in Fig. 1 we show the decay scheme of ^{144}Ce, as given in Ref. 5.

Two types of properties are present in this decay scheme. The first are those associated with the energy levels and include the following: atomic number (Z); mass number (A); mass; half-life; energy (for excited states); total angular momentum (spin); parity; and one or more static electromagnetic moments (and, for excited states, a number of transition moments, too). The second are those associated with the radiations which represent transitions between the individual levels and include the following: the radiation type (e.g., β, γ); energy; intensity; and total angular momentum and parity (multipolarity). It is generally the properties of the radiations rather than those of the levels that are of interest in the applications of decay data, the level-related data being of interest primarily in nuclear

†Work performed under the auspices of the Energy Research and Development Administration.

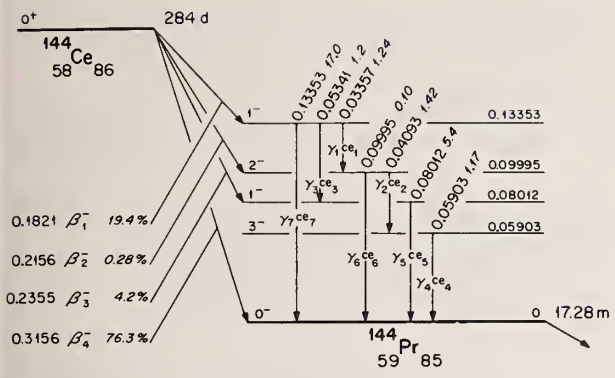

Fig. 1. Decay scheme of ^{144}Ce.

structure research. However, it should be emphasized that the level properties, where known, should be available to the compiler of a file of decay data for specialized applications. Such information may be necessary for the determination of radiation properties which have not been directly measured or for the estimation of errors.

The half-life is a level property of great importance, since it determines the fractional number of atoms of a given isotope which decay per unit time. As such, a knowledge of its value is required in any quantitative measurement of the radiations emitted by a radioisotope to determine the number of atoms present in a given sample. It is also needed in making decay corrections to data acquired at different times from a radioactive sample. The atomic masses of the parent and daughter ground states are of interest in some applications of decay data (e.g., decay heat) by virtue of the fact that the energy equivalent of their difference is the total energy available (Q value) for the decay process (β^- in Fig. 1).

The radiations emitted as the radioactive nucleus decays exhibit an energy and intensity pattern which is unique to, and characteristic of, that nucleus. For β^- (and β^+) decay, the individual transitions possess a continuous distribution of energies, ranging from zero up to a maximum value (the "endpoint" energy) which is the total energy available to that transition. This fact, and the experimental difficulties associated with β-ray spectroscopy, make the β radiation of little use as a tool for nuclide identification. However, a knowledge of the β energy distribution is important in a number of applications, e.g., decay heat and absorbed-dose estimates in biomedical studies. In α decay, on the other hand, the spectrum of emitted particles consists of discrete lines and is a useful tool in nuclide identification. One application of such information lies in the area of nuclear fuel safeguards, where the identification and quantitative assay of actinide isotopes associated with the nuclear fuel cycle is recognized as a critical problem.

The daughter nucleus formed in the decay of the radioactive parent is generally left in one of a number of excited states. These states generally decay via γ-ray emission (or the competing process of internal-conversion electron emission) to lower-lying states of the same nucleus. As is the case for the radiations emitted directly in the decay of a radioactive nucleus, the spectrum (i.e., energies and relative intensities) of γ radiation is uniquely characteristic of a given nuclide. This fact, and the relative ease with which γ-ray spectra can be measured using modern techniques, make the knowledge of the γ-ray spectrum one of the most powerful tools presently available for radioactive-nuclide identification. Of major importance in the applications of radioactivity are the branching ratios (the number of γ rays emitted per 100 decays) of the various γ rays. These data, together with the nuclide half-life, are essential quantities in all applications where the quantitative assay of radioactivity is required. Since both qualitative and quantitative radionuclide assay utilizing γ-ray spectroscopy are widely employed in many applications involving radioactivity, γ-ray data constitute a particularly important category of decay data.

The spectrum of internal-conversion electrons associated with a particular γ-ray transition is rather complicated and more difficult to determine experimentally than is the γ-ray spectrum. However, if the multipolarity of the γ-ray transition is known, this spectrum can be calculated with good accuracy in almost all cases using the theoretical internal-conversion coefficients.[6] Following the ejection of a conversion electron, x radiation and a rather complicated spectrum of low-energy secondary (Auger) electrons are emitted. A knowledge of these quantities is important in such applications as internal radiation-dose estimation, where not only the total released energy but also the form in which it appears is required. Where the contributions of these processes to the complete energy characterization are not measured (and this represents the majority of such cases), they can be calculated theoretically with sufficient realism to be adequate for most applications.

Under certain conditions, particle emission can take place from excited states of the daughter nucleus. A particularly important special case of such "delayed-particle" emission is delayed-neutron emission. As a result of the development of improved neutron counters[7] and the availability of isotope-separated samples for "on-line" study, delayed-neutron energy spectra, measured with good resolution, of a number of fission-product nuclides have recently begun to appear in the literature.[8]

In Table I, we list some of the quantities more commonly measured in radioactive-decay studies and indicate their relevance in several broad areas of application.

Nuclear Data for Summation Calculations of Decay Heat

The summation calculation of the fission-product decay-heat source term represents one important application of decay data. Because of its relevance to the subsequent discussion, we now present a brief description of this calculational procedure. More complete discussions are given in, e.g., Refs. 9-11 as well as in the following papers.[12,13] The summation approach to the decay-heat calculation involves first predicting the fission-product inventory of a reactor core at a given time. This involves an assumption of a power and operating history for the reactor as well as a knowledge of the direct fission yields, capture cross sections and half-lives of the individual fission products and nuclides produced by neutron capture. From this inventory, the energy release per fission as a function of time can be calculated for all times following shutdown by summing the contributions of the individual nuclides. To do this requires, for each isotopic species present, values of the half-life, the average β energy per decay, $\langle E_\beta \rangle$ and the average γ energy emitted per decay, $\langle E_\gamma \rangle$.

TABLE I

Several categories of decay data and areas of their application

Measured Quantity	End Use: Decay Heat	Nuclide Identification	Quantitative Nuclide Assay	Biomedical and Tracer	Basic Nuclear Physics
Half-life	X	X	X	X	X
γ-ray energy	X	X	X	X	X
γ-ray relative intensity		X	X	X	X
γ-ray branching ratio	X		X	X	
x-ray intensity	X			X	
electron energy	X			X	X
electron relative intensity				X	X
electron absolute intensity	X				
β-ray energy	X			X	X
β-ray relative intensity				X	X
β-ray branching ratio	X				
α-particle energy	X	X	X	X	X
α-particle relative intensity		X		X	X
α-particle branching ratio	X		X	X	
Q-value	X				X
level energy					X
level spin and parity					X

Nuclide-Decay Data for ENDF/B: An Example of a User-Oriented Special-Purpose Data File

In recognition of the pressing need for radioactive-nuclide decay data in a variety of reactor-related applications, a decision was made about two years ago to expand the scope of the Evaluated Nuclear Data File (ENDF/B) to include such information. The impetus for this was provided by the need for a reliable and common data base to be used in summation calculations of the decay-heat source term in power reactors. Our involvement in this expansion of ENDF/B has been twofold: (1) to establish the categories of decay data to be included in ENDF/B and to set up a framework within which they could be prepared; and (2) to evaluate the experimental data and prepare a file of such data for a number of nuclides. There were primarily fission products of priority interest for the decay-heat problem.

The Experimental Decay-Data File for ENDF/B

As seen above, a decay-data file adequate for the needs of the decay-heat problem could be set up with a quite modest data content (i.e., $T_{\frac{1}{2}}$, $\langle E_\beta \rangle$ and $\langle E_\gamma \rangle$) and a relatively simple format. However, in view of the importance of decay data for many reactor-related problems, it was felt that a file of decay data for ENDF/B should have sufficient content to adequately address the needs of several types of users. Thus it was decided at the outset to set up a data file of much broader scope than what would be required for the decay-heat problem alone. Since the content and format established for this file has been discussed in detail elsewhere[14], only a brief treatment of them is given here.

A sample case, the decay data for ^{144}Ce is illustrated in Table II. It should be pointed out that, in ENDF/B, these data are given in File 1, MT=457 under the standard ENDF/B conventions (e.g., energies in eV, half-lives in sec , etc.). Consequently, their appearance there differs somewhat from that of Table II, where they are given in the "people-readable" card-image format in which we prepare them. A computer program[15] (FIPP) has been written to carry out the translation to the ENDF/B format.

As indicated in Table II, each data set is headed by the Z and A value of the parent. In the following column an integer "isomer flag" is given. A zero indicates that the nuclide is in its ground state, a 1 indicates that the data are for the decay of the first excited isomeric state, a 2 indicates the decay of the second excited isomeric state, etc. (Isomers are arbitrarily restricted to nuclear states with half-lives $\geq$ 0.1 sec.) Following this first card is a group of cards giving any desired comments, such as the references for the data and how they have been treated.

The rest of the set is composed of data cards. The first contains the half-life together with its uncertainty and units, the number of decay modes of this nuclide and the number of "energy spectra" to be listed. This is followed by one card for each decay mode giving the following information: the type of radiation emitted in the decay of the parent state (e.g., a 1 indicates β^- emission); which final-nucleus isomeric state is fed (a 0 indicates population of the ground-state, a 1 indicates population of the first excited isomeric state, etc.); and the Q value and its uncertainty; and the branching ratio (in percent) for this decay mode and its uncertainty. With the feeding of the daughter-nucleus ground and isomeric states treated in this way, the series of daughter nuclides produced from a given parent isotope can be kept track of. Also, it should be noted that the decay data related to the daughter-nucleus isomeric state are not contained under the parent. They are given under a file entry for the isomeric state. In the present example, the 59-keV state in ^{144}Pr (see Fig. 1) is isomeric ($T_{\frac{1}{2}}$ = 7.2 min). Consequently, the 59-keV

Table II. Decay data for ^{144}Ce prepared in our laboratory-file format (prior to translation to the ENDF/B format).

Z	A	IS	Number of Comment Cards
581440	CE		8

Documentation and Comments

PREPARED FOR FILE: 7/74 CWR
REFERENCES: Q- 1973 REVISION OF WAPSTRA-GOVE MASS TABLE.
HALF-LIFE - N.E. HOLDEN, CHART OF THE NUCLIDES(1973); AND PRIVATE COMMUNICATION (SEPT.,1973).
OTHER- M.J. MARTIN AND P.H. BLICHERT-TOFT, NUCLEAR DATA TABLES A 8, NOS.1-2, (1970). J.L. FASCHING, W.B. WALTERS AND C.D. CORYELL, PHYS. REV. C 1, 1126 (1970).

Half-Life	Δ	Units	Number of Decay Modes	No. of Spectra
284.4	0.2	D	2	2

Decay Mode	Final State	Q	ΔQ	Branching
1	0	315.5	1.5	98.8
1	1	256.5	1.5	1.2

⟨E-Beta⟩	Δ	⟨E-Gamma⟩	Δ
82.96		28.87	

Normalization	Δ	Number of Transitions	Radiation Type
1.0		4	1

E	ΔE	I	ΔI
182.1	1.5	19.4	0.7
215.6	1.5	0.28	0.1
235.5	1.5	4.2	0.3
315.6	1.5	76.3	0.7

Normalization	Δ	Number of Transitions	Radiation Type
1.0		6	0

E	ΔE	I	ΔI	ICC	ΔICC
33.57	0.03	0.22	0.02	4.6	0.7
40.93	0.03	0.39	0.03	2.6	0.4
53.41	0.05	0.14	0.02	7.7	1.6
80.12	0.03	1.54	0.15	2.52	0.27
99.95	0.05	0.038	0.004	1.6	0.3
133.53	0.03	10.8	0.5	0.58	0.04

γ ray observed in the ^{144}Ce γ-ray spectrum is listed not in the ^{144}Ce data set but rather in the data set for ^{144m}Pr (identified as 591441).

Following the decay-mode cards is a card giving the average energy per decay for the different radiation types. Entered, sequentially, are the average β energy $\langle E_\beta \rangle$, its uncertainty, $\langle E_\gamma \rangle$, its uncertainty, $\langle E_\alpha \rangle$ and its uncertainty.

Next in the data set come the listings of the various radiation spectra. In the example there are two such spectra: β^-, denoted by the radiation-type 1, and γ, denoted by the radiation type 0. For each spectrum listed, two card types are present. The first is a single card which gives: a normalization factor, which provides a conversion from relative intensities to absolute intensities for the listed intensity data; its uncertainty; the number of transition energies; and a number denoting the type of radiation. The spectral data follow, with one card for each transition. These latter cards give: transition energy (keV) and its uncertainty; and the (relative) intensity and its uncertainty. For γ radiation, the fifth and sixth fields include the total internal-conversion coefficient and its uncertainty. The separation of relative and absolute intensities in this manner is done for the following reason. For γ radiation, it is the relative values that are customarily obtained from spectral measurements. The conversion of these to absolute intensities (i.e., photons per 100 disintegrations) is usually made from considerations of the specific decay scheme involved or from a separate measurement, this involving its own uncertainty. It is thus possible to treat the two measurement errors separately; and, if the basis for the absolute-intensity data should subsequently change, this can be taken into account simply by a single change in the normalization. For example, in the ^{144}Ce decay scheme shown in Fig. 1 the absolute γ-ray intensities are based upon a value of $\approx$ 76% for the ground-state β branch. Should this value eventually be found to be incorrect, these absolute intensities will have to be changed. The relative intensities, however, would remain unaffected.

In addition to β^- decay given in the example shown in Table II, the file is set up to include the following decay modes: electron capture and/or β^+; isomeric transition; α particle; delayed neutron; and spontaneous fission.

Status of Decay Data on ENDF/B-IV. The status of the nuclide-decay data on ENDF/B-IV, as of March 1974, and the relation of the various aspects of the data-preparation process are illustrated in Fig. 2.

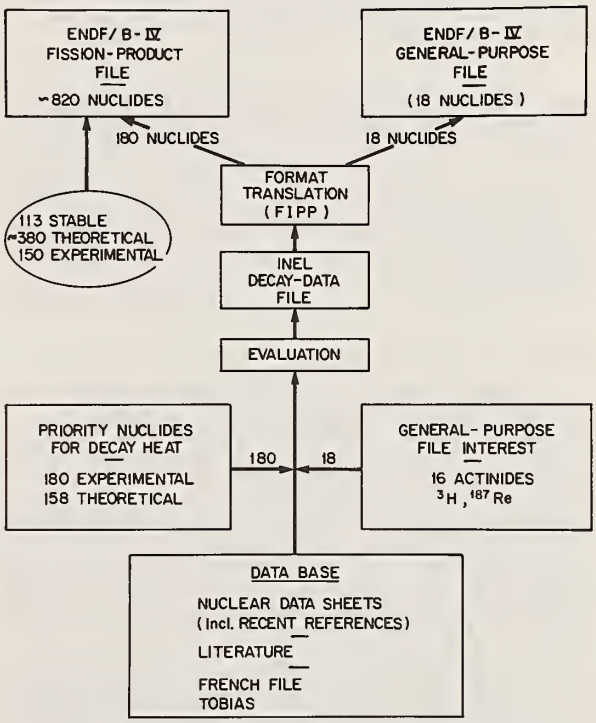

Fig. 2. Relation of the decay-data compilation effort to the present status of decay data on ENDF/B-IV.

The ENDF/B-IV Fission-Product File contains entries for ~ 820 nuclides, in mass chains ranging from A=72 through A=167. These are believed to constitute a sufficient data base for decay-heat calculations for decay times $\gtrsim$ 1 sec. Of these, 113 are stable ($T_{1/2} > 10^{10}$ y). Of the remaining ~ 710, the present experimental data are sufficiently complete to permit $\langle E_\beta \rangle$ and $\langle E_\gamma \rangle$ values to be extracted for only ~ 330 nuclides. For the remaining ~ 380, most all of which are short-lived, the $\langle E_\beta \rangle$ and $\langle E_\gamma \rangle$ values (and in some cases the half-lives as well) must be inferred from theoretical considerations[12] in order that their contribution to the decay heat can be taken into account.

In the Version-IV Fission-Product File data sets similar to that shown in Table II above have been prepared for 180 nuclides. These are the ones of primary[12] importance in the decay-heat problem for which decay-data exist. This data-compilation effort was helped considerably by the availability of other compilations of Fission-Product decay data[16,17], particularly that of the French groups. The entries for the remaining ∿ 150 experimentally studied fission products as well as for the ∿ 380 "theoretical" cases (this number includes the 158 "priority" nuclides shown in Fig. 2) are restricted to only the quantities needed for the decay-heat calculations; their $\langle E_\beta \rangle$ and $\langle E_\gamma \rangle$ values are derived from theoretical considerations.[12]

Data on 18 additional isotopes, mainly actinides, were also prepared as illustrated in Table II. These are included in the Version-IV General-Purpose File of ENDF/B.

Future Work. At the present time, the format and data content of the file are being expanded to include spin and parity values for the nuclides and to allow a more detailed treatment of x-ray and discrete-electron energy spectra. Also included will be a more unified and consistent approach to the incorporation of delayed-particle emission, of which delayed-neutron energy spectra are an important component.

In addition, decay data are being prepared for the remaining ∿ 150 "experimental" fission-product nuclides and for nuclides important in other applied areas. Examples of such areas include: fast-reactor dosimetry and reaction-rate determinations; decay heating from structural, control and fuel materials in fast-reactor systems; activation products important for determination of integral capture cross sections of fission-product nuclides; and environmental monitoring of effluents from nuclear-power facilities and determination of radioactivity source terms for safety analyses.

Specialized Data Files

The data content of the file described above, while much larger than required for the decay-heat problem, is nonetheless much more restricted than those of such broadly based data compilations as the Table of Isotopes[18] or the Nuclear Data Sheets[19]. This file treats only a specialized subset of the broader category of "decay data", a subset oriented toward certain areas of application. It thus represents a specialized data compilation. It also possesses another characteristic important for such a compilation, namely the data it contains are reduced to and presented in a form convenient for their intended use.

The need for specialized compilations of nuclear data has long been recognized. Numerous examples of such compilations in nuclear physics are contained in the journal Nuclear Data Tables.[20] Compilations of γ rays ordered by energy, nuclide and half-life are quite useful in applications involving γ-ray spectral analysis and isotopic identification; and a number of such tables exist.[21,22] In the fields of nuclear medicine and health physics, the decay-data requirements for internal-dose estimates have led to the so-called MIRD documents[23] as well as other compilations[5] providing such information. As the uses of radioactivity expand and the volume of data accumulates, it appears that the need for specialized data compilations (such as the present one) will increase.

Comments on the Current Status of Decay Data

In view of the effort which has been expended over the years in decay-scheme studies, it is natural to ask whether or not more such studies are in fact needed and whether the present base of decay data is adequate. This question cannot be considered meaningfully without a careful consideration of the uses for which the data are needed. We briefly treat two facets of the problem of the adequacy of the current base of decay data, namely the lack of certain information and the precision of already existing data.

Lack of Data

One obvious example of a gap in the present decay data is provided by nuclides for which few if any decay data exist. The bulk of such cases are the neutron-rich and neutron-deficient nuclides far off the line of stability. This lack of data is quite evident in the ENDF/B-IV decay-data file. As noted above, data on over half of the fission-product nuclides in this data file were sufficiently lacking that theoretical estimates rather than experimental data had to be used for their $\langle E_\beta \rangle$ and $\langle E_\gamma \rangle$ values. And, in some cases, even the half-lives were not available. Generally these nuclides are the shorter-lived fission products, whose major contribution to the decay-heat source term occurs at short times.

In this connection, it appears that rather specialized basic nuclear-physics measurements may have a direct application to this problem and provide $\langle E_\beta \rangle$ and $\langle E_\gamma \rangle$ values for some of these nuclei. Measurements of the β-strength functions of ≈ 90 fission-product nuclides with half-lives in the range from ∿ 1 to ∿ 200 sec have been carried out at the OSIRIS facility in Sweden[24,25]. These measurements provide information about the average β feeding per unit energy in the decay of these nuclides and hence provide a means of extracting $\langle E_\beta \rangle$ values. From the relation

$$Q_\beta = \langle E_\beta \rangle + \langle E_\nu \rangle + \langle E_\gamma \rangle ,$$

where $\langle E_\nu \rangle$ is the average (anti)neutrino energy per decay and is closely related to $\langle E_\beta \rangle$, it should be possible to obtain realistic values for $\langle E_\gamma \rangle$. Although somewhat over half of the nuclides investigated in these studies are already included in our data file, 43 of them represent cases for which only theoretical estimates of the $\langle E_\beta \rangle$ and $\langle E_\gamma \rangle$ values are presently available. Although these β-strength-function studies provide no detailed information about the discrete components of either the β- or the γ-ray spectrum and hence may not be relevant to many applications, they do appear to provide data specifically required by the decay-heat problem. This situation is also an illustration of the frequent need for compilers of files to consider data outside the specific file content in order to obtain values for certain of the file data.

Less obvious, but no less important, are cases where an otherwise large body of data on a given nuclide cannot be used because of a lack of certain information. A frequently occurring example of such data is provided by the γ -ray branching ratios. In the preparation of decay data for inclusion in the ENDF/B file, it was necessary to exclude data on roughly ten nuclides for which extensive spectral data were reported and for which rather detailed decay schemes had been proposed. This was done because no γ-ray branching ratio data were measured and hence no values for $\langle E_\beta \rangle$ and $\langle E_\gamma \rangle$ could be obtained.

The Question of Precision. In the use of decay data in specific areas, an important consideration is the precision of the data required in a given application. This question cannot be treated in general but must be evaluated for each specific case. Since nuclide half-life and γ-ray branching ratio data are required in all applications involving quantitative assay of

radioactivity using γ-ray spectroscopy, these two types of decay data warrant special attention. The range of reactor-related problems in which such assay is used is quite large, including, e.g., dosimetry, nondestructive assay, activation-analysis techniques for integral cross-section determinations[26], effluent monitoring, nuclear fuel safeguards and radioactive waste management.

The precision of the present half-life data appears adequate for most applications related to quantitative radionuclide assay. However, in the area of nuclear fuel safeguards and accountability, assay for actinide elements is frequently carried out using calorimetric measurements or absolute α counting. The interpretation of these data to provide nuclide assay with the necessary precision requires highly accurate half-life values (∿ 0.1%) in some cases. These requirements may in some instances lie beyond the capabilities of the present data. A specific instance of a lack of adequate precision in γ-ray branching-ratio data is given in a paper contributed to this conference.[27] In the determination of absolute reaction rates in "standard" neutron spectra with high precision (the ILRR program), absolute γ-ray counting of activation products in various irradiated foils was carried out. There it was found[27] that, while absolute γ-ray branching-ratio data existed for all the reaction products of interest, in a few cases the data did not possess the required precision of ±2½%.

The reasons why the absolute γ-ray branching ratio data are of such uneven quality are not difficult to understand. To make such measurements with high precision is generally a difficult and time-consuming task, requiring special instrumentation and techniques. Furthermore, a knowledge of these values frequently contributes very little to the basic-physics information which is obtained from the study of a decay scheme. As a result, few basic-physics investigations attempt to measure these quantities, a situation which is sometimes abetted by a lack of realization by the experimenter of the real value of such data to the applied user. Because of this unfortunate situation, it appears most appropriate to mount an effort to measure such data in a systematic fashion. This could be done as one aspect of a broadly scoped program of radioactive-nuclide metrology.

Conclusion

The field of radioactive-nuclide data is one with particular relevance for both basic nuclear physics and for other research as well. At present, it is characterized by a large and steadily increasing base of data. Effective use of this data base is being made by individuals and groups active in nuclear physics and related activities such as radiochemistry, who by and large are also its producers. However, improvements in its utilization by workers in other basic and applied scientific disciplines need to be made. Because of the expansion of the scope of ENDF/B to include decay data, it appears that this evaluated subset of these data will become available to an important group of users. The wide acceptance and use of ENDF/B as a source of nuclear data by the nuclear-power industry and its associated reactor research and development activities makes ENDF/B the logical mechanism for providing a commonly available base of evaluated decay data. The data content presented above was chosen with the eventuality in mind that all segments of the nuclear program, including the regulatory (e.g., effluent monitoring and reporting) and fuel-safeguards functions, as well as the CTR programs, would have access to a common base of evaluated, relevant decay data. Because of the international role of ENDF/B, this addition to its scope has had impact in international nuclear-data activities as well. It is most encouraging to observe the increasing international awareness of the importance of decay data, as evidenced by the results of the recent IAEA Fission Product Nuclear Data Panel Meeting[28], and to note the generally favorable reception of the ENDF/B decay-data content and format internationally.

In order to make more effective utilization of decay data in other areas, attention must be given to increasing the interaction between the users, producers and compilers of such data. It should be pointed out that a similar problem existed within the field of neutron cross-section data; and to solve it a fairly close, formal relation was set up between these three segments of the data effort. We can envision a similar pattern operating effectively within other areas of "nuclear data" as well. An example of one possible mechanism for accomplishing this is shown in Fig. 3.

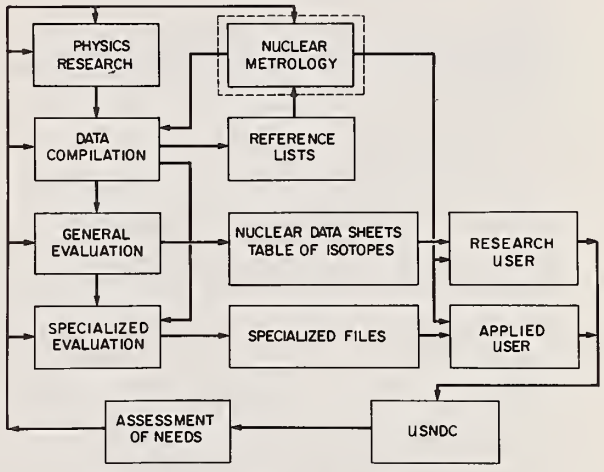

Fig. 3. One possible mechanism for coordinating the functions of measurement, compilation and application in the area of radioactive-nuclide decay data.

An especially important feature of such an interaction is the identification of "needs" and deficiencies in the data base. This identification will lead to improvements in this base and, in some instances, may lead to the production of specialized data evaluations intended for use in particular applied areas. The file of decay data set up for ENDF/B represents one example of such a specialized evaluation. Coordination of this effort is also important; and the U.S. Nuclear Data Committee, with the expanded scope of its interests, seems particularly suited for such a function. This would also provide a natural mechanism for establishing and maintaining communication between the U.S. efforts and international efforts in this field. One result of the Bologna meeting[28] was an articulation of the awareness of the importance of decay data, as one aspect of the broad category of "nuclear data", and of the need for international cooperation in this area.

An important component in the decay-data activities outlined in Fig. 3 is the radioactive-nuclide metrology function. The orientation of this function would be the development of experimental techniques for the measurement with high precision of basic radioactive-decay parameters such as, e.g., γ-ray branching ratios. As such, it would most effectively be carried out within the context of basic nuclear-measurement laboratories. One of its emphases would be the generation of specific high-precision decay data in support of the nuclear-data effort.

Acknowledgement

Helpful conversations with R. L. Heath are gratefully acknowledged.

References

1. See, e.g., R. L. Heath, Modern Trends in Activation Analysis, Nat. Bur. Stand. (U.S.) Spec. Publ. 312, Vol II, 959 (June 1969).
2. Proceedings of the International Symposium on Why and How Should We Investigate Nuclides Far Off the Stability Line, Lysekil, Sweden, Aug. 21-27, 1966, Ark. Fys. 36 (1967).
3. International Conference on the Properties of Nuclei Far from the Region of Beta-Stability, Leysin, Switzerland, Aug. 31-Sept. 4, 1970, CERN-70-30, Vols. I, II (Nov. 1970).
4. Proceedings of the 8th International EMIS Conference on Low Energy Ion Accelerators and Mass Separators, Skövde, Sweden, June 12-15, 1973, Eds. G. Andersson and G. Holmén (Chalmers University of Technology, Göteborg, 1973).
5. M. J. Martin and P. H. Blichert-Toft, Nucl. Data A 8, No.s 1-2, 1 (1970).
6. R. S. Hager and E. C. Seltzer, Nucl. Data A 4, 1 (1968).
7. G. Rudstam, S. Shalev and O. C. Jonsson, Nucl. Instrum. Methods 120, 333 (1974).
8. S. Shalev and G. Rudstam, Nucl. Phys. A230, 153 (1974); G. Rudstam and S. Shalev, Nucl. Phys. A235, 397 (1974).
9. R. O. Gumprecht, "Mathematical Basis of Computer Code RIBD", DUN-4136, Dougles-United Nuclear, Inc. (1968).
10. M. J. Bell, "ORIGEN - The ORNL Isotope Generation and Depletion Code", ORNL-4628, Oak Ridge National Laboratory (May 1973).
11. T. R. England, "CINDER - A One-Point Depletion and Fission-Product Program", WAPD-TM-334 (Rev.), (1964).
12. R. E. Schenter and F. Schmittroth, invited paper presented at this conference; and private communication.
13. C. Devillers, B. Nimal, C. Fiche, J. P. Noel, R. de Tourreil and J. Blachot, invited paper presented at this conference.
14. C. W. Reich, R. G. Helmer and M. H. Putnam, "Radioactive-Nuclide Decay Data for ENDF/B", USAEC Report ANCR-1157 (August 1974).
15. Program FIPP, written by B. Sapienza; private communication from O. Ozer (July 1973).
16. J. Blachot and R. de Tourreil, CEA.N. 1526 (March 1972); C. Devillers, J. Blachot, M. Lott, B. Nimal, N'Guyen Van Dat, J. P. Noel and R. de Tourreil, Proceedings of the International Conference on Nuclear Data and Technology, (IAEA, Vienna, 1973), Vol. 1, p. 477.
17. A. Tobias, Central Electricity Generating Board Report RD/B/M2669, CNDC (73) P4, (June 1973).
18. C. M. Lederer, J. M. Hollander and I. Perlman, Table of Isotopes, 6th Edition, (John Wiley and Sons, New York, 1967).
19. Nuclear Data Sheets (Academic Press, New York and London, continuing).
20. Nuclear Data Tables (Academic Press, New York and London, continuing).
21. G. Erdtmann and W. Soyka, Jül-1003-AC, Vols. 1-III (September 1973).
22. M. A. Wakat, Nucl. Data A 8, Nos. 5-6 (Jan. 1971).
23. L. T. Dillmann, J. Nucl. Med. 10, Suppl. 2 (1969); L. T. Dillmann, J. Nucl. Med. 11, Suppl. 4 (1970).
24. K. H. Johansen, K. Bonde Nielsen and G. Rudstam, Nucl. Phys. A 203, 481 (1973).
25. K. A. Johansson, G. Nyman and G. Rudstam, Swedish Research Council's Laboratory Report LF-58 (1974).
26. R. A. Anderl, Y. D. Harker, E. H. Turk, R. G. Nisle and J. R. Berreth, contributed paper presented at this conference.
27. R. G. Helmer and R. C. Greenwood, contributed paper presented at this conference.
28. Proceedings of the IAEA Fission Product Nuclear Data Panel Meeting, Bologna, Italy, November 26-30, 1973 (IAEA, Vienna, to be published).

RADIOACTIVE DECAY HEAT ANALYSES

R. E. Schenter and F. Schmittroth

Hanford Engineering Development Laboratory*
Richland, Washington 99352

Calculations of decay heat from fission products have been made using the summation method for fast and thermal reactor systems. Results of these calculations for both "burst" and long exposure times are presented and compared with previous experimental results and summation calculations. In addition, uncertainty estimate calculations are given which used both exact and approximate summation method formulas. The above calculations require as input libraries containing data for each individual fission product nuclide. Our source of data has been ENDF/B-IV, where fission yield, cross section and decay data (half lives, β and γ energies, branching, etc.) for 824 fission product nuclides are contained in the fission product and fissionable isotope files.

(Decay heat, fission products, $\bar{E}_\beta$, $\bar{E}_\gamma$, half lives, ^{235}U, ^{239}Pu, yields, ENDF/B-IV)

Introduction

The ENDF/B-IV "Fission Product Data File" has recently been released (January 1975). It contains cross section and decay data for 824 fission product nuclides (300,000 data entries). Of these, 181 nuclides have complete cross section evaluations (capture, elastic, inelastic, total, 10^{-5} eV to 20 MeV), 182 have experimental data on β end-point and γ "line data" energies and intensities.[1] All decaying nuclides (712) have evaluated data ($\bar{E}_\beta$, $\bar{E}_\gamma$, half lives, branching, etc.) needed to make decay heat analyses using summation calculations. In addition, fission yield data (13,000 entries) are part of the ENDF/B-IV "General Purpose File" and appear with the cross sections of the fissionable nuclides.

This extensive data set represents a recent two-year effort by the Cross Section Evaluation Working Group Task Force on "Nuclear Data for Fission Product Decay Heat and Burnup Calculations." The initial emphasis of the Task Force's work was on accurate calculations of fission-product decay heating during "loss-of-coolant accidents" (LOCA). The LOCA analyses require decay heating calculations for short cooling times (t_c<1000 sec). These same data, however, are also applicable to problems involving longer cooling times and additional related studies using calculations of radioactivity effects associated with fast and thermal reactor systems. Members and consultants to this Task Force (∿30) have included experts in the yield, decay and cross section fields from various industrial and government laboratories.

Major data sources used by the Task Force to construct this library include:

Half Lives - New GE "Chart of the Nuclides"[2]

Cumulative Yields Thermal - Walker - Rider 1973 combined evaluations[3,4]

Cumulative Yields Fast - Rider 1973 evaluation incorporating recent Maeck and Larsen measurements[4]

Direct Yield Models - Wahl, Wolfsberg et al., 1973[5]

β and γ Energies and Intensities - Experimental

- ANC Data Project[1]
- Fission Product Data File, Grenoble (3/73)[6]
- Nuclear Data Project - Nuclear Data Sheets, ORNL[7]
- Table of Isotopes[8]
- Fission Product Data File, Berkeley Nuclear Laboratories (10/72)[9]

β and γ Energies and Intensities - Theoretical

- Q values from mass law compilations[10,11]
- β-strength function theories[12,13]

Cross Sections

- Hauser Feshbach calculations.[14]
- BNL-325 (1973)[15]
- CFRMF Integral Results[16,17]
- CINDA 72, 73
- RPI Capture Measurements[18]

Because of the possibility of large numbers of fission product nuclides significantly contributing to summation calculations, it is important to answer questions of the following type: which nuclides and how many nuclides do we need accurate data for? This point was examined and considered in putting together the fission product library. A collection of 299 nuclides were identified which contribute to 99% of the decay heat for an operating reactor for cooling time intervals of 1 second to 30 years. Work on finding decay data for these nuclides was given first priority for ENDF/B-IV.

The following two sections of this paper give results using the ENDF/B-IV data library to produce decay power curves and their uncertainties. The uncertainty or sensitivity studies are not complete in the sense that they still require complete sets of uncertainty estimates of the individual decay parameters for each nuclide. Since quantitative uncertainty estimates are extremely important to decay heat analyses, our future work will emphasize obtaining the individual decay uncertainties and completing the calculations.

Decay Heat Calculation Results

Figures 1-9 show the results of decay heat calculations using the summation method with the ENDF/B-IV library. Also given are previous experimental results, evaluations of experimental results, and recent summation calculations. The ENDF/B-IV calculations were made using the RIBD-II[19] computer code. The main uncertainties in summation calculations stem from input data rather than from any numerical procedure.[20] Codes such as ORIGEN[21] and CINDER-7[22] would give essentially identical results. The basic summation formula is given as

$$P(t,T) = \sum_c \sum_i \varepsilon_{ic} \lambda_{ic} N_{ic}(t,T) , \qquad (1)$$

where P(t,T) is the decay power, for a reactor that has operated for a time T, at a time, t(cooling time), after shutdown. The quantities ε_{ic}, λ_{ic} and $N_{ic}(t,T)$ denote the decay energy ($\varepsilon_{ic} = \bar{E}_\beta + \bar{E}_\beta$), decay constant ($\lambda_{ic}$= ln2/half life), and nuclide concentration, respectively, for the i-th nuclide in mass chain, c. The quantities plotted in Fig.'s 1-9 represent two types of functions which are directly related to the decay power P(t,T) and naturally arise in the experimental situation. The first (FI(T)) is the "integral afterheat function" F(t,T)[23] which when multiplied by the fission rate equals P(t,T). Conventional units for F(t,T) are (Mev/sec)/(fissions/sec) = Mev/fission, or, alternatively, a fraction of the operation power. The second function (F(T)) is the "differential afterheat function" f(t)[23] which represents the energy release per unit time following an essentially-instantaneous burst of fissions. For the "burst" cases which are shown in Fig.'s 5-7, tf(t) (TF(T)) is actually plotted.

Figure 1 gives the ENDF/B-IV decay heat curve for thermal-neutron fission of U-235 with "infinite" exposure for the important cooling time interval of 10 to 10^3 seconds. Also given in Fig. 1 are the evaluations of experimental results by Perry et al.[23] (10% uncertainty bars are shown), the evaluation of Shure[24] which is the basis for the ANS 5.1 decay heat standard,[25] and the Shure curve "plus uncertainty" (20%) which has been used as an upper limit for thermal reactor design application. Figure 2 shows the same functions as those given in Fig. 1 except for the longer cooling time interval of 10^3 to 10^6 seconds. Figures 3 and 4 show the result of splitting up the curves of Fig. 1 into their β and γ energy components. The agreement with Perry et al.'s[23] evaluation is not as good for the split as for the total.

Burst results for ^{235}U are given in Fig.'s 5-7. The summation calculations of Tobias[26] and Devillers et al.[6] are also shown. The unfolded calorimetric results of Lott et al.[27] are given in Fig. 5 for the total differential afterheat function. Note the oscillation in the ENDF/B-IV curve follow that given by the Lott et al.[27] data. Figures 6 and 7 give results for β and γ energy release, respectively. Experimental data is shown with symbols and the references for these measurements are all given in Tobias.[26] Also shown in Fig. 7 are the early "statistical" calculations of Way and Wigner.[28]

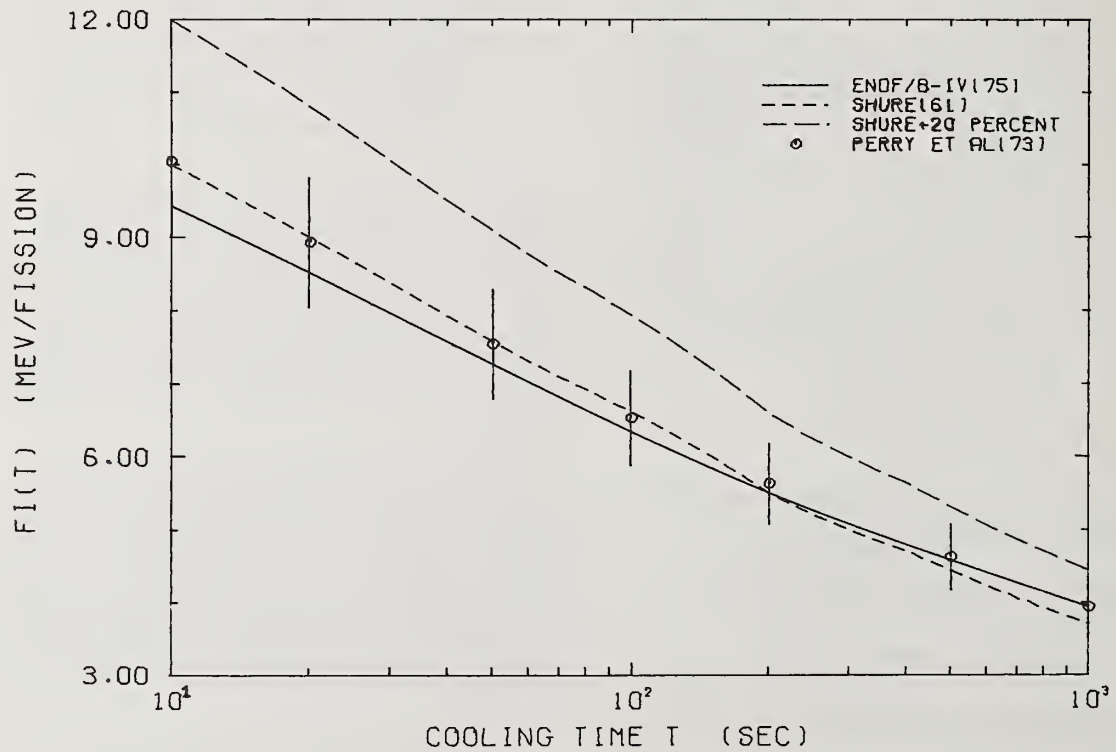

FIG. 1. Total integral afterheat for ^{235}U thermal, "infinite" exposure.

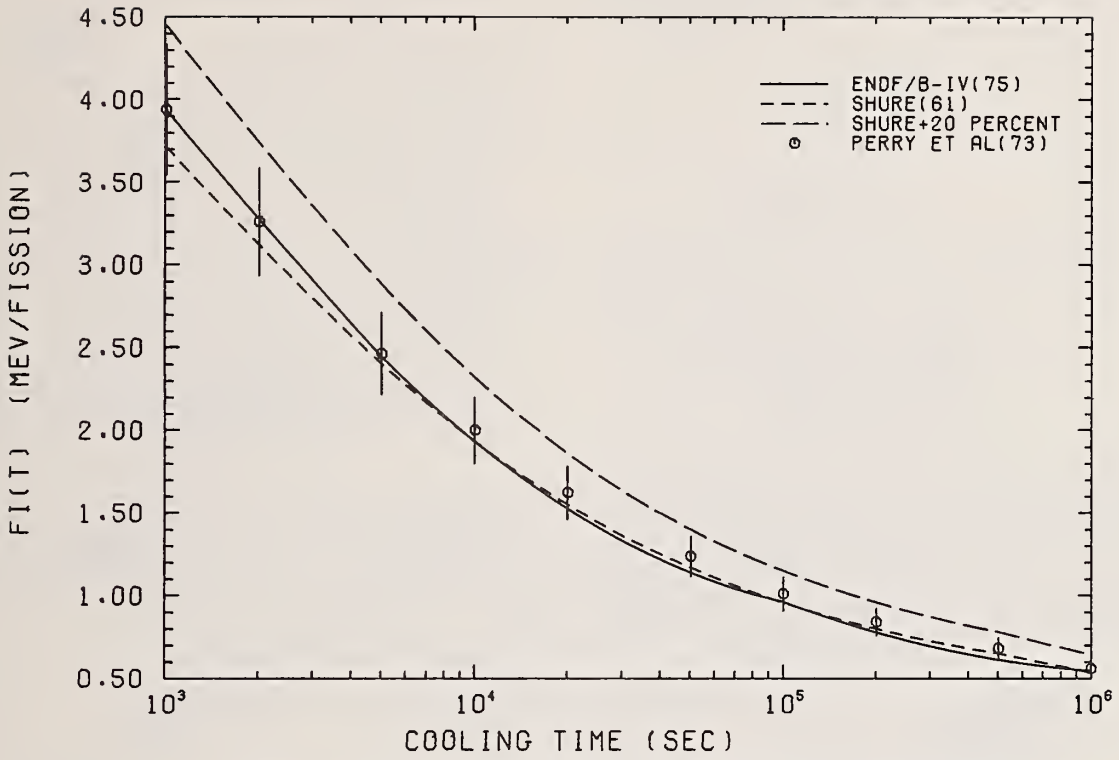

FIG. 2. Total integral afterheat for ^{235}U thermal, "infinite" exposure.

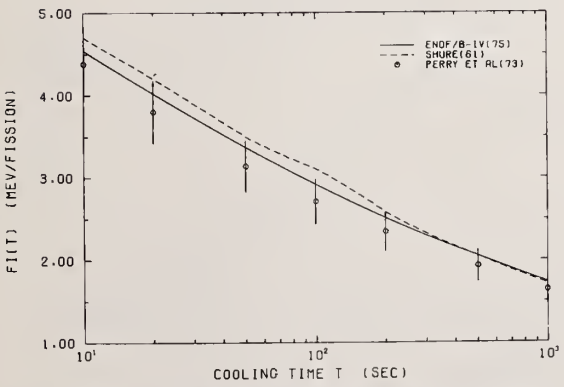

FIG. 3. Beta integral afterheat for ^{235}U thermal, "infinite" exposure.

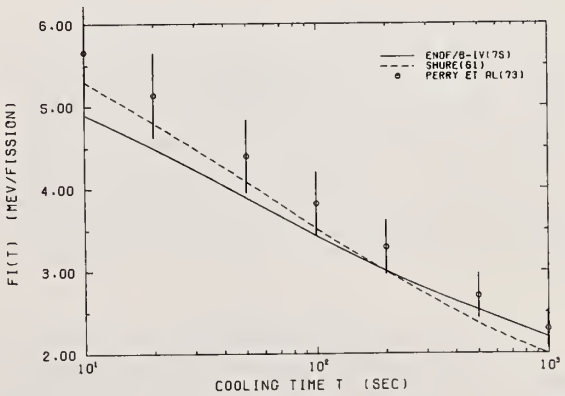

FIG. 4. Gamma integral afterheat for ^{235}U thermal, "infinite" exposure.

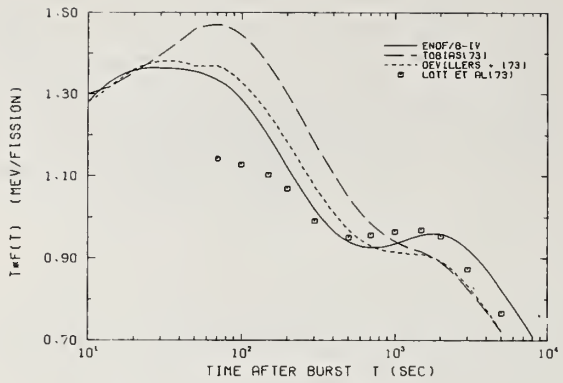

FIG. 5. Total differential afterheat for ^{235}U thermal.

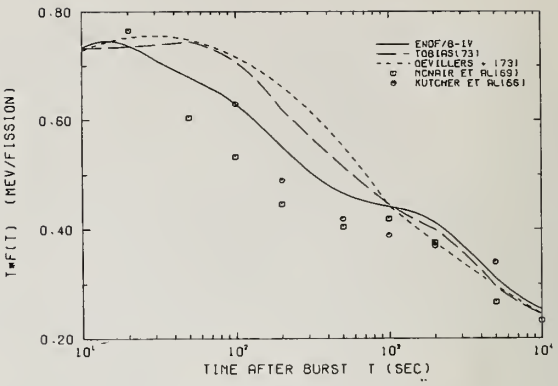

FIG. 6. Beta differential afterheat for ^{235}U thermal.

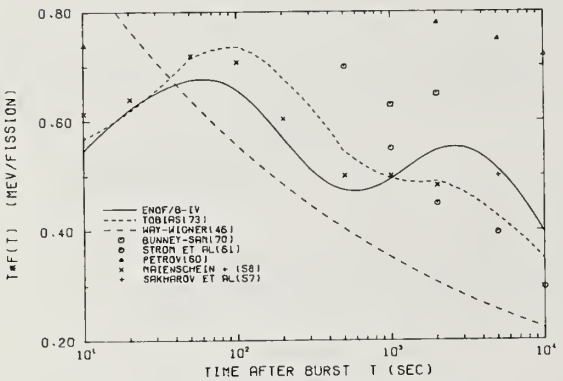

FIG. 7. Gamma differential afterheat for ^{235}U thermal.

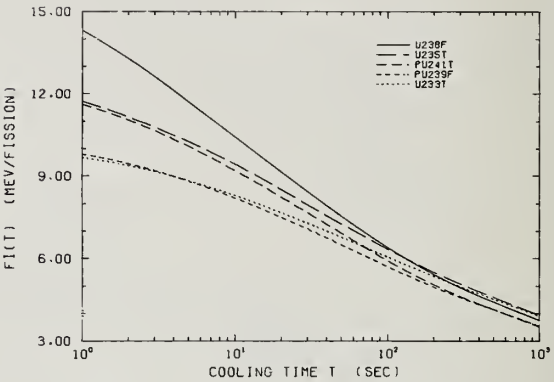

FIG. 8. Total integral afterheat showing variation with fissionable isotope for "infinite" exposure.

The two final figures in this section give integral afterheat functions calculated with the ENDF/B-IV library. Variation of these functions with fissionable nuclide is shown in Fig. 8. As expected, the more neutron rich isotopes (U238 versus U233 or U235) have the higher energy release. The symbols T and F represent thermal and fast neutron fission, respectively. Finite (1 yr and 42 days) versus "infinite" (165 yr) exposure results are indicated in Fig. 9. Also shown are capture effects (PHI=10^{14} vs. PHI=0) which are small for this cooling time interval.

Sensitivity Studies

An understanding of the sensitivity of decay-heat summation calculations to the basic input data is important for two distinct reasons. First of all, to estimate the inherent accuracy of the final answers and second, to pinpoint those areas where further refinement of the input data would be fruitful. Fortunately, with modern computers, the summation formalism can be applied in a way that does not introduce additional uncertainties due to the calculational methods. Any errors in the decay heat results must

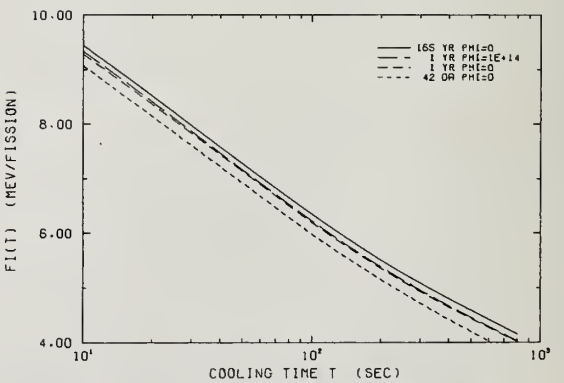

FIG. 9. Total integral afterheat showing variations with exposure time and flux values for ^{235}U thermal.

arise from the uncertainties in the basic data. In addition to errors in various parameters such as half-lives, yields, and decay energies, these uncertainties include other effects; for example, undetected metastable states, incorrect neutrino energies, and internal conversion corrections.

Because of the role experimental measurements play in the assignment of decay heat uncertainties, it is useful to consider separately short and long times after reactor shutdown. At short times (less than 100 seconds) where these integral measurements are very meager and often conflicting, the propagation of uncertainties in the basic data can provide the best estimate of the final errors. For the longer times, the integral experiments provide an important test of the input parameters. Even here, however, sensitivity studies can be very helpful. Many of the integral experiments concentrate on one or two fissionable nuclides, especially ^{235}U. Since the only parameters that vary from one nuclide to another or for varying neutron energies are the fission product yields, a knowledge of the propagation of yield uncertainties allows one to confidently predict decay heat for nuclides or energies in addition to the ones where high quality integral experiments exist.

Due to the form of the summation equations, the propagation of uncorrelated errors in the decay energies is the easiest to consider. It follows immediately that the variance, $V_\varepsilon(P)$, of P with respect to uncertainties in the decay energies is given by

$$V_\varepsilon(P) = \sum_c \sum_i v(\varepsilon_{ic})\, \lambda_{ic}^2\, N_{ic}^2 , \qquad (2)$$

where $v(\varepsilon_{ic})$ is the variance associated with nuclide, (i,c).

In order to obtain a quantitative feel for this expression, assume that all the energies are uncertain by a constant percentage:

$$\frac{v(\varepsilon_{ic})}{\varepsilon_{ic}^2} = \sigma_\varepsilon^2 \qquad (3)$$

One can then write

$$\frac{V_\varepsilon(P)}{P^2} = \frac{\sigma_\varepsilon^2}{\eta} \qquad (4)$$

where η is the effective number of contributing nuclides and is found from

$$\eta = \frac{\left[\sum_c \sum_i (\varepsilon_{ic}\, \lambda_{ic}\, N_{ic})\right]^2}{\sum_c \sum_i (\varepsilon_{ic}\, \lambda_{ic}\, N_{ic})^2} . \qquad (5)$$

In Fig. 10, values of $(1/\eta)$ based on the ENDF/B-IV decay heat file are plotted for various cooling times, t, after a $T=10^7$ sec (120 day) reactor operating period. The relative variance, $V_\varepsilon(P)/P^2$, can then be easily found for any specified variance, σ_ε^2, of the decay energies. The contributions from those nuclides whose decay energies were determined from experiment are shown separately from those whose energies were estimated

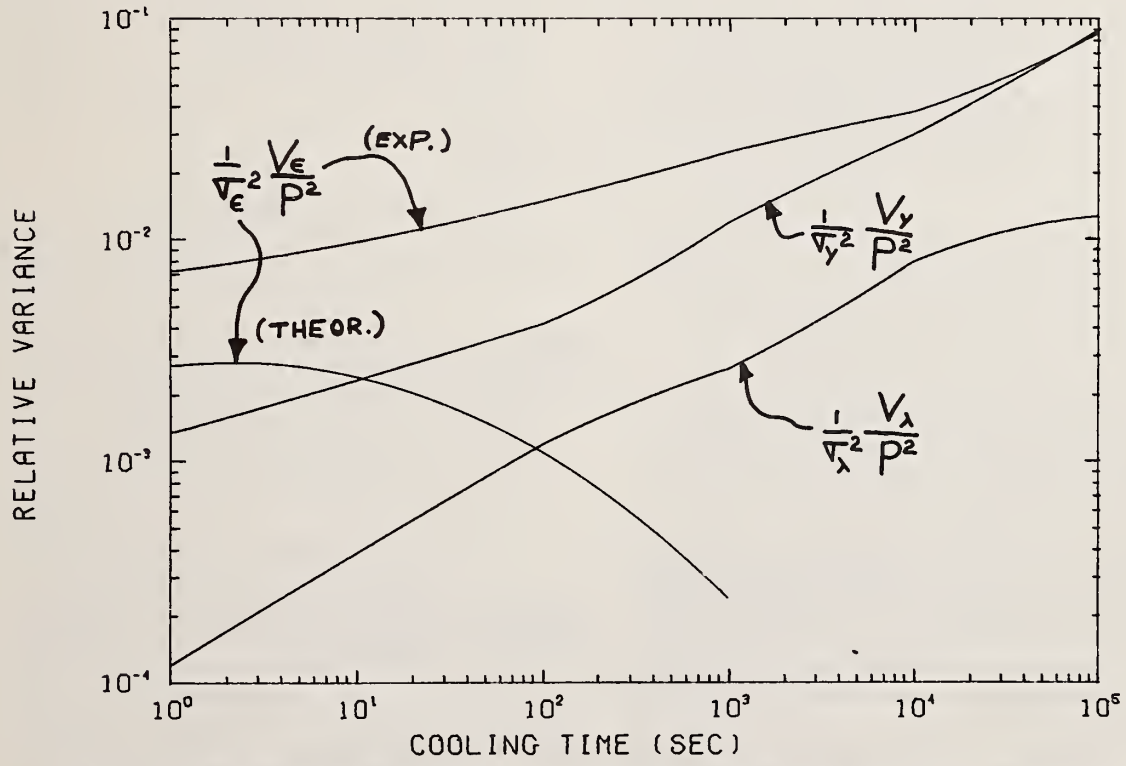

FIG. 10. Decay heat variance relative to the square of the expected value, P, for an exposure time, $T=10^7$ seconds. The subscripts, ε, λ, and Y denote the variance due to uncertainties, σ_i, in the decay energies, half-lives, and chain yields, respectively. The contributions from isotopes with theoretical and experimental decay energies are noted separately by "THEOR." and "EXP.".

from theoretical extrapolations. Notice that the ratio of variances for the experimental nuclides as compared to the theoretical ones is equal to 0.016/.001 ≃ 16. at a time, t = 100 sec. Therefore, the relative error in the theoretical nuclides could be larger by the factor, $\sqrt{16.} \simeq 4.0$ before the theoretical and experimental nuclides contributed equally to the overall variance. At times greater than 1000 seconds, the effect of the theoretical nuclides becomes negligible. Of course, correlated errors would change matters. If all the decay energies were 1% high, the decay power would be overestimated by this same 1%. Figure 11 shows the percent uncertainty in the decay power for a range of uncertainty values in the energy of the experimental and theoretical nuclides.

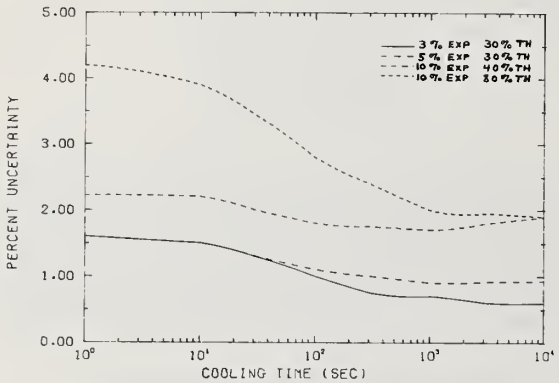

FIG. 11. Uncertainties in decay heat due to uncertainties in the average decay energies. EXP and TH represent experimental and theoretical nuclides, respectively.

Since the nuclide concentrations are nonlinear with respect to the decay constants, λ_{ic}, the variance of P(t,T) with respect to these constants is more difficult to compute. A Monte Carlo approach would be straightforward but very lengthy if one were not sufficiently clever. For each random sample, one would have to solve the decay equations for the concentrations, N_{ic}. Fortunately, at least for times less than about 10^4 seconds (∿3 hours), the exact expression for P(t,T), Eq. (1), can be replaced by a much simpler one along lines presented years ago by Way and Wigner.[28]

Because nuclides further away from the line of beta-stability have shorter half-lives on an average, one can assume that all the parent nuclides decay into each daughter nuclide in a time short compared to the decay time for that daughter. For a fission burst, for example, where the initial nuclide concentrations, $n_{ic}(o)$, are just the direct yields, y_{ic}, $(n_{ic}(o)=y_{ic})$, the nuclide concentrations as a function of time can be approximated by

$$n_{ic}(t) = Y_{ic}\, e^{-\lambda_{ic} t} \qquad (6)$$

where Y_{ic} is the cumulative yield. In the absence of neutron capture, one can integrate Eq. (6) to obtain nuclide concentrations for a finite operating period, T:

$$N_{ic}(t,T) = \int_t^{t+T} n_{ic}(t')\, dt'$$

$$= \frac{Y_{ic}}{\lambda_{ic}} \left[e^{-\lambda_{ic} t} - e^{-\lambda_{ic}(t+T)} \right] \qquad (7)$$

Note that if the concentrations, n_{ic}, are determined by the direct yields, then the integrated concentrations, N_{ic}, are relative to a normalized fission rate so that units for N_{ic} are expressed as (1/(fissions/sec)).

One should also note that even though Eq. (6) is seriously in error, at shutdown (t=o) for those nuclides whose cumulative yield differs appreciably from their direct yield, Eq. (7) for N_{ic} is much better. In fact, for a long operating period, T, when most of the concentrations have saturated, Eq. (7) is exact at shutdown:

$$N_{ic}(t=o,\ T=\infty) = \frac{Y_{ic}}{\lambda_{ic}} \,. \qquad (8)$$

Detailed calculations of P(t,T) based on Eq. (1) were compared with N_{ic} calculated exactly and with N_{ic} approximated by Eq. (7) for an infinite exposure, T=∞. At shutdown the two calculations coincide as noted above. At longer times the approximate method starts to fall away to become 20% low by 10^4 seconds.

With the approximation, Eq. (7), Eq. (1) becomes:

$$P(t,T) \simeq \sum_c \sum_i \varepsilon_{ic}\, Y_{ic} \left[e^{-\lambda_{ic} t} - e^{-\lambda_{ic}(t+T)} \right]. \qquad (9)$$

The variance of $e^{-\lambda_{ic} t}$ with respect to λ_{ic} can be approximated by

$$V_\lambda(e^{-\lambda t}) = \left(\frac{de^{-\lambda t}}{d\lambda}\right)^2 v(\lambda)$$

$$= (te^{-\lambda t})^2\, v(\lambda) \qquad (10)$$

where $v(\lambda)$ is the variance of λ. If for simplicity, the exposure is taken to be infinite, T=∞, the variance of P(t,T) with respect to the λ_{ic} now becomes

$$V_\lambda(P) \simeq \sum_c \sum_i \varepsilon_{ic}^2\, Y_{ic}^2\, (te^{-\lambda_{ic} t})^2\, v(\lambda_{ic})$$

$$\simeq \sum_c \sum_i \left[\varepsilon_{ic}^2\, N_{ic}^2\, (\lambda_{ic} t)^2\, v(\lambda_{ic}) \right] \qquad (11)$$

If $v(\lambda_{ic})$ is assumed proportional to λ_{ic}, as was done for the decay energies, ε_{ic}:

$$v(\lambda_{ic}) = \sigma_\lambda^2\, \lambda_{ic}^2 \,, \qquad (12)$$

then Eq. (11) becomes

$$\frac{V_\lambda(P)}{P^2} = \sigma_\lambda^2 \left\{ \frac{\sum_c \sum_i \varepsilon_{ic}^2\, \lambda_{ic}^2\, N_{ic}^2 (t\lambda_{ic})^2}{\left[\sum_c \sum_i \varepsilon_{ic} \lambda_{ic} N_{ic} \right]^2} \right\} . \qquad (13)$$

As before for the variance with respect to decay energies, the factor in brackets in Eq. (13) is shown in Fig. 10. In this case, most of the important nuclides have experimental values for the half-lives, and the variances from experimental and theoretical nuclides are not shown separately. Also note from Fig. 10 that the precision needed for the decay constants (or half-lives) is much less than for the decay energies.

Another source of uncertainty in the decay heat arises from the fission product yields. Both the uncertainties in the chain yields and the charge distribution were considered. First of all, for an exposure time of $T=10^7$ sec, the use of a strictly Gaussian charge distribution does not change the decay heat for any time after shutdown by more than 2% as compared to the direct yields taken from ENDF/B-IV. Secondly, within their normal uncertainties, variations of both the most probable charge values, Z_p, and the charge distribution width, σ, affect the decay heat by less than 2% for all shutdown times. In fact, the gross assumption that the charge is not redistributed at all during fission changes the decay heat by only 7% for times less than 1000 seconds. At longer times the effect is even smaller. All the above variations maintained the conservation of neutrons and protons as constraints on the yields.

Finally, uncertainties in the chain yields were considered. Although the decay heat summation formula depends linearly on the chain yields, the same as for the decay energies, calculation of the variance is complicated by the fact that the sum of the chain yields is constrained to equal 2. With the aid of a formula derived independently by B. L. Spinrad in an Oregon State Memo, the constrained variance, $V_y(P)$, with respect to chain yields, was computed. The following quantity is shown in Fig. 11, along with the other results:

$$R_y = \frac{1}{\sigma_y^2} \cdot \frac{V_y}{P^2} ,$$

where σ_y is an average error in the chain yields for the important mass chains. Unlike the corresponding quantities for decay constants and energies, R_y is not completely independent of σ_y. Nevertheless, R_y is a useful quantity for comparison purposes.

U^{235}. As an example, consider the thermal fission of U^{235}. Typical chain yield errors are less than 2% for many of the important isotopes.[4] And since R_y (see Fig. 10) is less than 10^{-2} for times less than 10^3 seconds, the corresponding decay heat uncertainty is only

$$2\% \times \sqrt{10^{-2}} = 0.2\% .$$

For typical reactor operating periods, metastable states contribute about 5-10% of the decay heat for all shutdown times up to about 10^5 sec. They must therefore be considered in any error assessment. If it were not for the effect of neutrinos, the sole effect of the metastable states would be to change the time of the release of decay heat, not the overall energy released. However, because a metastable state can alter the relative beta and gamma energies given off by an isotope, the neutrino fraction can be altered. Any change in total energy due to direct yields to metastable states turns out to be small. Since there is no obvious systematic way to study the effects of undetected metastable states or errors in their parameters, it was decided to simply note the overall effect of eliminating all known metastable states. Three changes were made to the decay heat file. All direct yields to the metastables were transferred to the ground state, the average gamma energies of neighboring nuclides were appropriately modified, and all branching to metastable states was set to zero. Only the last change produced a marked effect. For an exposure of 10^7 seconds, the maximum change up to 10^7 seconds (120 days) was a decrease in the decay heat of about 7% near 10^3 seconds after shutdown. It seems likely, for shorter times at least where many nuclides are contributing, that any errors introduced by the metastables must be smaller than the 7%. Most of the nuclides near the line of stability are relatively well studied, and for the more neutron-rich nuclides, the half-lives of both the metastable and ground states are short. Hence, only some alteration of the time dependence of the decay heat would occur. Any uncertainty due to neutrino energies could just as well be assigned to uncertainties in the corresponding beta and gamma energies.

References

*Operated by Westinghouse Hanford Company for the U.S. Energy Research and Development Administration.

[1] C. W. Reich and R. G. Helmer, "Radioactive-Nuclide Decay Data in Science and Technology," this conference.

[2] N. E. Holden and F. W. Walker, "CHART OF NUCLIDES," Eleventh Edition-Revised to April 1972.

[3] W. H. Walker, "Fission Product Data for Thermal Reactors Part II-Yields," AECL-3037, CRNL, (April 1973).

[4] M. E. Meek and B. F. Rider, "Compilation of Fission Product Yields Vallecitos Nuclear Center 1974," NEDO-12154-1 (January 1974).

[5] K. Wolfsberg, "Estimated Values of Fractional Yields from Low Energy Fission and a Compilation of Measured Fractional Yields," LA-5553-MS (May 1974).

[6] C. Devillers et al., 1973, IAEA-SM-170/63, Symp. on Appl. of Nuc. Data in Science and Technology, Paris.

[7] D. H. Horen et al., "Nuclear Data Sheets," edited by Nuclear Data Group, ORNL.

[8] C. M. Lederer et al., "Table of Isotopes, Sixth Edition (1967).

[9] A. Tobias, "Data for the Calculation of Gamma Radiation Spectra and Beta Heating from Fission Products (Revision 2)," RD/B/M2453 (October 1972).

[10] G. T. Garvey et al., Rev. Mod. Phys. 41 S1 (1969).

[11] A. H. Wapstra and N. B. Gove, Nuclear Data Tables A9, Nos. 4-5, 265 (1971).

[12] K. H. Johansen and K. Bonde Nielsen, Nucl. Phys. A203 (1973) 481.

[13] K. Takahashi et al., Atomic Data and Nuclear Data Tables, 12, 101 (1973).

[14] F. Schmittroth and R. E. Schenter, "Fast Neutron Capture Cross Sections for Fission Product Isotopes," HEDL TME 73-63 (August 1973).

[15] S. F. Mughabghab and D. I. Garber, "Neutron Cross Sections Volume 1, Resonance Parameters," BNL-325 (June 1973).

[16]Y. D. Harker and E. H. Turk, "The Use of CFRMF Integral Data in Cross-Section Evaluations," Kiamesha Lake Conference, CONF-720901 Book 2, p. 613 (September 1972).

[17]R. A. Anderl et al., "Integral Capture Cross-Section Measurements in CFRMF for LMFBR Control Materials," this conference.

[18]R. W. Hockenbury et al., "Fission Product Capture Cross Sections in the keV Region," this conference.

[19]D. R. Marr, "A Users' Manual for Computer Code RIBD-II, A Fission Product Inventory Code," HEDL TME 75-26 (to be published).

[20]C. W. Kee, C. R. Weisbin, and R. E. Schenter, Trans. Am. Nucl. Soc., 19, 398 (1974).

[21]M. J. Bell, "ORIGEN-The ORNL Isotope Generation and Depletion Code," ORNL-4628, Oak Ridge National Laboratory (May 1973).

[22]T. R. England, R. Wilczynski, and N. L. Whittemore, "CINDER-7; An Interim Users' Report," LA-5885-MS (to be published 1975).

[23]A. M. Perry, F. C. Maienschein, and D. R. Vondy, "Fission-Product Afterheat-A Review of Experiments Pertinent to the Thermal-Neutron Fission of ^{235}U," ORNL-4197, Oak Ridge National Laboratory (October 1973).

[24]K. Shure, "Fission-Product Decay Energy," Bettis Technical Review, WAPD-BT-24 (December 1961).

[25]American Nuclear Society, "Proposed ANS Standard Decay Energy Release Rates Following Shutdown of Uranium-Fueled Thermal Reactors," Draft Standard ANS 5.1, approved by Subcommittee ANS-5 of the ANS Standards Committee, October 1971, revised October 1973.

[26]A. Tobias, J. Nucl. Energy, 27, 725 (1973).

[27]P. M. Lott et al., "Mesures Calorimetriques De La Puissance Emise Par Les Produits De Fission De U-235 Pour Des Temps De Refroidissement Compris Entre 70 Secondes Et 7.10^6 Secondes," B.I.S.T. Commissariat A L'Energie Atomique, No. 181 (Mai 1973) (French).

[28]K. Way and E. P. Wigner, Phys. Rev., 70, 115 (1946).

SENSITIVITY OF THE AFTERHEAT FROM ^{235}U AND ^{239}Pu THERMAL FISSION TO ERRORS IN FISSION PRODUCT NUCLEAR DATA

C. Devillers*. B. Nimal*. C. Fiche**. J.P. Noël**
J. Blachot***. R. de Tourreil****.

Commissariat à l'Energie Atomique,
Centres d'Etudes Nucléaires,
de Saclay*, Fontenay-aux-Roses**, Grenoble***,
Institut de Physique Nucléaire d'Orsay**** - France -

This paper presents calculational results on the decay heat associated with the thermal fission of ^{235}U and ^{239}Pu. Calculations are based on the summation of the energies which are released by individual fission products. Two cases have been considered : the first corresponds to one instantaneous fission, the other to a 900 days irradiation time. In both cases the sensivities of the afterheat to respectively independent yields, half-lives, average beta plus gamma energies of 512 instable fission products have been derived. This information has been used to calculate the afterheat uncertainties from experimental and evaluated nuclear data errors, when available. Results relating to the instantaneous fission of ^{235}U and ^{239}Pu are compared to calorimetric measurements between 100 and 10^5 second cooling time. Errors in the afterheat corresponding to a 900 days irradiation time have been estimated for cooling times ranging from 1 to 1000 seconds which are appropriate for Loss of Coolant Accident analyses in light water reactors. The computer programmes which have been developed can be applied to any irradiation and cooling time condition.

(Fission products, decay heat, afterheat, sensitivity, error estimates, loss of coolant accident)

Introduction

The decay heat function required in the analysis of a Loss of Coolant Accident (LOCA) in light water reactors can be derived by two complementary methods. The first is based upon the integral measurement of the total beta and gamma power released after one fission. The second method, on the other hand consists of cumulating the individual energies released by each of the fission products ; it necessitates a detailed knowledge of independent yields and decay properties of the largest number of the isotopes produced by fission. The integral measurements should be used to test the validity of the "microscopic" calculational approach which in turn could be applied to more complex situations in a reactor, taking in account the reactor power variations and the evolution of fissionable isotopes as function of reactor operation. The various presently available integral results however, show numerous discrepancies which are incompatible with the degree of accuracy needed as set by the IAEA Panel on fission product nuclear data[1].The uncertainties in integral measurements could be reduced to a large extent by performing several benchmark experiments in different laboratories. It is worthwhile, in the mean time to develop computational methods capable of providing the sensitivities of the afterheat to inaccuracies in nuclear data. This might call the attention of physicists and evaluators on those nuclei and those data which are important for the afterheat problem. This paper presents sensitivity studies of the decay heat associated with the thermal fission of ^{235}U and ^{239}Pu. Both an instantaneous fission (zero irradiation time) and a long irradiation time (900 days) have been considered. The first case shows a highest sensitivity to short lived fission products, as can be observed in a benchmark experiment. The second case corresponds to reactor conditions. Error estimates based on calculated sensitivity factors and on compilations of nuclear data uncertainties are reported. The calculated decay heats corresponding to one instantaneous thermal fission of respectively ^{235}U and ^{239}Pu are compared to the experimental ones deduced from calorimetric measurements of the gamma and beta power released by ^{235}U and ^{239}Pu samples.

Principles of decay heat calculations

The energy released by fission products at time t after one fission is calculated by the summation formula :

$$f(t) = \sum_{i=1}^{M} E_i . \lambda_i . N_i(t)$$

where,

- M = number of fission products in the library
- Ei = average gamma plus beta energy per decay of nuclide i
- λi = decay constant
- $N_i(t)$ = number of atoms of nuclide i at time t in the fissionable sample under consideration.

The time dependent variation of the fission product density is derived from the following equation set :

$$N_i(t) = \sum_{k=1}^{i} p_{ik} \exp(-\lambda_k t)$$

$$p_{ik} = -\frac{1}{\lambda_i - \lambda_k} \sum_{j=k}^{i-1} \lambda_{ij} p_{jk}$$

the summation extending to all possible precursors of nuclide i,

$$p_{ii} = y_i - \sum_{k=1}^{i-1} p_{ik}$$

where,

y_i = independent yield of nuclide i
$\lambda_{ij} = b_{ij}\,\lambda_j$
b_{ij} = branching from j to i

These calculations are done by the computer programme PEPIN [2] ; nuclides are ordered such that daughter nuclei are treated after their precursors. PEPIN requires as input a library containing independent yields and decay data of individual fission products. The library content and format have been described in reference[3] ; the major recent improvements brought into the library have been :

- increase the number of fission product isotopes to 633
- adopt the last Meek and Rider's yield compilation[4]
- revise the decay data of more than one hundred isotopes (Blachot[5]).

The afterheat at time t following an irradiation at a constant fission rate of one fission per second can be calculated by the integration formula :

$$F(\theta,t) = \int_{t}^{\theta+t} f(u)\,du$$

where,

θ = irradiation time
f = decay heat function for one instantaneous fission

This formula is correct provided the effect of neutron captures on afterheat can be neglected. This effect is less than 1 % is case of a 900 days irradiation and for cooling times lower than 1000 seconds, which is the case of interest here[6]. If the function f is known at the boundaries of small time intervals, the integration can be performed by assuming a linear variation of f in each time interval, in a log x log scale :

$$F(\theta,t) = \sum_{k=k_1}^{k_2} \frac{(f.t)_{k+1} - (f.t)_k}{\alpha_k + 1}$$

with,

$$\alpha_k = \frac{\ln (f_{k+1}/f_k)}{\ln (t_{k+1}/t_k)}$$

$$t_{k1} = t \quad , \quad t_{k2} = \theta + t$$

From these analytical formulaes it is therefore possible to correlate sensitivity calculations for any irradiation condition, even for a time dependent fission rate, to sensitivity calculations for the decay heat associated with one instantaneous fission.

Definition of sensitivity

Given a function f depending upon N independent variables x_i, f (x_1, x_2 .... x_N), the uncertainty in f due to the inacurracy of one variable x_i is given by the expression :

$$\left(\frac{\Delta f}{f}\right)_i = \frac{\partial f}{\partial x_i}\,\frac{x_i}{f}\,\left(\frac{\Delta x_i}{x_i}\right)$$

The sensitivity of f to an error in x_i is simply defined as :

$$s_i = \frac{\partial f}{\partial x_i}\,\frac{x_i}{f}$$

The total uncertainty in f due to statistical errors in all the variables can therefore be estimated by the following relationship,

$$\frac{\Delta f}{f} = \left[\sum_{i=1}^{N} s_i^2 \left(\frac{\Delta x_i}{x_i}\right)^2\right]^{1/2}$$

Based on a first order expansion of the function around each of the variables, the above method provides good uncertainty estimates for error values that are not too high. Sensitivity factors can also be used of course to evaluate the effect on f of systematic errors in the variables :

$$\frac{\Delta f}{f} = \sum_{i=1}^{N} s_i\,\frac{\Delta x_i}{x_i}$$

Techniques for calculating sensitivities

The decay heat obtained by the summation formula is considered as a function of 3 N independent variables being respectively, the independent yield, the half-life and the average beta plus gamma decay energy of each of the N fission product isotopes. The sensivities to each of the three nuclear data types of any isotope m are derived as follows :

a) independent yield :

$$sy_m(t) = \sum_{i=m}^{M} E_i.\lambda_i.\,\frac{\partial N_i(t)}{\partial y_m}\cdot\frac{y_m}{f(t)}$$

b) half-life :

$$sT_m(t) = -\sum_{i=m}^{M} E_i.\left[\lambda_i.\frac{\partial N_i(t)}{\partial \lambda_i} + \delta_{im} N_i(t)\right].\frac{\lambda_m}{f(t)}$$

$\delta_{im} = 1$ for $i = m$, $\delta_{im} = 0$ for $i \neq m$

The summation in the two above formulaes begins with i=m, all the isotopes below m beeing independent of isotope m.

c) energy :

$$sE_m(t) = \frac{E_m.\lambda_m.N_m(t)}{f(t)}$$

This last sensitivity is nothing but the relative contribution to decay heat of nuclide m.

The derivatives of the isotope number density involved in the equations a) and b) can be written,

$$\frac{\partial N_i(t)}{\partial y_m} = \sum_{k=1}^{i} \frac{\partial pik}{\partial y_m}\,\exp(-\lambda_k t)$$

$$\frac{\partial N_i(t)}{\partial \lambda_m} = \sum_{k=1}^{i} \frac{\partial p_{ik}}{\partial \lambda_m} \exp(-\lambda_k t) - t\, p_{im} \exp(-\lambda_m t)$$

The matrix coefficient derivatives can in turn be calculated by recurrent formulaes which are too cumbersome to be detailed here.

The programme PEPIN has been extended to include these calculations. In addition to the decay heat it provides sensitivity factors with respect to each radioactive isotope of the library ; sensitivity factors are stored on tape for later use.

If one is concerned with the case of an irradiation at a constant fission rate, during time θ, the analytical integration technique explained previously provides a direct mean of obtaining sensitivity factors in this case. The sensitivity of the afterheat $F(\theta,t)$ to the independent yield of isotope m thus obtained is,

$$SY_m = \frac{1}{F(\theta,t)} \sum_{k=k_1}^{k_2} \frac{(sY_m.f.t)_{k+1} - (sY_m.f.t)_k - R_k}{\alpha_k + 1}$$

with,

$$R_k = \frac{(f.t)_{k+1} - (f.t)_k}{\alpha_{k+1}} \cdot \frac{(sY_m)_{k+1} - (sY_m)_k}{\ln(t_{k+1}/t_k)}$$

and,

$$\alpha_k = \frac{\ln(f_{k+1}/f_k)}{\ln(t_{k+1}/t_k)}$$

where,

f_k = decay heat at time t_k after one fission
$(sY_m)_k$ = sensitivity of f_k to independent yield Y_m of isotope m.

A similar expression holds for the sensitivity to the half-life. The sensitivity to the average beta plus gamma decay energy of one isotope m is the relative contribution of this isotope to the afterheat $F(\theta,t)$; this contribution can be easily calculated.

Uncertainties in nuclear data

Three types of data have been considered as bringing in errors :

- independent yields,
- half-lives,
- average beta and gamma decay energy.

Errors in branching ratios have not been taken into account here. Errors in fission product capture cross sections do no affect the afterheat at short times after shutdown and can therefore be ignored.

Errors in independent yields

The last Meek and Rider yield compilation[4] provides independent yield error values which have been affected to the 633 nuclides of our fission product library. Table I gives an overlook of the error distribution.

Table I. Independent yield errors (thermal fission)

Yield error (%)	Number of nuclides ^{235}U	^{239}Pu
2	1	-
2.8	4	-
4.	9	-
6.	14	4
8.	17	14
11.	21	6
16.	18	5
23.	17	18
32.	45	52
45.	23	16
64.	464	518

Summation of the independent yields over the 633 isotopes of our library gives respectively, for 100 fissions :

196.65 fission products for ^{235}U

196.16 fission products for ^{239}Pu

To insure a 200 % balance, fractional cumulative yields instead of independent are assigned to the first isotope of each decay chain. However, the energy released by the precursors of these isotopes will be lacking. Independent yields are calculated by using a Gaussian distribution with ZP and SIGMA values recommended in [4] ; the odd-even effect has not been included, its influence on the decay heat will be estimated below by the aid of sensitivity factors.

Errors in half-lives

The uncertainties in the half-lives have been compiled by Blachot[5] at the same time as his revision and updating of the decay properties in the library. About two thirds of the radioactive nuclei have known experimental errors. Table II shows how these errors distribute in function of the half-life value.

Table II. Half-life errors

Range	Number of nuclides	Average error (%)
0 - 3 s	87	13.
3 s - 1 m	148	8.
1 m - 5 m	48	5.
5 m - 1 h	81	2.
1 h - 5 h	31	1.4
5 h - 1 j	40	1.5
1 j - 20 j	22	0.85
20 j - 1 y	23	0.5
1 y - 3 y	5	0.7
> 3 y	27	4.
stable	121	

For unknown errors, the following rules have been applied :

from 0 to 3 seconds : error = 30 %
from 3 s to 1 minut : error = 10 %
other ranges : error = average error in range

About 30 unknown half-lives have been evaluated by de Tourreil ; a 100 % error has been affected to these values.

Errors in beta and gamma energy

Information on errors in decay schemes (beta transition energies and intensities) is still too scarce to allow systematical error estimates in the average beta and gamma decay energies. Three cases have been considered :

a) Isomeric transition : the beta plus gamma energy being equal to the reaction energy, the error is given by :

$$\Delta E = \Delta Q$$

b) Beta decay with known decay scheme : the average beta plus gamma energy is always normalized to the reaction energy minus the average neutrino energy :

$$E = Q - E_\nu$$

E_ν is calculated according to the FERMI model[7] for each beta transition and then averaged over the transition probability spectrum. The error is therefore calculated by :

$$\Delta E = \left[(\Delta Q)^2 + \left(\frac{\Delta E_\nu}{E_\nu} \right)^2 \cdot (Q-E)^2 \right]^{1/2}$$

a constant error of 5 % has been assumed in the calculation of the average neutrino energy, including uncertainties in the decay scheme and inaccuracy of the model.

c) Beta decay with unknown decay scheme : the average total beta and gamma energy is assumed a given (spin and parity dependent) fraction of the reaction energy :

$$E = \alpha Q$$

For short lived fission products contributing to the afterheat at short times after shutdown, α is on the average equal to 0.6. The average neutrino energy is therefore : $E_\nu = 0.4\ Q$; assuming that this factor might vary from 0.28 to 0.52 (30 % uncertainty) results in a relative error in α equal to 20 %. The error in E is therefore estimated as :

$$\frac{\Delta E}{E} = 0.2 + \frac{\Delta Q}{Q}$$

The errors in Q have been taken form WAPSTRA[8] or GARVEY[9] when lacking. When no errors were available, a 15 % relative error has been adopted. When different decay modes occured in a given nuclide, statistical rules were used to combine the errors obtained for each mode.

Decay heat error estimates

Computing procedure

A series of three programmes is utilized to perform decay heat and error estimate calculations :

DOP - nuclear data processing
- calculation of independent yields from chain yields, ZP and SIGMA
- calculation of average beta, gamma and neutrino energies
- normalization of average beta and gamma energies
- preparation of a library in PEPIN format

PEPIN - nuclide depletion, decay heat and sensitivity factor calculations (one fission)
- solution of Bateman equations
- calculation of activities and fractional decay heats
- calculation of sensitivity factors, storage on tape

PEPER - error estimate calculations
- error estimate in decay heat after one fission
- calculation of afterheat following any operation time
- derivation of afterheat sensitivities
- error estimate in afterheat.

The error estimates performed by PEPER are limited to statistical ones coming from statistical uncertainties in the data mentioned above . Errors due to systematic deviations of the data from the assumed values, such as the odd-even effect for example, can be evaluated by the aid of the sensitivity factors provided by PEPER.

Error in decay heat following one fission

Results of the sensitivity study are reported in Table III for ^{235}U and Table IV for ^{239}Pu. The error values quoted in these tables are one relative standard deviation.

Table III. ^{235}U decay heat error estimate
(one thermal fission - one standard deviation)

Cooling time (s)	Origin of the error: yields	half-lives	energies	Total (%)
10^0	4.7	3.5	4.7	7.5
10^1	3.6	4.0	3.8	6.6
10^2	3.5	5.0	3.0	6.8
10^3	3.7	1.1	1.8	4.3
10^4	1.8	1.4	1.0	2.5
10^5	5.4	1.5	1.3	5.7

Table IV. ^{239}Pu decay heat error estimate
(one thermal fission - one standard deviation

Cooling time (s)	Origin of the error: yields	half-lives	energies	Total (%)
10^0	7.0	4.2	5.6	9.9
10^1	5.2	4.7	4.0	8.0
10^2	4.5	4.3	4.0	7.4
10^3	4.2	0.7	3.0	5.2
10^4	4.1	0.6	1.	4.2
10^5	6.7	0.8	1.1	6.9

At short times after fission, up to 100 seconds, the three types of data contribute roughly by the same amount to the error, whereas for longer times the error coming from yields is predominant. These observations are of course strongly dependent upon the validity of the error values adopted in the calculation.

An analysis of the error estimate can be done by referring to Appendix 1/a to 1/f which presents the detailed nuclide dependent sensitivities and associated errors. The list is limited to the isotopes giving rate to sensitivity factors greater than 0.02. To the previous error estimate must be added firstly the systematic energy lack due to nuclides with unknown properties which have been ignored : 1.7 % of fission products for ^{235}U, 1,9 % for ^{239}Pu, and secondly the eventual consequences of the odd-even effect in independent yields : multiply even Z isotopes by 1.20, divide odd Z isotopes by 1.20, normalize to chain yield.

The first systematic error has been estimated by evaluating half-lives for the ten nuclides : ^{86}As, ^{99}Sr, ^{100}Y, ^{101}Y, ^{103}Zr, ^{104}Nb, ^{111}Ru, ^{147}Ba, ^{150}Ce, ^{151}Ce, which represent about 80 % of the total production of ignored nuclides. Half-lives were derived from correlations with Q taken from TASAKA[10]. The Q values were taken from GARVEY[9] whereas the average beta plus gamma decay energy was assumed to be 60 % of Q. Hand calculations of the total energy released by these isotopes provide a rough indication of the underestimate of the decay heat due to ignored fission products. An effect of about 6 % at one second and 1 % at ten second cooling time has been found for ^{235}U. Corresponding values for ^{239}Pu are respectively 6 % and 2 %. The effect vanishes very rapidly, 6 over the 10 evaluated half-lives having values lower than 3 seconds. The effect is then multiplied by 1.25 to account for the other neglected nuclides. It has been then assumed that the uncertainty in the systematic error estimate could be ± 50 %.

The other cause of error which has been investigated concerns the odd-even effect in independent yield ; instead of having included it in the independent yield library, as in the Meek and Rider compilation, its action on the decay heat has been calculated by using the yield sensitivity factors. Applying the odd-even effect to the independent yields : multiplying even Z isotopes by 1.20, dividing odd Z isotopes by 1.20 and normalizing to chain yields gives the following results : diminution of the decay heat by 4 % at 1 second, augmentation of the decay heat by 1 to 2 % within 10 to 10^5seconds.

The total uncertainty in the decay heat can therefore be estimated by the following way :

Lower bound = calculated decay heat
-2 relative standard deviations
+0.5 energy lack estimate

Upper bound = calculated decay heat
+2 relative standard deviations
+1.5 energy lack estimate
+ even-odd effect.

The calculated decay heat functions and their uncertainty range estimates are reported in Table V for ^{235}U and Table VI for ^{239}Pu. The credibility of theoretical uncertainty calculations will certainly increase in the future by improving nuclear data error files with a comprehensive analysis of experimental errors, especially in detecting systematic errors. In the mean time it is worthwhile to compare the theoretical decay heat uncertainty calculations to experimental integral measurements and to encourage further integral benchmark experiments.

In this study we have confined ourselves to the comparison with decay heat functions deduced from calorimetric measurements of the total beta and gamma power released by ^{235}U [11] and ^{239}Pu[12] samples after various irradiations times (100, 1000, 5000 seconds). Experimental results are available for cooling times greater than 100 seconds. The errors quoted for these results vary from 9 % at 100 seconds cooling time to 6 % at 1000 seconds onwards. The unfold decay heat value at 100 seconds is much sensitive to the inaccuracy of the heat transfer function of the calorimater and presents the highest error value. The experimentally determined decay heat functions are compared to theoretical ones in Tables V and VI and figures 1 and 2. This comparison shows that the deviations between calculations and measurements are consistent with the uncertainty of both calculations and experiments. In the case of ^{239}Pu however, the agreement between calculations and measurements is less good,the measured values lay in general outside the uncertainty range estimate of the theoretical decay heat as shown in fig.2. No explanation has yet been found to this discrepancy ; this point is now under study, both from the point of view of the nuclear data and by analyzing the possible causes of experimental errors.

Table V. ^{235}U decay heat uncertainty range (one thermal fission)

Cooling time (s)	Calcul. decay heat (MeV/s)	Uncertainty estimate (%)	Measured decay heat (MeV/s)	Exp. error (%)	Meas-Calc. Calc. (%)
10^0	6.00^{-1}	(-11.4,+22.0)	-		
10^1	1.27^{-1}	(-12.5,+16.5)	-		
10^2	1.31^{-2}	(-13.7,+15.4)	1.11^{-2}	(9.)	- 15.3
10^3	8.90^{-4}	(- 8.5,+11.0)	9.49^{-4}	(6.)	+ 6.6
10^4	5.67^{-5}	(- 4.9,+ 6.9)	5.89^{-5}	(6.)	+ 3.9
10^5	2.58^{-6}	(-11.5,+12.4)	2.67^{-6}	(6.)	+ 3.5

Table VI. ^{239}Pu decay heat uncertainty range (one thermal fission)

Cooling time (s)	Calcul. decay heat (MeV/s)	Uncertainty estimate (%)	Measured decay heat (MeV/s)	Exp. error (%)	Meas-Calc. Calc. (%)
10^0	4.55^{-1}	(-15.9,+27.5)			
10^1	9.99^{-2}	(-14.7,+21.4)			
10^2	1.16^{-2}	(-14.9,+15.8)	1.03^{-2}	(9.)	- 11.2
10^3	8.50^{-4}	(-10.5,+12.4)	9.70^{-4}	(6.)	+ 14.1
10^4	4.55^{-5}	(- 8.5,+10.5)	5.13^{-5}	(6.)	+ 12.7
10^5	2.42^{-6}	(-13.7,+14.2)	2.67^{-6}	(6.)	+ 10.3

Error on decay heat following a long irradiation time

Sensitivity calculations have also been performed in the case of a 900 days irradiation at a constant fission rate of one fission per second. The errors have been estimated by the same procedure as in the instantaneous fission case. Tables VII and VIII show the repartition of the errors due to the different data types.

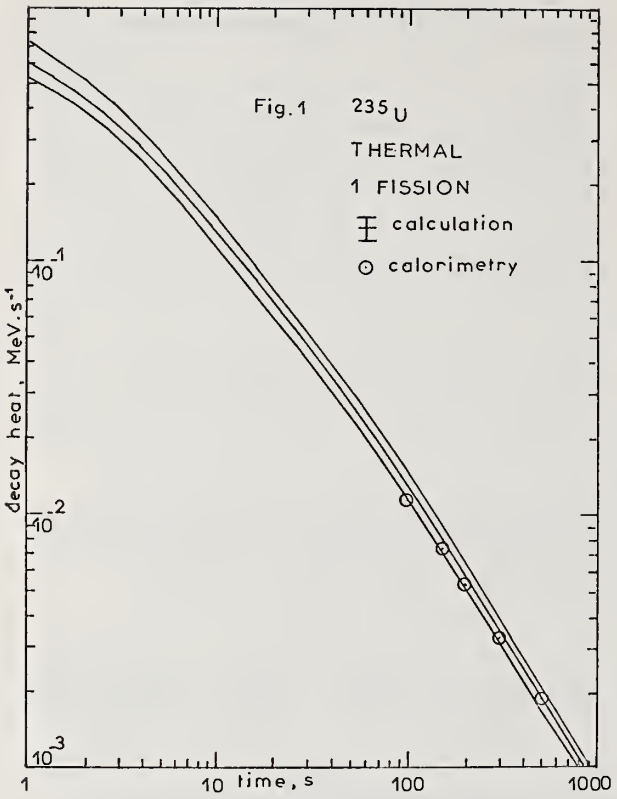
Fig.1 ^{235}U
THERMAL
1 FISSION
calculation
calorimetry
decay heat, MeV.s^{-1}
10^{-1}
10^{-2}
10^{-3}
1
10
time, s
100
1000

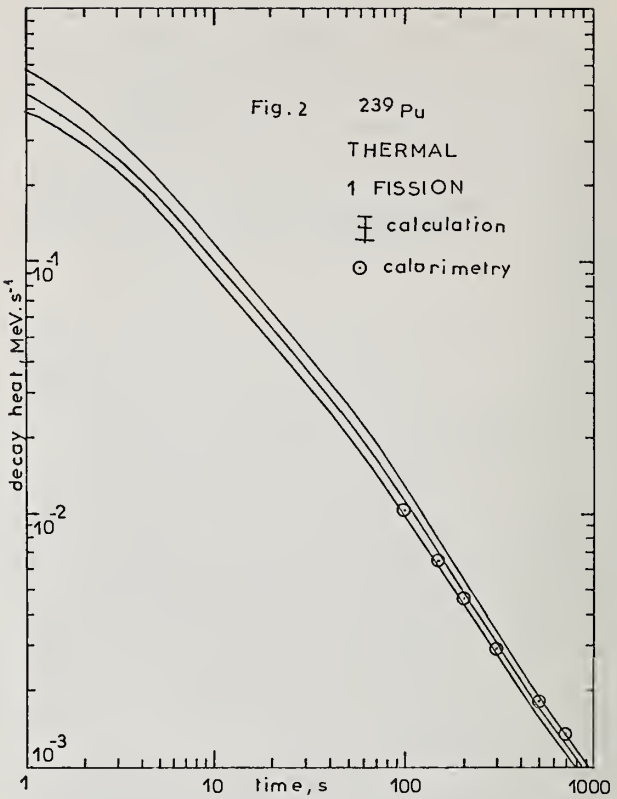
Fig.2 ^{239}Pu
THERMAL
1 FISSION
calculation
calorimetry
decay heat, MeV.s^{-1}
10^{-1}
10^{-2}
10^{-3}
1
10
time, s
100
1000

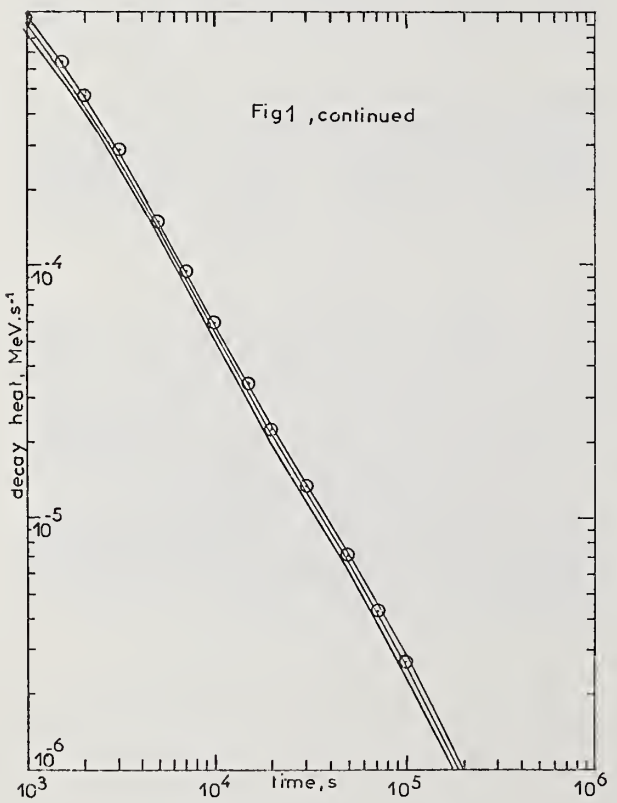
Fig1 ,continued
decay heat, MeV.s^{-1}
10^{-4}
10^{-5}
10^{-6}
10^3
10^4
time, s
10^5
10^6

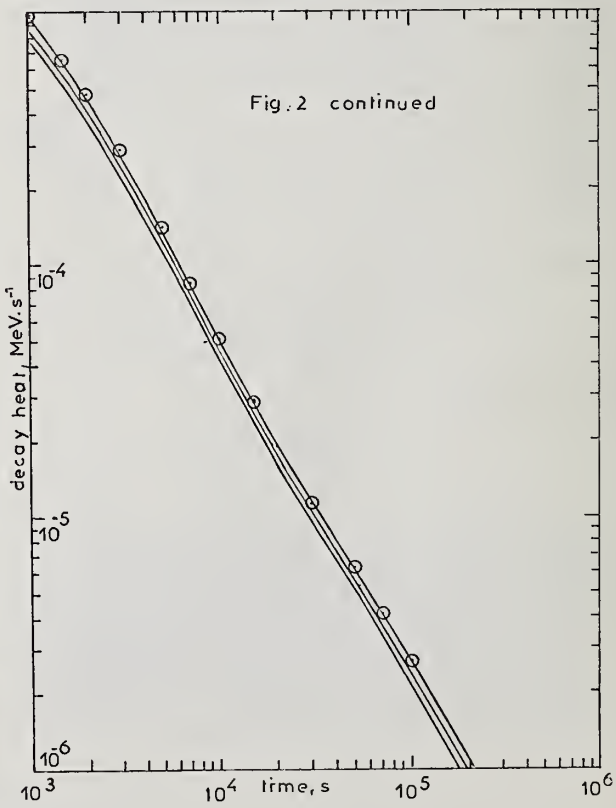
Fig.2 continued
decay heat, MeV.s^{-1}
10^{-4}
10^{-5}
10^{-6}
10^3
10^4
time, s
10^5
10^6

Table VII. ^{235}U afterheat error estimate (constant fission rate - one standard deviation)

Cooling time (s)	Origin of the error: Yields	Half-lives	Energies	Total (%)
10^0	2.6	0.4	1.7	3.1
10^1	2.6	0.8	1.6	3.1
10^2	2.5	0.8	1.2	2.8
10^3	2.4	0.7	0.8	2.6

Table VIII. ^{239}Pu afterheat error estimate (constant fission rate - one standard deviation)

Cooling time (s)	Origin of the error: Yields	Half-lives	Energies	Total (%)
10^0	3.3	0.3	1.9	3.9
10^1	3.2	0.7	1.9	3.8
10^2	3.2	0.6	1.6	3.6
10^3	3.4	0.2	1.0	3.6

The errors are significantly lower than in the previous case because the relative contribution of short lived nuclei is much lower now. In particular the errors in half-lives have much less influence than the errors in the two other data types. Appendix 2/a to 2/f show the list of nuclides important for the afterheat, the corresponding sensitivities (>0.02) and associated errors. The error due to ignored nuclides has been found only significant at 1 second cooling time where it is of the order of + 1 %. The influence of the even-odd effect in the independent yields is everywhere lower than + 2 %. The total resulting uncertainty ranges calculated by the same way as for one fission are shown in Tables IX and X.

Table IX. ^{235}U afterheat uncertainty range . (constant fission rate : 1 fission/s - duration : 900 days)

Cooling time (s)	Calcul. after-heat (MeV/s)	Uncertainty range (%)	Shure (ANS-5) evaluation (MeV/s)	Shure-pres.work(%) present work
10^0	11.30	(-6.7,+8.1)	12.5	10.6
10^1	9.04	(-6.3,+7.5)	10.0	10.6
10^2	5.98	(-5.6,+6.7)	6.62	10.7
10^3	3.56	(-5.2,+6.9)	3.70	3.9

Table X. ^{239}Pu afterheat uncertainty range (constant fission rate : 1 fission/s - duration : 900 days)

Cooloing time (s)	Calculated afterheat (MeV/s)	Uncertainty range (%)
10^0	9.68	(-7.2, +9.8)
10^1	7.95	(-7.5, +8.7)
10^2	5.35	(-7.2, +8.1)
10^3	3.20	(-7.2, +8.6)

In Table IX is given for comparison, the evaluation of the total afterheat for an infinite irradiation, proposed as standard by the ANS-5 subcommittee[13]. It is shown that this evaluation is roughly 10 % higher than calculational results obtained here below 100 seconds and does not fall into the uncertainty range estimate which is + 8 % at most.

Conclusion

From the comparison between calculations and calorimetric measurements in the cooling time range 10^2 to 10^5 it appears that the error estimate for the decay heat is not unrealistic. The contribution of this time region to the integral afterheat following a long operation time is respectively 45 % at 1 second, 56 % at 10 seconds and 84 % at 100 seconds cooling time, as found when integrating the decay heat function over the irradiation time. This kind of benchmark experiment is therefore capable of furnishing a significant test of the calculational methods in the region of interest for reactor safety problems. However it is necessary to complete them by measurements down to a few seconds after one fission. It is urgent, on the other hand, to understand the reasons why the calculated decay heats are systematically lower than the measured ones, by about 5 % for ^{235}U and 12 % for ^{239}Pu. Although there is not yet a sufficient proof of that, it is likely to think that the Shure's evaluation of the ^{235}U afterheat, which is 10 %higher than the calculations, is reasonably conservative and therefore needs no supplementary 20 % safety margin. Given the economical consequences that would result from confirming this assumption, it is payfull to continue our investigations in the fission product nuclear data field and especially to obtain reliable error values for the independent yields from thermal fission of ^{235}U, ^{239}Pu and higher plutonium isotopes.

References

1. M. Lott, Review paper 15, IAEA Panel on Fission Product Nuclear Data, Bologna, november 26, 1973
2. R. de Tourreil, note CEA.N 824 - 1967 -
3. C. Devillers et al, Bibliothèque de données relatives aux produits de fission, IAEA-SM-170/63 - 1973 -
4. M.E. Meek and B.F. Rider , Compilation of Fission Product Yields, NEDO-12154-1, January 1974 -
5. To be published
6. C. Devillers, Review paper 4, IAEA Panel on Fission Product Nuclear Data, Bologna, november 26, 1973
7. B. Barré, R. de Tourreil, Energie moyenne émise par les nuclides β instables, note CEA.N 1285 - 1970 -
8. A.H. Wapstra, N.B. Gove, Nuclear Data Tables 9 - 1971 -
9. G.T. Garvey et al, Review of Modern Physics - Vol. 41, n° 4, Part 2 - 1969 -
10. Kanji Tasaka, Nobuo Sasamoto, Calculation of Decay Heat Power of Fission Products, Nuclear Science and Engineering, Vol 54, Number 2 - june 1974 -

11. M. Lott et al, Puissance résiduelle totale émise par les produits de fission thermique de ^{235}U, Journal of Nuclear Energy, Vol 27 - 1973 -

12. To be published

13. Proposed ANS Standard - Decay Energy Rates Following Shutdown of Uranium Fueled Thermal Reactors, ANS-5.1 - 1971 - (draft).

ANALYSIS OF THE ERROR IN FISSION PRODUCT ENERGY RELEASE
U235 THERM. INSTANTANEOUS FISSION

IRRADIATION TIME	0.0 S
COOLING TIME	1.0000 00 S
ENERGY RELEASED	5.957E-01 (MEV/S)
ERROR DUE TO YIELDS	4.680 %
ERROR DUE TO HALF-LIVES	3.464 %
ERROR DUE TO Q	4.705 %
TOTAL ERROR	7.486 %

NUCLIDE	SENSIVITY OF DECAY HEAT TO YIELD	SENSIVITY OF DECAY HEAT TO H-LIFE	SENSIVITY OF DECAY HEAT TO EBGM	ERROR ON DECAY HEAT DUE TO YIELD (%)	ERROR ON DECAY HEAT DUE TO H-LIFE (%)	ERROR ON DECAY HEAT DUE TO EBGM (%)
BR 90	0.021	-0.012	0.021	0.66	-0.10	0.72
KR 92	0.022	-0.015	0.017	0.09	-0.01	0.11
RB 92	0.039	-0.037	0.044	0.11	-1.64	0.19
RB 93	0.024	-0.023	0.026	0.07	-0.02	0.09
RB 94	0.060	-0.047	0.063	0.24	-0.07	1.03
SR 97	0.056	0.015	0.031	1.78	1.13	1.10
Y 97	0.063	-0.040	0.085	2.02	-0.29	2.51
Y 99	0.064	-0.015	0.050	2.04	-1.31	1.76
ZR 99	0.030	-0.023	0.042	0.48	-0.28	0.40
ZR100	0.021	-0.020	0.012	0.49	-0.11	0.41
NB100F	0.011	-0.014	0.021	0.71	-0.27	0.21
ZR101	0.037	-0.025	0.034	1.18	-0.37	0.87
ZR102	0.024	-0.008	0.013	0.78	-0.32	0.47
NB102	0.030	-0.032	0.041	0.57	-1.90	1.44
NB103	0.038	-0.012	0.037	1.21	-0.36	1.30
CS142	0.047	-0.030	0.049	0.19	-0.18	1.06
CS143	0.021	-0.013	0.021	0.23	-0.38	0.74

Appendix I-a

COOLING TIME 1.0000 01 S

ENERGY RELEASED	1.271E-01 (MEV/S)
ERROR DUE TO YIELDS	3.557 %
ERROR DUE TO HALF-LIVES	4.004 %
ERROR DUE TO Q	3.789 %
TOTAL ERROR	6.560 %

NUCLIDE	SENSIVITY OF DECAY HEAT TO YIELD	SENSIVITY OF DECAY HEAT TO H-LIFE	SENSIVITY OF DECAY HEAT TO EBGM	ERROR ON DECAY HEAT DUE TO YIELD (%)	ERROR ON DECAY HEAT DUE TO H-LIFE (%)	ERROR ON DECAY HEAT DUE TO EBGM (%)
BR 88	0.024	-0.016	0.028	0.19	-0.16	0.96
BR 89	0.020	0.010	0.020	0.32	0.02	0.69
KR 91	0.027	-0.008	0.023	0.05	-0.08	0.74
KR 92	0.029	0.014	0.033	0.12	0.01	0.32
RB 92	0.046	0.025	0.074	0.13	1.08	0.21
RB 93	0.041	0.006	0.046	0.11	0.00	0.16
RB 94	0.028	0.046	0.029	0.11	0.07	0.47
SR 95	0.025	-0.023	0.030	1.13	-0.25	0.67
SR 96	0.022	0.013	0.019	0.70	0.06	0.68
Y 98	0.043	-0.030	0.045	1.39	-3.01	1.56
Y 99	0.021	0.006	0.000	0.67	0.50	0.00
ZR 99	0.025	0.031	0.021	0.40	0.26	0.20
N8 99F	0.000	-0.018	0.025	0.01	-0.02	0.81
ZR100	0.083	-0.017	0.023	1.92	-0.09	0.86
NB100F	0.001	0.012	0.061	0.05	0.23	0.61
ZR101	0.033	0.015	0.007	1.05	0.25	0.18
NB101	0.014	-0.005	0.039	0.44	-0.04	0.65
NB102	0.017	0.026	0.025	0.54	2.10	1.03
TE135	0.025	-0.016	0.026	0.20	-0.18	0.92
I138	0.026	-0.000	0.027	0.21	-0.00	0.92
XE140	0.023	-0.013	0.021	0.19	-0.13	0.40
EA143	0.019	-0.012	0.030	0.21	-0.12	1.04

Appendix I-b

COOLING TIME 1.0000 02 S

ENERGY RELEASED	1.311E-02 (MEV/S)
ERROR DUE TO YIELDS	3.542 %
ERROR DUE TO HALF-LIVES	4.985 %
ERROR DUE TO Q	3.032 %
TOTAL ERROR	6.825 %

NUCLIDE	SENSIVITY OF DECAY HEAT TO YIELD	SENSIVITY OF DECAY HEAT TO H-LIFE	SENSIVITY OF DECAY HEAT TO EBGM	ERROR ON DECAY HEAT DUE TO YIELD (%)	ERROR ON DECAY HEAT DUE TO H-LIFE (%)	ERROR ON DECAY HEAT DUE TO EBGM (%)
SE 86	0.020	0.009	0.002	0.65	0.09	0.05
BR 86	0.010	0.002	0.029	0.66	0.02	0.26
BR 87	0.017	0.005	0.024	0.07	0.00	0.62
KR 89	0.020	-0.022	0.031	0.12	-0.01	0.08
KR 90	0.059	0.018	0.025	0.65	0.00	0.07
RB 90F	0.007	-0.033	0.047	0.06	-0.53	0.13
KR 91	0.038	0.008	0.000	0.08	0.08	0.00
RB 91	0.032	0.007	0.072	0.13	0.07	0.29
SR 94	0.024	-0.005	0.034	1.11	-0.00	0.22
SR 95	0.032	0.045	0.032	1.46	0.49	0.70
SR 96	0.028	0.001	0.000	0.90	0.00	0.00
Y 96	0.027	-0.020	0.058	0.88	-0.48	2.02
Y 98	0.045	0.04E	0.009	1.45	4.80	0.31
ZR 98	0.012	0.033	0.021	0.27	0.33	0.18
NB 98F	0.0	0.003	0.034	0.0	0.09	0.27
NB103	0.028	0.000	0.000	0.88	0.01	0.00
MO133	0.010	-0.001	0.029	0.31	-0.01	1.00
SB132F	0.023	-0.013	0.027	0.14	-0.21	0.65
TE135	0.008	0.023	0.008	0.06	0.25	0.28
I136F	0.043	-0.009	0.059	1.00	-0.09	0.23
I137	0.013	0.026	0.014	0.21	0.01	0.49
XE135	0.029	0.017	0.027	0.17	0.03	0.14
XE140	0.037	0.015	0.002	0.30	0.15	0.04
CS140	0.038	-0.003	0.074	0.15	-0.02	0.21
CS141	0.015	0.027	0.016	0.04	0.27	0.34
BA144	0.024	0.014	0.001	0.27	0.16	0.05
LA144	0.008	0.011	0.035	0.18	0.02	0.85

Appendix I-c

ANALYSIS OF THE ERROR IN FISSION PRODUCT ENERGY RELEASE
FU235 THERM. INSTANTANEOUS FISSION

IRRADIATION TIME	0.0 S
COOLING TIME	1.0000 00 S
ENERGY RELEASED	4.555E-01 (MEV/S)
ERROR DUE TO YIELDS	7.025 %
ERROR DUE TO HALF-LIVES	4.179 %
ERROR DUE TO Q	5.590 %
TOTAL ERROR	9.903 %

NUCLIDE	SENSIVITY OF DECAY HEAT TO YIELD	SENSIVITY OF DECAY HEAT TO H-LIFE	SENSIVITY OF DECAY HEAT TO EBGM	ERROR ON DECAY HEAT DUE TO YIELD (%)	ERROR ON DECAY HEAT DUE TO H-LIFE (%)	ERROR ON DECAY HEAT DUE TO EBGM (%)
RB 92	0.025	-0.022	0.026	0.79	-0.98	0.11
RB 94	0.031	-0.024	0.032	1.59	-0.04	0.52
SR 97	0.029	0.010	0.021	2.48	0.78	0.75
Y 97	0.078	-0.041	0.096	2.50	-0.29	2.70
Y 99	0.054	-0.013	0.042	1.72	-1.10	1.48
ZR 99	0.045	-0.042	0.055	1.44	-0.35	0.51
ZR100	0.025	-0.023	0.014	0.81	-0.13	0.48
NB100F	0.026	-0.023	0.03E	1.68	-0.46	0.37
ZR101	0.036	-0.024	0.032	1.14	-0.36	0.85
ZR102	0.025	-0.009	0.014	0.79	-0.32	0.48
NB102	0.061	-0.056	0.072	1.96	-3.30	2.54
NB103	0.087	-0.027	0.086	2.80	-0.92	3.00
CS142	0.047	-0.029	0.048	1.49	-0.17	1.04

Appendix I-d

ANALYSIS OF THE ERROR IN FISSION PRODUCT ENERGY RELEASE

PU239 THERM.	INSTANTANEOUS FISSION
IRRADIATION TIME	C.C S
COOLING TIME	1.CCCE 01 S
ENERGY RELEASED	9.954E-C2 (MEV/S)
ERROR DUE TO YIELDS	5.173 %
ERROR DUE TO HALF-LIVES	4.710 %
ERROR DUE TO Q	3.969 %
TOTAL ERROR	E.043 %

NUCLIDE	SENSIVITY OF DECAY HEAT TO YIELD	TO H-LIFE	TO EBCM	ERROR ON DECAY HEAT DUE TO YIELD (%)	DUE TO H-LIFE (%)	DUE TO EBCM (%)
RB 92	0.029	C.015	0.037	0.92	0.66	0.16
RB 93	0.023	0.CC4	0.024	C.74	0.CC	C.0E
RB 94	0.014	C.C22	0.C14	0.88	0.03	0.23
SR 95	0.021	-C.C17	0.023	0.67	-0.19	0.51
Y 98	0.045	-0.025	0.044	I.45	-2.93	I.53
ZR 99	0.036	C.C27	0.C23	1.14	0.3C	0.22
NB 99F	0.0C0	-0.021	0.03C	0.03	-0.03	0.56
ZR100	0.095	-0.019	0.026	3.C5	-C.II	0.91
NB100F	0.0C2	C.C17	0.C7I	0.12	0.32	0.7C
ZR101	0.031	C.CIE	0.0C7	0.98	0.27	C.17
NB101	D.C29	-C.0C9	0.053	0.92	-0.04	0.93
NB102	0.033	C.C58	0.D45	I.C6	3.3B	I.5E
MO103	0.C09	-C.021	0.023	0.22	-C.21	0.79
TE135	0.024	-0.C15	0.025	0.56	-0.17	C.8E
I138	0.020	C.CCC	0.C21	0.22	0.0C	0.72
XE140	0.023	-C.012	0.02C	0.18	-0.12	0.39
CS141	0.017	-C.016	0.021	0.55	-0.16	0.46
BA143	0.019	-0.012	0.028	0.45	-C.12	C.97

Appendix I-e

ANALYSIS OF THE ERROR IN FISSION PRODUCT ENERGY RELEASE

U235 THERM.	CONSTANT FISSION RATE (1 FISSION/S)
IRRADIATION TIME	7.776E C7 S
COOLING TIME	1.CCOE CO S
ENERGY RELEASED	1.117E 01 (MEV/S)
ERROR DUE TO YIELDS	2.569 %
ERROR DUE TO HALF-LIVES	C.362 %
ERROR DUE TO Q	I.696 %
TOTAL ERROR	3.100 %

NUCLIDE	SENSIVITY OF DECAY HEAT TO YIELD	TO H-LIFE	TO EBCM	ERROR ON DECAY HEAT DUE TO YIELD (%)	DUE TO H-LIFE (%)	DUE TO EBCM (%)
KR 90	0.026	C.CC0	0.011	0.2B	0.0C	0.03
RB 91	0.016	-C.CCC	0.02C	0.C6	-0.00	C.CE
RB 92	0.024	-C.CC2	0.C19	0.07	-0.10	0.08
SR 95	0.028	0.CC1	0.017	1.27	C.01	C.37
Y 96	0.010	0.CCC	0.021	0.33	0.00	0.73
Y 98	0.024	C.CC1	0.016	0.78	0.05	C.57
ZR100	0.021	0.DC0	0.006	0.49	0.00	0.21
XE140	0.023	C.CC0	0.007	0.18	0.00	0.13
CS140	0.021	-C.CC0	0.02C	0.09	-0.00	0.0E

Appendix II-a

COOLING TIME	I.CCOE 02 S
ENERGY RELEASED	1.162E-02 (MEV/S)
ERROR DUE TO YIELDS	4.490 %
ERROR DUE TO HALF-LIVES	4.340 %
ERROR DUE TO Q	4.044 %
TOTAL ERROR	7.439 %

NUCLIDE	SENSIVITY OF DECAY HEAT TO YIELD	TO H-LIFE	TO EBCM	ERROR ON DECAY HEAT DUE TO YIELD (%)	DUE TO H-LIFE (%)	DUE TO EBCM (%)
RB 91	0.020	0.CC4	0.031	0.64	0.04	C.12
SR 94	0.021	-C.CC4	0.024	0.49	-0.00	C.15
SR 95	0.024	0.030	0.021	0.76	0.33	0.47
Y 96	0.032	-0.C26	0.050	1.01	-0.42	I.76
Y 98	0.042	0.042	0.C08	1.34	4.17	C.27
ZR 9E	0.019	0.035	0.022	0.45	C.35	C.18
NB 98F	0.0	0.CC3	0.035	0.0	0.05	C.28
NB103	0.055	0.CC1	0.030	1.75	0.02	0.0C
MO103	0.037	-0.0C1	0.C71	0.86	-0.01	2.4E
TC103	0.000	-C.CC7	0.021	0.03	-0.07	C.34
MO104	0.030	-0.CC1	0.025	0.70	-0.0D	C.85
MO105	0.C38	0.020	0.036	1.22	0.20	1.27
MO106	0.020	0.CC9	0.00D	0.64	0.1E	0.01
TC106	0.C18	0.C27	0.C38	0.42	0.27	1.14
TC107	0.013	0.C21	0.C10	0.40	0.02	0.34
SB132F	0.027	-C.CI4	0.03C	0.66	-0.23	C.71
I136F	0.050	-C.CC5	0.061	1.60	-0.05	C.23
I137	0.012	0.024	0.013	0.40	0.01	0.46
XE137	0.012	-0.016	0.023	0.20	-0.00	C.15
XE139	0.C26	0.C15	0.C24	0.29	0.03	0.12
XE140	0.032	0.C13	0.C02	0.25	0.13	0.03
CS140	0.040	-C.0C2	0.072	1.29	-0.02	D.30
CS141	0.015	0.C26	0.015	0.48	0.26	0.32
LA144	0.007	C.CC9	0.027	0.23	0.01	D.66

Appendix I-f

COOLING TIME	I.CCOE 01 S
ENERGY RELEASED	E.920E 00 (MEV/S)
ERROR DUE TO YIELDS	2.559 %
ERROR DUE TO HALF-LIVES	C.766 %
ERROR DUE TO Q	1.5E3 %
TOTAL ERROR	3.131 %

NUCLIDE	SENSIVITY OF DECAY HEAT TO YIELD	TO H-LIFE	TO EBCM	ERROR ON DECAY HEAT DUE TO YIELD (%)	DUE TO H-LIFE (%)	DUE TO EBCM (%)
KR 89	0.023	C.CC1	0.016	0.14	0.0C	0.04
KR 90	0.030	0.0C3	0.011	0.33	0.00	0.03
RB 90F	0.003	C.CC1	0.022	0.03	0.01	0.06
KR 91	0.020	0.CC3	0.004	0.04	0.03	0.12
RB 91	0.018	0.0C2	0.024	0.07	0.02	0.09
SR 94	0.020	0.CC1	0.012	0.90	0.00	0.08
SR 95	0.C32	0.CC5	0.016	1.42	0.05	C.8E
Y 96	0.012	0.CC1	0.025	0.41	0.02	C.8E
Y 98	0.024	0.CC7	0.014	0.77	0.67	0.48
TE134	0.021	0.CC1	0.005	0.17	0.00	0.13
I134F	0.CC7	C.CC1	0.024	0.04	0.00	0.06
XE138	0.024	-C.0C0	0.011	0.C7	-0.00	0.04
CS138F	0.003	0.CC1	0.025	0.03	0.00	D.0B
XE139	0.022	0.CC2	0.010	0.13	0.00	D.05
XE140	0.025	0.CC3	0.C05	0.20	C.03	0.10
CS140	0.025	D.CC1	0.023	0.10	0.01	0.10

Appendix II-b

COOLING TIME	1.0C0E 02 S
ENERGY RELEASED	5.856E C0 (MEV/S)
ERROR DUE TO YIELDS	2.45) %
ERROR DUE TO HALF-LIVES	C.802 %
ERROR DUE TO Q	1.208 %
TOTAL ERROR	2.847 %

NUCLIDE	SENSIVITY OF DECAY HEAT TO YIELD	SENSIVITY OF DECAY HEAT TO H-LIFE	SENSIVITY OF DECAY HEAT TO EBCM	ERROR ON DECAY HEAT DUE TO YIELD (%)	ERROR ON DECAY HEAT DUE TO H-LIFE (%)	ERROR ON DECAY HEAT DUE TO EBCM (%)
KR 89	0.030	0.007	0.018	0.18	0.00	0.05
RB 89	0.002	-0.001	0.026	0.04	-0.00	0.04
KR 90	0.027	0.009	0.002	0.30	0.00	0.01
RB 90F	0.004	0.008	0.025	0.03	0.13	0.07
RB 92	0.020	-0.009	0.000	0.06	-0.40	0.00
SR 93	0.013	0.004	0.024	0.43	0.01	0.19
SR 94	0.023	0.007	0.007	1.05	0.09	0.05
Y 94	0.002	0.000	0.030	0.16	0.00	0.22
SR 95	0.028	0.008	0.002	1.27	0.08	0.05
Y 95	0.010	0.001	0.021	0.61	0.00	0.11
Y 96	0.012	0.013	0.024	0.38	0.20	0.83
SB132F	0.023	0.006	0.010	0.14	0.09	0.25
TE134	0.031	0.001	0.007	0.25	0.00	0.19
I134F	0.010	0.001	0.037	0.06	0.00	0.10
XE138	0.036	0.001	0.016	0.10	0.00	0.06
CS138F	0.004	0.002	0.038	0.05	0.00	0.12
XE139	0.022	0.006	0.003	0.13	0.01	0.02
XE140	0.021	0.002	0.000	0.17	0.02	0.00
CS140	0.026	0.013	0.014	0.10	0.13	0.06
LA140	0.000	-0.000	0.027	0.00	-0.00	0.05
CS142	0.023	-0.021	0.000	0.09	-0.12	0.00
LA142	0.001	-0.000	0.030	0.03	-0.00	0.06

Appendix II-c

COOLING TIME	1.0CCE 01 S
ENERGY RELEASED	7.945E C0 (MEV/S)
ERROR DUE TO YIELDS	3.233 %
ERROR DUE TO HALF-LIVES	C.724 %
ERROR DUE TO Q	1.889 %
TOTAL ERROR	3.814 %

NUCLIDE	SENSIVITY OF DECAY HEAT TO YIELD	SENSIVITY OF DECAY HEAT TO H-LIFE	SENSIVITY OF DECAY HEAT TO EBCM	ERROR ON DECAY HEAT DUE TO YIELD (%)	ERROR ON DECAY HEAT DUE TO H-LIFE (%)	ERROR ON DECAY HEAT DUE TO EBCM (%)
SR 95	0.023	0.003	0.011	0.74	0.03	0.24
Y 96	0.014	0.001	0.022	0.45	0.01	0.76
Y 98	0.022	0.006	0.012	0.71	0.58	0.41
NB103	0.022	0.000	0.000	0.71	0.01	0.00
MO104	0.026	0.001	0.024	0.35	0.02	0.84
MO105	0.027	0.003	0.009	0.61	0.01	0.30
SB132F	0.022	0.001	0.012	0.70	0.01	0.39
I134F	0.011	0.001	0.026	0.09	0.00	0.29
I136F	0.018	0.002	0.021	0.59	0.02	0.77
XE138	0.023	-0.000	0.010	0.19	-0.00	0.08
CS138F	0.004	0.001	0.023	0.25	0.00	0.04
XE139	0.020	0.002	0.009	0.22	0.00	0.07
XE140	0.022	0.003	0.005	0.17	0.03	0.05
CS140	0.027	0.001	0.023	0.86	0.01	0.10

Appendix II-e

ANALYSIS OF THE ERROR IN FISSION PRODUCT ENERGY RELEASE	
FU239 THERM.	CONSTANT FISSION RATE (1 FISSION/S)
IRRADIATION TIME	7.776E C7 S
COOLING TIME	1.CCCE C0 S
ENERGY RELEASED	9.687E C0 (MEV/S)
ERROR DUE TO YIELDS	2.323 %
ERROR DUE TO HALF-LIVES	0.334 %
ERROR DUE TO Q	1.933 %
TOTAL ERROR	3.858 %

NUCLIDE	SENSIVITY OF DECAY HEAT TO YIELD	SENSIVITY OF DECAY HEAT TO H-LIFE	SENSIVITY OF DECAY HEAT TO EBCM	ERROR ON DECAY HEAT DUE TO YIELD (%)	ERROR ON DECAY HEAT DUE TO H-LIFE (%)	ERROR ON DECAY HEAT DUE TO EBCM (%)
SR 95	0.021	0.001	0.011	0.68	0.01	0.25
Y 98	0.023	0.001	0.014	0.74	0.05	0.51
ZR103	0.022	0.000	0.006	0.71	0.00	0.22
NB102	0.023	0.004	0.015	0.72	0.21	0.53
NB103	0.025	0.004	0.005	0.81	0.11	0.19
MO103	0.013	-0.000	0.022	0.31	-0.00	0.76
MO104	0.022	-0.000	0.008	0.52	-0.00	0.27
MO105	0.024	0.000	0.013	0.76	0.00	0.45
I134F	0.009	0.001	0.022	0.07	0.00	0.06
XE140	0.020	0.000	0.006	0.16	0.00	0.12
CS140	0.023	-0.000	0.020	0.75	-0.00	0.08

Appendix II-d

COOLING TIME	1.CCOE 02 S
ENERGY RELEASED	5.351E C0 (MEV/S)
ERROR DUE TO YIELDS	3.203 %
ERROR DUE TO HALF-LIVES	C.614 %
ERROR DUE TO Q	1.552 %
TOTAL ERROR	3.612 %

NUCLIDE	SENSIVITY OF DECAY HEAT TO YIELD	SENSIVITY OF DECAY HEAT TO H-LIFE	SENSIVITY OF DECAY HEAT TO EBCM	ERROR ON DECAY HEAT DUE TO YIELD (%)	ERROR ON DECAY HEAT DUE TO H-LIFE (%)	ERROR ON DECAY HEAT DUE TO EBCM (%)
Y 94	0.004	0.000	0.023	0.26	0.00	0.16
SR 95	0.020	0.005	0.002	0.65	0.05	0.04
TC102F	0.0	0.000	0.023	0.0	0.00	0.61
MO104	0.030	0.005	0.005	0.69	0.04	0.16
TC104	0.003	0.000	0.027	0.19	0.00	0.65
MO105	0.025	0.008	0.004	0.81	0.08	0.15
TC105	0.010	0.002	0.020	0.32	0.01	0.52
SR132F	0.026	0.006	0.011	0.82	0.10	0.26
I132F	0.001	-0.000	0.026	0.04	-0.00	0.04
TE134	0.029	0.001	0.006	0.23	0.00	0.16
I134F	0.016	0.002	0.035	0.13	0.00	0.10
I135	0.020	0.001	0.022	0.16	0.00	0.05
XE138	0.034	0.001	0.014	0.27	0.00	0.05
CS138F	0.006	0.002	0.034	0.36	0.00	0.11
CS140	0.027	0.012	0.013	0.86	0.12	0.05
LA140	0.000	-0.000	0.027	0.00	-0.00	0.05
LA142	0.001	0.000	0.028	0.07	0.00	0.06

Appendix II-f

SIGNIFICANCE OF NUCLEAR DATA ON THE DEVELOPMENT OF THE LMFBR INDUSTRY*

N. C. Paik
Westinghouse Advanced Reactors Division
Madison, Pennsylvania 15663

The overall interaction of nuclear data, methods and nuclear performance predictions of an LMFBR is described. Areas of successful applications of the recent Evaluated Neutron Data File (ENDF/B) to an LMFBR design are shown to be numerous. Design areas where improvements in the Evaluated Neutron Data File would have significant impact on the development of the LMFBR industry are listed. Specific cross sections where improvements in the neutron data would be beneficial to the LMFBR industry are enumerated. In order to provide insight into why these developments are required, an application of nuclear data to the determination of the intrinsic neutron source strength in an LMFBR are described in relation to the Ex-Vessel Low Level Flux Monitor system design.

(Data, neutron, LFMBR, flux.)

Introduction

This conference on Nuclear Cross Sections and Technology provides a unique opportunity for the measurers, users and evaluators of neutron cross sections and related nuclear data to review the present status of data and project future cross section needs. The present and future impact on LMFBR industry is summarized in this paper from the point of view of a user in the LMFBR community. An engineering approach to correct the nuclear data and analyses method uncertainty is first described, which requires analyses of integral experiments in simulated critical assemblies of an LMFBR. The use of critical assembly analyses is illustrated to show how an LMFBR designer obtains biased nuclear predictions and associated uncertainties in these predictions. Design areas are listed where the applications of the Evaluated Neutron Data File (ENDF/B) are successful utilizing the bias factor approach. General areas of future as well as present concerns where one cannot use the bias factor approach are described. These are also related to the ecological impact study of LMFBRs and the commercialization of LMFBR. Five specific cross section needs of future significance are elaborated. Finally, an application of nuclear data to the buildup analysis of the actinides is discussed with respect to the waste management aspect and the importance of the intrinsic neutron source from the actinides.

Overall Interaction of Nuclear Data, Methods and Nuclear Performance

The interaction of nuclear data, methods and nuclear performance predictions of an LMFBR is of interest to the nuclear experimental physicists. A common engineering approach in the determinations of a biased nuclear performance and associated uncertainty is shown in Figure 1. Utilization of the microscopic neutron data file (such as the ENDF/B-III or IV) in the analysis of the various experimental results performed in a series of simulated critical assemblies, leads to the development of bias factors for LMFBR nuclear performance. These bias factors account for the combined errors due to nuclear data and analysis method. These biases are often applied directly to nuclear performance predictions in an LMFBR under the assumption that the power reactor is similar to a simulated critical assembly or a series of critical assembly mockups. Analyses of large numbers of the same experiments in the critical assembly mockups can also be used in a statistical evaluation of the uncertainty in the ratio of E/C (Experiment/Calculation). The overall uncertainty in the biased nuclear performance of an LMFBR should account for this uncertainty from critical assembly analyses and other possible sources of uncertainties due to dissimilitude between a power reactor and critical assemblies.

A method to determine the accuracy of control rod worth calculations is a good example to elaborate this simple engineering approach. The accuracy of control rod worth predictions is a combination of a ±8 percent uncertainty (2σ) in the bias factor deduced from GE analyses[1] of critical assembly experiments performed by Argonne National Laboratory[2], a ±3 percent uncertainty due to the potential B^{10} loading variations, and a ±4 percent uncertainty due to extrapolation of critical assembly results to a power reactor design.

Design Areas of Successful Application Of The Recent ENDF/B Data

Refinements of the ENDF/B files based on the old and new microscopic cross section measurements make it possible for reactor designers to accurately predict the nuclear performance of an LMFBR using its bias factors and associated uncertainties. Table 1 shows the successful design applications of the ENDF/B data to an LMFBR design in the areas of Doppler effect, fuel enrichment specification, control enrichment specification, sodium voiding reactivity, fuel depletion and fission product worth, and power distribution.

South Eastern Fast Oxide Reactor (SEFOR) provided the first full scale experimental physics test to verify the negative Doppler effect utilizing mixed plutonium-uranium oxide fuel. Doppler sample tests and analyses of the experiments in ZPR-3, ZPR-6 and ZPPR critical assemblies were conducted for years at ANL. These experiments in addition to SEFOR tests confirmed the successful LMFBR Doppler prediction of the ENDF/B data file. This success of the ENDF/B is of course due to major contributions by nuclear experimental physicists (See Table 2) who made nuclear data available. The fuel and control enrichments can be specified with adequate margin for data uncertainty in designs of an LMFBR. In the future, where specific critical assemblies are not utilized, the LMFBR design will require further improvements in cross sections of fissile isotopes to more accurately predict the reactivity worth of the fuel and control material. The resolution of the high versus low fission cross sections of both ^{235}U and ^{239}Pu below the neutron energy of 100 keV is necessary for the LMFBR community to use the ENDF/B file with confidence in predicting nuclear performance parameter such as breeding ratio and in calculating the important safety parameter such as sodium void reactivity. Areas of fuel depletion and fission product worths, and power distribution calculation are thought to be adequate in the designs of an LMFBR.

*Work performed under U.S. ERDA Contract AT(11-1)-3045, Task 12.

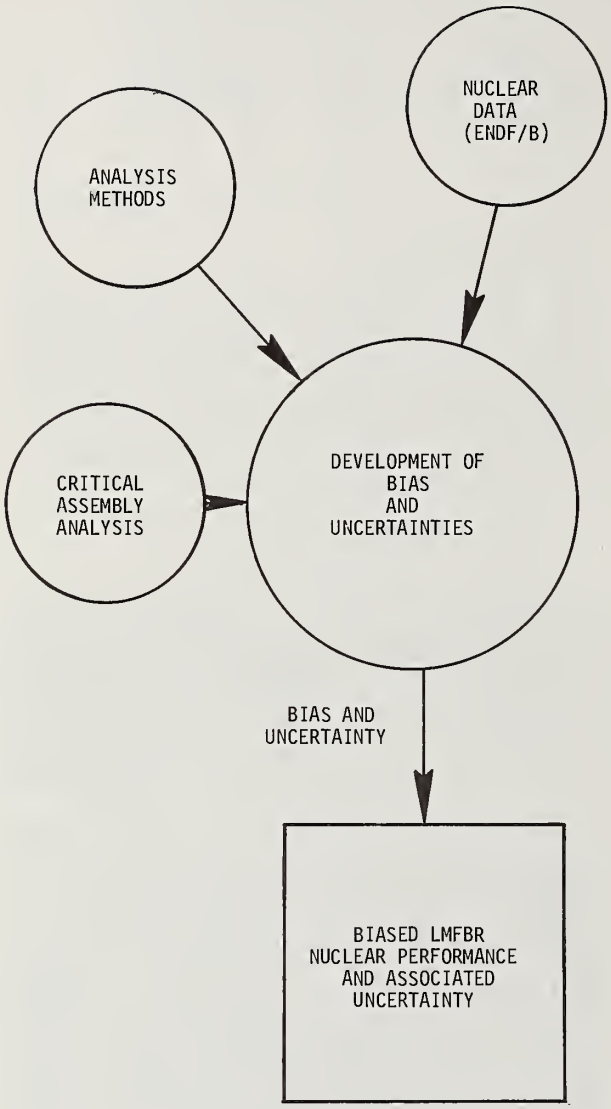

FIGURE 1

INTERACTION OF NUCLEAR DATA, METHODS AND NUCLEAR PERFORMANCE

TABLE 1

AREAS OF SUCCESSFUL DESIGN APPLICATION OF THE ENDF/B DATA

- DOPPLER EFFECT
- FUEL ENRICHMENT SPECIFICATION
- CONTROL ENRICHMENT SPECIFICATION
- SODIUM VOIDING REACTIVITY
- FUEL DEPLETION AND FISSION PRODUCT WORTH
- POWER DISTRIBUTION

TABLE 2

EXPERIMENTS AND MAJOR CONTRIBUTORS WHICH HAVE LED TO SUCCESSFUL LMFBR DOPPLER PREDICTIONS

EXPERIMENTS

- SEFOR TESTS (GE, AEC, KFK)
- DOPPLER SAMPLE TESTS AND ANALYSIS IN ZPR-6-7, ZPPR-2 and ZPR-3 (ANL)

MAJOR CONTRIBUTORS

ASGHAR, M. ET AL, NUCLEAR PHYSICS, 85,305 (1966),

BOLLINGER, L.M. ET AL, PHYSICS REV., 171, 1293 (1968),

CARRARO, G. ET AL, NUCL. DATA FOR REACTORS, VOL. 1, IAEA (1970) AND CONF-710301, 701 (1971),

RAHN, F. ET AL, PHYS. REV., 6C, 1854 (1972),

ROHR, G. ET AL, NUCL. DATA FOR REACTORS, VOL. 1, IAEA (1970),

DE SAUSSURE, G. ET AL, ORNL-TM-4059 (1973),

FRIESENHAHN, S.J. ET AL, GA-10194, JUNE (1970),

MENLOVE ET AL, NUCL. SCI. ENG. 33,24 (1968),

MOXON, AERE-R6074 (1969),

AND OTHERS.

Design Areas Where Improvements in the Evaluated Nuclear Data Files Would Have Significant Impact

In the previous section, the present status of nuclear data is shown to be adequate when supported by critical experiments. However, further improvements are required to improve the data to a point where LMFBR designs can be accomplished without critical assembly experiments, such as in the PWR industry today. Furthermore, there are other important design areas where improvements in the ENDF/B files would have significant impact in LMFBR development. These areas of design application are shown in Table 3.

TABLE 3

DESIGN AREAS WHERE IMPROVEMENTS IN THE EVALUATED NEUTRON DATA FILE WOULD HAVE SIGNIFICANT IMPACT

- WASTE MANAGEMENT AND DISPOSAL OF ACTINIDES AND FISSION PRODUCTS
- HANDLING AND SHIPPING OF IRRADIATED CORE AND RADIAL BLANKET ASSEMBLIES
- INTRINSIC NEUTRON SOURCE STRENGTH IN AN LMFBR
- OPERATING COST AND BREEDING PERFORMANCE
- SEISMIC, RELIABILITY AND SAFETY EVALUATION OF REACTOR PRIMARY SYSTEM COMPONENTS
- DEVELOPMENTS OF LOW SWELLING ALLOY FOR FUEL DESIGN

These areas of designs and analyses are becoming increasingly more important in relation to the ecological impact study of an LMFBR, the significance of LMFBRs in the national energy program and the eventual required commercialization of an LMFBR. To be more specific, cross sections which could have a significant impact on the LMFBR performance are listed in Table 4. Nickel cross sections are important because the amount of nickel content in potential commercial alloys of future (such as A-286 and PE-16) with low irradiation induced swelling and reduced creep rate will vary from 26% to 43.5%, respectively. The present content is only 12 percent in SS-316. As indicated in Table 4, the cross sections of ^{241}Pu will also become important due to the introduction of light water reactor discharge plutonium in LMFBRs. Capture cross sections and inelastic scattering cross sections of ^{238}U need to be improved because the breeding performance of an LMFBR is sensitive to changes to these cross sections. The nu-bar, average number of neutrons per fission of ^{252}Cf which is one of important standards in determination of nu-bars of other fissile isotopes should be resolved as soon as possible. The one percent uncertainty in $\bar{\nu}(^{252}Cf)$ is already too large to take into design with an adequate uncertainty. Cross sections of Actinides ^{237}Np, ^{242}Cm, ^{244}Cm, ^{241}Am and ^{243}Am are of considerable importance in the study of waste management and disposal. Furthermore, the intrinsic neutron source strength in an LMFBR is directly related to the buildup and burnup of transuranium elements.

TABLE 4

SPECIFIC CROSS SECTION AREAS WHICH WILL HAVE SIGNIFICANT IMPACT ON LMFBR PERFORMANCE

- LOW SWELLING ALLOY DEVELOPMENT FOR FUEL AND CONTROL ASSEMBLY USE (NICKEL CROSS SECTIONS)
- PU-241 (USE OF LWR DISCHARGE PLUTONIUM IN AN LMFBR: ∿10% PU-241)
- U-238 CAPTURE & INELASTIC CROSS SECTIONS (LMFBR BREEDING PERFORMANCE)
- $\bar{\nu}$- ^{252}Cf (IMPACT ON OTHER FISSILE ISOTOPES)
- ACTINIDE CROSS SECTIONS: Np, Cm, Am (WASTE MANAGEMENT AND DISPOSAL)

Because of increasing importance of the actinides as waste products and source of intrinsic neutrons in an LMFBR, the application of nuclear data to actinide buildups is discussed in the next section.

Application Of Nuclear Data To Actinide Buildup And In Turn On The Design Of A Low Level Flux Monitoring System

The safe and reliable operation of an LMFBR depends in part on the successful development of a Low Level Flux Monitor (LLFM) system. Functional requirements of the LLFM system for an LMFBR are:
(1) Continuous and reliable monitoring of reactor neutron flux during the power escalation from shutdown conditions to low power level;
(2) Assurance during refueling that the reactor never approaches criticality by an erroneous assembly interchange, with adequate margin for the uncertainties of the measurements.

One of the most important items in the feasibility verification of an Ex-Vessel LLFM is the determination of intrinsic neutron source strengths as a function of cycles and number of assemblies charged during refueling. Nuclear information used in the development of the intrinsic neutron source strengths of a typical LMFBR (such as Clinch River Breeder Reactor Plant) is presented below.

The transmutation chains of the actinides are shown in Figure 2. This figure illustrates the decay and buildup chains of the actinides in an LMFBR. One group cross sections of these actinides and other transuranium isotopes are given in Table 5. Using these one group cross sections, the amounts of the actinides in an equilibrium core were determined. These material inventories at the end of an equilibrium cycle in a typical LMFBR of the CRBR size[3] are summarized in Table 6. Neutron sources in mixed oxide fuel per Kg of various nuclides shown in Table 7 were determined using the basic nuclear information of the half lives and energies of α decay of each nuclide, and the half lives for spontaneous fission and the number (ν) of neutrons per fission from ANL-5800. Finally the intrinsic neutron source strengths were obtained using the material inventory in Table 6 and the basic nuclear data from Table 7. These results are summarized in

Table 8 for the inner and outer core zones of an LMFBR. The intrinsic neutron source strength from blanket regions were found to be about one percent of the core neutron source strength. One concludes on the basis of results in Table 8, that the most important nuclides in the determination of the neutron source strength are ^{242}Cm, ^{244}Cm, ^{238}Pu, ^{240}Pu and ^{242}Pu in the order of decreasing significance.

TABLE 5

ACTINIDE CROSS SECTIONS IN BARNS
FOR FAST REACTORS

Nuclide	σ_f	σ_c
^{238}U	.04	.29
^{237}Np	.32	1.49
^{238}Pu	1.13	.47
^{239}Pu	1.83	.47
^{240}Pu	.37	.39
^{241}Pu	2.45	.41
^{242}Pu	.30	.32
^{241}Am	.39	.99
^{243}Am	.20	.65
^{244}Cm	.5	.4

Concluding Remarks

The successful development of the microscopic data files (ENDF/B) in the past ten years by the measurers, users and evaluators was the result of the excellent technical coordination by the Cross Section Evaluation Working Group under the policy direction and funding from the Physics Branch of RRD, with technical assistance from the National Neutron Cross Section Center at BNL. In the design areas of immediate concerns, the ENDF/B data are shown to be adequate. However, the commercialization of LMFBRs where design conservatism should be greatly reduced, will require modifications and improvements to the ENDF/B files. New or improved experiments with noble concepts should, therefore, continue by the measurers in order to resolve cross section discrepancies and to supplement the existing ENDF/B data files for future applications.

References

1. Stewart, S. L., A. K. Hartman, and S. C. Crick, "Evaluation and Analysis of ZPPR Assembly 3 Critical Experiments," GEAP-14001, UC-79e, April 1974.
2. ZPPR-3 Monthly Report for February 1973 ZPR-TM-134, Argonne National Laboratory, March 1972.
3. Paik, N. C., R. A. Doncals, and J. A. Lake, "Fuel and Blanket Management For the Clinch River Breeder Reactor," Westinghouse Advanced Reactors Division paper presented at the ANS Topical Meeting on Advanced Reactors in Atlanta, Georgia, September, 1974.

TABLE 6 REACTOR MATERIAL INVENTORY(Kg), EQUILIBRIUM CORE (EOC)

REACTOR REGION	Pu-238	Pu-239	Pu-240	Pu-241	Pu-242
Inner Core	7.00	4.22×10^{2}	1.71×10^{2}	4.45×10^{1}	1.97×10^{1}
Outer Core	8.30	4.63×10^{2}	1.97×10^{2}	5.74×10^{1}	2.34×10^{1}

	U-235	U-238	Cm-242	Cm-244
Inner Core	3.2	2.69×10^{3}	1.08×10^{-1}	4.7×10^{-2}
Outer Core	2.6	2.03×10^{3}	1.18×10^{-1}	4.1×10^{-2}

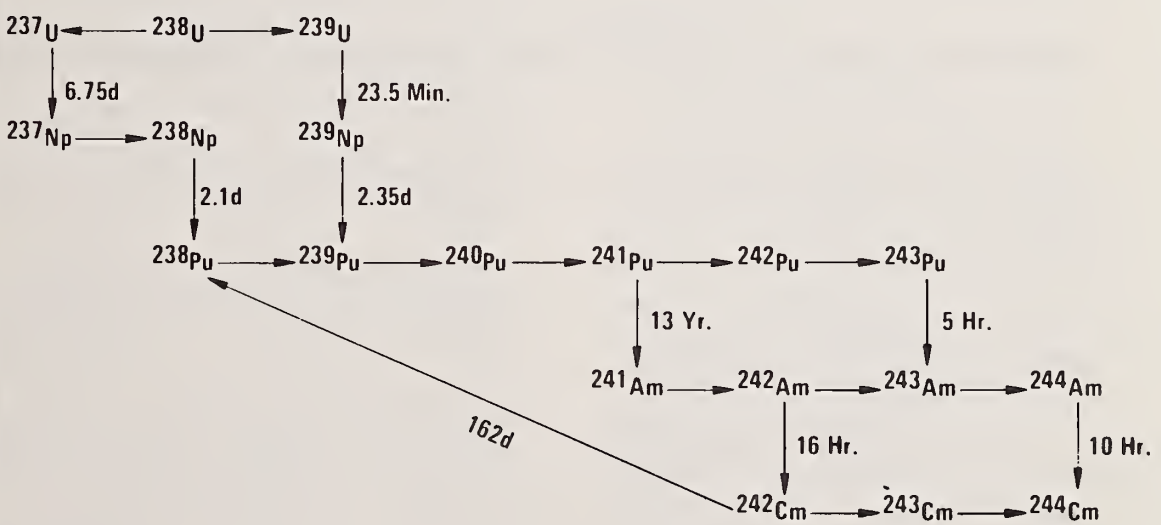

FIGURE 2 ACTINIDE TRANSMUTATIONS

TABLE 7 NEUTRON SOURCES IN MIXED OXIDE FUEL

NUCLIDE	(NEUTRONS/SEC) per Kg of NUCLIDE		
	(α,n) Reactions with Oxygen	Spontaneous Fission	Total
Pu-238	2.71×10^{7}	2.5×10^{6}	2.96×10^{7}
Pu-239	7.8×10^{4}	3.0×10^{1}	7.8×10^{4}
Pu-240	2.8×10^{5}	1.02×10^{6}	1.3×10^{6}
Pu-241	0.0	0.0	0.0
Pu-242	4.1×10^{3}	1.7×10^{6}	1.7×10^{6}
U-235	1.7	8.0×10^{-1}	2.5
U-238	2.0×10^{-1}	1.6×10^{1}	1.62×10^{1}
Cm-242	2.8×10^{9}	1.7×10^{10}	2.0×10^{10}
Cm-244	7.0×10^{7}	7.2×10^{9}	7.3×10^{9}

TABLE 8
NEUTRON SOURCE PER REACTOR REGION AND NUCLIDE EQUILIBRIUM CORE

	Neutron Source (n/sec.)				
REACTOR REGION	Pu-238	Pu-239	Pu-240	Pu-241	Pu-242
Inner Core	2.068×10^{8}	3.29×10^{7}	2.22×10^{8}	0.0	3.35×10^{7}
Outer Core	2.45×10^{8}	3.61×10^{7}	2.56×10^{8}	0.0	3.98×10^{8}
Percent Of Total	(6.9%)	(1.0%)	(7.3%)	(0.%)	(6.5%)
	U-235	U-238	Cm-242	Cm-244	
Inner Core	8.05	4.37×10^{4}	2.16×10^{9}	3.46×10^{8}	
Outer Core	6.58	3.29×10^{4}	2.35×10^{9}	2.99×10^{8}	
Percent of Total	(0.%)	(0.%)	(68.5%)	(9.8%)	

FAST REACTOR SAFETY*

Robert Avery
Reactor Analysis and Safety Division
Argonne National Laboratory
Argonne, Illinois 60439

The current state of knowledge with respect to the analysis of potential accident sequences in fast breeder reactors and the understanding of associated accident phenomena, as well as implications to reactor design, are reviewed.

(Safety, breeders, fast reactors, LMFBR, accidents, recriticality)

General Considerations

Safety is generally acknowledged to be one of the key items in feasibility considerations on the fast breeder reactor, if for no other reason, for reasons of public acceptance. In assessing the safety of any technology one must realize that safety is not an absolute, but that it must be related to a reasonable interpretation of how safe is safe enough.

In most other technologies the perception of safety generally held is based on experience. But reactors are properly thought to be different due to the potential of the low probability high consequence event. Much of my discussion will relate to considerations on the bounding accident.

My remarks will be made in the framework of the sodium cooled, oxide fueled fast breeder, or as generally referred to, the liquid metal fast breeder reactor (LMFBR). Most of the discussion will also be applicable to other fast breeder types, e.g., gas cooled (GCFR), or carbide fueled systems.

The fast breeder safety program has been developed within the framework of safety design and evaluation that evolved in this country over a period of years. This approach can be expressed in terms of three levels of safety. At the risk of oversimplification, Level 1 may be characterized as "building and operating it right"; Level 2 as the incorporation into the design of features to detect, prevent, and mitigate the effects of foreseeable malfunctions; and Level 3 as the provision of additional safety protection for the public in the event of severe hypothetical events arising from unforeseen low probability events and failures in Levels 1 or 2.

The objectives of the safety program, which includes both the development of the technology and the incorporation of this technology into the design, construction, and operation of fast breeder reactors, are the following:

a. Enable the designer to demonstrate that the probability of any major accident is negligibly small and that minor accidents and mishaps cannot escalate into a major occurrence.

b. Demonstrate that the containment, design, and site selection will be adequate to protect public health and safety.

c. Enable the designer to demonstrate that the probability of minor accidents is sufficiently small to not present any hazard to the operators of the plant. One must also sufficiently minimize the economic consequences of such minor events.

d. Develop improved engineered safety features and instrumentation.

e. Resolve public concern to the satisfaction of knowledgeable critics, or perhaps to put it better, obtain public acceptance. Actual safety is not enough. Also, a general perception of safety must hold.

The essential aspect of fast breeder reactor safety design is that the probability of significant release of radioactivity must be made vanishingly small. This assessment of safety must be one that is not only held to be true by the designers and operators, but one that is also generally accepted by regulatory bodies and responsible critics of nuclear power.

Reactor Characteristics Affecting Safety

The main relevant characteristics for LMFBRs include:

A small prompt neutron lifetime. This has been shown to be not important if there is a prompt negative feedback (which there is through the Doppler effect) and if there is no autocatalytic phase during disassembly (none have been found).

A small effective delayed neutron fraction. This has been shown to be not quantitatively significant.

A compact core with a high power density and a high plutonium content.

A coolant near atmospheric pressure, well below its boiling point, with excellent heat transfer properties, but the potential for thermal interaction with hot materials (fuel or clad) must be considered.

A chemically reactive coolant.

Inherent reactivity coefficients - Doppler and sodium void coefficients.
Doppler effect - its significance is firmly established; its magnitude does not matter too much if it is as large as believed certain for systems of interest.
Sodium void coefficient - more positive for larger systems and therefore more of a problem.

A core whose geometric configuration can be made more reactive by coolant, fuel, and clad relocations.

The last point should be emphasized. One key factor causing our concern over core meltdown is the recognition that the intact core is not in its most reactive configuration. Reactivity may be added from fuel or clad relocation, or from coolant voiding. Unlike water reactors, LMFBRs are very sensitive to dimensional changes or relocations. Reactivity additions, unless promptly offset by scram, tend to bring the

reactor to a threshold where it may continue to full core meltdown. Also, it is sometimes difficult to show a clear-cut subcriticality following an accident disassembly without a massive fuel removal. This raises the issue of recriticality.

In the event of a core disruptive accident, consideration of a possible recriticality subsequent to the initial core disruption, has received much attention recently. Detailed analyses of the early phases of hypothetical accidents indicate that the initial disassembly may not be severe enough to permanently disassemble the system and therefore the possibility of later recriticality arises. The major concern relates to establishing the upper limit of severity of the disassembly following the recriticality phase.

Structure of Fast Reactor Safety Field

In view of the complexity of safety considerations, it is obviously necessary to have some framework to organize the field. Generally we do safety assessment in two complementary ways; by way of accident delineation and by way of the study of accident phenomena. It is useful and it turns out to be possible to consider reactor safety in the framework of a reasonably small set of accidents. In each of the accidents we then follow the scenario through various phenomena. These phenomena may be reached through a branch point or thresholds. The various phenomena are frequently duplicated among different accidents. For example, such phenomena as fuel motion, clad motion, coolant motion, and fuel-clad-coolant interactions arise, in perhaps somewhat different conditions but also with generic resemblances, in the different accidents and, therefore, form suitable subjects for investigations somewhat independently of specific accident. Much of the safety work in actual performance is structured on these accident phenomena.

Among the small set of accidents that allow us to assess the safety of a fast reactor system, we generally include the loss of flow accident, the transient overpower accident, and the fuel element, including subassembly to subassembly, propagation accident. In order for such a small set of accidents to be reasonably representative for assessment of potential whole core accidents, it is necessary to treat these accidents in a generic way.

The scope of required safety studies is broad. Some of the contributing factors are:

(1) The scope of fast reactor safety must begin with and include all of the possible parameter ranges characterizing normal behavior. It must also address behavior characterizing all potential off normal conditions.

(2) In the accident scenario, we frequently find that we come to branch points where slight changes in either accident or design conditions could send us off into totally new regimes of phenomena. Considerations as to the effects of uncertainties thus attain much greater importance and further complicate the problem.

(3) We must follow accident sequences to their final end point of a coolable and subcritical configuration. This may carry us into additional areas in the accident scenario.

(4) Different size systems could lead to very different accident scenarios as could different fuel or coolant types.

Accident Sequences

In accidents, we look at things that can go wrong and the things that can be postulated to go wrong are unlimited. We, therefore, must categorize within generic classifications. One characteristic ingredient of most accidents is a mismatch between power and heat removal capability. One major example is the reactivity transient, from any cause, which causes the power to go up. The other major example is that heat removal capability is reduced, e.g., pump failure, pipe rupture, or flow blockage. One class of accident not necessarily involving overpower or undercooling is that of fuel failure, e.g., pin failure.

Another major categorization of accidents is between that of the whole core event and that of the local event, e.g., a subassembly event. A local event could, in principle, progress to a whole core event. Examples of whole core events are overpower transients or pump failure. An example of a local event is a subassembly flow blockage. An overpower event would not be a local event unless a small region of the core has the wrong enrichment. Another example of a local fault is a pin failure, which in principle could propagate to a full subassembly and perhaps even to the whole core.

Most of the accident analysis work is done with a mechanistic approach. In this approach we describe as realistically as we can the sequence of the accident as we believe it actually would occur under the hypothesized conditions. We seek experimental validation at each step of the way from both out-of-pile and in-pile experiments thus testing the validity of each of the relevant models used in the accident analysis. It is only after these individual parts, as well as some synthesized aspects of the entire accident sequence have been validated by integral experiments that we can assume some validity to the entire accident analysis methodology. For the most part, however, it would probably be excessively optimistic to believe that the mechanistic approach gives highly precise answers. In those instances where the geometry still remains intact, we have reason to believe that our methods may be quite good and, therefore, the mechanistic approach might be quite accurate, for example, in establishing a threshold of failure or a threshold of the onset of sodium boiling. When we get into the regime of disrupted geometry our uncertainties are so great that it is unreasonable to believe that the mechanistic approach can give quantitatively accurate answers. It is nevertheless still extremely useful for providing insight into the behavior of the system and for providing a tool for comparison of experiment with theory.

An alternative to the mechanistic approach is the bounding methodology. Here we do not necessarily attempt to trace the course of the accident as we believe it will occur but rather make extremely conservative assumptions which are perhaps not even related to possible physical behavior but are such that they give an upper bound to the severity of the accident. Here we must note that conclusions regarding worst cases may frequently require very subtle considerations. Because an accident that takes a branch point which at the moment seems to be in a less severe direction may, due to subsequent phenomena that it encounters, such as, for example, a later recriticality, turn out to have been worse.

A third approach, which has both overlapping and complementary features to the previous approaches is the probabilistic methodology. Here we introduce the concepts of probability for events happening and also

probability for various consequences resulting from specific events. We can use the latter probability distributions both for accounting for calculational uncertainties or for natural distributions in the results that might result from specific initial conditions.

The general approach relative to the bounding accident is to choose several hypothetical accidents to establish an envelope of design requirements covering unforeseen events. Typical accidents which might be considered are: (1) the transient overpower with failure to scram and (2) the loss-of-flow, e.g., loss of pump power and pump coastdown, with failure to scram. It should, of course, be noted that should the reactor scram or shut down, as it is designed to do with extremely high reliability, that the event would have been terminated benignly. Severe events can be postulated to occur only by such compounding of failures.

As an example, let us follow the accident sequence (as given by current analysis techniques) resulting from a pump coastdown without scram in a moderate sized fast reactor. (The moderate size manifests itself in the absence of a significant positive reactivity resulting from sodium voiding.) The sequence of events leads to a slow but progressive melting of the core. The specific sequence is as follows: The flow coasts down and perhaps 15 seconds later sodium starts to boil. The power has remained near full power in the absence of scram. After the sodium boils, the cladding melts, and then fuel begins to melt. The subassemblies successively progress through the stages of coolant voiding and melting, but the pressures generated are too low to cause a massive dispersal of molten fuel from the core region. The subassembly duct walls melt, and a growing region of molten fuel and steel begins to form in the hottest portion of the core. Enough local axial fuel dispersal has taken place by this time to lower the reactivity and to bring the reactor subcritical. Extended fuel dispersal is inhibited by blockages that form near the axial ends of the core because molten core materials refreeze in the colder regions near the axial ends. Continued decay heating causes further core melting and also causes the melted core materials to boil up and fill the available volume. If paths are available through the upper structure, material will begin to be ejected into the upper sodium pool. If the passages are blocked rapid melting attack on the upper structures will begin, allowing passages to be opened for ejection of molten core materials into the above-core sodium. This upward fuel removal should occur on a time scale that is short compared to the time required to melt down through the lower subassembly structure. If this ejection occurs as a result of the boil-up mechanism, it should have little or no damage potential. The materials will mix with the above-core sodium pool and come to rest upon the upper vessel surfaces where they may be coolable depending on the design. The remaining core materials will eventually come to rest on lower vessel surfaces where they also may be coolable. Needless to say, the accident sequence may be very dependent on design details.

Similar kinds of analyses can be made for other postulated accidents, such as transient overpower without scram. The details of the accident sequence would be quite different.

It should be kept in mind that at the current state of the art, a number of uncertainties still exist in the analysis. Much of the work being done in the safety field is aimed at removing these and similar uncertainties. We should also keep in mind that there may be major differences in the accident sequence between different sized systems or different fuels. In particular, the ability to cool the molten core debris in-vessel becomes progressively more difficult as the size of the core goes up (since the size of the vessel and surfaces within it on which core debris may be spread and cooled do not go up commensurately).

In the previous example, the analysis proceeded on the basis that disrupted core material would be basically dispersive and would not be prone to slump or compact causing recriticality. It is the current best judgment that the dispersive mechanism would dominate and that recriticality would not occur.

It is obvious that we need to obtain validated models for the various phenomena encountered in the fast reactor accidents. These include areas of fuel motion, clad motion, coolant motion, fuel-coolant interactions, and questions related to the sweeping out or conversely, the plugging or freezing of fuel and clad as they leave the core. The major analytical tool required relates to obtaining a methodology for handling neutronically and hydrodynamically extended motions of materials. The usually applied perturbation theory may not be applicable for neutronic calculations in largely distorted geometry. Similarly, the material motions have to be handled during fuel, coolant, and clad removals and re-entries. Frequently such re-entries would be occurring not under classical hydrodynamic forces but through such mechanisms as frozen material gradually heating up and dropping back into the system. Pressure driven motions due to fuel and steel interactions with sodium would also have to be accounted for, if present, although currently such is not believed to be the case.

An additional important required calculational tool relates to the analysis of the non-coherent behavior, of such items as sodium voiding and clad melting, within the fuel assembly as a result of temperature gradients within the subassembly. Such temperature distributions may be the result of the over-cooling of the outermost rows of the pins in the subassembly, or possibly relate to skewed power distributions over the subassembly.

Technology Areas

Most of the substantive safety research and development is performed in connection with the study of the technology areas related to phenomena that occur during hypothesized accident sequences. Only with an understanding of these phenomena can one hope to accurately describe the sequence of the accident and gain appropriate insight into it. The phenomena studied include the following:

Fuel Element Failure Propagation
Fuel and Clad Dynamics
Coolant Dynamics
Fuel Coolant Interactions
Post Accident Heat Removal
Structural Dynamics
Material Properties
Neutronics

Fuel Element Failure Propagation

This area is concerned with the basic phenomena that influence fuel failure and the propagation from pin to pin and possibly subassembly to subassembly. Information from both in-pile and supporting out-of-pile experiments provide explicit input to the development of analytical models needed to predict the effect of local abnormalities in liquid-metal-cooled fast

reactors. Included are: the determination of the influence of reactor design parameters and operational malfunctions on fuel failure; the measurement of the sensitivity and response of protective system sensors to the failure causative conditions; the investigation of fuel pin failure thresholds under abnormal operation; the propagation of single-pin failures to surrounding pins; and the potential propagation of damage beyond the boundaries of a single subassembly.

In this area the key remaining problems to be resolved relate to the issue of subassembly-to-subassembly propagation. We feel reasonably confident that pin-to-pin propagation or local fault propagation is not a serious concern, although some loose ends remain. However, the subassembly-to-subassembly problem remains with us. The key issue is whether such propagation can occur rapidly enough to pose a serious difficulty unless special instrumentation is inserted into the core to detect incipient subassembly blockage and meltdown prior to its complete occurrence.

Fuel and Clad Dynamics

This area is concerned with the basic phenomena involving fuel element failure and fuel and clad motion. An understanding is sought of the fuel failure thresholds and failure mechanisms which involve fuel and clad melting and subsequent motions, under power excursion and loss-of-flow conditions. Studies included are: (1) transient in-pile tests simulating reactor conditions, (2) the development of mathematical models of fuel failure, melting, and motion, and (3) transient experiments on fuel failure arising from local melting, power excursions, and loss of flow.

In the area of fuel dynamics perhaps the most important remaining problems are associated with the effects of fission gases entrapped within the fuel and their effect in providing early disassembly forces, particularly during short period excursions. We also need more information on reactivity changes associated with fuel movements.

Coolant Dynamics

This area is concerned with experimental and analytical studies of sodium boiling and two-phase flow. These are needed to describe void formation, coolant expulsion and re-entry, and pressure generation during reactor accidents. Tests are conducted with sodium and multi-pin geometries in test sections specifically designed to mock up reactor subassembly geometries.

In this area the main problems relate to the phenomena associated with the early onset of boiling and its propagation throughout the subassembly. Such phenomena related to the onset of boiling may be much more important in very large systems where the first void creates a significant reactivity effect that could profoundly affect the accident sequence. Another outstanding problem in coolant dynamics relates to the understanding of the combined and interacting effects of boiling and concurrent fission gas release from the fuel pins.

Fuel Coolant Interactions

A physical mechanism has been proposed and experimentally verified which provides for necessary conditions or requirements for large scale vapor explosions to occur. This mechanism indicates that oxide fuel and sodium under most reactor accident conditions will not produce large scale vapor explosions. However, the same mechanism indicates that the potential exists for molten steel and possibly other molten fuels (e.g., carbides or nitrides) to interact with sodium to produce a vapor explosion under some reactor accident conditions. Laboratory experiments on the basic mechanisms involved, and in-pile simulation tests under prototypic conditions need to be continued, in support of the development of phenomological models of coolant interacting with molten fuel and molten clad over the full range of conditions that may occur in both initiating and core-disruptive accidents. We also need to understand the behavior of molten fuel coolant interaction with respect to fuel sweepout, which is conjectured to occur in some transient overpower conditions.

Post Accident Heat Removal

The development and verification of mathematical models needed to describe the behavior of fuel, structural material, coolant and fission products subsequent to a hypothetical core-disruptive accident is an area of major concern. Sufficient information must be developed, through analysis and experimentation, to assure that effective means to contain the core debris following hypothetical accidents are either inherent or can be designed for. One is concerned whether the core debris can be retained within the primary system, and if not, within the containment system. Investigations included are: basic studies, out-of-pile simulations, in-pile simulations, the development of mathematical models, and engineering analyses of post accident containment and heat removal. The experimental investigations include studies of: molten-fuel motion, heat transfer, and interaction with structural materials and sodium; fission-product behavior and distribution between liquid, solid, and gaseous phases; molten-structural-material motion and heat transfer.

In this area the main current problems are to establish the practical considerations on core catcher materials and configurations to effectively preclude the continuing downward movement of molten materials through the reactor vessel and beyond.

Structural Dynamics

A quantitative understanding of the partition and absorption of sudden energy releases potentially associated with either initiating or core-disruptive reactor accidents is necessary. It is important to include the dynamic behavior of reactor structures in the analyses of the accident so that safety margins can be established. Included are: basic studies, code development, experimental simulations, and the development of mathematical models for structural effects and energy partition and absorption associated with potentially destructive energy releases. The codes yield material displacements, velocities, and accelerations; also pressures, densities, internal energies, and strains.

We feel reasonably confident about the understanding of the mechanical response of the reactor vessel to a given energy source term. However, considerable development has to be done in order to develop adequate codes for the response of the piping and other components such as the heat exchanger.

Material Properties

The determination and analysis of physical and chemical property information needed in fast reactor safety analysis also is essential. The current work is divided into two areas: (1) high temperature physical properties and equation-of-state of reactor materials (at temperature up to ~6000°K) and (2) chemical engineering data and modeling for post accident heat removal analyses. The first area provides information for use in the analysis of hypothetical core-disruptive

accidents; the second area deals with conditions that may arise after the core disruptive accident has terminated and decay heat removal from the system becomes necessary.

Neutronics - Sodium Void Reactivity Coefficient

Should all or part of a sodium cooled fast reactor become voided of sodium under accident conditions, the resulting reactivity changes could have a profound effect on the course of the accident. The essential point is that sodium removal in the central part of a (large) fast reactor adds reactivity. Sodium removal in the outer parts (axially and radially) of the core and in the blanket reduces reactivity. The reactivity history of the transient will thus crucially depend on the detailed space-time history of sodium voidage.

The neutronics problem consists of the accurate prediction of the reactivity change associated with any given voidage pattern. The problem is particularly difficult because of the great sensitivity of the reactivity coefficient to the details of the cross sections and because of the competition between the leakage and spectral components which are of opposite sign.

Neutronics - Doppler Effect

In a fast reactor transient, the Doppler coefficient is one of the major contributors to the safety of the system. It is effective both in terms of turning mild transients around and minimizing damage to the core or, in the case of very severe transients with violent disassembly, in very much reducing the destructive energy release. Its importance comes about primarily from the fact that in ceramic-fueled fast reactors, the Doppler effect is the only mechanism that yields an immediate negative reactivity feedback.

Some years back, there was not even complete certainty as to the sign of the Doppler coefficient. As long as there was an even remote possibility that the Doppler coefficient might be positive and hence act as an autocatalytic agent in an excursion, the Doppler effect posed a most serious problem. Both experimental and theoretical work have long since totally removed that possibility. It is now definitely known that in any fast breeder reactor composition of interest, the negative U^{238} Doppler coefficient will totally dominate the fissile component of the Doppler effect (which may or may not be positive, but in any event is extremely small in magnitude compared to the U^{238} component).

The main current problem with the Doppler effect is in predicting its magnitude with reasonable and proven accuracy. This is particularly important since it plays a quantitative role in safety analyses. Generally, it is not very important how large (negative) the Doppler coefficient is, providing it is known for sure that it is at least as large as some minimum value.

Some significant uncertainties relate to such questions as extrapolation to high temperature, mapping of the Doppler coefficient over the full core which might be complex due to insertion of control rods, various enrichments, buildup and burnup of fuel, presence of fission products, and spatial (as well as time dependent) temperature distributions.

Neutronics - Other Reactivity Coefficients

In addition to the Doppler and sodium coefficients, there are other reactivity coefficients that may be of importance to fast reactor design. One area relates to accurate means of establishing the power coefficient, including such contributions as may arise from small motions involved in fuel bowing or effects associated with the core restraint mechanism. Such reactivity effects are small but important. The magnitude and sign are determined by the details of small complex motions. Both the motions and also the associated reactivity effects may be very difficult to calculate.

Safety Approach and Impact on Design

There are various safety approaches under current discussion. Most of the debate centers on the relative emphasis to be given accident prevention relative to the emphasis to be given to accident mitigation. In assessment of causes, probability, and consequences of very rare events, a wide gray area of judgment as to appropriate conservatism is perhaps inevitable.

The incorporation of safety features usually involves tradeoffs. In those cases where features are clearly required and do not pose any major tradeoff questions there is little debate. The difficult problems arise when there is a tradeoff between safety and other factors, such as reliability, maintainability, performance, or economics, or even other considerations on safety. In the attempt to deal with a low probability event, one must always be on the lookout that we have not introduced a feature which perhaps causes problems in more likely events.

Some of the safety approach questions, as well as other considerations dependent on the status of accident analysis and accident phenomena, lead to a number of open design issues. This is perhaps the most important area in safety because it is most directly relates to the crucial issue of how we, in fact, build the reactor. As of now, a large number of uncertainties and differences of view exist in many of these areas.

a. Is an ex-vessel core catcher required?
b. Is an in-vessel core catcher required?
c. Is a sealed head compartment above the reactor vessel required?
d. Should one include specific design features against pipe rupture?
e. Should one have open or closed ducts enclosing the subassemblies?
f. Should an upper or a lower fission gas plenum be used?
g. What kind of core radial restraint system should be used?
h. Should the pumps trip on a scram signal?
i. What degree of subassembly instrumentation should be incorporated - should it be tied into the scram system?
j. What kind of diverse shutdown systems are required - should they all be dependent on ducts?
k. Should one design for a reduced sodium void coefficient in large systems?
l. What are the merits of alternate containment concepts - containment vs. confinement?

All of the above items may involve tradeoff considerations within the safety area, or with other considerations, e.g., economics or operational feasibility.

Conclusions

It is not my purpose here to argue the broad issue of the safety of the fast breeder reactor. However, it is certainly true that all the studies to date tend to show that accident related events are more benign than one might pessimistically conjecture. These studies support the conclusion that fast breeder reactors are safe by any reasonable definition of "safe."

There are a number of issues remaining, however. The solutions for many of these issues must evolve with the technology. The real question, I believe, is not whether fast breeder reactors are safe, but rather how far one must go, and pay, for protection against progressively more improbable events.

With respect to the subject of this conference, fast reactor safety is certainly a related field which rests in an important way on nuclear cross section technology, as it does also on a number of other disciplines and technologies. It is the neutronic aspects of the problem that produce the driving forces in most of the accident sequences and phenomena we study. The required neutronic calculations are frequently much more involved than those associated with more normal reactor operation. This is a result of the much more complex, time dependent geometries that may be involved. These calculations fully tax the current state of the art of reactor physics and cross section technology. Except possibly in the areas of the Doppler effect and the sodium void coefficient, I do not believe that cross section information deficiencies, play a significant limiting role in the state of our knowledge of fast reactor safety. This is clearly the result of the much more advanced state of the cross section field relative to the other technologies we encounter in fast reactor safety.

---

*Work supported by the U. S. Energy Research and Development Administration.

AFTER P H E N I X , WHAT IS THE IMPORTANCE OF NUCLEAR DATA PROGRAMS FOR THE F B R DEVELOPMENT ?

J.Y.BARRÉ [*] , J.BOUCHARD [**], J.P.CHAUDAT [*]

[*] C E A / C.E.N.CADARACHE

[**] C E A / C.E.N.FONTENAY-AUX-ROSES

FRANCE

In the fast reactor physics approach chosen in FRANCE, the integral experiments serve as a reference. The significance of differential nuclear measurements, in this philosophy, is presented.
The programs carried out on critical facilities and operating fast power reactors up to the end of this year will solve the last major problems arising from nuclear data inaccuracies for commercial plants. Results obtained on PHENIX during start-up and operation validate this approach. After the end of 1975, the nuclear data needs concern mainly safety, plant operation and fuel cycle analysis. Non-nuclear uncertainties largely dominate the effects of nuclear data uncertainties for these problems. Evaluations must be sufficient to reach the requested accuracies.

(PHENIX; nuclear data; FBR development; integral experiments)

1. INTRODUCTION

Fast neutron reactor physics in FRANCE aims at improving knowledge of parameters needed for the optimization, the safety and the operation of Plutonium-mixed-oxide-fuelled, sodium-cooled plants in the power range 250 up to 2000 MWe. Started in 1967, the program initially orientated towards PHENIX (250 MWe), in operation at full power since one year, is now focusing on SUPER-PHENIX. The construction of this 1200 MWe plant should start this year.

Major sources of uncertainties on calculated core and shielding design parameters were the inaccuracies of evaluated neutron data. To reach the design requested accuracies in the required times, the CEA has chosen an approach based on integral experiments performed either on critical facilities (MASURCA, HARMONIE, ERMINE), or on operating fast power reactors (RAPSODIE, PHENIX).

What are the CEA arguments to follow such a way and what will be the problems solved at the end of this year ? From the results previously obtained, it appears that no more major uncertainty caused by nuclear data inaccuracies will remain at the end of 1975. The three last important nuclear data problems concerning structural materials, higher Plutonium isotopes and fission products will be solved this year.

Results obtained on PHENIX during start-up (critical mass, power distribution, control rods, reactivity coefficients, shielding) and during a one-year normal operation (reactivity loss during burn-up) prove a posteriori the validity of this philosophy.

Then in the future, what are the results waited for from nuclear data programs ? No

more request of first priority for the design will exist. The remaining problems deal mainly with safety, plant operation and fuel cycle analysis. For these topics, the effects of nuclear data inaccuracies remain small and the broader accuracy requested should be reached from evaluations adjusted on integral experiments.

2. STATUS OF THE ART AT THE END OF 1975

2.1. CEA fast reactor physics approach

The main characteristic of this approach concerns the use of integral experiments as references for the improvement of the knowledge of design parameters. Among all the reasons justifying this choice [1], [2] the major one corresponds to the uncertainties caused by evaluated nuclear data inaccuracies, coming from differential measurements : these uncertainties were not acceptable for the designer. To reach the design accuracies requested in the required time did not allow to wait for a future possible improvement of differential nuclear data measurements : critical enrichments for PHENIX were defined in 1971, SUPER-PHENIX ones will have to be defined in the middle of 1976.

Integral experiments are planned at CEA to measure, in clean conditions, parameters directly related to the design requests in the range of interest. Due to the selected experimental conditions (fundamental mode) and to the improvements of the calculational methods, the uncertainties coming from the theoretical approximations remain negligible for these integral parameters. So the results of these experiments are used to adjust only nuclear data in the multigroup cross-section set. Then, the adjusted multigroup set together with the theoretical methods are applied to the design calculations.

The only problem lies in the transposition of integral experiments to the true design situation. The experiments are carefully selected to minimize the amplitude of that transposition and so, reduces the corresponding possible error sources.

Furthermore, this approach allows an accurate definition of the uncertainty on the calculated design parameters. These quantities are specially valuable for the design optimization (hot spot evaluation for example).

2.2. Program for PHENIX

The program of integral experiments have been initially oriented towards the range of 250 MWe plants for PHENIX. Comprehensive descriptions of this program have been previously presented [3] [4]. Only the main points related to nuclear data problems will be recalled here.

The reference program concerns the study of cell neutron balance parameters versus enrichment for Na lattices differing only by the fissile fuel, either Pu fuel (Z cores) or ^{235}U fuel (R cores). The variation of the averaged ^{238}U capture cross section versus the spectrum index r, typical of the whole cell spectrum, puts in evidence the direct contribution of R-Z program for power plants (Fig.1)

Complementary experiments have been performed to study specific problems of the neutron balance (Fig. 1) :

- .graphite program : variation of the graphite volumic composition for the same fuel pin either in Plutonium (PHUG cores) or in Uranium (HUG cores).
- .equivalence of graphite diluent and depleted UO_2 diluent for the neutron balance : PHRIXOS cores using PuO_2-UO_2 plates.
- .pure Uranium program in "K_∞=1" lattices with either metal fuel [5] (cores UK1, UK5, SCHERZO) or oxide fuel (cores OP10, OU10, OP20).

Three main parameters are measured in these lattices :

-material buckling by flux mapping and replacement method

-ratio total production over total absorption in zero leakage experiment

-reaction rate ratios in the fuel, by foils and detectors: fission rate ^{235}U,

^{238}U, ^{239}Pu, capture rate ^{238}U.
All these programs have been performed on the critical assembly MASURCA, the reactor source HARMONIE and the fast-thermal-coupled facility ERMINE.

Furthermore, irradiations performed on power reactors (OSIRIS, RAPSODIE) completed with mass spectrometry analyses give really accurate measurements of capture rate ratios for the main fissile and fertile isotopes [4]

Finally, together with measurements made available in the framework of cooperation with ZEBRA and SNEAK (Fig.1), all these integral results serve as references for the adjustment of the multigroup cross section set included in the Version III of the CARNAVAL system [6]. The production of this Version III has been made according to the standard BARRACA adjustment technique [6], [7]. The performances of this CARNAVAL III system can be summed up in the relative average discrepancies between experiments (E) and calculations (C) for all the integral results :

	$\frac{E-C}{C}$ %
Material buckling	: - 0.7 ± 0.8
Keff	: - 0.4 ± 0.4
σ_F $^{238}U/\sigma_F$ ^{235}U	: + 3.0 ± 2.5
σ_C $^{238}U/\sigma_F$ ^{235}U	: + 2.0 ± 3
σ_F $^{239}Pu/\sigma_F$ ^{235}U	: + 1.0 ± 2

Although some improvements could still be performed to reduce these small discrepancies (^{238}U fission), presently these figures correspond globally to the design needs.

As an example, the experimental and calculated (CARNAVAL III) fission rate ratios ^{239}Pu over ^{235}U are compared on Fig.2 versus the r spectrum index. Due to the large number of experimental results available, it can be clearly seen that a very high confidence level can be placed on the same calculated parameter for the design plants.

2.3. Results obtained on PHENIX

The start-up core of PHENIX and the operation parameters for each cycle are calculated with the standard CARNAVAL III system.

The experiments performed during the start-up represent the best check of the validity of the fast reactor physics approach. Comprehensive analyses of these start-up tests have shown the overall good agreement between calculations and experiments [8], [9]. The following points, more directly related to nuclear data, have to be outlined:

- The total discrepancy C/E on the start-up core was 1.4±1.5% on keff. This value has been corrected for various sources of errors, mainly discrepancies coming from calculated diluent reactivity worths. After these corrections, the discrepancy C/E directly related to the CARNAVAL III system is + 0.5 %.

- Calculated and measured power distributions agree to ± 2 %.

- Calculated control rod worths overestimate the experimental value by + 5 ± 5 %.

- Temperature and power reactivity coefficients, then the Doppler coefficient contributing to 50 % of these effects, appear to be correctly calculated.

This general agreement has been confirmed by the results of a one-year operation (4 cycles up to now). Furthermore, the reactivity loss during burn-up, a parameter strongly related to the internal breeding gain, is well predicted by calculation as shown for the first cycle on FiG. 7. The reactor operation up to now confirms the good agreement on this parameter which validates

the calculated detailed neutron balance.

2.4. New nuclear data problems related to SUPER PHENIX

For SUPER PHENIX (1200 MWe), three new problems coming from nuclear data inaccuracies exist : structural materials, higher Plutonium isotopes, fission products. The same integral approach applied to these problems will allow to solve them at the end of 1975.

2.4.1. Due to the better accuracy requested by the design at the SUPER PHENIX level, and to the increased volumic percentage of stainless steel in the core compared to PHENIX, an improvement of the stainless steel capture cross section is needed.

First, an evaluation work, based on capture measurements performed at CADARACHE, has been started for Fe, Cr and Ni.
First results are presented in companion papers to this Conference [10, 11, 12]
Second a program of integral experiments based on two types of techniques is being carried out. First reactivity worths of Ni, Cr, Fe and stainless steel samples are systematically measured by the oscillation technique in the centre of all lattices. Second the measurements of all the components of the cell neutron balance, material buckling or ratio production-absorption, and reaction rate ratios allow to define, by difference, the stainless steel capture rate. These experiments are performed in lattices with a very high stainless steel volumic content.

Such experiments are presently in progress in the fast-thermal coupled facility RB2 at BOLOGNE using micro-spheres of Carbone and ^{235}U mixed with Fe, Cr, Ni or stainless steel particles in zero leakage lattices.

2.4.2. The Plutonium fuel used in fast commercial plants will be produced in a large part from light water reactors and will contain a large amount of higher Plutonium isotopes. The experimental program aiming at improving the knowledge of the cross sections of these isotopes is based on four types of experiments :

- Cell neutron balance comparison for lattices differing only by the Plutonium isotopic compositions :

	Pu A	Pu B	Pu C
^{240}Pu	8 %	45 %	18 %
^{241}Pu	0.8 %	11 %	10 %
^{242}Pu	0 %	5 %	3 %

Measurements concern material buckling differences between these Pu fuels by the replacement method (ZONA cores Fig. 1) or ratios production over absorption in zero leakage lattices (OP10, 11 cores Fig. 1). This PLUTO program is carried out on MASURCA and ERMINE.

- Reactivity worths of Pu samples with variable isotopic composition by oscillation technique (MASURCA, ERMINE).

- Irradiations in fast power reactors (OSIRIS, RAPSODIE, PHENIX) and mass spectrometry analysis to measure the capture cross section ratios.

- Fission rate ratios by micro-fission-chambers in all the lattices, for the main Pu isotopes.

As an example the fission rate ratios for ^{240}Pu, ^{241}Pu and ^{242}Pu isotopes are presented Fig. 3, 4 and 5. From these experiment-calculation comparisons, it is already concluded that no problem exists to adjust the fission cross sections of these three isotopes :

- .the ^{242}Pu to ^{240}Pu fission ratio is correct to $\pm$ 3 %.
- .the ^{241}Pu to ^{239}Pu fission ratio has to be decreased by 8 $\pm$ 3 % globally
- .the ^{240}Pu to ^{238}U fission ratio has to be decreased by 11 $\pm$ 3 % to 5 $\pm$ 3 % according to the energy range.

2.4.3. The fission product reactivity effect in SUPER-PHENIX has an increased importance due to the cycle characteristics and core enrichments. An evaluation program for the major separated isotopes is in progress at CADARACHE.

The reference program of integral experiments consists of the reactivity worth measurements, on ERMINE by the oscillation technique, of fuel pins, or pure ^{239}Pu and ^{235}U samples, irradiated in RAPSODIE and PHENIX up to 10 % burn up. The measurements will be performed on three lattices, one uranium and two Pu fuelled, in the range of SUPER-PHENIX cores. Mass spectrometry analyses and complementary reactivity worths for fissile contents allow to separate the P.F. effect [14].

The global fission product capture cross section will be adjusted on these reference experiments.

Complementary experiments on separate fission product isotopes correspond to three types of measurements :

- reactivity worths by the oscillation technique in ERMINE and MASURCA
- activation in ERMINE
- irradiation in RAPSODIE and PHENIX.

2.5. Conclusion

All these programs will be completed in 1975 and the results will be applied to the adjustment of the CARNAVAL IV system that will be used for the definition of the SUPER-PHENIX enrichments in the middle of 1976.

At this time, all the new major specific problems coming from nuclear data inaccuracies will be solved for SUPER-PHENIX . The following accuracies should be reached on the three parameters previously mentionned (2σ) :

- stainless steel capture $\pm$ 5 -10 %
- higher Plutonium isotopes
  - Capture $\pm$ 5 -10 %
  - Fission $\pm$ 3 %
- global fission product capture $\pm$ 7%

Then, at the end of 1975, no more major uncertainty due to evaluated nuclear data inaccuracies will still remain for oxide-Sodium fast commercial plants. That applies to the main aspects of optimization (enrichment, power distribution, breeding gain), safety (control rod, Doppler and Sodium coefficient) and operation (reactivity loss with burn up).

- Finally, in this fast reactor physics integral approach, the complementary role of nuclear data programs is limited to three points :
  - .to give the more realistic initial evaluated nuclear data
  - .to define the inaccuracies acceptable from the nuclear physics and metrology point of view and the correlations between these data for the adjustment method
  - .to determine some nuclear data sufficiently well-known from evaluations.

For the most important parameters, all these aspects will be fulfilled at the end of this year.

3. NUCLEAR DATA NEEDS AFTER 1975

3.1. Introduction

For the design parameters previously mentionned, commercial plants restricted to the U-Pu fuel cycle and power range lower than 2000 MWe, no result of first priority is waited for from nuclear data programs after 1975. The systematic analysis of the results drawn from plant operation (PHENIX) and irradiated fuel analysis will represent a continuous check of the validity of the predictions. For different core designs (carbide fuel for example), a limited program of integral experiments will be carried out to confirm the calculations.

New topics where nuclear data needs exist are safety and plant operation on one hand , fuel cycle analysis on the other hand. But for these problems, the non-neutronic

uncertainties dominate the effects of nuclear data inaccuracies.

3.2. Goals

Safety and operation

.Outside the problems of Na void coefficient, Doppler coefficient and material worths included in the first part, the analysis of accident sequences deals with various characteristic phenomena such as fuel melting and vaporization. For these parameters, the determination of fission product migration and microscopic distribution in the fuel pins is needed to calculate the fuel dispersal : for nuclear data, that corresponds to the definition of fission yields and absorption cross sections for Xenon, then Cesium, Rubidium and Tellure F P isotopes.

.The accident diagnosis asks for a detailed knowledge of the detection system : for example, fuel failure detection needs, first the definition of non-F P Xenon and Krypton capture cross sections in the low energy range for the gas tag technique, second the gaseous F P yields for the gas analysis technique.

.Specific operation problems lead to some nuclear data requests : circuit contamination calculations (corrosion) for example, imply an estimate of activation cross sections for some structural material components :

51 Cr production	:	50 Cr (n, γ)
		54 Fe (n, α)
54 Mn production	:	54 Fe (n,p)
58 Co production	:	58 Ni (n,p)
60 Co production	:	59 Co (n, γ)
		60 Ni (n,p)

Furthermore, (n, 2n) cross sections contribute also to these productions at a lower level. Finally, some of these reactions (n,p) are also used for damage problems.

Fuel cycle analysis

.Nuclear data are useful for the improvement of the experimental techniquesused in fuel cycle measurements. However, these techniques are mainly relative ones [14], based on non-destructive physical methods such as γ spectrometry (γ scanning for power distribution), calorimetry and spontaneous neutron emission (Pu build-up in blankets). Nuclear data requests for these problems concern half-lives, (α,n) cross sections, γ production cross sections, relative fission product yields. Absolute measurements carried out to calibrate these relative techniques deal with destructive analyses using mass spectrometry, α spectrometry and chemical analyses. For the burn-up rate determination, for example, the Nd build-up measurements are completed with Nd fission yields in fast reactors considered to be sufficiently well-known to-day for the main U-Pu isotopes [15].

.Predictions of the fuel-cycle output lead first to the problems of fission product wastes : it is mainly fission yields that are requested in fast reactor field. Second, the points of fuel transportation, reprocessing and fabrication and the possible recovery and sales of some actinides require the knowledge of capture, fission and n, 2n cross sections for isotopes from ^{232}U to ^{244}Cm. Outside the problems solved in the cell neutron balance programs, the major isotopes requested are ^{236}Pu, ^{238}Pu, Americium and Curium ones. Third, the long term topics of waste recycling will imply the knowledge of production and absorption cross sections for some actinides, in a first step for Americium isotopes.

3.3. Nature of requests

All these requests for future nuclear data concern a large number of isotopes, especially fission products and actinides. But, in all cases, the required accuracy is largely broader than the accuracy needed for previous core and shielding requests : mostly, an order of magnitude is sufficient. In fact for the goals mentionned, non-neutronic uncertainties are usually more important than the consequences of nuclear data inaccuracies : the most evident example concerns the safety

problems.

In these conditions, evaluation works based on nuclear physics systematics should be able to answer the questions. Evaluators must then define whether new differential measurements are strictly necessary to satisfy the requested accuracies and delays taking into account that, in most cases, integral measurements represent the way to reach a more accurate result in a shorter time.

Among the new nuclear data requests, some ones will already be studied on an integral approach in 1975. For example, fission rate ratios for ^{241}Am and ^{238}Pu will be systematically measured by micro-fission-chambers in all fast lattices : that program will normally solve the question. Irradiations of ^{241}Am samples in several fast reactors and measurements of the ^{242}Cm production together with the values of branching ratios allow the determination of the ^{241}Am capture cross sections to $\pm$ 7 %. It is shown on fig. 6 that the ^{241}Am capture cross section in the CARNAVAL III system has to be reduced globally by 10 %. The result of the same irradiation experiment in 1974 in the centre of PHENIX will definitely answer this point in 1975. In the same way, activation cross sections will be measured in 1975 in specific irradiation experiments in RAPSODIE. Finally, a large program on PHENIX irradiated fuels will allow a good calibration of the evaluated nuclear data for the main problems mentionned in fuel cycle analysis.

4. CONCLUSION

At the end of 1975, the CEA fast reactor physics approach, based on integral experiments, will allow to solve the major problems due to nuclear data for oxide-sodium fast commercial plants in the power range 250 up to 2000 MWe. Results obtained during PHENIX start-up and one-year operation validate this approach. The whole conclusions drawn from that fast physics program will be included in the CARNAVAL Version IV system, to be used for the SUPER-PHENIX enrichment definition mid-1976. No major uncertainty caused by nuclear data inaccuracies will remain at the end of this year.

After that time, nuclear requests concern mainly safety, operation and fuel cycle analyses. For these topics, non-nuclear uncertainties largely dominate the effects of nuclear data inaccuracies. Due to the broader accuracy required, evaluations adjusted on integral experiments should be sufficient in most cases. The great number of fission product and actinide nuclear data required for the future still justifies an increase of the evaluation effort to be performed in the framework of an international cooperation which has been so successful in the past.

From the old ages, major fast reactor physics problems have moved from the knowledge of basic nuclear data, first to the study of spatial parameters, such as power distribution perturbations from the control rod system on SUPER-PHENIX (Fig.8) [16], and second to the analyses of plant operation, for example for the improvement of the breeding gain definition from irradiated fuel analyses. This orientation, due to the successful results obtained in the past in nuclear data and reactor physics programs, appears to be ineluctable.

REFERENCES

[1] J.Y.BARRÉ, J.P.CHAUDAT
Rôles respectifs des évaluations et des expériences intégrales pour la physique des réacteur rapides - Symposium on nuclear data in science and technology Vol.I p.143 IAEA-SM 170/69 PARIS (1973)

[2] J.Y.BARRÉ, J. BOUCHARD
Rôle complémentaire des expériences intégrales par rapport aux mesures différentielles pour un projet de réacteurs à neutrons rapides - Conference on nuclear data for reactors Vol.II p.465 IAEA-CN 26/73 HELSINKI (1970)

/3/ J.BUSSAC and al
The French fast reactor physics program International symposium on physics of fast reactors Vol.I A1 p.9 TOKYO (1973)

/4/ J.Y.BARRÉ and al
Fast reactor physics at CEA : study of the characteristics of the clean core, cell neutron balance, control rods, power distribution. Ibidem Vol.I A 21 p.396 TOKYO (1973)

/5/ M.DARROUZET and al
Studies of unit K_∞ lattices in metallic uranium assemblies ZEBRA 8H, SNEAK 8, ERMINE and HARMONIE UK. Ibidem Vol.I A 28 p.537 TOKYO (1973)

/6/ J.P.CHAUDAT and al
Improvements of the predicted characteristics for fast power reactors from integral experiments : CADARACHE Version III multigroup cross section set. Ibidem Vol.III A 34 p.1207 TOKYO (1973)

/7/ J.Y.BARRÉ and al
Lessons drawn from integral experiments on a set of multigroup cross sections BNES Conference on the physics and operation of fast reactors paper 1-15 p.165 LONDON (1969)

/8/ P.P.CLAUZON and al
Physics test program at the start-up of PHENIX. Ibidem Vol I A 12 p.215 TOKYO (1973)

/9/ P.P.CLAUZON and al
Experimental physics results at start-up of PHENIX "Fast reactor power stations" BNES Conference p.267 LONDON (1974)

/10/ A.ARNAUD and al
Self-shielding factor measurements for ^{23}Na and natural iron between 15 Kev and 160 Kev, presented to this conference

/11/ C. LE RIGOLEUR and al
Absolute measurement of the fast neutron radiative capture cross section for Cr, Ni, ^{103}Rh between 10 and 65 Kev, ^{23}Na, Fe, Ta between 10 and 160 Kev, ^{55}Mn, ^{238}U between 20 and 550 Kev, presented to this conference

/12/ D. ABRAMSON and al
Evaluation between 0 and 600 Kev of the capture cross section for Chromium and the resonance parameters, presented to this conference

/13/ J. BOUCHARD and al
Experimental study of burn up in fast breeder reactors ANS National meeting on new developments in reactor physics and shielding Vol.II 888 Conf 720901 KIAMESHA LAKE (1972)

/14/ J.BOUCHARD and al
Fast reactor physics at CEA : higher Plutonium isotopes and burn-up studies Ibidem Vol.II p.767 TOKYO (1973)

/15/ M.ROBIN and al
Determination of the ^{148}Nd yield in the fission of ^{235}U, ^{238}U and ^{239}Pu by thermal and fast neutrons BNES Conf. on chemical nuclear data 19 CANTERBURY (1971)

/16/ R. CARLE and al
Future programs and plans for prototype and prospects for CFRs. Ibidem BNES Conference p.605 LONDON (1974)

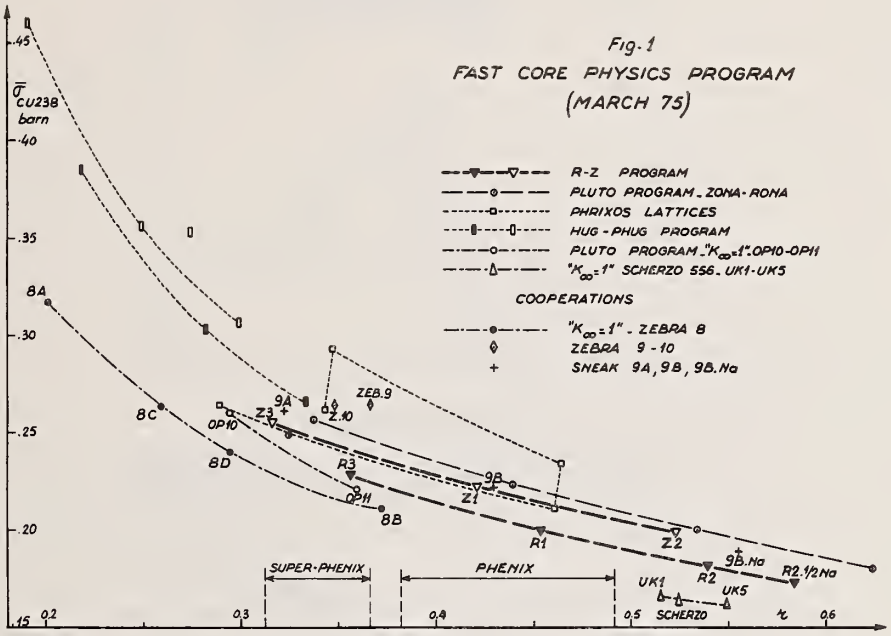
Fig. 1
FAST CORE PHYSICS PROGRAM
(MARCH 75)
R-Z PROGRAM
PLUTO PROGRAM - ZONA - RONA
PHRIXOS LATTICES
HUG - PHUG PROGRAM
PLUTO PROGRAM - "K∞=1" OP10 - OP11
"K∞=1" SCHERZO 556 - UK1 - UK5
COOPERATIONS
"K∞=1" - ZEBRA 8
ZEBRA 9 - 10
SNEAK 9A, 9B, 9B.Na
σ̄ cu238 barn
8A
8C
8D
8B
OP10
OP11
Z3
Z2
Z1
R3
R2
R1
9A
ZEB.9
Z.10
9B
9B.Na
R2.1/2Na
UK1
UK5
SCHERZO
SUPER-PHENIX
PHENIX
ν

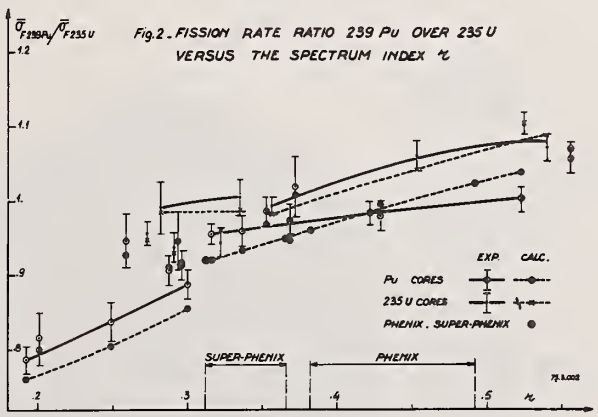
Fig. 2 - FISSION RATE RATIO 239 Pu OVER 235 U
VERSUS THE SPECTRUM INDEX ν
EXP. CALC.
Pu CORES
235 U CORES
PHENIX - SUPER-PHENIX
SUPER-PHENIX
PHENIX
ν

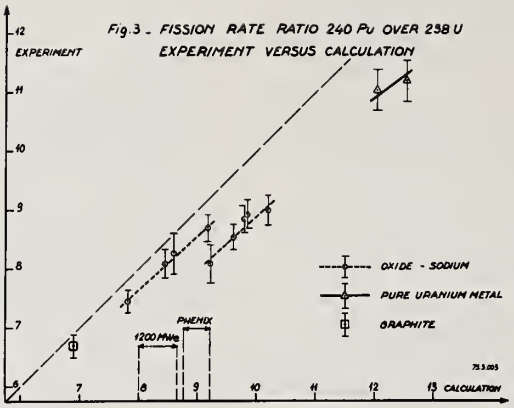
Fig.3 - FISSION RATE RATIO 240 Pu OVER 238 U
EXPERIMENT VERSUS CALCULATION
EXPERIMENT
CALCULATION
OXIDE - SODIUM
PURE URANIUM METAL
GRAPHITE
PHENIX
1200 MWe

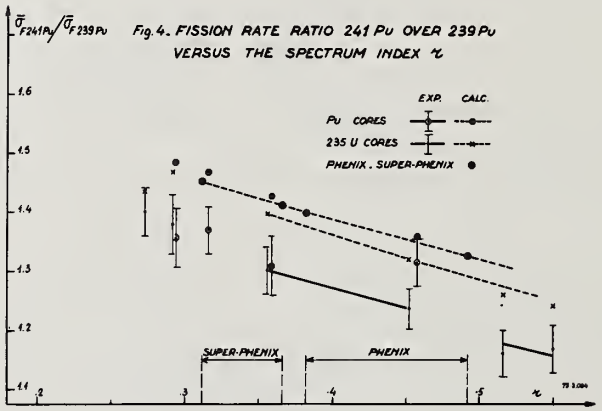
Fig.4 - FISSION RATE RATIO 241 Pu OVER 239 Pu
VERSUS THE SPECTRUM INDEX τ
EXP. CALC.
Pu CORES
235 U CORES
PHENIX . SUPER-PHENIX
SUPER-PHENIX
PHENIX

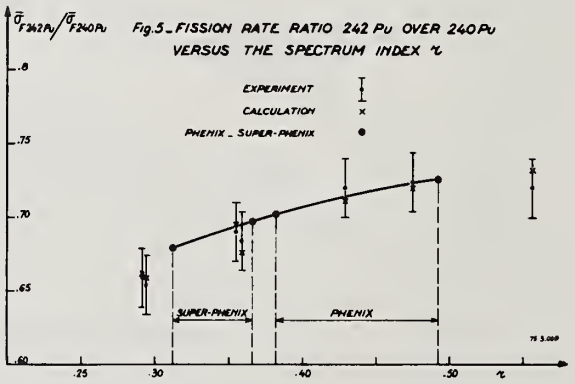
Fig.5 - FISSION RATE RATIO 242 Pu OVER 240 Pu
VERSUS THE SPECTRUM INDEX τ
EXPERIMENT
CALCULATION
PHENIX - SUPER-PHENIX
SUPER-PHENIX
PHENIX

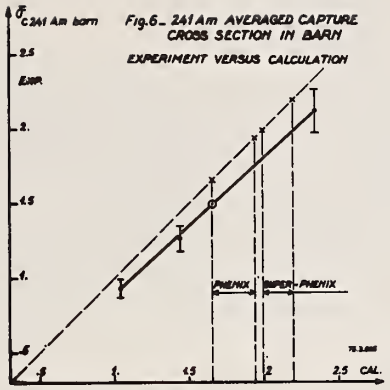

FIG. 7 - **REACTIVITY LOSS WITH BURN UP**

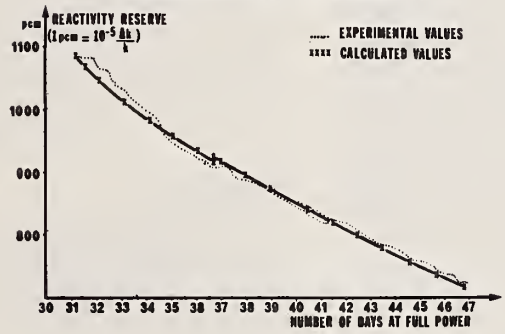

FIG.8

SUPER . PHENIX
CORE 1207

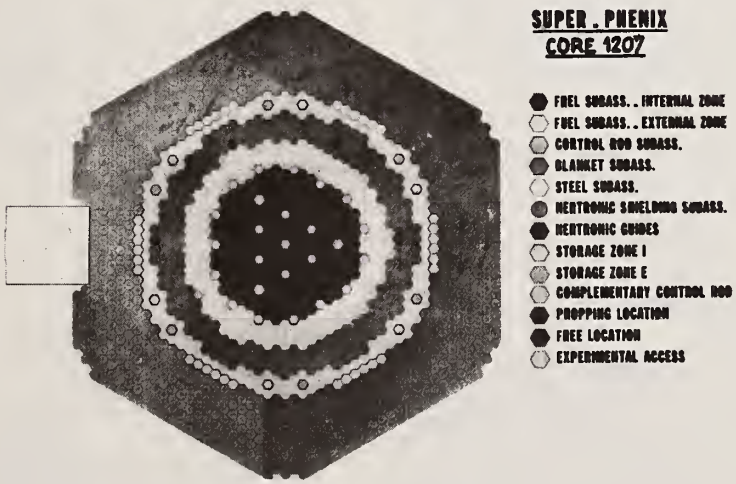

NE-213 NEUTRON SPECTROMETRY SYSTEM FOR MEASUREMENTS TO 15 MEV

R. H. Johnson, B. W. Wehring, and J. J. Dorning
University of Illinois at Urbana-Champaign
Urbana, Illinois 61801

A 5-cm by 5-cm NE-213 scintillator mounted on a 56AVP PM tube is used with a bridge utilizing two high voltage supplies and giving good linearity and good pulse shape discrimination. The cross-over timing method is used to discriminate against gamma-ray events. Measurements of a ^{252}Cf and a D-T source were used to test the linearity of the system. The ^{252}Cf measurement is in good agreement with earlier results and is fit by a Maxwellian distribution with a temperature of 1.43 MeV. A modified version of the COOLC unfolding code was used to obtain neutron spectra. This code, FORIST, optimizes the neutron energy resolution through an iterative process. A measured Pu-Be spectrum is used to demonstrate the benefits of the modified unfolding procedure. The Pu-Be spectrum is also in good agreement with earlier results. The 9.7 MeV peak of the Pu-Be neutron spectrum is resolved when the FORIST code is used, but not when the COOLC code is used with the window width data distributed with the COOLC and FERDOR code package.

(Proton-recoil spectrometry; spectra unfolding; Pu-Be and ^{252}Cf neutron spectra)

Introduction

An NE-213 neutron spectrometry system[1] has been assembled for measurements of neutron spectra in the range of 1 to 15 MeV. To test the system, which employs the data acquisition methods and data analysis techniques described below, the Pu-Be neutron spectrum and the ^{252}Cf fission neutron spectrum have been measured. Both spectra are in good agreement with recent measurements reported in the literature. This spectrometry system has been developed to measure neutron leakage spectra from homogeneous spherical-shell (benchmark-type) assemblies constructed of materials of interest in fission and fusion reactor technology. These measurements will be compared with calculations as a test of multigroup cross section sets and evaluated nuclear data files.

Data Acquisition

Electronics

A block diagram of the electronics used for data acquisition is shown in Fig. 1. A 5-cm by 5-cm NE-213 scintillator is coupled to a 56AVP photomultiplier tube with a 0.62 cm light pipe. Pulse shape discrimination is used to discriminate against gamma-ray events. The timing signal starts the TAC unit. The double-delay-line amplifier produces a bipolar energy pulse. The cross-over pickoff provides the stop pulse for the TAC unit. The output of the TAC unit is the rise time signal. This rise time signal varies linearly with the cross-over time of the double-delay-line amplifier which is related to the rise time of the energy signal from the photomultiplier tube. The single-channel analyzer is used to gate the multi-channel analyzer on the neutron event peak of the rise time spectrum which is well separated from the gamma-ray event peak. The multi-channel analyzer therefore accumulates energy pulses from the RC amplifier which are due only to neutron events.

Timing Walk

Timing walk was the major difficulty encountered in the cross-over-timing pulse shape discrimination. The walk of the electronics system was measured by replacing the photomultiplier tube and bridge with a precision pulser. The direct output of the pulser was used as the timing signal. The attenuated output of the pulser was used as the energy signal. Timing walk as a function of pulse height could then be measured by varying the attenuation of the energy signal.

The neutron unfolding code used with this spectrometry system requires measurements with two different gain settings. Pulse height spectra were measured over a 30-to-1 dynamic range for the high gain setting. The pulse-shape-discrimination circuitry was adjusted to minimize timing walk over this dynamic range. The

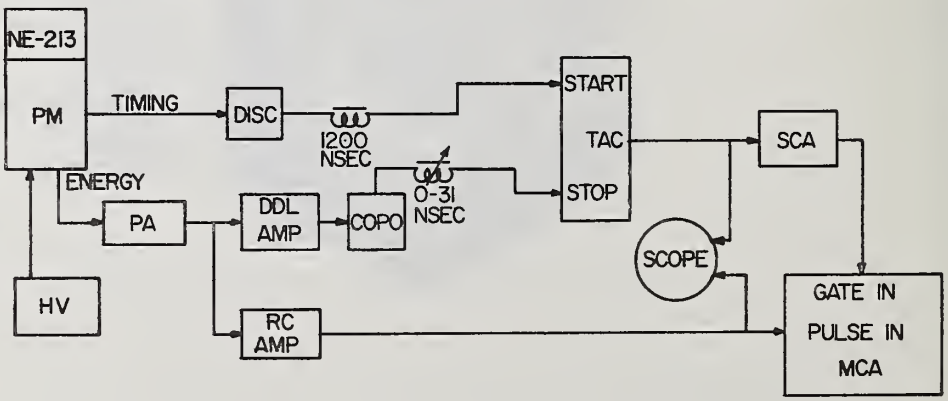

Fig. 1. Block diagram of electronics for NE-213 spectrometry system. The block labeled HV represents two high voltage supplies, one positive and one negative.

timing walk was found to be most sensitive to the reset voltage level of the cross-over pickoff. The timing walk with the pulser was measured to be ±2 nsec. The pulser was then replaced by the photomultiplier tube and the timing walk was measured over the same range for a gamma-ray source. Differences in the timing walks for the pulser and the gamma-ray source were negligible.

Photomultiplier Bridge

A schematic diagram of the photomultiplier bridge chosen for this spectrometry system is shown in Fig. 2. A number of photomultiplier bridge designs were tested for pulse shape discrimination and for energy linearity. The separation of the neutron and gamma-ray event peaks in rise-time spectra of a ^{252}Cf source ranged from 15 to 60 nsec. The design chosen gives both good energy linearity and good timing separation (34 nsec) for pulse shape discrimination. For the high gain spectrum measurements the voltages were +500 V and -1300 V; for the low gain spectrum measurements they were +500 V and -1200 V.

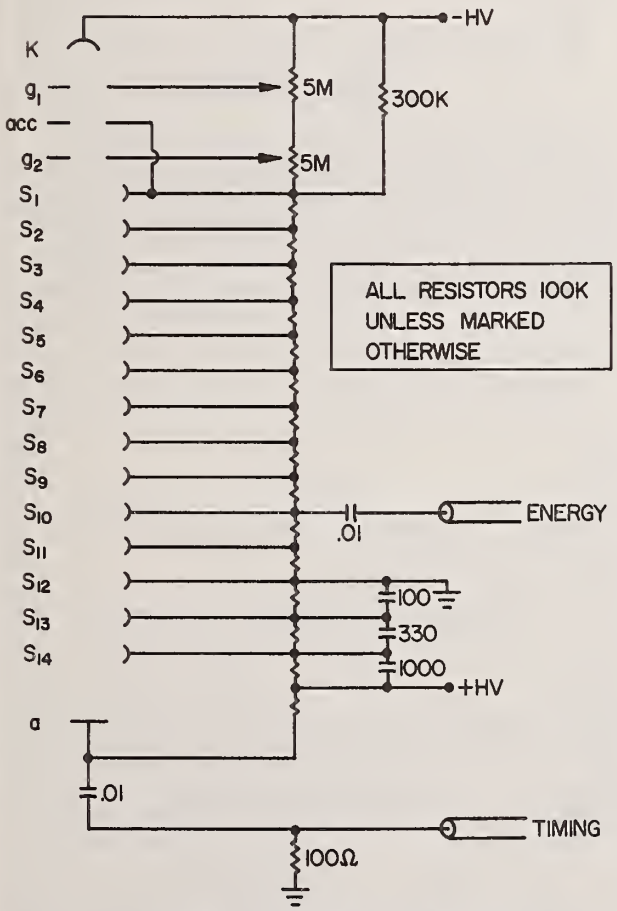

Fig. 2. Schematic diagram of photomultiplier bridge used in data acquisition system. The photomultiplier tube used was a Phillips 56AVP.

Data Analysis

Spectrum Unfolding

The FERDOR method[2,3] is used to unfold the measured pulse-height data. Because the response matrix used in the FERDOR method includes the resolution of the spectrometer, the elements of the solution vector $\underline{X}$ for the neutron flux have large statistical errors. The FERDOR method uses Gaussian window functions to smooth the solution and thereby reduces these statistical errors.

The smoothing equation used in FERDOR[3] is

$$\phi_k = \sum_{j=1}^{NC} G_{kj} X_j, \quad k=1, \ldots, NW, \tag{1}$$

where

$$G_{kj} = \frac{1}{\sqrt{2\pi}\,\sigma_k} \exp\left\{-\frac{1}{2}\left(\frac{E_k - E_j}{\sigma_k}\right)^2\right\} \tag{2}$$

and ϕ_k is the flux at neutron energy E_k. The resolution parameter σ_k is given by

$$\sigma_k = \frac{W_k E_k}{235.5} \tag{3}$$

where W_k is read into the FERDOR program and is called the window width. The window width is the full-width-at-half-maximum of the Gaussian smoothing function in percent.

Renormalization of Response Matrix

The FERDOR unfolding code is currently available in an IBM-360 version named COOLC.[4] The code package includes an NE-213 neutron response matrix which gave satisfactory results for our system after the response matrix was renormalized. Recent measurements[5] have shown that the 05S code[6] correctly calculates the neutron efficiency of NE-213 for energies above 2.5 MeV, but overestimates the efficiency below 2.5 MeV.

The response matrix was first renormalized to the efficiencies calculated by 05S for a 5-cm by 5-cm NE-213 scintillator.[7] The necessary renormalization below 2.5 MeV was determined by a measurement of a ^{252}Cf fission neutron spectrum. The measured spectrum was accurately fitted for energies above 2.5 MeV by a Maxwellian distribution. The response matrix below 2.5 MeV was then adjusted by a smoothly varying correction factor so that the spectrum below 2.5 MeV also fit the Maxwellian distribution.

Determination of Window Widths

The COOLC code package includes a sample set of window widths. These widths are not appropriate for some neutron spectra. The suitability of a set of window widths depends not only on the shape of the neutron spectrum, but also on the statistical error of the measured spectrum. A method[8] has been developed which optimizes a set of window widths for each spectrum unfolded. This method has been implemented in our modified version of COOLC, called FORIST.[8] The sample set of window widths, $\underline{W}^{(0)}$, distributed with COOLC is initially used in smoothing the unfolded

spectrum (zeroth iteration). The statistical errors thus obtained, $\underline{\varepsilon}^{(0)}$, are used in conjunction with a desired set of statistical errors, $\underline{\varepsilon}$, and an empirical expression motivated by information theory

$$W_k^{(n)} = \left[\frac{1}{W_k^{(n-1)}} + \frac{\ell n \left(\varepsilon_k / \varepsilon_k^{(n-1)} \right)}{40\exp(-0.08E_k)+50\exp(-0.7E_k)} \right]^{-1}, \quad (4)$$

to generate a new set of window widths. In this expression E_k is in MeV and both the window widths and the statistical errors are in percent. Equation 4 is used to choose the n^{th} set of window widths, within the constraint that they are $\leq$ 1.5 times the initial values, so that the resulting statistical errors $\underline{\varepsilon}^{(n)}$ approach the desired statistical errors $\underline{\varepsilon}$. The smoothing of the unfolded spectrum is then repeated using $\underline{W}^{(n)}$, the new set of window widths. This iterative smoothing process may be used repeatedly, but in practice one iteration has been found to suffice.

Pu-Be Neutron Spectrum

A pulse-height distribution was obtained with the data acquisition system for a 5-Curie Pu-Be neutron source. The zeroth iteration smoothed and unfolded spectrum is shown in Fig. 3. This zeroth iteration neutron spectrum obtained using FORIST is identical to the neutron spectrum obtained using COOLC. The sample set of window widths used is shown in Fig. 4 (solid line). The window widths obtained in the first iteration of FORIST for the Pu-Be data are also shown in Fig. 4 (broken line).

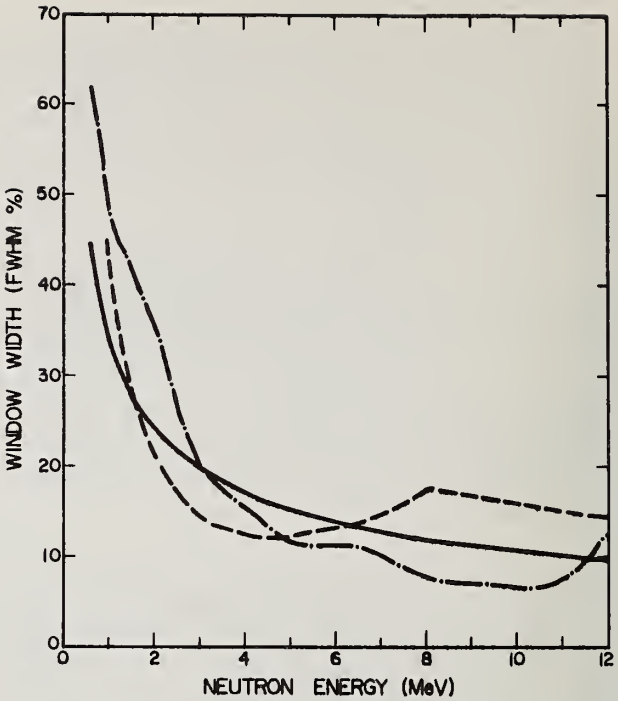

Fig. 4. Window widths used in FORIST. The solid line is the sample set of window widths obtained with COOLC and used in the zeroth iteration of FORIST. The broken line is the first iteration set of window widths for the Pu-Be spectrum. The dashed line is the first iteration set of window widths for the ^{252}Cf spectrum.

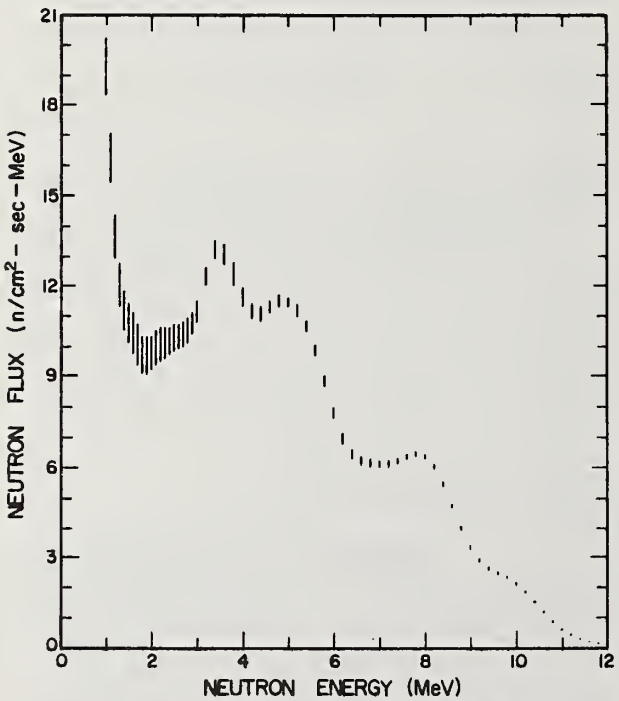

Fig. 3. Zeroth iteration neutron spectrum of a 5-Curie Pu-Be source using FORIST. The vertical lines represent ±1 standard deviation (statistical) error in the unfolded spectrum due to statistical error in the measured data.

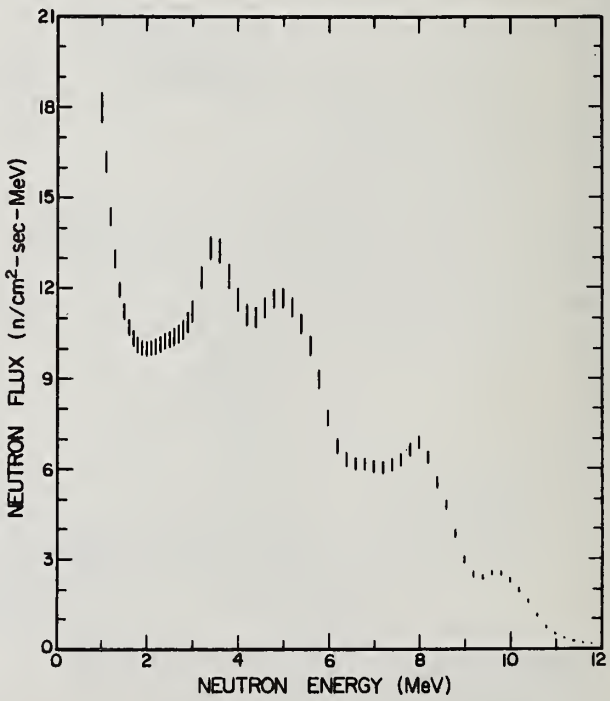

Fig. 5. First iteration neutron spectrum of a 5-Curie Pu-Be source using FORIST.

The first iteration neutron spectrum using FORIST to unfold the Pu-Be data is shown in Fig. 5. The desired statistical error for this run was ±3%. In this first iteration spectrum the statistical error in the 2-MeV valley has been noticeably reduced and the 9.7-MeV peak has been resolved. This illustrates the advantage of the FORIST unfolding procedure. The Pu-Be spectrum shown in Fig. 5 is in good general agreement with other recent measurements.[9,10]

^{252}Cf Neutron Spectrum

Measurement of a ^{252}Cf neutron spectrum was one test used in evaluating the linearity of several of the photomultiplier bridge designs. Distortion in the unfolded fission spectrum was evident when a bridge became nonlinear. A measurement using the bridge design in Fig. 2 is shown in Fig. 6. The first iteration set of window widths obtained by FORIST in unfolding this spectrum is shown if Fig. 4 (dashed line).

Maxwellian distributions were fitted to this measurement. A weighted least-squares fit in the range from 2.6 MeV to 15 MeV yielded a temperature of 1.44 ±0.05 MeV. A weighted least-squares fit in the range from 3 MeV to 11 MeV is plotted as the straight line in Fig. 6; this fit yielded a temperature of 1.43 ±0.05 MeV. The errors given for the temperatures are the systematic errors due to an estimated error in gain calibration of ±2%; the statistical errors are negligible in comparison. Systematic errors due to efficiency errors in the response matrix were not estimated.

The temperatures obtained are in good agreement with the recent measurements of Green et al.[5] However, those measurements[5] show a deviation from a Maxwellian distribution above 9 MeV. Recent calculations by Browne and Dietrich[11], on the other hand, show good agreement with a Maxwellian from 3 MeV to 14 MeV, but yield a temperature of 1.25 MeV.

Final confirmation of the linearity of this spectrometry system was obtained by a measurement of the neutron spectrum from a D-T reaction produced by a neutron generator.[12] The peak of the measured spectrum was within 0.1 MeV of the source energy.

Summary

The ^{252}Cf fission spectrum and the D-T reaction spectrum reported above confirm that the system described here has good linearity up to 15 MeV. The Pu-Be spectra reported here (Figs. 3 and 5) demonstrate the benefit of the modified unfolding procedure (FORIST) over the standard FERDOR method, and show that this modified procedure optimizes the energy resolution of the unfolded spectrum for a given statistical error.

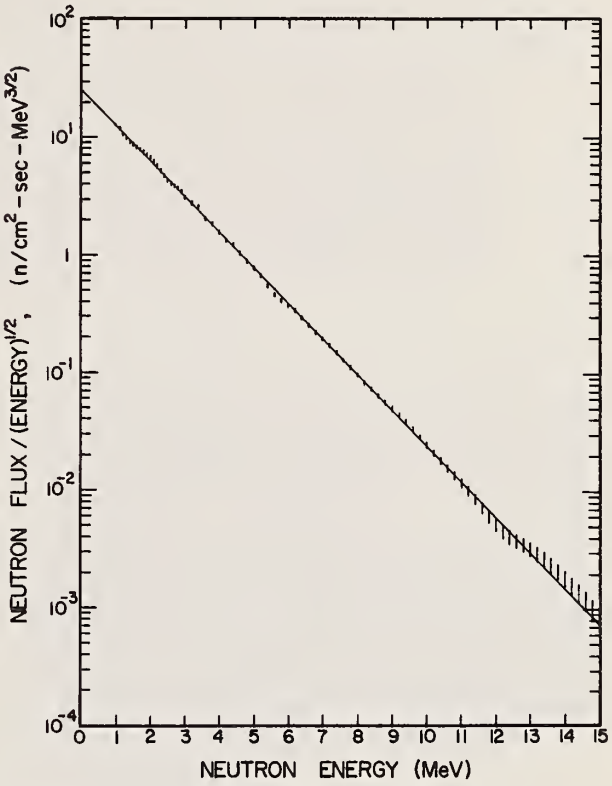

Fig. 6. First iteration neutron spectrum of a 4-microgram ^{252}Cf source using FORIST. The straight line is a weighted least-squares fit of a Maxwellian distribution (T=1.43 MeV) to the measurement in the energy range 3 MeV to 11 MeV.

[1] R. H. Johnson, B. W. Wehring, and J. J. Dorning, to be submitted to Nucl. Instr. and Meth.

[2] W. R. Burrus and V. V. Verbinski, Nucl. Instr. and Meth. 67, 181 (1969).

[3] H. Kendrick and S. M. Sperling, "An Introduction to the Principles and Use of the FERDOR Unfolding Code," GA-9882, Gulf Radiation Technology (1970).

[4] "COOLC and FERDOR Spectra Unfolding Codes," Radiation Shielding Information Center, Oak Ridge National Laboratory, PSR-17.

[5] L. Green, J. A. Mitchell, and N. M. Steen, Nucl. Sci. Eng. 50, 257 (1973).

[6] R. E. Textor and V. V. Verbinski, "05S: A Monte Carlo Code for Calculating Pulse Height Distributions Due to Monoenergetic Neutrons Incident on Organic Scintillators," ORNL-4160, Oak Ridge National Laboratory (1968).

[7] V. V. Verbinski, W. R. Burrus, T. A. Love, W. Zobel, and N. W. Hill, Nucl. Instr. and Meth. 65, 8 (1968).

[8] R. H. Johnson, J. J. Dorning, and B. W. Wehring, to be submitted to Nucl. Sci. Eng.

[9] D. F. Shook and C. R. Pierce, "A Comparison of Neutron Spectra Measured with Three Sizes of Organic Liquid Scintillators Using Differentiation Analysis," NASA TM X-2646 (1972).

[10] W. Meyer and D. W. Prigel, Trans. Am. Nucl. Soc. 16, 361 (1973).

[11] J. C. Browne and F. S. Dietrich, Phys. Rev. C 10, 2545 (1974).

[12] R. H. Johnson, J. J. Dorning, and B. W. Wehring, "Integral Test of Cross Sections Using Neutron Leakage Spectra from Spheres of Iron, Niobium, Beryllium, and Polyethylene," proceedings of this conference.

ABSOLUTE CALIBRATION OF NEUTRON DETECTORS IN THE 10-30 MEV ENERGY RANGE

J. A. Cookson,* M. Hussian,† and C. A. Uttley*
Atomic Energy Research Establishment, Harwell, Didcot, Oxon.

J. L. Fowler¶
AERE Harwell and Oak Ridge National Laboratory, Oak Ridge, Tenn.

R. B. Schwartz§
AERE Harwell and U. S. National Bureau of Standards, Washington, D. C.

A central problem in fast neutron research is that of finding the absolute efficiency of neutron detectors. Using the associated particle method for this purpose, we have designed a chamber to count He particles from the D(d,n)^{3}He or the T(d,n)^{4}He reaction in coincidence with neutron events. The reactions take place in deuterium or tritium gas and a ΔE solid state counter at 80°, 65°, or 43° to the 2-10 MeV deuteron beam direction detects the He particles with 100% efficiency. To reduce background we allow the deuterons to pass out of the gas chamber through a Ni window and stop the beam ∿ 150 cm from the counters. With the D(d,n)^{3}He reaction we have obtained ∿2% efficiency calibration of the central portion of a liquid scintillator in the 9-10 MeV energy range. With the T(d,n) reaction this calibration can be extended to ∿ 27 MeV and the efficiency can be mapped out as a function of position in the scintillator.

(Absolute Efficiency of Fast Neutron Detectors)

Determining the absolute efficiency of neutron detectors for energies > 10 MeV is a major problem in fast neutron research. Below ∿8 MeV neutron energy (n,p) scattering is sufficiently isotropic in the C.M. system[1] so that a proton recoil telescope allows an absolute neutron flux measurement provided the flux is large enough to compensate for the low efficiency of a telescope. But above 8 MeV the uncertainty in the differential cross section of (n,p) scattering makes precise absolute measurements with a telescope somewhat questionable. Between ∿8.0 MeV and 50 MeV only one more or less complete set of differential measurements of forward scattering of neutrons by protons appears in the literature[2] and these do not agree with theoretical expectations based on extrapolations from higher energies. Recently, measurements at 24 MeV with high statistical accuracy for two forward scattering angles have been published,[3] but these are inconsistent with the earlier results. Thus from an experimental point of view there is a lack of definite knowledge of differential scattering of neutrons from protons. This leads to an uncertainty in proton recoil telescope results ranging from ∿1% at 14 MeV to ∿3% at 30 MeV. Because of this as well as because of the basic significance of (n,p) scattering, we have set up an experiment at A.E.R.E. Harwell to measure forward scattering of neutrons from protons at energies below ∿30 MeV. In order to determine the absolute efficiency of our neutron detector we use the associated particle method[4] in which we detect neutrons from the D(d,n)^{3}He or the T(d,n)^{4}He reactions in coincidence with the He reaction products.

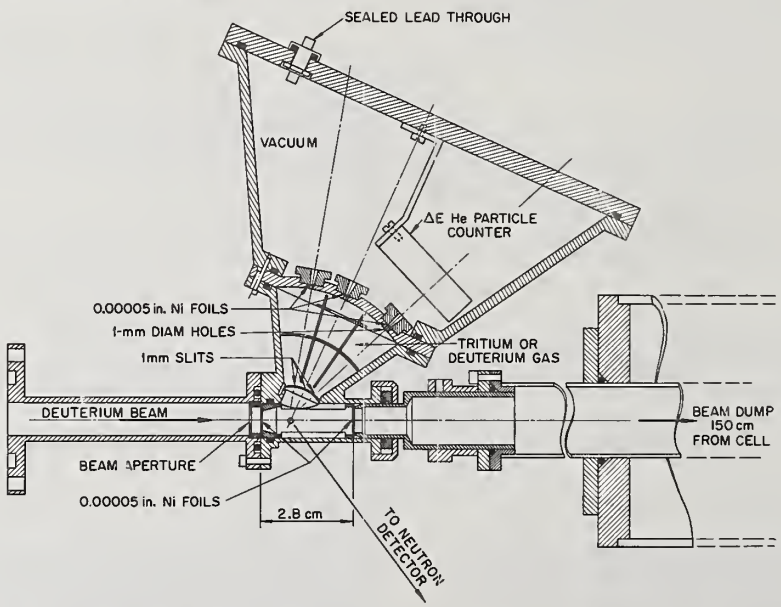

FIG. 1. Reaction chamber for absolute calibration of neutron detectors.

Figure 1 shows the reaction chamber for absolute calibration of neutron detectors. An aperture about 20 cm from the entrance foil limits the beam to ∿3 mm in dia. so that no direct beam is incident upon the aperture just in front of the entrance foil. After passing through the deuterium or tritium gas the beam leaves the reaction chamber through an exit foil and is stopped in a beam dump 150 cm from the cell. This reduces the neutron and γ-ray background in the vicinity of the He and neutron detectors. One mm slits and one mm dia. apertures define a column of reaction He particles which are counted by the ΔE solid state particle detector at 43^0, 65^0, or 80^0 to the incident deuteron beam direction.

The lower graph in Figure 2 shows the ^{3}He spectrum from the D(d,n)^{3}He reaction at 43^0 to a 9.9 MeV deuteron beam. The small background, which is found to be uniform under the peaks by substituting hydrogen for deuterium in the gas cell, is due to neutrons and or γ rays. In the upper part of the figure is the coincidence neutron time-of-flight spectrum as found with a 10.2 cm dia. 2.54 cm thick NE-213 scintillator centered on the ^{3}He associated neutron cone 25 cm from the reaction chamber. For this data the bias on the NE-123 scintillator was set to count neutrons above 4 MeV. The neutron detection efficiency in the center of the scintillator is the ratio of the neutron counts to the ^{3}He counts.

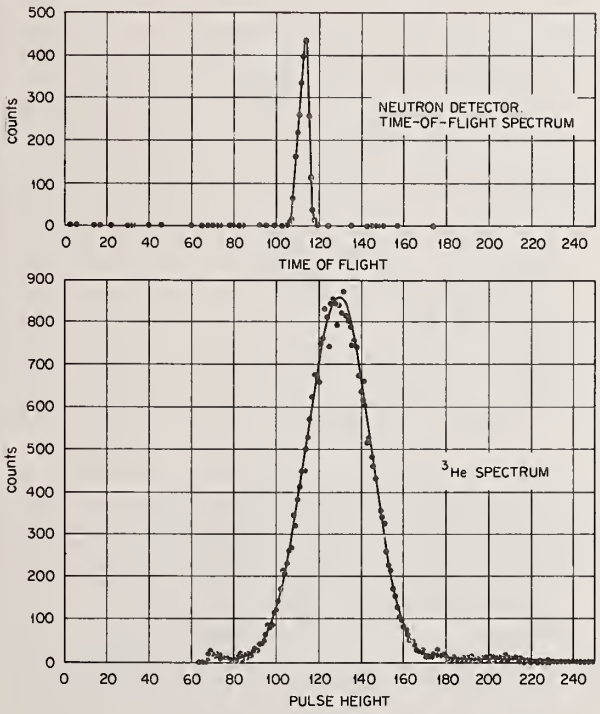

FIG. 2. Spectrum of ^{3}He particles from the D(d,n)^{3}He reaction for 9.9 MeV deuterons. An upper portion of the figure is the coincident neutron time-of-flight spectrum.

Figure 3 compares the measured efficiency for the 4 MeV detector bias with the average efficiency calculated with the computer program, DETEFF, written by R. J. Kurz[5] and altered by S. T. Thornton and J. R. Smith[6] and others. Recent scans across two perpindicular diameters of the scintillator indicates the average efficiency is within about 3% of the central efficiency at 9.3 MeV. Since the computer program is not expected to give efficiencies to better than 10%[5] the disagreement with the calculations is not significant. Nevertheless this 10% uncertainty in efficiency given by the computer program is not permissible in the (n,p) scattering measurements we are making at Harwell. With the bias set at 6 MeV on the NE-213 scintillator a very recent run with T(d,n)^{4}He neutrons shows the central efficiency which is about 4.3% at 9.3 MeV rises to a maximum of 4.9% at 14 MeV and then decreases to 4.2% at 25 MeV.

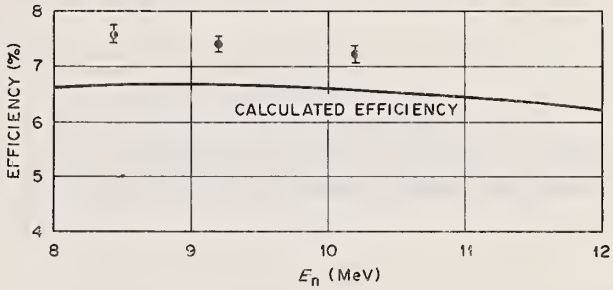

FIG. 3. Central efficiency of a 2.5 cm thick 10 cm dia. NE-213 scintillator compared with average efficiency calculated with the computer program of R. J. Kurz.

By moving the scintillator across the cone of neutrons associated with the He particles one scans the efficiency of the scintillator as a function of position in the detector. An interesting geometrical principle concerning the area of overlapping circles allows the average neutron efficiency of a detector to be readily evaluated from the results of such a scan. If one moves the small circle in Figure 4 across the large circle along a line passing through the two centers, and integrates the common area, A, as indicated below:

$$2\pi \int_0^{R_1 + R_2} \frac{AD\ dD}{\pi R_2^2} = \pi R_1^2$$

one obtains the area of the large circle for all radii of the small circle from 0 to R_1. Thus if the small circle represents the cross section of the neutron cone at the detector and the large circle represents the detector, then moving the small circle across the large one corresponds to mapping the efficiency of a detector of constant efficiency with an uniform beam of neutrons. Since neutron beams and detectors with cylindrical symmetry can be subdivided into circular discs with constant beam intensity or detector efficiency the integration indicated allows one to evaluate exactly the efficiency of a cylindrical symmetric detector with a beam of cylindrical symmetry.

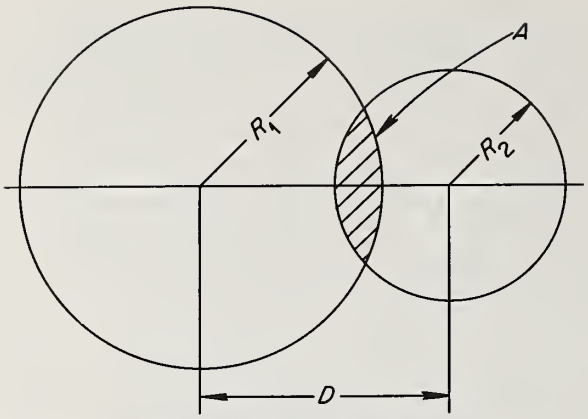

FIG. 4. Geometrical equivalent of mapping a neutron detector with uniform efficiency with a uniform circular cone of neutrons.

---

*Atomic Energy Research Establishment, Harwell, Didcot, Oxon.

†A.E.R.E. Harwell, on leave from the University of Dacca, Bangladesh.

¶A.E.R.E. Harwell, Exchange scientist from Oak Ridge National Laboratory, Oak Ridge, Tennessee.

§A.E.R.E. Harwell, on leave from U. S. National Bureau of Standards, Washington, D. C.

[1]L. N. Rothenberg, Phys. Rev. C1, 1226 (1970).

[2]Scanlan, Stafford, Thresher, Bowen, and Lansford, Nuclear Phys. 41, 401 (1963).

[3]T. G. Mastersen, Phys. Rev. C6, 690 (1972).

[4]B. R. Curtis, J. L. Fowler, and L. Rosen, Rev. Sci. Instr. 20, 388 (1949).

[5]R. J. Kurz, Lawrence Radiation Laboratory Report UCRL-11339 (1964) and Errata.

[6]S. T. Thornton and J. R. Smith, Nucl Instr. & Meth. 96, 551 (1971).

A THICK TARGET MEASUREMENT TECHNIQUE FOR DETERMINING NUCLEAR REACTION RATES*

N. A. Roughton
Regis College, Denver, Colo. and University of Colorado, Boulder, Colo. 80907
M. J. Fritts
University of Colorado, Boulder, Colo. and Science Applications, Inc., McLean, Va.
R. J. Peterson, C. J. Hansen, and C. S. Zaidins
University of Colorado, Boulder, Colo. 80907

A technique for measuring nuclear cross sections using thick targets and an empirical approximation for energy loss has been developed by our group at the Nuclear Physics Laboratory of the University of Colorado. Over the past two years we have measured thick target yields of over thirty nuclear reactions of interest in astrophysics and CTR applications. From these yields we can derive average cross sections and thermonuclear reaction rates, $N_A\langle\sigma v\rangle$. We will describe the technique and data analysis methods and give some examples of our results.

(Cross sections, thick targets, reaction rates, astrophysics, fusion)

For several years our group has been measuring thermonuclear reaction rates with the University of Colorado, Nuclear Physics Laboratory cyclotron by a technique which monitors the decay of radioactive products formed in a thick target through the reactions of interest. The details of this technique are what we wish to discuss in this talk. Further information may be found in the references cited at the end of the paper.

Our original interest in thermonuclear reaction rates was purely astrophysical. The study of the late stages of stellar evolution has reached a point where it is relatively well understood. One of the important tests of this understanding involves agreement between the predicted nucleosynthesis of elements and their measured abundances for our solar system. Detailed comparisons, however, not only require that the stellar environments be modeled very closely, but also that the nuclear reaction rates be reliable. Since nucleosynthesis calculations require knowledge of many more reactions than can be examined in the laboratory, the results of theoretical models are used for the most part. Our goal is to use our technique to examine a sufficient number of reactions on a wide class of nuclei to establish benchmark data. This will permit theoreticians, such as Prof. J. W. Truran and the group at Cal Tech, to refine the models used in the theoretical rate derivations. This should ultimately provide much better understanding of both nucleosynthesis and stellar evolution near the end-point of a star's life.

After we had established our technique as being reliable and after we had measured a number of astrophysically interesting thermonuclear rates, one additional area, thermonuclear fusion reactions of terrestial (applied) interest, gained our attention. In particular, there has been a great deal of interest in the reaction $^{11}B(p,3\alpha)$ as a clean thermonuclear energy source since no neutrons are produced. The rate for this reaction is promisingly large and Boron is a relatively abundant element in the earth's crust. However, natural Boron contains 19.8% ^{10}B and the reactions $^{10}B(p,\gamma)\ ^{11}C$ and $^{10}B(p,\alpha)\ ^{7}Be$ both lead to radioactive residual nuclei. We were able to measure, with the thick target technique, the thermonuclear rates for both of these reactions as a function of temperature. These rates can then be used in all further discussions of proposed Boron plus Hydrogen thermonuclear energy generation. It is important that the problem be considered, as the measured ^{10}B rates suggest the possibility of serious radioactive contamination, if the Boron fuel contains much ^{10}B.

With this introduction on the utility of our technique, let us examine the technique in detail. The quantity generally called the thermonuclear reaction rate is $N_A\langle\sigma v\rangle$ where N_A is Avogadro's number and $\langle\sigma v\rangle$ is the average value of the product of the nuclear cross section, σ, in cm^2 and the relative velocity of the reacting species, v, in cm/sec. This average is dependent upon the temperature, as the average is almost always taken over the velocities weighted by a Maxwell-Boltzman distribution function at a given temperature:

$$\langle\sigma v\rangle = \int_0^\infty \sigma(v)\cdot v \cdot \phi_{MB}(v)\, dv$$

The units of $N_A\langle\sigma v\rangle$ are $cm^3 gm^{-1} sec^{-1}$ and the actual reaction rate requires the knowledge of the density, temperature, and chemical composition at the location of the reactions. Since, except for ultra high density reactions, $N_A\langle\sigma v\rangle$ depends only on the temperature, it is necessary and sufficient to parametrize $N_A\langle\sigma v\rangle$ with respect to temperature. The formula we use for this is

$$N_A\langle\sigma v\rangle = T_9^{-3/2} \exp(A + BT_9^{-1/3} + CT_9^{-1})$$

where T_9 is the unit of temperature measured in 10^9 degrees Kelvin, and A, B, and C are free parameters, to be fit in a least squares sense to the individual rates over a range of relevant temperatures. Table 1 shows the reactions we have completed to date, the value of A, B, and C and the range of temperatures in T_9 over which we feel these rates are reliable.

TABLE I

Thermonuclear Reaction Rates as a Function of Temperature in Billions of Kelvins Fit to the Form

$$N_A\langle\sigma v\rangle = \exp(A + BT_9^{-1/3} + CT_9^{-1})/T_9^{3/2}$$

Reaction	A	B	C	T_9 Limits
$^{10}B(p,\alpha)\ ^{7}Be$	-30.24	-17.188	1.094	0.25-8.5
$^{10}B(p,\gamma)\ ^{11}C$	19.372	-15.977	0.218	2-7
$^{28}Si(p,\gamma)\ ^{29}P$	15.727	-4.815	-15.234	2-8
$^{29}Si(p,\gamma)\ ^{30}P$	25.647	-27.415	9.022	2-8
$^{40}Ca(p,\gamma)\ ^{41}Sc$	22.25	-27.014	1.695	3.5-6
$^{46}Ti(p,\gamma)\ ^{47}V$	22.854	-16.607	-3.644	1.5-5
$^{47}Ti(p,\gamma)\ ^{48}V$	23.617	-16.153	-5.131	1-6.5
$^{50}Cr(p,\gamma)\ ^{51}Mn$	22.866	-17.677	-5.294	1.5-6

*Work supported in part by U.S. Atomic Energy Comm.

TABLE I
(Continued)

Reaction	A	B	C	T_9 Limits
^{54}Fe(p,γ)^{55}Co	27.538	-31.484	6.697	2.5-5
^{56}Fe(p,γ)^{57}Co	26.94	-22.903	-4.310	2.5-5
^{58}Ni(p,γ)^{59}Cu	24.445	-24.38	-1.528	2-4
^{60}Ni(p,γ)^{61}Cu	21.995	-14.225	-9.859	1.5-4
^{61}Ni(p,γ)^{62}Cu	27.395	-22.956	-4.635	1.5-5
^{64}Zn(p,γ)^{65}Ga	25.567	-21.052	-7.521	2-7
^{67}Zn(p,γ)^{68}Ga	24.198	-15.855	-10.141	2-7
^{68}Zn(p,n)^{68}Ga	28.05	-10.463	-42.39	3-7
^{70}Ge(p,γ)^{71}As	30.403	-27.859	-6.857	2-7
^{74}Ge(p,n)^{74}As	27.367	-9.354	-39.324	2-7
^{76}Ge(p,n)^{76}As	36.098	-32.872	-8.707	2-7
^{92}Mo(p,γ)^{93}Tc	32.689	-38.769	-1.184	3-6
^{92}Mo(p,γ)^{93m}Tc	30.755	-36.298	-3.112	2-7
^{95}Mo(p,n)^{95}Tc	33.167	-29.973	-17.793	4-5
^{95}Mo(p,n)^{95m}Tc	35.572	-33.794	-14.453	4-5
^{95}Mo(p,γ)^{96}Tc	25.767	-21.425	-12.376	2-7
^{95}Mo(p,γ)^{96m}Tc	20.759	-12.716	-17.864	3-7
^{96}Mo(p,n)^{96}Tc	27.101	-11.386	-42.448	2-7
^{96}Mo(p,n)^{96m}Tc	25.917	-10.399	-43.287	2-7
^{98}Mo(p,γ)^{99}Tc	25.815	-16.671	-15.249	2-7
^{100}Mo(p,γ)^{101}Tc	28.373	-32.931	-10.217	3-6

The advantage of our technique lies in the fact that reliable values of $N_A\langle\sigma v\rangle$ can be calculated using "smoothed" average values for the cross section, since the integral which yields $\langle\sigma v\rangle$ would itself automatically smooth the cross section. The exception to this is the case of a strong resonance which dominates the cross section. When this occurs, as in the case of isobaric analog resonances, we treat the resonance contribution separately. However, for most cases the smooth cross section is all the input needed to find $N_A\langle\sigma v\rangle$, as the usual smaller fluctuations in the value of σ are not important.

Experimentally, we measure a different quantity, the yield, Y. We define the yield as the ratio of the number of reactions occurring (or the number of product nuclei formed) to the number of incident beam particles. This ratio, which depends on the center of mass energy E, is adjusted to the value that would have been measured on a target of isotopic purity, although we use primarily natural targets. We have accelerated both proton and alpha particles, but all the data totally analyzed to date is with the proton beam. Yields have been measured at c.m. energies from 250 KeV to 6 MeV at the C.U. cyclotron with one Boron point taken at 69 KeV on the positive ion linear accelerator of the C.U. Electrical Engineering Department. Since the C.U. cyclotron can accelerate 45 MeV ^{3}He ions, this accelerator has a proven dynamic energy range of about 180 to 1.

In the formalism we use, the yield could be measured for reactions leading to stable nuclei, by detecting prompt γ's, neutrons, or in a few cases charged particles. However, we have concentrated, thus far, on those reactions leading to residual nuclei which undergo delayed γ,β^-, or β^+ decay. The analysis is slightly more difficult, but the experimental technique is quite a bit easier. By keeping track of the timing, beam current, etc., we can relate the activity A of the target at the end of the bombardment directly to the prompt yield by the relation

$$A(E) = Y(E)\cdot t^{-1}\cdot(1 - e^{-\lambda t})$$

where λ is the decay constant of the residual nucleus and t is the bombardment time. The actual radioactivity that we measure is either β^+ anniliation quanta or β^- delayed γ-rays. Branching ratio correction, decay times, efficiencies, etc. are used in arriving at the actual activity of the target. The activities we have used range in half-life from 0.6 s to over a year. For the activities with half-lives under about two minutes we have a cycling irradiation facility called the ram which transfers the target and controls counting automatically. For those over two minutes, there is only one irradiation and every operation is done by hand except multi-spectral scaling, which is used whenever half-life information is needed to identify the radioactivity.

After we have our experimental results which consist of the Y(E) data points, we extract the values for $\sigma(E)$, which are used in $N_A\langle\sigma v\rangle$. As mentioned before, these are "smoothed" values and could be called "averages" over our entire energy range as they are extracted in the way described below.

The thick target yield is related to the cross section by

$$Y(E) = \frac{N_A}{M_T}\int_E^o \sigma(E)\left[\frac{dE}{d(\rho x)}\right]^{-1} d\,E \qquad (1)$$

where M_T is the molecular weight of the target and $\frac{dE}{d(\rho x)}$ is the stopping power of the target. This particular form assumes a target thickness which exceeds the range of the particle at energy E, so that the beam stops in the thick target. The expression used for the stopping power is given by

$$\frac{dE}{d(\rho x)} = \frac{C(1 - e^{-\alpha E})}{E^{3/4}}$$

where C and α are parameters which depend on the beam particle and the target material. This empirical expression is discussed along with the extraction of the values for C and α in reference 5, and will not be pursued in further detail here.

From Equation (1) we can derive an expression for the cross section by differentiating:

$$\sigma(E) = \frac{dY(E)}{dE}\cdot\frac{M_T}{N_A}\cdot\frac{dE}{d(\rho x)} \qquad (2)$$

We arrive at values for $\sigma(E)$ from the lowest to the highest value of E in the following way. Our values of Y(E) are least squares fit by a polynomial in powers of ln(E). The best fit to Y(E) is then differentiated analytically with respect to E and substituted into Equation (2) to obtain $\sigma(E)$.

This calculated array of numbers is then fit by a parametric form for $\sigma(E)$ which is given by

$$\sigma(E) = \frac{S}{E} \exp\left(-\frac{b}{E^{1/2}} + cE^{1/2} + gE\right) \qquad (3)$$

where the parameters S, b, c, and g are computed by least squares. Typical values of these parameters are given in Table II, for several cases. This form of $\sigma(E)$, Equation (3), is the "smoothed" or "averaged" cross section.

TABLE II

Coefficients for the Cross Section Fit*

Reaction	log S	b	c	g	CM Energy (MeV)
$^{64}_{30}Zn(p,\gamma)^{65}_{31}Ga$	3.446	-47.77	-30.95	5.215	0.8-5
$^{68}_{30}Zn(p,n)^{68}_{31}Ga$	-607.9	233.67	358.3	-70.70	3.8-4.9
$^{70}_{32}Ge(p,\gamma)^{71}_{33}As$	16.376	-59.62	-35.05	6.027	1.5-5
$^{76}_{32}Ge(p,n)^{76}_{33}As$	-45.97	-27.38	3.756	-1.025	1.8-5
$^{92}_{42}Mo(p,\gamma)^{93m}_{43}Tc$	22.97	-65.83	-42.77	8.18	1.5-5
$^{95}_{42}Mo(p,n)^{95}_{43}Tc$	1908.1	-1303.9	-995.9	169.1	2.4-5.2
$^{95}_{42}Mo(p,\gamma)^{96}_{43}Tc$	-43.39	-44.61	19.58	-9.06	1.8-3.3
"	-65.73	-5.326	4.053	-.3402	3.3-4.5
$^{98}_{42}Mo(p,\gamma)^{99}_{43}Tc$	541.5	-355.7	-339.3	63.611	1.4-5.2
$^{100}_{42}Mo(p,\gamma)^{101}_{43}Tc$	-95.12	-4.37	26.69	-5.064	1.9-5

* $\sigma = S \exp(b/\sqrt{E} + c\sqrt{E} + gE)/E$

Before we go on, mention must be made of several important exceptions to this procedure which must occasionally be used. These are the cases of strong resonances, thresholds, and rapidly changing yield curve slopes. In the case of a strong resonance, such as isobaric analog states, etc., a Breit-Wigner shape for the resonance is used and resonance parameters extracted from the yield curve. Then in the resonance region, this form is substituted for the usual parametric form of $\sigma(E)$. When a threshold is reached as in the (p,n) reactions, the yield curve is fit by a power of $(E - E_{th})^n$ near the threshold energy E_{th}. Otherwise the rest of the yield curve is fit as usual. Finally, there are cases where there are rapid changes of yield curve slopes not related to narrow resonances or to thresholds. In these cases, we break the energy range of the data into two or more regions to be treated separately. Each region then has its own values of the parameters for $\sigma(E)$. The predicted yield curve is still constrained, of course, to be continuous.

After we have the parametrized $\sigma(E)$, either by the usual method or by one of the exceptions noted, we are almost ready to proceed with our calculations of $N_A\langle\sigma v\rangle$. We must first test how good our function for $\sigma(E)$ is with respect to our original yield data. In order to do this, we use the form of σ given by Equation (3) and numerically integrate Equation (1). An example of the fit generated is given in Figure 1.

FIGURE 1

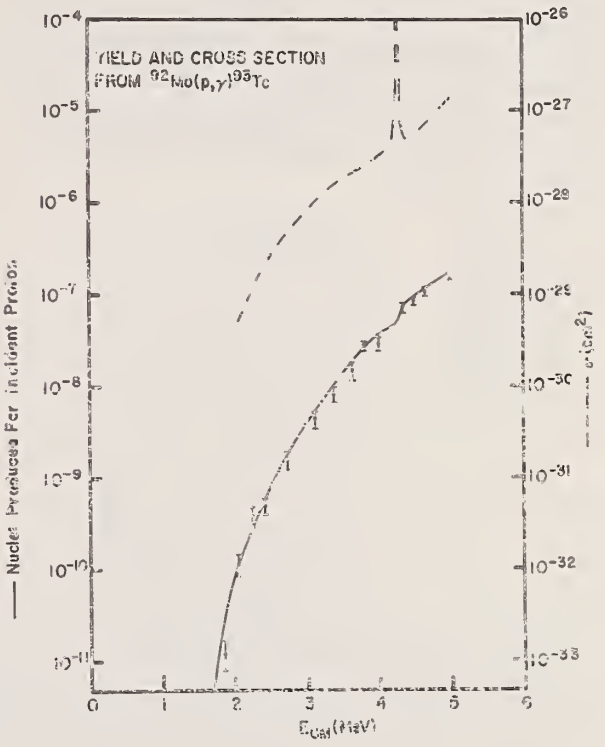

When we are satisfied that the form and parameters for σ are satisfactory as indicated by the fit and its associated χ^2, then we proceed to calculate $\langle\sigma v\rangle$.

The integral which defines $\langle\sigma v\rangle$ extends from zero ($v=0$ or $E=0$) to infinity ($v=\infty$ or $E=\infty$). However, our range of energies do not extend from zero to infinity, but rather from low energy (typically 1 MeV or less) to larger energy (ranging from 3 to 6 MeV, depending on the nucleus). (Of course for all these calculations, relativistic effects are neglected since our energies are quite non-relativistic.) Thus, the way in which we calculate $N_A\langle\sigma v\rangle$ is to evaluate the finite integral from the lowest energy E_{min} to the highest energy E_{max} by numerical methods such as Simpson's rule. We will typically use regular intervals in E from $T_9 = 0.25$ to $T_9 = 10$. At the same time we evaluate the numerical integral, we also can approximate the contribution from $E=0$ to E_{min} and from $E=E_{max}$ to infinity. Typically for low temperatures the low energy contribution is a few per cent of the total from the actually measured region. For values of T_9 above our selected range the high energy contribution approximation is also a few percent of the measured region's contribution. Thus we choose the range of integration's validity from those values of T_9 where the high and low energy contributions are a few percent and then fit the valid region of temperature to find the values of A_0, B_0, and C_0 as discussed above, which give a parametric form for $N_A\langle\sigma v\rangle$. These values are good over factors of 2-3 in T_9, typically. Although extrapolation outside the limited range of T_9 might yield correct rates there is no supporting evidence.

to substantiate this, and it is done at the user's risk.

In summary, the advantage of our technique is the relatively rapid way in which we can arrive at smoothed expressions for $\sigma(E)$ and thus $N_A\langle\sigma v\rangle$. The tedious method of measuring many values of $\sigma(E)$ with thin targets is not necessary since all that detail is lost in integrating to find $\langle\sigma v\rangle$. If the detail in σ is required, then this technique would have no advantage as many more values of Y(E) would be necessary than we presently use (approximately 5-10 measurements per MeV interval). We have presented this paper in the hope that you might find it useful for some measurement or that you may find modifications which will extend its usefulness.

Thank you.

REFERENCES

1. N. A. Roughton, M. J. Fritts, R. J. Peterson, C. S. Zaidins, and C. J. Hansen, "Thick Target Measurement of the (p,γ) Stellar Reaction Rates on the Nuclides ^{12}C, ^{29}Si, ^{46}Ti, ^{47}Ti, and ^{56}Fe," Ap. J. 188, 595 (1974).
2. _____, "Stellar Reaction Rates for Proton Captures on ^{28}Si, ^{50}Cr, ^{58}Ni, ^{60}Ni, and ^{61}Ni," Ap. J. 193, 187 (1974).
3. _____, "Stellar Rates for Proton Reactions on Isotopes of Ca, Ge, Zn, and Mo," submitted for publication to Ap. J.
4. R. J. Peterson, C. S. Zaidins, M. J. Fritts, N. A. Roughton, and C. J. Hansen, "Radioactive Products from Boron CTR Reactions," J. Nuc. Energy 00, 00 (1975).
5. C. S. Zaidins, "A Method for Energy-Loss and Range Calculations Based on Empirical Approximations," Nucl. Inst. and Methods 120, 125 (1974).

A BLACK DETECTOR FOR 250 KEV--1000 KEV NEUTRONS

G. P. Lamaze, M. M. Meier, and O. A. Wasson
National Bureau of Standards
Washington, D. C. 20234

A detector has been designed to have a greater than 95% efficiency in the range of 250--1000 keV neutron energy. The detector is modeled from a similar but larger detector by Poenitz.[1] The efficiency calculations were made with a modified version of Carlo Black,[1] which is a Monte Carlo calculation of multiple neutron scattering in a scintillator. The detector is a 12.6 cm x 17.78 cm cylinder of NE 110 with a 5.08 cm x 2.54 cm reentrant hole. The scintillator is mounted on an RCA 8854 photomultiplier tube which has been selected for low noise. Calculated efficiencies are presented as well as comparisons with experimental measurements.

(Neutrons; flux; scintillators; detector; Monte Carlo; time-of-flight)

One of the most important and difficult parts of any neutron cross section experiment is determining the neutron flux. Accurate flux measurements become more important as attempts are made to measure cross sections to better than 3% accuracy. There are several characteristics that are usually desired in a flux monitor. It should have a high efficiency and the efficiency should vary smoothly with energy; the efficiency should be easily calibrated and/or calculated; and the detector should have a fast response so that it can be used in time-of-flight and other coincidence experiments.

Organic scintillators are often used as flux monitors. Figure 1 shows a typical spectrum from a thin organic scintillator. Because of phototube noise, a discriminator is set to cut off the lower end of the spectrum (shown as E_d in the slide). This leaves the problem of determining what fraction of the spectrum is being rejected and this leads to an uncertainty in the flux measurement.

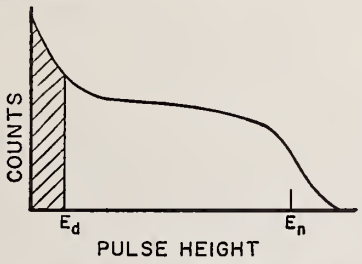

Figure 1. Typical spectrum from thin organic scintillator.

To overcome this problem of throwing away a large portion of the spectrum, Dr. Poenitz of Argonne has proposed a "black" detector, so called since it is designed to give a large pulse for each incoming neutron. Figure 2 shows the main idea behind this type of detector. Incoming neutrons are collimated into a reentrant hole in a large organic scintillator. The neutrons make several collisions and deposit most of their energy, giving a spectrum such as shown in the figure.

Since the neutron gives up most of its energy in three or four collisions, the time response of the detector is fast (~ 5-10 ns). Below 2 MeV the efficiency of the detector depends only on elastic scattering on hydrogen and carbon, so that the efficiency is easily calculated.

Dr. Poenitz was kind enough to give us a copy of his code Carlo Black,[1] which calculates spectra and efficiencies of black detectors. Using this code, we have designed a small, relatively inexpensive black detector. It is 12.7 cm in diameter by 17.78 cm long with a 5.08 cm x 2.54 cm reentrant hole. It is optically coupled to an RCA 8854 phototube. The small

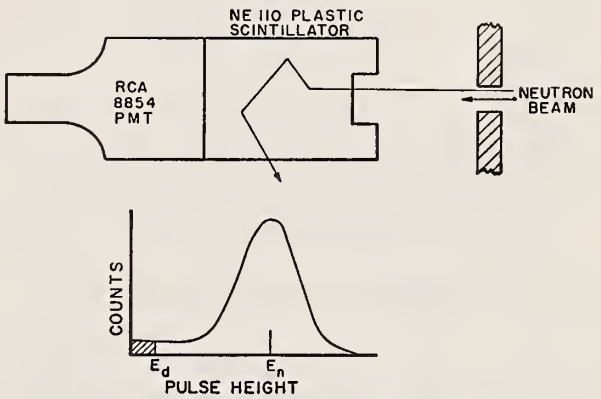

Figure 2. Schematic diagram of NBS black detector and ideal pulse height spectrum.

dimensions of this scintillator were chosen to maximize the efficiency below 1 MeV while minimizing costs.

Figure 3 shows some representative spectra obtained at the 200 m flight path of the NBS Linac above ground time-of-flight facility. The spectra show the expected characteristics of a peaked pulse height distribution and the pulse height increasing with energy. This figure also demonstrates one of our principal problems with this detector. The linac γ-flash generates a great deal of noise in the detector requiring the setting of a bias at about 100 keV neutron energy. This noise is believed to be due to after pulsing in the scintillator. The relative error caused by this high bias decreases for higher neutron energies.

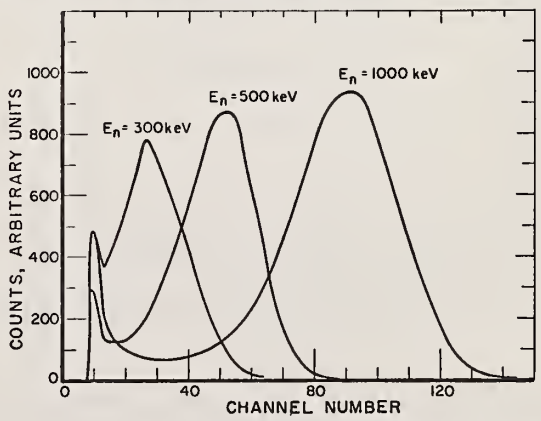

Figure 3. Typical spectra obtained with black detector at 200 m flight path of NBS Linac.

Figure 4 shows a comparison of a calculated spectrum and a Linac time-of-flight spectrum for 600 keV neutrons. The two spectra agree very well except for the shoulder on the calculated spectrum. We believe that this shoulder may be due to inaccuracies in the light tables. The light tables used in this program are taken from NE 213 light tables of Verbinski[2] and especially at low energies the NE 110 response may be much more linear. With this bias setting, the code predicts about 92% for the efficiency of the detector at this energy.

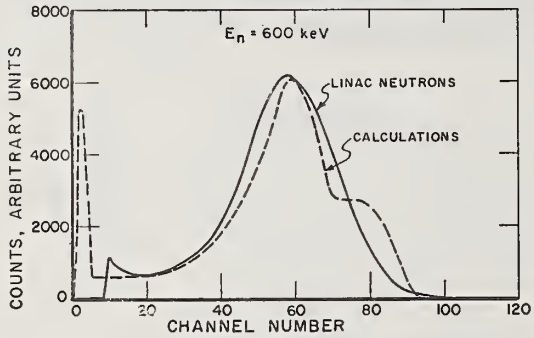

Figure 4. Comparison of calculated and experimental spectrum for E_n = 600 keV.

Figure 5 shows a comparison of a calculated spectrum and an experimental spectrum of 300 keV neutrons. This spectrum was produced with the NBS associated particle facility. Neutrons are produced with the $T(p,n)^3He$ reaction and are detected in coincidence with the outgoing ^3He particle. This facility is discussed in the following paper (BB5). There are two things I would like to point out about this spectrum. First, since there is no γ-flash in the Van de Graaff measurements, the lower level discriminator can be set down very low to essentially zero neutron energy. The second thing to point out is the obvious discrepancy between the calculated and observed spectrum. The explanation of this discrepancy is that for low neutron energies, only a small number of photons are produced in the scintillator and, of course, only a fraction of these produce photoelectrons. Hence, Poisson statistics should be folded into the calculated spectrum. For this spectrum, if you use 10 photoelectrons for 300 keV, the Poisson distribution reproduces the experimental spectrum fairly closely. Carlo Black does not presently take poor photon statistics into account, but we are planning to add this feature shortly.

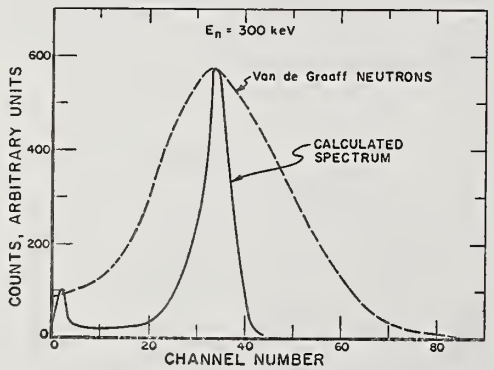

Figure 5. Comparison of calculated and experimental spectrum for E_n = 300 keV.

Figure 6 shows some efficiency curves predicted by Carlo Black. Curves for three different cutoffs are shown. These curves do not take into account Poisson statistics, so these lower energy values will still have to be corrected. But ignoring that for the moment, we see that for a 15 keV cutoff, the predicted efficiency is almost flat and is about 98%. As the cutoff is brought up to 100 keV, the efficiency drops to about 92%. Of course, for lower neutron energy, the efficiencies will be less after corrections are made for the poor photon statistics.

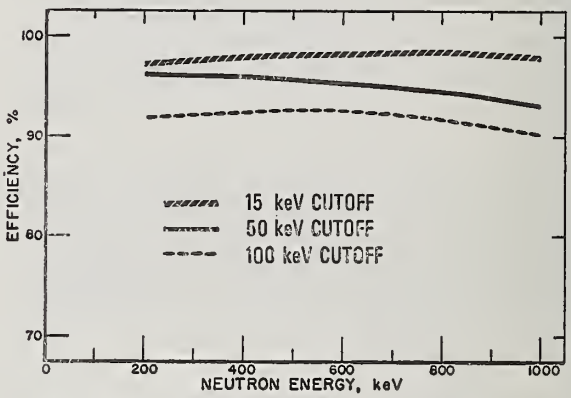

Figure 6. Calculated efficiencies of the black detector as a function of lower level cutoff.

This detector will be used as a flux monitor in both the Linac and Van de Graaff laboratories. At the Linac, the detector is presently being used as a flux monitor on the 200 meter flight path. At higher energies, we use the calculated efficiencies and at the lower energies we will rely on calibrations of this detector now underway at the Van de Graaff laboratory.

References

1 W. P. Poenitz, ANL-7915, Argonne National Laboratory (1972).

2 V. V. Verbinski, W. R. Burrus, T. A. Love, W. Zobel, N. W. Hill, R. Textor, Nucl. Inst. and Meth. 65 (1968) p. 8.

DETECTOR CALIBRATION WITH AN ASSOCIATED PARTICLE APPARATUS

M. M. Meier, A. D. Carlson and G. P. Lamaze
National Bureau of Standards
Washington, D. C. 20234

An associated particle apparatus employing the T(p,n)^{3}He reaction is now in routine use at the NBS. The apparatus consists of two target chambers with ports at 10° and 25° which give a useful neutron energy range of 100 keV to 1 MeV for protons from the 3 MV Van de Graaff. Electrostatic deflection, fast energy discrimination and pulsed beam time of flight techniques are used to reduce background in the neutron-associated $^3He^{++}$ pulse height spectrum to less than 1%. Neutron fluxes in the associated cone range between 30 and 100 n/sec at the lowest and highest bombarding energies. The spatial profile of the neutron cone is broadened by coulomb scattering of the $^3He^{++}$ in the tritiated titanium target and has a width less than 12° (Full width at one-tenth maximum) for neutron energies above 300 keV. The apparatus has been used to calibrate a "black" detector described by Lamaze.[1] The results of this calibration will be compared to a Monte Carlo calculation of the efficiency.

(Associated particle technique; neutron detector; neutron flux monitor; neutron standards; neutrons; T(p,n)^{3}He reaction)

Introduction

The black detector discussed in the previous paper will be used to monitor neutron flux in the energy range 100 keV to 1 MeV in a variety of NBS measurements using Van de Graaff and Linac. The utility of the detector is obviously limited by the determination of its efficiency in each of these various situations which will be characterized by quite different noise and background conditions. This presentation describes our scheme for calibrating the efficiency of the black detector in a way that satisfies the needs of different users, and reports our most recent results in implementing it. The calibration is our first application of the associated particle apparatus and, as such, also reflects its current state of development at NBS.

Associated Particle Apparatus

The associated particle technique employing the T(p,n)^{3}He reaction has been employed for neutron flux determination by Fort et al.[2] and by Paulsen et al.[3] Our approach follows most closely that of the latter authors and is schematically illustrated in Fig. 1.

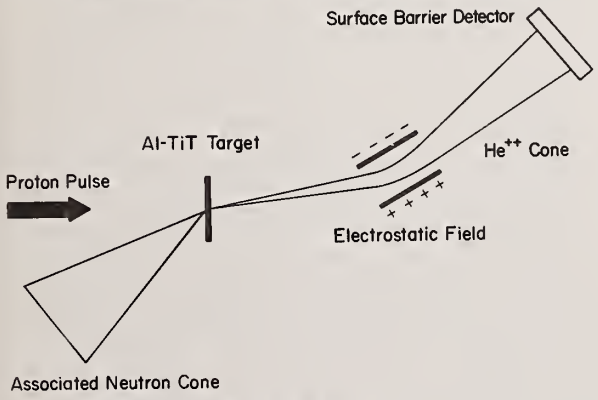

Figure 1. Associated particle apparatus.

The proton beam is collimated to 5 mm diameter and incident on a tritiated titanium target: 100 μg/cm^2 titanium deposited on a 100 μg/cm^2 Al substrate. After transmission, the unscattered beam is monitored at the end of the vacuum line, 80 cm from the target. Particles emitted at 10° are collimated to 8 mm before passing through a perpendicular electrostatic field. The field is adjusted so that $^3He^{++}$ particles are deflected through 4° and subsequently detected in a surface barrier detector (SBD) 160 cm from the target.

A block diagram of electronics which further separate the ^{3}He nuclei from background is shown in Fig. 2.

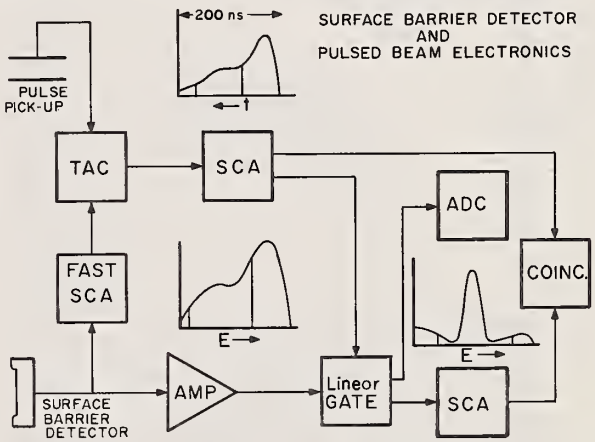

Figure 2. Electronics for ^{3}He identification.

A time of flight spectrum is generated by signals derived from the SBD and beam pulse pickoff. Timing from the SBD is derived with a fast single channel analyser with the upper baseline set somewhat below the energy of elastically scattered protons, to reduce the rate at the time to amplitude converter (TAC) to acceptable levels. Even with this discrimination the dominant feature of the time spectrum is the tail of energy degraded protons. From this spectrum a gate corresponding to the proper time of arrival of ^{3}He particles at the SBD is generated. This gate then passes the amplified and delayed SBD pulse height signal which is then stored in a single parameter array. Another single channel then generates gates which correspond to the appropriate ^{3}He pulse height. These, in coincidence with the true ^{3}He time of flight gates provide a gate indicating with high probability the detection of a $^3He^{++}$ event.

The procedure for a calibration or cross section measurement is clearly suggested. By turning on the electronics for neutron collection with this coincidence gate only events in the neutron detector that

are correlated with $^3He^{++}$ production are collected. In this way bias free pulse height spectra from neutron detectors are generated.

The magnitude of the problem of obtaining true ^3He events in the presence of a background of elastic protons and other reaction products is shown in the Fig. 3.

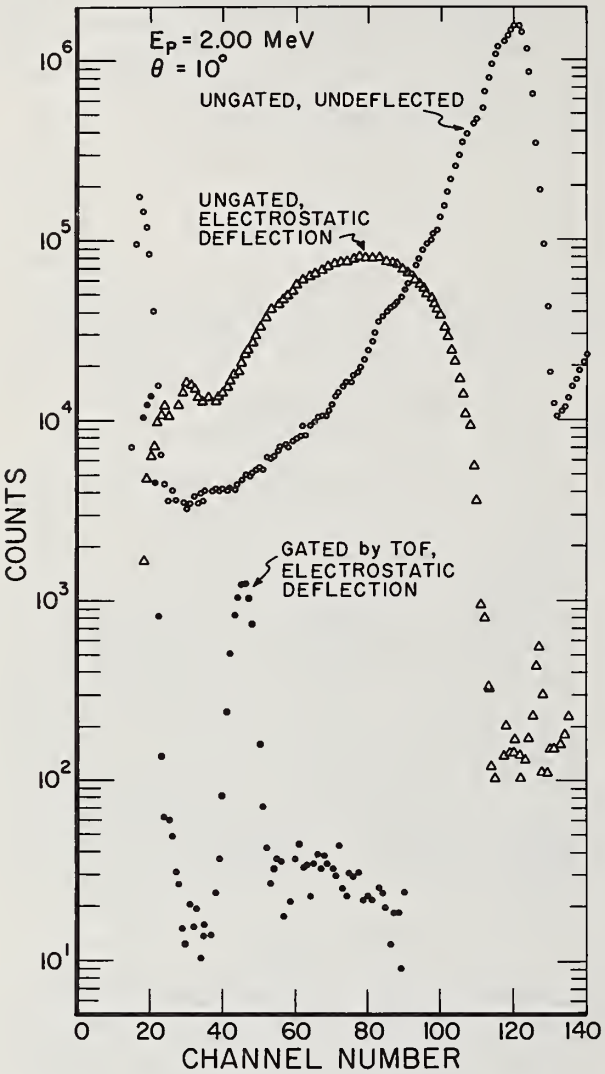

Figure 3. Spectra from the surface barrier detector. The curves are discussed in the text.

The spectrum labeled "Ungated, Undeflected" is the pulse height spectrum from the SBD viewing the target directly under conditions of very low beam intensity. The second spectrum labeled "Ungated, Electrostatic Deflection" is one taken with the SBD offset and the voltage on the parallel plates set to the appropriate value for the detection of $^3He^{++}$. The count rate is sufficiently reduced that the electronics are not overloaded at beam currents of the microampere level. Finally, the spectrum labeled "Gated by TOF, Electrostatic Deflection" shows the results of applying the ^3He - pulsed beam TOF gate to the second spectrum. A recent more detailed example of this reduced spectrum is shown in Fig. 4.

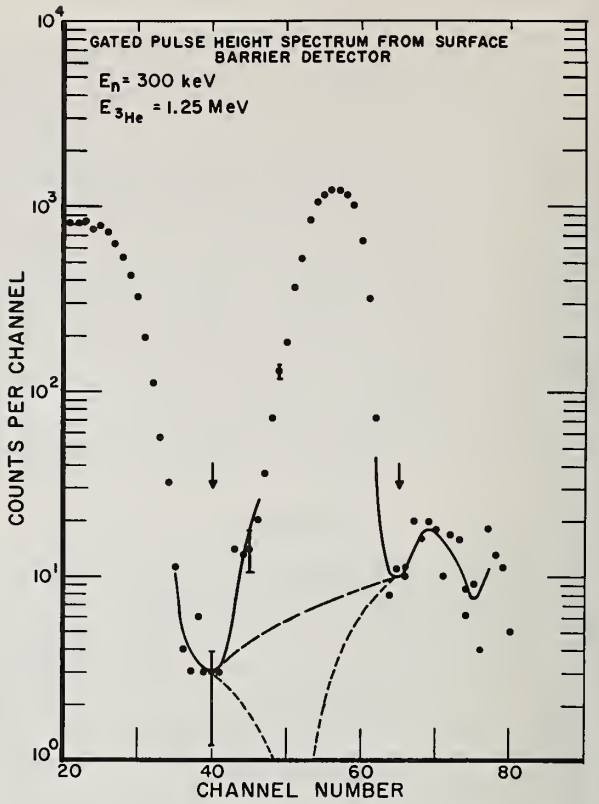

Figure 4. Gated pulse height spectrum from the surface barrier detector. The dashed curves indicate backgrounds of 1% and 0.5%.

This spectrum reflects our current ability to resolve true events from background. The dashed curves are straight lines on a linear plot which we feel overestimate and underestimate the background contamination below the peak. The upper dashed curve represents a background/corrected peak ratio of 1% and the lower estimates give a ratio of 1/2%. In calculating an efficiency we take the mean value of these two and assign it a conservative uncertainty equal to itself, i.e., the background here is taken to be 3/4% ± 3/4%.

Figure 5 shows an inherently less tractable problem inherent to associated particle techniques. If one measures the angular dependence of neutrons in the cone as a function of angle, the cone is found to be broadened more than would be expected from kinematics. This effect is due to the coulomb scattering of $^3He^{++}$ in the titanium layer. These are the results we obtain for a neutron energy of 300 keV. The angular width of the detector employed in this measurement is shown as the horizontal bar at 130°. The relevance of this measurement to the calibration is indicated by the two arrows. These show the angle subtended by the reentrant hole of the black detector while it is undergoing calibration. We estimate that at this energy less than 1% of the neutrons lie outside the reentrant hole.

Black Detector

As mentioned before, the black detector will be used at NBS under varying bias conditions depending on the particular experimental environment encountered. For this reason a single efficiency number for a given neutron energy is not a satisfactory calibration re-

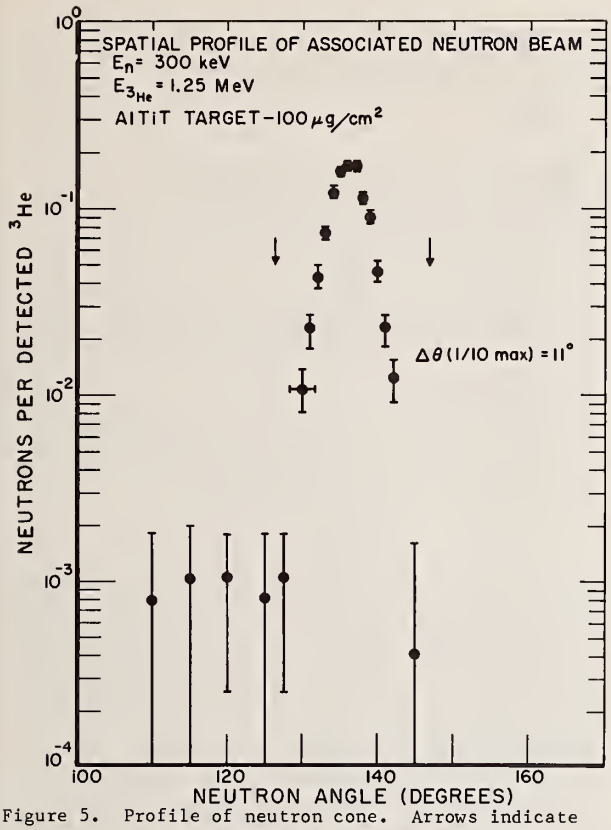

Figure 5. Profile of neutron cone. Arrows indicate the angle subtended by the reentrant hole of the black detector.

sult. Rather, the desired quantity is the differential efficiency; a curve with the shape of the pulse height spectrum for monoenergetic neutrons with an integral equal to the efficiency with zero bias. The electronics employed to generate the zero bias pulse height spectrum, corrected for background, are shown schematically in Fig. 6.

If there were no background, the pulse height spectrum from the black detector gated by the twofold coincidence of ^{3}He time and pulse height would be the needed zero bias pulse height spectrum. Dividing the value of such a spectrum by the corrected ^{3}He peak sum would give directly the desired differential efficiency curve. However, an accidental background exists which is due to events that are correlated with a given beam burst, but are not complementary reaction products. We simultaneously obtain this background spectrum by taking the data in two parameter format; detector pulse-height and SBD-black detector time of flight. The time spectrum exhibits this background as structure at intervals corresponding to the beam pulsing rate. The magnitude of this background is, of course, dependent on the beam intensity and, during the calibration runs, was kept to a value below 1%.

The price paid for this additional information is the imposition of a bias on the spectrum. To insure that this effect is negligible, spectra are taken for a series of increasing biases imposed at the SCA. When the shape of the spectrum at low pulse height is first observed to change, that bias is noted and the calibration bias is taken to be a factor of ten lower. A typical spectrum for 300 keV neutrons is shown in Fig. 7. The spectrum can be biased by other users of

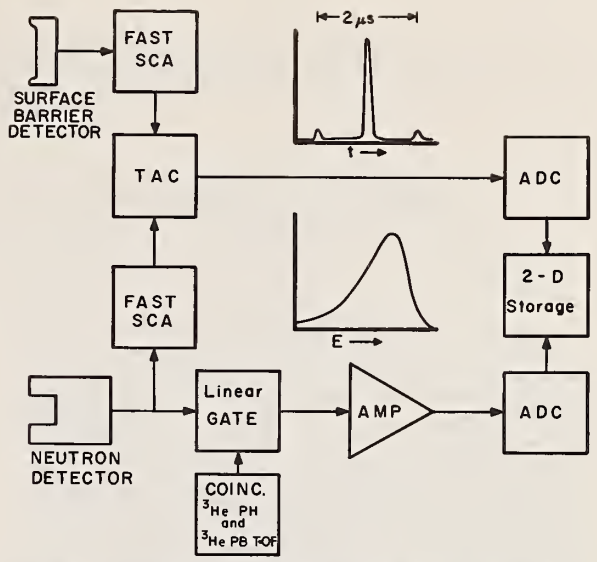

Figure 6. Electronics for collection of neutron events and background identification.

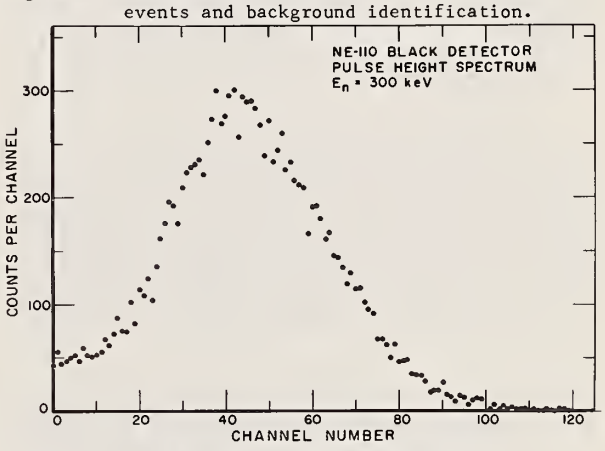

Figure 7. Pulse height spectrum of the black detector gated by ^{3}He events.

the black detector wherever necessary and the efficiency taken to be the appropriate fraction of the spectrum integral divided by ^{3}He peak sum. The integral of this curve normalized to ^{3}He is 0.94 with an uncertainty of around 5%. This uncertainty was somewhat disappointing in view of our desired accuracy of 3%. However, the systematic effects which contributed to the larger error are being corrected and future plans include recalibration of this point as well as calibration over the remainder of the range 100 keV to 1 MeV.

References

1 G. P. Lamaze, M. M. Meier and O. A. Wasson, Conference on Nuclear Cross Sections and Technology, 1975

2 E. Fort, J. L. Leroy and J. P. Marquette, Nucl. Instr. and Meth., 85, 115 (1970)

3 A. Paulsen, H. Liskien and M. Cosack, Nucl. Instr. and Meth., 105, 103 (1972)

USE OF GAS PROPORTIONAL COUNTERS FOR NEUTRON FLUX MONITORS AT THE NBS LINAC

O. A. Wasson
National Bureau of Standards
Washington, D. C. 20234

The use of a hydrogen filled proportional counter as a neutron flux monitor for standard neutron reaction cross section measurements at the 200 m flight path of the NBS linac is described. Efficiency uncertainties approaching 1% are obtainable.

(Neutron; flux; monitor; hydrogen; proportional; counter)

Introduction

The goal of the neutron standards program at the NBS Linac is to measure neutron reaction cross sections in the neutron energy interval from 1 eV to 20 MeV to a precision of a few percent. These reactions include $^{10}B(n,\alpha\gamma)$, $^{6}Li(n,\alpha)$, $^{235}U(n,f)$, and $^{237}Np(n,f)$ and require good neutron flux monitors. Since hydrogen scattering is the best known cross section in this energy region, we require either hydrogen containing detectors or else thick detectors containing other materials such that the efficiency is insensitive to uncertainties in the cross sections of the detector material. We also require that most energy intervals be covered by two or more detectors in order to determine the systematic errors. Our selection of the best available monitors and their range of operation is listed in Table I.

For the interval from 1 eV to 10 keV we have chosen a thick ^{10}B slab using the $^{10}B(n,\alpha\gamma)$ reaction. The slab must be thick since we will use it to measure the $^{10}B(n,\alpha\gamma)$ cross section. From 10 keV to several hundred kilovolts we use a hydrogen gas proportional counter. Use of a 2.02 x 10^5 Nm^{-2} (two atmosphere) methane gas filling extends the range of the gas counter to over 1 MeV. The region from 200 keV to 1 MeV is also covered with the thick NE 110 plastic scintillator described in the previous two papers[1,2] in this publication. Above 1 MeV we detect proton recoils from thin plastic radiators with a solid state detector.

TABLE I. Neutron Flux monitor for the neutron energy region from 1 eV to 15 MeV for the NBS Linac

Monitor	Energy Region
Thick ^{10}B Slab	1 eV-10 keV
Hydrogen Proportional Counter	10 keV-200 keV
Methane Proportional Counter	50 keV-1 MeV
NE 110 Plastic Scintillator	200 keV-1 MeV
Proton recoils	800 keV-15 MeV

This paper will be limited to a presentation of preliminary results obtained with a hydrogen filled gas proportional counter using the 200 m flight path at the NBS Linac which was built for use of slow response detectors like gas counters.

Experimental Geometry

The experimental arrangement on the 200 m flight path is shown in Fig 1. The entire beam line is in vacuum except for the target room, a 30 cm gap at 5 m for filters and beam pipe expansion, 1.3 m at 68 m where the reaction cross section samples are located, and, of course, several meters before the monitors at 200 m. We also plan to insert a 1/2 mm thick ^{6}Li glass transmission monitor inside the beam pipe at 60 m for normalization purposes. We measure relative cross sections by placing the samples and their associated detectors at 68 m while the flux monitors are placed in a neutron beam collimated to 2.5 cm diameter at 200 m. This collimation allows the interchange of the different monitors without requiring corrections for the different detector sizes. Various other neutron shields are located within the beam pipes and are not shown.

A more detailed view of the hydrogen gas counter at the 200 m station is shown in Fig 2. The gas mixtures contain 1.01 x 10^5 Nm^{-2} (1 atmosphere) of hydrogen with a 1.6% admixture of methane for quenching and has a detection efficiency of about 7% at 10 keV. The methane mixture was limited to 1.6% in order to keep the carbon scattering contribution below 0.4%. This counter detects neutrons by means of the gas ionization produced by the proton or carbon recoils. For a monoenergetic neutron the proton recoil response is a rectangular spectrum. The counter is 5.0 cm in diameter and has an active length of 60 cm. The neutron beam is collimated to a diameter of 2.5 cm in order to prevent a recoiling proton striking the outer

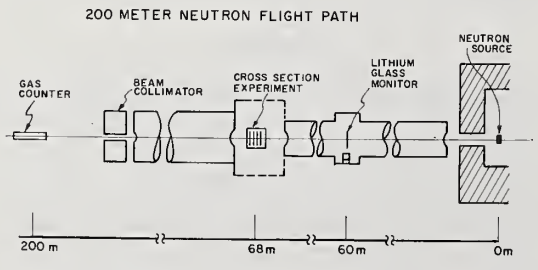

Figure 1. Experimental geometry for the 200 m flight path.

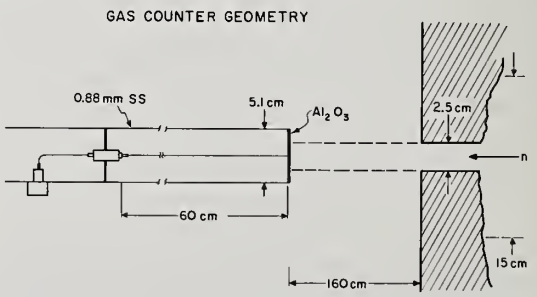

Figure 2. Shielding and dimensions of the gas proportional counter.

counter wall for neutron energies less than approximately 300 keV. Thus the spectral distortions produced by the wall effect are eliminated. The long length also keeps the spectral distortions for the end effect less than 3%.

Since we measure neutron energy by time of flight, we depend upon the shape of the recoil spectrum only to determine the number of neutron interactions and not to determine neutron energy. Thus distortions in spectral shape are not very important. However, processes which scatter neutrons and add or subtract events are important. The transmission of the front end of the counter is significant while the scattering from the back side, the sides, and air rescattering is small and calculable. The usefulness at higher energies is limited by the 1.1 μsec timing uncertainty which yields a 25 keV energy uncertainty at 300 keV and 160 keV uncertainty at 1 MeV.

Experimental Results

The response of the counter to 149 keV neutrons is shown in Fig 3 where the 16 keV neutron energy spread results from neutron flight time interval selected for the spectrum. The horizontal axis labels the recoiling proton energy. The slope of the spectrum is largely due to the end effect where the protons lose only part of their energy in the active volume of the counter. The range of a 150 keV proton

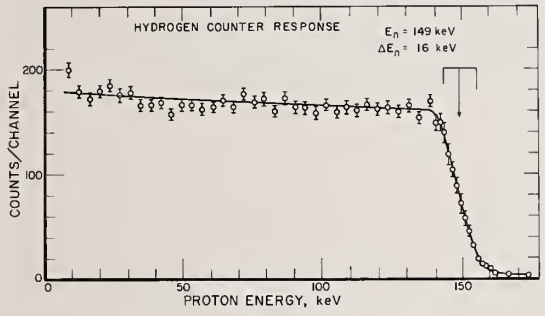

Figure 3. Response of the hydrogen counter to 149 keV neutrons. The arrow and bars indicate the spread in neutron energy. The horizontal axis indicate the recoiling proton energy.

is approximately 1.4 cm which means that the end effect distorts less than 3% of the spectrum.

The γ ray flash pulse is small, being equivalent to that of a 100 keV neutron with no filters in the beam. The flash thus generates no serious electronic overload problems and serves to determine the zero for the neutron flight time.

The low proton energy response of the counter to 1.2 keV, 7.5 keV, and 70 keV neutrons is shown in Fig 4. The high energy part of the 60-81 keV neutron spectrum is off scale to the right. The dominant source of the rise at low proton energies is γ ray background which will be reduced in future experiments. In operation we collect two parameter data and in the analysis bias the spectrum at several kilovolts. Thus the major uncertainty in the efficiency determination at low neutron energies is the extrapolation of the proton spectrum to zero energy. Since proportional counters measure the ionization produced by the recoiling proton and not the recoiling energy, the extrapolation is limited by the uncertainty of the energy loss required to produce an ion pair at low energies. This is sometimes called the ion-pair defect and has been found to vary widely for different hydrogen filled counters.[3-6] The results for the present counter are shown in Fig 5.

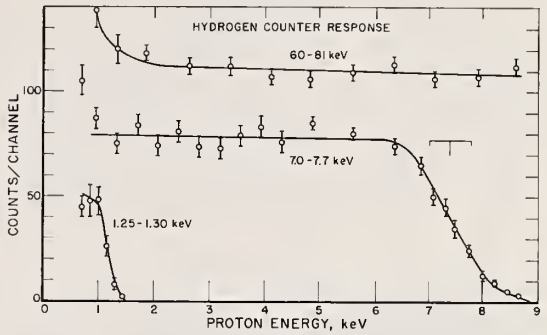

Figure 4. Low recoiling proton energy response for the various incident neutron energies indicated in the figure.

In Fig 5 is plotted the observed ionization divided by the maximum proton energy as a function of neutron energy. The ionization is determined from the half height of the upper edge of the spectrum while the maximum proton energy is determined from the neutron flight time. These results show that the proton energy loss required to produce an ion pair is constant within a few percent from energies above 2.5 keV. The change down to 1 keV is less than 20%. From these measurements I conclude that the uncertainty in the ion pair defect produces less than a 1% error in the efficiency determination for neutron energies greater than 10 keV.

Another important consideration is the background contribution. Fig 6 shows the hydrogen counter time-of-flight spectrum taken with a 5 keV bias for a blacking out natural lithium filter in the beam. Most of the 1% contribution to the 250 keV resonance dip is due to ambient background which is readily measurable. Below 10 keV the fraction of ambient background increases because of the low neutron flux produced by the bare neutron producing target.

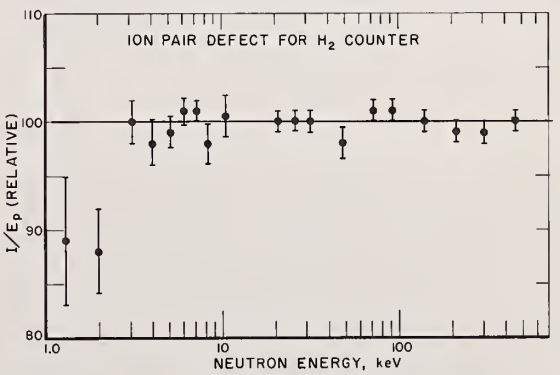

Figure 5. Ionization per unit energy less as a function of proton energy for the hydrogen counter.

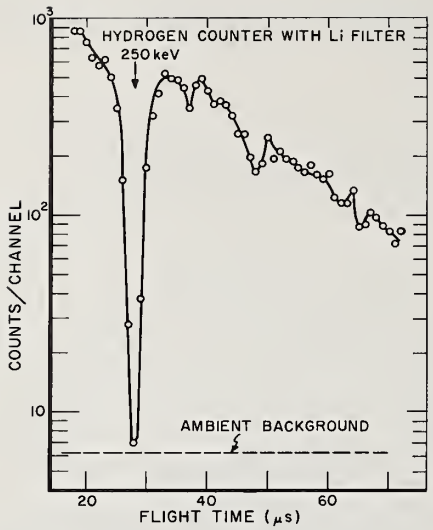

Figure 6. Background measurement of the hydrogen counter taken with a thick Li filter in the beam.

TABLE II. Systematic errors for the efficiency of the hydrogen filled proportional counter.

Effect	Uncertainty, %
Neutron scattering	0.3
Entrance Window transmission	1.8
Background	0.5
Gas Volume and pressure	0.5
Spectrum bias	1.0 for En = 10 keV
	0.2 En >100 keV

Conclusion

Table II summarizes the limitations or the efficiency determination of the hydrogen gas counter based on measurements to data. The largest uncertainty results from the density of the aluminum oxide entrance window. This error will be reduced by at least a factor of three in future measurements.

In conclusion, it appears that we can use the hydrogen gas counter to measure neutron fluxes at 200 m with a systematic uncertainty approaching 1%.

References

[1] G. P. Lamaze, M. M. Meier, and O. A. Wasson, Paper BB4 in this proceedings.

[2] M. M. Meier, A. D. Carlson, and G. P. Lamaze. Paper BB5 in this proceedings.

[3] E. F. Bennett, Nucl. Sci. and Eng. 27, 16 (1967).

[4] V. V. Verbinski and R. Giovannini, Nucl. Instr. and Meth. 114, 205 (1974)

[5] S. J. Friesenhahn, A. D. Carlson, V. J. Orphan, and M. P. Fricke. Measurements of the $^{10}B(n,\alpha)$ Cross Sections for Neutron Energies from 1 to 1000 keV. Gulf-RT-A12192 (July, 1972)

[6] J. W. Rogers. An Investigation of the Energy Dependence of the Specific Average Energy Loss Per Ion Pair in Methane and Hydrogen with a Proton-Recoil Spectrometer, Trans. Am. Nucl. Soc. 12, 936 (1969)

FISSION CROSS SECTION MEASUREMENTS ON SHORT-LIVED ALPHA EMITTERS

J. W. T. Dabbs, N. W. Hill, C. E. Bemis, and S. Raman
Oak Ridge National Laboratory*
Oak Ridge, Tennessee 37830

The large difference in initial ionization can be used to limit the size of alpha pulses relative to fission pulses in an ionization chamber, if the track lengths are both short. In parallel plate chambers this condition is not well met. We have developed a spherical plate chamber in which the ratio of maximum/minimum track length is 3. In the present (small sample) version, the maximum track is 6 mm, with deposit and neutron beam diameters of 1 cm. At optimum, with pure CH_4 gas, an electron collection time of ∿22 ns is expected across the 2mm gap. It is expected that the worst alpha/fission current pulse ratio will not exceed 1/14. Thus fissile isotopes with alpha half lives of 30 years or more (e.g. ^{243}Cm) may be studied with 1-2 nanosecond risetime current amplifiers; in addition, very small spontaneous fission branching ratios may be better determined. Comparisons of this new chamber with a parallel plate chamber and initial results on ^{245}Cm (∿16 μg sample) will be presented. The ORELA pulsed neutron source permits measurements below 20 eV which are inaccessible to underground explosion experiments.

(Fast Ionization Chamber, Spherical Electrodes, fission/alpha, σ_f, ^{245}Cm)

I. Introduction

Measurements of neutron fission cross sections can be severely hampered if the target nuclide is a short-lived alpha emitter, except in the underground nuclear explosion case. Neutron time-of-flight techniques are now almost invariably used; these normally require timing accuracies of ∿10 nsec. If solid state nuclear particle detectors are used, one finds that after $\sim 10^{11}$ alpha particles/cm^2 the detector is radiation damaged sufficiently to require replacement.[1] This problem is avoided if a gaseous ionization chamber can be used. Electron collection is the preferred mode of operation, since the positive ion drift velocities are very low, and collection times are too long, even for closely spaced electrodes. Electron drift velocities in pure CH_4 reach 10.5 cm/μsec, and vary nonlinearly with variations in electric field per unit of gas density.[2] Plates spaced apart by a few mm at most are desirable to keep electron collection times ∿20-30 nsec when highly alpha active targets are used, to reduce pileup of the alpha particle pulses. Fast risetime, low input impedance current sensitive amplifiers are needed both from the neutron time-of-flight and the α-pulse pileup points of view, and can be made fast enough that the electron collection time controls the pileup.[3]

In the first part of its range, a fission fragment gives an ionization density some 50 times greater than an alpha-particle. In Section II, we describe a geometrical approach which takes advantage of this difference, describe a chamber made following this approach, and give results of tests using ^{252}Cf. Section III contains a discussion of some of the factors involved in making measurements on short-lived alpha emitters and a discussion of pulse shapes and pulse pileup. Section IV contains preliminary results of a measurement of $\sigma_f(^{245}Cm)$ recently performed at ORELA, in which a sample of only 16 μg was used.

II. Spherical Plate Ionization Chamber

Geometrical Considerations

In a parallel plate chamber, the maximum alpha pulse size is determined by the smaller of 1) the alpha particle range at the density of the filling gas, 2) the sum of the radius of the deposit and the radius of the plates (both assumed circular). The minimum fission fragment pulse size is determined by the smaller of 1) the plate spacing, 2) the range at the gas density. In the limit of high gas density, one approaches a pulse height ratio of about 6 (30 MeV/5 MeV) when both types of particle are stopped in a distance ≤ the plate spacing. As we shall see later, this is a marginal ratio when pileup is considered in practical cases, if it is desired to approach an "absolute" separation of fission and alpha particle pulses by pulse height discrimination alone. Another method of improving the ratios of minimum fission to maximum alpha pulses is to restrict the ratio of maximum to minimum track lengths geometrically at lower pressures. This could be done by dividing the interplate volume into a number of small chambers, with attendant wall scattering, possible breakdown, and possible gas contamination from the nonconducting separators. We have taken a different approach. We have "closed off" those particle paths which are almost parallel to the surface of the active deposit by "enclosing" the deposit with the collector electrode. This is accomplished by placing the deposit spot on a convex spherical surface and using a spherical surface with a larger (concentric) radius as collector. A particle path tangent to the inner sphere then reaches the outer surface in a distance†

$$\ell_{max} = d \cdot \sqrt{(r+1)/(r-1)} \qquad (1)$$

where d is the difference and r is the ratio of the two radii (r>1). For the present case r = 1.25 and ℓ_{max}/d is 3.0.

It is clear that the active deposit should not be placed on the inner surface of the larger sphere, but on the convex surface of the inner sphere only. For low pressures where $\ell_{max} \leq 0.3$ of the α particle range, the smallest pulse/height ratio of fission to alpha particles should be ∿50/3, provided no degradation of the fission fragment energy occurs in the source deposit itself.

†We thank R. L. Macklin for pointing out this simple form.

Present Chamber

The experimental chamber contains three sets (pairs) of thin "hemispherical" plates, stacked to give a 6.25 mm separation of one set from the next. This separation of deposits is then less than the flight path uncertainty from the neutron moderator. The plate radii used were 8.66 mm and 10.82 mm (d = 2.16 mm) in each set, with a slight conical modification of the inner "hemisphere" to improve the stack spacing. The deposit spot on the inner sphere was 10 mm diameter and subtended a cone half angle of 35.3° about the chamber axis when viewed from the center of the "hemispheres".

The plates were made of 0.05 mm (2 mil) 304 stainless steel and formed between machined dies. An initial anneal, followed by a two-step process with intermediate annealing was found necessary to avoid rupture.†† Steel was chosen because the actinide recovery chemistry is better understood than for Al. An advantage of the spherical shape is great rigidity, which permits both accurate location and spacing of the plates, and freedom from microphonic pickup, even for very thin plates. The present design also provides an additional level of practical containment of the alpha active actinide by preventing straight line, recoil induced self-transfer to the region external to the plates. One thus reduces contamination of the chamber walls and capacitor and insulator surfaces.

††We are grateful to R. H. Ward and C. R. Hill of the ORNL Physics Division Staff Shop for the development of this process.

Results with ^{252}Cf

Chamber tests with a deposit of ^{252}Cf (1200 α/sec and 40 fission events/sec) and using a conventional slow amplifier and multichannel analyzer confirmed the expected 14:1 ratio (based on heaviest, lowest energy fragments/alpha) between the pulse heights corresponding to 1) the 4 percent point on the lower edge of the fission fragment group and 2) the 50 percent point on the high side of the alpha particle peak (a step from 2-alpha pileup was noted, even at this low α rate). The broad valley between the alpha peaks and the rather abrupt rise in fission events was filled in almost uniformly with an integrated total of 1.4 percent of the total fission events. These degraded pulses extended downward *under* the alpha peak with only a slight rise all the way to the lowest pulse heights measured. It was determined that 97 ± 3 percent of these events were fission events by using an external fission neutron detector in coincidence with the chamber pulses. These degraded pulses are related to deposit thickness or columnar recombination. More experience and experiments will be needed to establish the relative importance of these causes.

A similar set of measurements with parallel plates, otherwise identical as to spacing, overall diameter, deposit size, etc., and mounted in the same CH_4 gaseous environment, gave results about 2.5 times worse in terms of the ratio of the pulse height at the foot of the fission group/pulse height at the extreme upper edge of the alpha group (2:1 vs. 5:1 for the spherical plates). The height in the valley in the pulse height distribution (fissions only) varied from 0.3 percent to 3 percent of the fission maximum at very low pulse heights. The integral was 0.5 percent of the total number of fissions. It is not known if the flat plate deposit was of higher quality. The valley integral was 0.8 percent with a solid state detector from a similar deposit.

III. Pulse Shapes, Collection Times, and Deposit Thickness

An interesting difference in the pulses obtained in a spherical plate chamber of the type described here is that *all* tracks begin at the inner sphere and end at the outer sphere. To the extent that the ionization is uniform along the tracks, the current pulses, as seen with a very fast risetime amplifier, should then be triangular (sharp rise, followed by a linear fall) and all of the same duration. In methane, with an electron drift velocity (max) of 10.5 cm/μsec, and a spacing of 2.16 mm, one expects a pulse duration of 22.7 nsec. While this may be correct for lightly ionizing α particles (which cannot be seen above noise in present day fast amplifiers), we have observed fission pulse durations of ∿ 35-40 nsec. For the moment, we attribute the slower collection to columnar reduction in the electric field within the track.

It should be noted that improved collection times require a smaller gap and that such gaps *require* scaled down spherical radii and deposit area, if $\ell_{max}/d \sim 3$ is to be maintained. Similarly, large deposit or beam areas *require* larger spacing and longer collection times. The present size is considered a good compromise. Estimates of pulse pileup occurrence rates have not been attempted in a serious way for pileup greater than three times the height of a single pulse, except for the well-known rectangular pulse case. Various crude approximations based on the rectangular pulse formulas and the use of an effective width of a triangular pulse equal to the portion above $\sqrt[n]{0.5}$ where n is the "pileup depth number" suggest that the present chamber design should be capable of giving adequate fission-alpha pileup discrimination at alpha rates of 10^8/sec (50 μg, 30 year half-life).

The "valley" observed with ^{252}Cf was found to be substantially filled in (to 10 percent of peak) when a deposit thickness of 200 μg/cm^2 of ^{235}U was used in the experiments described below. With a very poor deposit (electroplated twice), the valley was even less well defined. This suggests that great care is necessary in deposit preparation; the greater possibilities for a good separation demand higher quality deposits to make the inherent advantages of the spherical plates truly useful.

IV. Measurements on $\sigma_f(^{245}Cm)$

Samples of 16 μg ^{245}Cm (99.96 percent pure) and 168 μg ^{235}U were placed on adjacent sets of spherical plates. Roughly 12 days of operation of ORELA at 52 kW, 800 pps have been carried out with both samples in a 2 cm diameter neutron beam at 9.5 M. Table I gives a list of energies at which fission resonances have been observed below 20 eV. A short run at 200 pps which will permit a normalization check at 0.025 eV is in progress.

Table I. New Fission Resonances in ^{245}Cm Below 20 eV.

E_o	Relative Height	E_o	Relative Height
15.65 eV	27	7.53	172
14.00	19	4.72	120
11.42	56	3.43	5*
10.10	14*	2.54	13*
9.22	32*	1.99	31
8.95	24*	0.98	7*

See Ref. 4 for resonances 21-60 eV.
*Broad.

*Operated by Union Carbide Corporation for the Energy Research and Development Administration.

[1]J.W.T. Dabbs *et al.*, Fission Cross Section of ^{249}Cf (to be published).

[2]T. L. Cottrell and I. C. Walker, Trans. Faraday Soc. 61, 1585 (1965).

[3]H. G. Jackson, Trans. IEEE, NS 20, No. 5, 3-16 (1973).

[4]M. S. Moore *et al.*, Phys. Rev. C3, 1656 (1971).

Systematic Discrepancy in Photoneutron Cross Sections for Medium and Heavy Nuclei

T. Tomimasu and S. Sugiyama
Electrotechnical Laboratory
Tanashi, Tokyo, Japan

The shape and magnitude of the photoneutron cross sections for Cu, Pr, Pb, and Bi are compared to find out a systematic discrepancy between the cross sections obtained using the NBS P-2 chamber as a bremsstrahlung beam monitor and those obtained by other experimental techniques such as the positron annihilation-in-flight. The former cross sections in general are observed to be systematically larger than the latter. The discrepancy of about 10 % is demonstrated in the peak cross section values for medium nuclei. This may be explained in the good direction by a systematic discrepancy of 6 % in the calibration constants of the NBS P 2 chamber given at several laboratories, because the lowest values in these calibrations have been widely used to determine the photoneutron cross sections from measured neutron yield curves. The highest values can almost eliminate the 10 % discrepancy. The definite discrepancy can not be demonstrated for heavy nuclei because of the large discrepancies of 20 % or more found in the cross sections obtained with γ -rays from positron annihilation-in-flight.

[NUCLEAR REACTIONS Cu, ^{63}Cu, Pr, Pb, ^{208}Pb, Bi(γ,n); Comparison of shape and magnitude of photoneutron cross sections. Calibrations of the NBS P2 chamber.]

1 INTRODUCTION

Precise measurements of the photonuclear cross sections for medium and heavy nuclei are of interest for (1) comparison with the theoretical predictions[1] on the shape of the cross section and (2) identification of giant quadrupole resonances as has been achived by (e,e') reactions.[2]

One more interest in accurate cross section measurements is to make a comparison of experimental values for the integrated cross sections with the theoretical predictions of the sum rules.[3,4]

In the past two decades, a large number of measurements of photonuclear cross sections have been made for various nuclei. Recently, some compilations of these data have been published[5,6] and another compilation of photoneutron cross sections obtained with monoenergetic photons is prepared.[7] Nevertheless, the existing data for an identical nucleus obtained in different laboratories are almost in disagreement with one another in both magnitude and shape of the cross section. Therefore, there is a number of articles[8-18] discussing the disagreement of the cross section magnitudes. The recent article by Bramblett et al.[18] has pointed out that there are some discrepancies between the Livermore and Saclay values of the integrated photoneutron cross sections measured with the annihilation-in-flight technique.[19]

The purpose of the present work is (1) to show a systematic discrepancy of 10 % or more found between the cross sections for medium and heavy nuclei obtained with bremsstrahlung beam using the NBS P·2 chamber as a beam monitor and those obtained by other experimental techniques such as the position annihilation-in-flight, and (2) to discuss a possible cause for this discrepancy.

2 THE PHOTONEUTRON CROSS SECTION FOR COPPER

Before monoenergetic γ -rays from positron annihilation in flight[19] (PAF γ-rays) or from photon tagging method (PT γ -rays)[20] have been available, most measurements of photonuclear cross sections have been using bremsstrahlung beams (BS γ -rays) from electron accelerators. On the other hand, measurements of photonuclear cross sections using monoenergetic γ -rays from nuclear reactions (NR γ-rays), while restricted to a few energies, provide an important check on the accuracy of these BS cross section data. Because the BS cross sections are subject to several uncertainties arising from (1) the unfolding of bremsstrahlung yield curves, (2) a lack of exact knowledge of the bremsstrahlung spectrum shape, and (3) the X-ray intensity monitoring methods commonly used.

However, the NR cross sections are also subject to several uncertainties arising from (1) low γ -ray intensity, (2) target irradiation in condisions of poor geometry, and (3) difficulties in calibrating the γ -ray intensity monitors, as pointed out by Coote et al.[10] Therefore, there are considerable discrepancies in absolute values of the NR cross sections for the ^{63}Cu (γ,n) ^{62}Cu reaction at 17.6 MeV, as discussed in the following section.

The (γ,n) cross section of natural copper or ^{63}Cu has been used as a standard for the normalization of new data and investigated frequently either using bremsstrahlung beams[21] or γ -rays[22] from the ^{7}Li (p,γ) ^{8}Be reaction. Nevertheless, the cross section values for the ^{63}Cu (γ,n) reaction do not agree with one another. As Nakamura et al.[9] and Coote et al. have pointed out, BS cross section values show reasonable agreement with peak cross sections of about 100 mb and most of NR γ -ray measurements yield results about half this value. These situations are almost same for the photoneutron cross section for natural copper.

Yasumi et al.[23] and Coote et al. have attempted careful measurements of NR cross section for the ^{63}Cu (γ,n) ^{62}Cu reaction and have obtained 76 $\pm$ 5 mb and 73 $\pm$ 8 mb at 17.6 MeV, respectively. Both NR values are in good agreement with each other and they are 25 % lower than the previous BS values and 50 % higher than the previous NR values.

In the past decade the PAF cross sections besides the BS and NR cross sections have been measured for more than 50 nuclei throughout the periodic table mainly by the Saclay[16,19] and Livermore[18,24,25] groups and recently by the San Diego[15] group using γ -rays from positron annihilation in flight (PAF γ-rays). Nevertheless, considerable discrepancies are found in absolute values of these PAF cross sections just as in the case of the BS and NR cross sections.

One of the authors[14] has pointed out that a systematic discrepancy of the order of 30 % is still found in the absolute values of the PAF cross sections [16,18,19] of copper and lead and that a discrepancy of 6 % found in the calibrations of the NBS P2 chamber[26] very carefully done at different laboratories[27,28] may be one of the possible causes for the discrepancy found in the BS cross section values obtained by the use of the NBS P-2 chamber as a beam monitor.

We have attempted an absolute measurement of BS photoneutron cross sections for natural copper and lead using an ETL (Electrotechnical Laboratory) type quantameter[14] and a 4 π paraffin moderated neutron detector.[29] The calibration constant of the ETL type quantameter and the detection efficiency (about 0.6 %) for photoneutrons of the 4 π neutron detector have been given in our laboratory.[14]

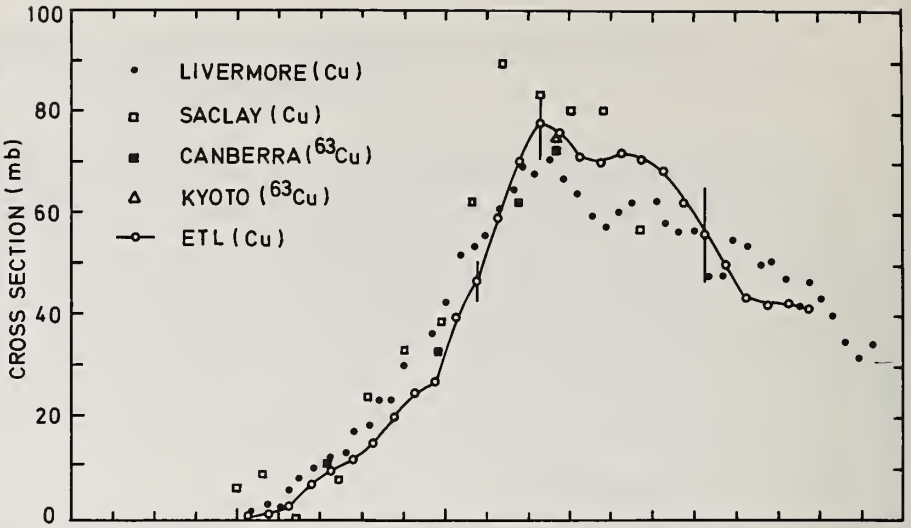

FIG.1(a) Comparison of the photoneutron cross sections for copper. The Livermore data were shifted upward in energy by 0.5 MeV for comparison.

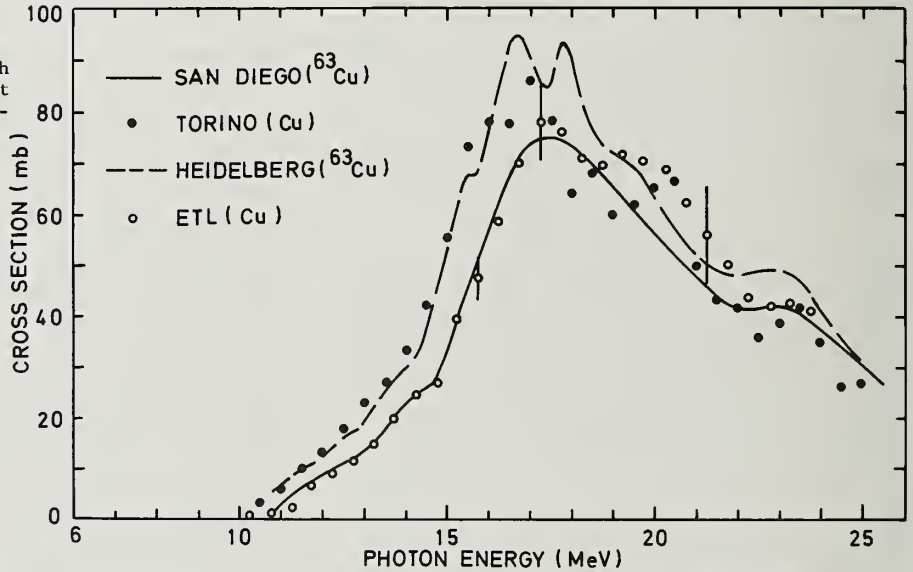

FIG.1(b) Comparison of the BS photoneutron cross sections with the PAF cross section of Sund et al. The latter data were shifted upward in energy by 0.25 MeV for comparison.

The peak values of our BS cross sections are 78 $\pm$ 8 mb* for copper and 660 $\pm$ 60 mb* for lead. They are about 20 % lower than the previous BS values. Fig.1(a) demonstrates that no significant discrepancy is found in our BS value for copper and the NR values for ^{63}Cu of Yasumi et al. at Kyoto and Coote et al. at Canberra but our BS value is about 15 % lower than the PAF value of Saclay[19] and several percent higher than that of Livermore.[24] Our BS value for lead will be discussed later in detail.

A little later Sund et al.[15] at San Diego have measured the (γ,n) and (γ,2n) cross sections for ^{63}Cu using the activation analysis method and PAF γ-rays. The activation analysis method for the determination of number of photoneutron events has the advantage that the detection efficiency is independent of the neutron energy spectrum, which may vary with the energy of the bombarding photons. Their attempt is of considerable interest because it may reveal the causes for the discrepancy found in the magnitude and shape of the PAF cross sections measured at Saclay and Livermore, where the detector or detecting method of Photoneutron events are different one another : Saclay, at early stage with a 4π paraffin moderated neutron detector having a neutron detecting efficiency of about 1.48 %[19] and later with a gadolinium loaded liquid scintillator having a neutron detecting efficiency of about 60 %;[16] Livermore, with a 4π paraffin moderated neutron detector having a neutron detecting efficiency of about 20 %.[24] However, the spectrum and photon flux measurements of PAF γ-rays have been made with a large NaI(Tl) spectrometer at each laboratory.

The peak value of the PAF cross section of Sund et al. is 75 $\pm$ 6 mb for ^{63}Cu and about 20 % lower than the previous BS values except our BS value. Fig.1(b) and Tab.1 show excellent agreement of their PAF cross section with our BS cross section for natural copper, although natural copper includes about 31 % ^{65}Cu other than ^{63}Cu. However, their PAF value is several percent higher than that (70 $\pm$ 7 mb) of Livermore and more than 10 % lower than that (90 $\pm$ 7 mb) of Saclay. These discrepancies exceed the experimental errors quoted in their PAF cross sections and may be due to inaccuracies in the detection efficiencies of photoneutron events.

Somewhat later, Dreyer et al.[17] at Heidelberg have reported that the peak values of their BS cross sections for ^{63}Cu and ^{141}Pr appear to be systematically higher (some 10 % to 20 %) than the corresponding

* $\pm$ 8 mb and $\pm$ 60 mb indicate total error (= 3 x sdm + net systematic error).

PAF values. Their cross sections were obtained using the activation analysis method and the NBS P2 chamber. Nevertheless, their BS value (92 mb) well agrees with the PAF value for copper of Miller et al. and is several percent higher than the BS value (86 ± 2 mb) of Baciu et al.[12] at Torino as shown in Fig.1 (b). Therefore the systematic discrepancy found between the BS and PAF values seems to be about 10 % or smaller.

A BS cross section for copper can be obtained from the neutron yield measurement by Gerstenberg and Fuller,[13] although this is not a direct BS cross section measurement. They attempted a careful study on the detection efficiency of the photoneutron detector used in the BS cross section measurement at NBS. Using this calibrated neutron detector and the NBS P2 chamber, the neutron yields from twelve nuclei throughout the periodic table including lead and copper were measured at peak bremsstrahlung energies from 12 to 29 MeV. These yields were compared with those calculated from the PAF cross sections measured at Saclay and Livermore. The ratios of the neutron yields from copper of Saclay and Livermore to that of NBS are 0.98 and 0.91.[13] The peak cross section for copper of NBS can be roughly estimated to be 85 ± 5 mb from these ratios and the peak values of Saclay[19] and Livermore.[24]

Of these BS cross sections, those of Baciu et al., Gerstenberg and Fuller, and Dreyer et al. have been obtained using the NBS P2 chamber as a detector of the photon beam energy. As shown in Tab.1, they give peak values converging towards 88 mb. On the other hand, the peak values of the PAF cross sections of Miller et al., Fultz et al., and Sund et al. considerably scatter from 70 mb to 90 mb, but the average value (78 mb) of them is just same with our BS value (78 mb). The discrepancy between the BS values except ours and the PAF values is about 10 %.

3 THE CALIBRATION CONSTANTS OF THE NBS P2 CHAMBER

A possible cause for the 10 % discrepancy is discussed here. Fig.2 shows the calibration constants of the NBS P2 chamber given at several laboratories. The NBS P2 chamber[26] is the most widely used chamber for X-ray beam energy measurement. The calibration constants at energies below 20 MeV, a region of importance to photonuclear cross section measurements, are of NBS[27], LPTI[28], and ETL (our laboratory).[14]

Target	σ_m (mb)	Γ (MeV)	$\int^x \sigma\, dE$ (MeV-mb)(x)	Reference
Cu	90		450 (19.6)	19(Saclay)
Cu	71 ± 7	10	635 (28)	24(Livermore)
^{63}Cu	70 ± 7	11	603 (28)	"
^{63}Cu	75 ± 6	8	586 (25)	15(San Diego)
Cu	86 ± 2	7.3	733 (28)	12(Torino)
Cu	85 ± 5			13(NBS)
Cu	78 ± 8	8	587 (24)	14(ETL)
^{63}Cu	92 ± 6	6.0	697 (33)	17(Heidelberg)

TAB.1 Parameters of the photoneutron cross sections for Cu and ^{63}Cu.

However, these calibration constants considerably scatter. A systematic discrepancy of 6 % is found between the NBS and LPTI values at the interested energy region. The 6 % discrepancy exceeds the estimated error shown in Fig.2.

The 10 % discrepancy discussed in Sec.2 may be explained in the good direction by the systematic discrepancy of 6 % in these calibration constants, because the lowest calibration constants given at NBS have been widely used to determine the BS cross sections from measured neutron yield curves. The highest calibration constants shown in Fig.2 can yield a lower peak cross section value by 6 % than that determined by the lowest ones. Therefore, the highest ones may almost eliminate the 10 % discrepancy, although other possible causes besides the 6 % discrepancy found in the calibration constants could be also considered.

However, it is, at least, justifiable that the 6 % discrepancy can lead to a reasonable agreement of the four BS cross sections (Torino, NBS, Heidelberg, and ETL) discussed above. The reason is that the three laboratories other than our laboratory have used the NBS calibration constants, which are the lowest ones as shown in Fig.2, whereas the ETL calibration constants given by the use of the ETL type quantameter belong to the highest ones in the calibration constants of the NBS P2 chamber. Therefore, the 10 % discrepancy found in the four BS cross sections can be almost explained in the good direction by the 6 % discrepancy.

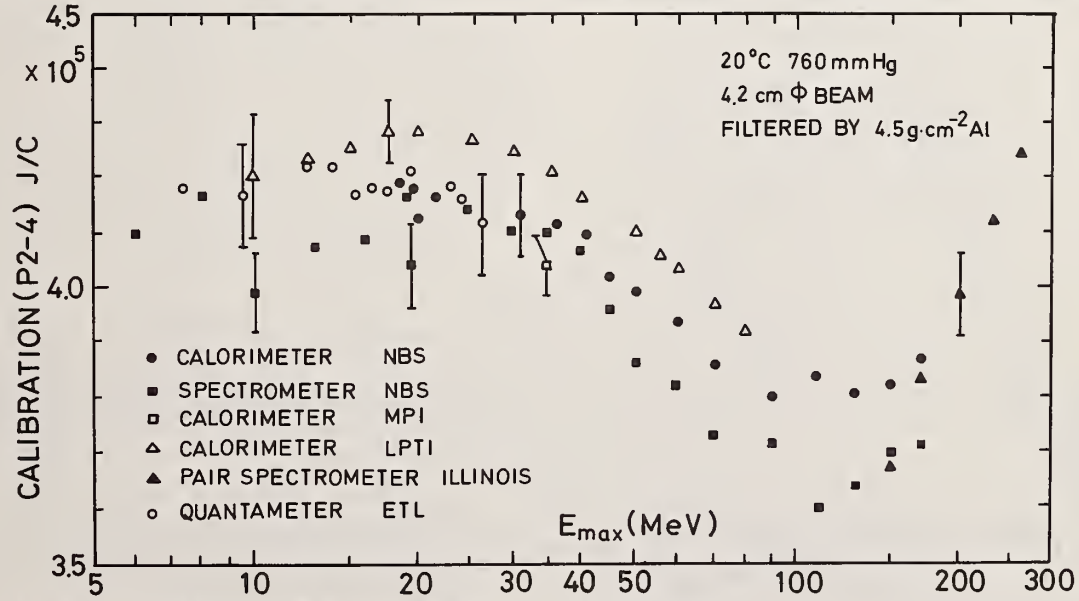

FIG.2 Calibration constants of the NBS P2 chamber at 20 °C and 760 mmHg.

4 THE PHOTONEUTRON CROSS SECTIONS FOR PRASEODYMIUM

Excellent critical accounts on recent works[30-33] on ^{141}Pr (γ,n) reaction are described in detail by Sund et al.[33] and Dreyer et al..[17] Their conclusions are (1) the giant resonance of ^{141}Pr (γ,n) reaction appears to be a near structureless broad resonance and (2) the BS cross section values appear to be systematically some 10 % higher than the PAF values.

The first of their conclusions has been confirmed by Beil et al.[34] at Saclay and Yound[35] at Illinois. Their second conclusion is well demonstrated by about 10 % discrepancy found in the peak cross section values σ_m shown in Tab.2. Among these parameters of the photoneutron cross section for praseodymium, those in the upper column are obtained by PAF γ -rays, those in the middle by PT γ-rays, and those in the lower by BS γ-rays.

The BS cross section[17,31] have been obtained by using the NBS P2 chamber as a detector of X-ray beam energy, but Cook et al. at Iowa have used a slightly modified version of the NBS chamber.[36] The BS cross sections shown in Tab.2 give peak values of about 390 mb.

On the other hand, the peak values of the PAF cross sections of Bramblett et al., Sund et al., and Beil et al. give an average value of about 340 mb, which well agrees with the peak value (332 mb) of the PT cross section of Young. The discrepancy between the BS and the PAF values is 10 % or more. Therefore, the BS cross section values for copper and praseodymium are systematically about 10 % higher than the corresponding PAF values. The 10 % discrepancy can be also explained by the same account discussed in Sec.3.

However, contrary to the comment of Bramblett[18] and the larger discrepancy of 20 % or more found in the PAF cross sections for copper, lead, and bismuth, the three PAF cross sections for praseodymium show a good agreement within several percent. The reason for this singularity is not know.

Target	σ_m (mb)	Γ (MeV)	$\int^x \sigma\, dE$ (MeV-mb)(x)	Reference
Pr	324	4.4	2062 (29.8)	30(Livermore)
Pr	348	4.0		33(San Diego)
Pr	347	4.5	1422 (16.9)	34(Saclay)
Pr	332	4.1	1395 (18.1)	35(Illinois)
Pr	390	4.0	1790 (30)	31(Iowa)
Pr	396	3.9	2100 (30)	17(Heidelberg)

TAB.2 Parameters of the photoneutron cross sections for ^{141}Pr.

5 THE PHOTONEUTRON CROSS SECTIONS FOR LEAD AND BISMUTH

The photoneutron cross sections for lead has been measured at several laboratories using BS γ-rays, PAF γ-rays, or PT γ-rays as a source of photons. These measurements are in good agreement as to the position and width of the giant resonance but not so as to the height and shape as shown in Fig.3 although some of them[14,17,20,35,37,38] have relealed structures on the low energy side of the giant resonance.

Of these measurements, our BS cross section is in excellent agreement with the PAF cross section of Miller et al. in the magnitude and shape of the giant resonance but not with that of Harvey et al.[25] The most recent PAF cross section of ^{208}Pb was obtained by Veyssiere et al.[16] at Saclay using the high detection efficiency neutron detector. The peak value of their latest PAF cross section is 640 $\pm$ 10 mb and in good agreement with our BS value of 660 $\pm$ 60 mb and their old PAF value of 650 $\pm$ 25 mb as shown in Tab.3.

Target	σ_m (mb)	Γ (MeV)	$\int^x \sigma\, dE$ (MeV-mb)(x)	Reference
Pb	650 $\pm$ 25	4.5	4100 (22)	19(Saclay)
^{208}Pb	491	3.9	2646 (26.4)	25(Livermore)
^{208}Pb	640 $\pm$ 10	4.05	3480 (25)	16(Saclay)
^{208}Pb	650 $\pm$ 60	4		20(Illinois)
^{208}Pb	645	3.94	2090 (14.9)	35(Illinois)
^{208}Pb	610	4		13(NBS)
Pb	660 $\pm$ 60	4.5	3480 (25)	14(ETL)
^{208}Pb	750-800	5.6	4000 (18.5)	37(Moscow)
^{208}Pb	510 $\pm$ 51	6	4320 (27)	41(Moscow)
Bi	650 $\pm$ 25	4.5	3730 (22)	19(Saclay)
Bi	521	3.97	3058 (26.4)	25(Livermore)
Bi	648	3.72	2129 (14.8)	35(Illinois)
Bi	650			42(Moscow)
Bi	565	4.5	3954 (58)	43(Iowa)
Bi	660 $\pm$ 80	4.7	4100 (24)	44(ETL)

TAB.3 Parameters of the photoneutron cross sections for Pb, ^{208}Pb, and ^{209}Bi.

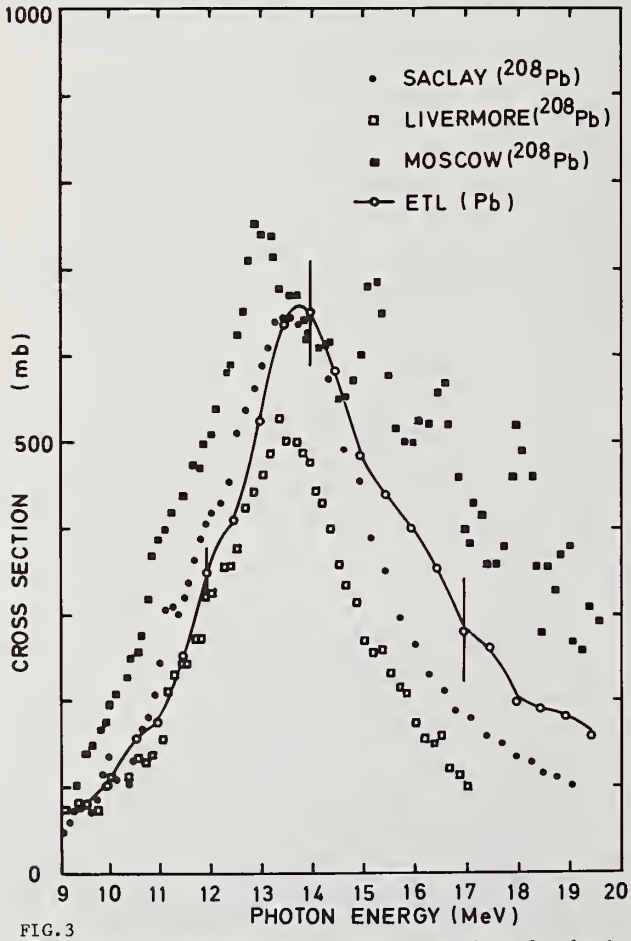

FIG.3
Comparison of the photoneutron cross sections for lead.

Other BS cross sections for lead are those obtained at NBS and Moscow. The original result of Fuller and Hayward[38] at NBS corrected by 30 %[13] was subsequently republished by Danos and Fuller.[39] The peak value of the corrected cross section is 610 mb. Goryachev et al.[37] at Moscow have measured the BS cross section of ^{208}Pb using a spherical neutron detector (efficiency, ~13 %) and a thick-wall aluminum ionization chamber.[40] The peak value of their cross section is 750-800 mb and 20 % higher than our BS value of 660 mb.

A further measurement of the BS cross sections for ^{206}Pb and ^{208}Pb has been made by Sorokin et al[41] using a neutron detector (efficiency,~26 %) employed a water moderator and BF_3 counters. The peak values of these cross sections are 470 $\pm$ 47 mb and 510 $\pm$ 51 mb. However, The resonance peaks (Γ, ~6 MeV) are considerably wider than the previously published half widths.[16,25]

Calarco at Illinois[20] has obtained a peak cross section of 650 $\pm$ 60 mb for ^{208}Pb using an associated particle method as a means of tagging the incident photons. The peak value of his PT cross section well agrees with our BS value. Somewhat later, the most recent PT cross section for ^{208}Pb was obtained by Young[35] at Illinois. His peak value is 645 mb and in good agreement with our BS value.

Furthermore, Sorokin[42] measured the BS cross sections for bismuth and gold. The peak values of them are 650 mb for bismuth and 600 mb for gold. The peak value of bismuth, neighboring nucleous of lead, can be seen as an approximate value of the peak cross section of lead. Nevertheless, these peak values of lead and bismuth obtained at Moscow are considerably scatter from 500 mb to 800 mb. The reason for this large discrepancy is not known.

Almost same time, Kocimski and Cook[43] at Iowa have measured the BS cross section of bismuth using a Gd loaded liquid scintillator having a neutron detecting efficiency of about 82 % and a slightly modified version of the NBS P2 chamber.[36] The measurement was taken for peak bremsstrahlung energies from 9 MeV to 59 MeV in 1 MeV steps. The peak value of their BS cross section is 565 mb.

A further measurement of the BS cross section for bismuth has been made by one of the authors using a high detection efficiency pair spectrometer and the attenuation method.[44] The peak value and half-value width of this cross section are 660 $\pm$ 80 mb and 4.5 MeV.

The peak values and half-value widths of these cross sections for lead and bismuth are shown in Tab.3. Of these cross sections, those obtained at Saclay (Pb, 650 mb; ^{208}Pb, 640 mb; Bi, 650 mb), NBS (^{208}Pb, 610 mb), ETL (Pb, 660 mb; Bi, 660 mb), and Illinois (^{208}Pb, 650 mb, 645 mb; Bi, 648 mb) were measured with different experimental methods each other. Neverthless, these laboratories give peak values converging towards 650 mb. A recent measurement of the PAF cross section for Bi by the Saclay group[45] gives a further support for this conclusion. However, the peak values obtained at the other laboratories considerably sctter from 500 mb to 800 mb. A systematic discrepancy between the BS and PAF cross sections, as observed for copper and praseodymium, is not found for lead and bismuth.

6 CONCLUSION

The agreement is good in the shape of the cross section between the BS and PAF data, at least, in the low energy side of the giant resonance. The agreement of these BS and PAF data on the shape of the cross section could provide more reliable consequences with regard to theoretical calculations on the shape of the cross section. However, a systematic discrepancy of 10 % or more is found between the BS cross section values for medium heavy nuclei obtained by the use of the NBS P-2 chamber as a beam monitor and the corresponding PAF cross section values. The 10 % discrepancy may be explained in good direction by the 6 % discrepancy found in the calibration constants of the NBS P2 chamber given by several laboratories. However, in order to make more clear the source of the discrepancy found between the BS and PAF cross sections, the calibration of the NBS P2 chamber should be investigated at other laboratories than NBS, and ETL. The definite discrepancy can not be demonstrated for heavy nuclei because of the large discrepancies of 20 % or more found even in the PAF cross sections. The PAF cross sections for heavy nuclei should be measured at other laboratories than Saclay, Livermore.

REFERENCES

1. M. G. Huber, M. Danos, H. J. Weber, and W. Greiner, Phys. Rev. 155, 1973 (1967). H. Arenhovel and H. J. Weber, Nucl. Phys. A91, 145 (1967). R. Ligensa and W. Greiner, ibid. A92, 673 (1967). R. F. Barrett and P. P. Delsanto, ibid. A173, 641 (1971). C. B. Dover, R. H. Lemmer, and F. J. W. Hahne, Annals of Physics 70, 458 (1972).
2. S. Fukuda and Y. Torizuka, Phys. Rev. Lett. 29, 1109 (1972). F. Busbrik, H. D. Graf, R. Pitthan, H. Theissen, O. Titze, and Th. Walcher, Phys. Lett. 42B, 194 (1972).
3. J. S. Levinger, Nuclear Photo-Disintegration (Oxford University Press, 1960) P.50
4. J. S. O'Connell, Proc. Int. Conf. Photonuclear Reactions and Applications, California, 1973, edited by B. L. Berman, P.71.
5. E. G. Fuller, H. M. Gerstenberg, H. Vander Molen, and T. C. Dunn, NBS special Publication 380 (1973).
6. B. Bulow and B. Forkman, IAEA Technical Reports No.156.
7. B. L. Berman, private communication (1974)
8. W. H. Hartley, W. E. Stephens, and E. J. Winhold, Phys. Rev. 104, 178 (1956).
9. T. Nakamura, K. Takamatsu, K. Fukunaga, M. Yata, and S. Yasumi, J. Phys. Soc. Japan 14, 693 (1959).
10. G. E. Coote, W. E. Turichinetz, and I. F. Wright, Nucl. Phys. 23 468 (1961).
11. W. E. Del Bianco and W. E. Stephens, Phys. Rev. 126, 706 (1962).
12. G. Baciu, G. C. Bonazzola, B. Minetti, C. Molino, L. Pasqualini, and G. Piragino, Nucl. Phys. 67, 178 (1965).
13. H. M. Gerstenberg and E. G. Fuller, Technical Note NBS 416 (1967).
14. T. Tomimasu, J. Phys. Soc. Japan 25, 655 (1968), Researches of Electrotechnical Laboratory No.679, PP1-54, (1967).
15. R. E. Sund, M. P. Baker, L. A. Kull, and R. B. Walton, Phys. Rev. 176, 1366 (1968).
16. A. Veyssiere, H. Beil, R. Bergere, P. Carlos, and A. Lepretre, Nucl. Phys. A159, 561 (1970).
17. F. Dreyer, H. Dreyer, H. Dahmen, J. Staude, and H. H. Thies, ibid. A181, 477 (1972).
18. R. L. Bramblett, S. C. Fultz, and B. L. Berman, Ref.4, P.13.
19. J. Miller, C. Schuhl, and C. Tzara, Nucl. Phys. 32, 236 (1962).
20. J. R. Calarco, Ph. D. Thesis, University of Illinois (1969).
21. See ref. 10 references contained therein.
22. See ref. 10 references contained therein.
23. S. Yasumi, M. Yata, K. Takamatsu, A. Masaike, and Y. Masuda, J. Phys. Soc. Japan 15, 1913 (1960).
24. S. C. Fultz, R. L. Bramblett, J. T. Caldwell, and R. R. Harvey, Phys. Rev. 133, B1149 (1964).
25. R. R. Harvey, J. T. Caldwell, R. L. Bramblett, and S. C. Fultz, ibid. 136, B126 (1964).
26. J. S. Pruitt and S. R. Domen, NBS Monograph 48 (1962).
27. J. S. Pruitt and S. R. Domen, J. Res. NBS, 68A, 703 (1964).

28. A. P. Komar, S. P. Kruglov, and I. V. Lopatin, Nucl. Instr. Meth. 42, 235 (1966).
29. E. Teranishi, B. Furubayashi, T. Michikawa, M. Kageyama, and O. Yura, Japan J. app. Phys. 3, 36 (1964).
30. R. L. Bramblett, J. T. Caldwell, B. L. Berman, R. R. Harvey, and S. C. Fultz, Phys. Rev. 148, 1198 (1966).
31. B. C. Cook, D. R. Hutchinson, R. C. Waring, J. N. Bradford, R. G. Johnson, and J. E. Griffin, ibid., 143, 730 (1966).
32. P. H. Cannington, R. J. J. Stewart, and B. M. Spicer, Nucl. Phys. A109, 385 (1966).
33. R. E. Sund, V. V. Verbinski, Hans Weber, and L. A. Kull, Phys. Rev. C2, 1129 (1970).
34. H. Beil, R. Bergere, P. Carlos, A. Lepretre, A. Veyssiere, and A. Parlag, Nucl. Phys. A172, 426 (1971)
35. L. M. Young, Ph. D. Thesis, University of Illinois (1972).
36. B. C. Cook, J. E. E. Baglin, J. N. Bradford, and J. E. Griffin, Phys. Rev. 143, 712 (1966).
37. B. I. Goryachev, V. S. Ishkanov, V. G. Schevchenko JETP Lett. (Sov. Phys.) 7, 161 (1968).
38. E. G. Fuller and E. Hayward, Nucl. Phys. 33, 431 (1962).
39. M. Danos and E. G. Fuller, Ann. Rev. Nucl. Sci. 15, 29 (1965).
40. B. H. Flowers, J. D. Lawson, and E. B. Fossey, Proc. Phys. Soc., 65B, 286 (1952).
41. Yu. I. Sorokin, V. A. Krushchev, and B. A. Yur'ev, Izv. Akad. Nauk SSSR. Ser. Fiz., 37, 156 (1973).
42. Yu. I. Sorokin, Izv. Akad. Nauk SSSR. Ser. Fig., 37, 1890 (1973).
43. S. M. Kocimski and B. C. Cook, Ref.4, P.1059.
44. S. Sugiyama, Researches of Electrotechnical Laboratory No.744 (1974).
45. R. Bergere, Private communication, 1975

THE 2-KEV FILTERED BEAM FACILITY AT THE NBS REACTOR*

I.G. Schroder and R.B. Schwartz
National Bureau of Standards
Washington, D.C. 20234

E.D. McGarry
Harry Diamond Laboratories
Adelphi, Maryland 20783

A scandium filter that views a manganese scatterer has been installed in a through tube of the National Bureau of Standards Reactor (NBSR). The use of a resonant scatterer eliminates unwanted core neutrons and core gamma rays. This produces a pure 2-keV neutron beam with only 3% higher energy neutron contamination and a 1 $mR \cdot hr^{-1}$ gamma-ray background. This should be compared with previously reported results in which the high energy contaminant was approximately 50%, thus severely limiting the utility of such a filter. Details of the filter construction, the use of titanium with the scandium to reduce background, the optimization of the beam for different types of experiments, and the application of 2-keV neutrons to neutron dosimetry, cross-section measurements and capture gamma-ray studies are discussed.

(Neutrons; Filtered Beams; Cross Sections; Capture Gamma Rays; Dosimetry)

Introduction

The existence of "neutron windows" in the total cross section (which arises from interference minima between the resonance and potential scattering for s-wave neutrons) has permitted the development of a series of neutron filters that transmit neutrons, in narrow energy bands, from a reactor spectrum. The production of such high-intensity, filtered beams was pioneered at the Materials Testing Reactor (MTR), Idaho, by Simpson and his co-workers[1] who produced neutron beams at 2, 25 and 144 keV by using filters of scandium, iron and silicon respectively. Unfortunately, the existence of neutron windows at other energies in these materials reduced the purity of the beams. This has proven, up to now, to be a major problem in the application of this technique. As the MTR was phased out before the full development of these beams could be completed, the scandium and silicon filters were transferred to NBS for further development and for use in the neutron standards program The object of this paper is to report on the progress made with 2-keV scandium-filtered beams at the NBSR.

The Scandium Filter

The 2-keV window in scandium results from the overlap of two interference minima from the s-wave resonances at 3.24 keV and 4.27 keV, producing a cross section with a minimum value[2] of only 50 mb. However, there are many other windows in scandium at higher energies. These windows are responsible for a neutron background in the energy region between 7 and 800 keV (Fig. 1). The high energy neutron background severely limits the utility of the scandium filter and constitutes a major source of uncertainty. In the work of Simpson et al[1], the background was approximately 50% of the 2-keV flux. The problem is inevitable in any facility in which a scandium filter looks at a reactor core.

* Work partially supported by the U.S. Energy Research and Development Administration.

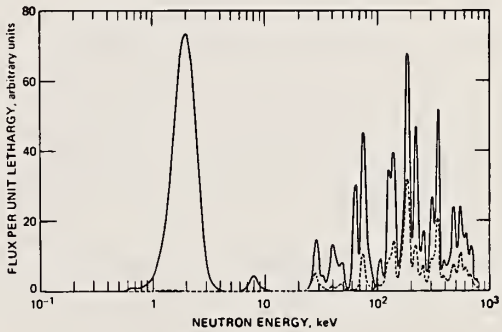

Fig. 1. Neutron spectrum obtained with the scandium filter at the Materials Testing Reactor (Ref. 1)

The Scandium-Filtered Beam at the NBSR

The elimination of the high energy neutron background was achieved at the NBSR by the use of a through tube in conjuction with a resonant scatterer that preferentially scatters 2-keV neutrons. To preferentially scatter 2-keV neutrons, use is made of the large 2.375-keV resonance in manganese. Although, the resonant energy does not exactly match the energy of the 2-keV window, the manganese resonance is sufficiently broad that at 2 keV the scattering cross section[3] is still greater than 100 b. Therefore, as the collimating system containing the scandium filter sees only the manganese scatterer at the center of the through tube (Fig. 2), the higher energy core neutrons are eliminated, as well as unwanted core gammas. The advantages of this design may be seen in the spectra shown in Fig. 4.

Physically, the through tube is a 2.63-m long, CO_2-filled aluminum tube (11.4-cm inside diameter) tangential to the reactor core and 10 cm from its

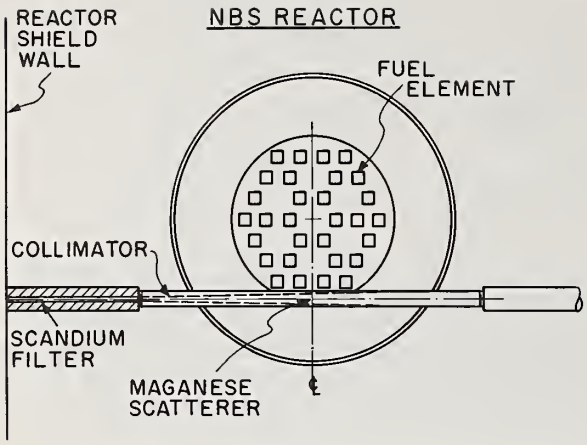

Fig. 2. Schematic representation of the NBS Reactor showing the filter, collimator and scatterer in the through tube. (Not to scale)

edge. At the center of this tube is a scatterer (Fig. 2) which is a 90-cm^2 by 3mm-thick manganese-aluminum alloy disc containing 57 atomic percent manganese and cooled by natural convection and radiation. The scatterer is 2.38 m from the inner edge of the scandium filter. The scandium filter is made of 99.9% scandium pressed into a 5-section converging collimator, 1.10 m-long, made of nickel and titanium sections. These sections are 17.5 cm in diameter and the scandium in them has an initial diameter of 2.22 cm and reduces in four steps (2.22, 2.06, 1.91, and 1.75 centimeters) to a final diameter of 1.75 cm as shown in Fig. 3. Needless to say, the filter only sees the manganese scatterer at the center of the through tube. A stainless steel, heavy-concrete-filled collimator (1.07-m long with 6.35-cm inner diameter and containing a 0.64-cm boral plate at its inner end) reduces further the presence of unwanted neutrons and gamma rays

The sectional character of the scandium filter permits one to vary the amount of filter material to optimize the beam requirements (both energy and intensity) for different experimental needs. Furthermore, space is provided in the precollimator, and in the 10-cm gap between the filter (Fig. 3), for additional materials to further collimate or attenuate the beam, should the need arise.

The Filtered Neutron Spectrum

An 1-atm hydrogen-filled proton-recoil spectrometer, 2.5 cm in diameter and 5-cm long was used to measure the energy distribution of the neutrons filtered through the 1.10 m of scandium. The counter was placed perpendicular to the beam to minimize proton-track distortions due to wall and end-of-field effects. The analysis of the proton-recoil data involved taking derivatives, accounting for gas concentration and adjusting for the variation of the hydrogen scattering cross section with energy. Wall effects and end-of-field truncations were neglected in the analysis. Furthermore, since the gamma field associated with the filtered beam is low (1 mR hr^{-1}), spectrum measurements were possible at, and slightly below, 2-keV without pulse rise-time discrimination against gammas.

Two typical spectra are shown in Fig. 4. The solid line shows the spectrum obtained with 1.10 m of scandium. A series of higher energy peaks were detected up to 132 keV but there were no other peaks observed at higher energies. In terms of total flux (i.e., the areas under the peaks), the higher energy contaminants amount to 6% of the 2-keV flux, the main contaminant being the peak at 29 keV which contributes 3% of the flux. The measured total flux was 6.5 x 10^5 $n \cdot s^{-1}$. The dashed curve in Fig. 4 shows the effect of adding 1 cm of titanium to the scandium. The addition of titanium reduces the peaks at 7, 15 and 40 keV by a factor of 2.5 at the cost of only 17% reduction of the 2-keV peak. The addition of the titanium reduces the higher energy contribution to approximately 3% of the 2-keV flux.

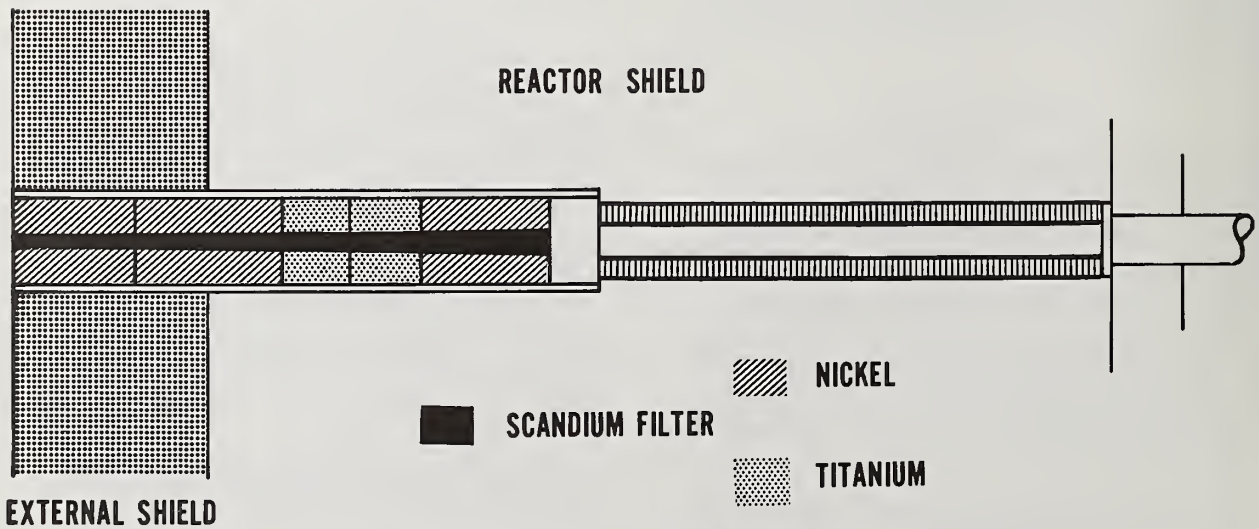

Fig. 3. Physical details of the scandium filter.

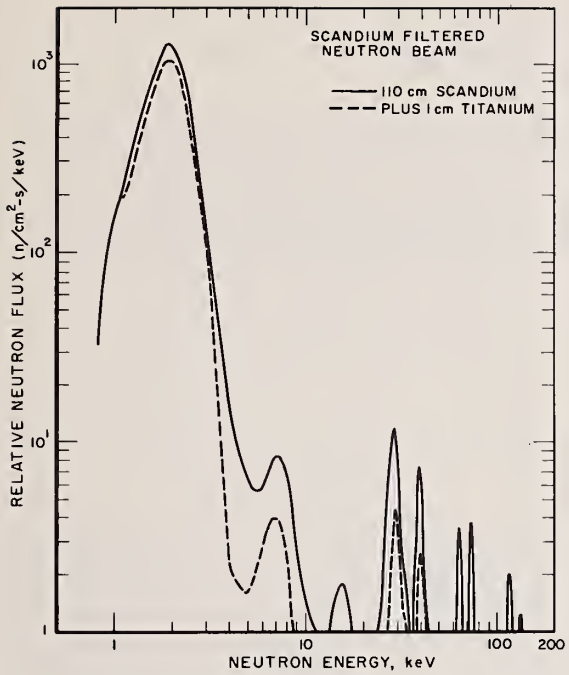

Fig. 4. Neutron spectrum through the scandium filter. The solid curve represents the spectrum with a 110-cm scandium filter; the dashed curve is the spectrum observed with the addition of 1 cm of titanium.

Personnel Dosimetry

The growing use of nuclear reactors as major sources of power has resulted in a renewal of interest in investigations related to routine and emergency monitoring of personnel and areas in the vicinity of modern reactor facilities. Recent studies[4] have shown that, on the average, 30 to 40% of the neutron dose in biological tissue comes from neutrons whose energies are between 0.5 keV and 0.1 MeV. For this reason, a number of laboratories in the United States under the auspices of the Energy Research and Development Administration (ERDA), are investigating the feasibility of replacing the conventional film badge by a system better suited to dosimetry in this neutron-energy range. This is, of course, where filtered beams from reactors can play a major role. To this effect, a program is under way (at NBS), under the auspices of the Health Protection Branch, Division of Operational Safety, ERDA, to use the 2-keV filtered beam facility, as well as the 25-keV facility,[5] and a 144-keV beam under development, as standard mono-energetic neutron fields for the calibration and development of health-physics-type neutron dosimeters.

Cross-Section Measurements

The need for cross section measurements in the low keV region for fast reactor applications makes the 2-keV filtered beam with its relative freedom from higher energy contaminants an extremely useful tool for the measurement of both total and partial cross sections. Furthermore, this beam can be used to great advantage in the determination of average resonance-neutron parameters that are important in the design and safety analysis of fast breeder reactors.[6]

Capture Gamma-Ray Studies

The marginal neutron fluxes available in the kilovolt region from charge-particle machines have made the study of the capture process in this region extremely difficult. For neutron energies greater than 1 keV, good capture gamma-ray data are relatively sparse compared to the vast amount of data available at lower energies. Yet, the energy region between one and a few hundred keV is important in furthering our understanding of the capture process and in applied work, such as shielding and radiation damage studies. In this energy region, filtered beams have proven to be an important tool in experiments where averaging over many neutron resonances is preferable to studying the detailed structure of each resonance (as afforded by the time-of-flight methods). In this technique, first investigated at the MTR, Idaho,[7] the broad, but well-defined, sources afforded by the beams encompass many capturing states thereby averaging out the statistical (Porter-Thomas) fluctuations in the partial radiation widths. This enables one to establish the s- and p-wave components and determine the spin and parity of final states.[8] Therefore, the combination of filtered and thermal beams provides a powerful means of studying the neutron-capture mechanism and the properties of nuclear levels. In this respect, a cooperative program with the Idaho National Engineering Laboratory (Aerojet Nuclear Company) has been initiated to study average neutron capture at the NBSR 2-keV beam facility.

Lastly, filtered beams from reactors can provide data on the prompt-gamma energy component in shielding materials for fast reactors. This information is not available from thermal capture where the primary gamma-ray transistions are governed by Porter-Thomas fluctuations and, therefore, do not resemble the spectra resulting from higher energy neutron capture where these fluctuations are averaged out.

Acknowledgements

We would like to thank R.M. Brugger and O.D. Simpson for making the scandium and silicon filters available to us. We would also like to thank JW Rogers for lending us the proton recoil counter used to characterize the beam and for useful discussion concerning the neutron spectrum measurements.

The assistance and cooperation of R.A. Dallatore in all phases of the fabrication and mechanical assembly of the filter system are gratefully acknowledged.

References

1. O.D. Simpson, J.R. Smith and JW Rogers, Proc. Symp, Neutron Standards and Flux Normalization, CONF-701002, USAEC p. 362, (1971).

2. W.L. Wilson, "Neutron Cross Section Measurements and Gamma Ray Studies of ^{45}Sc", M.S. Thesis, University of Idaho Graduate School, (December 1966); (unpublished).

3. M.D. Goldberg, S.F. Mughabghab, B.A. Magurno, and V.M. May, "Neutron Cross Sections, Vol. II A", BNL 325, Second Edition, Supplement No. 2, Physics-TID-4500 (February 1966).

4. J.R. Harvey and S. Beyon, International Symp. on Neutron Dosimetry in Biology and Medicine, Commission of European Communities and Gesellschaft fur Strahlenschutz and Umweltforschung mbH, Neuherberg/Muenchen (1972).

5. E.D. McGarry and I.G. Schroder, Contribution to this conference.

6. O.D. Simpson and L.G. Miller, Nucl. Instr. Meth. 61, 245 (1968).

7. R.C. Greenwood, R.A. Harlan, R.G. Helmer, and C.W. Reich, Proceedings of the Symposium on Neutron Capture Gamma Rays, IAEA, Studsvik, Vienna, (1969).

8. Second International Symposium on Neutron Capture Gamma Ray Sepctroscopy, Petten, the Netherlands, (1974) and references contained herein.

THE RENSSELAER INTENSE NEUTRON SPECTROMETER*

R. C. Block and R. W. Hockenbury
Rensselaer Polytechnic Institute, Troy N.Y. 12180
and
D. S. Cramer, E. Bean and R. E. Slovacek
Knolls Atomic Power Laboratory, Schenectady, N. Y. 12305

The Rensselaer Intense Neutron Spectrometer (RINS) is obtained by driving a a 75-ton lead slowing down spectrometer with the intense pulsed neutron source from the RPI 100-MeV electron linac. For the same linac beam power, RINS produces a useable neutron flux which is $10^3 \sim 10^4$ greater than that obtained with a conventional time-of-flight spectrometer . Fission measurements upon ^{238}U have shown strong subthreshold fission above 700 eV and have determined the fission widths of the 6.7, 21 and 37 eV resonances to be (10 ± 5), (70 ± 30) and (8 ± 6) neV respectively. No strong subthreshold fission was observed in ^{232}Th, and an upper limit of (15 ± 10) neV is obtained for $\bar{\Gamma}_f$ for the Th resonances below 260 eV. Measurements of ^{145}Nd (n, α) have shown that the RINS system is readily capable of measuring ~μeV partial widths with only several mg of sample.

(Measured ^{238}U fission below 35 keV, deduced $\bar{\Gamma}_f$ of 6.7, 21 and 37 eV resonances; measured Th fission and deduced $\bar{\Gamma}_f$ below 260 eV; measured $^{145}Nd(n,\alpha)$.

I Introduction

The Rensselaer Intense Neutron Spectrometer (RINS) is an extended form of a lead slowing down spectrometer system. Basically the RINS system contains the following components: (a) the RPI 100-MeV electron linac to provide a repetitively pulsed intense neutron source burst (50 nsec wide); (b) a cube of lead 1.8 m on edge which serves as a neutron slowing down medium with small leakage and absorption; (c) sample material located in the lead cube; (d) charged-particle detectors (which may contain the sample material) or neutron detectors located near the sample material to observe the interactions between the neutrons slowing down in the lead cube and the nuclei in the sample material; and (e) a time analyzer to record events occuring in the detectors at various slowing down times after the initial neutron source pulse.

Previous investigations with the original lead spectrometer[1] and subsequent setups at other laboratories were all conducted with pulsed DT neutron sources limited in intensity to about 10^9 n/sec. With the electron linear accelerator a source intensity of 10^{12} n/sec has easily been obtained with a gas (helium) cooled target. This large increase in source intensity has permitted some partial cross sections to be measured which have not been previously observed.

II Experimental Facility

Figure 1 shows a schematic arrangement of the equipment. A cube, 1.8 m on edge, was stacked containing 75 tons of 99.99% purity lead. All cube surfaces were covered with Cd to prevent room-return thermal neutrons from reentering the lead. The cube rests on a crossed I-beam base 61-cm high. Between the I-beams, packaged Li_2CO_3 is arranged to reduce neutrons backscattered from the floor.

Nine 10-cm x 10-cm channels penetrating through the cube and three reentrant ports are available for experimental equipment. One of the through channels is used to bring in the electron beam to a target located near the center of the cube. The unused parts of the channels and ports are normally filled with lead bricks.

The photo-neutron target is constructed of tantalum plates and is similar in geometry to the standard RPI target[2] but differs with respect to the cooling medium. The target is located 3cm from the cube center in an attempt to center the neutron source volume.

The electron beam leaves the linac vacuum system through a 0.0025-cm thick titanium window and passes through a 91-cm long helium-filled drift tube to the target. The target is cooled by helium which in turn is cooled by water in a heat exchanger. The designed cooling capacity is 500 watts.

Small (0.64-cm dia. x 2.54-cm long) fission chambers containing ^{233}U, ^{235}U, or ^{239}Pu are located near the cube corners to serve as flux monitors. A BF_3 detector (0.48-cm dia. x 2.54-cm long) is used to determine the flux at the various experimental locations.

A Hewlett-Packard 2116B on-line computer with a 32 MHz clock serves as a time analyzer. A routing circuit permits up to six detector inputs to be used simultaneously.

In the neutron energy range of interest, 10^5 to 1 eV, the elastic scattering of neutrons from the heavy lead nuclei produces less than a 1% energy loss per collision. The neutron behavior in a lead spectrometer is represented very accurately by the continuous slowing down approximation. Below 100 keV average neutron energy, E (in keV) is related to the slowing down time t (in μsec) by the expression[1]

$$E = \frac{183}{(t + t_o)^2}$$

where $t_o \simeq 0.3$ μsec is a correction to account for the time it takes neutrons to slow down from source energies. The constant corresponds to a 5.9-m flight path for neutrons. The instantaneous neutron density distribution is Gaussian in shape about the average neutron energy[1]. Between 1 keV and 1 eV the resolution is approximately constant given theoretically[1] by $(\Delta E/E)_{FWHM} = 2.35\sqrt{8/3A_{Pb}} = 0.27$; experimentally the data indicate $(\Delta E/E)_{FWHM} \simeq 0.33$ gives a better fit.

In the large lead slowing down medium with corresponding small leakage, most of the source neutrons are "recycled" so that the available flux is considerably greater than in a conventional beam time-of-flight (TOF) experiment. The neutron flux at a position 42 cm from the target has been determined

*Work supported by ERDA

with a BF_3 detector as $\phi = 1.9 \times 10^4 \, PE^{-0.77}$ $n/cm^2/sec/eV$ where P is the target power in watts and E is the neutron energy in eV. This flux is about 55% of the flux that was calculated by a Monte Carlo program.

The RINS flux is several orders of magnitude greater than fluxes typically obtained in a conventional TOF experiment. This is illustrated in Table 1 where the RINS flux ϕ_{RINS} and the flux ϕ_{TOF} obtained in a 5-m flight path TOF experiment are compared. The comparison is for the same electron beam power. The TOF flux is inversely proportional to the square of the flight path and the 5-m flight path was selected as the minimum practical flight path. This $\simeq 10^4$ increase in ϕ_{RINS} enables experiments to be carried out with this technique that cannot be carried out by conventional TOF experiments.

Table 1

E_n(eV)	ϕ_{RINS} / ϕ_{TOF}
1,000	9,200
100	12,400
10	16,600
1	22,600

III Experimental Results

The RINS system is characterized by an intense initial "gamma flash" of bremsstrahlung from the photoneutron target followed by an intense slowing-down flux of neutrons inside the lead assembly. This imposes stringent requirements upon the detectors - they must recover rapidly from the gamma flash and must be able to operate while bathed in the neutron flux. Three types of detectors have been tested so far for use with the RINS system: (a) a scintillator-photomultiplier detector, (2) fission cylindrical ionization chambers and (3) a Si diffused-junction solid state detector. The scintillator-photomultiplier detector exhibited severe problems with gamma-flash recovery and further development is indicated before this type of system can be successfully used. However, the fission ionization chambers and the solid state detector have performed very well with this system, and results with these two types of detectors are presented below.

(a) Measurements with Ionization Chambers - Fission cross section measurements were carried out with chambers coated with highly enriched ^{238}U (4ppm ^{235}U) and with Th. The ^{238}U chambers consisted of four 2.5-cm dia. cylinders each coated along a 20-cm length for a total ^{238}U content of $\simeq 0.8$ g. These chambers were placed in one of the 10-cm x 10-cm channels of RINS and were located 42-cm from the center of the assembly. Data were obtained over a period of 5 hours, with only 330 watts of electron beam power on the photo-neutron target. The net ^{238}U fission counts are plotted in Figure 2 over the neutron energy range from 1.5 eV to 35 keV. The data have been corrected for fission from the 4ppm of ^{235}U and the results are presented in terms of ^{238}U fission counts per μ sec of slowing down time. The ^{238}U resonances at 6.7 and 21 eV are clearly resolved, and the resonance at 37 eV shows up clearly as a shoulder on the high energy side of the 21 eV resonance. The subthreshold fission groups reported[3] at 720 and 1200 eV show up very strongly in these data, and substantial subthreshold fission is also seen above 5 keV. The fission widths of the 6.7, 21 and 37 eV resonances are (10 $\pm$ 5), (70 $\pm$ 30) and (8 $\pm$ 6) nanoelectronvolts (neV) respectively. (These rather large errors result from the uncertainty in the flux normalization; subsequent BF_3 flux measurements should improve the accuracy of these results by about a factor of two.) The fission width of the 6.7 eV resonance is considerably smaller than the 200 neV upper limit reported by Leonard and Odegaarden[4]; these widths are consistent with the (30 $\pm$ 50) neV average width reported by Silbert and Bergen[5] for the resonances between 37 and 327 eV. The cross section integrated over the two subthreshold groups at 720 and 1200 eV and the average cross section from 10 to 30 keV are in agreement with results from the earlier reported beam measurement[3].

A fission chamber containing about 0.2 gm of Th was located in RINS about 58 cm from the photoneutron target. Data were obtained over a 4.5 hr period with 210 watts of electron beam power. There was no evidence of Th subthreshold fission group structure below 50 keV (as, e.g., was observed in ^{238}U near 720, 1200 and above 5000 eV). Rather, the Th data exhibited little or no structure within the counting statistics. A total of 691 counts were observed over the energy interval from 0.07 to 258 eV. Since these counts may result from background or from fission events from ^{235}U or other impurities, only an upper limit to the Th average fission width is assigned for this energy interval pending further analysis of the sample material and possible background effects. The estimated upper limit for the average Th fission width for resonances below 260 eV is $\bar{\Gamma}_f \lesssim (15 \pm 10)$neV.

(b) Measurements with a Solid State Detector-Two 125 μ depletion depth, 2-cm^2 active area diffused-junction Si detectors were obtained from the Los Alamos Scientific Laboratory for evaluation in the RINS system. The better of these detectors had a resolution of $\simeq$110 keV for 5.3 MeV ^{210}Po alpha particles, and this detector was selected for these tests. The detector was placed in the RINS assembly about 86 cm from the photo-neutron target, and was subjected to a total of $\simeq 4$ kilowatt-hours of electron beam irradiation both with and without Cd covering. This irradiation produced no noticeable change in the detector resolution, but the leakage current did rise from an initial value of 1.4 μA to 2.6 μA.

A 7.2 mg sample of $^{145}Nd_2O_3$ was painted onto a 7.2 mg/cm^2 Al backing; the deposit was extremely granular and covered an area of approximately 1.2cm^2. The $^{145}Nd_2O_3$ sample was placed near the surface of the Si detector, and these were both placed inside a Cd-covered, evacuated container which was then placed in the RINS system. The detector was operated with a 65 μ depletion depth (equal to the range of a 9.5 MeV alpha particle). The results of the ^{145}Nd (n,α) measurement are shown in Figure 3 for a 2.5-hr run at 330 watts electron beam power. The counts represent alpha particles with energies greater than 4.6 MeV; the ^{145}Nd (n, α) ground state alpha particle energy is 8.5 MeV. A pulse height measurement of the Si detector spectrum showed that the counts were due to alpha particles and not to capture in the ^{145}Nd resonances. The peaks labeled 4.7 and 51 eV are due to the 4.4 and 43 eV ^{145}Nd resonances and are clearly resolved in this measurement. The peak labeled 110eV is an unresolved cluster of the 87, 97 and 102 eV resonances. The average alpha particle width for ^{145}Nd resonances is reported[6] to be 2.6 μeV. Thus RINS is capable of measuring very small charged-particle-emission cross sections with small quantities of sample.

IV Conclusion

The RINS system is a very intense neutron spectrometer which has already been demonstrated to have the sensitivity of measuring in a few hours time fission widths of $\sim 10^{-9}$ eV in ~ 1 g samples and alpha widths of $\sim 10^{-6}$ eV in several mg samples. The RINS intensity is presently limited to ≈ 500 watts by the gas-cooled target, but this power can be increased by over an order of magnitude by going to a liquid-cooled target. This system shall be used for alpha spectroscopy and fission studies (e.g. fragment mass and kinetic energy distributions) at discrete low-energy resonances and for neutron energies up to ≈ 50 keV. RINS should prove a complement to the intense nuclear explosion TOF measurements, since RINS can easily study the energy region below the ≈ 20 eV cutoff of the explosion technique(7).

References

1. Bergmann, Isakov, Murin, Shapiro, Shtranikh and Kazarnovsky, Proc. of Geneva Conf. Peaceful Uses Atomic Energy, 4, 135 (1955).

2. Hockenbury, Bartolome, Tatarczuk, Moyer and Block, Phys. Rev. 178, 1746 (1969). Bartolome, Hockenbury, Moyer, Tatarczuk and Block Nucl. Sci. & Eng. 37, 137 (1969).

3. R. C. Block, R. W. Hockenbury, R. E. Slovacek, E. B. Bean and D. S. Cramer, Phys. Lett. 31, 247 (1973).

4. Leonard and Odegaarden, Bull. Am. Phys. Soc. 6, 8 (1961).

5. M. G. Silbert and D. W. Bergen, Phys. Rev. C4, 200 (1971).

6. Popov, Pschitula, Rumi, Stepinsky, Florek and Furman, Proc. of Helsinki 2nd Int'l. Conf. on Nucl. Data for Reactors, I, 669, IAEA, Vienna (1970).

7. Diven, B. C. Nuclear Structure Studies with Neutrons, pg. 441, N. Holland Publ. Co., Amsterdam (1966).

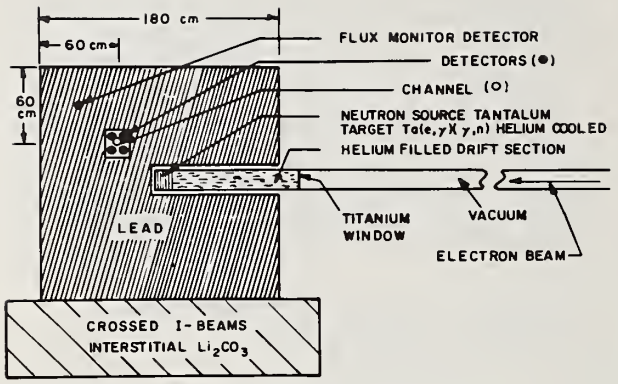

Fig. 1 - The 75-ton RINS lead slowing down spectrometer

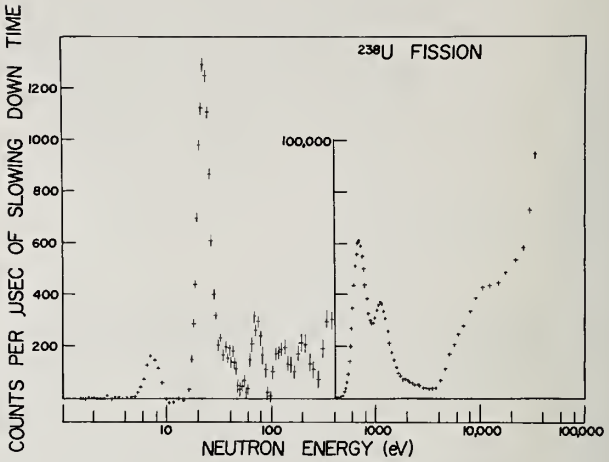

Fig. 2 - The $^{238}U(n,f)$ counts per μsec slowing down time vs. neutron energy.

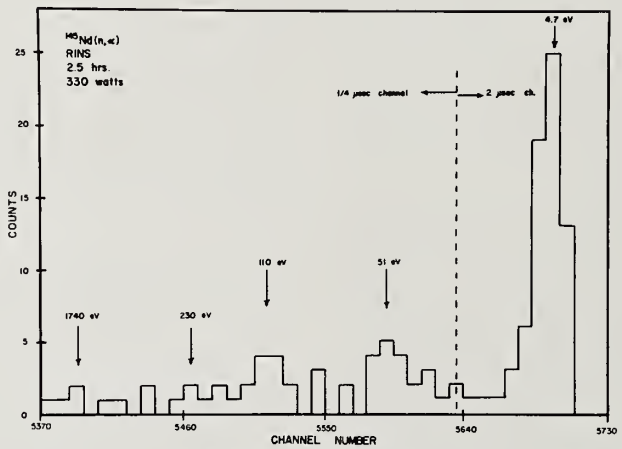

Fig. 3 - The $^{145}Nd(n,\alpha)$ counts vs. slowing down time.

A MODULAR MINICOMPUTER MULTIPARAMETER DATA GATHERING AND VIRTUAL MEMORY OPERATING SYSTEM FOR THE NBS NEUTRON STANDARDS PROGRAM

R. A. Schrack, H. T. Heaton II, and D. Green
National Bureau of Standards
Washington, D. C. 20234

A new aboveground neutron time-of-flight system has recently been completed at the National Bureau of Standards linear accelerator facility. A computer system has been developed that will permit the accumulation of multiparameter data simultaneously from several experiments, using an inexpensive minicomputer and a small moving head disc storage unit. The operating system is modular in form, allowing different experimenters to rapidly construct a software system to their requirements. Data gathering and analysis programs are interchanged between core and disc as required. Interfacing hardware has been modularized using the CAMAC system.

(Minicomputer; modular; multiparameter; disc; CAMAC; on-line)

Introduction

For the past ten years the experiments carried on at the National Bureau of Standards (NBS) Linac facility have used an on-line data gathering system named ROMEO.[1] We have been very satisfied with the system and it is used on almost every experiment to collect data, do brief on-line analysis, and control the progress of the experiment by automatic sample changing, etc. Several years ago the need for additional memory to provide large storage arrays for multiparameter data taking became evident. Economic considerations and the need for a faster basic cycle time and greater peripheral reliability led to the choice of a new computer system based on the Harris 6024/5 computer.* Our basic system includes a two-platter moving head disc having one removable platter with a total capacity of 1,800,000 words, a 200-line-per-minute line printer, tape unit, and teletype. We currently have a 16,000-word core in the CPU but will soon expand it to 24,000 words. Figure 1 shows a diagram of the system.

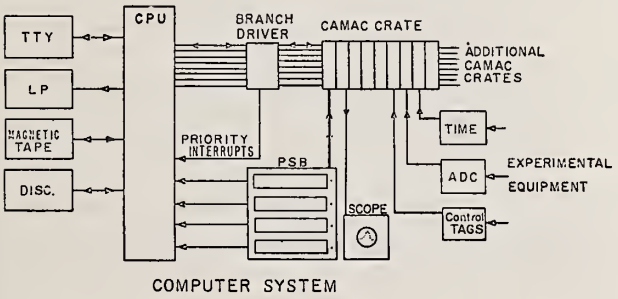

Figure 1. Block diagram of computer system components. Experimental equipment for a 2-parameter data taking system is shown.

Disc Storage System

A preliminary analysis of the optimum methods of using a disc and CPU to obtain the highest rate of random data storage indicated the need for a reasonably large core to hold the input data in buffers before it is finally stored on disc. While moving head disc systems can never approach the speed and efficiency of a fixed head disc system, it is surprising how efficient a buffered, moving head system can be.

The disc storage system is similar in concept to the technique discussed by Gonidec in France and used by Sinclair et al. at University of Indiana.[2,3]

The storage of a 20-bit address requires 2^{20} = 1,048,576 words. For convenience, each track on the disc holds 2,048 words; thus 512 tracks are required in all. As each event comes in, the address is divided by 2,048, the quotient is the track address, and the remainder is the word address on that track that is to be incremented. The word address is stored in the appropriate track buffer. Each track buffer can hold word addresses for up to 32 events that are to be stored somewhere on that track. This is part A of Fig. 2 of the track storage code and continues as long as events are being presented. Part B of the code operates independently of part A to continuously unload the track buffers (TB) and update the appropriate tracks on the disc. The track buffers are not uniquely related to a particular track on disc. There are two look-up tables that are used to keep a record of track assignments in the buffer. They are the buffer sequence (BS) and the track sequence (TS) tables. As each event comes in, the BS is searched to see if there is a buffer assigned to that track yet. If there is, the word is stored in the next available space in that buffer and word count is augmented in the TS. When the buffer area is full, a new buffer area is assigned to that track in the BS. If no buffer area has yet been assigned for a particular track, the next available unassigned buffer area is assigned to that track. If no more buffer areas are available, the data taking is halted and a track buffer overflow warning is given. The rate of data taking must be reduced to avoid another track buffer overflow.

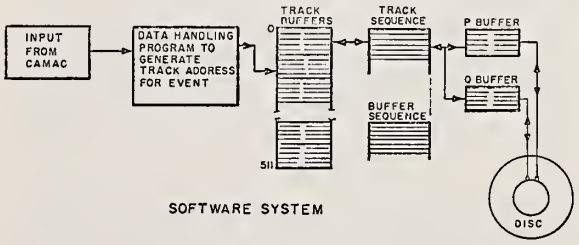

Figure 2. Block diagram of disc storage system.

* This particular piece of equipment is identified in this paper in order to adequately specify the experimental procedure. In no case does such identification imply recommendation or endorsement by NBS, nor does it imply that the material or equipment identified is necessarily the best available for the purpose.

After a track buffer area is stored on disc, the BS is searched to see which buffer area has the most words waiting. That track buffer area is then chosen to be the next one to be emptied onto the disc. When a particular TB is chosen to be placed on disc, that track is read off the disc into the P buffer. As that track is being updated by the CPU, another track at the same radius on the disc is being read into the Q buffer. As the Q buffer track is being updated by the CPU, the now updated P buffer is written back on the disc. When that is done, the updated Q buffer is written back on disc and the CPU searches for the next track buffer to be unloaded. The speed of data storage on the disc is related to the size of each track buffer. Since the track buffers require 8,192 words of core for the present systems and have a maximum data rate of 400 cps, expansion of the core by an additional 8,000 words would allow for a data rate of 800 cps. Reduction in the number of bits to be stored would also allow for a faster data taking rate. A detailed study of the relationship of word size and buffer area sizes can be used to determine optimum investment in core storage as compared to disc capabilities for any particular system design.

Our current system can store completely random data at an equilibrium rate of 400 counts per second. If the data is not random, the data storage rate rises to the asymptotic rate determined by the input/processing code for a fixed data input. For a fixed pulser input we have exceeded 3,000 counts per second input rates.

The maximum array size available on the disc is 1,048,576 words. This capacity can be used as a single parameter or in any multiparameter way desired. In experiments now going on at NBS we are using the disc as a three parameter array:

2 x 1024 x 512

where the parameters are a) experiment 1 or 2, b) 1024 words of time information, and c) 512 words of pulse height information.

An input program prepares the address of the memory location to be updated on the disc. The data is obtained from the experimental equipment via a CAMAC interfacing system. Control bits read in with the data determine how the data is to be interpreted and thus the appropriate address developed by the input data handling code. We recognize that the development of the disc address from the input data using softwear instead of hardware has the penalty of taking a longer time. We are, however, time-bound by the disc storage program, so that the flexibility and ease of development of the softwear approach are accompanied by no real penalty for the types of data we normally store.

CAMAC

We have chosen to interface the computer to the data taking system with a CAMAC interface system.[4,5] Just as the modularizing of nuclear instrumentation in the NIM system has become almost universal, we feel that the CAMAC interfacing system will be widely adopted because of the many advantages. The branch driver is the only part of the CAMAC system that must be tailored to the type of computer it is to be used with. The CAMAC system is well adapted for use with the computer it is used with because they both have a 24-bit word length. The pulse height and time information are digitized by other electronics and these signals, as well as control tag information, are presented to the CAMAC system on separate registers. All three types of data must be present to record an event. Internal checks in the software check for and record incomplete events of various types to permit rapid trouble-shooting.

Program Selector Board

In addition to obtaining data input through the CAMAC system, it is also used to initiate special user-oriented programs by means of a Program Selector Board (PSB) similar to the type we have been using in the ROMEO system. PSB programs can be initiated by the user at any time, but they will stop the data processing operation in the current limited core arrangement. Because maximum data taking rate demands maximum core utilization, we have placed the PSB programs on a section of the disc. When a PSB program is requested, data taking is halted, an area of core used for buffer storage is placed on the disc, and the desired PSB program is placed in core. After the PSB program is completed, the buffer area is restored to core from the disc and the data taking is resumed. After several months of operation we have about 30 PSB programs available for this system for general housekeeping operations. The programs have a standard format and are made sufficiently general in purpose so that they can be used by all users interchangeably. The request for a PSB program is initiated by the input of a standardized octal number sequence:

C.	I.	O.	S.
777	1	177	177

where S.: is the subject program (i.e. the program requested)
O.: is the object program (program where the data to be operated on is located)
I.: signifies the object program is a data taking (interrupt) program
C.: signifies constants that may be necessary to determine a choice in the subject program

The numbers shown represent the maximum allowable values that can be entered. We thus have a maximum capacity of 128 PSB programs for this system.

If a set of operations is to be performed, it can be built up of a sequence of separate program steps that are stored and then the whole set initiated in a sequencer type program.

Summary

We feel that the combination of modular software coordinated with a modular hardware system offers a maximum degree of flexibility and capacity at very low cost. Once a library of basic operations is accumulated, most experiments can be implemented with little or no specific software development for a particular experiment.

---

[1] J. Broberg, et al, IEEE Transactions on Nuclear Science, NS-11, No. 3, 331 (1964)
[2] J. P. Gonidec, Nucl. Instr. and Meth. 88, 125 (1970)
[3] J. W. D. Sinclair, et al, Nucl. Instr. and Meth. 111, 61 (1973)
[4] CAMAC Tutorial Issue, IEE Transactions on Nuclear Science, NS-18, No. 2 (1971)
[5] CAMAC Tutorial Issue, IEE Transactions on Nuclear Science, NS-20, No. 2 (1973)

TUNL FAST NEUTRON CROSS SECTION FACILITY*

D.W. Glasgow, F.O. Purser, J.C. Clement, G. Mack+, K. Stelzer++,
J.R. Boyce, D.H. Epperson, H.H. Hogue, E.G. Bilpuch, and H.W. Newson
Duke University and TUNL 27708
and C.R. Gould
North Carolina State U. and TUNL 27607

A fast neutron time-of-flight (TOF) facility has been constructed in order to measure neutron differential cross sections required for the CTR program. The facility combines the outstanding capabilities of the Cyclo-Graaff accelerator with those of a good energy resolution, high mechanical precision, very low background TOF spectrometer-goniometer. The facility provides the capability for measurements of scattering cross sections with magnitudes of a few mb/sr to $\approx$ 5% absolute accuracy in the energy range 6-15 MeV. The D(d,n)^{3}He source spectra at 0° are practically devoid of extraneous neutrons produced by deuteron reactions with the all-metal, ultra-clean beam transport system.

[NEUTRON TOF FACILITY; D(d,n)^{3}He and C(n,n) spectra; C(n,n), E = 9-15 MeV, measured $\sigma(E_n,\theta)$]

Introduction

In response to requests (USNDC-6) from DCTR for fast neutron cross section data required for the neutronic design of a prototype fusion reactor, personnel of TUNL have designed and constructed a fast neutron TOF facility at the Cyclo-Graaff Laboratory[1]. The facility unites the outstanding capabilities of the Cyclo-Graaff accelerator and its on-line computers with those of a heavy, optimum shielded, TOF spectrometer-goniometer. The system provides the capability for measurements of scattering cross sections (using the D(d,n)^{3}He source reaction) over the energy range 6-15 MeV with magnitudes of a few mb/sr to $\approx$ 5% absolute accuracy.

The techniques required to achieve this sensitivity and accuracy include: 1. Extreme reduction of time-correlated and-uncorrelated backgrounds by: (a) excellent vacuum (10^{-8}Torr) obtained in a wide aperture, all-metal beam line evacuated with a turbo-molecular pump(TM) and liquid nitrogen trapping; (b) intensive chemical cleaning of the last meter of beam line and gas cell source; (c) beam optics which minimize the interaction of the deuteron beam with the beam line components; (d) shielding of the primary neutron source by massive tungsten shadow shields; (e) double-truncated conical collimators for optimum transmission; (f) massive shielding of the neutron detectors; (g) increased laboratory shielding between the neutron hall and the accelerator bay. 2. Good resolution TOF spectroscopy involving: (a) NE218 liquid scintillators; (b) high quantum efficiency, low transit time-spread, photomultipliers (PM); (c) constant fraction and low-noise electronics; (d) neutron gamma discrimination (PSD) with high figures of merit over a large dynamic range; (e) pulsing and klystron bunching of the accelerator ion beam; (f) short, low-pressure gas targets. 3. Very stable tandem accellerator system. 4. Modular, high-precision fabrication of the mechanical goniometer. 5. Very stable neutron TOF monitor system. 6. Careful detector efficiency determinations. 7. Careful normalization of the measured cross sections to the n-p scattering cross section. 8. Monte Carlo simulation of finite sample size effects.

Cyclo-Graaff Facility

A plan view of the Cyclo-Graaff laboratory is shown in Fig. 1. For neutron scattering experiments below 17 MeV, the FN tandem accelerator is used. The ion source is an off-axis duoplasmatron designed for direct extraction of negative ions. The source typically provided 45 μA of deuterium ions at $\approx$ 50 keV. The pulsing and bunching of the d.c. beam is accomplished with a standard High Voltage Engineering Corporation pulsing and bunching system. The pulsed beam is accelerated to operating energies with $\approx$50% transmission through the accelerator. The time dispersion of a typical 1-2 μA beam at the gas cell target was 1.5-2 nsec

In order to eliminate inside surface contaminants the wide aperture, all-metal beam line was degreased and cleaned with NaOH and distilled H_2O, before assembly with Indium metal "O" rings. The last 50 cm of line was fabricated from tantulum tubing of 1 cm I.D. The Ta line, Ta collimators, a small gas cell and its associated Ta liner and beam stop, were cleaned with HF, NaOH, and distilled H_2O before assembly. The beam current integration system, 3.5 μm thick Mo entrance foil, indium metal "O" rings, and deuterium gas filling system were cleaned with NaOH and distilled H_2O before assembly. The gas cell was cleaned and the Mo entrance foil, Ta stop, and liner were replaced and cleaned before each experiment in order to minimize the buildup of contaminants such as carbon and drive-in deuterium from the preceding experiment. The beam-line vacuum (10^{-8}Torr) was obtained with a TM pump and an on-line liquid nitrogen trap. The line was continuously evacuated many days before an experiment. The gas cell and filling system were also evacuated days before a run with continuous cryogenic pumping. Filling with high-purity deuterium gas through a cryogenic trap occurred just before the experiment. This entire process greatly reduced contaminants which lead to time-correlated background in the source and scattering spectra.

Neutron TOF Spectrometer-Goniometer

The details of the mechanical goniometer and detector shielding have been given previously, hence only a brief discussion will be given here[2]. The goniometer (Fig. 2) is a heavily structured, high-precision device loaded with a 7300 kg, optimum designed, double-truncated conical collimator and shield. The shield system was designed to minimize the time-correlated and uncorrelated background in neutron scattering spectra. The collimator was designed to minimize the scattering from its own walls into the detector and to view as small a solid angle as is practical and still leave the detector a completely unobstructed view of the scattering sample. The precision machining of the collimator, together with the precision construction and leveling of the goniometer table and angular and radial carriages, allowed the detector to be easily positioned with an angular precision of better than ±0.2° while maintaining correct alignment of the scatterer, collimator, and detector. To further improve the shielding, the front of the shield was provided with a second and third stage of collimation. The

*Partially supported by USAEC
+Visiting scientist from Tubingen Univ.
++Visiting scientist from Frankfurt Univ.

second collimator was a 12.7-cm-long copper cylinder which also had a double-truncated cone aperture. The third stage was designed to shield the outer periphery of the main shield from source neutrons that were not intercepted by a 110kg shadow shield. The shadow shield,which is 62 cm long,was designed to shield the collimator throats and the detector from the primary neutron source. Figure 2 illustrates the scattering geometry. The sample was suspended with its axis vertical and located $\approx$ 9 cm from the center of the gas cell. The main neutron detector was an 8.89-cm-diam x 5.08-cm-thick NE 218 scintillator which was coupled to a Phillips 58 DVP PM tube and could be positioned at distances of 1.5 to 4.0 m from the scatterer. A second smaller neutron detector (NE218-56DVP) was housed in a cylindrical copper shield which was suspended above the scattering plane. This detector monitored the neutron flux incident onto the scattering sample during the experiment. The electronics for the TOF spectrometer are shown in Fig. 3. Fast timing signals from the main and monitor detectors and the beam pulse pickoff were converted to logic signals by constant-fraction pulse-height discriminators. The time difference between the detector pulses and the delayed pick-off pulses, as measured by time-to-amplitude converters (TAC), determined the flight times of the neutrons. The linear signals from both detectors were used for lower-level discrimination to reject pulses with amplitudes smaller than a predetermined value and for PSD to reject detected γ rays from the time spectra. The PSD, TOF, and routing pulses were fed through a computer interface to four ADCs. Neutron TOF, γ TOF and PSD cross-over timing spectra for the monitor and main detector systems were stored and displayed simultaneously by a DDP-224 computer for on-line diagnostic purposes. The computer also provided the capability for on-line calculations of peak yields, background subtraction, TOF energy calculations, kinematic energy calculations, plus a number of other calculations, and diagnostics.

Performance of the TOF Spectrometer-Goniometer

A number of primary neutron source and carbon scattering experiments were performed to evaluate the system at incident neutron energies of 8-15 MeV. Fig. 4 shows a neutron TOF spectrum of the $D(d,n)^3He$ source reaction taken at $\theta_L = 90°$, $E_n = 9.0$ MeV at 0°. The measurement utilized the heavily shielded collimator system, less intensive cleaning of the beam line components, and a non all-metal beam line evacuated with oil diffusion pumps. Fig. 4a was taken without PSD. The heavily shielded collimator system reduced the time-uncorrelated background down to low levels; however, interaction of the deuterons with beam line and gas cell contaminants such as C and Si produced time-correlated background in the source spectra. Fig. 5 shows the effect of contaminant neutron sources on the TOF measurement of inelastic scattering. At certain angles the inelastic scattering peak migrates over the background peaks, making an accurate subtraction of background very difficult. Fig. 6 shows the effect, on a C scattering spectrum, of deuterons driven into the Ta beam stop in a previous high energy C scattering experiment. It is obvious that the beam stop must be replaced after each experiment. Figs.7, 8,and 9 show the primary neutron source spectra and carbon scattering spectra taken with the TOF spectrometer-goniometer incorporating all of the background reduction techniques outlined in the introduction. The primary quasi-monoenergetic neutron peak of the $D(d,n)^3He$ reaction stands alone between channels 500-600. Approximately 70% of the neutron continuum that appears to the left of the $D(d,n)^3He$ group is due to the D(d,np)D, D(d,np) np reactions with the remaining 30 percent due to evaporation and stripping on the Ta beam stop. At about 11 MeV the neutron yield from the continuum > the yield from the $D(d,n)^3He$ reaction. Due to a Q value of 3.27 MeV and a breakup threshold of 4.45 MeV, there is a 7.4 MeV wide spectral region available for neutron scattering measurements of greatly reduced backgrounds. This allows one to measure up to $\approx$7.4 MeV excitation in the nucleus without appreciable interference from background. The background plateau between the continuum and the mono-energetic group is primarily the result of deuteron scattering into the cell walls and is subtracted with gas-out measurements. The C elastic and inelastic scattering (Q = -4.43) peaks are essentially free of time-uncorrelated background up to an incident neutron energy of $\approx$ 11 MeV at which point gas-out measurements must be made. The third distinct peak appearing in the 14.5 and 15 MeV work is due to inelastic scattering from the 7.66 MeV state. The quality of the TOF scattering spectra is comparable to charged particle pulse-height spectra.

Measurements were made of the angular distributions for the elastic and inelastic scattering (Q = -4.43 MeV) of neutrons by carbon at 28 angles each for 14 different energies spanning the range 9-15 MeV. Fig. 10 shows the angular distribution for the elastic scattering of 9 and 15 MeV neutrons from carbon. We will only point out the minimum amount of dispersion in the data and the accuracy which we believe to be of the order of 5%. Details of the measurements and discussion of items 6-8 of the Introduction to this report will be covered in paper IB4 of this conference. In addition we have nearly completed measurements of the scattering of 7-15 MeV neutrons from ^9Be, and have started measurements of the scattering of 9-15 MeV neutrons from ^{27}Al. We will start scattering measurements on ^6Li in a few weeks, and proceed on to ^7Li, O,F,B, and Nb. All of these measurements will be extended to the extreme forward angles using the small angle scattering system obtained on loan from the USA Ballistic Research Laboratories, Aberdeen, MD.

Conclusions

By utilizing techniques for extreme reduction of time-correlated and uncorrelated backgrounds, good resolution TOF spectroscopy, stable monitor system, accurate detector efficiency determinations, absolute normalization of the cross sections, and Monte Carlo simulation of finite sample size effects, measurements can be made of differential cross sections spanning the difficult energy range 6-15 MeV to an absolute uncertainty of $\approx$ 5 percent.

References

1. H.W. Newson, E.G. Bilpuch, F.O. Purser, J.R. Boyce and T.B. Clegg, Nucl. Instr. and Meth. 122, 99 (1974).

2. D.W. Glasgow, D.E. Velkley, J.D. Brandenberger, M.T. McEllistrem, H.J. Hennecke and D.V. Breitenbecher, Nucl. Instr. and Meth. 114, 521 (1974).

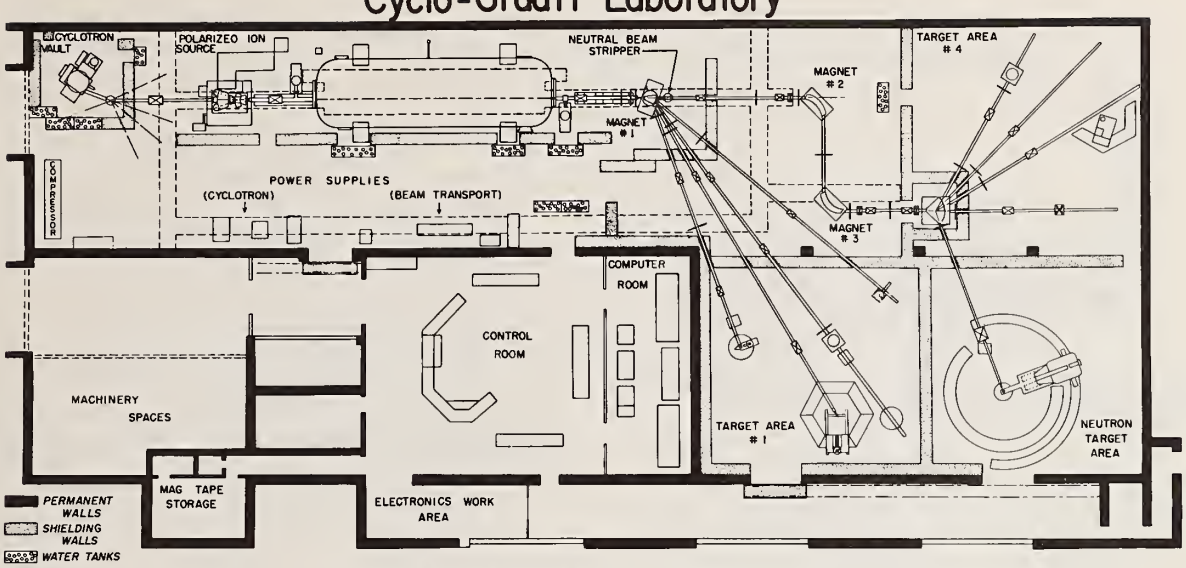

Fig. 1. Plan view of the Cyclo-Graaff Laboratory.

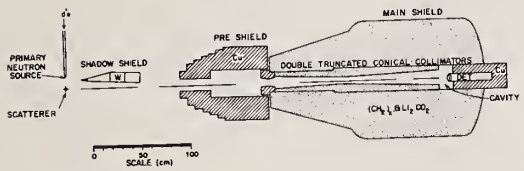

Fig. 2. The experimental scattering geometry used to measure the differential cross sections.

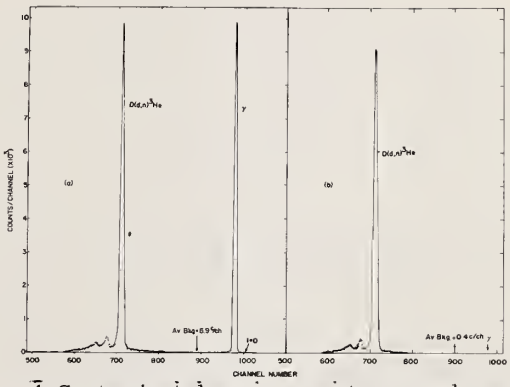

Fig. 4. Contaminated source spectrum produced by deuteron interactions with C and Si in the beam line. The primary neutron energy 9.0 MeV.

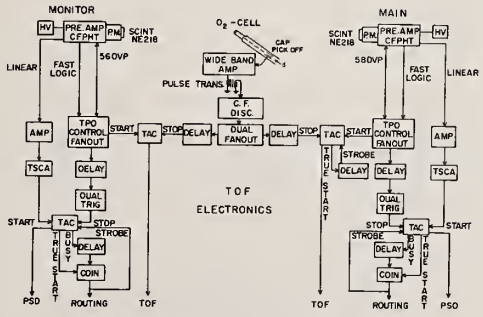

Fig. 3. Block diagram of the electronics used in the neutron TOF spectrometers.

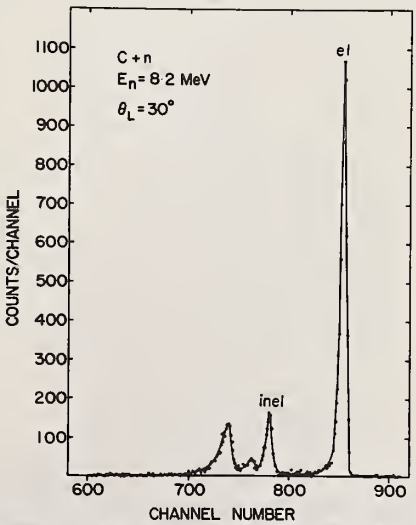

Fig. 5. Neutron TOF spectrum of 8.2 MeV neutrons scattered by C at θ_L = 30°. The two peaks to the left of the inelastic peak are due to contaminants.

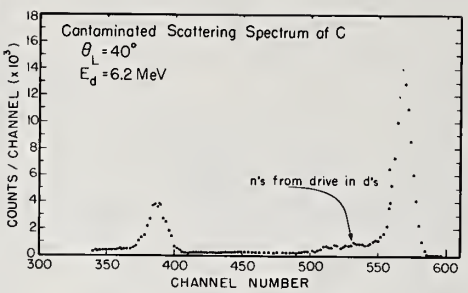

Fig. 6. Contaminated scattering spectrum produced from "drive in deuterons" in the Ta beam stop.

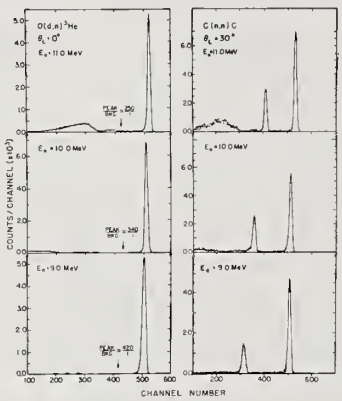

Fig. 7. Neutron source spectrum and carbon scattering spectrum for E_n = 9-11 MeV. The carbon elastic and inelastic scattering peaks in the C(n,n)C spectrum are on the right and left respectively. Notice the low background and that the continuum neutrons are also scattered by the carbon.

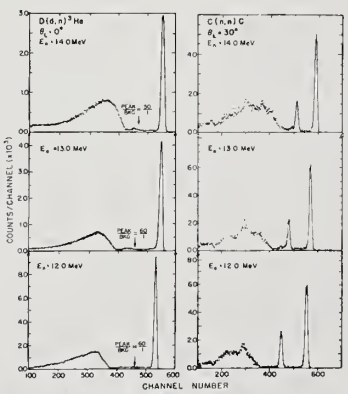

Fig. 8. Neutron source spectrum and carbon scattering spectrum for E_n = 12-14 MeV. The strong continuum forming to the left in the source reaction is due to the D(d,np)d and D(d,np)np reactions in the source gas; and evaporation and stripping on the Ta beam stop.

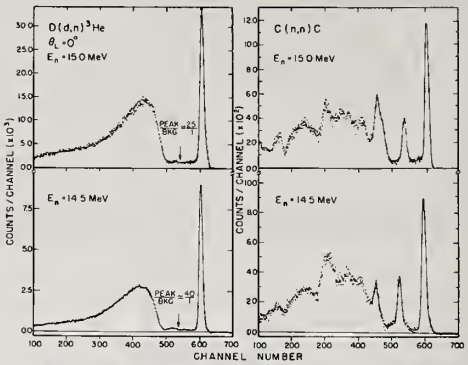

Fig. 9. Neutron source spectrum and carbon scattering spectrum for E_n = 14.5-15.0 MeV. The 2nd peak to the left of the carbon elastic peak is due to scattering from the 2nd excited state in C.

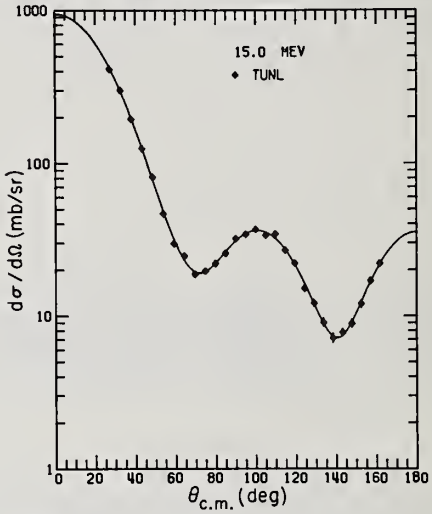

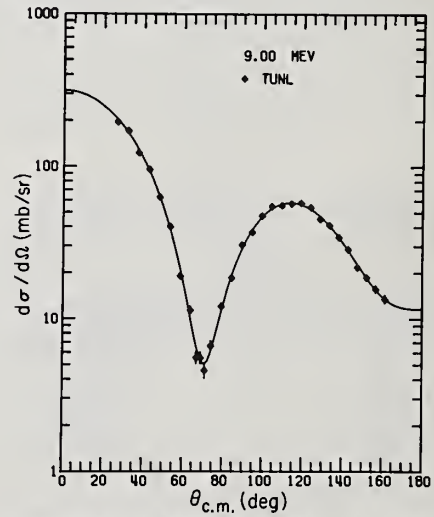

Fig. 10. Measured differential elastic scattering cross sections for E_n = 9.0 and 15.0 MeV. The curves are LSF fits to a sum of Legendre polynomials. The absolute errors are < the diagonals of the diamond symbols except in the minima.

A FACILITY FOR STUDYING NEUTRON-INDUCED CHARGED PARTICLE REACTIONS†

F. P. Brady, N. S. P. King, M. W. McNaughton,
and J. F. Harrison,
University of California, Davis, CA 95616
B. E. Bonner
Los Alamos Scientific Laboratory, Los Alamos, N.M. 87544

Nearly monoenergetic beams of neutrons, variable in energy from below 10 to above 60 MeV are produced via intense beams of protons and deuterons from the sector focussing isochronous cyclotron at Crocker Nuclear Laboratory. The neutron production target and collimation system are connected to a scattering chamber containing detector telescopes, all in vacuum. ΔE, E and time-of-flight signals from each telescope are interfaced to a PDP15/40 computer via CAMAC and sophisticated on-line and off-line data processing can be carried out. There are a number of examples of the use of these cross sections: Neutron induced reactions on carbon have provided us with a better understanding of energy dependence of neutron detection efficiencies in plastic scintillators. Data from carbon and other tissue-resident elements are necessary for an understanding of microscopic dose distributions produced by neutrons.

(Neutron-induced reactions, facility, ^{12}C data, 56 MeV)

Introduction

Charged particle measurements in neutron induced reaction experiments traditionally suffer from one or more of the usual problems associated with low neutron intensities: 1) poor beam energy resolution, 2) target thickness limitations arising from the low energy of the emitted charged particles, 3) poor resolution in charged particle detection systems and 4) normalization problems in obtaining absolute cross sections. As a consequence, the most successful efforts have involved either experiments in light nuclei in which energy resolution is not critical and cross sections are relatively high or use of good resolution neutron beams near 14 MeV generated by the T (d,n) reaction.

The present unpolarized neutron facility at Crocker Nuclear Laboratory has evolved from a system originally designed primarily for few nucleon experiments.[1] Emphasis has been placed on improving charged particle detectors for high energy protons, deuterons, and tritons and enclosing them in a vacuum system. Overall system resolution is now ≈1 MeV which allows individual nuclear states in low mass nuclei to be studied. Virtually no neutron-induced charged particle differential cross section data exist for individual nuclear levels at neutron bombarding energies above 25 MeV.

Recently we have made a survey of (n,z) reactions using 56 MeV neutrons incident on ^{4}He and ^{14}N in an LN_2 cooled gas target and on self-supporting ^{6}Li, ^{7}Li, ^{9}Be, ^{12}C, ^{27}Al and ^{209}Bi targets.[2] Particle identification permitted observation of proton, deuteron and triton energy spectra as well as ^{3}He and ^{4}He data for the ^{12}C target.

The ^{6}Li (n,p) ^{6}He, ^{12}C (n,p) ^{12}B, ^{27}Al (n,p) ^{27}Mg, and ^{209}Bi (n,p) ^{209}Pb reactions have provided evidence for the population of strongly collective states which form analogs to known giant resonances (M1, E1, M2 and E2) in the respective target nuclei.[2] These resonances tend to increase the cross sections for the (n,p) reaction above those expected on the basis of simple reaction models normally incorporated in higher energy neutron transport calculations.

The single and multinucleon transfer reactions provide a means for studying the isospin dependence of various reaction mechanisms by comparisons with known charge conjugate reaction data.

Application of neutron-induced charged particle data can be made to a wide range of problems which include calculation of energy deposition in tissue for tumor treatments, neutron transport codes, and calculation of neutron detector efficiencies. The latter topic will be expanded upon in another section of this paper.

Experimental facility

The isochronous cyclotron at Crocker Nuclear Laboratory produces intense proton beams variable in energy from below 10 to above 60 MeV as well as beams of deuterons to above 40 MeV and alpha particles to above 80 MeV. In the work described here a proton beam of 15 μA strikes a metallic ^{7}Li target, and neutrons from $^{7}Li(p,n)^{7}Be$ are collimated at 0° by a 1.55 meter-long steel collimator (figure 1). The neutron production targets such as ^{7}Li are mounted on a water-cooled, oscillating target wheel. More details of the target wheel, cyclotron, the arrangement of experimental areas and charged particle beam lines are given in ref. 1.

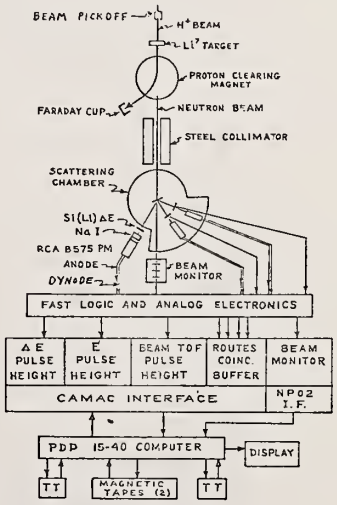

Figure 1. Schematic of overall set-up.

A well-defined beam of size 12 mm wide x 24 mm high and of intensity 5 x 10^5/cm^2-sec. per MeV of ^{7}Li target thickness is formed by the steel collimator. Roughly 60% of the neutrons produced in the reaction ^{7}Li(p,n)^{7}Be fall within a well-defined high-energy peak of 1 MeV FWHM corresponding to transitions principally to the ground state of ^{7}Be. The remaining neutrons are spread over a broad, lower-energy tail. The mean energy of the beam peak is determined to within ± 100 keV by a time-of-flight technique.[3]

The collimated beam passes into a scattering chamber and its intensity is monitored by a recoil-proton telescope.[1] Integration of the proton beam cleared into a Faraday cup provides a secondary neutron beam monitor accurate to 1-2%. Three DE-E telescopes mounted in the scattering chamber each consist of a solid-state detector and a NaI scintillator coupled to an 8575 phototube. One telescope is fixed at 15.5° on the right and two are movable, 20° apart, on the left-hand side of the beam. Zero-crossing timing signals, derived from the NaI detectors, and relative to a beam pick-off mounted just upstream of the ^{7}Li target are used to determine particle time-of-flight. This TOF then forms the basis for selecting only those charged particle events generated by the ∿1 MeV wide neutron peak.

With the clearing magnet turned off, a proton (or other) beam, typically less than 1 nA can be focussed through the neutron collimator and into the scattering chamber, all in vacuum. This "proton trickle" is most convenient for testing the detector systems in place and for tuning up the electronics more rapidly than can be accomplished with a neutron beam.

All detector arms share the same analog electronics for digitising pulse-height and time-of-flight parameters. Analog data, in addition to a detector identification signal, are transferred to an on-line PDP 15/40 computer via a CAMAC interface, and recorded, event by event on standard magnetic tape. The data are subsequently analyzed using interactive programs written for the PDP 15. An example of this data played back into the computer is shown in figure 2.

The upper half of figure 2 shows ΔE vs E and TOF vs E_D spectra. The lower half shows the ^{12}C(n,d) spectrum resulting from the appropriate cuts in the ΔE vs E and TOF vs E_D spectra.

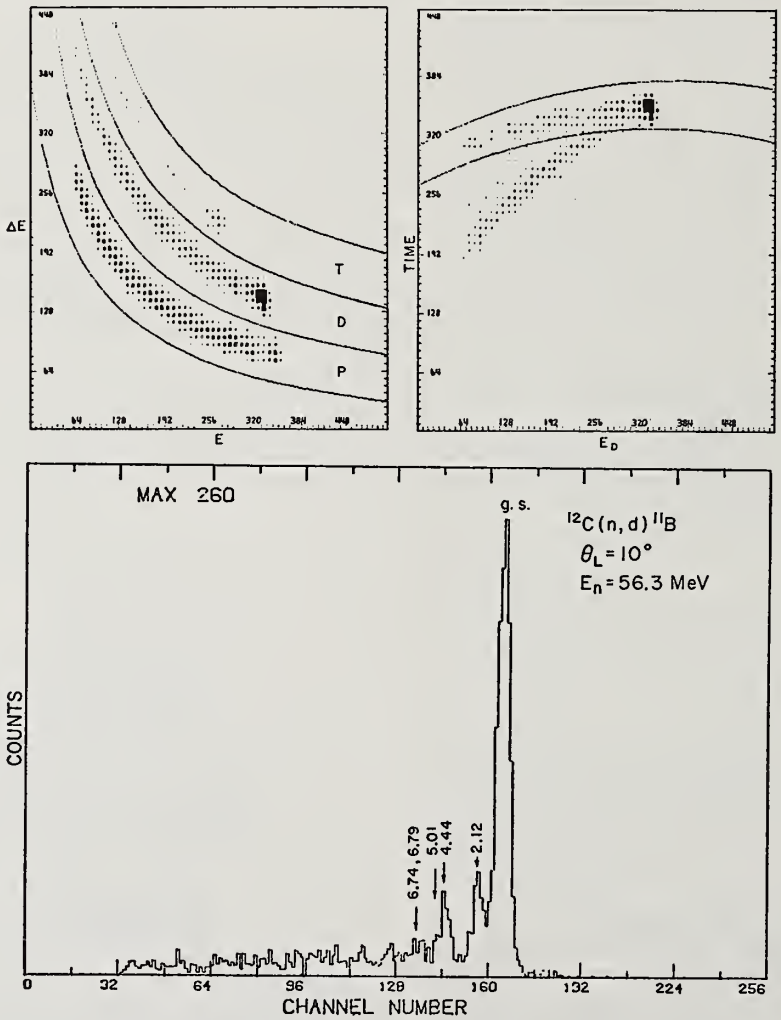

Figure 2. Top: ΔE vs E and TOF vs E.
Bottom: Deuteron spectrum from ^{12}C(n,d)^{11}B after particle and time cuts.

Data are also simultaneously sorted on-line according to restriction cuts on the DE vs E and TOF vs E histograms, and single parameter energy pulse height spectra are produced. These spectra can be displayed with a variety of formats. This allows continuous monitoring of the experiment. The number of parameters per event and the histograms which are produced are variable to allow a diversity of experiments.

Absolute (n,z) cross sections are obtained via normalization to n-p scattering. Recently, precision n-p differential cross sections at 50.0 MeV [5] and near 25 MeV [6] have been measured. These can be interpolated and extrapolated using an adjusted fit [7] to provide an absolute normalization of 3%.

Neutron detector efficiencies

One important application of neutron induced charged particle reactions from ^{12}C is in the prediction of neutron detection efficiencies for plastic scintillators. In principle these efficiencies are predictable from the n-p cross sections, which are well known, and the n-^{12}C cross sections, which are poorly known. For example, in three widely used computer codes to predict efficiencies, estimates made for unmeasured cross sections variously conclude that the $^{12}C(n,p)$ total reaction cross section at 50 MeV is 61.5 mb[8], 125 mb[9], and 204 mb[10]. Further estimates have to be made for the final state energy and angular distributions before these integrated cross sections can be used to predict efficiencies.

In a recent paper [11], we reported accurate measurements of neutron detection efficiencies, and observed significant discrepancies of up to 20% between the predictions and measurements at some energies. Since then we have made preliminary measurements of $^{12}C(n,p)$, $^{12}C(n,d)$ and $^{12}C(n,t)$ cross sections at 56 MeV and inserted these results into Stanton's code.[12] The predictions are thereby considerably improved, with no significant discrepancy for a 4.2 MeV detection threshold, and discrepancies of less than 7% for a 1 MeV threshold.

References

† Supported largely by the National Science Foundation.

1. J. A. Jungerman and F. P. Brady, Nucl. Instr. Meth. 89, 167 (1970).
2. Annual Report to the National Science Foundation, UCD-CNL 183.
3. F. P. Brady, W. J. Knox and S. W. Johnsen, Nucl. Instr. Meth. 89, 309 (1970).
4. F. P. Brady, W. J. Knox, J. A. Jungerman, M. R. McGie and R. L. Walraven, Phys. Rev. Lett. 25, 1638 (1970).
5. T. C. Montgomery, F. P. Brady, B. E. Bonner, W. B. Broste and M. W. McNaughton, Phys. Rev. Lett. 31, 640 (1973).
6. L. N. Rothenberg, Phys. Rev. C1, 1226 (1970), T. W. Burrows, B.A.P.S. 17, 151 (1972) and T. G. Masterson, Phys. Rev. C6, 690 (1972).
7. R. A. Bryan and A. Gersten, Phys. Rev. D6, 341 (1972).
8. R. E. Textor and V. V. Verbinski, ORNL-4160 (1968)
9. R. J. Kurz, UCRL-11339 (1964).
10. N. R. Stanton, COO-1545-92 (1971).
11. M. W. McNaughton et al., Nucl. Inst. 116 (74) 25.
12. M. W. McNaughton et al., Nucl. Inst. to be published.

AFTER-PULSE SUPPRESSION FOR 8850 AND 8854 PHOTOMULTIPLIERS

G. P. Lamaze, J. K. Whittaker, R. A. Schrack and O. A. Wasson
National Bureau of Standards
Washington, D. C. 20234

Spurious pulses occurring after large light output events in a scintillator (after pulsing) have been observed in semi-conducting first dynode photomultipliers (RCA 8850 series). The after-pulsing apparently has two components, an isochronous component occurring at a fixed time interval after the initial light pulse and an asynchronous component with a long duration lasting at least 40 μsec. The time interval between the isochronous bursts is related to the types of residual gases in the photomultiplier. In the RCA 8850 series tubes, the asynchronous after-pulsing consists of very low amplitude pulses and appears to be primarily due to single electron events, the number of these events being related to the main pulse amplitude. To obtain after pulse suppression, a fine stainless steel mesh was stretched tightly over the glass window of the photocathode. The mesh was then pulsed (FWHM = 250 ns) during the light flash to +300 volts relative to the photocathode potential. The isochronous and asynchronous after-pulsing was completely suppressed. Further details are presented.

(After-pulse; photomultiplier; gamma-flash; pulse suppression; scintillator; detector)

In neutron time-of-flight experiments performed with neutrons produced by an electron linac, the arrival of the neutrons at the detector is preceded by an intense burst of photons (usually referred to as the gamma flash). The time interval between the detection of the gamma flash and the detection of the neutron is dependent on the energy of the neutron and the length of the flight path. This gamma flash generates a long chain of after-pulses in the photomultiplier which are indistinguishable from neutron events in the scintillator.

This phenomenon of after-pulsing is well reported in the literature,[1-4] and is due to the ionization of residual gases in the photomultiplier by the photoelectrons. These ions are accelerated back to the photocathode and will excite further bursts of electrons. The after-pulsing apparently has two components, an isochronous component occurring at a fixed time interval after the initial light pulse and an asynchronous component with a long duration lasting at least 40 μs. The time interval between the isochronous bursts is related to the types of residual gases in the photomultiplier.[1] In the RCA 8850 series tubes, the asynchronous after-pulsing consists of very low amplitude pulses and appears to be primarily due to single electron events, the number of these events being related to the main pulse amplitude. This type of after-pulsing is probably present in most photomultipliers but the effect is more significant in the 8850 series tubes because of the possibility of resolving events due to single photoelectrons.

Schrack et al.[3] demonstrated that after-pulsing in Philips 58AVP photomultipliers could be suppressed by reversing the electric field at the photocathode and thus preventing the photoelectrons from reaching the first dynode and producing ion pairs. This was done by pulsing the voltage of the focus electrode 600 V negative, with respect to its normal operating potential, during the scintillator light flash. This method is ineffective in some photomultipliers, including the RCA 8850 series, due to their internal construction. Additionally, pulsing the focus electrode may produce noise in the photomultiplier.[3] Charpak[5] and Bartl[6] have demonstrated that photomultipliers can be pulsed off by applying a voltage to a fine transparent mesh placed over the front of the photomultiplier, thus reversing the field and preventing the electrons from leaving the photocathode. This latter technique has been used in the present investigation to suppress both types of after-pulsing for the RCA type 8850 and 8854 photomultipliers. Both tubes are of essentially the same construction, with gallium phosphide (GaP) first dynodes, and both have virtually identical after-pulsing characteristics.

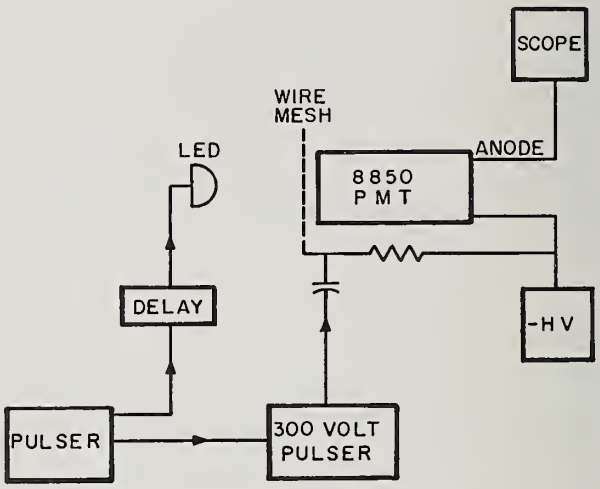

Figure 1. Circuit for testing after-pulsing characteristics and after-pulse suppression of phototubes.

Figure 1 indicates the experimental setup for measuring both after-pulse characteristics and the after-pulse suppression of the phototubes under test. A woven, stainless steel mesh ($\approx$60 μm thick of wire $\approx$ 30 μm diameter, mesh size $\approx$ 1.25 mm), looking like the fabric of a nylon stocking, and of estimated transparency of 96%, was stretched tightly over the glass window of the photocathode and held at cathode potential. A red light-emitting diode was used as a pulse light source (fwhm = 100 ns). With no pulse applied to the stainless steel mesh, two isochronous groups of after-pulses were observed about 600 ns and 1 μs after the light flash (see figure 2). Additionally, asynchronous pulses were observed up to 80 μs after the light flash with the largest number occurring 40 μs after the light flash (see figure 3). The mesh was then pulsed (fwhm = 250 ns) during the light flash to + 300 V relative to the photocathode potential.

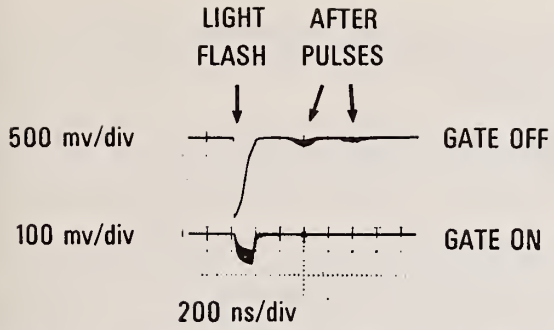

Figure 2. Observed phototube output. Top trace is with no after-pulse suppression; bottom trace is with 300 volt pulse applied to wire mesh.

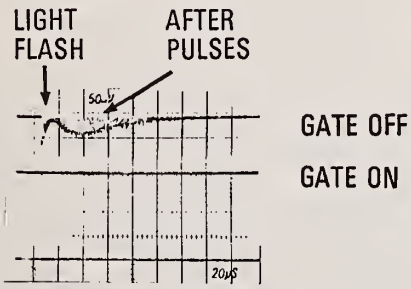

Figure 3. Observed phototube output for long times (20 μs/div). Top trace is with no after-pulse suppression; bottom trace is with 300 volt pulse applied to wire mesh.

Figure 2 demonstrates that the light flash signal was reduced by a factor of about 15 and the after pulses were completely eliminated. Figure 3 shows that the long time component after pulsing is also essentially completely eliminated.

After achieving these rather successful results, three new 8850 tubes were ordered and tested. One performed exactly as described above, but the other two exhibited a strange characteristic. When the pulse was applied to the mesh, a large amount of noise was created in the tube with a great deal of after-pulsing, effectively negating the beneficial results of pulsing off. We have no explanation for the differences in what should have been identical tubes.

References

[1] G. A. Morton, H. M. Smith and R. Wasserman, IEEE Trans. Nucl. Sci. NS-14, no. 1 (1967) 443.

[2] Y. M. Shin, S. H. Ku, C. Glavina and J. A. Rawlins, Nucl. Instr. and Meth. 58 (1968) 353.

[3] R. A. Schrack, H. T. Heaton II and R. B. Schwartz, Nucl. Instr. and Meth. 77 (1970) 175.

[4] C. F. G. Delaney and J. A. Harwood, Sci. Proc. Roy. Dublin. A3 (1967) 57.

[5] G. Charpak, Nucl. Instr. and Meth. 51 (1967) 125.

[6] W. Bartl, CERN 68-41 (1968).

A SECONDARY STANDARD NEUTRON DETECTOR FOR MEASURING TOTAL REACTION CROSS SECTIONS*

K. K. Sekharan, H. Laumer and F. Gabbard
University of Kentucky
Lexington, Kentucky 40506

A neutron detector has been constructed and calibrated for the accurate measurement of total neutron-production cross sections. The detector consists of a polyethylene sphere of 24" diameter in which 8-$^{10}BF_3$ counters have been installed radially. The relative efficiency of this detector has been determined for average neutron energies, from 30 keV to 1.5 MeV by counting neutrons from $^{7}Li(p,n)^{7}Be$. By adjusting the radial positions of the BF_3 counters in the polyethylene sphere the efficiency for neutron detection was made nearly constant for this energy range. Measurement of absolute efficiency for the same neutron energy range has been done by counting the neutrons from $^{51}V(p,n)^{51}Cr$ and $^{57}Fe(p,n)^{57}Co$ reactions and determining the absolute number of residual nuclei produced during the measurement of neutron yield. Details of absolute efficiency measurements and the use of the detector for measurement of total neutron yields from neutron producing reactions such as $^{23}Na(p,n)^{23}Mg$ are given.

(Neutron detector; Absolute Efficiency Determination; Cross Section Measurements)

Introduction

The determination of the absolute neutron reaction cross sections is important for the study of nuclear reactions in nucleosynthesis in stars[1] and also for reactor calculations. Many of these reaction cross sections cannot be determined directly because the target material does not exist in nature. Such reaction cross sections can be determined by measuring the inverse reaction and then calculating the reaction cross section of interest by using the reciprocity theorem.

The detector described here is a 4π neutron counter for use in measuring neutron production cross sections from charged particles such as alpha-particles and protons incident on various target nuclei.

The use of a 4π-counter eliminates the necessity for the measurement of the angular distribution of a reaction and subsequent calculation of integrated cross section. However, an accurate determination of the cross section is possible only if the efficiency of the detector is known accurately. Since the sphere counter we have used detects neutrons of any energy it is important that the efficiency of the detector as a function of the neutron energy be constant so that neutrons belonging to different energy groups can be detected with the same efficiency. It is also important that the efficiency of the detector be independent of the nature of angular distribution of the emerging neutrons in the reaction.

Experimental Method

Description of Sphere Counter

The sphere counter is shown in Fig. 1. The neutron detector consists of a 24" diameter polyethylene sphere in which 8 $^{10}BF_3$ proportional counters have been radially installed. The $^{10}BF_3$ counters are 5/8" in diameter and about 9" in length. These counters are distributed at angles 31°, 39°, 55°, 90°, 90°, 125°, 141° and 149° which are zeroes of the Legendre polynomials. The target is mounted in an aluminum chamber which is located at the center of the polyethylene sphere in a 5" diameter spherical cavity. There is a 2 3/8" diameter hole for the entrance and exit of the charged particle beam.

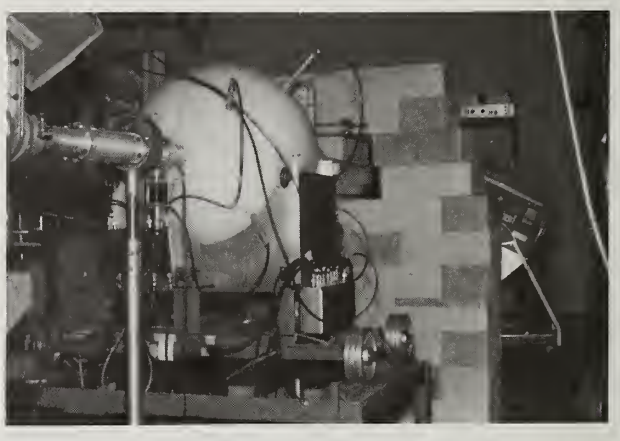

Fig. 1. Sphere counter. The detectors are 5/8" diameter BF_3 counters.

The neutrons are moderated in the polyethylene sphere and detected by the $^{10}BF_3$ counter by the reaction $^{10}B(n,\alpha)^{6}Li$. The signals from each BF_3 counter is separately amplified by a preamplifier for each detector. The signals from 4 preamplifiers connected to BF_3 counters at the forward angles

are fed into a mixing unit A and those from the 4 remaining preamplifiers connected to BF_3 counters at backward angles are fed into a second mixing unit B. Signals from the mixing units are further amplified and counted separately in decade scalars. Having two sets is helpful in reducing the dead time to an acceptable level.

The targets are mounted in the center of the sphere counter. The incident beam can be stopped in the sphere or be dumped in a Faraday cup approximately 6' away from the sphere to reduce background. In case the beam is stopped in the sphere a polyethylene plug is used to cover the 2 3/8" hole at 0°. The targets used in the sphere counter were either self supporting foils or materials evaporated on to a pure 0.4 mg/cm^2 thick aluminum foil.

Gamma Ray Detection System

A 35 cc ORTEC Ge(Li) gamma ray detector was used to determine the gamma ray yield from the bombarded targets ^{7}Li, ^{51}V and ^{57}Fe. 4" to 6" thick shielding of iron bricks were placed around the Ge(Li) detector to reduce the background gamma rays. The absolute efficiency of Ge(Li) detector was determined by direct calibration of the detector with standard ^{51}Cr and ^{57}Co sources obtained from National Bureau of Standards. Standard sources and the bombarded targets were placed exactly in the same location in front of the Ge(Li) detector for counting. We observed that slight lateral displacement of the sources, such as might be due to wandering of the beam on the target, from this position did not cause any significant change in the gamma ray yield.

^{7}Li(p,n)^{7}Be Reaction

The neutron yield from this reaction was measured in steps of 50 keV from threshold to 4.0 MeV incident proton energy. At the peak near 2.25 MeV the yield was measured in 25 keV steps. We observed that the neutron yield obtained in our measurement agreed well with the yield obtained by Gibbons and Macklin[2] using a carbon moderating detector. For determining the relative efficiency, several LiF targets evaporated onto pure aluminum foils were bombarded with protons at several incident proton energies. The bombarding time varied from 1 to 2 hours. These targets were immediately placed in front of the Ge(Li) detector to measure the 478 keV gamma ray yield. From the knowledge of neutron yield and gamma ray yield the relative efficiency was determined as explained in the next section. The relative efficiency decreased only by 3% at an average neutron energy of 1.5 MeV from the maximum relative efficiency at 300 keV. This was achieved by adjusting the radial position of the BF_3 counters in the sphere. The relative efficiency and the neutron yield as a function of E_p are shown in Fig. 2.

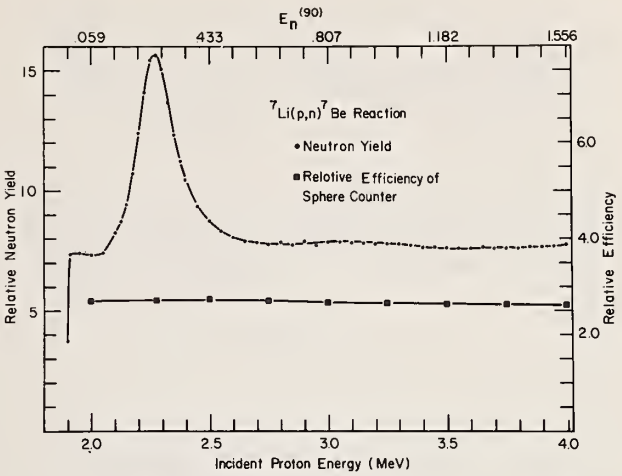

Fig. 2. Neutron yield from ^{7}Li(p,n)^{7}Be reaction. The flat curve shows the efficiency of the polyethylene sphere relative to the carbon sphere of Macklin and Gibbons.

Absolute Efficiency

There are many (p,n) reactions in which the residual nucleus decays back, at least partly, to an excited state of the target nucleus by positron emission or electron capture. This results in the emission of a gamma ray when the nucleus is de-excited to the ground state. Some of these reactions have long half lives. By determining the number of gamma rays emitted from the target nucleus which has been bombarded it is possible to determine accurately the number of residual nuclei produced in the (p,n) reaction. Therefore, if we measure the neutron yield from the (p,n) reaction with the sphere counter whenever the target is bombarded with the incident beam the ratio of neutrons detected to the total number of residual nuclei produced will give the efficiency of the sphere counter since one residual nucleus is produced for every neutron produced. This method is independent of current integration, target uniformity and target thickness measurements. The important factors are the half life for decay and the efficiency of the gamma ray detector for the particular geometry in which gamma ray counting is done.

We have chosen ^{51}V(p,n)^{51}Cr and ^{57}Fe(p,n)^{57}Co reactions for the absolute efficiency determination and ^{7}Li(p,n)^{7}Be reaction for its relative efficiency determination. A thick vanadium foil was bombarded with 2.05 MeV protons for 3 hours and the 320 keV gamma rays counted with the Ge(Li) detector. From this measurement the absolute efficiency of the sphere counter for neutrons of average energy 300 keV was found to be (0.56 ± .017)%. A thin iron target was bombarded with 3.0 MeV protons and from the gamma ray yield measurement the absolute efficiency for 1.35 MeV neutrons was obtained as (0.55 ± .016)%.

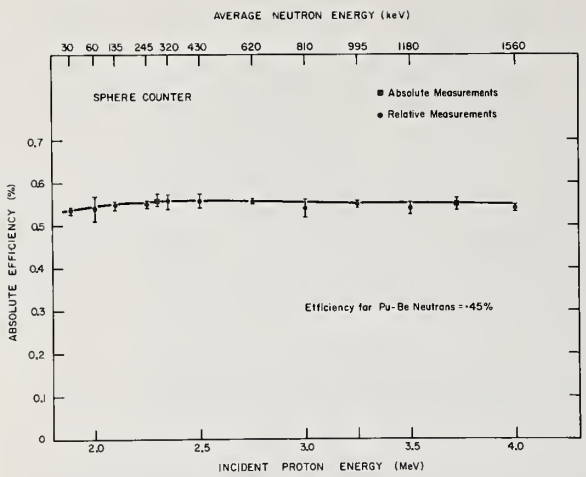

Fig. 3. Absolute efficiency of sphere counter. The error flags are an estimate of the standard error at each point.

By normalizing the relative efficiency values obtained from LiF target measurements the absolute efficiency was determined for the neutron energy range 30 keV to 1560 keV. The absolute efficiency for the neutrons from Pu-Be source was found to be (0.45 ± 0.01)%. The efficiency curve is shown in Fig. 3 and the measured values are tabulated in Table 1.

TABLE 1

Absolute Efficiency of Sphere Counter. $\bar{E}_n$ is the average neutron energy; ΔE_n is the full energy spread of the neutrons; ε is the absolute counting efficiency; and $\Delta\varepsilon$ is the estimated standard error in the efficiency determination.

$\bar{E}_n$ (keV)	ΔE_n (keV)	ε %	$\Delta\varepsilon$	Target
30[a]	35	.54	±.01	LiF
60	215	.54	±.03	"
135	300	.55	±.01	"
245	400	.55	±.01	"
~300	500	.56[b]	±.017	^{51}V Foil
320	460	.56	±.02	LiF
430	550	.56	±.015	"
621	680	.56	±.008	"
810	805	.54	±.02	"
995	925	.55	±.008	"
1180	1050	.54	±.015	"
1350[a]	140	.55[b]	±.016	$^{57}Fe_2O_3$
1560	1280	.54	±.01	LiF

[a] monoenergetic neutrons
[b] absolute measurements

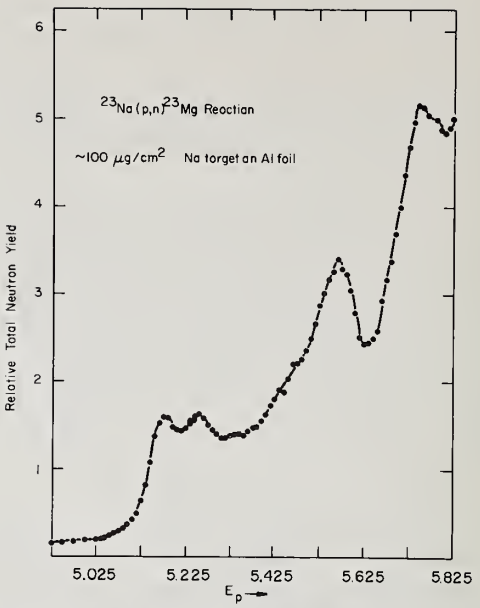

Fig. 4. Neutron yield from $^{23}Na(p,n)^{23}Mg$ reaction measured by sphere counter.

$^{23}Na(p,n)^{23}Mg$ and $^{27}Al(p,n)^{27}Si$ Reactions

The relative neutron yield from the $^{23}Na(p,n)^{23}Mg$ reaction was measured with the sphere counter. A sodium metal target evaporated on to a 0.4 mg/cm^2 aluminum foil was bombarded with protons. The yield measured from threshold to 5.8 MeV of incident proton energy is shown in Fig. 4. The neutron yield from $^{27}Al(p,n)^{27}Si$ reaction was measured from threshold to 6.4 MeV and is shown in Fig. 5.

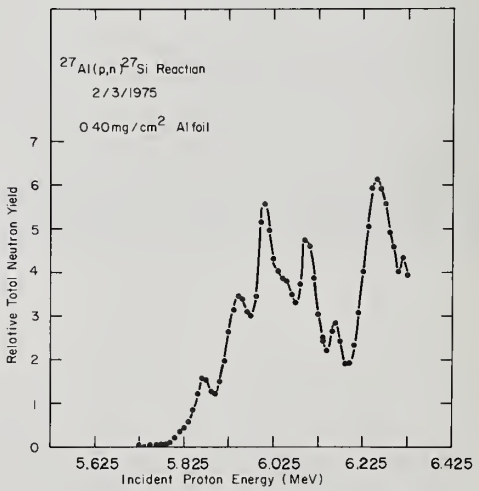

Fig. 5. Neutron yield from $^{27}Al(p,n)^{27}Si$ reaction measured by sphere counter.

Acknowledgements

The authors wish to thank Messrs Jim Dawson, Ron Harper and Douglas Miracle for helping to take some of the data. Many helpful discussions with Professors B. D. Kern and J. L. Weil are very much appreciated. Discussions with C. D. Bowman, Allan Carlson and R. S. Caswell at the National Bureau of Standards have been most helpful.

*Work supported in part by the National Science Foundation.

[1]D. D. Clayton and S. E. Woosley, Proc. Int. Conf. Nucl. Phys., MUNICH (1973), Vol. 2, p. 718; S. E. Woosley Bull. Amer. Phys. Soc. 20, 18 (1975).

[2]R. L. Macklin and J. H. Gibbons, Phys. Rev. 114, 571 (1959).

FACILITIES FOR CROSS SECTION MEASUREMENTS USING Na-D PHOTONEUTRON SOURCES

J. C. Robertson*, M. C. Davis and J. C. Engdahl
The University of Michigan
Ann Arbor, Michigan 48105

Photoneutron sources are a convenient source of neutrons in the intermediate energy range, and because of this they are often used to make absolute cross section measurements. In this paper, the construction of two sodium-deuterium sources is described. One of the sources uses deuterated polyethylene shells and the other utilizes heavy water. The methods used in the manipulation of the sources are outlined. The effects of radiolysis on the yields from the sources is discussed together with the unique features of the Michigan manganese bath system used in their calibration. The results of Monte Carlo calculations of the neutron spectra are given.

(Na-D photoneutron sources, construction, spectrum, calibration, radiolysis)

Introduction

Measurements of fission cross sections with photoneutron sources are a useful contribution to the available data for reactor design. However, in references[1,2] the existence of structure in the ^{235}U fission cross section in the low keV energy region has been established so that measurements of fission cross sections made with a Sb-Be source[3] are not so useful as was first thought. Consequently, measurements have been made using sodium-deuterium photoneutron sources which permit the absolute fission cross sections of ^{235}U and ^{239}Pu to be determined in an energy region where the problem of resonances in the cross sections is avoided. In this paper, the construction of the sources used in these measurements and the methods used in handling them are outlined. The unique features of the Michigan manganese bath system used in their calibration are discussed.

Source Construction

The spherical deuterated polyethylene source is constructed from a 2.38 cm diameter core of compacted NaF powder within an aluminum shell of thickness 0.32 cm. To prevent radiation damage to the deuterated polyethylene shells the core is separately irradiated in a reactor neutron flux of 10^{12} n/cm^2/sec for approximately 24 hrs. giving a ^{24}Na activity of about 10 Ci. Uniform activation of the core is assured by continuously rotating the source during the irradiation. After the irradiation, the core is transferred to an adjacent hot cave where the two shells of deuterated polyethylene are pressed to the core and attached using a small quantity of spray adhesive type 77 supplied by the 3M company. This adhesive holds the deuterated polyethylene target shells in position while the source is in use but permits easy removal of the shells when the ^{24}Na activity has decayed. The core can then be separately re-irradiated.

Table 1 gives the specifications of the source:

Table 1

NaF core diameter	2.38 cm
Aluminum shell - ID	2.38 cm
- OD	3.01 cm
deuterated polyethylene - ID	3.01 cm
- OD	3.65 cm
NaF mass	8.9 g
deuterated polyethylene mass	10.63 g
Aluminum mass	19.63 g

In its mounted form, the source is easily handled using vacuum pickups and is transferred from the hot cave to a low albedo laboratory (where the fission cross sections are made) in a lead shield manufactured from a standard therapy type shield used in hospitals.

The deuterated polyethylene half shells were formed by molding powdered deuterated polyethylene. The polyethylene was heated at 85°C for 2 hours after which it was allowed to cool slowly to room temperature when the half shells were removed from the mold. The polyethylene became colored during this process due to the oxidation of the trace metals used as catalysts in its manufacture. The shells and the mold in which they were formed are shown in Figure 1. The core of the source can also be seen in this figure. Figure 2 shows the mounted shells ready to be pressed to the core.

The heavy water source consists of a NaF core 2.54 cm in diameter within an aluminum shell of thickness 0.32 cm. A second aluminum shell of equal thickness was positioned around the inner core by using six spacers, 0.3 cm in length and 0.15 cm thick. In this way a cavity was left, 0.3 cm thick, which was filled with heavy water after irradiation of the central core. A syringe and intramedical polyethylene tubing were used in this remote filling operation. The heavy water was then sealed in position using a standard pipe fit type 1/16-27 N.T.P. Further details of this source are omitted since the observations given in the next section have led us to preferentially use the deuterated polyethylene source.

Source Yield

The yield from the sodium-deuterated polyethylene source was 2×10^7 n/sec immediately after irradiation, while that from the heavy water source was 1.7×10^7 n/sec. These yields were determined using the Michigan manganese bath system[4] which differs in several ways from previous systems.[5,6] The manganese activity is sampled by circulating part of the manganese solution through a detector chamber but instantaneous mixing of the solution is not used. This mixing is normally achieved by using mechanical stirring so that the activity produced is quickly distributed throughout the entire volume of the bath. When a source is placed at the center of the bath, even though most of the neutrons are captured in the region of solution surrounding the source, the sample of solution counted is of a uniformly mixed solution. Analysis of the counting data to give the source strength allows for decay of activity in transit from the bath to the detector chamber.

*On leave of absence from Dundee College of Technology, Dundee, Scotland

In the Michigan system there is no instantaneous mixing of the solution. A definite mixing interval, τ, is required before activity created at anytime, t, during the source calibration becomes uniformly mixed throughout the entire volume of the manganese solution. Past measurements have shown that this mixing interval is of the order of 500 sec. The sampled activity is a mixture of activity created prior to the sampling time, t, and which is well mixed by time, t, together with activity induced in the interval, τ, prior to t which has not been well mixed. Analysis of the counting data obtained from the sampled solution yields the saturated activity of the entire fluid volume (not just the volume of the manganese bath) so that no correction is required for the decay of activity in transit.

The source strength is obtained by comparing the saturated count rate with the count rate produced by the secondary standard Ra-Be source NBS II. In each case the saturated count rate is obtained from the counts measured in counting intervals, Δ, (typically 600 sec) throughout the calibration. The saturated count rate is obtained after correction for the lack of nonuniform sampling. This correction term, K, contains only the product of τ and δ where δ allows for any change in the detection efficiency of the well mixed and recently produced activity. The value of K is a function of the energy spectrum of the source since the concentration nonuniformity is a function of the source spectrum. For high energy sources, K tends to 1.0 since there is then no lack of uniform mixing in the solution. Neutrons from high energy sources produce activity in the bath which is effectively instantaneously mixed by the circulating system itself. The correction term, K, is only important during the early part of the source calibration. It becomes much less significant as the activity of the solution approaches saturation. Furthermore, after the source is removed from the bath the activity becomes thoroughly mixed in time, τ, so that no mixing correction is required for the decaying solution. K is determined by finding the value which brings the saturated count rate derived from the counting intervals at the beginning of the source calibration, into agreement with the saturated rate obtained from intervals in the near saturation period and ensuring that there is no mismatch between the growth and decay portions of the data.

Figure 3 shows a plot of K versus the average energy for several different types of neutron sources. The average energy of the Ra-Be (γ,n) source was derived from the spectrum given by Eggler and Hughes.[7] A value of 4.5 MeV was taken as the average energy of the Pu-Be source. The results indicate that a mean energy of about 1.8 MeV would be more appropriate. For the californium source a mean energy of 2.06 MeV was used. The error in K is directly related to the source strength since this determines how quickly the background becomes insignificant in the data obtained from the counting intervals at the start of the source calibration. By determining K, the Michigan manganese bath system permits the average source energy to be determined, for sources with average energy below about 2 MeV, at the same time as the source strength.

The yield from the Na-deuterated polyethylene source was observed to follow the ^{24}Na half life of 15.00 ± 0.02 h[9] but the yield from the Na-D_2O source did not. In every case where the heavy water source was used the yield decayed faster than it would have done were it following the ^{24}Na decay constant. This increased decay rate is attributed to the effect of radiolysis on the heavy water with a consequent loss of deuterium through the filler plug in the source. Each time, after the source was used, it was observed that there had been a decrease in the volume of the heavy water. Since the effect of the radiolysis is variable from irradiation to irradiation, the use of a heavy water source is not advocated for applications in which a highly accurate knowledge of the time-dependent neutron yield is important. The sodium-deuterated polyethylene source is much more convenient to use. In addition, since the outer shells are detachable, the material forming the central core is easily varied so that different γ-rays can be used to give different energy photoneutron sources. For example, the use of ^{72}Ga would give neutrons in the 140 keV energy region.

Source Spectrum

The emitted photoneutrons have a primary energy distribution determined by the kinematics of the photodisintegration process. The photoneutron energy, E_n, can be expressed as:

$$E_n = \left\{ \frac{1}{2} \frac{h\nu}{c} \frac{\sqrt{2m_n}}{m_n+M_R} \cos\theta + \sqrt{(h\nu - E_s)\frac{M_R}{m_n+M_R} - \frac{1}{2}\left(\frac{h\nu}{c}\right)^2 \left(\frac{1}{m_n+M_R} - \frac{m_n \cos^2\theta}{(m_n+M_R)^2}\right)} \right\}^2$$

where $h\nu$ = the primary gamma ray energy. For ^{24}Na this is 2.753 MeV.[10]

m_n = mass of neutron

M_R = mass of residual nuclide

E_s = the photodisintegration threshold energy, 2.226 MeV

c = speed of light, and

θ = angle between the incoming gamma ray and the emitted photoneutron.

For a Na-D source, E_n varies from 297 keV when $\theta = 0°$ to 232 keV when $\theta = 180°$.

This primary distribution is then further modified by the elastic and inelastic scattering of the neutrons in the source material and also as a result of Compton Scattering in the source of the 2.75 MeV gamma rays to energies above the photodisintegration threshold for deuterium. This results in neutrons of lower energy. The energy spectrum of the source is shown in Figure 4. This spectrum was calculated by adapting the Monte Carlo code developed by Veseley et al.[11] to the design of this particular source where the effect of the finite aluminum wall thickness has been taken into account.[12] The code calculates photon and neutron transport in the three regions of the source. 70% of the neutrons produced escape without any interaction in the source. The remaining 30% scatter either in the central core, the aluminum shell, or the deuterated polyethylene shells. The effect of the aluminum shell is to increase the Compton Scattering of the gamma rays, thus slightly degrading the neutron spectrum.

The code assumes a uniform photon distribution within the sodium core with an initial energy of 2.753 MeV. With each photon history, the photon is initially given a weighted value, ω, of 1. The probability of escape is calculated and ω is adjusted to account for this. The photon is thus forced to interact within one of the three regions; either by capture, Compton Scattering, or photodisintegration. The latter can only occur in the target shell.

When photodisintegration occurs in the target, a neutron history begins. It is assumed that photoneutrons are emitted isotropically in the laboratory system. The initial energy, position, and direction, of each neutron and the weight to attribute in the calculation to this neutron are calculated from the respective photon parameters. The neutron's path is followed throughout the source until is escapes the system or is captured. Upon escaping, its energy and angle of emission are recorded.

References

1. B. H. Patrick, M. G. Sowerby and M. G. Schomberg, J. Nucl. Energy, 24,(1970) 269.

2. C. D. Bowman, G. S. Sidhu, M. L. Stelts and J. C. Browne, Proceedings Third Conference on Neutron Cross Sections and Technology, Knoxville, CONF-710301, 2, (1971) 584.

3. J. L. Perkin, P. H. White, P. Fieldhouse, E. J. Axton, P. Cross and J. C. Robertson, J. Nucl. Energy, 19 (1965) 423.

4. D. M. Gilliam, Ph.D. Dissertation, Univ. of Michigan, (1973).

5. E. J. Axton, P. Cross and J. C. Robertson, J. Nucl. Energy, 17, (1963) 440.

6. M. C. Scott, Nuclear Instr. and Methods, 82, (1970) 237.

7. C. Eggler and D. J. Hughes, U.S.A.E.C., (1950) ANL 4476.

8. I.C.R.U. (1964) Report 10b, (NBS Handbook 85).

9. F. Lagoutine, Y. Le Gallic and J. LeGrand, (1960), Standardization of Radionuclides, p. 603, I.A.E.A. Vienna.

10. G. Murray, R. L. Graham and J. S. Geiger, Nucl. Phys., 63, (1965) 353.

11. F. Veseley, F. Bensch and H. Heztmanek, Nukleonik, 11, (1968) 300.

12. M. C. Davis, Master's Thesis, Univ. of Michigan, (1974).

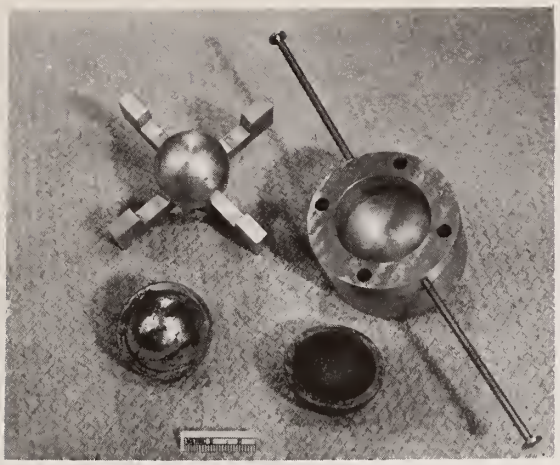

Figure 1. The NaF core, the deuterated polyethylene shells and the mold used in forming the shells.

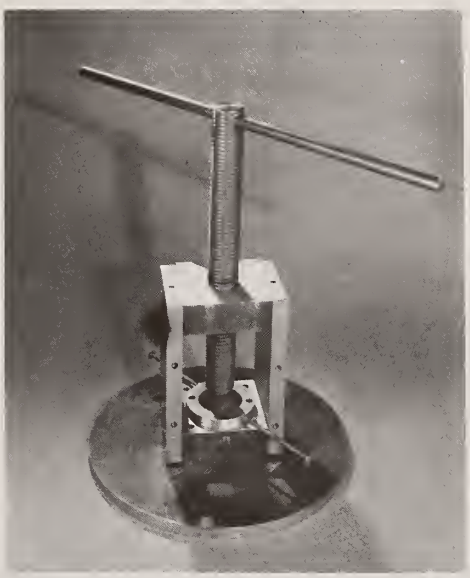

Figure 2. The press used to attach the deuterated polyethylene shells to the NaF core.

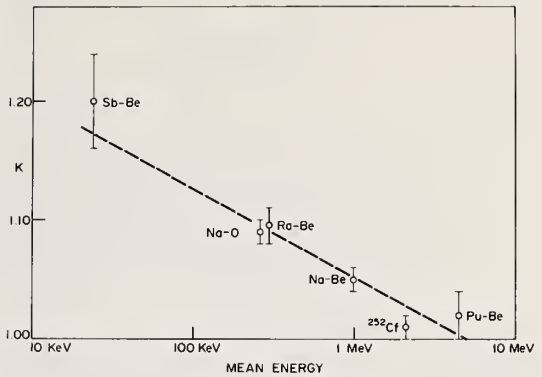

Figure 3. The correction term, K, for lack of nonuniform mixing versus the mean energy for several types of neutron source.

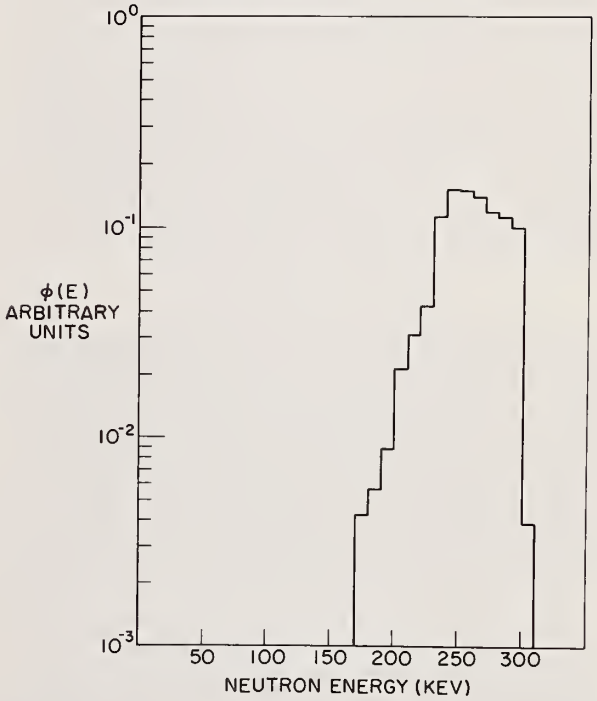

Figure 3 Calculated Neutron Energy Spectrum from ^{24}Na - Deuterated Polyethylene Source.

Figure 4. The calculated energy spectrum from the ^{24}Na deuterated polyethylene source.

A 25-KEV NEUTRON BEAM FACILITY AT NBS

E. D. McGarry
Harry Diamond Laboratories
Adelphi, Maryland 20783

I. G. Schroder
National Bureau of Standards
Washington, DC 20234

An iron-filtered, neutron-beam facility that provides a well collimated source of 25-keV neutrons has been developed at the National Bureau of Standards (NBS) Reactor. For selected physics experiments and monoenergetic calibration of neutron dosimeters, the beam flux may be tailored to provide $5 \times 10^5 n \cdot cm^{-2} \cdot s^{-1}$ with 99% 25-keV neutrons. For other experiments, such as calibration of fast-neutron spectrometers, fluxes of $10^6 n \cdot cm^{-2} \cdot s^{-1}$ may be obtained with as many as 13 identifiable peaks in the energy range 25 keV to 1.5 MeV. (Neutrons; Filtered Beams; Spectroscopy; Dosimetry)

Introduction

By placing thick filters in collimated beams of neutrons from nuclear reactors, it is possible to obtain transmitted neutrons whose energy spectra have well-defined peaks at energies corresponding to minima in the cross section of the filter. The production of such filtered beams was pioneered at the Materials Testing Reactor.[1] A similarly constructed 25-keV beam has been installed at the HIB beam port of the Brookhaven High Flux Beam Reactor.[2] Furthermore, filtered beams have been used as a new approach to enhance the capabilities of time-of-flight cross section measurements.[3] We wish to report improvements in filtered-beam methods that make the beams more monoenergetic and substantially reduce gamma background levels. Both of these objectives are accomplished by using a resonance scattering material in a region of high fast flux and positioning the collimator, which views the scatterer, so that it is not aimed at the reactor fuel. This paper describes such a facility to provide 25-keV neutrons at the NBS reactor.

The Physical Facility

The 25-keV neutron facility is shown in Fig. 1. It has been installed in a vertical, 6.4-cm-diameter thimble of the NBS reactor. It consists of four principal parts: (1) a collimating system, (2) an iron filter, (3) a secondary filter of aluminum, and (4) a titanium neutron scatterer. The facility is a sealed tubular configuration, 5.4-m long, filled with 1 atm of helium to minimize air scattering. The bottom section of the assembly is a 3.4-m-long by 4.5-cm-diameter aluminum tube that positions a titanium neutron-scattering disc in the immediate vicinity of the reactor fuel.

There are two collimator sections in the assembly. The lower collimator is composed of a carbon-steel pipe (1-cm inside diameter by 1.2-m long) in a lead sleeve which serves as shielding around the beam. The upper collimator is a titanium tube (1-cm diameter by 1-m long) also through a lead sleeve. Between the collimators is the principal neutron filter - 30 cm of ARMCO electromagnet iron. This iron is 99.9% pure natural iron (^{56}Fe-91.7%; ^{54}Fe-5.8%; ^{57}Fe-2.2%; ^{58}Fe-0.4%). The principal contaminents that contribute to the cross section at 25 keV are manganese and copper.

The Iron Filter

The neutron beam is due to a dominant minimum in the cross section of iron at 24.5±0.3 keV. This minimum, 0.430±0.005 b,[4] is caused by destructive interference between the potential and resonance scattering cross sections at the low energy side of the 27.9-keV resonance [5] in ^{56}Fe.

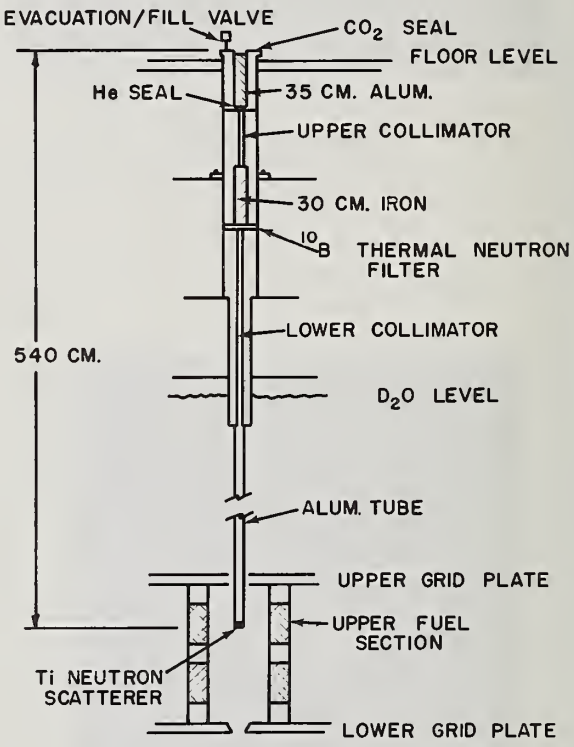

Fig. 1. The 25-keV neutron facility.

The Titanium Scatterer

The cross section of elemental titanium exhibits a large broad scattering peak[5] in the energy range from 10 to 30 keV. Although the maximum scattering takes place at 17.5 keV, because of the resonance in ^{48}Ti (naturally 74% abundant), the magnitude of the cross section at 25 keV is still 40 b (only down by 50% from the maximum). Therefore, the titanium scatters 25-keV neutrons into the iron filter. The use of a resonance scatterer between the fuel elements, as opposed to aiming the collimating system directly at the fuel, eliminates substantial quantities of core neutrons and core gammas.

Neutron Spectra

Measurements: The energy spectra were measured with a hydrogen-gas proton-recoil spectrometer. [6] The hydrogen, at 5 atm, is contained in a 2.5 cm-

diameter stainless-steel tube. The effective length of the electric field is 5 cm. When the 1-cm diameter 25-keV beam is directed into the side (at the center) of the hydrogen-filled tube, very few protons interact with the distorted electric field near the ends of the tube. Furthermore, the combination of 5-atm pressure and the 2.5-cm diameter is sufficient to give accurate flux measurements over the energy range of interest (10 to 400 keV). This is because the mean range of 25-keV protons in 5 atm of hydrogen (at 15° C) is only 0.025 cm. It is true that distortions, because of truncation of recoil protons with the walls, become significant as the range approaches the radius of the tube. This occurs at approximately 800 keV. Below 400 keV, however, greater than 85% of the pulses will correspond to the energies of protons that are completely stopped in the gas.

Reactor Neutrons Filtered Through Iron: The 30 cm of iron transmits 40% of the 24.5-keV neutrons with a full-width-at-half maximum of approximately 10%. The resulting neutron spectrum is shown in Fig. 2. The 25-keV neutron peak is separated from the next higher energy group, at 82 keV, by more than 50 keV. The principal contributions, from other less pronounced minima in the iron cross section between 50 keV and 1 MeV, are at 82, 137 and 270 keV.

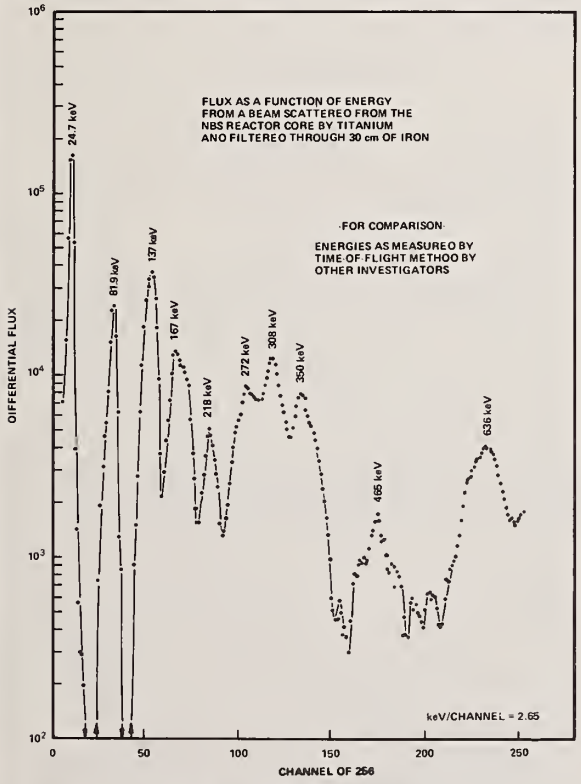

Fig. 2. Energy spectrum observed with only 30 cm of iron in the beam.

Because of extremely low gamma background, the spectra can be obtained without the use of gamma-discrimination techniques.[6] For example, Fig. 3 shows the raw proton-recoil pulse-height distribution from which the spectrum of Fig. 2 was obtained. The quality of the data is, to a large extent, attributable to the excellent low-noise properties of the charge-sensitive preamplifier.[7] The resolution of

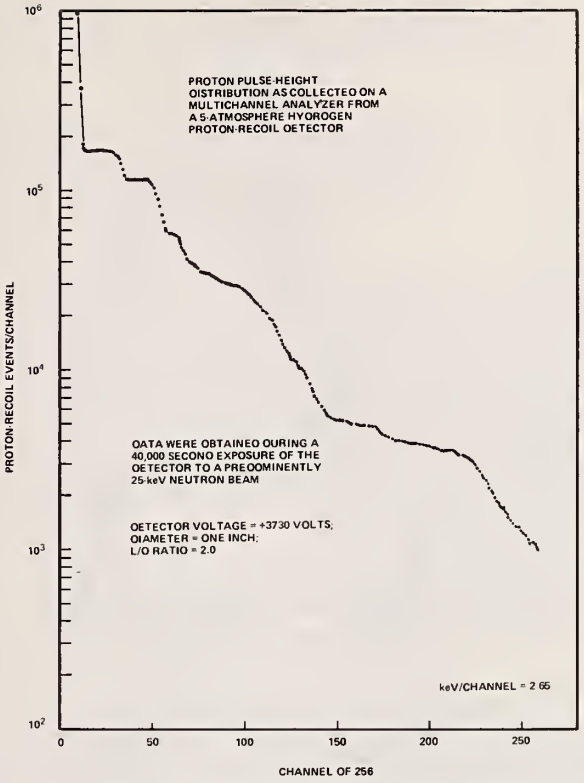

Fig. 3. Raw experimental data from the hydrogen-gas proton-recoil spectrometer. The spectrum in Fig. 2. was derived from these data.

the system at 25 keV is 9%. For the thermally-induced 615-keV reaction ^{14}N (n,p)$^{14}C12$, the resolution of the pulse-height peak is 5.5%. About 5% nitrogen was added to the hydrogen for energy calibration purposes.

A Monoenergetic 25-keV Beam: Because the titanium scatterer is not in the best geometry with the D_2O coolant immediately below it, we feel that more neutrons, with energies greater than 25 keV, are scattered into the collimator than would be if the titanium were surrounded by air or helium. A new design is being investigated with a titanium scatterer in the through tube of the NBS reactor where there is no D_2O environment.

With the present design, secondary filters of aluminum and sulfur were investigated to purify the neutron spectrum shown in Fig. 2. Although sulfur tends to suppress unwanted peaks in the iron spectrum, sulfur is more opaque to 25-keV neutrons than aluminum. Aluminum removes a greater percentage of higher energy neutrons than either sulfur or additional iron; therefore, 35 cm of aluminum is quite an acceptable filter. Fig. 4 shows a spectrum filtered through 30 cm of iron and 35 cm of aluminum.

Analyses of the areas under the peaks (shown in Fig. 4) reveals that 99% of the neutrons are in the 25-keV peak and the remaining 1% in the 137-and 270-keV peaks.

Gamma Radiation: For a neutron intensity of $5 \times 10^5 n \cdot cm^{-2} \cdot s^{-1}$ in the 1-cm-diameter beam, the gamma-ray background is less than two $mR \cdot hr^{-1}$. Our estimate of the gamma content is based upon measurements with

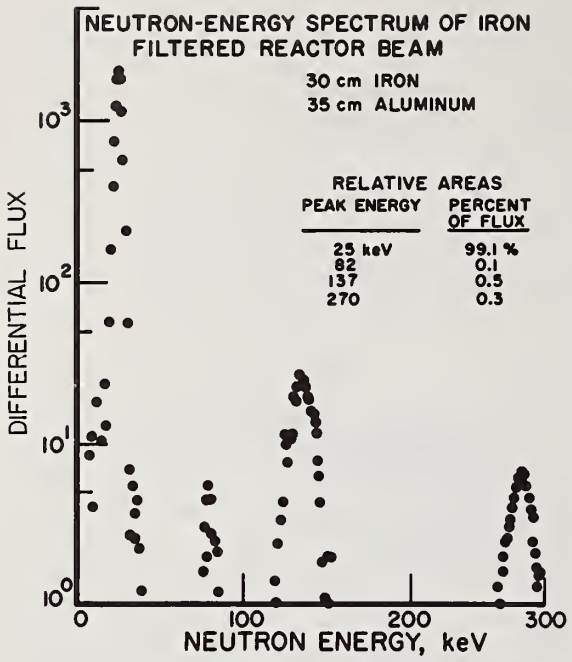

Fig. 4. Energy spectrum of the highly monoenergetic 25-keV beam facility.

a variety of health physics gamma-survey instruments held adjacent to and directly in the beam. The estimate does not include a correction for the fast-neutron response of the instruments.

Applications

Personnel Dosimetry: With the growing need of nuclear reactors as energy sources, there is a renewed interest in studies of routine and emergency radiation monitoring of personnel. With its high percentage of 25-keV neutrons and its low gamma background, this beam is well suited as a standard, monoenergetic-neutron field for the development and calibration of health-physics-type neutron dosimeters.

Furthermore, by placing external gamma-radioactive sources of varying intensity in the near vicinity of a dosimeter in the beam, it is possible to accurately determine the gamma sensitivity of the neutron dosimeters.

In a converse manner, the 25-keV beam can be used in conjunction with thermal neutrons, the existing 2-keV neutron facility (also reported on in this session) and a 144-keV neutron facility (under development) to study neutron sensitivity of gamma-radiation survey equipment.

Cross Section: Because the 25-keV flux peak is well isolated from other peaks, high peak-to-background ratios can easily be obtained for capture cross section measurements. Block, et al, [4] conclude that cross sections of materials can be measured at 25-keV, with a 10% energy spread, to accuracy of 4%.

Spectrometer Calibration: Fluxes of $10^6 n \cdot cm^{-2} \cdot s^{-1}$ are obtainable by shortening the aluminum filter. This provides a beam whose spectrum has many identifiable peaks in the energy range 25 keV to 1.5 MeV. Such a spectrum is useful for the intercalibration of fast-neutron spectrometers.[8]

Shielding: The application of the 25-keV neutron beam to shielding experiments is suggested by the fact that gamma spectra resulting from fast-neutron capture and fast fission are different from those produced with thermal neutrons. Consequently, the 25-keV beam (as well as the 2-and 144-keV beams) can be utilized to produce gamma fields for closely controlled studies of shielding for fast reactors.

Conclusions

An iron-filtered neutron-beam facility has been developed for the NBS Reactor. This facility provides a well collimated source of 99% 25-keV neutrons with a flux of $5 \times 10^5 n \cdot cm^{-2} \cdot s^{-1}$ and a gamma background of less than 2 $mR \cdot hr^{-1}$. The beam is obtained by preferentially scattering 25-keV neutrons from a titanium element placed tangential to the reactor fuel, by using iron filtering, and by optimizing a secondary aluminum filter to provide the desired purity.

The high purity 25-keV beam has direct application to measurements of cross sections, to capture gamma-ray studies, to development and monoenergetic calibration of neutron dosimeters to be used as personnel monitors, and to studies of neutron-detector response at 25-keV with a wide range of gamma-to-neutron ratios.

Acknowledgements

We wish to thank T. P. Wright and C. R. Heimbach for programming and data-processing assistance. A special thanks is due Robert A. Dallatore for his invaluable assistance in the fabrication and mechanical assembly of the filtered beam.

References

1. O. D. Simpson, J. R. Smith and J. W. Rogers, Proc. Symp. Neutron Standards and Flux Normalization; CONF-701002, U.S. Atomic Energy Commission, 362 (1971).

2. O. A. Wasson, K. Rimawi and R. E. Chrien, 2nd International Symp. on Neutron Capture Gamma Ray Spectroscopy, Petten, The Netherlands, (1974).

3. J. A. Harvey, National Topic Meeting on New Developments in Reactor Physics and Shielding, Kiamesha Lake, New York; CONF-720901, 2, 1075, USAEC (1972).

4. R. C. Block et al, Trans. Am. Nucl. Soc. 15, 531 (1972).

5. M. D. Goldberg, S. F. Mughabghab, B. A. Magurno and V. M. May; BNL-325, 2nd Ed. Suppl. 2, Vol IIA, Physics-TID-4500 (Feb 1966).

6. E. F. Bennett, Nucl. Sci. Eng. 27, 16 (1967).

7. V. Radeka, International Symp. on Nuclear Electronics, Varsailles, France (1968).

8. J. E. Powell and J. W. Rogers, Nucl. Instr. and Meth., 87, 1, 29 (1970).

NEW EXPERIMENTAL TECHNIQUES AND RESULTS IN NEUTRON SPECTROSCOPY

Charles D. Bowman
National Bureau of Standards
Washington, D. C. 20234

During the past several years there has been very little funding available for construction of new facilities for neutron measurements. The most important changes in the field have come through the development of new experimental techniques at existing facilities. These techniques and resulting measurements in the area of programmatic neutron data and neutron physics research will be discussed.

(Neutron cross sections; new results; new techniques; review)

Introduction

I will begin by briefly outlining the material which I hope to cover. First, I will give a perspective covering the period of the four conferences in this series. The proceedings of these conferences provide a resource which I have used to attempt to define some trends which might be of interest to you. I should provide a good base for the main subject of my talk which will be to review the new experimental techniques of the past four years and to present some results of those techniques. Of course, there is a great deal of measurement activity of high quality and great productivity using techniques which existed previously and I will not cover those topics as they will be adequately covered by other invited speakers and in contributed papers. In the area of the physics of fission, much progress has been made but I will only touch briefly on this since fission is the subject of invited papers at this conference by Drs. M. S. Moore and A. Michaudon.

Trends

Let me begin the first section of my talk by describing some trends growing out of the historical perspective of this series of four conferences which began in 1966. I have attempted to answer several questions on the assumption that the contributed papers to this series of four meetings represent a useful index of the emphasis of these conferences and perhaps of the actual activity in our field both in the U. S. and internationally.

Figure 1 addresses the measurements versus data evaluation. These efforts towards data improvements shown here surprised me. I had expected a strong trend of more evaluation efforts, whereas the results indicate a significant trend toward less activity in that area as opposed to measurements. Certainly the evaluation and compilation activities now have a greater impact on data improvement than they have had in the past. Perhaps there have been unconscious influences which have moved these conferences more towards the measurements and away from the evaluation community.

Figure 2 showing trends in neutron sources usage also surprised me a bit. White sources include any accelerator used as a white source with the exception of electrostatic accelerators. Under monoenergetic sources I classified all charged particle accelerators used this way. Reactor based measurements include any chopper work still underway and all integral measurements, filtered beam work, etc. Isotopic measurements here is shorthand for radioactive sources including, californium, Sb-Be, etc. I had expected that the monoenergetic sources would have decreased in use over the period of this survey and, in fact, that apparently happened during the late sixties. However, we see a rather clear resurgence of activity in that area to a point where it now appears just about equal to that carried out with white sources. During the period of this survey, as you know, a number of reactor facilities have been closed or staff reduced and yet there appears to be a steady trend upward in the use of this type of facility for measurements. The isotopic sources, which perhaps many of us felt to be archaic, have showed a surprising capability to produce interesting and useful results. A result again which surprises me is that these four types of facilities over a period of nearly ten years have all maintained nearly the same relative role in satisfying nuclear data needs.

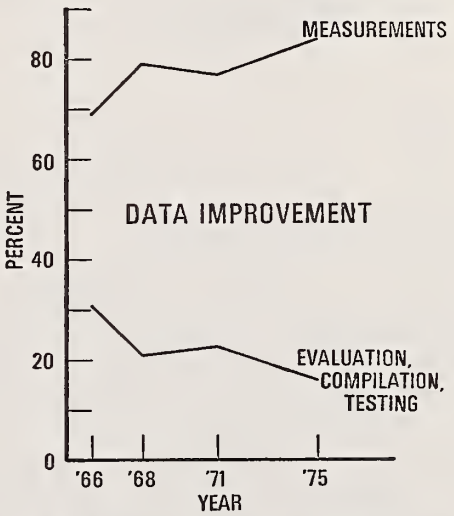

Figure 1. A comparison of activity in this series of conferences in the areas of measurements and evaluations. The comparison index is the fraction of contributed papers at this series of meetings devoted to these two areas of activity.

As a staff member of the Bureau of Standards, Fig. 3 on trends in standards is of particular interest to me. The period has seen rather strong fluctuations in interest and activity as is indicated by the slide, but if there is a trend it appears to be slightly upward with integral measurements and differential measurements being maintained at roughly the same level in relation to each other. I was surprised that, at present, standards measurements appear to represent almost 20% of all measurements presently underway in this field.

Figure 4 shows a comparison of target character--that is actinide targets as opposed to nonactinides. One can state from this slide that there appears to be no significant trend in this area--60% of the activity being devoted to actinide and about 40% over the long term being devoted to non-actinide targets. Likewise, in the area of basic versus applied research, there appears to be little trend and so no slide is included.

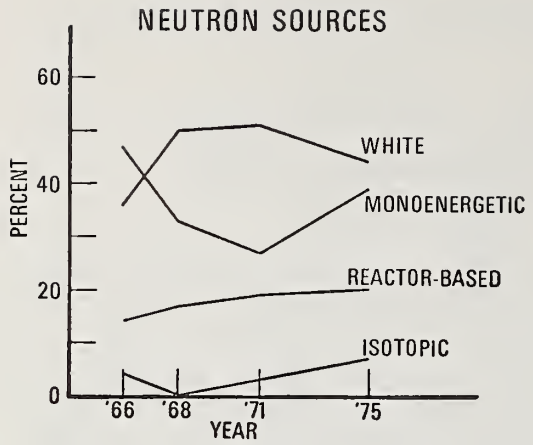

Figure 2. Trends in neutron source usage.

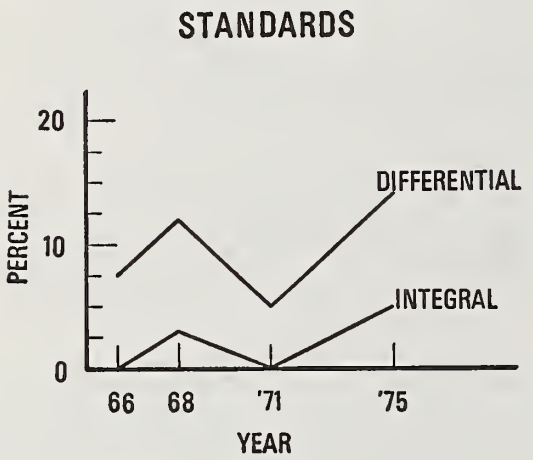

Figure 3. Trends in differential and integral neutron standards activity.

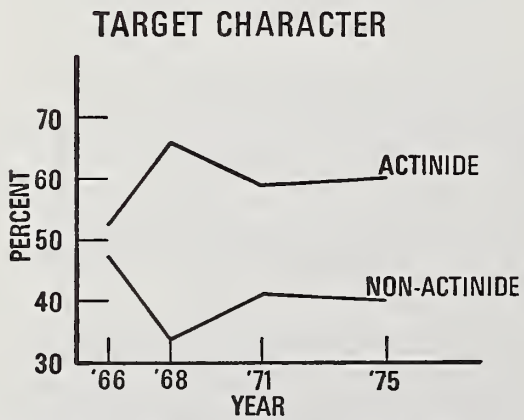

Figure 4. A comparison of target type under study in the area of neutron nuclear data measurements.

Over the years about 20% of the activities reported at these conferences were basic research as opposed to 80% applied.

New Techniques and Results

Let me move on now to look at some highlights of techniques development and results from these new techniques. As I mentioned earlier and as is of course clear to the audience, there is no way that I can cover the whole field of interesting measurements which has taken place during the past four years. I will only emphasize those which have required, in my view, significant new developments and some results which have arisen from such capabilities. I would like to begin this portion of my talk by devoting attention first to new developments relating to applications. As you all know, the linac has long been touted as a valuable tool for eV and keV neutron physics work. During recent years, particularly at the last conference and at the standards symposium[1] at Argonne, many of us associated with pulsed white sources have claimed useful capabilities in the MeV region as well. Some with monoenergetic neutron sources have asked "If this capability is really significant, why aren't there any results from reaction studies such as fission." I think finally that some good MeV work is starting to come from electron linacs in particular and I would like to give some examples of that now. Drs. Sidhu and Czirr of Lawrence Livermore Laboratory are reporting at this conference[2] on a measurement of the ^{235}U fission cross section in the 0.8 to 20 MeV range. Figure 5 shows their results in the 3 MeV to 20 MeV range compared with other measurements. A more complete exposition of their results is given in Fig. 5 of their contribution to this conference. The Livermore group claims a shape uncertainty of 2% or less across the region from 1 to 15 MeV. Their measurement was not an absolute measurement and is normalized in the lower MeV range. I think it is clear from the point density and statistics that significant measurements across the MeV range with high accuracy can be achieved with the white source technique.

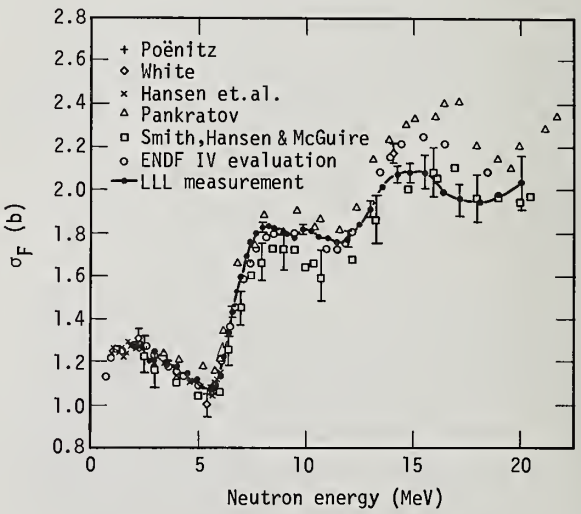

Figure 5. The fission cross section of ^{235}U as measured by the LLL group in the 3 to 20 MeV range and compared with some previously existing results.

Let me now show you a few details of the flux monitoring system which is the key to the successful measurement in this energy range. Figure 6 shows the geometry for flux measurement. The arrangement is situated 67 meters from the neutron source. A shadow bar creates an annular neutron beam which strikes the hydrogenous radiator. Protons are ejected from this thin foil and strike a solid-state detector located on the beam axis but shielded from the direct neutron beam by the shadow bar. The principal statistical uncertainty in the experiment is in getting adequate statistics in the flux monitor. Figure 7 shows the pulse height spectrum for 15 MeV neutrons from this system. Only a small background correction appears necessary even at this high energy. Figure 8 shows the similar spectrum at 3.1 MeV. It is important to remark at this point that both pulse height and time-of-flight information were stored for every event and sorted on line into a million word storage facility. These facilities now exist at a number of white source linacs, having been pioneered at ORELA.[3] In terms of facilities they represent a vitally important advance in the capability to perform high quality measurements at facilities where neutron time-of-flight is always a parameter.

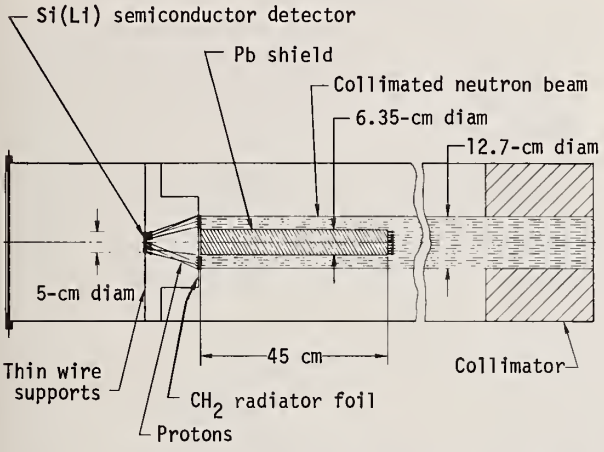

Figure 6. The geometry for flux measurements for the LLL MeV fission measurements on ^{235}U. An annular beam strikes a thin ring-shaped hydrogenous foil which ejects protons into a solid state detector located on the beam axis.

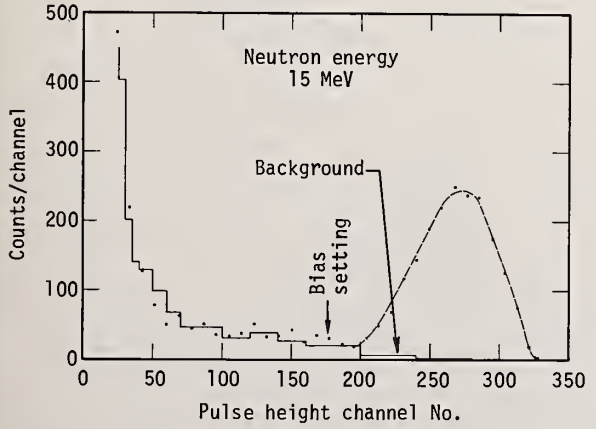

Figure 7. Pulse height spectrum for 15 MeV neutrons with the apparatus of Fig. 6.

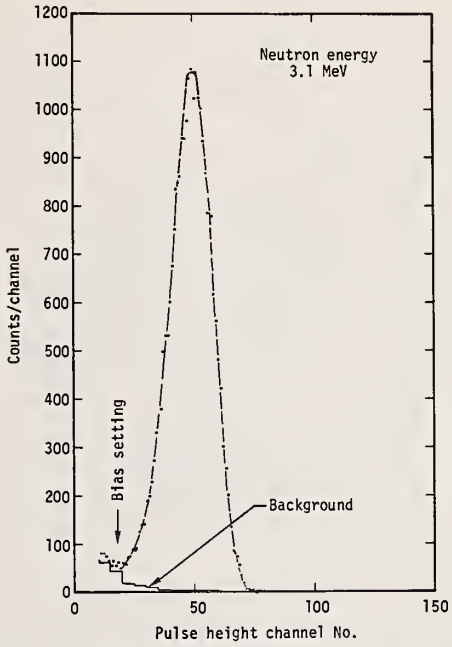

Figure 8. Pulse height spectrum for 3.1 MeV neutrons with the apparatus of Fig. 6.

This experiment is part of an integrated program at Livermore to measure in the 1 keV to 20 MeV range the fission cross section and $\bar{\nu}$ for all of the important fissile targets. The intent is to establish ^{235}U to high absolute accuracy and measure the ratio of the fission cross section of all other materials to that for ^{235}U. These ratio measurements are well underway and are reported in detail in a paper presented at this meeting[4] by Behrens, Carlson, and Bower of the Livermore laboratory. Statistical accuracy usually less than 1% is obtained over the energy range from a few kilovolts to 30 MeV for several isotopes.

Some of you might be wanting to ask, "But what about putting these measurements on an absolute scale?" Of course with the linac this can be done by extending the measurements down into the thermal region and normalizing the cross section measurements there. Up to this point this has not been done with high accuracy because an interesting alternative exists with regard to normalization through radioactive source measurements. Figure 9 shows apparatus for a measurement carried out at the University of Michigan by Gilliam and Knoll and reported at this meeting. A ^{24}Na source is placed inside the beryllium ball shown here. The neutron source strengths from this combination was calibrated in a manganese bath. Fission events were recorded by identical detector systems shown in both sides of the source. The fissile deposit, shown as the foil closest to the source, emitted fission fragments which were then collimated by a ring before they struck a track counter mounted in the outer-most ring in the figure. The irradiation was carried out in a helium atmosphere. An essential feature to obtain a high quality measurement in this experiment is the pair of detectors. This pairing arrangment eliminates the need for accurate source-to-fission foil measurements, since the important measurement in the geometry

of this experiment is the separation between the two fission foils.

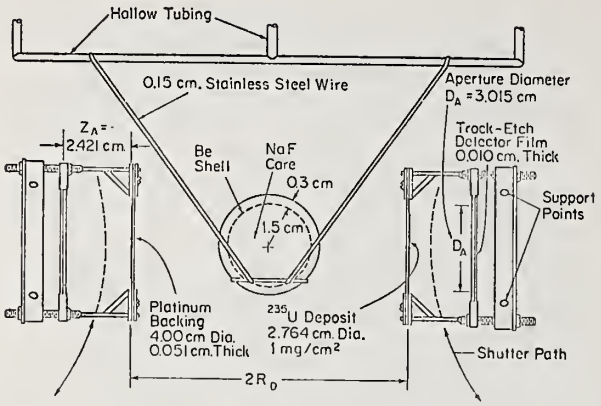

Figure 9. Apparatus for a measurement of fission cross sections at the University of Michigan using a monoenergetic ^{24}Na-Be neutron source. A fission foil and track detector system is located on opposite sides of the neutron source.

At the NBS we are currently measuring the ^{235}U cross section to high accuracy in the MeV range in the experiment similar to that at Livermore and we feel that we will be able to put high reliance on a measurement of this type to normalize the relative fission cross section as well as on measurements of the ^{235}U fission cross section in a californium neutron spectrum which is reported by Heaton et al.[6] of NBS in this meeting. An accuracy exceeding ± 2% is claimed for these techniques using radioactive sources. I view both techniques as valuable complements to the white source method.

Let me move on now to discuss some new techniques in inelastic neutron scattering. I'm sure that everyone at the conference is aware of the high quality of inelastic neutron scattering which has been carried out in recent years at a number of laboratories possessing monoenergetic neutron facilities in the neutron energy range below 8 MeV. These measurements are perhaps best exemplified by the high productivity and quality of measurements produced at ANL in A. Smith's laboratory. However, the regions between 8 and 14 MeV, which is becoming much more important with the increasing attention being given the controlled fusion programs, cannot be attacked with the same confidence using these techniques.

Dr. G. L. Morgan, working at ORELA, has adapted an old idea to the linac experimental conditions to produce a significant new capability[7] for inelastic scattering measurements in the energy region above 8 MeV and also below. The geometry is shown in Fig. 10. At the end of a 47 meter flight path, a shadow bar is positioned in the beam and a neutron scintillator is placed on the beam axis behind the shadow bar. A ring geometry for the scattered sample is used and neutrons from the beam are scattered into the detector. For each event both the time of flight and the pulse height are recorded and sorted into a million work array on line with the type of computer facility I mentioned earlier. By time-of-flight the incoming neutron energy is measured to high accuracy and by unfolding the pulse height spectrum in the scintillator the energy of the scattered neutron is determined.

Figure 11 shows the scattering from carbon, the highest energy peak being the elastic scattering peak and the lower energy peak being that from the 4.4 MeV level. The power of the technique is well demonstrated by Fig. 12 which shows the energy distribution of inelastically scattered neutrons from iron as a function of incident neutron energy which in this case varies from 6 MeV to 20 MeV.

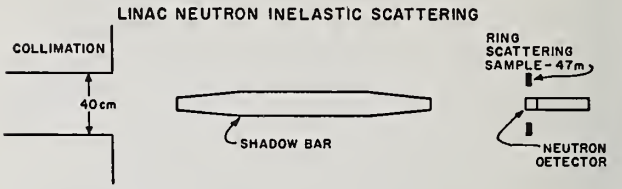

Figure 10. ORELA arrangement for neutron inelastic scattering measurements. The "ring" geometry is adapted to the linac. The angle is changed by moving the detector.

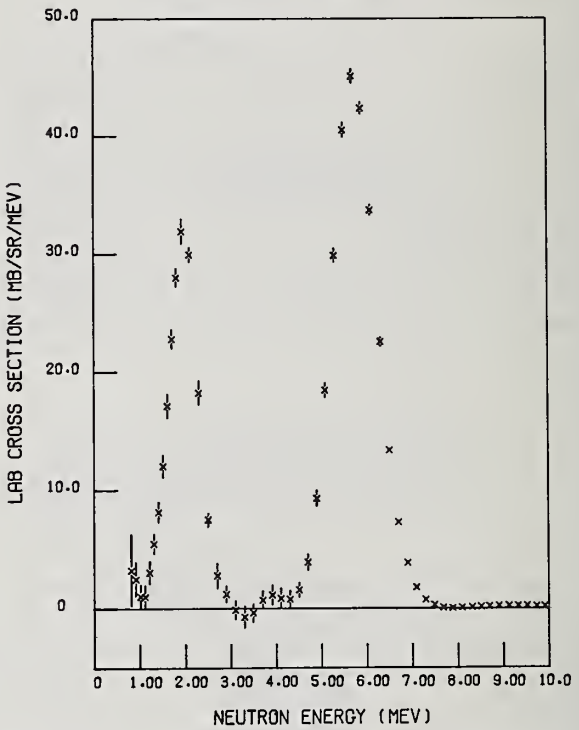

Figure 11. The scattering from ^{12}C obtained with the apparatus of Fig. 10 by unfolding the pulse height response from the measured spectra.

Let me move on to discuss another adaptation of an old technique to the linac experimental situation for a significant new advance in capabilities for gamma ray production measurements. Measurements of gamma ray production both at linacs and at electrostatic accelerators during the past several years have been carried out using Ge-Li detectors with the accompanying very high resolution in the lines but some uncertainties in the response. For shielding purposes, which represent the need for most of this data, the high resolution was not nearly so important as high absolute

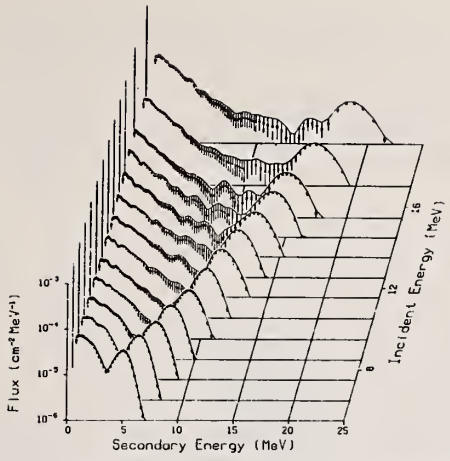

Figure 12. The inelastic scattering from iron measured using the apparatus of Fig. 10.

accuracy in the shape of the gamma ray spectrum. Figure 13 shows the adaptation of a 12.5 x 12.5 cm NaI crystal in heavily shielded geometry for gamma ray production measurements[8] at ORELA and at the same flight path. The NaI crystal, in addition to being heavily shielded by lead as is usually the case, is also shielded by lithium hydride and by lithiated paraffin. The response function of such a crystal is well known and again the time-of-flight and pulse height of each recorded event are stored and sorted on line and the results unfolded according to the response

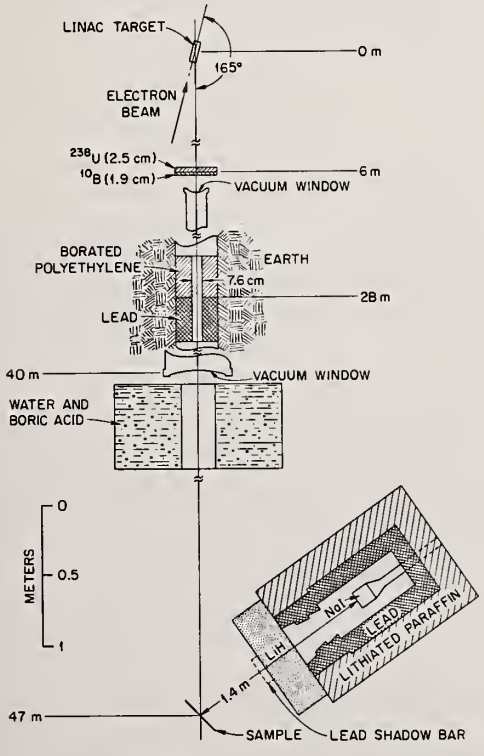

Figure 13. ORELA Facility for gamma ray production measurements using neutron time of flight and a NaI detector.

function. The results of measurements on silver at an angle of 125° in the incident neutron energy range from 1 to 18 MeV are shown in Fig. 14 which indicates the quality of the data and the capabilities of the technique.

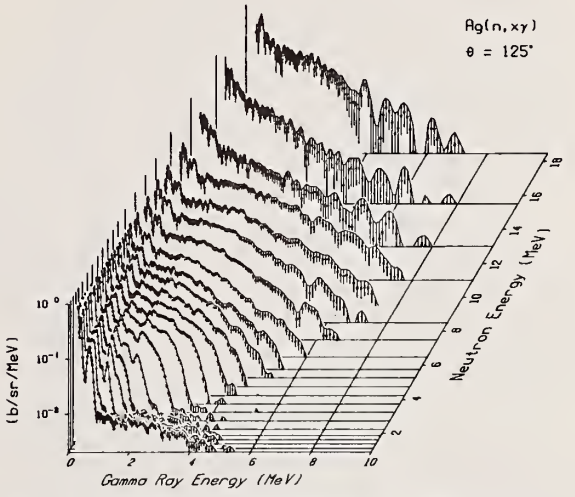

Figure 14. The results of gamma ray production measurements on Ag using the apparatus of Fig. 13.

The reactor filtered beams, which were first introduced by the MTR Laboratory[9] several years ago, are beginning to have a significant impact on basic and applied nuclear science activities. Such filtered beams now exist at several laboratories around the world, the repertoire generally limited to a 2-keV beam produced by a scandium window, a 24-keV beam produced by an iron window, and a 140-keV beam produced by a silicon window. The complete set of these facilities is installed at the NBS Reactor in geometries[10] which significantly improve the experimental conditions over that in the original MTR arrangement. The 2 keV scandium beam originally established at the MTR in Idaho, while being fairly intense, suffered from a 50% contamination of higher energy neutrons and also a large contamination of gamma rays. Such a beam was useless for the NBS neutron dosimetry program. Dr. Schroder of NBS rearranged these facilities at the NBS Reactor as shown in Fig. 15 with a resulting great improvement in both neutron and γ-ray background. He noted that manganese has a scattering peak right at the location of the minimum in the scandium cross section and took advantage of the through-hole geometry existing for two beam tubes at NBS and installed the manganese scatterer next to the reactor core such that the scattering of 2 keV neutrons was strongly enhanced over any other and

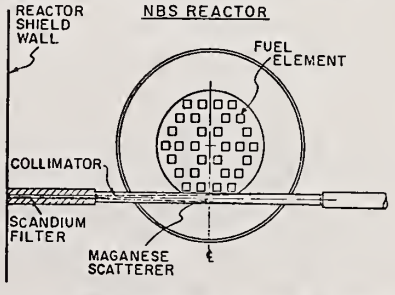

Figure 15. The NBS scandium-filtered beam installation for 2 keV neutrons.

these neutrons were then filtered by the scandium filter to yield a beam of intensity comparable to that at the MTR but with a neutron background reduced by a factor of 25 so that the number of higher energy neutrons is less than 3%. In addition, by avoiding having to look directly at the core, the gamma ray intensity in the beam is greatly reduced such that within the beam the gamma ray intensity is only a factor of 2 higher than the reactor experimental area room background. Improvements also were achieved in the case of the 24 keV beam using a titanium scatterer to selectively scatter 24 keV neutrons into the iron window, again using the through tube geometry. The silicon beam will be installed in the through-tube geometry also within the next week or two.

I am sure that Dr. Chrien will mention some of the important advantages of the use of these monoenergetic beams in neutron capture gamma ray spectroscopy in his talk on that subject later in the meeting. Thus far at NBS, these beams have been used to examine the angular distribution in the $^{6}Li(n,\alpha)$ reaction. Dr. Schroder et al. have measured[11] a surprising anisotropy in this cross section even at the low energy of 25 keV.

Let me move on now to discuss a new development in techniques for $\bar{\nu}$ measurements. Measurements of $\bar{\nu}$ have been of interest for three reasons during the last several years: (1) for greater accuracy in the MeV region; (2) for confirmation of the apparent rapid fluctuation of $\bar{\nu}$ around one MeV observed at Bruyeres le Chatel,[12] and (3) for possible fluctuations in $\bar{\nu}$ at low energy associated with resonant spin or other resonance properties. Until recently, a large liquid scintillator tank was used in nearly every experiment for detection of neutrons. Measurement with a different type of detector would represent a signficant advance since $\bar{\nu}$ plays as important a role in reactor neutron economy as cross sections. Weston and Todd[13] reported at the last meeting in this series their measurements on ^{239}Pu using proton recoil in plastic scintillators. The results obtained to high statistical accuracy indicated a significant change in $\bar{\nu}$ from resonance to resonance. However, an essential feature of a detector for $\bar{\nu}$ measurements is a flat response over the fission spectrum. Since the proton-recoil detector has a cutoff almost at the middle of the fission spectrum, it is not clear that the apparent fluctuation is not due to a change in the spectrum of the neutrons rather than a change in $\bar{\nu}$.

A system has been established by Howe et al.[14] at Livermore using proton recoil in liquid scintillators. The facility is shown in Fig. 16. At the end of a 14 meter flight path is located an assembly consisting of a spherical shell of ^{235}U surrounded by a shell of ^{6}Li and then by a shell of lead two inches thick. The total diameter of the system is twelve inches. The amount of ^{235}U in the central shell is 35 kilograms. The system has a k = .75 and it works in the following way. Neutrons from the Livermore linac strike the parallel-plate fission chamber located inside the shell at its center and fission neutrons are released. Essentially, all these neutrons then interact in the thick ^{235}U shell. Since uranium has a cross section across the fission neutron spectrum, which is fairly constant, and since the shell is thick, the probability for a neutron interacting in the shell is nearly constant with energy. Unless there are very large changes in the neutron spectrum one can therefore expect that the neutron interaction is independent of the neutron energy. As I mentioned earlier, the system has a criticality of .75 such that many more neutrons are made than are released from the fission, but the number made is proportional to the number which are released in the fission if one averages over a large number of fission events. Neutrons are detected with low efficiency in the liquid scintillators. Since the neutrons detected are not the original neutrons emitted in the fission event, the effective bias of .5 MeV introduces no sensitivity to spectrum changes. The system is, therefore, useful for measuring $\bar{\nu}$ since the number of neutrons detected per fission event in the fission chamber can be measured.

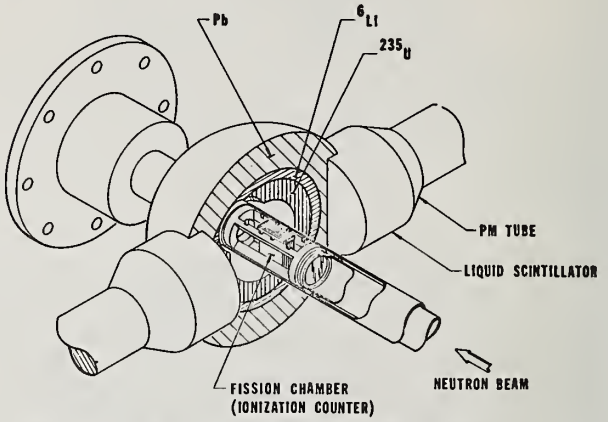

Figure 16. The LLL facility for $\bar{\nu}$ measurements in the .01 eV to 20 MeV range.

A major advantage of this system for linac use is the fact that the neutron detection takes place rapidly as opposed to the large tank so that time resolution is unimportant and also since the scintillators are shielded by thick uranium and lead shells, there is essentially no gamma-flash problem. Measurements with this system therefore should be possible from thermal neutron energies up to 20 MeV.

The results of a measurement on ^{235}U are shown in Fig. 17, where relative $\bar{\nu}$ is shown. The results were averaged over neutron energy in such a way as to achieve a constant ± .3% error in $\bar{\nu}$. This of course, means averaging over a number of resonances.

The point clearly indicated by this slide is that there are significant variations of $\bar{\nu}$ as a function of energy which appear to be related to groups of resonances rather than with individual resonances themselves. The source of the fluctuations is unknown, but the magnitude of this fluctuation in $\bar{\nu}$ for ^{235}U is ± .5%.

Recently, new measurements have been successfully carried out which extended from 100 eV all the way to 20 MeV. Unfortunately, these were finished too late to be reported in detail at this meeting but the experimenters are now confident of measurements from thermal to 20 MeV. The accuracy typically with 100 mg of sample will be ± 1% for a 10% energy bins and for two-weeks of running time on the Livermore linac.

Before I leave the subject of $\bar{\nu}$, I would like to mention the very interesting results of Shackelton, Trochon, Frehaut, and Lebars[15] working at Bruyeres le Chatel and Saclay who have demonstrated an anticorrelation between the number of neutrons emitted in fission and the average gamma ray energy. They find this anticorrelation most notable on resonances with narrow fission widths. They explain the effect by way of the n, γf reaction, arguing that when the fission widths become comparable in size to the gamma ray width, that the n, γf process can compete successfully

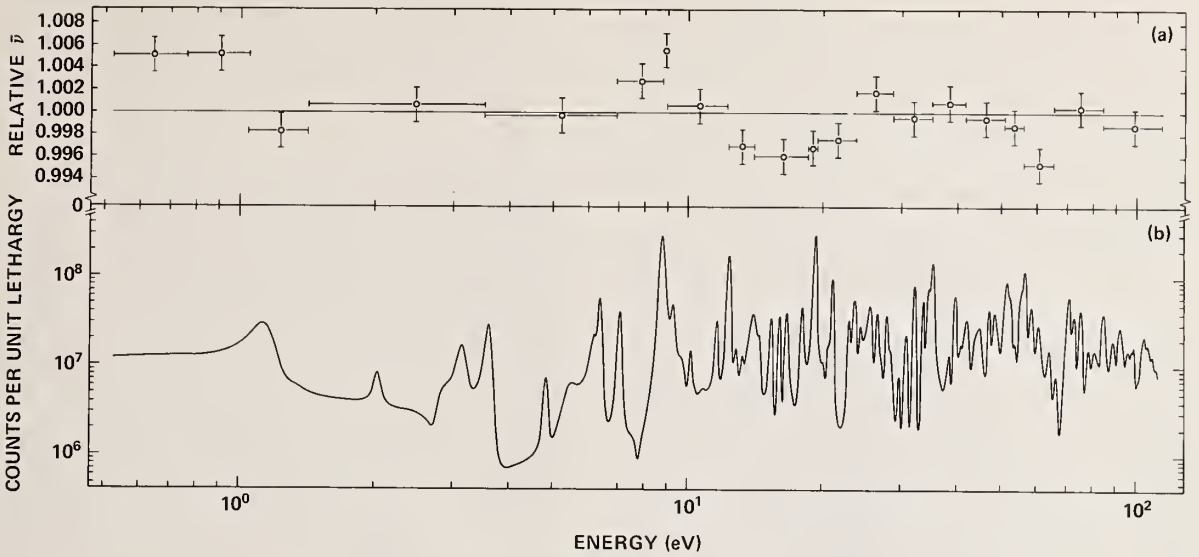

Figure 17. Low energy results of $\bar{\nu}$ measurements on ^{235}U averaged in energy to achieve constant statistical accuracy.

with the ordinary fission process. Since in the n, γf process less energy is available for fission, fewer neutrons on the average should be emitted while of course more gamma ray energy should be detected--in accordance with their experiment. This explanation clearly depends on the magnitude of the fission width rather than the spin of the resonance since one can encounter small fission widths for either spin regardless of the degree of barrier penetrability owing to the Porter-Thomas fluctuations in the individual fission widths. Thus the value of $\bar{\nu}$ for a resonance cannot be used in general to determine resonance spin.

Basic Measurements

These discussions of the source of fluctuations in $\bar{\nu}$ illustrate an interesting overlap between applied and basic measurements and provides a nice bridge for turning the discussion now to new techniques having their greatest impact in the area of basic science. I would like to begin by discussing the collaboration between Los Alamos Scientific Laboratory and Oak Ridge National Laboratory on an experiment involving polarized beams and targets.[16] Neutrons from the Oak Ridge Accelerator pass through a cryostat which polarizes a hydrogen-containing target. Since the triplet and singlet cross sections are greatly different and the target is thick, only the neutrons of one polarization are transmitted through the target. These neutrons then travel through a second cryostat where a target is polarized. In the case of a fission sample, fission is detected by twelve liquid scintillators which are five inches in diameter and which are placed in close proximity to the polarized fission sample. The transmission of the target also can be measured using the ^6Li glass detector placed behind the second cryostat.

A very nice exposition of the effectiveness of the transmission method for determining spin is illustrated in Fig. 18. In the lower portion of this figure we have transmission as measured with the target polarized in one direction, e.g., opposite to the spin of the neutron. The transmission experiment is then repeated with the target polarized in the other direction and then the difference between these two transmissions can be plotted as it is in the upper part of the curve. For the case of ^{237}Np shown here, the j = 2 and j = 3 spin states are clearly and cleanly separated. Dr. Keyworth from LASL refers to this as his spinsmanship slide and on safe ground challenges anyone to match it. Clearly the technique provides a means for measuring spins of any target so long as a sample of suitable size can be obtained and used. The most serious limitation is encountered with radioactivity where the heat generated by the natural radioactivity even in materials such as ^{239}Pu is perhaps too large for the existing system to adequately handle.

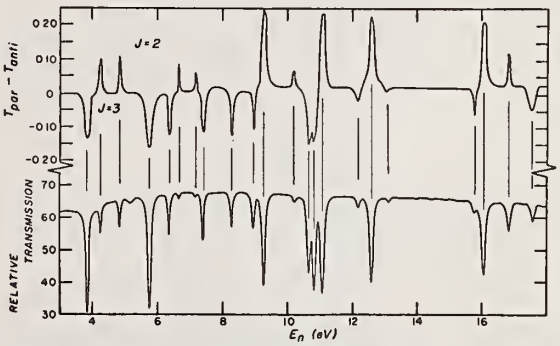

Figure 18. The LASL-ORELA measurement of the species of ^{237}Np using a polarized beam and target. The difference in transmission provides a sensitive measure of the resonance spin.

Let me move on now to the area of capture cross section measurements. Although no really new techniques have been developed in the past three years, the optimum matching of detector to neutron source has taken place and in this country the major emphasis in capture has gone to the weighted spectrum type of facility first applied by Czirr and Lindsey[17] at LLL in alpha measurements on ^{239}Pu. That work is being carried on now at Livermore by John Browne using deuterated benzene detectors and even more agressively,

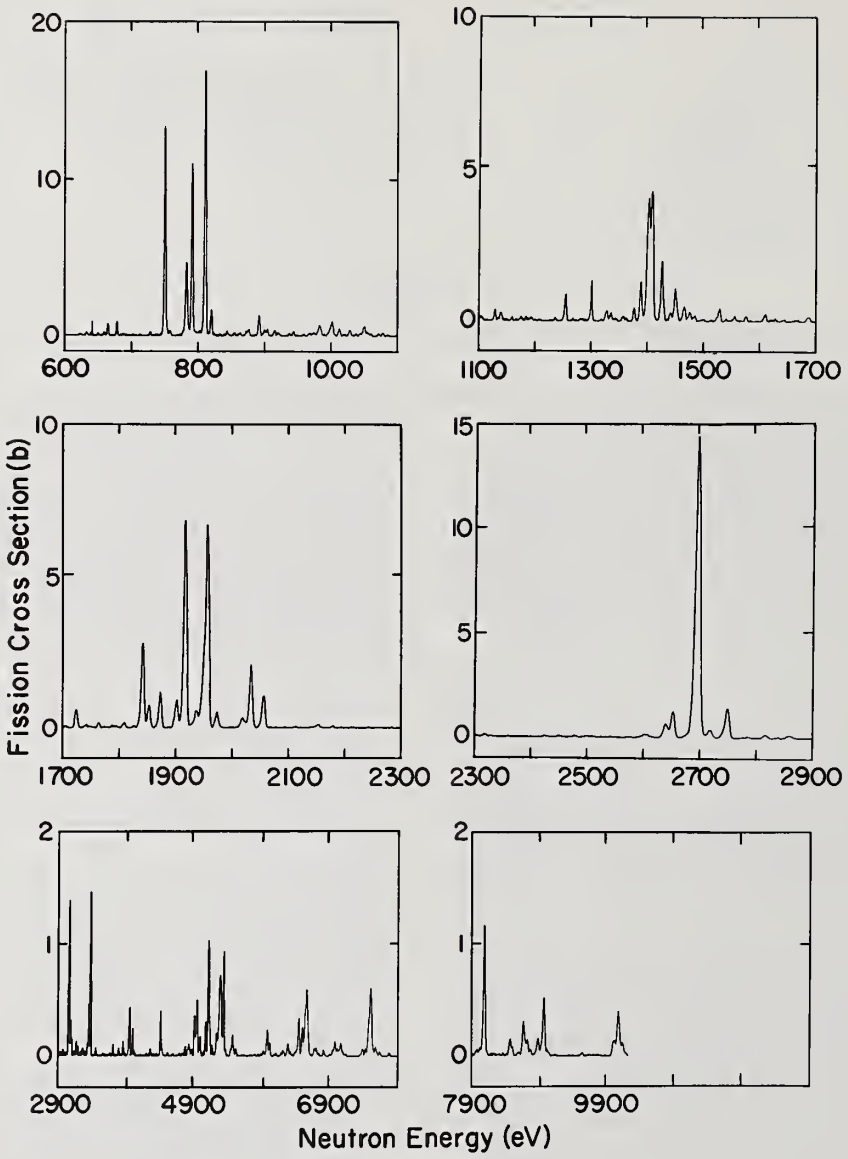

Figure 19. A LASL-ORELA measurement of the fission intermediate structure in ^{240}Pu indicating the high quality of data now attained with high powered linacs.

at ORELA by Macklin using a C_6F_6 scintillator. Most of the ORELA work has been concentrated in the keV region and I am sure most of you have seen the many very nice examples of the high quality work which the ORELA system can achieve.[18] The work at Livermore has been concentrated on eV measurements of importance in astrophysical problems.

A number of experiments have been done both in Europe and the United States using capture apparatus to search for γ-ray decay in the second well. To my knowledge no one has claimed success in a neutron-induced reaction, where the initial spin and excitation energy are accurately known, of seeing the γ-ray decay in the second well. I feel that those of us involved or interested in such measurements should consider this a severe embarrassment. It is still a major challenge to us and it is important that these gamma rays be found. If the model predicts γ-ray intensities which are sufficiently large to detect, and I believe it does, then we have to wonder why we are not seeing them. At the moment, this is the one missing link I know of between the intermediate structure in fission and its apparent relationship to the second minimum in the fission barrier.

We have slipped from capture into fission and I would like to go on now and discuss some interesting results in fission measurements which represent new advances in my opinion. In Fig. 19 I show a fission cross section measurement measured at ORELA on ^{240}Pu by Auchampaugh of LASL and by Weston of ORNL in another collaboration[20] for the purpose of indicating the quality of data which it is possible to obtain with the high intensity linacs now on line. I can remember the time when it was felt that the bomb technique was the only one which could produce data of this quality on a target with this level of radioactivity. I believe that both in terms of resolution and statistical accuracy, this experiment at ORELA on a moderately radioactive target, has surpassed the quality of the measurements on the bomb shot.

I would next like to describe another experiment done at ORELA by the Columbia group of Felvinci, Melkonian, and Havens.[21] A solid state detector with a ^{235}U fission foil adjacent to it was positioned about 10 m from the neutron source and the energy distribution of the fragments was measured. The experimenters take advantage of the fact that for the heavy fragment, the velocity of the fragment is rather closely correlated with the mass. They divided the pulse height spectrum up into a number of channels of equal numbers of events and plotted the fission cross section as a function of energy from 5 to 15 eV for these different fragment masses. The group claims to see some significant variations in the structure as a function of the bias window although the Geel group[22] contests this conclusion. It is clear that this kind of measurement is now possible and has the potential for interesting physics if it is carried out with adequate statistical accuracy.

I would finally like to mention a new technique showing the exceptionally high resolution which has been obtained with a ^3He spectrometer by Prestwich[23] at McMaster University. The capabilities here far exceeded anything I expected. In this experiment, Dr. Prestwich obtains a monoenergetic gamma ray from a reactor and directs it against a lead target. He thus excites the lower side of the giant resonance of ^{208}Pb where the resonances are overlapping and measures with a ^3He spectrometer, located in close proximity to the lead sample, the neutron spectrum being emitted to the ground state and other excited states of the various lead isotopes. In Fig. 20 we see a result of this spectrometry. The left side of the scale corresponds to an energy of about 1 MeV and the right-hand side to an energy of about 5 MeV. Looking at the tallest line corresponding to the emission to the 803 keV first excited state in ^{206}Pb, one can measure a resolution there of 3%. That resolution appears to hold down to significantly lower energies and, I think, is more than adequate for many measurements in neutron spectroscopy. Obviously, the sensitivity of such a system is not high, but when one compares the resolution capability of this system which can be placed very close to a source, compared with a time-of-flight experiment for example, where inverse r^2 is playing a major role, the technique might well be competitive.

Finally, I would like to mention the recent work at RPI with the lead slowing down spectrometer. This type of facility has been around for years, performing useful measurements but not exciting the interest of a large fraction of the neutron physics community. At RPI, the staff has taken the simple step of pulsing the lead spectrometer with their electron linac,[24] which results in an intensity in the spectrometer which is perhaps a factor of a thousand or more larger than that which has been used in the past. The RPI staff claims that the technique yields an intensity which is about four orders of magnitude above the comparable intensity obtained with the same resolution with the linac source. They have backed up their claim in practical terms by detection of an intermediate structure resonance in ^{238}U near 760 eV, which had previously escaped detection. For those measurements when high intensity is very important, this facility should play an important role.

In concluding I would like to thank especially those persons who forwarded their material to me. My time is insufficient to cover all of the progress in this field and I apologize to many of you for not being able to include an account of your work in this brief paper or for failing to recognize a significant new technique. I would also like to apologize to my European colleagues who perhaps have not received their due in this talk, but I have been forced to speak more about those programs in the United States with which I am most familiar. I hope I have been able to demonstrate that significant innovations are taking place in our field and that there are likely many other opportunities waiting to be explored. Thank you for your attention.

References

1. Neutron Standards and Flux Normalization, Proceedings of a Symposium held at Argonne National Laboratory, Argonne, Illinois, October 21-28, 1970.

2. G. S. Sidhu and J. B. Czirr, Paper GB-20, these proceedings.

3. N. A. Betz, J. W. Reynolds and G. G. Slaughter, Proceedings for the Skytop Conference on Computer Systems in Experimental Nuclear Physics (1969) AEC Div. of Technical Information, CONF-690301.

4. J. W. Behrins, G. W. Carlson and R. W. Bauer, Paper GB-14, these proceedings.

5. D. M. Gilliam and G. F. Knoll, Paper GB-25, these proceedings.

6. H. T. Heaton II, J. A. Grundl, V. Spiegel, Jr., D. M. Gilliam and C. Eisenhauer, Paper DB-10, these proceedings.

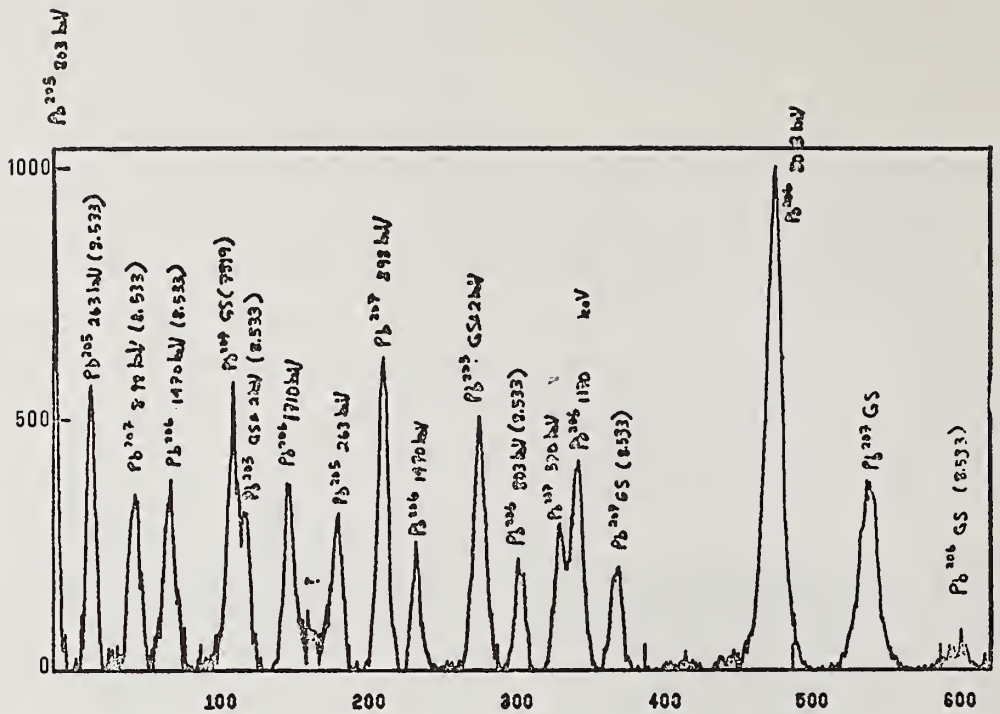

Figure 20. Neutron spectrum obtained at Mcgill University, with a ^{3}He proportional counter. (α,n) neutrons were detected from a material lead sample bombarded with monoenergetic γ-rays.

7. G. L. Morgan, T. A. Love, and F. G. Pevey, submitted to Nuclear Instruments and Methods.

8. G. T. Chapman, J. K. Dickens, T. A. Love. G. L. Morgan and E. Newman, Paper HB-9, these proceedings.

9. O. D. Simpson, J. R. Smith and J. W. Rogers, "Filtered-Beam Techniques," AEC Symposium Series 23, Neutron Standards and Flux Normalization Proceedings of a symposium held at Argonne National Lab., ARgonne, Ill,. Oct. 21-23, 1970, p. 362.

10. I. G. Schroder, R. B. Schwartz, and E. D. McGarry Papers GB-9 and GB-18, these proceedings.

11. I. G. Schroder, E. G. McGarry. S. de Leeuw, and C. de Leeuw-Gierts, Paper DB-3, these proceedings.

12. M. Soleilhac, J. Frehaut and J. Gauriau, J. Nucl. Energy, 33, 257, (1969).

13. L. W. Weston and J. H. Todd, p. 861, Vol II, Proceedings of the Third Conference on Neutron Cross Sections and Technology, March 15-17, 1971, University of Tennessee, Knoxville, Tennessee.

14. R. E. Howe, T. W. Phillips and C. D. Bowman, Paper IAEA-FM-174/61, p. 495, Third IAEA Symposium on the Chemistry and Physics of Fission, Rochester, N. Y., August 13-17, 1973.

15. D. Shackleton, J. Trochon, J. Frehaut and M. Le Bars, Physics Letters, 42B, 344 (1972).

16. G. A. Keyworth, C. E. Olsen, F. T. Seibel, J. W. T. Dabbs and N. W. Hill, Phys. Rev. Lett., 31, 1077 (1973).

17. J. B. Czirr and J. S. Lindsey, Nucl. Sci. and Eng. 41, 56 (1970).

18. For example see B. J. Allen, J. W. Boldeman, M. J. Kenny, A. R. Musgrove, and R. L. Macklin, Paper EB-16, these proceedings.

19. For example see B. L. Berman and J. E. Brown, Phys. Rev. C7, 2522, (1973).

20. G. F. Auchampaugh and L. W. Eston, Paper GB-5, these proceedings.

21. J. P. Felvinci, E. Melkonian, and W. W. Havens, Paper, GB-11, these proceedings.

22. G. Rohr, Private Communications, (1975).

23. M. V. Prestwich, Private Communications, (1975).

24. R. C. Block, R. W. Hockenbury and R. E. Slovacek, Paper BB-10, these proceedings.

MEASUREMENT, ANALYSIS, AND IMPLICATIONS OF THE FISSION CROSS SECTION OF THE IMPORTANT FISSIONABLE ISOTOPES*

M. S. Moore
Los Alamos Scientific Laboratory
Los Alamos, NM 87544

Recent measurements on the resonance cross sections of isotopes of uranium and plutonium are reviewed, with the objective of determining average parameters suitable for calculations at higher energies. The average parameters obtained are useful in two ways: they provide the necessary input for statistical calculations of resonance cross sections in the unresolved region, and they provide a normalization point for the calculation of smooth cross sections above the unresolved region. The particular problem we address is the systematic trend of average fission cross sections from 3-5 MeV, which have been found to follow the equation $\sigma_f = -39.031 + 17.231\ Z^2/A^{3/2}$. We find that a very simple statistical model calculation, based on R-matrix parameters which adequately describe the total cross section from 20 keV to 20 MeV, can provide a qualitative understanding of this systematic behavior.

[NUCLEAR REACTIONS, FISSION, U, Pu isotopes, calculated $\langle\sigma_f\rangle$, E = 3-5 MeV.
^{235}U(n,f), deduced channel spectrum.]

Introduction

It is often said that one of the justifications for making detailed measurements of cross sections of fissionable isotopes in the resonance region is that these data can be used in extrapolating to the unresolved resonance region and above. As one of the most promising techniques for providing cross sections in the unresolved resonance region, we recommend following the pioneering work of Brissenden and Dursten[1] with resonance ladders, and using the probability table method of Levitt.[2] While much remains to be done in this area, the technique is well known and will not be reviewed here. Instead, we should like to review significant new results at low energies with the objective of using these data as an evaluation guide in the region of smooth cross sections.

W. G. Davey[3] has suggested that a program to provide significantly improved cross section data for fissionable isotopes should be based on an interactive approach involving microscopic measurements, integral experiments, and model calculations. In such a program, it is the interactive feedback which is most important. The integral experiments and model calculations suggest areas where new measurements are needed; discrepancies in microscopic measurements and between measurement and calculation might be resolvable by carefully designed integral experiments; and both the integral and microscopic data can lead to refinements in the model. Ultimately, one might hope to be able to calculate, in a reasonable way, data sets for isotopes which are difficult or impossible to measure (e.g., the heavier actinides which may be important as radioactive wastes, heavy element production with underground nuclear explosions, and neutron production by medium energy charged particle beams).

It is this last area, in particular, which prompted the present study. We are involved in planning the experimental program for the Weapons Neutron Research (WNR) facility at the Los Alamos Scientific Laboratory. In this facility, neutrons are produced by short bursts of 800 MeV protons incident on a ^{238}U target. Below neutron energies of 20 MeV, calculations are based on a Monte Carlo treatment using ENDF/B cross sections. Above 20 MeV, we have been using the Nucleon-Meson Transport Code NMTC[4] which ignores fission. The results of the calculations, carried out by Russell and reported at this conference, show a discontinuity at 20 MeV and suggest that an improved treatment is needed.

Following Davey's suggestion that model calculations can play an important part in the refinement of nuclear data, we shall explore two questions: (1) how can the systematics derived from low energy microscopic measurements be used in nuclear model calculations, and (2) what can one hope to learn from such calculations?

To make a model calculation for fissionable isotopes, we find that we need the following input: (1) neutron transmission coefficients for elastic and inelastic scattering, (2) the low-lying level structure of the target nucleus with spins and parities, (3) a description of the variation of the nuclear level density with energy for saddle point and ground state deformation, (4) the variation of the radiation width with energy, (5) the fission channel spectrum at the saddle point with spins and parities, (6) the pairing gap for ground-state and saddle-point configurations, (7) the neutron binding energies and fission thresholds, and (8) the barrier curvature parameters for the formulation chosen to represent barrier penetration. Many of these are not very well known, and for the studies we have done, the keyword is simplicity: we shall try to use constant values for many of the parameters as possible over the limited range of target nuclides considered.

Neutron Transmission Coefficients

The measured neutron widths for resolved resonances provide the s- and p- wave strength functions, as taken from the recent compilation of recommended parameters by Mughabghab and Garber.[6] The weighted averages for the uranium and plutonium isotopes are 1.03×10^{-4} for the s-wave strength function, and 1.85×10^{-4} for the p-wave strength function. The usual approach to obtaining neutron transmission coefficients for model calculations is with the optical model. The optical model fits recently reported by Lagrange[7] represent the current state of the art. Lagrange used the coupled-channel model of Tamura[8] (the JUPITOR-I code), and fitted in decreasing order of importance the total cross sections, the s- and p- wave strength functions at low energies, and the elastic plus low-lying inelastic angular distributions. While calculations[9] using the Lagrange parameters give good agreement for ^{238}U, the description is less satisfactory for ^{239}Pu, suggesting that the optical model parameterization is not only energy dependent, but is different for each nuclide to be considered. For this reason, we have chosen a simpler representation for this study, which follows the R-matrix approach used by Uttley et al[10] in the analysis of total cross sections. We use the generalized one-level formula of Lane and Thomas[11] which leads to the following expressions for the average total, shape-elastic, and compound-nucleus reaction cross sections:

$$\langle\sigma_T\rangle = \frac{2\pi}{k^2}\sum_\ell (2\ell+1)\cdot$$

$$\cdot\left[\left(1-\cos 2\phi_\ell\right)\left(1-\frac{\pi\Gamma_n^{(\ell)}}{D}\right)+\frac{\pi\Gamma_n^{(\ell)}}{D}\right], \quad (1a)$$

$$\langle\sigma_{se}\rangle = \frac{2\pi}{k^2}\sum_\ell (2\ell+1)\left(1-\cos 2\phi_\ell\right)\left(1-\frac{\pi\Gamma_n^{(\ell)}}{D}\right), \quad (1b)$$

$$\langle\sigma_x\rangle = \frac{2\pi}{k^2}\sum_\ell (2\ell+1)\,\frac{\pi\Gamma_n^{(\ell)}}{D}\cdot\frac{\pi\Gamma_x^{(\ell)}}{D}\Big/\sum_x\frac{\pi\Gamma_x^{(\ell)}}{D}. \quad (1c)$$

In the above expressions, the wave number $k = \frac{1}{\lambda\!\!\!^{-}} = \frac{\mu v}{\hbar}$, where μ is the reduced mass and v is the relative velocity, ℓ is the neutron orbital angular momentum, $\Gamma_n^{(\ell)}$ is the average neutron width, $\Gamma_x^{(\ell)}$ is the average reaction width, and D is the average level spacing. The quantity $2\pi\Gamma_n^{(\ell)}/D$ is the neutron transmission coefficient we are seeking. The average compound-nucleus reaction cross section was written in the above form to show the relationship $\langle\sigma_T\rangle = \langle\sigma_{se}\rangle + \sum_x\langle\sigma_x\rangle$; it is properly written as a compound-nucleus spin expansion

$$\langle\sigma_x\rangle = \frac{2\pi^2}{k^2}\sum_{J,\ell} g_J\,\frac{\Gamma_n^{(J,\ell)}}{D_J}\,\frac{\Gamma_x^{(J)}}{D_J}\Big/\frac{\Gamma^{(J)}}{D_J}, \quad (2)$$

where g_J is the statistical factor $(2J+1)/2(2I+1)$, and where J is the spin of the compound nucleus and I is the spin of the target nucleus. The statistical factor g_J obeys the sum rule $\sum_J g_J = 2\ell+1$, and the total width $\frac{\Gamma^{(J)}}{D_J} = \sum_x\frac{\Gamma_x^{(J)}}{D_J}$. In this study, we assume that $\Gamma_n^{(J,\ell)}/D_J$ depends only on ℓ, and ignore width correlation corrections and multilevel interference, except for the diagonal R^∞ term. In the absence of R^∞, the transmission coefficients $2\pi\Gamma_n^{(\ell)}/D$ are related to the strength functions $\Gamma_n^{0(\ell)}/D$ by the expression

$$\frac{\Gamma_n^{(\ell)}}{D} = \frac{\Gamma_n^{0(\ell)}}{D}\cdot E\cdot P_\ell/\rho, \quad (3)$$

where $\rho = ka$, a is the nuclear radius, and P_ℓ and ϕ_ℓ in Eq. (1) are given by the Lane and Thomas recursion relations

$$P_0 = \rho;\ P_\ell = \rho^2 P_{\ell-1}/[(\ell - S_{\ell-1})^2 + (P_{\ell-1})^2],$$
$$S_0 = 0;\ S_\ell = \rho^2(\ell - S_{\ell-1}),$$
$$\phi_0 = \rho;\ \phi_\ell = \phi_{\ell-1} - \tan^{-1}[P_{\ell-1}/(\ell - S_{\ell-1})], \quad (4)$$

If R^∞_ℓ is non-zero and diagonal, the relations are modified as follows:

$$\frac{\Gamma_n^{(\ell)}}{D} = \frac{\Gamma_n^{0(\ell)}}{D}\cdot E\cdot P'_\ell/\rho,$$
$$P'_\ell = P_\ell/d_\ell,$$
$$S'_\ell = [S_\ell(1 - R^\infty_\ell S_\ell) - R^\infty_\ell P_\ell^2]/d_\ell,$$
$$\phi'_\ell = \phi_\ell - \tan^{-1}[R^\infty_\ell P_\ell/(1 - R^\infty_\ell S_\ell)],$$
$$d_\ell = (1 - R^\infty_\ell S_\ell)^2 + (R^\infty_\ell P_\ell)^2. \quad (5)$$

The purpose of this part of the exercise is to obtain the simplest possible parameterization of a set of neutron transmission coefficients which fairly well describe the total cross sections of the uranium and plutonium isotopes over a wide range of neutron energies. We note that recent measurements of Schwartz et al[12] of the total cross section of ^{235}U, ^{238}U, and ^{239}Pu between 10 keV and 15 MeV do not differ from one another by more than a few percent. The s- and p- wave average parameters provide a normalization point for obtaining these neutron transmission coefficients, but they give no information for higher partial waves. To obtain a reasonable set of parameters to use in the present formalism, we choose strength functions consistent with Lagrange's average transmission coefficients for ^{238}U in the energy regions where the partial cross sections are highest. Finally, we solve, by least-squares fitting the average of the measurements of Schwartz et al, for the R^∞ matrix elements. The results are given in Table 1, and the fit is shown in Fig. 1. The neutron transmission coefficients calculated from the parameters in Table 1 agree with those of Lagrange to about 10% in the energy regions of importance.

Table 1. Parameters used in calculating neutron transmission coefficients.

ℓ	Strength function	R^∞_ℓ
0	1.03×10^{-4}	-0.111
1	1.85×10^{-4}	+0.125
2	1.0×10^{-4}	+0.043
3	2.25×10^{-4}	-0.071
4	1.0×10^{-4}	-0.058
5	1.2×10^{-4}	+0.068
6	2.0×10^{-4}	0.0
≥ 7	1.0×10^{-4}	0.0

Discrete Levels for Inelastic Scattering

For this study, we are interested primarily in treating the average behavior of inelastic scattering. For simplicity, we construct a standard spectrum of levels which is used for all nuclides. For rotational band structure, there are three standard spectra: the K = 0 spectrum, the K > 0 spectrum, and the spin 1/2 spectrum which takes into account Coriolis coupling. All these are generated as averages of the known rotational structure for the uranium and plutonium isotopes as evaluated by Ellis.[13] The energies of

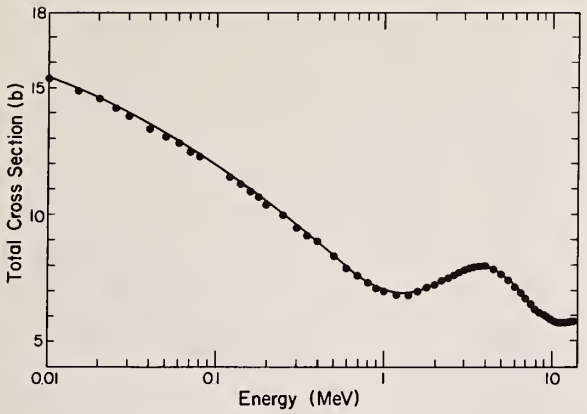

Fig. 1. Average total cross section of ^{235}U, ^{238}U, and ^{239}Pu from 0.01 to 15 MeV. Points show averaged data from measurements of Schwartz et al[11] and from ENDF/B-IV; the solid line shows the calculated curve using parameters of Table 1.

vibrational band heads again represent averages for the known low lying level structure of the even-even isotopes. Included as part of the vibrational spectrum are the negative parity octupole vibrations with K = 0, 1, 2, and 3, the positive parity beta and gamma vibrations with K = 0 and 2, and a second $K,J^{\pi} = 0,0^{+}$ band near 1 MeV. The spectra of intrinsic levels for the even-odd targets are constructed from average energy differences as tabulated by Ellis and Schmorak.[14] In some cases, it is necessary to extend the single-particle spectrum beyond the range of known levels. Additional levels (and the entire spectrum of single-particle fission channels) are taken from the level diagrams of Seeger and Howard[15] at the appropriate average deformation.

For the even-even nuclei, it is necessary to include certain of the two-quasiparticle states. From the ^{234}U spectrum evaluated by Ellis,[13] we conclude that these start to be important at ~1.5 MeV excitation. We construct a spectrum which looks reasonable by taking the appropriate energy differences for the single particle states and adding 1.5 times the pairing gap, for both neutrons and protons.

The calculation of inelastic scattering is done in the usual way,[16] using reciprocity. We find that the calculated inelastic scattering to the lowest rotational states in ^{238}U is low by 30-50%, probably because we ignore direct processes by using a diagonal representation for R^{∞}. There is reasonably good agreement with inelastic scattering to the higher states in ^{238}U, suggesting that this simplified approach may be adequate for describing compound nucleus processes, and in particular, competition between inelastic and fission.

Level Densities and the Radiation Width

The next step in model calculations is to obtain a description of the level density for continuum inelastic scattering and of the variation of the radiation width with neutron energy. The usual prescription is to use the Gilbert and Cameron level density formula,[17] normalizing the radiation width to the correct value in the resonance region. We follow Gilbert and Cameron in the assumption that the important parameter in the level density formula is $E_B + E - E_p$, where E_B is the binding energy, E is the neutron energy, and E_p is the pairing gap. We obtain an estimate of the pairing gap by looking at neutron and proton separation energy differences, and find, as show in Figs. 2 and 3, that these appear to depend on the mass number. The reduced level spacing (taking out the expected 2J + 1 dependence and applying the Gilbert and Cameron spin-cutoff correction) is plotted as a function of $E_B - E_p$ for the uranium through americium isotopes in Fig. 4, where the data points are again from the compilation of parameters recommended by Mughabghab and Garber.[6] The Gilbert and Cameron formula with parameters set equal to the average for this region of A does not fit the data points, so we assume the Weisskopf description,[18] $\rho = A \exp a\sqrt{E}$, solving for the parameters A and a by the method of least squares.

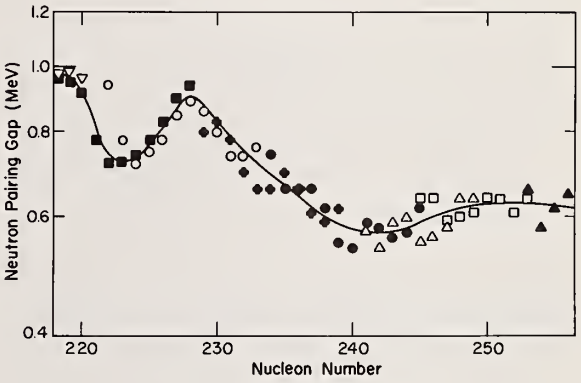

Fig. 2. Estimate of the pairing gap for neutrons, inferred from neutron separation energies for even-even and even-odd nuclei as a function of mass number.

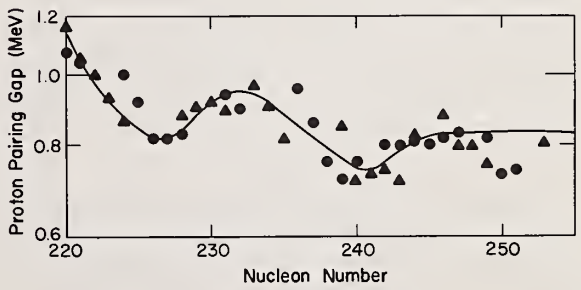

Fig. 3. Estimate of the pairing gap for protons, inferred from proton separation energies for even-even and odd-even nuclei as a function of mass number.

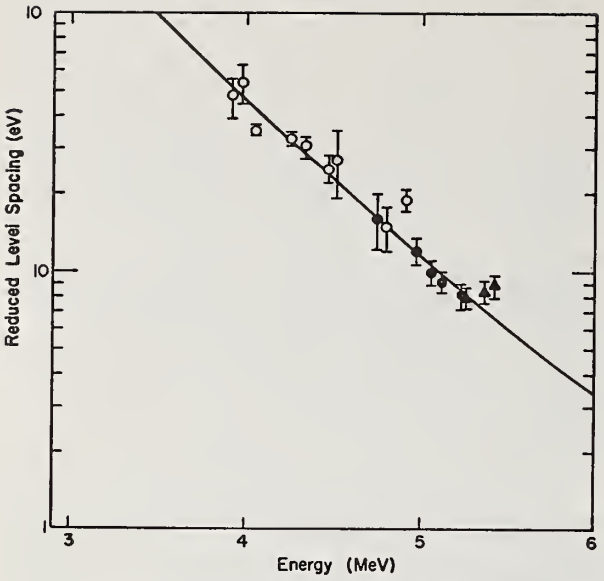

Fig. 4. Reduced level spacing for uranium through americium isotopes, as a function of $E_B - E_p$. The solid line shows the calculated curve used, given by $\rho = 0.145 \exp(5.88\sqrt{E})$.

The resonance parameters recommended by Mughabghab and Garber are also used in deriving a simple expression for the energy dependence of the radiation width. Figure 5 shows a plot of the radiation widths for the actinides of interest as a function of $E_B - E_p$. We follow the usual procedure of normalizing in the center of the range, calculating the energy dependence to be expected for $(\hbar\omega)^3$ and $(\hbar\omega)^5$, corresponding to El and E2 radiation. For purposes of this study, we conclude that the $(\hbar\omega)^3$ dependence is adequate. finally, as an internal consistency check, we calculate the radiative capture cross section of ^{238}U, and find satisfactory agreement with the recommended curve of ENDF/B-IV below 1 MeV, as shown in Fig. 6. We find that the Gilbert and Cameron level density formula tends to overpredict radiative capture at 1 MeV by a substantial amount (~50%). This is because the Gilbert and Cameron formula gives a stronger increase in the number of levels as the energy increases in this region of A than does the Weisskopf representation we are using; hence Γ_γ/D increases much faster.

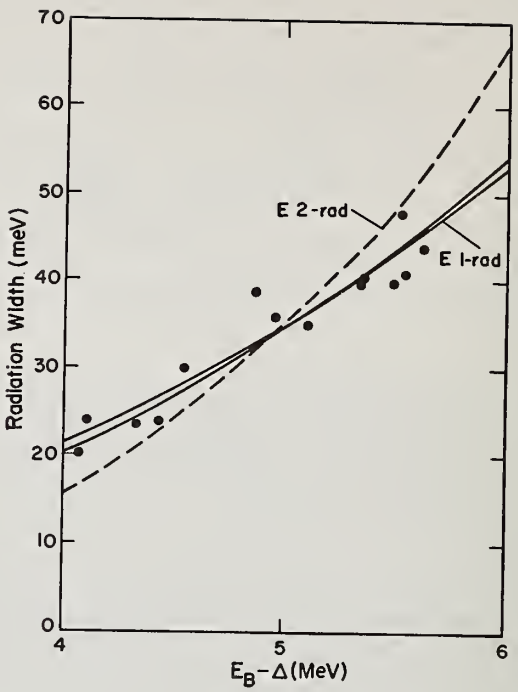

Fig. 5. Average recommended radiation widths[6] as a function of $E_B - E_p$. The dashed curve corresponds to an assumed $(\hbar\omega)^5$ dependence of the partial radiation width. The solid curves correspond to an assumed $(\hbar\omega)^3$ dependence, but the calculation is not sensitive to the expression used for the level density. The two solid curves correspond to the Gilbert and Cameron formula[17] and the one we use as described in the text.

Fission and Inelastic Competition from 3-5 MeV

Our simplified approach to including the fission contribution is based on the definitive analysis by Back et al[19,20] of charged-particle induced fission measurements. We use the double-humped barrier with curvature constants set equal to the averages given by Back et al for even-even and for even-odd fissioning species. We are interested primarily in fission above both barriers, so we use the strong coupling approximation, setting the matrix elements connecting Class I and Class II states equal to unity. The difference in first and second barrier heights appears to be slightly N-dependent, but we ignore it. The Z-dependence is taken into account by a linear fit to the average given by Back et al, as shown in Fig. 7.

One of the first things one finds in trying to calculate fission cross sections below the second-chance threshold is that both the magnitude and the slope of the cross section in the plateau region (3-5 MeV) are determined by competition between continuum inelastic scattering and continuum fission. (By the word "continuum," we mean the region in which the level density formula is applicable.)

Several years ago, Smith et al[21] measured fission cross sections for a number of the actinides, and found that the average cross sections between 3 and 5 MeV could be described within 5-10% by the empirical relationship $\sigma_f = -39.031 + 17.231\ Z^2/A^{3/2}$. If we plot the most recent evaluations, as given in ENDF/B-IV, for the average fission cross sections for uranium and plutonium from 3-5 MeV, we find that the relationship is still remarkably good, as shown in Fig. 8.

We know that the Smith et al empirical formula cannot be pushed to extremes; for example for ^{250}U, the fission cross section would be far negative and for ^{220}U it would greatly exceed the total. However, it would seem that any model calculation, even one as simplified as the one we are using for these studies,

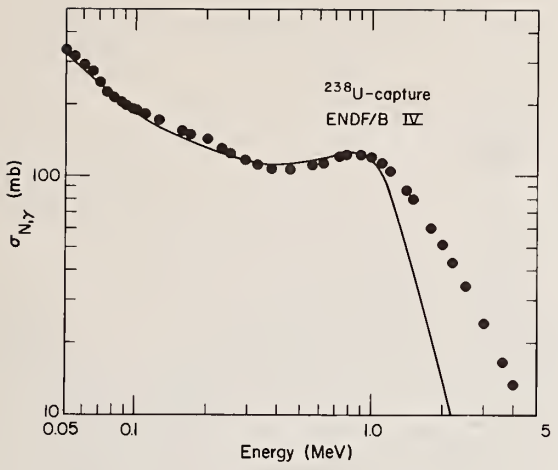

Fig. 6. The radiative capture cross section of ^{238}U. Data points are from ENDF/B-IV; the solid line represents the calculated curve.

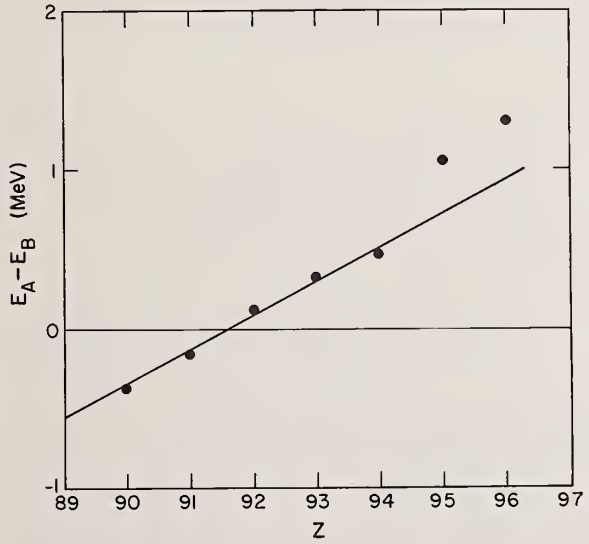

Fig. 7. Average energy difference between first and second barrier heights as a function of proton number, calculated from barrier heights derived by Back et al.[19,20]

should be able to explain physically this systematic behavior.

Before we can do a meaningful calculation, however, we still need two pieces of information: the level of density formula for continuum fission, and the pairing gap at the barrier. While it is reasonable to assume that the form of the level density formula is the same for continuum fission and continuum inelastic, we do not expect to be able to use exactly the same constants. If one carried out a Strutinsky calculation[22] of single-particle levels to find the barrier height as a function of deformation, he would find that the single-particle level density at the Fermi surface for barrier deformations is lower than for ground state deformations. At energies well above the barrier, the densities must eventually be the same on the average, although one still expects local fluctuations. In other words, the existence of the barrier is attributable to a lower level density in its vicinity, but at some energy above the barrier we should expect that the same level density formula would be applicable at both deformations.

To account for this effect we use the same level density formula for continuum inelastic and for continuum fission, but change the width of the interval over which the levels are counted in fission by a constant factor. For low energies, (i.e., 3-5 MeV) the value of this constant factor will be treated as a free parameter in fitting the data; at higher energies (i.e., where the level density for continuum fission becomes equal to that for first-well levels) it will be set equal to unity.

The best guesses for the pairing gap at the barrier are from Britt and Huizenga,[23] who suggest that it is roughly equal to the pairing gap at the ground state, or from Seeger and Howard,[15] whose results indicate that it is somewhat larger than the ground state gap. This is not good enough, and we are forced to introduce another free parameter, which we shall call the continuum fission barrier, E_c. This parameter is defined by the relation $E_c = E_{A,B} + E_p(\text{bar.}) - E_p(\text{g.s.})$, where $E_{A,B}$, the usual barrier parameter, is the height of either the first or second hump (whichever is greater) measured from the ground state, and $E_p(\text{bar.})$ and $E_p(\text{g.s.})$ are the pairing gaps at deformations corresponding to the barrier and to the ground state, respectively. (The introduction of E_c as a free parameter simply allows us to defer the problem of the pairing gap at the barrier; we can carry out the calculations without knowing what it is.)

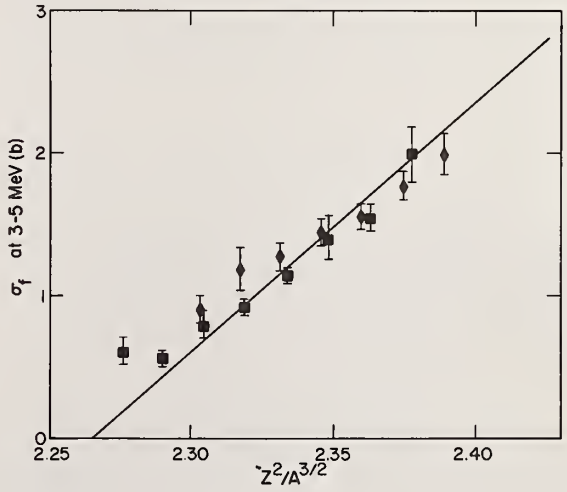

Fig. 8. Average fission cross sections of uranium and plutonium from 3-5 MeV, plotted against $Z^2/A^{3/2}$. The solid curve is the empirical relationship of Smith et al.[21]

The continuum barrier E_c lies above the usual barrier by the pairing gap at that deformation. If we assume that the pairing gap is only slightly dependent on Z and N (cf. Figs. 2 and 3), then it follows that E_c will show properties similar to $E_{A,B}$. In particular, we expect that the continuum barrier will have a slight N-dependence, which we neglect, and a fairly strong Z-dependence. We assume that the Z-dependence of the continuum barrier in going from uranium to plutonium is equal to the average given by Back et al[19] for the measured barriers for the even-even uranium and plutonium nuclei, which are presumably 0^+ at both deformations. This gives a difference of 0.24 MeV in the barriers for uranium and plutonium.

With this assumption, we need to fit only one target nucleus (value and slope) from 3 to 5 MeV in order to fix both the parameters we have left free. We choose to normalize to ^{235}U, and in particular, to the recent measurements of Hansen et al[24] which are the basis for ENDF/B-IV in this region. We find that the values which best describe the ^{235}U data give a continuum barrier of 6.02 MeV, and a continuum level density 6.5% higher at an energy of 1.5 MeV above the barrier than at the ground state deformation. For the plutonium isotopes, we use a continuum barrier which is 0.24 MeV lower, or 5.78 MeV.

The results of a calculation of the 3-5 MeV fission cross sections for all the uranium and plutonium isotopes, using these constants, are shown in Figs. 9 and 10. The calculated averages are plotted against the empirical curve of Smith et al in Fig. 11.

In the calculations, we find that the key parameter is the energy difference between the onset of continuum inelastic and continuum fission, as shown in Fig. 12. We have assumed that continuum inelastic occurs when the neutron energy exceeds the pairing gap of the target nucleus, and that continuum fission occurs when the neutron energy plus the binding energy exceeds the continuum fission barrier plus the pairing gap of the compound nucleus. The variable responsible for this systematic behavior is thus the binding energy plus or minus the ground-state pairing gap for the last neutron. It is the binding energy plus the pairing gap if the target nucleus is even-even, and minus if even-odd. The above results also suggest that the pairing gap at the barrier is roughly 10% larger than at the ground-state, in agreement with recent estimates.[15,23]

The most puzzling discrepancy in Figs. 9 and 10 is for ^{241}Pu. The calculations for ^{239}Pu and ^{242}Pu agree fairly well, and ^{240}Pu gives about the right average even though the slope is much too large. But ^{241}Pu, which should fit best, is underpredicted by 10-20%. Even though existing measurements on ^{241}Pu appear to agree to ~5%, we are tempted to suggest that a remeasurement may be in order. It should be noted that there is a small continuing effort at the Los Alamos Scientific Laboratory in the measurement of neutron cross sections with nuclear explosions. Forman et al,[26] who recently completed a measurement of the gamma-ray prodution cross section of ^{241}Am below 6 MeV by this technique, are planning to remeasure the fission cross section of ^{241}Pu to 6 MeV in the near future.

Using the results of these calculations, it is possible to predict the magnitude and slope of the plateau cross sections for second, third, fourth-chance fission, etc., which arise by the mechanism of inelastic scattering to continuum levels which lie above the fission threshold in the residual nucleus. The decay of these levels is again dominated by competition between neutron emission and fission.

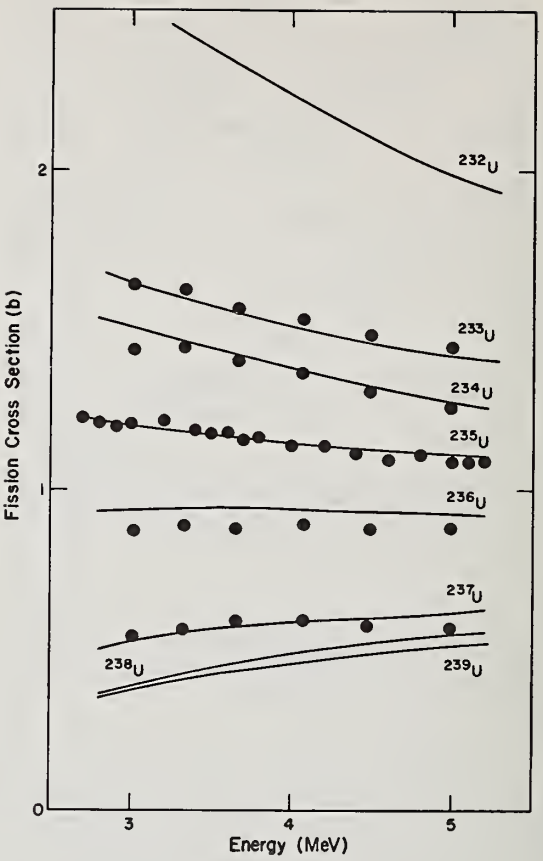

Fig. 9. Fission cross sections of the uranium isotopes from 3-5 MeV. The points are evaluated data; the curves represent the results of calculations as described in the text.

The results of such a calculation for ^{235}U below 25 MeV, compared to evaluated data from ENDF/B-IV, are shown in Fig. 13. These results are similar to those obtained by Jary,[27] who concluded that it is possible to calculate multiple-chance fission with a statistical model with no free parameters, using the magnitude of the observed plateau for first-chance fission.

Our results may also be compared to those of Gavron et al,[28] who use a microscopic calculation of level densities and a spherical optical model for neutron transmission coefficients. They find that they are able to fit fission probabilities for a wide range of fissioning species, primarily induced by charged particle reactions, again with no free parameters. From the fission probabilities, they expect to be able to obtain neutron cross sections for targets which would be unmeasurable by usual techniques, following methods similar to those of Cramer and Britt.[29]

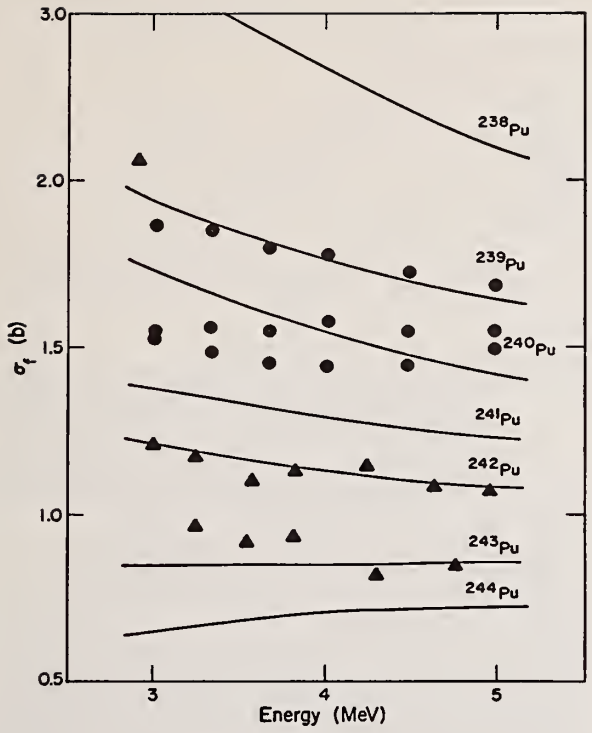

Fig. 10. Fission cross sections of the plutonium isotopes from 3-5 MeV. The points, except for ^{242}Pu and ^{244}Pu, are evaluated data, the curves represent the results of calculations as described in the text. For ^{242}Pu and ^{244}Pu, the points are taken from measurements reported by Auchampaugh and Bergen.[25]

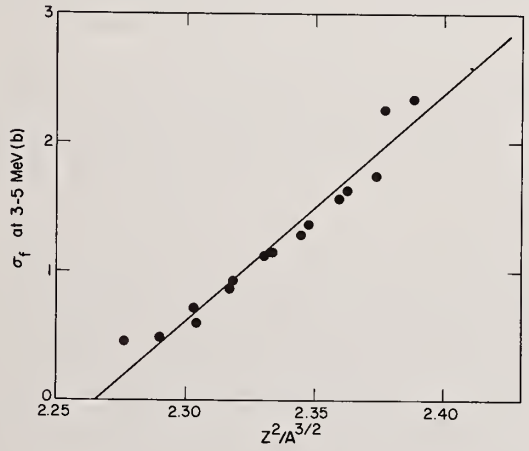

Fig. 11. Calculated average fission cross sections of the uranium and plutonium isotopes from 3-5 MeV, plotted against $Z^2/A^{3/2}$. The solid curve is the empirical relationship of Smith et al.[21]

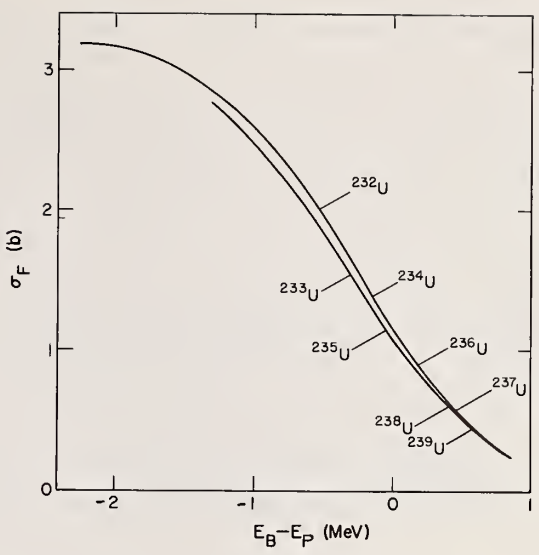

Fig. 12. Calculated average fission cross sections of the uranium isotopes as a function of the energy difference between the continuum fission threshold and the pairing gap governing continuum inelastic scattering.

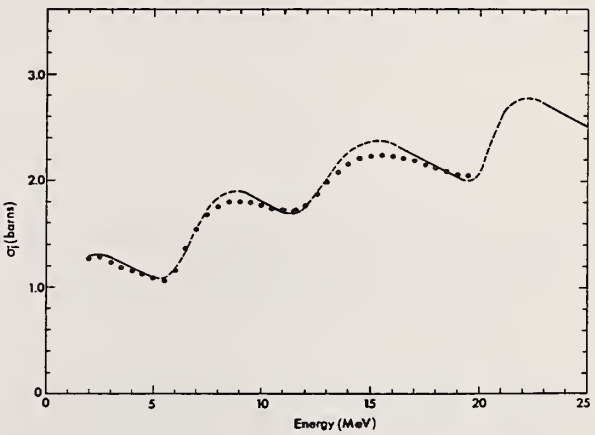

Fig. 13. Fission cross section of (^{235}U+n) from 2 to 25 MeV. Data points are taken from ENDF/B-IV; calculations were carried out only for the plateau regions corresponding to first-, second-, third-, and fourth-chance fission.

Discrete Fission Channels

The last question we should like to address is that of the discrete fission channel spectrum, and what we can expect to learn from the resonance region. The situation is best for ^{235}U; we have the definitive spin assignments from measurements by Keyworth et al[30] using polarized neutrons incident upon polarized targets. We also have effective anisotropies, leading to K-assignments, from the work of Pattenden and Postma[31] with aligned targets. These results suggest $\langle A_2 \rangle = -1.54$ for

J=3 and $\langle A_2 \rangle$ = -2.05 for J=4. For the fission widths, we have the results of a multilevel analysis carried out by Smith and Young[32] for ENDF/B-IV, which give average fission widths of 0.074 eV for J=4 and 0.186 eV for J=3. The purpose of this part of the excercise is to deduce, from the average resonance parameters and the assumed fission barrier description from Back et al,[19,20] the spectrum of the low-lying fission channels. We shall then test these in a statistical model calculation in the region of a few hundred keV.

If the resonances had pure K, Pattenden and Postma note that we should expect A_2 = -2.92, -2.19, 0, and +3.65 for (K,J) = (0,3), (1,3), (2,3), and (3,3), respectively. We expect A_2 = -2.48, -1.17, +1.02, and +4.08 for (K,J) = (1,4), (2,4), (3,4), and (4,4), respectively. From the average parameters, we set up the following equations:

For J=3,

$$(-2.92\langle\Gamma_{f_0}\rangle - 2.19\langle\Gamma_{f_1}\rangle + 0.0\langle\Gamma_{f_2}\rangle + 3.65\langle\Gamma_{f_3}\rangle)/\langle\Gamma_f\rangle = -1.54, \quad (6)$$

and

$$\langle\Gamma_f\rangle = \langle\Gamma_{f_0}\rangle + \langle\Gamma_{f_1}\rangle + \langle\Gamma_{f_2}\rangle + \langle\Gamma_{f_3}\rangle = 0.186 \text{ eV}, \quad (7)$$

where $\langle\Gamma_{fK}\rangle$ is the average width for the fission channel of the appropriate K.

For J=4, we have a similar expression,

$$(-2.48\langle\Gamma_{f_1}\rangle - 1.17\langle\Gamma_{f_2}\rangle + 1.02\langle\Gamma_{f_3}\rangle + 4.08\langle\Gamma_{f_4}\rangle)/\langle\Gamma_f\rangle = -2.05, \quad (8)$$

and

$$\langle\Gamma_f\rangle = \langle\Gamma_{f_1}\rangle + \langle\Gamma_{f_2}\rangle + \langle\Gamma_{f_3}\rangle + \langle\Gamma_{f_4}\rangle = 0.074 \text{ eV}. \quad (9)$$

In order to solve these equations, we use the conclusion reached by Pattenden and Postma, that channels with K=3 and 4 are effectively closed and that their contributions can be neglected. The equations for J=4 can be solved immediately, giving $\langle\Gamma_{f_1}\rangle$ = 0.049 eV and $\langle\Gamma_{f_2}\rangle$ = 0.025 eV.

We assume that these partially open channels for J=4 are rotational members of bands which also have J=3 members. In this case, knowledge of the energy difference between the 4⁻ members of these two bands can be used to give the energy difference between the 3⁻ members of the same two bands.

In order to solve Eqs. (6) and (7) for J=3, we calculate the fission penetrabilities, $2\pi\Gamma_f/D$, as a function of excitation energy, as shown in Fig. 14. Using D=1.65 eV and 1.41 eV for J=3 and 4, respectively (implying a 6% correction for missed levels below 30 eV), we find that the 4⁻ members of the K=1 and K=2 bands are separated by 0.065 MeV. We assume that this same number applies for the J=3 members. This permits the solution of the equations for J=3, for which we find $\langle\Gamma_{f_0}\rangle$ = 0.023 eV, $\langle\Gamma_{f_1}\rangle$ = 0.101 eV, and $\langle\Gamma_{f_2}\rangle$ = 0.062 eV. If we then assume that the lowest threshold for ^{236}U is at 5.70 MeV, as given by Back et al, we estimate the transition state band heads at 0.87, 0.72, and 0.85 MeV for K=0⁻, 1⁻, and 2⁻, respectively. These are quite different from the transition state energies suggested by Back et al for ^{236}U, 0.15 and 0.45 MeV for K=0⁻ and 1⁻, respectively. Our transition state energies are similar to the energies of negative parity bands observed near the ground state; 688 keV for the lowest (K = 0?),[33,34] and 970 keV for $K^\pi = 1^-$.[35] Using the channel sequence inferred from the low energy resonances, the calculated fission cross section agrees quite well with the measurements below 300 keV; we find, in particular, that the lowest 3^+ channel, presumably corresponding to gamma vibrations with K=2, cannot have a transition-state energy much below 1 MeV. This again is quite different from the transition-state energy of 0.18 MeV suggested by Back et al, but is quite close to the first well energy of 0.95 MeV. It may be noted that if the gamma-band transition state lies well below 1 MeV, the p-wave contribution to fission in (^{235}U + n) is much too large. We could, however, include the beta vibrational band with K=0 without changing the results. This occurs for the following reason: after the fission penetrability approaches unity for a given spin, fission dominates in compound nucleus decay. Increasing the fission width for this spin by a factor of two, by doubling the number of open channels, has no appreciable affect on the average decay probability.

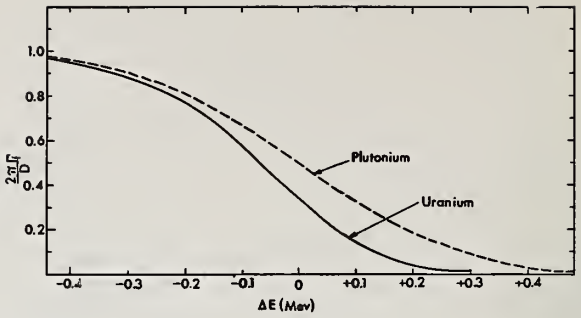

Fig. 14. Calculated fission penetrability, $2\pi\Gamma_f/D$, for uranium and plutonium, as a function of the difference between the barrier height and the excitation energy. The curve for uranium is different from that for plutonium because of the difference in height of the second hump.

It may also be noted, from Fig. 14, that $2\pi\Gamma_f/D$ changes quite rapidly with excitation energy. The surprising success we have had in describing the fission cross section below 300 keV, simply by pegging the channel structure at the neutron binding energy, gives us some confidence in the barrier parameterization we have used.

In order to fit the data above 400 keV, several additional channels are required, but their quantum numbers and exact locations are not critical. We construct these using the procedures described above for inelastic levels, and modify the energies slightly as required. Figure 15 shows the kind of fit one can achieve below the second-chance fission threshold. We divide the energy range into four regions of interest: (1) At the lowest energies, $\lesssim$ 50 keV, we find that fission through the s-wave channels is dominant, and the average cross section is determined primarily by competition between fission and radiative capture. (2) Between 50 and 400 keV, p-wave fission becomes important, and discrete inelastic channels need to be considered as well. (3) Between 400 keV and roughly 2 MeV, we find higher partial waves becoming important, and we see that competition between many discrete fission channels and inelastic channels is the dominant consideration. This

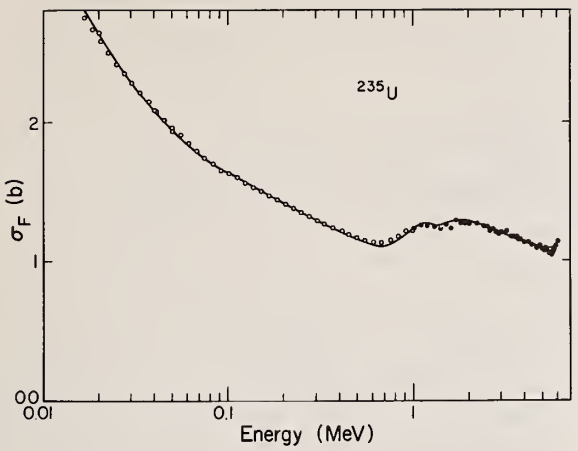

Fig. 15. The fission cross section of (^{235}U + n) below 6 MeV. The solid line represents the calculated curve, and shows the broad structure one expects to be able to reproduce by model calculations in the region of smooth cross sections.

is the region which gives the most difficulty, because we have very little knowledge of either spectrum. (4) Finally, above 2 MeV, we reach what we have called the continuum region, where the very rapidly increasing level density both for fission channels and inelastic levels gives the familiar plateau and quickly drives all other compound-nucleus cross sections to zero.

When we first began this study, we had hoped to find that the same approach, perhaps even the same parameters, would provide an adquate representation for all the isotopes of uranium and plutonium. We find that this is not the case. For (^{239}Pu + n), the resonance parameters suggest that there is one 0^+ channel fully open at the neutron binding energy, and a second is partially open; the 1^+ channel should correspond to an average fission width of 0.04 eV. In fitting the smooth cross sections below 400 keV, however, we find that this gives too much s-wave-neutron-induced fission. To achieve a fit, we must reduce the average width for 1^+ levels at the neutron binding energy by a factor of two. For both (^{233}U + n) and (^{241}Pu + n), placing the excitation energy of the transition state which produces 3^+ fission near the energy of the observed gamma vibrational band in ^{234}U and ^{242}Pu is not satisfactory; it must be nearly 300 keV lower if it is to provide enough 3^+ fission to describe the resonance fission widths and the fission cross sections below 400 keV. For fissile targets other than ^{235}U, we find that this simplified calculation tends to underpredict the fission cross section below 1.5 MeV and to overpredict significantly near 2 MeV. For the even-even targets, we have not seriously attempted to fit the data from threshold to 3 MeV. The fission channel spectrum is not well known, and the low energy resonances give no information. While this is an important region, it is not within the scope of the present study.

Discussion

The primary purpose of this review is to show how one might go about using average parameters obtained from neutron cross section measurements in the resonance region to extrapolate to substantially higher energies in describing the fission cross sections for actinide nuclei. For illustration purposes, we have chosen a greatly simplified nuclear model, holding as many parameters fixed as possible. We find that average resonance spacings provide a level density formula which seems to be adequate. Average s- and p-wave neutron widths provide input for a least-squares adjustment giving neutron transmission coefficients. Average radiation widths provide an expression for the energy dependence which is adequate for extrapolation over a limited range. Finally, we suggest a way in which average partial fission widths might be used to give some indication of the appropriate fission channel spectrum.

We feel that model calculations can be an extremly useful tool in both measurement and evaluation of nuclear data. We have shown how even a very simple calculation can provide qualitative understanding of certain systematic behavior. One can expect that a state-of-the-art programmatic effort in nuclear modeling can provide suggestions for important new areas where measurements are needed, either as input to the calculations or to resolve serious discrepancies. Finally, there is the problem of non-existent and unmeasurable data for which modeling is the only solution.

Acknowledgements

The author would like to express his appreciation to Philip A. Seeger of the Los Alamos Scientific Laboratory for countless helpful discussions and for a critical reading of the manuscript, to Augustus Prince of the Brookhaven National Laboratory for communicating his results of JUPITOR-1 calculations for ^{238}U and ^{239}Pu, and to William G. Davey of the Los Alamos Scientific Laboratory, who, in pointing out the connection between low energy measurements and nuclear modeling, suggested the outline for this study.

---

*Work performed under the auspices of the USERDA.

[1] R. J. Brissenden and C. Dursten, U.K.A.E.A., Winfrith, in Proceedings of the Conference on the Application of Computing Methods to Reactor Problems," May 17-19, 1965, Argonne National Laboratory, Illinois, USAEC Report ANL-7050, p. 51, August 1965.

[2] L. B. Levitt, Nuc. Sci, Eng. 49, 450 (1972).

[3] W. G. Davey, Private communication (1975).

[4] W. A. Coleman and T. W. Armstrong, USAEC Report ORNL-4606, October 1970.

[5] L. R. Veeser, G. J. Russell, E. D. Arthur, P. A. Seeger, W. F. Sommer, D. M. Drake, and R. G. Fluharty, in "Proceedings of the Conference on Nuclear Cross Sections and Technology," Washington, D.C., March 1975, paper FB3.

[6] S. F. Mughabghab and D. I. Garber, USAEC Report BNL-325, 3rd Ed., Vol. 1 (1973).

[7] Ch. Lagrange, in "Critique of Nuclear Models and their Validity in the Evaluation of Nuclear Data," EANDC Topical Discussion, Tokyo, March 1974 (to be published.)

[8] T. Tamura, Revs. Mod. Phys. 37, 679 (1965), and USAEC Report ORNL-4152 (1967).

[9] A. Prince, Private communication (1974). We are greatly indebted to Dr. Prince for communicating the results of these calculations.

[10] C. A. Uttley, C. M. Newstead, and K. M. Diment, in "Nuclear Data for Reactors," IAEA, Vienna, Vol. I, p. 165 (1967).

[11] A. M. Lane and R. G. Thomas, Revs. Mod. Phys. 30, 257 (1958).

[12] R. B. Schwartz, R. A. Schrack, and H. T. Heaton II, Nuc. Sci. Eng. 54, 322 (1974).

[13] Y. Ellis, Nuclear Data Sheets B4, 581, 623, 635, 661, 683 (1970).

[14]Y. A. Ellis and M. R. Schmorak, Nuclear Data Sheets B8, 345 (1972).
[15]P. A. Seeger and W. M. Howard, Nuc. Phys. A238, 491 (1975).
[16]W. Hauser and H. Feshbach, Phys. Rev. 87, 366 (1952).
[17]A. Gilbert and A. G. W. Cameron, Can. J. Phys. 43, 1446 (1965).
[18]J. M. Blatt and V. F. Weisskopf, Theoretical Nuclear Physics, John Wiley and Sons, New York (1952), p. 371.
[19]B. B. Back, O. Hansen, H. C. Britt, and J. D. Garrett, Phys. Rev. C9, 1924 (1974).
[20]B. B. Back, H. C. Britt, O. Hansen, B. Leroux, and J. D. Garrett, Phys. Rev. C10, 1948 (1974).
[21]H. L. Smith, R. K. Smith, and R. L. Henkel, Phys. Rev. 125, 1329 (1962).
[22]V. M. Strutinsky, Nuc. Phys. A95, 420 (1967).
[23]H. C. Britt and J. R. Huizenga, Phys. Rev. C9, 435 (1974).
[24]G. E. Hansen, D. M. Barton, G. A. Jarvis, P. G. Koontz, and R. K. Smith, Private communication (1973).
[25]G. F. Auchampaugh, J. A. Farrell, and D. W. Bergen, Nuc. Phys. A171, 31 (1971).
[26]L. Forman, M. G. Silbert, and A. D. Schelberg, to be published (1975).
[27]J. Jary, in "Critique of Nuclear Models and their Validity in the Evaluation of Nuclear Data," EANDC Topical Discussion, Tokyo, March 1974 (to be published).
[28]A. Gavron, H. C. Britt, E. Konecny, J. Weber, and J. B. Wilhelmy, Phys. Rev. Letters, to be published (1975).
[29]J. D. Cramer and H. C. Britt, Nuc. Sci. Eng. 41, 177 (1970).
[30]G. A. Keyworth, C. E. Olsen, F. T. Seibel, J. W. T. Dabbs, and N. W. Hill, Phys. Rev. Letters 31, 1077 (1973).
[31]N. J. Pattenden and H. Postma, Nuc. Phys. A167, 225 (1971).
[32]J. R. Smith and R. C. Young, USAEC Report ANCR-1044, ENDF-161 (1971)
[33]C. M. Lederer, J. M. Jaklevic, and S. G. Prussin, Nuc. Phys. A135, 36 (1969).
[34]F. K. McGowan, C. E. Bemis, Jr., W. T. Milner, J. L. C. Ford, Jr., R. L. Robinson, and P. H. Stelson, Phys. Rev. C10, 1146 (1974).
[35]K. Katori, A. M. Friedman, and J. R. Ershine, Phys. Rev. C8, 2336 (1973).

NEUTRON CAPTURE CROSS SECTION MEASUREMENT TECHNIQUES*

R. E. Chrien
Brookhaven National Laboratory
Upton, New York 11973

A review of currently-used techniques to measure neutron capture cross sections is presented. Measurements involving use of total absorption and Moxon-Rae detectors are based on low-resolution detection of the prompt γ-ray cascades following neutron captures. In certain energy ranges activation methods are convenient and useful. High resolution γ-ray measurements with germanium detectors can give information on the parameters of resonance capture states. The use of these techniques is described.

(Review; capture techniques; total absorption; Moxon-Rae; activation; high resolution methods)

I. Introduction

Neutron capture reactions are important in a wide range of nuclear applications from stellar nucleosynthesis to reactors. These reactions provide a means of populating states of many nuclides and hence are also important in determining nuclear structure and providing insight into capture reaction mechanisms. As knowledge concerning neutron interactions has developed a variety of techniques for capture studies have been made available to the experimenter. Some of these are quite specific as to energy range, source type, or nuclear species, others are generally applicable to many types of sources and samples.

In this review a description of some of the more useful techniques will be given in the hope of acquainting the non-specialist with activity in this field, and to impart some appreciation to the user of cross section information about the limitations and expected precision of capture cross section measurements. For the purposes of the present discussion, the term capture will be taken to indicate radiative capture.

The most commonly-used methods are based on direct detection of prompt photons emitted after capture with low resolution devices. These prompt detection methods are suitable for use with pulsed source, time-of-flight experiments. The use of high resolution techniques relevant to spin assignments and the systematic behavior of capture resonances will also be discussed.

II. Direct Detection Methods

The capture of neutrons in non-fissile targets is followed by the emission of electromagnetic radiation to states of the product nucleus. The spectral character of this radiation is quite complex. From first order perturbation theory, the electric dipole portion of a multipole expansion of this radiation may be expressed as a width amplitude in the following terms:[1]

$$\Gamma_{\gamma\lambda f}^{\frac{1}{2}} = \left(\frac{16\pi}{9} k_\gamma^3\right)^{\frac{1}{2}} \frac{|\langle \psi_f | \vec{r} | \psi_i \rangle|}{(2J_\lambda+1)^{\frac{1}{2}}} \quad .$$

The complexity of the resonance wave function ψ_i leads to a distribution of $\Gamma_{\gamma\lambda f}^{\frac{1}{2}}$ which is approximately Gaussian. The widths follow therefore approximately a chi-square distribution with one degree of freedom, similar to the distribution law for neutron widths. The angular momentum selection rules introduce an additional variability. The spectra from resonance to resonance display marked differences because of these factors, as is illustrated in Fig. 1 showing the spectra from the first three resonances of a typical heavy odd-A target, ^{173}Yb.

The primary transition is followed by a cascade of secondary radiation leading ultimately to the ground state. In a heavy nucleus a γ-ray multiplicity of three to four is typical.

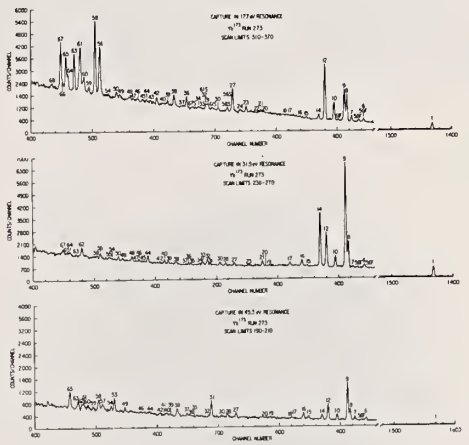

Fig. 1. Examples of high resolution γ-ray spectra recorded from several resonances of ^{173}Yb.

An ideal direct detection technique must exhibit an insensitivity to the spectral variability. This insensitivity can be accomplished by several means, which we shall discuss in some detail. We note that any γ-cascade proceeding from the initial state must have the energies of the individual members sum to the available energy for the reaction:

$$E_{available} = E_B + E_n$$

where: E_B is the neutron separation energy (usually 6-8 MeV) and E_n the center of mass energy for the incident neutron.

The two major detection techniques most commonly employed are the "total absorption" and the "Moxon-Rae" types.

A. Total Absorption Detection

The principle of this method is simple: one collects, insofar as practical, all of the prompt γ-rays following capture to produce a single pulse, one for each capture event. This is accomplished by making the detector subtend 4π solid angle and large enough so that all the γ rays in the de-excitation cascade are absorbed in the detector. In practice this ideal is never achieved, since a γ-ray of 8 MeV has an absorption mean length of about 41 cm in a liquid scintillator. Fortuantely γ-ray multiplicities usually range between 3 and 4 photons per capture, and a liquid scintillation tank of about 1 meter in diameter is practical to construct with efficiencies of 50% or more, overall.

Liquid scintillator tanks of this size range are in operation at many laboratories. An example which serves to illustrate many of the features of such devices is a detector used at ORELA called "ORELAST",[2] shown in Fig. 2. ORELAST is 1.56 meters in diameter and contains 3000 liters of NE-224 (1,2,4 trimethyl benzene) poisoned with trimethylborate to inhibit neutron capture by hydrogen. The tank is viewed by 32 5-inch phototubes and is coated with an epoxy-based titanium-oxide reflector. The detector is pierced by a 7 inch diameter through-tube fabricated from 0.015 inch aluminum and it contains a 5 foot liner of ^{6}LiH, 2.5 cm thick. Such a detector has a good signal to noise ratio. Figure 3 shows the observed count rates from the ORELAST from a 25 mil thick ^{238}U sample. The tank can be subdivided for coincidence operation; the upper curve represents events detected in one of the two halves of the tank, the bottom curve is the coincidence rate. The improvement in signal to noise ratio is about 8 for coincidence operation.

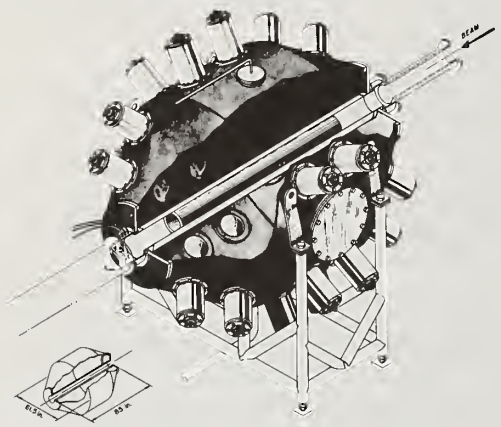

Fig. 2. The scintillation tank detector in use at the Oak Ridge Electron Linear Accelerator facility, "ORELAST".

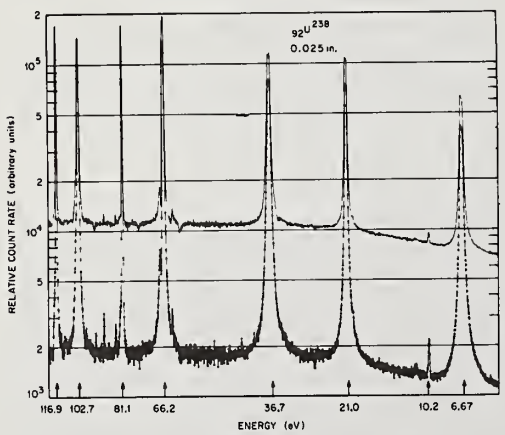

Fig. 3. A portion of the time-of-flight spectrum from neutron capture by ^{238}U obtained by ORELAST.

Modern capture tanks are relatively fast in response. The time resolution of ORELAST is about 5.7 ns, which is now typical for tank operation.

Due to the large size of the capture tank detector, however, a large background, typically several hundred counts/sec, exists with a bias of from 1-2 MeV applied to the tank. The total tank efficiency may be written as the product of two factors:

$$\varepsilon = \varepsilon_s \varepsilon_c,$$

where ε_c is the cascade efficiency and ε_s is the spectrum fraction determined by the detection bias level.

Block and Hockenbury[3] have calculated the cascade efficiency for a 1.25 meter diameter tank for cascades of γ-rays from medium-A nuclides, based on known thermal capture spectra. The efficiencies they deduce range from $0.85 \pm .02$ (for ^{60}Ni, E_B = 7.82 MeV) to 0.98 ± 0.01 (for ^{50}Cr, E_B = 9.27 MeV). The variation is evidently caused by the differences in spectra for these nuclides. The spectrum fraction ε_s can be estimated from extrapolation below the lowest possible bias which can be set--usually 0.5 MeV. Typical tank operation under running conditions, however, requires a bias level of about 2 MeV, at which the spectrum fraction is typically 70%. The estimated error of the extrapolation process is about 5% in the overall efficiency. The low energy bias of the tank is not altogether a disadvantage. It can be used effectively to suppress γ-rays due to inelastic neutron scattering.

Because of their large volume and high detection efficiency, capture tanks are sensitive to a number of background sources. Most of these backgrounds are in principle capable of subtraction. Table I, taken from a report of the Karlsruhe group by Spencer and Beer[4], lists the various types of background encountered.

Table I

	Source	Time Dependent
(1)	Tube Noise and Natural Radioactivity	No
(2)	Sample Activation	No
(3)	Accelerator Room Background	No
(4)	Capture in Sample Holder	Yes
(5)	Scattered neutrons moderated in tank and captured in tank or sample	No
(6)	Overlap Neutrons	Yes
(7)	Sample-scattered neutrons promptly captured in the tank	Yes
(8)	Rescattered neutrons captured in sample	Yes

Most of these backgrounds are determinable by either 1) use of resonance "notched" filters introduced in the beam, which remove all neutrons whose energies are properly related to time-of-flight in a pulsed neutron experiment, or 2) by background runs with dummy samples. The use of a ^{6}Li or equivalent liner is important in preventing scattered neutrons from entering the tank, or being rescattered to the sample. The suppression of the last two types of the table, (7) and (8) is particularly important, as they are not susceptible to correction by the notched-filter technique. Hockenbury,[5] however, has estimated the sensitivity of the 1.25 meter RPI tank to scattered neutrons at less than 10^{-5} at 80 keV. The Karlsruhe group[4] has likewise estimated a sensitivity of 2 to 3 parts in 10^{5} at 300 to 500 keV. It is especially important to ensure a low prompt neutron sensitivity in view of the large scattering to

capture ratio at higher neutron energies. An example of the need to suppress this kind of background arises in the interesting correlations between total radiation widths and capture widths that have been reported by the RPI group.[6] These correlations are important to establish because of their implications for nuclear reaction theory and for the prediction of average capture cross sections.

Multiple scattering corrections in the sample yield are readily calculable with modern high-speed computing techniques, and they are discussed in a later section.

B. Moxon-Rae Detectors

For many applications the large size, high background, and timing abilities of the scintillation tank detectors are disadvantages. The Moxon-Rae detector[7] was developed to overcome these deficiencies, providing a small detector with good timing at the expense of detector efficiency, which is reduced to a few percent, compared to the 70% of the tank detector.

The idea is to construct a detector whose efficiency is proportional to photon energy. If the detector subtends a reasonably small solid angle at the sample position, the probability of detection of more than one member of the photon cascade is small and thus to a good approximation,

$$\epsilon \cong \sum_{i=1}^{\nu} \epsilon_i(E_{\gamma i}); \quad \epsilon_i = kE_{\gamma i}$$

$$= k \sum_{i=1}^{\nu} E_{\gamma i} = kE_{total}$$

The detection efficiency is thus independent of the γ-ray cascade and dependent only on the total energy available in the reaction.

The idea developed by Moxon and Rae is shown schematically in Fig. 4. The photons from the capture sample are transformed to electrons by a graphite converter surrounding the sample. The emergent electrons are converted to light in thin sheets of plastic scintillator attached to photomultipliers. Since the electron range increases roughly linearly with photon energy, the number of electrons emerging from the graphite converter surface is approximately proportional to photon energy; hence detector efficiency is also proportional to photon energy.

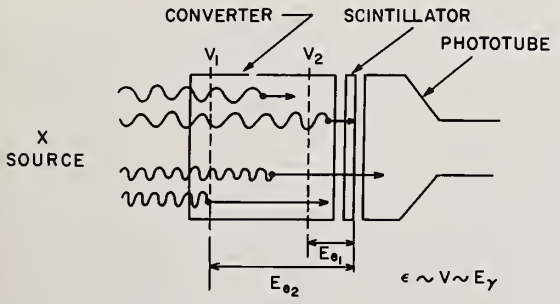

Fig. 4. A schematic view of the Moxon-Rae detector and its response to photons of different energies.

The constant of proportionality relating efficiency to photon energy has been studied by a number of experimenters; the most recent work is that of Iyengar, Tal and Jhingan[8] shown in Fig. 5. These data show the typical behavior of k: it rises rapidly from zero to a relatively constant value from below 1 MeV up to 12 MeV. The overall efficiency of the converter increases with Z; high Z elements tend to reach a plateau value at quite low

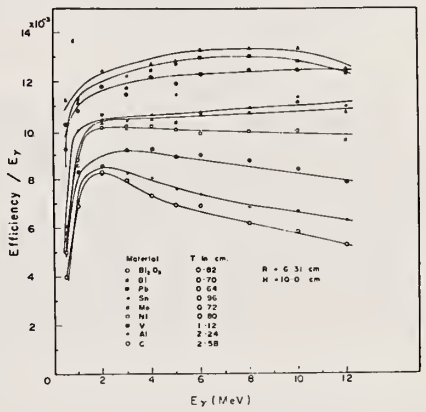

Fig. 5. The Moxon-Rae efficiency per unit photon efficiency, k, for a number of converter materials (ref. 8).

values of energy and to rise slowly with energy, while low Z values reach a maximum near 2 MeV and then fall off with increasing energy. The data suggest that the addition of a material such as Bi_2O_3 to the carbon converter should give an optimum response function; in practice about 9% (atomic) of the converter is bismuth.[9]

The Moxon-Rae detector, while offering efficiencies of only a few percent, is simple to construct and fast in response. It can be operated at relatively low bias levels at reasonable background rates. Because of these virtues it has been used extensively at time-of-flight facilities for capture measurements.

A higher-efficiency version of this detector type has been developed by Weigmann, Carraro and Böckhoff[10] at Geel. The device is shown schematically in Fig. 6. It consists of a series of thick plastic scintillators arrayed in a sandwich whose layers are alternately viewed by a pair of photomultipliers. A coincidence requirement on the phototubes requires the converted electron to travel in at least 2 scintillators, thus providing the essential property of the Moxon-Rae detector. A boron-loaded plastic sheet between scintillation elements reduces the effect of proton capture of neutrons. The advantage

of this detector is that it offers high efficiency--10% at 8 MeV--in a relatively small and simple detector.

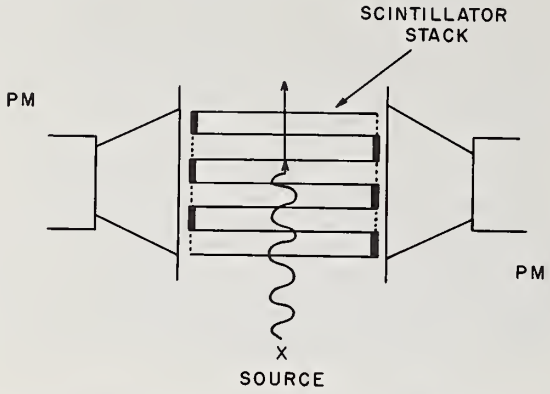

Fig. 6. The high efficiency Moxon-Rae detector developed at Geel.

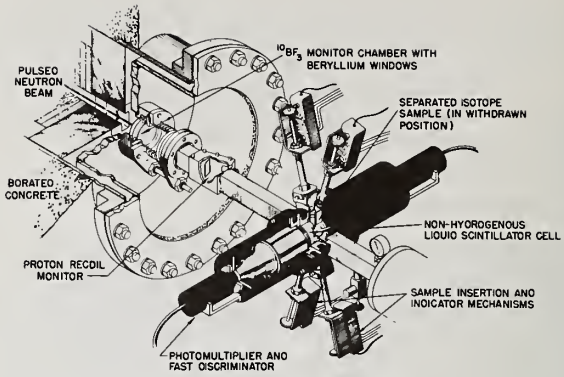

Fig. 7. The fluorocarbon detector developed at ORNL.

An elegant generalization of the Moxon-Rae detector has been developed by Macklin and Gibbons, based on a suggested attributed to Maier-Leibnitz.[11] The detector output is multiplied by a weighting factor, calculated to transform the response of an arbitrary detector--in practice a plastic scintillator--so that the energy proportionality is achieved. If the response function giving a pulse height within the range E and E+dE is $\rho(E)dE$, this condition calls for a weighting function w satisfying the following relation:

$$\int w(E_\gamma)\rho(E,E_\gamma)\cdot dE = E_\gamma .$$

The pulse height distributions to be expected from an incident photon of energy E_γ were calculated by Macklin and Gibbons[11] for right circular cylinders of plastic and liquid scintillators for energies up to 10 MeV in 50 keV steps. The interaction is dominated by Compton scattering, but the small pair production cross section and the resulting Compton interactions of the annihilation quanta were included, as were the various wall effects. The weight function is conveniently introduced by digital computer processing of the raw spectrum. Macklin has used this method in conjunction with a liquid scintillator, NE-226, based on hexafluorobenzene, (ρ=1.6) which is relatively insensitive to fast neutrons. Figure 7 shows the two fluorocarbon scintillators, 4 cm thick by 10 cm diameter, mounted on 5-in phototubes. The overall efficiency, at a bias level of 150 keV is about 15% per capture and the time resolution is less than two nonoseconds. A multiparameter detection scheme is used; a detector file is incremented at each event, the increment being determined by the weight function.

It is interesting to note, however, the relative insensitivity of the measured capture cross sections to the form of the weighting function used in this type of detector. This relative insensitivity partly results from the use of a γ-detector with no full energy peak. Figure 8 shows the experimental results from the average pulse height weighting factor as a function of neutron energy for indium and tantalum.

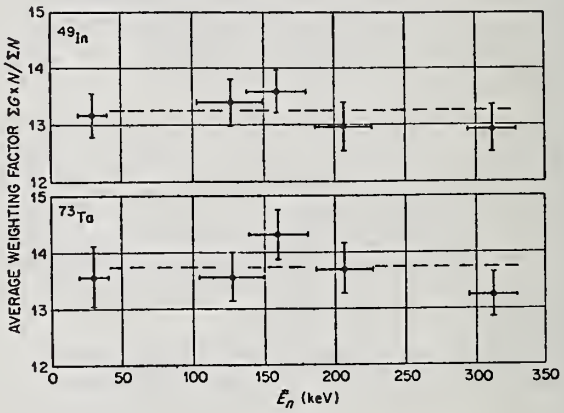

Fig. 8. The average weighting factor of the Macklin-Gibbons detector as a function of neutron energy for indium and tantalum (ref. 11).

Shown is the ratio of the weighted counts to those for the unweighted spectrum, with an electronic bias corresponding to 40 keV. As the neutron energy increases, the capture process changes from predominantly S-wave to predominantly P and D-wave, with corresponding parity reversals and spin changes for the compound levels. From these data there is observed little effect from the use of a weighting function, even though there must be a considerable change in at least the initial portions of the γ-cascades resulting from capture. Another point of interest is the behavior of the average weighting function with neutron binding energy, Fig. 9. Above 7 MeV, the plateau of Fig. 9 implies a multiplicity apparently proportional to total cascade energy; below 7 MeV the linear rise is what is expected if the multiplicity is constant, leading to an average photon energy proportional to total energy release.

The low bias achievable in this method makes it sensitive (and thus useful) for inelastic neutron γ-ray detection. In this case some attention must be paid to the anisotropic character of the radiation.

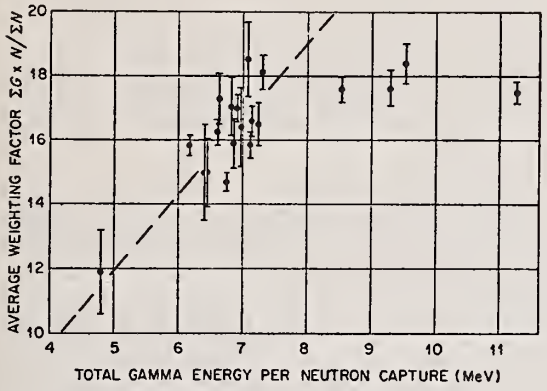

Fig. 9. The dependence of average weighting factor on neutron binding energy (ref. 11).

For multipoles up to ℓ=2, or quadrupole

$$\varphi(\theta) = 1 + aP_2(\cos\theta) + bP_4(\cos\theta).$$

Note that P_2 is a function of $\cos^2\theta$; at $\theta = 90^o$ this approaches a minimum. Figure 10 shows that for volumes exceeding 46 liters, the P_2 correction can be made zero, and the P_4 corrections are relatively small ($\approx$ 5%). While the use of hydrogenous scintillators is unacceptable because of their neutron sensitivity, deuterated liquid scintillators offer somewhat lower neutron sensitivity than do fluorocarbons,

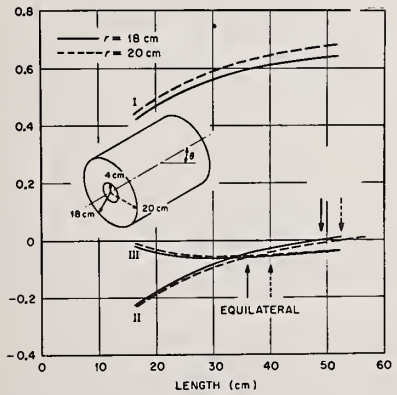

Fig. 10. Total efficiency in a C_6D_6 cylinder for 860 keV γ-rays as a function of cylinder length. I corresponds to isotropy; II corresponds to $1+P_2(\cos\theta)$; and III corresponds to $1+P_4(\cos\theta)$, (ref. 12).

are fast (1 ns timing), and can be used with pulse shaping to reject proton recoils.[12] The only resonance of concern with such a scintillation detector below 1.75 MeV is the ^{13}C resonance at 150 keV, with the natural abundance of ^{13}C only 1.1%. Other possible improvements in the simple detector as used at ORNL is the division of the scintillators into quandrants to reduce summing and the use of multiple phototubes to improve light collection and to reduce pulse height dependence on source position.

III. Analysis of Capture Yields

The extraction of cross sections and resonance parameters from capture yields is appreciably more complicated than the corresponding analysis of total cross section data. The relation between yields and cross sections may be written, ignoring resolution corrections:

$$Y_\gamma(E_n) = \left\{ \int_{DE_n} \left[1-\exp\left\{-n\sigma_{\Delta t}(E)\right\} \right] (\sigma_{\Delta\gamma}(E_n)/\sigma_{\Delta t}(E_n))dE_n \right\} \times \left\{1 + f_m\right\}/(\varepsilon\ \varphi\ (E_n))$$

where $\sigma_{\Delta t}$, $\sigma_{\Delta\gamma}$ are the total and partial Doppler-broadened cross sections
and f_m the multiple scattering and self absorption corrections,
$\varphi(E_n)$ the incident flux,
ε the detection efficiency.

In the thin sample approximation, for ℓ=0:

$$Y\varepsilon\varphi(E_n) = A_\gamma = 2\pi^2\lambda^2 g\Gamma_n\Gamma_\gamma/\Gamma.$$

The principal problems encountered in reducing yields to cross section information is the determination of the flux φ, the detector efficiency ε, and, especially where $\Gamma_n \gg \Gamma_\gamma$, the correction for multiple scattered neutrons. At low energies, where on an isolated resonance $\Gamma_\gamma \gg \Gamma_n$, a thick sample will show a saturated count rate at the resonance maximum. The saturated level fixes the product $\varepsilon\varphi$, and it remains only to establish the energy variation of φ (and possibly ε) over the energy range of the experiment. This is conventionally done with a beam monitor, usually $^6Li(n,\alpha)$, $^{10}B(n,\alpha)$ or a hydrogen recoil counter.

Figure 11 illustrates the normalization technique using the saturated resonance method as applied by de Saussure, et al.[13] at Oak Ridge. The data are compared to the ENDF/B-III resonance parameters for the ^{238}U 6.67 eV resonance. deSaussure estimates that the normalization error in this instance can be no larger than 2%.

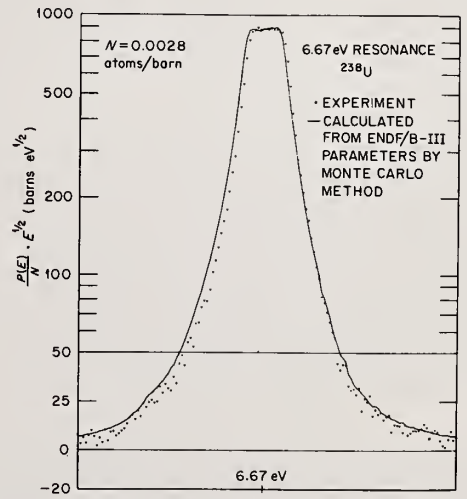

Fig. 11. Capture events recorded in a saturated resonance - 6.67 eV in ^{238}U.

The multiple scattering term, f_m, can be expanded in terms of orders ranging from single up to several scatterings before capture. The terms are complicated functions of resonance parameters and sample geometry, particularly at higher energies, where the loss of energy upon scattering can be larger than the resonance width. They can be adequately treated only by extensive Monte Carlo computations. Fortunately several reliable codes are available and in common use among various experimental laboratories.

Closed-form analytical expressions have been developed at BNL,[14] and San Diego,[15] which solve the multiple scattering corrections to second order for the near thermal region ($\sigma_\gamma >> \sigma_n$) and for infinite slab geometry. For the resolved resonance region, codes have been developed at BNL,[16] San Diego,[17] RPI,[18] and Harwell,[19] and those codes have been interchanged and checked for reliability. In the unresolved resonance region, one must have recourse to statistical simulations of the cross sections underlying the unresolved structure region, using the Wigner level distributions and the Porter-Thomas width distribution. Bogart[20] has discussed the effect of these calculations on spherical shell transmission results, while Fröhner[21] has applied these ideas to capture cross sections derived from white-source time-of-flight measurements. These corrections allow reasonable accuracies of about 1% in the resolved resonance region and 2 to 3% in the unresolved region.

IV. Supplementary Capture Techniques

Certain capture techniques are useful only for specific nuclides for selected energy regions using steady state neutron sources, or in specialized circumstances. They are important, however, in establishing useful normalization points or standards for the direct methods.

Indirect methods of high precision and sensitivity are the "danger coefficient" and "pile oscillator" techniques.[22] These methods refer to the effects on reactivity by introducing an absorber into a critical assembly. In the latter case, the sample is introduced periodically to improve sensitivity and to reduce the effects of secular reactivity variations due to barometric changes. Mass spectroscopy has also been employed to deduce the number of transmutations occurring in a sample placed in a high reactor flux. These methods suffer from the heterogeneous nature of the energy distribution of a reactor flux, and are not discussed further here.

A. Spherical Shell Transmission

An absolute method of absorption cross section is afforded by the spherical shell transmission technique.[23] The sample is arranged in a shell around either the source or detector and the number of neutrons reaching the detector is recorded by an energy insensitive neutron detector. In this geometry in-scattering exactly compensates out-scattering and only absorption is measured. In principle the method is absolute; no knowledge of neutron source strength or detector efficiency is needed, and in this regard it is analogous to a transmission measurement taken in a geometry where scattering events do not contribute.

It is of course impractical to use and construct spherical shells from most materials and for most neutron sources; they have been most often used with antimony-beryllium sources. Furthermore, in practice it has been shown that multiple scattering effects and self-shielding effects related to resonance structure introduce sizeable correction factors in sphere data.

Fröhner[21] has reanalyzed shell transmission data to take account of resonance structure in a Monte Carlo approximation. The value for σ_γ on gold at 24 keV reported by Schmitt and Cook[23] was changed from 532 ± 60 mb to 650 ± 35 mb when structural effects were included. This example demonstrates that the precision of shell transmission results is not so high as formerly believed. Nevertheless the method provides an alternate measurement of capture free of questions of source strength or detector efficiency.

B. Activation

Some nuclides, after neutron absprption, produce daughters which decay subsequently by β-emission with characteristic half lives. The β or γ radiation accompanying this decay can be counted either during or after irradiation and the intensity may be related to the number of captures through knowledge of the decay scheme and half lives. By using modern high-resolution solid state detectors, the characteristic radiations can usually be easily separated and recorded, even for isotopic mixtures. Efficiencies and source strengths are such that relatively thin samples requiring only modest corrections for γ ray and neutron absorptions (1 to 10%) are useful.

This method may be applied with a well known standard so that flux and efficiency corrections need not be known. An example is that of Fig. 12, showing the 412 keV γ-ray (the $2^+ \rightarrow 0^+$ transition in ^{198}Hg following the 2.7 day beta decay of ^{198}Au), and the 417 keV γ-ray (a 4^+ to 2^+ transition in ^{116}Sn). These spectra were obtained by activating gold and indium with the 24.3 keV neutron beam produced through an iron filter at the BNL High Flux Reactor.[24]

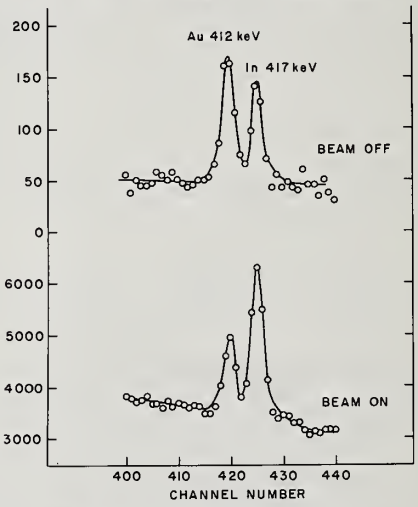

Fig. 12. Gamma decays from gold and indium foils after activation with 24.3 keV neutrons from an iron filter in HFBR.

Only the relative detector efficiency between 417 and 412 keV need be known, with appropriate branching ratios, half lives and small corrections for sample absorption effects, to deduce the cross section ratio between indium and gold. An alternate technique involves comparison between a measurement at thermal and the energy in question. This requires a knowledge of the thermal cross sections for the standard and the sample, but avoids knowledge of flux and efficiencies.

In any activation measurements it is essential

to know the energy distributions of the incident neutron flux, and, in particular, to guard against the interaction of neutrons degraded in energy by scattering processes. The ratio of cross sections, for a straight 1/v absorber, is 1000 between thermal and 25 keV, for example, and in many cases the thermal region is dominated by a resonance leading to cross sections even higher. The historical tendency of activation cross sections to decrease as measurements are made with improved sources and techniques testifies to the influence of this affect. However, at high neutron energies (> 1 MeV) and for small cross sections, the activation method is extremely effective. The specific nature of the activity discriminates against inelastic scattering competition, and the activity can be counted under conditions of low background.

It is only recently, however, that MeV activation cross section measurements have properly taken account of the influences of secondary and degraded neutrons on the sample. Kantele and Valkonen[25] have pointed out the influence of secondary neutrons produced in the tritium target head for 14 MeV activation work, and they have stressed the importance of extrapolating to zero sample thickness to provide reliable cross sections. Following this work, Rigaud, et al.[26] did systematic studies of capture at 14 MeV on $^{27}A\ell$, ^{50}Ti, ^{51}V, ^{103}Rh, ^{127}I and ^{139}La. They show that the apparent cross sections depend largely on the geometry, and the mass and material of the target heads. Cross sections ranging from 2 to 7 mb for ^{127}I and from 0.5 to 1 mb for ^{51}V, for example, were obtained by variations in the above parameters with resulting modification of the secondary neutron spectra. The apparent cross section increases as the mass of the target backing material increases, for nuclides far from magic neutron numbers. Rigaud, et al. conclude that even with the use of an $A\ell$ target backing, corrections of up to 58% for ^{103}Rh were necessary. The results of their studies (Fig. 13) allow Rigaud to conclude that (n,γ) cross sections near 14 MeV are in the range 1.0 ± 0.5 mb, independent of neutron number, in contrast to previous measurements (triangles in Fig. 13), which gave up to 20 mb from samples away from magic neutron numbers. Vuletin, Kulisic and Cindro[27] have confirmed the importance of secondary neutron reactions such as (n,2n) in activation studies, and they have shown that with proper corrections, the long-standing discrepancy between activation results and those obtained by direct integration of unfolded spectra for plastic scintillation electron pair detectors is removed. These recent measurements have eliminated the disagreement between the observed cross sections and those predicted by the Clement, Lane and Rook[28] model of semi-direct capture in the 14 MeV region, as indicated in Fig. 13.

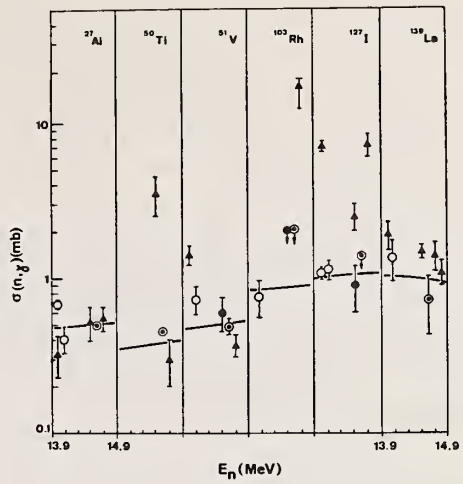

Fig. 13. A comparison of recent activation measurements at 14 MeV with theoretical predictions of the semi-direct model (ref. 26).

V. High Resolution Capture Studies

The study of electromagnetic transitions to individual final states has given us much detailed information on the nuclear structure of nuclides formed in the (n,γ) reaction, and on the nature of the (n,γ) reaction mechanism. This area is beyond the scope of the present review. High resolution techniques, however, can be interpreted also to provide information about individual capture states, such as their spins and parities, and on their average properties such as strength functions and level spacings. Those aspects are of direct interest to the applications of capture cross sections.

In a number of cases, especially in light nuclides with well known level schemes mapped out in excitation up to the region of the neutron binding energy, it is possible to integrate partial cross sections directly to obtain the total capture. At Los Alamos, for example, Jurney[29] has used the Omega West thermal capture γ-ray facility with a detector consisting of a Ge(Li) detector and an optically divided NaI annulus to measure partial cross sections. The annulus is operated in an anti-coincidence mode for Compton suppression up to 3 MeV γ-energy, and in a pair spectrometer mode in the 2-7 MeV range. Normalization is provided by observing the 2.2 MeV hydrogen capture line. Cross sections for radiative capture by ^{9}Be, ^{6}Li and ^{7}Li have been derived with quoted accuracies of about 10%.

The selection rules for electromagnetic transitions have long been used to establish resonance spins, and this technique is straightforwardly applied to high-energy primary γ rays populating states of known spin. Significant information is also available in the low energy portion of the γ-spectrum.

It has long been established that the population of low-lying states by γ-ray cascades following capture shows a strong spin dependence. Following a suggestion by Huizenga and Vandenbosch,[30] and elaborated by Poenitz,[31] a plausible explanation for this spin dependence can be based on the argument that the population of final states depends simply on the number of possible routes available for γ-cascades of a given multipole order and multiplicity to reach a given final state. The subsequent decay rate of the state is then largely a function of the difference in spins between the compound nucleus capturing state and the level in question. For a large difference the effect is large, since for a given cascade multiplicity, the number of possible de-excitation sequences decreases rapidly with the net spin change between initial and final states. For the assignment of resonance spins, it is apparent that absolute decay rates need not be measured; it suffices to examine the ratios of decay rates of final states with known spin, since the ratios are highly spin dependent.

The technique has been exploited as a simple and effective method of resonance spin determinations, Corvi, Stefanon, Coceva, and Giacobbe at Geel have demonstrated this most remarkably in a measurement on the spin of ^{235}U.[32] They studied the de-excitation of the 6^+ member (160.6 keV) of the gs rotational band compared to the de-excitation of the 2^- level at

687 keV, which emits a 642 keV γ-ray to the first excited state. Although several fission and background lines lie near the 160.6 keV peak, Fig. 15 shows a varying ratio for the 160.6 line compared to the 642 keV monitor line, depending on resonance spin. As expected the 6^+ level is more heavily populated for a J=4 resonance. The 14 resonant spins assigned by Corvi, et al. were later confirmed by a much more elaborate polarized neutron experiment carried on by Keyworth et al.[33] at Oak Ridge.

Recently similar methods have been extended to the unresolved resonance region. Of particular interest in this regard is the question of possible intermediate structure in the neutron strength functions in the various channel spin states. A novel method using these high resolution methods has recently been used by Coceva[34] and his collaborators at Geel.

Consider two low-lying levels a and b, with $J_a \geq I + 1/2$ and $J_b \leq I - 1/2$, where I is the target spin. Let P_a^+ be the probability that a γ-cascade from an I+1/2 level populates a, P_a^- be the probability of population from an I-1/2 state, and similarly for P_B^+ and P_b^-. Further define $R^+ = P_a^+/P_b^+$ $R^- = P_a^-/P_b^-$, and $R_b = P_b^+/P_b^-$ (Fig. 16). The average ratio, in a given interval containing many resonances, between the populations of levels a and b can be related to the 1+1/2 and 1-1/2 capture rates by

$$X = \frac{1}{R_b}\,\frac{\langle R\rangle - R^-}{R^+ - \langle R\rangle}$$

where $X = \sigma(I+1/2)/\sigma(I-1/2)$.

The values of R_b, R^- and R^+ can be determined from isolated resonances. From X one can thus derive the spin dependent strength functions S_o^+ and S_o^-

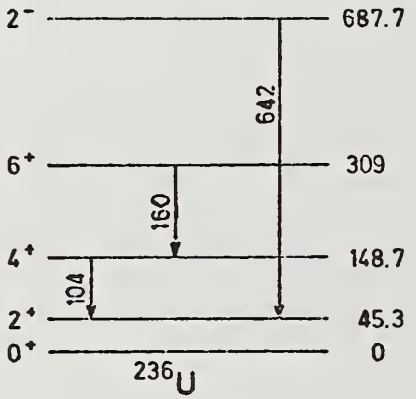

14. A portion of the level scheme for ^{236}U.

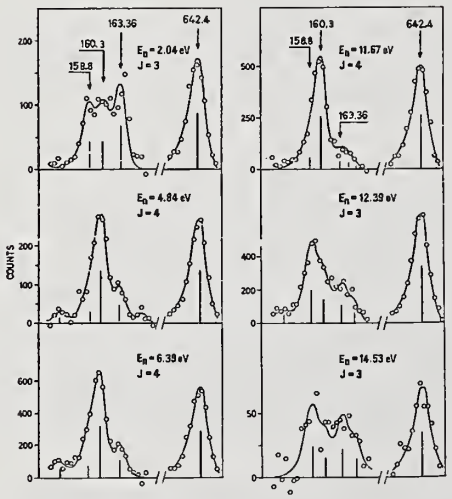

Fig. 15. Portions of the low-energy γ-ray spectra following neutron capture in ^{235}U. The de-excitation of the 6^+ member of the g.s. rotational band results in a peak at 160.6 keV.

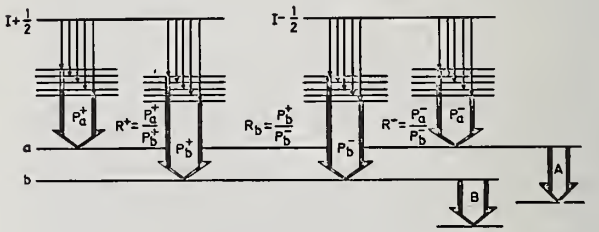

Fig. 16. Illustration of population systematics to establish the spin dependence of the neutron strength function. The ratios of the populations of levels a and b may be related to the capture state spin.

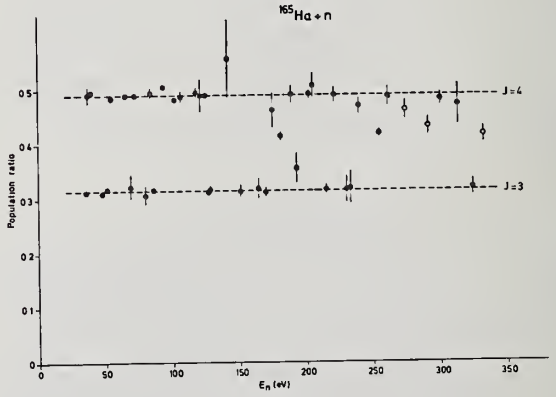

Fig. 17. The population ratios for spin 5 levels (at 330 and 348 keV) and spin 3 levels (at 171 and 482 keV) in ^{166}Ho.

Table II

Ratios of Averaged Reduced Widths as a Function of σ in ^{115}In

	σ=∞	5	4	3.6	3.0
$\langle S_5\rangle/\langle S_4\rangle$:E1	1.42±0.2	1.16±.16	1.04±.15	0.97±.12	0.81 ±.11
$\langle S_5\rangle/\langle S_4\rangle$:M1	1.52± .22	1.24±.18	1.11±.16	1.03±.14	.87 ±.13

$$S_o^+/S_o^- = X\ (\frac{I}{1+I}),$$

which is valid so long as $\Gamma_\gamma > \Gamma_n$; i.e., at reasonably low neutron energies. At higher energies suitable corrections must be introduced. Figure 17 shows the population ratios for spin 5 levels at 330 and 348 keV, and spin 3 levels at 171 and 482 keV in ^{166}Ho. A clear division into 2 groups, as expected, is seen. In the region between 170 and 340 eV there is preponderance of J=4 resonances, and the value $S^+/S^- = 1.83$ obtained by this method is in good agreement with the corresponding neutron widths of Tellier.

Measurements of high energy primary transitions can be used to determine level density parameters, such as the spin cut-off parameter σ:

$$\rho(J) = (2J+1)\ \exp\{-J(J+1)/2\sigma^2\}.$$

A direct way to determine σ is to deduce it from D(I-1/2) and D(I+1/2) by simply counting levels. An alternate way, which is insensitive to missed levels, is to make use of the expectation that the photon strength function is spin independent:

$$S_J = \Gamma_{\gamma i}(J)/D_J(E_\gamma^3),$$

hence:

$$\Gamma_{\gamma i}(I+1/2)/\Gamma_{\gamma i}(I-1/2) = D(I+1/2)/D(I-1/2).$$

Coceva[34] has tested this method for 30 resonances in ^{115}In, 14 J=4 and 16 J=5, and for γ-rays to 41 low-lying states of ^{116}In. The results were averaged separately for E-1 and M-1 transitions and are summarized in Table II.

From this table a value of $3.6\ ^{+1.0}_{-0.4}$ is deduced, which is in good agreement with typical values for nuclides of A>100 as obtained from direct spacing measurements.

From the several illustrations given above it can be seen that high-resolution γ-ray spectroscopy is capable of providing useful supplementary information for interpreting capture cross section measurements.

Acknowledgements

I wish to acknowledge the assistance of the following in providing material included in this review, and for their permission to use it: R. L. Macklin, G. B. deSaussure, C. Coceva, K. V. K. Iyengar, J. L. Irigaray, and E. Jurney.

References

*Work supported by the Energy Research and Development Administration.

[1]J. E. Lynn, "The Theory of Neutron Resonance Reactions" Clarendon Press, Oxford (1967).

[2]Neutron Physics Div. Progress Report, Oak Ridge Natl. Lab. (ORNL 4997) Aug 31, 1974.

[3]R. C. Block and R. W. Hockenbury, "Neutron Standards and Flux Normalization", CONF-701002, National Technical Information Service, Springfield, Va. (1971), p. 355.

[4]R. R. Spencer and H. Beer, "Total Capture Cross Section of ^{59}Co in the Neutron Energy Region 6-200 keV", Report KFK 1951 (1974).

[5]R. W. Hockenbury, Z. M. Bartolome, J. R. Tatarczuk, W. R. Moyer, and R. C. Block, Phys. Rev. 178, 1746 (1969).

[6]R. G. Stieglitz, R. W. Hockenbury, and R. C. Block, Nucl. Phys. A163, 1592 (1971).

[7]M. C. Moxon and E. R. Rae, Nucl. Instr. Methods 24, 445 (1963).

[8]K. V. K. Iyengar, B. Lal, and M. L. Jhingan, Nucl. Instr. Methods 121, 33 (1974).

[9]R. L. Macklin, J. H. Gibbons, and T. Inada, Nucl. Physics 43, 353 (1963).

[10]H. Weigmann, G. Carraro, and K. H. Böckhoff, Nucl. Instr. Methods 50, 267 (1967).

[11]R. L. Macklin and J. H. Gibbons, Phys. Rev. 159, 1007 (1967).

[12]R. L. Macklin, private communication, and ORNL-TM 4128 (unpublished)(1973).

[13]ORNL 4997, see ref. 2.

[14]S. S. Malik, G. Brunhart, F. J. Shore, and V. L. Sailor, Nucl. Instr. Methods 86, 83 (1970).

[15]S. J. Friesenhalm, E. Haddad, F. H. Fröhner, and W. M. Lopez, Nucl. Sci. Eng. 26, 487 (1966).

[16]J. L. Friedes, "Multiple Scattering Corrections to Partial Cross Section Measurements," BNL 8028 (1964).

[17]F. H. Fröehner, "TACASI, A Fortran-IV Code for Least Squares Analysis of Neutron Resonance Data", USAEC Report GA 6906 (1966).

[18]J. C. Sullivan, G. G. Warner, R. C. Block, and R. W. Hockenbury, "A Monte-Carlo Code for Neutron Capture Experiments", USAEC Report RPI - 328-155 (1969)

[19]J. E. Lynn, quoted in "Experimental Neutron Resonance Spectroscopy", J. A. Harvey, Ed., Academic Press, New York 1970, p. 163.

[20]D. Bogart and T. Semler in "Conf. on Neutron Cross Section Technology, P. B. Hemmig, Ed., USAEC Report CONF 660303 (1966), p. 502.

[21]F. H. Fröehner, "Nuclear Data for Reactors", International Atomic Energy Agency, Vienna (1970), paper CN-26/8.

[22]D. J. Hughes, "Pile Neutron Research", John Wiley and Sons, N. Y., 1956.

[23]H. W. Schmitt and C. W. Cook, Nucl. Phys. 20, 202 (1960).

[24]K. Rimawi and R. E. Chrien, contribution to this conference.

[25]J. Kantele and M. Valkonen, Phys. Letters 39B, 625 (1972).

[26]F. Rigaud, M. G. Desthuilliers, G. Y. Petit, J. L. Irigaray, G. Longo, and F. Saporetti, "Radiative Capture by Nuclei from Aℓ to La", contributed to Second Intl. Symposium on Neutron Capture γ-Ray Spectroscopy and Related Topics, Sept. 2-6, 1974, Petten (to be published).

[27]J. Vuletin, P. Kulisic, and N. Cindro, Lettere al Nuono Ciento (1974).

[28]C. F. Clement, A. M. Lane, and J. R. Rook, Nucl. Phys. 66, 273 (1965)

[29]E. Jurney (Los Alamos Scientific Laboratory, private communication.
[30]J. R. Huizenga and R. Vandenbosch, Phys. Rev. 120, 1305 (1960).
[31]W. P. Poenitz, Z. Phys. 197, 262 (1966).
[32]F. Corvi, N. Stefanon, C. Coceva, P. Giacobbe, Nucl. Phys. A203, 145 (1973).
[33]G. A. Keyworth, C. E. Olsen, F. T. Seibel, J. W. T. Dabbs, and N. W. Hill, Phys. Rev. Lett. 31, 1077 (1973).
[34]C. Coceva, "Some Aspects of Neutron Resonance Research", in II International School on Neutron Physics, Joint Inst. for Nuclear Research D3-7991, Dubna (1974).

NUCLEAR MODELS AND DATA FOR GAMMA-RAY PRODUCTION*

P. G. Young

Los Alamos Scientific Laboratory, University of California

Los Alamos, N.M. 87544

The current Evaluated Nuclear Data File (ENDF/B, Version IV) contains information on prompt gamma-ray production from neutron-induced reactions for some 38 nuclides. In addition, there is a mass of fission product yield, capture, and radioactive decay data from which certain time-dependent gamma-ray results can be calculated. These data are needed in such applications as gamma-ray heating calculations for reactors, estimates of radiation levels near nuclear facilities and weapons, shielding design calculations, and materials damage estimates. The prompt results are comprised of production cross sections, multiplicities, angular distributions, and energy spectra for secondary gamma-rays from a variety of reactions up to an incident neutron energy of 20 MeV. These data are based in many instances on experimental measurements, but nuclear model calculations, generally of a statistical nature, are also frequently used to smooth data, to interpolate between measurements, and to calculate data in unmeasured regions. The techniques and data used in determining the ENDF/B evaluations will be reviewed in this paper, and comparisons of model-code calculations and ENDF data with recent experimental results will be given.

(NUCLEAR REACTIONS ^{14}N, ^{27}Al, ^{56}Fe, Mo, ^{93}Nb, ^{181}Ta, W, ^{238}U; review selected (n,xγ) measurements, evaluations, $\sigma(E_n)$, $\sigma(E_\gamma)$. $^{93}Nb(n,x\gamma)$, E = 14.2 MeV; calculated $\sigma(E_\gamma)$. $^{181}Ta(n,x\gamma)$, E = thermal; calculated $\sigma(E_\gamma)$.)

Introduction

The need for neutron-induced gamma-ray production data in such applications as reactor heating calculations, weapon effects predictions, shielding design calculations, and materials damage estimates has motivated a rather large scale effort in recent years to provide reliable gamma-ray production evaluations through the national evaluated nuclear data system ENDF/B. Prior to the issuance of Version III of ENDF/B in 1972, formats and procedures were devised for inputting gamma-ray production cross sections, multiplicities, angular distributions and energy distributions from prompt neutron-induced reactions, and such data were included in both Versions III and IV of ENDF/B. As described in earlier papers[1,2], a mass of fission yield and radioactive decay data has also been assembled in ENDF that can be used in summation calculations to generate gamma-ray yields and spectra as a function of time following fission reactions for times greater than ~ 1 sec. There is also provision in ENDF/B for directly inputting time-dependent yields and spectra. No data of this latter type are presently in the national system, although we have recently utilized these formats at Los Alamos to include time-dependent gamma-ray spectra from ^{235}U and ^{239}Pu at times between prompt and ~ 1 second.

In this paper I will concentrate on the prompt gamma-ray data and will briefly summarize techniques, theoretical models, and experimental data that have been used to obtain evaluated data. I will not discuss individual evaluations in any detail, but I will show some examples of evaluated and calculated data and will present comparisons with experimental data.

*Work supported by the Defense Nuclear Agency and the Atomic Energy Commission.

Although the ENDF/B(IV) evaluations span the neutron energy region from 10^{-11} to 20 MeV, most of my discussion will involve either the thermal or the MeV region, mainly because most available measurements are at these energies. In the case of thermal neutrons, the principal gamma-ray-producing reaction is almost always radiative capture. The dominant reactions in the MeV region are (n,n'γ), (n,2nγ), and (n,3nγ), although charged-particle-producing reactions are frequently important for lighter elements and, of course, fission reactions in the heaviest nuclei.

Experimental Data

There are now evaluations of neutron-induced prompt gamma-ray cross sections for some 38 elements in ENDF/B, and the data for almost all materials are based at least in part on experimental data. For many years most experimental data were obtained in measurements of well-resolved, discrete gamma rays, usually with CsI, NaI, or more recently, Ge(Li) detectors. The measurements were generally made with monoenergetic neutrons from a charged-particle-induced source reaction or with thermal neutrons from a reactor. The essential elements of the experiments are determination of the incident neutron flux, measurement of the yield for a given target and experimental geometry, and determination of the detector efficiency over the relevant range of gamma-ray energy.

A sampling of results from such measurements for the 1.632- and 4.913-MeV gamma-rays that result from neutron inelastic scattering by ^{14}N is shown in Fig. 1. The solid curves represent the ENDF/B (III) evaluation[3]. There are significant discrepancies among some of the measurements, but the more recent data are generally in reasonable agreement.

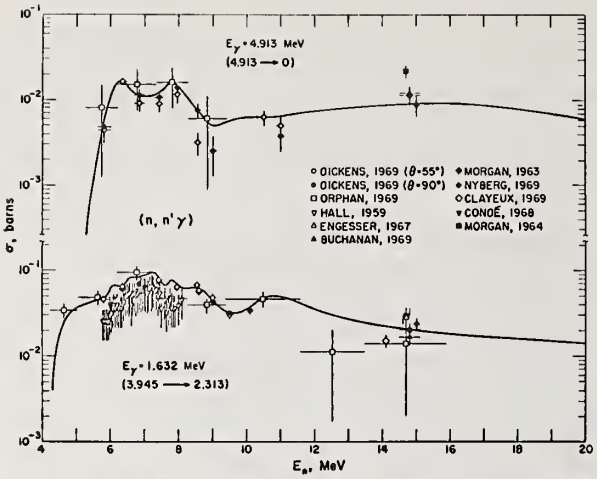

Fig. 1. Measured and evaluated photon production cross sections for the predominant gamma rays from the second and third excited states of ^{14}N. The experimental data are described in reference 3.

The experimental data by Orphan[4] in Fig. 1 were obtained in an early measurement using a continuous source of bremstrahlung neutrons from an electron linear accelerator, together with time-of-flight measurements to determine incident neutron energies. This type of measurement has been of great use in providing gamma-ray data for applications, primarily because data for a wide assortment of incident neutron energies can be obtained simultaneously in an experiment. This technique has been widely used at the Oak Ridge Electron Linear Accelerator (ORELA) in gamma-ray measurements for an assortment of materials[5], and several examples of these data are shown later.

Measurements of individual gamma-ray cross sections, such as those given in Fig. 1, have been very useful for light elements where levels are relatively widely spaced and most important gamma rays can be experimentally resolved. For nuclei with $Z \gtrsim 10$, however, levels rapidly become closely enough spaced that much of the gamma-ray cross section is in unresolved or continuum gamma rays, even for high-resolution measurements with Ge(Li) detectors. In the past few years much effort has been directed at developing and improving techniques for measuring continuum gamma rays. These measurements involve the additional complication that detector response functions for gamma rays of various energies must be obtained, usually with standard sources, and the pulse-height spectra from the actual experiment must be unfolded or stripped to obtain the gamma-ray continua.

An example of a measurement that includes both resolved and unresolved gamma rays is given in Fig. 2. Here we have the gamma-ray spectrum that results from 12-14 MeV neutron bombardment of ^{27}Al, as measured by Dickens et al.[6] at ORELA. The sharp peaks below E_γ = 4 MeV result mainly from discrete gamma-ray transitions between known levels below 5-MeV excitation in ^{27}Al. The peaks are superimposed on a relatively smooth continuum that results principally from transitions originating in states with $E_x > 5$ MeV.

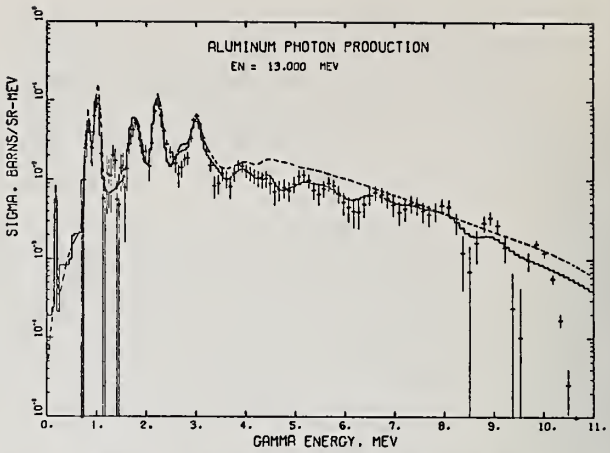

Fig. 2. Energy spectrum of gamma rays produced by 12-14 MeV bombardment of ^{27}Al for $\theta = 125^o$.

The solid curve in Fig. 2 is the ENDF/B(IV) evaluation, and the dashed curve represents the earlier Version III evaluation[7]. The latter evaluation was performed before these measurements became available and was based on a simple spin-independent model calculation that will be described later. The evaluated data in this case are represented partially as discrete gamma rays and partially as continua, and have been smeared and averaged to match the experimental conditions.

As might be expected, some difficulties have been experienced in developing techniques, and discrepancies still exist among some of the data. For example, the status in 1973 of measurements of the 0.846-MeV gamma-ray from the Fe(n,n'γ) reaction is shown in Fig. 3. The LASL[8] and TNC[9] measurements were made with monoenergetic neutron sources; the ORNL[10] and GRT[11] data were obtained with continuous energy neutron sources. NaI detectors were used in the LASL, TNC, and ORNL measurements, whereas a Ge(Li)

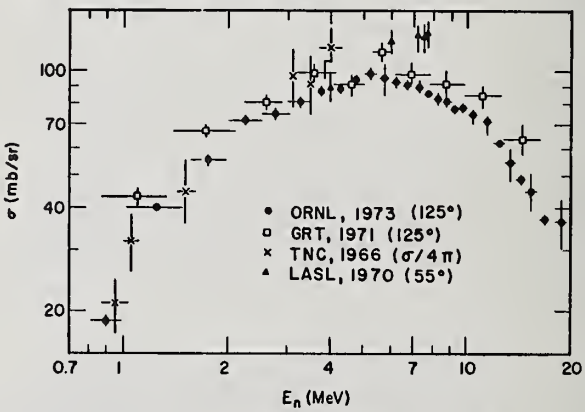

Fig. 3. Status of several measurements of the Fe(n,xγ) cross section for production of the 0.846-MeV gamma ray from ^{56}Fe in ~ 1973. The data are from experimental groups at Oak Ridge National Laboratory[10], Gulf Radiation Technology[11], Texas Nuclear Corporation[9], and Los Alamos Scientific Laboratory[8].

detector was employed in the GRT experiment. The measurements are for roughly equivalent gamma-ray energy bins. There is clear disagreement between the measurements with continuous energy and monoenergetic neutron sources, with the former results falling as much as 50% lower than the latter.

Because of the discrepancies in Fig. 3, the Fe(n,xγ) results have been examined rather closely. Corrections for Compton downscattering in the target sample have been made to the original GRT data[13]. An error of the order of 10% is suspected in the original LASL results, and those measurements have been repeated at somewhat higher energies[12]. Similarly, the original ORNL results are thought to have a normalization error at higher neutron energies, and those measurements have also been repeated[5].

The present status of the measurements is shown in Fig. 4. Except for the ORNL measurements, all the data are for the discrete 0.846-MeV line. The ORNL results were obtained by integrating the gamma-ray spectrum for E_γ = 0.71-0.95 MeV, which means there are additional contributions from unresolved gamma-rays and from the 0.930-MeV line from ^{56}Fe(n,2nγ) reactions above 12 MeV.

The line data from TNC[9], GRT[13], and LASL[12] are in reasonable agreement for E_n = 2-13 MeV, and are supported by results from Bruyères-le-Châtel[14] and Trieste[15]. The apparent discrepancy with the new ORNL[5] results is partially accounted for by the continuum gamma rays and the 0.930-MeV line that are included in the ORNL results. However, it is difficult to account for the entire difference in this way, and a discrepancy of the order of 20% is probably present at some energies. In addition, there are differences between the GRT data and the other results for E_n < 2 MeV and E_n > 13 MeV.

Thusfar, I have only discussed gamma-ray measurements for neutrons in the MeV energy region. Another class of gamma-ray data that are important for applications are measurements of gamma-ray spectra induced by thermal neutrons. Typically the same gamma-ray detection techniques that I outlined earlier are used but with thermal neutron sources. For example, at the Los Alamos neutron capture gamma-ray facility, samples are located inside the thermal column of the Omega West reactor and are viewed through a collimator by an external NaI or Ge(Li) detector.

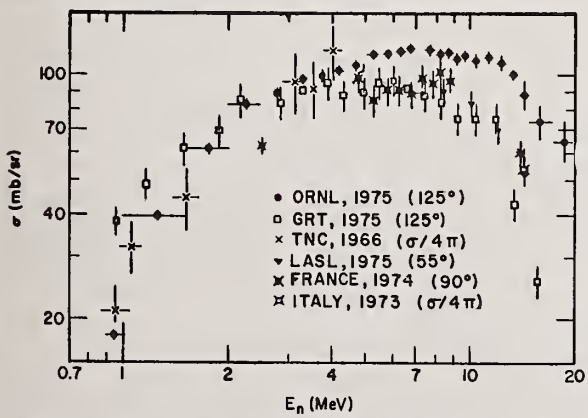

Fig. 4. Present status of measurements of the Fe(n,xγ) production cross section for the 0.846-MeV gamma ray. The data are from groups at Oak Ridge National Laboratory[5], Gulf Radiation Technology[13], Texas Nuclear Corp.[9], Los Alamos Scientific Laboratory[12], Bruyères-le-Châtel in France[14], and Trieste[15].

Recent measurements of spectra from the ^{93}Nb(n,γ) and ^{238}U(n,γ) reactions by Jurney[16] at the Los Alamos facility are shown in Fig. 5. For these measurements, a 10 cm diameter by 15 cm long NaI detector was operated in anti-coincidence with a surrounding NaI annulus.

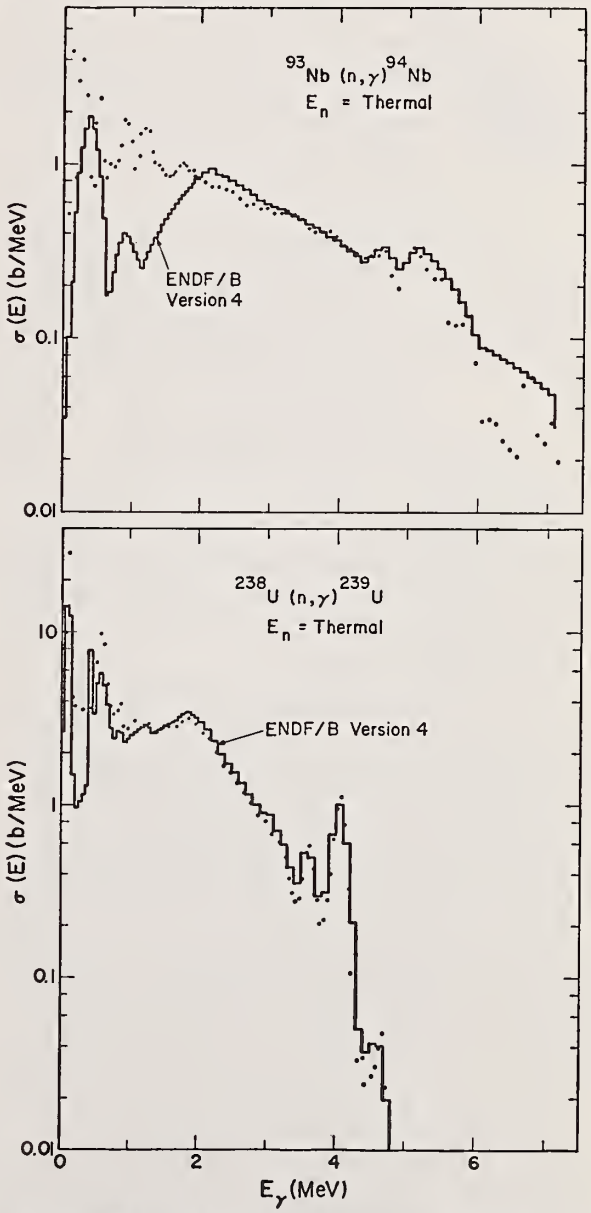

Fig. 5. Gamma-ray spectra from radiative capture of thermal neutrons by ^{93}Nb and ^{238}U. The experimental data are from a measurement by Jurney[16].

The curves given in Fig. 5 are ENDF/B(IV) evaluated spectra. The ^{93}Nb evaluation[17] was performed without the benefit of the new measurements, so the differences are not surprising. The evaluated spectrum for ^{238}U capture is based on a preliminary measurement by Jurney, and the difference between evaluation and experiment mainly reflects differences in the preliminary and final experimental data.

Nuclear Models

I would now like to very briefly describe some of the nuclear model calculations that are being used to obtain gamma-ray data for applications.

The simplest model, and one which has been frequently used, is based on a semi-empirical representation of secondary gamma-ray spectra by Howerton and Plechaty[18]. The gamma-ray spectrum from any given reaction [i.e.,(n,γ), (n,n'γ), (n,2nγ), etc.] is assumed to be of the form

$$N(E_\gamma) \propto E_\gamma \exp(-R\, E_\gamma) \quad , \qquad (1)$$

in analogy to the shape of a neutron evaporation spectrum, that is, R is analogous to an inverse nuclear temperature. This representation has recently been refined by Perkins et al.[19] to include an empirical factor that forces the above expression to zero at the maximum possible γ-ray energy, as follows:

$$N(E_\gamma) \propto E_\gamma \exp(-R\, E_\gamma) \left[\frac{E_\gamma^{max} - E_\gamma}{E_\gamma^{max} - \bar{E}_\gamma^{T}}\right] \qquad (2)$$

where E_γ^{max} is the maximum γ-ray energy for the reaction under consideration, and $\bar{E}_\gamma^{T}$ is the total energy removed by gamma rays. The new formulation specifies the use of Eq. 1 for $E_\gamma < \bar{E}_\gamma^{T}$, and the use of Eq. 2 for higher gamma energies.

This representation has been applied[19] to parameterize extensive ORELA measurements of Ta(n,xγ) reactions by Morgan et al.[20]. The shape parameter R, when represented as a function of excitation energy of the gamma-ray-producing nucleus, was found to be reasonably smoothly varying with excitation energy and reasonably insensitive to the exact nucleus involved. A comparison between the results of that analysis, which were used in the Version IV ENDF/B evaluation, and a recent measurement by Drake et al.[21] with 14.2-MeV neutrons is shown in Fig. 6. Except for very low gamma-ray energies, the shape of the spectrum is well represented by Eqs. 1 and 2. The good agreement between evaluation and experiment also indicates consistency between the Van de Graaff data of Drake et al. and the ORELA measurement by Dickens et al.

The application of Eqs. 1 and 2 for lighter elements is more problematical. A comparison is given in Fig. 7 of the Drake et al.[21] measurement at 14.2 MeV for Mo and the ENDF/B(IV) evaluation which utilized Eqs. 1 and 2. In this instance the parameters used in the calculations were necessarily based on systematics, and agreement with the recent measurement is not good.

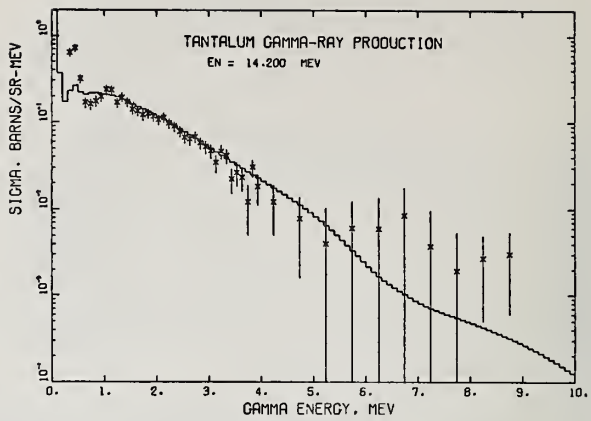

Fig. 6. Energy spectrum of gamma rays from 14.2-MeV neutron bombardment of Ta for θ = 125°.

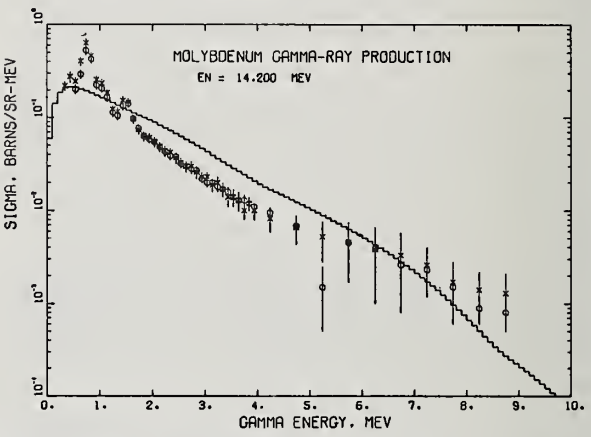

Fig. 7. Energy spectrum of gamma rays from 14.2-MeV neutron bombardment of Mo for θ = 90° and 125°.

Another relatively simple but somewhat more realistic model that has been used in evaluations is based on a spin-independent statistical theory described by Troubetzkoy[22]. To illustrate this case, a schematic diagram is given in Fig. 8 showing formation of a compound nucleus [A+1] by a neutron interaction with nucleus [A] and successive de-excitation of the system by neutron and gamma-ray emission. Each residual nucleus is divided at excitation energy E_c into continuum and discrete regions. At excitation energies below E_c, the experimentally determined gamma decay schemes for known levels are input directly into the calculation. At higher excitation energies, a continuum of levels represented by a level density function is assumed to exist.

The probability of neutron emission from continuum states is assumed to be of the form

$$N_n(\varepsilon)\,\Delta E \propto \varepsilon\, \sigma_I(\varepsilon)\, \rho(E)\Delta E \qquad (3)$$

where ε is the energy of the emitted neutron, $\sigma_I(\varepsilon)$ is the usual inverse reaction cross section (generally assumed constant), and ρ(E) is the density of states at excitation energy E in the final nucleus.

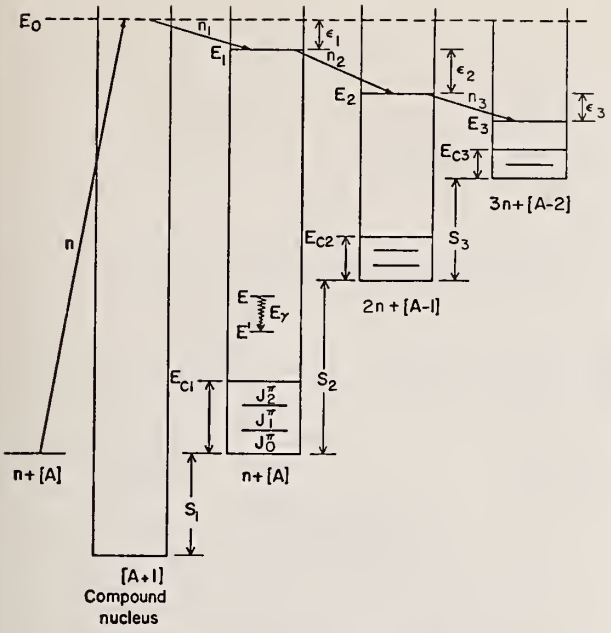

Fig. 8. Schematic representation of neutron and gamma-ray emission from (n,n'γ), (n,2nγ), and (n,3nγ) reactions.

The gamma-ray transition probability is assumed to have the energy dependence of the Weisskopf single-particle model[23]:

$$N_\gamma(E,E')\,\Delta E' \propto (E-E')^{2\ell+1}\,\rho(E')\Delta E' \qquad (4)$$

where E and E' are excitation energies of the initial and final states and ℓ is the multipole order of the transition. Competition between gamma-ray and neutron emission is ignored; the latter is assumed to always occur when energetically possible.

This model was used to calculate the unresolved part of the Al(n,xγ) spectrum for the Version III ENDF/B curve that was shown in Fig. 2. More recently, this method was used[24] to fit extensive ORELA measurements by Dickens et al.[25] of W(n,xγ) spectra at neutron energies between 1 and 20 MeV. Two parameters were varied at each neutron energy in fitting the tungsten data: the overall normalization and the level density parameter 'a' used in the Gilbert and Cameron[26] form of the level density expression. The four major W isotopes were included in the calculations, weighted according to natural abundance and using the same level density parameter for each isotope.

The fits that resulted for the capture part of the data at $\bar{E}_n$ = 1.25 MeV and for the (n,n'γ) and (n,2nγ) part at $\bar{E}_n$ = 13 MeV are shown in Fig. 9. The abrupt rise in the 1.25-MeV measured spectrum below E_γ = 1.5 MeV results from (n,n'γ) reactions which were not included in that calculation. Similarly, the 13-MeV calculation did not include (n,γ) reactions, which are responsible for the high energy gamma rays in the measured spectrum.

The fits achieved at most other neutron energies were of roughly similar quality. While these results were quite useful in smoothing, interpolating, and

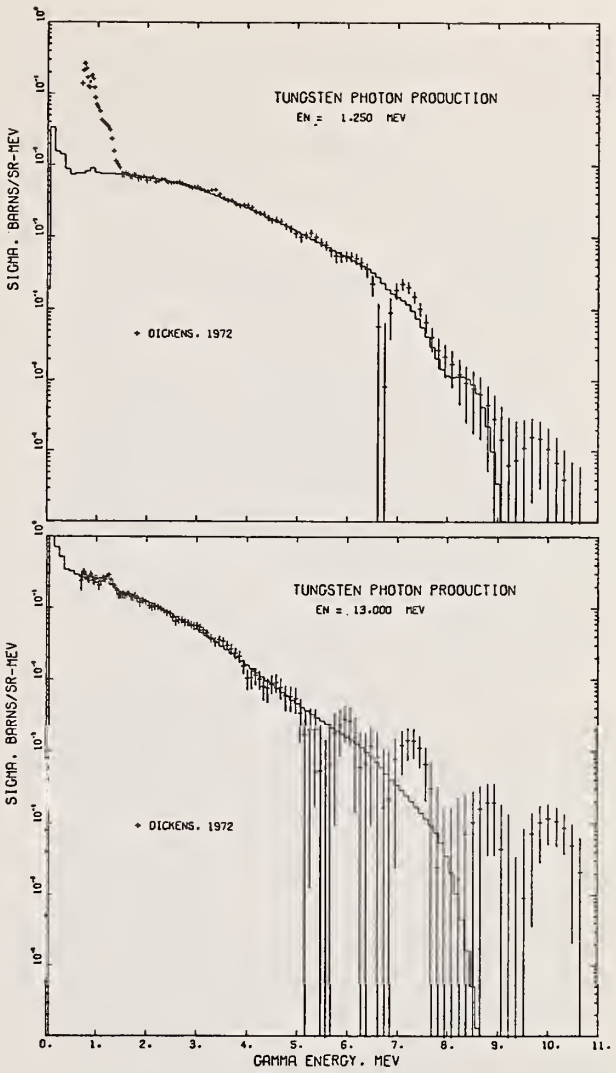

Fig. 9. Gamma-ray spectra from 1.0-1.5 and 12-14 MeV neutron bombardment of W for θ = 125°.

extrapolating the measurement, the level density parameters obtained in the analysis lie in the range a = 12 ± 2 MeV^{-1}, whereas the values tabulated for tungsten isotopes by Gilbert and Cameron[26] are roughly twice as large. Clearly, a more realistic model is desirable for cases where absolute calculations are needed and measurements are not available.

More detailed statistical calculations that include spin and parity effects and competition between gamma ray and particle emission have been performed at various laboratories (for example, see references 27-31). At Los Alamos we have recently developed a code that follows closely the theory described by Uhl[28]. This code handles de-excitation of up to ten nuclei in the decay sequence, and each decaying nucleus can emit up to six types of radiation. Externally calculated optical model transmission coefficients are used to compute particle-decay widths, and either the Weisskopf[23] single particle estimate or the Brink-Axel[32] giant dipole resonance model is used to estimate

gamma-ray widths. Gamma-ray emission by electric and magnetic dipole or quadrupole transitions are allowed. The Gilbert and Cameron[26] form of level density function is used and is matched with inputted discrete level data for up to 50 low-lying states per residual nucleus. Output information includes energy spectra from all reactions in the calculation and level excitation and gamma-ray de-excitation cross sections for all discrete states.

Preliminary calculations of the gamma-ray spectrum from 14.2-MeV neutron bombardment of ^{93}Nb are compared in Fig. 10 to a new measurement by Drake et al.[21] (crosses) and the ENDF/B(IV) evaluation[17] (solid curve) which was obtained using the semi-empirical technique[18,19] described earlier. The dashed curve shows the calculation using the Brink-Axel model to compute gamma-ray widths, and the dash-dot curve shows a similar calculation with the Weisskopf approximation. In each case, neutron transmission coefficients computed from optical model parameters by Wilmore and Hodgson[33] were used, together with a value of a = 14 MeV^{-1} for the level density parameter which is ~ 15% higher than the value tabulated by Gilbert and Cameron[26].

The Brink-Axel expression results in better overall agreement with the experiment for reasonable values of the level density parameter. The shape obtained with the Weisskopf expression fits the data very well for E_γ < 4 MeV, but falls off too rapidly at higher energies where capture is important.

Gardner[29] has observed similar effects in calculations of relative spectra from radiative capture in ^{181}Ta using a modified version of a code by Uhl[28]. Some of these results are shown in Fig. 11, where the crosses indicate the Brink-Axel calculation, the solid circles represent the Weisskopf calculation, and the solid histogram shows a measurement by Orphan et al.[34] for thermal incident neutrons. The dashed curve indicates a Los Alamos calculation made with a slightly different level density. The Brink-Axel calculations agree reasonably well with the measurements for E_γ > 2 MeV, where the experimental data

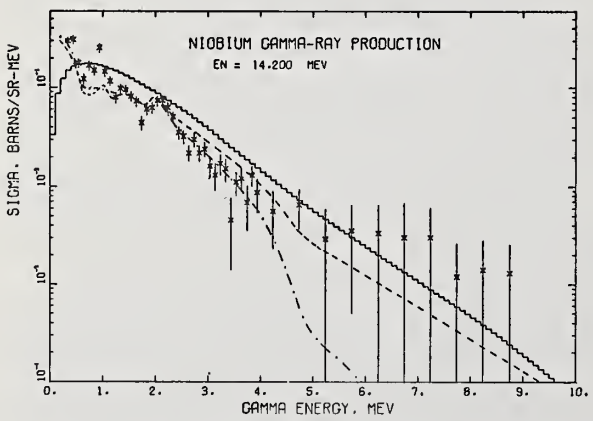

Fig. 10. Energy spectrum of gamma rays from 14.2-MeV neutron bombardment of ^{93}Nb for θ = 125°.

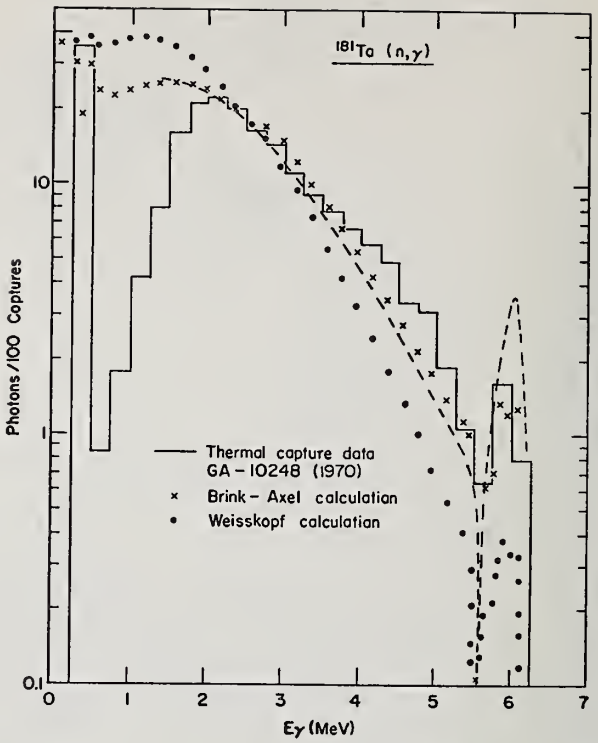

Fig. 11. Energy spectrum of gamma rays from radiative capture of thermal neutrons by Ta.

are believed to be most reliable. Gardner has found that the agreement is further improved by including a small "pigmy resonance" with $E_R \simeq 5.5$ MeV and $\Gamma \simeq 1.5$ MeV.

Conclusions

While the quality of many evaluated data sets is reasonably good, there is a good deal of new experimental data available that should be incorporated into the evaluations. There still remain some discrepancies between different modern measurements of gamma-ray production that need resolution, and an important example is the production cross section for the 0.846-MeV line from the Fe(n,n'γ) reaction. Although progress has been made in developing model code capabilities, improvements are still needed, particularly in understanding gamma-ray transition probabilities.

In closing, I wish to recognize that there are at least two major areas that I have not even touched on: gamma-ray spectra from resonance capture at epithermal neutron energies, and gamma-ray production from fissionable nuclei. These areas are both quite important and have been omitted only because of space and time limitations. In both cases there is need for further experimental data and development of improved theoretical tools.

References

1. C. W. Reich and R. G. Helmer, Bull. Am. Phys. Soc. 20, 134 (1975).

2. R. E. Schenter and F. Schmittroth, Bull. Am. Phys. Soc. 20, 135 (1975).

3. P. G. Young and D. G. Foster, Jr., "An Evaluation of the Neutron and Gamma-Ray Production Cross Sections for Nitrogen," Los Alamos Scientific Laboratory report LA-4725 (1972).

4. V. J. Orphan and C. G. Hoot, "Neutron Cross Section Data for Radiation Transport Calculations," Gulf General Atomic report GA-8006 (1969).

5. G. T. Chapman, J. K. Dickens, T. A. Love, G. L. Morgan, and E. Newman, Bull. Am. Phys. Soc. 20, 166 (1975).

6. J. K. Dickens, T. A. Love, and G. L. Morgan, "Gamma-Ray Production Due to Neutron Interactions with Aluminum for Incident Neutron Energies between 0.85 and 20-MeV: Tabulated Differential Cross Sections," Oak Ridge National Laboratory report ORNL-TM-4232 (1973).

7. P. G. Young and D. G. Foster, Jr., "A Preliminary Evaluation of the Neutron and Photon-Production Cross Sections for Aluminum," Los Alamos Scientific Laboratory report LA-4726 (1972).

8. D. M. Drake, J. C. Hopkins, C. S. Young, and H. Conde, Nucl. Sci. Eng. 40, 294 (1970).

9. R. W. Benjamin, P. S. Buchanan, and I. L. Morgan, Nucl. Phys. 79, 241 (1966).

10. J. K. Dickens, G. L. Morgan, and F. G. Perey, Nucl. Sci. Eng. 50, 311 (1973).

11. V. J. Orphan, C. G. Hoot, and J. John, "Gamma Ray Production Cross Sections for Iron and Aluminum," Gulf Radiation Technology report RT-A10743, (1971).

12. D. M. Drake, L. R. Veeser, G. Jensen, and M. Drosg, Bull. Am. Phys. Soc. 20, 168 (1975).

13. V. C. Rogers, V. J. Orphan, C. G. Hoot, V. V. Verbinski, D. G. Costello, and S. J. Friesenhahn, Bull. Am. Phys. Soc. 20, 166 (1975).

14. J. Lachkar, J. Sigaud, Y. Patin, and G. Haouat, Nucl. Sci. Engr. 55, 168 (1974).

15. U. Abbondanno, R. Giacomich, M. Lagonegro, and G. Pauli, J. Nucl. En. 27, 227 (1973).

16. E. T. Jurney, Los Alamos Scientific Laboratory, private communication (1975).

17. R. Howerton, A. Smith, P. Guenther, and J. Whalen, "Evaluated Neutronic Cross Section File for Niobium," Argonne National Laboratory report ANL/NDM-6 (1974).

18. R. J. Howerton and E. F. Plechaty, Nucl. Sci. Eng. 32, 178 (1968).

19. S. T. Perkins, R. C. Haight, and R. J. Howerton, to be published.

20. G. L. Morgan, T. A. Love, J. K. Dickens, and F. G. Perey, "Gamma-Ray Production Cross Sections of Tantalum and Carbon for Incident Neutron Energies between 0.007 and 20.0 MeV," Oak Ridge National Laboratory report ORNL-TM-3702 (1972).

21. D. M. Drake, E. D. Arthur, and M. G. Silbert, "Fourteen-MeV, Neutron-Induced Gamma-Ray Production Cross Sections," Los Alamos Scientific Laboratory report LA-5662-MS, (1974); E. D. Arthur, D. M. Drake, M. G. Silbert, and P. G. Young, Bull. Am. Phys. Soc. 20, 166 (1975).

22. E. S. Troubetzkoy, Phys. Rev. 122, 212 (1961).

23. J. M. Blatt and V. F. Weisskopf, Theoretical Nuclear Physics, Wiley, New York (1952).

24. P. G. Young, "An Evaluation of Gamma-Ray Production Cross Sections from Neutron-Induced Reactions on Tungsten," Los Alamos Scientific Laboratory report LA-5793, to be issued.

25. J. K. Dickens, T. A. Love, and G. L. Morgan, "Gamma-Ray Production Due to Neutron Interactions with Tungsten for Incident Neutron Energies between 1.0 and 20 MeV: Tabulated Differential Cross Sections," Oak Ridge National Laboratory report ORNL-4847, (1973).

26. A. Gilbert and A. G. W. Cameron, Can. J. Phys. 43, 1446 (1965).

27. J. Gilat, "GROGI2 - A Nuclear Evaporation Computer Code Description and User's Manual," Brookhaven National Laboratory report BNL-50246 (1970).

28. M. Uhl, Acta Physica Aust. 31, 245 (1970).

29. D. G. Gardner, Bull. Am. Phys. Soc. 19, 1017 (1974); and private communication.

30. C. Y. Fu, Bull. Am. Phys. Soc. 20, 149 (1975).

31. K. J. Yost, Nucl. Sci. Engr. 32, 62 (1968).

32. D. M. Brink, Thesis, Oxford University,(1955); P. Axel, Phys. Rev. 126, 671 (1962).

33. D. Wilmore and P. E. Hodgson, Nucl. Phys. 55, 673 (1964).

34. V. J. Orphan, N. C. Rasmussen, and T. L. Harper, "Line and Continuum Gamma-Ray Yields from Thermal Neutron Capture in 75 Elements," Gulf General Atomic report GA-10248,(1970).

TECHNIQUES FOR THE DETERMINATION OF NEUTRON INDUCED CHARGED PARTICLE REACTIONS

H. Liskien
Central Bureau for Nuclear Measurements
Geel, Belgium

Several fields of practical importance are existing for neutron induced charged particle reactions despite their low position within the cross section hierarchy. A survey is given on the experimental techniques employed to obtain information on cross sections, energy and angular distribution for this class of reactions. The obtainable accuracies are discussed and compared with the accuracies requested for the practical applications. The main areas of work, presently neglected, requiring future attention can be identified: (1) Reactions on medium mass nuclei not accessible by the activation method and (2) The neutron energy region between 6 and 12 MeV where suited neutron sources are not easily available.

(Neutron; cross section; charged particle; emission; techniques; application)

Introduction

Charged particles are emitted in nearly all neutron induced reactions as recoiling nuclei; as usual we are calling here a reaction a charged particle reaction, if one of the reaction products is charged and has a mass number $A \leq 4$, but exclude spallation and ternary fission. Q-values are such, that below 14 MeV neutron energy the charged particle emission cross section is mainly determined by the (n,p) and (n,α) reaction. Above that energy (n,d), (n,np), and (n,nα), also become important, while (n,t) and (n,^{3}He) are less probable. There will be later during this conference a paper on cross section systematics.[1] Here we should only remember that the low mass region is favouring charged particle emission not only due to the lower Coulomb barriers but also by the fact that here also (n,n') and (n,2n) reactions may contribute to the charged particle emission cross section via the break-up of the residual nucleus as in ^{9}Be(n,2n) or in ^{6}Li(n,n') (above 1.7 MeV) and ^{12}C(n,n') (above 8 MeV). In the following it is intended to find an answer to three questions:

- In which fields of applied physics neutron induced charged particle reactions play a part and what are the quantities of interest?
- What techniques are presently available to investigate such reactions ?
- What should be the future areas of work and what accuracies can be expected ?

Fields of Application

In Table 1 below, those application fields have been compiled for which the knowledge of neutron induced charged particle emission cross sections is essential. Especially the production of He bubbles and the stabilization of voids by He gas have been recognized as important phenomena which determine the long term behaviour of mechanical properties of structural material used in fission reactors. They are also responsible for heat conductivity defects in claddings. Most of the information stems from world request lists.[2-4] The quantity of interest is in most cases the integrated cross section. Information on the energy spectrum is only of importance in the case of neutron therapy where it is needed for KERMA calculations and in the case of ^{10}B(n,α) where the population of the first excited state in ^{7}Li has to be known. Its γ-deexcitation is observed in the boron slab detector which is frequently used for fast timing in neutron TOF-experiments. Information on angular distribution is essential for the n-p scattering process when proton recoil telescopes are used and for the ^{6}Li(n,α) reaction when ^{6}Li/solid state sandwich detectors are employed. All differential data and also information on polarization are of great value for the understanding of nuclear processes and for testing nuclear models. Their inclusion in simultaneous fits also introduces additional constraints on the possible values of the integrated cross sections. But for most of the applications it is only the integrated cross section which is of direct interest.

Available Techniques

There is nothing specific with respect to the used neutron sources and the applied techniques for flux (density) or fluence determination. What is specific, is the determination of the reaction rates and the following will be restricted to this.

Sample activation technique

Most of our experimental knowledge on cross sections for neutron induced charged particles reactions has been obtained by using the activation technique; this means the reaction rates were determined not by the number of emitted charged particles but by the number of produced residual nuclei and this via their characteristic decay. A, the activity at the end of a neutron irradiation, is related to the integrated reaction rate R by

$$R = A \frac{T}{1 - \exp(-\lambda T)}$$

$$R = A/\lambda \quad \text{if} \quad \lambda T \ll 1$$

$$R = A\,T \quad \text{if} \quad \lambda T \gg 1 \quad \text{(saturation)}$$

T is the irradiation time and λthe decay constant of the residual nucleus. This relation assumes a time constant neutron flux; a correction factor can be easily calculated, if this is not the case.
With decreasing cross section and increasing half-life the method becomes more and more difficult to apply. Using chemical separation S.M. Qaim[5] succeeded in the determination of (n,^{3}He) cross section as small as 3μb while the excitation function for the reaction ^{63}Cu(n,α) leading to the 5.2 y ^{60}Co have been determined at Geel[6]. Induced activities in this case were in the order of pCi/g and demanded low-level counting using γ-γcoincidence techniques. When extreme short half-lives are involved, attention must be paid to rapid transport between the place of irradiation and the counting position. When determining the ^{6}Li(n,p)^{6}He (0.8 s) cross section, R. Prasad and D.C. Sarkar[7] used a sample-transferring rabbit device. Another possibilitiy is not to move the sample but to pulse the source, a method which has been successfully applied by R.H. Augustson and H.O. Menlove[8] when determining delayed neutron production cross sections for the ^{9}Be(n,p)^{9}Li (170 ms)

Application field	Reactions (not complete)	Quantity needed	Energy region (MeV)	Accuracy demanded
Cross section standards for accurate flux determination	H(n,pn) $^{3}He(n,p)T$, $^{6}Li(n,t)^{4}He$, $^{10}B(n,\alpha)^{7}Li$	σ, $\frac{d\sigma}{d\Omega}$ (θ) for $^{10}B(n,\alpha)$ also branching ratio ^{7}Li / ^{7}Li	< 20 < 0.5	1 - 3 %
Spectrometry and Dosimetry in reactor, shielding and health physics problems	$^{3}He(n,p)T$, $^{6}Li(n,t)^{4}He$ ^{46}Ti, ^{54}Fe, ^{58}Ni ..... (n,p) ^{27}Al, ^{58}Ni, ^{63}Cu ..... (n,α)	for $^{6}Li(n,t)$ also $\frac{d\sigma}{d\Omega}$ (θ)	< 0.5 < 20	3 - 5 %
Long term behaviour of structural material, gas production and activation	Al, Ti, V, Cr, Fe ...(n,p)(n,α) $^{63}Cu(n,\alpha)^{60}Co$	σ	< 15	10 %
Therapy (KERMA calculations)	$^{12}C(n,\alpha)^{9}Be$, $^{12}C(n,n'\alpha)2^{4}He$ $^{14}N(n,p)^{14}C$, $^{14}N(n,d)^{13}C$ $^{16}O(n,p)^{16}N$, $^{16}O(n,\alpha)^{13}C$	$\frac{d\sigma}{dE'}$	< 20	10 %
Tritium breeding in CTR and connected problems	$^{6}Li(n,t)^{4}He$, $^{6}Li(n,n'd)^{4}He$ $^{7}Li(n,n't)^{4}He$, $^{9}Be(n,2n)2^{4}He$ $^{19}F(n,\alpha)^{16}N$	σ	< 15	3 - 10 %
Activation analysis	^{16}O, ^{27}Al, ^{37}Cl.....(n,p) ^{19}F, ^{31}P, ^{55}Mn.....(n,α)	σ	$\simeq$ 14	5 %
Safe-guards, production of delayed neutron precursors	$^{9}Be(n,p)^{9}Li$, $^{17}O(n,p)^{17}N$ $^{18}O(n,d)^{17}N$	delayed neutron emission	$\simeq$ 14	10 %

Table 1

reaction. In this special case the delayed neutron yield was of interest and therefore a neutron long counter served as activity counter. In general whenever it is feasible γ-counting is prefered compared to β-counting, especially since the availability of Ge(Li) detectors. To establish a reliable photopeak efficiency curve of such Ge(Li) detectors is at present still a rather time consuming job. Therefore the concern of the International Nuclear Data Committee (INDC) with respect to the development of multi-γ-emission rate standards[9] like ^{152}Eu, ^{133}Ba and ^{56}Co is of large interest also for this field.

Obviously the activation method demands monoenergetic neutron sources if neutron energy dependent data are wanted and it yields cross sections already integrated over emission angle and secondary energy. But this is just the information of interest for most of the applications as we have seen earlier. Also the facts that the method is not able to distinguish between (n, np), (n,pn) and (n,d) processes and that, if sample material in its natural isotopic composition is used, the induced activity may in special cases be allocated to different reactions (for example $^{46}Ti(n,p)^{46}Sc$ and $^{47}Ti(n,d)^{46}Sc$) are no serious drawbacks. The main disadvandage of the sample activation method is simply, that it demands a radioactive residual nucleus and this with suited half-life and radiation(s). This restriction can only be by-passed in the case of (n,t) reactions where the emitted charged particle itself is radioactive. Determination of (n,t) cross sections by vacuum separation of tritium followed by low level gas phase β^- counting has been performed rather recently [10]

Direct detection methods

We are now turning to those methods where the reaction rates are determined by direct observation of the emitted charged particles. In principle this demands that the sample material has to be thin compared to the range of the charged particles and that possibilities exist to discriminate against other charged particles (and gammas) which may be produced by neutrons in the sample, the structural material of the sample/detector housing or in the detector itself. Technically it is difficult to realize a 4 π geometry. Both points, thin sample and the geometry, are only partly compensated by the efficiency of 1 for the charged particle detector. Therefore the largest difficulty in performing such experiments is the low reaction rate and consequently most of the existing measurements have been performed around 14 MeV, where with the 110keV T(d,n)

resonance an intense neutron source is available.

4 π geometry

There is a group of experiments where one has tried to overcome the intensity problem by studying those reactions where the charged particle detector could serve at the same time as sample. In this way a 4 π geometry is realized, integration over all emission angles is performed by the method itself, and background events in the structural material are of minor importance. Distinction between the various kinds of emitted charged particles(p,d,α...) is often simply based on the knowledge of the various Q-values or pulse shape analysis is performed, if this was feasible. In the following Table 2 are summarized the cases which have been studied in this way. The detectors comprise all kinds of scintillators, semiconductors, proportional counters with different gas fillings and specially loaded photo-plates.

Reaction studied	Sample/detector
$^{3}He(n,p)T$	^{3}He-filled proportional counter[11]
$^{3}He(n,d)D$	
$^{6}Li(n,t)^{4}He$	^{6}LiI (Eu) scintillator[12]
$^{6}Li(n,t)^{4}He$	^{6}Li loaded glass scintillator[13]
$^{7}Li(n,n't)^{4}He$	Li loaded Ilford K_o emulsion[14]
$^{10}B(n,\alpha)^{7}Li$	BF_3-CH_4 filled proportional counter[15]
$^{14}N(n,t)^{12}C$	Ar-N_2 filled gridded ionisation chamber[16]
$^{14}N(n,\alpha)^{11}B$	P-9-O emulsion[17]
$^{14}N(n,\alpha)^{11}B$	
$^{16}O(n,\alpha)^{13}C$	
$^{28}Si(n,p)^{28}Al$	Si(Li) and Si surface barrier detector[18]
$^{28}Si(n,\alpha)^{25}Mg$	
$^{39}K(n,p)^{39}Ar$	KI(Tl) scintillator[19]
$^{39}K(n,\alpha)^{36}Cl$	
$^{40}Ca(n,p)^{40}K$	CaF_2 (Eu) scintillator[20]
$^{40}Ca(n,\alpha)^{37}Ar$	
$^{73}Ge(n,\alpha)^{70}Zn$	Ge(Li) detector[21]
$^{127}Cs^{133}I(n,\alpha)$	CsI (Tl) scintillator[22]

Table 2

Other geometries

The first systematic studies of charged particle spectra and their angular dependece of neutron induced reactions have been made by using photographic plates.[22] Presently employed experimental set-ups to determine double differential cross sections are discussed on the basis of two recent publications:
Bormann et al.[21] studied (n,α)-reactions on ^{63}Cu, Nb, Rh, and ^{107}Ag. Neutrons of 14 MeV are produced via the $T(d,n)^{4}He$ reaction by bombarding a T-Ti target with 150 keV deuterons. Under this condition the associated particle method is conveniently applied and allows the determination of the neutron flux. The sample foil is mounted in a low-mass chamber and observed by a CsI(Tl) crystal. Chamber and scintillation detector are turnable to allow different emission angles (relative to the neutron direction) to be observed. There are two measures to reduce the background from the reaction chamber and from the CsI-crystal itself:

(a) A lead wedge between neutron source and charged particle detector; and
(b) The demand of a fast coincidence between the α-particle associated with each neutron and the charged particle count. For this the sample foil is only irradiated by those neutrons which correspond kinematically to the associated α-particles observed in this case at 90°. A variable aperture allows fine adjustment.

Pulse shape discrimination for the pulses from the CsI-(Tl)-scintillator are used for particle identification.

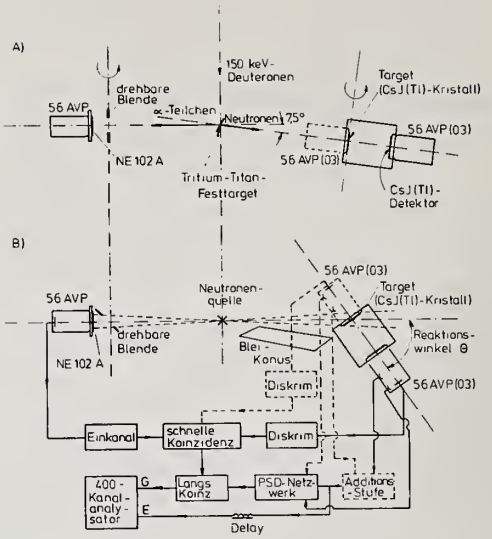

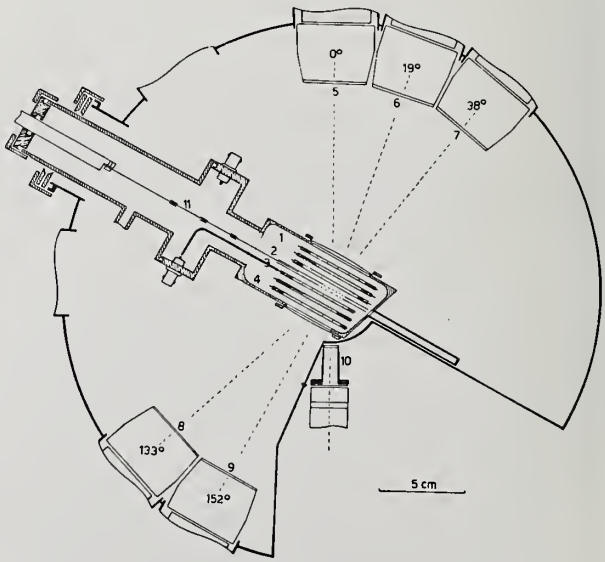

Salathe et al.[23] have determined double differential (n,α)-cross sections for C and N in the 15 to 19 MeV energy range. The neutron producing target is in this a double window tritium gas cell and the determination of the neutron flux is performed relative to the n-p scattering cross section by employing a calibrated plastic scintillator. The reaction chamber contains essentially five telescope counters. Each consists of two proportional counters for $\Delta E/\Delta x$-determination and one CsI(Tl)-scintillator for energy determination, all three working in coincidence. By this the background is reduced drastically. By an analog electronics a function $0.48 \log (E + 0.12\,\Delta E) + \log \Delta E$ is constructed which is constant whithin ± 3 % for α-particles and serves for particle identification. In practice there are only two $\Delta E/\Delta x$ counter at each side of the sample foil which are common for all relevant E-counters. To obtain a decoupling of the two counters they are separated by a highly transparent metallic grid while a 0.6 mg/cm^2 Ni foil seperates the proportional counters from the reaction chamber. The above described two apparatus are used with monoenergetic neutrons. In connection with the Karlsruhe Isochronous Cyclotron, which is partly also used as ns-pulsed neutron source, a set of semiconductor telescopes have been successfully employed to study the ^{9}Be(n,α) reaction above 8 MeV neutron energy[24]. Additional fast signals from the silicon detector which served as E-counter were used for neutron energy determination by the time-of-flight method.

Accuracies and Future Areas of Work

A presently organized international comparison of fluences of fast monoenergetic neutrons confirms that ± 3 % is a realistic uncertainty contribution for this factor.[29] The uncertainty due to sample assay is normally negligible. An exception is the assay of scintillation crystals (e.g. the ^{6}Li content of glass scintillators) when they serve at the same time as sample.

Most accurate results on integrated cross sections - namely 5 to 6 %, if the relevant decay scheme is well established - can be expected from the sample activation method. The direct detection method is capable to produce data in the 10 to 15 % accuracy range. This uncertainty includes contributions due to the necessary integration over all emission angles and the full range of secondary energies, due to the necessary particle discrimination, and due to statistics which is in this case often not at all negligible.

Nevertheless there are discrepancies up to a factor of two as seen in the figure 3.
This discrepancy becomes even more severe, if one notes that all the results are very recent (1972 or later) and that it concerns a reaction which is regarded at lower energies as a standard.

The experimental information on microscopic cross sections is to a very large extent compiled by the four Neutron Data Centers and available through them. Comparison with the needs in the field which is covered here yields immediately two main areas of work which require future attention.

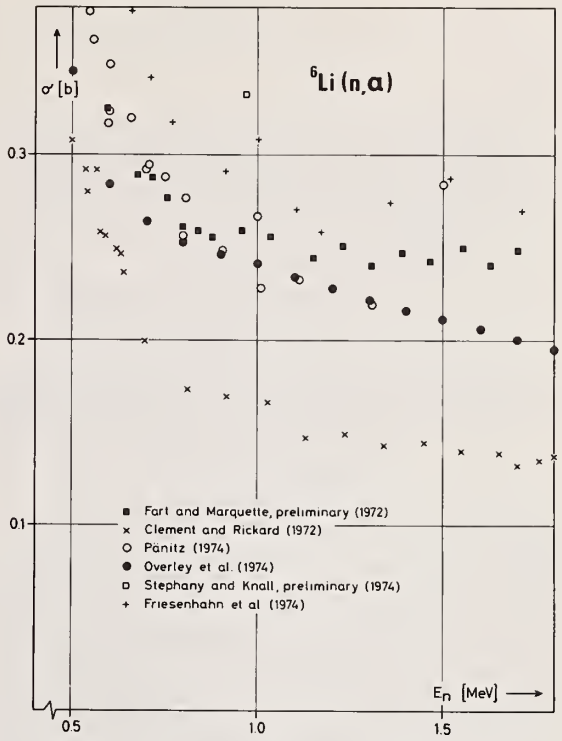

Those reactions which are not accessible to the sample activation method have mostly been studied only under especially convenient conditions (14 MeV T-D neutrons, sample identical with charged particle detector). Unfortunately the demands for cross section determination are governed by the needs and do not care for the experimental difficulties. A special effort to determine (n,p) and (n,α) cross sections for medium mass nuclei especially of structural material is requested. Data in the 6 to 12 MeV range are extremely scarce even if the relative simple sample activation method would be applicable. This is due to the difficulties to produce monoenergetic neutrons in this energy range. Figure 4 demonstrates that accelerators with energies of 5 to 8 MeV are needed to produce neutrons of this energy and there are only a few of this machines which have sufficient ion current and are available for neutron work.

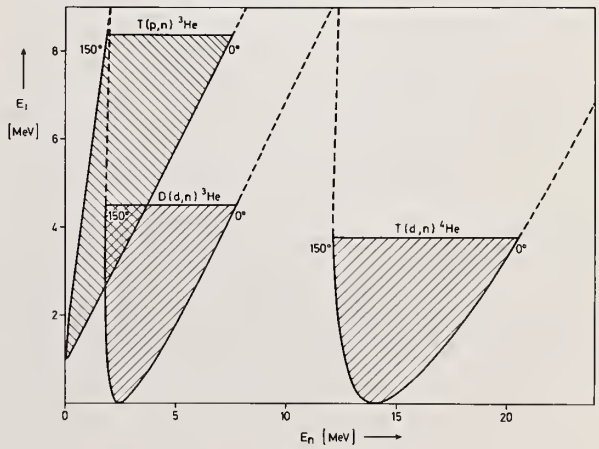

[1] S. Pearlstein, Presented at the Conference on Nuclear Cross Sections and Technology, March 3-7, Washington, DC (1975)
[2] World Request List for Neutron Data Measurements for Nuclear Reactors, INDC(SEC)-38/U (1974)
[3] Request Lists of Nuclear Data for Controlled Fusion Research as submitted to IAEA by Member States, INDC(NDS)-57/U+F (1973)
[4] Request List of Nuclear Data for Safeguards Development Purposes as submitted to IAEA by Member States, INDC(NDS)-50/U+S (1973)
[5] S.M. Qaim, J. Inorg. Nucl. Chem. 36, 239 (1974)
[6] H. Liskien and A. Paulsen, Nukleonik 8, 315 (1966) A. Paulsen, Nukleonik 10, 91 (1967)
[7] R. Prasad and D.C. Sarkar, Nuovo Cim. 3A, 467 (1971)
[8] R.H. Augustson and H.O. Menlove, Nucl. Sci. Eng. 54, 190 (1974)
[9] Technical Minutes of the 7th INDC Meeting to be published (1975)
[10] S.M. Qaim, R. Wölfle, and G. Stöckling, J. Radioanalyt. Chem. 21, 395 (1974)
[11] A.R. Sayres, K.W. Jones, and C.S. Wu, Phys. Rev. 122, 1853 (1961)
[12] F. Gabbard, R.H. Davis, and T.W. Bonner, Phys. Rev. 114, 201 (1959)
[13] W.P. Poenitz, Z. Physik 268, 359 (1974)
[14] B. Antolkovic, Nucl. Phys. A219, 332 (1974)
[15] S.J. Friesenhahn, V.J. Orphan, A.D. Carlson, M.P. Fricke, and W.M. Lopez, INTEL-RT 7011-001 (1974)
[16] W. Scobel, R.W. Fink, and M. Borman, Z. Phys 197, 124 (1966)
[17] M.V. Kirichenko and Z.I. Solov'eva, Sov. J. Nucl. Phys. 16, 9 (1973)
[18] D.W. Mingay, J.P.F. Sellschop, and P.M. Johnson, Nucl. Instr. Meth. 94, 497 (1971)
[19] C.M. Bartle, P.B. Johnson, and N.G. Chapman, Nucl. Phys. A220, 395 (1974)
[20] P. Huber, W. Hunn, E. Steiner, and R. Wagner, Helv. Phys. Acta 38, 217 (1965)
[21] M. Bormann, W. Schmidt, V. Schröder, W. Scobel, and U. Seebeck, Nucl. Phys. A186, 65 (1972)
[22] D.L. Allan, Proc. Phys. Soc. A70, 195 (1957)
[23] W. Salathe, E. Baumgartner, and P. Huber, Helv. Phys. Acta 44, 815 (1971)
[24] L. Kropp and P. Forti, Nucl. Instr. Meth. 104, 381 (1972)
[25] E. Fort and J.P. Marquette, EANDC(E)-148'U' (1972)
[26] P.J. Clements and I.C. Rickard, AERE-R 7075 (1972)
[27] J.C. Overley, R.M. Sealock and D.H. Ehlers, Nucl. Phys. A221, 573 (1974)
[28] W.P. Stephany and G.F. Knoll, EANDC(US)-186'U' (1973)
[29] H. Liskien, CONF-701002 p. 343 (1970)

INTEGRAL MEASUREMENTS TO TEST SHIELDING CROSS SECTIONS*

L. Harris, Jr., J. C. Young, N. A. Lurie, D. K. Steinman,
S. J. Friesenhahn, D. E. Bryan, W. E. Gober, and L. Schänzler**
IRT Corporation
San Diego, California 92138

The pulsed-white-neutron-source, time-of-flight method and an NE-213 detector have been used for two integral shielding measurements. Incident-neutron-energy-dependent measurements of scattered neutrons and secondary gamma rays from small samples of Be, C, N, H_2O and Fe have been performed. Results for N, including unfolded energy spectra of scattered neutrons and secondary gamma rays at 125°, are presented. Time-dependent measurements of leakage neutrons and secondary gamma rays from a thick concrete and steel shield are described, and some data are presented.

(Integral measurements; nitrogen cross sections; concrete and steel shield; NE-213 detector; neutron spectrum unfolding; gamma-ray spectrum unfolding)

Introduction

The pulsed-white-neutron source, time-of-flight (TOF) method developed for the 1969 integral measurements of Harris and Kendrick[1-3] has been used for two new measurements at the IRT electron linear accelerator (Linac) facility. The general geometry used for the measurements is shown in Figure 1. A high-power, water-cooled Ta/Aℓ/Be Linac target was used to produce 50-nsec (FWHM) pulses of photoneutrons with energies from thermal to above 20 MeV. In contrast with many earlier pulsed-neutron-source, TOF shielding experiments, the shielding material under study was located at the detector end of the neutron flight path, rather than at the source end. As a consequence, when the average residence time of neutrons in the shielding material is very small compared to the neutron TOF, the measured time-of-arrival at the detector is very nearly equal to the neutron TOF, and thus can be correlated directly with incident neutron energy. Because, for example, count rates can be measured as a function of incident neutron energy and the same quantity can be calculated directly using adjoint transport methods, these measurements are sometimes described as adjoint measurements.

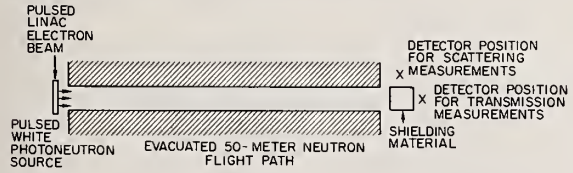

Figure 1. General geometry used for IRT integral shielding measurements

The first of the measurements reported here clearly meets the criteria of an adjoint measurement. The shielding materials consist of small samples of Be, C (graphite), N (liquid nitrogen), H_2O and Fe. The liquid nitrogen and water were held in low-density (0.03 g/cm^3) styrofoam (C_8H_8) containers. Separate scattering measurements, performed for each sample, provide data for high-sensitivity tests of differential neutron scattering and gamma-ray production cross sections. Several results of the nitrogen measurements will be presented.

The second experiment, which involved a thick concrete and steel shield, also demonstrated certain features of adjoint measurements. Some results of the transmission measurements will be presented also. Before discussing the measurements further, some new data on the NE-213 detector, which was used for most of the measurements, will be presented.

NE-213 Detector

NE-213 is a clear liquid organic ($CH_{1.21}$) scintillator. The 4.78-cm-high by 4.60-cm-diameter scintillator was contained in a Nuclear Enterprise type-V clear pyrex cell. The pyrex cell was enclosed by an Aℓ foil reflector, black plastic electrical tape, and a Perfection Mica Model 22P70N co-netic magnetic shield. Neutrons and gamma rays were measured simultaneously using this detector. Three parameters (time, pulse height, and pulse shape) were recorded for each detection event using an on-line computer for data acquisition. Pulse-shape discrimination was used to distinguish between neutrons and gamma rays. For neutrons, the detector functions as a proton-recoil spectrometer, and for gamma rays it functions as a Compton spectrometer. Two types of neutron and gamma-ray data, count rates and unfolded energy spectra, were obtained. Spectrum unfolding was performed using the FERDOR code.[4-6] A 140 x 70 neutron response matrix was measured using the pulsed-white-neutron-source, TOF method[7] and normalized to efficiencies (0.1 light unit bias) derived from the calculated efficiency tables reported by Verbinski et al.[8] Verbinski's light unit is defined as one light unit equals 1.13 times the Compton-edge half-height of the pulse-height spectrum due to 1.275-MeV gamma rays from ^{22}Na.

The new data reported here for this detector are a set of gamma-ray response functions shown in Figure 2. These were calculated using the 3-D, Monte Carlo, coupled photon-electron transport code, SANDYL.[9] Absolute efficiencies (0.4 light unit bias) derived from these calculated response functions agree well with measured efficiencies. A 186 x 93 gamma-ray response matrix, which was generated by interpolation from the calculated response functions, has been used successfully for unfolding a variety of gamma-ray energy spectra. Some of these will be shown below.

When a gamma-ray detector is used in mixed neutron and gamma-ray fluxes, as for the measurements reported here, neutron-induced gamma-ray production in the detector produces gamma-ray counts. The effect can be important when the neutron-to-gamma-ray ratio is high. For this NE-213 detector, the effect can be estimated and corrected for using the data on neutron-induced gamma-ray counts shown in Figure 3.

*Work supported by Defense Nuclear Agency and U.S. Air Force Space and Missile Systems Organization.

**Visiting Scientist, West German Ministry of Defense.

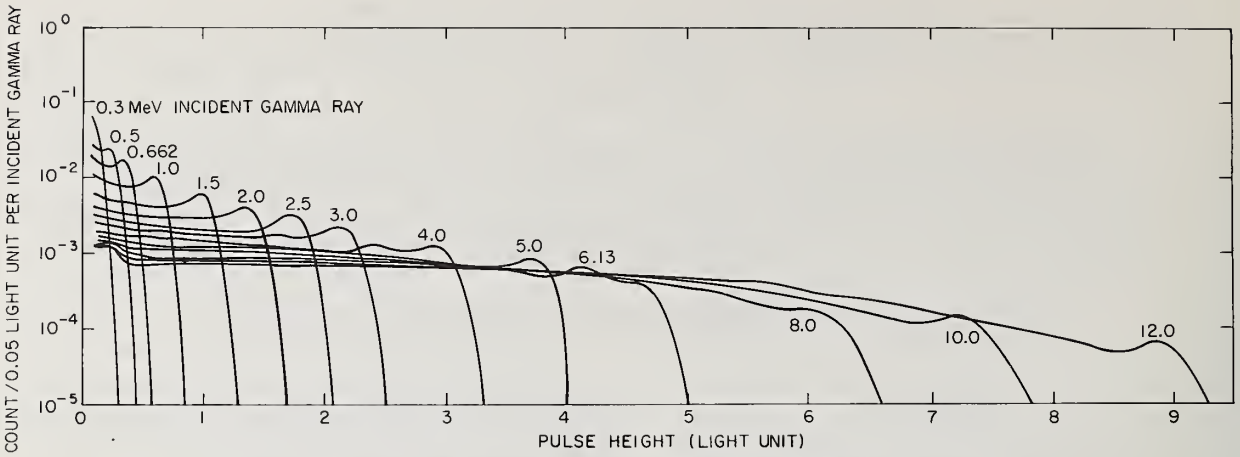

Figure 2. Calculated gamma-ray response functions for NE-213 detector

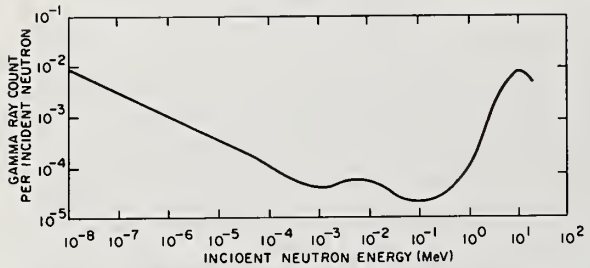

Figure 3. Gamma-ray counts due to neutron-induced gamma-ray production in NE-213 detector

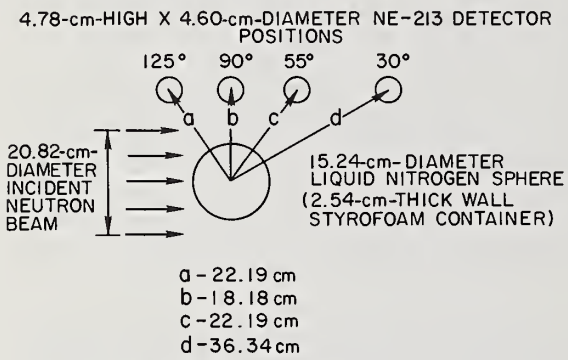

Figure 4. Geometry used for small-sample scattering measurements for N

Small-Sample Scattering Measurements

The geometry used for the small-sample scattering measurements for N is shown in Figure 4. The measurements were performed for incident neutrons from 2 to 20 MeV, average scattering angles of 30, 55, 90, and 125°, scattered neutrons from 1 to 12 MeV, and secondary gamma rays from 0.5 to 8 MeV. The liquid nitrogen sample was held in a spherical styrofoam container which was gravity-filled from an overhead reservoir.

Data reduction included: (1) correcting for dead time and pulse pileup rejection; (2) separating neutron and gamma-ray counts; (3) normalizing count rates to source monitor; (4) calculating standard deviations due to counting statistics; (5) subtracting time-dependent background measured with no sample present; (6) transforming from TOF to incident neutron energy; and (7) dividing the resulting energy-dependent count rate (count/MeV-source monitor) by the source spectrum (incident neutron/MeV-cm^2-source monitor) to obtain count per incident neutron/cm^2. The resulting data due to scattered neutrons and secondary gamma rays from N at 125° are shown in Figure 5.

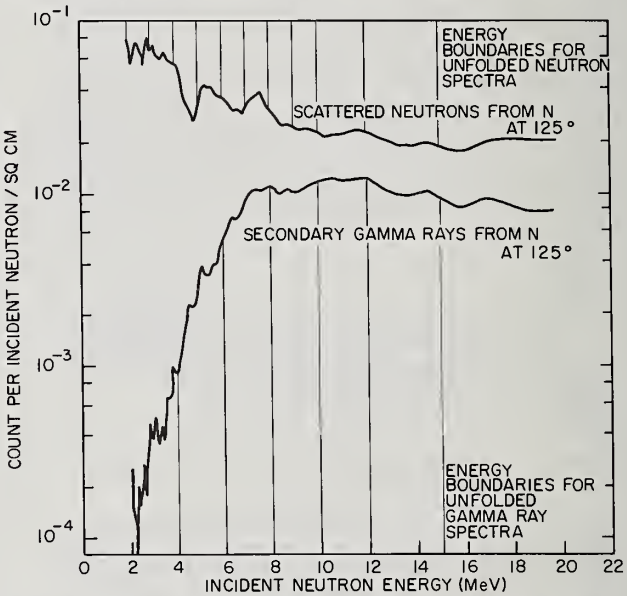

Figure 5. Measured count per incident neutron/cm^2 due to scattered neutrons and secondary gamma rays from N at 125°

The thin vertical lines in Figure 5 show the incident neutron energy boundaries used for the unfolded energy spectra. Ten unfolded scattered neutron spectra are shown in Figure 6, and five unfolded secondary gamma-ray spectra are shown in Figure 7. Both sets of spectra show considerable variation with incident neutron energy. The neutron spectra are dominated by peaks due to single elastic scattering interactions in the N sample. The gamma-ray spectra seem to be dominated by gamma-ray lines near 2.0, 4.8, and 6.2 MeV. Preliminary data for the C and N measurements were published earlier.[10-12] A report presenting final data

(figures and tables) for the Be, C, N, H_2O, and Fe measurements is in preparation.

Similar measurements, which include unfolded neutron energy spectra, have been reported by Morgan et al.[13,14] for scattered neutrons from annular samples of C and Fe.

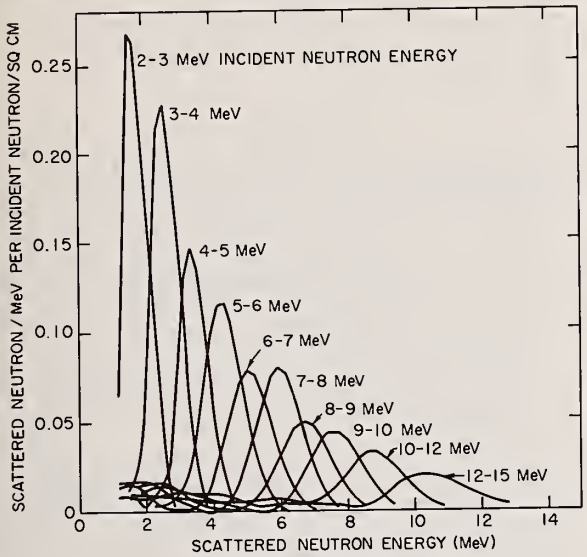

Figure 6. Measured energy spectra of scattered neutrons from N at 125°

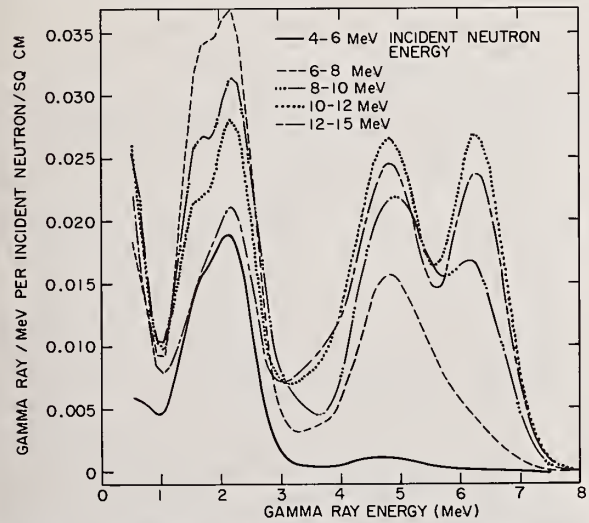

Figure 7. Measured energy spectra of secondary gamma rays from N at 125°

Thick-Shield Transmission Measurements

The geometry used for the transmission measurements through the thick concrete and steel (23 wt %) shield is shown in Figure 8. The 88.42-cm-thick shield consists of 81.28 cm of ordinary concrete (2.25 g/cm^3 and 5.10 wt % H_2O) and 7.14 cm of hot-rolled steel (7.85 g/cm^3), with the concrete slabs and steel plates alternating as indicated in the figure. The same NE-213 detector was used at the centerline detector position to measure time-dependent neutron and gamma-ray count rates. The resulting data are shown in Figure 9. The incident neutron count rate, measured immediately before the concrete and steel shield was set up, is shown at the top of the figure. The separation between the count rates due to incident neutrons and leakage neutrons is a measure of the neutron attenuation properties of the shield. The peaks in the count rates at 2.5 μsec are due to neutron streaming through the 2.35-MeV antiresonance in the total cross section of oxygen, the major constituent (60 atom %) of concrete. Unfolded energy spectra of leakage neutrons and leakage secondary gamma rays were obtained for the incident neutron energy intervals indicated in the figure, and will be included in a report which is in preparation.

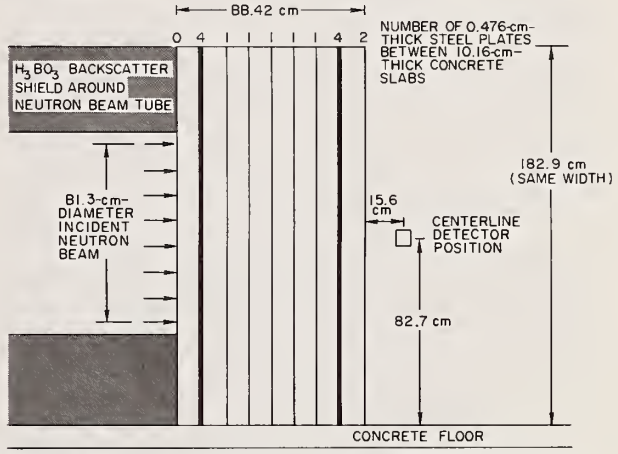

Figure 8. Geometry used for thick-shield transmission measurements for concrete and steel shield

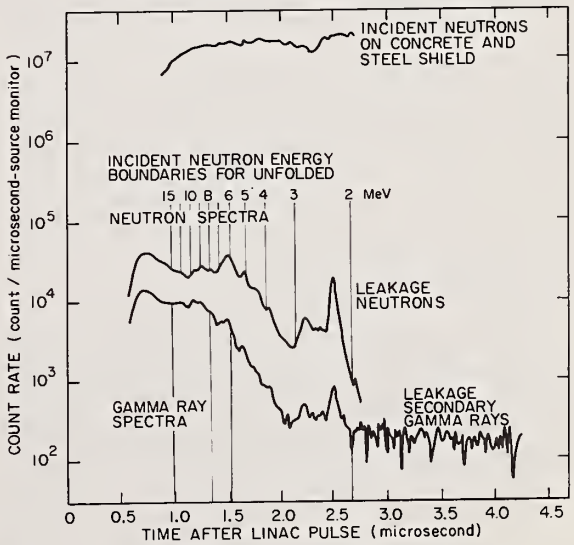

Figure 9. Time-dependent count rates measured with NE-213 detector behind concrete and steel shield

Time-dependent count rates due to capture gamma rays leaking from the shield were measured for times out to 500 μsec. These count rates, which after about 125 μsec decrease exponentially with a 280-μsec die-away time, are shown in Figure 10. In addition, time dependent count rates due to thermal neutrons leaking from the shield were measured using a 20-cm-long by 5-cm-diameter, 4-atm, ^{3}He proportional counter. These

count rates were multiplied by 0.22 and plotted on Figure 10 for comparison with those due to capture gamma rays. The thermal neutron count rates build up to a maximum near 80 μsec, and then begin an exponential dieaway. After about 125 μsec, the slopes of both count rates are about the same.

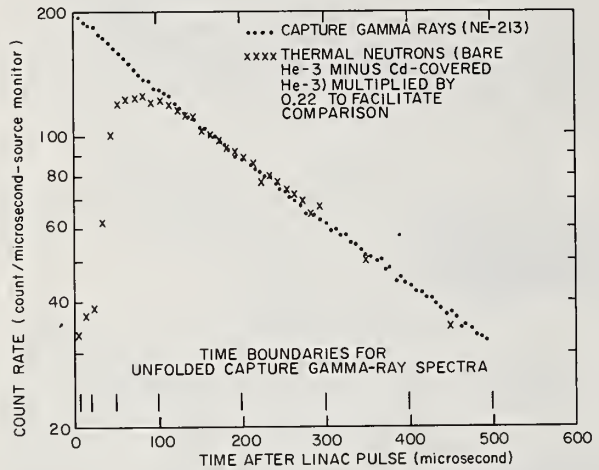

Figure 10. Time-dependent count rates measured with NE-213 and ^{3}He detectors behind concrete and steel shield

Conclusions

The two integral shielding measurements reported here have rather different cross-section sensitivities. The small-sample scattering measurements are dominated by first-collision interactions. The measured data are closely correlated with differential neutron scattering and gamma-ray production cross sections as functions of incident neutron energy from 2 to 20 MeV, scattering angle from 30 to 125°, scattered neutron energy from 1 to 12 MeV, and secondary gamma-ray energy from 0.5 to 8 MeV. For the cross section evaluator, differences between the measured small-sample data and data calculated using transport codes should be readily interpreted in terms of specific cross-section deficiencies over the full range of well-defined incident neutron energies from 2 to 20 MeV.

The thick-shield transmission measurements are dominated by multiple-collision interactions. Comparison of the measured thick-shield data with data calculated using time-dependent transport codes will test both the codes and cross sections for 2-D, deep-penetration transport through two important shielding materials, concrete and steel.

References

1. L. Harris, Jr., et al., "Time-Dependent Fast-Neutron and Secondary Gamma-Ray Spectrum Measurements in Concrete - Volumes I and II," DASA 2401-1 and DASA 2401-2, Gulf General Atomic Incorporated (1969).

2. L. Harris, Jr. and H. Kendrick, "Time-Dependent Fast-Neutron and Secondary Gamma-Ray Spectrum Measurements in Concrete - Volume III," DNA 2401-3, Gulf Radiation Technology (1972).

3. L. Harris, Jr., "Developments in Integral Shielding Experiments Involving Fast-Neutron Transport," CONF-720901, Book 1, 385-396, American Nuclear Society National Topical Meeting on New Developments in Reactor Physics and Shielding (1972).

4. W. R. Burrus, "Utilization of *a priori* Information by Means of Mathematical Programming in the Statistical Interpretation of Measured Distributions," ORNL-3743, Oak Ridge National Laboratory (1965).

5. W. R. Burrus and V. V. Verbinski, "Fast Neutron Spectroscopy with Thick Organic Scintillators," Nucl. Instr. Methods 67, 181 (1969).

6. H. Kendrick and S. M. Sperling, "An Introduction to the Principles and Use of the FERDOR Unfolding Code," GA-9882, Gulf Radiation Technology (1970).

7. H. Kendrick and L. Harris, Jr., "Numerical and Experimental Studies of Spectral Unfolding - Vol. I," DASA 2720-1, Gulf Radiation Technology (1971).

8. V. V. Verbinski, et al., "Calibration of an Organic Scintillator for Neutron Spectrometry," Nucl. Instr. Methods 65, 8 (1968).

9. H. M. Colbert, "SANDYL: A Computer Program for Calculating Combined Photon-Electron Transport in Complex Systems," SLL-74-0012, Sandia Livermore Laboratories (1974).

10. L. Harris, Jr., G. D. Trimble, and J. C. Young, "Integral Experiment to Test Carbon and Nitrogen Cross Sections," DNA-2986F, Gulf Radiation Technology (1972).

11. L. Harris, Jr., G. D. Trimble, and J. C. Young, "Integral Experiment to Test Gamma-Ray Production and Neutron Scattering Cross Sections," Trans. Am. Nucl. Soc. 15, 960 (1972).

12. L. Harris, Jr. and J. C. Young, "Energy Spectrum Measurements of Scattered Neutrons from Nitrogen," Trans. Am. Nucl. Soc. 17, 550 (1973).

13. G. L. Morgan, T. A. Love, and F. G. Perey, "Integral Neutron Scattering Measurements on Carbon from 1 to 20 MeV," ORNL-TM-4157, Oak Ridge National Laboratory (1973).

14. G. L. Morgan, T. A. Love, and F. G. Perey, "Integral Neutron Scattering Measurements on Iron from 1 to 20 MeV," ORNL-TM-4193, Oak Ridge National Laboratory (1973).

EVALUATION, UNCERTAINTY ESTIMATION AND ADJUSTMENT OF CAPTURE CROSS SECTIONS FOR FISSION PRODUCT NUCLEI

H. Gruppelaar, J.B. Dragt, A.J. Janssen and J.W.M. Dekker
Reactor Centrum Nederland, Petten, The Netherlands

Part of the results of integral measurements, which have been performed in the STEK-facility for about 60 fission product nuclei, have been analysed and used for adjustment of capture cross sections needed for fast breeders. This paper gives an outline of the method used to obtain these adjusted cross sections as well as some conclusions for σ_c of $^{101,102,104}Ru$, ^{127}I).

(Evaluation, sensitivity analysis, adjustment, σ_c, fission products, $^{101,102,104}Ru$, ^{127}I).

Introduction

This paper describes part of the results which have been obtained from the STEK project[1], which is a Dutch contribution to the DeBeNeLux co-operation on fast breeder development. The main goal of this project is to improve the knowledge of σ_c for a number of about 60 long-lived fission products by means of integral (central reactivity worth) measurements in the STEK reactor. Results obtained from lumped fission-product samples have been published[2] previously. The methods for the interpretation of the integral data for individual isotopes are based on our previous experiences[1-5], however, with a number of important changes, viz.: (i) a more sophisticated cross section and uncertainty evaluation than in the past[4,5], (ii) the introduction of self-shielded reactivity worths in the group constant adjustment scheme, and (iii) adjustment of some nuclear parameters. The presently adopted methods are briefly explained in the following sections, referring to fig. 1 for the links between the various parts. In the last section some results are reported for σ_c of $^{101,102,104}Ru$, ^{127}I.

Evaluation and calculation of group constants

For each nuclide measured, the point cross sections σ_t, σ_{el}, σ_c, σ_{in} and σ_{n2n} are being evaluated, with emphasis on σ_c for which an uncertainty analysis consistent with the evaluation is given. The word evaluation in this context means the calculation of cross sections from nuclear parameters with the possibility of manual adjustments of these parameters in order to obtain agreement with the (few) experimental point cross sections.

In the resolved resonance region a modified version of the code SIGMA-2 is used.[6] Above this energy region Hauser-Feshbach theory with width fluctuation correction is applied. Below a few tens of keV the transmission coefficients are calculated from strength functions, whereas at higher energies the optical model[7] is used. The codes for this calculation have been derived from codes developed at Bologna.[8,9] All codes have been coupled together in order to produce a consistent cross section file (RCN-2 library in KEDAK format) in one computer run. In the field of parameter evaluation an extensive co-operation with experienced groups in France and Italy has been established.

For the calculation of group constants and inelastic scattering matrices a code has been developed which reads from a file in KEDAK format and produces group constants in the 26-group ABBN scheme.[10] As a weighting spectrum an averaged flux spectrum for all five STEK cores has been used. Self-shielding factors for the group constants of the measured samples are calculated with an improved version of the code TRIX.[11] With these codes a macroscopic group constant library is obtained for the measured samples, including infinite dilution group constants (fig. 1).

Uncertainty estimation

Uncertainty estimation here means the calculation of standard deviations and correlation coefficients for σ_c, condensed to 26-group constants. This error calculation is based on calculated cross sections rather than on measured point cross sections. The method used follows ref.[5] with the following modifications: (i) the use of a better nuclear model, (ii) treatment of errors in self-shielded cross sections in the resonance region, and (iii) a better treatment of errors due to uncertainties in the weighting spectrum in the resolved resonance region.

It can be seen from fig. 1 that the uncertainty calculation is split up into three parts, which are finally combined to obtain the complete co-variance matrix for all group constants involved in the adjustment calculation. The error calculation of σ_c above the resonance region is identical for infinitely diluted and self-shielded group constants.

Statistical model errors

Under this subheading errors due to the statistical nature of the model itself are intended, which arise from: (i) fluctuations in the number of resonances per energy group (Dyson-Mehta statistics), (ii) fluctuations in the level widths (Porter-Thomas statistics), and (iii) fluctuations in the number of bound levels of the target nucleus at energies where these levels are calculated with a statistical model (Poisson statistics). Expressions to calculate the co-variance matrix resulting from these fluctuations have been given in ref.[12].

Parameter sensitivities

For the calculation of the sensitivities of σ_c for a change of one standard deviation of a statistical-model parameter, the same model as described before is used, except that the neutron transmission coefficients are calculated from strength functions S_ℓ (ℓ=0 to 4). The following parameters are varied: S_ℓ; the average radiation width at neutron binding energy, $\langle\Gamma_\gamma\rangle$; the giant resonance energy and width, E_r and Γ_r; the level density parameters for the compound nucleus and target nucleus, a_c and a_t. No correlations are assumed between different parameters; correlations for the same parameter but different isotopes are admitted.

Resolved resonance region

The error calculation in the resolved region is based on the single level Breit-Wigner formula.[5] The weighting spectrum within one energy group is assumed to have E^α-energy dependence. Uncertainties in the resonance parameters g, Γ_n and Γ_γ and in α are considered using the error propagation law. The calculated σ_c can be adjusted to fit the measured value of

Table 2

Calculated capture group constants σ_i (in b) from the RCN-2 set[a] together with initial standard deviations Δ_i, adjustments δ and final standard deviations Δ_f, in %.

N[b]	^{127}I σ_i (Δ_i, δ, Δ_f)	^{101}Ru σ_i (Δ_i, δ, Δ_f)	^{102}Ru[d] σ_i ($\pm\Delta_i$, δ, $\pm\Delta_f$)	^{104}Ru[d] σ_i ($\pm\Delta_i$, δ, $\pm\Delta_f$)
1	.0005(95,-0.2,95)	.003(80,+5.8,75)	.005($^{500}_{80}$,-83,$^{110}_{50}$)	.007($^{300}_{75}$,-69,$^{160}_{62}$)
2	.006 (60,-0.8,60)	.013(75,+6.6,65)	.026($^{200}_{70}$,-69,$^{60}_{40}$)	.031($^{150}_{60}$,-55,$^{90}_{50}$)
3	.030 (50,-0.6,50)	.028(60,+6.1,55)	.052($^{150}_{60}$,-59,35)	.048($^{95}_{50}$,-45,$^{50}_{30}$)
4	.059 (35,-0.4,35)	.038(45,+5.6,40)	.052($^{95}_{50}$,-52,35)	.043($^{70}_{40}$,-36,35)
5	.084 (30,-0.0,25)	.051(40,+5.3,30)	.063($^{80}_{45}$,-43,30)	.045($^{60}_{40}$,-35,25)
6	.13 (20,+0.5,18)	.11 (30,+4.1,19)	.082($^{70}_{40}$,-43,25)	.047($^{60}_{40}$,-32,30)
7	.19 (25,+0.4,19)	.22 (25,+3.4,15)	.092($^{60}_{40}$,-39,20)	.077($^{55}_{35}$,-27,20)
8	.27 (20,+0.4,16)	.37 (20,+3.5,15)	.10 ($^{70}_{40}$,-42,20)	.081(35,-30,20)
9	.49 (20,+1.5,12)	.60 (20,+2.9,12)	.15 ($^{70}_{40}$,-41,20)	.12 (35,-31,20)
10	.78 (25,+2.0,14)	.94 (25,+4.0,20)	.26 ($^{65}_{40}$,-42,30)	.20 (35,-29,25)
11	1.09 (30,+2.2,17)	1.36(25,-0.4,13)	.43 ($^{60}_{35}$,-27,13)	.34 (40,-30,13)
12	1.44 (25,+1.9,14)	1.90(30,-1.4,16)	.63 ($^{55}_{40}$,-18,20)	.51 (35,-28,16)
13	1.78 (11,+0.3, 6)	2.56(30,-1.5,15)	.85 ($^{60}_{40}$,-11,30)	.71 (40,-26,20)
14	2.64 (12,-0.5, 7)	3.72(25,-1.4,14)	1.22($^{45}_{30}$,+0.8,30)	1.13(30,-17,20)
15	5.59 (11,-0.4, 6)	4.69(20,-3.2,16)	.008[4](12,-0.0,12)	.95 (20,+2.5,20)
16	9.66 (9,-0.3, 6)	13.4(11,-3.5,10)	.55 (15,+0.6,16)	2.86(16,+1.5,15)
17	21.8 (15,-0.5, 9)	7.86(25,-2.2,25)	.16 (15,+0.1,15)	.018(30,+2.4,30)
18	27.6 (7,-0.1, 6)	18.0(6,-0.6, 6)	.024(12,-0.1,12)	.009[4](40,+0.8,40)
19	140 (7,-0.2, 5)	22.8(13,-0.6,13)	.035(12,-0.2,12)	.013(40,+0.7,40)
20	20.8 (8,-0.2, 8)	46.6(7,-0.1, 7)	.051(12,-0.2,12)	.019(40,+0.6,40)
21	.462 (15,-0.6, 9)	.440(10,-3.0,10)	.075(12,-0.2,12)	.027(40,+0.6,40)
22	.583 (14,-0.5, 8)	.352(11,-3.5,10)	.11 (12,-0.2,12)	.040(40,+0.6,40)
23	.795 (13,-0.5, 8)	.427(12,-3.6,11)	.16 (12,-0.2,12)	.058(40,+0.6,40)
24	1.12 (13,-0.5, 8)	.575(12,-3.7,11)	.23 (12,-0.2,12)	.083(40,+0.6,40)
25	1.65 (13,-0.5, 8)	.800(12,-3.8,11)	.34 (12,-0.2,12)	.12 (40,+0.6,40)
26[c]	6.15 (11,-0.4, 7)	1.27(12,-3.8,11)	1.45(12,-0.1,12)	.47 (45,+0.6,45)

a) Weighting spectrum of KFKINR set.[15]
b) Number of ABBN energy group.[10]
c) Energy group from 0.001 to 0.215 eV, different from definition in ref.[10].
d) It is assumed that $\ln \sigma_i$ is normally distributed.

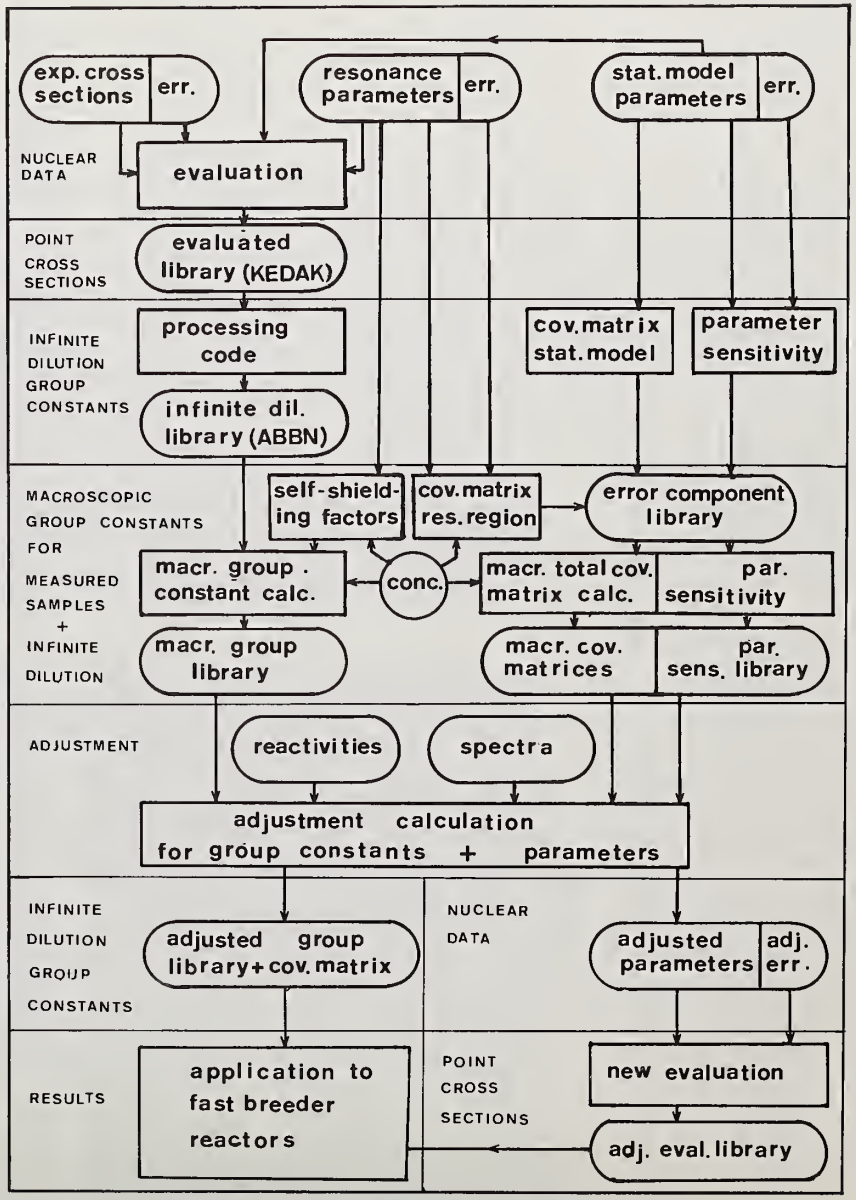

FIG.1 SCHEME FOR ADJUSTMENT CALCULATIONS

σ_{2200} by means of a 1/v term. The uncertainty in σ_{2200} is taken into account in the error calculation.

Resonance self-shielding in the actual samples is accounted for in the error calculation using the intermediate resonance approximation without Doppler broadening.[13] The parameters λ and s, defined in ref.[13], are obtained with the code TRIX.[11] The uncertainty in the potential scattering cross section appearing in the formula for the self-shielded resonance integral is also taken into account. The adequacy of the model used in TRIX has been checked with the more sophisticated code RABBLE.[14]

Correlations between the errors in group constants for a specific isotope in different concentrations (including infinite dilution) are calculated. Errors in Γ_γ of all resonances may be taken fully correlated or fully independent. Other resonance parameters are considered to be independent. Correlations between errors in the α-factors of different energy groups are usually taken as +1.

Complete co-variance matrix

Preceding subsections describe the computation of co-variance matrices for capture group constants $\sigma_{c,g}$ of isotopes, possibly with different degrees of self-shielding. These data are stored in an error component library (fig. 1). The next step is to calculate the co-variance matrix for a vector containing the $\sigma_{c,g}$ of each of the mixtures and infinite dilution group constants of each of the constituting isotopes. This macroscopic total co-variance matrix is computed by the code CONPRO, which takes into account all standard deviations and correlations mentioned before. In addition the sensitivities of the macroscopic group constants for statistical model parameters are calculated.

Adjustment calculation

The vector of group constants with its co-variance matrix is used in the adjustment code ADJ3. This code also reads capture reactivity worths (including co-variances) of the mixtures in different STEK cores, $\rho = \Sigma_g \sigma_{c,g} \phi_g \phi_g^+$, with properly normalized product of group flux and adjoint flux $\phi_g \phi_g^+$ (see next section). These "spectra" $\phi_g \phi_g^+$ are seen to be the sensitivities of reactivities with respect to group constants. From this entire information ADJ3 computes adjusted group constants as much as possible within the error margins, accounting for existing correlations, to produce optimal agreement with the measured reactivity worths.[3] A χ^2-test checks the statistical consistency. The infinite dilution isotopic group constants have been included in the group constant vector and follow the adjustment due to the correlations with the group constants of the measured samples. These adjusted data will be better than the prior ones, at least when used for calculation of integral quantities of a fast breeder reactor.

The sensitivities of cross sections with respect to the underlying statistical model parameters are used to translate group constant adjustments into parameter adjustments. These adjusted parameters may be used to obtain improved point cross sections.

Spectra and reactivities

The central STEK spectra ϕ_g and ϕ_g^+ have been determined by means of calculations and measurements. The calculations were made with two-dimensional diffusion and transport codes using the 26-group KFKINR cross section set.[15] The flux spectra were measured by four differential techniques in the energy range from 10 eV to 10 MeV. Also integral spectrum index measurements have been performed. All this spectral information has been combined[16] by means of a least-squares code, which produces ϕ_g together with a co-variance matrix. This code uses as input the co-variances of the calculated ϕ_g (derived from uncertainties in the cross sections) and estimated standard deviations in the measurements. The calculated adjoint spectrum ϕ_g^+ has been checked with measurements in one STEK core.

Central reactivity worths of the samples were measured in the five STEK cores.[3] To avoid the problem of calculating the normalization integral in the first-order perturbation formula for a zoned reactor, the reactivities ρ have been normalized to a standard ρ_o, for which was taken the product of the apparent reactivity worth of a calibrated ^{252}Cf neutron source and the absolute fission rate of ^{235}U.[17] In formula: $\rho/\rho_o = \Sigma_g \sigma_{c,g} \phi_g \phi_g^+ / \Sigma_g \sigma_{f,g} \phi_g \Sigma_g \chi_g \phi_g^+$, where $\sigma_{f,g}$ is the ^{235}U fission cross section[15] and χ_g the ^{252}Cf fission spectrum. The use of this standard leads to a reasonable agreement between experimental and calculated reactivities for the main STEK core constituents ^{235}U and graphite, although in the softer spectra the ^{235}U reactivity is systematically overpredicted. For boron the reactivity is systematically underpredicted by 15%, which is in agreement with results obtained in various SNEAK assemblies.[18-20] The reason for these discrepancies is not clear yet and is being investigated to be sure that no systematic error is made in the present normalization. Therefore, the numerical results in this paper are given with some reservation.

Before adjustment of σ_c, the measured reactivities are corrected for scattering effects and for the effect of non-fission products present in the samples. Errors in the measured worths and in the corrections are taken into account, as well as errors in the calculated capture effects due to spectrum uncertainties, sample composition uncertainties and uncertainties in ρ_o. Correlations between all sources of errors are accounted for.

Results and discussion

In this section some results obtained for σ_c of ^{127}I and $^{101,102,104}Ru$ are reported. These isotopes were selected for this paper, because the ^{127}I capture cross section is rather well known and may therefore serve as a general check, whereas the capture cross sections of the Ru-isotopes (in particular those of ^{101}Ru) are important for fast breeder reactors.

The results are presented with some reservations due to reactivity normalization problems as mentioned in the previous section.

^{127}I

The most important parameters used in the calculation of σ_c of ^{127}I are listed in table 1. Above 4 keV σ_c is in good agreement with the eye-guided line through the points as given in ref.[22] The deviations from the cross section values recommended by Pönitz[21] vary from -16% to +13%. Compared to the ENDF/B-IV evaluation, the RCN-2 capture cross sections are up to 10% higher for energies in between 10 keV and 1 MeV. In table 2 the group constants and uncertainties are listed. At low energies the main source of uncertainty originates from the fact that no measurements on Γ_γ for resolved resonances have been reported.

Integral measurements for five PbI_2-samples in different thicknesses have been performed in five STEK cores. As a result of the adjustment (with a value of χ^2 of 0.84) only very small changes in the group constants are obtained (see table 2). This result gives confidence in the applied method of reactivity normalization, discussed in the previous section.

Table 1

Some statistical model parameters p_i used in the evaluation, together with initial standard deviations Δ_i, adjustments δ, and final standard deviations Δ_f, in %.

parameter (unit)	^{127}I		^{101}Ru		^{102}Ru		^{104}Ru	
	p_i	(Δ_i, δ, Δ_f)	p_i	(Δ_i, δ, Δ_f)	p_i	(Δ_i, δ, Δ_f)	p_i	(Δ_i, δ, Δ_f)
S_o (10^{-4} eV$^{-\frac{1}{2}}$)	0.62[a]	(15,+.2, 15)	0.56[a]	(25,-2 , 25)	0.32	(100,+15, 95)	0.32	(100,-5 ,100)
S_1 (10^{-4} eV$^{-\frac{1}{2}}$)	2.24	(100,+8 , 60)	7.30	(100,-10, 55)	7.30	(100,+35, 70)	7.00	(100,-30, 70)
$\langle\Gamma_\gamma\rangle$ (meV)	130	(25,+.6, 17)	172	(25,+4 , 14)	275[b]	(50,-35, 30)	97.0	(25,-13, 19)
D_{obs} (eV)	13.0[a]	(0.5,+.0,0.5)	16.7[a]	(10,-1 , 8)	573[a]	(30,+20, 15)	265[a]	(25,+30, 10)
a_c (MeV^{-1})	17.35[a]	(0.4,+.0,0.4)	16.2[a]	(1.0,+.1,0.9)	17.94[a]	(3,-2 ,1.6)	20.85[a]	(4,-3 ,1.7)
a_t (MeV^{-1})	20.7[c]	(10,+.0, 10)	16.3	(18,-.2, 18)	16.2[a]	(1.0,+.0,1.0)	17.0	(12,+.1, 12)

a) Derived from resolved resonance parameters; b) Manually adjusted to fit the recent capture cross section values given in refs. [24,25]; c) Manually adjusted to fit the measured point cross sections in the MeV range.

After the adjustment the uncertainty in the group cross sections is improved appreciably, as can be seen from table 2. Moreover the statistical uncertainty in the capture rate of ^{127}I in a fast breeder reactor (SNR-300) is improved from 15% to 7%.

^{101,102,104}Ru

For these nuclei only a few measured capture cross sections have been reported.[22-29] Therefore, the evaluation heavily depends on the knowledge of resolved resonance parameters, which are scarcely known for ^{102,104}Ru. The parameters listed in table 1 have been derived from systematics or theory, unless otherwise stated. In table 2 the calculated group constants and uncertainties are listed.

Good agreement ($\chi^2 = 1.2$) is obtained between the calculated values of σ_c of ^{101}Ru and values derived[23] from differential measurements on natural Ru and ^{96,102,104}Ru, at 220 and 830 keV.

Both for ^{102}Ru and ^{104}Ru there is good agreement between calculated σ_c-values and results from activation measurements[24-29] at 2 and 24 keV (except the data of ref.[27] for ^{104}Ru). At 195 keV the measured value[28] of the capture cross section of ^{102}Ru is about twice as high as calculated, whereas for ^{104}Ru the experimental values[28,29] at 195 keV and 3 MeV are about 2.6 times lower than calculated. Part of these discrepancies might be due to the use of obsolete values for the standards. Therefore the recent measurements by Schuman[24] and Murty et al.[25] are to be preferred. The RCN-2 evaluation is in good agreement with the latter measurements.

In the energy range from 10 keV to 1 MeV the ENDF/B-IV evaluation gives, on the average, 15%, 10% and 20% lower values compared to the RCN-2 evaluation for σ_c of ^{101}Ru, ^{102}Ru and ^{104}Ru, respectively.

For the integral measurements, samples enriched to 97.7%, 96.9% and 99.7% in ^{101}Ru, ^{102}Ru and ^{104}Ru, respectively, have been used. These samples have been obtained from the USAEC isotope loan pool. For each isotope samples in two thicknesses have been oscillated in the five STEK cores. From the simultaneous adjustment of these 30 reactivity worth measurements ($\chi^2 = 0.52$) the following conclusions can be drawn (see table 2): (i) very small adjustments occur in the resolved resonance region for all Ru isotopes considered, (ii) a +5% adjustment is found for σ_c of ^{101}Ru above a few keV, (iii) adjustments of -40% and -30% occur for the two even Ru isotopes above a few keV, (iv) the uncertainties in the group constants are significantly improved for energies above a few keV.

Comparison of adjusted cross sections with measured point cross sections for the two even Ru isotopes leads to the conclusion that for ^{102}Ru the discrepancies between differentially measured points and the calculated cross section have become larger after the adjustment, whereas for ^{104}Ru the adjusted cross section is still not in disagreement with the recent measurements[24,25] and the discrepancies with regard to the other measurements[28,29] have become smaller.

The evaluated ENDF/B-IV capture cross section is on the average -20%, +30% and +10% different from the adjusted RCN-2 cross sections for ^{101}Ru, ^{102}Ru and ^{104}Ru, respectively, at energies between 10 keV and 1 MeV.

Parameter adjustment

The parameter adjustments and new standard deviations are included in table 1. For ^{127}I and ^{101}Ru the changes in the parameters are small. The main change in parameters for ^{102,104}Ru occurs in the ratio $\langle\Gamma_\gamma\rangle/D_{obs}$.

The authors thank Ir.R.J. Heyboer for many stimulating discussions. Mr. J. Nederkoorn and Mr. R. Jost are acknowledged for their contributions in code development.

References

1 M. Bustraan et al., Proc.Int.Symp. on Physics of Fast Reactors, Tokyo, Vol.II (1973) 665.
2 H. Gruppelaar (comp.), RCN-205 (1974).
3 M. Bustraan (comp.), RCN-122 (1970).
4 G. Lautenbach, RCN-191 (1973).
5 J.B. Dragt and H. Gruppelaar, RCN-192 (1973).
6 M.R. Bhat, BNL-50296 (1971).
7 S. Igarasi in: JAERI-M5752 (1974).
8 V. Benzi et al., RT-FI(69)44 (1969).
9 V. Benzi et al., RT-FI(71)6 (1971).
10 L.P. Abagyan et al., Group constants for nuclear reactor calculations, New York, Consultants Bureau,1964.
11 J.M. Otter, NAA-SR-Memo-11538 (1965).
12 H. Gruppelaar, paper presented at Second Int.Symp.on (n,γ) Spectroscopy and Related Topics, Petten (1974).
13 R. Goldstein and H. Brooks, Nucl.Sci. and Eng. 20 (1964) 331.
14 P.H. Kier and A.A. Robba, ANL-7326 (1967).
15 E. Kiefhaber, KFK-1572 (1972).
16 J.W.M. Dekker, paper submitted to Reaktortagung 1975, Deutsches Atomforum, Neurenberg.
17 R.A. Karam, Nucl.Sci. and Eng. 37 (1969) 192.
18 E.A. Fischer and P.E. McGrath (compilers), KFK-1939 (1974).
19 M. Pinter, KFK-2028 (1974).
20 G. Jourdan, KFK-2012 (1974).
21 W.P. Pönitz in: Nuclear Data for Reactors, Vol. I, Vienna, IAEA (1967) 277.
22 M.D. Goldberg et al., BNL-325 (1966) ed.2, suppl.2.
23 T.S. Belanova and O.D. Kazachkovskii, Atomnaya Énergiya 14 (1963) 185.
24 R.P. Schuman, WASH-1127 (1969) 72. HH
25 M.S.Murty et al., J.Phys.Soc.Japan 35 (1973) 8.
26 R.L.Macklin et al., Phys.Rev. 114 (1959) 6.
27 A.K.Chauby and M.L.Sehgal, Phys.Rev.152(1966)1055.
28 W.S.Lyon and R.L.Macklin, Phys.Rev.114(1959)6.
29 G.Peto et al., J.Nucl.Energy 21 (1967) 797.

INTEGRAL TEST OF CROSS SECTIONS USING NEUTRON LEAKAGE SPECTRA FROM SPHERES OF IRON, NIOBIUM, BERYLLIUM, AND POLYETHYLENE

R. H. Johnson, J. J. Dorning, and B. W. Wehring
University of Illinois at Urbana-Champaign
Urbana, Illinois 61801

Measurements of neutron leakage spectra in the energy range 1 to 15 MeV from homogeneous spherical assemblies have been made using an NE-213 spectrometry system. These benchmark-type measured spectra will be compared with detailed computed spectra as an integral test of evaluated nuclear data. Preliminary ANISN calculations using cross section sets based on ENDF/B-III are presented and compared with the measurements. Measurements on a 22-cm diam beryllium sphere, a 25-cm diam niobium sphere, and a 46-cm diam polyethylene (CH_2) sphere, each with a ^{252}Cf source at the sphere center, have been made. The niobium calculation slightly underpredicts the leakage spectrum below 9 MeV. The beryllium and polyethylene calculations are in general agreement with the measurements, though discrepancies are seen for small energy ranges. Measurements have also been made for a 76-cm diam iron sphere with a 14-MeV source at the sphere center. The preliminary iron calculation (ENDF/B-III) greatly underpredicts the leakage spectrum from 1 to 8 MeV.

(Integral cross section tests; iron; niobium; beryllium; carbon)

Introduction

An NE-213 spectrometry system[1] was used to measure the neutron leakage spectra from homogeneous spherical assemblies as an integral test of neutron cross section data. Measurements using a ^{252}Cf source have been made for spheres of beryllium, niobium, and polyethylene. Measurements have also been made using a 14-MeV neutron source in the center of an iron sphere. Preliminary calculations using cross section sets based on ENDF/B-III data have been done for these four experiments.

^{252}Cf Source

Experimental Procedure

Leakage spectra have been measured for niobium, beryllium, and polyethylene spheres using a ^{252}Cf source. Similar measurements were made at NASA-Lewis Research Center using these spheres with an Am-Be source.[2] The dimensions and compositions of the spheres are discussed in Ref. 2.

For each measurement the sphere was supported by an iron pipe 2 m above a concrete floor. The source was positioned at the center of a 6-cm diam void in the center of each sphere. The NE-213 detector was supported 2 m above the floor and positioned at a distance of 2.00 $\pm$0.01 m from the sphere center. Background measurements were made by placing a paraffin shadow cone between the sphere and the neutron detector.

The bare source spectrum is reported in a paper[1] describing the NE-213 spectrometry system used in these measurements. The measured bare source spectrum was found to be fit well by a Maxwellian distribution with a temperature of 1.43 $\pm$0.05 MeV.[1] The error given for the temperature is systematic error due to an estimated gain calibration error of $\pm$2%.

Accurate gain calibration is particularly important when a ^{252}Cf neutron source is used. The shape of the fission spectrum causes the measured flux at high energies to be very sensitive to the gain. A measured source spectrum was unfolded with two gains differing by 1%. The unfolded fluxes differed by 16% at 15 MeV, 3% at 7 MeV, and less than 1% at 2 MeV. This sensitivity of the high energy flux to gain calibration results in an estimated experimental error at high energies which is greater than the statistical error calculated by the spectra unfolding code.

Niobium Sphere

The leakage spectrum measured for the 25-cm diam niobium sphere is shown in Fig. 1 as the vertical lines ($\pm$1 standard deviation error bars due to statistical errors). An S_{32}, P_3 ANISN[3] calculation of the leakage spectrum is shown in Fig. 1 as the histogram. The source spectrum used for the ANISN calculation was a Maxwellian fission spectrum with a temperature of 1.43 MeV. This calculation was made using the DLC-2D cross section set[4] which was constructed from ENDF/B-III data. A second shorter measurement of the leakage spectrum is not shown but is in good agreement with the measurement in Fig. 1.

Above 9 MeV the calculation is in good general agreement with the measurements. Between 2 and 9 MeV, however, the calculation underpredicts the measured spectrum by 5 to 10%. Below 2 MeV the calculation underpredicts the measured spectrum by 15 to 50%. The discrepancies between 1.5 and 9 MeV are consistent with those observed in the NASA experiment.[2] Causes for these discrepancies, including possible errors in nonelastic cross sections, will be investigated.

Beryllium Sphere

The leakage spectrum measured for the 22-cm diam beryllium sphere is shown in Fig. 2 with an S_{32}, P_3 ANISN calculation made using the DLC-2D cross section set (ENDF/B-III).

Above 5 MeV the measurement is lower than the calculation. A second shorter measurement of the beryllium leakage spectrum was slightly higher than this calculation for energies above 5 MeV. The two beryllium measurements illustrate that the spectrometry system has good reproducibility for low neutron energies, but that this reproducibility decreases at higher energies. We attribute this to error in gain calibration. Hence, we conclude that above 3 MeV the beryllium measurements and calculations agree within experimental errors.

Between 1 and 3 MeV, however, the calculation underpredicts the measured spectrum by approximately 15%. Similar discrepancies in this energy range were observed in the NASA experiment.[2] Possible causes for these discrepancies, including the (n,2n) cross sections, will be investigated.

Polyethylene Sphere

The leakage spectrum measured from the 46-cm diam polyethylene sphere is shown in Fig. 3 with an S_{32}, P_3 ANISN calculation. The calculation was done using the DLC-28 cross section set[5] which was constructed using ENDF/B-III neutron data.

The calculation and measurement are in generally good agreement between 2.5 and 9 MeV, although the measurement does not resolve the structure between 7 and 9 MeV apparent in the calculation. This structure will be investigated by smoothing a more detailed multigroup calculation with the resolution of the unfolded measured neutron spectrum. Above 9 MeV the measured spectrum is below the calculated spectrum, but, due to the sensitivity at high energies to errors in gain calibration, we believe that above 9 MeV the polyethylene measurement and calculation agree within experimental errors.

The calculation underpredicts the measured leakage by approximately 10% between 1.5 and 2.5 MeV. Such a discrepancy was not observed in the NASA experiment.[2] Possible causes for the discrepancies, including errors in the carbon nonelastic cross sections, will be investigated.

D-T Source

Experimental Procedure

A neutron generator was used as a source of 14-MeV neutrons from the D-T reaction. A deuteron beam of approximately 50 kV and 20 μA was used. In the spectrum measurements using the 14-MeV source the problem of sensitivity to gain calibration does not arise.

A measurement of the bare source spectrum is shown in Fig. 4. This measurement was taken at an angle of 90° to the deuteron beam. At this angle the source energy is 14.08 MeV. The measured peak energy is 14.1 ±0.1 MeV. Oscillations in the unfolded spectrum are evident below the peak energy, especially at 10 MeV. Such oscillations are common, however, when monoenergetic spectra are unfolded.

Iron Sphere

The target of the neutron generator was centered in a 76-cm diam iron sphere. The sphere has a central void of 15-cm diam and a reentrant hole of 9.5-cm diam

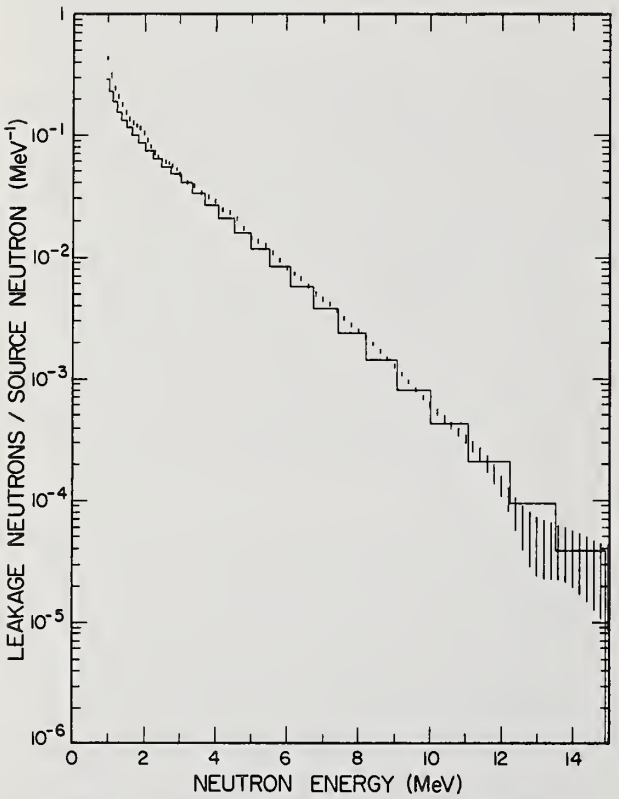

Fig. 1. Measured (vertical error bars denoting ±1 standard deviation error due to counting statistics) and calculated (histogram) leakage spectra for 25-cm diam niobium sphere.

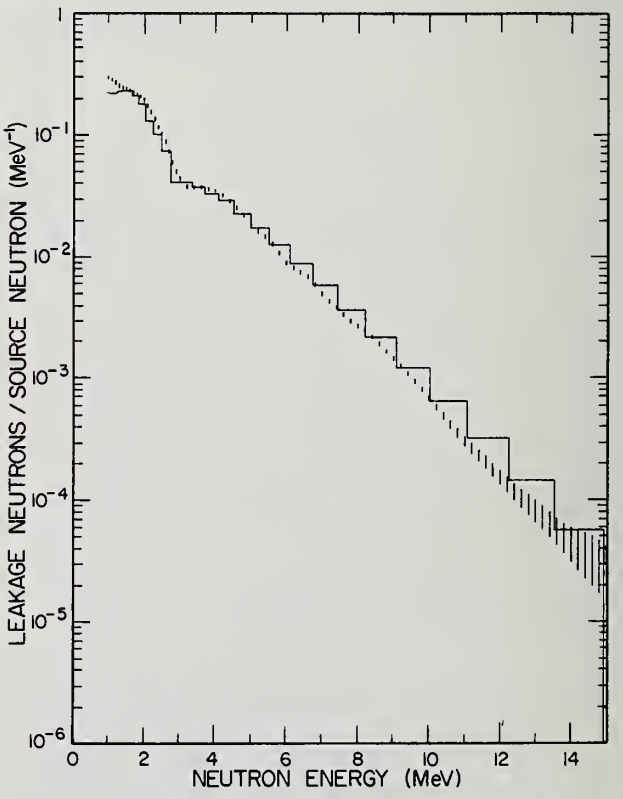

Fig. 2. Measured (vertical error bars) and calculated (histogram) leakage spectra for 22-cm diam beryllium sphere.

for the neutron generator beam tube. This sphere was previously used in time-of-flight spectrum measurements.[6,7] A detailed description of the dimensions and composition of the sphere is given in Ref. 6. The iron sphere was supported 1 m above a concrete floor. The NE-213 detector was positioned 1 m above the floor, 2.00 +0.01 m from the sphere center, and at an angle of 90° from the deuteron beam tube. A paraffin shadow cone was positioned between the detector and the sphere for background measurements.

The measured leakage spectrum from the iron sphere is shown in Fig. 5 along with an S_{32}, P_3 ANISN calculation of the leakage spectrum done using the DLC-2D cross section set (ENDF/B-III). The measurement is normalized to the calculation by equating the integrated leakage above 10 MeV.

The 14-MeV peak is somewhat broader than the bare source measurement because of poorer counting statistics. Downscattering of source neutrons also contributes to broadening of the source peak. The oscillation at 10 MeV in the measured leakage spectrum is attributed in part to the spectrum unfolding (see Fig. 4 for comparison).

In the energy range 1 to 8 MeV the measured neutron leakage flux is 2.5 to 5 times the calculated leakage flux.

Similar measurements using the time-of-flight method were performed at Lawrence Livermore Laboratory (LLL) for iron spheres of 9, 27, and 45 cm diam using a pulsed 14-MeV source.[8] The iron sphere used in the present measurements has a shell thickness that is 36% larger than the radius of the largest iron sphere studied at LLL. The LLL measurements covered the ranges of several keV to 1 MeV and 2 to 15 MeV and have been compared with Monte Carlo calculations using ENDF/B-III data.[8,9]

Between 3 and 8 MeV the discrepancies between the present measurements and calculations are slightly larger than the discrepancies for the largest LLL sphere. This appears to be consistent with the LLL discrepancies (which are also large) because the discrepancies for the three LLL spheres increase with sphere size.

At 2 MeV, however, we observe a much larger discrepancy than the discrepancy for the largest LLL sphere. Our largest discrepancy is near 1 MeV where the present measurement of the leakage is about 5 times the calculated leakage. The LLL measured leakage at 1 MeV for the 27-cm diam iron sphere, however, is less than the calculated leakage.[8] Below 3 MeV, therefore, our measurements appear to be in poor agreement with the LLL measurements.

Sensitivity studies at Oak Ridge National Laboratory (ORNL) have singled out continuum inelastic-scattering data as the probable cause for the large discrepancies between the LLL measurements and Monte Carlo calculations using ENDF/B-III data.[9] The evaluations for the ENDF/B-IV cross sections for iron were evaluated partly based on the LLL iron sphere measurements. We will calculate the leakage spectrum from the 76-cm diam iron sphere using ENDF/B-IV and compare those calculations based on the new iron evaluation with the measured spectrum reported here.

Studies at ORNL have also indicated that possible errors may exist in the evaluation of the iron total cross section between 1 and 3 MeV.[10] The measurements reported here using a 14-MeV source with the iron sphere may be sensitive to such errors. However, a more definitive test of the total neutron cross section in this energy range should be leakage spectrum measurements which are currently being planned using the ^{252}Cf fission neutron source.

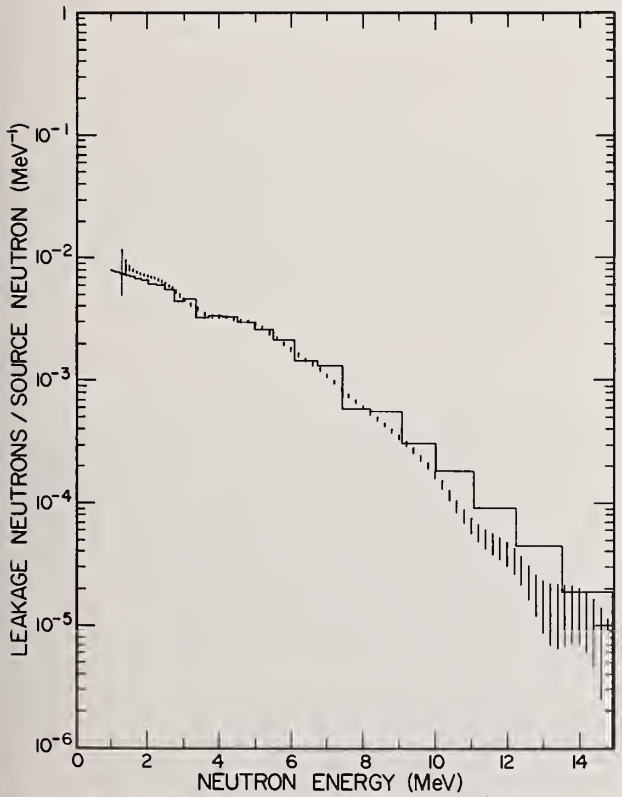

Fig. 3. Measured (vertical error bars) and calculated (histogram) leakage spectra for 46-cm diam polyethylene sphere.

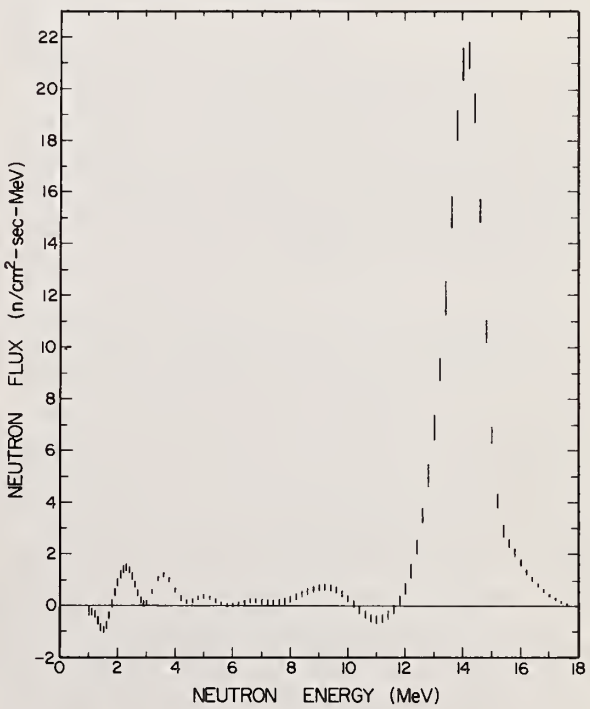

Fig. 4. Measured D-T source spectrum at 90° to deuteron beam.

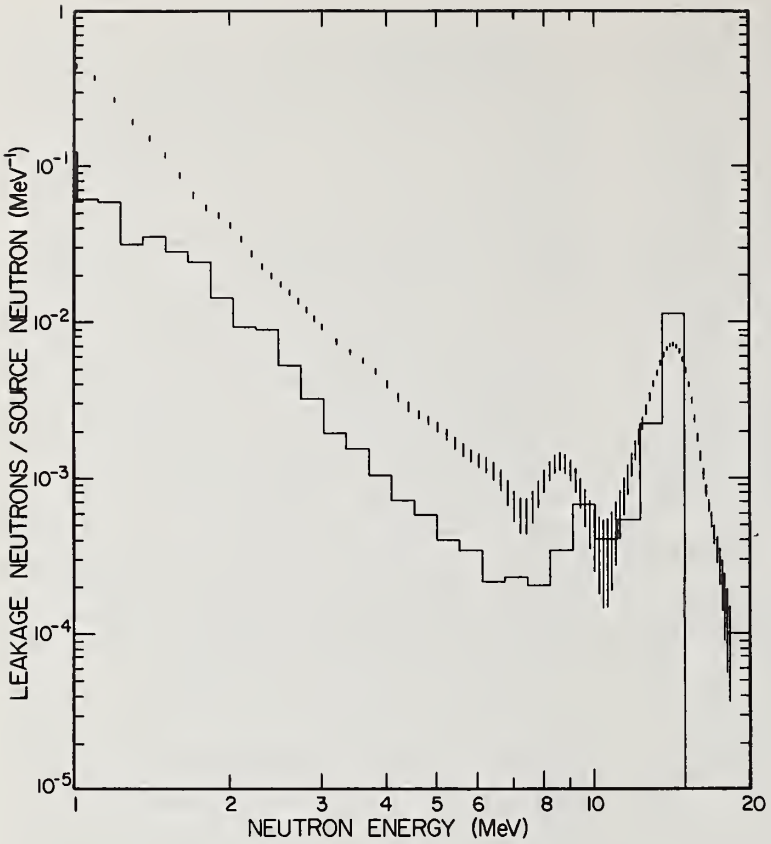

Fig. 5. Measured (vertical error bars) and calculated (histogram) leakage spectra for 76-cm diam iron sphere. The measurement is normalized to the calculation by equating the integrated leakage above 10 MeV.

Summary

Leakage neutron spectra have been measured for spheres of niobium, beryllium, polyethylene, and iron. The measurements have been compared to preliminary ANISN calculations using ENDF/B-III data. Large discrepancies have been observed for iron. Smaller discrepancies have been observed for the other materials. Detailed calculations will be made using ENDF/B-IV data. Leakage measurements for the iron sphere using the ^{252}Cf source will be made to test total cross sections between 1 and 3 MeV.

Acknowledgements

Discussions with Dr. Donald Bogart and Dr. Donald F. Shook of NASA during the early part of this work are gratefully acknowledged. Dr. Ralph J. Cerbone and Dr. John M. Neill's assistance in the transfer of the iron sphere is acknowledged. The other assemblies used in this work are on loan from NASA. The ^{252}Cf source is provided on loan through the University Loan Program of the AEC.

[1] R. H. Johnson, B. W. Wehring, and J. J. Dorning, "NE-213 Neutron Spectrometry System for Measurements to 15 MeV," proceedings of this conference.

[2] D. Bogart, D. F. Shook, and D. Fieno, Nucl. Sci. Eng. 53, 285 (1974).

[3] W. W. Engle, Jr., "A User's Manual for ANISN," Union Carbide Corp., 1967 (K-1693).

[4] "100G, 100 Group Neutron Cross-Section Data Based on ENDF/B," Radiation Shielding Information Center, Oak Ridge National Laboratory (DLC-2D).

[5] J. T. Kriese, "Coupled Neutron and Gamma-Ray Cross Section Sets for Fusion Reactor Calculations," Oak Ridge National Laboratory, 1973 (ORNL-TM-4277).

[6] R. J. Cerbone, "Measurement of Neutron Penetration Standards, Vol. I, Angular Neutron and Gamma-Ray Spectrum Measurements in a Bulk Iron Assembly," Gulf General Atomic, 1969, DASA Report No. 2289 (GA-9149).

[7] R. J. Cerbone, "Reanalysis of the Neutron Spectrum Measurements in an Iron Bulk Assembly," Gulf Radiation Technology, 1971 (DNA-2779F, Gulf-RT-A10859).

[8] L. F. Hansen, J. D. Anderson, P. S. Brown, R. J. Howerton, J. L. Kammerdiener, C. M. Logan, E. F. Plechaty, and C. Wong, Nucl. Sci. Eng. 51, 278 (1973).

[9] S. N. Cramer, R. W. Roussin, and E. M. Oblow, "Monte Carlo Calculations and Sensitivity Studies of the LLL Pulsed Sphere Program," Oak Ridge National Laboratory, 1973 (ORNL-TM-4072).

[10] E. M. Oblow, private communication.

UNCERTAINTIES AND CORRELATIONS IN EVALUATED DATA SETS INDUCED BY USE OF STANDARD CROSS SECTIONS*

R. W. Peelle

Oak Ridge National Laboratory
Oak Ridge, Tennessee 37830

A file of cross-section uncertainty information for use in reactor performance uncertainty analysis should take into account the propagated effects of uncertainties in the standard cross sections used. This problem has been analyzed using first-order error theory in terms of the uncertainties in the standard cross sections and the energy-dependent weight given to each underlying experimental result in obtaining an evaluated cross section. Three cases occur depending on whether the energy dependence of the standard was utilized, and if so whether the absolute magnitude or only the shape of the standard cross section was used in an underlying experiment. The analysis yields the uncertainties in and correlations among the evaluated cross sections. The resulting uncertainty files need not refer explicitly to the uncertainties in standards and can use the same set of formats employed for other uncertainty data.

(Uncertainty file; standard cross section; ENDF/B; covariance; correlation)

Introduction

Energy-dependent capture and fission cross sections in the energy region below a few hundred keV have often been measured relative to the $^{10}B(n,\alpha)$ or $^{6}Li(n,\alpha)$ standard cross sections, and at higher energies the ^{235}U fission and n,p scattering cross sections have been employed. In other cases energy-independent standards such as the $\overline{\nu}(^{252}Cf)$ or 2200 m/sec cross sections have been employed. Any significant uncertainties in these standards propagate to the measured values. Such uncertainties cannot be discovered by comparing experimental results if these results were based on the same standard cross section. Moreover, this contribution to uncertainty in evaluated cross sections induces marked correlations among the various cross sections which have been measured relative to the same standards. Several authors have recognized the sensitivity of computed uncertainties in reactor parameters to the correlation properties assumed for the input data.[1]

The analysis described here assumed a context of a thorough and detailed analysis of the uncertainty in some reactor parameter P, leading to the variance in that parameter $\langle \Delta P^2 \rangle = \sum S_i S_j V_{ij}$, where in the language of group cross sections the V_{ij} is the covariance matrix of the complete set of group cross sections (the indices i and j run over all materials, energy groups, and reaction types) and the "sensitivity coefficients" S_i are the partial derivatives of the parameter P to the i^{th} group partial cross section. The covariance matrix V_{ij} is obtained by processing uncertainty files so they correspond to the utilized group structure. The uncertainty file structure defined for ENDF/B-IV[2] contains a set of mutually incoherent segments, each of which lists piece-wise constant uncertainties or variances with energy-dependent correlation patterns defined by an indicator flag. This ENDF uncertainty file structure and this paper are confined to energy-dependent cross sections, excluding resonance representations. (See Appendix A.)

The uncertainty evaluator faces the problem that he cannot complete the file for a given material (MAT) or reaction type (MT) without having the uncertainty file for the standard cross sections referred to in the data being evaluated. To enter the covariance files which link MAT, MT to cross sections for other materials, our evaluator must also know about all other cross sections which depend on the same standard cross section. This situation would be entirely impractical since one man cannot do all the work and each evaluator cannot be the last.

This paper indicates the main features of a method for practical handling of the propagation of uncertainties in standard cross sections.

How Evaluated Cross Sections Depend on Standards

Consider two examples which illustrate how the uncertainty in an energy-dependent cross section measurement depends on the uncertainties in a standard cross section used.

Suppose the $^{239}Pu(n,f)$ cross section is being measured against the $^{10}B(n,\alpha)$ cross section as an absolute standard; the numbers of fission fragments and alpha particles, respectively, are measured in the same flux for a measured number of atoms of each material.

$$\sigma_{nf}(E) = (n_B/n_{Pu})(C_f/C_\alpha)\ \sigma_{n\alpha}(E) \quad , \tag{1}$$

and one can write a small relative error in σ_{nf} as

$$\Delta\sigma_{nf}/\sigma_{nf} \equiv x_{nf}(E) = x_{n\alpha}(E) + \text{res} \quad , \tag{2}$$

where $x_{n\alpha} \equiv \Delta\sigma_{n\alpha}/\sigma_{n\alpha}$ and res represents residual relative uncertainties not associated with standards. By direct inspection the relative covariance of this fission measurement includes that of the standard,

$$\frac{\mathrm{Cov}[\sigma_{nf}(E),\sigma_{nf}(E')]}{\sigma_{nf}(E)\ \sigma_{nf}(E')} \equiv \langle x_{nf}(E)\ x_{nf}(E')\rangle = \langle x_{n\alpha}(E)\ x_{n\alpha}(E')\rangle + \ldots \quad . \tag{3}$$

The above does not include any correlation among the residual terms at the two energies. The angle brackets denote the expectation value, or average over an ensemble of equivalent experiments. If the energy-dependent covariance terms in the standard $\sigma_{n\alpha}$ can be represented, the result carries over directly to the fission cross section.

As a second example take a $^{233}U(n,f)$ measurement in the same energy region based on the shape vs energy of the $^{10}B(n,\alpha)$ cross section and on the 2200 m/sec $^{233}U(n,f)$ cross section σ^0_{nf} for absolute normalization:

$$\sigma_{nf}(E) = R(E)\ \sigma^0_{nf}\ [\sigma_{n\alpha}(E)/\sigma^0_{n\alpha}] \quad , \tag{4}$$

where R is the ratio of fission to alpha counts at E divided by the same ratio at the reference energy E_r = 0.0253 eV. Then if x(E) is a small relative error in cross section X at E, one can write

$$x_{nf}(E) = x^0_{nf} + x_{n\alpha}(E) - x^0_{n\alpha} + \text{res} \quad . \tag{5}$$

The sign difference is important if (n,α) values at E and 0.025 eV are correlated.

$$\langle x_{nf}(E)\ x_{nf}(E')\rangle = \langle (x^0_{nf})^2\rangle + \langle [x_{n\alpha}(E) - x^0_{n\alpha}][x_{n\alpha}(E') - x^0_{n\alpha}]\rangle + \ldots, \tag{6}$$

where we have assumed $\langle x^0_{nf}[x_{n\alpha}(E) - x^0_{n\alpha}]\rangle = 0$. Note how the shape uncertainty is expressed; an error in the

normalization of the (n,α) standard cancels out. Equation (6) simplifies if $x_{n\alpha}$ is taken as zero.

The above examples illustrate the three principal types of dependence on cross section standards. In a real evaluation, data from more than one experiment will influence the output and its uncertainties; each may have used the same standard cross section in a different way or with a different reference energy, and some may have used a different standard. In a given energy region an evaluated cross section is a weighted average (or more complex fit) of several experimental results; these weights can be estimated even though the evaluator may not have displayed them explicitly. Within each energy region ΔE_i where these weights w_i are constant, a small relative error x_i in the evaluated cross section can be written $x_i = \sum_\alpha w_i^\alpha x_i^\alpha$, where α runs over the experiments considered important and the w_i sum to unity. The x_i^α for experiment α may depend on standards as in Eqs. (2) or (5) above; in some cases two or more experiments have used the same standard and weights must be combined. The combination process is tricky where the same standard has been used both as an absolute and a relative standard, or where the same relative standard has been employed with two different reference energies. Each such case must be looked at in small error theory and correlations taken into account before reduction of the following general expression for the relative covariance between cross section X anywhere within the region ΔE_i and Y within the region ΔE_j:

$$\langle x_i y_j \rangle = \langle \sum_{\alpha,\beta} w_i^\alpha x_i^\alpha w_j^\beta y_j^\beta \rangle \quad , \qquad (7)$$

where $x_i^\alpha = \Delta X_i^\alpha / X_i$, $y_j^\beta = \Delta Y_j^\beta / Y_j$, and α and β run over the various experiments. Each x_i^α or y_j^β may have a relation to standards like Eqs. (2), (5), or something more complex, depending on the formula from which the cross section was derived. That is, the important components of x_i^α will be s_r^ℓ, s_i^m, and/or $(s_i^n - s_r^n)$, where s^m etc. are small relative errors in standard cross sections ℓ, m, or n and the subscripts indicate whether the error is evaluated at the reference energy or in the energy range ΔE_i where the uncertainty is desired.

Since several measurements are combined in an evaluation and since the weights given these experiments will differ from one energy region to another, the relatively simple ideas described above can lead to considerable detail in execution.

Organization of a Solution

Any solution to the problem posed in the introduction requires effective division of effort. Here it is assumed that files of uncertainty information in ENDF-like formats are available for the standard cross sections, that the uncertainty evaluator for the nuclide of interest knows the weight given to each set of experimental results by the cross-section evaluator for that nuclide, and that the mode of dependence of these measured values on standard cross sections is known. It is also assumed that uncertainty files delivered to a user must be in some standard format easy to process to a group cross-section covariance matrix. (See Appendix A for the present ENDF approach.)

The solution investigated here requires that each uncertainty evaluator list for each energy region the fractional weight each standard had upon the evaluated cross section and the mode of this dependence. This is done (by collecting like terms in the sums produced when $\sum_\alpha w_i^\alpha x_i$ of Eq. (7) is expanded in terms of relative errors in standard cross sections) without reference to which other partial cross sections may depend on some of these same standards. The proposed solution includes an "uncertainty file pre-processor" stage in which these fractional dependence files are combined with the uncertainty files for the standards themselves to obtain a complete set of uncertainty files in which no reference to a standard requires further action. If new or revised "source" uncertainty files with references to standards later become available, part or all of the uncertainty file pre-processing must be repeated, but it will not be necessary to bother the evaluator who produced the source uncertainty file. The pre-processing step allows the proper variance and covariance file segments to be inserted in a semi-automatic way corresponding to correlations not even recognized by individual uncertainty evaluators.

Before the above concept can be adopted, it must be sure that pre-processing can be accomplished with a limited number of passes through the source uncertainty file. One example of a possible procedure would give assurance. It must also be shown possible for a pre-processor to construct practical output uncertainty files for any pattern of uncertainty correlation in the standard cross sections and any combination of modes of dependence of important cross sections upon these standards. An existance theorem has not been sought to prove the second requirement satisfied, but one can be rather sure that all combinations of circumstances can be handled precisely enough. It is important to have formulations prepared at the outset for the most important cases.

A Procedure for an Uncertainty File Pre-processor

This section gives the elements of a pre-processor procedure. It is assumed that one "spins" through the source uncertainty file in a monodirectional manner, producing after a few such passes an output "applications" file. In the process one develops a random-access standards file which is not relayed to the user. The procedure applies only for point-wise energy-dependent files giving uncertainty information for various partial cross sections (File 33 in the ENDF system).

First Pass Through Source Uncertainty File

a. The uncertainty files for materials (MATS) and partial cross sections (MTS) used as standards are abstracted and placed in the random-access standards file. If any absolute uncertainties appear there, they are converted by approximation in small energy intervals to the appropriate form of relative cross sections.

b. Every sub-subsection which is found in the source file and which refers to a given standard is copied into the standards file and "attached" to that standard.

c. To prevent the list of all energy boundaries referenced in the source file from being excessive, values can be rounded to one of a prearranged but large set to bound the number of energy entries which can be required in the cross-section processor.

d. Once the information giving fractional dependence on several standards has been copied from the source file, it can either be deleted or held in the source file for historical purposes.

e. If one standard [say $^{235}U(n,f)$] was partially measured using another standard [say $^{10}B(n,\alpha)$], the linkages involved must be clarified. At the end of the first pass through the source file the standards file

is scanned for any such cases and the propagation explicitly carried out. New file segments expressing direct dependence on the primary standard are formed for each of the fractional-dependence segments attached to the secondary standard. This process is tricky when a given region in a partial cross section in the source file has direct dependence on both the primary and secondary standard.

Second Pass Through the Source Uncertainty File

During this pass the output uncertainty file is prepared. For each material and reaction type (MAT,MT) the file segments which do not relate to standard cross sections are passed along to the applications file, and sections are added for each incoherent contribution induced by dependence on a standard. These will include the energy-dependent file subsections which link MAT,MT to itself, the subsections linking MAT1,MT1 to itself, and those linking MAT,MT to MAT1,MT1. The only reason for the second pass through the source file is to place the new subsections in the proper locations, since all the information needed to produce these uncertainty files was attached to the standards file during the first pass.

Uncertainty File Structure

Appendix A indicates in short form the presently-approved uncertainty-file structure for ENDF.[2] These definitions maintain the condition that the uncertainty files can be processed by simple additions to any processing code based on summations over a super-group structure. Note that in every case piecewise-constant uncertainty information as a function of energy is given, while the patterns of correlation among the various energy regions are indicated by an index (LB).

A compatible source uncertainty file structure to contain the necessary information concerning dependence on standards needs to give the standard involved, the mode of dependence, the reference energy if applicable, and a table with energy labels and the fractional dependence on the indicated standard between successive energy boundaries.

For clarity, one possible way of carrying this information within the ENDF/B system[3] is described; if a system similar to the one recommended here is adopted, the appropriate evaluation groups will have to determine the most desirable format arrangement. (The author's apologies are extended to those who work with a cross section file structure completely different from the ENDF system.)

In File 33 for a given material, there can be a section expressing the covariance information for MAT, MT as a function of energy. The segments expressing dependence on standards should be introduced in this region of the file, probably at the location indicated in Appendix A. The required information will be in a file subsection linking the material and reaction type of interest (MAT,MT) with the material and reaction type corresponding to a standard (MATS,MTS), and could appear as follows:

[MAT,33,MT/b,b;MATS,MTS:NC,NI] CONT

[MAT,33,MT/b,E_r;b,LR;2*NM,NM/{E_m,R_m}] LIST

(other sub-subsections) .

This combination represents the fractional dependence of the partial cross section MAT,MT on the standard partial cross section MATS,MTS with one sub-subsection of type N_c. The second line indicates a mode dependence LR with a reference energy E_r. The energy dependence is given by the set of NM couplets {E_m,R_m}. There may be adjacent sub-subsections also giving dependence on standards. The format suggests sub-subsections are present giving covariance information of other types, but NI is likely to be zero here.

The tag LR = 0 has been defined for ENDF to label a record of "covariance flag indicators;" definitions for some other values of LR are proposed here:

LR = 3. The R_m give the fractional dependence of MAT,MT on the absolute standard cross section in the same energy interval (E_m, E_{m+1}).

LR = 4. The R_m give the fractional dependence of MAT,MT in the region E_m, E_{m+1} on the shape of the standard cross section, or more precisely on the ratio of the standard cross section in the region ΔE_m to its value at E_r.

LR = 5. The R_m give the fractional dependence of MAT,MT in the region ΔE_m on the value of the standard cross section at E_r.

Sequences of source uncertainty segments of the type described above give the uncertainty file pre-processor sufficient information to allow production of the output uncertainty file if uncertainty files for the standard cross sections have been given.

Examples of Output Uncertainty Files

A few of the most likely combinations of file structures are handled here as examples.

Suppose the partial cross section MATS,MTS is utilized as a standard, and the uncertainties in this standard are expressed in one LB = 1 segment (sub-subsection) with the couplets {E_s,^1F_s} and one LB = 2 segment with the couplets {E_t,^2F_t}. (See Appendix A.) Then suppose that the File 33 subsection for MAT,MT; MATS,MTS contains an LR = 3 segment containing {E_m,^3R_m} to show an absolute dependence on the standard as a function of energy, and that MAT1,MT1; MATS,MTS has an LR = 4 segment with E_r, {E_ℓ, $^4R_\ell$} to show a relative dependence upon the same standard cross section with reference energy E_r. What file segments should be produced by the uncertainty file pre-processor?

In MAT,MT; 0,0, the subsection giving information on $\mathrm{Cov}(X_i,X_j)$, incoherent contributions must be generated for the LB = 1 and 2 segments in MATS,MTS. For the former, there is induced an LB = 4 segment in which the two tables are taken directly from the inputs; one is appended directly behind the other,

$$\{E_k,{}^4F_k\} = \{E_s,{}^1F_s\} \; ; \; \{E_m,{}^3R_m\} \quad .$$

The file segment induced by the LB = 2 segment in MATS,MTS has LB = 2. The set of E_k are obtained by merging the $\{E_t\}$ with the $\{E_m\}$, and the corresponding F_k are:

$$^2F_k = \sum_{t,m} I_k^{t,m} \, {}^3R_m \, {}^2F_t \quad ,$$

where $I_k^{t,m}$ is unity if ΔE_k is contained within ΔE_t and ΔE_m, and zero otherwise. Summations like that above have but one nonzero summand.

In MAT1,MT1; 0,0, the subsection giving information on $\mathrm{Cov}\,(Y_i, Y_j)$, at least three segments are generated.

The segments based on the LB = 1 input must recognize that the LB = 4 reference produces a coherent effect so that there is a null output within the $\Delta E_{\hat{s}}$ which includes E_r. The result could be written as a sequence of segments, one for each ΔE_s region of the uncertainty in the standard. As an alternate one can write an LB = 4 segment with the dual table:

$$\{E_k,{}^4F_k\} = \{E_s,{}^1F_s'\}; \{E_\ell,{}^4R_\ell\} \quad ,$$

where $^1F_s'$ equals the input ^1F_s except that $^1F_{\hat{s}}'$ equals zero for the region $\Delta E_{\hat{s}}$ which includes E_r. There is

also produced an LB = 2 segment $\{E_k, {}^2F_k\}$ with $\{E_\ell\}$, $E_{\hat{s}}$, and $E_{\hat{s}+1}$ merged to form $\{E_k\}$ and

$$ {}^2F_k = ({}^1F_{\hat{s}})^{1/2} \sum_\ell {}^4R_\ell (1 - I_k^{\hat{s}}) I_k^\ell \quad . $$

The LB = 2 segment in the standard induces one LB = 2 output segment $\{E_k, {}^2F_k\}$. The $\{E_t\}$ and the $\{E_\ell\}$ are merged to $\{E_k\}$, and

$$ {}^2F_k = \sum_{\ell,t} {}^4R_\ell ({}^2F_t - {}^2F_{\hat{t}}) I_k^{\ell,t} \quad , $$

where ${}^2F_{\hat{t}}$ is the coefficient in the energy interval which includes the reference energy. The above formula can lead to correct negative values.

In MAT,MT; MAT1,MT1, and vice versa, the subsection giving information on $\mathrm{Cov}(X_i, Y_j)$, one must generate segments to represent the formula below:

$$ \langle x_i y_j \rangle = {}^3R_i \, {}^4R_j \, \langle s_i (s_j - s_r) \rangle $$

The LB = 1 sub-subsection associated with the standard will produce a sequence of LB = 3 sub-subsections, one for each ΔE_s, of the form $\{E_k, {}^3F_k^s\}$; $\{E_{k'}, {}^3F_{k'}^s\}$. In each case the $\{E_k\}$ is obtained by merging E_s, E_{s+1}, and all E_m within ΔE_s. The $\{E_s\}$ and $\{E_\ell\}$ are merged to $\{E_{k'}\}$. Then the s^{th} such sub-subsection has components:

$$ {}^3F_k^s = {}^1F_s \sum_m {}^3R_m \, I_k^{m,s} \quad , \text{ and} $$

$$ {}^3F_{k'}^s = \sum_\ell {}^4R_\ell \, I_{k'}^\ell \, (I_k^s - \delta_{s\hat{s}}) \quad , $$

where $\delta_{s\hat{s}}$ is 1 if $s = \hat{s}$ and zero otherwise. (Instead of these sub-subsections, two sub-subsections would suffice if one combined the features of LB = 3 and 4.)

The LB = 2 segment in the standard uncertainty produces a dual-table LB = 3 segment $\{E_k, {}^3F_k\}$; $\{E_{k'}, {}^3F_{k'}\}$. The $\{E_t\}$ and $\{E_m\}$ are merged to $\{E_k\}$ for the first table, while the $\{E_t\}$ and $\{E_\ell\}$ are merged to $\{E_{k'}\}$.

$$ {}^3F_k = \sum_{m,t} {}^3R_m \, {}^2F_t \, I_k^{m,t} \quad , \text{ and} $$

$$ {}^3F_{k'} = \sum_{\ell,t} {}^4R_\ell ({}^2F_t - {}^2F_{\hat{t}}) I_{k'}^{\ell,t} \quad . $$

It will be wise to let further enumeration of examples like those above await experience to be gained in an initial practical trial.

Acknowledgment

The work outlined here benefited greatly from numerous discussions with F. G. Perey on uncertainty file structures and propagation.

References

*Research sponsored by the Energy Research and Development Administration under contract with the Union Carbide Corporation.

[1]For example, L. N. Usachev and Yu. G. Bobkov, INDC (CCP)-19/U, (Jan. 1972 for English translation); H. H. Hummel and W. M. Stacey, Jr., Nucl. Sci. Eng. 54, 35 (1974).

[2]F. G. Perey, ENDF/B format modification 73-7, Dec. 1973. This document amends F. G. Perey, Formats and Procedures for ENDF/B Error Files, May 1973, in the minutes of the May 1973 meeting of the Cross Section Evaluation Working Group, Sol Pearlstein, BNL, Chairman.

[3]ENDF files are described in ENDF 102, M. K. Drake ed., Data Formats and Procedures for the ENDF Neutron Cross Section Library (1970), National Neutron Cross Section Center, BNL [also denoted BNL-50274 (T601)].

Appendix A. ENDF/B Uncertainty File Representations

From F. G. Perey,[2] the section of ENDF File MF=33 giving uncertainties for material MAT and partial cross section MT appears as follows: (b for blank)

[MAT,33,MT/ZA,AWR;b,NL;b,b] HEAD

a { [MAT,33,MT/b,b;MAT1,MT1;NC,NI] CONT

b { [MAT,33,MT/b,b;b,b;2*NCI,NCI/CI(E)] LIST

[MAT,33,MT/b,E_r;b,LR;2*NM,NM/{E_m,R_m}] LIST[c]

d { [MAT,33,MT/b,b;LT,LB;2*NP,NP/{E_k,F_k}] LIST[e]

[MAT,33,0/b,b;b,b;b,b] SEND

An "NC-type" sub-subsection has been included as proposed in this paper.

The interpretations that have been assigned to "NI-type" subsections for five LB-values are given below.[2] In these definitions X_i and Y_j are ENDF/B cross-section values for partial cross section X at E_i and Y at E_j. $\mathrm{Cov}(X_i, Y_j) = \langle \Delta X_i \, \Delta Y_j \rangle_{av}$ over an hypothetical ensemble of cross section evaluations on equivalent data bases. Definitions are shown as sums for convenience; in use only one summand is nonzero. The coefficients $P_{j;m,n}^{i;k,\ell} = S_i^k \, S_i^\ell \, S_j^m \, S_j^n$, where $S_i^k = 1$ if $E_k \le E_i < E_{k+1}$ and zero otherwise. The F_k and F_ℓ in these definitions are those listed in the NI-type sub-subsections.

LB = 0. $\mathrm{Cov}(X_i, Y_j) = \sum_k P_{j;k}^{i;k} \, {}^0F_k$

LB = 1. $\mathrm{Cov}(X_i, Y_j) = \sum_k P_{j;k}^{i;k} \, {}^1F_k \, X_i Y_j$

LB = 2. $\mathrm{Cov}(X_i, Y_j) = \sum_{k,k'} P_{j;k'}^{i;k} \, {}^2F_k \, {}^2F_{k'} \, X_i Y_j$

LB = 3. $\mathrm{Cov}(X_i, Y_j) = \sum_{k,\ell} P_{j;\ell}^{i;k} \, F_{x,k} \, F_{y,\ell} \, X_i Y_j$

LB = 4. $\mathrm{Cov}(X_i, Y_j) = \sum_{k,\ell,\ell'} P_{j;k,\ell'}^{i;k,\ell} \, F_k \, F_\ell \, F_{\ell'} \, X_i \, Y_j$

For LB = 0,1,2 a single set of couplets $\{E_k, F_k\}$ is provided, while LB = 3 and 4 segments each contain two tables. Note that the F-tables sometimes are like relative standard errors (LB = 2,3) while some are more like variances or relative variances (LB = 0,1).

---

[a]NL subsections of this type for different MAT1, MT1.

[b]NC of these sub-subsections.

[c]This format was provided for in ref 2 but has not been assigned to show information on relative dependence on standards as proposed here.

[d]NI of these sub-sections.

[e]The notation $\{E_k, F_k\}$ for a set of couplets is used here rather than the FR(E) used by Perey.[2] No difference in meaning is intended.

SHIELDING BENCHMARK EXPERIMENTS AND SENSITIVITY STUDIES IN PROGRESS AT SOME EUROPEAN LABORATORIES

G. Hehn, M. Mattes
IKE, Institut für Kernenergetik
University of Stuttgart
7 Stuttgart 80 - Germany
W. Matthes, R. Nicks, H. Rief
Euratom, JRC
21020 Ispra - Italy

A 100 group standard library based on ENDF/B3 has been prepared by IKE° and JRC°°. This library is used for the analysis of the current European and Japanese iron benchmark experiments. Further measurements are planned for checking the data sets for graphite, sodium and water.
In a cooperation between the IKE and JRC groups coupled neutron-photon cross section sets will be produced.
Point data are processed at IKE by the modular program system RSYST (CDC 6600) for elaborating the ENDFB data, whereas the JRC group, apart from using standard codes such as SUPERTOG 3, GAMLEG etc., has developed a series of auxiliary programs (IBM 360) for handling the DLC 2D and POPOP libraries and for producing the combined neutron-plus gamma library EL4 (119 groups).
Sensitivity studies (in progress at IKE) make possible improvements in methods and optimization of calculation efforts for establishing group data. A tentative sensitivity study for a 3 dimensional MC approach is in progress at Ispra. As for nuclear data evaluation, the JRC group is calculating barium cross sections and their associated gamma spectra.

(Benchmark; neutron; cross sections; graphite; sodium; water.)

I. Introduction

A specialist meeting on Shielding Benchmark Experiments was held at Ispra, on the 17,18 and 19 April, 1974, under the joint sponsorship of NEA and EURATOM.[1] The meeting had been arranged (at the request of the European American Committee on Reactor Physics -EACRP-), in order to examine the current work and future plans in the experimental field with a view to co-ordinating the programmes and exchange results.
The items covered by the discussions were concerned also with energy heating, besides radiation penetration.
The meeting was attended by 24 delegates representing 12 European and Japanese Organizations or Establishments. One US observer was present, too.
Right from the opening of the session it was realised that defining a shielding benchmark experiment was an arduous task, which was further complicated by the inclusion of energy-deposition studies. The distinction between data testing and/or methods testing benchmark is seldomly clearcut.
The meeting finally agreed that a benchmark experiment is one which involves negligeable error due to the representation of source characteristics, shield composition, geometry and the detector response function.

°"Institut für Kernenergetik", University of Stuttgart -Germany-

°°Joint Research Center, Euratom Ispra-Italy-

II. Facilities for Shielding Benchmark Experiments

The neutron sources involved in European and Japanese experimental shielding research are:

-the fast sources Harmonie (CEA,Cadarache) and Tapiro (CNEN, Casaccia)

-the disk sources (converters) ASPIS (UKAEA, Winfrith) and EURACOS II (EURATOM, JRC, Ispra)

-the fast source YAYOI (Tokyo University), used in a gun mode.

Harmonie is a 2KW power source reactor using a highly enriched Uranium core surrounded by a blanket of depleted Uranium and a reflector of stainless Steel.

Tapiro is a fast source reactor which has a maximum power of 5 KW with a small enriched Uranium metal core surrounded by a copper reflector.

YAYOI is basically similar to Harmonie with a blanket of depleted Uranium, but the reflector is made of lead and the core can be moved horizontally to operate at five separate stations, including a beam hole, fast, intermediate and thermal neutron columns and a special "bare reactor" facility.

ASPIS is a conventional fission converter plate of natural Uranium installed at the low power source reactor Nestor; the converter power is about 7 W.

The new EURACOS facility is a 90% enriched converter disk accomodated in the thermal column of the TRIGA-Reactor at the University of Pavia. The converter power is about 400 W.

III. The Collaborative Benchmark Programme

At the Ispra meeting, the various laboratories agreed on a benchmark experiment on neutron penetration in mild steel. At a later stage, also graphite and Na could be investigated. A common set of activation detectors has also been defined without precluding, however, the use of neutron spectrometers such as organic scintillators, proportional counters, miniature semiconductor telescope spectrometer with identification of recoil protons, etc. The experiments should be presented in a common format close to that used in the benchmark experiments published by the European Shielding Information Service (ESIS). Moreover it was decided that a standard energy group structure for iron and other environmental materials to be used for the first round of calculations should be fixed.

Iron has already been studied in the Harmonie columns and the results are available. Experiments in Iron have been started at Yayoi; it is intended to extend this work to cover a penetration range up to 80 cm. An integral experiment in Iron slabs has already been carried out with the TRIGA converter-plate at Casaccia; the accomodation of the iron block into the horizontal facility Tapiro is in preparation. Measurements on ASPIS are underway, whereas the work on EURACOS has to be postponed because of the transfer of this facility from the JRC Ispra to the TRIGA reactor at Pavia.

A restrictive meeting on the Iron benchmark experiments is to be held at Winfrith on 24th and 25th of April 1975. This meeting is intended to provide an opportunity for those organizations who have embarked on the first single-material benchmark experiment to discuss the practicalities of measurements, such as intercalibration of detectors, sources, unfolding spectra etc., and also problems arising from the preliminary analysis using the standard 99-groups data sets prepared by the "Institut für Kernenergetik" at the University of Stuttgart (IKE) and the European Shielding Information Service (ESIS).

IV. Cross Sections for the Interpretation of the Benchmark Experiments

a. The Standard Library (EURLIB)

The basic cross section data for the common data set come from ENDFB/3. At its present state of development it contains the following elements or isotopes, in addition to iron: H, C12, O16, A27, Si, Ca, Cu, U235, U238. In fact, the set of energy limits used in the standard library represents a subset of the energy bounds for the Standard CSEWG Multigroup File, as proposed in a paper by C.R. Weisbin and R.J. Labauve.[2] The present energy subdivision has been chosen in such a way as to take account of the following particular requirements: adequate representation of the main resonances of materials involved in the benchmark experiments, acceptable representation of the resonance detector cross sections commonly used in the various laboratories.

For all the isotopes (or elements) except iron, the weighting spectrum 1/E has been chosen for $E \leqslant 0{,}8$ Mev; for energies greater than 0,8 Mev the weighting function was a fission spectrum. All the data are limited to a P_3-approximation. Special attention has been paid to iron, inso far as the 1/E spectrum was replaced by the function $\frac{1}{E.\Sigma_t(E)}$.

As for the thermal cross sections the IKE group calculated them from a multigroup thermal library with 123 groups, taking into account downand upscattering as well as linear anisotropy. All the data are available in the FIDO format, as required by the ANISN, DOT, MORSE programs.

A 100 group structure is too large for the treatment of the 2 or 3 dimensional geometrical representation which might be necessary for the interpretation of the benchmark experiments. Therefore, 2 collapsed structures, one to 33 groups and one to 15 groups, have been proposed. As for the detector library, the Casaccia group prepared multigroup cross sections for $Al^{27}(n,\alpha)$, $Fe^{56}(n,p)$, $Ni^{58}(n,p)$, $S^{32}(n,p)$, $In^{115}(n,n')$ in the standard scheme, whereas ESIS prepared the activation cross sections for Au^{197} and Mn^{55} for different foil thicknesses.

b. Data Processing Codes

The common effort realised in the field of benchmark experiments fall into the context of a broader cooperation agreement between the IKE and the JRC groups, for producing coupled neutron-photon cross section tests. There are already collections of neutron cross section data since many years, as DLC-2 or GAMII. But they are not sufficient for many shielding problems for the following reasons: 1) they were set up for core calculations, thus they do not describe well enough the sharp antiresonances ("windows") in some important shielding materials (f.i. Fe, O, C). Second, they contain only few gamma data -or none of them at all. (The last ENDF/B files contribute at least somewhat to this problem). An obvious consequence of the gamma data lack is that -third point- there are only few coupled libraries available (neutron-plus-gamma data), moreover they are often classified and exist only for few nuclides. Thus the ESIS staff tried to solve these four problems:

1) generation of neutron libraries taking into account explicitly the shielding needs (especially the "windows");
2) generating gamma data (n-γ and γ-γ);
3) generation of coupled n-plus-gamma libraries;
4) free publication and distribution of all results for all important nuclides (not only few nuclides needed in some specific cases).

Referring to point 1) -special shielding neutron libraries- the EURLIB activity was already explained. Moreover, a similar library HUND (for hundred groups) was set up

for H, B^{10}, C, O, Na, Mg, Al, Si, Ca, Fe, Mo) using SUPERTOG and ENDFB/3, plus a collapsed version for 24 groups.
In order to solve the second group of problems-gamma data- two $\gamma - \gamma$ libraries were calculated with the GAMLEG code starting from the data in the Hubbell compilation, EL1, for 19 groups in P5 approximation and EL2 for 21 groups in P3, both of them for 33 elements°.
The neutron-induced gamma production cross sections were calculated with the code POPOP4 starting from the DLC 12 (POPLIB) data. The classic 100 neutron groups (99 of GAM plus 1 thermal), and the 19 gamma groups of EL1 were used. This (n,γ)-library-called EL3- now contains 31 nuclides. But -third problem- for a complete shield calculation one usually must run twice a transport code -for neutrons and gammas separately- and between the runs an integration (folding) code in order to convert the neutron fluxes to gamma sources. In order to speed up this lengthy procedure, the (n,n), (n,γ), and (γ,γ) libraries were combined in form of a coupled particle library, in FIDO format suitable for ANISN, DOT and MORSE. The 100-group neutron data are those of DLC-2D (alternatively GAM II), the gamma-data are those of EL1, the (n,γ)- data those of EL3. A flow chart of the calculation procedure of EL1-EL3 and the following coupling process leading to EL4 is given in Fig. 1 below.
The data processing codes at IKE, Stuttgart, are applied mainly in two fields: first for producing group cross sections for thermal reactor cores and secondly for processing of datas needed for reactor shielding including biomedical radiation applications. In cross section data generation a great number of different codes must be used with large data input and output. For such kind of problems the modular program system RSYST[3], has been developed, which works with a central data pool from which the individual modul gets all data and writes the results back.

The main codes which process the point data to group libraries in different stages are shown in Fig. 2. Most of them are commonly used programs like SUPERTOG, LAPHAN, and SMUG which we have integrated in our data processing system.

Since cross section requirements and accuracy needed vary strongly from project to project, a data processing system must be flexible. Special resonance effects of fast neutrons are often important for shielding problems, so that a higher calculation effort in resonance energy regions is required. Spectral variations of thermal neutrons in thick iron layers of PWRs may change the effective neutron absorption appreciably and herewith the production of gamma radiation.

With appropriate flux weighting a multigroup structure of approximately 120 groups can have all the details needed for a standard shielding library with combined neutron and gamma cross sections.

°ESIS Newsletters No.10 (July 1974) and No.12 (January 1975)

The IKE multigroup libraries have such energy structure[4], a 1/E weighting and a P_5-approximation of the scatter matrix. A better treatment of resonances by narrow resonance approximation or fine group treatment is done only problem dependent for important energy regions. Transport corrected cross sections[5] are used with advantage especially in calculations of multidimensional geometries. For biomedical application combined electron and gamma cross section libraries have been produced. In the case of electrons transport correction is required to reduce the high number of P_L-moments of the scatter matrix even for one-dimensional S_N-calculations.

c. Nuclear Cross Section Calculation

The purpose of this work is to arrive at a program for the calculation of the production cross-sections for some kinds of particles in the form:

$$\sigma_a(E).f_{ab}(E,E')dE'$$

where:

$\sigma_a(E)$ is the total reaction cross section for a particle of type a and energy E, and

$f_{ab}(E,E')dE'$ is the mean number of particles of type b with an energy in the intervall dE' around E' emitted in a reaction initiated by an incoming particle of type a and energy E (a,b may be a γ, n, p, d or α)

If for example the incoming particles are neutrons and let $\phi(E,x)$ be the neutron flux at position x and energy E, then the expression:

$$\int dE\ \phi(E,x)\,\sigma_n(E)f_{nb}(E,E')dE'$$

gives us the mean number of b-type particles produced per sec per cm^3 at position x with an energy in dE' around E'. The work will develop in two phases:

a) in the first phase (work in course at the moment) we restrict our considerations to an energy range where only reactions of the type (a;b) or (a;b,c) are possible. The computer-code we use for these investigations was written by Mr. Uhl of the Institute for Nuclear Physics, University Vienna. This code is based on the statistical nuclear model and designed to follow only one decay-chain which can be chosen arbitrarily out of the whole set of possible decay-chains for the compound nucleus.

b) In the second phase we want to extend the energy region to allow for reactions with longer decay-chains. As the UHL-code follows only one specific decay-channel, our need however is an average over the whole set of possible decay chains, we plan to simulate the nuclear decay cascade by a Monte Carlo procedure. This concept leads to a clear separation of the external (angular momentum geometry) aspects of the cascade and the pure nuclear physics aspects.

At each step in the history of a cascade full information is given about all physical parameters describing the decay-process. Storing many individual histories we can afterwards scan the whole set of these histories for some interesting physical quantity and perform the proper average.

To reduce the time-consuming preparation of input data we intend to create an input-tape containing model independent standard information (e.g. Nuclear masses, Binding energies for all interesting particles, Nuclear levels (energy, spin and parity), Branching ratios for the discrete levelts etc.) and model dependent information (e.g. parameters for the level-densities, as function of mass-number, optical potential parameters for the calculation of the transmission coefficients and data concerning γ -decay.

V. Sensitivity Calculations

For most configurations of radiation source, shielding material and detector, an experienced "shielder" will be able to explain qualitatively the main features and correlations observed in radiation penetration -he will have a feel for the sensitivity of a given detector quantity to the change of property or configuration in the source or shielding material. In many shielding applications such qualitative knowledge is fully sufficient, since some important correlations may be evident and further details are not required.
Generally shielding measurements serve as integral checks of both calculational design codes and all input data used for special shielding problems. In contrary to this integral benchmark experiments of single materials or better of single elements are designed primarily for testing particular aspects of nuclear cross sections important for shielding or other reactor applications. In the second kind of experiments we have normally simple geometries, sources and isotopic compositions, so that the methodical error of the transport code becomes negligeably small and we get a good check of the cross section input. Here sensitivity studies are of great value giving the quantitative correlations between every detector quantity and all particular cross sections.

Sensitivity studies have been applied at IKE Stuttgart, both to help in evaluating iron benchmark experiments and to show in detail the special cross section requirements for shielding of a PWR and a fast reactor. Forward S_N- calculations had been performed when the influence of a few different cross section sets had to be compared. Source effects can be studied economically by adjoint calculations. But large amounts of various cross section data can best be handled in using forward and adjoint calculations in the context of linear perturbation theory according to Bartine et al.[6], of course restricted to simplified geometries. Sensitivity studies in complicated geometry will be done with the Monte Carlo method at JRC Ispra.

a) Sensitivity Studies for Iron Benchmark Experiments

Since iron is widely used in reactor technology as most important structural and shielding material and in biomedical application of fast neutrons as the primary collimator material with substantial thicknesses ($\sim$ 70 cm), integral checks of iron cross sections are of high interest. A large number of benchmark measurements become available and should be evaluated. Of particular interest are good checks of the neutron transport in the KeV resonance region, of neutron slowing down by inelastic scattering in the MeV-region and of the total gamma production.

Special attention had been paid to the treatment of resonances in production of group data. In Fig. 3 the effect of different flux weighting is shown on the total cross section for the 100 group library EURLIB. The narrow resonance approximation results in substantial changes of the group data up to 60% in comparison to the normal 1/E -flux weighting. Such resonance problems can best be checked with extreme thick layers of iron as used for benchmark experiments and are of special importance to neutron collimators. Since iron is an excellent slowing down medium for neutrons in the upper MeV-energy region and therefore specially used for shielding, checks of the inelastic scattering cross section and particularly of the energy distribution of the scattered neutrons are important. We made special sensitivity studies of the neutron flux to the anisotropy of inelastic scattering[7]. The calculations were done for a fission source with 10 cm diameter at the center of an iron sphere with 100 cm radius. As shown in Fig. 4 slowing down of neutrons is reduced, if the anisotropy of the inelastic scatter process is taken into account, resulting in a 23% decrease of the mean neutron flux below 10 KeV for the inner region 1 (0-20 cm radius) near the source and a 7% increase of fast neutrons above 1 MeV for the outer zone 5 (80-100 cm radius).

b) Sensitivity Studies for Reactor Projects

In sensitivity studies for reactor shielding one starts from integral target quantities of interest like biological dose outside the primary shield, gamma heating in pressure vessel and concrete shield or radiation damage in essential structural components outside the core.
For these target quantities one has to determine the importance and contribution

1. of different large source and shielding regions like core region or thermal shields,
2. of single isotopes or elements as Fe, U-38 etc.,
3. of partial cross sections for dominant neutron or gamma reactions,
4. of the most effective energy groups and last not least
5. of the angular moments needed.

Such studies had been done to show the requirements of cross section data for shielding of a PWR and fast reactor in simplified spherical geometry. In Fig. 5 the sensitivity

of radiation damage (production rate of atomic dislocations) in the pressure vessel of a fast reactor (SNR) to total cross section of nuclides is given. The cross section of sodium is most important, with the dominant part of reactions below 1 MeV. This relation changes for the next important isotope U-238, where the reactions above 1 MeV are essential. Iron takes the third position followed by O, Cr, Ni, Pu-39, Si, Zr, and U-35.
A sensitivity profile of radiation damage in the pressure vessel of a PWR to total reactions of material zones is given in Fig.6. The material zones represent the reactor core, the core cage (Fe 1), the first coolant region (H_2O1), the thermal shield (Fe 2) and the outer coolant region (H_2O2).

In every material region the cross sections above 1 MeV are of primary importance showing broad maxima about 3 and 5 MeV and a shift to lower energies for regions near to the pressure vessel.

c) Sensitivity Studies in Complicated Geometries

So far most of the sensitivity studies were carried out for one-dimensional problems only. In shielding calculations, where ducts and other heterogeneities are of importance, two and three-dimensional sensitivity calculations are, however, requested by several authors.
On the basis of experience of calculating differential effects in three-dimensional systems by the Monte Carlo method the possibilities of performing sensitivity studies by introducing appropriate modifications into the TIMOC code were investigated.[8]
For this purpose a sampling scheme was formulated which allows the estimation of fluxes at points and which is combined with a perturbation method based on correlated sampling. The method which was devised does not make use of the "straight-forward approach" of sampling the uncollided contribution to the detector points from each collision point, since this method is shown to have infinite variance and, therefore, a slow convergence of the mean of the flux. In the deviced scheme an intermediate collision point is sampled from a probability density function which includes explicitly the $1/r^2$ term so as to make the variance finite.[9]

In the first step of our program development the following sensitivity studies (cross section variation) will be possible:

- change of the total cross section for each isotope separatly under the assumption of a constant ratio between the differential cross sections
- change of the ratio absorption to non absorption cross sections
- change of the anisotropic scattering distribution.

References

1) - U. Farinelli and M. Martini, Facilities for Shielding Benchmark Experiments at CNEN Casaccia.
   - C. Devillers and Y. Oceries, Neutron Propagation in the Steel Column of the Source Reactor HARMONIE.
   - G. Hehn, Sensitivity Studies and Integral Benchmark Experiments.
   - R. J. Labauve, D. R. Harris, D. W. Muir and P. B. Hemmig, The Application of Shielding Benchmark Experiments to the Testing of Nuclear Data, Calculational Methods, and Procedures.
   - J. Butler, P. C. Miller, M. D. Carter and A. Packwood, The UK Programme of DATAM Experiments on Energy-Deposition and Radiation Penetration.
   - R. Richmond, Measurement of Radiation Penetration in the Iron Shield of a Gas-Cooled Fast Reactor Lattice.
   - R. Nicks and G. Perlini, Compilation of Integral Shielding Experiments.
   - S. An et al., Review of Published Results, Current Work and Future Plans of Benchmark Shielding Experiments in Japan.
   - M. D. Belli, U. Farinelli, and M. Martini, A Benchmark Experiment to Test Activation Detector Cross Sections on the TAPIRO Reactor.
   - A. K. McCracken, The RADAK Unfolding Code.
   - A. D. Knipe, A Gamma-Ray Energy Deposition Benchmark Experiment.
   - R. Nicks and G. Perlini, ESIS Exp 1: Neutron Propagation in Laminated Iron-Water Shields.
   Papers presented at the Benchmark Meeting, Ispra, April 1974.
2) C. R. Weisbin, R. J. Labauve, Specification of a Generally Useful Multigroup Structure for Neutron Transport.
3) R. Rühle: RSYST, ein integriertes Modulsystem mit Datenbasis zur automatisierten Berechnung von Kernreaktoren; IKE 4-12 (1973).
4) D. Keinert, M. Mattes, P. Stiller, NG98-18, gekoppelte Neutronen-und Gamma-Datenbibliothek mit Wärmeproduktionfaktoren; IKE 6-74 (1973).
5) Bell et al, Multitable Treatments of Anisotropic Scattering in S_N Multigroup Transport Calculations; NSE, 28 (1967).
6) Bartine et al, SWANLAKE, A Computer Code Utilizing ANISN Radiation Transport Calculations for Cross Section Sensitivity Analysis; ORNL-TM-3809.
7) Roller, Berechnung der Anisotropie der inelastischen Streuung im Eisen; IKE report in press, 1975.
8) R. Jaarsma and H. Rief, TIMOC 72 Code Manual EUR 5016 e (1973).
9) M. H. Kalos, On the Estimation of Flux at a Point by Monte Carlo, Nucl.Sci.Eng. 16, 111-117 (1963).

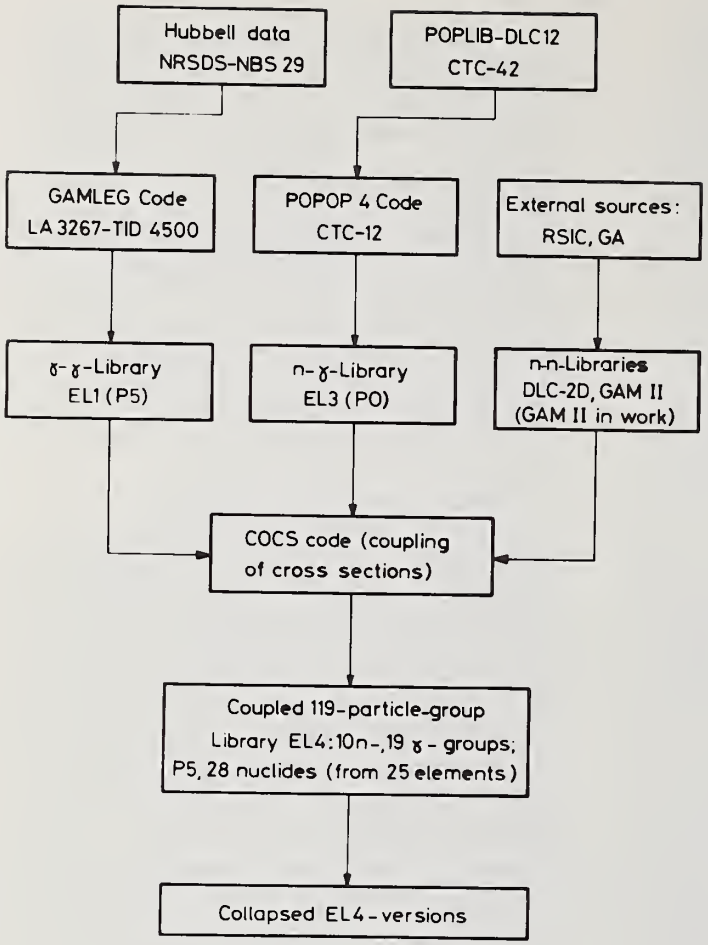

Fig. 1

CALCULATION PROCEDURE OF JRC. DATA PROCESSING.

IKE Stuttgart

Fig. 2: DATA PROCESSING IN RSYST

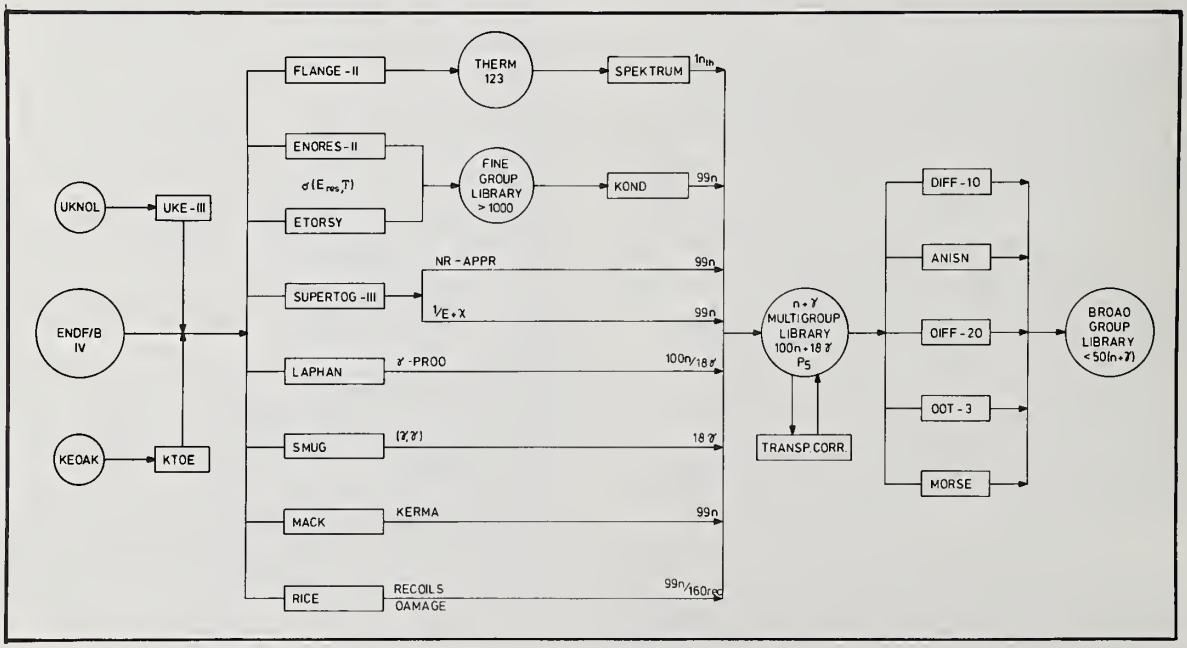

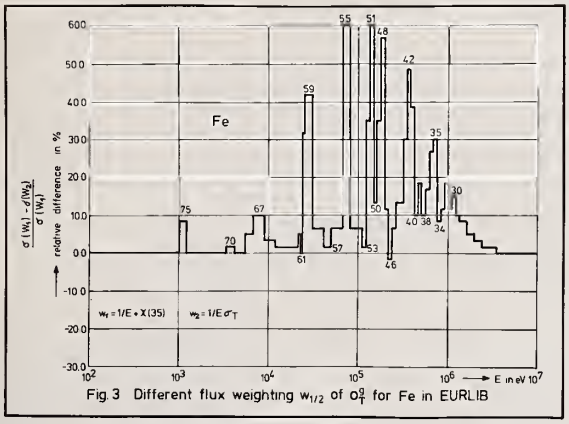

Fig. 3 Different flux weighting $w_{1/2}$ of σ_T^0 for Fe in EURLIB

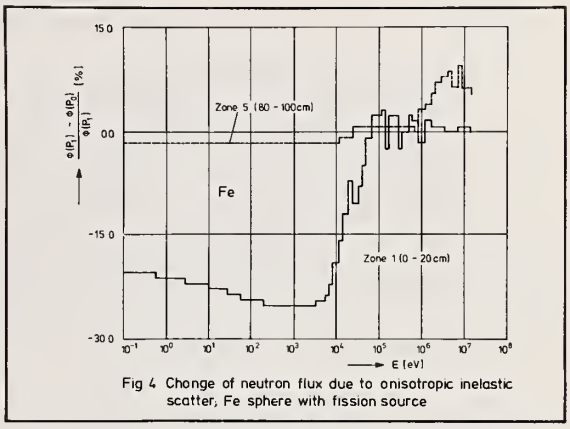

Fig 4 Chonge of neutron flux due to onisotropic inelastic scatter, Fe sphere with fission source

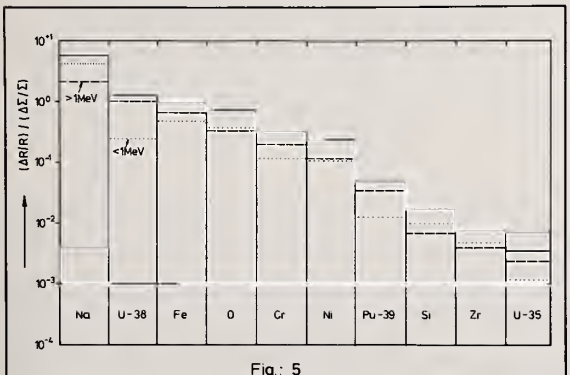

Fig.: 5

IKE Stuttgart	Sensitivity of rod. domage in pressure vessel (SNR) to totol cross section of nuclides	160.05.003.4 1974

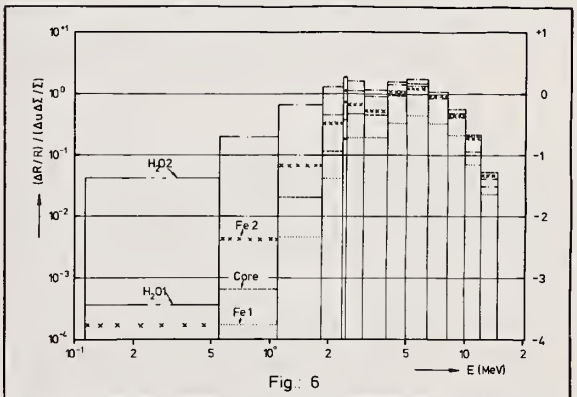

Fig.: 6

IKE Stuttgart	Sensitivity of rod. domage in pressure vessel (PWR) to totol cross section of moteriol zones	160.05.002.4 1974

ASSESSMENT OF NEUTRON GROUP CONSTANTS FOR IRON AND STAINLESS STEEL THROUGH MEASUREMENTS AND ANALYSES OF ENERGY AND SPACE DISTRIBUTIONS OF NEUTRONS IN TEST ASSEMBLIES

Itsuro Kimura, Katsuhei Kobayashi, Shu A. Hayashi, Shuji Yamamoto
Research Reactor Institute, Kyoto University
Kumatori, Sennan-gun, Osaka, Japan
Hiroshi Nishihara, Masato Ando, Satoshi Kanazawa
Department of Nuclear Engineering, Kyoto University
Sakyo-ku, Kyoto, Japan
and Masayuki Nakagawa
Japan Atomic Energy Research Institute
Tokai, Naka-gun, Ibaraki, Japan

In order to assess group constants (JAERI-FAST, ABBN, DLC-2D etc.) for iron and stainless steel, neutron energy spectra from 1keV to a few MeV in iron and stainless steel assemblies were measured by the linac-time-of-flight method. Neutron spatial distributions measured by the activation method ($^{58}Ni(n,p)^{58}Co$ and $^{197}Au(n,\gamma)^{198}Au$) showed a spherical symmetry around the photoneutron source, and enabled us to use one-dimensional transport codes (ANISN, DTF-IV etc.). The measured neutron spectra agree with the predicted by ANISN code with DLC-2D for both materials. However, C/E agreement is poorer below the 25 keV resonance when JAERI-FAST constants for iron are used in calculation. This disagreement was considerably reduced by using a modified set of constants. General shape of fast-neutron spatial distributions agrees with the theoretically predicted for all cases.

(Group constants; iron; stainless steel; neutron spectrum; time-of-flight; activation method; one-dimensional transport calculation)

Introduction

Accurate information of neutron distribution function in a reactor core is requested to predict nuclear characteristics of a reactor. Multi-group diffusion or transport calculation is often performed to obtain the neutron distribution functions by making use of multi-group constants. However, remarkable discrepancies exist among different group constants. Therefore, several methods have been proposed and tried to assess group constants.

Studies of neutron distribution function especially energy spectrum in bulk test assemblies of homogeneous materials in simple geometry have been recently performed by several groups by making use of an intense pulsed neutron source such as an electron linear accelerator[1~8]. Since it employs a single material in simple configuration, ambiguities of this method must be smaller than those of other methods.

In the present work neutron energy spectra in iron and stainless steel assemblies have been measured by neutron time-of-flight method with an electron linear accelerator as a pulsed neutron source and the results are compared with those obtained by one-dimentional multi-group transport calculation with several group constants. In addition to the spectrum measurement, spatial distribution of neutrons in both pile, that none of previous experimenters had measured, was experimentally determined by the activtion method with nickel wires and gold foils in parallel with the spectrum measurement. From this spatial distribution, the spherical symmetry of the system is demonstrated; besides, by comparing the obtained spatial distribution of neutrons with the calculated, the group constants could also be evaluated.

As the group constants to be assessed, we selected JAERI-FAST set (J-F)[9], ABBN set (ABBN)[10] and DLC-2D set[11] principally. For iron newly modified group constants of JAERI-FAST type[12] were comparatively adopted in the calculation.

Experimental Arrangement and Procedure

Sample Piles

The iron assembly was a stack of iron blocks of soft steel, JIS SS-41. The standard size of a block was 10cm X 10cm X 50cm. The constants of main impurities are tabulated in Table 1. The size of the assembly was 90cm wide, 1m long and 1m high. Electron beam enters into a reentrant hole, 5cm X 5cm. At the bottom of the hole a lead photoneutron target was located. For the purpose of extracting neutron beam from the assembly, it has a square reentrant hole, 5cm X 5cm, of which central axis was 22cm apart from the center of the assembly. By inserting an iron plug into the hole in appropriate depth, space and angular dependent neutron spectrum $\Phi(r,\mu,E)$ could be measured. For background measurement the plug was removed. Nickel wires and gold foils were distributed on the central horizontal plane.

TABLE 1 Contents of samples

Iron sample		Stainless steel	
Element	Percent(w/o)	Element	Percent(w/o)
C	0.24	Cr	18.5
Si	0.065	Ni	9.1
P	0.012	P	0.028
Mn	0.42	Mn	0.98
S	0.015	Si	0.66
		C	0.05

The stainless steel assembly was a 75cm cube and was composed of stainless steel plates, JIS SUS 304, 1cm thick. The contents except iron are also given in Table 1. Experimental arrangements for this assembly are similar to those for the iron assembly.

Pulse Neutron source

Fast neutron pulses were generated with the electron linear accelerator of Research Reactor Institute, Kyoto University. The typical operating conditions of the accelerator were as follows: electron energy, about 33 MeV; repetition rate, 100~166 pps; pulse width, 30~50 nsec; target current, 300~500 mA. A photoneutron target of lead, 5cm in diameter and 5cm thick was placed at the center of the assembly. The target was cooled by air. The energy distribution of photoneutron from the target had been measured and was found to be a composite of two Maxwellians:

$$\phi(E) \propto \begin{cases} E \exp(-E/0.89) & \text{for } E < 3.8 \text{ MeV} \\ E \exp(-E/1.70) & \text{for } E \geq 3.8 \text{ MeV} \end{cases}$$

The target was electrically insulated from the assembly and connected to the ground through a resistance of 50 ohms, from which we obtained a beam pulse that was used as a start pulse of the time-of-flight measurement.

Collimator and Flight Tube

The general configuration of a collimator and an evacuated flight tube of neutron is depicted in Fig. 1.

In order to eliminate gamma flash in the early part of time analysis, a natural uranium plate of 1cm or 2cm in thickness was used as a filter. Loss of neutrons due to collisions in this uranium plate, in its stainless steel clad, and in the aluminum windows of the flight tube is corrected by using the transmission probability through these filtering layers.

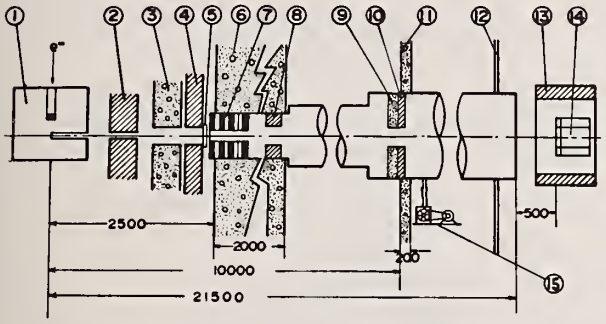

Fig. 1 Geometrical arrangement of experiment (Numbers which show distance in the figure are in mm)

① Assembly
② Lead pre-collimator (22mmϕ, 250mm thick)
③ Heavy concrete, 40cm
④ Lead, 30cm
⑤ Uranium filter
⑥ Concrete wall, 2m
⑦ Lead and B_4C collimator (47mm lead+47mm B_4C)X4 50mmϕ
⑧ Lead collimator, 20cm, 10cmϕ
⑨ B_4C collimator, 8cm } 16cmϕ
⑩ Lead collimator, 6cm }
⑪ Concrete wall, 20cm
⑫ Wall of hut
⑬ Lead Shield for detector
⑭ ^{6}Li Glass Scintillation counter bank
⑮ Rotary pump

Measurements of Spatial Distributions of Neutrons

Nickel wires of 1mm in diameter and gold foils of 3mm in diameter and of 0.05mm in thickness were used for the measurements of fast neutron flux by the ^{58}Ni(n,p)^{58}Co reaction and intermediate neutron flux by the ^{197}Au(n,γ)^{198}Au reaction, respectively. The induced gamma activities of both ^{58}Co and ^{198}Au were measured with a Ge(Li) detector.

Neutron Detector

As a neutron detector, we used a bank of three ^{6}Li glass scintillation counters of type NE 912 of Nuclear Enterprises, Ltd., 12.7cm in diameter and 1.27cm thick. By making use of a quartz light guide 1.65cm thick between the scintillator and the photomultiplier EMI-9618 R, the full width at half maximum of thermal neutron peak on the pulse height distribution of its output became less than 30%. The detection efficiency of this bank was experimentally determined by a standard neutron spectrum field with a boronated graphite pile. The result shows rather higher efficiency above several hundred keV than that obtaied by Neill et al.[13]. Details about the calibration of the detector will be given elsewhere[14].

Two ^{235}U fission chamber were used as the neutron flux monitor.

Electronics

The block diagram of the electronic circuits is shown in Fig. 2. A new fast time analyzer with a plated wire memory[15], HISTA-1000 was successfully applied to the time-of-flight analysis. On account of its short dead time (t_d= 270 nsec) no correction of dead time was necessary.

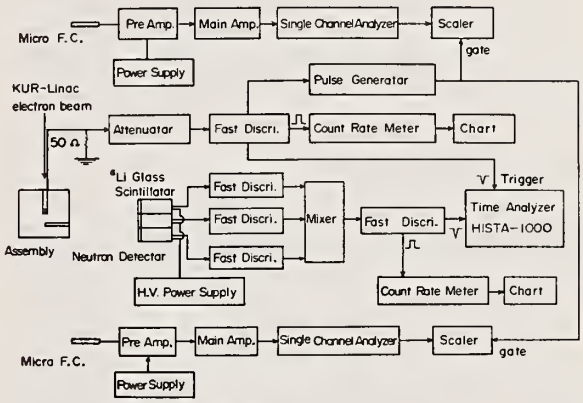

Fig. 2 Block diagram of electronic circuits

Background Measurement

The background counting rate was mainly determined by the tunnel method; the plugs were removed from the neutron extraction hole to form a through tunnel. Complementary two methods, one with a ^{7}Li glass scintillation counter and the other with a polyethylene scatterer, were also tried. The result was that the background counts by these methods were also the same as that by the tunnel method.

Data Treatment

Calibration of time versus energy scale was achieved by identifying dips and peaks on time spectra. For derivation of the energy- or lethargy-spectrum from an observed time distribution, the data were processed by well known relation between time and energy or lethargy.

Theoretical Calculation

Configuration and Assumption

In the theoretical calculation both assemblies were assumed to be spheres which had the same geometrical buckling as the test assemblies. We assumed uniform and isotropic photoneutron source in the part of spherical lead target.

In typical calculations, space mesh was taken to be 1cm and number of angular quadrature points to be sixteen, respectively.

Computer Codes

Calculation was performed by two multi-group Sn codes DTF-IV[16] and ANISN[17] assuming spherical symmetry.

Group Constants

As the neutron group constants to be assessed, we

selected the 70 group JAERI-FAST constants[9] (J-F), the 26 group constants compiled by Abagyan et al.[10] (ABBN) and the 100 group constants compiled at the Radiation Shielding Information Center of ORNL from the ENDF/B nuclear data library[11] (DLC-2D). The first two constants and the last one were used in DTF-IV and ANISN, respectively.

It has been pointed out that the original 70 group J-F constants for iron seems to have some problems below several ten keV. Our preliminary work also suggested that the original group constants could not explain the experimental results satisfactorily[7]. The main reason was thought that the self-shielding factors for the elastic slowing-down cross sections of the energy groups near the largest scattering resonance were not exactly estimated. Therefore, one of the authors recently modified the group constants (J-E)[12] by using the weighting neutron spectrum which was obtained by a code for neutron slowing-down calculation, ESELEM[18] with the same source data for J-F.

Scattering Anisotropy

In the calculation by the ANISN code with the DLC-2D constants we usually took eight terms of Legendre polynomials for anisotropic scattering cross sections. On the other hand the linearly anisotropic scattering law i.e. the P_1 approximation was adopted in the DTF-IV calculation.

Neutron spectrum in the iron assembly calculated by the ANISN code with the P_1 approximation was compared with that with the P_8 approximation, and the result showed that both spectra at the measured position and direction agreed each other in so far as at energies below 1 MeV.

Results and Discussion

Spatial Distribution of Neutron Flux

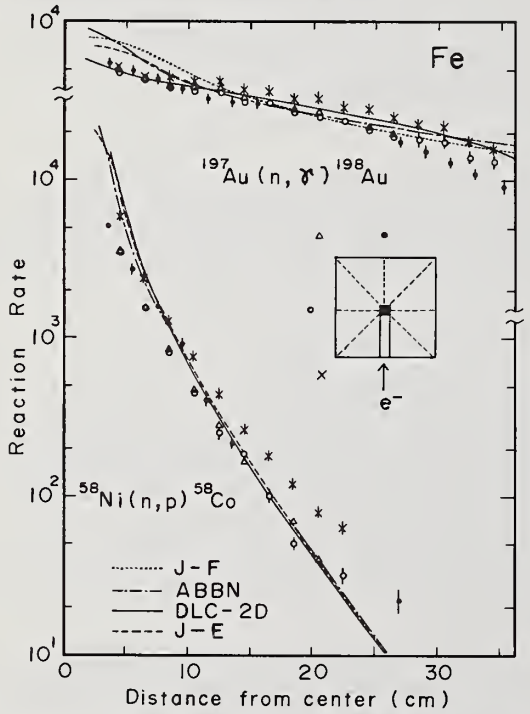

Fig. 3 Spatial distributions of the ^{58}Ni(n,p)^{58}Co and ^{197}Au(n,γ)^{198}Au reactions in the iron assembly

Spatial distributions of the ^{58}Ni(n,p)^{58}Co and ^{197}Au(n,γ)^{198}Au reactions in the iron assembly are shown in Fig. 3, from which we can see the followings: (1) The measured activities of both ^{58}Co and ^{198}Au distribute symmetrically around the lead target, especially in the forward half of the assembly where there is the reentrant hole for extracting neutrons. Activation in the backward direction ($\theta = 135^{o}$) is significantly higher and is probably due to excess production of photoneutrons in iron. (2) Theoretical predictions of ^{58}Co activity distribution are all in good agreement, and fit well to the experimental results in the forward half. (3) The radial attenuation of ^{198}Au predicted with DLC-2D agrees fairly with the measured. (4) J-F gives too rapid radial attenuation. This evidently means that the low energy tail of the J-F spectrum is unreasonably short as shown later. (5) Over-all agreement is good with those calculated using ABBN and J-F.

Figure 4 shows spatial distributions of both reactions for the stainless steel assembly. With regard to ^{58}Co activity distribution we can see a tendency similar to iron. Satisfactory agreement between the measured and the predicted with DLC-2D and ABBN can be found in the radial distribution of the ^{197}Au(n,γ)^{198}Au reaction in contrast with that for iron.

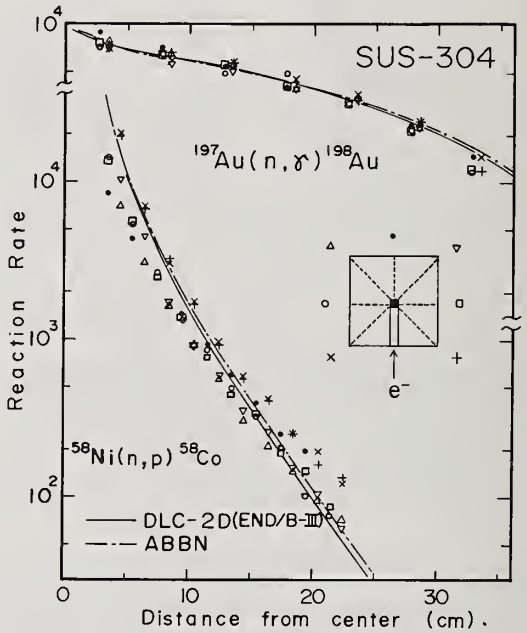

Fig. 4 Spatial distributions of the ^{58}Ni(n,p)^{58}Co and ^{197}Au(n,γ)^{198}Au reactions in the stainless steel assembly

Neutron Spectra in Iron

The space- and energy-distributions of neutron angular flux were calculated by ANISN with DLC-2B, -2C and -2D which were processed from the source data ENDF/B-I, -II and -III, respectively. The results for r = 22 ± 1cm and μ = 0 ($\theta = 90^{o}$) are shown in Fig. 5.

Although fine structure of the spectra considerably differs from each other, not big difference seems to exist among their gross structures. Therefore only the spectra calculated by ANISN with DLC-2D are used for comparison with experimental data, as shown in Fig. 6. At the same time, the experimental data are compared with the predicted by DTF-IV with J-F, J-E and ABBN. In this figure, two values have been plotted for the calculated, i.e. r = 28 and 31cm for the top, r = 21 and 23cm for the middle and r = 28 and 31cm for the bottom. (1) General agreement between the measured

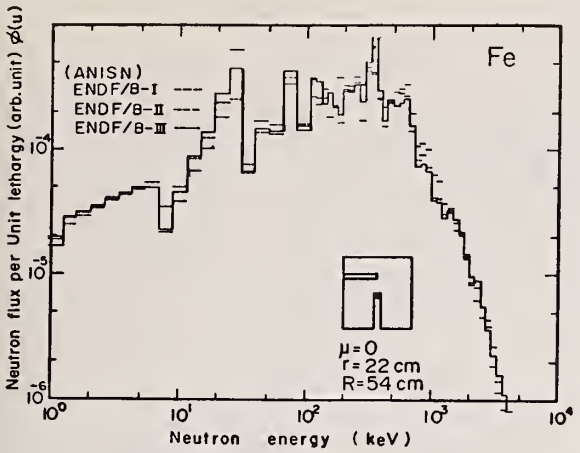

Fig. 5 Intercomparison of neutron spectra in the iron assembly calculated by ANISN with DLC-2B, -2C and -2D (ENDF/B-I, -II and -III, respectively)

and the DLC-2D spectra can be seen in the figure. (2) The low-energy tail of the J-F spectra are apparently too short. This is evidently due to insufficient slowing-down of neutrons passing through the 28 keV resonance of iron. (3) This disagreement was remarkably improved by J-E spectra which were close to those obtained with ABBN.

In this experiment, the energy resolution of time-of-flight analysis is estimated to be about 1.6% at 10 keV, 2.2% at 100 keV, and 5.4% at 1 MeV. The error mainly due to counting statistics is about 10%.

The measured and the calculated spectra are independently normalized with regard to the integral values of flux in the energy range from 100 keV to 400 keV, where the total counting rate is the highest and the experimental results are considered the most reliable in all respects.

Since, as mentioned in the previous section, the efficiency of the present neutron detector seems to be remarkably higher than that published by Neill et al.[3], at energies above several hundred keV, we compared our experimental spectrum in the iron assembly with that obtained by Cerbone et al.[2] who used the Neill's efficiency for their ^{6}Li counter. The result was that both spectra agreed satisfactorily with each other. Furthermore, we set up an iron assembly similar to that used by Malaviya et al.[5] in order to simulate their experiment. The results also agreed with Malaviya's considerably. It may be concluded, as the results of these intercomparisons, the present detector efficiency is reasonable but different from Neill's.

Neutron Spectra in Stainless Steel

Energy spectra of neutrons at three different positions and angles in the stainless steel assembly are depicted in Fig. 7. As same as in Fig. 6, the calculated spectra for two positions are shown together. In contrast with the case of iron, we can find that the

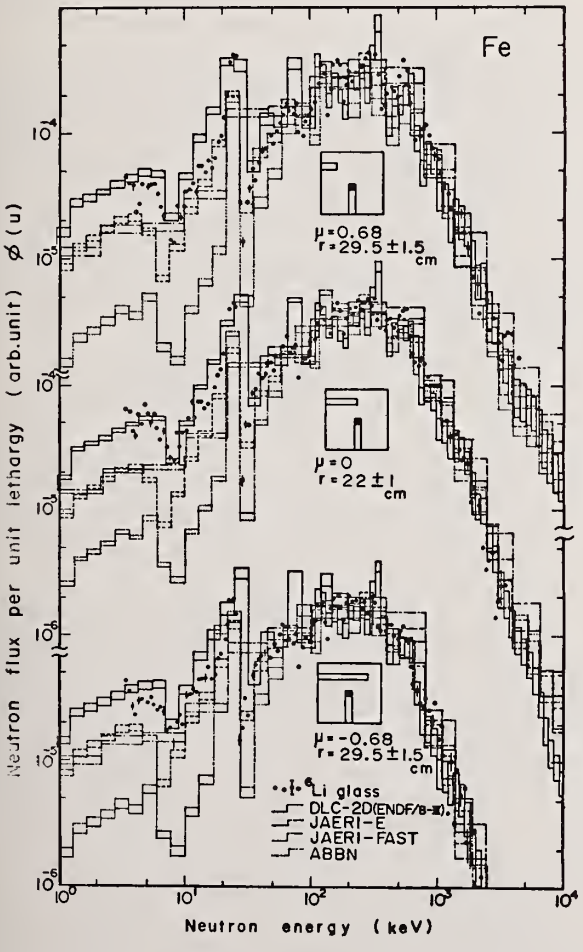

Fig. 6 Neutron spectra in the iron assembly

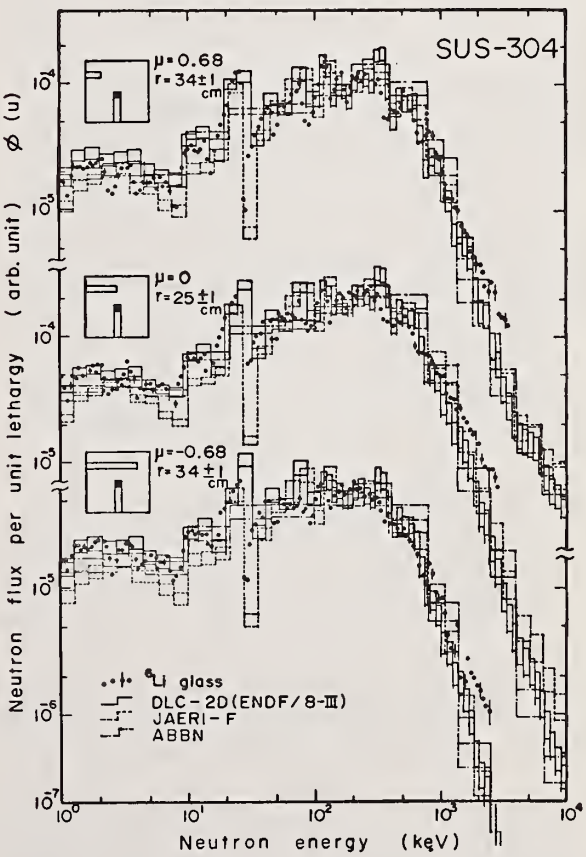

Fig. 7 Neutron spectra in the stainless steel assembly

measured spectra satisfactorily agree with the calculated with the three group constants, DLC-2D, J-F and ABBN, though the J-F and ABBN spectra are still slightly lower than the DLC-2D spectra.

Concluding Remarks

In calculating neutron flux distributions in the iron assembly with a group constant set of ABBN- or J-F-type, the background cross section must be taken to be zero. In such an extremal case, the resonance self-shielding for elastic slowing-down becomes considerably different from that for elastic scattering, especially near a large scattering resonance. In both ABBN and J-F, however, the self-shielding factor is assumed to be common to total elastic scattering and elastic slowing-down. This assumption seems to be the major reason for the unduely small estimation of the number of neutrons slowing-down through the iron resonance.

In the case of J-E set, the elastic slowing-down cross section for pure iron was directly calculated from the source data (UK library) using the exact spectrum generated by the ESELEM code. Even with J-E set, the C/E ratio below the resonance is still too small. This should be attributed either to an overestimation of the capture cross section of iron in this energy range or to neglection of neutrons produced with energies below the resonance by the n-gamma-n' reaction in the MeV region. Before going further into this problem, we are now trying to apply the variational formulation by Stacey[19] to the cross section-to-spectrum sensitivity analysis.

Ni and Cr (and probably Mn also) in stainless steel present a considerable magnitude of background cross section around the large anti-resonance of iron. Consequently, the self-shielding factor of elsatic slowing-down approaches unity. Then the above mentioned unfavorable effect of the assumption that the correction is common to elastic scattering and slowing-down is expected to become much smaller than in the case of pure iron.

DLC-2D constants were produced by the processing code SUPERTOG from the ENDF/B data. The correction for the resonance self-shielding is not taken into account in this process. Therefore, we have a plan to incorporate this correction into a processing code of SUPERTOG-type.

Acknowledgement

This study was financially supported by the Visiting Researchers Program of Research Reactor Institute, Kyoto University and also by the Grant in Aid for Fundamental Research of the Ministry of Education of Japan. The authors would like to acknowledge the continuing support of Prof. T. Shibata, Director of KURRI, and the coorperation of Mr. Y. Fujita, Chief of the LINAC crew. They also wish to express their appreciation to the considerable guidance and coorperation of Drs. S. Katsuragi, T. Tone of JAERI. Acknowledgement is also due to Drs. R. C. Block and K. Kanda for the valuable discussions on this work. The authors are deeply indebted to Messrs. Y. Katayama and T. Matsumura of Kyoto University for their assistance in both experiment and computation.

References

1. M. S. Coates et al., AERE-R 5364 (1968)
2. R. J. Cerbone et al., GA-9149 Vol.1 (1969)
3. I. Kimura et al.; Annual Reports, Res. Reactor Inst., Kyoto Univ., 3, 58 (1970)
4. K. Kanda et al., *ibid.*, 4, 25 (1971)
5. B. K. Malaviya et al., Nucl. Sci. Eng., 47, 329 (1972)
6. N. N. Kaushal et al., *ibid.*, 49, 330 (1972)
7. H. Nishihara et al., *Proceedings of International Symposium on Physics of Fast Reactors*, Tokyo, Vol. 2, p. 861 (1973)
8. A. J. H. Goddard et al., Annals of Nucl. Sci. Eng., 1, 139 (1974)
9. S. Katsuragi et al., JAERI-1195 (1970)
10. I. I. Bondarenko, *Group Constants for Nuclear Reactor Calculations*, Consultants Bureau, New York, 1964
11. Magnetic Tapes from Radiation Shielding Information Center, ORNL
12. M. Nakagawa, *unpublished*
13. J. M. Neill et al., Nucl. Instr. Meth. 82, 162 (1970)
14. I. Kimura et al., *ibid., to be submitted.*
15. I. Kimura, *ibid.*, 111, 169 (1973)
16. K. D. Lathrop, LA-3373 (1965)
17. W. W. Engle, Jr., K-1693 (1967)
18. S. Katsuragi et al., JAERI-1109 (1966)
19. W. Stacey, Jr., *Variational Methods in Nuclear Reactor Physics*, Academic Press, New York, 1974

ENDF/B DOSIMETRY CROSS SECTION FILE BENCHMARK NEUTRON FLUX-SPECTRAL UNCERTAINTIES

W. N. McElroy
Hanford Engineering Development Laboratory
Richland, WA 99352

An ENDF/B file of evaluated energy dependent cross sections for dosimetry applications has been established. The fission and most reliable non-fission reaction cross sections on this file are used with current recommended sets of evaluated measured reaction rates for several benchmark spectra to establish multiple foil derived flux-spectra with Monte Carlo uncertainties for comparison with spectrometry and calculated spectra. It is concluded that integral data testing of cross sections on the ENDF/B-IV file is presently limited to the ±5 to 10% (1σ) range because of uncertainties in the benchmark flux-spectra.

(Neutrons; spectra; flux; reaction rates; cross sections)

Introduction

An ENDF/B file of evaluated energy dependent cross sections for dosimetry applications has been established by the Cross Section Evaluation Working Group (CSEWG) and the file will be maintained by the National Neutron Cross Section Center at BNL.[1]

The USAEC established Interlaboratory LMFBR Reaction Rate (ILRR) program, the Center for Radiation Research Neutron Standards program at the National Bureau of Standards, and the CEN-SCK Standard Neutron Field program at Mol, Belgium, are in the process of establishing absolute values of reaction rates and ratios for a series of benchmark neutron spectra for data testing of this and other evaluated data files. Preliminary results of data testing of the ENDF/B-IV and other files are reported elsewhere.[1-3]

In this paper, the fission and most reliable non-fission reaction cross sections on the ENDF/B-IV file are used with current recommended sets of absolute measured reaction rates for several benchmark spectra to establish SAND-II multiple foil derived flux-spectra with Monte Carlo uncertainties. These spectra are then compared with available spectrometry and calculated spectra, which were used as input for the SAND-II analysis, to establish uncertainty estimates for currently recommended benchmark flux-spectral shapes. These uncertainties are presently limiting the accuracy of integral data testing of evaluated dosimetry cross section data files.

Data Testing, Benchmark Flux-Spectra, and Reaction Rates

Based on previous studies which made use of ENDF/B-III, SAND-II, KEDAK, and CEN-SCK evaluated cross section files, it is concluded that integral data testing of evaluated dosimetry cross sections is presently limited to the ±5 to 10% (1σ) range because of uncertainties in benchmark flux-spectra.[2-5]

Magurno and Ozer have described the ENDF/B-IV dosimetry file, which contains 36 reactions in 26 isotopes, and have provided preliminary results of CSEWG data testing.[1] At present, three fast neutron benchmark spectra are being used for this data testing; they are the CFRMF, ΣΣ, and ^{235}U fission spectra. Detailed information on these spectra and the selection of recommended sets of evaluated absolute measured reaction rates are provided in a series of ILRR program related papers in a special issue of Nuclear Technology[1-4] and a separate paper by Fabry.[5]

The currently recommended sets of evaluated absolute measured reaction rates, taken from references 2, 3, and 5, are given in Table I with estimated uncertainties for the fission and most reliable non-fission reaction cross sections on the ENDF/B-IV file. These values of reaction rates and errors are used in the next section to determine error estimates for multiple foil derived flux-spectra for the three benchmark spectra.

Flux-Spectral Determinations

Discussion

Significant differences still exist between spectrometry, multiple-foil-derived and calculated flux-spectra.[2-8] Inconsistencies between different calculated and measured flux-spectra can generally be attributed to a combination of modeling, nuclear data uncertainties, and coding problems.[3,4,7] Inconsistencies between multiple-foil-derived and spectrometry flux-spectra are less well understood, at least at present, and continue to be a serious problem.[1-5,8]

In this study, a combination of calculated, spectrometry, and multiple-foil-derived flux-spectra are used to help establish uncertainty estimates for currently recommended benchmark flux-spectra.

Multiple-Foil-Derived Flux-Spectra

Discussion. The reader is referred elsewhere for a discussion of the SAND-II method of multiple-foil-derived flux-spectral determination.[2,6,8,9] Since the previous SAND-II studies of the CFRMF, ΣΣ, and ^{235}U fission benchmark flux-spectra,[2,8] some important modifications have been made in the SAND-II Monte Carlo code.

The modifications are based on an in depth study of different weighting procedures which use measured reaction rate and evaluated cross section uncertainties to obtain a "best" SAND-II solution flux-spectrum. The modified code uses a weighting procedure based on the use of the square root of the sum of the variances of the individual foil reaction rate and evaluated energy-dependent cross section error assignments. Except for this modification, the SAND-II procedure is essentially the same as that described in reference 9.

Since the current ENDF/B-IV dosimetry cross section file does not contain error assignments, the SAND-II evaluated cross section error assignments given in reference 2 were used for this study. This was considered reasonable, since the previous error assignments were based on studies of different evaluated data files, including ENDF/B-III and-IV.

Results. As input for the SAND-II Monte Carlo code, the reference 2 cross section error assignments and Table I sets of evaluated absolute measured reaction rates, with assigned uncertainties, were used for the CFRMF, ΣΣ, and ^{235}U fission spectra.

A one-dimensional SCAMP transport calculation by Rogers, Millsap, and Harker[4] was used as the starting spectral approximation for CFRMF, an evaluated spectrometry spectrum by Fabry, G. DeLeeuw and S. DeLeeuw[3] was used for ΣΣ, and an evaluated Maxwellian fission

spectrum was used for the ^{235}U fission spectrum.

The multiple-foil-derived 20th-iteration solutions for these three spectra are shown in Figure 1, with assigned (1σ) uncertainties. They are compared with available calculated and evaluated-measured spectrometry results, which are normalized to the same area (integral flux) as the SAND-II solutions. The reader is referred to previous studies of similar results based on the use of ENDF/B-III and SAND-II cross sections.[2,8]

The SAND-II Monte Carlo code derived values of absolute total flux are $7.6_0 \times 10^{10}$(n/cm^2-sec) ±2.2%(1σ), $7.6_4 \times 10^{-1}$(n/cm^2-sec) ±3.6%(1σ), and 1.0_4(n/cm^2-sec) ±2.0%(1σ), respectively, for the CFRMF, ΣΣ, and fission spectrum based on the Table I sets of evaluated absolute measured reaction rates. The corresponding neutron mean energies are 0.74_4 ±2.2%(1σ)MeV, 0.79_7 ±2.1%(1σ)MeV, and 2.0_5 ±2.0%(1σ)MeV, respectively. The above values of total flux can be divided into the corresponding Table I sets of reaction rates to establish up-dated evaluated sets of measured CFRMF, ΣΣ, and fission spectrum averaged cross sections for integral data testing.[1]

Although there are some important differences between the results of this and previous studies (such as the higher multiple-foil-derived components of the low energy spectrum for CFRMF and ΣΣ which are in better agreement with proton recoil results), the previously observed multiple-foil-derived increases in the high energy component of each spectrum still persist with the ENDF/B-IV cross sections and current sets of evaluated measured reaction rates.

For the present study with the new SAND-II weighting procedure, the fission reactions have the greatest effect on determining the shape and magnitude of the solution spectrum because of smaller assigned reaction rate and cross section errors. Next in order would be the $^{10}B(n,\alpha)$, $^{6}Li(n,\alpha)$, $^{197}Au(n,\gamma)$, $^{58}Ni(n,p)$, etc. reactions. Most of the measured reaction rates, Table I, have very small assigned errors and the most important reaction cross sections have 3 to 8% assigned errors for their energy regions of maximum neutron response (see reference 2). It would appear, therefore, that the larger observed spectral differences, Figure 1, can be attributed to uncertainties in the current specification of the benchmark spectra rather than to reaction rate and dosimetry cross section errors. These spectral uncertainties are currently placed in the ±5 to 25% (1σ) range for the more important energy regions for the CFRMF, ΣΣ, and ^{235}U fission spectra.

Conclusions

The results of this study support previous conclusions using ENDF/B-III and other data files that integral data testing of evaluated dosimetry cross sections is presently limited to the ±5 to 10% (1σ) range because of benchmark flux-spectral uncertainties. For the more important energy regions, the spectral uncertainty are presently placed in the ±5 to 25% (1σ) range, depending on the benchmark spectrum. The uncertainties associated with multiple-foil-derived values of absolute total flux, which are needed to define measured value of spectral averaged cross sections, are much smaller and are in the ±2 to 4% (1σ) range.

References

1. B. A. Magurno and O. Ozer, Nucl. Technol. 25, 376 (1975).
2. W. N. McElroy and L. S. Kellogg, Nucl. Technol. 25, 180 (1975).
3. A. Fabry, G. DeLeeuw, and S. DeLeeuw, Nucl. Technol. 25, 349 (1975).
4. J. W. Rogers, D. A. Millsap, and Y. D. Harker, Nucl. Technol. 45, 330 (1975).
5. A. Fabry, "Evaluation of Microscopic Cross Sections Averaged in the Uranium-235 Thermal Fission Neutron Spectrum", BLG-465, Centre d'Etude de L'Energie Nucléaire, Mol, Belgium (1972).
6. J. L. Jackson, W. N. McElroy, J. A. Ulseth, and L. S. Kellogg, "EBR-II Dosimetry Tests", ANS Mtg. Irradiation Experimentation in Fast Reactors, Jackson, Wyoming, Sept. 10-12, 1973.
7. B. R. Sehgal and R. H. Rempert, Nucl. Technol. 25, 390 (1975).
8. W. N. McElroy, R. J. Armani, and E. Tochilin, Nucl. Sci. Eng. 48, 51 (1972).
9. C. A. Oster, W. N. McElroy, and J. M. Marr, "A Monte Carlo Program for SAND-II Error Analysis", HEDL-TME 73-20, Hanford Engineering Development Laboratory (1973).

Acknowledgments

The author is indebted to the members of a working committee on the improvement of error estimates for multiple-foil-derived flux-spectra. In particular to C. A. Oster (BNW), G. R. Odette (UCSB), R. Gold (JCGS), and E. P. Lippincott and R. L. Simons of HEDL. Special credit is also given to G. E. Shook and N. J. Graves of HEDL for their valuable work in helping to complete the current SAND-II Monte Carlo code error analysis studies. For ILRR and CSEWG related program guidance and support, the efforts of T. C. Reuther and P. B. Hemmig of ERDA are gratefully acknowledged. This work was supported by the Energy Research and Development Administration (ERDA).

TABLE I

BENCHMARK SPECTRA EVALUATED ABSOLUTE MEASURED REACTION RATES

REACTION	REACTION RATES (React./sec.-nucleus)		
	CFRMF[a] ($\times 10^{15}$)	$\Sigma\Sigma$[b] ($\times 10^{27}$)	FISSION[c] ($\times 10^{27}$)
^{6}Li (n,total ^{4}He)	66.2 (±3.2%)[d]	-	-
^{10}B (n,total ^{4}He)	142.9 (±1.5%)	-	-
^{235}U (n,f)FP	122.1 (±1.4%)	1171 (±3.5%)[d]	1250[e] (±3.0%)[d]
^{239}Pu (n,f)FP	142.1 (±1.6%)	1382 (±3.5%)	1859 (±3.2%)
^{237}Np (n,f)FP	43.5 (±1.9%)	467 (±3.5%)	1370 (±5.5%)
^{238}U (n,f)FP	5.96 (±1.9%)	64.4 (±3.5%)	328 (±3.1%)
^{232}Th (n,f)FP	-	15.5 (±6%)	83 (±4.2%)
^{197}Au (n,γ)^{198}Au	33.3 (±1.0%)	326 (±2%)	88 (±5.1%)
^{27}Al (n,p)^{27}Mg	0.0685 (±2.0%)	0.761 (±10%)	4.0 (±10%)
^{27}Al (n,α)^{24}Na	0.01267 (±1.2%)	0.134 (±3%)	0.725 (±2.8%)
^{54}Fe (n,p)^{54}Mn	1.367 (±1.0%)	-	82.5 (±2.4%)
^{56}Fe (n,p)^{56}Mn	-	0.201 (±3%)	1.07 (±5.6%)
^{58}Ni (n,p)^{58}Co	1.885 (±1.0%)	21.25 (±2.5%)	113 (±2.2%)
^{115}In (n,n')^{115m}In	3.90 (±4.4%)	43.2 (±2%)	188 (±2.1%)

a) Reference 2, reaction rate at a stated reaction power of 6.0 KW.

b) Reference 3, reaction rate per unit available thermal flux.

c) Reference 5, reaction rate per unit flux (or fission spectrum averaged cross section).

d) One standard deviation error estimates.

e) Reference reaction for assessment of the absolute cross-section scale--all other errors are assigned relative to this reaction. For this study, a value of ±3.0% was assigned to ^{235}U (n,f)FP.

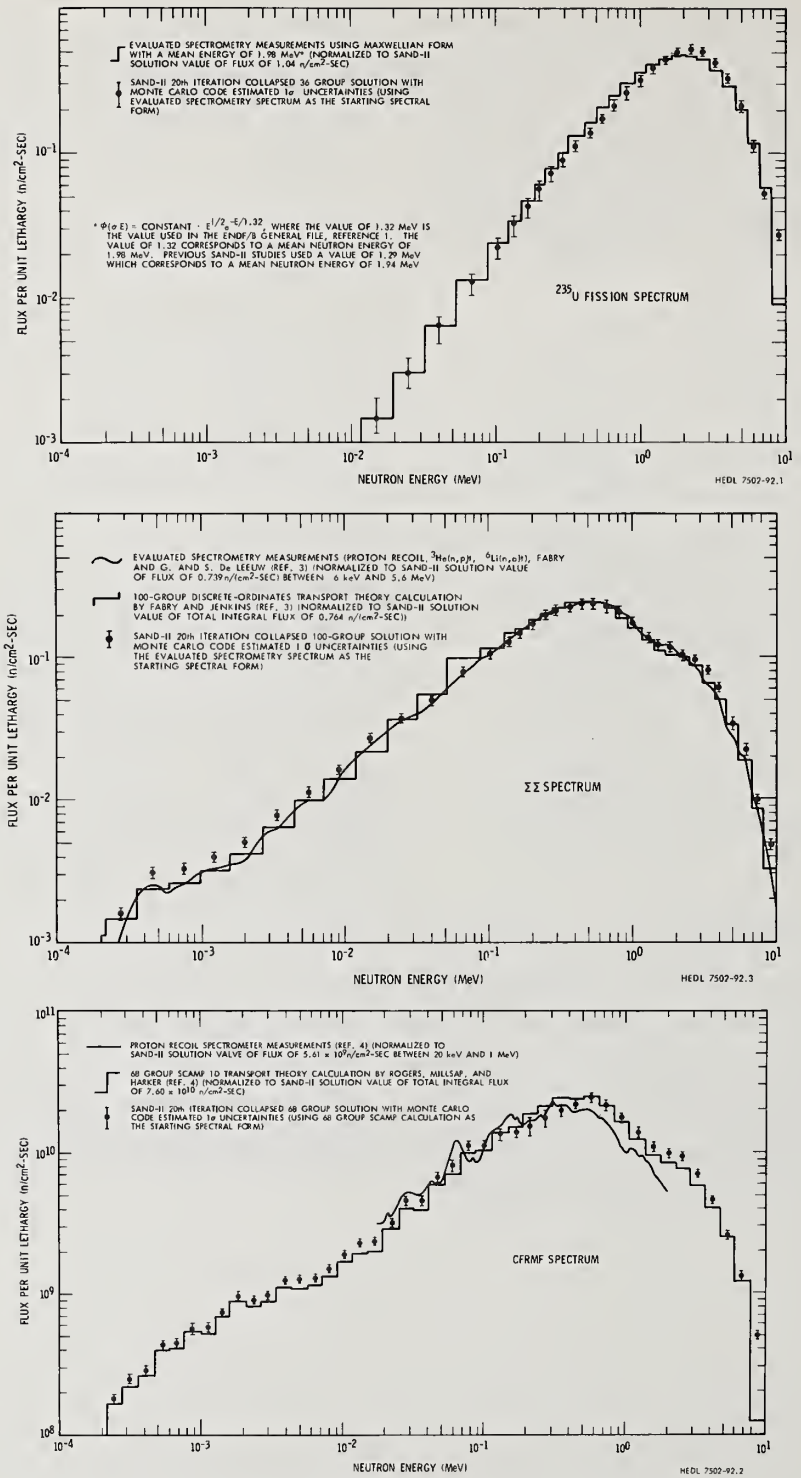

FIGURE 1. COMPARISON OF MEASURED AND CALCULATED SPECTRA

FISSION-PRODUCT GAMMA-RAY AND PHOTONEUTRON SPECTRA*

M. G. Stamatelatos and T. R. England
Los Alamos Scientific Laboratory, University of California
Los Alamos, New Mexico 87544

Fission-product gamma-ray and photoneutron spectra from thermal and fast fission of ^{233}U, ^{235}U, ^{238}U, and ^{239}Pu have been calculated at 27 time intervals between 1 and 1000 hours following reactor shutdown. The gamma spectral calculations were made using CINDER, a depletion and fission-product code, which has been revised, extended, and variably dimensioned for applications to many problems involving irradiated materials. ENDF/B-IV yield and decay data for all fission products with half-lives $\gtrsim$ 15 minutes and gamma energies above $^{9}Be(\gamma,n)^{8}Be$ threshold were used. An interesting general feature of the spectra is that they harden with time. The photoneutron spectra were calculated with PHONEX, a program general enough to operate on arbitrary gamma spectra incident on specific materials, e.g., ^{9}Be and ^{2}H. Time-dependent distributions of photons and photoneutrons/fission were calculated in 66 energy groups (50 keV grids). The constancy of these source strengths between ~ 10 and 200 hours following reactor shutdown indicates the possibility of sourceless start-ups.

(Gamma spectra; photoneutron spectra; fission products; ^{9}Be; ^{2}H; reactors)

Introduction

The importance of fission-product and other nuclide decay radiation in many areas of applied nuclear science and technology is thoroughly recognized today. The importance of decay-heating to reactor safety, for example, is currently receiving considerable attention. Nevertheless, few experimental data and even fewer detailed calculations have been available until recently.

Fission-product decay-heat experiments are difficult, especially when designed to distinguish between the various types of decays of which the gamma and the beta are by far the most important.

Theoretical calculations are also very difficult to perform, not in distinguishing between the various types of decays, but because they require sophisticated computer codes as well as a complete and accurate set of data including fission yields, decay parameters, and cross sections. A number of nuclide-chain and fission-product computer codes are currently available in the U.S. and abroad. To the best of the authors' knowledge CINDER[1] is the only computer code which can currently calculate nuclide decay spectra in an arbitrary energy grid and for arbitrary irradiation histories and fuel mixtures. The spectral feature was coded as part of the general effort to reevaluate fission-product decay heating.

Until recently, the data necessary for performing even aggregate decay-heat calculations were believed by many people to be inadequate; extensive libraries were compiled by a few people but no library was exclusively accepted in the U.S. Approximately two years ago, a large task-force was organized to expand the fission-product data in the Evaluated Nuclear Data Files (ENDF/B) from an inadequate 55-nuclide cross section set to a comprehensive set including, at present, significant cross section, decay parameters, and fission yields for 824 nuclides. The ENDF/B-IV fission-product data files were compiled and evaluated by many people at industrial and government laboratories in a cooperative, coordinated effort. The existence of such a data set makes accurate fission-product decay-heat, absorption, and spectral calculations possible for any irradiation history and for most fuels.

Reported here are fission-product gamma-ray and photoneutron spectra from thermal and fast fission of uranium and plutonium isotopes calculated at 27 time-steps between 1 and 1000 hours following fission. The nominal neutron irradiation period prior to reactor shutdown was chosen to be one month at constant power. The reported data are per Watt of operating power. The photoneutron spectra were calculated for the two most important photoneutron contributors in nuclear reactors, ^{9}Be and ^{2}H.

Computer Code Descriptions

The fission-product gamma-ray spectra were calculated using the latest version of CINDER,[1] a general nuclide depletion and fission-product computer code. CINDER calculates temporal compositions of coupled nuclides in a time-dependent flux environment. The nuclides can be coupled in any sequential mixture of radioactive decay types and neutron-, or other particle-, induced reactions. The neutron fluxes (or fission power), nuclide parameters, coupling forming nuclide chains etc. are specified by the user. The code computes concentrations of coupled fission products generated by fission in fuel chains, absorption build-up, fuel depletion, decay heating, activity and decay spectra.

Versions of the basic code or its derivatives have been in use for more than ten years. Since the existence of the first version of the code, the amount of basic nuclide data has greatly increased to the present 824-nuclide set in ENDF/B-IV. The latest version of CINDER is a reprogramming and extension of the basic code using new coding techniques which permit variable dimensioning, dynamic storage, and free-form input formats. It is capable of treating a wider variety of coupled nuclides than the previous versions for a wide class of users. The data input is greatly simplified and less subject to input preparation errors. The output options have also been extended. The capability of calculating fission-product gamma spectra in energy groups of arbitrary width is also a new feature.

The photoneutron spectra from ^{9}Be and ^{2}H based on fission-product gamma spectra from CINDER were calculated with PHONEX,[2] a new photoneutron spectrum code general enough to operate on arbitrary input gamma-ray spectra. As a convenience for the calculations reported here, the input format of the version of PHONEX we used was made compatible with the CINDER output format. Although the fission-product gamma energy range does not require it, PHONEX uses general relativistic kinematic calculations. These are mandatory for high-energy gamma-ray spectra which can be used as input to PHONEX. The

calculations in the code are conveniently broken down into a number of subroutines. Besides the gamma-ray spectra, the PHONEX input requires energy-dependent photoneutron cross sections and the functional dependence of the double-differential photoneutron cross section on the neutron center-of-mass angle. A form of the latter,[3] valid for ^{2}H and ^{9}Be at low gamma energies, is embedded in the code. It can be easily replaced when not applicable.

Input Data

The input data for the fission-product gamma spectra calculations are, primarily, ENDF/B-IV yields, branching and decay parameters for all products and their precursors which have half-lives $\gtrsim$ 15 minutes and gamma energies above the $^{9}Be(\gamma,n)^{8}Be$ threshold (~1.67 MeV). Within these criteria, there are 32 nuclides emiting gammas above the (γ,n) threshold and 25 precursors which significantly affect their concentrations. These 57 nuclides were formed into 29 nuclide chains. One of the nuclides emits 68 resolved gammas above 1.67 MeV, but the average is ~16 per nuclide.

The cross section data on photoneutron reactions are sparse, especially near the threshold. The cross sections used in the photoneutron spectral calculations are believed to be the best set currently available.[3-10] The center-of-mass neutron angular distribution for the $^{9}Be(\gamma,n)^{8}Be$ reaction is poorly known but we found that even the isotropic neutron emission assumption makes unnoticeable differences in the calculated photoneutron spectra.

Results and Discussions

The fission-product gamma spectra were calculated in 66 energy groups (50 keV uniform grid). The major contributors to the spectra at the various time intervals folling fission are listed in Table I. Listed are nuclides which contribute $\gtrsim$ 10% to the decay energy in any 50 keV bin contributing $\gtrsim$ 5% to the total gammas per fission. For each such energy bin, the nuclides are listed in order of decreasing contribution. Table II shows the major contributors to the total energy at cooling times of 1, 10, 100, and 1000 hours following fission, i.e., nuclides which contribute $\gtrsim$ 5% to the total gamma energy release rate.

The calculated gamma spectra were normalized to the total gamma yield above the (γ,n) threshold. Examples from ^{235}U thermal fission and from ^{238}U fast fission are shown in Figs. 1-3. The total gamma yield as a function of cooling time were also calculated (see, for example, Figs. 5-7); these results for $^{2}H(\gamma,n)^{1}H$ are normalized to the value at 1 hour.

All total time-dependent gamma yields have two common features: 1) they decrease rapidly up to ~10 hours, remain relatively flat up to ~200 hours and then decrease again quite rapidly and 2) the spectrum averaged gamma energies (Fig. 4) decrease slightly from 1 to 10 hours and then steadily increase up to 1000 hours. Both the spectrum hardening and the near-constant source result from the presence of energetic gamma-rays from short-lived nuclides in transient equilibrium with long-lived precursors. The most important of these are ^{140}La and ^{144}Pr, which dominate the gamma spectrum above the $^{2}H(\gamma,n)^{1}H$ threshold at large time intervals after fission. The ^{140}La contribution in the 2.3-2.35 and 2.5-2.55 MeV energy bins is visible at all times from 1 to 1000 hours. The spectral effect of the 12.8-day ^{140}Ba to ^{140}La chain has already been confirmed experimentally.[11]

The photoneutron spectra from the $^{2}H(\gamma,n)^{1}H$ and $^{9}Be(\gamma,n)^{8}Be$ reactions as well as the total time-dependent photoneutron yields follow to a great extent the behavior of the corresponding gamma distributions (Figs. 8-10). For the $^{2}H(\gamma,n)^{1}H$ reaction, the spectrum-averaged photoneutron energy remains fairly constant. The $^{9}Be(\gamma,n)^{8}Be$ average photoneutron energy, however, increases between ~10 and ~1000 hours by almost a factor of 3 (Fig. 11). The relatively flat total $^{2}H(\gamma,n)^{1}H$ photoneutron intensity between 10 and 200 hours (Fig. 12) indicates that if light water reactor photoneutrons are of measurable intensity at ~10 hours after shutdown, they should also be readily detectable more than a week later. It is, therefore, possible for reactors to use this neutron source safely to restart after shutdown periods of a few days without any other neutron source. This possibility, of course, depends on the operating power level prior to shutdown.

These general results apply to all the fuels and neutron fission energies which we examined. Table III provides a comparison of the total gamma and photoneutron source from various fuels at various fission energies. Detailed results and nuclide data will be reported separately.

References

1. T. R. England, R. Wilczynski, and N. L. Whittemore, "CINDER-7: An Interim Users Report," Los Alamos Scientific Laboratory report LA-5885-MS, to be published.

2. M. G. Stamatelatos, "PHONEX, A Computer Program to Calculate Photoneutron Spectra," Los Alamos Scientific Laboratory report LA-5860-MS, February 1975.

3. L. Hulthén and M. Sugawara, "The Two-Nucleon Problem," in Encyclopedia of Physics, S. Flugge, Ed., Vol. 39 (Springer Verlag, Berlin) 1957, Chap. 1, p. 6.

4. E. G. Fuller, private communication.

5. L. Hulthén and B. C. H. Nagel, Phys. Rev. 90, 62 (1953).

6. K. J. Jakobsen, Phys. Rev. 123, 229 (1961).

7. R. Bosch, J. Lang, R. Müller, and W. Wölfli, Helv. Phys. Acta 35, 288 (1962).

8. B. L. Berman, R. L. VanHemert and C. D. Bowman, Phys. Rev. 163, 958 (1967).

9. F. C. Barker and B. M. Fitzpatrick, Aust. J. Phys. 21, 415 (1968).

10. B. Bülow and B. Forkman, "Photonuclear Cross Sections," in Handbook of Nuclear Activation Cross Sections (International Atomic Energy Agency, Vienna, 1974) p. 475.

11. C. A. Polaski and R. G. Cochran, "Experimental Determination of the Source of Photoneutrons in a Water Moderated Nuclear Reactor," Texas A&M report 17, 1966.

*Work performed under the auspices of the United States Atomic Energy Commission.

TABLE I

MAJOR CONTRIBUTORS TO PEAKS IN GAMMA SPECTRA
(^{235}U thermal fission)

--1 HOURS COOLING--

ENERGY BIN (MeV)	NUCLIDE(S)
1.67-1.75	^{135}I, ^{98}Nb, ^{134}I
1.75-1.80	^{135}I, ^{142}La, ^{97}Zr
1.80-1.85	^{88}Rb, ^{134}I
1.90-1.95	^{142}La, ^{93}Y, ^{132}I, ^{135}I
2.00-2.05	^{88}Kr, ^{142}La
2.15-2.20	^{88}Kr, ^{142}La, ^{89}Rb
2.20-2.25	^{138}Cs, ^{88}Kr
2.35-2.40	^{88}Kr, ^{142}La
2.50-2.55	^{142}La, ^{140}La

--10 HOURS COOLING--

1.67-1.75	^{135}I
1.75-1.80	^{135}I, ^{97}Zr
1.80-1.85	^{88}Rb, ^{135}I
1.90-1.95	^{132}I, ^{93}Y
2.00-2.05	^{132}I, ^{88}Kr, ^{135}I, ^{131M}Te
2.15-2.20	^{88}Kr, ^{93}Y, ^{132}I
2.35-2.40	^{88}Kr, ^{142}La
2.50-2.55	^{140}La

--100 HOURS COOLING--

1.90-1.95	^{132}I
2.00-2.05	^{132}I
2.30-2.35	^{140}La
2.50-2.55	^{140}La

--1000 HOURS COOLING--

2.15-2.20	^{144}Pr
2.30-2.35	^{140}La
2.50-2.55	^{140}La

TABLE II

MAJOR CONTRIBUTORS TO TOTAL ENERGY
(^{235}U thermal fission)

COOLING TIME(HRS)	NUCLIDES
1	^{88}Kr, ^{135}I, ^{138}Cs, ^{88}Rb
10	^{135}I, ^{140}La, ^{88}Kr, ^{132}I, ^{88}Rb, ^{142}La
100	^{140}La, ^{132}I
1000	^{140}La, ^{144}Pr

TABLE III

GAMMA AND PHOTONEUTRON SOURCES
(Normalization Factors)

Fission Set	Shutdown Time (hrs)	γ/fiss/W (E_γ>2.225) (X 10^{-5})	γ/fiss/W (E_γ>1.67) (X 10^{-5})
^{235}U thermal	1	95.958	217.940
	10	8.942	29.686
	100	4.185	5.572
	1000	0.549	0.602
^{235}U fast	1	91.560	209.280
	10	8.639	28.946
	100	4.003	5.504
	1000	0.523	0.574
^{235}U 14 MeV	1	78.118	174.972
	10	7.377	24.268
	100	2.982	4.459
	1000	0.384	0.420
^{238}U fast	1	77.368	184.612
	10	7.597	27.596
	100	3.936	5.534
	1000	0.514	0.563
^{238}U 14 MeV	1	68.706	166.510
	10	6.773	25.494
	100	3.136	4.779
	1000	0.403	0.443
^{239}Pu thermal	1	66.216	160.342
	10	6.666	25.082
	100	3.734	5.412
	1000	0.486	0.528
^{239}Pu fast	1	79.130	179.108
	10	6.609	26.020
	100	3.575	5.265
	1000	0.464	0.505
^{233}U thermal	1	110.510	233.040
	10	10.296	30.628
	100	4.257	5.748
	1000	0.557	0.602

		n/fiss/b/W [^{2}H(γ,n)^{1}H] (X 10^{-8})	n/fiss/b/W [^{9}Be(γ,n)^{8}Be] (X 10^{-8})
^{235}U thermal	1	96.210	135.996
	10	8.441	21.454
	100	4.262	2.976
	1000	0.569	0.291
^{235}U fast	1	91.156	130.312
	10	8.118	20.838
	100	4.067	2.958
	1000	0.541	0.277
^{235}U 14 MeV	1	79.576	108.342
	10	6.922	17.326
	100	3.016	2.433
	1000	0.397	0.205
^{238}U fast	1	77.500	114.230
	10	7.221	19.925
	100	3.992	2.988
	1000	0.532	0.275
^{238}U 14 MeV	1	69.920	102.578
	10	6.424	18.252
	100	3.165	2.615
	1000	0.417	0.217
^{239}Pu thermal	1	68.034	98.220
	10	6.419	18.231
	100	3.779	2.938
	1000	0.502	0.260
^{239}Pu fast	1	83.390	106.978
	10	6.373	18.698
	100	3.614	2.866
	1000	0.480	0.249
^{233}U thermal	1	113.310	147.854
	10	9.580	21.542
	100	4.331	3.073
	1000	0.577	0.292

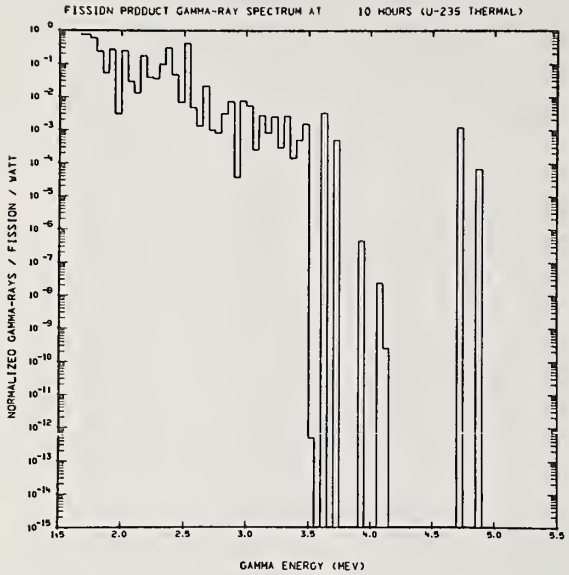

Fig. 1. ^{235}U-thermal fission-product gamma-ray spectrum at 10 hours after fission. Normalization constant = 8.9416 X 10^{-5}.

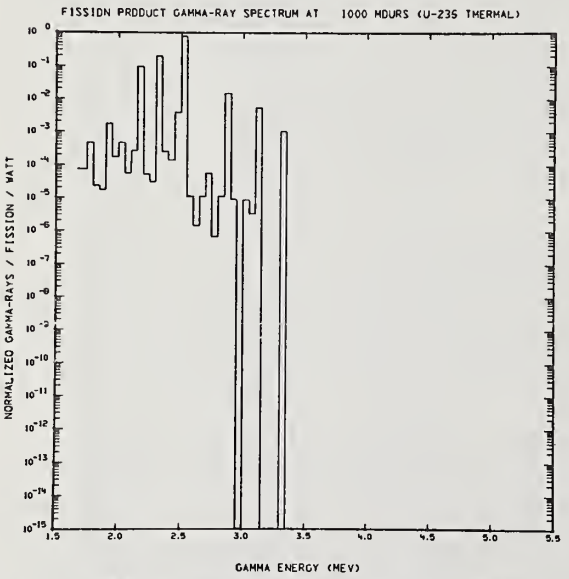

Fig. 2. ^{235}U-thermal fission-product gamma-ray spectrum at 1000 hours after fission. Normalization constant = 5.4928 X 10^{-6}.

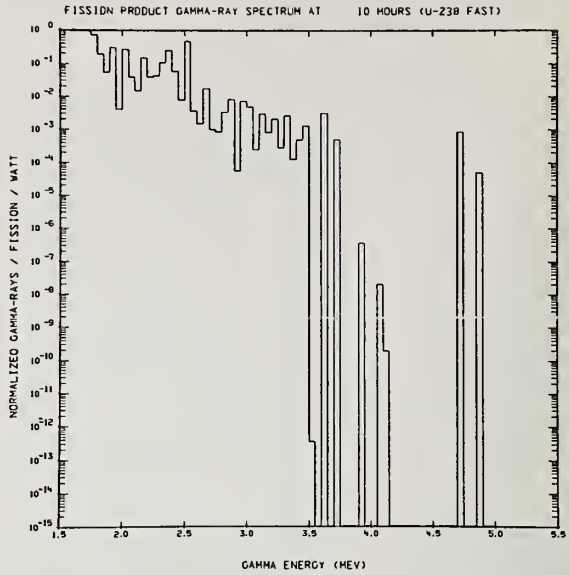

Fig. 3. ^{238}U-fast fission-product gamma-ray spectrum at 10 hours after fission. Normalization constant = 7.5968 X 10^{-5}.

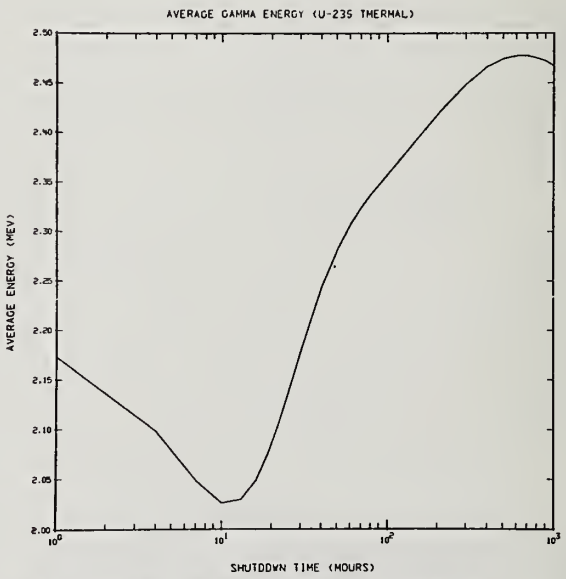

Fig. 4. Spectrum-averaged gamma-ray energy from ^{235}U-thermal fission-products.

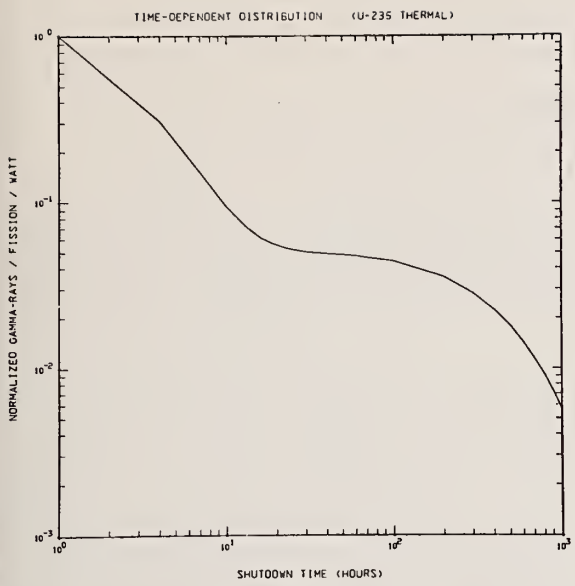

Fig. 5. Time-dependent total fission-product gamma-ray yield for ^{235}U thermal fission. Normalization constant = 9.5958 X 10^{-4}.

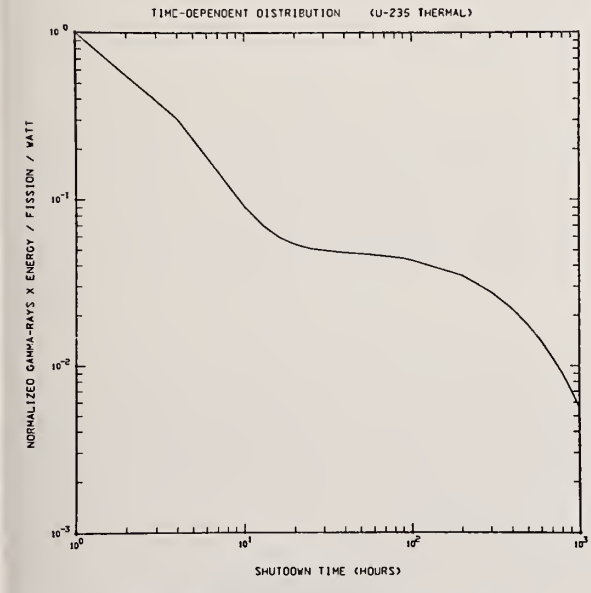

Fig. 6. Time-dependent total fission-product gamma decay-heat for ^{235}U thermal fission. Normalization constant = 2.4344 X 10^{-3}.

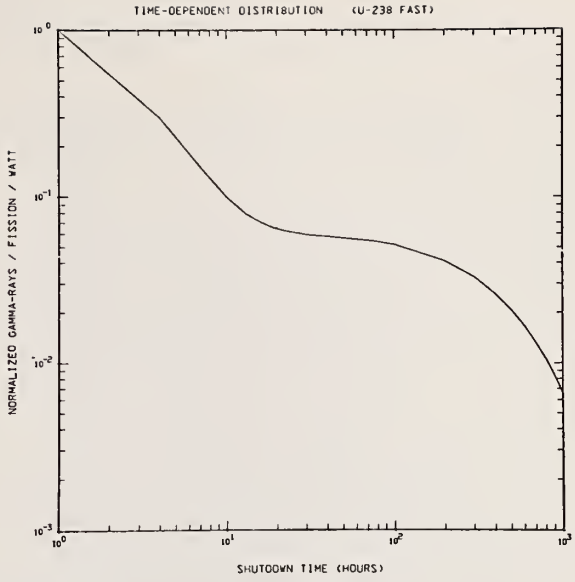

Fig. 7. Time-dependent total fission-product gamma-ray yield for ^{238}U fast fission. Normalization constant = 7.7368 X 10^{-4}.

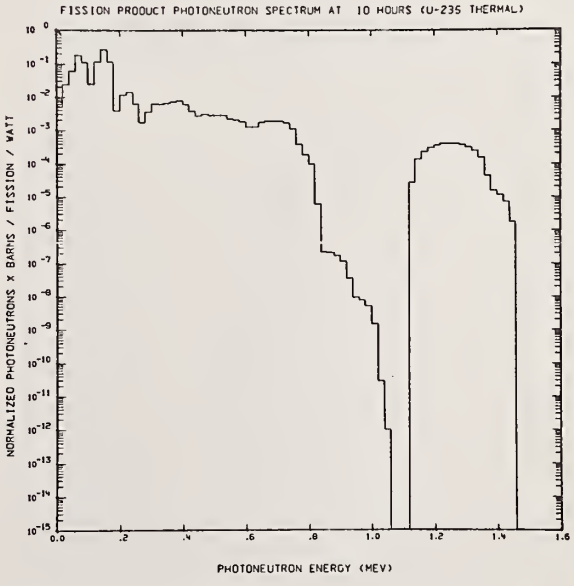

Fig. 8. ^{235}U-thermal fission-product $^{2}H(\gamma,n)^{1}H$ photoneutron spectrum at 10 hours after fission. Normalization constant = 8.4408 X 10^{-8} barn.

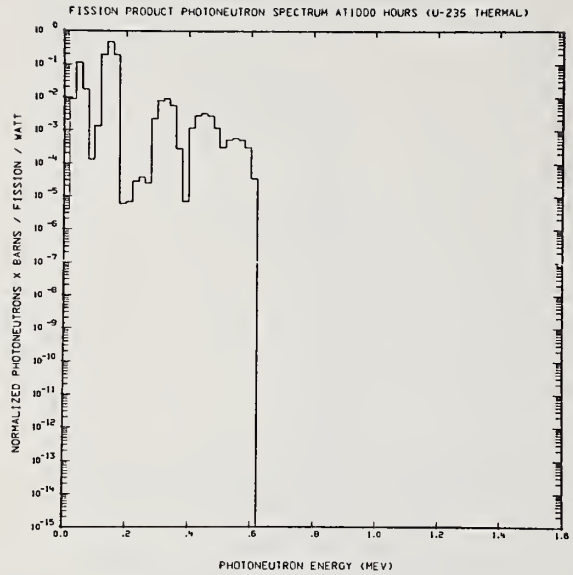

Fig. 9. ^{235}U thermal fission-product $^{2}H(\gamma,n)^{1}H$ photoneutron spectrum at 1000 hours after fission. Normalization constant = 5.6872 X 10^{-9} barn.

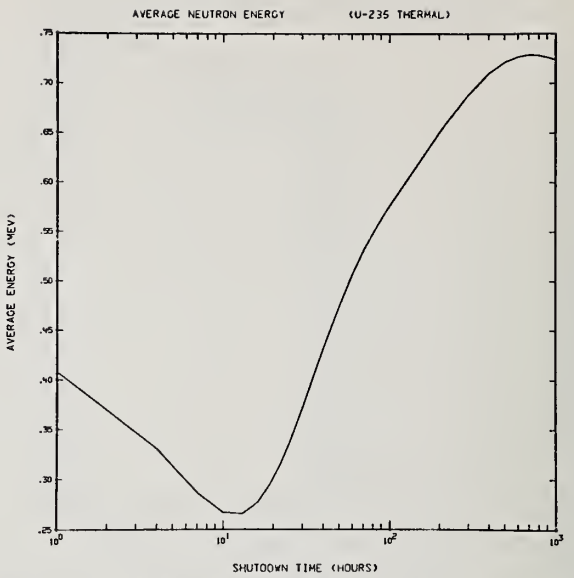

Fig. 11. Spectrum-averaged $^{9}Be(\gamma,n)^{8}Be$ photoneutron energy based on ^{235}U thermal fission-product gamma-rays.

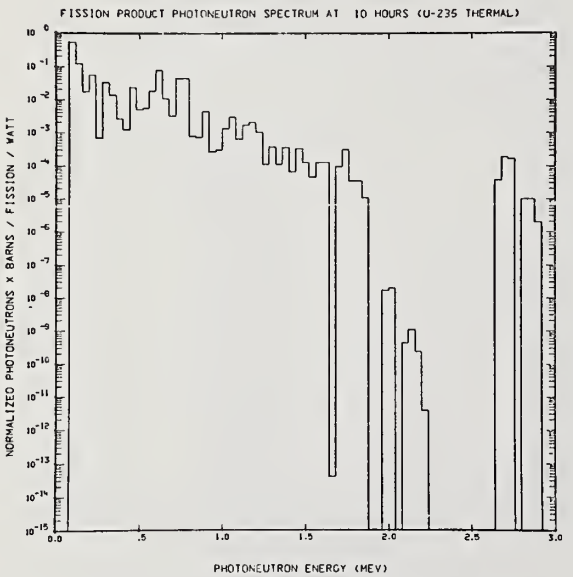

Fig. 10. ^{235}U-thermal fission-product $^{9}Be(\gamma,n)^{8}Be$ photoneutron spectrum at 10 hours after fission. Normalization constant = 2.1457 X 10^{-7} barn.

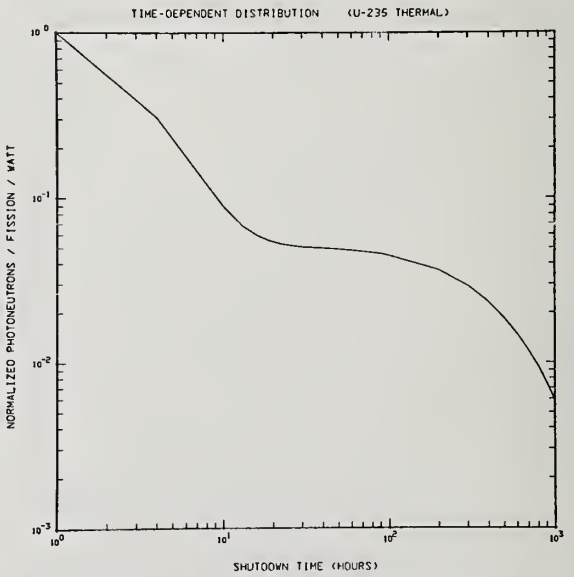

Fig. 12. Time-dependent total $^{2}H(\gamma,n)^{1}H$ photoneutron yield based on ^{235}U-thermal fission-product gamma-rays. Normalization constant = 9.621 X 10^{-7} barn.

SAFEGUARDS AGAINST THEFT OR DIVERSION OF NUCLEAR MATERIALS

T.B. Taylor
International Research and Technology Corporation
1501 Wilson Boulevard
Arlington, Virginia 22209

An overview of the risks and safeguards relevant to the possible theft or national diversion of special nuclear materials from peaceful nuclear enterprises is presented.

This paper is a brief overview of the risks of theft or diversion of nuclear materials from components of non-military nuclear technology and present and possible future safeguards designed to reduce those risks. Various technical and non technical aspects of this subject are covered in much greater detail in a number of recent publications. (1-7)

The information and non-nuclear materials needed to make fission explosives are now widely distributed and available to the general public. Dozens of nations have or could acquire the skills and facilities required to design and build reliable, lightweight, and efficient fission explosives. Crude, inefficient, and statistically variable yield, but nonetheless highly destructive fission explosives that could be transported by automobile could be designed and built by small groups of people, conceivably by individuals working alone, if they somehow managed to acquire the needed quantities of special nuclear materials. Under some conditions this could be done in an ordinary home workshop, using equipment and materials that are commercially easily available worldwide.

Plutonium, highly enriched uranium, or U-233 of the isotopic compositions used or produced in all types of power reactors could be used as core materials for fission explosives. Metallic, oxide, and some other chemical forms of these could all be used. The required amounts and the resulting explosion efficiencies, however, would depend on the chemical forms, as well as the specific type of supercriticality assembly system used.

The presence of Pu-240 and Pu-242, and the associated neutrons released by their spontaneous fission does not preclude the use of reactor grade plutonium in fission explosives. Under some conditions the minimum yield of such explosives might be comparatively low, of the order of the equivalent of 100 tons of high explosive, and the actual yield of a specific device could only be predicted to be within a rather wide range; i.e., a probability distribution of a yield, rather than a specific yield, is all that could be predicted.

It is well known that imposion-type fission explosives achieve supercriticality by compressing the special nuclear material core. Thus fission explosives can be made with amounts of special nuclear material that are initially subcritical at normal densities. The normal density critical masses of metallic spheres of uranium enriched to 93% in U-235, plutonium containing a volume fraction of 30% of Pu-240 plus Pu-242, and 95% of U-233, each in a thick natural uranium reflector, are, respectively, about 17 kilograms, 8 kilograms, and 6 kilograms. In the form of oxides at crystal density, the corresponding critical masses are 20% to 30% greater.

Plutonium, if dispersed in micron-size or smaller particles suspended in air, could also be used as a means for causing large numbers of human casualties and considerable property damage in a densely populated area. As little as a few grams of plutonium more or less uniformly distributed in the air inside an office or residential building area of several thousand square feet for fifteen minutes could deliver an inhalation dose to the occupants that would be likely to cause death from cancer some years later. Dispersal of somewhat larger quantities of plutonium in outside air could cause the evacuation from and decontamination of significant fractions of a large metropolitan area, the actually affected areas depending on weather conditions, the characteristics of buildings in the area, and a number of other factors.

Thus the presence of special nuclear materials within components of the world's nuclear energy system carries with it the risks of their diversion by nations from peaceful to military purposes, or of their theft by criminals for extortionist, terrorist, or other criminal purposes. The extent of these risks depends not only the motives of national governments and non-national groups of people, but also on the numbers and geographical distribution of places where these materials exist, the quantities of special nuclear materials at such places, and the types of safeguards against national diversion or criminal theft to which the materials are subjected.

The total amount of plutonium that has already been produced in the world's nuclear power plants (excluding the reactors in the United States, the Soviet Union, and the Peoples' Republic of China that have been used only for production of nuclear materials for weapons) is roughly 60,000 kilograms, a majority of which is still contained in irradiated reactor fuel assemblies that have not been reprocessed. Of this, about 12,000 kilograms are accounted for in 15 countries that have operating power reactors, but that have not publicly announced nuclear weapons systems: Argentina, Belgium, Bulgaria, Canada, Czechoslovakia, Western Germany, Eastern Germany, India, Italy, Japan, the Netherlands, Pakistan, Spain, Sweden, and Switzerland. (8) In addition, the following 30 countries have announced intentions to acquire large nuclear power plants within the next ten years: Australia, Austria, Bangladesh (perhaps recently cancelled), Brazil, Chile, Egypt, Finland, Greece, Hong Kong, Hungary, Iran, Ireland, Israel, Jamaica, South Korea, Luxembourg, Mexico, New Zealand, Norway, Pakistan, the Phillipines, Poland, Portugal, Romania, Singapore, South Africa, Taiwan, Thailand, Turkey, and Yugoslavia. (9) This brings to at least 50 the total number of countries that can be expected to have sufficient quantities of plutonium for at least dozens of fission explosives by 1985. By 1980 the world's total rate of production of plutonium in power reactors in about 30 countries is expected to be more than 40,000 kilograms per year, and the cumulative total produced by then will be more than 200,000 kilograms.

At least ten countries--the United States, the Soviet Union, the United Kingdom, france, the Peoples' Republic of China, Belgium, Western Germany, Italy, Japan, and India--have or are constructing nuclear fuel reprocessing plants capable of separating several hundred kilograms or more of plutonium per year. No

commercial reprocessing plant has been in operation in the United States since early 1972, and none will be until mid 1976, at the earliest. In Western Europe, on the other hand, substantial reprocessing facilities now exist in several countries.

The International Atomic Energy Agency (IAEA) in Vienna has the responsibility for safeguards to detect diversion of nuclear materials from peaceful purposes to destructive purposes by nations that are parties to the Treaty on Non-Proliferation of Nuclear Weapons (NPT) or that have otherwise agreed to place their civilian nuclear materials under international safeguards. It is not responsible, however, for applying physical security safeguards to prevent overt theft or clandestine diversion by non-national groups, such as terrorists or other criminals. This is left to individual countries to take care of.

Although the IAEA has served an international safeguarding function for more than 15 years, its present safeguards system requires additional strengthening to assure that national diversion of significant quantities of nuclear weapons materials will be promptly detected. The present IAEA annual budget for this purpose is roughly $5 million. Somewhere around 50 IAEA inspectors have the job of performing audits of nuclear material balances and periodically inspecting nuclear facilities in several dozen countries, a huge task for such a small group.

Present U.S. physical security applied to special nuclear materials for civilian purposes, though strengthened substantially during the last two years, is still inadequate to prevent theft by determined groups having resources and skills similar to these that have been used for successful bank robberies or hijacking of valuable shipments in the past.(10) Serious consideration is now being given by the Nuclear Regulatory Commission to possible new regulatory actions designed to protect special nuclear materials in the United States against overt theft or clandestine diversion considerably more effectively than is implied by current regulations and regulatory guides. There are also indications that other countries are planning to do the same. The remainder of the paper is concerned with possible new safeguards measures that might be adopted in the United States and other countries to provide much better physical security for special nuclear materials than at present.

A guiding principle, called the "principle of containment" has been proposed for the design and assessment of security systems for the protection of special nuclear materials. (11) According to this principle, all materials that could be used to make fission explosives and that are used, produced, or processed in the nuclear power industry would be contained in areas circumscribed by a well defined set of barriers. These barriers would exclude unauthorized persons. A minimum number of authorized channels for the flow of such materials through the barriers would be established. All other channels would be continuously monitored, by means of the best available technology, to detect any unauthorized flow of materials. In addition to the physical barriers, and other deterrents to theft, a network of alarms, communications, and security forces would be set up in such a way that no credible attempt to remove nuclear materials from authorized channels, whether by employees, outsiders, or a combination, would be successful.

Some of the specific security measures that might effectively be used in applying this principle and that are under study are the following:

- Co-location of fuel reprocessing and fuel fabrication plants at the same site, to remove the particularly vulnerable transportation link for recycled plutonium in concentrated form. This is not current practice.

- Dilution of separated plutonium by slightly enriched or natural uranium at the output stages of reprocessing plants, to produce the mixed oxide fuel materials before transfer to a fuel fabrication plant. (12) In equilibrium, the concentration of plutonium in mixed oxide fuel would be about 0.6% if all refabricated fuel for a light water reactor power system consisted of mixed oxides. This would not only lead to a requirement for chemical separation of the plutonium from stolen fuel material before it could be used for making fission explosives, but also, and perhaps more importantly, increase by more than a factor of 100 the total weight of fuel material that would have to be stolen to provide a given weight of contained plutonium.

- "Spiking" of plutonium, or, where applicable, highly enriched uranium or U-233 with intensive gamma ray emitters in sufficient quantities to require massive shielding to prevent lethal doses of gamma radiation from being delivered, in an hour or less, to people handling kilogram quantities of these special nuclear materials. The "spiking" materials could be retained fission products with relatively low thermal neutron cross sections, or added isotopes, such as Co-60. "Spiking" at such high levels (in the range of hundreds of REM's per hour per kilogram of plutonium at one meter, for example) would require use of massive shielding at all subsequent steps in a fuel cycle, to keep radiation exposures to workers at acceptable levels. Although some preliminary studies of this possibility are underway, it is not yet clear whether it will be cost effective.

- "Spiking" of special nuclear materials with gamma ray or neutron emitters in order to make them easier to detect with passive monitoring equipment. Routine use of this technique could lower the threshold for detection of unshielded special nuclear materials at doorway monitors, for example, to less than one gram, without requiring anywhere near as much shielding to keep worker exposures at acceptable limits as if "spiking" were used to make the materials "self-protecting."

- Use of specially designed motor vehicles and shipment vans designed to protect shipments of special nuclear materials from rather massive and sophisticated attempts to penetrate the van or commandeer the vehicle for sufficiently long times to allow large law enforcement, or even military forces to arrive at the scene of an attempted hijacking before it can be completed.

- As an alternative to the above measure, the use of rail transport of all special nuclear materials inside shipping containers similar to the roughly 100 ton containers contemplated for use in shipping irradiated fuel from reactors to reprocessing plants.

- The establishment of a Federal protective service for the explicit purpose of safeguarding nuclear materials in transit and also at fixed sites. This possibility is currently being assessed by the Nuclear Regulatory Commission.

A common reaction to these and other proposed major new safeguards measures is that, taken together, their costs are likely to make nuclear power economically uncompetitive with alternative sources of energy. Preliminary studies of the capital and operating costs of considerably more effective safeguards than those called for by present regulations, however, strongly suggest that this is not the case. One such set of estimates, for example, leads to the conclusion that the operating costs of a rather massive security system applied to light water reactor fuel cycles, with routine recycle of plutonium, would correspond to less than 1% of the cost of nuclear electric power produced by the system. (13) The total number of physical security personnel employed for the safeguarding of an 80,000 MW(e) light water reactor fuel cycle, with 20 separately sited power plants, was taken to be about 800, of whom approximately 150 would be on duty at any particular time.

Thus, from technical and economic standpoints, it appears to be possible to design physical security systems that would require skills and resources greater than those used for major thefts of valuables in the past for successful theft of potentially dangerous quantities of special nuclear materials. Whether or not the institutional and political obstacles confronting efforts to implement such effective safeguards against theft, and also against national diversion of special nuclear materials, can be overcome within the next few years, however, remains to be seen.

References

1. Leachman, R.B., Althoff, P., ed., *Preventing Nuclear Theft: Guidelines for Industry and Government.* New York: Praeger, 1972.
2. Willrich, M., ed., *International Safeguards and Nuclear Industry.* Baltimore, Md: Johns Hopkins University Press, 1973.
3. Comptroller General of the United States, *Improvements Needed in the Program for the Protection of Special Nuclear Materials.* Report to the Congress by the General Accounting Office, Washington, 1974, and *Protecting Special Nuclear Material in Transit: Improvements Made and Existing Problems (B-184105),* GAO, 1974.
4. McPhee, J., *The Curve of Binding Energy.* New York: Farrar, Straus, and Giroux, 1974.
5. Willrich, M., Taylor, T.B., *Nuclear Theft: Risks and Safeguards.* Cambridge, Mass: Ballinger, 1974.
6. Rosenbaum, D.M., et al., *Special Safeguards Study.* Prepared for the AEC's Director of Licensing in the spring of 1974.
7. U.S. Atomic Energy Commission. Tech. Rep. WASH-1535 *Proposed Final Environmental Statement, Liquid Metal Fast Breeder Reactor Program,* 1974.
8. U.S. Atomic Energy Commission, *Nuclear Power Growth, 1974-2000,* WASH-1139, 1974.
9. Ibid.
10. See References 1-7.
11. See Reference 5.
12. Private communication: Puechl, Karl, 1975.
13. See Reference 7.

FISSION THEORY AND ACTINIDE FISSION DATA

A. Michaudon
Service de Physique Nucléaire - Centre d'Etudes de Bruyères-le-Châtel
B.P n° 61 - 92120 Montrouge , France

Abstract

The understanding of the fission process has made great progress recently, as a result of the calculation of fission barriers, using the Strutinsky prescription . Double-humped shapes were obtained for nuclei in the actinide region . Such shapes could explain, in a coherent manner, many different phenomena : fission isomers, structure in near-threshold fission cross sections, intermediate structure in subthreshold fission cross sections and anisotropy in the emission of the fission fragments . A brief review of fission barrier calculations and relevant experimental data is presented. Calculations of fission cross sections, using double-humped barrier shapes and fission channel properties, as obtained from the data discussed previously, are given for some U and Pu isotopes .

The fission channel theory of A. Bohr has greatly influenced the study of low-energy fission .However, recent investigation of the yields of prompt neutrons and γ rays emitted in the resonances of ^{235}U and ^{239}Pu, together with the spin determination for many resonances of these two nuclei cannot be explained purely in terms of the Bohr theory . Variation in the prompt neutron and γ-ray yields from resonance to resonance does not seem to be due to such fission channels, as was thought previously, but to the effect of the (n, γ f) reaction .

The number of prompt fission neutrons and the kinetic energy of the fission fragments are affected by the energy balance and damping or viscosity effects in the last stage of the fission process, from saddle point to scission . These effects are discussed for some nuclei, especially for ^{240}Pu .

1 - Introduction

The design of nuclear reactors, especially for the fast breeders, requires the knowledge of a great variety of accurate fission data ; among them are i) the neutron-induced reactions for the fuel elements and for the transuranic nuclei formed during the operation of the reactor ii) the average number $\bar{\nu}_p$ and the spectrum of the prompt neutrons which are emitted per fission . These data are often needed over a wide range of incident neutron energies (for example from thermal energy to 20 MeV) and sometimes with an accuracy equal to or better than 1 % . It is obvious that such data cannot be obtained from the nuclear theory of a very complex phenomenon which is not very well known yet, despite extensive studies carried out for more than 35 years . Therefore, most of the accurate fission data come from measurements supplemented by evaluation . But fission theory plays an important role . It is essential, indeed, to have a good understanding of the fission process in order to know what the available fission data actually mean and to treat them adequately . For example, the intermediate structure effect in some subthreshold fission cross sections has changed completely the picture previously accepted of statistical properties of fission resonance parameters . This effect had not been understood until double-humped fission barrier shapes were obtained in Strutinsky's calculations and a new fission mechanism was proposed .Also, calculations based on reliable fission models, hence on fission theory, are needed to provide good evaluated fission data not only by fitting the experimental data but also and mainly by interpolating and extrapolating the known data to energy regions and/or to nuclei where no experimental results are available yet . This type of "model calculations" is more and more used by the evaluators and must be based on good fission theory .

An extensive and detailed assessment of the contribution of fission theory to fission data is largely beyond the scope of this paper . Rather, we shall focus our attention on some aspects of the fission process which may be useful for obtaining or understanding various fission data . This explains the following organization of the talk :

- Fission barriers (static and dynamical aspects) .
- Fission channel theory of Bohr .Application to the ^{239}Pu resonances . The (n, γ f) reaction .
- Damping effects . Application to the fission of ^{240}Pu at low energy .

2 - Fission barriers

2.A - The fission barrier of a nucleus is determined from the knowledge of the multidimensional potential energy surface over a wide range of deformations, from the ground state to scission through the saddle point . This potential energy cannot yet be calculated accurately by fundamental methods . Though Hartree-Fock methods are making rapid progress for the treatment of largely deformed nuclear systems[1] , they cannot be used at present to calculate fission barriers with a good precision . The most reliable method consists in using the phenomenological prescription of Strutinsky[2] in which the total energy $E_{\{s\}}$ of the nuclear system at a given deformation $\{s\}$ is obtained by adding to the liquid drop energy E_{LD} ($\{s\}$) a shell energy correction ΔE_{sh} ($\{s\}$) which takes into account the bunching of the single-particle levels near the Fermi surface :

$$E_{(\{s\})} = E_{LD}(\{s\}) + \Delta E_{sh}(\{s\}) \qquad (1)$$

Several groups are actively engaged in such macroscopic-microscopic calculations in which the correction ΔE_{sh} ($\{s\}$) is obtained by using different types of shell-model potentials : Harmonic oscillator[2,3] , Woods-Saxon[4] , folded Yukawa[5] , two-centre potentials[6,7,8] . These calculations give fission barrier shapes with two humps for nuclei in the actinide region, as is illustrated in Fig.1 . Such barrier shapes can explain in a coherent manner many different aspects of the fission phenomenon which were discovered independently one from another, for example : fission isomers, intermediate structure in subthreshold fission cross sections, structure in near-threshold fission cross sections, angular distribution of the fission fragments . This subject has been treated already in several review papers[9,10,11,12] .

2.B - Let us sum up the main aspects of the situation. About 45 fission isomers have been identified in nuclei from U through Cf isotopes with half-lives between 5.10^{-11} s. (^{242}Cm) and $1.4.10^{-2}$ s. (^{241}Am)
The subnanosecond time region has been explored for even-even U and Cm fission isomers using a geometrical magnifying effect in the fission-in-flight method[13] . No doubt that other fission isomers having shorter life-times and formed with lower isomeric ratios could be observed using improved techniques . Strong odd-even effects in the life-time values, sometimes as large as 10^3 in ratio, are observed for most of the

fission isomers . It is not clear at present whether these effects are due to a change in barrier height (as modified by pairing and/or specialization energies) or in barrier penetration (caused by a different curvature and/or mass inertia parameters) or both . Delayed fission deexcitation of the fission isomers seems to come not only from the ground state but also from excited states in the second well of the fission barrier . Prompt γ-ray transition between excited states of the ground state rotational band in the second well, preceding delayed fission deexcitation, has been detected through conversion electrons for the 4 ns ^{240}Pu fission isomer[14]. The low value of their measured energy gives the first piece of evidence that the fission isomers have a large moment of inertia, hence a large deformation, in agreement with the double-humped barrier representation[14]. The γ-ray decay of a shape isomer by tunneling through the inner barrier (the γ-branch) has been observed for ^{238}U (ref.15). Information on the spin and parity I^{π} of the fission isomers is extremely scarce . Indication on the I^{π} values for some of them is obtained from the angular distributions or the anisotropy of the fission fragments[16,17] .Unambiguous I^{π} values are very difficult to determine since i) several combinations of I and K quantum numbers can fit the data iii) it is not sure that value of K for the nuclear system is conserved when crossing the outer barrier and ii) the initial alignment of the compound nucleus formed by the reaction can be modified by neutrons and γ rays emitted before the formation of the shape isomer and also by the perturbation brought about by extra nuclear fields .

The intermediate structure in subthreshold fission cross sections has been observed for several non-fissile isotopes (a review of the subject is given in[9]) This phenomenon has been interpreted as being due to the existence of compound nucleus states in the second well of the double-humped fission barrier (class-II states)[18] as is illustrated in Fig.2 . The fine structure of the narrow resonances due to the compound nucleus states in the first well (class-I states) is then modulated by the coupling of these states to the fission exit channels through the class-II states acting as intermediate states . According to this proposed mechanism, all the large fission resonances belonging to a given cluster should have the same spin, that of the class-II state responsible for their enhanced fission width . This has been verified experimentally for ^{237}Np where the intermediate structure effect is quite pronounced[19] and where the "s" wave resonances can have two J values (J=2 and 3) . An unambiguous experiment using polarized neutrons and a polarized ^{237}Np target, clearly demonstrates that the fission contribution in the first cluster at 40 eV comes essentially from one spin state (J=3) (See Fig. 3)[20] . This mechanism also predicts that, in a given cluster, the large fission resonances should have their fission widths distributed, on the average, along a lorentzian, as a function of incident neutron energy . In addition to this smooth behavior these fission widths should exhibit-Porter-Thomas fluctuations . Such a distribution is actually observed in presently available data[9,21] .

Analysis of available fission data relevant to an interpretation in terms of the double-humped barrier can yield information on barrier parameters such as the heights of the two maxima and of the second minimum relative to the energy of the ground state . Comparison of such "experimental" fission barrier parameters with calculated values shows in general, good overall agreement but with a few areas of discrepancies ; for instance, in the Th region , the measured inner barrier is definitely higher than all values obtained from calculations[9] .

Another interesting aspect to investigate in the potential energy landscape of the fissioning nucleus is the behavior of the surface as a function of odd deformation parameters . It is a well-known fact that low-energy fission is an asymmetric fragmentation for most actinides except for the lighter ones where a mixture of symmetric and asymmetric yields can appear (see ^{227}Ac, for example) and also for ^{258}Fm which seems to prefer symmetric fragmentation only . Compilation of fragment mass distributions for the actinides shows also that, for increasing mass of the fissioning nucleus, the leading side of the heavy fragment peak seems very stable (around Z=50 and N=82) whereas the light fragment peak moves toward higher masses . These features seem connected to shell effects but no satisfactory explanation could be provided before extensive calculations for odd and even deformation parameters, using the Strutinsky prescription, could be available . An illustration of calculations of this type is shown for ^{236}U in Fig.4[8] , where it can be seen that asymmetry in the fission fragment yields is apparent in the potential energy surface at scission . A closer examination of the picture indicates that asymmetry in the nuclear system already appears at the second saddle point, between the shape isomer and scission, where a double valley starts to develop and deepens for increasing deformation as the shell structure of the nascent fragments plays a more important role due to a more pronounced necking-in . Comparison of experimental mass distributions with those obtained from such calculations shows qualitative agreement . In particular, it is of interest to note that, for light actinides (^{226}Ac), the threshold for symmetric fission appears a few MeV higher than that for asymmetric fission[22] . Nevertheless, a quantitative account of the experimental results cannot be obtained from the theory yet[12],especially since these potential energy calculations should be supplemented by a satisfactory theory of the fission dynamics which is started being studied .

2.C - <u>The calculation of fission cross sections or fission life-times</u> (for example for the ground state), requires the knowledge of the equation of motion for the fissioning system all the way to scission . This cannot be achieved without some theory of fission dynamics which, on the other hand, is poorly understood at present. One does not even know what type of fission dynamics is to be applied since it seems to depend strongly on the excitation energy (See Section 4). In the absence of an appropriate theory, one is led to make very crude assumptions in actual calculations .

- <u>At low energy</u>, in the sub-barrier region, it is generally assumed that the phase corresponding to the crossing of the barrier (i.e. where $E(\{s\})$ is greater than the energy E of the system) is adiabatic. This hypothesis means that the fission mode does not induce real intrinsic excitations in the system. After the crossing of the barrier, when the nucleus moves, in an irreversible manner, from the point of exit (where $E = E(\{s\})$) to scission, the fastness of the process is such that the adiabatic approximation is questionable. Viscosity effects may then appear in which real intrinsic excitations can be produced due to their coupling to the fission mode . These effects can affect the properties of the fragments (kinetic and excitation energies) but do not modify the fission probability since they appear in the last stage of the process only.

- <u>At higher excitation energy</u>, above the barrier, the situation is more complicated since viscosity (or damping) effects can appear at a much earlier stage of the process and therefore modify the value of the fission probability . In this energy range, general use is made of the Bohr-Wheeler formula :

$$2\pi \frac{\langle \Gamma_f \rangle}{\langle D \rangle} = N_f \qquad (2)$$

where :

- $\langle \Gamma_f \rangle$ and $\langle D \rangle$ are respectively the average fission width and spacing of the compound nucleus states taken into account .

and - N_f is the number of states available at the saddle point .

This formula, which will be discussed in more detail in Section 3, is derived by assuming statistical equilibrium and is generally verified experimentally . It has been pointed out, nevertheless, that this relation requires finite viscosity for the collective motion .

Let us now comment on these two hypotheses and illustrate how they can be used for the calculation of some fission data .

- The adiabatic approximation is certainly justified for the calculation of life-times $\tau_{g.s}$ for spontaneous fission of nuclei in their ground state . In that case, the fission probability λ per unit time ($\lambda = (\tau_{g.s})^{-1}$) is equal to the frequency $2\pi\omega_f$ for the zero-point motion mode, multiplied by the barrier penetrability P .

$$\lambda = 2\pi\omega_f \times P \qquad (3)$$

In actual calculations, it is generally assumed that $1/2\hbar\omega_f = 0.5$ MeV and the value of P can be obtained by standard WKB techniques[25] . The calculations of P are greatly simplified for one dimensional fission barriers and constant mass parameters B . One then obtains :

$$P \cong \exp\left(-2\frac{S}{\hbar}\right) \text{ if } S \gg \hbar \qquad (4)$$

with $$S = \int_{s'}^{s''} \sqrt{2\,|\,E - E(s)\,|\,.\,B}\;.\;ds \qquad (5)$$

In this last expression :

- s is the deformation parameter along the fission path .
- s' and s" (with s" > s') are the values of s, respectively at the entrance and exit of the barrier for which the total energy E of the system is equal to that of the barrier (E = E(s') = E(s")).

Improvements to life-time calculations have been brought about recently by a more sophisticated approach [4,26], that we shall summarize below .

It is first considered that the potential energy is known in a multidimensional space with a set $\{s\} = (s_1, s_2, \ldots s_i \ldots s_j \ldots)$ of deformation coordinates, using the Strutinsky procedure . But the major step forward is to consider that the mass inertia parameter B is no longer constant but can vary with $\{s\}$. This is justified by noting that the shell structure, which is so important in the calculation of the potential energy also plays a major role in the value of the mass tensor B_{ij} (the indices i and j refer to the deformation coordinates s_i and s_j respectively) . Actual calculations of B_{ij}, using the "cranking" formula show oscillations in these values with deformation quite similar to those of ΔE_{Sh} discussed previously . In this multidimensional representation, with possible variations in B_{ij} with $\{s\}$ taken into account explicitly, the expression for S now reads :

$$S = \int_{\sigma'}^{\sigma''} \sqrt{2\,|\,E - E(\{s\})\,|\;B(\sigma)}\,d\sigma \qquad (6)$$

where :

- the deformation parameters s_i, s_j, are supposed to be functions of some arbitrary parameter σ .
- σ' and σ'' are the end-point values of the parameter σ , similar to s' and s" defined in (5), for which E = E (σ') = E (σ'') .
- B (σ) is the effective mass defined by the following relation :

$$B(\sigma) = \sum_{i,j} B_{ij}\left(s_1(\sigma), s_2(\sigma) \cdots s_i(\sigma)\, s_j(\sigma) \cdots\right) \frac{\partial s_i}{\partial \sigma} \cdot \frac{\partial s_j}{\partial \sigma} \qquad (7)$$

In the adiabatic approximation, the collective motion in the fission mode is supposed to be slow enough so that, for each deformation $\{s\}$,(or a given σ value) the nucleons have enough time to rearrange themselves . It is then justified to consider the state of the system (including the single-particle states $|m\rangle$) at any deformation $\{s\}$ in the sub-barrier region . In these conditions, it is possible to derive an expression for B_{ij} , in terms of the single-particle states $|m\rangle$,having eigenvalue E_m, using the cranking formula :

$$B_{ij}(\sigma) = 2\hbar^2 \sum_{m \geq 1} \frac{\langle o|\partial/\partial s_i|m\rangle\langle m|\partial/\partial s_j|o\rangle}{E_m - E_o} \qquad (8)$$

The calculation of S, with equation (6), can be carried out provided that a trajectory, the fission path, is defined between the two end points σ' and σ'' . If B had a constant value, the fission path would follow the extremal values of the potential energy surface . This condition defines what is called the "static barrier" . The fission path is no longer the static barrier if B varies with deformation . For example, the fission trajectory may reach higher potential energy if the mass parameter takes there a smaller value . The fission path is then determined by the least-action principle ,which leads to the smallest possible value for S and, consequently, for $\tau_{g.s}$. Such a path gives the so-called "dynamical barrier" which is illustrated in Fig.5 for ^{240}Pu. It is interesting to note that the least-action trajectory does not pass through the "static" saddle points, but prefers a path at a somewhat higher energy . This seems to apply to most of the cases studied so far and appears to be a consequance of a large mass parameter at the saddle point . This effect itself is due to the shell structure which gives a large positive shell-energy correction at that deformation .

The validity of this method can be checked by comparing the fission life-time values obtained from such calculations with the experimental ones . This comparison must be carried out with great care since, according to the authors themselves[4,26] the calculations seem to be extremely sensitive to both microscopic and macroscopic properties of the nucleus . Some of these properties are not well known and the uncertainty associated with their values can drastically change the results of the calculations .For example,the variation of the pairing strength with deformation is practically unknown but plays a crucial role in the derivation of the mass tensor B_{ij} from expression (8) . In the absence of more detailed information, it is generally assumed that the pairing strength is either constant or proportional to the surface area of the nucleus. But switching from one to the other of these two assumptions changes the $\tau_{g.s.}$ values by an enormous factor, from 8 to 10 orders of magnitude for Uranium isotopes . A change as small as 10 % in the pairing strength can bring about as large as about five orders of magnitude in the life-time determination . Such variations can be expected in the deformation dependence of the pairing strength . For example, self-consistent calculations of the properties of Sm isotopes for various deformations, using the Hartree-Fock-Bogolyubov method with external constraint, show oscillations in the pairing strength as high as 20 % over a limited range of deformations, much smaller than that met in fission[28]. Also, the liquid drop parameters need to be correctly adjusted to reproduce the experimental data. For example, in Fig.6, where a good overall agreement is achieved between experimental and calculated values of $\tau_{g.s}$, not only a simple assumption was made on pairing but also the reduced fissility parameter ζ,as defined in[5], had to be adjusted separately for the various series of isotopes

Therefore, it would seem that this very interesting method needs to be supplemented by a more accurate knowledge of both microscopic (pairing strength) and macroscopic (LD parameters) properties of the fissioning nucleus as a function of deformation .

-The difficulty in calculating, from basic theory, such a simple quantity as the fission life-time for the ground state is still more pronounced for the calculation of fission cross sections. For example, the theory cannot predict as yet the detailed sequence and the exact energies of the available transition states above the two saddle points of the double-humped barrier. All practical calculations make very crude assumptions about the physical quantities which are needed. In fact, most of the calculations still assume a single-humped barrier with a constant mass parameter B .

A more sophisticated approach, though far from being completely satisfactory, has been developed recently in terms of the double-humped shape, including damping in the two wells of the barrier, and in which the physical quantities needed in the calculations are adjusted by fitting as many relevant fission data as possible[29]. We summarize below this method which makes use of the statistical model for the calculation of the neutron cross sections (including that for fission) of heavy nuclei between 3 keV and 1 MeV .

The main difficulty of the calculations lies in the determination of the fission probability at a given energy and for a well-defined set $\{c\}$ of quantum numbers (generally J,π,M and K). For all sets $\{c\}$, one-dimensional fission barriers are considered, all of them having the same shape, as sketched in Fig.7 . This shape is obtained by smoothly joining three parabolas having parameters extracted from fits to relevant fission data such as those discussed in Section 2[9,30]. For each set $\{c\}$,the barrier is shifted as a whole of an energy ΔE ($\{c\}$) determined by the fitting procedure. Damping is introduced through the form of an imaginary part in the potential in order to simulate the coupling of the fission mode to the intrinsic degrees of freedom .

The transmission of the barrier is calculated by solving the Schrödinger equation in the complex potential thus obtained .

The experimental data Di, used in this procedure when they are available, are the followings :

D_1 - the total fission cross section σ_f (E_n) at incident neutron energy E_n .

D_2 - the angular distribution σ_f (θ,E_n) of the fission fragments emitted at angle θ relative to the direction of the incident neutron beam .

D_3 - the coefficients G_L (E_n) of the Legendre polynomial expansion $\sigma_f(\theta,E_n)=\sum_L G_L(E_n)\cdot P_L(\cos\theta)$ used to fit the σ_f (θ,E_n) data .

D_4 - The anisotropy $a_s(E_n)=\sigma_{f(0°,En)}/\sigma_{f(90°,En)}$

The fission parameters P_i , determined by fitting the above data are :

P_1 - the energy shift ΔE ($\{c\}$) for the lowest fission channel having quantum numbers $\{c\}$.

P_2 - the effective number N ($\{c\}$) of fission channels having quantum numbers $\{c\}$. This takes into account the possible opening of more fission channels for increasing E_n .

P_3 - the coefficients α_n of an analytical expression $N(\{c\}) = f(E_n, \alpha_n)$ describing the variation of N ($\{c\}$) with E_n .

P_4 - the maximum depth W_m of the imaginary part of the potential supposed to have a parabolic shape, in the 2nd well.(Full damping is assumed in the first well)

These parameters Pi are determined by a least-square fit to the data Dj . In order to simplify the fitting procedure, only the most important of the 16 combinations Pi x Dj are taken into account, those which connect the available data Dj with the most sensitive parameters Pi .

Illustration of the results obtained in such calculations is given in Fig. 8 and 9 where the calculated fission and capture cross sections for ^{236}U, ^{238}Pu and ^{240}Pu are plotted as a function of E_n . Other cross sections such as those for elastic and inelastic scattering are also obtained with this procedure . All the cross sections are calculated by using a coupled-channel optical model potential with the parameters obtained by fitting ^{238}U data (ref. 31) .

It is interesting to note that not only the calculated results are in agreement with the experimental data (in fact most of the data have been used in the fitting procedure) but also that this method can give calculated cross sections where no experimental data are available (for example $\sigma(n,\gamma)$ for ^{232}U, ^{236}U and ^{238}Pu).

In summary, despite the lack of a good fission theory to calculate fission data such as life-times or cross sections, it is nevertheless possible to make use of the fairly good knowledge of the fission barriers and of simple fission models provided that their parameters can be adjusted to accurate and relevant experimental data .We shall now discuss the fission theory of A.Bohr which is commonly used in the interpretation and the calculation of fission data .

3 - Fission Channel Theory of A. Bohr : Application to ^{239}Pu resonances . The (n, γf) reaction .

As we have seen in Section 2, it is far beyond the present capabilities of fission theory to predict the fission properties of a specific fissioning state having spin and parity J^π and at an excitation energy above the neutron emission threshold and, a fortiori, to predict how these properties vary with J^π . Nevertheless, a simplification in this very complex problem appeared when A. Bohr showed that many properties of the fission process through these individual excited states could be discussed in terms of a small set of reaction alternatives or channels, even though the number of different fragment pairs is very large in binary fission of a heavy nucleus[32]. In this approach, A. Bohr proposed the concept of fission exit channels by considering that the passage from saddle point to scission is so rapid that the properties of fission, though strongly dependent on several factors, are nevertheless influenced by those of the transition states at the saddle point. In this picture, the fission exit channels are therefore these transition states whose spectrum, according to A. Bohr, is very similar to that of the first excited states of the nucleus at ground-state deformation .

This channel theory of fission provides also another interpretation of the number N_f of fission exit channels[23]. This concept of "open" fission channels was expressed in terms of fission saddle-point configurations which were energetically available . Their number N_f is given by expression (2) . This expression simply comes from the fact that the ensemble of nucleons finds itself in all allowed configurations (including the N saddle-point configurations) once every period $\tau \sim 2\pi\hbar/\langle D\rangle$. The life time τ_f for fission is thus $\tau_f \sim 2\pi\hbar/N\langle D\rangle$ from which the average fission width and Eq.(2) are then deduced .

Within the framework of the channel theory of Bohr, an effective number of fission channels, called $(N_{eff})_{J^\pi}$, is now defined for each spin and parity J^π . This number $(N_{eff})_{J^\pi}$ is also expressed in terms of the average fission width and spacing as in (2) , but, in addition, is equal to the sum of the penetrabilities P_i

for each fission channel i having spin and parity J^π. Each P_i is calculated for the fission barrier associated with the transition state i . Thus :

$$(N_{eff})_{J^\pi} = 2\pi \frac{\langle \Gamma_f \rangle_{J^\pi}}{\langle D \rangle_{J^\pi}} = \sum_i P_i \qquad (9)$$

Let us now examine how the predictions of the Bohr theory are verified in the case of ^{239}Pu resonances which are fairly well known (including their spin J) and for which the fission channel properties are very different for the two possible J^π values ($J^\pi = 0^+$ and 1^+) obtained in the capture of "s"-wave neutrons by ^{239}Pu . Whereas the lowest $J^\pi = 0^+$ transition state is symmetric and below the neutron separation energy S_n in ^{240}Pu (this is in fact the ground state of the system), the lowest $J^\pi = 1^+$ transition state seems to be asymmetric, since it has been postulated to be a combination of the two $K^\pi = 0^-$ and $K^\pi = 1^-$ octupole vibrations, and at an excitation energy above S_n .

The discussion of this subject , as already published in a previous paper[9], is summarized below and supplemented by new results obtained for prompt neutron and γ-ray emission in the ^{239}Pu resonances .

The fission width distribution for the ^{239}Pu resonances shows, as for the other fissile nuclei, large fluctuations due to the small number of available fission exit channels defined in terms of the Bohr theory . But, in contrast to all similar distributions, the one for ^{239}Pu shows clearly a break, explained by the existence of two families of resonances having widely different average fission width values . This interpretation is supported by the spin determination for a large number of resonances, as obtained by both direct and indirect methods . The values of N_{eff}, for $J^\pi = 0^+$ and 1^+ from the average widths and spacings of the resonances are respectively $(N_{eff})_{0^+} = 1.48$ and $(N_{eff})_{1^+} = 0.07$. This is in agreement with the Bohr theory if the existence of a 1^+ transition state of collective character is postulated below the 2-quasiparticle excitations.

The different symmetry properties of the transition states should be reflected in the fission properties of the 0^+ and 1^+ resonances .

The mass distribution of the fission products was measured by the "wheel technique" using a nuclear explosion as a pulsed-neutron source[33]. By radiochemical analysis, the valley-to-peak ratio of the mass distribution, or more exactly the $^{115}Cd/^{99}Mo$ ratio R was obtained for more than twenty resonances with energies ranging from 15 to 82 eV. The R-values seem to fall into two categories having average values of R in ratio 3.5 . High and low values of R are associated respectively with 0^+ and 1^+ spin states, in agreement with the theory. Moreover , there is also a correlation between the R values and the fission widths, as expected : the fission widths are larger, on the average for the group of resonances having high values of R (Fig. 10).

Variations of the total kinetic energy of the fission fragments were observed and they can also be correlated with the spin states and the variations of R in the way predicted by theory of Bohr[34] .

The behavior of $\overline{\nu}$, the average number of prompt neutrons per fission, from resonance to resonance, has been more difficult to understand for quite a long time. The situation was very puzzling several years ago when the most complete set of data available at that time showed definite variations in $\overline{\nu}$, but in opposite directions[35,36] . Moreover, these variations could be correlated with J, but in a different manner ; the high values of $\overline{\nu}$ were associated with $J^\pi = 1^+$ for one set of data[35] but with $J^\pi = 0^+$ for the other one[36]. Nevertheless, both results could find an interpretation in terms of the Bohr theory . For one case[35] it is possible to justify the observed correlation between $\overline{\nu}$ and J^π by postulating that, neglecting viscosity effects, the fission barrier associated with the 1^+ transition state remains higher than for $J^\pi = 0^+$ all the way to scission. This energy difference can them be found in an increase in the excitation energy of the fission fragments, hence in a larger $\overline{\nu}$ value. A different argument can be invoked to explain the other set of results[36] ; since the 1^+ transition state is asymmetric, a more asymmetric mass division is expected and is actually found for the 1^+ resonances, as we discussed above. This effect should be accompanied by a lower value due to the well-known saw-tooth behavior of $\overline{\nu}(A_f)$ as a function of the fragment mass A_f (ref.37) .

This confusion was not dissipated by other experiments, carried out a little later, since they concluded to the existence of fluctuations, but not correlated with J^π [38,39]. The situation has been clarified by more recent measurements of $\overline{\nu}$ and $\overline{E_\gamma}$,the mean γ-ray energy emitted per fission[40,41].The Saclay results[40] were obtained by using a big (520 l) Gd-loaded liquid scintillator for the detection of the prompt neutrons and γ rays emitted per fission. Large fluctuations are observed both in $\overline{\nu}$ and $\overline{E_\gamma}$ measured values which appear to be strongly anticorrelated . This means that high values are generally associated with low $\overline{E_\gamma}$ values . These data can be better understood if they are plotted separately for the 0^+ and 1^+ resonances which have been analysed below 200 eV. The fluctuations in $\overline{\nu}$ and $\overline{E_\gamma}$ values together with the anticorrelation between these two quantities clearly appear for the 1^+ resonances (see Fig.11) but are much less significant for the 0^+ resonances. Statistical tests applied to these data confirm this effect. The probability that the fluctuations in $\overline{\nu}$ and $\overline{E_\gamma}$ are of purely statistical nature is below 5.10^{-5} for the 1^+ resonances but as large as 0.1 and 0.63 respectively for the $\overline{\nu}$ and $\overline{E_\gamma}$ values of the 0^+ resonances. Also the correlation coefficient between $\overline{\nu}_i$ and $\overline{E_{\gamma i}}$,for a set of resonances i, is -0.84 and 0.07 respectively for the two sets of 1^+ and 0^+ resonances. There is respectively 7 % and 77 % probability that these two coefficients can be caused by statistical fluctuations only .

A closer examination of the data shows that the fluctuations in $\overline{\nu}$ and $\overline{E_\gamma}$ are larger for the 1^+ resonances having smaller fission widths. This effect appears more clearly in Fig.12 where both $\overline{\nu}$ and $\overline{E_\gamma}$ are consistent with a linear dependence with $1/\Gamma_f$.

An interpretation of this phenomenon has been put forward[42] in terms of the $(n,\gamma f)$ reaction already considered in a more general context[43] . The width $\Gamma_{\gamma f}$ for the reaction $(n,\gamma f)$ is expected to be fairly small (a few meV according to calculations[43]) and constant from resonance to resonance since it corresponds to a many-exit-channel process. It may occur that, due to the large fluctuations of Γ_f discussed previously, $\Gamma_{\gamma f}$ becomes comparable to Γ_f for some resonances, more likely to have $J^\pi = 1^+$ rather than $J^\pi = 0^+$ since $\langle \Gamma_f \rangle_{0^+} \gg \langle \Gamma_f \rangle_{1^+}$.For these resonances,the $(n,\gamma f)$ process competes with comparable probability with "direct fission", called (n,fd) in which the initial compound nucleus deexcites directly by fission. This competition explains the properties observed in $\overline{\nu}$ and $\overline{E_\gamma}$. In the $(n,\gamma f)$ reaction, more γ rays and therefore less neutrons are emitted because i) γ rays are emitted before scission by the compound nucleus which is thus less excited and ii) the final γ-ray emission by the fragments below their neutron emission threshold is common to both $(n,\gamma f)$ and $(n, f\, d)$ processes .

These considerations lead to the following relations :

$$\Gamma_f = \Gamma_{\gamma f} + \Gamma_{fd} \quad (10)$$

$$\overline{E}_{\gamma f} = \overline{E}_{\gamma fd} + \overline{e}_{\gamma} \quad (11)$$

$$\overline{\nu}_{\gamma f} = \overline{\nu}_{fd} - \overline{e}_{\gamma} \frac{\partial \overline{\nu}}{\partial E^*} \quad (12)$$

where - the subscripts f, γf and fd refer to the total fission, (n,γf) and (n,f d) processes

- $-\frac{\partial \overline{\nu}}{\partial E^*}$ is the variation of $\overline{\nu}$ with excitation energy E in "direct fission"

- $\overline{e}_{\gamma}$ is the mean energy of the pre-scission γrays emitted in the (n, γf) reaction

In the resonances where the (n, γf) and (n,f d) reactions compete, the neutron and γ-ray yields are as follows :

$$\overline{E}_{\gamma} = \overline{E}_{\gamma fd} + \overline{e}_{\gamma} \, \Gamma_{\gamma f}/\Gamma_f \quad (13)$$

$$\overline{\nu} = \overline{\nu}_{fd} - \overline{e}_{\gamma} \frac{\partial \overline{\nu}}{\partial E^*} \cdot \Gamma_{\gamma f}/\Gamma_f \quad (14)$$

These calculated yields show a linear variation with $1/\Gamma_f$ which is actually found in the experimental results for the 1^+ resonances. The phenomenon is certainly present in the $J^\pi = 0^+$ resonances but is masked by their large fission width .

This seems to be the first piece of evidence for the existence of the (n, γf) reaction which is also confirmed by the fact that the average multiplicity $\overline{n}_{\gamma}$ of the fission γ rays emitted in the ^{239}Pu resonances shows a linear dependence with $1/\Gamma_f$ in the same manner as $\overline{\nu}$ and $\overline{E}_{\gamma}$ [42] .

Analysis of the $\overline{\nu}$ and $\overline{E}_{\gamma}$ data, by a least-square fit to the experimental values, is consistent with the conservation of the energy for the sum of the prompt neutron and γ-ray yields. This analysis gives the following value :

$$\Gamma_{\gamma f} \cdot \overline{e}_{\gamma} = (4.6 \pm 0.4) \times 10^3 \text{ eV}^2 \quad (J^\pi = 1^+) \quad (15)$$

For the 0^+ resonances, a similar expression can be derived though the phenomenon is much less pronounced :

$$\Gamma_{\gamma f} \cdot \overline{e}_{\gamma} = (8.0 \pm 1.9) \times 10^3 \text{ eV}^2 \quad (J^\pi = 0^+) \quad (16)$$

These values are in agreement with recent calculations making conventional assumptions about the fission and γ-ray decay of compound nucleus states[40] .

The existence and the influence of the (n, γf) reaction for the ^{239}Pu resonances seems to be clearly established and explains most of the variations observed in $\overline{\nu}$ and $\overline{E}_{\gamma}$. It explains also the fact that no resonances have been observed with a fission width smaller than 4 meV, which is very close to the expected value for $\Gamma_{\gamma f}$.

After removal of the effect of the (n, γf) reaction in the ^{239}Pu resonances, one obtains for the neutron and γ-ray yields and for the two spin states :

$$(\overline{\nu}_{fd})_{0^+} - (\overline{\nu}_{fd})_{1^+} = 0.0130 \pm 0.0055 \text{ neutrons} \quad (17)$$

$$(\overline{E}_{\gamma fd})_{0^+} - (\overline{E}_{\gamma fd})_{1^+} = 10 \pm 10 \text{ keV} \quad (18)$$

This results in the following difference in the excitation energy E_f^x for the fission fragments and for the two spin states :

$$(E_f^x)_{0^+} - (E_f^x)_{1^+} = 109 \pm 43 \text{ keV} \quad (19)$$

It seems therefore that there is a weak effect of the fission exit channels on the prompt neutron and possibly on the γ-ray yields and also on the excitation energy of the fission fragments .

Similar studies have been carried out on ^{235}U (ref. 40) and ^{241}Pu (ref. 44) but show much smaller effects in the first case and practically none in the second case.

In summary, the fission channel theory of A. Bohr seems generally verified in the fission data, in particular for the case of the ^{239}Pu resonances which are fairly well known . A careful study of the prompt fission neutron yields supplemented by that of the prompt fission γ rays, in the ^{239}Pu resonances, has clarified a situation which was previously rather confusing . The fluctuations in $\overline{\nu}$ from resonance to resonance seem to be caused by the (n, γf) reaction rather than by the effect of fission channels .

4 - Damping effects in fission. (Application to the fission of ^{240}Pu at low energy)

A complete theory of fission must take into account not only the static aspects, essentially the potential energy surface as a function of deformation coordinates but also the dynamical aspects which include inertial and damping effects . In Section 2, we described the present status of the potential energy surface which is now known with a relatively good accuracy, in contrast to the dynamics of the process . A discussion of a derivation of mass inertia parameter for spontaneous fission, supposed to be adiabatic during the crossing of the barrier, has shown the limitations of the calculational method. But even less is known about damping or viscosity effects which describe the coupling of the fission mode to other degrees of freedom . It seems that damping is quite large in the first well, moderate in the second well, but very little is known about the damping in the last phase, i.e in the descent from the second saddle point to scission. This information is nevertheless very important for predicting the energy share between the kinetic and excitation energies of the fission fragments and therefore the prompt neutron emission . Many contradictory assumptions have been made between the two following extremes : i) full damping in which all the available energy at scission is dissipated into excitation energy with no pre-scission kinetic energy ii) weak damping in which this available energy appears almost completely in the form of pre-scission kinetic energy without intrinsic excitation of the fissioning system .[45,46,47] It is very difficult to find out from the experimental results, what type of damping actually occurs in the descent to scission and how this damping varies with excitation energy . The fragment total kinetic energy $\overline{TKE}$ for the low energy fission of actinides shows a linear dependence with $Z^2 A^{-1/3}$ over a wide range of mass numbers[49] . Under simple assumptions, the Coulomb energy V_c of the two fragments at scission can also show a linear dependence with $Z^2 A^{-1/3}$:

$$V_c = \frac{Z_{f1} \times Z_{f2}}{d} e^2 \quad (20)$$

where :

- Z_{f1} and Z_{f2} are the atomic numbers of the two fragments

and - d is the distance of the two charge centers at scission .

The $Z^2 A^{-1/3}$ dependence, for a given fragment mass ratio, can be derived by assuming that the distance d is proportional to $A^{1/3}$. One then obtains :

$$V_c \propto \frac{Z^2}{A^{1/3}} \quad (21)$$

This linear dependence of V_c with $Z^2 A^{-1/3}$ could suggest that, at scission, there is no appreciable kinetic energy and that the total kinetic energy $\overline{TKE}$ comes from Coulomb repulsion only . This would tend to favor the strong damping hypothesis. Nevertheless, this simple picture is unrealistic as has been pointed out already[47]. In fact, at scission, the distance d depends not only on A but also on Z . For higher Z values,

the scission configuration is relatively more elongated, therefore with lower Coulomb energy . Liquid drop calculations[45] show that the variation of V_c with Z^2/A actually flatens and even decreases for increasing Z^2/A for large Z^2/A values . But, assuming this time the zero-damping hypothesis to apply, the pre-scission kinetic energy added to V_c gives $\overline{TKE}$ values which are also in fairly good agreement with the experimental results[45] .

Ternary-fission data cannot help much in clarifying this complex situation since they can be explained equally well in terms of either weak damping[50] or full damping[46] .

In spite of our poor knowledge of damping effects in the last phase of fission, let us examine how they can play a role by comparing TKE and $\overline{\nu}$ data for spontaneous and neutron-induced fission of some even-even nuclei . Special attention is given to the ^{240}Pu case for which (d,p f) data are also considered[48] .

It can be seen in Fig.13 that, for a given even-even nucleus, $\overline{TKE}$ is systematically higher for thermal-neutron-induced fission that for spontaneous fission . Therefore, the full damping condition is not met for the cases plotted in Fig.13 since the excess S_n of excitation energy for neutron-induced fission is found, at least partially, in the form of kinetic energy . But the difference $\Delta\overline{TKE}$ in $\overline{TKE}$ is less than 6 MeV (the approximate value of S_n for such nuclei), implying that some damping can nevertheless occur which causes the rest ($S_n - \Delta\overline{TKE}$) of the excitation energy to appear in the form of dissipation . This is actually reflected in prompt-neutron emission since the $\overline{\nu}$-values, as plotted in Fig.14, are systematically higher for thermal-neutron-induced fission than for spontaneous fission, in agreement with $\overline{TKE}$ data . From these results, it would seem that moderate damping could apply to the low-energy fission of even-even actinides .

A closer examination of neutron-induced-fission for a wide range of neutron energies E_n (below the threshold for second-chance fission) can help to know better what fraction of the increase in excitation energy E^* of the fissioning nucleus goes into fragment excitation and how this fraction varies with E^* . Many studies have been made on the variation of $\overline{\nu}$ with E_n for a great variety of actinides[51] . An illustration of this $\overline{\nu}$ energy dependence for ^{240}Pu is given in Fig.15 where it can be seen that $\overline{\nu}$ increases linearly with E_n . No attention is paid here to the details of the energy dependence, in particular to the fine structure which may exist at low energy, but rather the gross behavior of $\overline{\nu}$ versus E_n is considered . These results show that the excitation energy of the fission fragments increases at a fast rate as a function of the excitation energy E^* . If this effect, probably due to damping , is supposed to be present in the same manner for all excitation energies below S_n, the linear variation of $\overline{\nu}$ with E_n can be extended down to zero-excitation energy to obtain the extrapolated value of $\overline{\nu}_{ext}$ (called $\overline{\nu}_{ext}$) for spontaneous fission. Comparison of extrapolated and measured values of $\overline{\nu}$ for ^{240}Pu spontaneous fission shows that the first one is lower than the second one (Fig.15). This effect is found for all even-even actinides for which relevant $\overline{\nu}$ data are available (Fig.14) . Therefore, it seems that the amount of damping would decrease for excitation energies somewhat below S_n .

Ir is possible to pursue further this type of investigation for the low-energy fission of ^{240}Pu since a fairly large amount of experimental results are available on the properties of the fission fragments and their variation with excitation energy[48,52]. The variation of the total kinetic energy $\overline{TKE}$ for the fragments emitted in the low-energy fission of ^{240}Pu is plotted in Fig.15 which includes data for the spontaneous fission of the ground state (G.S), the 4 ns isomeric state (I.S), to the ^{239}Pu thermal-neutron induced fission and for the ^{239}Pu (d,p f) reaction. Also, the variation $d\overline{E_K}/dE^*$ of the kinetic energy $\overline{E_K}$ of the fission fragments as a function of excitation energy E^* is plotted in Fig.16 for several groups of fragment mass ratios. Moreover the average mass $\langle m_H^* \rangle$ of the heavy primary fission fragments is plotted as a function of E^* in Fig. 17 .

Examination of these data seems to demonstrate the existence of two types of fission . The first one (called type I) includes the G.S and I.S spontaneous fission and ^{239}Pu (d,p f) reaction at $E^* = 4.65$ MeV and for the fragments emitted at an angle $\Theta = 0°$ relative to the recoil axis of the ^{240}Pu compound nucleus . A 200 keV wide resonance appears at $E^* = 4.65$ MeV in the anisotropy data and is interpreted as being due to a vibrational level in the 2nd well of the ^{240}Pu double-humped fission barrier. The second one (called type II) refers to all other ^{239}Pu (d, p f) results and to the ^{239}Pu (n,f) reaction induced by thermal neutrons .

In the fission of type I, the kinetic energy $\overline{TKE}$ increases linearly as a function of E^* with a slope of about + 1 . This means that practically all the excitation energy E^* is found as an increase of the kinetic energy of the fission fragments and this holds for all types of fragmentations (Fig.16) . The average mass $\langle m_H^* \rangle$ is the same for the three fission reactions of this type . This strongly suggests that damping, if present, must be very small and the fission of type I may very well be an illustration of superfluid motion already envisaged[47] in which the nucleons remain coupled by the pairing force all the way to scission. In this hypothesis, no intrinsic excitation occurs in the descent to scission and the available energy at that point then appears as pre-scission kinetic energy . All increase in E^* is then found entirely as an increase in pre-scission kinetic energy and therefore in $\overline{TKE}$ since the Coulomb energy does not change with E^* in this picture. This applies to all types of fragmentation since all fission properties but the kinetic energy do not vary E^* . The experimental results obtained for fission of the type I are consistent with this superfluid motion of the fissioning system .

In the fission of type II, on the contrary, the kinetic energy $\overline{TKE}$ decreases linearly as a function of E^* with a slope of about -0.43 . This is consistent with the increase of $\overline{\nu}$ with E^* observed above S_n .Nevertheless the energy balance in fission calculated with these data leads to a fairly large value $\langle S_n^f \rangle$ of the average neutron separation energy in the fission fragments ($S_n^f \simeq 8.3$ MeV) . The type of fragmentation is different from that of type I since $\langle m_H^* \rangle$ takes a different value (Fig.17) . There does not seem to be a satisfactory interpretation of such a behavior of $\overline{TKE}$ and $\overline{\nu}$ with E^*. Several explanations have been proposed in terms either of damping or variation in stiffness of the fission fragments with E^*.[48] In the first case, the coupling of the fission mode to the other degrees of freedom reduces the pre-scission kinetic energy and induces intrinsic excitations which lead to a greater excitation of the fission fragments, hence to an increase in $\overline{\nu}$.[47] In the second case, the greater excitation energy reduces the stiffness of the nascent fragments which then become softer to deform. At scission they are more elongated and the increase in the distance d between their charge centers decreases the Coulomb energy[52,53]. In these interpretations, shell effects seem to play an important role in agreement with the experimental results since the rate of decrease $d\overline{E_K}/dE^*$ of the kinetic energy $\overline{E_K}$ with increasing E^* strongly depends on the fragment mass ratio (Fig.16) .

The existence of these two types of fission having different variations of $\overline{TKE}$ and $\overline{\nu}$ with excitation energy seems justified from these experimental data and has to be taken into account for the prediction of some fission properties such as the prompt neutron emission. From the discussion presented above, it does not seem correct to assume the same amount of damping in fission for all excitation energies, starting from the ground state. In particular, it is certainly erroneous to extrapolate at higher energy the $\overline{\nu}$ or $\overline{TKE}$ data obtained for spontaneous and thermal-neutron-induced fission.

5 - Conclusion

In summary, though our understanding of the fission process has recently greatly improved, a reliable fission theory does not yet exist ; we are far from completely understanding this very complex phenomenon and from calculating accurately all its properties .

Fission barriers can be calculated with a good accuracy by using the Strutinsky macroscopic-microscopic approach . More fundamental Hartree-Fock approaches are also making rapid progress. The double-humped barrier shapes which are obtained for the actinides can explain many aspects of fission, among them are fission isomers and intermediate structure in fission cross sections .

In contrast to the statics, the fission dynamics which includes inertial and damping effects is very poorly known . Attempts to calculate life-time for ground state spontaneous fission with a microscopic approach have shown the limitations of the method . Fission cross sections are still more difficult to obtain on a fundamental basis . Nevertheless, approximate values can be obtained, not from pure theory, but from simple models having parameters adjusted to selected available fission data . The fission channel theory of A. Bohr, generally verified experimentally, is widely used in such calculations. A similar situation seems to apply also for other fission properties such as prompt neutron emission. Correct treatment of the subject requires the knowledge of damping effects in the descent from the second saddle point to scission. At present one cannot but speculate on such effects though new data on fission fragment kinetic energy and prompt neutron emission start to throw some light on this difficult aspect of fission . Again, in this case, simple models can be used to predict $\overline{\nu}$-values when they are not measured, provided that the model parameters employed in the calculations are adjusted on reliable fission data . But, it has been shown that these data must be used with great care before being introduced in the calculations .

It is worth noting at this point, that damping effects are studied not only in fission but also in heavy-ion induced reactions and a lot of information on such matters is expected in the few years to come when the new heavy-ion accelerators, now under construction, will be put into operation .

References

1 H. Flocard, P. Quentin, D. Vautherin, A.K. Kerman P.C.F.+ (IAEA, Vienna 1974) Vol I, p. 231 .

2 V.M. Strutinsky, Nucl. Phys. A 95 (1967), 420 . Nucl. Phys. A 122 (1968), 1 .

3 S.G. Nilsson, Chin Fu Tsang, A. Sobiczewski, Z. Szymanski, S. Wycech, C. Gustafson, I.L. Lamm, P. Möller and B. Nilsson, Nucl. Phys. A 131, (1969),1

4 M. Brack, J. Damgaard, A.S. Jensen, H.C. Pauli, V.M. Strutinsky and C.Y. Wong, Rev. Mod. Phys. 44, (1972), 320 .

5 J.R. Nix, Ann. Rev. of Nucl. Sc. 22, (1972), 65 .

6 B.L. Andersen, F. Dickman and K. Dietrich, Nucl. Phys A 159, (1970), 337 .

7 P. Holzer, U. Mosel and W. Greiner, Nucl. Phys.A 138 (1969), 241 .

8 M.G. Mustafa, U. Mosel and H.W. Schmitt, Phys. Rev. C 7 (1973), 1519 .

9 A. Michaudon, Advances in Nuclear Physics - Ed. by M. Baranger and E. Vogt ; Vol 6, p.1 (Plenum Press, 1973) .

10 a) V.M. Strutinsky and H.C. Pauli,P.C.F.++(IAEA,Vienna 1969) p. 155 .
b) J.E. Lynn, P.C.F.++(IAEA, Vienna 1969) p.249 .

11 J.R. Nix, Ann. Rev. of Nucl. Sc. 22, (1972), 65 .

12 a) H.J. Specht, Rev. Mod. Phys. 46 ,Nb 4 (1974) 773 .
b) V. Metag, E. Liukkonen, O. Glomset and A. Bergman P.C.F.+(IAEA, Vienna 1974) Vol I, p. 317 .

13 P. Limkilde and G. Sletten, Nucl. Phys. A 199 (1973), 504 .

14 H.J. Specht, J. Weber, E. Konecny and D. Heunemann, Phys. Let. B 41, (1972), 43 .

15 P.A. Russo, J. Pedersen and R. Vandenbosch, P.C.F.+ (IAEA, Vienna 1974) Vol 1, p. 271 .

16 R. Vandenbosch, P.C.F+ (IAEA, Vienna 1974) Vol I, p. 251 .

17 H.J. Specht, E. Konecny, J. Weber and C. Kozhuharov, P.C.F + (IAEA, Vienna 1974) Vol I, p. 285 .

18 a) J.E. Lynn, Nuclear Structure (IAEA, Vienna 1969) p. 249 .
b) J.E. Lynn, Report A.E.R.E Harwell R 5891 (1968) .
c) H. Weigmann, Z. Phys. 214 (1968), 7 .

19 a) D. Paya, H. Derrien, A. Fubini, A. Michaudon and P. Ribon, Nuclear Data for Reactors (IAEA, Vienna 1967) Vol III, p. 128 .
b) A. Michaudon, Nuclear Structure (IAEA, Vienna 1968) p. 427 .
c) A. Fubini, J. Blons, A. Michaudon and D. Paya, Phys. Rev. Let. 20 (24) (1968) 1373 (C) .

20 G.A. Keyworth, J.R. Lemley, C.E. Olsen, F.T. Seibel, J.W.T. Dabbs, P.C.F.+ (IAEA, Vienna 1974) Vol I, p.85.

21 a) A. Michaudon, New Developments in reactor physics and Shielding Calculations, Kiamesha Lake 12-15 Sept 1972, Vol II, p. 1087 - CONF 720-901 .
b) A. Michaudon, Statistical Properties of Nuclei (Albany 23-27 August 1971) (Plenum Press) 1972, p.149

22 E. Konecny, H.J. Specht and J. Weber, P.C.F.+ (IAEA, Vienna 1974) Vol II, p. 3 .

+ Physics and Chemistry of Fission (Proceedings of a IAEA Symposium, Rochester (N.Y) 13-17 August 1973) .

++ Physics and Chemistry of Fission (Proceedings of the second IAEA Symposium, Vienna 28 July-1 August 1969)

[23]N. Bohr and J.A. Wheeler, Phys. Rev. 56 (1939) 426 .

[24]H.A. Kramers, Physica 7 , (1940), 284 .

[25]P.O. Fröman and N. Fröman, J.W.K.B. Approximation, Contribution to the Theory, North-Holland, Amsterdam (1965) .

[26]H.C. Pauli and T. Ledergerber, P.C.F.+ (IAEA,Vienna 1974) Vol I, p. 463 .

[27]D. Inglis, Phys. Rev. 96 , (1954), 1059 .

[28]D. Gogny, private communication (1974) .

[29]a) P. Thomet, EANDC Topical Discussion (Tokyo, March 27, 1974) CEA-CONF 2855 .
b) P. Thomet, CEA-Report R-4631 (1974) .

[30]H. Weigmann and J.P. Theobald, Nucl. Phys. A 187 , (1972) , 305 .

[31]C. Lagrange, EANDC Topical Discussion (Tokyo, March 27, 1974) CEA-CONF 2852 - 2853

[32]A. Bohr, Proc. Int. Conf. Peaceful Uses of Atomic Energy (Geneva 1955) Vol II, United Nations, New York (1956) p. 220 .

[33]G.A. Cowan, B.P. Bayhurst, R.J. Prestwood,J.S. Gilmore and G.W. Knobeloch, Phys. Rev. 144 (3), (1966), 979 .

[34]E. Melkonian and G.K. Mehta, P.C.F.+++ (IAEA, Vienna 1965) Vol II, p. 355 .

[35]F.L. Shapiro, Nuclear Structure (IAEA, Vienna 1968) p. 283 .

[36]S. Weinstein, R. Reed and R.C. Block, P.C.F.++ (IAEA, Vienna 1969) p. 477 .

[37]J. Terrell, Phys. Rev. 127 , (1962), 880 .

[38]L. Weston and J. Todd, Conf. Neutron Cross Sections and Technology (U. of Tennessee, 1971) Vol II, p.961.

[39]J. Trochon, B. Lucas, A. Michaudon, D. Paya and Y. Ryabov, J. Physique 34 , (1973), 131 .

[40]a) D. Shackleton, J. Trochon, J. Fréhaut and M. Le Bars, Phys. Let. 42 B , (1972), p.344 .
b) J. Fréhaut and D. Shackleton, P.C.F.+ (IAEA, Vienna 1974) Vol II, p. 201 .
c) D. Shackleton, D. Sc. Thesis (Paris 1974) .

[41]L.W. Weston and J. Todd, Phys. Rev. 10 (4),(1974), 1402 .

[42]a)J. Trochon, Private Communication (1972) .
b)Y. Ryabov, J. Trochon, D. Shackleton and J.Fréhaut Nucl. Phys. A 216 , (1973), 395 .

[43]J.E. Lynn, The Theory of Neutron Resonance Reactions (Clarendon, Oxford, 1968) .

[44]J. Fréhaut, G. Simon, J. Trochon, Private Communication (1974) .

[45]J.R. Nix,Nucl. Phys. A 130 (1969), 241 .

[46]P.Fong P.C.F.++ (IAEA, Vienna 1969) p. 133 .

[47]W.J. Swiatecki and S. Bjørnholm, Physics Reports 4, (6) (1972), 325 .

[48]a) J. Lachkar, Y. Patin and J. Sigaud, J. de Physique Lettre (to be published)
b) Journées d'Etudes de la Fission (Cadarache, France 1974) (unpublished) .

[49]R. Vandenbosch and J.R. Huizenga "Nuclear Fission" Academic Press (1973) .

[50]J. Halpern and E.M. Henley, Comments on Nuclear and Particle Physics 3 , (1969), 52 .

[51]F. Manero and V.A. Konshin "Atomic Energy Review" (IAEA, Vienna 1972) Vol 10, (4), p.637 .

[52]E. Konecny, H.J. Specht and J. Weber Phys. Let. 45 B, (1973), 329 .

[53]W. Nöremberg, P.C.F.++(IAEA, Vienna 1969) p. 51 .

[54]R. Vandenbosch, Comments on Nuclear and Particle Physics , Vol V, (6), (1972), p. 161 .

[55]J.P. Unik, J.E. Gindler, L.E. Glendenin, K.F. Flynn, A. Gorski and R.K. Sjoblom, P.C.F.+ (IAEA, Vienna 1974) Vol II, p. 19 .

[56]A.J. Deruytter and G. Wegener-Penning P.C.F.+ (IAEA, Vienna 1974) Vol II, p. 51 .

+++Physics and Chemistry of Fission (Proceedings of a IAEA Symposium, Salzburg 22-26 March 1965) .

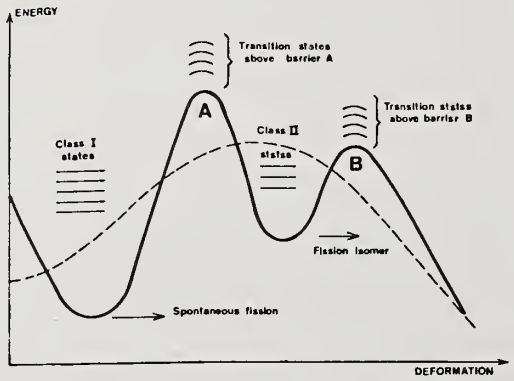

Fig. 1
Double-humped fission barrier (solid line) resulting from shell-energy corrections to the LD barrier (dashed line)

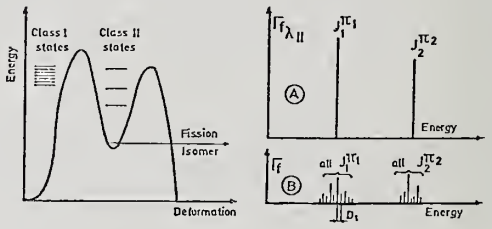

Fig. 2

Mechanism of intermediate structure in subthreshold fission cross sections . Clusters appear in the fission cross section when energy, spin and parity of a class-II state match those of the class-I resonances (at most two J^{π} values are possible for "s" wave neutrons) . The fission widths are drawn at the energy of the respective levels for class-II states (diagram A) and for the observed resonances (diagram B) .

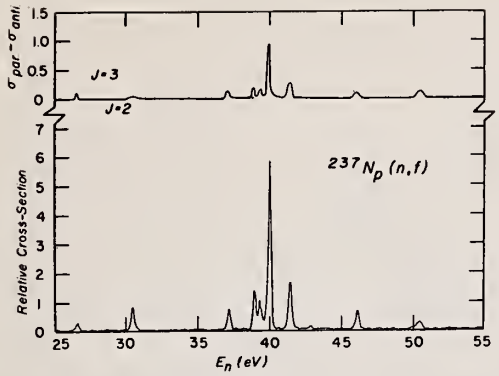

Fig. 3
Fission data obtained in the neighborhood of the first cluster at 40 eV in the ^{237}Np subthreshold fission cross section using a polarized neutron beam and a polarized ^{237}Np target[20]. The upper curve represents the difference between the cross sections measured with beam and target polarizations parallel and antiparallel These data demonstrate that most of the cross section in this cluster is due to J = 3 resonances[20].

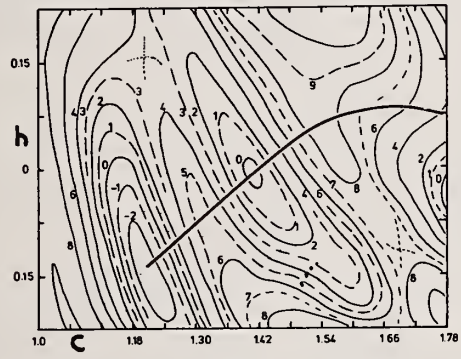

Fig. 5
The calculated deformation energy of ^{240}Pu versus the two symmetric deformations c(elongation) and h (constriction) is shown as a contour plot. Contour intervals are 1 MeV. The projection of the least action trajectory into the symmetric subspace (c,h) is shown by the thick solid line. Note the discrepancy between the static and dynamical barriers[26].

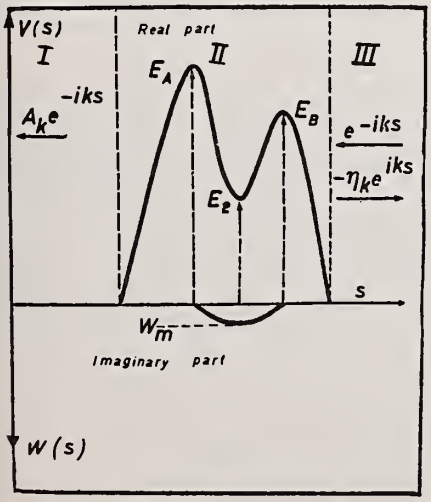

Fig. 7

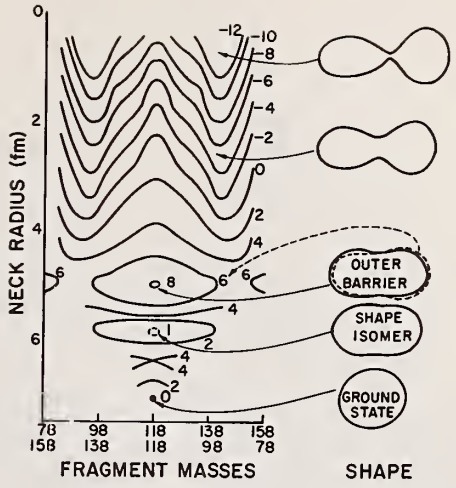

Fig. 4
Potential energy surface for ^{236}U as obtained from calculations using the Strutinsky procedure. Contour intervals are 2 MeV except for the shape isomer [8,54].

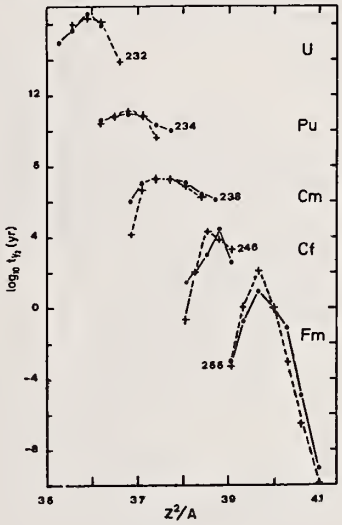

Fig. 6
Theoretical (•) and experimental (+) half-lives (in years) for ground-state spontaneous fission plotted versus Z^2/A (ref.[26]). The parameterization of the fissionability parameter for each set of isotopes is given in [26]. A pairing strength proportional to the surface area of the deformed nucleus is assumed in the calculations.

Fig. 7
Real and imaginary parts of the potential, as a function of deformation s, used in the cross section calculations described in the text and in [29]. The real part V(s) represents the double-humped fission barrier obtained by smoothly joining three paraboles. The imaginary part is supposed to be parabolic with maximum W_m in the second well. Full absorption is assumed in the first well.

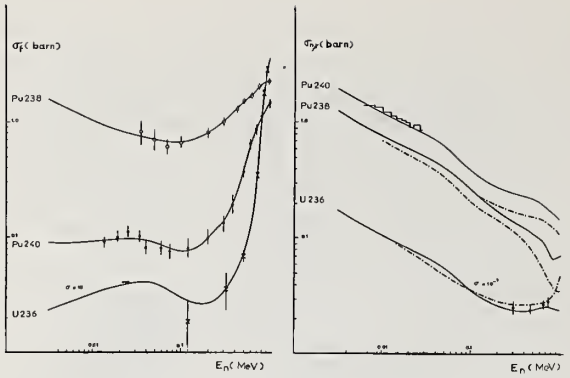

Fig. 8

Fig. 9

Fig. 8 - Fission cross sections of ^{236}U, ^{238}Pu and ^{240}Pu as a function of neutron energy E_n calculated with the method described in [29] (solid lines). The references for the experimental data are given in [29].

Fig. 9 - Capture cross sections of ^{236}U, ^{238}Pu and ^{240}Pu as a function of neutron energy E_n calculated with the method described in [29] (solid lines). The references for the experimental data are given in [29]. The lines _._ come from ENDFB/III.

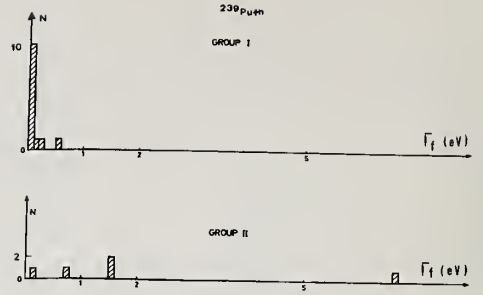

Fig. 10

Frequency distribution of the Γ_f values for the two groups of ^{239}Pu resonances separated according to their R-values, as discussed in the text [9,33].

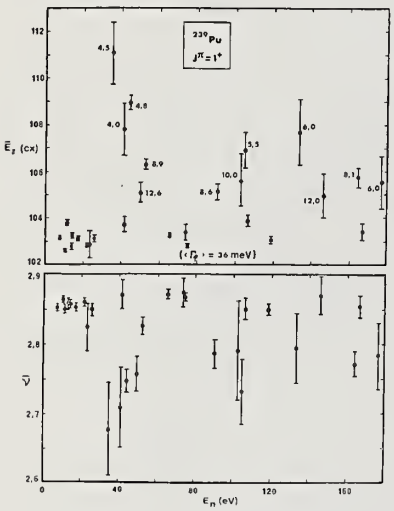

Fig. 11

The fission prompt neutron and γ-ray yields (respectively $\bar{\nu}$ and $\bar{E}_\gamma$) are plotted as a function of resonance energy for the ^{239}Pu resonances having $J = 1^+$ and analysed below 180 eV neutron energy [40]. The value of Γ_f is indicate in meV near the $\bar{E}_\gamma$ point for the resonances having a small fission width.

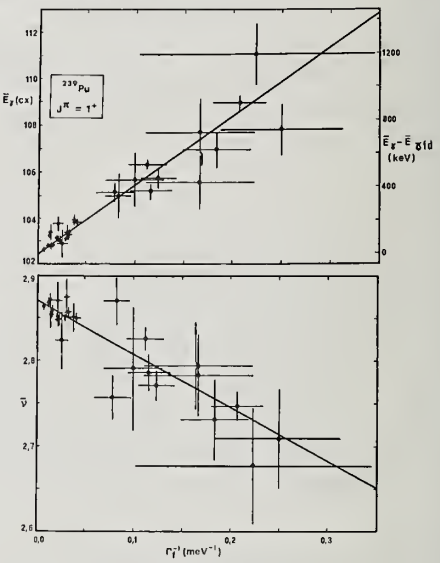

Fig. 12

The prompt-neutron and γ-ray yields (respectively $\bar{\nu}$ and $\bar{E}_\gamma$) are plotted as a function of $1/\Gamma_f$ for the ^{239}Pu resonances having $J^\pi = 1^+$ and analysed below 200 eV neutron energy, to demonstrate the effect of the $(n,\gamma f)$ reaction (ref.40). The solid lines are least-squares fits to the data.

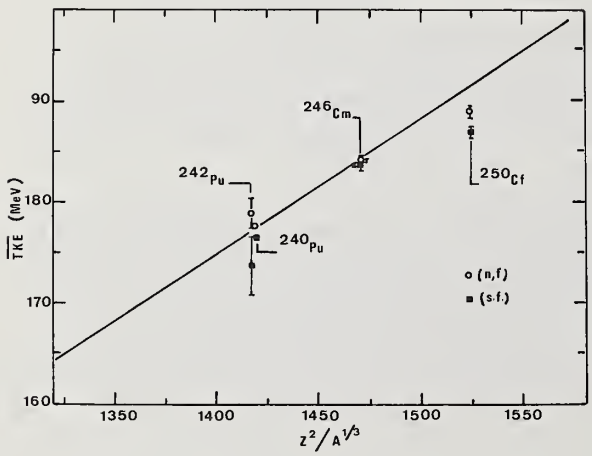

Fig. 13

Comparison of the total kinetic energy $\overline{TKE}$ of the fragments for the ground state spontaneous fission (■) the thermal-neutron-induced fission (o) of some even-even nuclei. The references for these data can be found in [55,56]. The solid line is a fit to the available data [55].

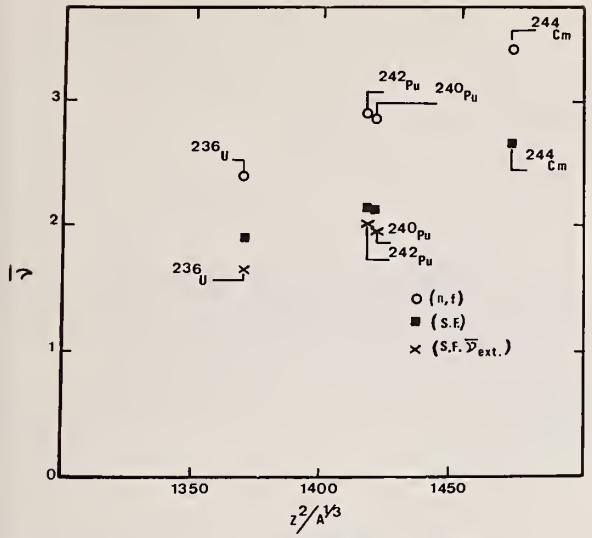

Fig. 14

Comparison of the average fission neutron multiplicity $\bar{\nu}$ for the ground state spontaneous fission (■) and the thermal-neutron induced fission (o) of some even-even nuclei. The value $\bar{\nu}_{ext}$ is obtained by extrapolating to zero excitation energy the $\bar{\nu}$ energy dependence observed for the neutron-induced fission .

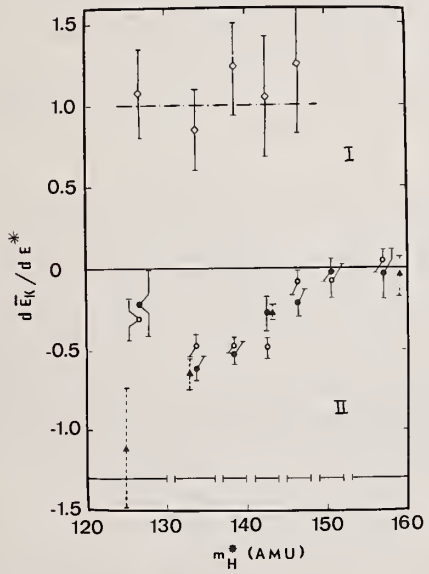

Fig. 16

Variation $\frac{d\bar{E}_K}{dE^*}$ of the fragment kinetic energy $\bar{E}_K$ with excitation energy E^* of the fissioning nucleus ^{240}Pu for various groups of the mass $^*m_H$ of the heavy fission fragment (ref.48) . This variation $\frac{d\bar{E}_K}{dE^*}$ has been plotted for the two types of fission (I and II) discussed in the text. References for the data plotted in this figure can be found in[48] .

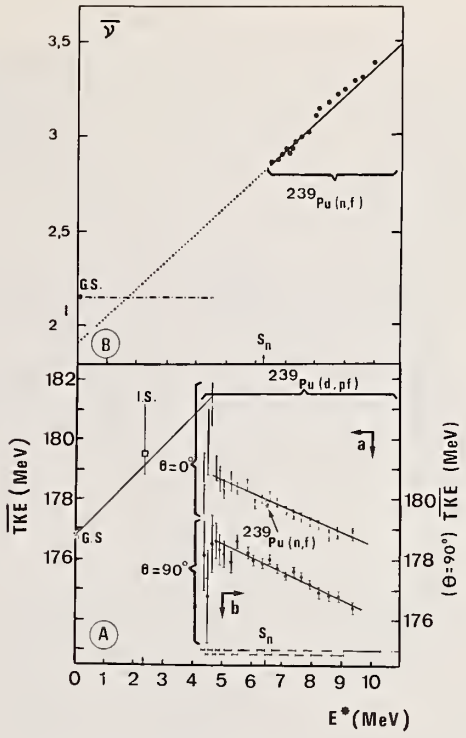

Fig. 15

Plots of the fragment total kinetic energy $\overline{TKE}$ (graph A) and prompt-neutron yield $\bar{\nu}$ (graph B) for the fission of ^{240}Pu as a function of excitation energy E^* (ref.48) . References fot the various data plotted in this figure can be found in[48] .

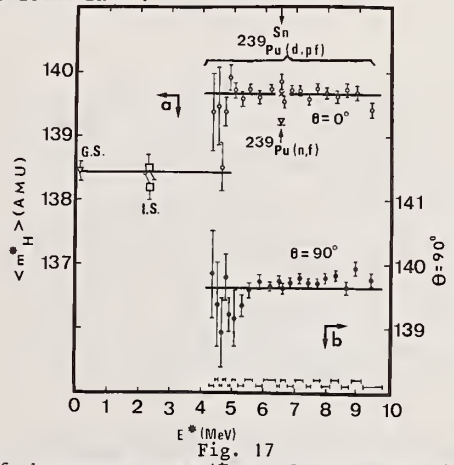

Fig. 17

Plot of the average mass $<^*m_H>$ of the heavy primary fragments emitted in the fission of ^{240}Pu as a function of excitation energy E^* (ref. 48). Note the difference in $<^*m_H>$ for the two types of fission discussed in the text .

NUCLEAR DATA FOR ACTINIDE RECYCLE

E. J. Hennelly
Savannah River Laboratory
E. I. du Pont de Nemours & Co.
Aiken, S. C. 29801

ABSTRACT

Large quantities of heavy actinides will be byproducts of burning plutonium and uranium fuel in nuclear power reactors. Chemical recovery and subsequent recycle in reactors will be for the production of ^{238}Pu and ^{244}Cm as heat sources and ^{252}Cf as a unique source of neutrons or for the ultimate conversion of heavy actinides to shorter-lived fission products to reduce long-term waste storage problems. Test measurements and production yields have provided data for developing a consistent set of multigroup cross sections which give excellent predictions of actinide concentrations in a variety of reactor environments and exposures. These multigroup cross sections are compatible with advanced reactor theory calculational codes.

(Key Words: transplutonium, cross section sets, actinide burnup, yield, waste management, neutron spectrum)

Introduction

The actinides found in sizable quantities in nature are thorium and the isotopes of uranium. Heavier actinides have become available in substantial quantities from the operation of fission reactors. Large-scale recycling of these actinides has occurred for about 15 years.[1] For example, current ERDA production programs have resulted in transmutation of significant quantities of actinides to ^{238}Pu, ^{241,243}Am, ^{244}Cm, and ^{252}Cf, in addition to plutonium for reactor fuel and nuclear weapons uses. These production programs are continuing. They have been successful because there are efficient chemical separation and target reprocessing facilities that permit recycling of unique target material for further irradiation.

Four years ago at the last conference,[2] a self-consistent two-group set of cross sections for the isotopes of curium and californium was presented. It was based primarily on data obtained from the ^{244}Cm and ^{252}Cf production programs. An improved 84-group set has been reported at this conference.[3] It is based on the original data plus many additional detailed measurements and analyses. The cross sections are available for conversion to the pointwise ENDF/B format for use in advanced reactor calculational codes. This paper concentrates on the applicability of the new neutron cross section data to the evaluation of concepts that have been suggested for the management of recycling heavy transplutonium actinides.

In the future, the largest actinide recycle program will involve the recycle of uranium and plutonium fuel in power reactors. The recycle of these fuels is of economic importance to nuclear power. Proposed sodium-cooled fast-breeder reactors also require plutonium recycle to burn the bred plutonium as fuel. Nuclear data for these operations as well as recyclings involving thorium-^{233}U systems, such as for the gas-cooled reactors and the molten salt reactor, are available, but they are not covered in this paper. Recycle of ^{241,243}Am and ^{237}Np is discussed briefly.

One consequence of uranium and plutonium recycle in nuclear power reactors is the gradual buildup of the heavy actinides neptunium, americium, curium and californium. This prospect stimulated projections, six years ago, that very large quantities would become available for applications.[4] Applications include ^{238}Pu and ^{244}Cm as isotopic heat source material for space or terrestrial missions and ^{252}Cf as a unique portable source of neutrons, already useful for such widely diverse applications as the treatment of tumors and neutron radiography in industry. Recently others have suggested that large accumulations of byproduct heavy actinides in process waste or separate residues provide a serious problem for long-range storage in safe repositories because half-lives are long (>10^3 years). It has been suggested that transmutation and/or fission would reduce storage to the more manageable hazard of fission products.[5]

A study was made to determine if the current nuclear data are adequate for evaluating heavy actinide production and/or removal programs. The results show the data to be adequate for such purposes. Large-scale actinide burnup late in this century may require improved fission data because irradiation of the expected large quantities could alter reactor charge design characteristics and reactivity transient effects. Such data can certainly be provided within the required time span, particularly as more actinide material becomes available. There is no urgency for the improved data to begin to recycle the lesser amounts expected in the next decade or two.

Actinide Production

Actinide production calculated on the basis of the 84-group set of cross sections[3] agreed very well with actual transplutonium production programs. To apply these new cross sections to other studies, users must realize the sensitivity of calculations to possible errors from uncertainties in neutron exposure and neutron spectrum. Possible errors are comparable to experimental errors in the data used to derive the cross section set originally (Figures 1-3). Figure 1 shows the calculated-to-experimental yield ratio for three of the data sets used to verify the cross section set. Figure 2 shows the effect of 10% lower neutron exposures on nuclide yields for three typical exposures. Figure 3 shows the sensitivity of neutron spectrum to nuclide yields at two typical exposures for 10% reductions in the fast-to-thermal flux ratio (ϕ_f/ϕ_{th}). In these calculated

cases, ^{244}Cm is assumed as the starting target material. The plots in Figures 2 and 3 show how important correct determination of irradiation conditions is in making initial projections of transplutonium production. The production calculations were made using two-group cross sections derived from the new 84-group cross section set. The consistency of the cross sections and most of the experimental data for a variety of irradiation conditions suggests that experimental values in Figure 1 lying outside ±10% are possibly suspect and that any data trends similar to those calculated for Figures 2 and 3 indicate that possible errors in the estimates of irradiation conditions should be investigated. Equivalent overestimates of these variables would give mirror image plots rotated about the yield ratio of unity.

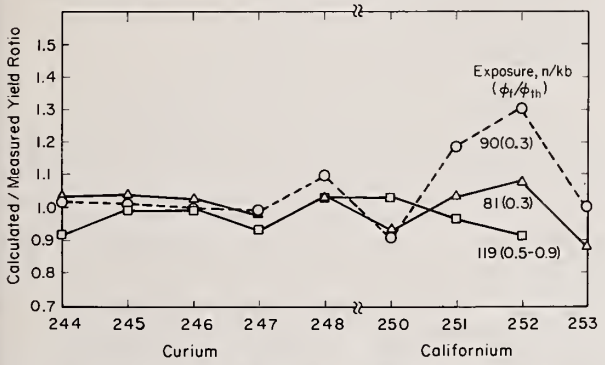

FIG. 1 Transplutonium Burnup: Comparison of Calc/Meas Yield Ratio for Typical Test Samples

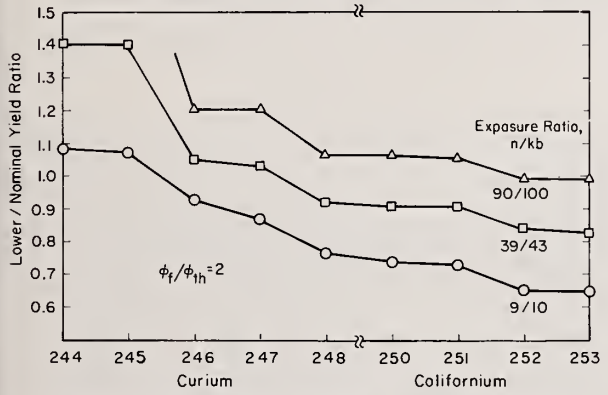

FIG. 2 Calculated ^{244}Cm Burnup: Effect of 10% Lower Exposure on Yield Estimates

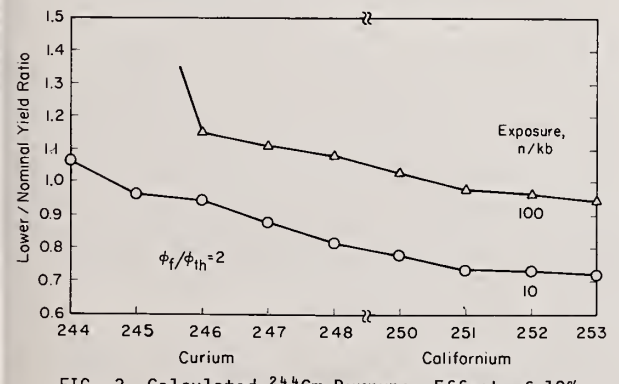

FIG. 3 Calculated ^{244}Cm Burnup: Effect of 10% Lower ϕ_f/ϕ_{th} Ratio on Yield Estimates

Actinide Burnup

Official criteria for setting goals for actinide burnup have not been established. The goal for decay of fission products has been set nominally to be ~600 years of storage[5], equivalent to about 20 half-lives of ^{137}Cs and ^{90}Sr or a 10^6 reduction. Using similar criteria, the goal for the burnup of transplutonium actinides could be set to be ~40 years, equivalent to a professional career or to the approximate lifetime of the nuclear plant in which the actinides were generated. An effective burnup half-life of about two years to give the 20 half-lives or the 10^6 reduction, seems to be a reasonable burnup rate and will be used as a goal in this recycle study.

Two important aspects of any burnup program are yield (Table 1) and rate (Table 2). The heavy actinides can be fissioned; transmutation to an inactive nuclide is not feasible. The amount fissioned in present day reactors on a single irradiation is 99.44% through ^{252}Cf and subsequent burnup can reduce the actinide reduction to the goal of ~10^6. Use of another consistent two-group cross section set developed at HFIR[6] shows a nearly identical fission yield of 99.42%. The ORNL set provides similar but not identical cross sections. Thus, two independently developed and tested production cross section sets give nearly identical high fission yields for the transplutonium chain.

TABLE 1

ACTINIDE BURNUP YIELDS

Nuclide	Fiss/Abs	Fissioned*
^{243}Am	0	0
^{244}Cm	0.05	5
^{245}Cm	0.86	87
^{246}Cm	0.09	88
^{247}Cm	0.59	95
^{248}Cm	0.05	95
^{250}Cf	0	95
^{251}Cf	0.65	98.4
^{252}Cf	0.65	99.44

* Cummulative percent of original mass that is fissioned.

TABLE 2

ACTINIDE REMOVAL RATE

	Half-Life, years			
		Burnup		
Nuclide	Decay	PWR	D_2O	HPD
^{243}Am	7370	1.5	1.3	0.14
^{244}Cm	18	4.9	4.9	0.48
^{245}Cm	8500	0.75	0.12	0.04
^{246}Cm	4760	23	24	2.2
^{247}Cm	15 x 10^6	2.1	1.2	0.18
^{248}Cm	35 x 10^4	10.7	11.6	1.05
^{249}Bk	0.85	0.6	0.1	0.03
^{249}Cf	352	0.5	0.1	0.03
^{250}Cf	13	0.2	0.1	0.02
^{251}Cf	900	0.17	0.04	0.01
^{252}Cf	2.6	13	4.6	0.92
^{253}Cf	0.05	0.9	0.2	0.05

α, β, α

The rate can be evaluated by simple two-group calculation of burnup half-lives, i.e., the time it takes for a neutron exposure to reduce a nuclide concentration by 50%. Burnup half-life, years = $2.17 \times 10^{16}/\phi\sigma$, where ϕ_{th} = n/(cm²-sec) and σ = cross section, barns. Table 2 compares calculated actinide burnup half-lives to decay half-lives for three nominal irradiations. The column labeled PWR is for a nominal pressurized water reactor ($\bar{\phi}_{th} = 2 \times 10^{13}$ n/(cm²-sec); $\phi_f/\phi_{th} = 6$). The column labeled D_2O is for a nominal D_2O reactor ($\phi_{th} = 10^{14}$ n/(cm²-sec); $\phi_f/\phi_{th} = 2$). The column labeled HPD is for a special high power density reactor charge ($\bar{\phi}_{th} = 4 \times 10^{14}$ n/(cm²-sec); $\phi_f/\phi_{th} = 3$). This latter concept is similar to a modified Savannah River high flux charge.[7] It was created, calculationally, because the other two reactor types gave unacceptably long burnup half-lives for the rate-limiting isotope ^{246}Cm. The net effective calculated half-life for ^{244}Cm burnup to 10^{-6} total actinides is ~42 years for the HPD charge, a reasonable expectation. The burnup and the resulting actinide residues are shown in Figure 4. The effective burnup half-life in a PWR for the precursor plutonium isotope chain is short (<4 years) and is accomplished to improve fuel cycle efficiency.

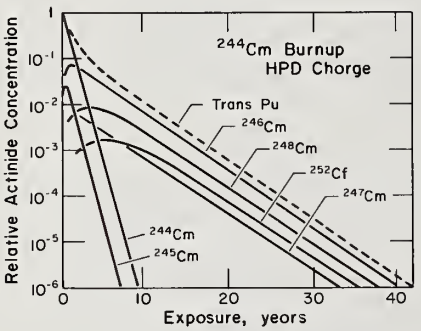

FIG. 4 ^{244}Cm Burnup in HPD Charge

Burnup halflives computed with ORIGEN[8] built-in two-group cross sections would be similar to the PWR results in Table 2, differing only in detail for the heavier curium isotopes. However, the 84-group, new cross sections can be used with modern reactor codes to give more precise calculations and to account correctly for self shielding of the even numbered curium isotopes in practical irradiation environments.

The data in Table 2 show that burnup can be achieved in a reasonable time by using a reactor with high power density but not with conventional thermal reactors. The cross section set is sufficiently precise so that this important conclusion will not be modified by future refinements in the data. If few applications are developed for ^{244}Cm and if large quantities of transplutonium actinides are to be burned up, it may be necessary to operate in two stages. The first would be in conventional thermal reactors to burn up large quantities of ^{243}Am-^{244}Cm mixtures and to remove the substantial heat from ^{245}Cm fission (87% of the transplutonium fissions occur at this isotope of curium). The second stage at high power density would be to burn up the remaining actinide residues, predominately ^{246}Cm, the burnup rate-limiting nuclide. The ultimate goal could be either a ^{252}Cf product or fission products. Both goals, production or burnup, are served better in a high power density reactor charge.

Fission product yield data for the actinides are available and show that no additional unwanted fission product is produced in excess of that already made by conventional fissions in ^{235}U and Pu.[9] From the projected fissile plutonium inventory, world wide, of about 680 tons[10] by the year 2000, we could expect the accumulated transplutonium actinides to approach at least 100 tons at that time. Either burnup or production techniques would need to displace substantial portions of thermal reactor charges selected for such operations. Actinide irradiation in LMFBR's might also be possible, at that time, and cross section data now available can be used to estimate the feasibility if the permissible LMFBR irradiation conditions of exposure and spectrum could be defined for the large quantities involved. The potential adverse effect of actinide burnup on the breeding of plutonium fuel would be a major concern to LMFBR irradiations of actinides. However, large-scale LMFBR operation is expected to reduce actinide residue output substantial because of increased plutonium fissioning.

Large-scale transplutonium actinide recycle will of course involve substantial development work. Targets to contain the actinides would require special handling, would generate heat from curium alpha decay, and would operate as fuel during early burnup stages. Concentration of actinides in target assemblies would provide self-shielding that would reduce rate-limiting burnup rates of ^{246}Cm and ^{248}Cm, thus extending actinide burnup times. Large-scale chemical processing facilities would also have to be built to separate the actinides for initial irradiation and for recycle to new targets as irradiation proceeds. In the forecast of 1968, it was projected that there would be "Tons of Curium and Pounds of Californium."[4] The magnitude of an actual recycle late in this century, for whatever purpose, could approach a "Ton of Californium."

^{238}Pu Production

Both ^{237}Np and ^{241}Am will accumulate in large quantities as a consequence of nuclear power operation and growth.[10] The ^{237}Np can be recycled to produce large amounts of ^{238}Pu, a product that has been useful as a power source in space exploration, and that is also intended for heart pacemakers and heart assist devices. ^{241}Am is separated from power reactor fuel along with a companion isotope, ^{243}Am. If recycled and burned up, it can be a source of very high-purity ^{238}Pu via alpha decay of the separated irradiation product ^{242}Cm.[11] The eventual burnup of the other isotope, ^{243}Am, has already been discussed. Nuclear data for these types of irradiation are well established and have been applied to plant-type operations.

In the burnup of ^{241}Am, some minor uncertainties seem to exist in the choice of a branching ratio for ^{242}Am, which leads to the simultaneous formation of of ^{242}Cm and ^{242}Pu. ^{242}Am is formed by neutron capture in ^{241}Am. Resolution of the uncertainties presented by differing data would be achieved promptly if a large-scale irradiation program were ever to become a reality. In short, for recycle of ^{237}Np and ^{241,243}Am, current ENDF/B data appear to be quite adequate for recycle estimation and planning. ^{236}Pu, an unwanted impurity in ^{238}Pu and in recycled plutonium fuel,* is formed by high energy (n,2n) and (γ,n) reactions on ^{237}Np. The nuclear data for these reactions are also well understood and readily available.[12]

* ^{236}Pu daughters emit hard gammas that make handling plutonium more difficult as ^{236}Pu decays.

Acknowledgement

The author wishes to thank Thomas C. Gorrell at the Savannah River Laboratory for his many helpful suggestions and calculations during the preparation of the manuscript.

References

1. D. Perlman. "The Atomic Archeologist: Dr. Glenn T. Seaborg." *Saturday Review*, p 52 (March 5, 1960).

2. E. J. Hennelly. "The Californium Cross Section Story." p 494 in *Third Conference on Neutron Cross Sections and Technology*. CONF-710302, Vol II (1971).

3. R. W. Benjamin, et al. "A Consistent Set of Transplutonium Multigroup Cross Sections." Presented at the *Conference on Nuclear Cross Sections and Technology*, Washington, DC, March 3-7, 1974.

4. J. L. Crandall. "Tons of Curium and Pounds of Californium." p 193, *Proceedings of International Conference of Constructive Uses of Atomic Energy*. R. Franks (Ed.), American Nuclear Society, Hinsdale, Ill. (1968).

5. *Atomic Energy Clearing House*, Vol. 21, No. 1, p 7, Congressional Information Bureau, Inc., Washington, DC (January 6, 1975). "High Level Radioactive Waste Management Alternatives - Vol. 4. Sec. 9, BNWL-1900 (May 1974).

6. J. L. King, J. E. Bigelow, and E. D. Collins. *Transuranium Processing Plant Semiannual Report of Production, Status, and Plans for Period Ending December 31, 1973*. USAEC Report ORNL-4965 p 24, Oak Ridge National Laboratory, Oak Ridge, TN (1974).

7. E. J. Hennelly. "Large-Scale Production of Radioisotopes." Ch. 2, p 86 in *Radioisotope Engineering*, (G. G. Eichholz, ed.), Marcel Dekker, Inc., NY (1972).

8. M. J. Bell. *ORIGEN*. USAEC Report ORNL-4628, Oak Ridge National Laboratory, Oak Ridge, TN (1973).

9. K. W. MacMurdo and R. M. Harbour. "Mass Yields from Thermal-Neutron Induced Fission of ^{245}Cm." *J. Inorg. Nucl. Chem 34*, 2109 (1972).

10. *Nuclear Power Growth: 1974-2000*, USAEC Report WASH-1139, p 33-34, U. S. Government Printing Office, Washington, DC (1974).

11. C. J. Banick and M. H. Goosey. *Improved Methods for Determination of ^{236}Pu in ^{238}Pu*. USAEC Report DP-1291, Savannah River Laboratory, E. I. du Pont de Nemours & Co., Aiken, SC (1972).

12. C. K. Paulson and E. J. Hennelly. "Cross-Section Measurement of Plutonium-236 Formation in Plutonium-238 by ^{237}Np (η,2n) Reactions." *Nucl. Sci. Eng. 55*, 24 (1974).

This work was done under Contract No. AT(07-2)-1 with the U. S. Energy Research and Development Administration.

(n,f) CROSS SECTIONS FOR EXOTIC ACTINIDES*

J. B. Wilhelmy, H. C. Britt, A. Gavron, E. Konecny,†
and J. Weber
University of California, Los Alamos Scientific Laboratory
Los Alamos, N. M. 87544

ABSTRACT

Neutron induced fission cross sections have been obtained for 26 actinide nuclei using (^{3}He,df) and (^{3}He,tf) reactions to determine fission probabilities and then multiplying these values by calculated compound nuclear neutron reaction cross sections. Comparison with existing (n,f) data shows this to be a feasible approach for obtaining reliable estimates for (n,f) cross sections where direct measurements are not possible. Theoretical developments in interpreting fission probability measurements are discussed.

[NUCLEAR REACTIONS Measured P_f $^{230\text{-}233}$Pa, ^{231,232}U, $^{233\text{-}239}$Np, ^{237,238}Pu, $^{239\text{-}243}$Am, $^{241\text{-}244}$Cm, ^{248,249}Bk using (^{3}He,df), (^{3}He,tf), E = threshold - ∿12 MeV; deduced $\sigma_{n,f}$.]

Introduction

We have extracted equivalent neutron induced fission cross sections for actinide nuclei using experimentally measured charged particle induced fission probabilities and calculated total compound nuclear neutron cross sections. Using a charged particle direct reaction it is possible to produce excited nuclei for which the equivalent neutron induced reaction target isotope is precluded from direct laboratory study due to its non availability and/or short half life. Microscopic cross sectional information on such isotopes can nevertheless be important in regions of high neutron fluences such as CTR and fast breeder reactor applications.

Using the (^{3}He,df) and (^{3}He,tf) reactions on available actinide targets we were able to measure fission probabilities [$P_f = \Gamma_f/(\Gamma_f+\Gamma_n+\Gamma_\gamma)$] for 26 actinide nuclei at an excitation energy range from fission threshold up to ∿ 11-12 MeV.[1] Estimates for the (n,f) cross sections were obtained by multiplying the experimental P_f values by optical model calculated total compound nuclear neutron reaction cross sections. We have also developed a theoretical model which produces good fits to the measured P_f values over the entire excitation energy range.

Experimental

A 25 MeV ^{3}He beam of ∿ 120 n amps was obtained from the LASL FN tandem Van de Graaff. Targets were prepared by vacuum evaporation onto ∿ 50 μg/cm^2 carbon foils and were usually around 100 μg/cm^2. The experimental configuration is shown in Fig. 1. A ΔE-E counter telescope arrangement was used for energy determination and particle identification of the outgoing direct reaction charged particle. The two fission fragment detectors were independently coincidenced with the counter telescope. Knowing the Q value of the reactions and measuring the outgoing particle energy enabled determination of the excitation energy in the residual nucleus. The fission probability was then extracted by ratioing the geometry corrected number of measured fission events to the number of times the nucleus was produced in that excited state. The data were recorded and processed using an on-line SDS-930 computer. The energy resolution obtained in the counter telescope for this very close in geometry was ∿ 150 keV.

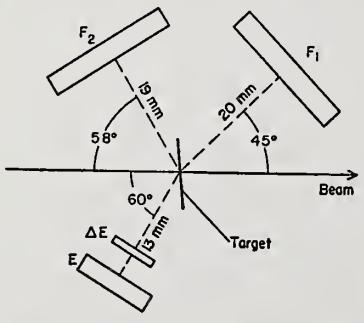

Fig. 1. Schematic representation of the experimental configuration as viewed from above. The particle identifying counter telescope is indicated by ΔE and E and the two independent fission fragment detectors as F_1 and F_2.

(n,f) Cross Sections

Estimates for n,f cross sections were obtained from the measured P_f data by simply multiplying the appropriate excitation energy corrected fission probabilities by calculated total compound nuclear neutron reaction cross sections:

$$\sigma_{n,f}(E_n) = P_f(E_n+B_n) \cdot \sigma_{C.N.}(E_n). \qquad (1)$$

where E_n is the incident neutron energy and B_n is the neutron binding energy. The underlying motivation for pursuing this hybrid approach is the assumption that the most difficult to theoretically predict portion of the (n,f) cross sections are the competition in the excited nucleus between fission and other modes of de-excitation. These are just the quantities which we have experimentally determined in the P_f measurements. We, therefore, have only to rely on the theory to provide the total compound nuclear reaction cross section. The use of fission probabilities, determined with direct charged particle reactions, to obtain (n,f) cross section estimates has been attempted previously using the (t,pf) reaction.[2,3] The limitation with this reaction is that the maximum equivalent neutron energy obtainable is only ∿ 2 MeV whereas with the ^{3}He reactions excitations corresponding to as high as ∿ 8 MeV incident neutrons can be reached.

The most serious assumption in this procedure is that the fission probabilities are independent of the reaction mechanism. For several cases we were able to produce the same compound nucleus with (^{3}He,d) and (^{3}He,t) reactions on different targets. Within our accuracy (∿ 10%) there was no measured difference between the P_f values and thus for these reactions there is no apparent dependence on the specific reaction mechanism. However, the difference in angular momentum transfer between neutron induced reactions and those formed with (^{3}He,d) and (^{3}He,t) reactions is of potential concern. Figure 2 presents calculated values for the relative ℓ wave dependent transmission coefficients for reactions induced with neutrons and ^{3}He. The

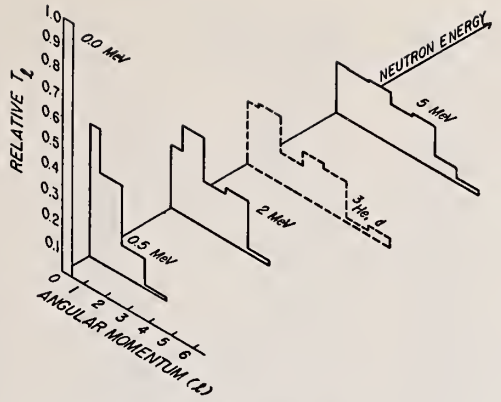

Fig. 2. A three dimensional histogram representation of the calculated[5,14] relative transmission coefficients, T_ℓ, for a typical actinide nucleus (^{240}Pu) as a function of the transferred angular momentum, ℓ, evaluated at various incident neutron energies (solid curves) and for a (^{3}He,d) direct reaction (dashed curve). The charged particle reaction has been arbitarily located on the neutron energy axis. This was done because the angular momentum transferred by the direct reaction will not appreciably vary over the excitation energy range reached with the indicated incident neutrons. The purpose of the figure is to demonstrate that the angular momentum transferred in the (^{3}He,d) reaction is similar to that transferred by neutrons in the few MeV range.

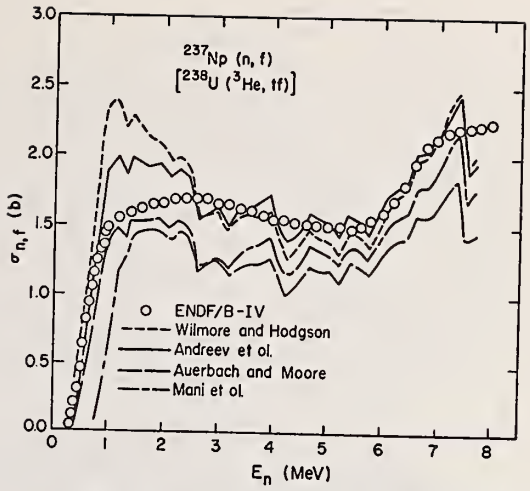

Fig. 3. The ^{237}Np(n,f) cross section as a function of neutron energy. The open circles are the ENDF/B-IV[7] recommended experimental values. The fission probability for the compound nucleus ^{238}Np* was also obtained using the ^{238}U(^{3}He,tf) reaction. The four curves give the predicted cross sections (Eq. 1) for the reaction using our experimental P_f values and different sets of optical model parameters.[3-6] The apparent oscillatory structure in the calculated curves is caused by statistical fluctuations in the measured P_f values.

important feature is that in the incident neutron energy range of a few MeV the angular momentum transferred by neutrons is similar to that transferred by the (^{3}He,d) direct reaction. This reasonable matching of angular momentum transfer should minimize any intrinsic effects due to specific spin levels available in the fissioning nucleus. As the neutron energy is decreased the ℓ transfer distribution becomes smaller and there are major discrepancies between the neutron and charged particle angular momentum transfer. We would, therefore, expect possible deviation caused by angular momentum effects to be most prevalent in this (n,f) simulation approach for equivalent neutron energies of less than $\sim$ 1-2 MeV.

To have an accurate prediction of the (n,f) cross section requires a reliable estimate for the compound nuclear neutron cross section. Unfortunately these calculated cross sections show a large variation depending on the optical model parameters used for the determination. We have taken, as a representative sampling, four sets of recommended parameters from the literature[3-6] and using Eq. 1 transformed our P_f values to equivalent (n,f) cross sections. The results for ^{237}Np(n,f) are shown in Fig. 3 along with the ENDF/B-IV[7] recommended compilation from the existing experimental data. No set of parameters gives complete agreement with the recommended cross section. With the parameters of Andreev et al.[3] a good agreement with the data is obtained above $\sim$ 2 MeV. Since the lower energies are the most suspect for this technique from non angular momentum transfer matching it was felt that of the four parameter sets those of Andreev et al. were favored. Certainly a more complete investigation of available optical model parameters is possible and could result in an improved agreement with the data. Conversely the measured P_f data could be used to adjust the optical model parameters in such a way as to improve the fit. For our present purposes we wanted only to demonstrate that the charged particle simulation technique was viable and that reasonable estimates of the (n,f) cross section could be obtained using established optical model parameter sets.

Using the parameters of Andreev et al.[7] we have generated (n,f) excitation functions for the three additional isotopes for which there are both (n,f) experimental data and our P_f results. These are presented in Figs. 4-6. The predictions for the ^{231}Pa(n,f) cross section (Fig. 4) agree fairly well with the existing data. The spread in the data is at such a level as to make the predictions from our simulated approach as credible as the direct experiments. This is an encouraging case since the fission probabilities for this light actinide are quite low ($P_f \sim 0.2$-0.4) and thus we are able to predict accurate (n,f) cross sections even for cases in which the majority of the decay is not by fission.

The ^{241}Am cross section (Fig. 5) is similar to the ^{237}Np(n,f) case. The predicted values are substantially high in the 1-2 MeV neutron range and then agree better with, but are still $\sim$ 10% higher than, the recommended cross section at higher neutron energies. The ENDF/B-IV recommended cross sections for ^{241}Am are lower than most existing data (an example of which for 2.5 MeV neutrons from two different experimenters is shown in Fig. 5 with the appropriate experimental error) and this may be a case where a new evaluation of experimental data may be needed. The final example is for ^{242m}Am (Fig. 6) and here there is only one experiment and the data, except for the one indicated point, have estimated uncertainties of 50%. Though the agreement between the experiment and our prediction is satisfactory, with such large (n,f) experimental uncertainty, it is not a very stringent test for the procedure. This large uncertainty in the experimental data does, however, emphasize the usefulness of the charged

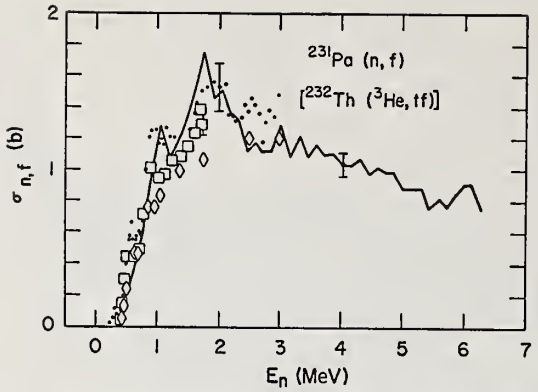

Fig. 4. The $^{231}Pa(n,f)$ cross section. The experimental data are • [15], ◇ [16], □ [17]. Typical reported experimental errors are shown on selected data points. The solid curve is the predicted cross section (Eq. 1) using Andreev et al. optical model parameters[3] and experimental P_f values from the $^{232}Th(^3He,tf)$ reaction. A typical statistical error for the P_f points is indicated on the line.

particle simulation technique. Direct (n,f) cross sectional determinations for all of the nuclei we have studied through charged particle reactions are difficult and subject, when done, to large errors. This demonstrated feasibility of the charged particle simulation technique should make this a useful approach for applications where it is necessary to have estimates for (n,f) cross sections on these inaccessible nuclei.

As a further example Fig. 7 presents the extracted (n,f) cross sections for seven Np isotopes. The feature we want to stress in this figure is that there are substantial differences in the fission cross section among fissile nuclei even well above the fission threshold. In Table I we list the 26 compound nuclei we have produced with the (^{3}He,d) and (^{3}He,t) reactions. Also listed are the corresponding "neutron targets" to produce these compound nuclei, the half lives of these isotopes, and the maximum equivalent neutron bombarding energies for which we have obtained fission probability data. As seen, the half lives for some of the neutron

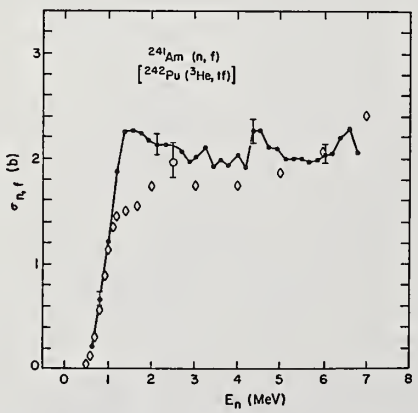

Fig. 5. The $^{241}Am(n,f)$ cross section. Similar to Fig. 4 except ◇ [7], ○ [8,9].

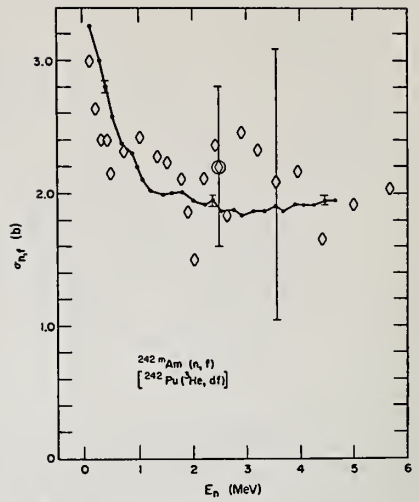

Fig. 6. The $^{242m}Am(n,f)$ cross section. Similar to Fig. 4 except all data points are from ref. 8. All experimental points, except the one circled point, are estimated to have uncertainties of 50%.

target isotopes are as short as minutes and are clearly not available for direct measurement.

Calculated Fission Probabilities

We have recently successfully produced a theoretical model for quantitatively fitting our measured P_f data.[1] As in a prior development[10] the model incorporates a double peaked fission barrier, uses realistic single particle based level densities, and a solution to the microscopic pairing equations. The major new feature which allows, for the first time, a good absolute value fit to all the experimental data without arbitrary adjustable scaling parameters is the inclusion of enhancement effects[11] at the inner saddle point caused by a predicted[12,13] potential energy surface

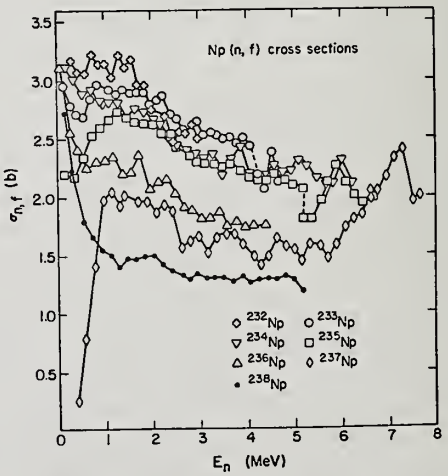

Fig. 7. The (n,f) cross sections for seven Np isotopes. The points are generated using Eq. 1 with the appropriate experimental P_f data and the Andreev et al. optical model parameters.[3]

Table I

'Neutron Target'	$t_{1/2}$	Max Energy Neutron (MeV)	Compound Nucleus
^{229}Pa	1.4 d	5.2	^{230}Pa
^{230}Pa	17.4 d	3.7	^{231}Pa
^{231}Pa	3.25×10^4 y	6.3	^{232}Pa
^{232}Pa	1.32 d	4.4	^{233}Pa
^{230}U	20.8 d	7.0	^{231}U
^{231}U	4.2 d	5.2	^{232}U
^{232}Np	14.7 m	3.0	^{233}Np
^{233}Np	35 m	3.9	^{234}Np
^{234}Np	4.4 d	6.2	^{235}Np
^{235}Np	396. d	6.6	^{236}Np
^{236}Np	1.3×10^6 y	4.3	^{237}Np
^{237}Np	2.1×10^6 y	7.7	^{238}Np
^{238}Np	2.12 d	5.2	^{239}Np
^{236}Pu	2.85 y	7.2	^{237}Pu
^{237}Pu	45.6 d	5.6	^{238}Pu
^{238}Pu	1.63 h	5.1	^{239}Am
^{239}Am	11.9 h	5.5	^{240}Am
^{240}Am	51. h	3.9	^{241}Am
^{241}Am	433. y	6.8	^{242}Am
^{242}Am	152. y	4.6	^{243}Am
^{240}Cm	26.8 d	6.2	^{241}Cm
^{241}Cm	36. d	4.6	^{242}Cm
^{242}Cm	163. d	7.1	^{243}Cm
^{243}Cm	28. y	5.3	^{244}Cm
^{247}Cm	1.4×10^3 y	5.9	^{248}Bk
^{248}Bk	18. h	4.2	^{249}Bk

which prefers non axially symmetric shapes. Representative examples of the fitted data are shown in Fig. 8. The significant parameters which enter into the model are the heights and curvatures of the two barriers. In all cases the values used for these parameters are consistent with previous experimental determinations of these quantities.

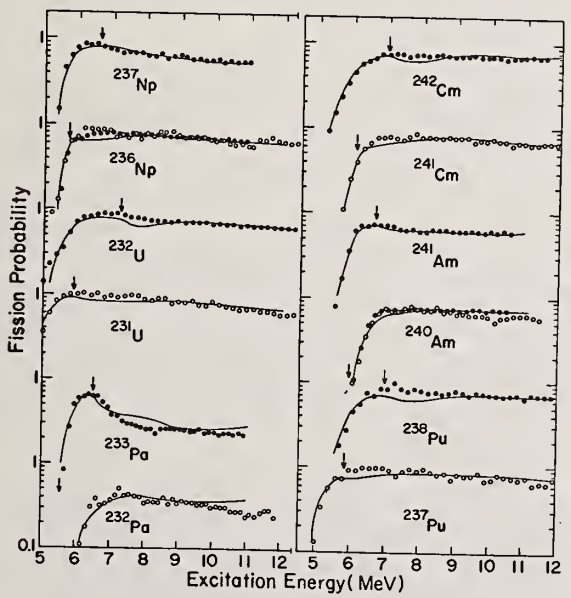

Fig. 8. Measured fission probabilities for several actinide nuclei. The closed circles are from (^{3}He,d) reactions and the open circles from (^{3}He,t) reactions. The solid lines show the fits to the data using the improved microscopic statistical model.[1] The arrows indicate the locations of the neutron binding energies.

Conclusions

With the charged particle simulation techniques we have been able to extract equivalent (n,f) cross sections on a wide variety of nuclei which are not available for direct laboratory study. With the (^{3}He,d) and (^{3}He,t) reactions we have been able to reach excitation energies in some cases as high as those induced with ∿8 MeV incident neutrons. This technique seems to work well for neutron energies > ∿ 2 MeV. For lower energy neutrons the (n,f) cross sections tend to be overestimated. We are investigating the calculated low energy optical model cross sections in an attempt to improve this situation. Finally we have developed a theoretical model which gives good quantitative fits to existing experimental data and has hopefully extended our microscopic understanding of the fission process.

References

*Work performed under the auspices of the U. S. Atomic Energy Commission.

†Present address: Technische Universität Munchen

1. A. Gavron, H. C. Britt, E. Konecny, J. Weber, and J. B. Wilhelmy, submitted to Phys. Rev. Letters, Los Alamos Scientific Laboratory Report, LA-UR-75-161 (1975).
2. J. D. Cramer and H. C. Britt, Nuclear Science and Eng., 41, 177 (1970).
3. M. F. Andreev, V. V. Gladkov, V. A. Zavgorodnii, V. I. Serov, and V. M. Sunn, Sov. J. Nucl. Phys. 17, 243 (1973).
4. D. Wilmore and P. E. Hodgson, Nucl. Phys. 55, 673 (1964).
5. E. H. Auerbach and S. O. Moore, Phys. Rev. 135, B895 (1964).
6. G. S. Mani, M. A. Melkanoff, and I. Ion, Centre D'Etudes Nucleaires de Saclay, Rapports (EA-2379, 2380 (1963)).
7. ENDF/B-IV, USAEC, ^{237}Np (MAT-1263), ^{241}Am (MAT-1056).
8. C. D. Bowman, G. F. Auchampaugh, S. C. Fultz, and R. W. Hoff, Phys. Rev. 166, 1219 (1968).
9. M. I. Kazarinova, Yu. S. Zamyatin, V. M. Gorbacher, At. Energ. (USSR) 8, 139 (1960).
10. B. B. Back, H. C. Britt, Ole Hansen, B. Leroux and J. D. Garrett, Phys. Rev. C 10, 1948 (1974).
11. S. Bjørnholm, A. Bohr and B. R. Mottelson, in Proceeding of the Third International Atomic Energy Symposium on the Physics and Chemistry of Fission, Rochester, 1973. (International Atomic Energy Agency, Vienna, 1974), Vol. I, p. 367.
12. P. Moller and S. G. Nilsson, Phys. Lett. 31B, 283 (1970).
13. H. C. Pauli, T. Ledergerber, and M. Brack, Phys. Lett. 34B, 264 (1971).
14. Computer Code DWUCK, P. D. Kunz, private communication.
15. D. W. Muir and L. R. Veeser, Los Alamos Scientific Laboratory Report LA-4648-MS (1971).
16. J. Williams, Los Alamos Scientific Laboratory Report LA-150 (1944). Renormalized by BNL compilation group.
17. S. M. Dubrovina and V. A. Shigin, Doklady Physics Sections (Eng. Translation), 9, 579, (1965).

A STUDY OF THE ^{233}U-^{232}Th REACTOR AS A BURNER FOR ACTINIDE WASTES*

S. Raman, C. W. Nestor, Jr., and J. W. T. Dabbs
Oak Ridge National Laboratory, Oak Ridge, Tennessee 37830

A plausible method for reducing the storage problems and hazards now associated with long-lived actinide wastes might be to recycle and convert these to fission products. Several reactor types can be envisaged for this purpose. We note that in a ^{233}U-^{232}Th reactor, the production of ^{237}Np, Pu and transplutonium isotopes is greatly reduced compared to a ^{235}U-^{238}U reactor because several additional neutron captures are required to reach the same mass. Hence, the ^{233}U-^{232}Th reactor can be employed to effectively reduce Np, Pu, Am and Cm wastes to fission-product wastes which entail shorter (≈1000 yr) storage times.

(Actinide fuel, fertile material, and wastes; recycle concept; transuranium element production; waste recycling in a ^{233}U-^{232}Th reactor)

Introduction

A major problem in connection with the development of large-scale nuclear energy is the potential hazard associated with the fuel, fertile material and wastes. These products must be processed, transported, stored and safeguarded with extreme care. Reactor fuel elements need to be processed in order to recover reusable fuel and fertile material. The unrecovered portions are usually termed "wastes", which can be broadly divided into fission products and actinides (Ac and higher Z elements). Most fission products decay to harmless natural elements in a relatively short span of ≈ 1000 years. It is generally believed that adequate storage means, either underground or above ground, can be found to handle fission product wastes safely. The fuel, fertile material and actinide wastes pose a different type of problem because several isotopes among them possess very long half-lives. For example, the main new fuel produced in a light-water ^{235}U-^{238}U reactor is ^{239}Pu which has $T_{1/2}$ = 24390 yr. The half-life of ^{243}Am, a waste material, is 7370 yr. The hazards associated with the fissionable isotopes of the fuel are, however, of secondary concern because these isotopes can be depleted through their use in a reactor. Since the fertile materials *ab initio* came from the earth, whether or not they should be viewed as hazards newly created by reactor operations is debatable.

The Actinide Recycle Concept

A plausible method which has been suggested for reducing the hazards associated with the remaining actinides might be to recycle these also in a suitable reactor. Among Pu, Am, and Cm isotopes, alternate ones (^{239}Pu, ^{241}Pu; ^{242}Am, ^{244}Am; ^{243}Cm, ^{245}Cm) possess appreciable fission cross-sections and the remaining isotopes for the above elements can be transmuted to these by neutron capture. Therefore, in principle, the actinides can be partly converted into more manageable fission products.

Recycling requires a neutron source which might be the same reactor producing the wastes or a specially designed burner reactor or even a fusion reactor. Claiborne[1] has shown that a reduction by an order of magnitude in the hazard potential of the actinide wastes can be achieved through recycling in the same reactors (pressurized light-water reactors, operating on the 3.3% ^{235}U-^{238}U cycle) producing the bulk of the wastes. This reduction occurs because when recycled, the inventory of Am and Cm isotopes, for example, approaches a maximum value, an asymptote, rather than increasing linearly with time. Despite this reduction, the overall inventory of the actinides will be appreciable by the end of this century. There remains a problem of final disposal of reactor inventories if and when the nuclear fission power program draws to a close and is replaced by alternate energy sources.

The ^{233}U-^{232}Th Reactor

The last-mentioned problem, among other things, led us to consider the reactor type operating on the ^{233}U-^{232}Th cycle. In this case, the capture of neutrons by the ^{232}Th fertile material leads to the replenishment of the original ^{233}U fuel. Successive neutron captures by ^{233}U result in higher U isotopes until ^{237}U is reached, when a higher Z isotope, ^{237}Np, is produced. It is further obvious that Pu and transplutonium isotopes are generated to a far lesser extent in a ^{233}U-^{232}Th reactor when compared to a ^{235}U-^{238}U reactor. For nuclides above ^{238}Pu, the typical reduction factor is > 10^6 because in the ^{233}U case, five additional neutron captures are required to reach the same mass. Therefore, in the absence of substantial new production of these elements, the ^{233}U-^{232}Th reactor can be effectively employed to reduce the Np, Pu, Am and Cm inventories. By contrast, the best that can be contrived through recycling in a ^{235}U-^{238}U reactor is a situation in which these materials are transmuted at essentially the same rate as they are freshly produced.

To test these ideas, we have carried out some preliminary calculations with the ORIGEN (Oak Ridge Isotope Generation and Depletion Code) computer program originally written by Bell.[2] To keep the calculations as simple as possible we selected a 1000 MW(e) pressurized light-water reactor in which the fuel was 3.3% ^{235}U-^{238}U in the first instance and ^{233}U-^{232}Th in the other. The calculations are hypothetical in two senses--the fuel loadings are idealized and the ^{233}U-^{232}Th reactor of this type might not be practical. An operating cycle included a 3 yr power generation period followed by a 3 yr cooling off period. Table 1 shows the amounts of selected transuranium isotopes present at the end of 1 cycle. As expected, the production of these isotopes is greatly reduced in the case of the ^{233}U-^{232}Th reactor. This conclusion would remain valid notwithstanding the differences in the flux levels of the two reactors.

The recycle concept was tested next as follows. The Np, Am, Cm and higher isotopes together with 0.5% of U and Pu isotopes from a ^{235}U-^{238}U reactor were considered as wastes. Such wastes from a 1 cycle operation of 10 reactors were recycled repeatedly in a ^{233}U-^{232}Th reactor. The resulting growths and decays of several selected isotopes are shown in the figure. In 60 years (10 cycles), negative gradients have been established for all isotopes except ^{246}Cm and ^{252}Cf. The negative gradients would have been steeper were it not for the presence of the ^{238}U material (200 gram atoms) which replenishes the transuranium isotopes. Further operation should establish negative gradients for ^{246}Cm and ^{252}Cf also. The rapid increase in the ^{252}Cf build-up, endemic to all recycling schemes, requires additional shielding for transportation and fuel reprocessing.

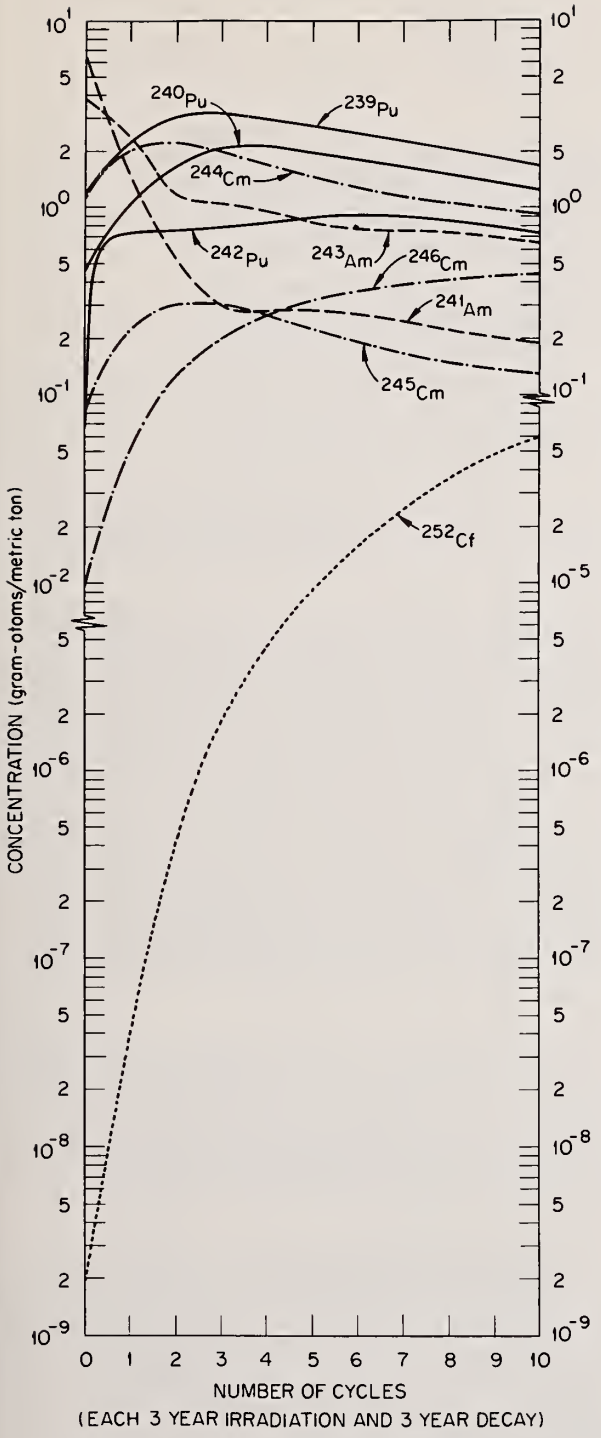

FIG. 1. Behavior of selected transuranium isotopes recycled in a ^{233}U-^{232}Th reactor. The ^{233}U and ^{232}Th concentrations were 240 and 4060 gram atoms, respectively, per metric ton of heavy elements charged to the reactor. To obtain the approximate quantities in kilograms in the actual reactor, multiply the ordinate numbers by 20. Note also the different scale for ^{252}Cf.

Table I. Comparison between transuranium production in two 1000 MW(e) reactors with different fuels at the end of 1 cycle (3 yr power generation, 3 yr cooling).

Fuel		Fuel
^{235}U - 2630 Kg ^{234}U - 20 Kg ^{238}U - 77350 Kg		^{233}U - 4500 Kg ^{232}Th - 75500 Kg
Flux		Flux
2.9×10^{13} n/cm^2 sec		1.2×10^{13} n/cm^2 sec
Quantity (Kg)	Isotope	Quantity (Kg)
39	^{237}Np	0.04
14	^{238}Pu	0.003
422	^{239}Pu	0.0002
174	^{240}Pu	$< 2 \times 10^{-5}$
72	^{241}Pu	$< 2 \times 10^{-6}$
28	^{242}Pu	$< 8 \times 10^{-8}$
13	^{241}Am	$< 3 \times 10^{-7}$
0.07	^{242m}Am	$< 4 \times 10^{-10}$
8	^{243}Am	$< 4 \times 10^{-9}$
0.008	^{242}Cm	$< 2 \times 10^{-11}$
0.006	^{243}Cm	$< 3 \times 10^{-12}$
2.2	^{244}Cm	$< 3 \times 10^{-10}$
0.16	^{245}Cm	$< 5 \times 10^{-12}$

We find that it is possible to further reduce the inventories of several transuranium isotopes through sustained recycling in a ^{233}U-^{232}Th reactor. The operation of a ^{233}U-^{232}Th reactor, of course, results in a different set of actinides with attendant hazards. Therefore, an answer to the important question of whether or not recycling the wastes in a ^{233}U-^{232}Th reactor results in a significant net reduction in the hazard requires more detailed calculations than what have been attempted here. In particular, such calculations require a broader scheme in which the required nuclear power generating capacity is suitably apportioned among the different types of reactors. Several factors such as (i) the degree of chemical separation that can be achieved for different elements, (ii) which elements are discharged into the waste streams, (iii) the hazards associated with transportation, reprocessing and fuel fabrication, (iv) both the short and long-term hazards associated with the fuel, (v) conversion ratios, (vi) safety, etc., need to be considered. On a more fundamental level, there are significant gaps in the cross-section data needed for predicting in advance the amount and nature of actinide wastes that will be generated and for detailed testing of the several proposed recycle schemes. We note, for example, that ^{245}Cm is a doorway leading to Bk and Cf isotopes. Therefore, fission cross-section measurements on ^{245}Cm have been initiated, as described elsewhere in these Proceedings, at the Oak Ridge Electron Linear Accelerator (ORELA) as part of a comprehensive program aimed at providing basic data for the recycle concept.

* Research sponsored by the U. S. Atomic Energy Commission under contract with the Union Carbide Corp.

[1] H. C. Claiborne, Neutron-Induced Transmutation of High-Level Radioactive Wastes, ORNL-TM-3964 (Dec., 1972).

[2] M. J. Bell, Origen - The ORNL Isotope Generation and Depletion Code, ORNL-4628 (May, 1973). Program modified by C. W. Kee and by O. W. Hermann.

A CONSISTENT SET OF TRANSPLUTONIUM MULTIGROUP CROSS SECTIONS*

R. W. Benjamin, V. D. Vandervelde,
T. C. Gorrell, and F. J. McCrosson
E. I. du Pont de Nemours and Company
Savannah River Laboratory,
Aiken, SC 29801

A consistent set of multigroup neutron cross sections was developed for nuclides in the chain from ^{242}Pu to ^{253}Es. Evaluated multigroup cross section data were combined with experimental test measurements and production yields from long-term reactor irradiations in flux spectra of varying hardness. Thus 37- and 84-group data were derived in part from ENDF/B and existing Savannah River Laboratory evaluated libraries. Where differential data were lacking, resonance-region model calculations and integral cross section values were combined to form the multigroup data. The data were tested with the JOSHUA system to calculate the reactor environment as a function of time and to predict the concentration of actinide nuclides in the chain. Cross section data were modified within experimental uncertainties until predicted nuclide concentrations matched experimental results within reasonable limits over the range of neutron flux spectra.

(Neutron reactions, heavy actinides; multigroup cross sections; heavy actinide burnup; reactor production experiments)

Introduction

A consistent set of multigroup neutron cross section data suitable for quantitative burnup or production studies of the heavier actinides has been developed. When used in conjunction with multigroup reactor production codes, these cross section data sets are capable of predicting actinide yields over a wide range of neutron energy spectra. Isotopes included in the set are in the production chain from ^{242}Pu to ^{253}Es and are shown in Figure 1.

Data Sources

Multigroup Data Sets

The basic data sets used in these determinations consist of smooth cross sections and resonance parameters, and span the energy region from zero to 10 MeV with a thermal cutoff at 0.625 eV. The 30-group THERMOS structure is used for the thermal region, and the 54-group MUFT structure is used for the epithermal region. Resonance parameters include resolved and unresolved resonances above the thermal cutoff to 10 keV. The 84-group sets have also been collapsed to 37 groups (12 thermal and 25 epithermal groups) which may be used to reduce computer time.

Data sets for nuclides below ^{244}Cm were from the SRL STANDARD library, which is made up of tested ENDF/B data sets and Savannah River Laboratory (SRL) evaluations. The two key nuclides, ^{242}Pu and ^{243}Am, were re-evaluated shortly before this study to include the most recent experimental work. Data sets beginning with ^{244}Cm and extending through the higher mass region were based on differential experimental data where possible, and on a combination of integral data and nuclear model calculations where differential data were inadequate or nonexistent. The techniques for generating differential data from integral data and nuclear model calculations are described by F. J. McCrosson.[1] Brief descriptions of the major data sets in these studies are listed in Table 1. Many of the experimental data sets for specific nuclides are incomplete; however, realistic, consistent, and functional multigroup evaluations can be made for most of these nuclides with the techniques described in this paper.

Reactor Production Experiments

Data from five independent reactor experiments, each including up to six targets with differing conditions, were used in the testing and adjustment of the consistent cross section data sets. The general properties of each of the experiments are listed in Table 2, and a brief description of each experiment follows.

HIFLUX: Four plutonium-oxide and aluminum rods containing about 98% ^{242}Pu with small quantities of other plutonium isotopes were irradiated in 1965. Target rods were removed from the reactor at successive intervals to determine the buildup of transplutonium isotopes as a function of time. Concentrations of isotopes of the actinides in the rods were determined by SRL. A consistent set of two-group data, based upon this experiment, was reported in 1968.[2]

Cf-I-Foils: This was part of a campaign to produce significant quantities of heavier actinides. The target rods of actinide oxides and aluminum contained mixtures of ^{243}Am and ^{244}Cm with small quantities of the higher curium isotopes. Isotopic analysis of the actinides following discharge was done by the transuranium (TRU) facility at Oak Ridge. These data are as yet unpublished.

Cf-I-Housings: The fuel housings (and flow guides) for the Cf-I campaign contained a filler of plutonium oxide which was about 99% ^{242}Pu. There were substantial variations in the fast-to-slow flux ratios during the exposure of these housings, and their flux history is mixed; i.e., all experienced significant zero flux time during their exposure. Final actinide analyses were determined by TRU facility personnel. These data are also still unpublished.

Resonance Spectrum Assemblies: This study was done to evaluate the resonance-spectrum reactor for transplutonium actinide production. Several pure and mixed heavy actinides were deposited on aluminum foils, sealed in quartz ampoules, and irradiated inside lithium-aluminum filter assemblies. The Li-Al assemblies served to harden the neutron spectrum. This HARDSPEC series had a fast-to-slow flux ratio of about 10. Similar foils with primarily ^{244}Cm were irradiated without the filters (BARELAT series) to obtain a fast-to-slow flux ratio of about 1.9. The flux history for these exposures was mixed, with some zero flux times occurring. A review of these measurements was done by J. D. Spencer and K. W. MacMurdo.[3]

With each of the above experiments, full account was taken of the flux history and of the energy dependence of the incident neutron flux for input to the

production codes. Isotopic decay during zero flux time was explicitly included.

Cross Section Testing and Modification

The Reactor Production Code GOSPEL

Actinide concentration as a function of time in the reactor environment is calculated by the production code GOSPEL, a code operating on the SRL JOSHUA system. GOSPEL can determine the production of actinides from ^{230}Th to ^{257}Fm using cross sections computed from multigroup cross section sets and multigroup neutron spectra.

GOSPEL uses the Runge-Kutta routine, stepping through time to solve a set of 53 differential equations, which express the rate of change of concentration of each isotope as the difference between the production and loss of that isotope. The loss for a given isotope is through decay (spontaneous fission, alpha, beta, or electron capture) or through neutron capture (nγ to the ground state of the subsequent nucleus, nγ to an isomeric state, or n-fission). The production of a given isotope is determined by the losses of all the other isotopes which contribute to it through their decay or neutron interaction.

The reaction rate was obtained by multiplying the effective cross section for a particular reaction type by the thermal neutron flux and the concentration. The effective cross section for the reaction was made up of two parts, σ_{th} and σ_{epi}, which were obtained by folding in the multigroup cross sections with the calculated multigroup neutron spectra. Spatially-dependent multigroup fluxes were calculated with the JOSHUA module RAHAB, which uses integral transport theory and the Nordheim treatment. The neutron spectra and the resulting effective cross section sets were identified by a spectral index to obtain cross sections which may vary with time. The thermal component (σ_{th}) was the cross section averaged over the thermal groups of the spectrum. The epithermal component (σ_{epi}), averaged over the epithermal groups, was a function of the isotopic concentration due to the self shielding of the resonances.

Iterations

The following approach was taken in deriving these cross section sets:

1. Establish the best, experimentally-based neutron cross section evaluations for each isotope, either through differential data, or integral data plus nuclear model calculations.

2. Prepare the reactor environment input data for GOSPEL as a function of time, i.e., flux, temperature, and neutron energy spectra.

3. Calculate actinide production with GOSPEL and compare with the measured experimental concentrations.

4. Examine deviations of the calculated from the experimental concentrations for a variety of neutron energy spectra.

5. Modify selected reaction cross sections in the appropriate energy region, i.e., thermal or epithermal. Ideally, cross sections should only have to be modified within the experimental uncertainty of the original measured sections.

6. Run GOSPEL again with the modified data set.

Iterations continue until acceptable agreement between calculated and experimental concentrations is reached. Once a complete and consistent set of multigroup cross sections has been established, any change in a single isotopic cross section set may alter significantly the predicted concentrations of that isotope and others above it in the chain.

Results and Conclusions

A complete set of multigroup cross sections for nuclides in the production chain from ^{242}Pu to ^{253}Es has been established with the techniques described above. Because of the limited space available, it is not possible to tabulate the 84-group data sets with their associated resonance parameters. The resulting data, however, may be characterized by the real 2200 m/s cross sections, a g-factor which is a convenient measure of the departure from 1/v dependence,[4] and the resonance integral (with a thermal cutoff of 0.625 eV). These values are listed in Table 3. For two-group calculations, the thermal value used should be the product of the 2200 m/s cross section and the g-factor.

Generally, the concentrations of actinide nuclides predicted with the newly-formulated consistent set are within ±10% of the experimentally-measured concentrations. Plots of the percent variation of the calculated from the measured concentrations versus the nuclides in the production chain are shown in Figure 2. Agreement of calculated and measured concentrations is very good through all of the curium isotopes for all the energy spectra. Variations are well within 10% with few exceptions. Agreement for the limited measured values of ^{249}Bk and ^{249}Cf is mixed. This may be attributed to the difficulty in measuring the concentrations of these isotopes and referring the concentrations back to the time of discharge from the reactor, particularly since ^{249}Bk β-decays to ^{249}Cf with a 314-day half-life and ^{253}Es α-decays to ^{249}Bk with a 20.47-day half-life. The growth of californium isotopes above ^{249}Cf is relatively insensitive to the ^{249}Bk cross sections, so these should be regarded as tentative values. The ^{249}Bk cross sections in both the thermal and resonance regions must, however, be significantly larger than indicated in earlier measurements.[5]

Agreement in the californium region is reasonably good in the thermal and near-thermal spectra, but less consistent in the harder spectra. Resonance-region data for ^{250}Cf. ^{251}Cf, and ^{252}Cf are based upon resonance integrals determined at ORNL by Halperin, et al.[6,7] and Bemis, et al.,[8] whose results were corroborated through mock-up of their experiments with the SRL codes. Significantly better agreement for the two aberrant points (Figure 2) in BARELAT (^{250}Cf) and HARDLAT (^{252}Cf) cannot be achieved with reasonable adjustments of the californium cross sections. Results for the isotopes above ^{252}Cf are only indicative of the cross sections because of the paucity of the data and the difficulty of dependable measurements of isotopes with low concentrations and relatively short half-lives.

A document detailing the studies described above is in preparation. In conclusion, 1) multigroup cross sections for the heavy actinides through ^{248}Cm are very suitable for general reactor studies in a wide range of neutron spectra, and 2) multigroup cross sections for berkelium and californium isotopes are adequate for good quantitative studies in the thermal and near-thermal regions, but probably only useful for qualitative studies in the epithermal region.

References

1. F. J. McCrosson, *Proceedings of the Third Conference on Neutron Cross Sections and Technology, March 15-17, 1971, Knoxville, Tennessee*, USAEC Report CONF-710301, vol. 2, ERDA-TIC, Oak Ridge, Tennessee, pp. 714-21 (1971).

2. J. A. Smith, C. J. Banick, R. L. Folger, H. P Holcomb, and I. B. Richter, *Neutron Cross Sections and Technology-Proceedings of a Conference, Washington, D. C., March 4-7, 1968*, NBS Special Publ. 299, vol. II, pp. 1285-90 (1968).

3. J. D. Spencer and K. W. MacMurdo, *Transplutonium Cross Sections Determined in a Resonance Spectrum Irradiation Assembly*, USAEC Report DP-1311, E. I. du Pont de Nemours & Co., Savannah River Laboratory, Aiken, South Carolina (1974).

4. C. H. Westcott, *Effective Cross Section Values for Well-Moderated Thermal Reactor Spectra*, Report CRRP-787 (AECL-670), Atomic Energy of Canada, Ltd. (1968).

5. R. L. Folger, J. A. Smith, L. C. Brown, R. F. Overman, and H. P. Holcomb, *Neutron Cross Sections and Technology - Proceedings of a Conference, Washington, D. C., March 4-7, 1968*, NBS Special Publ. 299, vol II, pp. 1279-1284 (1968).

6. J. Halperin, C. E. Bemis, Jr., R. E. Droschel, and R. E. Eby, *Chemistry Division Annual Progress Report for Period Ending May 20, 1971*, USAEC Report ORNL-4706, Oak Ridge National Laboratory, Oak Ridge, Tennessee, pp. 47-51 (1971).

7. J. Halperin, J. N. Oliver, and R. W. Stoughton (Reference 6), pp. 53-55 (1971).

8. C. E. Bemis, Jr., R. D. Druschel, R. D. Baybarz, and J. Halperin (Reference 6), pp. 51-53 (1971).

* Work performed under ERDA Contract No. AT(07-2)-1.

TABLE 1. Description of Cross Section Data Sets

Nuclide	Experimental Data	First Resonance, eV	Comments
^{242}Pu	Differential	2.68	Good data.[a]
^{243}Am	Differential	0.42	Good data.[a]
^{244}Cm	Differential	7.67	Good data.[a]
^{245}Cm	Differential	1.96	Incomplete differential data; need low energy fission.[a]
^{246}Cm	Differential	4.32	Reasonable differential data, though incomplete.[a]
^{247}Cm	Integral	Unknown	No differential data, <20eV.[b]
^{248}Cm	Differential	7.25	Good data.[a]
^{249}Bk	Integral	Unknown	Very little data of any sort.[b]
^{249}Cf	Differential	0.70	Reasonable differential fission data.[a]
^{250}Cf	Integral	Unknown	No differential data.[b]
^{251}Cf	Integral	Unknown	No differential data.[b]
^{252}Cf	Integral	Unknown	No differential data.[b]
^{253}Cf	Integral	Unknown	No differential data, incomplete integral data.[b]
^{254}Cf	Integral	Unknown	No differential data, no integral data.[b]
^{253}Es	Integral	Unknown	No differential data.[b]
^{254}Es	Integral	Unknown	No differential data, incomplete integral data.[b]

a. Data set based on experimental data.

b. Data set based on integral data and nuclear model calculations; differential data and resonance parameters were generated by the technique of McCrosson.[1]

Table 2. General Properties of Reactor Experiments

Experiment	Unit Name	Exposure Time, days	Initial Major Isotope(s)	Integrated Flux, n/cm^2	Fast-to-Slow Flux Ratio Range	Brief Description
HIFLUX	Slug I	157	^{242}Pu	3.82×10^{22}	0.296	Target rods of plutonium oxide and aluminum.
	Slug II	213	^{242}Pu	5.18×10^{22}	0.296	
	Slug III	296	^{242}Pu	7.20×10^{22}	0.296	
	Slug IV	370	^{242}Pu	9.00×10^{22}	0.296	
Q-FOILS	K-7	370	^{243}Am, ^{244}Cm	1.15×10^{23}	0.256 to 0.302	Target rods of americium oxide, curium oxide, and aluminum.
	K-10	350	^{243}Am, ^{244}Cm	1.06×10^{23}	0.256 to 0.302	
	K-37	280	^{243}Am, ^{244}Cm	8.12×10^{22}	0.278 to 0.312	
	K-40	260	^{243}Am, ^{244}Cm	7.62×10^{22}	0.278 to 0.312	
	K-41	260	^{243}Am, ^{244}Cm	7.74×10^{22}	0.278 to 0.312	
	K-42	250	^{243}Am, ^{244}Cm	7.11×10^{22}	0.278 to 0.312	
HOUSINGS	TRU1	670	^{242}Pu	1.11×10^{23}	0.563 to 0.920	Cylindrical tubes of plutonium oxide and aluminum.
	TRU2	710	^{242}Pu	1.13×10^{23}	0.520 to 0.920	
	TRU3	830	^{242}Pu	1.16×10^{23}	0.520 to 0.920	
	TRU4	830	^{242}Pu	1.22×10^{23}	0.473 to 0.920	
	TRU6	830	^{242}Pu	1.20×10^{23}	0.520 to 0.920	
SOFTSPEC	BARELAT	165	^{244}Cm	1.83×10^{21}	1.630 to 2.110	Deposits on aluminum foils in quartz ampoules.
HARDSPEC	HARDLAT	165	^{244}Cm	2.47×10^{20}	7.438 to 12.451	Deposits on aluminum foils in

TABLE 3. Characteristic Cross Sections from the Multigroup Data Sets

Isotope	σ_c^{2200} (barns)	σ_f^{2200} (barns)	g-factor	I_c ≥0.625 eV (barns)	I_f ≥0.625 eV (barns)
^{242}Pu	18.7	0	1.0	1,280	4.74
^{243}Pu	87.4	180	1.0	264	541
^{243}Am	74.4	0	1.015	2,159	3.4
^{244}Cm	10.0	1.5	0.995	585	17.1
^{245}Cm	383	2161	0.971	104	766
^{246}Cm	1.4	0.17	1.0	119	10.0
^{247}Cm	58.0	72.3	1.0	500	761
^{248}Cm	2.89	0.11	1.0	251	14.7
^{249}Bk	1600	0	1.0	4,000	0
^{249}Cf	495	1720	0.969	777	1863
^{250}Cf	1701	0	1.0	11,600	0
^{251}Cf	2849	4801	1.0	1,600	5400
^{252}Cf	20.4	32.0	1.0	43.5	110
^{253}Cf	12.0	1100	1.0	12.0	2000
^{253}Es	155	0	1.0	7,300	0

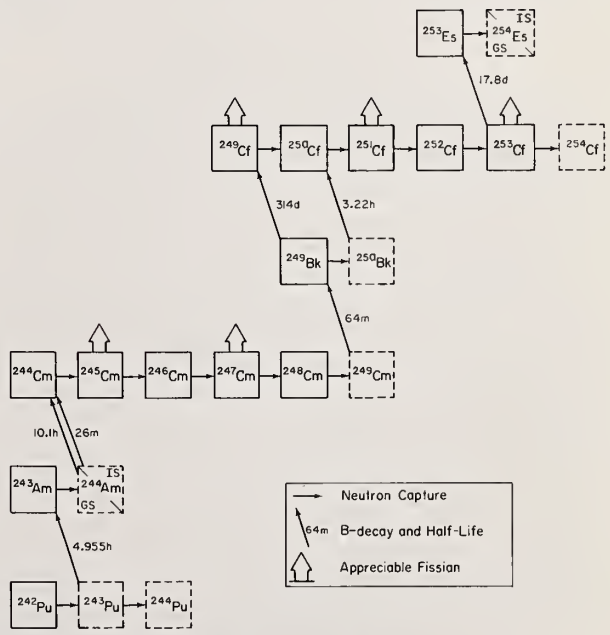

FIG. 1 The ^{252}Cf Production Chain

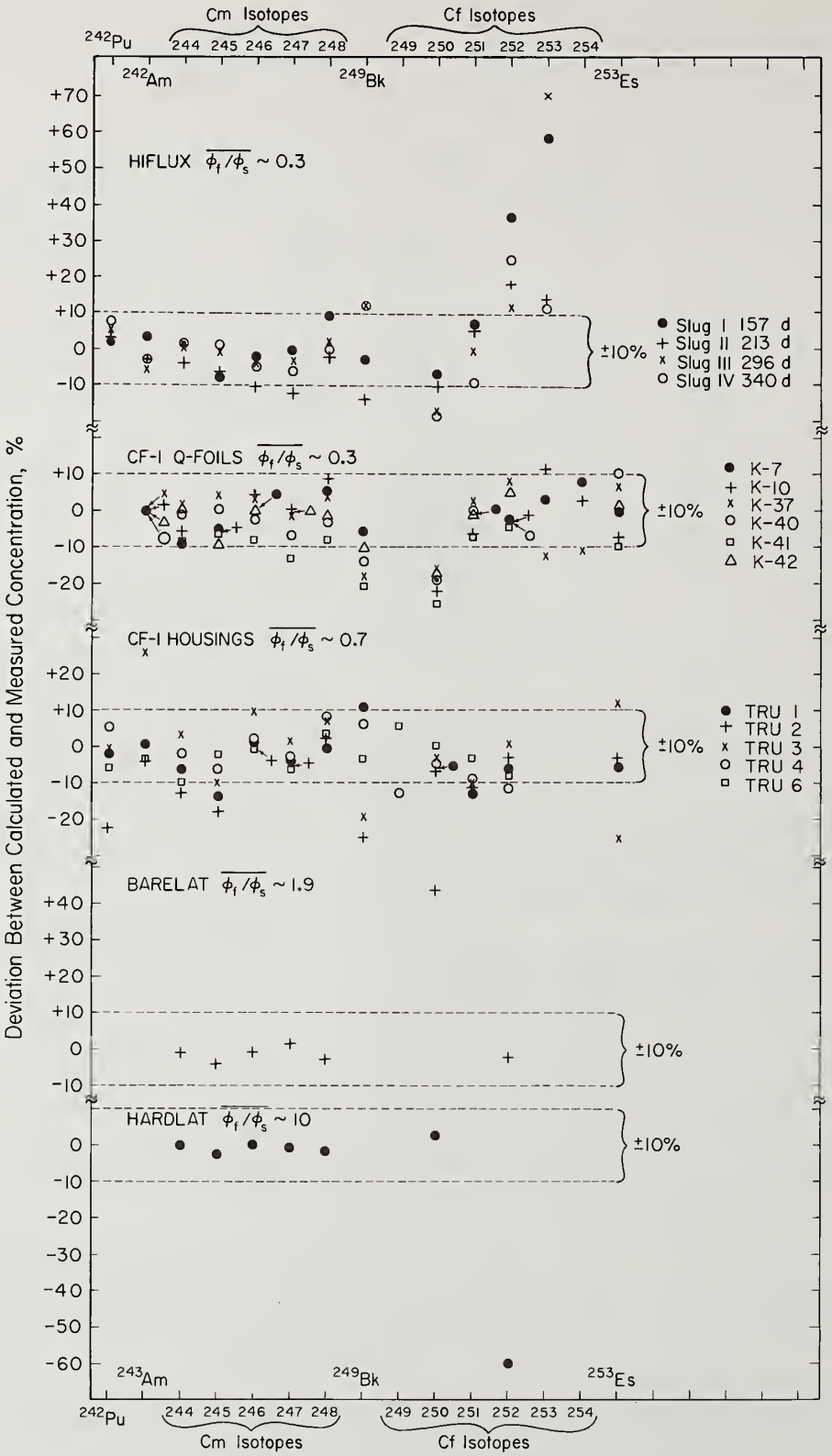

FIG. 2 Reactor Experiments

MEASUREMENT OF THE NEUTRON CAPTURE CROSS SECTIONS OF THE ACTINIDES*

L. W. Weston and J. H. Todd

Oak Ridge National Laboratory
Oak Ridge, Tennessee 37830

The capture cross sections of the isotopes heavier than ^{239}Pu are of great importance for the core physics, fuel recycle, and waste management for power reactors. Since total cross sections are not sufficient, a program for the measurement of these needed capture cross sections is being carried out at ORNL. Measurements have been almost completed on ^{240}Pu, ^{241}Pu, and ^{241}Am and have been planned for ^{242}Pu and possible ^{237}Np and ^{243}Am. The capture gamma-ray detector used is the "total energy detector" which is a modification of the Moxon-Rae detector. Fission, when present, is detected with fast neutron counters. Results obtained on ^{240}Pu, ^{241}Pu, and ^{241}Am will extend continuously from thermal neutron energies to 350 keV. The cross sections are normalized at thermal neutron energies and the neutron flux is measured relative to the $^{10}B(n,\alpha)$ cross section up to 2 keV and $^{6}Li(n,\alpha)$ at higher neutron energies. The accuracy of the techniques used varies with the sample but is about 8%. With such cross sections the long range management of the actinides produced in power reactors can be planned on a more systematic basis.

(Actinide management; neutron capture cross sections; Pu isotopes, ^{241}Am)

Introduction

The actinide nuclides of higher mass than ^{239}Pu are produced in reactors via successive neutron capture. In U fueled reactors they are produced with ^{238}U as the principal progenitor and in a Pu fueled reactor it is ^{239}Pu. With the exception of ^{241}Pu these nuclides as a group are of little value as fuel for the reactor. In terms of fuel and waste management these actinide isotopes are important. The higher Pu isotopes, $^{240,241,242}Pu$, are about 26%, 12%, and 3% respectively of the total Pu discharged from a water reactor.[1] These isotopes must be considered in the core physics of a Pu-fueled reactor. Other actinide elements which are of importance to fuel and waste management are Np, Am, Cm, and Cf.

The isotopes of Np, Am, and Cm plus unrecovered U and Pu constitute the major long term (> 500 years) radiological hazard from reactor waste.[2] After the decay of fission products to innocuous levels as compared to naturally occurring minerals in about 500 years, the radiological hazard of these actinides will continue for a million years. Therefore, a knowledge of the neutron cross sections for the production (and transmutation) of these isotopes is essential. Because of the long term radiological hazard (> 500 years) of these nuclides, it has been proposed that they be recycled in reactors to be transmuted into fission products which are a shorter-term hazard.[2,3] Since the projected quantity of these nuclides to be produced by the year 2000 is 1,269 metric tons,[4] the conversion would be no minor undertaking. The burden on the neutron economy of the transmutation reactor may be acceptable since every other isotope of the actinides tends to have an appreciable fission cross section. If the actinide recycle concept is to be implemented or adequately assessed, the capture and fission cross sections of the nuclides involved need to be known over the whole neutron energy spectrum of potential waste-burning systems. The underground nuclear explosion technique[5] has provided a wealth of fission cross sections of these nuclides; however, the capture cross sections are not nearly as well known. Total cross sections and integral measurements[6] are of great value in deriving capture cross sections but are not sufficient in all cases, particularly above the resolved resonance region. One of the major problems in measuring the capture cross sections for the long-lived actinide isotopes is obtaining pure samples. Isotopes with appreciable spontaneous fission, even if present only as impurities, can cause prohibitive backgrounds.

Of particular importance to those involved in fuel recycle are the spontaneous fissioning isotopes of Pu, Cm, and Cf which make additional shielding necessary in the fabrication and shipping of fuel elements. The cross sections leading to the production of the spontaneous fissioning nuclides are needed for the various types of reactors. Additional shielding necessary for fission neutrons could be costly and needs advance consideration. If the long lived actinides are to be transmuted in reactors before disposal, there will be more of these spontaneously fissioning nuclides formed. Predictions of this additional neutron activity is dependent on the cross sections as well as the neutron energy spectrum of the type reactor used.

Since one of the major objectives of the Oak Ridge Electron Linear Accelerator (ORELA) is to produce the neutron cross sections needed by the power reactor program, there is a program to measure the needed capture and fission cross sections of the actinide nuclides of mass higher than ^{239}Pu. The purpose of this paper is to discuss this measurement program and techniques involved.

Experimental Procedure

The ORELA is used as a source of pulsed neutrons. Neutron energies are measured by time-of-flight along a flight path of 20 or 85 meters. Since ORELA has multiple flight paths which can be used simultaneously, the measurements can be carried out at the same time as other experiments.

In order to directly measure a capture cross section, means must be available to detect the capture gamma-ray cascade following a neutron capture event. The detection efficiency for the capture event must be independent of changes in the gamma-ray cascade. If a low-efficiency detector has an efficiency which is proportional to gamma-ray energy then its efficiency for detecting a capture event is proportional to the (constant) binding energy of the nucleus. Such detectors were first approximated by thick walled geiger counters, then Moxon-Rae detectors,[7] and finally the "total energy detector."[8] The "total energy detector" can be any gamma-ray detector whose pulse-height response to gamma-rays of different energies is known. Sets of weighting factors for different pulse height events have been developed to force the net efficiency to be proportional to gamma-ray energy. This method was suggested by Maier-Leibnitz[9] and developed by R. L. Macklin.[8] Fission events are also detected by such a detector because of the prompt fission gamma-rays.

The gamma-ray detectors used in these experiments are 2 by 10 cm diameter liquid scintillators of NE-226, a nonhydrogenous scintillator. Such a scintillator was desired to reduce the efficiency of response to fast

neutrons from fission events in the sample. The gamma-ray event weighting factors as a function of pulse-height derived by R. L. Macklin[8] were altered slightly to account for the 0.32 cm of Pb which was necessary between the sample and the detectors because of the high activity of low energy gamma-rays (< 100 keV) from most of the samples. No statistically significant differences were observed in the capture rate vs neutron energy when the capture events were not weighted according to their pulse-height. This infers that changes in the prompt gamma-ray spectrum following a capture event were not significant for the cases studied in these measurements. The efficiency for the detection of a capture or fission event by these detectors was about 1.5% per detector.

To detect fission events in the samples where there is a measurable fission cross section, fast neutron counters are used. These fast neutron detectors are liquid scintillators (NE-213) which are 10 cm in diameter and 5 cm thick. Pulse-shape discrimination is done on the pulses from the scintillators in order to discriminate between fast neutrons and gamma rays. These two fission neutron detectors are used in the same geometry as the gamma-ray detectors so that there is a total of four detectors facing the sample with their axis in the plane perpendicular to the neutron beam.

The shape of the neutron flux from thermal neutron energies to 2 keV is measured with a parallel-plate $^{10}BF_3$ chamber which intercepts the full neutron beam. Above 2 keV this chamber was calibrated vs a ^{6}Li glass detector of 0.5 mm thickness and 7.62 cm diameter. Thus the shape of the cross sections is based on the ^{6}Li cross section above 2 keV. The ^{6}Li cross section and corrections for scattering in the Li glass were these proposed by Macklin.[10] The $^{10}B(n,\alpha)$ cross section assumed is that proposed by Sowerby;[11] this evaluated cross section is nearly 1/v up to 2 keV.

The time-dependent background in the gamma-ray, neutron, and flux detectors is measured by means of the black resonance technique. Filters of S, Na, and Au were used to deplete all primary neutrons at their resonances at 105 keV, 2 keV, and 5 eV respectively and determine the background at these neutron energies. These backgrounds were used to normalize the shape of the time-dependent background as determined with a mock-up sample container. A relatively large background which is independent of time is usually caused by the radioactivity of the sample. The level of this background is determined at long times following the accelerator burst when essentially all neutrons have passed the sample position or have been depleted by a ^{10}B overlap filter.

The shape of the neutron cross sections vs neutron energy which is derived in these experiments is normalized to the absolute value of the cross section at 0.025 eV as listed in ENDF/B-IV. Resonance self-protection corrections were relatively small since 2-gram samples of 7.62 cm diameter have been used at eV neutron energies and 9-gram samples at keV neutron energies. The effects of multiple neutron scattering in the sample in most cases were negligible.

Experimental Results

With the experimental techniques described, measurements have been carried out on ^{240}Pu, ^{241}Pu, and ^{241}Am. The results of these experiments have not quite been finalized. In addition, measurements of $\alpha(\langle\sigma_c\rangle/\langle\sigma_F\rangle)$ have been done on ^{239}Pu in order to make a direct comparison of the present techniques with those using a fission chamber sample in a large liquid scintillator tank. The results of this comparison are discussed in another paper in these proceedings.[12] Preliminary results on ^{241}Pu have been described previously.[13]

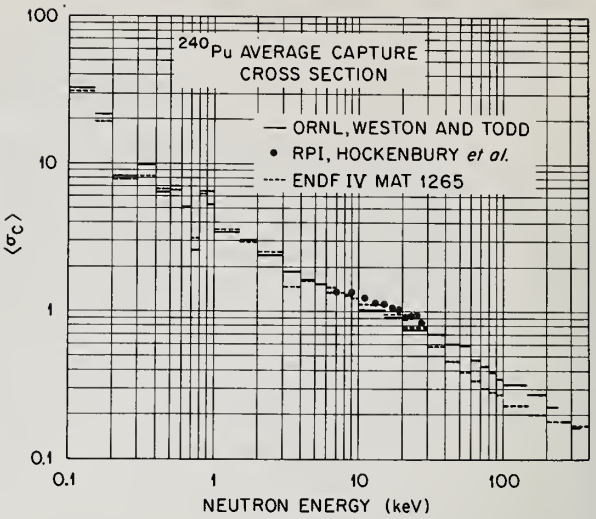

Figure 1

Figure 1 shows the results on the average capture cross section of ^{240}Pu. These data were normalized at 0.025 eV to the ENDF/B-IV evaluation and the normalization was confirmed by using the black resonance technique of normalization with the large 1-eV resonance in ^{240}Pu. Also shown for comparison are the results of Hockenbury et al.[14] and ENDF/B-IV MAT 1265 evaluation. The results of Hockenbury et al. are in agreement within experimental errors with the present results. The ENDF evaluation in the neutron energy range shown is based on the results of Hockenbury and preliminary results of these experiments. Measurements on the subthreshold fission of ^{240}Pu are discussed elsewhere in these proceedings.[15]

Figure 2 is the average absorption cross section of ^{241}Am. The cross section is predominately capture since fission is small at these neutron energies. The ENDF/B-IV MAT 1056 evaluation is shown for comparison. The ENDF evaluation at keV neutron energies is based almost entirely on resonance parameters from total cross sections in the resolved resonance region so the agreement is considered satisfactory. The increase in the cross section above the ENDF/B-IV evaluation starting at 20 keV was indicated by measurements both at the 20 and 85 meter flight paths.

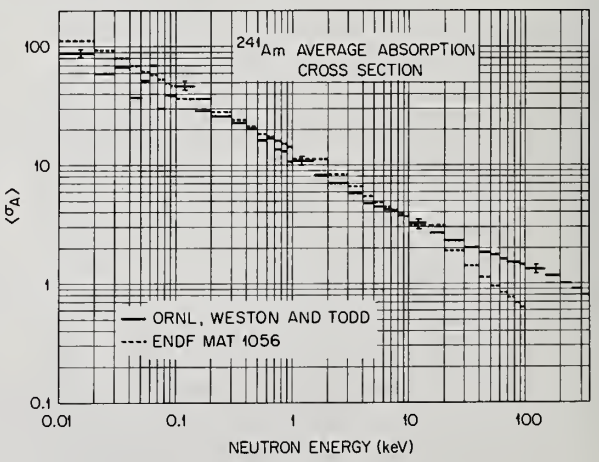

Figure 2

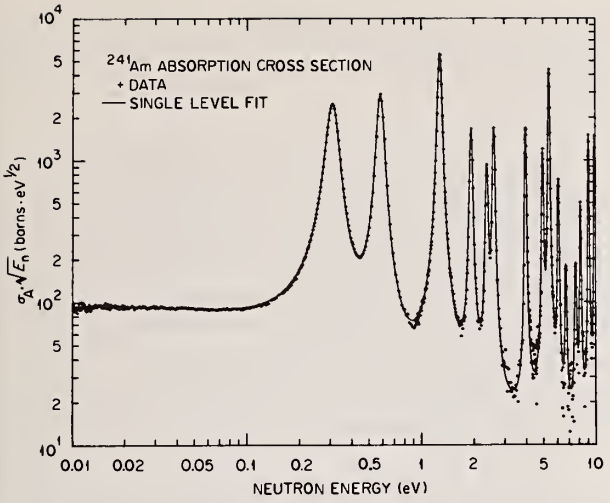

Figure 3

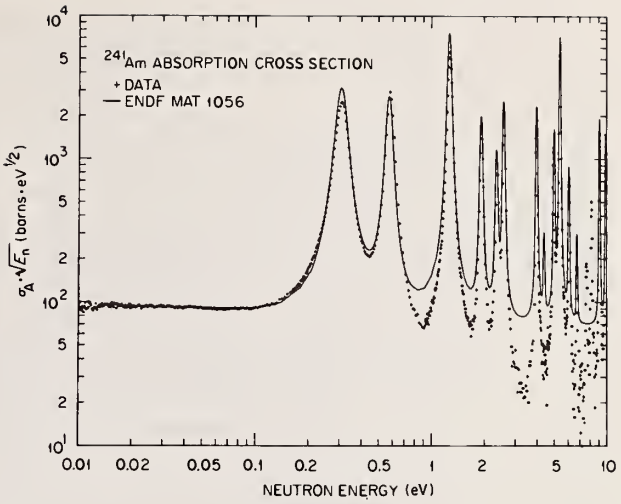

Figure 4

Figure 3 is the absorption cross section data in the eV region of neutron energies with the solid line being the single-level fit to the data. The fission cross section of ^{241}Am was not measured in this experiment because of an inexplicably high spontaneous fission rate in the sample. Figure 4 is a comparison of ENDF/B-IV MAT 1056 with the present data. The ENDF evaluation in the resonance region of ^{241}Am was based on total cross section measurements.[16] The agreement is not satisfactory, especially between the resonances where the ENDF evaluation is appreciably higher than the present data.

The neutron cross section data taken with this technique are of high neutron energy resolution as can be seen in Fig. 3. There is resonance structure which extends far above the nominal resolved resonance region. Average cross sections were used in the comparisons at keV neutron energies since the fine structure in the cross sections makes direct comparison difficult.

Summary

Measurements have been made with the described techniques on the capture and fission cross sections of some of the nuclides of higher mass than ^{239}Pu which are important to fast reactor core physics. Additional measurements are planned for ^{242}Pu and perhaps ^{237}Np and ^{243}Am. If the actinide recycle concept is to be implemented or adequately assessed as an appropriate method of reducing the long term radiological hazard of the actinide waste, other similar measurements are possible and will be needed. Several of the long lived isotopes of Am and Cm are succeptable to cross section measurements with the present techniques. Sample preparation will be a major problem.

Total cross sections and integral measurements are of great value; however, measurement of the capture and fission cross sections are needed to produce the needed knowledge of the cross sections. With these cross sections the fuel and waste management for Pu fueled reactors can be planned on a systematic basis.

References

*Research sponsored by the Energy Research and Development Administration under contract with the Union Carbide Corporation.

[1]P. Greebler, B. A. Hutchins, and C. L. Cowan, Proc. Conf. Nuclear Data for Reactors, vol. I, p. 19 (1972) Helsinki, IAEA.

[2]H. C. Claiborne, "Effect of Actinide Removal on the Long-term Hazard of High-level Waste," ORNL-TM-4724 (1975); also see ORNL-TM-3964 (1972).

[3]"High-level Radioactive Waste Management Alternatives," BNWL-1900, vols. 1-4, May 1974.

[4]J. O. Blomeke, C. W. Kee, and J. P. Nichols, "Projections of Radioactive Wastes to be Generated by the U. S. Nuclear Power Industry," ORNL-TM-3965, February 1974.

[5]B. C. Diven, Ann. Rev. Nucl. Sci. 20, 79 (1970); also A. Hemmendinger, Am. Scientist 58, 622 (1970).

[6]R. W. Benjamin, "Survey of Experimentally Determined Neutron Cross Sections of the Actinides," DP-1324 (1973).

[7]M. C. Moxon and E. R. Rae, in Neutron Time-of-Flight Methods, ed. J. Spaepen, European Atomic Energy Committee, Brussels, 1961.

[8]R. L. Macklin and J. H. Gibbons, Phys. Rev., vol. 159, No. 4, 1007 (1967).

[9]H. Maier-Leibnitz (private communication to R. L. Macklin).

[10]R. L. Macklin, J. Halperin, and R. R. Winters, "Gold Neutron Capture Cross Section from 3 to 550 keV," accepted for publication in Phys. Rev. C. See also B. J. Allen et al., Phys. Rev. C 8, 1504 (1973).

[11]M. G. Sowerby et al., Proc. Conf. Nuclear Data for Reactors, vol. I, p. 161 (1970) Helsinki, IAEA.

[12]R. Gwin et al., "A Direct Comparison of Different Experimental Techniques for Measuring Neutron Capture and Fission Cross Sections," Proc. Conf. Nuclear Cross Sections and Technology, March 3-7, Washington, D.C. (1975).

[13]L. W. Weston and J. H. Todd, "Neutron Fission and Absorption Cross Sections Measurements of ^{239}Pu and ^{241}Pu," Trans. Am. Nucl. Soc. 15, 480 (1972).

[14]R. W. Hockenbury, W. R. Moyer, and R. C. Block, Nucl. Sci. Eng. 49, 153 (1972).

[15]G. F. Auchampaugh and L. W. Weston, "Subthreshold Fission in ^{240}Pu+n," Proc. Conf. Nuclear Cross Sections and Technology, March 3-7, Washington, D. C. (1975).

[16]For references on individual measurements see ref 6.

MEASUREMENTS OF THE ^{6}Li and ^{10}B PARTIAL CROSS SECTIONS FROM 1 TO 1500 keV

S. J. Friesenhahn, V. J. Orphan, A. D. Carlson,
M. P. Fricke, and W. M. Lopez
IRT Corporation
San Diego, California 92138

The $^{10}B(n,\alpha_0+\alpha_1)^{7}Li$, $^{10}B(n,\alpha_1)^{7}Li^*$ and $^{6}Li(n,\alpha)T$ cross sections have been measured between 1- and 1500-keV neutron energy. The neutron spectrum was measured using proton scattering as observed in a methane-filled proportional counter. Gamma rays from the $^{10}B(n,\alpha_1)^{7}Li^*$ reaction were observed with a high-resolution Ge(Li) spectrometer, and the reaction products from the $^{10}B(n,\alpha_0+\alpha_1)^{7}Li$ and $^{6}Li(n,\alpha)T$ reactions were observed in a large ion chamber. In an auxiliary measurement, the ratio of the $^{10}B(n,\alpha_0+\alpha_1)^{7}Li$ cross section to the hydrogen scattering cross section was obtained between 200 and 1000 keV by observation of interactions in a specially constructed $^{10}BF_3$ proportional counter containing a methane additive.

(Neutron cross section; ^{10}B; ^{6}Li; standard)

Introduction

The large, smoothly varying reaction cross sections of ^{10}B and ^{6}Li, combined with the ease of their implementation in neutron detectors, has resulted in the use of these isotopes as standard cross sections for neutron flux determinations. The reaction energies are sufficiently large to make event detection relatively easy, and in the case of ^{10}B, the interactions may be detected via both charged-particle and gamma-ray detectors. However, relatively few measurements of these cross sections have been made. Many of the direct measurements made previously may contain systematic errors from long-counter flux determinations, and are subject to a variety of uncertainties associated with background determinations. The indirect results [e.g., the $^{10}B(n,\alpha)$ cross sections deduced from the total and scattering cross sections] may contain substantial systematic errors inherent in such determinations. The present measurements were undertaken to remove or reduce these uncertainties, by making high-accuracy, direct measurements relative to the H(n,n) standard cross section.

Measurements and Data Reduction

The measurements were made using a 226-meter evacuated flight path and the IRT Linac as a neutron source. The 70-MeV Linac electron beam of 0.1-μsec duration struck a tungsten alloy target located at the center of a 7-inch-diameter ^{238}U cylinder. The emergent neutron spectrum was partially moderated in a 1-inch-thick slab of polyethylene before entering the flight path. Thick aluminum, sodium, or polyethylene filters were inserted at the 45-meter position for determining the background. Data were acquired with an on-line CDC-1700 computer, which employed interfaces to three analog-to-digital converters and a time digitizer to store data in multiparameter form on magnetic tape. These four-parameter data were subsequently sorted on a Univac-1108 computer.

The neutron flux measurements were performed using a 24-inch-long, 2-inch-diameter ceramic end window methane counter. The filling pressure of 2 atmospheres is sufficient to produce high-quality proton-recoil response functions which are relatively free of wall and end effects up to 1 MeV. The response was improved further by use of a collimator just upstream from the counter, which confined the neutron beam to the central region of the counter, thus further reducing the wall-interaction effect.

Since the ionization/eV of recoiling proton energy is not constant, the energy dependence of this effect was measured in the course of the flux determination by sorting the multiparameter data into proton-recoil response functions at various neutron energies. The location of the leading edge of the distribution divided by the incident neutron energy was taken as a measure of the relative number of ion pairs/eV produced. This function, along with the calculated wall and resolution effects, was used to calculate the bias efficiency for the proton-recoil data, which had been sorted with an energy-dependent bias equal to 35% of the incident neutron energy.

One of the parameters stored on the magnetic tape is a rate-of-rise signal, which is derived by differentiating the pulse from the counter in a fast amplification system. This pulse rise-time information was used to discriminate between neutron and gamma-ray interactions in the counter. Gamma-ray background subtractions were quite small throughout the region of interest.

Since the only material with appreciable neutron cross section between the neutron source and the detection position was a ^{10}B filter used to avoid neutron burst overlap, the measured spectrum is quite smooth, with the exception of a small dip in the vicinity of the oxygen resonance at 432 keV. Part of this dip is due to the mylar vacuum windows in the flight path, and part is due to the Al_2O_3 end window of the counter. The end window transmission was corrected for in determining the neutron spectrum.

Considerable effort was expended in developing detection devices exhibiting desirable response functions and a minimum of multiple scattering. We next briefly describe each of these devices and their implementation in the measurements.

The 478-keV gamma ray from the $^{10}B(n,\alpha_1)^{7}Li^*$ reaction was observed by locating an 80-cc high-resolution (4-keV) Ge(Li) spectrometer in the center of the 9-inch-diameter neutron beam. The Ge(Li) spectrometer and its cryostat were shielded from the incident neutron beam. The remaining portion of the beam struck a thin slab of ^{10}B powder contained between mylar sheets. The slab was evacuated to hold the powder in a uniform layer. Doppler broadening of the gamma ray required the use of a 10-keV-wide gamma-ray energy window. A small background correction was obtained by replacing the ^{10}B

slab with a graphite slab having approximately the same macroscopic scattering cross section. This background agreed well with that obtained by moving the gamma-ray bias window just above the 478-keV position.

The $^{10}B(n,\alpha_0+\alpha_1)^7Li$ and $^6Li(n,\alpha)T$ reactions were observed in a large, gridded ion chamber. An identical background chamber was constructed, but backgrounds were too small to be observable, and no correction was necessary. All of the chamber elements, with the exception of the source plates, were formed by 10-inch x 10-inch grids composed of No. 36 aluminum wire spaced ∿1/8 inch apart. The chambers were long enough (54 inches) to contain several source plates of ^{10}B and ^6Li simultaneously. It was thus possible to accumulate simultaneously data on both ^{10}B and ^6Li cross sections under nearly identical conditions. The chambers were operated at atmospheric pressure with a gas flow of ≈15 liters per minute of 90% argon, 10% CO_2.

The large energy-loss rate and relatively low energy of the ^7Li reaction product results in a poor response function for a useful thickness of ^{10}B deposited on a thick substrate. This is a serious problem, since the range of neutron energies covered in these measurements is sufficient to produce large changes in the response function due to the incident neutron kinetic energy. For this reason, a technique was developed for producing thin, self-supporting ^{10}B films for the 10-inch x 10-inch ion chamber source plates. These self-supporting plates allow observation of the sum of the α and ^7Li energies, thus greatly improving the response function and reducing bias efficiency corrections.

The films were formed from a liquid plastic solution containing a ^{10}B dispersion. The plastic was coated on a large glass plate, and then an ion chamber frame was cemented to the dried film. The film was made conductive by rubbing with graphite powder, and then stripped from the glass plate under water. The completed films contained ≈30% ^{10}B by weight. The sum response function is illustrated in Figure 1. Since the films contained hydrogen, it was necessary to use a neutron-energy-dependent bias in sorting the data. The bias efficiency corrections were obtained via calculated response functions (example given in Figure 1), which included detailed treatment of energy loss, particle ranges, branching ratio, angular distributions, etc. The energy dependence of the bias efficiency corrections, along with those of other detectors used in these measurements, is illustrated in Figure 2.

Because of the reactive nature of lithium and its compounds, it was not possible to produce self-supporting films containing this material. For this reason, ^6Li metal was evaporated on 1-mil aluminum foil. Two deposit thicknesses of ≈50 and ≈250 μg/cm^2 were used. The thinner deposit yielded the response function illustrated in Figure 3, and several plates of this thickness were used to obtain cross-section data of moderate statistical precision. The data from several of the thick deposits were then divided by the thin deposit data to obtain the ratio of the bias efficiencies. This ratio was grouped and smoothed to obtain the relative thick deposit biasing efficiency as a function of neutron energy. The thin deposit bias efficiency was calculated using a computer code similar to that used for the ^{10}B efficiency calculations. A comparison of calculated versus measured distributions is illustrated in Figure 3.

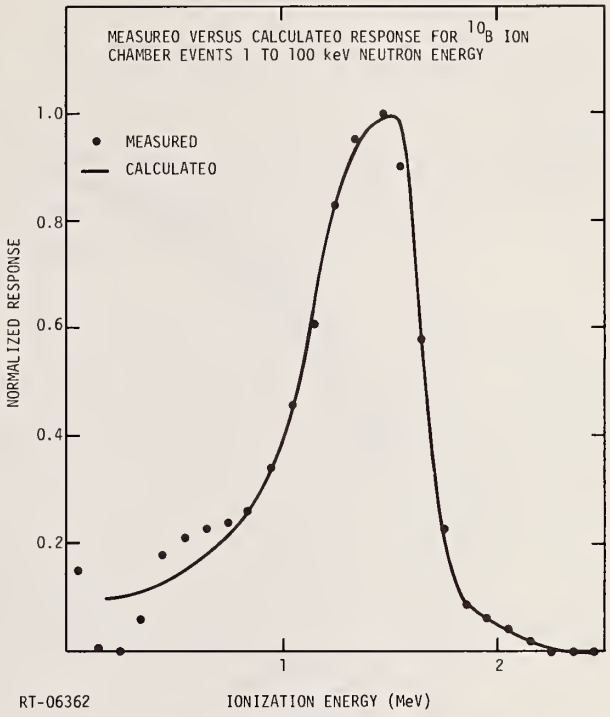

Figure 1. Measured versus calculated response for ^{10}B ion chamber events 1 to 100 keV neutron energy

The cross-section data were normalized to 1/V extrapolations of thermal values near 4 keV. This normalization energy was dictated by the large statistical fluctuations in the ion pairs produced in methane below 1 keV, which limited the flux bias efficiency calculations to energies above ≈3 keV.

Since it is desirable to obtain an independent check on the normalization, a BF_3 counter was fabricated which contained an admixture of methane. This allowed the observation of proton recoils in the same environment as the $^{10}B(n,\alpha)$ reactions. The two reactions are well separated on the basis of pulse height. After completion of the measurements, the counter was tapped and a chemical analysis of the gas composition performed. This allowed a determination of the $^{10}B(n,\alpha_0+\alpha_1)^7Li$ cross section, which is based only on the results of the gas analysis. When the inferior time resolution of these data relative to those obtained with the ion chamber is taken into account, the agreement of the two determinations of the cross section is satisfactory

Results and Conclusions

Comparison of the present cross-section results with those of other workers is illustrated in Figures 4, 5, and 6. The present $^{10}B(n,\alpha)$ data, shown in Figure 4, are in good agreement with all previous measurements below 100 keV. In general, the present $^{10}B(n,\alpha)$ cross sections are in good agreement with

ENDF/B-Version III values, with the exception of the 450-keV resonance, which is seen more distinctly, and the sharpness of the decrease in the cross section above the resonance. The absolute $^{10}B(n,\alpha)$ cross-section measurement obtained using the BF_3/CH_4 proportional counter confirmed the ion chamber results from 200 to 1000 keV. The $^{10}B(n,\alpha_1)^7Li^*/^{10}B(n,\alpha_{0+}\alpha_1)^7Li^*$ branching ratio is compared to the Irving[1] evaluation in Figure 4. The agreement is quite good, except above 600 keV where the present results tend to be slightly lower. The ^6Li data illustrated in Figure 5 exhibit a higher and sharper peak at the 250-keV resonance than observed in previous measurements. This may be due in part to the good time resolution and small multiple scattering effects in the present data. $^{10}B(n,\alpha)/^6Li(n,\alpha)$ cross-section ratios, relatively free of systematic uncertainties, were also determined over the neutron energy range 1 to 1500 keV from the ion chamber results.

References

1. D. C. Irving, "Evaluation of Neutron Cross Sections for Boron 10," ORNL-TM-1872 (1967).

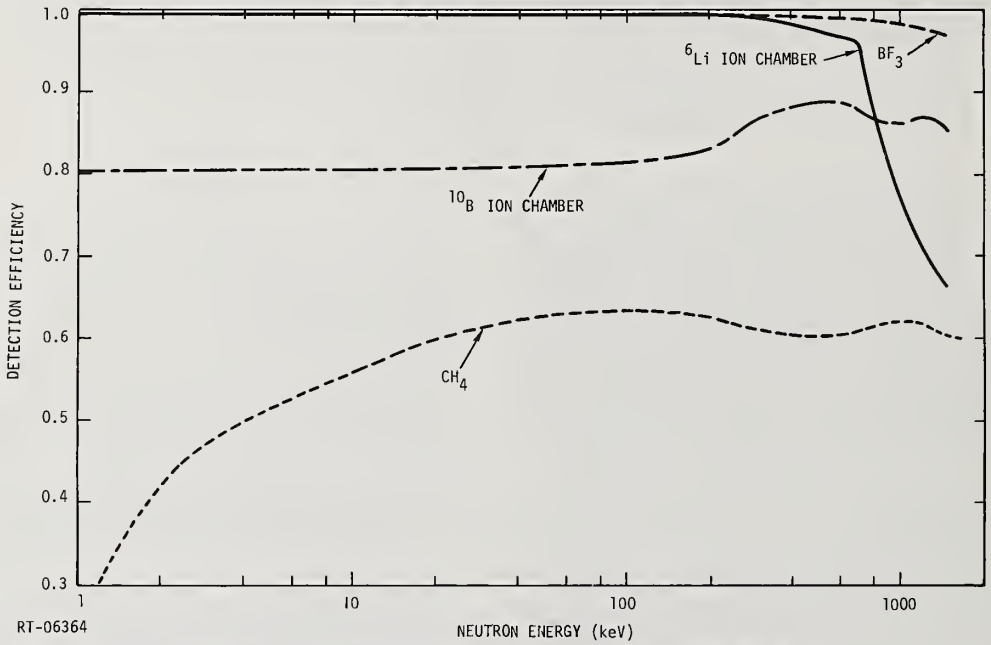

Figure 2. Detection efficiencies versus neutron energy

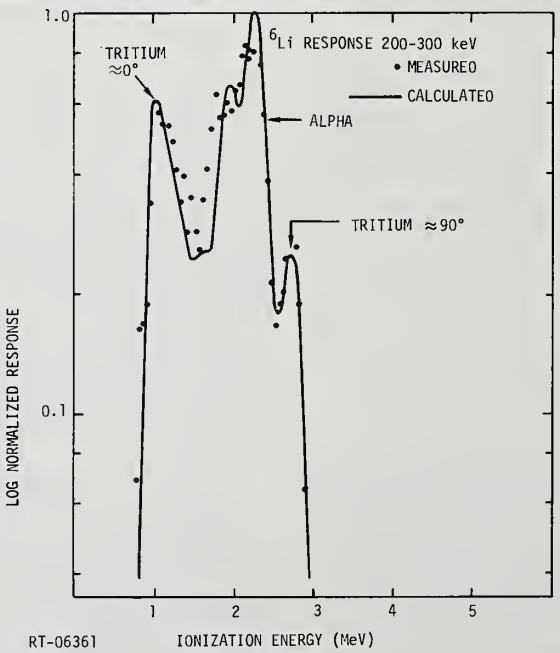

Figure 3. Calculated versus measured ^6Li ion chamber response

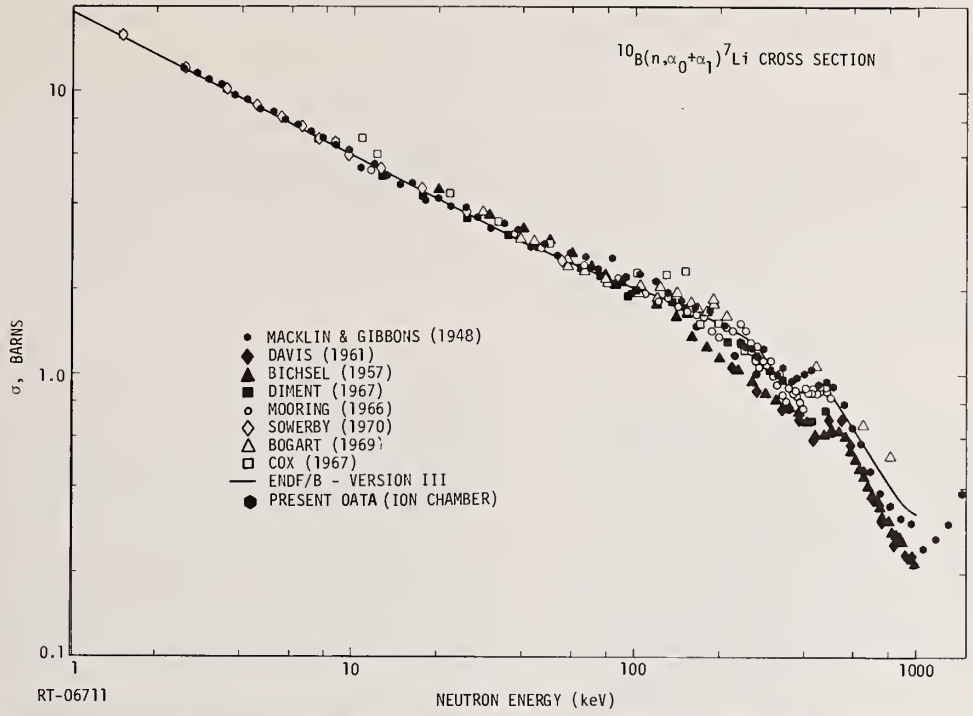

Figure 4. Comparison of present ion chamber measurements of $^{10}B(n,\alpha_0+\alpha_1)^7Li$ cross section to those of other workers

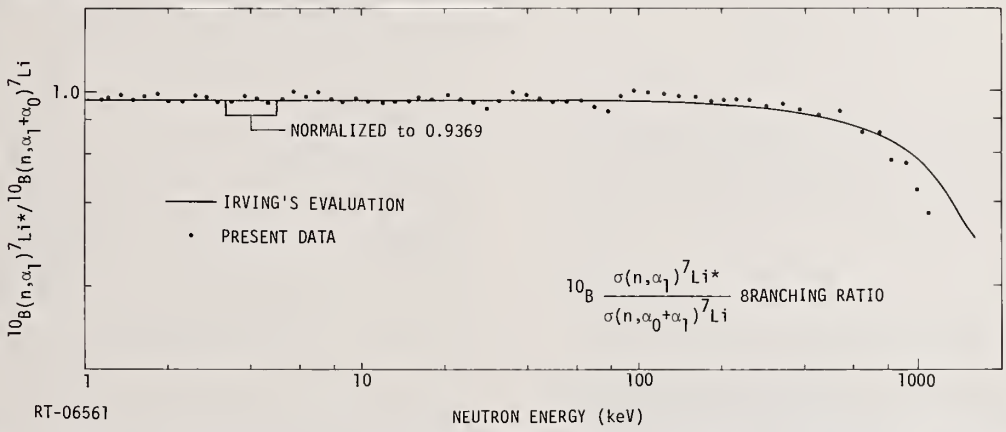

Figure 5. $^{10}B(n,\alpha_1)^7Li^*/^{10}B(n,\alpha_0+\alpha_1)^7Li$ branching ratio obtained from Ge(Li) versus BF_3 measurements

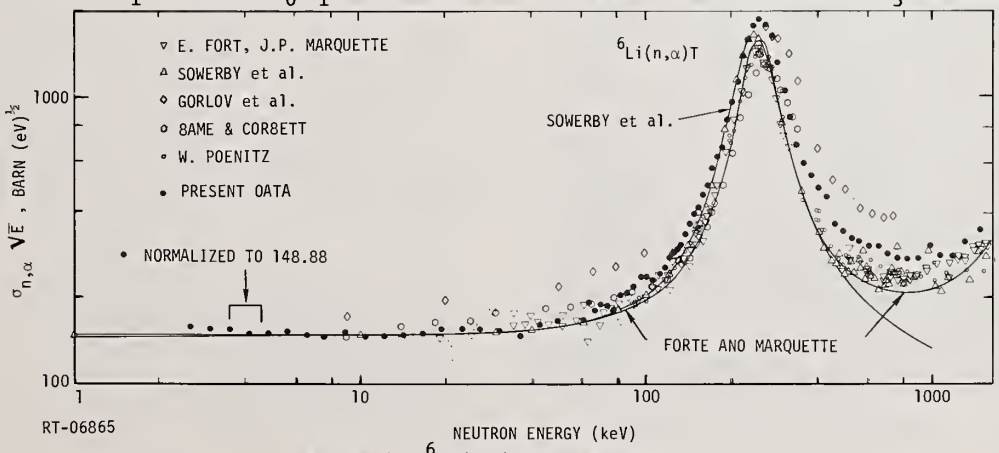

Figure 6. $^6Li(n,\alpha)T$ cross section

AN ABSOLUTE MEASUREMENT OF THE $^{6}Li(n,\alpha)$ CROSS SECTION AT 964 keV

W. P. Stephany and G. F. Knoll
The University of Michigan
Ann Arbor, Michigan 48104

A value of 356 mb ± 12% was obtained for the $^{6}Li(n,\alpha)$ cross section at 964 keV. Neutrons were produced using a spherical Na-Be photoneutron source, calibrated relative to NBS-II using The University of Michigan manganese bath. Thin ^{6}LiF targets enriched to 95 atom percent ^{6}Li were vapor deposited onto the electrode surfaces of a 42 micron thick, fully depleted Si surface barrier detector. A summary of the data, corrections, and error analysis is presented.

(Neutron cross sections; $^{6}Li(n,\alpha)$; absolute cross section measurements; photoneutron sources; manganese bath; surface barrier detectors)

Introduction

The measurement was undertaken as an attempt to resolve the substantial discrepancies reported during the last few years for the $^{6}Li(n,\alpha)$ cross section in the energy range near 1 MeV. Accurate knowledge of the cross section would enhance the usefulness of ^{6}Li for neutron flux measurements in this energy range. The use of thin targets, having mass thickness of about 175 μgms/cm^2, as well as accurate data on the isotopic composition of the Li, eliminated two of the well known systematic error sources encountered in previous measurements. The limits of the present measurement were determined by the effects of the intense gamma activity of the photoneutron source (about 35 Ci of ^{24}Na) on the detector response and by the uncertainties in the correction to the neutron flux due to local inscattering.

Experimental Procedure

Facilities

The experimental facilities for performing the cross section measurements are described elsewhere in these proceedings.[1] In particular, the experimental aspects and primary data reduction for determination of the neutron activity of the Na-Be source are credited to D. Gilliam.[2]

Procedure

The detector, rigidly supported in the low scatter stainless steel tubular frame, is shown in Figure 1.

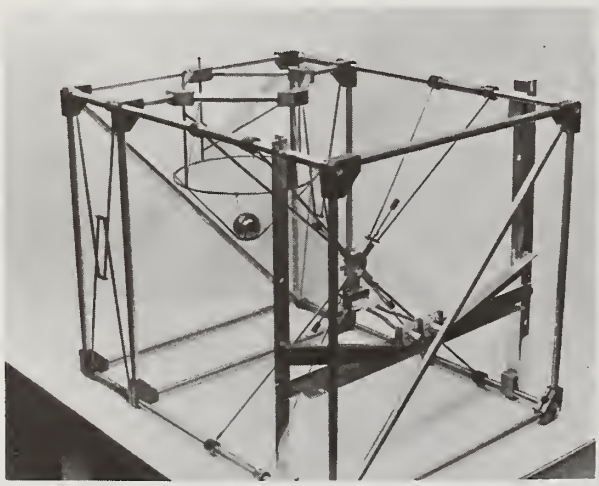

Figure 1. Source-Detector Support Frame

This frame allowed accurate positioning of the photoneutron source relative to the detector, using a positioning jig to obtain approximate alignment, followed by measurement of the exact source-detector separation distance using calibrated micrometers. Experiments were done at two source-detector spacings to allow direct elimination of the room return flux contribution. Each experiment consisted of two measurements. First a ^{24}Na-aluminum clad photon source of equivalent gamma activity to the Na-Be photoneutron source was run, duplicating the system response to all background characteristics encountered during the photoneutron source run; then the photoneutron source was run. Data was accumulated in counting periods of short duration, usually 8000 seconds, to allow monitoring of the stability of the system and subsequent statistical evaluation. After each experiment, the photoneutron source was calibrated by direct comparison with NBS-II. The source-detector arrangement is schematically shown in Figure 2.

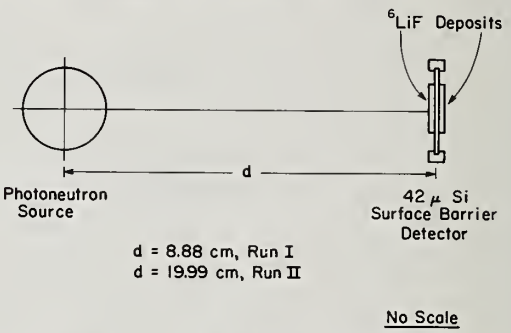

Figure 2. Source-Detector Arrangement

Detector-Target Composite

A 42 μ thick Si surface barrier, with the ^{6}LiF targets directly vapor deposited on the electrode surfaces was used to record the events, which in turn were processed by a fast electronic system to minimize pulse pile-up caused by the high gamma event rate. Energy discrimination was used to suppress the gamma background. The target deposits had an area of approximately 1 cm^2 whereas the active area of the detector was 2 cm^2.

Summary of the Data

To determine the cross section three primary factors or their equivalents must be known:

1. the number of target nuclei
2. the neutron flux
3. the reaction rate

The results will be presented in this order.

Number of Target Nuclei

The vapor deposition of the targets onto the electrode surfaces was done at the Isotope Target Laboratory of ORNL. Target mass was inferred from the weight gain of three monitor foils symmetrically positioned around the detector during each deposition. Measurements of the deposit diameters of both sets of monitor foils and of the target deposits themselves, using a calibrated optical microscope, enabled values for the number of ^{6}Li nuclei to be calculated. One of the monitor foils was used to determine the ^{6}Li to ^{7}Li ratio by mass spectrographic analysis. The following results were obtained:

^{6}Li content:	95 ± .01%
^{7}Li content:	5 ± .01%

Mean Scalar Fluence

The neutron activity of the photoneutron source is obtained from the manganese bath system at the time of insertion into the bath. Using a ^{24}Na half life value of 15.00 ± 0.03 hours, the neutron activity of the source is calculated at the starting time of each counting interval.[3,4] The mean scalar fluence is determined by calculation of the flux per unit source strength, taking into account the source-detector spacing and the spatial distribution of the source and target, and the decay of the source over the duration of the experiment.

Integrated Neutron Activities. The University of Michigan manganese bath system was used, in conjunction with the data reduction code SAT2, to obtain a ^{56}Mn saturated count rate at the time of insertion of the source into the bath.[2] SAT2 corrects the bath data for decay of the ^{24}Na (for the Na-Be source), activation and decay of the ^{56}Mn, detector background, counting system deadtime and mixing delays. The neutron activity of the source is obtained from the ratio of its saturated count rate to that obtained using the national secondary neutron standard source, NBS-II, since the activity of NBS-II is known to high precision. Corrections for small differences in self absorption, leakage, and photoneutron production in the bath solution need to be made.

The neutron activity value of NBS-II used in this analysis is 1.174×10^{6} sec^{-1} ± 0.37%, as of June, 1973, based on independent calibrations by four laboratories.[5]

The results of this calculation, including time correction to the start of the first counting interval are summarized in Table 1, where I and II denote the close and far spacing runs, respectively. Here t_0 is the time of insertion of the source into the bath and t_1 is the start time of the first counting interval for either of the cross section data acquisition runs.

Table 1

Summary of Results for Neutron Activity Determinations

	Source	Saturated Count Rate at t_0, counts/sec	Neutron Activity 10^6 neutrons/sec t_0	t_1
I	Na-Be	1090.3±.14	4.381±.56%	35.1±.7%
	NBS-II	288.2±.07	STND	STND
II	Na-Be	727.0±.15	2.292±.56%	36.1±.7%
	NBS-II	288.1±.07	STND	STND

Source-Detector Spacing. For both the near and far spacing runs, the source-detector spacing was inferred from measurements of the distance from the surface of a precision chrome sphere to a 49 mil thick aluminum plate attached to the detector mount surface. Alignment was accomplished using a positioning jig. The plate thickness and the distance from the plate to the target surface were accurately measured using an optical microscope. Values of 8.882 cm and 19.985 cm were obtained for the source center to detector center distance for the close and far spacing runs, respectively. The plate to chrome sphere measurements were made before and after each run and showed agreement to ± .003 cm. A maximum error of ± 0.050 cm is assigned to the spacing values, leading to ± 0.56% and to ± 0.25% uncertainties in the close and far distances, respectively.

Target Fluence. The average scalar flux over the target surface was obtained from the source-detector geometry and vacuum streaming calculations. Good agreement was obtained from independent calculations, one based on integration of the current over the deposit surface and the other an integration of the angular flux. Both results are very close to the neutron current obtained for a point source and point detector at a distance equal to the source center to detector center spacing. The mean scalar fluence calculated over the course of each run carried an overall estimated uncertainty of about ± 1%.

Reaction Rate

Primary Data. The data from each decaying source was accumulated in 7 to 12 sequential counting intervals.

In order to facilitate subtraction of photon-induced events from the detector output, the intervals were matched for the paired runs of photoneutron and photon-only sources. A typical pulse height spectrum obtained using the photoneutron source is shown in Figure 3. This illustrates the three pulse height regions in which neutron-induced events are separately evaluated. In region I, only neutron events occur. In region II, the number of neutron events is obtained by subtraction of the gamma response from the photoneutron induced response after smoothing both data sets.[6] In region III, this subtraction procedure is statistically meaningless and the neutron response was estimated from data obtained by exposing the detector-target composite to a thermal neutron beam. The results are shown in Table 2.

Table 2

Neutron Counts by Energy Region

Experiment	Number of Neutron Counts			
	I	II	III	Total
I (close)	4400±66	433±46	67±67	4900±105
II (far)	1151±34	195±64	11±11	1357±73

The errors quoted above are one standard deviation for regions I and II, the latter reflecting the error due to the photon background subtraction procedure. The predicted neutron events for region III were arbitrarily assigned a 100% error. The error for the total number of events is the quadrature sum of the errors of the three regions.

The detector malfunctioned during the fourth counting interval of the close spacing run due to microplasma breakdown induced by the very high gamma

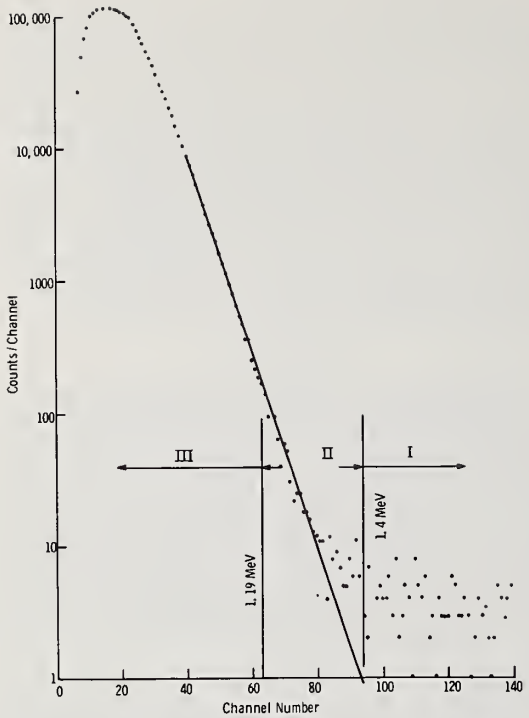

Figure 3. Typical Pulse Height Spectrum

flux of the experiment. This malfunctioning was evidenced by a fluctuation in leakage current together with the appearance of high-rate large-amplitude pulses. The experiment was interrupted to allow the detector to stabilize and no further instability was observed. This data set was not used in the cross section evaluation. The sixth data set from the far spacing run was also eliminated. Although there was no evidence for anamolous behavior during the actual data acquisition, the neutron count obtained in region II by subtraction of the photon response was five standard deviations above the expected value. The data from all regions of this set were therefore not used.

Statistical Evaluation. The total neutron counts for each counting interval were compared with the mean. Taking into account the starting time and duration of each interval, an equivalent count to that obtained during the first interval was calculated. Figure 4 is a plot of these results for the close

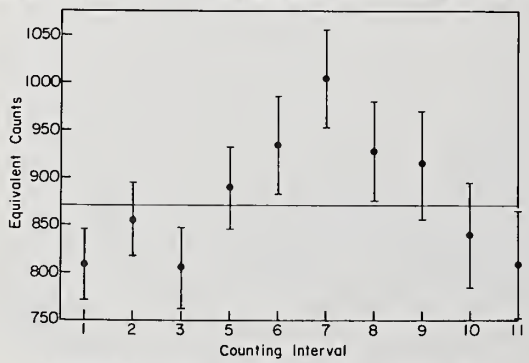

Figure 4. Equivalent Neutron Counts Per Counting Interval Compared With the Mean. (Close Spacing Run)

spacing experiment. This plot led to our introducing a systematic error term into the final cross section evaluation of ± 1%, the variation due to including or excluding the seventh data set from the close spacing experiment which appears to be high as evidenced in Figure 4.

Corrections

Detection Efficiency

The intrinsic efficiency of the detector-target composite was calculated separately for the near and far targets. Calculated efficiencies were 100% for the near target and 81.7% for the far target (i.e., the deposit on surface facing away from the source.) The difference arises because of the forward peaking of the reaction products in the laboratory coordinate system. The overall efficiency is relatively insensitive to the degree of anisotropy of the reaction and carries an estimated uncertainty of ± 2.1%.

Local Inscatter

The correction for scattering from objects near the target is divided into two cases: first, the inscatter from hydrogen contained in the epoxy used to fix the detector to the insulating lavite ring; secondly, all other scattering treated as elastic scattering from point sources. The geometric extent of the numerous sources was treated by calculating an effective position of the scatterer relative to the photoneutron source and target deposits. The detector mount materials were selected to minimize the inscatter correction.

Inscatter Due to Hydrogen. The epoxy chemical composition was determined by elemental analysis. The geometry of the epoxy was determined by actual measurement using a dial gage arrangement on an optical microscope. Because of the forward scattering from hydrogen and the small solid angle subtended at the target by the epoxy, the increase in the reaction rate was found to be of the order of 0.1%.

Inscatter Due to Other Components. The increase in the flux at the target was calculated for all materials near the source or detector, i.e., the detector itself including the lavite ring, the detector mount, electrical leads, and all support members. The total increase in the flux was calculated to be 7.56% and 9.21% for the near and far spacing runs, respectively. Because of the large uncertainties in the inscatter calculations, the error in this correction was conservatively assumed to be 100%.

Cross Section Determination

The equation

$$N_{obs}/\varepsilon = N\sigma F(1+\frac{\delta\phi}{\phi_o}) + kA \qquad (1)$$

where N_{obs} = Number of neutron counts
ε = Detection efficiency
N = Number of target nuclei
σ = Integral cross section
F = Mean scalar fluence
$\delta\phi/\phi_o$ = Local inscatter correction
A = Integrated source neutron activity
k = Proportionality constant

was solved using parameter values for the near and far spacing runs. The term kA represents the number of neutron events due to the room return flux, assumed to be independent of source-detector spacing. By simultaneous solution of the equations obtained at the two spacings, k is eliminated and the value for the cross section obtained. The integral cross section, relative to the Na-Be source spectrum, is 375 mb. The photoneutron source spectrum obtained from a Monte Carlo code developed at NPL was used with the energy dependence of the $^{6}Li(n,\alpha)$ cross section measured by Friesenhahn (see Figure 5) to obtain a value of 356 mb at the mean source energy, 964 keV.[7,8] A summary of results and estimated errors (one standard deviation) is given in Table 3.

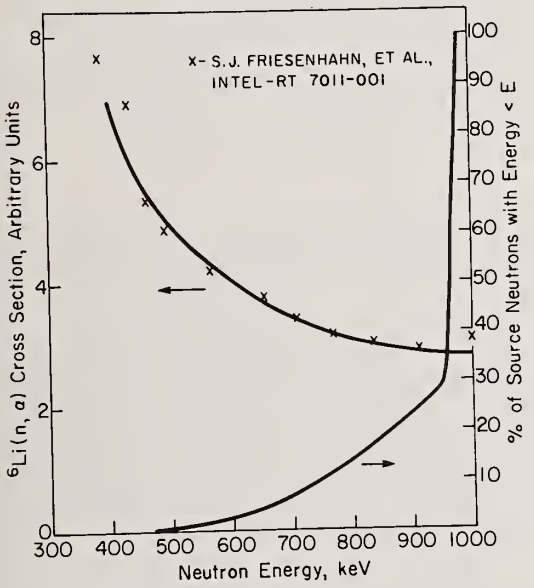

Figure 5. Integral Source Spectrum Compared with $^{6}Li(n,\alpha)$ Cross Section

Table 3

Summary of Results and Errors

RESULT	VALUE	ERROR, AS % OF VALUE
Number of ^{6}Li Nuclei	8.28×10^{18}	1.7
Observed Neutron Events	I - 4900 II- 1357	2.1 5.4
Mean Scalar Fluence Neutrons/cm^2	I - 1.530×10^{9} II- 3.496×10^{8}	1.0 0.92
-Source/Target Spacing, cm	I - 8.88 II-19.99	.56 .25
-Integrated Neutron Activity	I - 1.504×10^{12} II- 1.752×10^{12}	.81 .86
Detection Efficiency	0.905	2.1
Local Inscatter, $\delta\phi/\phi$	I - .076 II- .092	100 100
$^{6}Li(n,\alpha)$ Cross Section at 964 keV	356 mb	12

References

1. J. C. Robertson, M. C. Davis and J. C. Engdahl, "Facilities for Cross Section Measurements Using Na-D Photoneutron Sources", Paper BB16, this conference.

2. D. M. Gilliam, "An Absolute Determination of the ^{235}U Fission Cross Section at 964 keV", Doctoral Dissertation, University of Michigan, 1973.

3. J. F. Emery, S. A. Reynolds, E. I. Wyatt and G. I. Gleason, Nucl. Sci. Engng. 48, 319 (1972).

4. J. S. Merritt and J. G. V. Taylor, Progress Report AECL-3912, 43 (1971).

5. D. M. Gilliam and G. F. Knoll, "An Absolute Determination of the ^{235}U Fission Cross Section at 964 keV", to be published in Annals of Nucl. Sci. Engng.

6. B. Garbow, "Smoothing by Cubic Splines", from ANL code center, ANL E3505, (1968).

7. T. B. Ryves and J. C. Robertson, National Physical Laboratory, private communication, 1971.

8. S. J. Friesenhahn, V. J. Orphan, A. D. Carlson, M. P. Fricke and W. M. Lopez, INTEL-RT 7011-001 (1974).

Angular Anisotropy in the $^6Li(n,\alpha)^3H$ Reaction at 25 keV

I.G. Schroder, National Bureau of Standards
Washington, D.C. 20234

E.D. McGarry, Harry Diamond Laboratories
Adelphi, Maryland 20783

G. de Leeuw-Gierts and S. de Leeuw
SCK-CEN Mol, Belgium

The angular anisotropy in the $^6Li(n,\alpha)^3H$ reaction at 25 keV has been measured in two sets of experiments performed at an iron-filtered beam facility (99% of the flux at 25 keV) at the NBS Reactor. First, a surface-barrier detector coated with 80 $\mu g \cdot cm^{-2}$ of ^6LiF (front face) was used as a 2π detector. This detector was placed in four different angular positions with respect to the neutron beam: front face at 90° and 45° to the beam; back face at 90° and 45° to the beam. The pulse-height distributions of both the ^3H and ^4He were recorded for these four positions yielding a forward-to-backward asymmetry of 1.59 $\pm$0.11 in the center-of-mass system. A second detector was placed coaxially with the first (at 90° to the beam) and in such a way as to substend a 45° cone. Coincidence measurements, that simultaneously recorded the distributions in both detectors, yielded an asymmetry in the backward-to-forward 45° cone of 1.80 $\pm$0.06 in the center-of-mass system. The existence of such a large anisotropy at this low energy and the possibility of similar behavior at still lower energies (i.e., 1 - 2 keV) should result from s-p wave interference. This would give rise to a constant anisotropy that is experimentally masked by the 1/v behavior of the isotropic s-s interference terms at lower energies.

(Cross sections; (n,α) cross sections; Nuclear reactions; Fast-Neutron Reactions; Lithium)

Introduction

The $^6Li(n,\alpha)^3H$ reaction is widely used as a standard in partial cross-section measurements, for flux normalization, for neutron detection and in neutron spectroscopy. For this reason, the reaction has been extensively studied.[1] However, very little data exists in the energy region between 10 and 100 keV. In particular, differential (n,α) measurements in this region are few and mainly unpublished.[2,3] As is known, in the region below 10 keV the (n,α) cross section follows the 1/v dependence to within $\pm$1% while above this energy, and up to 500 keV, the cross section is dominated by the large $5/2^-$ resonance at 250 keV. The recent installation of a monoenergetic 25-keV iron-filtered-beam facility at the NBS reactor[4] and the fact that so little is known about the behavior of the differential (n,α) cross section in this region, are the principal reasons for undertaking the present experiment.

The 25-keV Filtered-Beam Facility

The 25-keV neutron beam is described in detail elswhere in these proceedings.[4] This facility provides a well-collimated, 1-cm-diameter beam with an intensity of 5×10^5 $n \cdot cm^{-2} \cdot s^{-1}$. To minimize possible thermal-neutron contamination, no beam stop was used in this experiment and the emergent beam was allowed to hit the roof of the reactor, which is 11.3 meters away. The composition of the neutron beam was measured with a proton-recoil spectrometer. Analysis shows that 99% of the beam is composed of 25-keV neutrons and the remaining 1% is made up of contaminants at 82, 137 and 270 KeV. No thermal-neutron contaminant was found in the beam.

The ^6Li Detector and Associated Electronics

To measure the angular anisotropy of the charged particles emitted in the $^6Li(n,\alpha)^3H$ reaction, a silicon surface-barrier detector was built and mounted on a pyrofilite (non-hydrogenous) ring. A 3-cm^2 circular area on the front face of the detector was coated (by evaporation) with 80 $\mu g \cdot cm^{-2}$(0.3 μm) of ^6LiF. This detector (referred to subsequently as the ^6Li detector) was then enclosed in the aluminum holder shown in Fig. 1. The holder is made of a base (4), over which the detector fits, and a cap (5). The purpose of the cap is two-fold: it serves as a light seal and allows the pressure contacts (2) and (3) to operate. One pressure contact (2) is insulated from the holder by a Teflon insert (6) and constitutes the bias voltage and signal lead to the detector. The other pressure contact (3) provides the grounding for the front surface of the detector, which contains the ^6Li deposit (1). Both the base and the cap have 0.025-cm windows (7) to minimize scattering of the neutron beam (8).

The electronics used with the ^6Li detector is quite conventional: an FET charge-sensitive preamplifier followed by a low-noise RC-clipped amplifier (1 μs differentiation and 1 μs integration) and a 2048-channel pulse-height analyzer (with a 100-Mhz ADC). A temperature-controlled, dekapot pulser was used to monitor any drifts in the system.

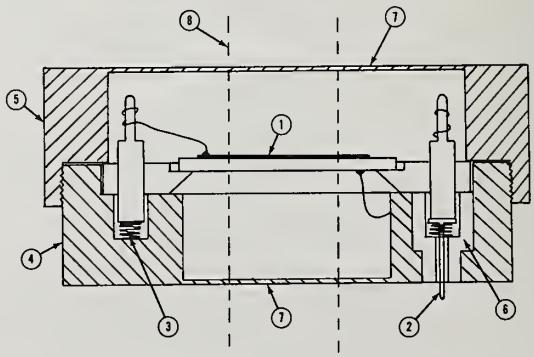

Fig. 1. Physical details of the "^6Li detector"

Thermal-Neutron Calibration of the ^{6}Li Detector

Prior to the measurements at 25 keV, four sets of thermal calibrations were performed. The first was made with the neutron beam incident perpendicular to the front face of the detector i.e., the surface containing the ^{6}Li deposit. The second calibration was made with the beam perpendicular to the backside of the detector. The other two sets of measurements were made with the beam 45° to the front and then 45° to the back of the ^{6}Li detector. No differences in the pulse-height distributions were observed among the four sets of measurements. Between the runs, a series of pulser calibrations were made which showed there were no gain shifts. At the termination of the calibration runs, the equipment was moved to the 25-keV beam facility.

25-keV Measurements with the ^{6}Li Detector

The ^{6}Li detector in the holder was mounted on a support that allowed the detector to rotate from 0° to 360° with respect to the axis of the neutron beam. Once the equipment was set up, pulser calibrations were again performed to insure that no gain shifts had occurred (none had) during movement of the equipment. Four series of runs were then performed similar to those made at the thermal column. That is, front face at 90° and 45° to the beam then, back face at 90° and 45° to the beam. At the termination of each run, pulser calibrations were also performed. These showed that there were no variations in gain among the runs. This essentially completed what we have called the "2π measurements" with the ^{6}Li detector in the 25-keV beam.

Subsequently, the ^{6}Li detector, in its holder, was taken back to the thermal beam and calibrated. As no energy shifts were detected (confirming the pulser calibrations), energy corrections to the data at 25 keV were not necessary. A comparison of the 25-keV data to that taken at thermal, shows (besides the energy shifts in the peaks that arise from kinematics) that the number of tritons emitted in the forward 2π direction (in the laboratory system) is 65% higher than those emitted in the backward direction (Fig. 2). This should be compared to a 5% asymmetry in the laboratory system that is present, because of kinematics, when the emission in the center-of-mass system is isotropic.

Coincidence Measurements

Once the 2π measurements were concluded, the ^{6}Li detector was mounted in an evacuated, aluminum chamber together with a second detector (D2), placed parallel to, and coaxial with, the first. The D2 detector was at such a distance that it would detect any particle emitted from the lithium surface at an angle of approximately $\pm 45°$ to the beam. The D2 detector was a commercial, partially-depleted, surface-barrier detector with an active area of 200 mm^2 and with an alpha (5.5 MeV) resolution of 19 keV (FWHM). A coincidence circuit was set up (with a resolving time of 80 ns) so the coincidence response of both detectors could be registered simultaneously in two ADCs. The response of the system was studied in a thermal beam. The purpose was twofold: to provide proper alignment of the system and to provide an energy calibration. The proper operation of the system was further checked by observing that equal numbers of tritons and alphas were detected under both coincident and non-coincident conditions. The equipment was then taken to the 25-keV beam facility and the chamber mounted with the two detectors perpendicular to, and coaxial with, the neutron beam, and

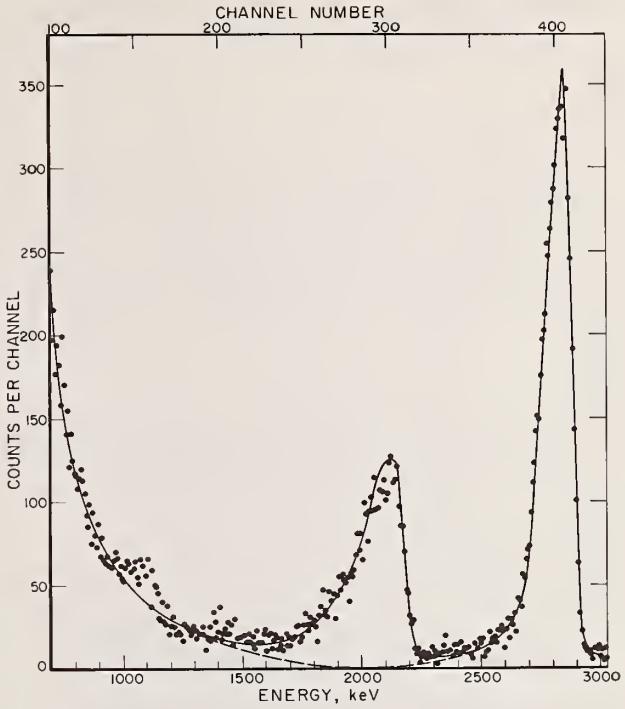

Fig. 2. Experimental pulse-height distribution obtained in the forward 2π measurements made at 25 keV.

such that the ^{6}Li detector was between the beam and the D2 detector. As no subsequent thermal calibration could be made at the termination of the coincidence experiment (because of reactor maintenance shutdown), a pulser was used throughout the thermal and 25-keV runs to insure that no gain shifts had occurred (again, none had). The results of this experiment are shown in Fig. 3. The figure shows the superposition of the data obtained with the two ADCs. The two upper peaks, at approximately 2850 and 2650 keV, correspond to the forward and backward triton distributions, respectively. The peaks at 2150 and 1950 keV correspond to the backward and forward alpha particle distributions. One can see in this figure two small peaks at about 2730 and 2050 keV. These correspond to thermal tritons (2728 keV) and thermal alphas (2056 keV), not present in the previous runs, that were caused by hydrogenous material in the D2 detector.

Analysis of the Data

The first thing to note is that in the thermal runs the number of tritons is equal to the number of alphas, and remains the same no matter what angle the detector makes with the beam. Also, regardless of the angle, the energy of the tritons, and alphas, remains constant at thermal energy. This is no longer true when the energy of the neutron is different from zero. In this case, the energy of the triton (and, therefore, also of the alpha particle) depends not only on the neutron energy but also on the angle of emission. Furthermore, even if in the center-of-mass system the distribution of outgoing particles is isotropic, in the laboratory system the distribution is anisotropic, and becomes more so as the incoming neutron energy increases. These of course, are all kinematic effects that have to be taken into consideration in the analysis of the data.

First, one has to find the number of tritons and

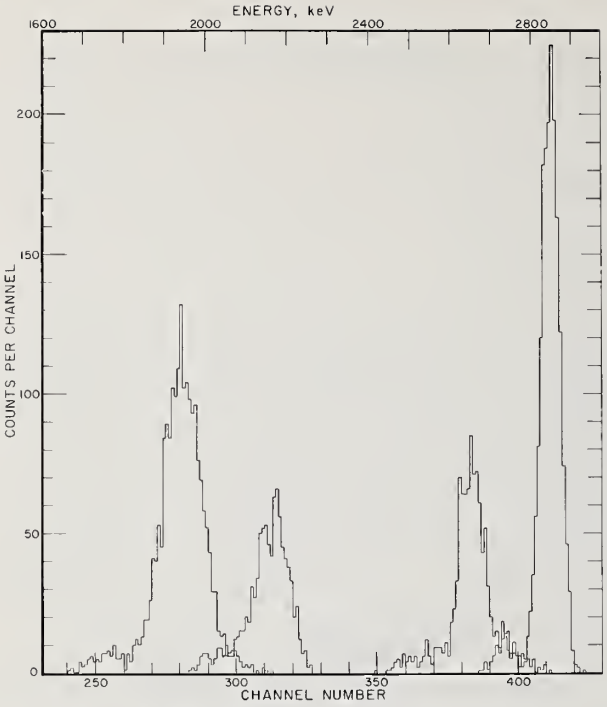

Fig. 3. Experimental pulse-height distribution obtained in the coincident experiment at 25 keV.

alphas emitted in each of the experimental conditions. From these numbers, which correspond to laboratory distributions, one can determine the degree of asymmetry involved in each case and deduce the corresponding anisotropy in the center-of-mass system. The main source of error in the 2π experiments is in the proper subtraction of the background. This is especially true in the case of the alpha-particle distributions, as can be seen in Fig. 2. The background in this figure is typical of that observed in the other 2π measurements. No such problem arises in the coincidence measurements (Fig. 3) where the sources of error arise from the need to subtract the small peaks due to thermal-neutron contamination and counting statistics.

Once the background was determined, the numbers of tritons and alphas were estimated for each of the 2π measurements. The data were then normalized to the average number of particles observed in the forward and backward distributions. This was done under the assumption that, to the first approximation, tritons and alphas are emitted in opposite directions in the laboratory system. Therefore, one obtains for the 2π forward and backward distributions:

$$N_f = T_f + A_f = (8248 \pm 106) + (4976 \pm 202) \quad (1)$$

$$N_b = T_b + A_b = (4936 \pm 103) + (8288 \pm 334) \quad (2)$$

where T and A denote the triton and the alpha particle and f and b denote the forward and backward directions. Similarly, for the 45° distributions, one obtains:

$$N_f^{45} = T_f^{45} + A_f^{45} = (7697 \pm 321) + (5527 \pm 352) \quad (3)$$

$$N_b^{45} = T_b^{45} + A_b^{45} = (5540 \pm 126) + (7684 \pm 347) \quad (4)$$

The errors in these distributions come from both the estimation of the background (main source) and from the counting statistics. No such normalization can be undertaken with the results of the coincidence measurements. This is not necessary, of course, because both the forward and backward tritons (or alphas) are measured simultaneously. Thus, for the coincidence experiment, one obtains an asymmetry in the forward-to-backward 45° cone of

$$R_c = 1.96 \pm 0.06 \quad (5)$$

where the error arises from the thermal contamination present and from the counting statistics. Similarly, from Eqs. (1) and (2) one obtains the ratio, R, for the forward-to-backward 2π asymmetry; from Eqs. (3) and (4) one obtains the ratio, R_{45}, for the backward-to-forward 45° 2π asymmetry. These results are shown in Table I in both the laboratory and the center-of-mass systems.

TABLE I.

Ratio	Lab.	C.M.
R	1.67±0.11	1.59±0.11
R_{45}	1.39±0.11	1.35±0.11
R_c	1.96±0.06	1.80±0.06

The Angular Distribution

From the results obtained in the four 2π measurements and from the coincidence experiment (Eqs. 1 to 5), we can obtain a coarse-grided angular distribution. To see this, consider Fig. 4a. This figure represents a unit sphere that is intersected by two planes: one horizontal and the other at 45°. These planes represent the orientations of the 2π detectors. In Fig. 4a, the coincidence experiment is represented by a 45° cone whose axis goes through the center of the sphere and is oriented perpendicular to the horizontal plane. If we now consider the first experiment, i.e., tritons and alphas emitted in the forward direction

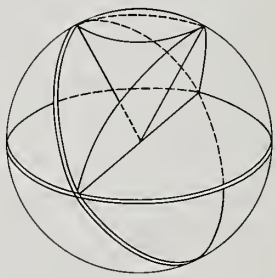

Fig. 4a

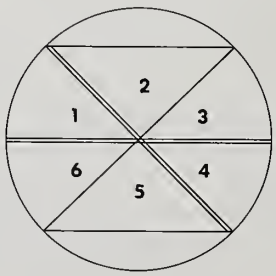

Fig. 4b

Fig. 4. Geometrical configurations used to describe the coincidence and 2π experiments.

and restrict ourselves to the tritons, we see that any triton detected corresponds to a triton being emitted at the center of the sphere and passing through the upper hemispherical surface. On the other hand, in the 2π forward 45^o experiment, the tritons detected correspond to those tritons emitted from the center of the sphere and that pass through the right-half hemispherical surface which is intersected by the 45^o plane. Lastly, the tritons detected in the forward direction, in the coincidence experiment, correspond to tritons being emitted at the center of the sphere but restricted to the 45^o cone. Similar considerations apply to the backward emitted particles. Let us now consider dividing the sphere into 45^o regions. There are only four such regions. The 0^o to 45^o region, i.e., the surface defined by the intersection of the forward cone and the unit sphere; the 45^o to 90^o region which is the upper hemispherical surface minus the 0^o to 45^o region; two similar backward regions in the lower hemisphere: a 90^o to 135^o region and a 135^o to 180^o region. Also (to further confuse the reader), we divide the unit sphere into six sections by three 45^o planes, as shown schematically in Fig. 4b.

With these ideas in mind, let us consider the tritons emitted in the forward direction in the first 2π experiment. If T_f is the number of tritons detected, these are composed of the tritons emitted in the forward 45^o cone plus those emitted between 45^o and 90^o. Calling f_1 and f_2 the triton densities in these two regions, we can write:

$$a_{11}f_1 + a_{21}f_1 + a_{31}f_1 + a_{22}f_2 = T_f \qquad (6)$$

where the a_{jk} represent the areas in the different spherical regions. That is, j denotes one of the six areas shown in Fig. 4b and k denotes the triton density. For instance, area a_{31} is the area of section 3, while area a_{21} is the area of section 2 minus the area a_{22} (which is that cap-like area defined by the intersection of the cone and the unit sphere). Similarily, for the tritons emitted in the backward direction, T_b, one can write:

$$a_{41}b_1 + a_{51}b_1 + a_{61}b_1 + a_{52}b_2 = T_b \qquad (7)$$

where b_1 and b_2 are the triton densities of the backward emitted tritons between 90^o and 135^o, and 135^o and 180^o respectively. If we now consider the 45^o forward 2π experiment we can write:

$$a_{21}f_1 + a_{31}f_1 + a_{41}b_1 + a_{22}f_2 = T_{45} \qquad (8)$$

where T_{45} is the number of tritons observed in the experiment. Lastly, from the coincidence experiment one can write:

$$a_{22}f_2 = R_c a_{52}b_2 \qquad (9)$$

Eqs. (6) to (9) represent a system of four equations from which the unknown densities f_1, f_2, b_1 and b_2 can be obtained. These densities are directly proportional to $d\sigma/d\Omega$ (barns per steradian) so that the solution of the above equations yields a coarse angular distribution. This angular distribution in both the lab system and the center-of-mass system is shown in Fig. 5. The two dashed lines in these distribution represent the errors arising from the uncertainty in the determination of the background. The dotted lines in the lab distribution correspond to an isotropic distribution in the center-of-mass system.

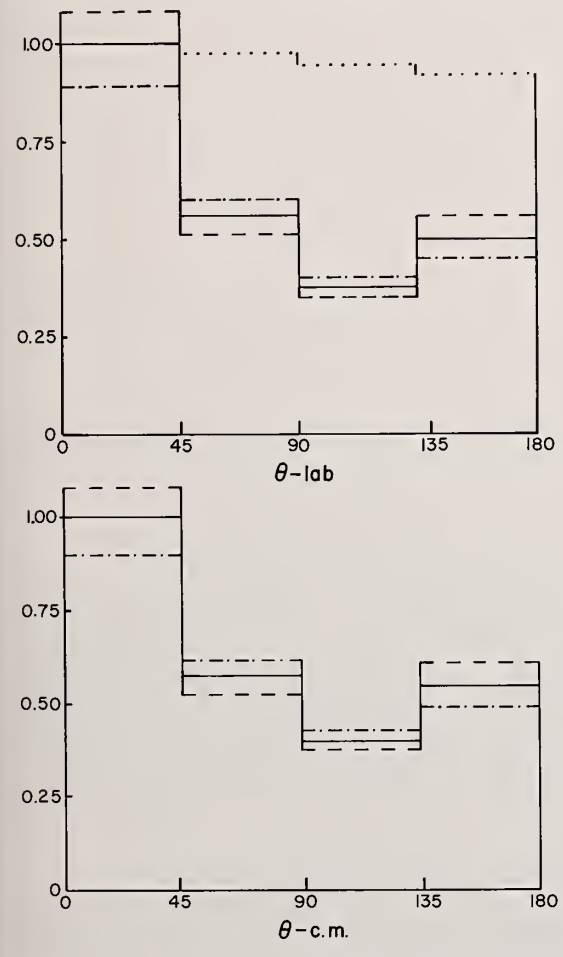

Fig. 5. Angular anisotropy of the $^6Li(n,\alpha)^3H$ reaction at 25 keV in the lab and center-of-mass systems.

Conclusions

The results of the present experiment show a large angular anisotropy in the $^6Li(n, \alpha)^3H$ reaction at 25 keV. The existence of this anisotropy at such a low energy and the possibility of similar behavior at still lower energies (i.e., 1 - 2keV) should result from s-p wave interference. This would give rise to a constant anisotropy that is experimentally masked by the 1/v behavior of the isotropic s-s interference terms at lower energies.[5]

References

1. J.C. Overly, R.M. Sealock and D.H. Ehlers, Nucl. Phys. A221, 573 (1974) and references therein.

2. G. de Leeuw-Gierts, PhD Thesis, Faculte de Sciences Universite Libre de Bruxelles, (1968).

3. C. Beets, G. de Leeuw-Gierts, S. de Leeuw, Y. Baudinet-Robinet, G. Robaye, and L. Winand, Nucl. Phys., 69, 145 (1965).

4. E.D. McGarry and I.G. Schroder, paper BB18, (this conference).

5. G.M. Hale, private communication and paper EA4 (this conference).

NEUTRON TOTAL CROSS SECTION OF ^{6}Li FROM 10 eV TO 10 MeV

J. A. Harvey and N. W. Hill
Oak Ridge National Laboratory*
Oak Ridge, Tennessee 37830

Transmission measurements have been made at ORELA upon two metal samples of ^{6}Li(98.72%) with inverse sample thicknesses of ^{6}Li of 11.99 and 2.987 b/atom. The measurements at low energies (from 10 eV to 300 keV) were made using a ^{6}Li glass scintillation detector at 17.878 m and 78.203 m and at high energies (from 50 keV to ∿10 MeV) using an NE-110 scintillation detector at 78.203 m. The total cross section data from both samples and detectors are in good agreement and are believed to be accurate to 1 to 2% below 1 MeV. Total cross section data obtained from both samples at ∿25 discrete energies up to 1 MeV using an iron-filtered beam are in good agreement with the continuous spectra data.

(Nuclear Reactions: ^{6}Li, σ_{nT}, En = 10 eV to 10 MeV)

Introduction

One of the more useful neutron standards in the energy region below 1 MeV is the ^{6}Li(n,α) reaction since fast, efficient, stable neutron detectors utilizing this reaction can be readily constructed. Below ∿10 keV the ^{6}Li(n,α) cross section follows a 1/v law and is known to ∿1% accuracy.[1] However, at high energies the accuracy varies from 5 to 15%. Values from recent measurements[2,3] differ by ∿10% at the peak of the resonance at 246 keV. It is well known[1,4] that total cross section data are valuable in establishing the (n,α) cross section particularly in the region of the 246-keV resonance. Many total cross section measurements have been made upon ^{6}Li in the past 20 years; these data were reviewed in 1970 by Uttley *et al.*[1] The two most recent measurements[5,6] agree in cross section but show an 8-keV energy discrepancy in the region of the 246-keV resonance. One of the recommendations made by Uttley *et al.*[1] was that the total cross section should be remeasured from a few eV to a few MeV.

Experimental Measurements

Transmission measurements have been made upon two metal samples of ^{6}Li (98.72%) with inverse sample thickness of ^{6}Li of 11.99 and 2.987 b/atom. The samples were contained in stainless steel cylinders 3.0 cm diameter and sealed to prevent the formation of nitrides and oxides. Data were taken at the higher neutron energies (> 30 keV) using an NE-110 scintillation detector located 78.203 m from the standard neutron target[7] at ORELA. For these higher energy measurements, 5 nsec bursts 1000 pps were used resulting in an energy resolution $\Delta E/E$ of $0.001\sqrt{1+4\ E(\text{in MeV})}$. A 1.1-cm-thick uranium filter was used to reduce the gamma flash and a ^{10}B filter (0.6 gm/cm^2) to eliminate overlap neutrons. For the lower energy measurements, a ^{6}Li glass scintillator (1.27 cm thick, 11 cm dia) was used at both the 78.203 m and 17.878 m flight paths. At the longer flight path 22-nsec bursts 800 pps were used with a 7-mm Pb filter and a ^{10}B filter (0.6 gm/cm^2) to reduce overlap neutrons. At the shorter flight path 7.5-nsec bursts 180 pps were used with a 7-mm Pb filter and a 1-mm Cd filter to prevent overlap. In addition to these continuous energy measurements, measurements at ∿25 discrete energies (with energy spreads of from ∿0.7 to 5 keV) have been made using iron window neutrons produced by a 29-cm iron filter in the beam and the NE-110 detector located at the 78.203 m flight path.

Experimental Results

The time-of-flight spectra measured with the NE-110 detector must be corrected for 3 backgrounds, each < 1%: first, the presence of 2.23-MeV gamma rays from neutron capture by the water moderator which decays with a ∿17.6-μsec decay time; second, the 478-keV gamma rays produced by capture in the boron in the pyrex of the phototube which has a 1-2 μsec decay time for the 2-cm-thick NE-110 scintillator; finally, a constant room background which is mainly due to gamma rays. Figure 1 shows the total cross section of ^{6}Li from 50 to 550 keV obtained with the NE-110 detector. The data below 5.5 barns was obtained from the thick sample and above 5.5 barns from the thin sample. Comparison of the thin and thick sample data (excluding the thick sample data above ∿8 barns) showed a difference of ∿0.1 barns which was explained by assuming that there was a slight amount of nitrogen in the thin sample. The data obtained using the iron-filtered neutrons also showed this ∿0.1-barn difference between the thick and thin samples. Hence, the thin data are only used in the energy region where the cross section is > 5.5 barns and, hence, any error in applying the ∿0.1-barn correction is very small. The values for the cross section in Fig. 1 are actually 0.987 $\sigma(^{6}\text{Li})$ + 0.013 $\sigma(^{7}\text{Li})$ rather than $\sigma(^{6}\text{Li})$. However, since the cross section of ^{7}Li is nearly the same as that of ^{6}Li the difference is small (< 1%) over the entire energy range. Nevertheless we plan to measure the ^{7}Li total cross section in order to make this small correction accurately. The peak cross section at 246 keV was 10.95 ± 0.10 barns. Data obtained using the ^{6}Li glass detector and the thin sample in the region of this

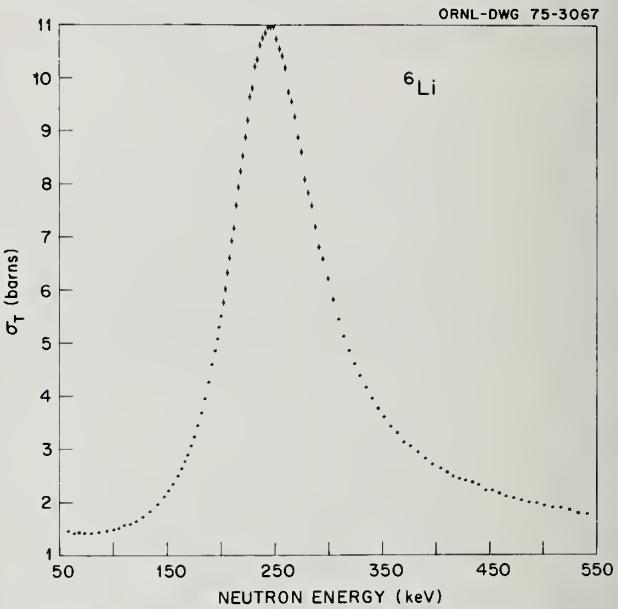

Fig. 1. Neutron Total Cross Section of ^{6}Li.

246-keV resonance are in good agreement within ∿1%. The peak cross section at 246 keV was 10.97 ± 0.10 barns.

Figure 2 shows the total cross section of ^{6}Li from 0.5 to 10.5 MeV obtained from the thick sample using the NE-110 detector. Above ∿3 MeV the statistical accuracy is relatively poor since the intensity of high energy neutrons is quite low from the water-moderated Ta(γ,n) target. We have shown recently that a greatly increased intensity of these higher energy neutrons can be realized by looking directly at the ORELA Ta target through a thick uranium filter, especially when only a small amount of sample is available. We plan to make new measurements up to ∿20 MeV using these unmoderated Ta(γ,n) neutrons.

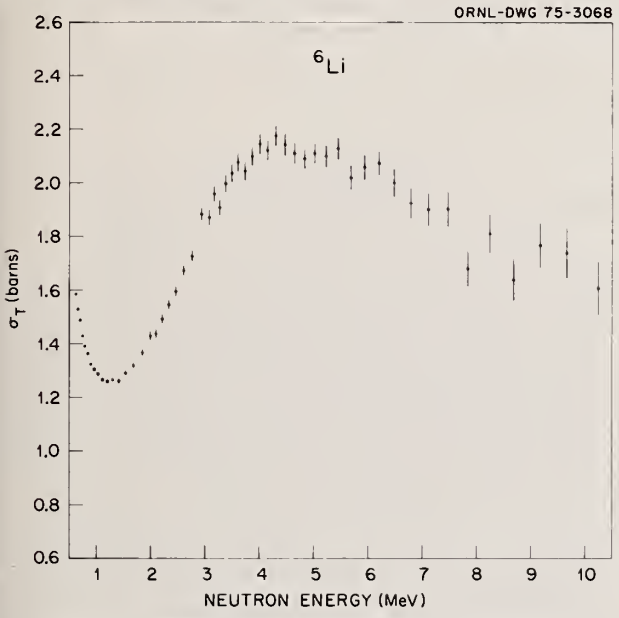

Fig. 2. Neutron Total Cross Section of ^{6}Li.

The total cross section data obtained using iron-filtered neutrons are listed in Table 1. These data agree with the data shown in Figure 1 to an accuracy of ∿1%.

The low-energy total cross section data obtained with the ^{6}Li glass scintillator are in excellent agreement up to several keV with the formula proposed by Uttley,[1] namely σ_T = constant × $149.5/\sqrt{E\ (\text{in eV})}$. Data from 10 eV to 10 keV were obtained using the 17.878-m flight path and from ∿100 eV to 300 keV using the 78.203-m flight path. Since the ^{6}Li(n,α) thermal cross section is known accurately (∿0.5%), it follows that the 1/v part of the total cross section in the eV energy region has an uncertainty of only ±0.5%. Thus the excellent agreement (∿1%) between the total cross section data and the equation confirms the accuracy of the thicknesses of the samples.

Conclusions

The total cross section of ^{6}Li has been measured to an accuracy of 1 to 2% below 1 MeV. The data are in good agreement with the data reported in references 5 and 6 except that the energy values in the region of the 246-keV resonance from reference 6 are ∿8 keV higher than from the present measurement or from reference 5. The energy scale in the present measurement is accurate to ∿0.1%. From 0.5 to 3 MeV the total cross sections have been measured to an accuracy of from 2% to 3% but the uncertainty increases to ∿10% at 10 MeV.

Table 1. Neutron Total Cross Section of ^{6}Li Determined from Iron Window Measurements

Energy (keV)	Energy Spread (keV)	σ_T (barns)
24.6	1.1	1.79 ± 0.02
81.6	0.7	1.45 ± 0.02
128.6	0.7	1.74 ± 0.02
137.2	1.4	1.90 ± 0.02
167.7	1.0	2.86 ± 0.03
183.7	1.4	3.91 ± 0.04
219.1	1.1	8.46 ± 0.08
244.1	0.9	10.85 ± 0.10
273.6	1.5	8.68 ± 0.08
312.5	1.3	5.29 ± 0.05
352.0	2.2	3.64 ± 0.03
375.7	1.6	3.09 ± 0.03
404.1	1.8	2.66 ± 0.05
436.9	2.1	2.34 ± 0.03
468.1	2.3	2.11 ± 0.02
497.8	2.5	1.94 ± 0.02
556.0	2.9	1.77 ± 0.03
610.0	5.0	1.61 ± 0.02
645.0	10.0	1.56 ± 0.02
703.0	4.0	1.48 ± 0.02
836.0	5.0	1.35 ± 0.03
954.0	3.0	1.30 ± 0.03

*Operated by Union Carbide Corporation for the Energy Research and Development Administration.

[1] C. A. Uttley, M. G. Sowerby, B. H. Patrick, and E. R. Rae, *Proceedings of Conf on Neutron Standards and Flux Normalization*, AEC Symposium Series 23 (1971), p. 80.

[2] W. P. Poenitz, Z. Physik 268, 359 (1974).

[3] S. J. Friesenhahn, V. J. Orphan, A. D. Carlson, M. P. Fricke, and W. M. Lopez, Bull. Am. Phys. Soc. 20, 144 (1975).

[4] G. M. Hale, Bull. Am. Phys. Soc. 20, 148 (1975).

[5] C. A. Uttley and K. M. Diment, British Reports AERE-PR/NP-14, 1968; AERE-PR/NP-15, 1969; AERE-PR/NP-16, 1969.

[6] J. W. Meadows and J. F. Whalen, Nucl. Sci. and Eng. 48, 221 (1972).

[7] R. L. Macklin, NIM 91, 79-84 (1971).

OBSERVATION AND ANALYSIS OF ELASTIC NEUTRON SCATTERING FROM ^{12}C*

R. J. Holt, A. B. Smith and J. F. Whalen
Argonne National Laboratory
Argonne, Illinois 60440

Angular distributions of neutrons elastically scattered from ^{12}C were measured from 1.8-4.0 MeV at intervals of $\leq$ 20 scattering angles distributed between 20-160 deg. Incident neutron energy resolutions were 20-50 keV. All differential cross sections were determined relative to those of the H(n,n) reaction. In addition, total neutron cross sections were deduced from monoenergetic (ΔE=2 keV) neutron transmissions in the energy range 1.5-5.0 MeV. The experimental results were interpreted in terms of a multi-level R-matrix analysis including considerations of previously reported cross sections and polarizations. The resulting R-matrix parameters are compared with the Yale values deduced from observed scattered neutron polarizations. The measured values and analysis suggest physically consistent standard carbon total and scattering cross sections readily referenced in measurement applications.

(Nuclear reaction $^{12}C(n,n)^{12}C$; measured $\sigma_T(E)$, E=1.5-5.0 MeV, $\sigma(\theta,E)$, E=1.8-4.0 MeV, θ_{lab} = 20° to 160°; R-function analysis).

Introduction

Studies of the ^{12}C + n system play an important part in the design of nuclear energy systems, the development of neutron flux calibration standards and the understanding of nuclear structure[1,2]. In particular, the $^{12}C(n,n)^{12}C$ reaction is of great importance for the construction of moderators, reflectors and fuel-structural elements in both fission and fusion powered reactors. In addition, the total and differential scattering cross sections of ^{12}C provide convenient reference standards for neutron flux measurements in the MeV region. A precise understanding of neutron scattering from ^{12}C would allow one to use ^{12}C directly as a reference standard rather than the usual hydrogen standard which is often employed in the form of a hydrocarbon (CH_2) anyway. Moreover, certain well-defined resonances in the total cross section of ^{12}C are widely used for energy calibration standards[3].

The ^{12}C+n system is well-suited for studies of basic reaction mechanisms and nucleus structure, since the $^{12}C(n,n)^{12}C$ reaction is dominated by four major resonances below 5 MeV[4]. This reaction has been extensively analyzed using the R-matrix formalism. The most notable analysis[5] was based upon an interpretation of neutron polarization data over the energy range 2 to 5 MeV and the total cross section was predicted from 0 to 5 MeV. The validity of the total cross section prediction was difficult to assay since several measured total neutron cross section sets were not consistent, particularly in the 2 to 3-MeV region[6,7]. In addition, the p-wave phase shifts deduced from an analysis[5] of the polarization data are in disagreement with those found from an interpretation of angular distribution measurements[8].

In view of the importance of the $^{12}C(n,n)^{12}C$ reactions, we have measured the total cross section of ^{12}C from 1.5 to 5.0 MeV. In addition, we have measured the angular distributions of neutrons scattered from ^{12}C throughout the energy region 1.8 to 4.0 MeV and at 20 to 90 angles between 20° and 160°. These measurements were interpreted in terms of a multi-level R-function analysis in which the R-function parameters were fitted to the observed angular distributions and the total cross section and polarizations were predicted. The final parameters are found to be in good agreement with those reported[5] by the Yale group, and hence, provide a unified description of the ^{12}C+n system below 5 MeV.

Experimental Methods

Total Neutron Cross Sections

The total neutron cross section measurements employed a variation of the monoenergetic source techniques discussed by Miller[9]. The neutron source was the $^7Li(p,n)$ reaction with the neutron energy determined from the kinematics and the reaction threshold of 1.8815 MeV[10]. The incident neutron energy spread was approximately 2 keV. All carbon samples were fabricated out of high-purity, pile-grade graphite. The neutrons from the source traveled along a 5-m, well-collimated flight path before being detected in a liquid scintillator. The pulsed source provided proton bursts with widths of 1 ns and conventional time-of-flight techniques were employed in order to assure that the detector response was confined to the primary neutron-source group and to reduce the background. In-scattering corrections were found to be negligible.

Elastic Neutron Scattering Cross Sections

The scattering measurements were made using the time-of-flight spectrometer and the 10-angle detector system in conjunction with the $^7Li(p,n)$ pulsed neutron source available at the Argonne Tandem Neutron Laboratory[11]. Scattered neutron flight paths were 5 to 6 meters and velocity resolutions ranged from 0.4 to 0.8 nsec/meter. Incident neutron resolutions were 20 to 50 keV. The scattering samples were 2 cm in diameter by 2 cm long cylinders of high-purity pile-grade graphite placed 13 cm from the source at a reaction angle of 0°. The scattering angles ranged from 20 deg. to 160 deg. The relative scattering angles were optically determined to an accuracy of 0.1 deg. The angular zero was determined to 0.5 deg. by observing the energies of neutrons scattered from the hydrogen of a CH_2 sample both left and right of the center line. The relative efficiencies of these detectors were determined by observation of the scattering of neutrons from hydrogen in a CH_2 sample. Subsequently, the normalization of the relative detector efficiencies was determined relative to the well-known H(n,n) scattering cross section[12]. The calibration of each of the 10 detectors was essentially independent and repeated at each of the numerous measurement periods. All of the scattering results including those associated with the normalization of the detector

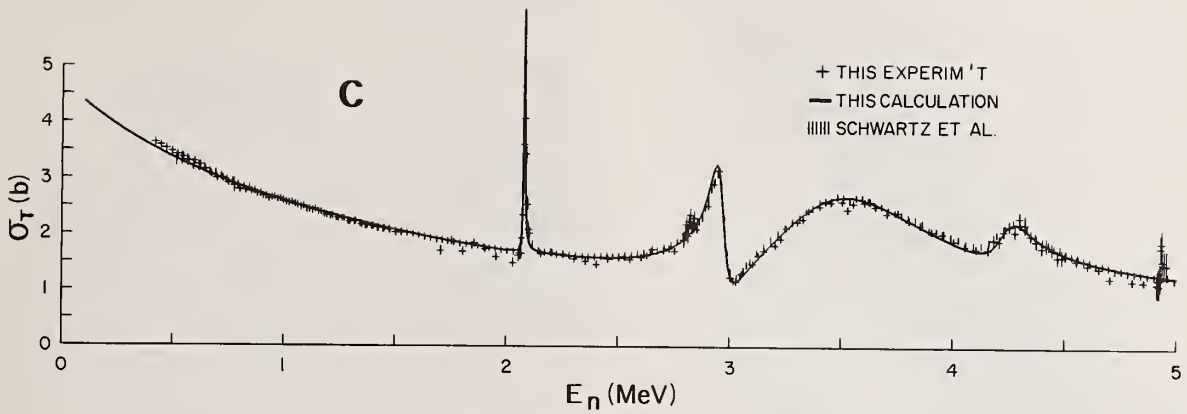

Fig. 1. Total neutron cross sections of carbon. The data of Schwartz et al. are taken from ref. 6. The curve indicates present R-matrix result. The present measurements and those of ref. 18 are indicated by crosses.

sensitivities, were corrected for incident beam attenuation, angular resolution and multiple event effects using analytical and Monte-Carlo techniques[13]. It is unlikely that the angular distribution measurements will be appreciably effected by many systematic uncertainties in energy and angle since the measurements were made with different detectors and at different times over a period of four years.

Experimental Results

Total Neutron Cross Sections

The total neutron cross sections were measured from 1.5 to 5.0 MeV with incident energy resolutions of 2 to 5 keVand at energy intervals which were sufficiently small to define the previously reported structure in the n+ ^{12}C system. The present results are outlined and compared with the work of Schwartz et al.[6] in Fig. 1. At the 2.08 MeV resonance the present resolution is better than that of Schwartz et al. but not as good as that reported by Cierjacks et al.[7]. Near 5.0 MeV the present resolutions are superior to those of either ref. 6 or 7. In the energy regions where the excitation function is slowly varying with energy, the magnitudes of the present measurements agree very well with those of Schwartz et al. with an average deviation between the two sets of $\tilde{\sim}$ 3.4 percent. This deviation was generally random in sign with possibly a slight tendency for the present results to have lower average magnitudes. Over wide energy ranges, the present results are remarkably lower than those of ref. 7. The results of Foster and Glasgow[14] and, to a lesser extent, Fossan et al.[15] and Bockelman et al.[16] are consistent with the present values. Two prominent and narrow resonances were observed at 2080 ± 5 keV and 2821 ± 5 keV, respectively. These observed energies are in very good agreement with those reported by Schwartz et al.[6], Davis and Noda[17] and that determined from ^{11}B(^{3}He,p)^{13}C reaction studies[4].

Generally, the present results, together with lower energy values previously reported from this laboratory[18], strongly support the results of Schwartz et al. obtained with an alternative method. Over the range 0.1 to 5.0 MeV, the discrepancy in energy-average normalization between the two results is $\tilde{\sim}$ 1-2 percent.

Elastic Neutron Scattering

The elastic neutron scattering results were obsained in more than ten measurement periods distributed over four years. Some of these results are illustrated in Fig. 2. The individual distributions contained from 16 to as many as 90 differential values. The differential-cross-section uncertainties varied from $\tilde{\sim}$ 5 percent to as much as 20 percent including relative and normalization contributions. The total average deviation of the measured values from Legendre polynomial fits was $\tilde{\sim}$ 6.5 percent. This value is consistent with the individual uncertainties. The average deviation between the total cross section, determined from polynomial fits to the observed angular distributions, and those values reported by Schwartz et al.[6] was found to be small (3.3%) compared to the uncertainties of the two measurements. Some impression of the general quality and scope of the present work can be obtained from Fig. 3.

There have been several previously reported measurements of elastic neutron scattering from carbon[19]. The most recent are those of Lane et al.[20] and Galati et al.[21]. The latter work is particularly detailed and is reported at incident energies near those of the present work. The Galati et al. results compare favorably with many of the present values as illustrated in Fig. 3.

R-Function Analysis

A five-level R-matrix analysis was used to fit the observed angular distributions between 1.8 and 4.0 MeV including resonance states in the n+ ^{12}C system at 2.076($d_{5/2}$), 2.92($d_{3/2}$), 3.50($d_{3/2}$) and 4.20($p_{1/2}$) MeV[4,22]. In addition, bound states at -1.86($s_{1/2}$) and -1.270($p_{3/2}$) MeV were included in order to achieve a good description of reported polarizations over the range 2 to 5 MeV and scattering results from 0 to 1.8 MeV[5,19].

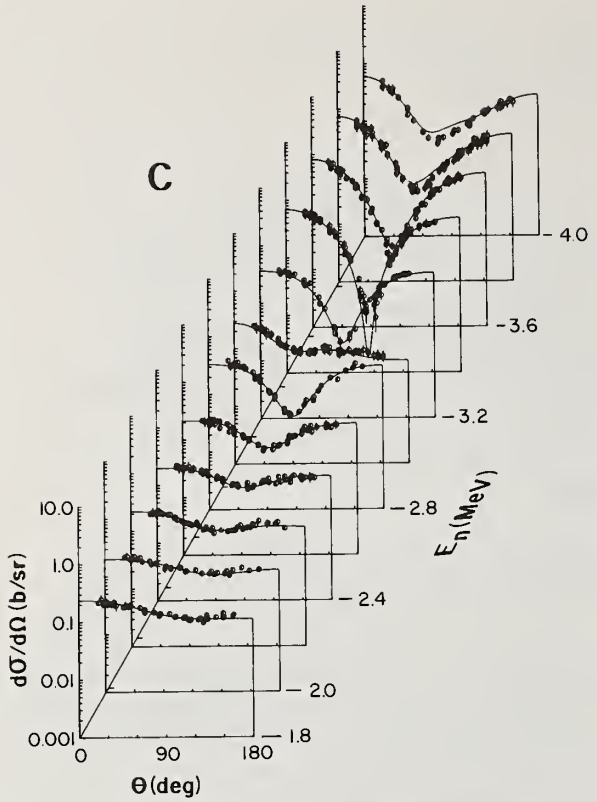

Fig. 2. Present measured (circles) and calculated (curves) differential elastic scattering cross sections of carbon.

Elastic scattering is the dominant process in the n+ ^{12}C reaction at energies below 4.0 MeV. Hence the R-matrix reduces to the R-function:

$$R_{nn}^{\ell J} = \sum_{\lambda} \frac{\gamma^2_{\lambda \ell J}}{E_{\lambda \ell J} - E} + R^{\infty}_{\ell J} \qquad (1)$$

where $\gamma^2_{\lambda \ell J}$ and $E_{\lambda \ell J}$ are reduced widths and level energies, respectively, for resonances λ with orbital momentum ℓ and spin J. In addition to explicitly defined levels there is the contribution from distant levels, μ, given by:

$$R^{\infty}_{\ell J} = \sum_{\mu=\lambda} \frac{\gamma^2_{\mu \ell J}}{E_{\mu \ell J} - E} \qquad (2)$$

Here $E_{\mu \ell J} >> E$ and only two leading terms are significant:

$$R^{\infty}_{\ell J} = R_o^{\ell J} + R_1^{\ell J} \cdot E \qquad (3)$$

where

$$R_o^{\ell J} = \sum_{\mu} \frac{\gamma^2_{\mu J}}{E_{\mu \ell J}} \quad \text{and} \quad R_1^{\ell J} = \sum_{\mu} \frac{\gamma^2_{\mu \ell J}}{E^2_{\mu \ell J}}$$

These approximations are applicable to the present case since $E << E_{\mu}$ is satisfied. The observables are computed from the collision function which is expressed in terms of the R-function by:

$$U_{nn} = e^{-2i\phi_\ell} \frac{1 - R_{nn}^{\ell J}(S_\ell - B_{\ell J} - iP_\ell)}{1 - R_{nn}^{\ell J}(S_\ell - B_{\ell J} + iP_\ell)} \qquad (4)$$

where ϕ_ℓ, P_ℓ and S_ℓ are hard-sphere phase-shift, penetration factor and level-shift factor, respectively. The $B_{\ell J}$ quantity is the boundary condition factor chosen to cancel the level-shift factor at the resonance energy, (i.e., the same as used in the Yale analysis).

The analysis of all of the angular distributions was carried out concurrently for all measured angles and energies. The Yale[5] R-matrix values were used as a starting point for the fitting procedures and the channel radius, α, was fixed at the Yale value of 4.61 fermis. The reduced width of the 2.076 MeV level is small (0.014 MeV), and consequently, was held constant in the present analysis. In addition, the s-wave bound-state reduced width (0.69 MeV) was not varied since it was determined from an analysis of the thermal total cross section. The $p_{3/2}$ bound state reduced width was fixed at 0.5 MeV since it provides a significantly better prediction of the neutron polarization[5]. The analysis of the angular distribution was found to be relatively insensitive to the p-wave parameters over a fairly wide range of variation. However, the present analysis was sensitive to the d-wave parameters. The reduced widths of the 2.92, 3.5 and 4.20 MeV resonances were allowed to vary in the analysis. In addition, the $R^{\infty}_{\ell J}$'s for all partial waves were varied in order to find the optimum fit to the angular distribution measurements.

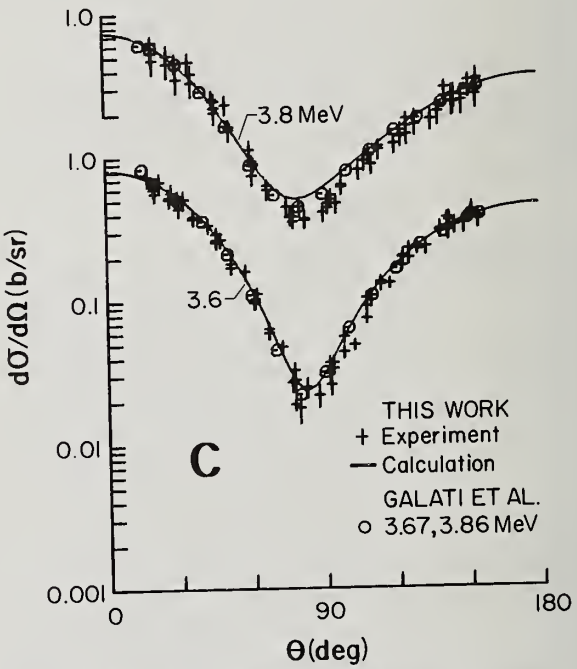

Fig. 3. Comparison of present angular distribution measurements with the work of Galati et al.[21].

Results of the R-Function Analysis

The final R-function parameters are compared with the Yale values in Table 1. The agreement between the two sets of parameters is excellent. This good agreement indicates that the present measurements are consistent with the neutron polarization work. Using the present values of the R-matrix parameters, the total cross section was predicted (see Fig. 1). The overall quality of the

R-function fit to the angular distributions is shown in Fig. 2. A detailed comparison of the R-function analysis with the data is given in Fig. 3. Finally, the R-function analysis is compared with measurements of neutron polarization in the energy range 2 to 5 MeV in Fig. 4.

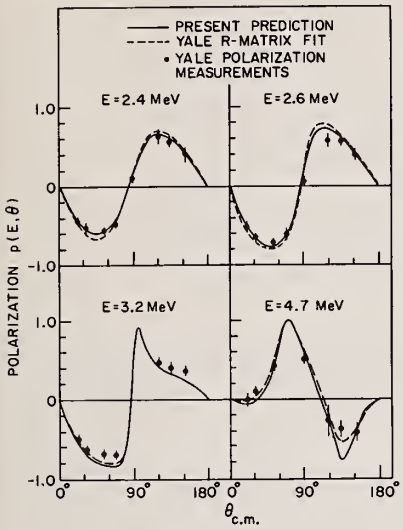

Fig.4. R-matrix predictions of the neutron polarization. The data were taken from the work of Holt et al.[5] The dashed curve represents the R-matrix fit to the polarization data of ref. 5.

Conclusions

In conclusion, the total neutron cross section for the $^{12}C(n,n)^{12}C$ reaction was measured in the energy range 1.5 to 5.0 MeV with an energy resolution of 2 to 5 keV. In addition, the angular distributions were measured at 20 to 90 angles between 20° and 150° throughout the energy region 1.8 to 4.0 MeV. These observations were interpreted in terms of the R-matrix theory and a self-consistent set of R-matrix parameters was found. These parameters were found to describe all observations of the $^{12}C+n$ system throughout the energy range 0 to 5 MeV. It is hoped that these nuclear reaction mechanisms can now be interpreted in terms of the underlying nuclear structure. Finally, this R-function description of the $^{12}C+n$ system provides a convenient means for simulating and extrapolating the neutron scattering from ^{12}C by using extremely simple computer calculations.

References

*This work supported by E.R.D.A.

1. E. Straker, Proc. Nat. Topical Conf. on New Developments in Reactor Physics and Shielding, CONF-720901, (1972).
2. N. Francis, C. Lubitz, J. Reynolds, C. Slavik and R. Stieglitz, Proc. of Sym. on Neut. Standards and Flux Normalization,CONF-701002,(1971).
3. For example, see Technical Minutes of 6th INDC meeting, (1973).
4. F. Ajzenberg-Selove, Nucl.Phys.,A152 6 (1970).
5. R. Holt, F. Firk, R. Nath and H. Schultz, Nucl. Phys., A213 147 (1973).
6. R. Schwartz, R. Schrack and H. Heaton, National Bureau of Standards Report, NBS-138, (1974).
7. S. Cierjacks, P. Forti, D. Kopsch, L. Kropp, J. Nebe and H. Unseld, Gesellschaft für Kernforschung Report, KFK-1000, (1968).
8. J. Wills, J. Blair, H. Cohn and H. Willard,Phys. Rev., 109 891 (1958).
9. D. Miller, Fast Neutron Physics, Part-2, p-985, Ed. J. Marion and J. Fowler,Interscience Pub., New York (1963).
10. H. Newson and J. Gibbons, Fast Neutron Physics, Part 2, P-1601, Ed. J. Marion and J. Fowler, Interscience Pub., New York (1963).
11. J. Whalen,R. Roge and A.Smith, Nucl. Inst. and Methods, 39 185, (1966).
12. J. Hopkins and G. Breit, Nucl.Data,A9 137,(1971).
13. P. Guenther and S. Smith, Private Communication.
14. D. Glasgow and D. Foster,Phys.Rev.,C3 604,(1971).
15. D. Fossan, R. Walter, W. Wilson and H. Barschall, Phys. Rev., 123 209, (1961).
16. C. Bockelman, D. Miller, R. Adair and H. Barschall,Phys. Rev., 84 69, (1951).
17. J.Davis and F.Noda, Nucl. Phys.,A134 361, (1969).
18. J.Meadows and J.Whalen,Nucl.Sci.and Eng.,41 351, (1970).
19. D. Garber, L. Stromberg, M. Goldberg, D. Cullen and V. May. Brookhaven National Lab. Report, BNL-325, 3rd Ed.,(1970); See also J.Stehn, M. Goldberg, B. Magurno and R. Wiener-Chassman, BNL-325, 2nd Ed.,2nd Supplement (1964).
20. R. Lane et al., Ohio University,Private Com.
21. W. Galati, J. Brandenberger and J. Weil, Phys. Rev., C5 1508,(1972).
22. A.Lane and R.Thomas,Rev.Mod.Phys.,30 257,(1958).

TABLE 1

R-Function Parameters with a=4.61 fm

ℓJ	λ = 1		λ = 2				
	$E_{\ell J}$(MeV)	$\gamma^2_{\ell J}$	$E_{\ell J}$(MeV)	$\gamma^2_{\ell J}$	$R_o^{\ell J}$(MeV^{-1})	$R_1^{\ell J}$	$B_{\ell J}$(MeV^{-1})
$s_{1/2}$	-1.86	0.69			0.4 (0)	0	0
$p_{1/2}$			4.20	0.70 (0.654)[a]	0.16 (0.15)[a]	0.02	-0.2
$p_{3/2}$	-1.27	0.5			0.34 (0.37)[a]	0.055	-0.18
$d_{3/2}$	2.92	0.17 (0.16)[a]	3.50	0.87 (0.93)[a]	0.15 (0.18)[a]	0.02 (0.025)[a]	-1.00
$d_{5/2}$			2.076	0.014	0.05 (0.03)[a]	0.0	-1.3

[a] values are those from the Yale analysis which differ from the present values.

FISSION SPECTRUM NEUTRONS FOR CROSS SECTION VALIDATION AND NEUTRON FLUX TRANSFER

J. A. Grundl and C. M. Eisenhauer
National Bureau of Standards
Washington, D. C. 20234

A variety of measurement methods over more than two decades provides a base for proper evaluation of the fission spectrum shape. The evaluation presented recommends a Maxwellian reference description for ^{252}Cf (spontaneous fission) and ^{235}U (thermal-neutron-induced fission) with average energy parameters of 2.13 MeV and 1.97 MeV respectively over the energy range 0.25 to 8 MeV. A further multigroup summary of the experimental data presents the final evaluation as an empirical adjustment of Maxwellian segments and includes an estimate of credible departures from the true spectrum shape. The reference Maxwellian shapes differ from the final evaluated shape by $\lesssim$ 2% over the above energy range. A few basic integral quantities, fission neutron age in water and the fission-spectrum-averaged fission cross section for ^{238}U, ^{235}U and ^{237}Np, are reviewed briefly, based on the results of the evaluation. Two features of fission neutrons make them a useful reference for certain measurement problems in nuclear technology: the fission spectrum shape is preserved above $\sim$ 1 MeV in important reactor-associated neutron environments, and small, intense sources of pure ^{252}Cf fission neutrons are now available. A restricted class of related applications using fission neutron sources is discussed.

(Cross sections; dosimetry; evaluation; fission spectrum; neutron flux; neutrons)

Introduction

The most widely studied neutron energy distribution in existence is that from nuclear fission. Sustained interest for well over two decades with an unmatched variety of measurement methods provides a data base for proper evaluation of the fission neutron spectrum shape. The results of such an evaluation of empirical data, aimed at reactor development needs rather than physical understanding, will be presented along with a truncated discussion of the evaluation criteria and the data manipulations employed. The final evaluated fission spectrum shape obtained for ^{235}U (thermal-neutron-induced fission) and ^{252}Cf (spontaneous fission) includes an estimate of credible departures of the recommended shape from the true spectrum shape.

Two features of fission neutrons make them a useful reference for certain measurement problems in nuclear technology. First, the fission spectrum shape is qualitatively preserved (in some cases very well) above about one MeV in breeder, fuels test, and light water reactor cores, as well as in clean and prototype critical assemblies; second, highly-localized, intense sources of pure ^{252}Cf fission neutrons have become available and their absolute source strength can be determined to ± 1.5% and better. These circumstances lead to the application of fission neutrons 1) for normalization of fission cross sections that do not vary greatly with energy; 2) for the validation of a generality of fission, absorption and threshold cross sections; and 3) for simple flux transfer measurements from isolated fission neutron fields of known intensity to reactor-associated neutron fields of importance for technology. A restricted class of such applications is described, and some established areas where cross section validation measurements exist are reviewed briefly.

Fission Neutron Spectrum Evaluation

Measurements and Maxwellian Fits

The voluminous body of literature describing all fission neutron spectrum measurements up to 1971 is satisfactorily referenced in recent review articles.[1] Sixteen published fission spectrum measurements for ^{235}U and ^{252}Cf, covering the period 1952 through 1974 and employing every perfected technique of neutron spectrometry, were chosen for the final stages of this evaluation. They are listed in Table I along with the energy range covered and a brief annotation of the experimental techniques employed.

The most consistent feature of fission neutron spectrum data is its pure exponential behavior when plotted as $N(E)/\sqrt{E}$ where $N(E)$ is the observed spectrum density. There is no physical theory to justify this behavior of the spectrum even though it is observed over several orders of magnitude.[2] For purposes of evaluation, however, the resulting one-parameter description is ideal and all data manipulation and fits were undertaken on the basis of the Maxwellian density function $\chi(E) \simeq \sqrt{E}\exp(-1.5E/E_{av})$. The results of a least-squares fit of the Maxwellian to each data set are shown in columns 3 and 4 of Table I. First given is the E_{av}-parameter for all data as reported by the experimenter, and in the adjacent column the E_{av}-parameter for a least-squares fit to the data over the energy region 0.25 to 8 MeV that excludes 6% of the spectrum where there is less measurement confidence. The latter values of E_{av}, shown underlined in Table I, were obtained by fits at NBS using data tabulations and assigned errors obtained from the original documentation or kindly provided on a short time scale by the experimenters. Consistent statistical weights were applied and the effects of alternate weighting schemes investigated. In almost all cases the fits obtained at NBS gave standard deviations for the E_{av}-parameter that were less than those assigned to the data fits undertaken by the original experimenters. The latter more conservative fitting errors are listed under "all data" while the NBS errors for E_{av} are assigned to the fits obtained between 0.25 and 8 MeV.

A weighted average and standard deviation of the E_{av}-parameters is given for each spectrum in Table I. The final recommendation for a reference Maxwellian description for each spectra is listed only for the restricted energy range, and includes subjective estimates for that energy range of the (1σ) uncertainty corresponding to the 67% and 95% confidence level. Overall consideration of each data set, including the energy range covered and the establishment of the neutron detection efficiency vs. energy, is involved in this recommendation.

Evaluation

With a reference Maxwellian fit established, the departures of individual data sets may be examined. A suitable normalization method was developed and departure plots like the one shown in Figure 1 were prepared. On the basis of such data displays estimates were made of the fission spectrum shape and uncertainties in five energy groups between 0.25 and 8 MeV and in the energy regions outside of this range. The results of this empirical data analysis are collected in Table II,

TABLE I, DIFFERENTIAL FISSION NEUTRON SPECTRUM MEASUREMENTS

Reference	Date	[a] E_{av}(MeV), Average Energy Parameter: [b] All Data	[c] Data Between 0.25 and 8 MeV	Measurement Range (MeV)	Detection Scheme
CALIFORNIUM - 252 SPONTANEOUS FISSION					
Green et al.[2]	1973	2.11 ± .02	2.12 ± .01	0.5 - 13	Time-of-flight (TOF); energy scale based on carbon scattering resonances. Scintillator NE-213 efficiency from long counter response (E < 4 MeV); calculations by Verbinski for E > 4 MeV.
Knitter et al.[2]	1973	2.13 ± .08	2.09 ± .02	0.15 - 15	TOF; energy scale calibrated with monoenergetic neutrons (0.4 to 2.3 MeV). Liq. scint. eff. from angular distribution of T(p,n), D(d,n), Li(p,n), H(n,n), etc. (0.05 to 8.2 MeV).
Werle and Bluhm[3]	1972				Proton-recoil proportional counters (PR); response functions from monoenergetic response. ^{3}He-spectrometer and prop. gas counter.
(n,p)		2.16 ± .02	2.15 ± .02	1.5 - 7	
(^{3}He)		2.13 ± .02	2.00 ± .03	1 - 4	
Meyer et al.[2]	1974	(1.98)		0.05 - 8	PR (0.05 to 1.2 MeV). Scint. NE-213; unfolded spectrum (1.1 to 8 MeV).
Jeki et al.[2]	1972	(1.95)		0.002 - 1	TOF; ^{6}Li glass scint. efficiency same as Meadows.
Meadows[3]	1967	2.35	2.33 ± .02	0.003- 15	TOF; ^{6}Li glass scint. (E < 2.6 MeV); liq. scint. (E > 1.0 MeV); calculated efficiencies.
Condé and During[3]	1965	2.08 ± .06		0.07 - 7.5	TOF; ^{6}Li Glass scint. (E < 1.1 MeV), Calc. eff.; NE 102A plastic scint. (E > 0.3 MeV), eff. measured against calibrated long counter.
Zamyatnin et al.[3]	1970	2.22 ± .05		0.04 - 6	TOF; ^{6}Li glass and plastic scint.
Weighted Average		2.13$_5$ ± .013	2.13 ± .027		
[d] Final Recommendation			2.13		
U - 235 THERMAL-NEUTRON-INDUCED FISSION					
Rosen	1956	1.95 ± .02	1.97 ± .02	0.3 - 13	Incident neutron energy (E_{in}) = thermal. Photographic plate method, background measurements.
Islam and Knitter[4]	1973	2.05 ± .05	2.06 ± .01	0.55 - 7	E_{in} = 0.4 MeV. TOF; energy scale checked with monoenergetic neutrons. NE 102 scint. eff. from H(n,n) up to 5.75 MeV.
Barnard et al.[5]	1965	1.94 ± .05	1.95 ± .01	0.3 - 4	E_{in} = 0.1 MeV. TOF. Plastic scint. calibrated with long ctr. (E < 2.3 MeV).
Condé and During[3]	1965	1.86 ± .06		1 - 7.5	E_{in} = 0.04 MeV. TOF. Plastic scint. only, same as Condé above.
Werle and Bluhm[3]	1972				Same as for ^{252}Cf by Werle and Bluhm. E_{in} = thermal.
(n,p)		1.96 ± .01	1.92 ± .01	1.5 - 7	
(^{3}He)		2.02 ± .02	1.91 ± .04	1 - 4	
Cranberg[5]	1956	1.92 ± .04	1.92 ± .03	0.18 - 2.7	E_{in} = 0.08 MeV. TOF. Plastic scint. calibrated against long ctr. (0.1 - 3.4 MeV).
Johansson and Almen[4]	1975	1.96 ± .05	1.96 ± .01	0.5 - 14	E_{in} = 0.1-2.0 MeV. TOF; energy scale based on scattering resonances (0.5 - 21 MeV). NE 213 scint. eff. from H(n,n) and T(p,n) angular distribution.
Watt[5]	1952	1.85 ± .01	1.86 ± .03	2.6 - 16	E_{in} = thermal. Proton-recoil, gas counter telescope.
Weighted Average		1.92 ± .022	1.97 ± .014		
[d] Final Recommendation			1.97		

[a] For ^{235}U all E_{av} values are corrected to E_{in} = 0 by the relation $\Delta E_{av} \simeq 0.024\ E_{in}$.
[b] Parameter of Maxwellian as given by the experimenters, or where lacking, from Ref. 6.
[c] Least-squares fits at NBS with a consistent statistical weighting scheme.
[d] Includes weighting of experiments according to coverage of energy range and determination of detector efficiency vs. energy. Final recommendation applies only to restricted energy range.

where the fission spectrum evaluation is presented in seven groups as segments of the reference Maxwellian adjusted up or down so as to give a best fit to the entire data collection without the constraint of a Maxwellian fit over all energies. The reference Maxwellians are listed for comparison. The errors for each group value (both 1σ and 2σ) are judged from departures of the data subsets after the Maxwellian segment adjustment.

The evaluation of the extremities of the fission spectrum were undertaken with all relevant data from Table I. The 1% of the spectrum above 8 MeV is most easily estimated since the data do not greatly differ from a Maxwellian shape except at the very highest energies. Measurements that extend to low energies do not contradict the common assumption that prompt neutrons are emitted predominantly, and without severe anisotropy, from fully accelerated fission fragments. The consequence of this assumption, namely that $\chi(E) \sim \sqrt{E}$ at low energies, is accepted here and the evaluation of the spectrum component below 0.25 MeV is anchored in this manner.[6] Delayed neutrons were specifically included in this part of the evaluation.

The final result of this fission spectrum evaluation for technology applications as presented in Table II are (1) a reference Maxwellian shape which fits the bulk of the selected spectrum measurements over a large energy range (0.25 to 8 MeV) to within a few percent; and (2) a coarse group description which represents a best free fit to the collection of data based on adjusted segments of the reference Maxwellian. The uncertainties for the latter, the segment-adjusted evaluation, vary between ± 3% (2σ) and ± 6% (2σ) for the primary spectrum range and between ± 11% (2σ) and ± 30% (2σ) for the energy range below 0.25 MeV and above 8 MeV.

Application of Fission Spectrum Neutrons

Fission neutron sources employed for nuclear measurements arise in a variety of situations and the literature is not widely available nor easily summarized. Three reviews, each of restricted concern, present important information and some technology import as of about 1971.[7, 8, 9] In this brief report a small set of crucial integral microscopic and macroscopic fission spectrum measurements will be summarized and the implications up-dated on the basis of the

fission spectrum evaluation just completed. Finally, a new look is given at the question of performing neutron flux transfer measurements from absolutely calibrated fission neutron sources to reactor cores, fuels and materials tests, and out-of-core neutron environments.

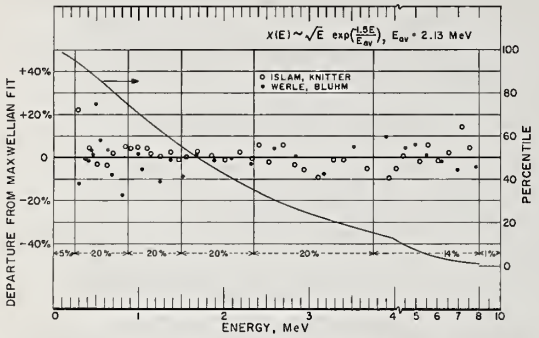

Fig. 1 Example of departures from reference Maxwellian

TABLE III, SPECTRUM SENSITIVE INTEGRAL MEASUREMENTS

	Age in Light water (cm^2)	$\bar{\sigma}(\chi, ^{238}U)$ (barns)	$\bar{\sigma}(\chi, ^{237}Np)$ (barns)
Californium - 252 (spontaneous fission)			
Observed[10, 11]	28.7 ± 0.4	0.320 ± .008	1.330 ± .04
[a]Computed	27.7 ± 0.4	0.313 ± .003	1.343 ± .009
[b]E_{av}: obs./comp.	1.05 ± .02$_5$	1.023 ± .03	–
U-235 (thermal-neutron-induced-fission)			
Observed[7, 12]	27.3 ± 0.6	0.310 ± .005	1.302 ± .05
[a]Computed	25.9 ± 0.3	0.295 ± .005	1.319 ± .013
[b]E_{av}: obs./comp.	1.06 ± .03	1.057 ± .02	–

[a]Computed values of Age in light water are from moments method calculations using the reference Maxwellians (Table II)[10]; average cross sections are based on ENDF/B-IV and the segment-adjusted Maxwellians (Table II). Errors apply only to 1σ fission spectrum uncertainties from Table II.

[b]Ratio of Maxwellian E_{av}-parameters implied by the ratio of observed to computed values.

TABLE II. FISSION SPECTRUM EVALUATION IN SEVEN GROUP STRUCTURE

Energy Boundaries (MeV)	Californium-252 (Spontaneous Fission) [a]Reference Maxwellian [E_{av} = 2.13 MeV]	Californium-252 (Spontaneous Fission) [b]Evaluated Fission Spectrum 1σ	2σ	Uranium-235 (Thermal-neutron-induced) [a]Reference Maxwellian [E_{av} = 1.97 MeV]	Uranium-235 (Thermal-neutron-induced) [b]Evaluated Fission Spectrum 1σ	2σ
0.0						
	(0.050)	0.054	± .007, ± .014	(0.056)	0.058	± .009, ± .018
0.25						
	0.179	0.182	± .002, ± .006	0.195	0.194	± .008, ± .012
0.8						
	0.222	0.221	± .004, ± .008	0.233	0.230	± .007, ± .011
1.5						
	0.193	0.193	± .002, ± .006	0.195	0.193	± .006, ± .010
2.3						
	0.199	0.196	± .004, ± .006	0.190	0.194	± .004, ± .006
3.7						
	0.147	0.145	± .003, ± .007	0.124	0.125	± .006, ± .010
8						
	(0.0104)	0.0094	± .0008, ± .0016	(0.0068)	0.0057	± .0003, ± .0006
12						

[a]Reference Maxwellian from the weighted average of least-squares fits of $\chi(E) \sim \sqrt{E}\ \exp(-1.5\ E/E_{av})$ to each selected data set over the energy range 0.25 to 8 MeV (see Table I).

[b]Group flux based on evaluation of data subsets in that group without the constraint of a Maxwellian fit over the full energy range. Segments of the reference Maxwellian were adjusted to give minimum departures. Listed uncertainties, 1σ and 2σ, are judged from departures of data subsets after adjustment.

Spectrum-Sensitive Integral Measurements

Two integral quantities have received the extensive attention of experimenters. The age-to-indium-resonance of fission neutrons in ordinary water and the fission-spectrum-averaged fission cross section of ^{238}U.[7] Evaluated results for these quantities along with those obtained for the important threshold reaction, $^{237}Np(n,f)$, are shown in Table III, [7, 10, 11, 12] Computed cross section values in the Table are based on ENDF/B-IV cross sections and the segment-adjusted evaluated fission spectra from Table II. Computed age values were obtained from recent moments method calculations at NBS using the reference Maxwellian spectra (see Table II).[10] The observed to computed ratio is presented in Table III as the implied ratio of Maxwellian E_{av} parameters. The discrepancy between observed and computed E_{av} values for two basic integral quantities (^{237}Np is not included because of too large errors and less well established differential cross sections) are in better agreement than in times past. For ^{252}Cf, where experiments are recent and less ambiguous than with ^{235}U, the discrepancies in Table III are agreeably small.

Normalization of Differential Fission Cross Sections

The fissile isotopes, ^{239}Pu, ^{235}U, and ^{233}U, display fission cross sections that do not vary severely over the energy range of fission neutrons. This circumstance makes it attractive to normalize measurements of fission cross sections vs. energy to absolute cross section determinations made under ideal experimental conditions with small but intense Cf fission sources. (Typical sources now available emit up to 5×10^9 neutrons per second from 0.35cc cylindrical capsules that are ~ 99% effectively uncollided. The Cf material is localized to within ± 1 mm and the source strength can be determined to better than ± 1½%.) Californium fission spectrum measurements for $^{239}Pu(n,f)$ and $^{235}U(n,f)$ are presented at this conference.[11, 13]

The low-energy fission spectrum component is of concern for estimating the potential accuracy of such a normalization procedure. In Table IV the fission spectrum response of $^{235}U(n,f)$ is given for the ^{252}Cf Reference Maxwellian from Table II, and for the same spectrum with an enhanced low-energy component, namely, the 2σ uncertainty limit given in Table II. The average cross section change for $^{235}U(n,f)$ is 0.4%; similarly, for $^{239}Pu(n,f)$ the average cross section change is 0.1%.

TABLE IV, LOW ENERGY FISSION SPECTRUM RESPONSE OF $^{236}U(n,f)$

Energy Boundaries (MeV)	Reference Maxwellian χ_i	Reference Maxwellian $\sigma_i\chi_i/\bar{\sigma}$	*Enhanced Low-energy Component $\sigma_i\chi_i/\bar{\sigma}$	$\frac{\sigma_i}{\bar{\sigma}}$
0.0				
	0.0049	0.0099	0.013	2.0
0.05				
	0.0086	0.0122	0.016	1.4
0.1				
	0.0368	0.0434	0.052	1.2
0.25				
	0.9497	0.9345	0.919	0.98
∞				
$\bar{\sigma}(^{235}U)$:		1245mb	1250mb	
			0.4%	

* ^{252}Cf fission spectrum component below 0.25 MeV enhanced by a maximum of 30%, which is the 2σ uncertainty limit given in Table II.

The normalization of fission cross sections to an absolute fission neutron source, therefore, is not limited by any credible uncertainty in the fission spectrum shape. Source strength and fissionable deposit mass errors would dominate.

Absolute Neutron Flux Transfer

Neutron fields which exhibit a near-fission spectrum energy distribution above about 1 MeV exist in environments of high technological interest. Prototype design and fuels test reactors, cores of breeder and light water reactors, fast and fusion reactor blankets, andnuclear weapons are common examples. Even in more remote regions near a thermal power reactor pressure vessel, the fission neutron distribution in the MeV range is not largely distorted over the response range of a threshold detector. It is feasible and simple to consider the measurement of fast neutron fluxes in such environments by a transfer of activation detector responses from a calibrated californium fission neutron source. No absolute detection measurements are required and the effects of cross section errors, often considerable, are relaxed. For threshold detectors which sample a large fraction of the fission spectrum (e.g., ^{237}Np(n,f), ^{238}U(n,f), and In(n,n')), detailed issues of fission spectrum shape are of little consequence. As with any method of neutron flux determination, extraneous information regarding the neutron spectrum of interest is required for a correction that depends upon the departure of the spectrum from that of the californium fission spectrum. Table V shows spectrum-averaged cross sections above 1.4 MeV for ^{238}U(n,f) accompanied by an estimate of the response fraction below 1.4 MeV. As an example, the spectrum correction for a fast flux transfer measurement using ^{238}U(n,f) in a Light Water Power Reactor Core would be only a few percent.

The ^{252}Cf fission sources mentioned in the previous section can be set up for isolated detector irradiations, providing fission neutron fluences in the range of 10^{13} n/cm^2. Such fluences make it possible to calibrate activation detectors with half-lives as long as one year. Computational capabilities also exist for estimating source and detector single-scattering corrections to the ideal free-field flux given by a distance measurement and the neutron source strength.

Neutron fields which do not have a significant low-energy component also can be subject to a total flux transfer method. The fission cross section of ^{239}Pu is energy-independent to within ± 6% between 10 keV and 5 MeV. Spectrum-averaged cross sections for ^{239}Pu(n,f) in Table V indicate the range of neutron environments in which a Pu fission detector may be used to obtain total neutron fluxes based on exposure to known fluences of californium fissions neutrons. For the Fast Test Reactor (FTR) Core, a spectrum typical of existing or planned sodium-cooled fast breeder reactors, the spectrum correction for a total neutron flux transfer from ^{252}Cf is about 5%.

TABLE V, SPECTRUM AVERAGE CROSS SECTIONS FOR ^{239}Pu(n,f) AND ^{238}U(n,f) IN NEUTRON FIELDS OF TECHNOLOGICAL IMPORTANCE

	Average Energy E_{av}(MeV)	$\sigma_f(^{239}Pu)$ $\overline{E > 0.4\ eV}$ (barns)	$\sigma_f(^{238}U)$ $\overline{E > 1.4\ MeV}$ (barns)	$\sigma_f(^{238}U)$ Response below 1.4 MeV
FISSION SPECTRA				
^{252}Cf	2.13	1.790	0.53	2.2%
^{235}U	1.97	1.783	0.52	2.5%
ISNF	1.07	1.852	0.51	3.6%
SIGMA SIGMA	0.76	1.79	0.51	4.2%
BIG TEN	0.58	1.62	0.51	5.1%
CPRMF	0.71	1.79	0.51	4.6%
FTR CORE	0.53	1.87	0.49	5.4%
LWR CORE	0.59	~ 15	0.52	2.8%
LWR PRESSURE VESSEL		~ 16	0.56	1.8%

Conclusion

Fission neutrons from ^{235}U (thermal-neutron-induced fission) and ^{252}Cf (spontaneous fission) are two of the best known fast neutron spectra available for nuclear technology application. This assertion is based upon the large number of measurements which exist and the multiplicity of neutron spectrometry techniques employed. An evaluation of the most important of these energy distribution measurements gives a two-fold result:

1. The collection of data may be represented over a primary energy range (0.25 to 8 MeV, 94% of the spectrum) by a conventional Maxwellian description ($\chi(E) \sim \sqrt{E}\ \exp(-1.5\ E/E_{av})$) with $E_{av} = 2.13$ MeV for ^{252}Cf and $E_{av} = 1.97$ MeV for ^{235}U. The average departure of experimental data from these reference Maxwellian shapes is $\lesssim$ 5% over the primary energy range.

2. A seven-group spectrum of adjusted Maxwellian segments describes the data over all energies. Estimated uncertainties over the primary energy range are between ± 1% to ± 4% (1σ) and ± 3% to ± 8% (2σ). Outside of this energy range (6% of the spectrum) uncertainties are between ± 5% and ± 15% (1σ) (see Table II).

The reference Maxwellian shape which differs by $\lesssim$ 2% from the final segment-adjusted spectrum between 0.25 and 8 MeV is adequate for many applications. It may be used also as a normalization to obtain critically evaluated quantities with the segment-adjusted spectrum (e.g., computed fission-spectrum-averaged cross sections).

A brief examination of two important integral measurements with fission neutrons (see Table III) indicates better agreement with prediction than has been the case for some time. The application of measurements with fission neutrons to differential cross section normalization and neutron flux transfer are described as feasible procedures.

References

1. T. Wiedling, Proc. Symp. on Neutron Stds. and Flux Normalization, ANL (1970). A. B. Smith, Proc. Consultants Mtg on Prompt Fission Neutron Spectra, Vienna (1971). A. Koster, Ibid., Vienna (1971).

2. L. Green, et al., Nucl. Sci, Eng., 50, 257 (1973). H. Knitter et al., Atomkernenergie, Bd. 22, p84 (1973). W. Meyer et al., Trans. Am. Nucl. Soc., 19, 480 (1974). L. Jeki et al., Proc. Mtg. on Prompt Fiss. Neut. Spectra, Vienna (1971).

3. H. Werle and H. Bluhm, Jour. of Nucl. Energy, 26, p.165 (1972). J. Meadows, Phys. Rev. 157, 1076 (1967). H. Conde and G. During, Arkiv for Fysik, 29, 313 (1965). Yu. S. Zamyatin et al., Nucl. Data for Reactors (Proc. Conf.), Helsinki (1970).

4. N. Islam and H. Knitter, Nucl. Sci. Eng; 50, 108 (1973). P. Johansson et al., Nucl. Data for Reactors (Proc. Conf.), Helsiniki (1970); also this conference.

5. L. Cranberg, G. Frye, N. Nereson, and L. Rosen, Phys. Rev. 103, 662 (1956). E. Barnard et al., Nucl. Phys. 71, 228 (1965). R. Watt, Phys. Rev. 87, 1037 (1952).

6. J. Terrell, Phys. Rev. 113, 527 (1959).

7. J. Grundl, Proc. Symp. on Neutron Stds. and Flux Normalization, p. 417, CONF-701002 (1971).

8. A. Fabry, Report BLG 463, SCK/CEN; Mol, Belgium (1972).

9. E. Kiefhaber, D. Thiem, Proc. Consult. Mtg. on Prompt Piss. Neut. Spectra, p. 129, Vienna (1972).

10. V. Spiegel, Nucl. Sci. Eng., 54, 28 (1974).

11. D. Gilliam et. al. This conference.

12. A. Fabry et al. This conference.

13. T. Heaton et al. This conference.

FUNDAMENTAL INTEGRAL CROSS SECTION RATIO MEASUREMENTS IN THE THERMAL-NEUTRON-INDUCED URANIUM-235 FISSION NEUTRON SPECTRUM

A. Fabry
C.E.N.-S.C.K.
2400 Mol, Belgium

J. A. Grundl and C. Eisenhauer
National Bureau of Standards
Washington, D.C. 20234

High-accuracy integral cross section ratio measurements have been performed in the thermal-neutron-induced uranium-235 fission neutron spectrum. This involves the basic fission reactions $^{235}U(n,f)$, $^{239}Pu(n,f)$, $^{238}U(n,f)$ and $^{237}Np(n,f)$; and the gold capture and $^{115}In(n,n')^{115m}In$ dosimetry reactions. The uranium-235 fission neutron spectrum is generated at the center of a one meter diameter spherical cavity within a graphite thermal column. Simple and variable geometrical arrangements were used and evaluated for neutron field purity. The fission rates were determined with the NBS double fission chamber as well as with others of different size and design. All fission detectors were validated within a parallel program of interlaboratory comparisons in the MOL-ΣΣ Standard Neutron Field. The activation rates have been measured with calibrated gamma-ray spectrometers. The resulting integral cross section ratios relative to the $^{238}U(n,f)$ reaction are, for $^{235}U(n,f)$: 3.94 ± 0.08; $^{239}Pu(n,f)$: 5.93 ± 0.13; $^{237}Np(n,f)$: 4.35 ± 0.13; $^{115}In(n,n')^{115m}In$: 0.620 ± 0.019 and; $^{197}Au(n,\gamma)^{198}Au$: 0.287 ± 0.014.

(Neutron Standards; Uranium-235 Cavity Fission Spectrum; Fission Cross Sections; Dosimetry)

Scope and Objectives

The uranium-235 thermal-neutron-induced fission neutron spectrum is a key standard neutron field[1] for the validation of differential nuclear data needed for fast reactor physics and for neutron dosimetry. In particular, it is one of the few benchmarks identified by CSEWG for the phase II Data Testing of the ENDF/B-IV Dosimetry file,[2] and it has also been selected for similar purposes at the IAEA panel on Nuclear Data for Reactor Neutron Dosimetry.[3] The ratio, $\bar{\sigma}_f(^{235}U, \chi_{25})/\bar{\sigma}_f(^{238}U, \chi_{25})$, of the uranium-235 to uranium-238 fission cross sections in the uranium-235 thermal fission neutron spectrum has been a long-standing challenge to experimenters and evaluators. Predictions from current differential fission neutron spectrum and fission cross section data have persistently and significantly disagreed with direct and indirect integral measurements.[1, 4, 5, 6] Additional integral determinations of this fundamental quantity have been requested in priority 1 by WRENDA 74.

The objective of this work is to provide new, accurate integral cross sections in this standard neutron field for $^{235}U(n,f)$, $^{238}U(n,f)$, $^{237}Np(n,f)$, $^{239}Pu(n,f)$, $^{115}In(n,n')^{115m}In$ and $^{197}Au(n,\gamma)^{198}Au$. Because absolute results are still preliminary, cross section ratios only are presented here. The two non-fission reactions above have been studied in view of their importance for neutron dosimetry.[7] A more extensive documentation of this interlaboratory effort will be published separately.

Impetus for undertaking the present joint experiments come from,

a. the existence of a cooperative links between the National Bureau of Standards Neutron Standard Program and the C.E.N.-S.C.K. Fast Reactor Physics Program;

b. the design, implementation and use of a one meter diameter spherical cavity within the vertical graphite thermal column of the Belgian BR1 reactor.[8] This facility generates intense thermal fission neutron spectrum fields in clean and well controlled environmental conditions;

c. the development at NBS of a capability to measure absolute fission rates per nucleus at remote laboratory sites.[9]

Experimental Approach

Various arrangements are employed to produce thermal neutron-induced fission neutron spectra in the MOL one meter cavity. For most of the work reported here, a cylindrical geometry of the fission source was selected for routine use of fission chambers. Gold results were derived from observations in a separate disk-to-disk source-detector configuration.[10]

In the principal experimental set-up, the exposure zone is within a 1 mm thick co-extruded, homogeneous cadmium tube of inner diameter 3.1 cm and about 2 meter long. The tube is placed vertically along the polar axis of the spherical cavity in the BR-1 thermal column. The bottom of this tube is tightly closed by a cadmium plate while the top is open just above the reactor shielding, in order to allow easy access for fission chamber traverses with the reactor operating at full power. The fission source is a 93% enriched, 0.1 mm thick and 7.7 cm long metallic uranium sheet, coaxially fixed around the cadmium tube at the cavity center. This uranium converter is protected by a very thin (< 0.02 mm) aluminium wrapping. A sketch of this experimental configuration is shown in Figure 1.

Systematic fission chamber and activation traverse measurements, with and without the fission source in place, were performed. In addition further extensive systematic errors were investigated as follows:

a. Four different types of fission chambers have been applied: the NBS gas-flow absolute double chamber,[9] the GfK sealed absolute chambers placed back-to-back,[11] and two types of French chambers [12] calibrated by exposure in a known thermal neutron field and/or in the ΣΣ standard neutron field.[13] All chambers are light in design and holders were either extremely thin aluminium pieces or could be placed very far from the sensitive area. Fig. 2 is a schematic illustration for the three types of instruments.

b. A number of perturbed source configurations were studied. They include doubling the uranium thickness, shortening its length, doubling the cadmium thickness, and for the miniature chambers, exposure within a sleeve of 1.0 cm outer diameter associated with a 0.1 mm thick uranium source 6.3 cm long.

Indium activation foils were exposed within the NBS fission chamber and in a mock up of parallel-plate type French chambers[12] (not illustrated here).

Corrections and Uncertainties

Corrections for fission responses are discussed in References 9 and 11. Corrections associated with the source-detector configuration are amenable to both measurement and computation. Comparisons of experiment and calculation involve three distinct steps that arise from simple arguments of superposition:

1. Exact geometrical calculations of the spatial distribution of the uncollided flux per unit source strength are carried out by means of an NBS code, INTRAN. Radially centered circular foils or annuli, with axis parallel or perpendicular to the cylindrical source axis, are both treated by the code (e.g., all cases of fig. 2). Excellent agreement with experimental traverses is found after suitable corrections have been applied. Figure 3 shows typical axial traverses. The computed flux is used to replace the actual geometry by an idealized one. This flux is equated to $1/4\ \pi z^2$, where z is an effective separation distance between an equivalent point source and point detector configuration.

2. Space and energy dependent wall return neutron fluxes due to both centered and off-centered point sources in graphite cavities are computed by one dimensional spherical discrete-ordinates transport theory. The graphite wall return background responses, which are significant only for non-threshold reactions, are measured by making use of wall return neutron flux spectra at intermediate and epithermal energies in spherical cavities.[14] They are obtained directly from observations made far away from the source and allow unfolding of the reaction rate traverses into pure fission spectrum and wall return contributions. In the principal experimental configuration, the percent central wall return response for $^{235}U(n,f)$ is approximately 14%. This value was checked by varying z over a large range. Resulting wall-returns varied from ~ 2% to ~ 50%. The fission spectrum responses inferred from these measurements were all consistent. Table I presents a comparison of computed and measured ratios, σ_w / σ_χ, of the wall return spectrum average to fission spectrum average cross sections.

Table I. Ratios of integral cross sections: graphite wall return to fission neutron spectra

Reaction	σ_w / σ_χ	
	Computed	Measured
$^{235}U(n,f)$	9.37	9.07
$^{239}Pu(n,f)$	6.67	6.88

3. The neutron field perturbations due to neutron scattering and absorption within the source - detector assemblies can be computed by two-dimensional cylindrical transport theory. This study is still in progress. At present a one-dimensional cylindrical model of the cadmium sleeve has been applied. These S_N calculations indicate an enhancement of the $^{235}U(n,f)$ response by 1%, essentially due to an increase of the total flux (neutron inscattering more important than neutron removal), and a decrease of 1% for the $^{238}U(n,f)$ response, associated with spectral distortion by neutron downscattering. Comparative INTRAN single-scattering, geometrically exact estimates lead to a flux enhancement of 2%. The spectral distortion has not been computed with the INTRAN code. It was used, however, to provide estimates of flux perturbations by the NBS fission chamber (≤ 0.6%). These intrinsic source-detector perturbation corrections are at present the dominating source of uncertainty in the evaluation of these experiments.

Table II presents an inventory of all components of the total central response for the NBS fission chamber in the principal measurement geometry. It was determined that contributions of fast neutron leakage from reactor core are entirely negligible. Photofission is induced primarily by cadmium capture gamma rays with energies of 9.04 MeV, 8.48 MeV and a group around 7.7 MeV. The response from photofission and epithermal core leakage neutrons was derived from background runs (without fission plate*) after subtracting the response to thermal neutron penetration. These neutron intensities were studied by means of bare and cadmium covered dysprosium foils.

Table II. Response components of the NBS fission chambers[a]

Type of data	^{238}U	^{235}U	^{239}Pu	^{237}Np
Total response	41.73	194.9	287.1	182.6
Background responses				
Wall return	0.09	26.8	30.8	0.45
Photofission and epithermal	0.27	0.93	3.20	0.60
Thermal neutron penetration	-	0.63	0.87	-
Impurity isotopes	-	-	1.66	1.68
Fission spectrum response[b]	41.37[c]	166.5	250.5	179.9

[a] Fission/sec. nucleus per monitor count x 10.[20]

[b] Uncorrected for neutron scattering and absorption within the source-detector assembly.

[c] From highly depleted uranium-238 fissionable deposit. A figure of 41.0 is obtained similarly from exposure of a natural uranium deposit.

Table III is a typical example of error appraisal for these experiments. The results of interlaboratory comparisons of the MOL-ΣΣ Standard Neutron Field have been taken into consideration when assigning uncertainties to the isotopic fission rates per nucleus.

The experimental details and error assignments for activation measurements are similar to those outlined elsewhere.[10] Gold was studied in a coaxial disc-to-disc fission source configuration[10] in order to reduce wall return corrections. The relationship to fission rates obtained in cylindrical geometry was established by means of the indium foil monitors. The spectral purity was also extensively investigated.

* TLD measurements have established that the contribution to the total gamma dose due to fission product gamma rays in the source is negligible.

Table III. Major corrections and uncertainties for an NBS fission chamber measurement

Error source	^{235}U	^{238}U	$^{235}U/^{238}U$
Fission chamber response	± 1.5%	± 1.5%	± 1.5%
Cavity wall return background	0.95 - 0.60 (± 0.3%)	1.000 (± 0%)	± 0.3%
Other backgrounds	0.992 (± 0.1%)	0.993 (± 0.1%)	± 0.2%
Intrinsic neutron field perturbation	0.991 (± 1%)	1.010 (± 1%)	± 1%
Instrumental perturbation	1.000 (± 0.3%)	1.006 (± 0.3%)	± 0.6%
Experimental precision	± 0.2%	± 0.2%	± 0.2%
Total uncertainties	± 1.8%	± 1.8%	± 2.0%

Results

Table IV presents the ^{235}U to ^{238}U fission cross section ratios as obtained by means of the three types of fission chambers employed. Each individual value is the average of many different runs in the principal irradiation geometry. Data from the tighter cylindrical assembly used for the French chamber does not differ appreciably and has been included in the final results. It is worth mentioning that the fissionable layers in the GfK and NBS chambers have been used in parts of the MOL-ΣΣ intercomparison measurements.[11]

Table IV. Integral cross section ratios for three types of fission chambers

Fission chamber	$\bar{\sigma}_f(^{235}U,\chi_{25})/\bar{\sigma}_f(^{238}U,\chi_{25})$
NBS	3.94 ± 0.08
GfK	3.93 ± 0.09
SACLAY	3.88 ± 0.10

Table V presents the final cross section ratios measured in this work. They are compared to the predictions of ENDF/B-IV using the DETAN 74 code[15] for integration. The uranium-235 thermal fission spectrum is represented by an evaluated Maxwellian of 1.97 MeV average energy.[16]

Table V. Observed Fission-spectrum-averaged cross section ratios and comparison with prediction

Reaction, r	$\bar{\sigma}(r,\chi_{25})/\bar{\sigma}(^{238}U,\chi_{25})$	
	Measured	Predicted
$^{235}U(n,f)$	3.94 ± 0.08	4.23
$^{239}Pu(n,f)$	5.93 ± 0.13	6.06
$^{237}Np(n,f)$	4.35 ± 0.13	4.49
$^{115}In(n,n')^{115m}In$	0.620 ± 0.019	0.565
$^{197}Au(n,\gamma)^{198}Au$	0.287 ± 0.014	0.291

References

1. "Prompt Fission Neutron Spectra" - Proceedings of a Consultants' Meeting, Vienna, 25-27 August 1971, IAEA.
2. B. A. Magurno, O. Ozer - Trans. Am. Nucl. Soc. 17, 528-529 (1973).
3. Nuclear Data for Reactor Neutron Dosimetry, INDC (NDS)-56/U (1973).
4. A. Fabry - Report Blg-456 (1972).
5. J. A. Grundl, in CONF-701002 (1970).
6. W. N. McElroy, R. J. Armani and E. Tochilin, NSE 48, 51 (1972).
7. W. N. McElroy - Trans. ANS 17, 515 (1973).
8. CEN-SCK Annual Report, Blg-481 (1972).
9. J. A. Grundl et al. - Trans. ANS 17, 516 (1973).
10. A. Fabry, K. H. Czock - Report IAEA/RL 27 (1974).
11. M. Pinter et al. - This conference.
12. M. Guery, A. Jarrige - Revue Physique Appliquée, 6, 121.
13. A. Fabry et al. - Trans. ANS 17, 527 (1973).
14. A. Fabry, J. D. Jenkins - Trans. ANS 15, 940 (1972).
15. C. Eisenhauer, A. Fabry - Code available on request.
16. J. Grundl, C. Eisenhauer - This conference.

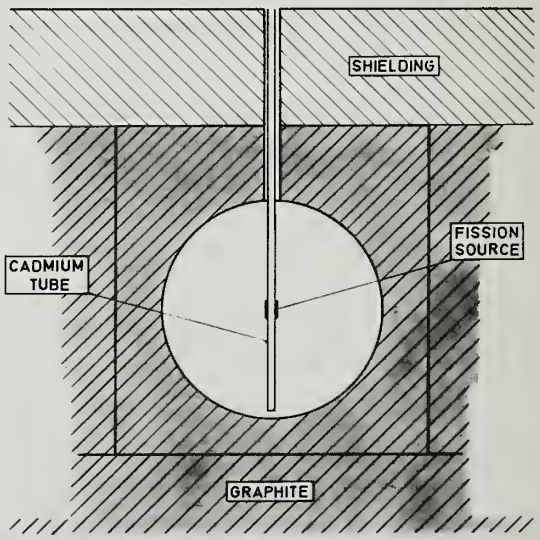

FIG. 1. EXPERIMENTAL CONFIGURATION IN THE SPHERICAL CAVITY OF THE BR-1 THERMAL COLUMN.

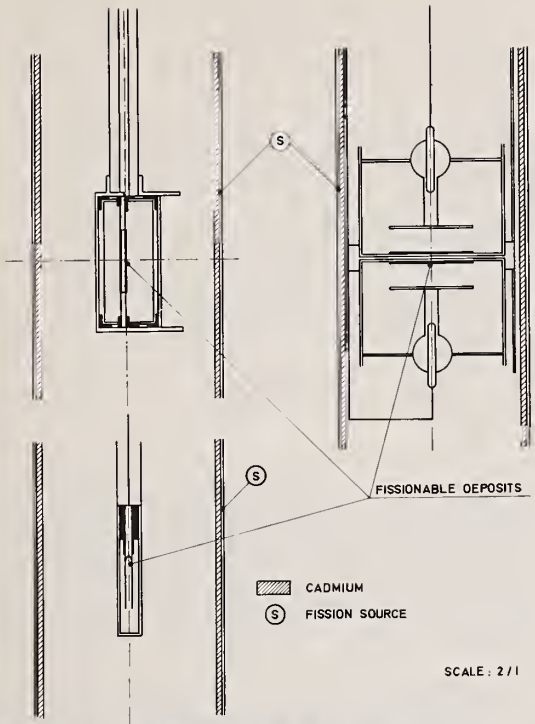

FIG. 2. FISSION CHAMBERS IN THE MOL CAVITY FISSION SPECTRUM NEUTRON FIELD.

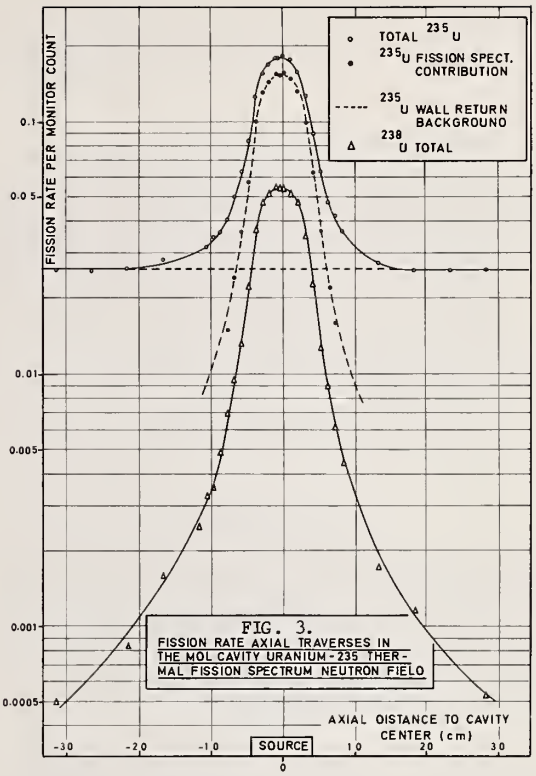

FIG. 3.
FISSION RATE AXIAL TRAVERSES IN THE MOL CAVITY URANIUM-235 THERMAL FISSION SPECTRUM NEUTRON FIELD

INTERLABORATORY COMPARISON OF ABSOLUTE FISSION RATE AND URANIUM-238 CAPTURE RATE MEASUREMENTS IN THE MOL-ΣΣ SECONDARY INTERMEDIATE-ENERGY STANDARD NEUTRON FIELD

M. Pinter, W. Scholtyssek, P. Fehsenfeld (GfK, Karlsruhe, Germany)
H.A.J. van der Kamp, W.H.J. Quaadvliet (RCN, Petten, Netherlands)
A. Fabry, G. and S. De Leeuw, F. Cops (CEN-SCK, Mol, Belgium)
J.A. Grundl, D. Gilliam, C. Eisenhauer (NBS, USA)

Interlaboratory comparisons have been made during the past two years, of techniques that are currently applied for the measurement of fission rates and uranium-238 capture rates in a number of zero-power fast assemblies related to the LMFBR program. This effort has involved the exposure of absolute fission chambers and of activation foils, to the Mol-ΣΣ central neutron field. Long term flux level monitoring accuracy of better than ± 0.5% in Mol-ΣΣ has been achieved. The perturbation of the neutron field by the access hole has been studied extensively. Uncertainties in measured reaction rates estimated by each laboratory relative to flux monitors are between ± 1.5% and ± 3.5%. Interlaboratory agreement for ^{235}U, ^{238}U, and ^{239}Pu fission rates is in the range ± 0.5% to ± 1.3%. Poor agreement is obtained for the ^{238}U capture rate measurements and further interlaboratory efforts are recommended including complementary experimental techniques. A set of ΣΣ preferred values of central fission rate ratios and uncertainties is presented.

(Fission rates, uranium-238 capture rates, Mol-ΣΣ facility, fission chambers, mass assay, fast reactors)

Scope and Objectives

The present work has primarily been accomplished in order to afford a realistic evaluation of the accuracy of the techniques currently applied in zero-power fast assemblies for the measurement of reaction rates important in terms of the fast breeder reactor development. Such measurements are to an appreciable extent the basic benchmark data upon which the assessment of neutron cross-section files ultimately hinge.

The decision to undertake this work programmatically belongs to the German-Dutch-Belgian tripartite Fast Reactor Physics project; a cooperation link has been established in 1972 with the National Bureau of Standards (NBS) Neutron Standard program and the USAEC Interlaboratory LMFBR Reaction Rate (ILRR) program.

The reaction rates investigated in this interlaboratory effort encompass fission in uranium-235, uranium-238, plutonium-239, neptunium-237 and capture in uranium-238. The place selected for the systematic comparison campaigns is the ΣΣ Secondary Intermediate-Energy Standard Neutron Field[1] in the Mol-ΣΣ facility. The choice of this simple, one-dimensional fast source assembly allows to intercompare techniques under clean and constant experimental conditions. In views of its rather extensive neutron spectral characterization, ΣΣ is furthermore a relevant neutron field in which to obtain accurate integral reaction rates for nuclear data testing purposes: this has been the second objective of this work.

The status presented in this paper is limited to the data obtained by experts from RCN (Petten,Netherlands), GfK (Karlsruhe, Germany), CEN-SCK (Mol, Belgium) and NBS (Washington, USA); the last two groups worked jointly and are not identified as separate but it must be noted, that NBS has not participated in the uranium-238 capture rate measurements.

Measurement Techniques

Full and detailed information on measurement techniques, evaluation of data and uncertainties involved in this intercomparison work will be presented elsewhere.[2] In this paper only brief descriptions can be given.

Table 1 Mass assay methods applied by the different laboratories.

	Method of mass assay			
	Mass isotopic dilution	Gravimetric analysis	Quantitative deposition	α-assay 1π, 2π and low geometry
RCN			U-235	U-238 Pu-239 Np-237
NBS	Pu-239		U-235 U-238 Pu-239	U-235 U-238 Pu-239 Np-237
GfK		U-235 U-238	U-235 U-238	U-235 U-238 Pu-239

Fission Rates

The basic technique applied in all laboratories for fission rate measurements is fission fragment counting by ionization chambers. For this purpose small parallel plate type chambers have been developed with as little structural material as possible.[3] While Mol-NBS and RCN use gas flow double fission chambers, GfK prefers the sealed single chamber type. In each case fission rate ratios are accurately measured by back to back operation of two fission foils or two chambers.

Absolute fission rate measurements have two distinct features:

(a) the mass and the isotopic composition of the fissile deposit must be accurately known;

(b) a well determined percentage of fission fragments has to be counted with high precision and reproducibility.

Manufacturing of the deposits and mass assay was done independently by each group. Selected manufacturing methods - molecular plating and vacuum evaporation - yielded layer thickness of 20 $\mu gr/cm^2$ up to 200 $\mu gr/cm^2$ with good homogeneity over the whole active surface. Thus corrections necessary for losses due to fission fragment absorption and low energy corrections for fragments masked by α and γ pulses and electronic noise are small and accurate.

Highly intricate and delicate methods have been applied to determine the fissionable masses of the deposits. Up to three independent techniques were used for certain isotopes (Table 1). In addition, cross checks by fission counting comparison in thermal and fast neutron spectra have been undertaken. Accuracies of $\sim$ 1.5% and less are claimed for deposit masses of the most important isotopes (uranium-235, uranium-238, plutonium-239).

To limit possible error sources in $\Sigma\Sigma$-intercomparison, α-sources were circulated among the laboratories to cross check the α-detectors applied for deposit mass assay. Moreover, RCN and GfK agreed in using a standard set of literature half lifes, needed for evaluation of the α-measurements. Here the values recommended by Vaninbroux[4] were taken.

Standard procedures have been developed by each laboratory for operation of the chambers and evaluation of the measurements to check chamber characteristics and performance continuously. Thus a maximum in reliability and reproducibility is achieved even for experiments in very different neutron fluxes and over long time ranges.

Uranium-238 Capture Rates

Uranium-238 capture rates are determined in all cases by neptunium-239 activity measurement of irradiated uranium foils. Depleted and natural uranium in pure metallic form and as alloy is used. Thicknesses range from 2 - 200 mg/cm^2 uranium. All laboratories count the 277 keV-γ-line of neptunium-239 with a Ge(Li)-detector[5], RCN additionally does coincidence counting with NaI-crystals in the 104 keV region.[6] The efficiencies of the detectors are determined by α-assayed americium-243 sources (RCN, GfK) or by absolute thermal flux calibration and using the well known thermal capture cross-section of uranium-238 (Mol).

γ-ray self absorption, contributing appreciably to the uncertainty of the capture value, especially in the case of the coincidence method, has been determined experimentally by all groups. In some cases significant differences from literature and calculated values were found.

Operation of the Detecting Devices in $\Sigma\Sigma$

The Mol-$\Sigma\Sigma$ facility basically consists of a natural uranium shell centered in a spherical cavity of a graphite thermal column. An inner boron carbide shell is placed concentrically to this source in order to generate the intermediate energy standard neutron field $\Sigma\Sigma$.

Table 2 Corrections and errors associated with unperturbed $\Sigma\Sigma$-centre flux reaction rates

Type of correction	Range of correction	1σ-error/%
A) Fission rates		
Uncertainties related to fission chambers:		
Mass assay		.7 -1.6
Dead time loss	< 1.001	negligible
Counting statistics		.2 - .4
Undetected fragments		
extrapolation to zero	1.002-1.025	.2 - .9
absorption in deposit	1.001-1.038	.35-1.0
Fission in other isotopes[1]	1.000- .995	.0 - .2
Uncertainties related to $\Sigma\Sigma$:		
Monitoring accuracy		.5
Chamber positioning		.2
Neutron scattering and absorption	1.0/1.006	.6
Access hole perturbation	.995/1.0	.5/.2
B) Uranium-238 capture rates		
Uncertainties related to activation foil data and γ-counting:		
Foil mass		negligible
Purity/enrichment	1.000-1.004	negligible
Counting statistics		.2 - .4
γ-self absorption	1.05 -1.35	.3 -2.0
Calibration of γ-detector		.5 -2.0
Neptunium-239 half life		.5
Fission product activity correction	1.000- .995	.2
Uncertainties related to $\Sigma\Sigma$:		
Monitoring accuracy		.5
Neutron self-shielding	1.000	.3

[1] .885 $\pm$ 0.02 in the case of natural uranium deposits

All detecting devices were fixed at the $\Sigma\Sigma$ center with their sensitive part (radius $\leq$ 13 mm) in the horizontal midplane. Reaction rate gradients are weak and never exceed 1.6%/cm; furthermore they are spatially self-compensating. Activation foils have been exposed on a light aluminium support in a strictly identical and fully closed configuration, but structural differences between fission chambers entailed small variations in mounting; e.g. in the way in which the access hole for cables and gas lines (if any) was shielded against thermal neutron penetration.

This is schematized on Figure 1. Each experimenter provided the best possible cadmium screen for his chamber, so as to reduce to a minimum the corrections for response to eventual background thermal neutrons. Such corrections have been extensively scrutinized, using activation techniques, solid state track recorders and various fission chambers whose design allowed exposure in any of the three illustrated setups.

A simple geometrical model predicts that a thermal beam should be rendered unmeasurable (< 0.1% fission rate increase) by adding a slotted cadmium-shield on the uranium outer surface at its intersection with the hole; this was confirmed by experiment, but it was also found that such a screen was unnecessary for application of the NBS and RCN chambers, owing to neutron outscattering and absorption throughout intercepting structures as stem, cable, gas line and support. It has been firmly established on another hand that the epicadmium access hole perturbation is as low as $(0.5 \pm 0.5)\%$; it is spatially uniform and identical for all instruments.

The intrinsic neutron field perturbation due to fast and intermediate energy neutron scattering and absorption within the instruments has been considered identical for all threshold fissionable isotopes and negligible for non-threshold ones. The highest applied correction of 0.6% is taken from detailed single scattering computations for the NBS fission chamber in a similar benchmark neutron field. It is acknowledged that further work regarding this effect might be warranted.

Accurate, long term, run-to-run flux level normalization is a delicate and demanding issue. Up to four independent and redundant activation monitors have been systematically applied; more recently, a permanent fission chamber has also been installed. Though more precise than activation foils, this monitor displayed a slow drift amounting to $\sim$ 2.5% over a period of about eight months. An overall run-to-run normalization accuracy of 0.5% could be achieved only as a result of extremely sustained efforts.

In Table 2 all corrections necessary to get final reaction rates in the unperturbed $\Sigma\Sigma$ center flux are compiled. They are divided according to those related to techniques and those related to $\Sigma\Sigma$.

Results

Reaction rates per nucleus in terms of one of the monitors — the central In-115(n,n') reaction as determined by RCN, Mol-NBS and GfK — are shown in the first three columns of Table 3. They are valid for the unperturbed flux of the $\Sigma\Sigma$ facility. The errors given are 1σ-errors including all sources listed in Table 2. Some of the systematic errors contribute in the same way to the individual values, e.g., those due to half lives necessary for mass assay. Thus the combined errors may overestimate the range in which the intercomparison values can vary. Nevertheless, the fission rates do agree in terms of the requested accuracies for the most important fuel-isotopes in fast reactor studies, although systematic errors of the order of 1% cannot be excluded.

More severe differences exist for uranium-238 capture rates. Different methods show discrepancies of up to 5 percent indicating systematic errors of the same order.

Recommended values for the $\Sigma\Sigma$ center flux are given in the last column. They are the unweighted averages of the individual values with exception of plutonium. Here the GfK rate is weighted by 0.5 because it was measured only one in 1973. At that time some difficulties still existed with the monitoring system.

Table 3 Reaction rates in the unperturbed $\Sigma\Sigma$-centre flux

	Reaction rate per nucleus per ^{115}In(n,n') normalization count			
	RCN	Mol-NBS	GfK	Recommended[5] values for $\Sigma\Sigma$
U-235 (n,f)	27.10 (.3/1.1)[1]	27.00 (.4/1.4)	26.85 (.3/1.2)	26.98 ± 1.3%
U-238 (n,f)	1.515(.4/1.2)	1.522(.3/1.65)	1.500(.4/1.5)	1.512 ± 1.6%
Pu-239(n,f)	31.50 (.35/1.1)	31.85 (.6/1.5)	31.11 (.4/2.0)[3]	[4] 31.56 ± 1.8%
Np-237(n,f)	10.70 (.6/.8)	10.25 (.6/1.8)		10.47 ± 2.5%
U-238 (n,γ) a)[2]	3.011(.7/1.0)	3.107	2.986(.4/1.2)	
b)	3.115(.6/2.6)			
c)		3.143		
f_8/f_5	.0560(.8/1.9)	.0564(.2/1.5)	.0558(.5/1.0)	.0561 ± 1.5%
f_9/f_5	1.162 (.7/1.8)	1.178 (.5/2.0)	1.161 (.5/1.5)	1.167 ± 2.0%
f_7/f_5	.395 (.9/1.6)	.380 (.7/2.2)		.388 ± 2.5%
c_8/f_5 a)	.1106(.6/2.0)	.1151(.6/2.2)	.1112(.5/2.2)	
b)	.1144(.6/2.8)			
c)		.1165(.6/2.5)		

1) Numbers in parentheses give 1-σ random (first) and systematic errors in percent.

2) Detector/Calibration a) Ge(Li)/^{243}Am
b) NaI /^{243}Am
c) Ge(Li)/thermal flux

3) Large systematic error is partly due to monitoring uncertainties.

4) GfK-value was weighted by 0.5

5) Total 1σ errors

Conclusions

Differential and integral reaction rate measurements address the same basic problem: to what accuracy can a quantity of fundamental importance be established as compared to the requirements?

An answer to this question can be obtained by proper comparison of independent techniques, preferably on an interlaboratory basis. For integral measurers standard neutron fields offer a way to do so. The present work is a limited example of the organization effort required for such an interlaboratory undertaking A notable result of this effort has been the improvement of individual laboratory methods and techniques.

Specific conclusions of this intercomparison are:

Fission reaction rates for ^{235}U, ^{238}U, and ^{239}Pu measured independently by three laboratories agree to $\sim \pm 1\%$.

Ratios of integral fission rates are measured to an accuracy of about $\pm$ 2%.

No consistency could be reached in this work regarding the results of uranium-238 capture rate measurements. New intercomparison efforts on a broader basis should be undertaken.

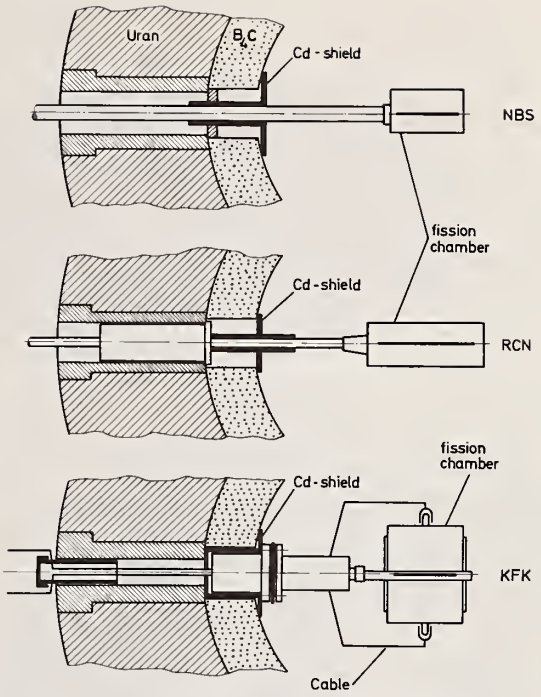

Fig.1 Cross sectional view of fission chambers used by RCN, MOL-NBS and KFK in ΣΣ

References

/1/ A. Fabry, G. De Leeuw, S. De Leeuw: The Secondary Intermediate-Energy Standard Neutron Field at the Mol-ΣΣ Facility. Nuclear Technology 25 2, 349-375 (1975)

/2/ Common Report, in preparation

/3/ J.A. Grundl, D.M. Gilliam, N.D. Dudey, R.J. Popek: Measurement of Absolute Fission Rates. Nuclear Technology 25, 237-257 (1975)

/4/ R. Vaninbroux: The Half-Live of Some Long-Lived Actinides: A Compilation. EUR-5194e, 1974

/5/ A.M. Bresesti et al.: A Method for Absolute Determination of ^{238}U Capture Rates. Journal Nuclear Energy 23, 379-386 (1969

/6/ H. Seufert, D. Stegemann: A Method for Absolute Determination of ^{238}U Capture Rates in Fast Zero-Power Reactors. Nucl. Sci. Eng. 28, 277-285 (1967)

MANGANESE BATH SYSTEMATIC EFFECTS IN MEASUREMENTS OF NU-BAR AND ETA[†]

J. R. Smith
Idaho National Engineering Laboratory
Aerojet Nuclear Company
Idaho Falls, Idaho 83401

Measurements using the manganese bath technique are central to the discrepancy that has existed between measured values of $\bar{\nu}$ for ^{252}Cf. Manganese bath measurements of $\bar{\nu}$ belong to the lower group of values, while the η measurements are consistent with the higher $\bar{\nu}$ values. A three-part study was performed to see if the discrepancy could be explained by differences in manganese bath techniques: (1) A ^{252}Cf source previously calibrated by De Volpi was calibrated in the MTR manganese bath; (2) The recommendations made by De Volpi for altering the MTR eta values were carefully considered; and (3) The results of the Monte Carlo calculation of the MTR experiment, carried out at Bettis Atomic Power Laboratory, were examined in detail. The study produced insignificant changes in the η values.

(Fissile nuclei, eta, ^{252}Cf, nu-bar, manganese bath)

I. Introduction

For several years there has persisted a discrepancy in measured values of $\bar{\nu}$ for ^{252}Cf. This discrepancy has from time to time been declared resolved,[1,2] but continues to cause concern. One way to view this discrepancy is to examine the results of pertinent measurements made using the manganese bath. De Volpi et al[3] and Axton et al[4] have both measured $\bar{\nu}$, the average number of neutrons per fission, for ^{252}Cf. Both have obtained the value 3.725, and both estimate errors of slightly less than 0.5%. Macklin and deSaussure and Smith et al[7,8] measured η, the average number of neutrons per absorption, for the fissile nuclei. Their results agree well, and again accuracies of 0.5% are claimed. Values of $\bar{\nu}$ for the fissile nuclei are derived from measurements of their ratios to $\bar{\nu}$ for ^{252}Cf. Then α, the absorption-to-fission ratio, can be used to connect $\bar{\nu}$ and η through the well-known relation

$$\bar{\nu} = \eta(1+\alpha). \qquad (1)$$

By way of Eq. (1), using the values for α and the $\bar{\nu}$ which were input to the 1968 IAEA evaluation of the fission constants,[9] we can derive the values for $\bar{\nu}$ for ^{252}Cf which are consistent with the η measurements. Table I shows the $\bar{\nu}$ values derived in this manner from the η measurements made at the Materials Testing Reactor (MTR) in 1964.

TABLE I

^{252}Cf $\bar{\nu}$ VALUES CONSISTENT WITH η VALUES

Nucleus	η	α	$\bar{\nu}/\bar{\nu}_{Cf}$	$\bar{\nu}_{Cf}$ Derived
^{233}U	2.298	.09001	.6635	3.775
^{235}U	2.079	.17011	.6417	3.791
^{239}Pu	2.108	.35975	.7618	3.763
			Average	3.776

The average value indicated for ^{252}Cf is 3.776. This is about 1.4% higher than the value measured directly by De Volpi and Axton. Thus, the "hard core" of the discrepancy is of the order of 1%.

The problem of reducing the residual 1% spread is a difficult one. It may be that no single source of error is present in any experiment, but a composite of several small differences in several experiments. In view of efforts to attribute the problem primarily to errors in the η measurements,[1,4] it seemed appropriate to reexamine the systematics of the experiments. The investigation has the following three principal lines of inquiry.

1. The data from a measurements in the MTR manganese bath of the strength of a ^{252}Cf source previously calibrated in the ANL bath were carefully examined. The purpose was to look for any evidence that the MTR bath had an intrinsically greater sensitivity to neutrons, real or spurious, which might explain the difference between the η and $\bar{\nu}$ results.

2. Careful consideration was given to the recommendations of De Volpi[1] for modifying the MTR η values using revisions of three manganese bath corrections.

3. A detailed comparison was made of the corrections to the MTR η experiments, as originally applied,[7] with those indicated by the Monte Carlo calculation performed by Mitchell and Emert.[10] This calculation agreed very well with the original analysis overall, but there remained the question of whether this agreement was really good throughout the experiment or merely resulted from chance compensation of differences in individual corrections.

II. Source Strength Comparison

The ^{252}Cf source which was measured in the MTR manganese bath was designated MB-4. De Volpi had calibrated this source as having an emission rate of 7.467 X 10 neutrons per second as of May 1, 1968.[11] The disintegration constant he recommended was $7.212 \times 10^{-4} day^{-1}$.

The source was used to irradiate the manganese bath seven times during a period of four weeks in August 1969. The average saturated activity observed, corrected for system efficiency and reduced to De Volpi's calibration date, was 2.553×10^{6} sec^{-1}. From this activity, the source strength was derived by means of two different sets of corrections. One was consistent with the corrections used in the η measurements, while the other used corrections consistent with De Volpi's systematics.[12] Since the measurement was made at only one concentration, it was necessary to assume a value for σ_H/σ_{Mn}, the ratio of the thermal absorption cross sections of hydrogen and manganese. Axton's value, 0.024965,[13] was used with the MTR corrections, while De Volpi's value, 0.02531 was used with the second set. The results are summarized in Table II.

[†]Work supported by the Energy Research and Development Administration

TABLE II

^{252}Cf SOURCE COMPARISON

^{56}Mn saturated activity: 2.553×10^6 sec^{-1}
(total bath, corrected to 1 May 1968)

	Correction Factors	
Effect	Original MTR	De Volpi
Leakage	.9988	.9946
High Energy Abs	.9941	.99941†
Fraction Abs in Mn	.34849*	.34475†
Other	.99740	.99740
Total (Product)	.34512	.34180
Source Strength	7.399×10^6sec^{-1}	7.471×10^6sec^{-1}
Difference from De Volpi	-.92%	+.05%
De Volpi calibration		7.467×10^6sec^{-1}

* Assume Axton Value $\sigma_H/\sigma_{Mn} = 0.024965$

† Assume De Volpi Value $\sigma_H/\sigma_{Mn} = 0.02531$

While the agreement with De Volpi's calibration appears excellent, it is evident that the difference in the hydrogen-to-manganese cross section ratio dominates the observed differences. Moreover, the MTR counter calibration turns out to have been accurate to only about 1%. Thus, the agreement seems somewhat fortuitous. This comparison appears to preclude the existence of any large systematic sensitivity to neutrons between the two manganese baths, but is otherwise not particularly revealing as to the validity of systematic corrections employed.

III. The De Volpi Recommendations

Alex De Volpi[1] has recommended certain changes in three corrections applied to the MTR η experiments. If appropriate, these would lower the values by about 0.4%, and go far toward eliminating the discrepancy between ν and η. Specifically, De Volpi would change the MTR η values by +0.3%, -0.5%, and -0.2% through use of modified values for corrections for neutron escape, high energy parasitic absorption, and manganese resonance absorption, respectively.

The author continues to prefer the leakage calculation of Goldstein[14] to De Volpi's recommended leakage correction. For the present purpose, however, it seems unnecessary to discuss the leakage correction separately. This is because De Volpi's leakage and parasitic absorption corrections are inseparably entwined. His determination of parasitic absorption directly depends upon the value he uses for leakage of neutrons from the manganese bath. Therefore, the appropriate correction to discuss is -0.2% for the combination of leakage and parasitic absorption. An adjustment in this direction may be appropriate, as is discussed below.

De Volpi's third recommendation, a decrease in η of 0.2% for manganese resonance absorption, is not appropriate. It apparently resulted from overlooking the fact that the resonance absorption correction for the η experiments enters in a form slightly different from that appropriate for source strength measurements. The intent was to apply Axton's method,[15] which differs from the original correction only in applying a self-shielding correction to the manganese resonance absorption. When correctly applied, this method results in a rise in η of 0.2%, rather than a drop of the same magnitude. Thus De Volpi's "corrected" recommendations would result in no net change in the MTR η values.

IV. Monte Carlo Calculation of the MTR Experiment

Mitchell and Emert[11] have made a thorough Monte Carlo (RECAP) analysis of the MTR measurement of η for ^{233}U. The results agreed extremely well with the original analysis, returning a value of 2.296, compared with the original value of 2.298. Nevertheless, such an agreement could have resulted from a fortuitous cancellation of individually discrepant effects. It was felt that a review of the manganese bath corrections should include a detailed comparison of the correction values implied by the Monte Carlo calculation with those evaluated separately. Mitchell and Emert very kindly made the RECAP output listings available for such a study.

The results of this comparison are summarized in Table III.

TABLE III

COMPARISON OF CORRECTIONS TO Mn BATH EXPERIMENT

	Neutron Fraction	
	Original	RECAP
Incident Beam Effects		
Abs. in sample	0.99302 (E, C)	0.99321
Scatter	0.00430 (C)	0.00485
Abs. in Cd backup	0.00069 (E)	0.00067
Abs. in Cd sleeves	0.00160 (C)	0.00129
Abs. in Al cladding	0.00044(C)	-------
Abs. in Al snout	0.0114 (E)	0.0078
Fission Neutrons		
Leakage	0.012 (C)	0.00246
Absorbed in Al	0.0008 (E)	0.0002
Abs. in Cd	0.0136 (E)	0.0123
Return to sample	0.00286 (C)	0.00519
Mn resonances abs.	0.0098 (C)	0.0099
Oxygen & sulfur abs.	0.0059 (C)	0.0037
Fast mult.	1.0307 (C)	-------

E = Experimental
C = Calculated

Regrettably RECAP did not record the tallies necessary for a direct comparison of the fast multiplication factor for the sample foils. Among those corrections that could be derived, the agreement is on the whole very good. However, there were three effects where differences seemed significant enough to warrant more detailed inquiry.

The RECAP calculation showed about 0.3% less absorption of open beam neutrons in the structural aluminum of the sample "snout" than measurements indicated. In this case the measured value is preferred. The calculation assumed the snout extension was made of pure aluminum, whereas it was 6061 aluminum. The material was unfortunately incompletely specified to the Bettis group when the RECAP model was set up.

The RECAP results indicated a little higher absorption of thermal neutrons in the fissile samples than the original corrections allowed. Upon closer examination, it appeared that the difference was principally due to absorption in the unprotected edges of the sample foils. The original corrections considered such absorptions in the face of the first foil, where the beam struck the sample, but neglected the edges. The RECAP results suggested that these edges

should be considered.

The third significant difference is in the high energy parasitic absorption in oxygen. RECAP yielded 0.285% for this absorption, compared to 0.48% resulting from the calculation by Goldstein.[14] Since this result agreed both in direction and magnitude with De Volpi's net correction, revision of this correction seemed in order.

V. Revisions of the Corrections

Oxygen Absorption

The RECAP analysis and De Volpi's results indicated that the loss to $^{16}O(n,\alpha)^{13}C$ was not as great as given by Goldstein's calculation. Further confirmation came from a 46-group diffusion theory calculation of the MTR η experiment made with the MONA[16] code. MONA agreed very well with the RECAP results. Since both these calculations used ENDF/B cross section, it was appropriate to investigate the cross section file used by Goldstein.

Goldstein used $^{16}O(n,\alpha)^{13}C$ cross sections from the evaluation by Kalos et al.[17] The ENDF/B file is lower in the 6-8 Mev region, due principally to differences between the preliminary and final values for the measurements of Davis et al.[18] A repetition of the Goldstein calculation is appropriate, but not at hand. Therefore, a renormalization of his result for the oxygen correction was attempted in terms of the average over the manganese bath spectrum of the oxygen absorption cross section. As shown in Table IV, the renormalized Goldstein calculation is in good agreement with the RECAP and MONA results, yielding 0.32% absorption compared to 0.28%. On the other hand, Version IV of ENDF/B is now available, and shows slightly increased cross sections for $^{16}O(n,\alpha)^{13}C$. As long as renormalization was in order, it was decided to renormalize to Version IV. The average oxygen absorption for the three renormalized calculations is 0.35%. Retaining Goldstein's value of 0.11% for the loss to $^{32}S(n,p)^{32}P$, we have a total parasitic absorption correction of 0.46%.

Other Adjustments

To the adjustments in corrections already mentioned were added recalculation of all fast multiplication corrections, using our original Monte Carlo program with ENDF/B-III cross sections, and recalculation of scattering by the sample cladding material, which was neglected in the original analysis. The revised manganese resonance absorption correction is based on Axton's method[15] to include self-shielding effects, but is normalized to an above - 1/V resonance integral of 8.4 barns[20] instead of the 8.0 barns used by Axton. The correction changes are summarized in Table V. The changes are of fairly random sign and mainly small, except for the scattering correction for the nickel-clad ^{239}Pu sample. The latter change had only a modest effect on the ^{239}Pu η value, as only a part of the data taken involved nickel-clad samples.

TABLE IV

NEUTRON LOSS BY $^{16}O(n,\alpha)^{13}C$

Calculation	Calc. Loss (%)	Norm to ENDF/B-III	Norm to ENDF/B-IV
GOLDSTEIN	.48	.323	.381
RECAP	.285	.285	.336
MONA	.283	.283	.334
		Ave. .297	Ave. .350
Loss to $^{32}S(n,p)^{32}P$		.11	.11
Total loss to charged particle interactions		.407	.407

Adopted correction factor: 1-.0046 = .9954 ± .0010

Cross Section Set	$\bar{\sigma}$ *
Kalos et al	.0842
ENDF/B-III	.0566
ENDF/B-IV	.0668

*$^{16}O(n,\alpha)^{13}C$ average cross section, weighted over spectrum of MTR Manganese Bath

VI. Readjustment by Least Squares Analysis

With the revised correction outlined above, it is appropriate to reanalyze the whole system of MTR η measurements by the method of least squares. The values to be shown here must for the present by considered interim values, pending consideration of the results of new Bettis Monte Carlo calculations[19] and of experimental studies now being made of fast multiplication and indirect multiplication effects. Preliminary indications are that any changes forthcoming from either of these sources will be in the neighborhood of one or two tenths of a percent. Such results will not appreciably affect the picture presented here.

TABLE V

REVISIONS OF CORRECTIONS TO THE η EXPERIMENTS

Effect	Original	Revised	Effect on η
$^{16}O(n,\alpha)^{13}C$ & $^{32}S(n,p)^{32}P$	0.9941 ± .002	0.9954 ± .002	-.17%
Mn Res. Abs.	1.0098 ± .002	1.0083 ± .002	+.15%
*Indirect Mult, foil edges	sample - dependent		-.15%
*Scatter (Al clad)	sample - dependent		+.1%
*Scatter (Ni clad Pu)	0.9988 ± .0012	0.9899 ± .0013	+.9%
*Fast Mult., ^{233}U	no change		0.0%
*Fast Mult., ^{235}U	1.0149 ± .002	1.0146 ± .002	+.03%
*Fast Mult., ^{239}Pu	1.0237 ± .002	1.0240 ± .002	-.03%
*Fast Mult., ^{241}Pu	1.0149 ± .002	1.0130 ± .002	+.19%

*Representative examples

Table VI summarizes the results of the reanalysis for the data at 0.0253 eV. The 0.060 eV data have not yet been reanalyzed. Shown in separate columns are the results for the original 0.0253 eV data, the data taken in 1967 when the ^{241}Pu measurements were made, and a composite analysis including both sets of data simultaneously. Since the third set of values comes from a separate least-squares run, it does not necessarily represent averages from the first two columns.

For the second two columns the errors include not only the values yielded by the least-squares analysis, but an enlarged error including a contribution of 0.2% representing an ambiguity in the effect of solution concentration changes. The ^{241}Pu result includes also a 0.1% contribution convoluted to the ^{241}Pu error for uncertainties in the decay corrections.

TABLE VI

REANALYZED η VALUES

Nucleus	η (1964 data)	η (1967 data)	η (All data)
^{233}U	2.298 ± .009	2.291 ± .010	2.295 ± .009
^{235}U	2.080 ± .010	2.082 ± .009	2.081 ± .009
^{239}Pu	2.110 ± .008	2.106 ± .009	2.110 ± .008
^{241}Pu	not measured	2.166 ± .010	2.165 ± .010

After all the additional analysis that has gone into this revision, it appears that the errors in the corrections are reasonably random in sign. They almost balance out, leaving the η values essentially unchanged. The differences between the revised values and the originally published values are not statistically significant. This study revealed no justification for either lowering the η values or for expanding their errors to allow better agreement with the manganese bath measurements of $\bar{\nu}$ for ^{252}Cf. The discrepancy of 1% remains.

VII. Acknowledgments

The author would like to express his appreciation to A. De Volpi for discussions concerning manganese bath techniques, to J. A. Mitchel and C. J. Emert for providing the RECAP output and its interpretation, and to F. W. Spraktes for counsel in the least-squares reevaluation.

References

1. A. De Volpi, ANL-7830 (1971)
2. J. W. Boldeman, Nucl. Sci. Eng. 55, 188 (1974)
3. A. De Volpi and K. G. Porges, Phys. Rev. C 1, 683 (1970)
4. E. J. Axton, EANDC (E)-754 "U", p. 20 (1972)
5. R. L. Macklin et al, Nucl. Sci. Eng. 8, 210 (1960)
6. R. L. Macklin et al, Nucl. Sci. Eng. 14, 101 (1962)
7. J. R. Smith et al, IDO-17083 (1966)
8. J. R. Smith and S. D. Reeder, in "Neutron Cross Sections and Technology," NBS Spec. Publ. 299 1, 590 (1968)
9. G. C. Hanna et al, At. Energy Review, Vol. VII, No. 4, p.3 (1969)
10. J. A. Mitchell and C. J. Emert, Proc. 3rd Conf. Neutron Cross Sections and Technology CONF-710301 (Vol. 2) p. 605, (1971)
11. A. De Volpi, private communication
12. A. De Volpi and K. G. Porges, Metrologia 5, 128 (1969)
13. E. J. Axton et al, J. Nucl. Energy Parts A/B 19, 409 (1965)
14. H. Goldstein, Trans. Am. Nucl. Soc. 5, 89 (1962)
15. E. J. Axton and T. B. Ryves, J. Nucl. Energy Parts A/B 21, 543 (1967)
16. G. E. Putnam, ANCR-1051 (1972)
17. M. H. Kalos et al, UNC-5038 (1962)
18. E. A. Davis et al, Nucl. Phys. 48, 169 (1963)
19. J. J. Ullo and M. Goldsmith, Paper GB3, this conference
20. R. Sher, in "Neutron Cross Sections and Technology," NBS Spec. Publ. 299 1, 253 (1968)

ABSOLUTE ^{235}U FISSION CROSS SECTION FOR ^{252}Cf SPONTANEOUS FISSION NEUTRONS

H. T. Heaton II, J. A. Grundl, V. Spiegel, Jr., D. M. Gilliam, and C. Eisenhauer
National Bureau of Standards
Washington, D. C. 20234

A measurement of the absolute ^{235}U fission cross section for ^{252}Cf spontaneous fission neutrons has been performed with two double fission chambers in compensated beam geometry. The fission chambers are mounted 10 cm apart on opposite sides of a small volume, single encapsulated ^{252}Cf source (4×10^9 n/sec, 0.34 cm^3 capsule vol; ∿2 g steel and aluminum). In this geometry the effect of source position errors is small. The ^{252}Cf neutron source strength was determined with a Manganous Sulfate Bath relative to the internationally compared Ra-Be photoneutron standard neutron source, NBS-I, presently known to ±1.1%. Uncertainty in the Manganous Bath comparison of NBS-I and the Cf source was ±0.4%; the ^{235}U fissionable deposit masses have been ascertained to ±1.3%. Five scattering corrections were applied to the data: source capsule (0.6 ± 0.8)%, fission chamber (1.1 ± 0.4)%, support structure (0.6 ± 0.5)%, platinum deposit backing (1.3 ± 0.8)% and total room return (0.5 ± 0.2)%. The observed ^{235}U fission cross section is 1204± 29 mb. A computed value of 1245 mb is obtained using an evaluated ^{252}Cf fission neutron spectrum and ENDF/B-IV for the $^{235}U(n,f)$ cross section.

(^{235}U (n,f); ^{252}Cf; spectrum averaged cross section; fission spectrum)

Introduction

Intense ^{252}Cf spontaneous fission sources of known source strength and small volume and mass, are attractive neutron sources for performing absolute cross section measurements in elementary geometry. An absolute determination of the ^{235}U fission cross section for ^{252}Cf neutrons has been carried out with two double fission chambers, the NBS set reference and working fissionable deposits, and the NBS Manganous Sulfate Bath Facility.

Important features of the measurement are: (1) establishment of the ^{252}Cf source strength relative to the internationally compared Ra-Be photoneutron standard neutron source, NBS-I; (2) two fission chambers in "compensated beam geometry" for reduced sensitivity to source position; (3) residual scattering corrections for the fission chambers, deposit backings, and the neutron source based on both computation and experiment; (4) investigation of the neutron return from the environment by employing the ^{252}Cf source itself as a background probe; and (5) ^{235}U deposit masses based on absolute alpha counting, quantitative deposition, and thermal fission comparison counting.

The purpose of this measurement is to provide normalization data for differential cross section measurements and for the validation of evaluated nuclear data. The results of this experiment are directly applicable for these purposes because the fission spectrum shape uncertainties are of little significance. For any credible departure of the fission spectrum shape from its normal Maxwellian description, the value of the $^{235}U(n,f)$ cross section will not vary by more than ∿0.4%.[1]

Source Detector Arrangement

Two double fission chambers were mounted in a light frame on opposite sides of a single ^{252}Cf source as shown in Fig. 1. This "compensated beam geometry" reduces source position errors in all directions to second order. A source displacement of 1 mm changes the sum of the two chamber responses by less than 0.1%. With such an experimental geometry, all of the important distance measurements can be undertaken without the source in place.

Data were taken in the orientation shown in the figure and also with both chambers rotated by 180°. This rotation eliminates the need for fission fragment momentum corrections. The count rate for each ^{235}U deposit was obtained by means of a triple-scaler counting system. These pulse recording systems provide on-line checks of chamber performance and

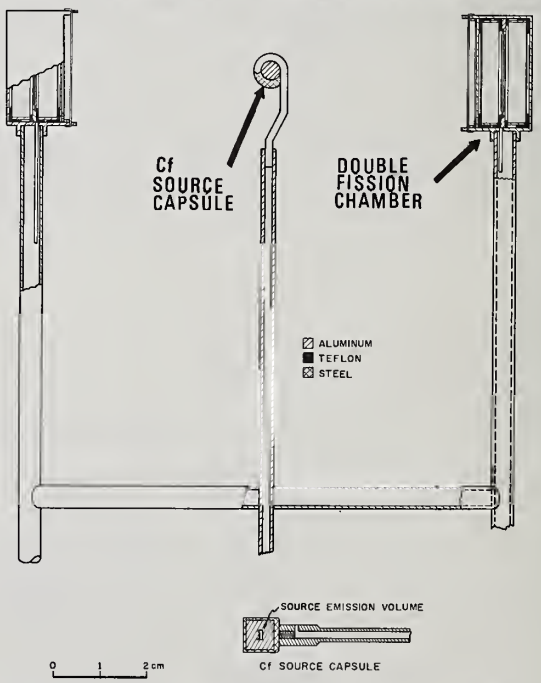

Figure 1. Experimental arrangement of Cf source and two NBS double fission chambers.

redundancy of pulse counting.[2]

The determination of fissionable deposit separation distances also involved redundant procedures. Three distance measurements were performed with a theodolite before each placement of the neutron source for a fission rate measurement: (1) chamber separation between the front or back faces of each chamber; (2) the distance between reference scribe marks on the chamber stems; and (3) the position of a replicated dummy source capsule and holder in place as shown in Fig. 1. The angle readings of the theodolite were transferred to a distance scale by means of a steel rule (calibrated to ±18 μm) mounted at the chambers in the same plane as the scribe marks. The reproducibility of the theodolite measurement is ±75 μm. The position of each fissionable deposit relative to the top of the chamber was determined in separate bench measurements with a depth micrometer fitted with an electrical contact. For three of the deposits used, internal positions were determined to an accuracy of ±45 μm; a fourth platinum deposit backing which had a dimple in it was uncertain to ±90 μm. These various position errors lead to an uncertainty in the ^{235}U fission cross section of ±0.6% for a 10 cm deposit separation.

The distance measurements were verified in two ways. First, the optically determined distance obtained from the scribe separation and from the chamber face separation was compared with the distance between the chamber faces determined mechanically with hand-held calipers. Agreement with the theodolite measurements was within ±0.1%. The second and more comprehensive distance check made use of position measurements of the dummy source which was also recorded routinely with the theodolite. This distance, which was measured to ±0.3%, along with the counting rate in each chamber, predict a mass ratio for the deposits in the two chambers. This can be compared with the mass ratio obtained directly from back-to-back thermal beam comparisons. For the seven measurements used in determining the absolute ^{235}U cross section, the distance determined ratios agreed with the thermal beam comparison to (0.1 ± 0.4)%.

Two corrections must be applied to the fission rate data: (1) 0.75% for the finite size of the fissionable deposit (12.7 mm-diameter oxides on polished platinum discs 19.1 mm-diameter and 0.13 mm thick); and (2) an average 0.1% for combined effects of small displacements of the exact midpoint source position, and deposit mass differences.

Fission Source Strength Calibration

An internal detail of the ^{252}Cf fission source is shown in Fig. 2. The source approaches an idealized point source with a source emission volume of about 1.4 mm^3 and a maximum extension of 1.5 mm. The $(CfO)_2SO_4$ pellets are encapsulated in a steel and aluminum capsule of ∿2 g and 0.34 cm^3. The x-ray photograph of the source show the emission volume to be centered to within 80 μm axially and 170 μm radially.

Figure 2. X-ray of ^{252}Cf fission neutron source. Californium deposit is at the center of the cylindrical capsule.

The Cf source was calibrated in the NBS Manganous Sulfate Bath Facility against the internationally compared Ra-Be photoneutron standard source, NBS-I. The induced, saturated manganese-56 activity of the bath is counted with two gain stabilized scintillation counting systems at a well-shielded remote location by continuously pumping a fraction of the bath volume to them, while simultaneously mixing the bath solution containing the neutron source. One scintillation counter samples the activity at the center of the volume and the second views a fraction of the same volume through a collimator. The first counter operates at about 200 cps for NBS-I (1.25×10^6 neutrons/sec) and would be paralyzed for the Cf source. The second counter operates at about 2500 cps for the Cf source but close to background for NBS-I. Relative counter efficiencies are obtained with intermediate strength sources of about 10^8 neutrons/sec. The counter ratio was measured to be 262.3 ± 0.15% by continuously multiscaling the saturated count recorded by both systems at a count rate of 12 Kcps for the first counter. In addition, the saturated activity for the first counter was calculated from multiscaled data started about 10 hours after the circulation system was stopped. This calculated activity agrees with that obtained from the two counter ratio method within the quoted accuracy.

With the help of a least-squares-fitting program extensive dead-time studies as a function of count rate were made on decaying bath activities from several Cf sources. At 12 Kcps the error of 0.15 microseconds determined from these studies, causes an uncertainty of ±0.2% in count rate. Combining this error in quadrature with the ±0.15% error in the counter ratio gives a total random error of ±0.24%.

The Manganous Sulfate Bath Method has been described in detail by Geiger.[3] The error in the absolute calibration of NBS-I as reported by Noyce[4] is ±1.1%, which is two-thirds the linear sum of all errors. The following percent corrections with errors have been applied to the bath activity for the Cf source: (0.9 ± 0.3)% for fast neutron capture by oxygen and sulfur,[5] (0.11 ± 0.05)% and (0.02 ± 0.01)% for fast and thermal neutron absorption by fluorine in the tetrafluoroethylene source holder, and (0.01 ± 0.01)% for thermal neutron absorption in the source.[6] The bath corrections for NBS-I are: 0.26% for thermal neutron absorption in the source and 0.04% for thermal neutron absorption in the source holder. Adding these systematic errors in quadrature to the 1.1% error associated with the calibration of NBS-I gives a total correction and systematic error of (1.30 ± 1.16)%. Adding the systematic and random errors in quadrature gives a total error in the calibration of the Cf source of ±1.18%.

The effective decay constant of the Cf source is determined from the fractional atomic percent of the neutron emitters, (californium 250, 252, and 254), the ratio of alpha particle to spontaneous fission, and the half-lives of the three isotopes. The isotopic content of the source was supplied by the fabricator, Oak Ridge National Laboratory. The half-lives and alpha to fission ratios are contained in a Technical Note by Spiegel.[7] The ^{252}Cf half-life used was 2.638 years.

Fission Fragment Detection

The design and operation of the NBS double fission chamber, and corrections developed for fission fragments undetected - extrapolation of the pulse height distribution to zero energy, and absorption of fission fragments in the deposit -- are discussed by Grundl et al.[2] Only a summary will be presented here.

The experiment was run with a single ^{235}U deposit in each fission chamber back-to-back with a ^{238}U deposit (or other fissionable deposit employed in the fission cross section ratio measurements performed by Gilliam et al.[8]). Two sets of ^{235}U fissionable deposits were used in matched pairs. The nominal areal densities of the two deposit pairs were 190 μg/cm^2 and 460 μg/cm^2, and the masses were matched to 2.7% and 5.5%, respectively. The count rate data from each of the ^{235}U deposits is recorded separately by a set of triple scalers. The uppermost discriminator level is set such that about half of the fission pulses are recorded above it; this serves as a gain stability monitor. The discriminator levels for the other two scalers are set in the valley region of the pulse height distribution and are a factor of 2 apart. The correction for extrapolation to zero pulse height assumes the valley region is flat. For the 190 μg/cm^2 deposits this correction is 0.9%, and for the 460 μg/cm^{2}deposits it is 1.7%.

Corrections for fission fragments absorbed in the deposits are based on a simple t/2r factor, where t is the thickness of the deposit and r is the average range of the fission fragment in the deposit. This correction is 1.3% for the 190 μg/cm^2 deposits and 3.2% for the 460 μg/cm^2 deposit.

The mass assay of the fissionable deposits, enriched to 99.7%, is based on two methods: (1) quantitative deposition from prepared solutions of known concentration, and (2) absolute alpha counting (performed by the NBS Radioactivity Section) combined with isotopic assay from mass spectrometry and alpha decay constants from the literature. The alpha counting results were also compared with mass ratio determinations by measuring back-to-back fission rate ratios in a thermal beam at the NBS Research Reactor. The mass of the NBS reference deposit for ^{235}U has been determined to an accuracy of ±1.2%. The overall mass determination error including that of the reference deposit is ±1.3%.

Neutron Scattering

Five main scattering corrections must be determined. Scattering from aluminum support structures was calculated to be 0.6%. Net scattering from structural components of the source and detector, also estimated by calculation, are 0.6% and 1.1% respectively. Scattering effects of the platinum foil backings were determined on the basis of rotation averaged fission rate data. A correction of 1.3% was applied based on measurements with 0.13, 0.25, and 0.41 mm thick platinum backings. This agrees well with a 1.1% value calculated for neutrons scattered by platinum.

Neutron scattering from the entire room was studied in two ways. First, the source was used to drive local areas of the room with the fission chambers in their normal position 188 cm above the floor. As an example, the return background from the floor was estimated in this way to be 1% with a similar amount from the rest of the room. The second method for examining room return was to measure fission rates versus distance and scale them according to the response of the ^{238}U deposit in its back to back position with the ^{235}U. The total room return background determined from measurements at 10 and 20 cm deposit separation, was about 2%. For all of the cross section measurements reported here, this room return background was greatly reduced by placing a cylinder of cadmium (90 cm long by 69 cm-diameter) around the source-detector assembly. With this room return shield in place the final total room return background correction is 0.45%. Neutrons scattered from the cadimum add < 0.1% to the ^{235}U fission rate.

TABLE I

Error Components
for ^{235}U Fission Cross Section Measurement

	Correction	*Percent Error
Mass of Fission Deposit Pairs (381.4 and 934.0 μg/cm²)		1.3
Source Strength (4×10^9 n/sec)		1.2
Fission in other isotopes	0.9987	0.1
Geometrical Measurements		
Fissionable Deposit Separation		0.6
Finite deposit diameter	1.0075	0.1
Source not at mid-point	1.001	0.2
Undetected Fission Fragments (light deposit)		
Extrapolation to zero pulse height	1.0090	0.5
Absorption in fissionable deposit	1.0132	0.3
Neutron Scattering		
Total room return	0.9955	0.2
Source capsule	0.9940	0.8
Fission chamber	0.9888	0.4
Support Structures	0.9945	0.5
Platinum deposit backing	0.9870	0.8
Total Error		2.4%

*Error in $^{235}U(n,f)$ cross section due to uncertainty in the listed component.

Results and Summary

Absolute fission rates, taken with two double fission chambers in compensated beam geometry, were obtained with a statistical precision of better than ±0.2%. Rotation-averaged results from three runs with matched pairs of ^{235}U deposits show an internal precision of ±0.55%. Other component errors for judging the accuracy of the measurements are listed in Table I. The column "Percent Error" refers to the uncertainty in the fission cross section due to the measured quantity and not to the error in the quantity itself. The correction sum for the three classes shown in the table are (+0.85 ± 0.64)% for geometrical measurement, (+2.23 ± .42)% for undetected fission fragments in the light pair of deposits, and (-3.96 ± 1.32)% for neutron scattering. The total rms uncertainty in the measuring cross section is ±2.4%.

The final result of this experiment for the ^{252}Cf fission-spectrum-averaged ^{235}U fission cross section is 1204 ± 29 mb at a confidence level of 67%. A computed cross section value of 1245 mb is obtained with the ENDF/B-IV ^{235}U fission cross section and the evaluated Cf fission spectrum from reference 1. The error in the computed value due to fission spectrum shape uncertainties alone, at the 95% confidence level, is 0.4%

References

1. J.A. Grundl and C. Eisenhauer, "Fission Spectrum Neutrons for Cross Section Validation and Neutron Flux Transfer, "Proceedings of the Conf. on Nuclear Cross Sections and Technology, March 3-7, 1975.

2. J.A. Grundl, D.M. Gilliam, N.D. Dudey and R.J. Popek, "Measurement of Absolute Fission Rates," Nuclear Technology, 25, 237 (1975)

3. K.W. Geiger, "Recent Improvements in the Absolute Calibration of Neutron Sources," Metrologia, 4, 8 (1968).

4. R.H. Noyce, E.R. Mosburg, Jr., J.B. Garfinkel, and R.S. Caswell, "Absolute Calibration of the National Bureau of Standards Photoneutron Source III Absorption in a Heavy Water Solution of Manganous Sulfate," Reactor Sci. Technol. (J. Nucl. Energy, Part A/B) 17, 313 (1963).

5. W.M. Murphy, "The Correction Factor For Fast Neutron Reactions on Sulphur and Oxygen in the Manganous-Sulfate-Bath Calibration of Neutron Sources, Nucl. Instr. and Methods, 37, 13 (1965).

6. V. Spiegel, Jr. and W.M. Murphy, "Calibration of Thermal Neutron Absorption in Cyclindrical and Spherical Neutron Sources," Metrologia, 7, 34 (1971).

7. V. Spiegel, Jr., "The Effective Half-life of Californium-252, Nuclear Science and Engineering," 53, 326 (1974).

8. D.M. Gilliam, C. Eisenhauer, H.T. Heaton II and J. A. Grundl, "Fission Cross Section Ratios in the ^{252}Cf Neutron Spectrum (^{235}U:^{238}U:^{239}Pu:^{237}Np)," Proceedings of the Conf. on Nuclear Cross Sections and Technology, March 3-7, 1975.

FISSION CROSS SECTION RATIOS IN THE ^{252}Cf NEUTRON SPECTRUM (^{235}U: ^{238}U: ^{239}Pu: ^{237}Np)

D. M. Gilliam, C. Eisenhauer, H. T. Heaton II, and J. A. Grundl
National Bureau of Standards
Washington, D. C. 20234

In a ^{252}Cf neutron field, ratios of spectrum-averaged fission cross sections have been measured by back-to-back counting in a double fission ionization chamber with interchangeable deposits of ^{235}U, ^{238}U, ^{239}Pu, and ^{237}Np. These ratio measurements provide integral tests for evaluated cross section data. The dominant error in the ratio measurements was the ±1.4% to ±2.1% uncertainty in the fissionable deposit masses. Redundant mass assay methods were employed for all deposit nuclides. Corrections of up to (1.4 ± .7)% were necessary for inelastic scattering effects on the neutron energy distribution in the cases of ^{238}U and ^{237}Np. For ^{235}U and ^{239}Pu fission rates, a correction of (0.45 ± .20)% was made for the contribution of neutrons moderated and back-scattered by laboratory structures. The cross section ratios observed in the present measurements were as follows: 1.000: 0.266 ± 1.7%: 1.500 ± 1.6%: 1.105 ± 2.2% for ^{235}U: ^{238}U: ^{239}Pu: ^{237}Np, respectively. In comparison to the observed integral cross section ratios, the corresponding values derived from ENDF/B-IV data were 2.3% to 6.0% lower.

(Fission cross section; ^{252}Cf; fission spectrum; ^{235}U; ^{238}U; ^{239}Pu; ^{237}Np)

Introduction

Measurements of integral cross sections for neutron induced fission in the ^{252}Cf spontaneous fission spectrum have been carried out for several different purposes as part of the NBS program in Neutron Standards. The ratios of the integral cross sections of ^{238}U, ^{239}Pu, and ^{237}Np to the integral cross section of ^{235}U were determined in measurements conducted simultaneously with the absolute determination of the ^{235}U cross section as reported in a companion paper by Heaton et al.[1] One purpose served by the present ratio measurements is that of providing stringent integral tests of evaluated nuclear data files. A more direct, but slightly less accurate test of such data files is provided by the absolute cross section values for ^{238}U, ^{239}Pu, and ^{237}Np which are derived from the combination of the present ratio results and the results of the companion paper on ^{235}U. The integral cross section values may also serve as absolute normalization integrals for relative cross section data from time-of-flight experiments, particularly in the case of ^{239}Pu (or ^{235}U) in which the normalization is insensitive to uncertainties in the ^{252}Cf fission neutron spectrum. Finally, the fission-spectrum averaged cross section of ^{238}U is useful for the purpose of flux transfer measurements in both fast and thermal reactors, because of the dominance of the fission spectrum in the flux above 1.4 MeV in many regions of these reactors.[2]

Experimental Method

The experimental arrangement is shown in Fig. 1. Each of the double fission chambers contains two independent fast ionization chambers. Counts were recorded by triple-scaler systems which have been described in detail in a previous paper.[3] In all runs, a highly enriched ^{235}U deposit was positioned facing the "bottom" chamber of both of the double chambers, and two deposits of either ^{238}U, ^{239}Pu, or ^{237}Np were positioned facing the "top" chambers. The platinum foil backings of the deposits were each 0.013 cm thick so that the back-to-back deposits were separated by 0.026 cm in the radial direction from the neutron source. Fission rate ratios were observed in two different orientations as shown in the figure. Depending on the selection of isotope in the top chamber, the fission rate ratio was found to change by 2% to 4% upon reversal of the orientation. The dependence of the observed ratio on orientation is due to three factors: (a) the flux gradient over the 0.026 cm separation of the deposits, (b) neutron scattering in the platinum backings, and (c) the change in fragment absorption due to recoil of the compound nucleus before fissioning. The fission rate ratios appropriate to the ^{252}Cf fission neutron field were derived from equally weighted averages of the counts in the two orientations.

The mass assay of the NBS set of fissionable deposits and the absolute efficiency of the double fission chamber have been discussed previously,[3] but some special considerations relevant to the present measurements warrant mention here. Deposit thicknesses ranging from 80 to 540 μg/cm^2 were employed over the course of the experiment, but in any given run the thicknesses of the back-to-back deposits were matched within 120 μg/cm^2 so that only small net corrections for detector counting losses were required. Natural uranium deposits (0.720 atom % ^{235}U) rather than depleted uranium deposits were employed in determination of the ^{238}U fission rates. This choice permitted a second path of $^{235}U/^{238}U$ deposit mass ratio determination in addition to the conventional alpha counting assay method. The ^{235}U content of the normal uranium deposits was determined relative to the ^{235}U content of the highly enriched ^{235}U deposits by counting in a thermal neutron beam, while the relative isotopic concentrations for natural uranium are known from mass spectrographic analysis. Fission counting in monoenergetic (2200 m/s) beams and in thermal beams has also been employed to intercompare the NBS reference deposits of ^{235}U and ^{239}Pu.

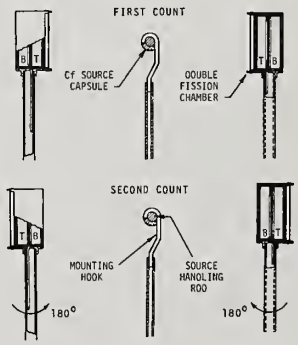

Figure 1. The experimental arrangement. Fissionable deposits of two different isotopes are positioned back-to-back between the two chambers. The "top" and "bottom" chambers are labeled T and B respectively. Fission rate ratios were observed in the two different orientations shown.

The measurements were carried out in an isolated building of lightweight construction. The chambers and source were positioned about 2 meters above the concrete floor. A cadmium enclosure of 69 cm diameter was employed to reduce the laboratory albedo contribution to the fission rate of the fissile isotopes. Back-scattering from the Cd enclosure was calculated to be less than 0.1%. The albedo contribution to the ^{235}U and ^{239}Pu fission rates was found to be (0.45 ± 0.20)% at 5 cm from the source by $1/r^2$-extrapolation of fission rate ratios observed at source-deposit spacings of 5 cm and 10 cm. The $1/r^2$-extrapolation of the fission rate ratios is free of the large geometric uncertainties normally associated with $1/r^2$-extrapolation of absolute count rates. An independent determination of the room albedo was also made by taking counts with the neutron source removed from its normal position and placed near various scattering structures in the room. By driving these scattering structures with the source, it was confirmed that the albedo for the ^{238}U and ^{237}Np was negligible and that the albedo for the fissile isotopes was on the order of 0.5% (within the cadmium enclosure).

Corrections and Estimated Errors

Several underlying sources of systematic bias were eliminated experimentally by averaging the fission rate ratios from the two orientations in which the deposit positions were reversed. Because of the symmetry of the deposit positions in the two irradiation orientations, any bias in the fission rate ratio due to elastic scattering in the platinum backings must be exactly reversed in the transposed orientation. Hence, no correction is required in the rotation-averaged fission rate ratio, in which the two orientations are weighed equally. The same sort of bias cancellation also applies to the biases associated with the flux gradient and with changes in fragment absorption due to compound nucleus recoil.

The correction for pulses falling below the lower integral discriminator of the tripel-scaler systems has been discussed at length previously.[3] This correction is proportional to the magnitude of the differential pulse height spectrum at the discriminator level and has been found to be approximately proportional to the thickness of the deposit. In the present measurements, recoil effects were found to cause slight perturbations in the magnitude of the differential pulse height spectrum at the discriminator level; however, these perturbations also cancel out in the rotation-averaged fission rate ratios.

The corrections for fissions in isotopes other than the principal isotope of a deposit were very small for the highly enriched ^{235}U deposits and high purity ^{237}Np deposits; however, a correction of (0.65 ± 0.3)% was necessary for ^{240}Pu content of the ^{239}Pu deposits, and a correction of (2.76 ± 0.10)% was required for ^{235}U content of the natural uranium deposits. The fission counting corrections are summarized in Table I.

For the isotopes ^{238}U and ^{237}Np, inelastic scattering of neutrons below the fission threshold introduces an additional loss term in the balance of in-scatter and out-scatter. The 16 group transfer cross sections from a LASL compilation[4] were employed in estimating these losses. In addition, an experimental check of the inelastic scattering effect of the platinum backings was made by adding extra platinum between the back-to-back deposits. The corrections for inelastic scattering losses in the source capsule, fission chamber structure, and platinum backings are listed separately in Table II.

TABLE I, FISSION COUNTING CORRECTIONS AND UNCERTAINTIES

TYPE OF CORRECTION OR UNCERTAINTY	MAGNITUDE OF CORRECTION TO FISSION RATE [a] (%)	UNCERTAINTY IN FISSION RATE RATIO [b] (%)
Fragment Absorption	0.54 - 3.42	0.20 - 0.28
Counts Below Discriminator	0.57 - 1.85	0.20 - 0.33
Isotopic Impurities	0.03 - 2.76	0.00 - 0.30
Dead Time	<0.02	0
Electronic Background	~0.05	0
Contamination	<0.02	0
Statistical Precision	——	0.15

[a] The corrections apply to the fission rates observed for each target deposit separately. Back-to-back deposit masses were matched to reduce the resulting uncertainty in the ratio.

[b] The uncertainties listed represent the resulting propagated error in the ratio of the fission rates in the back-to-back deposits.

TABLE II, INELASTIC SCATTERING PERTURBATIONS

STRUCTURAL COMPONENT	CORRECTION FOR ^{238}U (%)	CORRECTION FOR ^{237}Np (%)
Source Capsule	0.7 ± .35	0.35 ± .25
Fission Chamber	0.5 ± .25	0.25 ± .15
Platinum Backings	0.2 ± .40	0.1 ± .20
Total	1.4 ± .7	0.7 ± .5

Results and Comparisons with ENDF/B-IV Data

In Table III the fission-spectrum averaged fission cross section ratios determined from the present measurements are tabulated along with their estimated uncertainties. The errors quoted are "1σ" errors or standard deviations. The error propagation method employed was that described by Bevington,[5] in which it is assumed that residual systematic uncertainties are randomly distributed about zero. The deposit mass assay uncertainty is listed alongside the total propagated uncertainty, because the dominance of this single error factor warrants explicit mention. The present results are also compared in Table III to the corresponding spectrum-averaged cross section ratios derived from ENDF/B-IV data. The discrepancy for the $^{238}U/^{235}U$ cross section ratio is 6.0%, about 3.5 standard deviations.

Table IV shows the absolute cross section values derived from the present work and the absolute measurement of the ^{235}U cross section performed simultaneously.[1] The errors quoted for these absolute cross

TABLE III, FISSION CROSS SECTION RATIOS FOR ^{252}Cf FISSION-SPECTRUM NEUTRONS

NUCLIDES	σ_f RATIO	TOTAL UNCERTAINTY	MASS ASSAY UNCERTAINTY	σ_f RATIO, ENDF/B-IV[a]	DISCREPANCY PRESENT WORK/ENDF
	PRESENT WORK				
$^{238}U/^{235}U$	0.266	± 1.7%	± 1.5%	0.251	6.0%
$^{239}Pu/^{235}U$	1.500	± 1.6%	± 1.4%	1.440	4.2%
$^{237}Np/^{235}U$	1.105	± 2.2%	± 2.1%	1.080	2.3%

[a]The convolution of point-wise cross section data with the ^{252}Cf spectrum was performed using the evaluated spectrum reported in Reference 2.

TABLE IV, ABSOLUTE CROSS SECTION VALUES
(10^{-24} cm^2)

NUCLIDE	$\sigma_f(\chi_{Cf})$ PRESENT WORK	$\sigma_f(\chi_{Cf})$ ENDF/B-IV[a]	DISCREPANCY PRESENT WORK/ENDF
^{238}U	$0.320 \pm 2.8\%$	0.312_6	2.4%
^{239}Pu	$1.80_4 \pm 2.5\%$	1.79_0	0.8%
^{237}Np	$1.33_2 \pm 2.8\%$	1.34_3	-0.8%

[a]See footnote for Table III.

section values include the neutron source strength uncertainty (±1.2%), elastic scattering correction uncertainties (±1.3%), and geometrical errors (±0.6%) as described in Reference 1. Again a comparison with ENDF/B-IV values is given. The discrepancies between ENDF and the present absolute cross section results in Table IV are within the "1σ" error limits of the present work.

Only a very small portion of the discrepancies can be attributed to uncertainties in the ^{252}Cf fission spectrum. Since the ^{239}Pu and ^{235}U fission cross sections are rather flat over the peak region of the fission neutron spectrum, the uncertainties in the spectrum-averaged ENDF/B-IV data due to uncertainty in the ^{252}Cf fission spectrum are small: about 0.1% for ^{239}Pu and about 0.2% for ^{235}U. The thresholds for fission in ^{237}Np and ^{238}U occur near the peak of the ^{252}Cf fission spectrum, so that the uncertainties in the spectrum-averaged ENDF/B-IV data due to uncertainty in the ^{252}Cf spectrum are larger: about 1% for ^{238}U and about 0.7% for ^{237}Np.

It is somewhat surprising that the absolute cross sections (Table IV) are in better agreement than the ratios (Table III), because in this work and in most other cross section experiments, ratios are measured more easily and have smaller quoted errors. It is expected that a further reduction of the present uncertainties will be achieved by continued efforts in fission deposit mass assay and further experimental and analytic studies of the major scattering corrections. The 6% discrepancy in the $^{238}U/^{235}U$ fission cross section ratio is excessive in relation to the accuracy sought for reactor calculations, so that further efforts to resolve this discrepancy are warranted.

References

1 H. T. Heaton II, J. A. Grundl, V. Spiegel, Jr., D. M. Gilliam, C. Eisenhauer, "Absolute ^{235}U Fission Cross Section for ^{252}Cf Spontaneous Fission Neutrons". This conference.

2 J. A. Grundl and C. M. Eisenhauer, "Fission Spectrum Neutrons for Cross Section Validation and Neutron Flux Transfer". This conference.

3 J. A. Grundl, D. M. Gilliam, N. D. Dudey, and R. J. Popek, "Measurement of Absolute Fission Rates". Nuclear Technology, 25, 237 (1975).

4 G. E. Hansen and W. H. Roach, "Six and Sixteen Group Cross Sections For Fast and Intermediate Critical Assemblies". LAMS-2543, (1961).

5 P. R. Bevington, "Data Reduction and Error Analysis For the Physical Sciences", McGraw-Hill Book Company, New York, 59 (1969).

MEASUREMENT OF CROSS SECTIONS FOR THRESHOLD REACTIONS INDUCED BY CALIFORNIUM-252 SPONTANEOUS FISSION NEUTRONS

W.G. Alberts, J. Bortfeldt, E. Günther, K. Knauf,
M. Matzke, G. Rassl, V. Siegel, and K.F. Walz
Physikalisch-Technische Bundesanstalt
D-3300 Braunschweig, F.R. Germany

An open-air experiment for measuring cross sections averaged over the californium-252 spontaneous fission neutron spectrum is described. In a low-scattering arrangement the ^{252}Cf source was enclosed by the sample materials for irradiation. From the source strength (3×10^{-9} s^{-1} as of Jan. 1973) and the activities of the generated nuclides, average cross sections for the reactions $^{27}Al(n,\alpha)^{24}Na$, $^{54}Fe(n,p)^{54}Mn$, $^{56}Fe(n,p)^{56}Mn$, and $^{46}Ti(n,p)^{46}Sc$ were derived. The influence of neutron scattering in the source and samples has been taken into account by means of Monte Carlo calculations; in addition this influence in the samples was studied experimentally by activating samples of various thicknesses.

(Cross sections, neutron source, fission spectrum, threshold detectors, activity measurement, scattering corrections)

Introduction

An important requirement for reactor neutron measurements is a consistent cross section set for threshold detectors. If we look at requests for neutron cross sections for fission reactor measurements[1] or for neutron dosimetry purposes[2] we often find remarks concerning large discrepancies between spectrum-averaged neutron cross sections as calculated from energy-dependent cross sections and mean cross sections measured in what is assumed to be the same neutron spectrum. In our present work we attempt to obtain such a set by measuring reaction rates in the neutron field of a ^{252}Cf spontaneous fission neutron source. The reactions considered - $^{27}Al(n,\alpha)^{24}Na$, $^{54}Fe(n,p)^{54}Mn$, $^{56}Fe(n,p)^{56}Mn$, and $^{46}Ti(n,p)^{46}Sc$ - are included in the list of Category I and II neutron dosimetry reactions[2]. The ^{252}Cf source provides - except for half-life influences - a constant neutron field as to energy distribution and time and therefore seems to be particularly suited for measurements of this kind. In this paper an irradiation facility for low-scattering experiments is described and results for the above reactions are presented.

General Considerations

The reaction rate in a sample irradiated by neutrons is usually expressed in terms of the neutron flux density, atomic cross section and number of atoms in the sample. If a plane foil is irradiated close to a neutron source we find that the neutron flux density varies strongly along the foil surface and the accuracy of determining the flux density depends on the accuracy of measuring small distances.

In our experiment we start from a somewhat different consideration. The reaction rate R can be expressed simply by the product of the source strength Q and the probability p that an emitted neutron interacts within the sample: $R = Q \cdot p$. The quantity p contains all influences on R such as solid angle, path length of the neutron in the sample and sample characteristics. p can be calculated easily in the special geometry of a point source in the middle of a thin spherical shell of the sample material: the reaction probability becomes $p = \Sigma \cdot d$, where Σ is the cross section density and d the thickness of the shell. The measurement of the neutron flux density has thus been reduced to a measurement of the source strength; in addition, small deviations in the relative position between source and sample do not influence the generated activity as much as in a linear geometry.

If the source is not infinitely small and the surrounding sample material is not a sphere, the above equation still holds if the wall thickness d is replaced by an "effective thickness" d_{eff} which contains the corrections for the actual geometry and other effects which change the average path length of the neutrons in the sample. These considerations lead to an expression for the specific reaction rate R/m (averaged over the whole sample):

$$\frac{R}{m} = Q \cdot \frac{N_A}{M \cdot V} \cdot d_{eff} \cdot \langle\sigma\rangle \cdot P \qquad (1)$$

(N_A Avogadro constant
M molar mass
V volume of the sample material
m mass of the sample material
$\langle\sigma\rangle$ atomic cross section averaged over all neutron energies
P relative amount of the respective isotope in the sample).

Therefore we have to determine the source strength Q, the average specific saturation activity of the sample $a = R/m$ and the "effective wall thickness" d_{eff} for our special geometry.

Irradiation Arrangement

The irradiations in the open using a cylindrical ^{252}Cf source were performed in a low-scattering geometry on a 17 meter pole. The sample is mounted around the source behind a water tank near the ground and then moved into the 15m-high irradiation position by a closed circuit of nickel-wire and perlon-cord. Fig. 1 shows the actual shape of the source and the surrounding sample. At the end of the irradiation the sample is separated from the source in the irradiation position within a few seconds, thus determining accurately the end of the irradiation period. In this arrangement we irradiated samples of aluminum (purity 99.999%), iron (99.9%) and titanium (99.4%) for inducing the reactions $^{27}Al(n,\alpha)^{24}Na$, $^{54}Fe(n,p)^{54}Mn$, $^{56}Fe(n,p)^{56}Mn$ and $^{46}Ti(n,p)^{46}Sc$.

Source Strength Determination

The source strength of the two sources was determined using our water-bath facility[3]. Three measure-

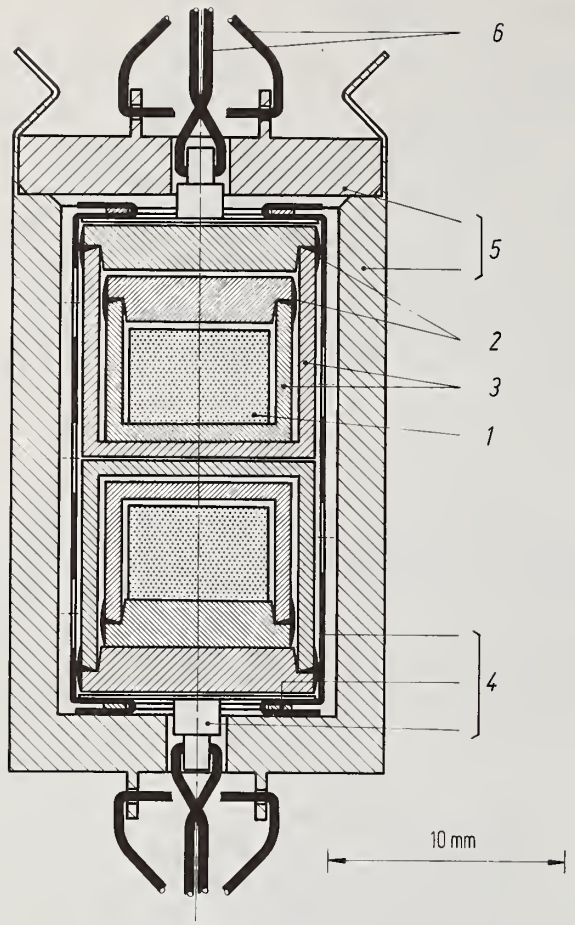

Fig. 1: Cross section through the source-sample combination. Two sources containing the californium-252 in ceramic tablets (1) in double gastight-welded (2) zirkaloy capsules (3) are combined in a thin aluminum hull (4). These sources are enclosed by the sample material in form of a cylindrical case (5). Source and sample are separately movable by the attached nickel wires (6).

ments were performed between January and December 1973, reproducing the source strength value within ± 0.6 %. In our calculations we used an adopted value for the ^{252}Cf half-life of (2.64± 0.02) years[4]. The source strength of both sources was $(2.92\pm0.05)\cdot10^{-9}$ s^{-1} as of January 1, 1973. This value contains corrections for the neutron absorption in the oxygen of the water (0.4 %) and the absorption of fast and intermediary neutrons in hydrogen (1.6 %). The stated uncertainty of the source strength value is the combined statistical (0.6 %) and estimated systematic (1.5%) uncertainty at a confidence level of 68 %.

Activity Determination

The specific saturation activity a of each sample was determined by comparison of the γ-ray emission rate of the sample with that of a standardized solution of the respective nuclide, the specific activity of which was determined by ionization chamber and 4πβ-γ coincidence measurements.

The samples were chemically dissolved and, after sufficient decay of short-lived impurity activities, pulse-height spectra of the γ-radiation were measured with Ge(Li) (30 cm^3) and NaI(Tl) (7.6 cm x 7.6 cm) detectors; integral measurements were used for evaluation as well as full absorption peak area determination. Then, following complete decay of the sample activity in the cases of ^{24}Na and ^{56}Mn, a small quantity of standard solution was added which had about the same activity as the sample solution in order to minimize corrections caused by counting rate effects. The measurement was then repeated in the same counting geometry.

Table 1 shows some details of the measurements. Again the statistical and estimated systematic uncertainties are stated; all uncertainties quoted in this paper are treated as random uncertainties at a confidence level of 68 %.

Table 1: Activity measurements of irradiated samples

Reaction	No. of Samples	γ-ray Detector	γ-energy in keV	Activity Measurement Uncertainty stat.	syst.
$^{27}Al(n,\alpha)^{24}Na$	15	NaI(Tl) Ge(Li)	1369 2754	0.15%	0.5 %
$^{54}Fe(n,p)^{54}Mn$	12	NaI(Tl)	835	0.5 %	0.4 %
$^{56}Fe(n,p)^{56}Mn$	10	NaI(Tl)	847 1811	0.2 %	0.8 %
$^{46}Ti(n,p)^{46}Sc$	6	NaI(Tl) Ge(Li)	889	0.4 %	0.5 %

Geometry and Scattering Corrections

The introduction of an "effective" thickness d_{eff} in eq. (1) for calculating the activation cross sections is advantageous only if d_{eff} is practically independent of material characteristics and cross sections of the detectors, i.e. if d_{eff} depends only on the geometry of the arrangement.

A Monte Carlo code was developed which permits following the path of neutrons - originating at a random position within the sources and having isotropic directional distribution - through source, capsules, and detector. The code was extended step by step to calculate the different interfering influences in different parts of the arrangement; we attempted to limit the uncertainty of d_{eff} to about 1 %. The calculation showed that it was sufficient to use a first collision approximation by considering monoenergetic neutrons, elastic scattering and a mean scattering angle. Thus d_{eff} was determined by averaging the path length in the sample material; the statistical uncertainty of the mean was 0.4 %. Cross sections and average scattering angles were taken from the ENDF/B-IV library and averaged over the energy regions corresponding to the respective detector response functions and over all isotope abundances in sources, hull and detector material.

In the relevant neutron energy region between 3 MeV and 10 MeV about 12 % of the neutrons produced are scattered in the sources and the zirkaloy capsules; the aluminum hull is neglected. The contribution of the scattering processes to the geometrical d_{eff} is only -0.4 % and is hardly energy dependent, as average scattering angle and cross section do not change considerably in this energy region. The neutron absorption in this energy region in source and capsules is assumed to be energy independent; the absorbed neutrons

do not influence these calculations since they are not included in the source strength determination.

Since the influence of neutron energy is neglected we can simply add the corrections for scattering and absorption in the source to the geometrical effective thickness. For the monoenergetic first-collision approximation we assume a systematic uncertainty of 0.6 %. A further uncertainty of 0.6 % is added to account for the uncertain spatial distribution of the ^{252}Cf in the ceramic tablets; this value was determined using the Monte Carlo code by varying position and shape of the tablets.

Considering effects in the detector material itself the self-shielding effect was calculated using the total cross section density Σ_t of the sample material which reduced the geometrical effective thickness by a value δ_t (e.g. 0.8 % to 2 % for Al of 1 mm to 2.5 mm wall thickness and 2 % to 4 % for Fe). Part of the δ_t correction is eliminated by a positive correction δ_s originating from the activation probability of neutrons after a scattering process in the detector material. If one assumes $\Sigma_t = \Sigma_s$ it turns out that $\delta_t + \delta_s \approx 0$; influences of inelastic scattering were not taken into account. Thus d_{eff} was not corrected for self shielding and scattering in the detector material; the uncertainty of this zero correction is estimated to be about $0.25 \cdot \delta_t$ (i.e. 0.5 % for Al and Ti, 1 % for Fe).

The neutron scattering in the surrounding air has not been considered in the calculations. According to ref.[9] the assumption of an additional uncertainty of 0.6 % seems reasonable. All stated uncertainties sum up to an overall uncertainty for d_{eff} of $\pm$ 1.5 % for Fe and $\pm$ 1.2 % for Al and Ti. The following table shows the calculated effective thicknesses of the various samples:

d	0.1	0.16	0.21/0.25+	0.25	cm
d_{eff}	0.1243	0.1978	0.2657	0.3105	cm

The ratio d_{eff}/d shows only minimal dependence on the wall thickness: it denotes essentially the difference between our geometry and the concentrical arrangement of point source and spherical shell.

Results and Conclusions

Table 2 shows the physical quantities used for the evaluation of eq. (1).

Table 2: Input data for eq. (1) for the different reactions

Reaction	Half-Life of the Generated Nuclide	Sample Material[8] Density in $g \cdot cm^{-3}$	Molar Mass in $g \cdot mol^{-1}$	Isotope Abundance in %
$^{27}Al(n,\alpha)^{24}Na$	14.98 h[5]	2.698	26.9815	100
$^{54}Fe(n,p)^{54}Mn$	312.6 d[6]	7.87	55.847	5.82
$^{56}Fe(n,p)^{56}Mn$	2.578 h[7]	7.87	55.847	91.66
$^{46}Ti(n,p)^{46}Sc$	83.85 d[6]	4.505	47.90	7.93

+cylinder jacket 0.21 cm, faces 0.25 cm

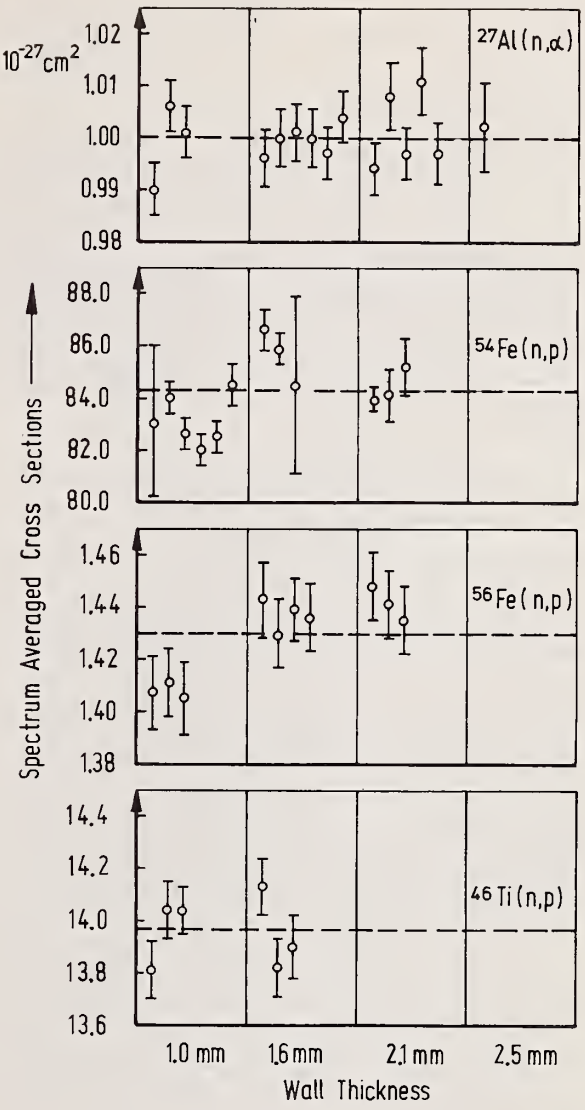

Fig. 2 Cross sections derived from each single measurement. The mean value $\langle\sigma\rangle$ for each reaction is indicated by the dashed line.

Fig. 2 shows the obtained $\langle\sigma\rangle$ values calculated with eq. (1) for each irradiated sample. The error bars indicated do not contain the uncertainty of the source strength nor the systematic uncertainty of d_{eff} since these quantities are common factors to all values.

The mean value of $\langle\sigma\rangle$ averaged over all measurements of one reaction was not obtained by averaging the single $\langle\sigma\rangle$ values but by calculating the weighted mean of the expression $\frac{a \cdot V}{d_{eff}}$ (cf. eq. (1)), where the specific saturated activity a is corrected for the decay of the ^{252}Cf since January 1, 1973, and averaged over all measurements within one sample group with equal wall thickness. We get the following results (cross sections in $10^{-27}cm^2$):

	This Work[§]	Ref.[10]	Calc.[+] Value
$\langle\sigma_{n,\alpha}(^{27}Al,\chi_{82})\rangle$	1.00 ± 0.02	0.86 ± 0.05	0.9994
$\langle\sigma_{n,p}(^{54}Fe,\chi_{82})\rangle$	84.3 ± 1.9	87 ± 3	86.95
$\langle\sigma_{n,p}(^{56}Fe,\chi_{82})\rangle$	1.43 ± 0.03	1.18 ± 0.08	1.527
$\langle\sigma_{n,p}(^{46}Ti,\chi_{82})\rangle$	14.0 ± 0.3[†]	12.4 ± 1.2	13.68

Generally we find better agreement of the experimental values than Kirouac, Eiland and Slavik[10] when comparing with values calculated using energy dependent data evaluated by Simons and McElroy[12]. The aluminum and titanium values are in good agreement whereas both iron cross sections are about 3 % and 6 % lower than the calculated values. This discrepancy may be explained only partly by the inelastic scattering processes not yet regarded.

The technical assistance of Mr. H. Becher and his group, who were responsible for the irradiation experiments, is gratefully acknowledged.

[§]The given uncertainties contain the uncertainties of the source strength, activity measurement and effective thickness as stated above.

[+]Calculation[11] with the energy dependent data of ref.[12] and the fission spectrum representation of ref.[13].

[†]This value ignores possible corrections for competing reactions $^{47}Ti(n,d)^{46}Sc$ and $^{47}Ti(n,pn)^{46}Sc$ (ref.[14]). For practical use the corresponding cross section density is given for the reaction $Ti(n,x)^{46}Sc$: $\Sigma = (6.28 \pm 0.13)\cdot 10^{-5}$ cm^{-1}.

References

[1]World Request List for Nuclear Data Measurements, Report INDC (SEC) - 38/U, Vienna 1974

[2]Proceedings of a Consultants Meeting on Nuclear Data for Reactor Neutron Dosimetry, Report INDC (NDS) - 56/U, Vienna 1973

[3]J. Bortfeldt and M. Matzke, PTB-Mitteilungen 84 (1974), p. 254

[4]R. Vaninbroukx, Report EUR 5194 e, Geel 1974

[5]M.J. Martin and P.H. Blichert-Toft, Nucl. Data Tables A8, 1970

[6]R.G. Helmer and R.C. Greenwood, ANCR-1129 (1973),p.20

[7]L. Varnell and J. Trishuk, Nucl. Instr. and Meth. 76 (1969), p. 109

[8]W. Seelmann-Eggebert, G. Pfennig, and H. Münzel, Chart of the Nuclides, Karlsruhe 1968

[9]C.F. Cook and T.R. Strayhorn in: Fast Neutron Physics, Ed.: J.B. Marion and J.L. Fowler, New York (1960), p. 807

[10]G.J. Kirouac, H.M. Eiland and C.J. Slavic, Topical Meeting on Irradiation Experimentation in Fast Reactors, Jackson Lake Lodge (1973), p. 412

[11]W.G. Alberts, Report PTB-FMRB-60 (1975)

[12]R.L. Simons and W.N. McElroy, Report BNWL-1312 (1970)

[13]L. Green, J.A. Mitchell, N.M. Steen, Nucl. Sci. Eng. 50 (1973), p. 257

[14]W.L. Zijp in ref.[2] p. 103

ABSOLUTE NEUTRON FLUX DETERMINATION IN FAST NEUTRON SPECTRA

I. Schouky, S. Cierjacks, P. Brotz, D. Gröschel, B. Leugers

Institut für Angewandte Kernphysik
Kernforschungszentrum Karlsruhe, F.R. Germany

A flux detector system was developed in order to determine the fast neutron flux between 1-30 MeV obtained with the Karlsruhe isochronous cyclotron. The counter system represents a telescope-like proton recoil device using solid radiatiors and gas scintillation transmission counters. Flux determination is accomplished separately between about 1-6 MeV and ∿5-30 MeV, with a small energy interval of overlap. Below 6 MeV, recoil protons are detected in a single gas scintillation chamber viewed by three photomultipliers requiring a fast coincidence. Above this range, high energy recoil protons are identified by coincidences in three adjacent chambers and by their specific energy losses. Since the transmission of the entire flux counter system is better than 99 %, it can be used for simultaneous flux measurements in partial cross section determination. The accuracy for the determination of the neutron flux is about 5 %.

(Neutron flux determination, gas scintillation transmission counters, $1 \leq E_n \leq 30$ MeV)

Introduction

For partial fast neutron cross section work employing nanosecond time-of-flight techniques, there is a continuing need for neutron flux counters having a flat energy response over a wide energy range and a time resolution of the order of a few nanoseconds. For neutron flux measurements between about 100 keV and several MeV, an excellent detector with such specifications is the black neutron detector invented by W.P. Pönitz[1]. This detector provides simultaneously a high efficiency, a wide flat response and a good timing resolution of only a few nanoseconds, Although the detector is presently used only in the range below about 5 MeV, it is, in principle, applicable for use in the many MeV range. A black neutron detector, which will be employed for flux measurements up to 14 MeV is, presently under construction at Bruyêres-le-Châtel[2].

A completely different approach is presented in this paper. For use with the fast neutron time-of-flight spectrometer at Karlsruhe, a flux detector was developped which represents a telescope-like proton recoil device, using thin solid radiator foils in a gas-scintillation transmission counter. The important characteristics of this system are:

- i) It provides fast time response of a few nonoseconds, due to the gas scintillation counting of the recoil protons.
- ii) It is extremely insensitive for γ-ray counting.
- iii) It provides an essentially flat energy dependence for proton detection over most of the intire energy region between 1-30 MeV.
- iv) The counter device can be used for simultaneous flux measurements during a partial cross section experiment in the same beam in which the sample is irradiated. This is due to the fact that the overall transmission was kept very close to unity (better than 99 %), thus introducing negligible distortion of the incident beam. This possibility is particularly of importance for white neutron sources with a complex and rapidly changing energy dependence of the neutron spectrum on the neutron emission angle.

Of course, the latter advantage of simultaneous measurements can be only achieved on the expense of a low overall neutron detection efficiency of the order of 10^{-4}. But this is of minor importance, if high intensity neutron sources are involved so that counting statistics is not a crucial problem.

Detector operation and design

Principle and arrangement of the detector

Neutron flux measurements over the entire energy region between 1-30 MeV is being accomplished with two different counters, because of the wide range of proton recoil energies and the different background reactions involved in this energy region. In particular, flux measurements are performed separately between ∿1-6 MeV and 5-30 MeV with a small energy range of overlap. In the energy range below ∿6 MeV, where no spurious background from neutron induced charged particle reactions is obtained, the protons from a thin radiator foil are detected in a single gas scintillation chamber viewed by three photomultipliers. For observation of a proton recoil event, a threefold coincidence within ≤ 30 nsec is required. Above the energy range of ∿5 MeV high energy protons from a thick radiator foil are identified by coincidences in three different scintillation chambers, which are arranged in series along the neutron beam axis, and by determination of their specific energy losses.
The arrangement of the flux counters in the neutron beam is shown in fig. 1. Both flux counter systems are placed beyond the last neutron collimator, shown here. In total, three of such collimators along the flight path define a narrow almost parallel neutron beam of $\sim 2 \cdot 10^{-6}$ sr. The two flux counters are set at a distance of ∿1-2 m apart from the simultaneously irradiated scattering samples. The diameter of the cylindrical chamber is chosen sufficiently large compared to the diameter of the traversing neutron beam, so that all massive parts of the chamber are well shielded from neutrons and γ-rays coming from the cyclotron source. Thus the neutron beam traverses only the thin entrance and exit windows of the chambers, the two radiator foils, and ∿25 cm plus 10.5 cm, respectively of the scintillation gas at atmospheric pressure. This results for the present chamber designs in an overall transmission for neutrons ranging between 99,4 % and 99,96 % depending on the incident neutron energy. The lower value of 99,4 % represents the worse case in the narrow resonance regions of argon, where peak cross sections of 10 barns as the worse case are assumed. Detector efficiencies of both flux counters are due to those of geometrically purely decoupled systems. For flux detector II, electronic thresholds are adjusted such that the counter can only detect protons from its own radiator foil.

Detector design

A schematic drawing of the neutron flux detector used for the measurements in the 5-30 MeV range is

shown in fig. 2. The gas scintillation chamber, having an inner diameter of 12.5 cm is made of 4 mm thick stainless steel. Nickel is plated on the wall as reflector material. Each scintillation chamber is viewed by one 56 DUVP Valvo photomultiplier tube. Photomultiplier windows are of 2 mm thick quartz glass. A mixture of 85 % argon and 15 % nitrogen serves as the scintillator gas. The gas is continuously flowing through the chamber at slightly above atmospheric pressure. The solid radiator foil of 20 µm thickness is mounted on a 10.6 cm diameter, 3 mm thick brass ring. The ring diameter is large enough to prevent it to be hitted by the incoming neutron beam. Special radiator foils of polypropylen were selected, which were particularly uniform in thickness. The foils were provided by KALLE AG, Wiesbaden. For background determination, the radiator foil can be moved manually out of beam without opening the chamber.

The design of the second counter (system II of fig. 1) is similar. For this detector, where only one scintillator chamber is used, the three photomultipliers are symmetrically placed on the circumference of the cylindrical part of the detector at relative angles of 120°. The polypropylen foil used in this chamber has a thickness of 10 µm.

Electronics and data acquisition

Fig. 3 shows a simplified block diagram of the electronics, which is essentially the same for both neutron flux counters. From each photomultiplier both, a time and an analog signal is derived. Requiring a fast coincidence within 30 ns, the time-of-flight information is recorded in a digital time-of-flight analyser and accumulated in 4096 time-channels of 2 ns width of a CDC-3100 on-line computer. The corresponding analog signals are combined in a sum amplifier and the sum signal is analysed in 512 channels of a LABEN-FC 60 fast analog-to-digital converter. In the case of the counter system I, the analog information is used for on-line selection of the specific energy loss of the recoil proton, which depends in a particular analytical manner on the neutron time-of-flight. The actual time dependence of the corresponding energy range, defined by the maximum and the minimum employed proton recoil angles are taken from a calibration run prior to the actual flux measurement. All events falling in the allowed dE/dx-band of the plane spanned by the time and the analog information are stored in 4096 channels according to their time-of-flight identification only. For purposes of the calculation of detector efficiencies and simulation of pulse height spectra, a largely channel grouped set of the two-dimensional input data is kept in addition in a 32-time-of-flight channel x 512-analog-channel matrix and stored on a magnetic disc.

An equivalent data acquisition procedure is performed for the other flux counter (system II). For this detector, no on-line data reduction due to dE/dx selection is necessary. Therefore, the time-of-flight information for each event is stored on the magnetic disc. In addition, a 32-time-of-flight channel x 512 analog channel information of the two dimensional data is taken also for this counter. In this case the information serves mainly for off-line determination of the detector threshold and the obtained energy resolution of the detector.

Computer code

In order to calculate the detector efficiencies and to simulate the proton recoil pulse height spectra, a Monte-Carlo program was written for use with an IBM 360/165 computer[3]. In the program, an incoming parallel neutron beam is assumed, hitting the circular radiator foil. The laboratory scattering angles of the produced recoil protons are calculated from the appropriate analytical equations, and are suitably sampled. From the incoming neutron energy and the selected proton scattering angle, the proton energy can be determined. Such calculations are carried out for different depths in the radiator and for different circular zones of the same area in the radiator plane. Energy losses in the radiator, the scintillator gas and the separating tantalum foils (comp. fig. 2) are calculated from the known energy-range and specific-energy-loss relationships.[4,5] In the present program, the tabulated values of Williamson and Boujet[5] were used. A particularly sensitive check of the reliability of these energy loss calculations comes from a comparison of the measured and the calculated cut-off-energy for the counter system I: Here the cut-off energy means that coincident events from recoil protons can be obtained only, if the incident neutron energy is high enough, so that the forward scattered proton can reach the third scintillation chamber. This minimum, or cut-off energy can independently be obtained by both, the cut-off channel in the time-of-flight spectrum and the minimum energy derived from energy loss calculations. The results for such calculated and measured cut-off energies differed only by ∿50 keV.

Results and discussions

Fig. 4 shows the probabilities for proton detection in the flux counter system II. The solid curve is the result calculated for an idealized, i.e. step-like detector threshold, set at a value of 100 keV proton energy. The dotted line is the efficiency obtained in a recent measurement with a realistic detector threshold , which is spread over 300 keV. It can be seen that the proton detection efficiencies are flat over most of the energy range. The rapid decrease below ∿2 Mev indicates the present limitation of the system, which is mainly due to the limitations in the energy resolution for the present detector. Typical pulse-height spectra obtained for three different neutron energies are shown in fig. 5. The spectra for both detectors are channel grouped results in the sense described in section 3, i.e. the figures combine results from 128 time-of-flight channels of 2 nsec widths. Fig. 5 a shows three typical proton recoil spectra of the detector system II. In fig. 5 b, the results for specific energy losses in the detector system I are illustrated. Typical time resolutions of both detectors have been derived from remaining prompt γ-ray peaks in the neutron time-of-flight spectra. The present values are ∿5 nsec for detector I and 25 nsec for detector II. With the present thicknesses of the radiator foils of 10 µm and 20 µm, the overall efficiencies of the flux detectors range between 1-3 x 10^{-4} for flux measurements between 1-6 MeV, and 2-4 x 10^{-4} for measurements between 5-30 MeV.

References

1 W.P. Pönitz, Black neutron detector, Report, ANL-7915, 1972

2 P. Nicolas, Etude d'un détecteur de neutrons de type détecteur noir, Rapport interne. DO.0094(1974)

3 P. Brotz, Diplom Thesis, University Karlsruhe, 1973.

4 W. Whaling, Handbuch der Physik, 34 (1958) 193

5 C. Williamson, J.P. Boujet, CEA-Report, CEA-2189, Saclay 1962

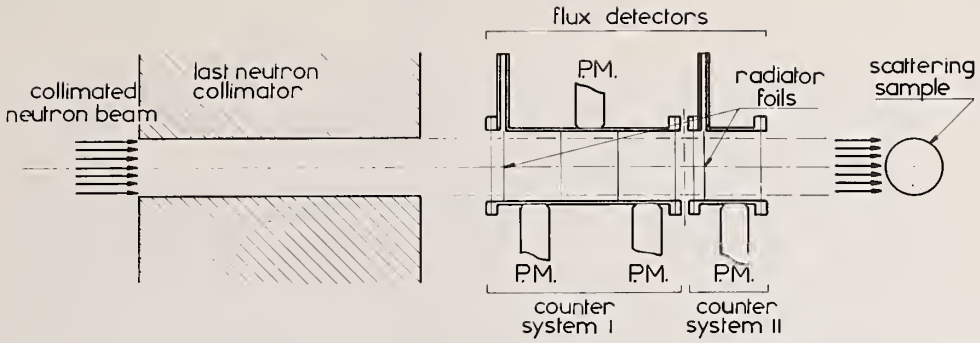

Fig. 1 Schematic drawing of the geometrical arrangement of the flux detector

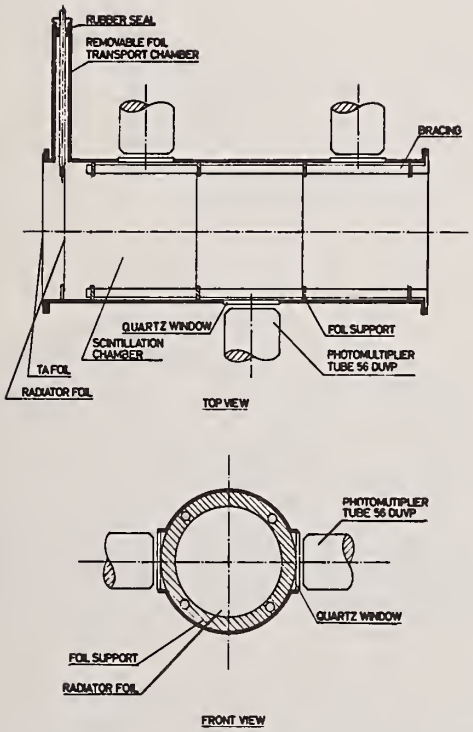

Fig. 2 Schematic drawing of the neutron flux detector I

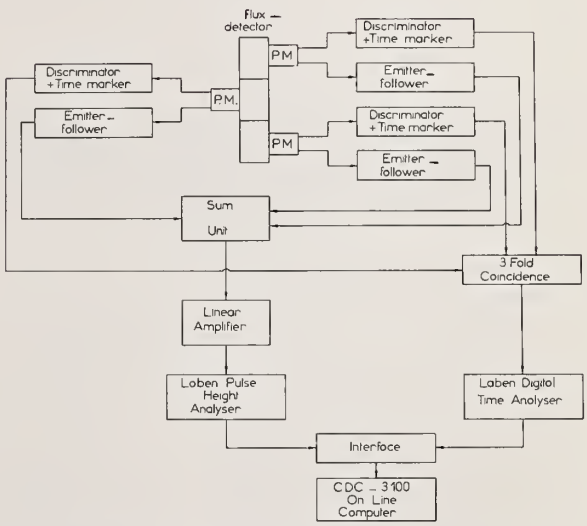

Fig. 3 Simplified block diagram of the electronics for flux detector system I

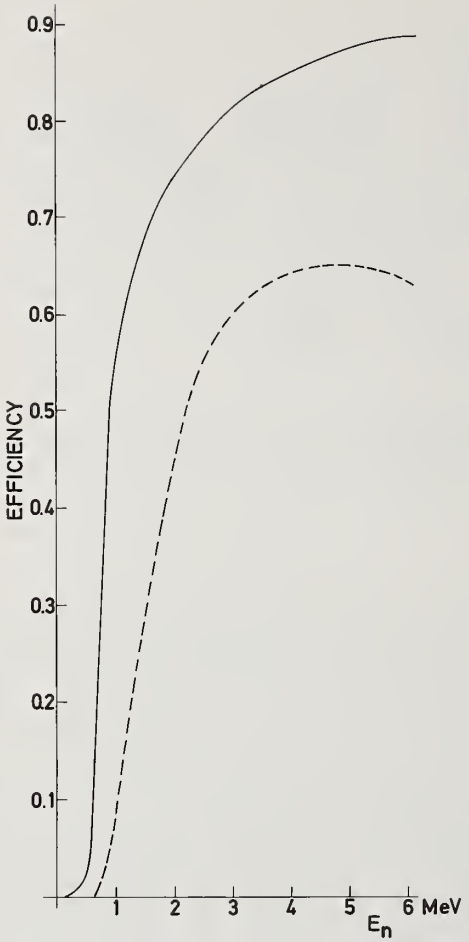

Fig. 4 Efficiency of detector II for proton detection for an idealized threshold at 100 keV (solid curve) and a realistic threshold (dotted curve)

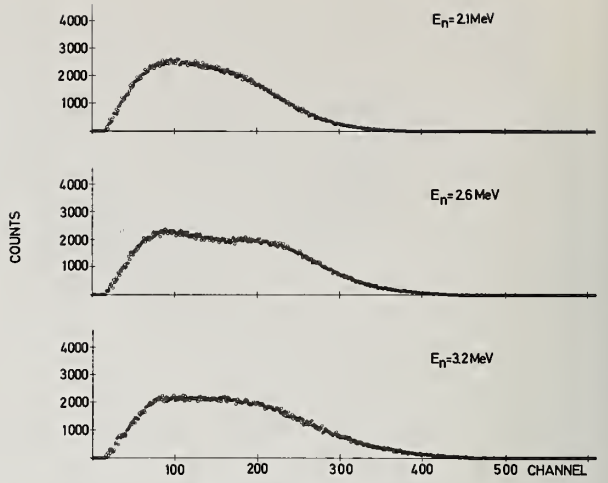

Fig. 5a Proton recoil spectra of detector II

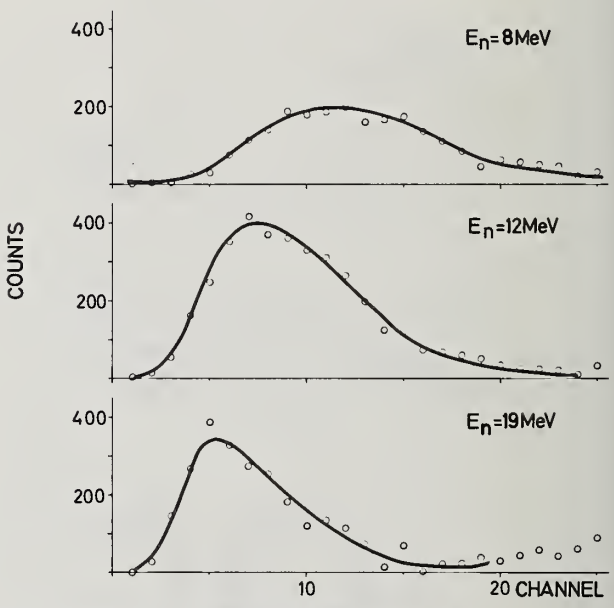

Fig. 5b Spectra of energy losses in detector I

THERMAL PARAMETERS OF THE FISSILE ISOTOPES

Bowen R. Leonard, Jr.
Battelle-Northwest
Richland, Washington 99352

Evaluations have continued to better define the 2200 m/s nuclear data for the fissile isotopes. The author has been participating in such evaluations with both the International Atomic Energy Agency (IAEA) and the USAEC National Neutron Cross Section Center (NNCSC). Each study is faced with the same dilemma: the measured values of a given parameter form a set which is reasonably self-consistent, yet the average values of the interrelated parameters constitute a set which is significantly inconsistent. The obvious discrepancy is between the values of alpha deduced with high accuracy from irradiation experiments with the values which result from the ensemble of values of the other parameters which by themselves form a reasonably self-consistent set. However, the inconsistency could result from error assignments which are too small for two or more parameters, e.g., fission and eta. In order to expedite ENDF/B-IV, the NNCSC evaluation fixed certain input parameters including the thermal shapes which are in good agreement with differential data. As a result the least-squares-compromise adjusted absorption, fission, and nubar values by several tenths percent. In the IAEA evaluation, the primary adjustments of the LSQ fit were in nubar and g_γ values which implicitly infer significant systematic errors in the directly measured capture shapes. The Electric Power Research Institute has initiated studies to attempt to resolve this dilemma which is crucial to analyses of fission power reactors. These are:

1. A simultaneous LSQ fit to energy-dependent differential partial and total data.
2. A reevaluation of the accuracy assignment of absolute fission cross section values.
3. A reexamination of irradiation alpha experiments with sophisticated analytical methods.

Further experiments which would improve the knowledge of the thermal parameters include:

1. Confirmatory measurements of capture shapes extended to lower neutron energies.
2. Confirmatory measurements relative to the monoenergetic eta experiments.
3. Accurate coherent scattering amplitude measurements in the thermal region for all isotopes.
4. Measurement of the total cross section of ^{233}U from thermal to several tenths eV.
5. Improved thermal fission critical experiments and analysis for ^{239}Pu.
6. Confirmatory high accuracy absolute fission cross-section experiments.

(NUCLEAR REACTIONS ^{233}U, ^{235}U, ^{239}Pu, ^{241}Pu (n,F) (n,γ) (n,n) $\bar{\nu}$, E = 0 - 1 eV, evaluation)

Introduction

Beginning in 1962[1] attempts have been made to improve the knowledge of the thermal parameters of the fissile nuclei through least-squares adjustments (LSQ) of experimental values and their ratios, including ratios of values for different nuclei. Since 1965,[2] the International Atomic Energy Agency (IAEA) has maintained a continued evaluation effort of this type to produce periodic[3,4] updated LSQ values of the 2200 m/s constants. The author participated as a consultant in the 1969 IAEA review[4] and an IAEA review which has been in progress since 1972. He has also participated in related, independent reviews for the National Neutron cross Section Center (NNCSC) to provide thermal data for ENDF/B.[5]

It has been apparent for several years that the experimental data for the fissile nuclei are internally inconsistent. These inconsistencies have not only remained, but have become more apparent, with the advent of new experimental data with claimed high accuracy. These new data include, primarily, nubar experiments of Axton[6] and of Boldeman[7] and absolute fission cross section values of Deruytter.[8,9,10,11] The basic inconsistency of the thermal data has frequently been referred to as the eta-nubar discrepancy. The obvious discrepancy, however, is between alpha values deduced from irradiation experiments and alpha values derived from other combinations of experimental data. Alpha values can be derived from total, scattering and fission data and, almost independently, from the ratio of nubar to eta. Values derived in this way for ^{233}U and ^{235}U are shown as the first two entries in Table I using averaged input values currently in use at NNCSC.[5]

Table I. 2200 m/s Alpha Values for ^{233}U and ^{235}U Input Data

Method	Alpha ^{233}U	Alpha ^{235}U
$\frac{\sigma_T-\sigma_s}{\sigma_f}$	0.079 ± 0.007	0.158 ± 0.005
$\bar{\nu}/\eta$	0.074 ± 0.005	0.155 ± 0.006
Critical Exps.	0.078 ± 0.007	0.153 ± 0.005
Mean	0.076 ± 0.004	0.155 ± 0.003
Irradiation Exps.	0.087 ± 0.002	0.169 ± 0.003

The third line shows alpha values deduced from the analysis of critical experiments which includes the nubar value and not only the total, scattering and fission values of line one but the shapes of the cross sections as well. All of these values are seen to form reasonably consistent sets of data although their mean values differ by 3 or 4 standard deviations from the average alpha values deduced from irradiation experiments, shown on the last line. Similar comparisons are

shown in Table II for ^{239}Pu data.

Table II. 2200 m/s Alpha Values for ^{239}Pu from Input Data

Method	Alpha ^{239}Pu
$\frac{\sigma_T-\sigma_s}{\sigma_f}$	0.364 ± 0.010
$\bar{\nu}/\eta$	0.350 ± 0.010
Mean	0.357 ± 0.007
Irradiation Exps.	0.366 ± 0.008

For the case of ^{239}Pu, no alpha value was derived from critical experiments because the precision of these experiments does not allow derivation of a meaningful value. The apparent alpha discrepancy for ^{239}Pu is similar to that shown for ^{233}U and ^{235}U although not as pronounced relative to the assigned errors.

The demonstrated inconsistencies in the basic data open the question of the possible value of a further LSQ adjustment at this time. It is clear that such an adjustment can only compromise the existing discrepancies and that the compromise values will be strongly influenced by the exact choices of input values and errors. In the absence of any understanding of the reasons for the discrepancies there is no a priori reason to believe that a new LSQ set will have a more valid base than sets currently in use. For these reasons, the present author proposes that the logical course of action is an extensive program of reevaluation in the hope that at least some of the apparent discrepancies can be removed. In addition, a number of new experimental investigations are proposed which may resolve discrepancies or otherwise improve the knowledge of the thermal parameters. The evaluation and new experimental data needs which have so far been identified are the subject of the present paper.

Discussion

Cross Section Shapes

The shapes of the partial cross sections of the fissile nuclei in the thermal region enter into the LSQ adjustment in two ways. In the first way, the interpretation of data from integral experiments depends, in general, on the cross section shapes used to derive 2200 m/s values from spectrum-averaged ones. In principle, all integral experiments are interpreted with identical cross section shapes to deduce 2200 m/s values. In addition, the Westcott g factors[12] which are the indices of these shapes can be allowed as adjustable parameters in the LSQ adjustment. By assigning unreasonably large errors to the g factors input to the LSQ adjustment, it has been determined that the LSQ compromise can produce output values of g which are significantly different from best-estimate differential data. Secondly, the 2200 m/s values deduced from differential data only rarely represent a single datum at 2200 m/s but are values deduced from σ vs E data using methods which have not yet been consistently applied to all experiments.

As a first step in the overall reevaluation, D. A. Kottwitz and the author[13] have started a study of cross section fitting to derive best-estimate shapes, 2200 m/s values, and error estimates on g-factors. We have programmed a modification of Adler-Adler[14] multi-level resonance fission theory along with MLBW scattering into the non-linear LSQ program LEARN.[15,16] The intent of using the chosen resonance formulation is to allow all of the physically possible energy dependencies while avoiding shape biases which might result from having to specify the exact details of the fission interference which might result from use of e.g., the Reich-Moore[17] formalism. The non-linear LSQ approach is indicated by the several non-linear energy dependent parameters of the theory. To date we have performed simultaneous fits to capture, fission and eta data for ^{235}U. We hope to add scattering and total cross section restraints in the near future.

Cross Section Data and Evaluation Problems

Capture Cross Sections. The direct measurement of $\sigma_\gamma(E)$ in the thermal region at ORNL and RPI for ^{233}U and for ^{235}U is a valuable type of experiment.[18,19] In particular, Steen[20] has found that the ^{233}U results significantly improved the internal consistency of ^{233}U data aside from the alpha discrepancy. Rather remarkably, however, the ^{235}U capture data were predicted quite well from the shape drived indirectly from total, fission and eta data as shown on Fig. 1. Also shown for comparison is a shape resulting from a provisional simultaneous fit to selected capture, fission and eta data.

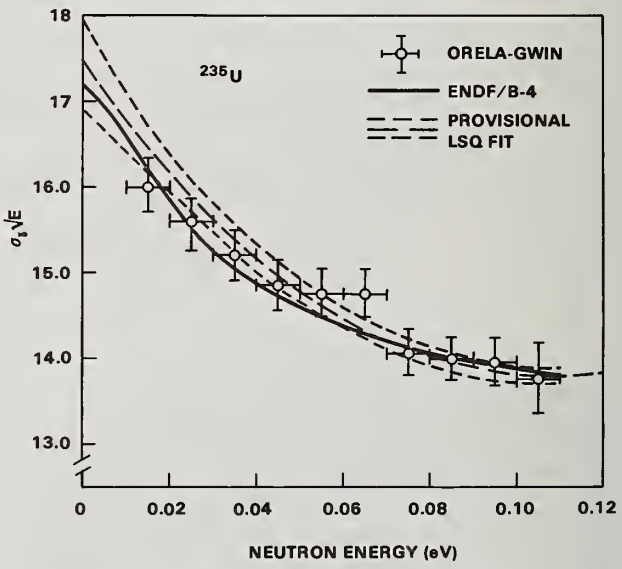

Figure 1. The direct capture data of Gwin et al[19] compared with shapes given on ENDF/B-IV and with LSQ fits to capture, fission and eta.

Although both ^{233}U and ^{235}U capture data appear to be in good agreement with expectations of correlated data it should be pointed out that this is a difficult experiment. Indeed, the high backgrounds encountered lead at least one of the authors to not place much reliance on the data below 0.03 eV. Independent measurements, extending to lower neutron energies, would be of value. Also, similar measurements on ^{239}Pu and ^{241}Pu are needed.

Scattering Cross Sections. A thermal spectrum scattering cross section measurement by Green and Mitchell[21] has given a value of 12.3 ± 0.7 b for ^{233}U. This value is in good agreement with expectation values of potential scattering of 10 to 12 b and existing resonance analyses which indicate that the thermal scattering should not be significantly larger than the

potential scattering. Most evaluations of ^{233}U data, however, propose thermal scattering cross-section values of 14.5 to 16 barns.[22,20] At the present time it is not known whether this is a real internal inconsistency in ^{233}U data or an evaluation deficiency. In an earlier paper,[23] the author pointed out that coherent scattering amplitude measurements could give valid estimates of total scattering cross sections for the fissile nuclei since the uncertainties in incoherent scattering effects and neutron energy dependence were much smaller than other uncertainties. He further pointed out problems in the existing single measurements for ^{235}U and ^{239}Pu. A programmatic study of coherent scattering values could greatly improve our confidence in thermal fissile constants.

A previously unnoticed problem with scattering cross sections in the LSQ adjustment is in the treatment of effective cross sections in transmission measurements. We expect extinction effects with metallic samples to produce lower effective scattering values than with liquid samples. The only experiments in which liquid and metal samples were measured simultaneously, however, yielded the same or higher total cross section values for the metal samples.[24,25] Thus, there may be scattering or other effects present which have not been identified in the evaluation process. At best, it seems doubtful that the procedures presently used for scattering in the LSQ adjustments should be continued.

Fission Cross Sections. The experiments which determine absolute values of fission cross sections are dominated by claimed accuracy by those of Deruytter.[8-11] Evaluation of these experiments, however, raises significant questions both as to the values and errors assigned to these measurements. First, it should be recognized that the quoted 2200 m/s values and errors are based on analytical fits to not terribly precise TOF fission data near 2200 m/s. We expect that better estimate values will be obtained in the simultaneous fits of Kottwitz and Leonard[13] to all partial and total cross section data. In addition, the contribution to absolute error of the uncertainty due to the analytical fits treats the dispersion of fitted values from the mean as computer experiments in which the assigned uncertainty is the precision of the mean. This procedure is, at best, a new adventure in statistical theory. Other problems are outstanding in the evaluation of Deruytter's measurements. The first is that the fission backgrounds were rather high; 8.5% and 10% in the two ^{235}U sample foil measurements.[8] To account for the backgrounds, the measured data were fitted to a harmonic function and the fitted function was subtracted for the background. No error estimate was assigned for the background subtraction even though: 1) there was presumably some statistical precision of the fit, 2) no physical basis for the energy dependence forced on the background was presented, and 3) the background as measured may differ from that present during the fission measurements. The treatment of the background may manifest itself in another problem of the measurement - the shape of the cross section. Deruytter's ^{235}U fission data are shown on Fig. 2 compared with other experiments designed to determine the fission shape at low energies. Also shown is the result of a simultaneous fit[13] to capture, eta, and fission data not including Deruytter's latest result.

The other three data sets shown, including Deruytter's 1961 experiment[11] all show a distinct non 1/v behavior below 0.02 eV. The simultaneous fit shown, which did not include the 1970 Deruytter data, indicates a total deviation from 1/v of 4.3 percent. Deruytter interprets his data to indicate no deviation from 1/v below 0.02 eV. If they did not, there would be a distinct shape difference. However, the display of the 1970 data shown on Fig. 1 indicates little real disagreement between the shape of the fitted curve and Deruytter's data.

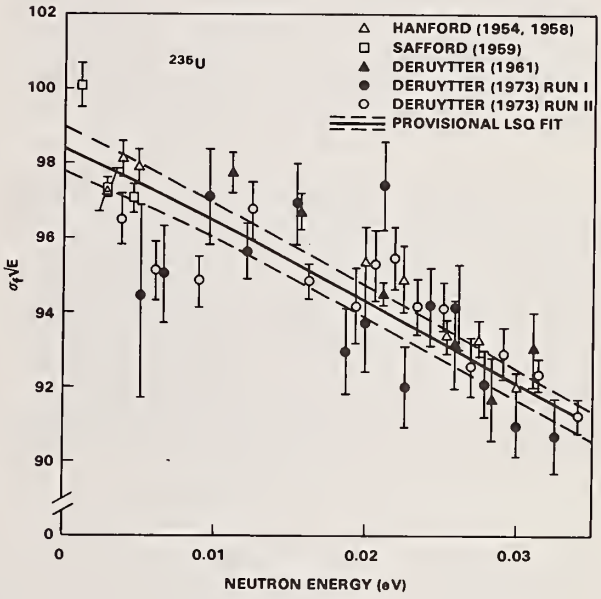

Figure 2. Low Energy Fission Data for ^{235}U

Another factor in this experiment is the procedure by which foil weights were established. Four boron and four fissile foils of differing weights were prepared and each weight obtained gravimetrically. The foils were then placed in a neutron beam and their fission or boron rates measured. The authors then plotted the fission rates vs the gravimetric weights. By fitting a straight line through zero to these data they claim to improve the knowledge of the gravimetric weights. Thus, the fissile and boron weights used in the analysis were the fitted weights and the error assigned to the boron weights was significantly reduced from the gravimetric uncertainty. This is a valuable experiment. However, the present author does not accept the conclusion that the fitted weights are either the best estimate weights nor that their error estimate has been improved since each type of determination contains a different and uncorrelated set of elements to effect the measurements and their interpretation.

Another facet of this experiment is the question of possible effects of non-uniformity of deposit. The authors also measured fission rates and boron rates for a neutron beam of smaller cross sectional area. Comparing these weights with the gravimetric weights they obtained weights for the two boron foils used in the absolute fission analysis which were 0.8% larger and 0.6% smaller than the boron weights actually used to derive final fission cross section values. These

substantial differences remain unexplained but may be due to non-uniformity or background effects. No error estimate due to this observation was included in the final error assignment of the absolute fission cross section.

A further fission data deficiency is the lack of adequate data for ^{241}Pu at very low energies. Because of problems with ^{241}Pu total cross section in this region, improved fission measurements would be of value.

Eta. The dominant experiments are the monoenergetic eta values reported by Smith, et al[26,27] for all fissile nuclei at 0.0253 eV and other selected neutron energies. Extensive studies of these experiments using sophisticated calculational techniques have confirmed the reported values to high accuracy. Results of studies of these and possible systematic errors are reported in another paper at this Conference.[28]

The shape of eta in the thermal region is also important in determining 2200 m/s values. For ^{235}U there is a single set of data which definitely shows a shape, other than a constant value below some 0.1 eV. These data of Palevsky et al[29] yield a maximum value of eta near 0.08 eV some two percent larger than values near zero eV. Independent measurements of eta (E) for ^{235}U made by the author[29] also indicate such a shape but with less conviction. The evaluated shape of eta given on ENDF/B-IV shows a maximum value near 0.04 eV which is 0.6% larger than the zero eV value. On Fig. 3 is shown the eta data of Palevsky et al[29] compared with a provisional result of the simultaneous fitting of capture, fission and eta data.

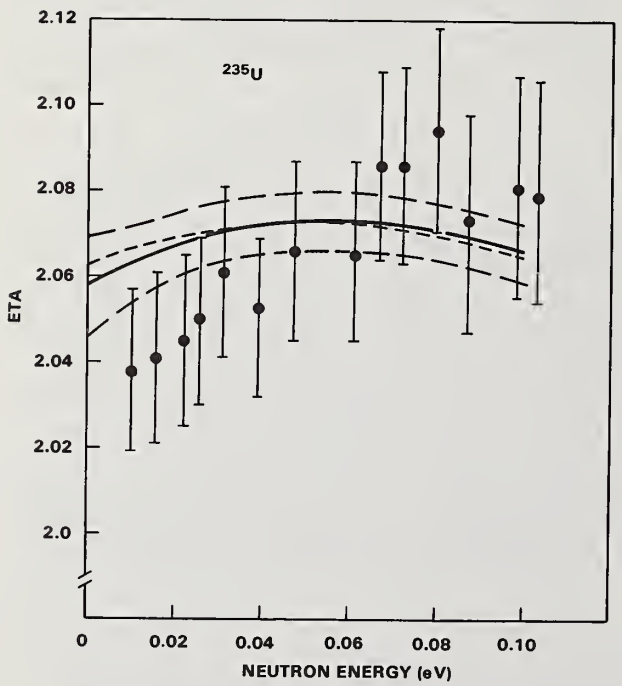

Figure 3. The low-energy eta (E) data of Palevsky et al[29] compared with LSQ fits to capture, fission and eta.

The fitted (solid) curve shows systematic departures from the data and a shape which differs only slightly from that of ENDF/B-IV. The dotted curve is a LSQ with the data of Palevsky et al not included. It is apparent that these data are having but small influence on the fit. For a new measurement to have a significant influence on the knowledge of eta (E) in the thermal region the data would need to be obtained with precisions of 0.5% or less.

Total Cross Sections. Although a large number of accurate total cross section measurements exist, there are measurements which could improve the knowledge of the thermal parameters. The authors of the ORNL-RPI capture and fission measurements[18] on ^{233}U normalized their data to total cross section data using calculated values of scattering cross sections. Nevertheless, their summed cross section values differ systematically from existing total cross section values in the energy region 0.1 to 0.2 eV. In addition, the existing total cross section data sets of Pattenden and Harvey[30] and of the MTR group[31] are not in particularly good agreement in this region. This is a very important energy region for ^{233}U and improved total cross section data would improve the understanding of problems here.

Irradiation Values of Alpha. The values of alpha derived from irradiation experiments are dominated by the results of Lounsbury et al[32] reported with errors even smaller than assigned in Tables I and II. Most other alpha values reported by others are similar in magnitude to those of Lounsbury et al. Noticeable exceptions are the values reported by Conway[33,20] which are consistent within errors with the mean values shown on Table I. While Conway's experiments were subjected to the most rigorous analysis of neutron spectrum effects of any of the alpha measurements the errors assigned to these values causes them to carry little weight in determining the average value. If a problem exists in the measurements of Lounsbury et al, it would appear to be in the definition of the thermal neutron flux spectrum and the epithermal flux. Kalos[34] has now started a study of spectrum problems in this experiment. It should be noted that the ^{233}U alpha value reported by Lounsbury et al has not yet been fully corrected for the present best-estimate shape of the ^{233}U capture cross section based on their own thermal spectrum analysis. A first order correction applied by Steen[20] reduced the reported value by 0.3%.

Nubar Values. The experimental values of nubar for ^{252}Cf and for ratios to fissile nuclei presently form a reasonably self-consistent set with no apparent systematic or undue flyers. The new values reported[7] by Boldeman for ^{252}Cf are, e.g., in good agreement with precise values of Devolpi[35] and of Axton.[6] In addition, the author has reviewed the Boron Pile experiments of Colvin and Sowerby[36] and proposes that these results be removed as discrepant values due to a number of factors, all of which tend to both increase the nubar values and their relative errors. These factors are:

1. The correction for the time gate used was typically 4.3% with an assigned error of 0.1%. The reported measurements indicate the correction was determined to a precision of about ± 0.5%.

2. The measured shape of the efficiency versus neutron energy was linear in the region 0-2 MeV where it was normalized to the calculated efficiency which was significantly nonlinear in shape. Any choice of normalization procedure other than that chosen by the authors would result in higher nubar values. An

additional error needs to be assigned due to this discrepancy.

3. Copper (n,p) and (n,α) and carbon (n,α) reactions were neglected in the efficiency calculations. Inclusion will increase nubar and the corrections will differ for different neutron emission spectra and the standard source calibration.

Discussion

The review of the status of the thermal cross sections of the fissile nuclei indicates that inconsistencies of the same type have persisted for the last several years. Previously, however, internal inconsistencies in nubar results allowed LSQ adjusted values of nubar to fall within data uncertainties. With the dimunition of the internal nubar discrepancy, however, a LSQ adjustment can only produce nubar and cross section values with definite and predictable biases from best-estimate input data. The only escapes from this dilemma are that 1) the error estimates on irradiation experiment values of alpha are significantly too small or 2) error estimates on other correlated quantities are similarly underestimated. The studies of cross section shapes and values and the reevaluation of irradiation alpha experiments are fundamental steps to the possible solution to the dilemma.

Acknowledgment

This work was supported by the Electric Power Research Institute.

References

1. R. Sher and J. Felberbaum. BNL-722 (1962) and BNL-918 (1965).

2. C. H. Westcott, K. Ekberg, G. C. Hanna, N. J. Pattenden, S. Sanatani and P. M. Attree, At. En. Rev. 3, No. 2 (1965).

3. C. H. Westcott, Nucl. Oata for Reactors, Paris, Vol. 2, 44, IAEA (1967).

4. G. C. Hanna, C. H. Westcott, H. O. Lemmel, B. R. Leonard, Jr., J. S. Story and P. M. Attree, At. En. Rev. VII, No. 4 (1969).

5. R. J. Stehn, TANSAO 18, 351 (1974).

6. E. J. Axton, A. G. Bardell and B. N. Andru, JNE A/B 23, 457 (1969) and Private Communication (1974).

7. J. W. Boldeman, NSE 55, 188 (1974).

8. A. J. Oeruytter, J. Spaepen and P. Pelfer, JNE, 27, 645 (1973).

9. A. J. Deruytter and C. Wagemans, NSE, 54, 423, (1974).

10. A. J. Deruytter and W. Becker, Ann. NSE, I, 311 (1974).

11. A. J. Oeruytter, JNE A/B 15, 165 (1961).

12. C. H. Westcott, (CRRP-960), AECL-1101 (1960).

13. D. A. Kottwitz and B. R. Leonard, Jr. Submitted for June ANS Meeting (1975).

14. D. B. Adler and F. T. Adler, TANSAO 5, 53 (1962).

15. B. H. Ouane, USAEC Report BNWL-390 (1967).

16. D. A. Kottwitz, USAEC Report BNWL-1590 (1971).

17. C. W. Reich and M. S. Moore, Phys. Rev. 111, 929 (1958).

18. L. Weston, R. Gwin, G. deSaussure, R. W. Ingle, J. H. Todd, C. W. Craven, R. W. Hockenbury and R. C. Block, NSE 42, 143 (1970).

19. R. Gwin, E. G. Silver, R. Ingle and H. Weaver, ORNL, to be published (1975).

20. N. M. Steen, Neutron Cross Sections and Technology, Knoxville, Conf-710301, 2, 566 (1971).

21. L. Green and J. A. Mitchell, NSE 54, 18 (1974).

22. ENDF/B, MAT 1260 (1974).

23. B. R. Leonard, Jr., Conf-720901, Book 1, 81 (1972).

24. G. J. Safford, W. W. Havens, Jr. and B. M. Rustad, Phys. Rev. 118, 799 (1960).

25. G. J. Safford, W. W. Havens, Jr. and B. M. Rustad, NSE 6, 433 (1959).

26. J. R. Smith, S. D. Reeder and R. G. Fluharty, IDO-17083 (1966).

27. J. R. Smith and S. D. Reeder, NBS Spec. Publ. 299, I, 591 (1968).

28. J. R. Smith, paper DB9, This Conference.

29. H. Palevsky, D. J. Hughes, R. L. Zimmerman and R. Eisberg, J. Nucl. Energy 1, 177 (1956).

30. N. J. Pattenden and J. A. Harvey, NSE 17, 404 (1963).

31. M. S. Moore, L. G. Miller and O. O. Simpson, Phys. Rev. 118, 714 (1960).

32. M. Lounsbury, R. W. Durham and G. C. Hanna, Nucl. Data for Reactors, Helsinki, I, 287, IAEA (1970).

33. D. E. Conway, WAPO-TM-613 (1967).

34. M. Kalos, Math. Applications Group, Inc., N. Y., Private Communication (1975).

35. A. Devolpi and K. G. Porges, Phys. Rev. C1, 683 (1970).

36. D. W. Colvin and M. G. Sowerby, Phys and Chem. of Fission, Salzburg, 2, 25, IAEA, Vienna (1965).

THE THIRD IAEA EVALUATION OF THE 2200 m/s AND 20°C MAXWELLIAN NEUTRON DATA FOR U-233, U-235, Pu-239 AND Pu-241

H.D. Lemmel
Nuclear Data Section
International Atomic Energy Agency
A-1011 Vienna, Austria

The paper presents a new consistent set of best values of 2200 m/s and 20°C Maxwellian neutron cross-sections, fission-neutron yields, and Westcott g-factors for U-233, U-235, Pu-239 and Pu-241, and of related reference values such as the spontaneous fission-neutron yield of Cf-252, the mean fission-neutron spectrum energies of the five nuclides named, the α-decay half-lives of U-233, U-234 and Pu-239 and others.

This consistent set of values is derived from a multi-parameter least-squares fit of all available experimental data, after reviewing and, where feasible, re-assessing the authors' quoted values and errors usually after consultation with the authors.

The new best set of values is significantly different from that of the Second IAEA Review of 1969 [2]. The major changes are due to new lower experimental values of $\bar{\nu}$ (Cf-252) and of half-lives. Also discussed are some disturbing unresolved discrepancies among experimental data, which leave the accuracies of some parameters, for example the uranium fission cross-sections, still unsatisfactory.

(Neutron data evaluation. U-233; U-235; Pu-239; Pu-241; neutron cross-sections; fission-neutron yields; mean energy of fission neutron spectrum; Westcott g-factors; E = 0.0253 eV and 20°C Maxwellian. Cf-252 spontaneous fission neutron yield; half-lives of U-233, U-234, Pu-239.)

Introduction

In 1965 [1] and 1969 [2] consultants groups convened by the IAEA Nuclear Data Section and led by C.H. Westcott and G.C. Hanna, published consistent sets of recommended best values of the thermal neutron data of the fissile nuclides. Recently, we have finished a third review with the active support of a consultants group composed of E.J. Axton, A.J. Deruytter, B.R. Leonard Jr. and J.S. Story [3].

In 1969 it was known that the recommended data suffered mainly from two uncertainties: firstly from the 2.5% spread in the experimental results of the Cf-252 fission neutron yield, $\bar{\nu}$, which is the reference value for most $\bar{\nu}$ values of all other fissile nuclides; and secondly from the 2% uncertainty in half-life values, especially that of U-234, which is a basic parameter in important measurements of the U-235 fission cross-section. At that time there were arguments in favor of assuming rather high values for $\bar{\nu}$ of Cf-252 and for the half-life of U-234, assumptions which later turned out to be wrong. Meanwhile these two main sources of uncertainty appear to be resolved and consequently revisions to the 1969 recommended values for $\bar{\nu}$ and the fission cross-sections by about two standard deviations appeared to be indicated. In addition to these two major changes a number of further adjustments became necessary concerning Westcott g-factors, standard cross-sections, mean fission spectrum energies, scattering cross-sections and other quantities.

Therefore, a complete new evaluation of the thermal neutron cross-sections and related parameters of the fissile nuclides was made by the IAEA group, and this paper gives a summary of the results and conclusions. It can be said that some of the disturbing discrepancies encountered earlier between experimental data can be regarded as resolved, but that other significant discrepancies which continue to exist require some further investigation.

The evaluation was made by fitting all available experimental data by means of a least-squares fitting program written by D. McPherson et al. [4]. The weight of each input datum is given by $1/e^2$ where e is the relative standard-deviation error including statistical and systematic error contributions. All thermal neutron data of U-233, U-235, Pu-239 and Pu-241 were simultaneously fitted together with Westcott g-factors and reference data such as $\bar{\nu}$ (Cf-252) and the half-lives of U-233, U-234 and Pu-239. Furthermore, the 2200 m/s standard cross-sections for boron, cobalt, gold and others were updated. Altogether there are about 200 experimental input data, which were carefully reviewed, mostly by pertinent specialists and, where possible, in contact with the authors. Values and errors were adjusted, when necessary, only for physical reasons inherent in the experiment; discrepancy with other input data was not recognized as a reason for downweighting. Error correlations between different input data were carefully considered and, as far as possible, reflected in the fit.

Brief review of the input data

Let us first consider the experiments made with monoenergetic neutrons. Since 1969 there were no new total cross-section measurements for the nuclides considered. However some new scattering cross-section measurements stimulated a re-evaluation by B.R. Leonard Jr.[S3], resulting in an increase of the scattering cross-section for U-233 and a decrease for U-235.

The knowledge of the 2200 m/s fission cross-sections of U-235 and Pu-239 was much improved by two accurate new measurements with monoenergetic neutrons by Deruytter et al. at Geel [F9, F10] and by Petrascu et al in Bucarest [F2, F3, F17]. Both are in good agreement, although they used somewhat different methods.

The disturbing spread of earlier fission cross-section values has been much reduced by Deruytter in his paper at the 1970 Argonne Symposium [F7], in which he discussed systematic errors in some earlier experiments due to erroneous extrapolations to zero sample thickness. Furthermore, a revised new value for the half-life of U-234 has been established by three recent agreeing experiments [H19]. The new value of 2.447×10^5 years improves the consistency between the

different fission cross-section measursments. Also for U-233 the half-life seems now to be well established, but for Pu-239 the knowledge of the fission cross-section still suffers from an unresolved 1.2% spread of expsrimental half-life data. Thers are however several indications that a low value close to Oetting's calorimetric value of 1970 [H14] may be corrsct, rather than the highsr values obtained by α-counting. A comparison of the half-life dependent fission cross-section measursments with the half-life independent ones clearly supports a lower value of the Pu-239 half-lifs.

If ons fits all ths experimental 2200 m/s data, using the revised half-life value of U-234, one obtains for U-235 a fission cross-section of 588±2 barns, which is 1.3% or four standard deviations higher than the 1969 value of 580±2 barns. However, there remains a ssrious 1.5% discrepancy between the U-235 fission cross-section obtained with monoenergetic neutrons and that obtained in integral experiments in a thermal neutron spectrum.

Considerable improvement has been reached with the fission-neutron yield of Cf-252. At the time of our 1969 review, experimental data formed two distinct groups with a discrepancy of 2.5%. The data of the two liquid scintillator experiments and one of the manganese bath data formed the high group close to a value of 3.8, all the other manganese bath data and the boron pile data formed the low group close to 3.7.

This discrepancy among the Cf-252 $\bar{\nu}$ data no longer exists, partly because their spread was reduced by rsvisions which had to be made to some of the previously extreme values, and partly because the new liquid-scintillator measurement by Boldeman, which gave a relatively low result, reconciled the previous systematic discrepancy between the liquid-scintillator method and the other methods [N9]. At present, five of the nine values for the prompt fission-neutron yield of Cf-252 are in excellent agreement in the range between 3.715 and 3.735, including the thrse most recent and most accurate determinations by De Volpi[N21], Axton [N3] and Boldeman[N9]. The present weighted mean is a prompt $\bar{\nu}$ value of 3.731±0.008. This is 0.8% lower than the 1969 IAEA value but somewhat higher than the value given by Axton in his 1972 evaluation [N4]. Compared to Axton's evaluation thsre are a few changes. Firstly, the present fit treats the mean energy of the fission neutron spectrum, which is an essential source of uncertainty, as a variable to be fitted. Secondly, the rather low Harwell boron pile results [N11,N12] were slightly downweighted due to neutron absorption by carbon and copper, which had previously been neglected. A quantitative assessment of this effect has, however, not yet been done, and improved Monte-Carlo calculations would be desirable. Furthermors, a new Monte-Carlo simulation, by Poitou and Signarbieux [N41], of the capture and detection of neutronswith large liquid scintillators added to previous calculations a new element, which is the emission of gamma cascades and their interaction with the scintillator. On this basis, Diven [N23] suggested reducing his relatively high $\bar{\nu}$ value [N27] by about 0.4%. The possible impact of this effect on the othsr liquid scintillator experiments has not yet been assessed, but it would support the trend to lower $\bar{\nu}$ values.

The consistency between the $\bar{\nu}$ data is satisfactory. If one makes a fit of all $\bar{\nu}$ data alone, one finds that only two out of 13 absolute experimental values, and seven out of 28 experimental $\bar{\nu}$ ratios deviate from the fitted mean value by more than their respective experimental errors. This is better than can be statistically expected.

In such a fit of the $\bar{\nu}$ data one obtains a prompt $\bar{\nu}$ value for U-235 of 2.387±0.006, which is 0.8% lower than ths 1969 valus of 2.407. Howsver, this low value is not quite consistent with other, in particular thermal Maxwellian, input data, so that finally one obtains somewhat higher $\bar{\nu}$ valuss.

After the rather low $\bar{\nu}$ values became more certain, great efforts have been spent by various scientists on careful examination of the measurements of eta, the nsutron yield per absorption, by J.R. Smith st al. [E16, E17, E18, E19] and by Macklin et al.[E11, E12]. It appeared that the low $\bar{\nu}$ values and ths high eta values were not consistent. However, only minor insignificant changes in the experimental η values could be established. And in fact, the relatively low $\bar{\nu}$ values and the relatively high eta values are indeed consistent, if one compares them with the experimental values of the monoenergetic fission and absorption cross-sections:

$$\bar{\nu}_t / \eta^o = \sigma_a^o / \sigma_f^o .$$

The low $\bar{\nu}$ values and the high eta values are, however, not consistent, if one compares them with the experimental values of the thermal Maxwellian cross-ssctions $\hat{\sigma}_a$ and $\hat{\sigma}_f$, resp. their ratio $1 + \hat{\alpha}$.

The agreement between the $\bar{\nu}$ data and the 2200 m/s data is indeed extraordinary. If one performs first a least-squares fit of the 2200 m/s cross-sections and eta data only, and then a fit of these same data together with the $\bar{\nu}$ data, one obtains identical results. In the worst casss, the inaccurately known values of σ_f^o(U-233) and $T_{1/2}$(Pu-239) are shifted by the $\bar{\nu}$ data by as little as one half of their errors. Almost all other data are shifted by only less than one tenth of their respective errors.

Among the 43 experimental 2200 m/s cross-section and eta data, only one total cross-section value and one fission cross-section value deviate from the fitted value by more than their experimental error. Both of these values are anyway rather inaccurate and have no significancs in ths fit.

We conclude that the neutron-yield data and the 2200 m/s cross-section data are absolutely consistent. It should be noted however, that the U-233 fission cross-section is determined in this fit only indirectly from $\sigma_f^o = \eta^o \sigma_a^o / \bar{\nu}_t$, because there is no direct measurement of σ_f^o(U-233) with monoenergetic neutrons, except for an old inaccurate one.

Let us now consider the thermal Maxwellian or integral cross-section data. The group of data measured in a thermal Maxwellian neutron spectrum is highly determined by various Chalk River measurements claiming rather good accuracy. Since our 1969 evaluation a number of new experiments have been published. The fission and capture-to-fission cross-section ratios by Lounsbury et al, of which preliminary values were available in 1969, were subsequently published with insignificant changes [C11]. Since then, the U-233/U-235 fission cross-section ratio was measured by Vidal et al. in France [F24], and the Pu-239/U-235 fission cross-section ratio by Sweet in Winfrith[F23]. The U-233 capture-to-fission cross-section ratio was measured by Cabell and Wilkins at Harwell [C3]. A set of Pu-239 and Pu-241 ratios versus U-235 of $\hat{\sigma}_a$ and $(\hat{\eta}-1)\hat{\sigma}_a$ was measured by Laponche at Saclay [E10]. The revised values [E13] of the "reactivity" and "liquid critical" experiments by Gwin and Magnuson were available already in our 1969 evaluation, but some further revisions were made by updating some cross-sections of other nuclides present in the experiment. The capture and absorption cross-section values measured earlier by various authors were reduced by 0.8% due to a revision by Dilg et al.[R2] of the thermal cobalt activation cross-section used as reference value for these data.

All these new results are in excellent agreement with the earlier ones. The whole set of data taken in a thermal Maxwellian spectrum is extremely consistent. In a least-squares fit of all Maxwellian data together, one encounters among the uranium $\hat{\alpha}$ data some spread which is however statistically insignificant. Among the other 43 experimental Maxwellian cross-section and eta data only three deviate from the fitted value by more than their aesigned error. These are, besides an inaccurate $\hat{\eta}\hat{\sigma}_a$ ratio, the Pu-239/U-235 fission cross-section ratio by Sweet, and the U-233/U-235 $\hat{\eta}$ ratio by DeBoisblanc and Fast [E5].

After reviewing the three groups of experimental data, 2200 m/s data, $\bar{\nu}$ data, and thermal Maxwellian data, one ends up with a disturbing systematic discrepancy. The 2200 m/s data together with the $\bar{\nu}$ data form a very consistent set; the thermal Maxwellian data form another very consistent set; however, both sets are discrepant. They agree for the plutonium isotopes, but they dieagree for the uranium isotopes. This is shown in Table 1.

	Fit of 2200 m/s data and $\bar{\nu}$ data together	δ	Fit of thermal Maxwellian data alone
σ_f^o	$\sigma_f^o = \sigma_a^o \eta^o / \bar{\nu}_t$		$\hat{\sigma}_f / g_f$
U-233	532.6 ± 3.0	4.0	528.6 ± 3.6
U-235	587.7 ± 1.9	9.0	578.7 ± 4.0
U-233/U-235	0.906 ± 0.005	0.007	0.913 ± 0.003
Pu-239/U-235	1.269 ± 0.007	0.019	1.288 ± 0.006
$1 + \hat{\alpha}$	$\frac{g_a}{g_f}\frac{\sigma_a^o}{\sigma_f^o} = \frac{\bar{\nu}_t}{\eta^o}\frac{g_a}{g_f}$		$1 + \hat{\alpha}$
U-233	1.080 ± 0.006	0.010	1.090 ± 0.001
U-235	1.157 ± 0.006	0.015	1.172 ± 0.001
$\bar{\nu}_t$	$\bar{\nu}_t = \eta^o \sigma_a^o / \sigma_f^o$		$\hat{\eta}(1 + \hat{\alpha})$
U-233	2.469 ± 0.008	0.034	2.503 ± 0.021
U-235	2.403 ± 0.006	0.048	2.451 ± 0.019

Table 1: Discrepancies

The most disturbing discrepancies are in the fission cross-section, in $(1 + \hat{\alpha})$ and in $\bar{\nu}$, of U-235 and, to somewhat lesser extent, of U-233. Also the Pu-239/U-235 fission cross-section ratio shows a serioue discrepancy. In these cases the differences between monoenergetic and thermal Maxwellian data are of the order of 1.5% corresponding to more than two standard deviations. The origin of this discrepancy is not known. On the first view one may suspect that there is eomething wrong with the Westcott g-factors. However, as the last item in Table 1 ehows, the discrepancy between $\bar{\nu}_t$ and $\hat{\eta}(1+\hat{\alpha})$ is independent of g-factors.

If one wants to find a single common source for these discrepancies the first suspicion falls on the fission counting with uranium samples in thermal neutron spectra. But due to the complexity of the interrelations of the various data in the fit, the uncertainty may poseibly be somewhere else.

This discrepancy aleo pertains to the continuing diecuesions [E21] about the parameter $(\hat{\eta}-1)\delta_a$ obtained from the analyeis of the critical systems. Fitting the monoenergetic and neutron yield data, one obtains $(\hat{\eta}-1)\delta_a = 737 \pm 6$ and 716 ± 6 barns for U-233 and U-235 respectively; from the fit of Maxwellian data one obtains 744 ± 10 and 723 ± 9 respectively. Both fits are in good agreement with each other and with experimental values of $(\hat{\eta}-1)\delta_a$. If one fits, however, all data together, one obtains the disturbingly low values of 733 ± 3 and 709 ± 3 for U-233 and U-235 respectively. In this fit, $(\hat{\eta}-1)\delta_a$ is mainly determined indirectly through the equation $(\hat{\eta}-1)\delta_a = \bar{\nu}_t \delta_f - (1+\hat{\alpha})\delta_f$. It appears again, that the too low experimental values for δ_f are among the possible sources for this disturbance.

Although the Westcott g-factors are not the main source for the encountered discrepancies, they require further attention.

In the past few years cross-section curve shapes at low energies have been measured by Weston [G12] for U-233 and by Deruytter and Wagemans [G1, F9, G2, G9] for $\sigma_f(E)$ of all four nuclides considered. In the case of fission, the g-factors adopted in 1969 have essentially been confirmed. But for U-233 capture the g-factor now appears to be significantly larger than aesumed earlier.

It seems however that the accuracy of the g-factors has been much over-estimated in the past, in particular for the uranium isotopes. The g-factor is defined by the integral

$$g\sigma_o\sqrt{E_o} = \int_o^\infty \sigma(E)\sqrt{E}\, M(E)\, dE$$

$$\text{with } \int_o^\infty M(E)\, dE = 1 \quad \text{resp.} \quad M(E) = 2\sqrt{E/\pi}\,(kT)^{-3/2} e^{-E/kT}$$

Assuming that $\sigma(E)\sqrt{E}$ is approximately constant, the characteristics of the integral are mainly determined by the density distribution M(E), which has its maximum at kT/2, that is at 0.0126 eV for a 20°C spectrum temperature. Of the integral $\int M(E)\, dE$ about one half is situated below the energy of 0.0253 eV; see Figure 1. But the cross-section curve shapes below this energy are rather poorly known. In previous g-factor calculations rather linear extrapolations of $\sigma\sqrt{E}$ towards zero energy were assumed. However, for the uranium isotopes, the shape of the cross-section curves is possibly governed by a negative-energy resonance near zerò energy as shown in Fig 2 [G4]. The experimental data available in this energy range suffer from statistical and systematic uncertainties. At present it seems impossible to decide which of the curves shown in Figure 2 may be correct, except that the extreme case "C" is rather unlikely. The curves are

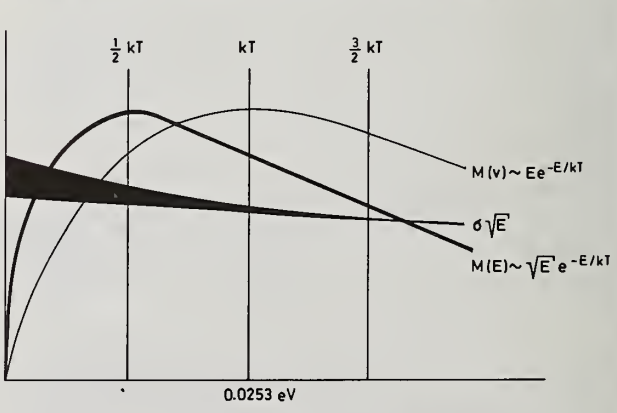

FIG.1 ILLUSTRATION OF THE INTEGRAL $g \sim \int_o^\infty \sigma\sqrt{E}\, M(E)\, dE$ AND ITS UNCERTAINTY BELOW E = kT = 0.0253 eV.

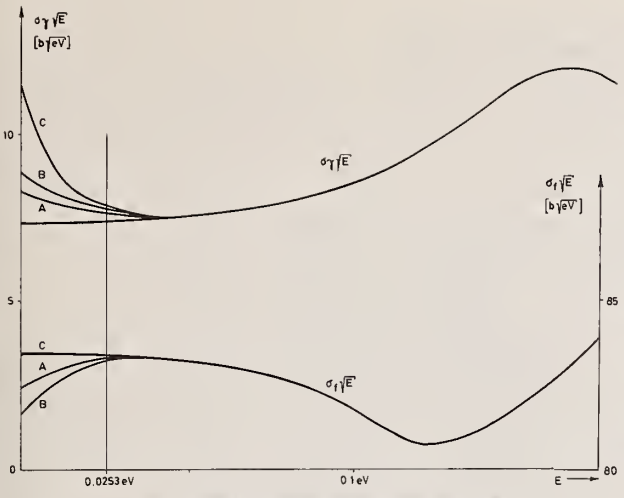

FIG.2 POSSIBLE LOW-ENERGY CROSS-SECTION CURVES FOR U-233

based on different parameters assumed for a resonance near -0.01 eV, and the resulting g-factors may well be discrepant by 3% in the case of capture or 0.5% in the case of absorption. Particularly for the capture cross-section, the uncertainty in the lowest-energy curve shape is the predominant error source, not only for the 20°C g-factor, but also for the temperature-dependence of the g-factor. If one corrects an integral capture cross-section or $\hat{\alpha}$ value from a spectrum of 100°C to one of 20°C one may have to assume a 2% uncertainty in $\hat{\alpha}$ and $\hat{\sigma}_\gamma$ due to the lowest-energy cross-section curve shape. In the least-squares fit, the errors of the experimental data were increased accordingly. This uncertainty may be responsible for the spread among the different experimental $\hat{\alpha}$ data but does not, however, account for the discrepancies between monoenergetic and thermal Maxwellian data.

Furthermore, one has to consider certain correlations between the absorption g-factors and the 2200 m/s cross-sections for scattering and absorption. Such correlations, which were not considered in earlier g-factor evaluations, were reflected in the present least-squares fit.

Results and conclusions

The results of the least-squares fit of all data together are shown in Table 2. For the uranium isotopes the fit presents a compromise between the 2200 m/s data and the Maxwellian data. The dilemma with this discrepancy becomes evident from the fact that two recent evaluations of the thermal data for U-233 and U-235, namely that by Steen [G7] and that used in ENDF/B-4, are discrepant by up to 1.4% where the data claim accuracies of 0.2% only.

The data resulting from the present fit have very good accuracies, e.g. 0.2-0.4% for the fission and absorption cross-sections. The errors given in Table 2 are the standard deviation errors resulting from the fit. They are determined by the internal errors of the experimental data. Except for some of the uranium data, the external errors are much smaller than the internal errors. The χ^2 value is about one half of its expectation value, an improvement compared to the 1969 evaluation where χ^2 values were about equal to their expectation values. Since a large fraction of the χ^2 value comes from σ_f and α of the uranium isotopes, the errors for all other data appear to be very reliable.

But for those data of the uranium isotopes, where the discrepancy between 2200 m/s data and Maxwellian data significantly exceeds one standard error, an increased error covering approximately this discrepancy is also given in Table 2. This error may be unsymmetric.

Compared to the 1969 IAEA values the main changes are (see Table 3):

The fission cross-sections for U-235, Pu-239 and Pu-241 are increased by more than one standard error, based on the lower half-life values for U-234 and Pu-239.

The absorption cross-section decreased for U-233 and increased for U-235 by more than one standard error.

The fission-neutron yields for all nuclides are decreased by more than one standard deviation, but the values of eta remain approximately unchanged.

The absorption g-factor is increased by more than two standard deviations in the case of U-233, and by about one standard deviation in the cases of the three other nuclides.

The increase in fission cross-sections and the decrease in fission-neutron yields would be considerably more drastic, were there not the discrepancy with the Maxwellian data.

Compared to the 1971 evaluation by De Volpi [5] there is agreement in the U-233 and Pu-239 cross-sections, but De Volpi's $\bar{\nu}$ and eta data are considerably lower than the present ones.

In the 1972 evaluation for the uranium isotopes by Steen [G7] the $\bar{\nu}$ data agree but all of Steen's cross-sections and eta data are significantly lower than the present values.

In ENDF/B-4 a preliminary version of the present evaluation was used. However, in order to avoid revision in curve shapes, the 1969 g-factors were kept unchanged. Some adjustment in the lowest-energy curve shapes seems to be indicated, although the g-factors of the uranium isotopes may be somewhat distorted in the present fit by the encountered discrepancies. The fission and absorption cross-sections of the uranium isotopes in ENDF-B are 2 or 3 barns higher than the present values.

The main conclusions are:

1. The low $\bar{\nu}$ values and the relatively high eta values are consistent if they are compared with the 2200m/s fission and absorption cross-sections $\bar{\nu}_t/\eta^o = \sigma_a^o/\sigma_f^o$, but they are inconsistent with the integral $\hat{\alpha}$ data of the uranium isotopes $\bar{\nu}_t/\eta^o = (1 + \hat{\alpha})\, g_f/g_a$.
2. The 2200 m/s cross-sections and the neutron yield data form one very consistent set, and the thermal Maxwellian cross-section data form another very consistent set. Both sets are consistent for the plutonium isotopes but discrepant for the uranium isotopes. The origin of this discrepancy is not known and requires further investigations.
3. The common source for the discrepancies encountered may be connected with the fission counting on uranium samples in a thermal neutron spectrum. Investigations in this direction appear to be indicated, but the source of the uncertainties may equally well be elsewhere.
4. The low-energy cross-section curve shapes between 0.005 and 0.025 eV are a significant source of uncertainty for g-factors and Maxwellian data. Accurate cross-section measurements are required in this low neutron energy range. Integral cross-section measurements in a "cold" neutron spectrum may also be useful.

Table 2: Consistent set of recommended values

Cross-sections in barns

		U-233	U-235	Pu-239	Pu-241	Cf-252
Cross-sections						
σ_T	metal sample	587.3 ± 1.3	695.3 ± 1.4	1018.5 ± 4.1	1389 ± 9	
	liquid sample	588.5 ± 1.3	697.0 ± 1.4	1019.2 ± 4.1	390 ± 9	
σ_s	metal sample	12.1 ± 0.7	14.4 ± 1.3	7.2 ± 1.4	10.8 ± 2.6	
	liquid sample	13.3 ± 0.7	16.1 ± 1.1	8.0 ± 1.0	12.0 ± 2.6	
σ_a	2200 m/s	575.2 ± 1.3	680.9 ± 1.7	1011.2 ± 4.1	1378 ± 9	
	20°C Maxw.	575.5 ± 1.3	667.1 ± 1.5	1092.9 ± 2.9	1432 ± 9	
σ_f	2200 m/s	529.9 ± 1.4*	583.5 ± 1.3*	744.0 ± 2.5	1015 ± 7	
	20°C Maxw.	528.1 ± 1.2* * ± 2	569.4 ± 1.2* * ± 4	785.3 ± 2.2	1060 ± 7	
$\frac{\sigma_f}{\sigma_f(U\text{-}235)}$	2200 m/s	0.908 ± 0.003		1.275 ± 0.004*	1.740 ± 0.012	
	20°C Maxw.	0.928 ± 0.002		1.379 ± 0.004* * ± 0.007	1.862 ± 0.012	
σ_γ	2200 m/s	45.3 ± 0.9*	97.4 ± 1.6*	267.2 ± 3.3	362 ± 6	
	20°C Maxw.	47.4 ± 0.3* * − 3	97.7 ± 0.6* * − 5	307.6 ± 1.5	371 ± 6	
$\alpha = \frac{\sigma_\gamma}{\sigma_f}$	2200 m/s	0.086 ± 0.002*	0.167 ± 0.003*	0.359 ± 0.005	0.357 ± 0.007	
	20°C Maxw.	0.090 ± 0.001* * − 0.005	0.172 ± 0.001* * − 0.008	0.392 ± 0.002	0.350 ± 0.006	
Neutron yields						
η	2200 m/s	2.283 ± 0.006	2.071 ± 0.006	2.106 ± 0.007	2.155 ± 0.010	
	20°C Maxw.	2.274 ± 0.005	2.062 ± 0.005	2.057 ± 0.006	2.166 ± 0.011	
$\eta\sigma_a = \bar{\nu}_t\sigma_f$	2200 m/s	1313 ± 4	1410 ± 4*	2129 ± 8	2969 ± 21	
	20°C Maxw.	1308 ± 4	1376 ± 4* *+ 5	2248 ± 8	3101 ± 21	
$(\eta-1)\sigma_a$	2200 m/s	738 ± 3	729 ± 4*	1118 ± 6	1592 ± 16	
	20°C Maxw.	733 ± 3	709 ± 3* * + 5	1155 ± 7	1669 ± 16	
$\bar{\nu}$	total	2.479 ± 0.006	2.416 ± 0.005*	2.862 ± 0.008	2.924 ± 0.010	3.746 ± 0.009
	prompt	2.472 ± 0.006	2.400 ± 0.005* *+0.02/−0.01	2.856 ± 0.008	2.908 ± 0.009	3.737 ± 0.008
	delayed	0.0067 ± 0.0002	0.0158 ± 0.0005	0.0063 ± 0.0004	0.0157 ± 0.0015	0.009 ± 0.004
$\frac{\bar{\nu}}{\bar{\nu}(Cf\text{-}252)}$	total	0.662 ± 0.002	0.645 ± 0.002	0.764 ± 0.002	0.781 ± 0.003	
	prompt	0.662 ± 0.002	0.642 ± 0.002	0.764 ± 0.002	0.778 ± 0.003	
g-factors (20°C)						
g_a		1.0006 ± 0.0018	0.9797 ± 0.0025	1.0808 ± 0.0039	1.0392 ± 0.0028	
g_f		0.9967 ± 0.0017	0.9758 ± 0.0014* *+0.002	1.0555 ± 0.0024	1.0442 ± 0.0048	
$g_\eta = g_f/g_a$		0.9962 ± 0.0017	0.9960 ± 0.0026	0.9766 ± 0.0034	1.0049 ± 0.0050	
g_γ		1.045 ± 0.021	1.003 ± 0.018	1.151 ± 0.015	1.025 ± 0.016	
The above data are consistent with the following values of the mean fission neutron spectrum energies $\bar{E}$ and of the half-live $T_{1/2}$:						
$\bar{E}$ [MeV]		2.09 ± 0.07	2.06 ± 0.06	2.13 ± 0.07	2.10 ± 0.07	2.19 ± 0.08
$T_{1/2}$ [y]		159000 ± 200	U-234 244700 ± 200	24290 ± 70	(14.5 ± 0.4)	

* An increased error is given for those data where the systematic discrepancy between 2200 m/s and 20° C Maxwellian experimental data exceeds significantly one standard error.

Table 3: Comparison with other evaluations

(cross-sections in barns, half-lives in years)

		Present Work (1975)	IAEA 1969 [2]	Change	De Volpi [5] (1971)	Steen [G7] (1972)	ENDF/B-4	Fit of 2200m/s data and $\bar{\nu}$ data (present work)
U-233	σ_a	575.2 ± 1.3	577.6 ± 1.8	- 2.4	575.6	572.2 ± 0.9	579.9 ± 1.5	573.8 ± 1.8
	σ_f	529.9 ± 1.4	530.6 ± 1.9	- 0.7	531.9	526.3 ± 0.8	533.7 ± 1.3	532.6 ± 3.0
	η	2.283 ± 0.006	2.284 ± 0.006	- 0.001	2.284	2.277 ± 0.005	2.284 ± 0.004	2.291 ± 0.009
	$\bar{\nu}_t$	2.479 ± 0.006	2.487 ± 0.007	- 0.008	2.472	2.476 ± 0.005	2.482 ± 0.005	2.468 ± 0.008
	g_a	1.001 ± 0.002	0.997 ± 0.001	+ 0.004			0.999	
	g_f	0.997 ± 0.002	0.995 ± 0.002	+ 0.002			0.997	
	$T_{1/2}$	159000 ± 200	159300 ± 2400	- 300				
U-235	σ_a	680.9 ± 1.7	678.5 ± 1.9	+ 2.4	683.0 ± 1.9	675.8 ± 1.3	682.9 ± 1.4	680.6 ± 1.8
	σ_f	583.5 ± 1.3	580.2 ± 1.8	+ 3.3	585.7 ± 1.8	577.5 ± 1.1	585.7 ± 1.1	587.7 ± 1.9
	η	2.071 ± 0.006	2.072 ± 0.006	- 0.001	2.058 ± 0.006	2.062 ± 0.005	2.074 ± 0.003	2.075 ± 0.008
	$\bar{\nu}_t$	2.416 ± 0.005	2.423 ± 0.007	- 0.007	2.400 ± 0.007	2.412 ± 0.005	2.419 ± 0.004	2.403 ± 0.006
	g_a	0.980 ± 0.003	0.979 ± 0.001	+ 0.001			0.979	
	g_f	0.976 ± 0.002	0.977 ± 0.002	- 0.001			0.977	
U-234	$T_{1/2}$	244700 ± 200	248800 ± 1600	- 4100				
Pu-239	σ_a	1011.2 ± 4.1	1012.9 ± 4.1	- 1.3	1013.4 ± 4.6		1011.8 ± 3.6	1010.8 ± 4.7
	σ_f	744.0 ± 2.5	741.6 ± 3.1	+ 2.4	742.5 ± 3.1		742.0 ± 2.1	745.9 ± 3.8
	η	2.106 ± 0.007	2.109 ± 0.007	- 0.003	2.091 ± 0.007		2.107 ± 0.007	2.112 ± 0.008
	$\bar{\nu}_t$	2.862 ± 0.008	2.880 ± 0.009	- 0.018	2.854 ± 0.007		2.873 ± 0.008	2.862 ± 0.010
	g_a	1.081 ± 0.004	1.075 ± 0.003	+ 0.006			1.075	
	g_f	1.056 ± 0.003	1.055 ± 0.003	+ 0.001			1.055	
	$T_{1/2}$	24290 ± 70	24380 ± 50	- 90				
Pu-241	σ_a	1378 ± 9	1375 ± 9	+ 3			1373 ± 7	1377 ± 13
	σ_f	1015 ± 7	1007 ± 7	+ 8			1009 ± 4	1021 ± 11
	η	2.155 ± 0.010	2.149 ± 0.014	+ 0.006			2.156 ± 0.007	2.162 ± 0.013
	$\bar{\nu}_t$	2.924 ± 0.010	2.934 ± 0.012	- 0.010			2.934 ± 0.008	2.915 ± 0.010
	g_a	1.039 ± 0.003	1.038 ± 0.001	+ 0.001			1.038	
	g_f	1.044 ± 0.005	1.049 ± 0.005	- 0.005		Axton [N4] (1972)	1.049	
Cf-252	$\bar{\nu}_t$	3.746 ± 0.009	3.765 ± 0.012	- 0.019		3.734 ± 0.008	3.757 ± 0.007	3.740 ± 0.009

5. As long as such measurements do not exist, the uncertainty of g-factors, due to the insufficient knowledge of the lowest-energy cross-section curves, should be investigated, in particular for the uranium isotopes. A variety of negative-energy resonance parameters should be tested to obtain a measure for the range of possible lowest-energy curve shapes. The uncertainty in the temperature corrections g(20°C)/g(T) should also be reviewed.

6. Of the 2200 m/s fission cross-section of U-233 only one inaccurate direct determination exists. A precise measurement of this quantity, being planned at Geel, is expected to improve considerably the knowledge of this quantity.

7. The Pu-239 half-life is insufficiently known. Several measurements of this quantity, being made in the US and at Geel, will noticeably improve the knowledge of the Pu-239 fission cross-section

8. The reason for the discrepancies among experimental half-life values should be investigated. In the case of a systematic error in the α-counting technique being verified, it would be desirable to know whether the same systematic error has also affected those fission cross-section measurements where the sample assay involved α-counting.

It is hoped that within one or two years from now at least some of the discrepancies and uncertainties mentioned can be eliminated. Whenever this will be the case, a revision of the present set of recommended values is likely to become necessary. In the meantime I shall be grateful to receive any comments or experimental results to be considered in the forthcoming revision.

REFERENCES

[1] WESTCOTT C.H., EKBERG K., HANNA G.C., PATTENDEN N.S., SANATANI S., ATREE P.M., Atomic Energy Review 3 2 (1965) 3.

[2] HANNA G.C., WESTCOTT C.H., LEMMEL H.D., LEONARD Jr. B.R., STORY J.S., ATTREE P.M., Atomic Energy Review 7 (1969) No. 4 p. 3.

[3] LEMMEL H.D., AXTON E.J., DERUYTTER A.J., LEONARD Jr., B.R., STORY J.S., INDC(NDS)-64 (1975), to be ordered from IAEA Nuclear Data Section, A-1011 Vienna, Austria, Box 590. Also to be published in Atomic Energy Review.

[4] McPHERSON D., JOHNSON J.H., AECL-3415(Apr.1972).

[5] DE VOLPI A., ANL-7830 (June 1971).

[C3] CAHELL M.J., WILKINS M., J.of Inorg.and Nucl. Chem. 33 (1971) 3972.

[C11] LOUNSBURY M., DURHAM R.W., HANNA G.C., Second Int.Conf.on Nucl.Data for Reactors, Helsinki 1970, Proc.Vienna (1970),vol.1, p.287. Supplemented by private communications from HANNA G.C.

[E5] DEBOISBLANC D.R., FAST E., Trans.Amer.nucl. Soc.4 2 (1961) 270.

[E10] LAPONCHE B., BRUNET M., BOUEDO Y., Nucl.Sci.and Engng 48 (1971) 305.

[E11] MACKLIN R.L., DESAUSSURE G., KINGTON J.D., LYON W.S., USAEC Rep.ORNL-60-2-84 (1960) and Nucl.Sci.Engng 8 (1960) 210.

[E12] MACKLIN R.L., DESAUSSURE G., KINGTON J.D., LYON W.S., Nucl.Sci.Engng 14 (1962) 101.

[E13] MAGNUSON D.W., Nucl.Sci. and Engng 44 (1971)266.

[E16] SMITH J.R., private communication (Dec. 1972) and (Aug. 1973).

[E17] SMITH J.R., USNDC-11 (June 1974) 12.

[E18] SMITH J.R., REEDER S.D., FLUHARTY R.G., IDO-17083 (1966).

[E19] SMITH J.R., REEDER S.D., Second Conf.on Nucl. Cross-Sections and Technology, Washington 1968, Proc.NBS Spec.Publication 299 (1968)vol.1,p.591.

[E21] GWIN R., ORNL-TM-4550 (Jan 1975).

[F2] BORCEA C., BORZA A., BUTA A., ISBASESCU A., MARINESCU L., MIHAI I., MASCUTIU T., PETRASCU M., SAVU V., SIMION V., IFA-NR-33(1970) Supplemented by private communication. Compare [F17].

[F3] BORCEA C., BORZA A., BUTA A., CIRSTOIU F., MARTINESCU L., MIHAI I., ISABASESCU A., MIHAILESCU I.M., NASCUTIU T., PETRASCU M., SAVU V., SIMION V., IFA-NR-47 (1973). Supplemented by private communication. Compare [F17].

[F7] DERUYTTER A.J., Symposium on Neutron Standards and Flux Normalization, Argonne 1970, Proc.AEC Symposium Series 23, CONF-701002 (1971) 221.

[F9] DERUYTTER A.J., SPAEPEN J., PELFER P., J.Nucl. Energy 27 (1973) 645. See also [F6], and DERUYTTER A.J., WAGEMANS C., J.Nucl.Energy 25 (1971) 263.

[F10] DERUYTTER A.J., BECKER W., Annals of Nucl.Sci. and Engng 1 (1974) 311. See also [F6] and [F8].

[F17] PETRASCU M., IFA-NR-22 (1965).

[F23] SWEET D.W., A.E.E. Winfrith, int.memorandum to J.S. Story of 26 July 1973. To be published.

[F24] VIDAL R., ROBIN M., CARNEIRO DA SILVA C., Second Int.Conf.on Nucl.Data for Reactors, Helsinki 1970, Proc.Vienna (1970),vol.1 p.295. Supplemented by private communication.

[G1] DERUYTTER A.J., WAGEMANS C., Nucl.Sci.and Engng 54 (1974) 423.

[G1] DERUYTTER A.J., WAGEMANS C., to be published in Annals of Nucl.Sci.and Engng (1975).

[G4] MOORE M.S., private communication (Sept 1973).

[G7] STEEN N.M., WAPD-TM-1052 (Sept 1972).

[G9] WAGEMANS C., DERUYTTER A.J., Conf.on Nucl.Cross-Sections and Technology, Washington D.C., March 1975, paper GB 17; and same authors, to be published in Annals of Nucl.Sci.and Engng(1975).

[G12] SMITH J.R., IAEA Conf.on Nucl.Data for Reactors, Paris 1966, Proc. INDC-156 (1966).

[H14] OETTING F.L., Symp.on "Plutonium 1970" and other Actinides, Santa Fe, New Mexico,Oct 1970, Proc. p.154, and OETTING F.L., RFP-1469 (1970).

[H19] VANINBROUKX R. EUR-5194e (Sept 1974).

[N3] AXTON E.J., CROSS P., ROSERTSON J.C., J.of Nucl.En. A/B 19 (1965) 409, and: AXTON E.J., BARDELL A.G., AUDRIC B.N., J.of Nucl.En. A/B 23 (1969) 457, and: RYVES T.B., HARDEN D., J.of Nucl.En. A/B 19 (1965) 607, and [N4].

[N4] AXTON E.J., Second IAEA Panel on Neutron Standard Reference Data,Vienna,Nov.1972,Proc.Vienna (1974), p.261.

[N9] BOLDEMAN J.W., Second IAEA Panel on Neutron Standard Reference Data,Vienna,Nov.1972, Proc.Vienna (1974) p.291.

[N11] COLVIN D.W., SOWERBY M.G., in Physics & Chemistry of Fission (Proc.Symp.Salzburg, 1965),2, IAEA, Vienna (1965) 25.

[N12] COLVIN D.W., SOWERBY M.G., MACDONALD R.I., in Nucl.Data for Reactors (Proc.Conf.Paris 1966) 1, IAEA, Vienna (1967) 307.

[N21] DE VOLPI A., PORGES K.G., Phys.Rev.C 1 (1970) 683, and: same authors, Metrologia 5 (1969)129, and: DE VOLPI A., ANL-7642 (1969). Revised value: DE VOLPI A.,J.of Nucl.En.26(1972) 75.

[N23] DIVEN B.C., private communications (1973).

[N27] HOPKINS J.C., DIVEN B.C., Nucl.Phys.48 (1963) 433.

[N41] POITOU J., SIGNARBIEUX C., Nucl.Instr. and Methods 114 (1974) 113.

[R2] DILG W., MANNHART W., STEICHELE E., ARNOLD P., Z. f. Physik 264 (1973) 427.

[S3] LEONARD Jr. B.R., Meeting on New Developments in Reactor Physics and Shielding, Kiamesha Lake 1972, Prov.CONF-720901 (1972),vol.1, p.81.

Acknowledgments: This work is based on the earlier works by C.H. Westcott, G.C. Hanna and their coworkers; on the active support and considerable contributions of E.J. Axton, A.J. Deruytter, B.R. Leonard Jr. and J.S. Story; on the advice of many scientists, both authors of experimental data and specialists for specific problems, whom all to name here is impossible; on the computer program by D.McPherson and J.H. Johnson, which was adapted to the IAEA computer by C.L. Dunford; and last not least on the assistance of neutron data centers and IAEA staff. All their contributions are gratefully acknowledged.

NEUTRON CROSS SECTION STANDARDS AND FLUX DETERMINATIONS ABOVE THERMAL ENERGIES

A. D. Carlson
National Bureau of Standards
Washington, D. C. 20234

The recent worldwide advances in nuclear technology, particularly fast fission and fusion reactors, have revealed the need for accurate neutron reaction cross sections for the design of these systems. The accuracies of these cross sections are generally limited by the standard cross sections relative to which they are measured. With the exception of the hydrogen scattering cross section, there have been serious problems with each of the standards in the energy region where it is being used as a standard. New measurements of many of these standards have been recently completed which will have a strong impact on the quality of these cross sections. A review will be presented of the status of the neutron cross section standards presently employed for measurements of neutron cross sections. Light element, capture and fission standards will be included. Special emphasis will be placed on the techniques which have been used to obtain the neutron flux for measurements of neutron cross section standards.

(Standard cross sections; H(n,n); ^{3}He(n,p); ^{6}Li(n,α); ^{10}B(n,α); C(n,n); Au(n,γ); ^{235}U(n,f); ^{237}Np(n,f); neutron flux determination)

Introduction

Although the subject of this paper is neutron cross section standards and flux determinations above thermal energies, it is clear that the topic is really the determination of neutron flux. The cross section standards are basically used as convenient means of determining the neutron flux. In the measurement of a given cross section for the design of a nuclear system, it is much easier to employ a standard cross section as a reference standard than to use the basic flux measuring techniques. It is often possible to choose a standard which is of the same type as the cross section to be measured. For example, in capture cross section measurements, replacing the sample for which the cross section is to be measured with a gold sample permits the determination of the neutron flux without any extensive changes in the electronics employed.

In this short paper I will briefly give the status of the standard cross sections, in my opinion, and then review the flux measurement techniques employed in standard cross section measurements.

Standard Cross Sections

Hydrogen Cross Section

The most accurately determined standard cross section is the hydrogen cross section. The total is known to ~1% up to 20 MeV and for standards work no additional measurements need to be made. The need at this time is for accurate measurements of the differential scattering cross section for neutron energies up to about 20 MeV. This need results from the use of counter telescopes for the determination of the neutron flux. In Fig. 1 recent measurements of the differential scattering cross section at 14.1 MeV are shown. The latest measurements, those of Shirato[1] (revised Shirato), agree with the calculations of Hopkins and Breit[2] within the errors of the measurements of ~3%. At this time the general feeling is that the Hopkins-Breit calculations are quite satisfactory in describing the hydrogen cross section. However, very accurate measurements (~1%) need to be made to substantiate these calculations. Measurements at this level of accuracy are extremely difficult and may be beyond the state of the art at this time. Measurements are now underway in the 20 MeV region at Harwell by Cookson and work is planned at Michigan by Shamu.

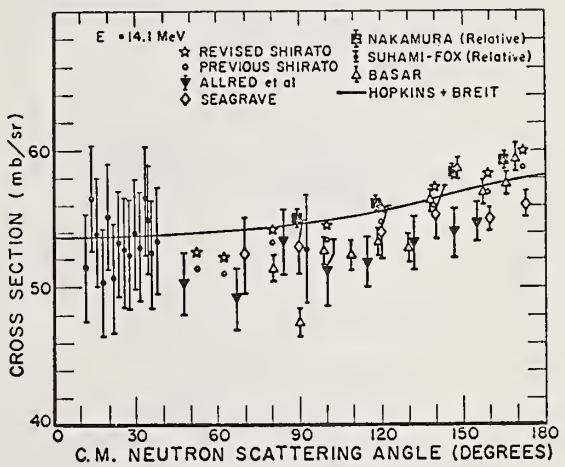

Figure 1. Measurements of the n-p scattering cross section at 14.1 MeV neutron energy. The references to the experimental work are contained in Ref. 1. The curve is the calculations of Hopkins and Breit.[2]

^{3}He(n,p)T Cross Section

The ^{3}He(n,p)T cross section has not been actively investigated in the last few years. It has many good features including a very large cross section and less structure than any of the other standards except hydrogen. One of its drawbacks is in its implementation. Its use has been limited to gas proportional counters which are too slow for fast timing applications. However recently ^{3}He has been employed in gas scintillators which do provide fast timing.[3,4] Although the pulse height resolution of these scintillators is not satisfactory for standards work at this time, further improvement in these detectors is anticipated.

In Figs. 2 and 3 measurements of the ^{3}He(n,p)T cross section are shown. It should be noted that the measurements of Lopez are relative to the ^{10}B(n,α_0+$\alpha_1\gamma$)^{7}Li reaction and thus the discrepancy near 100 keV may be a result of errors in this cross section. At this time the uncertainty in this cross section is ~1% at 1 keV, ~3% at 10 keV and ~7% above 100 keV. No measurements are currently underway or planned for this cross section but I believe this cross section deserves further consideration in view of improvements in technology and its many good points.

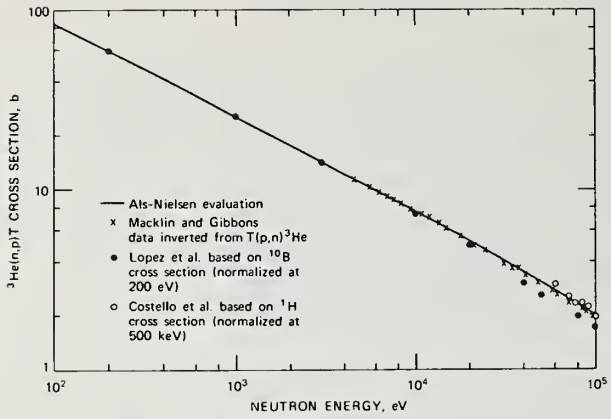

Figure 2. Measurements of the ^{3}He(n,p)T cross section from 100 eV to 100 keV compared with the evaluation of Als-Nielsen. The references to the experimental work and evaluation are contained in Ref. 5.

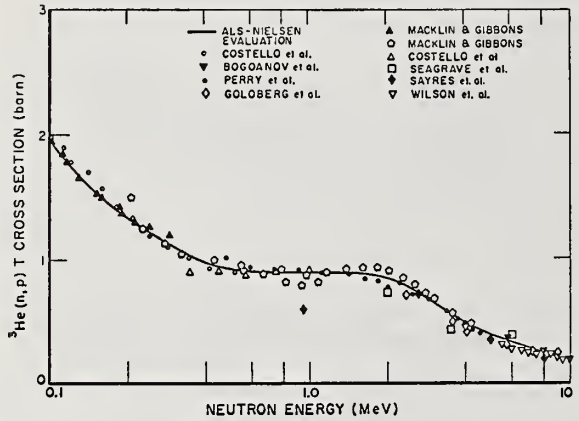

Figure 3. Measurements of the ^{3}He(n,p)T cross section from 0.1 to 10 MeV compared with the evaluation of Als-Nielsen. The references to all the experimental work (except Goldberg[6]) and the evaluation are contained in Ref. 5.

^{6}Li(n,α)T Cross Section

The ^{6}Li(n,α)T cross section has received more attention in the last few years than any other standard, except possibly ^{235}U(n,f). The interest in this cross section results from its ease of implementation with thin lithium glasses with which good timing can be obtained. Particular care has been given to determining the multiple scattering from the constituents of the lithium glass and scattering from surrounding materials. Recent measurements of this cross section are shown in Figs. 4 and 5. The measurements shown as Sowerby are obtained from the determinations of the ratio of the ^{6}Li(n,α)T to the ^{10}B(n,α_o+$\alpha_1\gamma$)^{7}Li cross sections by Sowerby combined with the ENDF/B-III evaluation for the ^{10}B(n,α_o+$\alpha_1\gamma$)^{7}Li cross section. The cross section is known to ~1% up to 1 keV and ~2-3% at 10 keV. Above 50 keV the recent ion chamber measurements of Friesenhahn are definitely higher than the lithium glass measurements of Coates and Poenitz.

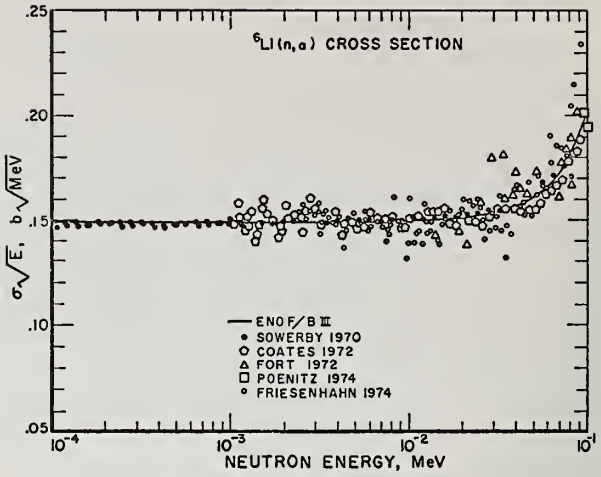

Figure 4. Measurements[7,8,9,10,11] of the ^{6}Li(n,α)T cross section from 100 eV to 100 keV compared with ENDF/B-III.

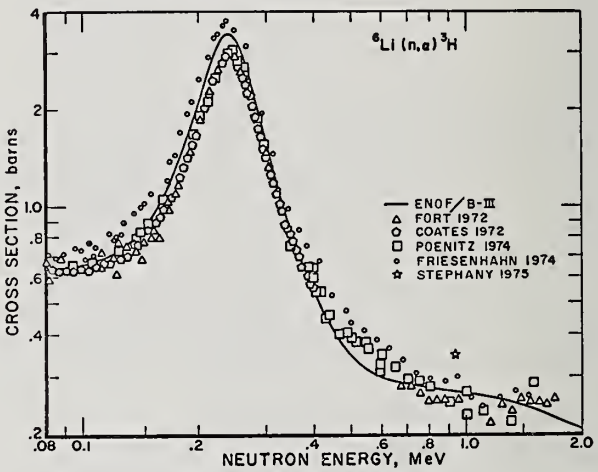

Figure 5. Measurements[9,8,10,11,12] of the ^{6}Li(n,α)T cross section from 80 keV to 2 MeV compared with ENDF/B-III.

Fort has recently reanalyzed his lithium glass for ^{6}Li content. The new determinations are 11% lower than those obtained previously. This would imply an 11% increase in the Fort values shown on Figs. 4 and 5. Fort is presently trying to resolve this discrepancy, but to my knowledge this problem has not been solved. A recent measurement by Stephany at 964 keV is higher than any other measurement at this energy; however, the uncertainty in this measurement is large. Useful standard cross sections should have a smooth energy dependence. The rapid change of the ^{6}Li(n,α)T cross section with energy near the 246 keV resonance may make this cross section unsuitable as a standard in this energy region.

Further work on this cross section is necessary to resolve the discrepancies. Work is planned at NBS and CBNM and new measurements have been recently completed and are being analyzed by Fort.

$^{10}B(n,\alpha)^{7}Li$ Cross Section

The interaction of neutrons with ^{10}B provides two commonly used standards. The $^{10}B(n,\alpha_1\gamma)^{7}Li$ reaction is convenient to use since the gamma ray produced is monoenergetic (478 keV) and hence complicated neutron energy dependent response functions are not required in implementing this cross section. The measurements of this cross section are shown in Fig. 6. The cross section is known to ~1% at 1 keV and ~2% at 10 keV. Above 50 keV discrepancies appear. In fact, no two data sets which have a reasonable range of overlap in energy agree even in shape. More work is necessary on this cross section. Measurements were recently begun at NBS and there is a high probability that new Harwell measurements will be initiated soon.

The $^{10}B(n,\alpha_0+\alpha_1\gamma)^{7}Li$ reaction has often been employed in neutron flux determination through the use of $^{10}BF_3$ gas proportional counters. Structure in the cross section in the hundred keV region must be properly taken into account when employing this cross section as a standard. In Fig. 7 measurements of this cross section are shown. The uncertainty in this cross section is ~1% at 1 keV and ~2-3% at 10 keV. Above 80 keV discrepancies become apparent. The measurements of Bichsel should not be included in evaluations of this cross section due to errors in the flux determination for these measurements. Note the large range in the determinations of this cross section near 400 keV where there is structure in this cross section. Clearly more work is required on this cross section, however at the present time there is no activity on this "standard". The discussion of the ^{6}Li and ^{10}B standards has been necessarily short in this paper. Further discussion of these standards is contained in the following paper by Hale.[23]

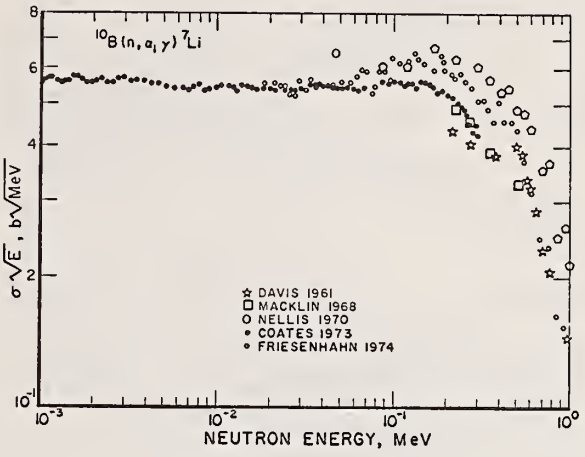

Figure 6. Measurements[13,14,15,16,11] of the $^{10}B(n,\alpha_1\gamma)^{7}Li$ cross section from 1 keV to 1 MeV.

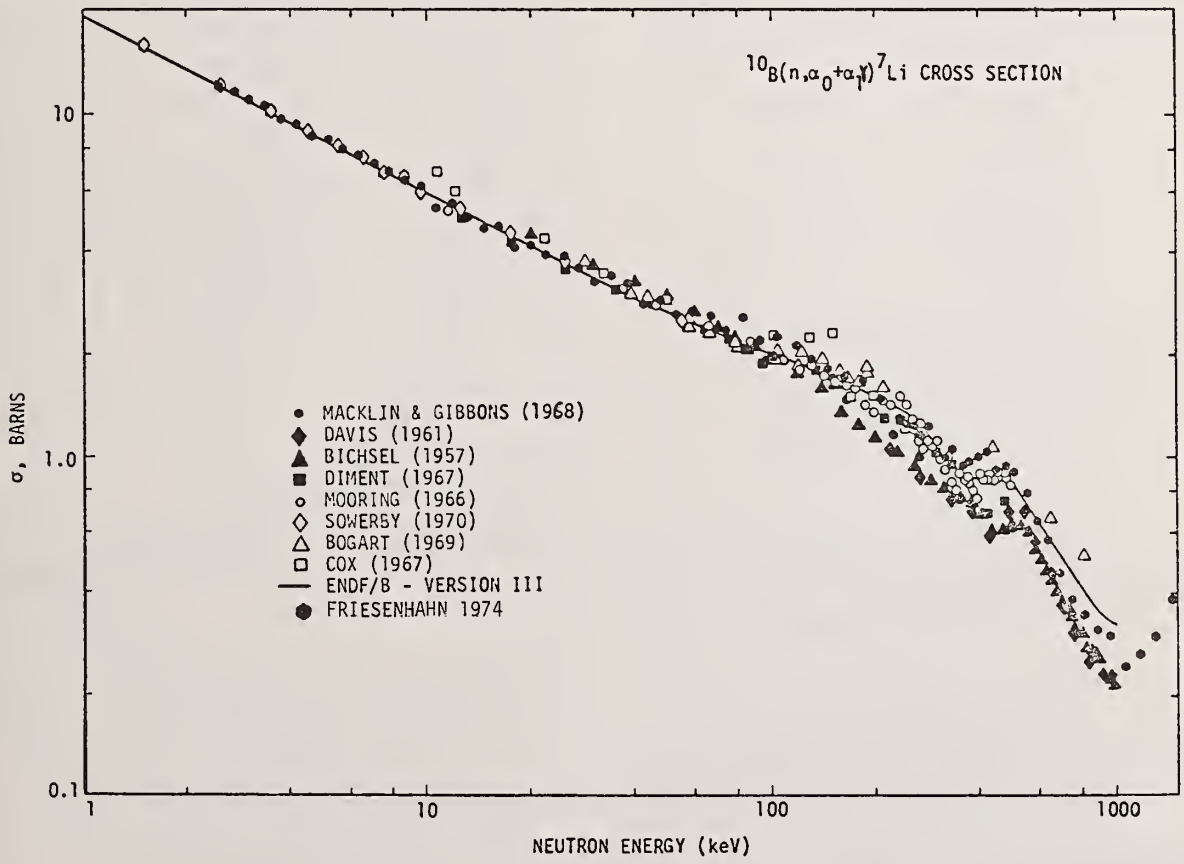

Figure 7. Measurements[14,13,17,18,19,20,21,22,11] of the $^{10}B(n,\alpha_0 + \alpha_1\gamma)^{7}Li$ cross section from 1 keV to 1 MeV compared with ENDF/B-III.

Carbon Cross Section

In the measurement of scattering cross sections, the carbon differential elastic scattering cross section is a useful standard. Measurements of the total neutron cross section provide a means of checking for consistency of these scattering cross sections. However two relatively recent precision measurements[25,26] differ by over 2% near 100 keV. As is shown in Fig. 8, recent measurements at NBS by Heaton[29], I think, have improved the knowledge of this cross section to the 1% level.

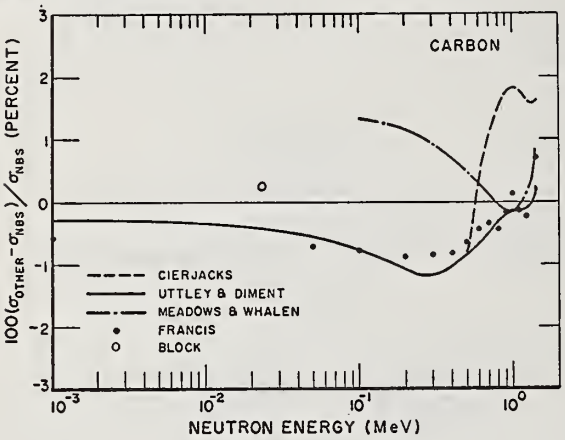

Figure 8. Measurements[24,25,26,28] and an evaluation[27] of the carbon total cross section compared with the NBS measurements of Heaton.[29]

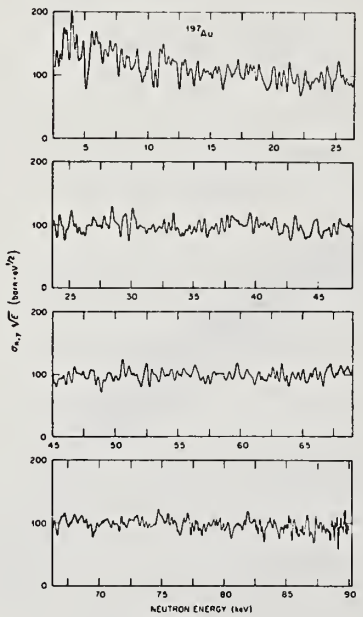

Figure 9. Measurements of the gold capture cross section by Macklin.[31] The data have been grouped to a constant resolution of 175 eV FWHM.

Capture Standards

Although a number of nuclides[30] may be potentially better standards than gold as capture standards, gold seems to have won by default largely due to difficulties in funding for cross section research. Fig. 9 shows measurements by Macklin of the gold capture cross section below 90 keV grouped to a resolution of 175 eV. The structure in this cross section must be taken into consideration when employing it as a cross section standard. Recent measurements of the gold capture cross section above 10 keV are shown in Figs. 10 and 11. The curve is the recent ENDF/B-IV evaluation by Murrey Goldberg. The agreement between the measurements and the evaluation is quite good, generally within the error bars. Unfortunately, this does not mean that the cross section is known accurately since the uncertainties are large on most of the measurements. The gold cross section is probably known to ~ 5% over most of this energy region. There is some concern over the measurement by Robertson at 964 keV which has a quoted accuracy of about 2% but is 12% higher than the ENDF/B-IV evaluation. Very recent measurements by Liskien[42] in this energy region indicate that there may be some structure at this energy which could explain the high value of Robertson. Though the gold capture cross section has improved considerably in the last five years, the uncertainties should be reduced to at least the 2% level. Measurements have recently been completed on this cross section (too late to be included in Figs. 10 and 11) by Liskien[42], Fort[43] and Macklin.[31] However, I am not aware of any measurements underway at this time.

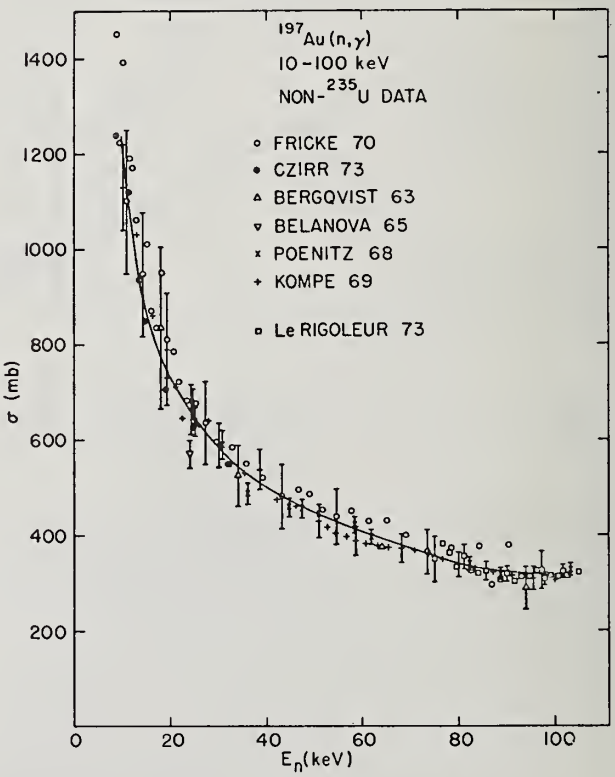

Figure 10. Measurements[32,33,34,35,36,37,38] of the gold capture cross section from 10 to 100 keV compared with ENDF/B-IV.

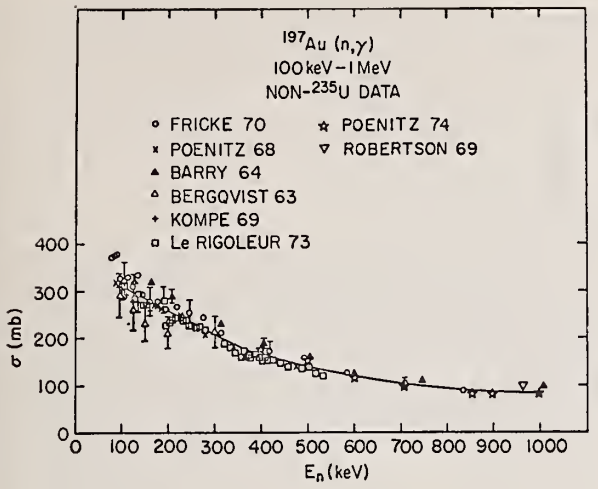

Figure 11. Measurements[32,36,39,34,37,38,40,41] of the gold capture cross section from 100 keV to 1 MeV compared with ENDF/B-IV.

Fission Standards

The status of the ^{235}U fission cross section has improved considerably in the last few years. Below 100 keV it must be used with caution as a result of structure in the cross section. Recent measurements of this cross section above 100 keV are shown in Figs. 12, 13 and 14. The ENDF/B-III curve is shown to permit an evaluation of the changes in the cross section values in the last few years. In the energy region from 100 keV to 1 MeV the cross section is known to an accuracy of about 3-4%; from 1 to 5 MeV, 3-5% and above 5 MeV the uncertainty is 7-10%. The need is for 1% uncertainties in this cross section throughout this entire energy region. There are disturbing discrepancies which need to be resolved before this accuracy will be achieved. For example, at 4 MeV the two most recent sets[51,52] of measurements of this cross section, each with an estimated uncertainty of about 1%, disagree by about 5%. Above 6 MeV very few high accuracy

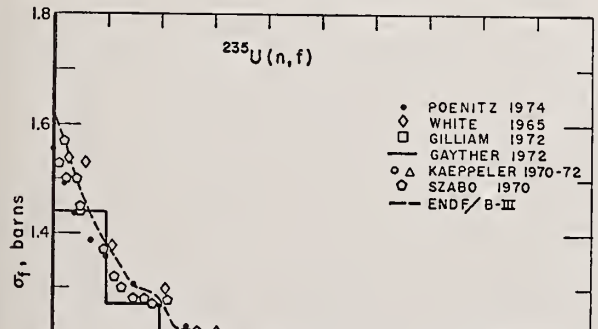

Figure 12. Measurements[44,45,46,47,48,49] of the ^{235}U fission cross section from 100 keV to 1 MeV compared with ENDF/B-III.

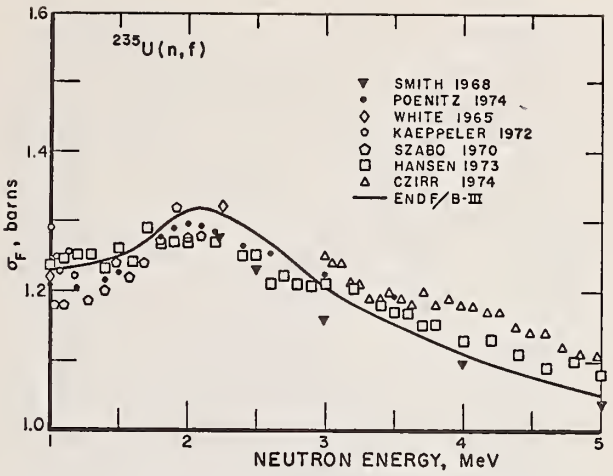

Figure 13. Measurements[50,44,45,48,49,51,52] of the ^{235}U fission cross section from 1 MeV to 5 MeV compared with ENDF/B-III.

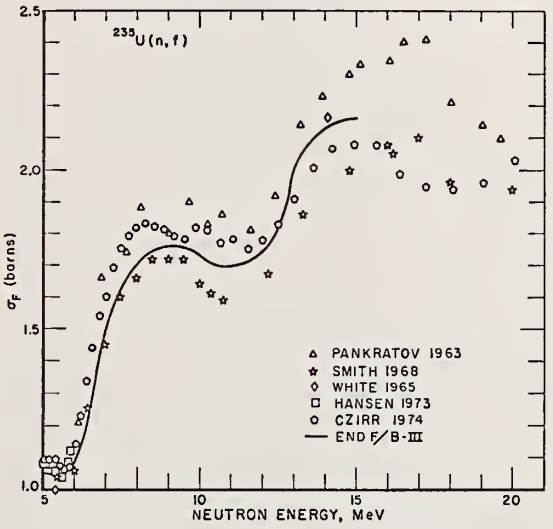

Figure 14. Measurements[53,50,45,51,52] of the ^{235}U fission cross section from 5 MeV to 20 MeV compared with ENDF/B-III.

measurements have been made. At this conference new measurements by Sidhu and Czirr[54] have extended the Livermore measurements from 3 MeV down to 0.8 MeV. They have also made new measurements relative to the $^{6}Li(n,\alpha)T$ cross section. In addition, new measurements have begun at NBS, Bruyerès-le-châtel and are planned at Argonne.

There is a need for a fission standard in the MeV region which does not have a large thermal cross section. With this standard, thermal and epithermal neutrons would not produce a significant background problem. In Fig. 15 the fission cross sections of ^{235}U, ^{238}U and ^{237}Np are compared. Above 1 MeV ^{237}Np has a larger cross section than ^{235}U. The effective threshold for ^{237}Np occurs at a considerably lower energy and the cross section varies more slowly with neutron energy above threshold than ^{238}U. The ^{237}Np fission cross section should be seriously considered for this standard.

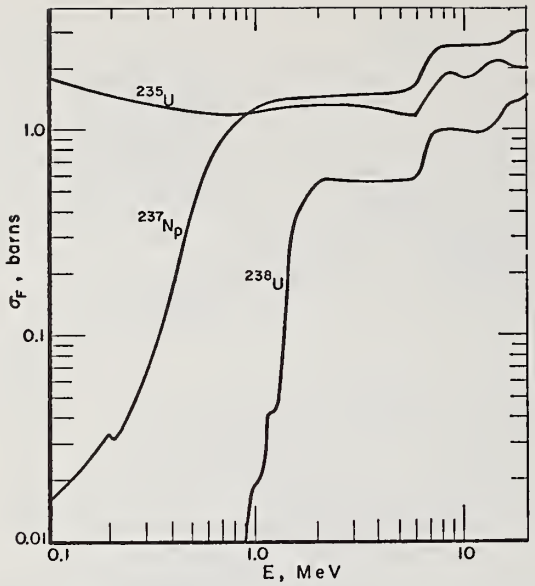

Figure 15. The fission cross sections of ^{235}U, ^{238}U and ^{237}Np from 0.1 to 20 MeV.

Flux Determination for Standard Cross Section Measurements

Associated Particle and Activity Methods

The associated particle technique has been employed effectively in the past with the $D(d,n)^3He$ and $T(d,n)^4He$ reactions. More recently Fort,[55] Liskien[56] and Meier[57] have utilized the $T(p,n)^3He$ reaction.

This reaction is well suited for many of the standards where the interest is in measurements from 100 keV to 1.5 MeV. Basically the associated particle technique permits a determination of the neutron flux in a given solid angle by counting the associated particles (^3He in this case) in the associated kinematic solid angle. Various techniques are employed to eliminate unwanted charged particles present in the associated cone. At NBS both time-of-flight and an electrostatic field are employed. With this system, background from unwanted charged particles has been reduced to less than 1%, however problems with the neutron cone may limit the accuracy to ≈2%.

The associated activity technique requires that the neutron producing reaction produces a radioactive final nucleus for every neutron emitted. By counting the activity of the target a determination of the total number of neutrons emitted can be obtained. This technique works very well near threshold where the neutrons are kinematically collimated into a forward cone. At higher energies however it is necessary to employ a spherical sample or detector to surround the entire target and a relatively large neutron energy spread must be tolerable.

Gray Detectors

In the recent past a number of gray neutron detectors have been designed.[44,58] They all depend on the moderation of neutrons in the detector and either detection of the moderated neutrons or gamma rays produced by capture of these neutrons in the constituents of the detector. The efficiency of these detectors is generally quite insensitive to neutron energy e.g. the detector of Gabbard[59] reported at this conference has an efficiency that is constant within the uncertainty of the measurements for neutron energies from 30 keV to 1.5 MeV. Unfortunately, the basic design which yields a very slow change in the energy dependence of the efficiency causes the detector to have rather poor timing. These detectors are used for relative measurements of the neutron flux.

Black Neutron Detector

The use of relatively thin hydrogenous scintillators for flux determination depends to first order on neutron interaction cross sections of the constituents of the scintillator, the size of the detector and neutron multiple scattering calculations. Therefore, generally, the efficiency of these detectors cannot be calculated with high accuracy. Poenitz[44] has designed a large hydrogenous scintillator which has a very large efficiency and depends only weakly on the above mentioned effects. The detector is a large cylinder with an entrance channel terminating near the center of the cylinder. A collimated neutron beam with a diameter smaller than the diameter of the channel enters the channel. As a result of the size of the scintillator each neutron will lose most of its kinetic energy in successive collisions with the hydrogen and carbon nuclei in the scintillator. The pulse height distribution from this detector will exhibit a pronounced sum peak with a relatively small tail extending to zero pulse height. Only a relatively small correction is made for the extrapolation to zero pulse height. In addition to providing an absolute determination of the neutron flux, the detector has a fast time response and can be employed in fast timing experiments. This detector should provide accuracies of ≈1% at suitable neutron energies. A modified version of this counter[60] is being used at NBS for flux determination for neutron energies from 250 keV to 1 MeV.

Techniques Involving Hydrogen Scattering

The hydrogen cross section is considered to be so well known that detectors which rely directly upon this cross section which have only small counter effects are considered as absolute neutron flux detectors. The implementation of the hydrogen cross section with gas proportional counters has been carefully investigated[45,61,62] in the recent past. The ideal pulse height distribution for such a counter for monoenergetic incident neutrons is proportional to the center of mass angular distribution for n-p scattering. Thus in the normal range of use for these counters, below 2 MeV, the distribution should be essentially flat. A major source of uncertainty in flux measurements with these counters at low neutron energies is the extrapolation below the bias to zero pulse height. Though proton recoils have been observed with energies as low as ~200 eV, uncertainties in the energy loss required to produce an ion pair are so large that accurate neutron flux measurements have been limited to energies above a few keV. Only recently have these counters been employed[11,63] in linac measurements. This is partly a result of the relatively poor timing of these counters so that high power linacs with long flight paths are necessary in their use. The background conditions for the linac measurements are generally much superior to those with monoenergetic sources. It should be possible to make flux measurements with uncertainties of ≈1% with these counters.

Proton counter telescopes have been used extensively in the past[64] for absolute measurements of the neutron flux in the MeV neutron energy region.

Frequently these counters were used in high background areas so that the telescope contained one or more dE/dx detectors between the proton emitting foil and the main proton detector. By demanding a coincidence between all the detectors a significant background reduction was possible. In extreme background conditions anti-coincidence detectors around the detector are used. Recently[52] a telescope in ring geometry was designed for linac use. A lead cylinder is used to shield the proton detector from direct neutrons and gamma-flash. The angle between the incoming neutrons and the scattered protons can be selected to minimize errors resulting from uncertainties in the n-p scattering cross section. The detected protons produce a well defined peak with only a small background. Measurements have been made up to 20 MeV neutron energy with this counter. A similar telescope has been designed and constructed at NBS. Though the telescope in principle can be used to determine the flux absolutely, its use has been as a relative flux detector. In this mode relative flux measurements with an accuracy of 1% are possible.

Bath Techniques

The physics involved in manganese or vanadium baths is similar to that for the gray detectors. Neutrons from a source to be calibrated are moderated in the bath and absorbed in Mn or V nuclei. The rate at which gamma rays are detected from decay of these radioactive nuclei is proportional to the neutron flux. However, bath techniques[65] involve accurate sampling of the liquid in the bath and a thorough understanding of neutron loss and corrections. The technique allows absolute determinations to be made with an accuracy of ≃ 1%. In addition to the calibration of encapsulated sources which are placed in the bath, this technique can be used for the measurement of neutron flux both from reactor filtered beams and from charged particle accelerator targets.

Normalization of Relative Measurements

A number of the detectors mentioned above are used to determine the relative flux. Various approaches can be followed in the use of these detectors in cross section measurements. One possibility is to calibrate the detector in a known neutron flux; however, then in a cross section measurement details of the reaction rate detector such as the amount of uranium in a fission foil must be known accurately. There are some compromise situations, for example, in some capture cross section measurements the saturated resonance technique can be applied. This method allows a determination of the product of the neutron flux and the gamma ray detector efficiency at the energy of the saturated resonance. Thus cross section measurements can be made from relative flux measurements and the thickness of the capture sample. Another method is to make relative cross section measurements and normalize to the cross section at one energy or the average over an energy interval. This technique is particularly good when the normalization can be done at thermal energies where the cross sections are generally known very accurately. Another means of normalization which is being considered for the ^{235}U fission cross section measurements at NBS involves the ^{235}U fission cross section averaged over the ^{252}Cf neutron spectrum, $\bar{\sigma}_f(X_{Cf}, {}^{235}U)$. Measurements of this quantity can be made with high accuracy.[66] The normalization then involves folding a best estimate of the ^{252}Cf neutron spectrum into the relative measurements and normalizing this to the measured $\bar{\sigma}_f(X_{Cf}, {}^{235}U)$. The result is very insensitive to uncertainties in the ^{252}Cf neutron spectrum. The weak dependence on the shape of the spectrum chosen can be seen from Fig. 16. The ^{235}U fission

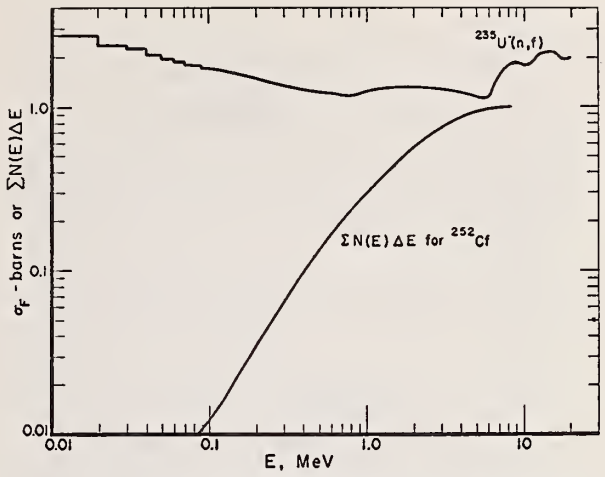

Figure 16. The normalized integral of the ^{252}Cf neutron spectrum (the fraction of the neutrons in the spectrum having an energy less than E) and the ^{235}U fission cross section for neutron energies from 0.01 MeV to 20 MeV.

cross section changes by less than a factor of 2 in the energy interval in which 98% of the ^{252}Cf neutrons are contained. There would be no dependence on the spectrum if the ^{235}U fission cross section were constant. A correction must be applied since the relative measurements will not cover the entire energy region of the ^{252}Cf fission spectrum. This procedure should provide ≈ a 2% normalization of the relative measurements.

Special Techniques

The ultimate objective is the measurement of standard cross sections. In some special cases these measurements can be made without a determination of the neutron flux. Some examples of the use of special techniques will be described. Measurements of the transmission of neutrons through a spherical shell[22] provide a determination of the total absorption cross section. If it is known that only one reaction contributes (or if corrections can be made for other reactions that can occur) then the spherical shell transmission measurement provides that reaction cross section. Unfortunately spherical shell transmission measurements often have large uncertainties due to the multiple scattering corrections and statistical uncertainty.

Another example is given by the technique employed by Costello[5] in measurements of the $^{3}He(n,p)T$ cross section. The pulse height distribution for about 500 keV neutrons incident on a ^{3}He gas proportional counter used in this experiment is shown in Fig. 17. Neutrons which interact with the ^{3}He nuclei must either scatter or be absorbed in the $^{3}He(n,p)T$ reaction. Thus the total neutron cross section is directly proportional to the total area in the pulse height distribution. The $^{3}He(n,p)T$ cross section is equal to the ratio of the area of the $^{3}He(n,p)T$ peak plus wall effect tail to the total area times the measured $^{3}He(n,p)T$ total cross section. The measurement is limited by the uncertainty in the total cross section and the area ratio.

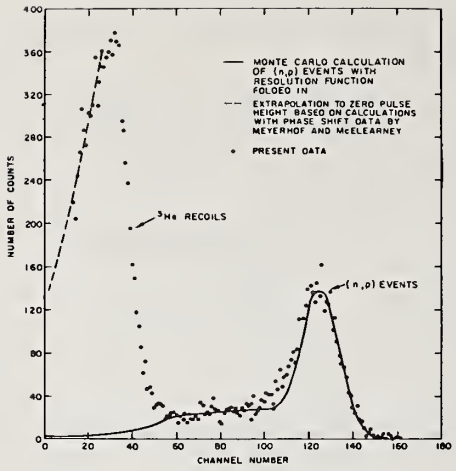

Figure 17. The pulse height distribution[5] for approximately 500 keV neutrons incident on a ^{3}He gas proportional counter.

Conclusion

There are discrepancies in many of the standard cross sections, particularly above 100 keV. It is generally not possible to resolve a discrepancy at one energy in a standard cross section by making just one measurement. One must employ as many redundant measuring techniques as is feasible for the determinations of both the neutron flux and the reaction rate. Only by showing the cross section community that consistent results are obtained from these redundant measurements, will the discrepancies in the standards be removed.

References

1 S. Shirato and K. Saitoh, J. Phys. Soc. Jap. 36 (1974) 331

2 J. C. Hopkins and G. Breit, Nuclear Data Tables A9 (1971) 137

3 M. M. Hoffman, G. J. Berzins, W. M. Sanders, L. J. Brown and D. D. Phillips, Proc. Conf. Neutron Cross Sections and Technology, CONF-710301, p. 868, U.S.A.E.C. (1971)

4 L. Mewissen, F. Poortmans, G. Rohr, J. Theobald, H. Weigmann and G. Vanpraet, these proceedings

5 D. G. Costello, Proc. Symp. Neutron Standards and Flux Normalization, CONF-701002, p. 74, U.S.A.E.C. (1971) and D. G. Costello, S. J. Friesenhahn, and W. M. Lopez, Nucl. Sci. Eng. 39 (1970) 409

6 M. D. Goldberg, J. D. Anderson, J. P. Stoering and C. Wong, Phys. Rev. 122 (1961) 1510

7 M. G. Sowerby, B. H. Patrick, C. A. Uttley and K. M. Diment, "The Ratio of the ^{6}Li(n,α) to the ^{10}B(n,α) Cross Section from 10 eV to 80 keV and Recommended Values of the ^{10}B(n,α) Cross Section", AERE-R-6316 (1970)

8 M. S. Coates, G. J. Hunt and C. A. Uttley, "Measurements of the Relative ^{6}Li(n,α)T Cross Section in the Energy Range 1 keV to 500 keV", Proc. Second IAEA Panel on Neutron Standard Reference Data, Vienna, (to be published)

9 E. Fort and J. P. Marquette, "Etude De La Section Efficace ^{6}Li(n,α)T Dans La Gamme D'Energie Comprise Entre 20 keV et 1700 keV", EANDC(E) 148 "U" (1972)

10 W. P. Poenitz, Z. Phys. 268 (1974) 359

11 S. J. Friesenhahn, V. J. Orphan, A. D. Carlson, M. P. Fricke and W. M. Lopez, "The (n,α) Cross Sections of ^{6}Li and ^{10}B Between 1 and 1500 keV", USAEC Report INTEL-RT 7011-001 (1974)

12 W. P. Stephany and G. F. Knoll, these proceedings

13 E. A. Davis, F. Gabbard, T. W. Bonner and R. Bass, Nucl. Phys. 27 (1961) 448

14 R. L. Macklin and J. H. Gibbons, Phys. Rev. 165 (1968) 1147

15 D. O. Nellis, W. E. Tucker and I. L. Morgan, Phys. Rev. C1 (1970) 847

16 M. S. Coates, G. J. Hunt and C. A. Uttley, "A Preliminary Measurement of the Relative ^{10}B(n,α$_1\gamma$) Cross Section", Proc. Second IAEA Panel on Neutron Standard Reference Data, Vienna (to be published)

17 H. Bichsel and T. W. Bonner, Phys. Rev. 108 (1957) 1025

18 K. M. Diment, "The Average Neutron Total Cross Section of ^{10}B from 100 eV to 10 MeV and Absorption Cross Section Up to 500 keV", AERE-R-5224 (1967) and private communication from M. G. Sowerby (1972)

19 F. P. Mooring, J. E. Monahan and C. M. Huddleston, Nucl. Phys. 82 (1966) 16

20 M. G. Sowerby, B. H. Patrick, C. A. Uttley and K. M. Diment, J. Nucl. Energy 24 (1970) 323 and private communication from M. G. Sowerby (1972)

21 D. Bogart and L. L. Nichols, Nucl. Phys. A125 (1969) 463

22 S. A. Cox and F. R. Pontet, J. Nucl. Energy 21 (1967) 271

23 G. M. Hale, these proceedings

24 S. Cierjacks, P. Forti, D. Kopsch, L. Kropp and J. Nebe, Proc. Conf. Neutron Cross Sections and Technology, p. 743, NBS Special Publication 299, National Bureau of Standards (1968)

25 C. A. Uttley and K. M. Diment, Proc. Symp. Neutron Standards and Flux Normalization, CONF-701002, p. 201, U.S.A.E.C. (1971)

26 J. W. Meadows and J. F. Whalen, Nucl. Sci. Eng., 41 (1970) 351

27 N. C. Francis, C. R. Lubitz, J. T. Reynolds, C. J. Slavik and R. G. Stieglitz, Proc. Symp. Neutron Standards and Flux Normalization, CONF-701002, p. 166, U.S.A.E.C. (1971)

28 R. C. Block, Y. Fujita, K. Kobayashi and T. Oosaki, J. Nucl. Sci. Eng. 12 (1975) 1

29 H. T. Heaton II, J. L. Menke, R. A. Schrack and R. B. Schwartz, Nucl. Sci. Eng. 56 (1975) 27

30 A. D. Carlson, Proc. Symp. Neutron Standards and Flux Normalization, CONF-701002, p. 285, U.S.A.E.C. (1971)

[31] R. L. Macklin, J. Halperin and R. R. Winters "Gold Neutron Capture Cross Section from 3 to 550 keV , to be published in Phys. Rev.

[32] M. P. Fricke, W. M. Lopez, S. J. Friesenhahn, A. D. Carlson and D. G. Costello, Proc. Second Conf. on Nucl. Data for Reactors, Helsinki, 1970, paper CN-26/43, I.A.E.A., Vienna

[33] J. B. Czirr and M. L. Stelts, Nucl. Sci. Eng. 52 (1973) 299

[34] I. Bergqvist, Ark. Fys. 23 (1963) 425

[35] T. S. Belanova, A. A. Van'kov, F. F. Mikhailus and Yu. Ya. Stavisski, J. Nucl. Energy 20 (1966) 411

[36] W. P. Poenitz, D. Kompe and H. O. Menlove, J. Nucl. Energy 22 (1968) 505

[37] D. Kompe, Nucl. Phys. A133 (1969) 513

[38] C. Le Rigoleur, A. Arnaud and J. Taste, "Mesure de la Section Efficace de Capture Radiative des Neutrons par l"Or Entre 75 keV et 550 keV", CEA-N-1662 (1973)

[39] J. F. Barry, J. Nucl. Energy 18 (1964) 491

[40] W. P. Poenitz, "Neutron Capture Cross Section Measurements of ^{197}Au and ^{238}U from 20-3500 keV", to be published

[41] J. C. Robertson, T. B. Ryves, E. J. Axton, I. Goodier and A. Williams, J. Nucl. Energy 23 (1969) 205

[42] H. Liskien, private communication (1975)

[43] C. Le Rigoleur, private communication (1975)

[44] W. P. Poenitz, Nucl. Sci. Eng. 53 (1974) 370

[45] P. H. White, J. Nucl. Energy A/B 19 (1965) 325

[46] D. M. Gilliam and G. F. Knoll, Trans. Am. Nucl. Soc. 15 (1972) 946 and these proceedings.

[47] D. B. Gayther, D. A. Boyce and J. B. Brisland, "Measurement of the ^{235}U Fission Cross Section in the Energy Range 1 keV to 1 MeV", Proc. Second IAEA Panel on Neutron Standard Reference Data, Vienna (to be published)

[48] F. Kaeppeler, Proc. Symp. Neutron Standards and Flux Normalization, CONF-701002, p. 272, U.S.A.E.C. (1971) and "A Measurement of the Neutron Fission Cross Section of ^{235}U Between 0.5 and 1.2 MeV", Proc. Second IAEA Panel on Neutron Standard Reference Data, Vienna (to be published)

[49] I. Szabo, G. Filippi, J. L. Huet, J. L. Leroy and J. P. Marquette, Proc. Symp. Neutron Standards and Flux Normalization, CONF-701002, p. 257, U.S.A.E.C. (1971); also Proc. Conf. Neutron Cross Sections and Technology, CONF-710301, p. 573, U.S.A.E.C. (1971) and I. Szabo, J. L. Leroy and J. P. Marquette, "On The Discrepancies Observed in Fission Cross Section Measurements Using Fission Foils From Difference Origins", Proc. Second IAEA Panel on Neutron Standard Reference Data, Vienna (to be published)

[50] R. K. Smith, G. E. Hansen and S. McGuire, Bull. Am. Phys. Soc. 2 (1957) 196 and Corrections to this data (1968)

[51] G. E. Hansen, private communication (1973)

[52] J. B. Czirr and G. S. Sidhu, "Fission Cross Section of ^{235}U from 3 to 20 MeV", UCRL-76041 (1974)

[53] V. M. Pankratov, Soviet Atomic Energy 14 (1963) 167

[54] G. S. Sidhu and J. B. Czirr, these proceedings, also J. B. Czirr and G. S. Sidhu, these proceedings

[55] E. Fort, J. L. Leroy and J. P. Marquette, Nucl. Instr. and Meth. 85 (1970) 115

[56] H. Liskien and A. Paulsen, Nucl. Instr. and Meth. 69 (1969) 70

[57] M. M. Meier, A. D. Carlson and G. P. Lamaze, these proceedings

[58] M. S. Coates, G. J. Hunt, C. A. Uttley and E. R. Rae, Proc. Symp. Neutron Standards and Flux Normalization, CONF-701002, p. 401, U.S.A.E.C. (1971)

[59] K. K. Sekharan, H. Laumer and F. Gabbard, these proceedings

[60] G. P. Lamaze, M. M. Meier and O. A. Wasson, these proceedings

[61] E. F. Bennett, Nucl. Sci. Eng. 27 (1967) 16 and also E. F. Bennett and T. J. Yule, "Techniques and Analyses of Fast-Reactor Neutron Spectroscopy with Proton-Recoil Proportional Counters, ANL-7763 (1971)

[62] J. W. Rogers, Nucl. Instr. and Meth. 80 (1970) 313

[63] O. A. Wasson, these proceedings

[64] C. H. Johnson in Fast Neutron Physics, ed. J. B. Marion and J. L. Fowler (Interscience Publishers, Inc., New York, 1960) Part I, p. 247

[65] K. W. Geiger, Metrologia 4 (1968) 8

[66] H. Heaton II, J. Grundl, V. Spiegel, Jr., D. Gilliam and C. Eisenhauer, these proceedings

R-MATRIX ANALYSIS OF THE LIGHT ELEMENT STANDARDS*

G. M. Hale
Los Alamos Scientific Laboratory, University of California
Los Alamos, New Mexico 87544

The application of multilevel, multichannel R-matrix theory to the analysis of reactions in light nuclear systems is outlined. The discussion then specializes to describe analyses of reactions in the ^{7}Li and ^{11}B systems, which contain (n,α) cross sections widely used as neutron standards. Comprehensive R-matrix analyses which were incorporated in Version IV of the Evaluated Nuclear Data File (ENDF/B-IV) for neutron reactions from ^{6}Li and ^{10}B are described, giving the reactions and data analyzed, the resulting parameters, and predicted cross sections. The effects of new experimental information on the ENDF/B-IV results are discussed for both lithium and boron. Particular attention is given to the perplexing question of determining the ^{6}Li(n,α) cross section in the region of the 240 keV resonance. Suggestions for further experimental work are given.

(Standards; cross sections; R-matrix; light elements; ^{6}Li; ^{10}B)

Introduction

I will begin this talk with a few introductory remarks about the analyses of nuclear reactions based on R-matrix theory, and then discuss applications of this approach to two light systems, ^{7}Li and ^{11}B. These systems contain (n,α) reactions having cross sections that are widely used as neutron "standards", since they follow the well-known 1/v dependence at low neutron energies. At energies above ~80 keV, however, these cross sections begin to deviate from the 1/v behavior due to the presence of resonances. In order that the cross sections be useful standards at neutron energies up to ~1 MeV, it is important to understand them in this resonance region. Both the 1/v behavior of the cross sections and the resonance effects come naturally from describing the reactions in terms of the R-matrix, introduced originally by Wigner and Eisenbud[1] in 1947.

It follows from the short range of nuclear forces that any quantity measured asymptotically for a nuclear scattering process -- cross section, polarization, or whatever -- can be related to the logarithmic derivative of the nuclear wavefunction evaluated on a surface having finite radii in configuration space. Outside of this "channel" surface, the particles are assumed to be grouped in separated pairs of fragments (two-body channels) between which no nuclear forces act. The R-matrix is essentially the reciprocal of the matrix formed by projecting the logarithmic derivative onto channel (spin-angle) eigenfunctions of total angular momentum and parity (J^{P}) at the nuclear surface.

The expansion

$$R_{c'c}(E) = \sum_{\lambda} \frac{\gamma_{\lambda c'}\gamma_{\lambda c}}{E_{\lambda}-E} \quad ,$$

results for elements of the R-matrix when the wavefunction inside the channel surface is expressed as a superposition of eigenfunctions created by imposing arbitrary boundary conditions at the channel surface on regular solutions of the total Hamilonian. The $\gamma_{\lambda c}$, or reduced width amplitudes, are essentially projections of these eigenfunctions onto the channel spin-angle functions at the surface, and the E_{λ} are the eigenvalues. A set of the R-matrix poles can be made to correspond with resonances of the physical system in the energy region of interest, while the remaining terms comprise the "distant level," or "background" contribution.

Many non-resonant features of nuclear reactions come from properties of the "known" (Coulomb) wavefunctions in the region exterior to the channel surface. The behavior of cross sections at and near thresholds is determined to a large extent by these functions, as is the dependence of the partial-wave amplitudes on orbital angular momentum, ℓ. In particular, anomolies in cross sections at thresholds for neutron channels, and the 1/v behavior of certain neutron-induced reaction cross sections at low energies, come directly from the energy dependence of these functions for s-wave neutrons.

The procedure for calculating the observables of a nuclear scattering process from the R-matrix is well established. Expressions for the unitary collision matrix, U, and the transition matrix, T, in terms of the R-matrix are given in the extensive review article of Lane and Thomas.[2] Transformation of the T-matrix to a different representation yields Wolfenstein's M-matrix[3] in terms of which arbitrary scattering observables may be calculated. This procedure has been implemented in its general form in a Los Alamos code called EDA[4] (for Energy Dependent Analysis), which accepts two-body channels having particles of arbitrary spins, masses, charges, parities, and relative angular momentum. Practical limitations on storage have thus far restricted the application of the code to light nuclear systems (A < 20).

Starting from a parameterization of the multichannel R-matrix in terms of channel radii a_c, reduced width amplitudes $\gamma_{\lambda c}$, and eigenvalues E_{λ}, the code calculates values for measured observables included from any of the two-body reactions possible in a given A-nucleon system. An automated search adjusts the parameters to obtain a best fit to all the data included in a least-squares sense. If the data analyzed are sufficent to determine the correct level structure in the region of interest, observables calculated from the best-fit parameters are likely to be quite reliable smoothed representations of the data. This is because experimental information from all the reactions considered influence the R-matrix parameters through unitarity, and incorrect experimental points should be "overruled" by the main body of the data, and by the general physical constraints R-matrix theory imposes. For this reason, we felt that comprehensive, multi-reaction R-matrix analyses would be well-suited to evaluating light-element standard cross sections. In the following, I will describe some results of applying this approach to the ^{7}Li and ^{11}B systems.

^{7}Li System

At energies between 0.1 and 1 MeV, the dominant feature of the neutron-induced reactions on ^{6}Li is a large

$J^P = 5/2^-$ resonance located at E_n = 240 keV. Disagreements among even recent measurements of the ^{6}Li(n,α) cross section over this resonance have been alarmingly large (as much as 25%) for a standard cross section. Furthermore, measured values of the neutron total cross section at the peak of the resonance appear to exceed the sum of the measured elastic scattering cross section and the measured (n,α) cross sections by more than 0.5 barn in most cases.

Although knowledge of the level structure of ^{7}Li is fairly complete at energies corresponding to E_n below ~2 MeV, most R-matrix calculations of the neutron cross sections near the 240 keV resonance have used the single-level approximation. In this approximation, the cross sections at the peak of the resonance depend on a single parameter (it is assumed that effects of the hard-sphere phases are neglected in the neutron elastic scattering), say

$$r = \frac{\Gamma_\alpha}{\Gamma_n} \quad ,$$

the ratio of the experimental width in the α-t channel to that in the n-^{6}Li channel. The experimental widths are related to the reduced widths of the R-matrix for a single level by

$$\Gamma_c = 2P_c\gamma_c^2 \quad ,$$

where P_c is the penetrability in channel c evaluated at resonance energy. The resonance in question has most of its width in the n-^{6}Li channel, so that r is a small number (~.25). An interesting consequence of the fact that r < 1 is that increasing the calculated value of the total cross section at the peak decreases the calculated peak value of the (n,α) cross section, and vice versa. The calculated value of the elastic cross section adjusts, of course, to maintian particle flux conservation.

This effect was evident in the single-level fits of Uttley and Diment[5] to measurements by Diment[6] of the neutron total cross section over the resonance. The calculated (n,α) cross section then peaked at a value 0.4 barn higher than the 3 barn figure indicated by several recent experiments.[7-9] Uttley has noted that reducing the calculated (n,α) cross section to agree with these measurements would force the calculated total cross section unacceptably far above Diment's measurements. He has speculated that the difficulty lies in the single-level approximation, since it neglects interference with a second $5/2^-$ level known to exist below the neutron threshold from measurements of α + t elastic scattering.[10,11] On the other hand, a very recent measurement of the (n,α) cross section by Friesenhahn[12] which gives a peak value of 3.77 barns has unsettled any comfortable feelings that this cross section is well-determined experimentally over the resonance.

Our R-matrix analysis of this system is directed at obtaining reliable cross sections despite discrepancies among these different sets of measurements by including simultaneously almost all available experimental information for the reactions ^{6}Li(n,n)^{6}Li, ^{6}Li(n,α)T, and T(α,α)T, and at assessing multi-level effects by including all known levels in the region of interest (this region extends below the n-^{6}Li threshold to the ground state of ^{7}Li). In addition, we are confronted with the interesting question of explaining the origin of the large 1/v portion of the ^{6}Li(n,α) cross section in a region where no positive-parity resonances have been identified.

Table I shows schematically the types of data that were included for the different reactions at an earlier stage of the analysis which was incorporated in the ENDF/B-IV evaluation for ^{6}Li. The multilevel fit to all these data behaved essentially the same over the resonance as did the single-level calculations. Parameters which reproduced Diment's total cross section measurements well gave good fits to all other data analyzed, with the exception of the (n,α) points over the resonance. The calculated (n,α) cross section was consistently above the measurements[8] over the resonance, although the difference was not simply a normalization factor. Attempts to reduce the calculated peak cross section from its value of 3.5 barns to 3.0 barns forced the calculated total cross section well above Diment's values in the peak, and deteriorated the fit to α + t elastic angular distributions[10] measured near the resonance.

These considerations showed, among other things, a substantial sensitivity of the (n,α) cross section near the resonance to values of the α + t angular distributions, which could be determined quite accurately using present charged-particle measuring techniques. An indication of this sensitivity can be obtained from considering, again, the single-level approximation. The fact that $r = \Gamma_\alpha/\Gamma_n < 1$ implies that the "resonant" part of the $5/2^-$ phase shift in the α-t channel does not, in fact, resonate. Instead, it rises to a maximum just in front of the resonant energy, drops sharply through zero at resonance, and falls to an equally deep minimum just behind the resonant energy. The total excursion of the "resonant" phase from maximum to minimum is given by $\mathrm{Tan}^{-1}\frac{r}{\sqrt{1-r^2}}$. As will be shown in later figs. excitation curves for the α + t elastic differential cross section over the resonance follow this excursion in the phase shift quite closely, so that they are sensitive to small variaitons in the parameter r. The neutron total cross section, on the other hand, is proportional to $\frac{1}{1+r}$, which is not so sensitive to small variations in r. Thus, accurate measurements of the α + t angular distributions over the resonance offer the possibility of determining the (n,α) cross sections more stringently than do accurate measurements of the total cross section.

Such measurements for t + α scattering have just been completed at Los Alamos.[13] The results of including these data in our analysis are shown in the first four figures. Figure 1 shows the first four angles at which excitation functions were measured. The relative errors on the data are generally less than 0.5%. Notice that the 69 degree excitation curve, in particular, follows closely the behavior described for the "resonant" α - t phase shift. Another interesting feature in the data is the threshold effect evident in the 49.6 degree excitation at the n+^{6}Li threshold (E_t = 8.4 MeV), which is well reproduced by the calculations. Figure 2 shows the 150 degree excitation curve, which overlaps earlier data taken at lower energies,[11] so that the effect of both $5/2^-$ resonances may be seen. Fits to four of the newly-measured t + α angular distributions are shown in Fig. 3. Figure 4 shows the calculated values for $\sigma_{n,T}$ and $\sigma_{n,\alpha}$ in the region of the resonance.

TABLE I

TYPES OF DATA INCLUDED IN THE ^{7}Li ANALYSIS

^{7}Li SYSTEM

Reaction	Observable Types Analyzed:			
	Total Neutron Cross Section	Integrated Cross Section	Differential Cross Section	Polarization
^{6}Li	X			
^{6}Li(n,n)^{6}Li		X	X	X
^{6}Li(n,α)T		X	X	
^{4}He(t,t)^{4}He			X	X

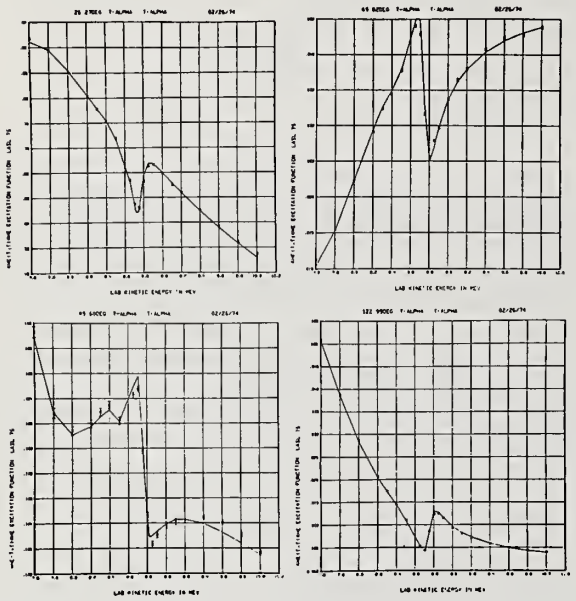

Fig. 1. ^{4}He(t,t)^{4}He excitation functions at center-of-mass angles of 26.3, 49.6, 69.0, and 123.0 degrees. The solid curve in this, and all subsequent figures, gives the R-matrix calculation. The data points are from Ref. 13.

The new t + α data appear to be demanding a total cross section that peaks at a value of 11.1 barns (somewhat above Diment's value, and more in agreement with Harvey's new measurements[14] at ORNL), while the peak value of the (n,α) cross section has dropped somewhat below our previous result to 3.4 barns.

The next figure shows selected (n,t) angular distributions, including predicted values at 25 keV. These predictions are of interest, since recent measurements of Schröder[15] at NBS indicate pronounced forward peaking of the triton angular distribution in the reaction at 25 keV. Our analysis originally did not predict the amount of asymmetry observed, but a minor adjustment of parameters reproduced the effect quite well at lower energies, as well as the data of Overley[16] at higher energies.

Space limitations allow only a brief discussion of the level structure which resulted from the analysis. Current assignments for the known levels in this region

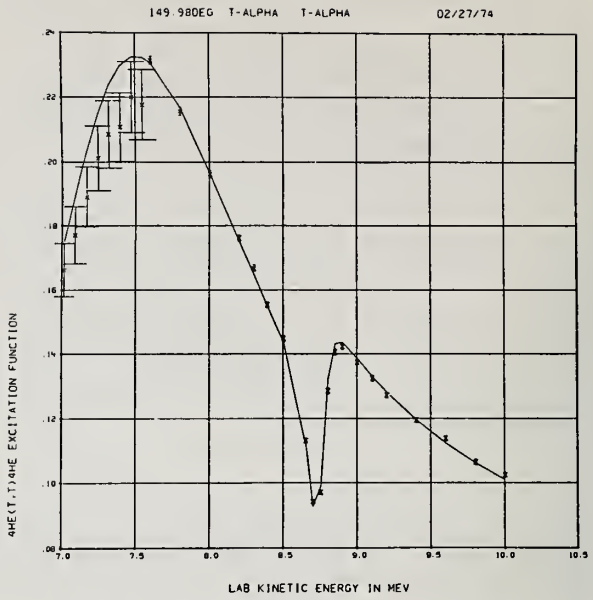

Fig. 2. ^{4}He(t,t)^{4}He excitation function at 150 degrees center-of-mass angle, showing the effects of both 5/2^{-} resonances. The data at the lower energies are those of Ivanovich et al. (Ref. 11); data at the upper energies are from Ref. 13.

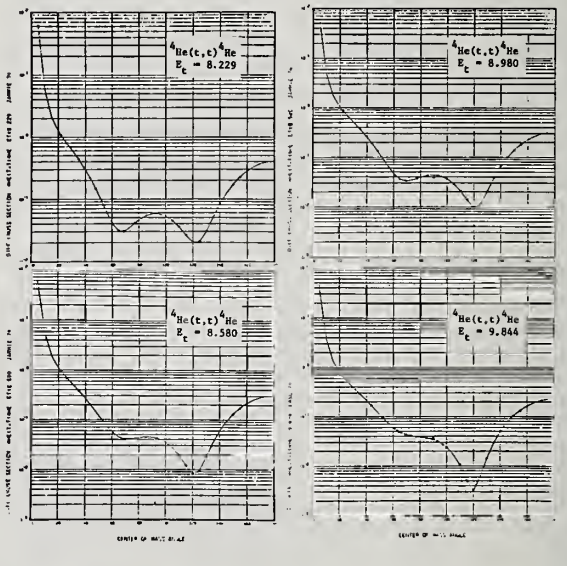

Fig. 3. ^{4}He(t,t) ^{4}He angular distributions at E_t = 8.229, 8.580, 8.980, and 9.844 MeV. The measurements are from Ref. 13.

appear consistent with almost all data measured for the three reactions considered. It is interesting that we seem to be seeing the tails of higher-lying levels of the $^{4}P_J$(n-^{6}Li) triplet, of which the J = 5/2 level at 240 keV is the lowest member, ordered according to ℓ·s splitting. We also find 3/2^{+} and 5/2^{+} levels with large

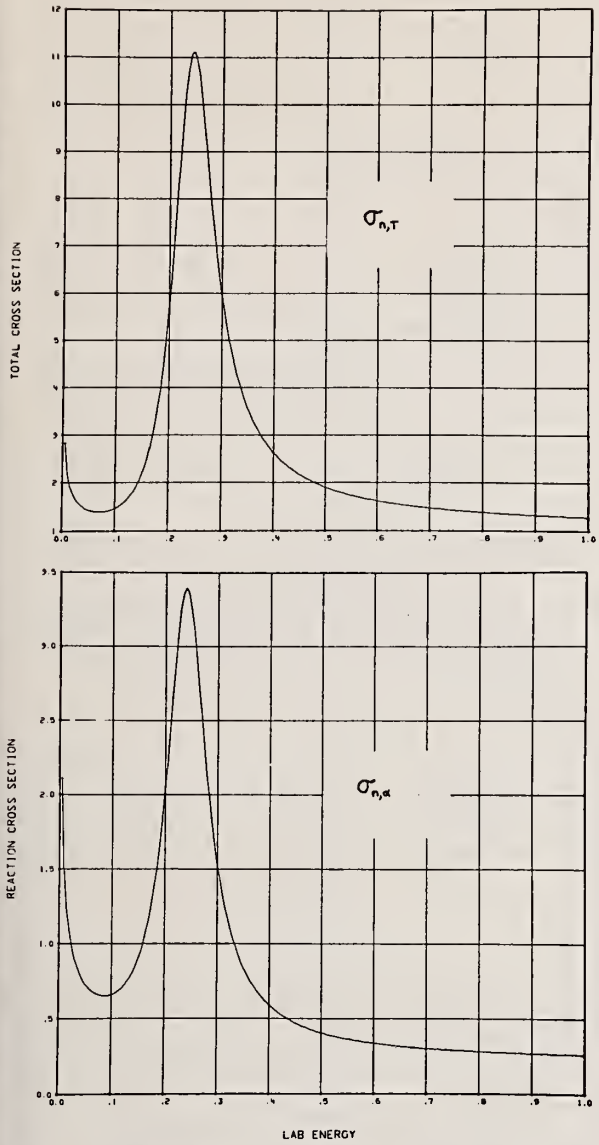

Fig. 4. Predicted values of the neutron total cross section (upper curve) and of the $^{6}Li(n,\alpha)$ reaction cross section (lower curve).

$^{2}D(\alpha\text{-}t)$ widths lying above the highest energy at which measurements were included. The $3/2^{+}$ level appears to be responsible for a portion of the 1/v (n,α) cross section at low energies. The remainder of the 1/v cross section comes, of course, from the $1/2^{+}$ state, in which large distant-level contributions seem to dominate.

Recent experimental information described here from reactions in the ^{7}Li system indicate values of the peak cross sections like 3.4 ± 0.1 for $\sigma_{n,\alpha}$ and 11.1 ± 0.2 barns for $\sigma_{n,T}$. The uncertainties in these values probably can be reduced as refinements in the new data are made. It would be worthwhile to resolve even small discrepancies in the measurements of the total cross section, as for instance, exist between the data of Diment and Harvey. However, direct measurements of the (n,α) cross section over the resonance continue to be

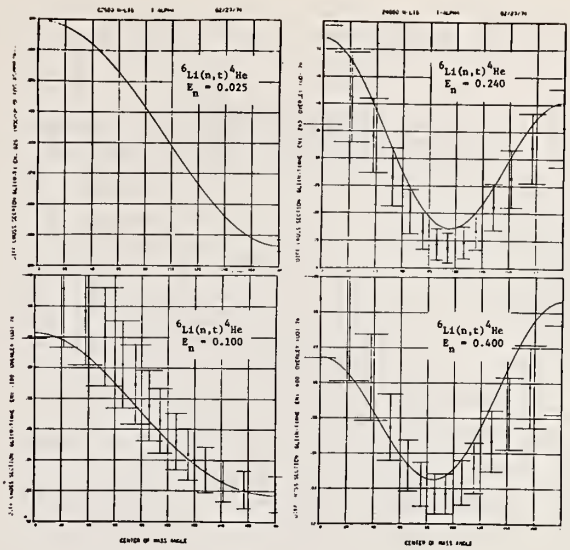

Fig. 5. $^{6}Li(n,t)^{4}He$ angular distributions at E_n = .025, .100, .240, and .400 MeV. Data at the upper three energies are those of Overley et al. (Ref. 16).

the most desirable, and most elusive, confirmation of the results of the analysis.

^{11}B System

Discrepant measurements are also a problem in determining reliable cross sections for the (n,α) reactions on ^{10}B (actually, there are two such reactions open, $^{10}B(n,\alpha_0)^{7}Li$, and $^{10}B(n,\alpha_1)^{7}Li^{*}$ [.478]) at energies below 1 MeV. In this case, however, R-matrix calculations are limited by incomplete knowledge about the level structure of ^{11}B in this region. Although the dominant levels at these energies, a broad $7/2^{+}$ level at $E_n \sim 0.3$ MeV and a $5/2^{-}$ level at $E_n \sim 0.5$ MeV, were identified by R. Lane and his colleagues from $n\text{-}^{10}B$ elastic scattering measurements,[17] at least three other levels occur in this region which could affect the detailed behavior of the (n,α) cross sections. These levels are clearly evident in the $\alpha\text{-}^{7}Li$ reactions, but have not, as yet, received definite J^{P} assignments.

A multi-reaction R-matrix analysis has been performed for the ^{11}B system which takes account of a limited amount of data from the $\alpha\text{-}^{7}Li$ reactions. The types of data included for the various reactions considered are listed in Table II. The fits to a selection of the data included for the neutron-induced reactions are shown in Figs. 6-8. These results were incorporated in the ENDF/B-IV evaluation of ^{10}B at low neutron energies. The fits to data from the $\alpha\text{-}^{7}Li$ reactions indicated, however, that this analysis had not successfully identified the unknown levels mentioned above.

Therefore, a separate analysis of the $\alpha\text{-}^{7}Li$ reactions alone that uses a more extensive data set has been undertaken with some success. Representative results

TABLE II

TYPES OF DATA INCLUDED IN THE ^{11}B ANALYSIS

^{11}B SYSTEM

Reaction	Observable Types Analyzed: Total Neutron Cross Section	Integrated Cross Section	Differential Cross Section	Polarization
^{10}B	X			
$^{10}B(n,n)^{10}B$		X	X	X
$^{10}B(n,\alpha_0)^7Li$		X	X	
$^{10}B(n,\alpha_1)^7Li^*$		X	X	
$^7Li(\alpha,\alpha_0)^7Li$			X	
$^7Li(\alpha,\alpha_1)^7Li^*$		X		

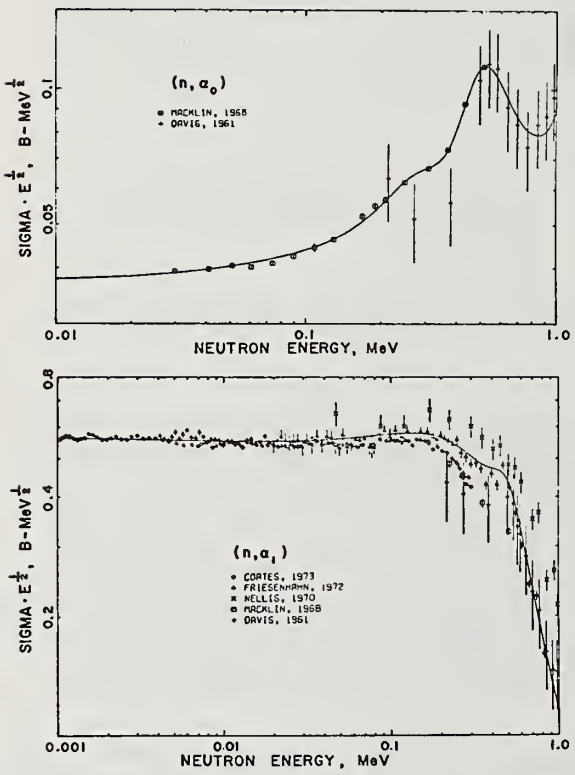

Fig. 6. Integrated $^{10}B(n,\alpha_0)^7Li$ and $^{10}B(n,\alpha_1)^7Li^*$ cross sections below E_n = 1 MeV.

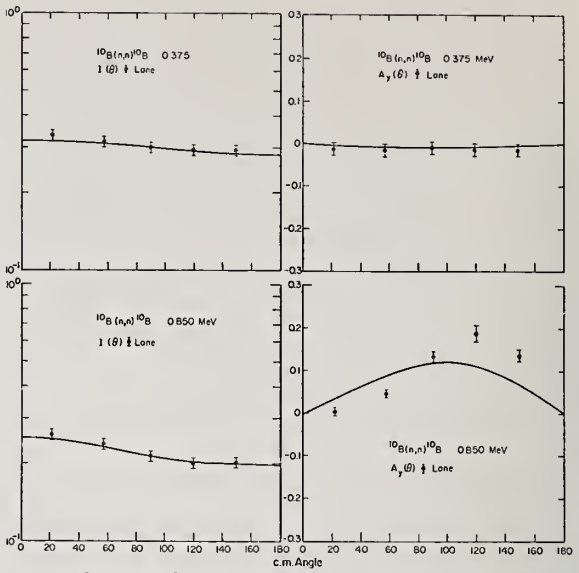

Fig. 7. $^{10}B(n,n)^{10}B$ differential cross sections and neutron polarizations at E_n = 0.375 and 0.850 MeV. The data are those of Lane et al. (Ref. 17).

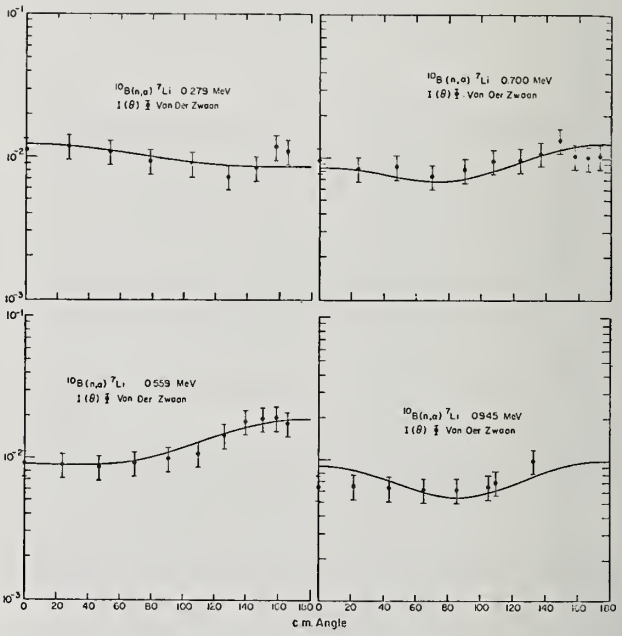

Fig. 8. $^{10}B(n,\alpha_0)^7Li$ differential cross sections for E_n between 0.28 and 0.95 MeV. The data are those of Van der Zwaan and Geiger (Ref. 21).

are given in the last three figures. The experimental data shown in these figures are those of Cusson,[18] who also attempted an R-matrix analysis of his measurement. Figure 9 shows the fit to the $^7Li(\alpha_0,\alpha_1)$ integrated cross section and indicates the tentative level assignments found. The three levels that could affect the (n,α) cross sections are located at E_α = 4.39, 4.60, and 6.01 MeV. The level at E_α = 4.6 MeV, (E_n = 0.150 MeV) is, in fact, visible in both the $^{10}B(n,\alpha_0)$ and $^{10}B(n,\alpha_1)$ cross sections (see Fig. 6). The $5/2^+$ assignment at E_α = 3.03 MeV disagrees with Cusson's "firm" assignment of $7/2^+$, but the angular distributions at that energy (Figs. 10 and 11) are clearly inconsistent with a $7/2^+$ level. This new information about the level structure of ^{11}B is currently being used in the full analysis that now includes new measurements of the $^{10}B(n,\alpha)$ integrated cross sections from Friesenhahn,[19] and of the $^{10}B(n,\alpha_0)$ and $^{10}B(n,\alpha_1)$ angular distributions from Sealock.[20]

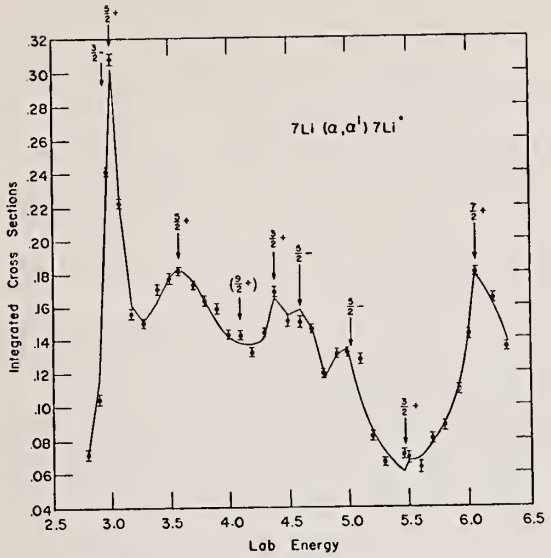

Fig. 9. Integrated $^{7}Li(\alpha_0,\alpha_1)^{7}Li^*$ cross section for E_α between 2.8 and 6.3 MeV. The data are those of Cusson (Ref. 18). Arrows mark tentative assignments made for the levels.

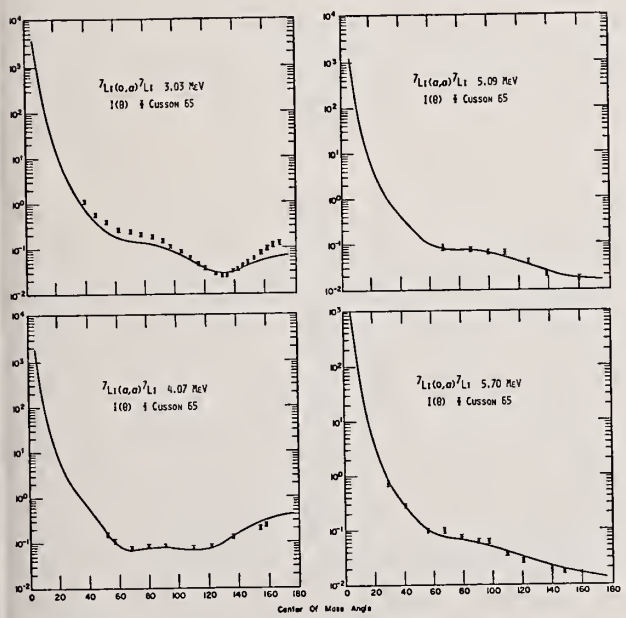

Fig. 10. $^{7}Li(\alpha,\alpha)^{7}Li$ angular distributions at energies between 3.0 and 5.7 MeV. The data are those of Cusson (Ref. 18). The calculated curves result from the level scheme of Fig. 9.

Measurements of $^{10}B(n,\alpha_0),\alpha_1$ or $^{7}Li(\alpha,\alpha_0),\alpha_1$ angular distributions in the region of E_n = 0.150 MeV, or E_α = 4.60 MeV could be most helpful in determining the J^P of the resonance that occurs there. Although integrated cross sections and excitation functions exist ata few angles over the resonance, these are not sufficient to identify it.

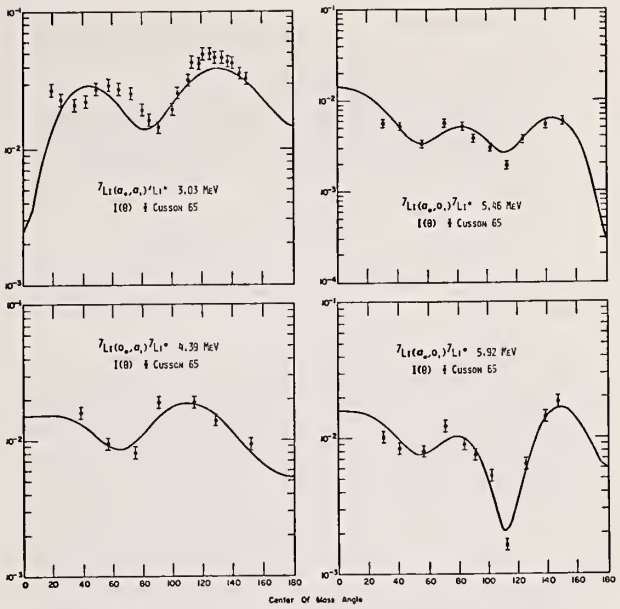

Fig. 11. $^{7}Li(\alpha_0,\alpha_1)^{7}Li^*$ angular distributions at energies between 3.0 and 5.9 MeV. The data are those of Cusson (Ref. 18). The calculated curves result from the level scheme of Fig. 9.

Conclusions

The R-matrix analyses described here show that it is practical and desirable to consider standard cross sections for the light elements in conjunction with other experimental information available from reactions in the same system. This approach provides a valuable check on the consistency of the standard cross section that cannot be obtained from considering it in isolation.

Both analyses illustrate the value of analyzing data for charged-particle reactions along with neutron data. In the case of lithium, the high precision of the charged-particle measurements allowed a closer determination of all the cross sections of interest. In the case of boron, the charged-particle data contained information about the level structure of the system that was not apparent from the neutron measurements.

Given the correct level structure, R-matrix calculations applied with few, if any, approximations can be expected to provide detailed fits to data from nuclear reactions. Such calculations appear to be particularly well-suited for obtaining smoothed representations of the standard cross sections for light elements.

References

1. E. P. Wigner and L. Eisenbud, Phys. Rev. 72, 29 (1947).

2. A. M. Lane and R. G. Thomas, Rev. Mod. Phys. 30, 257 (1958).

3. L. Wolfenstein, Ann. Rev. Nucl. Sci. 6, 43 (1956).

4. D. Dodder, K. Witte, and G. Hale, unpublished.

5. K. M. Diment and C. A. Uttley, Harwell report AERE-PR/NP 16, p. 3 (1969).

6. K. M. Diment and C. A. Uttley, Harwell report AERE-PR/NP 14, p. 20 (1968) and K. M. Diment and C. A. Uttley, Harwell report AERE PR/NP 15, p. 12 (1969).

7. E. Fort and J. P. Marquette, in Neutron Reference Standard Data, IAEA, Vienna, p. 113 (1974).

8. M. S. Coates, G. J. Hunt, and C. A. Uttley, ibid., p. 105.

9. W. P. Poenitz, Z. Phys. 268, 359 (1974).

10. R. J. Spiger and T. A. Tombrello, Phys. Rev. 163, 964 (1970).

11. M. Ivanovich, P. G. Young, and G. G. Ohlsen, Nucl. Phys. A110, 441 (1968).

12. S. J. Friesenhahn, to be published in the Proc. of the Conf. on Nucl. Cross Sections and Technology, Washington, D. C. (1975).

13. N. Jarmie et al., private communication.

14. J. A. Harvey and N. W. Hill, to be published in the Proc. of the Conf. on Nuclear Cross Sections and Technology, Washington, D. C. (1975).

15. I. G. Schroder et al., to be published in the Proc. of the Conf. on Nuclear Cross Sections and Technology, Washington, D. C. (1975).

16. J. C. Overley, R. M. Sealock, and D. H. Ehlers, Nucl. Phys. A221, 573 (1974).

17. R. O. Lane et al., Phys. Rev. C4, 380 (1971).

18. R. Y. Cusson, Nucl. Phys. 86, 481 (1966) and Thesis, California Institute of Technology (1965).

19. S. J. Friesenhahn et al., to be published in the Proc. of the Conf. on Nuclear Cross Sections and Technology, Washington, D. C. (1975).

20. R. M. Sealock, Thesis, University of Oregon (1974), and private communication.

21. L. Van der Zwaan and K. W. Geiger, Nucl. Phys A180, 615 (1972).

*Work performed under the auspices of the United States Atomic Energy Commission.

COMPUTER-READABLE "NUCLEAR DATA SHEETS"*

W. Bruce Ewbank
Oak Ridge National Laboratory, Oak Ridge, Tennessee 37830

The evaluated nuclear structure data contained in "Nuclear Data Sheets" are available in computer-readable form. Experimentally established properties of nuclear levels are included as well as radiations from nuclear reactions and radioactive decay. Portions of the data can be selected for distribution in several formats on magnetic tape or computer cards. A variety of different listing and drawing formats are also available.

(Nuclear structure; data; levels; decay; γ-rays; radiations; reactions; files; tables; formats; computers; ENSDF; evaluation)

Introduction

The Nuclear Data Project is engaged in the continuous evaluation of new experimental results in nuclear structure physics. The conclusions of these evaluations are published in the journal "Nuclear Data Sheets" (Academic Press, New York). For each nuclear reaction and radioactive decay, the "Nuclear Data Sheets" contain numerical data which describe the current status of knowledge about that reaction or decay. The "best estimates" of nuclear level properties (derived from all nuclear measurements) are also presented in an "Adopted" level scheme for each nucleus.

Over the past several years, the production of "Nuclear Data Sheets" has become increasingly automated. The level properties and radiation properties contained in the "Nuclear Data Sheets" have been entered into punched cards, and the cards have been organized into a comprehensive Evaluated Nuclear Structure Data File (ENSDF) for all nuclei. The Data File is used routinely by the Nuclear Data Project to prepare level schemes and selected tables of nuclear properties.

The "Nuclear Data Sheets" serve as a basic source of evaluated nuclear structure data for users in many areas of basic and applied research. Reactor shielding, reactor heat generation, activation analysis, medical dosimetry are but a few areas where the evaluated data have been repeatedly copied from the "Nuclear Data Sheets" into computer-readable format for use in further calculations. The growth of ENSDF removes the need for much duplicative effort. The standard sets of evaluated data contained in ENSDF should find wide application in many areas of science and technology. Already a tape of over 300 radioactive decay schemes has been extracted from the 1000+ sets of numerical data on the permanent ENSDF disk. Copies of this tape have been made available for testing of the compatibility of the standard data formats with requirements of additional programs. Copies of standard sets of data for specific decay schemes have also been distributed on computer cards.

This report describes the data content and organization of ENSDF, as well as several useful output formats which have been developed to handle selected portions of the data.

ENSDF Content

The basic outline of ENSDF content evolved from many years of experience by the Nuclear Data Project in preparing the "Nuclear Data Sheets". Specific formats for the Data File were formalized in 1971 by M. R. Schmorak, F.E. Bertrand, and D.J. Horen. The formats allow the convenient entry of the properties of nuclear levels and nuclear radiations. A partial listing of properties included in ENSDF is shown here:

for levels: E, J, π, $T_{1/2}$, μ, Q, decay modes
for γ-rays: E_γ, I_γ, Λ, δ, α, B(Λ), ce-ratios
for $\beta^{\pm}$-radiations: E_β(max), E_β(avg), I_β, log ft
for α-radiations: E_α, I_α, hindrance factors.

The uncertainties on all measured values are included. The ENSDF structure is readily extendible to additional types of data whenever the need arises.

The Data File includes very little redundant information. A set of data for radioactive decay does not need to include absolute photon intensity or total transition intensity. Measurements are usually made of relative photon intensity, and this is the intensity required by ENSDF. Absolute photon intensity or total transition intensity can be calculated from the measurement, by means of included normalization factors, decay branching ratios, and internal conversion coefficients. The decay scheme is also more easily updated. A reinterpretation of the level scheme may change the absolute normalization factor, but it will have no effect on the measured relative photon intensities.

A set of data obtained from a neutron-capture experiment will likewise include only measured relative photon intensity. A normalization factor is included to obtain the absolute number of photons per n-capture. New information about the (n, γ) cross section can be easily incorporated into tables of absolute intensity without the need for changing the entire γ-ray file.

ENSDF Organization

The Data File is organized into "data sets", each of which contains all nuclear structure information obtained from the study of a single nuclear reaction or radioactive decay. For example, a β-decay data set includes information about all daughter levels observed in the decay, the

*Research sponsored by Energy Research & Development Administration under contract with the Union Carbide Corporation.

energies and intensities of β- and γ-radiations, log ft for each β-branch, and multipolarity and internal conversion coefficients for each γ-ray. The decay data set also includes information about the parent nucleus (half-life and decay energy) when it is available. Each data set includes reference codes to identify sources of data and as many comments as may be needed to explain the particular data choices.

A data set for (n, γ) includes the levels populated in the reaction, the γ-ray energies, and relative photon intensities. If it is available, a normalization factor can also be included to convert relative photon intensity to absolute photon intensity per 100 neutron captures in the target isotope. A (d,p)-reaction data set includes level energies, ℓ-transfers, spectroscopic factors, and J-values if obtained from the (d,p)-reaction.

A data set is stored in ENSDF as a sequence of card images. Part of a simple data set for ^{62}Zn decay is shown in Figure 1. The data have been entered in the standard formats illustrated at the bottom of the figure. The names of most fields on the data cards are self-explanatory. An empty field means that a value has not been determined.

Each data set in ENSDF is labeled by a short description of the type of experiment [α-decay, EC-decay, (n, γ)-reaction, etc.] and by one or more reference codes to identify data sources. "ADOPTED" is reserved for those data sets which summarize the best nuclear level structure information from all experiments. Data sets included in published Nuclear Data Sheets have special reference codes. The data set labels, ordered by A and Z, are used as an index for efficient searching of ENSDF. A section of the index for A = 62 is shown in Figure 2.

```
 62CU    62ZN EC DECAY                    74NDS                          740612

62ZN    P 0            0+                9.255 H 14          1631       11
 62CU   Q -1631      11
62CU    L 0            1+                9.74 M   2
 62CU   E 1631       11 8.6        31.1    5.0
62CU    CE 660       10B+ MEASURED
62CU    L 40.85      6  2+
62CU    G 40.85      6 25.4     13M1                          42.9       13 C
62CU    L 243.41     8  2+
62CU    G 202.67     6 .010     2                             .010       2
62CU    G 243.36     6 2.5      1 M1+E2                       2.5        1  C
62CU    L 287.80     9  1+,2+
62CU    G 246.95     6 1.9      1 M1+E2                       1.9        1  CC
62CU    L 426.16     11 3+
62CU    G 385.31     9 .018     2 M1+E2                       .018       2
62CU    L 548.33     6 1+
 62CU   E  1083                    31.4     4.6
62CU    G 260.43     7 1.3      1 M1                          1.3        1  C
62CU    G 304.88     9 .29      2                             .29        2  C
62CU    G 507.60     1014.7     8 M1+E2                       14.8       8  C
62CU    G 548.35     1 15.1     8 M1+E2                       15.3       8
62CU    L 637.40     5  1+
62CU    E 994                    28.6     4.6
62CU    G 349.60     13.44      3 M1+E2                       0.44       11 C
62CU    G 394.03     6 2.2      1 M1+E2                       2.2        1  C
62CU    G 596.56     1325.7       M1                          26            C
62CU    G 637.41     7 .25      2                             .25        2
 62CU   L 644.82     6 (2)
 62CU   G 644.82      6 0.014    1 M1+E2                       0.014      1
62CU    L 698.3      5  2+,3+
62CU    G 657.5      5 .0012    3 M1+E2                       .0012      3
62CU    L 915.27     9
 62CU   E  716                    .036     7.2      GT
62CU    G 489.17     7 .016     2                             .0016      2
62CU    G 627.8      4 .001                                   .001
```

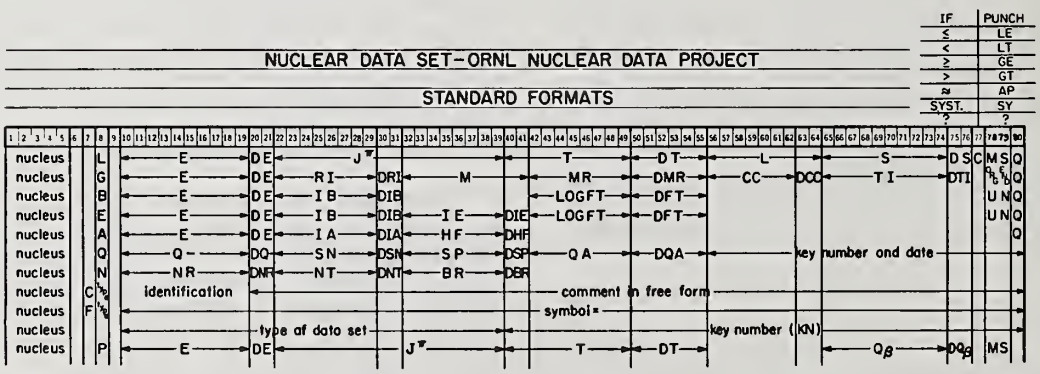

Figure 1. A simple decay data set.

```
62CO    ADOPTED LEVELS                    74NDS
62CO    DRAWING 1                         74NDS
62NI    ADOPTED LEVELS                    74NDS
62NI    COULOMB EXCITATION                74NDS
62NI    RESONANT SCATTERING               74NDS
62NI    1.5-M 62CO B- DECAY               74NDS
62NI    13.9-M 62CO B- DECAY              74NDS
62NI    59CO(A,P)                         74NDS 7DBU13
62NI    6DNI(T,P)                         74NDS 71DA16
62NI    61NI(D,P)                         74NDS
62NI     61NI(N,G) PRIMARY GAMMAS         74NDS
62NI    61NI(N,G)                         74NDS 7DFA06
62NI    62CU EC DECAY                     74NDS
62NI    62NI(D,D')                        74NDS
62NI    62NI(E,E')                        74NDS
62NI    62NI(P,P')                        74NDS
62NI    62NI(P,PG)                        74NDS
62NI    62NI(3HE,3HE')                    74NDS
62NI    62NI(4HE,4HE')                    74NDS
62NI    63CU(D,3HE)                       74NDS
62NI    63CU(G,P)                         74NDS
62NI    63CU(N,D)                         74NDS
62NI    64NI(P,T)                         74NDS
62NI    65CU(P,4HE)                       74NDS
62NI    66ZN(D,6LI)                       74NDS
62CU    ADOPTED LEVELS                    74NDS
62CU    6DNI(A,D)                         74NDS
62CU    6DNI(A,NPG)                       74NDS
62CU    61NI(3HE,D)                       74NDS
62CU    62NI(P,N)                         74NDS
62CU    62NI(P,NG), 61NI(D,NG)            74NDS
62CU    62NI(3HE,T)                       74NDS
62CU    62ZN EC DECAY                     74NDS
62CU    63CU(D,T)                         74NDS
62CU    63CU(3HE,A)                       74NDS
62CU    64ZN(D,A)                         74NDS
62ZN    ADOPTED LEVELS                    74NDS
62ZN    58NI(16O,12C)                     74NDS
62ZN    58NI(6LI,D)                       74NDS
62ZN    6DNI(3HE,N)                       74NDS
62ZN    63CU(P,2NG)                       74NDS
62ZN    64ZN(P,T)                         74NDS
62GA    ADOPTED LEVEL                     74NDS
```

Figure 2. ENSDF index for A = 62.

The Data File is maintained in two separate parts (each with its own index) — an "active" file of data sets currently being revised and updated for future issues of Nuclear Data Sheets and an "inactive" file of data sets from Nuclear Data Sheets already published. The active file can be searched and modified interactively from our remote terminal or from the central computer. The inactive file may be edited and searched only from the central computer. Data sets can be easily switched between the active file and the inactive file.

ENSDF Output Forms

Several programs have been developed to retrieve certain sets of data from ENSDF and then to prepare special tables or other output. The descriptions of these programs and their respective products should give a potential user some understanding of what kinds of information can be obtained from the Data File.

The level-scheme figures in the "Nuclear Data Sheets" are prepared from information retrieved from ENSDF. This pictorial representation was the first standard presentation of data from the Data File. The effort required to produce the level-scheme drawings was dramatically reduced. A computer drawing can be made in minutes for a complex scheme that previously required many hours of drafting time.

Tables of γ-ray energy and photon intensity ordered by energy have been prepared for radioactive decay and for nuclear reactions accompanied by γ-rays. The listing programs are simple enough that a table of γ-rays ordered by intensity or of level energies ordered by nuclear spin could be generated if needed. A listing of γ-ray energy, absolute photon intensity, and multipolarity produced from the decay data set in Figure 1 is shown in Figure 3.

```
62CU     62ZN EC DECAY          74NDS          740612
  40.85  6          25.4  13                    M1
 202.67  6           .010  2
 243.36  6          2.5   1                     M1+E2
 246.95  6          1.9   1                     M1+E2
 260.43  7          1.3   1                     M1
 304.88  9           .29  2
 349.60  13          .44  3                     M1+E2
 385.31  9           .018 2                     M1+E2
 394.03  6          2.2   1                     M1+E2
 489.17  7           .016 2
 507.60  10         14.7   8                     M1+E2
 548.35  1          15.1   8                     M1+E2
 596.56  13         25.7                         M1
 627.8   4           .001
 637.41  7           .25  2
 644.82  6          0.014  1                     M1+E2
 657.5   5           .0012 3                     M1+E2
 671.84  9           .004  1
 731.23  15          .0023 3
 792.03  7           .008  1
 827.59  14          .0030 4
 881.4   3           .015  1
 915.44  6           .016  1
1141.91  11          .034  2
1186.2   3           .004  1
1389.1   4           .011  1
1429.9   7           .027  3
1485.1   5           .0005 3
1525.9   6           .005  1
```

Figure 3. γ-rays from ^{62}Zn decay

The listing program is now being extended to prepare page copy for "Nuclear Data Sheets", i.e., including footnotes and comments from the data sets. These pages can be printed on the special line printer at ORNL or passed to a photocomposition device for completely automatic preparation of the "Nuclear Data Sheets".

A comprehensive program (MEDLIST) has been developed to operate on ENSDF decay data sets and produce complete lists of all radiations (including X-rays, conversion electrons, and Auger electrons as well as β- and γ-radiations) from a radioactive atom. Such lists (example, Figure 4) have particular value for dose calculations in medical applications.

85SR EC DECAY $T_{1/2}$ = 64.85 D 3

Type	Radiations Energy (keV)	Intensity (%)
Auger-L	1.68	108.3 23
Auger-K	11.4	29.1 9
ce-K- 1	498.790 10	0.617 21
ce-L- 1	511.925 10	0.070 3
ce-MNO- 1	513.668 10	0.024 3
X-ray L	1.69	1.6 6
X-ray $K\alpha_2$	13.33580 20	17.1 5
X-ray $K\alpha_1$	13.39530 20	33.0 7
X-ray Kβ	15	8.7 3
γ 1	513.990 10	98.0 10
γ 2	868.5 5	0.0140 20

Figure 4. MEDLIST output from ENSDF

The existence of a standard format for recording all nuclear structure data has greatly simplified the process of evaluating new measurements and re-evaluating previous conclusions in light of new results. Computer programs which calculate log ft, internal conversion coefficients, and α-hindrance factors have been modified to operate on the standard data sets. If the data from a new measurement are prepared in the standard format, then the preparation of new level schemes and tables for comparison with previous results can proceed automatically.

A program for calculating level energies by least-squares adjustment from measured γ-ray energies has been adapted to operate on standard data sets. After the adjustment, each input number is compared with its adjusted value and discrepancies are marked for special examination. Adjusted γ-ray energies are also calculated for all possible transitions among the levels (for comparison with energies of unplaced γ-rays). An example of the output from this program is shown in Figure 5 for a set of precision measurements of γ-ray energies in ^{192}Ir decay. The data are shown to be consistent, and very precise energies are obtained for the level energies.

	192PT	192IR	B- DECAY (74.02 01)		748E26 (PRECISION G-ENERGIES)
BOTTOM (OUT)		0	316.4985 10	612.4471 14	784.5537 17	920.8936 17	1201.004 5
LEVEL (IN)		0	315.497	612.450	784.560	920.896	1201.02
0		---	---	---	---	---	---
316.4985 10	316.4982 10		---	---	---	---	---
	316.4982 10						
612.4471 14	612.4460 14		295.9484 10	---	---	---	---
	612.446 9		295.9486 10				
784.5537 17	784.5520 17		468.0546 14	172.1065 12	---	---	---
			468.052 3				
920.8936 17	920.8913 17		604.3941 13	308.4463 11	136.3399 5	---	---
			604.396 8	308.4467 11	136.3398 5		
1201.004 5	1201.000 5		884.504 5	588.550 5	416.450 5	280.110 5	---
			884.513 24	588.551 8	416.452 5		

Figure 5. Least-squares adjustment of γ-ray energies.

Additional programs are under development to provide further assistance in the evaluation of nuclear structure data.

RECENT EVALUATION FOR THE GERMAN NUCLEAR DATA LIBRARY KEDAK-3

B.Goel, H.Küsters and F.Weller
Institut für Neutronenphysik und Reaktortechnik
Kernforschungszentrum Karlsruhe

For the design and optimization of reactors a precise knowledge of the microscopic neutron data is needed. For this purpose new evaluations for a number of important fast reactor materials have been performed at this laboratory. In the paper we discuss reevaluations of U^{238} and Pu^{239}. To check the quality of the presently evaluated data in reactor physics calculations, their effect on k_{eff} for a large variety of critical assemblies is studied. Calculation shows that with the evaluated data for U^{235}, U^{238}, Pu^{239}, Pu^{240}, Pu^{241} and Pu^{242} the value of k_{eff} for a large number of critical assemblies can be reasonable well reproduced without any adjustment of the data.

(Evaluation; nuclear data; uranium; plutonium)

The last version of KEDAK was released[1] in 1971. Since then a large number of new experiments has been published by various laboratories. The new experimental information has not only increased the quantity of the data available, but due to the application of advanced techniques the quality of the data, e.g. the energy resolution, has also been improved considerably and therefore, in many cases discrepancies in various experimental data sets are reduced substantially. In addition, the codes used for reactor physics calculations have also experienced substantial improvements; they are presently considered as sufficiently reliable tools. In some cases the nuclear data measurements have not yet converged to a unique cross section basis, thus the evaluators are forced to revise their nuclear data files. The new version of UKNDL was released[2] in 1973, the ENDF/B-4 was released[3] in 1974, and the new version of KEDAK (KEDAK-3) will be released in the near future.

In KEDAK-3 the highest priority was assigned to the reevaluation of the neutron cross sections of the heavy materials, U^{235}, U^{238}, Pu^{239}, Pu^{240}, Pu^{241} and Pu^{242}. The evaluation of U^{235} data has already been published[39] in 1973. After this publication the total cross section for U^{235} is changed following similar arguments as in the case of Pu^{239} which will be discussed below. The data for Pu^{240}, Pu^{241} and Pu^{242} on KEDAK originates from the evaluation of Caner and Yiftah[40] in cooperation with Karlsruhe. In case of σ_γ for Pu^{240}, however, recent measurements of Moxon[41] have shown that the older data of Geel[42] and Harwell[43] have to be renormalized. And thus the discrepancy between these data and the RPI data[44] is now resolved. The reevaluation of the cross sections of structural and coolant materials is in progress.

In this report only some of the evaluations done by the Karlsruhe group for KEDAK-3 are discussed, mainly the cross sections for U^{238} and Pu^{239} for the energy region above the resolved resonances. The effect of the new evaluation on the value of k_{eff} of a large variety of critical assemblies is also demonstrated.

Total Cross Section for Pu^{239}

In the energy region above 100 keV new experimental data have been published after 1970 by Foster and Glasgow[4], Cabé et al.[5], Smith et al.[6] and Schwartz et al.[7]. There are also unpublished data of Nadolny at RPI which are in agreement with those of Schwartz et al. according to ref.7. Figure 1 shows the available experimental data together with the previously and presently recommended data on KEDAK. In this figure the experimental data are averaged over 0.2 MeV. It is seen that the agreement in the experimental data of Foster, Smith and Schwartz is good, whereas, the data of Cabé are higher by 3 - 5 % throughout. (This trend is also observed in the case of Cabé's U^{235} data). The reason for this deviation might be a systematic error in Cabé's experiments. The recommended curve is is based on the above cited data sets (ref. 4, 6 and 7) and of the Cabé data reduced by 3 %.

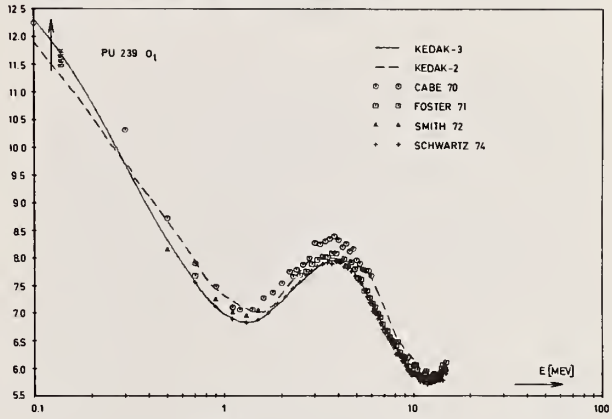

Fig. 1

All the data mentioned above were measured with the time of flight technique and the uncertainties given by the authors vary between 2 to 5%. Since except the data of Cabé all other data agree within 2% throughout the shown energy range, we assume that in this energy region the total cross section for Pu^{239} is well known and the uncertainty of the evaluated data is less than 3%.

Fission Cross Section for Pu^{239}

With respect to KEDAK-2 the fission cross section for Pu^{239} is revised from 1 keV to 30 keV. In this energy range the experimental discrepancies have been reduced considerably in the last few years. In Fig.2 the fission cross section, averaged over 1 keV intervals is plotted for 9 intervals from 1 keV to 10 keV. The experimental data are divided in two groups, the data published before 1970 (used for the KEDAK-2 evaluation) and those published after 1970 (Gwin et al.[8], Weston and Todd[9], Blons[10] and Lehto[11]). With the exception of Lehto the agreement of the data, published after 1970, is good. Therefore, the KEDAK-3 evaluation does not include the data of Lehto. The recommended curve is the weighted average of the data of Gwin et al., Weston and Todd and Blons. The uncertainty of this evaluation is estimated to be below 5%.

The difference between this evaluation and that of Sowerby et al.[12] which is also shown in Fig.2 may have two reasons; firstly Sowerby has simultaneously evaluated σ_f for U^{235}, U^{238}, Pu^{239} and σ_c for U^{238} and secondly (perhaps mainly) we have used revised Gwin data which were not available at the time of Sowerby's evaluation .

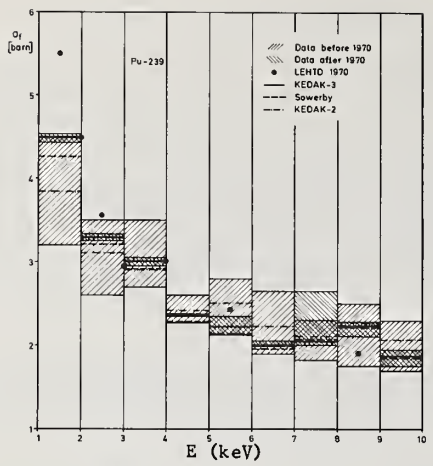

Fig. 2

Alpha and Capture Cross Section for Pu^{239}

For the evaluation of the capture to fission ratio of Pu^{239}, in the energy range 1 keV to 30 keV the scheme of Sowerby and Konshin[13] in their 1972 evaluation was used, in addition only the revised data of Gwin et al.[8] and Weston and Todd[9] were included. In the energy range above 30 keV the KEDAK-3 evaluation is based on weighted values of the data of the Saussure et al.[14], Bandl[15], Hopkins and Diven[16] and Kononov et al.[17]. The result is shown in Fig. 3.

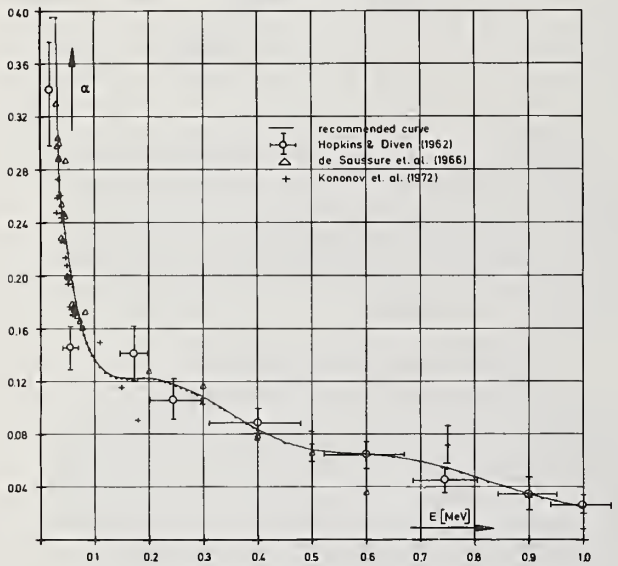

Fig. 3

The uncertainty of the evaluation of α between 1 keV and 30 keV is estimated to be between 5 and 10% and increases up to 25% at 1 MeV.

Above 1 MeV there are no measurements either for α or for σ_γ. A E^{-n} dependence for σ_γ was assumed. Considering the systematics of the neighbouring nuclei, n was chosen to be 1.65. In doing so, any contribution due to the direct reaction mechanism is neglected, which is expected to start at about 5 to 7 MeV. But due to the small absolute value of this cross section in the upper MeV range and its relative unimportance in reactor physics calculations, this neglect was tolerated at the moment.

Fission Cross Section for U^{238}

For the evaluation of σ_f for U^{238} we have first evaluated the ratio measurements of σ_f (U^{238}) / σ_f (U^{235}) (the lowest curve in Fig. 4). The evaluation above 6 MeV is based mainly on the data of Cierjacks et al.[18], and Hansen et al.[19] (the measurements of Smith, Henkel and Nobles[20], corrected for scattering effects[19]). Below 6 MeV the experiments considered are those of White and Warner[29], Stein et al.[22] and Meadows[23]. Following Davy[25] and Sowerby[12] the original data of Lamphere[24] were reduced by 6% to match the more precise measurements of Stein et al.

The evaluated ratio value was then multiplied by the σ_f of U^{235} evaluated in 1971 [39] to obtain σ_f for U^{238} (dotted curve). Compared to the absolute values of the U^{238} fission cross section this curve is too low, especially in the energy region above 7 MeV. Therefore, we considered also the absolute data, but due to the normalization uncertainties of these data, particularly the old Kalinin[26] measurements, with reduced weight. The resulting fission cross section is shown in Fig. 4 by the solid line. The reason for the difference between the solid and the dotted lines is most probably due to a too low U^{235} fission cross section above 8 MeV in the 1971 evaluation[39]. This point is being investigated.

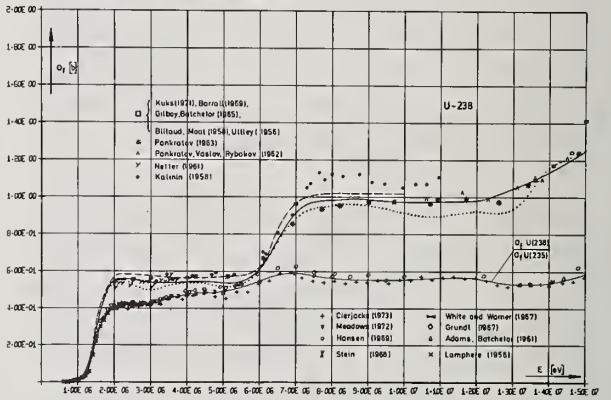

Fig. 4

The dashed curve shows the previously recommended data on KEDAK. The effect of the present evaluation is the reduction of σ_f for U^{238} by 3-4% in the energy region above 2 MeV.

The average of the evaluated data over the U^{235} neutron spectrum is 0.2963 b which is about 2% lower than the older experimental values of 0.304±0.007 [27], 0.312±0.004 [28] and 0.31±0.01 [29]. The uncertainty of the evaluated data is estimated to be 5% up to 10 MeV and 2.5 to 5% between 10 and 15 MeV.

Capture Cross Section for U^{238}

The data considered for the evaluation of σ_γ for U^{238} in the energy range 4.0 keV to 100 keV are those of Moxon[30], de Saussure et al.[31] and Friesenhahn et al.[32]. De Saussure et al. and Friesenhahn et al. have used the same experimental technique but in the lower energy region Friesenhahn gives much lower values for the capture cross section than de Saussure et al.. This may be due to the high gamma-detector bias at 4 MeV used by Friesenhahn as compared to 2.8 MeV used by de Saussure. We have, therefore, reduced the weight of Friesenhahn's data below 20 keV. Above 100 keV we used the data evaluated by Sowerby et

al.[12]. The uncertainty of the evaluation is estimated to be 10-7% in the energy region 4 keV to 100 keV. Above 100 keV Sowerby et al. gives an uncertainty of 7% up to 1 MeV, increasing to 10% at 3 MeV and 33% at 7 MeV.

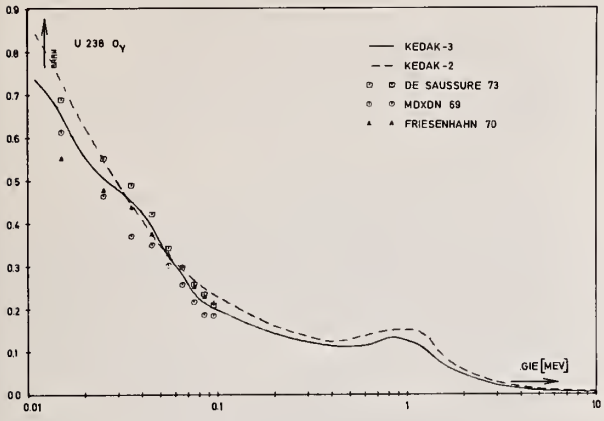

Fig. 5

Figure 5 shows the comparison of the presently recommended data on KEDAK with the previously recommended curve. The capture cross section σ_γ has been reduced almost throughout the energy range. Experimental data are averaged over 1 keV intervals in this figure.

Scattering Cross Section for U^{238}

A combined evaluation of the elastic, inelastic and nonelastic cross sections was performed using the relation

$$\sigma_t = \sigma_{el} + \sigma_a + \sigma_{in} = \sigma_{el} + \sigma_{nel}$$

(The evaluation of σ_t for KEDAK-3 is not described in this short paper).
In principle there are the following three different methods for the evaluation of the total inelastic scattering cross section

$$\sigma_{in} = \sum_k \sigma_{in}^{(k)} \qquad (1)$$

$$\sigma_{in} = \sigma_t - \sigma_{el} - \sigma_a \qquad (2)$$

$$\sigma_{in} = \sigma_{nel} - \sigma_a \qquad (3)$$

In the energy region below 1.8 MeV, where the discrete excited levels can be resolved, the partial inelastic scattering cross sections of these levels are measured and method (1) can be used. Thus, the error in the total inelastic scattering cross section derived in this way is determined by the error in the measurements of the individual levels or groups of levels. On the other hand if the inelastic cross section is inferred from methods (2) or (3), the uncertainties in the cross sections σ_t, σ_a, σ_{el} or σ_{nel} determine the uncertainty in the resulting total inelastic cross section. Therefore it has to be decided for each energy region which of the possible methods leads to the smallest uncertainties in the resulting cross section.

The method (3) is not possible below 2 MeV because the nonelastic cross section is measured only in the region above 2 MeV. As has been shown in a paper of Smith[35] the uncertainties of method (2) in the energy region below 0.8 MeV are rather large (~25%) and are estimated to be larger than those of method (1). Therefore up to 0.8 MeV method (1) was chosen for the evaluation of σ_{in}; the resulting cross section corresponds to the evaluation of Kanda[34]. Between 1 and 2 MeV error analysis does not allow a unique decision between the methods (1) and (2), because the uncertainties in both methods are estimated to be about 15-25%. In this case we consider the results of the neutron spectrum measurements as an independent physical criteria. Although the neutron spectrum measurements cannot reproduce the exact shape of the inelastic cross section, they provide decisive information about its overall behavior. Thus method (2) was chosen because it leads to a cross section which is more similar to that inferred from neutron spectrum measurements[33].

In the energy region between 2 and 5 MeV the method (2) was preferred because the uncertainties of the old nonelastic cross section measurements[36] lead to uncertainties of the resulting cross section of the method (3) which are estimated to be larger or not smaller than those of method (2). The evaluation of the elastic scattering cross section in the energy range from 1 MeV to 5 MeV is based mainly on the new microscopic data of Smith[35]. In the energy range above 6 MeV the nonelastic cross section was evaluated. In addition to the data sets used for the KEDAK-2 evaluation of the nonelastic cross section[36], the only data published after 1966 (Voignier[37]) were included for KEDAK-3. The difference between the previous and the present data for σ_{in} on KEDAK in this energy region is therefore mainly due to the different values of σ_a.

In Fig. 6 the results for the inelastic cross section are presented together with the previously recommended data on KEDAK, the results of the neutron spectrum measurements of Bluhm[33] and the KFKINR-set[38]. The present evaluation is characterized by a reduction of the previously recommended data on KEDAK in the energy region from 0.5 MeV to 5 MeV, amounting to 60% about 1.5 MeV. The uncertainty of these recommended data is estimated to be less than 20% below 5 MeV and of the order of 30-35% above 6 MeV which is primarily due to the uncertainty in σ_a. A new inelastic scattering matrix for U^{238} was generated using partly the data of Smith[35].

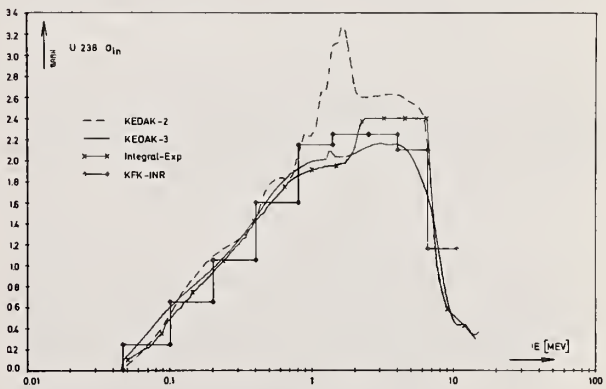

Fig. 6

Check of the Evaluated Data

To check the quality of the evaluated data for U^{235}, U^{238}, Pu^{239}, Pu^{240}, Pu^{241} and Pu^{242}, group cross sections were generated in the well-known Russian ABBN-26 group structure. These group constants were incorporated in the KFKINR-set[38], which is not based on KEDAK, but rather has been established by a careful investigation of both differential and especially integral physics experiments. With a few exceptions this set reproduces the experimental k_{eff}-values within a ± 1% margin (column a). With the modified KFKINR-

set zero-dimensional calculations were performed for a variety of critical assemblies with different neutron spectra. The results of these calculations for some assemblies are listed in table 1 (column b) and are compared with the corresponding results of the KFKINR-set (column b). The bucklings in the zero-dimensional calculations were taken unchanged from the original KFKINR-set. In all cases the $\bar{\nu}$-values have not been replaced in the KFKINR-set. This was done because it was intended to study the cross section effect separately. The present uncertainty in $\bar{\nu}$ is of the order of 1% which leads to almost the same uncertainty in the value of k_{eff}.

Table 1

No.	Critical assembly	k_{eff} KFK 1NR-set a)	b)	k_{eff} KFK INR-set modified with KEOAK-3 b)	% change in k_{eff} c)	k_{eff} KFK INR-set modified with KEDAK-2 b)	% change in k_{eff} c)
1	SNEAK 3A1	1.004	0.995	0.998	+ 0.30	0.984	- 1.12
2	SNEAK 3A2	1.001	0.990	0.993	+ 0.37	0.980	- 0.92
3	ZPR 111 55	1.011	0.995	0.975	- 2.02	0.930	- 6.57
4	ZPR IX 25	0.995	0.995	0.990	- 0.55	0.946	- 4.99
5	SNEAK-8	0.999	0.999	0.994	- 0.51	0.947	- 5.17
6	SNEAK-7A	1.012	1.017	1.007	- 1.0	0.999	- 1.78
7	VERA 11A	1.0064	0.954	0.944	- 0.98	0.946	- 0.76
8	ZPR III-48	1.007	0.976	0.968	- 0.82	0.953	- 2.39
9	SNEAK-2AR1	1.013	1.011	1.015	+ 0.34	1.002	- 0.91
10	SNEAK 6A-Z1	1.007	1.006	0.996	- 1.05	0.979	- 2.70
11	SNR 300	-	1.037	1.025	- 1.17	1.010	- 2.58

a) 2-dimensional calculation with all required correction, e.g. heterogeneity and transport corrections, (ref. 38)

b) zero-dimensional calculations

c) with respect to zero dimensional calculations with KFK 1NR-set

It is seen in table 1 that good agreement between the k_{eff}-values obtained with the KFKINR-set (column 4) and those with the KFKINR-set modified with KEDAK-3 (column 5) is achieved without requiring any adjustment of group cross sections. The good quality of the KEDAK-3 data is further emphasized if compared with the k_{eff}-values obtained with similar calculations using the KEDAK-2 cross sections (column 7).

The authors wish to acknowledge assistance in the work leading to the preparation of this paper from J.Braun, C.Broeders, I.Broeders, E.Kiefhaber, B.Krieg, I.Langner, M.Mangelmann, E.Stein and A.Wengeler.

References

1 B.Hinkelmann, B.Krieg, I.Langner, J.J.Schmidt, D.Woll, KFK 1340 (1971)

2 A.L.Pope, AEEW-M 1208 (1973)

3 Delivered to us in parts by CCCDN/Saclay

4 D.G.Foster and D.W.Glasgow, Phys.Rev.C3, 576 (1971) & Nucl.Instr.&Methods 36.1 (1965)

5 J.Cabé, M.Cance, A.Adam, M.Beaufour and M.Labat, Conf.Nucl.Data for Reactors, Helsinki, Vol.2 31 (1970)

6 A.B.Smith, P.Guenther and J.Whalen, J.Nucl.Energy 27, 317 (1973)

7 R.B.Schwartz, R.A.Schrack and H.T.Heaton,II, Nucl.Sc.Eng. 54, 322 (1974)

8 R.Gwin, L.W.Weston, G.de Saussure, R.W.Ingle, J.H.Todd, F.W.Gillespie, R.W.Hockenburry and R.C.Block, Nucl.Sci.Eng. 45, 25 (1971) and private communication 1973

9 L.W.Weston and J.H.Todd, Trans.Am.Nucl.Soc.15, 480 (1972) and private communication

10 J.Blons, Nucl.Sci.Eng., 51, 130 (1973)

11 W.K.Lehto, Nucl.Sci.Eng., 39, 361 (1970)

12 M.G.Sowerby, B.H.Patrick and D.S.Mather, AERE-R 7273 (1973) and Annals Nucl.Sci.Eng., 1, 409 (1974)

13 M.G. Sowerby and V.A.Konshin, Atomic Energy Review IAEA 10 453 (1972)

14 G.de Saussure, L.W.Weston, R.Gwin, R.W.Ingle, J.H.Todd, R.W.Hockenbury, R.R.Wood, and A.Lottin, Nucl.Data for Reactors Paris, 1966, 233

15 R.E.Bandl, H.Meissner and F.H.Fröhner, Conf. Neutron Cross-section and Technology, Knoxville Rep. CONF 710301 273 (1971)

16 J.E. Hopkins and B.C.Diven, Nucl.Sci.Engng. 12 169 (1962)

17 V.N.Kononov, E.D.Poletaev, Yu.S.Prokoptes, A.A.Metlev, and Yu.Ya.Staviskii, Rep FEI-274 (1971). Atomn. Energy. 32, 85 (1972)

18 S.Cierjacks, private communication (1973)

19 G.Hansen, S.McGuire, R.K.Smith (1969) quoted in ref.12

20 R.K.Smith, R.L.Henkel and R.A.Nobles, Bull.Am. Phys.Soc. 2, 196 (1957)

21 P.H.White, D.P.Warner, J.Nucl.Energ. 21, 671 (1967)

22 W.E.Stein, R.K.Smith, H.L.Smith, Washington Conf. Neutron Cross-sections and Technology, Vol.1, 627 (1968).

23 J.W.Meadows, Nucl.Sci.Eng. 49, 310 (1972)

24 R.W.Lamphere, Phys.Rev. 104, 1654 (1956)

25 W.G.Davey, Nucl.Sci.Eng. 32, 35 (1968)

26 S.P.Kalinin, V.M.Pankratov, Geneva Conf., Vol.16 136 (1958)

27 R.Richmond, quoted by W.D.Allen and R.L.Hendel, Progress Nuclear Energy, Vol.2, 29 (1958)

28 R.B.Leachman, H.W.Schmitt, J.Nucl.Energy 4, 48 (1957)

29 M.N.Nikolaev, V.I.Golubev, I.I.Bondarenko, Soviet.Phys. JETP 34(7), 517 (1958)

30 M.C.Moxon, AERE-R-6074 (1969)

31 G.de Saussure, R.B.Perez, R.Ingle and H.Weaver, ORNL-TM-4059 (1973)

32 S.J.Friesenhahn, W.M.Lopez, M.P.Fricke, D.G.Costello and A.D.Carlson, GA-10194 (1970)

33 H.Bluhm, KFK 1798 (1973)

34 Y.Kanda, NNDEN/13 (1974)

35 A.B.Smith, private communication (1973)

36 J.J.Schmidt, KFK-120 (1966)

37 J.J.Voignier, CEA 3503 (1968)

38 E.Kiefhaber, KFK 1572 (1972)

39 B.Schatz, KFK 1629 (1972) EANDC(E) 151 "U"

40 M.Canev, S.Yiftah IA-1243 (1973)

41 M.C.Moxon, private communication to H.Weigmann and J.P.Theobald, J.Nucl. Energy 26 643 (1972)

42 N.G.Cao, E.Migneco, J.P.Theobald and J.A.Wartena, Conf.Neutron Cross-section & Technology Washington 1968 P 513

43 M.Ashgar, M.C.Moxon and N.J.Pattenden, Conf.Nucl. Data, Paris 1966 P.CN-23/31 and EANDC(UK) 103 AL (1968)

44 R.W.Hockenbury, W.R.Moyer, R.C.Block, NCSAC-42, 213 (1971)

DESCRIPTION OF THE ENDF/B-IV SILICON EVALUATION ENERGY DISTRIBUTIONS OF OUTGOING PARTICLES*

D. Larson
Oak Ridge National Laboratory
Oak Ridge, Tennessee 37830

Calculations are presented for the energy distributions of secondary particles resulting from neutron-induced binary and tertiary reactions on ^{28}Si.

(Cross sections, energy distributions, tertiary, photon, theoretical)

Introduction

Silicon is an important shielding material for reactor design and weapons effects, as well as being generally used in semiconductor devices. Especially because of the latter use, radiation damage due to secondary particles and recoiling nuclei is important and for this reason we have made an effort to include energy distributions of all outgoing particles in the ENDF/B-IV evaluation for this material. Since very little data exist for the energy distributions of secondary neutrons, and there are no available data for secondary proton and alpha energy distributions except to the lowest few discrete states, we had to rely on calculations for the desired quantities. In addition, above incident neutron energies of 13 MeV, tertiary reactions are allowed and become important. Virtually no data for either the cross section or energy distributions of these reactions exist, and again we must rely upon calculations. For these reasons much effort was put into generating a consistent set of calculations which reproduce as well as possible energy-averaged data of many types. In this evaluation, the available eperimental data serve two purposes; where it appears reliable it is transferred directly into the evaluation, and it also serves to firmly anchor the calculations, which are used for interpolation and extrapolation to energy regions and to reaction types for which no reliable data exist. In this paper we concern ourselves with the energy distributions of the outgoing particles, both from binary and tertiary reactions. Details of these results as well as a description of the remainder of the evaluation will be reported elsewhere.[1]

Energy Distributions of Outgoing Particles

We present below a description of the calculations for the energy distributions of outgoing particles. Figure 1 displays the major partial cross sections which make up the nonelastic cross section. The first step is to obtain cross sections for the binary reactions (n,n'), (n,p') and (n,α'), which are the only important binary reactions.These binary cross sections are obtained from standard Hauser-Feshbach[2] (HF) calculations. The neutron optical model parameters for the HF calculations were obtained by fitting to elastic scattering data from 4 MeV to 14 MeV, and requiring the parameters to reproduce the measured total cross section on the average, as well as the only measured value of the nonelastic cross section which is at 14 MeV.[3] The proton parameters were taken from the work of Becchetti and Greenlees[4] and were adjusted via HF calculations to reproduce the experimentally measured cross sections to the low lying states in ^{28}Al. In a similar manner, the initial alpha parameters were taken from the work of S. S. So et al.[5] and adjusted to reproduce the cross sections to low lying states in ^{25}Mg.

Other important pieces of input for the HF calculations are the parameters for the level density in the residual nuclei. Since the relative level densities of the residual nuclei ^{28}Si, ^{28}Al and ^{25}Mg determine the percentage of the nonelastic cross section which goes into the (n,n'), (n,p) and (n,α) channels, the level densities must be carefully determined. For ^{28}Si we have a good experimentally measured estimate of the level density up to 13.5 MeV excitation energy.[6] The ^{28}Al level density is known from $^{27}Al(d,p)$ and $^{27}Al(n,\gamma)$ measurements, while the ^{25}Mg density has been observed up to about 8 MeV with various charged particle reactions. The level density parameters of Gilbert and Cameron[7] have been adjusted so as to produce a level density equal to or greater than the experimental densities, and in addition reproduce the average total (n,n'), (n,p) and (n,α) cross sections via HF calculations. In addition to the compound nucleus contributions to (n,n'), direct interaction components were included for the first 2^+ and 4^+ levels in ^{28}Si. These calculations yield results which are in good average agreement with available data.

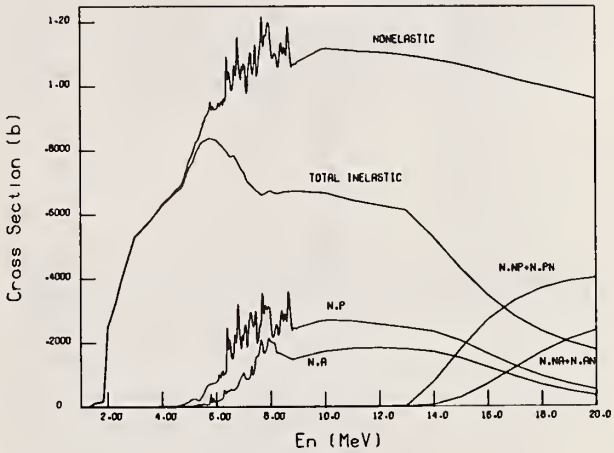

Figure 1. This figure shows the major components of the silicon nonelastic cross section. The effect of the onset of the tertiary reactions (n,n'p) and (n,n'α) can be seen in the total inelastic cross section near 13 MeV. The (n,np) and (n,pn), as well as the (n,nα) and (n,αn) cross sections have been summed because there is presently no facility in ENDF/B formats for entering them individually.

One method of demonstrating the overall quality of the calculations is to calculate the $Si(n,x\gamma)$ cross section -- i.e. the gamma production resulting from all neutron-induced reactions. Such a comparison is shown in Fig. 2. The data are those of Dickens, Love and Morgan[8] and are for the incident neutron energy bin from 9.5 to 10 MeV. The quality of the fit is directly related to the proper choices of optical model parameters and level densities in the residual nuclei. The required branching ratios are taken from the literature for the discrete states and calculated assuming dipole radiation for the continuum to discrete transitions. The calculations have been smeared to match the experimental resolution for display purposes.

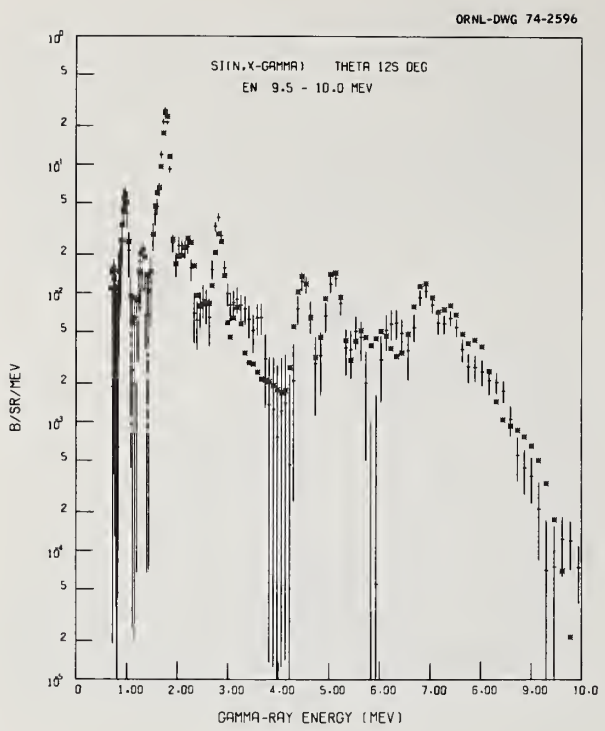

Figure 2. This figure is a comparison of the calculated Si(n,xγ) cross section with the data of Dickens, Love and Morgan.[8] The cross section scale is from 10^{-5} to 10° b/sr/MeV. The calculation was performed at E_n = 9.8 MeV, and the results are indicated by asterisks. The gamma ray near 1 MeV is from (n,p'γ) + (n,α'γ); the gamma ray near 1.4 MeV is from (n,αγ); the large peak near 1.8 MeV is mostly (n,n'γ), while the peak near 2.2 MeV is (n,pγ). The large gamma rays above 2.5 MeV are all from (n,n'γ) reactions.

Our results for the energy distribution dσ/dE' resulting from a 16-MeV incident neutron are shown in Figs. 3 through 5. Only the portion of the particle spectrum due to the continuum states in the residual nucleus is shown; the cross section to discrete final states lie at higher outgoing particle energy. The calculations were performed within the Hauser-Feshbach formalism, calculating the cross section to 50 keV wide bins in the residual nucleus. We note for the case of neutrons out from the (n,n') reaction in Fig. 3, the spectrum peaks near 1.2 MeV; lower energy neutrons are inhibited by the angular momentum barrier, while the slope of the distribution of the higher energy neutrons is governed mainly by the level density of the residual nucleus. The proton continuum from the (n,p) reaction shown in Fig. 4 peaks about 3.5 MeV, since low energy protons are inhibited by both the angular momentum and coulomb barriers. The alpha energy spectrum in Fig. 5 is even harder for the same reasons, peaking about 5.5 MeV.

We have also calculated the significant tertiary reaction cross sections, based on a development[9] of the complete statistical model. For the case where only discrete levels in the final nucleus are reached, which is the case here, the tertiary cross section is given by

$$\sigma_{xyz} = \sigma_{xy} \frac{k_z^2(2j_z+1)\,\sigma_c(z)}{\sum_z k_z^2(2j_z+1)\,\sigma_c(z)} \qquad (1)$$

where σ_{xy} is the binary cross section of interest and is is taken from the Hauser-Feshbach calculation, k_z^2 is the wave number of the second outgoing particle with intrinsic spin j_z, and $\sigma_c(z)$ is the cross section for the formation of the state y through the inverse channel z. $\sigma_c(z)$ is taken as the reaction cross section of the inverse system calculated from the optical model. For example, in the (n,n'α) calculation, $\sigma_{xy} = \sigma_{n,n'}$, and $\sigma_c(z)$ is the reaction cross section for α + ^{24}Mg. The sum in the denominator is over the open channels (n,n'γ) + (n,n'p) + (n,n'α). The model described above is rather crude; its major shortcoming being the lack of a correct treatment of angular momentum effects.

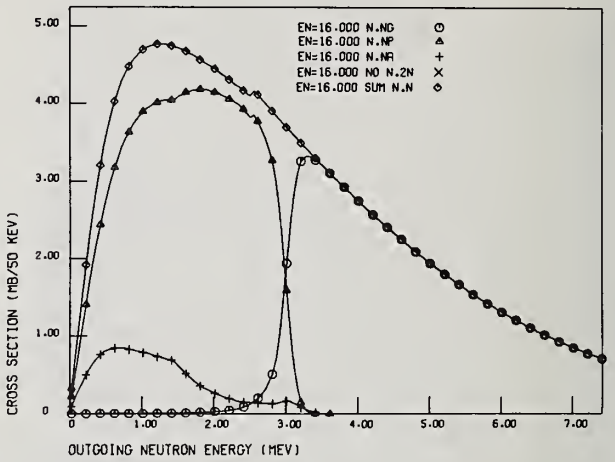

Figure 3. This figure shows the (n,n') energy distribution, and the breakdown into its tertiary components (n,n'γ), (n,n'p) and (n,n'α). At E_n = 16 MeV, the (n,n'p) cross section is much larger than the (n,n'α) cross section, but at 20 MeV they become more nearly equal. The energy distributions of the outgoing neutron, proton and alpha particles are uncorrelated, as required by the present ENDF/B format.

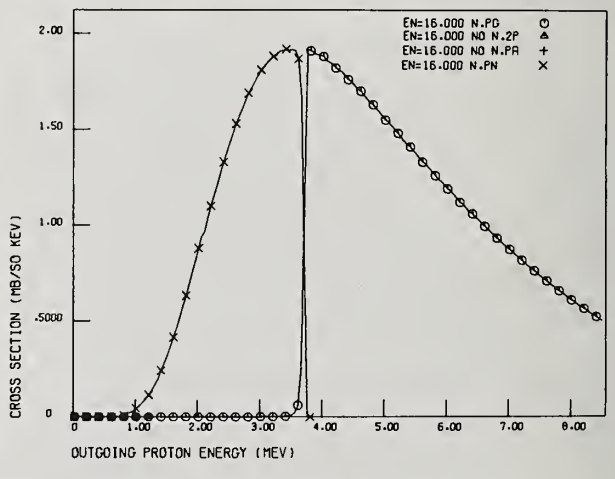

Figure 4. This figure shows the energy distribution of the outgoing proton for a 16-MeV incident neutron. The sum (n,p) curve is not drawn since it is made up only of the two components (n,pγ) + (n,pn).

The (n,n') spectrum consists of (n,n'γ) + (n,n'p) + (n,n'α) since the (n,2n) reaction is not allowed at

16 MeV due to its Q value. Figure 3 shows the breakup of the (n,n') spectrum into these component parts. We see that most secondary neutrons greater than 3 MeV are followed by gamma emission, while secondary neutrons less than 3 MeV are followed by either a proton or an alpha particle. Of course there is a corresponding figure for the energy distribution of the protons and alphas from the (n,n'p) and (n,n'α) reactions, but these are not shown. Figures 4 and 5, which show the proton and alpha energy distributions, are also split up into (n,pγ) + (n,pn) and (n,$\alpha\gamma$) + (n,αn) components, respectively. The reactions (n,pα), (n,2α), etc., are strongly inhibited by the coulomb barrier and are thus negligible, even if allowed by their Q value. Thus we see that at an incident neutron energy of 16 MeV, neutrons are produced not only from the (n,n') reaction but also a significant number from the (n,pn) and (n,αn) reactions. The secondary neutrons from these reactions are low energy, as seen in the figures, and are a substantial contributor to the low energy neutron spectrum.

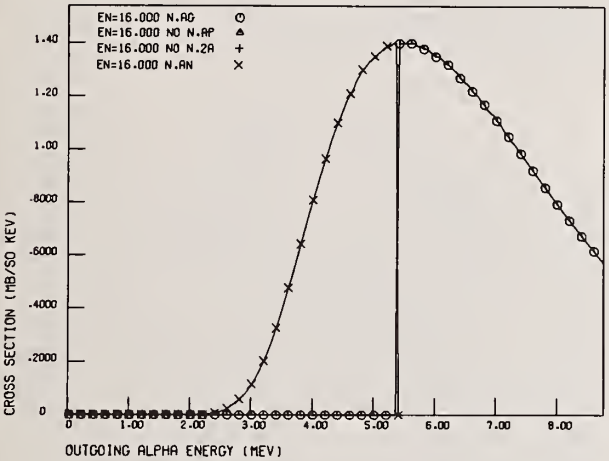

Figure 5. This figure shows the energy distribution of the outgoing alpha for a 16-MeV incident neutron. Again, the sum (n,α) curve is not drawn since it is made up only of two components (n,$\alpha\gamma$) + (n,αn).

The measurement of tertiary reaction cross sections is very difficult, and most of the present information is obtained by observing the gamma-ray production in the residual nuclei ^{27}Al and ^{24}Mg, in the case of ^{28}Si as the target material. Gamma rays associated with these nuclei begin to be observed when tertiary reactions become allowed, as demonstrated in the gamma-ray-production data of Dickens et al.[8] However, proper calculation of the associated gamma-ray production from tertiary reactions[9] has indicated that one must do better than the simple statistical model used above because of the sensitivity to angular momentum effects in the residual nuclei. The calculations for tertiary reactions shown here were done based on a statistical model, with an empirical correction for angular momentum effects. A correct treatment of the tertiary reaction process has been developed by C. Y. Fu[10] and will be discussed in a later paper in this session.

Using the correct treatment of angular momentum effects, combined with careful, consistent calculations which fit available experimental data, we feel confident we can make reasonable predictions of energy distributions which may be required for future applications, including fusion project requirements.

References

*Research sponsored by the Defense Nuclear Agency at Oak Ridge National Laboratory, operated by Union Carbide Corporation for the Energy Research and Development Administration.

1. D. Larson, to be published.
2. W. Hauser and H. Feshbach, Phys. Rev. 87, 366 (1952); A. M. Lane and R. G. Thomas, Rev. Mod. Phys. 30, 257 (1958).
3. N. N. Flerov and V. M. Talyzin, At. Energy (USSR) 1, 155 (1956).
4. F. D. Becchetti, Jr. and G. W. Greenlees, Phys. Rev. 183, 1190 (1969).
5. S. S. So et al., Nucl. Phys 84, 641 (1966).
6. P. M. Endt and C. Van der Leun, Nucl. Phys. A214, 194 (1973).
7. A. Gilbert and A. G. W. Cameron, Can. J. Phys. 43, 1446 (1965).
8. J. K. Dickens, T. A. Love and G. L. Morgan, ORNL-TM-4389 (1973).
9. C. Y. Fu, to be published.
10. C. Y. Fu, Paper EB-6 in this conference.

EVALUATION OF FISSION PRODUCT NUCLEAR DATA FOR 28 IMPORTANT NUCLIDES*

S. Igarasi, S. Iijima†, M. Kawai†, T. Nakagawa,
Y. Kikuchi, K. Maki††, and H. Matsunobu†††
Japan Atomic Energy Research Institute,
Tokai-mura, Ibaraki, Japan
†Nippon Atomic Industry Group Co., Ltd.
Kawasaki-shi, Kanagawa, Japan
††Atomic Energy Research Laboratory, Hitachi Ltd.
Kawasaki-shi, Kanagawa, Japan
†††Sumitomo Atomic Energy Industries, Ltd.
Tokyo, Japan

Evaluation of 28 fission product nuclear data for fast reactors is performed for total, capture, elastic scattering and inelastic scattering cross sections up to 15.0 MeV. Resonance parameters as well as the data of resonance integrals are surveyed. The cross sections reproduced with these parameters are adjusted so as to fit the thermal values and are connected smoothly with the cross sections obtained by the statistical model calculations. For some nuclides whose resonance parameters are not experimentally obtained yet, the statistical model calculations are carried out down to fairly low energy point. The cross section values thus obtained are used as the expectation values of averaged cross sections in the resonance region. Numerical data obtained are stored on the magnetic tape in the ENDF/B format.

(Evaluation; fission product; total cross section; capture cross section; elastic and inelastic scattering cross sections; resonance cross section; statistical model; optical model)

Introduction

A working group of JNDC has performed evaluation for total, capture, elastic scattering and inelastic scattering cross sections of the following 28 fission product nuclides; Sr-90, Zr-93, Mo-95, Mo-97, Tc-99, Ru-101, Ru-102, Rh-103, Ru-104, Pd-105, Ru-106, Pd-107, Ag-109, I-129, Xe-131, Cs-133, Cs-135, Cs-137, Nd-143, Ce-144, Nd-144, Nd-145, Pm-147, Sm-147, Sm-149, Sm-151, Eu-153, Eu-155.
These nuclides provide presumably about 80% of macroscopic capture cross section of all fission products in equilibrium core of a typical fast reactor. Preliminary results of this evaluation work were already published[1] and were used to produce a set of group constants[2] for fast reactors. After this publication, an effort has been made for revision of the evaluation. This is a short report on the revision work.

There are some shortcomings in the preliminary evaluation. One of these is that resonance structure of the cross sections was not taken into account but statistical model calculation was simply extrapolated down to 100 eV. While this may be a reasonable method to calculate the cross sections for lumped fission product, it is naturally incorrect for the cross sections of individual nuclides. Another defect is adoption of cross section formula without width-fluctuation correction. This formula overestimates the capture cross section below a few hundred keV. In fact, our evaluated values were often larger than those supplied by Benzi et al.[3,4,5] or by others.[6,7]

For improving these drawbacks, a new method was developed in this revision work. Cross-section formulas were modified for both statistical model and resonances. Resonance parameters as well as the data of resonance integrals were collected and surveyed in order to reproduce the resonance structures of the cross sections. Connection between the resonance and smooth cross sections was made at fairly reasonable energy point. An outline of this method is given in this report. Though the evaluation was carried out also for total, elastic scattering and inelastic scattering cross sections, discussion given in this report is mainly on the capture cross section.

* This work was performed as one of the projects of the Japanese Nuclear Data Committee (JNDC).

Evaluation Method

In the previous work[1], the optical and statistical model calculations were extrapolated by force down to 100 eV. Besides, the capture cross section was obtained without using the width-fluctuation corrections. These drawbacks were excluded in the present work by the use of the resonance formulas and of modified formulas[8] for the statistical model calculations.

It is well known that the optical model calculation provides the neutron total cross section σ_{tot}, shape elastic scattering cross section $\sigma_{el.s}$ and formation cross section of the compound nucleus σ_c that is composed of the capture ($\sigma_{n,\gamma}$), compound elastic ($\sigma_{el.c}$) and inelastic scattering (σ_{in}) cross sections. Relation between these cross sections is

$$\sigma_{tot}=\sigma_{el.s}+\sigma_c=\sigma_{el.s}+\sigma_{el.c}+\sigma_{in}+\sigma_{n,\gamma}\ , \quad (1)$$

In order to ensure this relation, the cross sections are calculated by the following formulas[8]

$$\sigma_{n,\gamma}(E_n)=\frac{\pi}{k_n^2}\sum_{J\pi jl} g^J \frac{\langle \Theta^{J\pi}_{njl}\rangle}{\langle \Theta^{J\pi}\rangle}\left\{\langle \Theta^{J\pi}_{\gamma 1}\rangle-\langle \Theta^{J\pi}_{\gamma 2}\rangle \times\left[\frac{\Delta\Theta^{J\pi}_{\gamma}}{\langle \Theta^{J\pi}\rangle}S^{J\pi}_{njl;\gamma 2}-1+S^{J\pi}_{njl;\gamma 2}\right]\right\}, \quad (2)$$

and

$$\sigma_{n,n'}(E_n)=\frac{\pi}{k_n^2}\sum_{J\pi jlj'l'} g^J\left\{\frac{\langle \Theta^{J\pi}_{njl}\rangle\cdot\langle \Theta^{J\pi}_{n'j'l'}\rangle}{\langle \Theta^{J\pi}\rangle}S^{J\pi}_{njl;n'j'l'} \times\left(1+\frac{\Delta\Theta^{J\pi}_{\gamma}}{\langle \Theta^{J\pi}\rangle}\right)-\delta_{njl;n'j'l'}\frac{1}{4}Q^{J\pi}(\langle \Theta^{J\pi}\rangle)\cdot\langle \Theta^{J\pi}_{njl}\rangle^2\right\}, \quad (3)$$

where n and n', in addition to indication of neutrons, stand for level energy, spin and parity for ground state of the target nucleus and for excited state of the residual nucleus, respectively. The quantities $\langle \Theta^{J\pi}_{njl}\rangle$ and $\langle \Theta^{J\pi}_{\gamma i}\rangle$ are obtained[9,10] using the neutron transmission coefficient $\langle T^{J\pi}_{njl}\rangle$ and gamma-ray transmission coefficient $\langle T^{J\pi}_{\gamma i}\rangle$,

$$\langle \Theta^{J\pi}_{njl}\rangle-\frac{1}{4}Q^{J\pi}(\langle \Theta^{J\pi}\rangle)\cdot\langle \Theta^{J\pi}_{njl}\rangle^2=\langle T^{J\pi}_{njl}\rangle, \quad (4)$$

$$\langle \Theta^{J\pi}_{\gamma i}\rangle-\frac{1}{4}Q^{J\pi}(\langle \Theta^{J\pi}\rangle)\cdot\langle \Theta^{J\pi}_{\gamma i}\rangle^2=\langle T^{J\pi}_{\gamma i}\rangle. \quad (5)$$

Two kinds of gamma-ray transmission coefficients[11,12] $\langle T^{J\pi}_{\gamma 1}\rangle$ and $\langle T^{J\pi}_{\gamma 2}\rangle$ correspond to the gamma-ray absorption and total gamma-ray widths respectively. Quantity $\Delta\Theta^{J\pi}_{\gamma}$ plays an important role in the cross-section formulas (2) and (3), and is given

$$\Delta\Theta^{J\pi}_{\gamma} = \langle\Theta^{J\pi}_{\gamma 2}\rangle - \langle\Theta^{J\pi}_{\gamma 1}\rangle \quad . \tag{6}$$

This quantity corresponds to the sum of the probability for neutron and gamma-ray emissions through cascade process from the compound nuclear states above the neutron separation energy. Quantities $Q^{J\pi}$ and $S^{J\pi}_{\text{inelc}}$ are correction factors for the resonance-interference and width-fluctuation effects [9,10]. It is easily seen that the relation (1) is satisfied by the cross-section formulas (2) and (3).

With simple sum of the single-level Breit-Wigner formula, negative values have often appeared at some energy points in the elastic scattering cross section. This unreason can be overcome by adopting the multi-level Breit-Wigner formula which takes account of interference between different levels. In applying this formula, the spins must be known for all the levels considered. For most of the fission product nuclides, however, there are many levels whose spins are not yet assigned. Hence the following approximation was taken in the present work. In the followings, suffices λ and μ denotes the spin assigned and unassigned levels respectively, and $P_{J\pi}$ is the probability that an unassigned level belongs to the (J,π) state. Then, the capture cross section is expressed as

$$\sigma_{n,\gamma}(E_n) = \frac{\pi}{k_n^2}\sum_{\ell}\left\{\sum_{J\pi} g^J \sum_{\lambda} \frac{\Gamma^{J\pi}_{\lambda n\ell}\cdot\Gamma^{J\pi}_{\lambda\gamma}}{(E^{J\pi}_{\lambda}-E_n)^2+(\frac{1}{2}\Gamma^{J\pi}_{\lambda})^2} + \left(\sum_{J\pi} g^J P_{J\pi}\right)\sum_{\mu}\frac{\Gamma_{\mu n\ell}\cdot\Gamma_{\mu\gamma}}{(E_\mu-E_n)^2+(\frac{1}{2}\Gamma_\mu)^2}\right\} , \tag{7}$$

and the elastic scattering cross section is

$$\sigma_{n,n}(E_n) = \frac{\pi}{k_n^2}\sum_{\ell}\left\{4(2\ell+1)\cdot\sin^2\phi_\ell + \sum_{J\pi} g^J\left[\langle\!\langle F^{J\pi}_{1\ell}\rangle\!\rangle^2 + \langle\!\langle \tfrac{1}{2}F^{J\pi}_{2\ell}\rangle\!\rangle^2 + 2\sin 2\phi_\ell\cdot F^{J\pi}_{1\ell} - (1-\cos 2\phi_\ell)\cdot F^{J\pi}_{2\ell}\right]\right\} , \tag{8}$$

where

$$F^{J\pi}_{i\ell} = \sum_{\lambda} f^{J\pi}_{i\ell\lambda} + P_{J\pi}\sum_{\mu} f_{i\ell\mu} \quad , \tag{9}$$

$$\left.\begin{aligned} f_{1\ell\lambda} &= \frac{(E_n-E_\lambda)\cdot\Gamma_{\lambda n\ell}}{(E_\lambda-E_n)^2+(\frac{1}{2}\Gamma_\lambda)^2} \quad , \\ f_{2\ell\lambda} &= \frac{\Gamma_{\lambda n\ell}\cdot\Gamma_\lambda}{(E_\lambda-E_n)^2+(\frac{1}{2}\Gamma_\lambda)^2} \quad . \end{aligned}\right\} \tag{10}$$

$\langle\!\langle \;\rangle\!\rangle^2$ means

$$\sum_{J\pi} g^J\langle\!\langle F^{J\pi}_{i\ell}\rangle\!\rangle^2 = \sum_{J\pi} g^J\left(\sum_{\lambda} f^{J\pi}_{i\ell\lambda}\right)^2 + 2\left(\sum_{J\pi} g^J P_{J\pi}\cdot\sum_{\lambda} f^{J\pi}_{i\ell\lambda}\right)\cdot\sum_{\mu} f_{i\ell\mu} + \left(\sum_{J\pi} g^J P_{J\pi}\right)\cdot\sum_{\mu} f^2_{i\ell\mu} + 2\left(\sum_{J\pi} g^J P^2_{J\pi}\right)\cdot\sum_{\mu<\mu'} f_{i\ell\mu}\cdot f_{i\ell\mu'} . \tag{11}$$

Here, the factor $P_{J\pi}$ is assumed to be proportional to $(2J+1)$.

The resonance cross sections were calculated by the use of the existing experimental data of the resonance parameters. The results of the calculations were adjusted by adding background cross sections so as to fit the thermal cross sections. The resonance integrals were also calculated and compared with the experimental data in order to confirm the reliability of the resonance cross sections. Agreement was fairly well between calculations and experiments.

The resonance cross sections thus obtained were connected with smooth cross sections calculated with the optical and statistical models. The energy point for the connection was chosen so that the discontinuity at this point can be explained as the statistical fluctuation of resonances. That is to say, if there were much more resonance levels observed, difference between the smooth cross section and averaged cross section of resonances should be within two times as large as a standard deviation of the latter, at this energy point. For the nuclides with no experimental data of the resonance parameters, the energy point for the connection was taken tentatively at a half distance of average level spacing from the thermal energy. The average level spacing and gamma-ray width were used in the statistical model calculations for giving the normalization factors of the gamma-ray transmission coefficients $\langle T^{J\pi}_{\gamma 1}\rangle$ and $\langle T^{J\pi}_{\gamma 2}\rangle$.

Survey of Parameters

Theoretical estimation is very useful for such data as fission product nuclear data whose experimental data are not enough for evaluation. In general, many parameters are used in the theory and their systematic trends must be known for many nuclides in wide energy range. In the previous work, parameters of the optical potential were investigated so as to reproduce the experimental data for total cross section, elastic scattering cross section and neutron strength function. Discrepancies between calculated and experimental data were 20 to 30% at most.

In the present work, the same potential parameters as before were used, because necessary revision is not due to the optical potential. The potential form is

$$V(r) = -(V_0 + iW_1)\cdot f_1(r) - iW_S\cdot f_2(r) - V_{so}\left(\frac{\hbar}{m_\pi c}\right)^2\frac{1}{r}\left|\frac{df_1(r)}{dr}\right|\cdot(\vec{\sigma}\cdot\vec{l}) , \tag{12}$$

$$f_1(r) = \left\{1+\exp[(r-R_1)/a_0]\right\}^{-1} , \tag{13}$$

$$f_2(r) = 4\exp\{(r-R_2)/b\}\Big/\left\{1+\exp[(r-R_2)/b]\right\}^2 , \tag{14}$$

and the parameters are

$$\left.\begin{aligned} V_0 &= 46 - 0.25E_n , \quad (A<147) \\ &= 52.5 - 40\frac{(N-Z)}{A} - 0.25E_n , \quad (A\geq 147) \\ W_1 &= 0.125E_n - 0.0004E_n^2 , \\ W_S &= 7.0 , \quad V_{so} = 7.0 , \quad a_0 = 0.62 , \quad b = 0.35 , \\ R_1 &= 1.16A^{1/3} + 0.6 , \\ R_2 &= 1.16A^{1/3} + 1.1 , \quad (A<147) \\ &= 1.16A^{1/3} + 1.3 , \quad (A\geq 147) \end{aligned}\right\} \tag{15}$$

Many examples calculated with this potential are illustrated in Refs. 1 and 13, for demonstrating the reliability of the parameters.

For level density, the formula of Gilbert and Cameron[14] was slightly modified[8] by taking account of parity distribution for highly excited states. Neutron separation energies from the compound nuclei were adopted from a compilation by Wapstra and Gove[15]. In the previous work, level schemes for 28 nuclides were surveyed for determining the energies, spins and parities. While this determination was rather tentative, no essential change of the values was made for the present work.

Average gamma-ray width and level spacing are very important parameters for the statistical model calcula-

tions, because their ratios are normalization factors of the gamma-ray transmission coefficients, namely of the capture cross sections. In the previous work, these parameters were adopted by surveying the experimental data or estimating them from the data of neighboring nuclei. They were used as the starting values of the normalization factors in the present evaluation, because the capture cross sections were expected to be smaller than the previous ones owing to the width-fluctuation effect. For nuclides with no experimental data, neither resonance parameters nor the smooth cross sections, the starting values of the parameters could be only useful data for noramlization of the capture cross sections. For the nuclides with no data of capture cross sections above the resonance energy region, the cross sections were calculated with the starting values and were connected reasonably with the resonance cross sections, through iterative calculations changing the normalization factors. Hence, the parameters were different from the starting values for these nuclides.

For the nuclides with the experimental data of capture cross sections, the parameters were adjusted so as to reproduce the cross sections. Such procedure as the adjustment might distort the meaning of parameters. The adjusted parameters are made to take all variations in behalf of the other fixed parameters such as the neutron transmission coefficients. Therefore, these adjusted parameters are not necessarily consistent with the data obtained from resolved resonance parameters.

After surveying many literatures, resonance parameters, resonance integrals of the capture cross sections (RI) and capture cross sections for thermal neutrons (σ_{th}) were collected. Numbers of resonance levels, their minimum and maximum energies are shown in the table, as well as the adopted values of σ_{th} and RI. Numbers of levels whose spins are not assigned yet are illustrated in parentheses. The spin values were guessed for Ru-102, Ru-104 and Nd-144, which have 3, 4 and 35 observed levels respectively. For Ru-102 and Ru-104, their levels were assumed to be s-wave resonances, because the neutron widths increase gradually with energy and show characteristic energy dependence of s-wave neutron widths. While fifteen of 35 levels for Nd-144 were also assumed to be s-wave resonances, the others seemed to be p-wave resonances.

	Numbers of Resonance Levels	E_{min} (eV)	E_{max} (eV)	σ_{th} (barns)	RI (barns)
Sr - 90	0			0.9±0.5	2.0
Zr - 93	0+ (1)	110	110	1.3~4	~33
Mo- 95	14+(39)	44.9	2112.2	14.5±0.5	105±7
Mo- 97	10+(52)	16.3	1835.9	2.2±0.7	13±3
Tc- 99	0+(11)	5.64	280.0	19±2	340±20
Ru-101	19+ (3)	15.9	670.0	3.1±0.9	85±12
Ru-102	3+ (0)	166.0	1296.0	1.3±0.15	4.1±0.4
Ru-104	4+ (0)	226.5	1055.0	0.47±0.2	4.6±1.0
Ru-106	0			0.146±0.045	2.6±0.6
Rh-103	59+(216)	1.257	4140.3	150±5	1100±50
Pd-105	12+ (1)	11.8	152.0	14.0	90±10
Pd-107	0			10.0	36
Ag-109	22+(59)	5.19	2506.0	91±3	1450±40
I -129	0+(5)	72.4	153.0	27±3	36±4
Xe-131	21+(17)	14.4	3945.3	90±10	870±40
Cs-133	12+(148)	5.9	3500.0	29.0±1.5	415±15
Cs-135	0			8.7±0.5	80.5
Cs-137	0			0.11±0.033	0.08
Ce-144	0			1.0±0.1	2.6±0.3
Nd-143	17+(93)+B	55.3	5503.0	325±1	140±30
Nd-144	15+(20)	373.8	19407.0	3.6±0.3	5.0±0.5
Nd-145	15+(170)	4.036	4637.0	42±2	240±35
Pm-147	0+(38)+B	5.36	316.5	181±7	2300±290
Sm-147	56+(75)+B	3.42	1161.0	64±5	714±50
Sm-149	80+(5) + B	0.0976	248.7	41000±2000	3183
Sm-151	0+(10)+B	1.103	12.75	15000±1800	3300±700
Eu-153	1+(71)	0.457	97.6	390±30	1635±200
Eu-155	0			4040±125	7000

Table. Numbers of observed resonance levels, their minimum and maximum energies, capture cross sections for thermal neutrons and resonance integrals of capture cross sections. Numbers in parentheses are numbers of levels whose spins are neither assigned nor guessed. Symbol B means that a bound level is considered in the present work.

Results and Discussion

For Sr-90, Ru-106, Pd-107, Cs-135, Cs-137, Ce-144 and Eu-155, neither capture cross sections nor resonance parameters are measured yet, except the thermal cross sections. Results with the optical and statistical models were taken for these nuclides. These are expectation values of the average cross sections and, in general, do not reproduce the thermal cross sections. Thermal and 1/v parts of the capture cross sections were obtained using experimental thermal cross sections, and were connected at one-half distance of the average level spacing from the thermal energy. Since the average level spacing for these seven nuclides was estimated from the data of the neighboring nuclides, uncertainties may be larger than those of the other 21 nuclides.

There are ten nuclides whose resonance parameters are observed but capture cross sections are not yet measured above 1 keV. They are Zr-93, Ru-101, Pd-105, I-129, Xe-131, Nd-143, Nd-144, Nd-145, Pm-147 and Sm-151. Resonance and thermal cross sections for these nuclides were calculated using the resonance parameters. Calculated thermal cross sections,however, did not necessarily fit to the experimental data. In order to reproduce the measured data, background cross sections were added to the thermal cross sections. The background cross sections were assumed to have 1/v form. Therefore, the resonance cross sections were also changed by this addition. The smooth cross sections calculated with the statistical model were connected reasonably with the resonance cross sections. For neodymium isotopes, the smooth cross sections were larger than those expected from the resonance cross sections. Reasonable connections were obtained reducing the smooth cross sections by 20% for Nd-143 and Nd-145, and by 50% for Nd-144, respectively. These reductions were carried out by reducing the normalization factors of the gamma-ray strength functions.

The smooth cross sections above 1 keV are experimentally known as well as the resonance parameters for Mo-95, Mo-97, Tc-99, Ru-102, Ru-104, Rh-103, Ag-109, Cs-133, Sm-147, Sm-149 and Eu-153. In general, the experimental data of the smooth cross sections are scattered and their uncertainties are fairly large. Therefore, the curve of the cross sections must be in the range of the scattered data and must connect reasonably with the resonance cross sections. Effects of the width fluctuation and resonance interference make the capture cross sections change considerably from those calculated by the simple Hauser-Feshbach theory. Therefore, the parameters in the previous work must be modified to fit the calculated curve to the experimental data. The average level spacing was taken as the adjustable parameters in this work. The average level spacing thus adjusted did not necessarily agree with those obtained from the resolved resonance parameters. This problem should be further investigated.

The cross-section curves were changed considerably for Cs-133 and Tc-99, in the present work. Larger values of the experimental data were selected for Cs-133 in the previous work. The smaller ones were adopted,

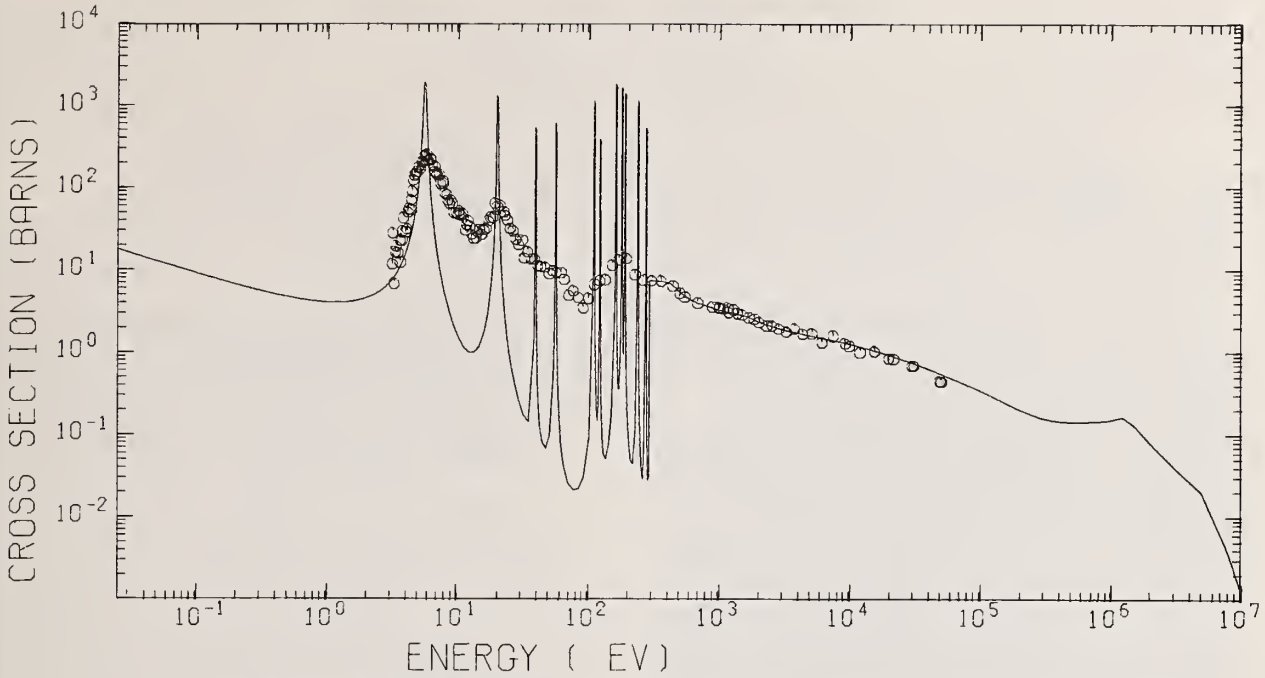

Figure. Neutron capture cross section of Tc-99.
Comparison is made between experimental and calculated data. The curve between 300 eV to 3 keV is drawn by eye-guide. Statistical model calculation is performed above 3 keV. Eleven levels of resonance are not assigned their spins at all. Thermal cross section is reproduced without background cross section, in this case.

in the present work, so as to obtain reasonable connection between the smooth and resonance cross sections. This choice is supported by the benchmark test[2] performed by using the group constants produced from the previous data.

For Tc-99, previous curve was normalized to the experimental data at 1 keV. Below 3 keV, however, the experimental data reveal fluctuation which cannot be reproduced by the statistical model calculation. In the present work, the eye-guide method was taken between 300 eV and 3 keV, and the smooth curve was normalized at 3 keV. The agreement was much improved with this method. Similar eye-guide method was applied for Mo-97 below 20 keV and for Eu-153 in the region from 100 eV to 5 keV.

In this report, the capture cross section was mainly discussed. The other cross sections were also evaluated in this work. Their numerical data were stored on the magnetic tape in the ENDF/B format.

References

1. Fission Product Nuclear Data Working Group, JNDC; JAERI-M 5752 (1974).
2. Y. Kikuchi, A. Hasegawa, I. Otake, K. Tasaka, H. Nishimura and S. Katsuragi; JAERI-M 6001 (1975).
3. V. Benzi and G. Reffo; CCDN/NW/10 (1969).
4. V. Benzi, R. D'Orazi, G. Reffo and M. Vaccari; Doc. CEC(71) 9 (1971).
5. V. Benzi, G.C. Panini, G. Reffo and M. Vaccari; Doc. CEC(71) 2 (1971).
6. J.L. Cook, AAEC/TM 549 (1969).
7. R.E. Shenter and A.F. Schmittroth; HEDL-TM-71-143 (1971).
8. S. Igarasi; J. Nucl.Sci.Technol. 12 67 (1975).
9. P.A. Moldauer; Phys.Rev. 135 B642 (1964).
10. Y. Tomita; JAERI 1191 (1970).
11. A.M. Lane and J.E. Lynn; Nucl.Phys. 11 646 (1959).
12. P.A. Moldauer; Proceedings of Conf. on Neutron Cross Section Technology, 613 (1966).
13. S. Igarasi, M. Kawai, T. Nakagawa, T. Suehiro and T. Murata; JAERI 1228 41 (1973).
14. A. Gilbert and A.G.W. Cameron; Can.J.Phys. 43 1446 (1965).
15. A.H. Wapstra and N.B. Gove; Nuclear Data Table 9 267 (1971).

EVALUATED DECAY-SCHEME DATA FOR THE ILRR PROGRAM†

R. G. Helmer and R. C. Greenwood
Aerojet Nuclear Company
Idaho National Engineering Laboratory
Idaho Falls, Idaho 83401

The half-lives and γ-ray intensities associated with radioactive decay have been evaluated for nuclides of interest to the Interlaboratory LMFBR Reaction Rate program. The results indicate that for most of the isotopes the decay parameters are known sufficiently well to meet the ILRR goals of 2½ or 5% accuracy in reaction rate measurements.

(Evaluted γ-ray intensities, evaluated half-lives, ILRR program)

For many years, the nuclear physics community has had available two general files of decay scheme data. These are the data sheets from the Nuclear Data Group at ORNL and the Table of Isotopes from LBL. These files have attempted to include essentially all quantities related to nuclear structure and radioactive decay. These files represent both a compilation (i.e., a list of all data or, at least, all references) and an evaluation (i.e., a judgment as to the best information). I will not review the quantities that can be included in a file of decay scheme data since this has been done by C. W. Reich at this Conference.[1]

In the last few years, a great use has developed for a number of specialized files of decay scheme data. These specialized files are usually needed for some of the following three reasons. First, due to the large amount of experimental data to be treated, it has not been possible to keep the evaluation work of the two general files up to date. For example, out of 218 A chains above A=44 for which the Nuclear Data Group has published data, 90 are dated before 1970 and 143 are dated before 1972. Second, some special files can justify more evaluation effort in obtaining specific quantities (e.g., absolute γ intensities) than can be warranted for these quantities in assembling the general files. Third, some special files may need particular quantities that are not available in the general files.

In assembling any data file, one must decide what level of evaluation is to be carried out. For example, in a decay data file for reactor decay heat calculations it seems quite reasonable to use data from one publication for each quantity. A more detailed evaluation which involved combining the results from several references would not be justified from the point of the manpower required.

In this paper, we wish to illustrate a specialized evaluation of decay scheme data by describing the data file for the Interlaboratory LMFBR Reaction Rate (ILRR) program.[2] This program was organized in 1971 for the purpose of making a series of precise measurements of rates of neutron induced reactions for a set of well-defined and reproducible neutron spectra. For most of these reactions, the rates are determined by measurements of the γ-ray spectra from the decay of radioactive reaction products. These reaction rates are determined in the ILRR program for two purposes. First, the rates for neutron induced reactions on certain nonfissile elements are measured in order to obtain information on the neutron spectrum or the integral cross section. The second purpose is to determine production rates for several fission products from four fissionable nuclides. (Combined with fission rate measurements, these data give fission yields.)

With respect to the γ-ray counting, the goals of the ILRR program are:

1. to obtain an estimate of the systematic errors in the γ-ray counting by comparing the results from several laboratories;
2. to provide absolute nonfission reaction rates which are accurate to ±5% (at the 68% confidence level); and
3. to provide absolute fission-product production rates accurate to ±2½%.

These reaction rates are given by

$$R = C \frac{A}{B \cdot \varepsilon} \frac{\lambda e^{\lambda \tau}}{(1-e^{-\lambda T})(1-e^{-\lambda t})}$$

where

- A = area of γ-ray peak
- ε = detector efficiency (energy dependent)
- B = absolute γ-ray intensity
- C = other factors, including sample mass
- λ = decay constant = $\ln 2/T_{½}$ and $T_{½}$ = half-life
- τ = decay time from end of irradiation to start of count
- T = count time
- t = irradiation time.

As shown, the reaction rate R depends on two parameters of the decay scheme: the half-life and the absolute γ-ray intensity (or branching ratio).

For the calculation of the reaction rates for the ILRR program, a careful determination of the associated uncertainties is needed. Differentiation of the above expression and rearrangement gives the following contributions to the fractional error, σ(R)/R.

$$\frac{\sigma(R)}{R} = -\frac{\sigma(\varepsilon)}{\varepsilon}$$

$$\frac{\sigma(R)}{R} = \frac{\sigma(A)}{A}$$

from the γ-ray counting and

$$\frac{\sigma(R)}{R} = -\frac{\sigma(B)}{B}$$

$$\frac{\sigma(R)}{R} = -\frac{\sigma(T_{½})}{T_{½}} \left(1 + \lambda\tau - \frac{\lambda T e^{-\lambda T}}{1-e^{-\lambda T}} - \frac{\lambda t e^{-\lambda t}}{1-e^{-\lambda t}}\right)$$

from the decay scheme parameters.

Although there are several other error contributions from the experimental counting, the above are generally the dominant terms in the error in R. For comparison of results from different irradiations or targets, relative reaction rates are sometimes

†Work performed under the auspices of the Energy Research and Development Administration.

sufficient. In these cases experiments can at times be done in a manner such as to cancel any error contribution from ε (same detector at same energy), B (same isotope counted) and $T_{1/2}$ (similar irradiation, decay and count times). In less than ideal situations, residual uncertainties from these contributions will be present but may still be small. The error in R may then be limited by $\sigma(A)/A$ and can be made quite small.

For careful γ counting, the $\sigma(\varepsilon)/\varepsilon$ contribution to $\sigma(R)$ is taken to be between 1% and 2% by the various laboratories involved in the ILRR measurements. This means that to meet a goal of $\sigma(R)/R < 2\frac{1}{2}\%$ with a typical value of $\sigma(\varepsilon)/\varepsilon = 1\frac{1}{2}\%$, the remaining terms above must total (when added in quadrature) $\leq 2\%$ for the fission products. Because of these rather stringent goals, an evaluation effort was needed within the ILRR program to provide the current best values of these parameters. In this case, published evaluations were not completely satisfactory because they either were out of date by several years or did not place a sufficient emphasis on obtaining precise values of these particular quantities.

The decay-scheme parameters from our most recent evaluation for the ILRR program are given in Table I for both the fission products and the nonfission reaction products. (These evaluations are documented in Ref. 3.) The uncertainties are estimated standard deviations. Since the γ-ray energies are used in the ILRR program only to identify the appropriate peaks, these quantities were not extensively evaluated and are generally from a single reference. In contrast, the half-lives and γ-ray intensities are the "average" of the various published values of comparable quality. In addition to providing (hopefully) the "best" values, this procedure has the advantage of indicating those cases where the quoted uncertainties are probably too small. (See illustration below.)

In determining an evaluated value for cases where several measurements exist and are of about the same quality, a weighted average of the values is used. Generally, the weight is taken to be $1/\sigma$ where σ is the reported uncertainty. An indication of the consistency of the individual values is determined from the reduced-χ^2 value, or ε^2.

$$\varepsilon^2 = \frac{\chi^2}{N-1} = \frac{1}{N-1} \sum_{i=1}^{N} \frac{1}{\sigma_i^2} (y_i - A)^2$$

where A is the average and $y_i \pm \sigma_i$ are the reported values. Then the "internal" estimate of the uncertainty in A is

$$\sigma(A)_{int} = \sqrt{N} \Big/ \sum_{i=1}^{N} \frac{1}{\sigma_i} \quad ,$$

and the "external" estimate of the uncertainty is

$$(A)_{ext} = \sqrt{\varepsilon^2}\, \sigma_{(int)} \quad .$$

A set of values is inconsistent if ε^2 is significantly greater than 1.0. The larger of σ_{int} and σ_{ext} is taken as the uncertainty in A.

There are basically two ways of determining the absolute γ-ray intensities. The first involves measuring the disintegration rate of a source (generally by 4π β or α counting) and the corresponding γ-ray emission rate. The ratio of these quantities is the absolute γ intensity. The second method consists of adding up the intensities of all of the radiations populating the ground state. The simplest cases of this are when only one γ ray, and no β rays, feed the ground state (e.g., ^{46}Sc). The most complex cases are those with strong βray transitions to the ground state and the γ rays have significant internal conversion (e.g., ^{144}Ce-^{144}Pr).

In several of the evaluated decay schemes in Table I, there is a γ-ray transition that occurs in $\sim$ 100% of the decays. In these cases, we have made an attempt to estimate the small effects (i.e., internal conversion, internal pair formation and unobserved, highly forbidden beta decay transitions) that would cause the γ-ray intensity to be less than 100%. Only in this way can a meaningful value of the uncertainty in the γ-ray intensity be obtained.

One of the purposes of any specialized data evaluation is to identify those experimental data which are not accurate enough for the program. To facilitate the comparison of the quality of the values in Table I with the ILRR goals, the contributions to $\sigma(R)/R$ from the γ-ray intensity and half-life errors are given in Table II. The latter contribution is given for typical irradiation and count times (namely, 2.2 and 8.3 hours, respectively) and two decay times (0 and the lesser of $2T_{1/2}$ and 60 days). These data indicate that the $\pm 5\%$ goal for the nonfission reactions can be met, but that more stringent goals would be impossible for several isotopes (e.g., ^{64}Cu, ^{115m}In). With the present parameters, the fission reaction goal of $\pm 2\frac{1}{2}\%$ cannot be met for ^{103}Ru, ^{132}Te and ^{144}Ce-Pr due to the large uncertainty in the absolute γ-ray intensities. In no case is the uncertainty in the half-life a limiting factor with respect to these goals.

Finally, we would like to illustrate one of the problems associated with the evalution of published experimental values. For many of the half-lives in Table I there have been a large number of measurements. For example, Table III lists nine values for ^{198}Au decay. It can be seen that these values are quite consistent since $\varepsilon^2 = 0.5$. However, a more typical situation is given in Table IV for eight reported values of the ^{24}Na half-life. Three different averages are shown. From the average of the three "best" values (i.e., those with the smallest quoted uncertainties), one obtains an ε^2 value of 54. This means that in order to be consistent, each of the reported errors would have to be multiplied by $\sqrt{54} \approx 7$. The effect of the "best", and latest, value is also illustrated by the comparison of the average of the first seven and all eight values. Between these two averages there is a large change in the deduced half-life as well as a large increase in ε^2, from 5 to 17. In this situation it would be tempting to use only the "best" value. However, since the best values often are inconsistent, we feel that this would be unacceptable. We, therefore, have taken the average value and used the external uncertainty estimate which takes into account the inconsistency within the set. It is reasonable to assume that the inconsistency in Table IV results in part, if not primarily, from the failure of experimentalists to include systematic error contributions in their quoted uncertainties.

References

1. C. W. Reich and R. G. Helmer, paper AA4 of this conference.
2. W. N. McElroy, Nucl. Tech. 25, 177 (1975) and following articles.
3. R. G. Helmer and R. C. Greenwood, Nucl. Tech. 25, 258 (1975).

TABLE I

EVALUATED NUCLEAR DECAY SCHEME DATA

Isotope	Half-Life	Gamma-Ray Energy (keV)	Gamma-Ray Intensity (%)
		nonfission reactions	
^{24}Na	15.00(2) h[a]	1368.60(3)	99.993(2)
		2753.98(10)	99.84(3)
^{27}Mg	9.46(2) m	843.73(4)	71.4(5)
		1014.44(5)	28.6(5)
			sum=99.964(4)
^{46}Sc	83.85(10) d	889.258(18)	99.984(6)
		1120.516(25)	99.987(6)
^{47}Sc	3.39(4) d	159.39(5)	69.0(25)
^{48}Sc	43.8(1) h	983.4(2)	99.987(2)
		1037.4(2)	97.5(3)
		1311.8(4)	99.992(2)
^{54}Mn	312.6(3) d	834.827(21)	99.97(2)
^{58}Co	71.23(15) d	810.757(21)	99.44(5)
^{59}Fe	44.6(1) d	1099.224(25)	55.5(17)
		1291.564(28)	44.1(12)
			sum=99.6(1)
^{60}Co	5.268(5) y	1173.208(25)	99.86(2)
		1332.464(30)	99.986(2)
^{64}Cu	12.701(7) h	511.002	36.8(16)[b]
^{115m}In	4.50(2) h	336.2(1)	47.(2)
^{116m}In	54.03(20) m	1293.4(3)	83.4(15)
		2112.1(4)	16.5(15)
			sum=99.94(1)
^{198}Au	2.696(2) d	411.794(8)	95.48(10)
^{239}Np	2.355(4) d	228.19(1)	11.3(2)
		277.60(3)	14.3(2)
		fission reactions	
^{95}Zr	64.4(5) d	724.184(18)	44.2(5)
		756.715(19)	54.8(5)
			sum=99.0(5)
^{103}Ru	39.43(10) d	497.08(1)	89.(3)
^{132}Te	77.9(5) h	228.16(6)	88.5(60)
^{137}Cs	30.03(15) y	661.638(19)	85.0(3)
^{140}Ba	12.79(1) d		
^{140}La	40.26(2) h	1596.18(5)	95.33(16)
^{144}Ce	284.4(4) d	133.53(3)	10.7(4)
^{144}Pr	17.28(5) m	696.492(19)	1.49(15)
		2185.608(46)	0.77(4)

[a]The numbers in the parentheses are the uncertainties in the last digit(s).

[b]This intensity assumes conversion of all positrons to photon pairs at the source.

TABLE II

UNCERTAINTY IN REACTION RATE R

Contributions to $\sigma(R)/R$ from the errors in decay scheme parameters for an irradiation of 30,000 sec and count duration of 8,000 sec. τ is the decay time.

Isotope	Half-Life	Fractional Uncertainty in R (%) from γ-Intensity	from Half-Life τ=0	from Half-Life τ=2T½	from Half-Life τ=60 d
		nonfission reactions			
^{24}Na	15 h	0.002	0.10	0.08	
^{27}Mg	9.5 m	0.7; 0.004[a]	0.21	0.50	
^{46}Sc	84 d	0.006	0.12		0.06
^{47}Sc	3.4 d	3.6	1.1	0.51	
^{48}Sc	44 h	0.002	0.21	0.11	
^{54}Mn	313 d	0.02	0.10		0.08
^{58}Co	71 d	0.05	0.21		0.09
^{59}Fe	45 d	2.7; 0.1[a]	0.22		0.01
^{60}Co	5.3 y	0.002	0.09		0.09
^{64}Cu	13 h	4.3	0.04	0.04	
^{115m}In	4.5 h	4.3	0.15	0.47	
^{116m}In	54 m	1.8; 0.01[a]	0.23	0.74	
^{198}Au	2.7 d	0.10	0.07	0.03	
^{239}Np	2.4 d	1.4	0.16	0.08	
		fission reactions			
^{95}Zr	64 d	0.9	0.77		0.27
^{103}Ru	39 d	3.4	0.25		0.01
^{132}Te	78 h	6.8	0.61	0.28	
^{137}Cs	30 y	0.35	0.50		0.50
^{140}Ba-La	13 d	0.17	0.08	0.03	
^{144}Ce-Pr	284 d	5.2[b]	0.14		0.12

[a]The second value applies if the sum of the intensities of two γ rays is used.

[b]For 2185-keV γ ray.

TABLE III

EXAMPLE OF CONSISTENT SET OF REPORTED HALF-LIFE VALUES - ^{198}Au

Half-Life (days)	Uncertainty (days)
2.697	0.003
2.699	0.003
2.697	0.005
2.699	0.004
2.697	0.005
2.693	0.005
2.695	0.002
2.6946	0.0010
2.696	0.004

Weighted Average = 2.696 ± 0.001

$\varepsilon^2 = 0.5$

TABLE IV

EXAMPLE OF INCONSISTENT SET OF REPORTED HALF-LIFE VALUES - ^{24}Na

Half-Life (hours)	Uncertainty (hours)
14.970	0.020
14.980	0.020
14.959	0.010
14.953	0.013
15.050	0.030
15.050	0.020
15.000	0.020
15.030	0.003

Weighted Averages

Values Used	Half-Life (hr)	Internal Uncertainty	ε^2	External Uncertainty
first seven	14.985	0.006	5	0.014
all eight	15.005	0.004	17	0.016
best three	15.004	0.003	54	0.025

DEVELOPMENT OF A TWO-STEP HAUSER-FESHBACH CODE WITH PRECOMPOUND DECAYS AND GAMMA-RAY CASCADES--A THEORETICAL TOOL FOR CROSS SECTION EVALUATIONS*

C. Y. Fu
Oak Ridge National Laboratory
Oak Ridge, Tennessee 37830

The code is used to calculate neutron-induced binary reaction, tertiary reaction and associated gamma-ray-production cross sections of ^{19}F, ^{40}Ca and ^{56}Fe. Comparisons with experimental data show much improved agreements over those previously possible.

(Fluorine; calcium; iron; tertiary; photon; reaction)

Introduction

The ENDF/B-IV evaluations of certain neutron-reaction and associated photon-production cross sections in the 10- to 20-MeV range remain speculative for many important materials[1] due to minimal or non-existent data and the lack of a satisfactory theoretical tool. Yet for weapons effects analysis and fusion reactor study the energy range mentioned is rather important. We have for this reason developed the new code with which one may analyze certain cross sections much more rigorously than previously feasible, as illustrated via ^{19}F, ^{40}Ca and ^{56}Fe.

Theory

Binary reaction part of the code, including width-fluctuation corrections, is based on the Hauser-Feshbach program HELENE.[2] Theories underlying the major additions made are very briefly discussed. More detailed descriptions will be reported elsewhere.[3]

The Hauser-Feshbach formula[4] for binary reaction cross sections is extended to include the emission of a second particle, assuming sequential decays without correlation between the two outgoing particles. The partial excitation cross section of a discrete level in the residual nucleus from deexcitation of an unbound state in the intermediate nucleus is of the form:

$$\sigma_{\alpha\alpha'\alpha''} = \sigma_{\alpha\alpha'} \frac{\sum_{s''\ell''} T^{I'}_{\alpha''s''\ell''}}{D(I'\pi')} \qquad (1)$$

where $\sigma_{\alpha\alpha'}$ is the usual Hauser-Feshbach formula for binary reaction cross sections for an entrance channel α and exit channel α'. The double primed quantities refer to tertiary channels. Each tertiary channel α'' has orbital angular momentum ℓ'' and channel spin s", leading to the binary level spin I'. In other words, we have $\vec{I}' = \vec{\ell}'' + \vec{s}''$ and $\vec{s}'' = \vec{I}'' + \vec{i}''$ where I" and i" denote spins of the two tertiary products. The transmission coefficients $T^{I'}_{\alpha''s''\ell''}$ are calculated for each energy of the outgoing particle using an inhouse optical model. The denominator $D(I'\pi')$ includes all decay modes open to the unbound binary state α' having spin I' and parity π'.

Gamma rays emitted in $(n,x\gamma)$ reactions are calculated in competition with other tertiary particles through the use of transmission coefficients derived from the widths of El transitions given by the giant dipole resonance.[5] By assuming that the transitions are predominantly El and that the gamma-ray partial widths are functions only of the gamma-ray energy E_γ, the initial level spin I'_i and the final level spin I'_f, we have for a level at excitation energy E'_x the following gamma-ray transmission coefficients:

$$T^{\gamma}_{I'\pi'} = \frac{1}{\pi\hbar^2c^2} \sum_{E_x=0}^{E'_x} E_\gamma^2 \, \sigma_c / g(I'_i, I'_f) \qquad (2)$$

where the sum is over all accessible levels with the restrictions $\Delta I' \leq 1$ and $\Delta\pi' \neq 0$. The quantity σ_c is the cross section of the El giant resonance and $g(I'_i,I'_f) = (2I'_i+1)/2(2I'_f+1)$. To calculate gamma-ray-production cross sections, we need only to define the gamma-ray-branching ratios for transitions which have not been experimentally measured. Consistent with Eq. (2) the gamma-ray branching ratio from a level at E'_x to a level at E_x is given by

$$B_\gamma(E'_x,E_x) = \frac{E_\gamma^2 \, \sigma_c/g}{\sum_{E_x=0}^{E'_x} (E_\gamma^2 \sigma_c/g)} \qquad (3)$$

with the same $\Delta I'$ and $\Delta\pi'$ restrictions as defined for Eq. (2).

The binary reaction cross section $\sigma_{\alpha\alpha'}$ may be modified, prior to its use in Eq. (1), by including the precompound contributions. The precompound binary cross section is taken to be proportional to

$$\frac{\sigma_{\alpha\alpha'}}{\rho(E_x)} \sum_{\substack{n=n_0 \\ \Delta n=2}}^{\bar{n}} \left(\frac{E_x}{E}\right)^{n-2} (n^2-n)$$

where E is the excitation energy in the compound nucleus, n refers to the exciton number and $\rho(E_x)$ the total level density at E_x in the residual nucleus. The above quantity is summed over all channels of a given reaction, and the sum is normalized to a desired fraction of that reaction. The above quantity is simply $\sigma_{\alpha\alpha'}$ times the ratio of the precompound decay rates given by Blann[6] and the compound decay rates given by the Weisskopf evaporation model.[7] The only reason for including the precompound contribution in this manner is to be able to include it for a discrete level so as not to cause a discontinuity in the energy distribution of the secondary particles at the energy which separates the discrete level region from the continuum.

For simplicity we have restricted Eqs. (1), (2) and (3) to the case of discrete levels only. Extensions of these equations to the case of continuum states are straightforward and will be given elsewhere.[3] Equations (1), (2) and (3) were formulated for the conservation of angular momentum; unfortunately we cannot say the same thing for the precompound emission. Eventually one might hope to use the formulation of Feshbach[8] for a consistent analysis of compound and precompound reactions.

Illustrations

Selected calculations near 14 MeV for ^{19}F, ^{40}Ca and ^{56}Fe are presented and compared with experiments. Optical model and level density parameters used are the

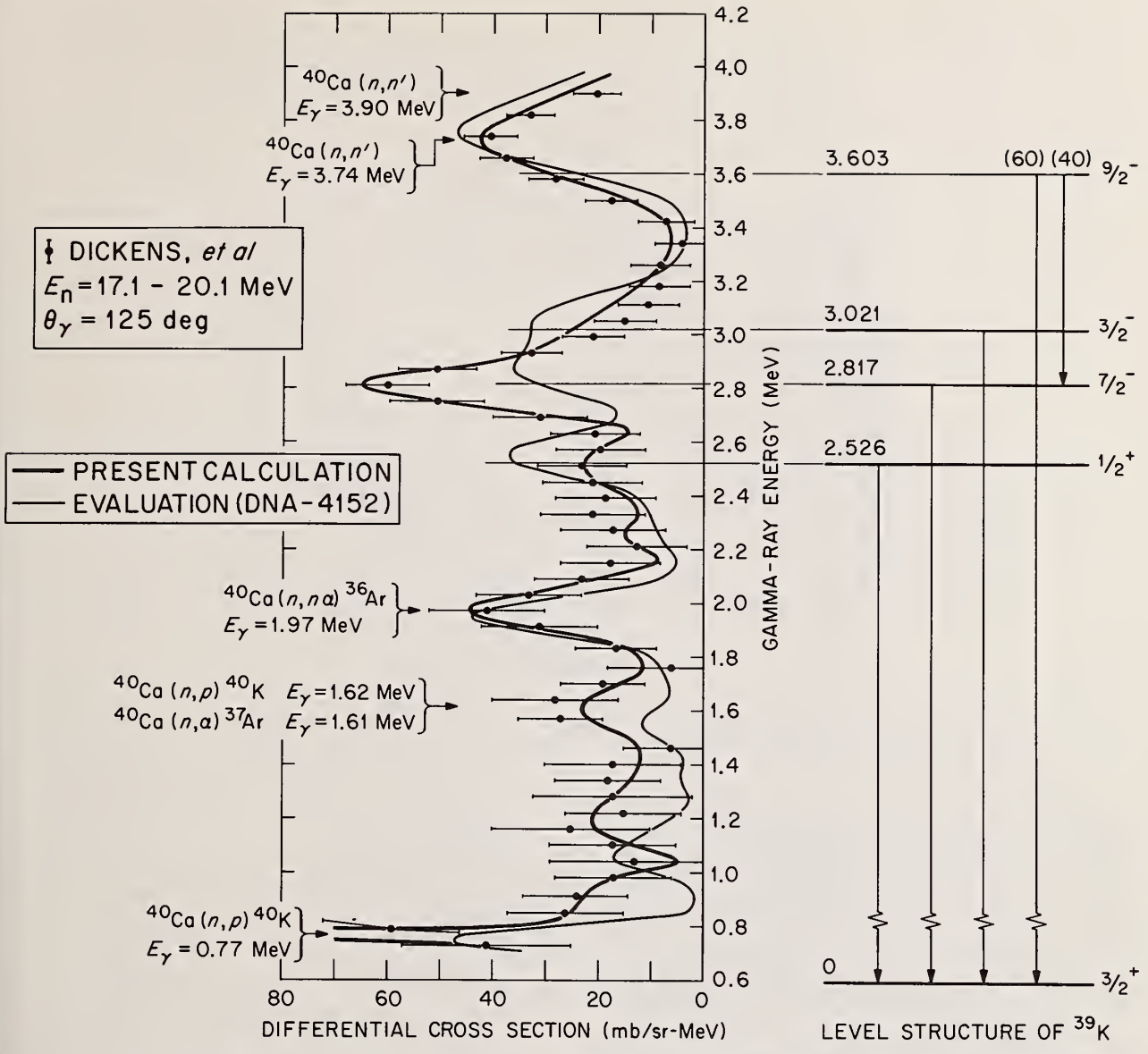

Fig. 1. Pronounced gamma rays arising from ^{40}Ca(n,xγ) reaction for 18.5-MeV incident neutrons. Levels excited in ^{40}Ca(n,np)^{39}K reaction are shown.

same as those optimized for ENDF/B-IV evaluations, so as to maintain consistency with elastic scattering and lower-energy reaction cross sections, on which the present code has little impact.

Calculated ^{40}Ca(n,xγ) cross sections at 18.5 MeV are shown in Fig. 1, together with the data of Dickens et al.[9] The calculated cross sections have been broadened in energy to correspond to the measurement. An early calculation (adopted in our evaluation before the data of Dickens et al. became available) based on the Weiskopf evapoation model[7] is also shown. The superiority of the present calculation is quite obvious. Although the result is expected, the significance is that, prior to the present development, the evaporation model had been the only available one. The three gamma rays (2.526, 2.817, and 3.021 MeV), produced in (n,np) reaction and as shown in the decay scheme in Fig. 1, illustrate the sensitivity of the Hauser-Feshbach calculations to the residual level spins. It is seen that the excitation cross sections of the I = 1/2 and 3/2 levels are much smaller than that of the I = 7/2 level, even though the excitation energies of these levels are comparable. Therefore, if only a small number of residual levels are excited in a tertiary reaction, the evaporation model is practically hopeless and the Hauser-Feshbach model should be used.

Calculated ^{19}F(n,xγ) cross sections for 15.5-MeV incident neutrons are compared in Fig. 2 with the data of Dickens et al.[10] The origins of the more pronounced gamma rays are: 0.937 MeV from (n,2n) reaction, 1.4 MeV from (n,n'), 1.982 MeV from (n,np), 2.58 MeV from (n,n') and 5.271 MeV from (n,nα). The calculated production cross section for the 0.937-MeV gamma ray appears too high, although we have obtained good agreement with the (n,2n) cross section itself.[11] On the other hand, calculation based on the evaporation model yields very poor results.

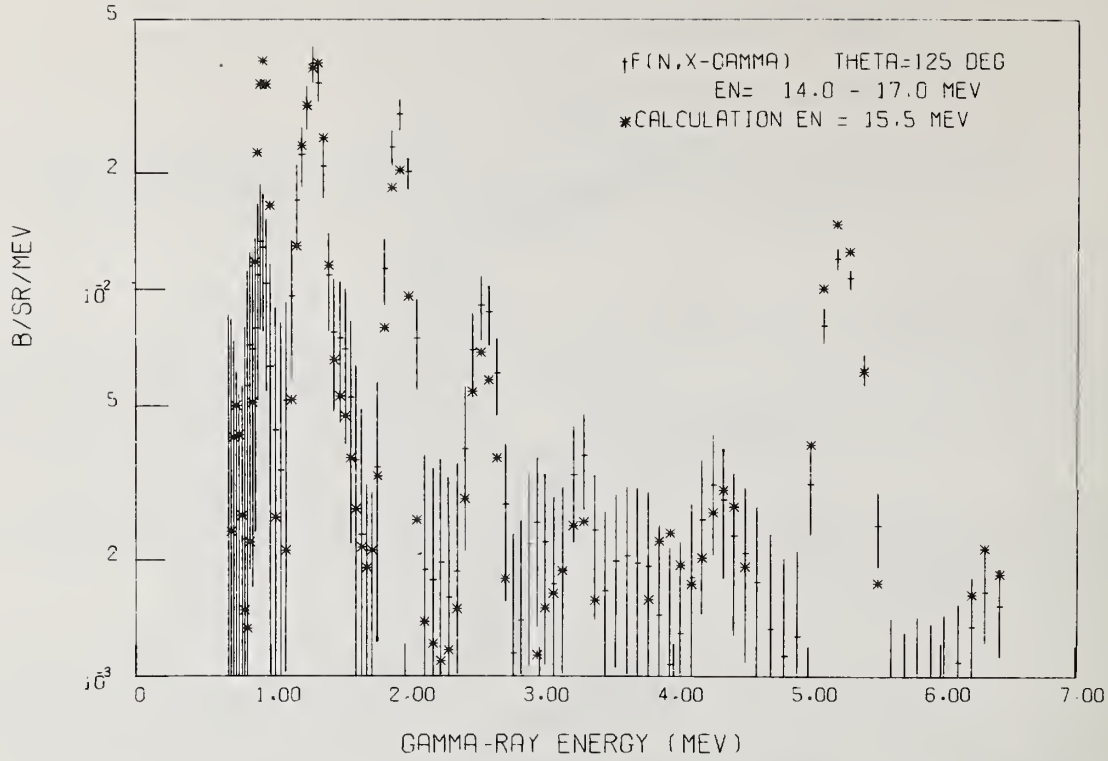

Fig. 2. Cross sections of gamma rays produced in $^{19}F(n,x)$ reaction at 15.5 MeV. Data shown are due to Dickens et al. (Ref. 10). Large contributions come from (n,2n), (n,np) and (n,nα) reactions. See text for origin of each peak.

Finally we compare in Fig. 3 the calculated differential cross sections of the secondary neutrons from ^{56}Fe bombarded with 14.5-MeV neutrons with available data.[12] Various calculated components shown have the following magnitudes: direct (n,n') = 100 mb, precompound (n,n')+(n,nx) = 365 mb, compound (n,n')+(n,nx) = 710 mb, (n,2n) = 496 mb and (n,pn) = 32 mb. The precompound cross section was adjusted to fit the high energy end of the spectrum and was limited to excitation energies greater than 4.51 MeV. Below 4.51 MeV we have calculated direct interaction contributions to (n,n') cross sections for 15 of the 26 discrete levels. Because only a few levels in ^{55}Fe are significantly excited in (n,2n) reaction, the energy distribution of the second neutron is sensitive to the spins and parities of these levels, and is therefore not describable by an evaporation model.

References

1. D. Steiner, editor, "The Status of Neutron-Induced Nuclear Data for Controlled Thermonuclear Research Applications: Critical Reveiws of Current Evaluations," U.S. Nuclear Data Committee Report USNDC-CTR-1(1974).

2. S. K. Penny, "HELENE - A Computer Program to Calculate Nuclear Cross Sections Employing the Hauser-Feshbach Model, Porter-Thomas Width Fluctuation, and Continuum States," ORNL-TM-2590, Oak Ridge National Laboratory (1969).

3. C. Y. Fu, "Consistent Calculations of Neutron and Gamma-Ray-Production Cross Sections for ^{40}Ca from 1 MeV to 20 MeV," to be published.

4. W. Hauser and H. Feshbach, Phys. Rev. 87, 366 (1952); A. M. Lane and R. G. Thomas, Rev. Mod. Phys. 30, 257 (1958).

5. P. Axel, Phys. Rev. 126, 671 (1962); P. Oliva and D. Prosperi, Nuova Cimento ILB, 161 (1967).

6. M. Blann, Phys. Rev. Lett. 21, 1357 (1968).

7. V. F. Weisskopf, Phys. Rev. 52, 295 (1937).

8. H. Feshbach, Rev. Mod. Phys. 46, 1 (1974), and private communication (1974).

9. J. K. Dickens, T. A. Love and G. L. Morgan, Nucl. Sci. Eng. 53, 277 (1974).

10. J. K. Dickens, T. A. Love and G. L. Morgan, Oak Ridge National Laboratory, ORNL-TM-4538 (1974).

11. P. Jensen et al., Nuclear Data A1, No. 2 (1966).

12. J. L. Kammerdiener, "Neutron Spectra Emitted by ^{239}Pu, ^{238}U, ^{235}U, Pb, Nb, Ni, Fe, Al, and C Irradiated by 14-MeV Neutrons," Lawrence Livermore Laboratory UCRL-51232 (1972).
R. M. Schectman and J. D. Anderson, Nucl. Phys. 77, 241 (1965).
G. C. Bonazzola et al., Nucl. Phys. 51, 353 (1965).
S. C. Mathur, P. S. Buchanan, and I. L. Morgan, Phys. Rev. 186, 1038 (1969).
G. Clayeux et al., Centre d'Etudes de Limeil CEA-R-4279 (1972).

*Research sponsored by the Defense Nuclear Agency at Oak Ridge National Laboratory, operated by Union Carbide Corp. for the Energy Res. and Dev. Administration

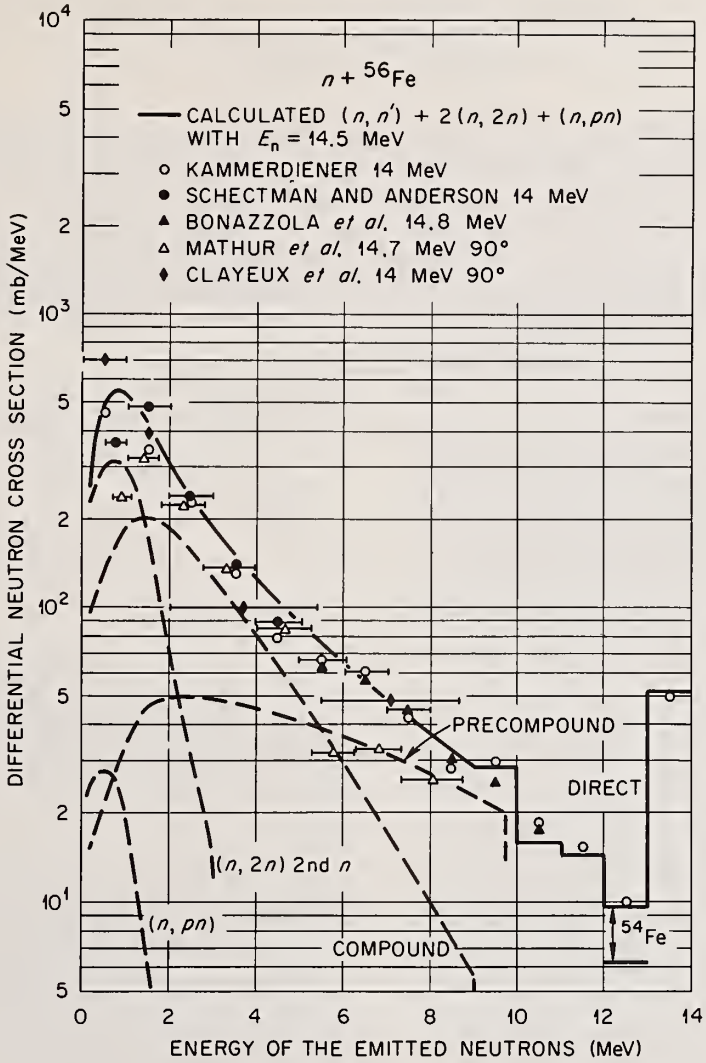

Fig. 3. Differential cross sections of secondary neutrons from iron bombarded with 14.5-MeV neutrons. See text for magnitude of each component.

NEUTRON CROSS SECTIONS AND THEIR UNCERTAINTIES OBTAINED FROM NUCLEAR SYSTEMATICS*

S. Pearlstein
Brookhaven National Laboratory
Upton, New York 11973

Previously, neutron cross sections in the MeV range for nuclei ranging in Z from 21 through 41 were calculated using a hybrid empirical-statistical model code THRESH. The formalism includes level density, Coulomb barrier, and competing reaction effects and has been useful in the prediction of unmeasured cross sections or normalized to point measurements to generate complete excitation curves. Reaction data up to 20 MeV in the Z range 21 through 83 are used to refine the model and extend its range of validity. A least squares fitting technique optimizes the choice of parameters with the resulting matrix used to determine parameter uncertainties and correlations. Fitted cross sections and their calculated uncertainties are compared with measurements and quoted errors. A range of uncertainty is assigned to predicted cross sections.

(Neutrons; cross section; nuclear model)

Introduction

Nuclear models can be used to provide physical insight to nuclear reaction mechanisms and to supplement experimental information that is either incomplete or discrepant while also yielding data in continuous form. The nuclear model parameters can be adjusted so that the calculations agree with good experimental data thereby extending the validity of the model but due to the spread of experimental data the nuclear model results will also have a range of uncertainty. The nuclear model code THRESH[1] has been improved and used to fit (n,2n), (n,p), and (n,α) data in the nuclear charge range 21 through 83.

The THRESH code calculates (n,particle) reactions in the MeV range using a hybrid empirical-statistical model but the results are not expected to be accurate in detail. No discrete level information is used and de-excitation of the compound nucleus by photon emission is ignored. Approximate formulas for components of the reaction mechanism are employed. In fact, only Z and A of the target nucleus is required as input although the calculated binding energies and any of 13 stored parameters may be overridden by the user if desired. The code has been very useful in evaluations of neutron cross sections for primary and secondary particle emission in the energy range to 20 MeV mainly because of the scarcity of experimental data and the detailed information required as input by other nuclear model codes.

Cross Section Systematics

The 14 MeV cross sections appear to vary in a systematic way with the neutron asymmetry parameter

$$s = \frac{N-Z}{N+Z} . \tag{1}$$

The (n,2n) reaction has been studied by several authors[2,3,4,5] with the premise that the channel for emitting neutrons $\sigma_{n,N}$ is in ratio to the nonelastic cross section σ_{ne} according to the following formula

$$\frac{\sigma_{n,N}}{\sigma_{ne}} = 1 - \alpha_N e^{-\beta_N s} \tag{2}$$

It is therefore not surprising that the remainder of the nonelastic cross section channels leading to charged particle emission are expected to vary exponentially with s according to

$$\frac{\sigma_{n,p}}{\sigma_{ne}} = \alpha_p e^{-\beta_p s} \quad \text{and} \tag{3}$$

$$\frac{\sigma_{n,A}}{\sigma_{ne}} = \alpha_A e^{-\beta_A s} \tag{4}$$

for (n,p) and (n,α) reactions respectively. Several authors[6,7,8,9] have proposed exponential formulas for the (n,p) and (n,α) cross sections at 14 MeV as described in Table I. There are significant differences among the proposed formulae that suggest it would be difficult to describe 14 MeV cross sections for emitting charged particles by a simple exponential formula.

Typical (n,p) cross section excitation curves are shown schematically as a function of energy and s in Figure 1. For small s, tending to describe a light nucleus with a small Coulomb barrier, (n,p) cross section has already peaked below 14 MeV and is decreasing due to competing reactions that are energetically possible. At intermediate values of s, for the cross section peak occurs at about 14 MeV. For large values of s, indicating a heavy nucleus with a high Coulomb barrier, the 14 MeV cross section occurs between threshold and the peak and is strongly dependent on barrier penetration characteristics. Thus 14 MeV cross sections sample widely different reaction phenomena and do not lend themselves to a few parameter fit. On the other hand the magnitude of the reaction channel which is approached by the peak cross section appears to vary systematically with s which serves as a simple indicator of a competion between neutron and charged particle emission.

Fitting Procedure

The cross section at energy E_n can be calculated using a nuclear model code with M parameters P_m

$$\sigma_n(E) = f\,(P_1, P_2 \text{----} P_M, E_n) \tag{5}$$

Denoting chi-square for N data points D_n of weight W_n as

$$\chi^2 = \sum_{n=1}^{N} W_n\,(D_n - \sigma_n) \tag{6}$$

*Research supported by U.S. Energy Research and Development Administration.

and creating a Taylor expansion about σ^o, determined from an initial set of parameter guesses, leads to the following minimization of χ^2 with respect to P_k

$$\sum_{n=1}^{N} W_n \sum_{m=1}^{M} \frac{\partial \sigma_n}{\partial P_m} \frac{\partial \sigma_n}{\partial P_k} \, dP_m = \sum_{n=1}^{N} W_n (D_n - \sigma_n^o) \frac{\partial \sigma_n}{\partial P_k} \qquad (7)$$

Equation 7 represents the normal equations to be solved simultaneously for a least squares fitting of the data. The matrix equation of the form

$$A \cdot dP = B \qquad (8)$$

is solved by inverting the A matrix to yield the column matrix dP, whose elements are the increments to the trial parameters P.

$$P_k^1 = P_k^0 + dP_k \qquad (9)$$

The process is repeated with the help of acceleration techniques until the solution has converged.

The uncertainties in the cross sections are expressed by the following equation.

$$d\sigma_n^2 = \sum_{k=1}^{M} \sum_{\ell=1}^{M} \left(\frac{\partial \sigma_n}{\partial P_k}\right)\left(\frac{\partial \sigma_n}{\partial P_\ell}\right) \langle dP_k \cdot dP_\ell \rangle \qquad (10)$$

where

$$\langle dP_k \cdot dP_\ell \rangle = A^{-1}_{k\ell} \frac{\chi^2}{N-M} \qquad (11)$$

and the correlation $C_{k\ell}$ between parameters dP_k and dP_ℓ is

$$C_{k\ell} = \frac{\langle dP_k \cdot dP_\ell \rangle}{dP_k \cdot dP_\ell} \leq 1 \qquad (12)$$

For 14 MeV (n,2n) data an evaluation[10] consisting of 98 nuclides and for (n,p) data a 132 nuclide evaluation[11] were used for fitting. For 14 MeV (n,α) data the experimental results of several authors[7,9,12,13,14,15] consisting of 90 data points for 66 nuclides was used. Energy dependent data for several nuclides were taken from the ENDF/B-IV library for cases where it could be ascertained that the evaluations were based on measured data.

Results

The range of uncertainties indicated by equation 10 is shown in Table II. Included is the estimated 10% uncertainty in the nonelastic cross section. In 30 to 50 percent of the cases the measured data lie outside the range of its fitted cross section and estimated uncertainty. For heavy nuclides the (n,2n) cross section approaches the nonelastic cross section whose error dominates the uncertainty the (n,p) and (n,α) cross sections are small and often highly uncertain.

The results of using the generalized parameters obtained from the least squares fitting of experimental data to fit the ^{56}Fe (n,p) cross section is shown in Figure 2. The ENDF/B-IV data are based on measurements. The agreement between calculation and experiment is improved by particularizing the parameters to the ^{56}Fe (n,p) cross section. However, the calculation does not agree near threshold due to deficiencies of the model in the calculation of threshold effects and excitation of particular states.

Some specific cases for the (n,α) reaction are shown in Table III. The two measurements for the ^{51}V (n,α) cross sections differ by a factor of 2 1/2 despite the assignment of small uncertainties. The results of the adjusted THRESH calculations have a 45% uncertainty but support the measurement of Levkowski[9]. For similar reasons the Sato[14] results are preferred over the measurements of other authors for ^{68}Zn, ^{79}Br, and ^{81}Br. These are a few examples of how the uncertainties in the cross sections obtained from nuclear model fitting of experimental data can be helpful in the selection of preferred values from among discrepant measurements.

References

1. S. Pearlstein, J. Nucl Energy 27 (1973) 81
2. D. W. Barr et al, Phys. Rev. 123 (1961) 859
3. S. Pearlstein, Nuc. Sci. and Eng 23 (1965) 238
4. W. Lu et al, Phys. Rev. C1 (1970) 350
5. E. Kondaiah, J. Phys A: Math., Nucl. Gen., 7 (1974) 1457
6. B. P. Bayhurst and R. J. Prestwood, J In. Nuc. Chem. 23 (1961) 173
7. E. Havlik, Acta Phys. Austriaca 34 (1971) 209
8. S. R. Choudhury and O. N. Kaul, J. Pure and Applied Phys. 10 (1973) 197
9. V. N. Levkowsky and O. Y. Artembya, Yad-Fiz., 13 (1971) 923
10. Z. T. Bödy et al, IAEA-153 (1971) 173
11. G. Eder et al, Z. Physik 253 (1972) 335
12. A. Chatterjee, Nuc. Phys. 49 (1963) 686
13. S. M. Quaim et al, Int. Conf. Brit. Nuc. Energy Soc. (1971)
14. J. Sato et al, Radiochimica Acta 16 (1971) 71
15. P. Venugopala et al, Phys. Rev. C3 (1971) 629

Table I

14 MEV SYSTEMATICS

$\frac{\sigma_{n,p}}{\sigma_{ne}} = ke^{-25.2\frac{N-Z}{N+Z}}$, $\frac{\sigma_{n,\alpha}}{\sigma_{ne}} = ke^{-31.1\frac{N-Z}{N+Z}}$ Bayhurst 1961

$\sigma_{n,p} = 0.60\,(N-Z)^2 e^{-62.8\frac{N-Z}{N+Z}}$, $\sigma_{n,\alpha} = 0.70e^{-28\frac{N-Z+1}{N+Z}}$ Havlik 1971

$\sigma_{n,\alpha} = 45.2\,(A^{\frac{1}{3}}+1)^2 e^{-45\frac{N-Z-L}{N+Z-L}}$ Choudhury 1971

$\frac{\sigma_{n,p}}{\sigma_{ne}} = 0.73e^{-33\frac{N-Z}{N+Z}}$, $\frac{\sigma_{n,\alpha}}{\sigma_{ne}} = 0.29e^{-33\frac{N-Z}{N+Z}}$ Levkowski 1971

Table II

RANGE OF UNCERTAINTIES (%)

Reaction	$\frac{N-Z}{N+Z}$ .03-.05	.05-.10	.10-.15	.15-.20
n,2n	20-50	10	10	10
n,p	20-25	20-30	20-40	30-150
n,α	25	25-40	30-60	40-150

Table III

EXAMPLES OF FITTED AND MEASURED RESULTS

Reaction	THRESH	Measurements		
^{51}V (n,α)	18 ± 3	43 ± 4	Chatterjee	1963
		18 ± 3	Levkowski	1971
^{68}Zn (n,α)	6.6 ± 1.8	15 ± 2.5	Quaim	1971
		8 ± 0.5	Sato	1971
		9 ± 1	Levkowski	1971
^{79}Br (n,α)	8 ± 2	20 ± 2	Venugopala	1971
		10.8 ± 0.7	Sato	1971
		15 ± 3	Levkowski	1971
^{81}Br (n,α)	3.6 ± 1.4	19 ± 2	Venugopala	1971
		3.7 ± 0.3	Sato	1971
		7 ± 1	Levkowski	1971

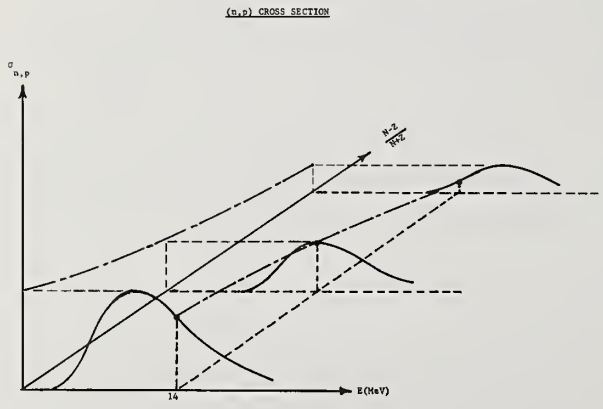

Figure 1

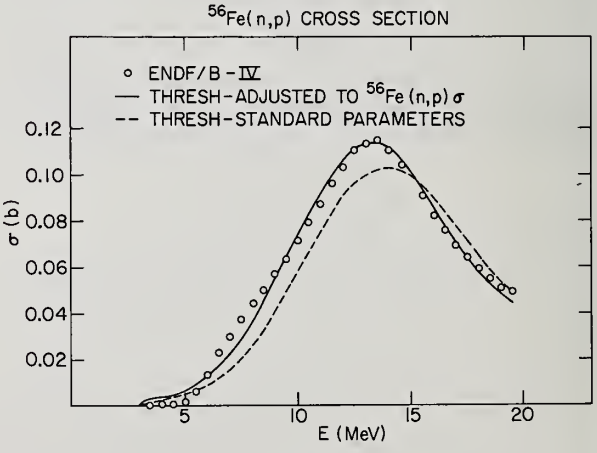

Figure 2

LEVEL DENSITY CALCULATION FOR DEFORMED NUCLEI *

J.P. Felvinci, D. Cacuci, and E. Melkonian
Columbia University
New York, New York 10027

Level densities for the rare earth and actinide nuclei have been calculated using a modified version of the Ericson formalism. The assumption was made, that K (the projection of J on the symmetry axis of the nucleus) is a good quantum number in the compound nucleus. Individual level densities for the different (K,J) values of the compound nucleus formed by low energy neutron interactions were calculated. The results show good agreement with the interpretation of recent results obtained on U-235 in this laboratory. Using the above calculations it is also possible to infer from the measured level densities the locations of the band heads of different K bands in the compound nucleus. The results also indicate that the K bands responsible for the level densities exclude the ground state rotational band. Levels built on the higher lying β and γ vibrational bands and their composites are sufficient in number to explain the observed level densities.

(Level densities and positions of K-bands in rare earth and actinide nuclei)

Calculation of level densities is one of the ways to compare the validity of a nuclear model with experimental results. Many such calculations have been performed in the past[1,2] but they frequently suffered from the comparisons with inadequate experimental data. Because of improved level spacing measurements in the recent years it is worthwhile to re-evaluate models used earlier in the light of the new data.

We have speculated in other papers[3] on the possibility that the K quantum number (the projection of the angular momentum J on the nuclear symmetry axis) is conserved during the lifetime of the compound nucleus. This assumption not only offered one possible explanation to some results we obtained in low energy fission resonances[3], but also gave us some understanding of certain non-statistical effects observed in other nuclei. As one of the checks on our assumptions, we performed a level density calculation incorporating these ideas.

Ericson[4], in an earlier paper, did include K in the level density calculations, but did not consider it a good quantum number at excitations corresponding to the neutron separation energy. He assumed a Gaussian distribution for K, centered about K = 0, and then integrated over this quantum number to retain in his final results a dependence of the level density on J only.

As mentioned earlier[3], we make the assumption that when s-wave neutrons interact with deformed nuclei, K is a good quantum number in the resulting compound nucleus. Thus the levels observed in slow neutron spectroscopy will be associated with a definite (J,K) value. The sequence of levels with (J,K) quantum numbers will be built on low lying vibrational states which have the same quantum numbers. Thus the excitation energy for each (J,K) sequence will differ depending on the position of the vibrational band. In an even-even target nucleus the addition of an s-wave neutron will populate levels in the even-odd compound nucleus with (1/2,1/2) quantum numbers. In an even-even compound nucleus there will be the possibility of more than two sequences of levels, corresponding to different (J,K) quantum numbers.

In this spirit we have used the Ericson level density formula, and instead of assuming a distribution of K, we calculated partial level densities corresponding to definite J and K values. The formula used could be written as

$$\rho(J,K,U) = \frac{\pi^{1/2}\, g_n^{n-1/2}\, g_z^{z-1/2}}{4n!z!} \left[\frac{\pi\, U_1}{F(U_1)+\frac{n+z-1}{2}}\right]^{n+z-2} \frac{\exp\,(2F(U_1))}{(F(U_1))^{1/2}}$$

with

$$F(U_1) = \left[\frac{\pi^2}{12}(g_n + g_z)U_1 + \left(\frac{n+z-1}{2}\right)^2\right]^{1/2}$$

In this relation g_n and g_z are the single neutron and proton spacings, n and z are the numbers of unpaired neutrons and protons respectively. The effective excitation energy is

$$U_1 = U - \frac{1}{\pi^2}\left[\frac{n(n-1)}{g_n} + \frac{z(z-1)}{g_z}\right]$$

where $U = S_n - E_k - \mu\Delta$ with S_n the neutron separation energy, Δ the pairing energy, μ is the number of broken pairs and

$$E_k = U(K) + \frac{h^2}{2\mathcal{I}}\,(J(J+1)-K^2)$$

where U(K) is the energy of the lowest level of the vibrational band in question; the second term is the energy of the rotational levels built on this vibrational state. The strong K dependence is in the value of U(K), it has a 2K + 1 degeneracy.

In this calculation we assume that the single particle level densities vary smoothly with the nuclear mass, and that the pairing energy varies smoothly with the inverse of $A^{1/2}$. These relations have been noted and used in earlier works[4-5]. The exact form we used was $g_n = g_z = 60.5/A$ and $\Delta = 15.65/A^{1/2}$. These values were obtained from the overall best fit to the data and also from comparisons with other constants in the literature. It should be noted here, that in other evaluations[2] both the single particle density and the pairing energy show appreciable local

variations connected with the shell structure. In our approach this variation is removed and is reflected in the actual locations of the vibrational bands. We feel that this view may offer a deeper understanding into the nuclear structure.

Using the known experimental neutron separation energies[6] we can calculate the level densities if we know the locations of the low lying vibrational bands, or, inversely, we can calculate the location of these bands from the experimentally determined level densities. For many even-odd compound nuclei we determined the experimental s-wave neutron level spacings from the known position of the (1/2,1/2) bands[7,8]. These results are given in Table I. It can be seen that in cases where both the location of the band and the level densities are well known, our calculations give the correct values. It has to be pointed out, that we assumed that it was mostly the (400) Nilsson band which contributed to the level spacing. This would be so, because this is the band which has the closest structural resemblance to the state, resulting from the capture of an s-wave neutron by an even-even target nucleus.

Table I. Experimental and Calculated Level Densities for Even-Even Target Nuclei for which the Position of the Vibration Band is Known.

Compound nucleus	Sn (MeV)	U(K) exp.	D exp. (eV)	D calc. (eV)	Nilsson
^{153}Sm	5.867	0.415	51.8 ± 4.3	56.5	400
^{155}Gd	6.446	0.368	14.5 ± 1.5	22.1	400
^{159}Gd	6.000	0.973	81	78.2	400
^{165}Er	5.808	0.745	20 ± 3	17.2	400
^{167}Er	6.436	1.135	37.6	37.0	400
^{239}U	4.800	0.698	20.8	19.3	620

It is clear that any agreement between the experimental and the theoretical level spacings is much more meaningful, if one knows that the experimentally determined values correspond to a pure s-wave sequence. In other words, one should be sure that there are no small s-wave levels missed and that all p-wave levels have been eliminated. In order to assure a pure s-wave sequence, we used published level spacings which were tested by the Dyson-Mehta statistics[9].

In Table II, we present calculated positions of vibrational bands which were obtained for even-odd compound nuclei by adjusting the theoretical level densities to the experimentally determined values. It can be seen, that the position of the (400) band, which we suspect of being the base for the levels in the rare earths is shifted to higher energies as we increase A. This is what would be expected from the systematics of other bands. For the actinide nuclei the basic band configuration should be a (620) and we determined the position of these bands also. These again correspond to the trend in the Nilsson diagrams.

In cases of even-even compound nuclei the calculations and comparisons are more involved, as many separate bands of the two possible spins can be formed. Some of these sequences may not be so probable as others, as will be discussed later. One interesting fact can already be noted in the case of the simplest even-even compound nucleus, that with spin 0^+ or 1^+. The level density calculations show, that to reproduce the experimental values in cases of $J = 0^+$ compound state we have to base our levels on a vibrational band and not on the ground state rotational band. A good example to this is Pu-240, for which the results are presented in Table III. The calculated $J = 0^+$ level spacing is based on the β-vibrational band located at 861 keV above the ground state. A sequence based on the ground state would give a much smaller level spacing than observed. A second, K = 0, J = 0, two phonon vibrational state exists at 1.41 MeV above ground state which results in a larger level spacing and possibly also larger average reduced neutron width. The $J = 1^+$ levels are based on a band located about 1.4 - 1.5 MeV above ground state and thus would expect a level spacing of 2.7 eV. These values are compared with the experimental spacing[6].

As can be seen from Table III, the levels based on the β-vibrational band have a spacing of 2.54 eV, the levels based on the two-phonon vibrational band have a spacing of 6.94 eV. It is interesting to note that many of the wide and most of them identified as $J = 0^+$ levels are very close together, (1.5 - 2.0 eV apart). The probability for the spacing to be so small with an average D of 8.2 eV is quite small, only a few percent. The possibility suggests itself that the basic $J = 0^+$ level spacing of 2.54 eV is modulated by the wider, 6.94 eV spacings.

In Table IV, we present results of our calculations for the even-even compound nucleus of U-236. The partial level spacings for each possible channel are given. In another paper[3] we assumed that the probability of the formation of compound states with K very different from the highest possible value

Table II. Calculated Vibrational Bands for Selected Nuclei by Adjusting Calculated and Experimental Level Densities.

Compound nuclei	Sn (MeV)	D exp (eV)	D calc (eV)	U(K) calc. (MeV)
Er^{169}	6.003	94 ± 10	92.7	1.38
Yb^{173}	6.367	70 ± 3	69.0	1.65
W^{183}	6.191	66 ± 5	65.0	1.68
W^{185}	5.750	82 ± 3	80.4	1.42
Th^{233}	4.787	17.7 ± 1.0	19.7	0.60
U^{235}	5.298	12.3 ± 1.5	12.4	0.90
U^{237}	5.124	15.4 ± 1.0	16.1	0.90
Pu^{241}	5.240	13.6 ± 0.4	13.7	1.00

Table III. Calculated and Experimental Level Spacing for ^{240}Pu Compound Nucleus.

J	<D> exp (eV)	K	J	<D> calc. (eV)	Remarks	U(K)* (MeV)
0^+	8.2	0	0^+	0.58	ground state rotation a½ band	0
		0	0^+	2.54	β-vibrational band	0.861
1^+	2.8	0	0^+	6.94	2-phonon vibrational band	1.410
		1	1^+	2.70		1.50

* Energies from ref. 13.

(corresponding to maximum possible alignment of the angular momentum along the symmetry axis) is small. This fact would explain the spacing. As it is reported in another paper[3] the only observed resonances in U-236 correspond to the (4,4), (4,3), and (3,3) channels.

From these results we predict 0.3 eV for the level spacing for U-235. Our experimental results presented in another paper seem to indicate the same value. Some time ago Garrison[11] predicted a real level spacing U-235 of 0.38 eV. Recently from a statistical analysis of the U-235 cross section he deduced a value of 0.37 eV, a value not too different from the one we find.

It has been observed previously and also confirmed by us that in some nuclei the correlation coefficient of successive reduced neutron widths is significantly different from zero. The value is negative for Er-168[11] and for the $J = 2^+$ levels of Au-197[12]; we calculated it to be positive for U-238 and Th-232. A possible interpretation of this effect is the addition of a second sequence of s-wave levels, based on a Nilsson band of different configuration at a higher excitation energy. Indeed, in the U-239 compound nucleus, the (600) band is calculated to be about 2 MeV above ground state for the stable deformation of $\delta = 0.3$. We calculated the level spacing, which would result from this assumption and obtained an average of approximately 200 eV. But this is the average spacing of the enhancements in U-238. Further discussion of this result is presented in another paper.[15]

Table IV. Calculated Level Spacing for ^{236}U for Different Channels.

K	J	U(K)* MeV	<D> eV
0	3^-	0.70	2.56
1	3^-	1.00	1.44
	4^-		1.62
2	3^-	0.85	0.63
	4^-		0.71
3	3^-	1.15	0.73
	4^-		0.81
4	4^-	2.00	2.79

*Energies from ref. 14.

These level density calculations, if they have some relation to reality, would present a good method of determining the position of the different bands, in case the complete sequence of definite (J,K) levels is known. This possibility gives an added incentive to measure both J and K for the s-wave neutron resonances in even-even and odd-odd compound nuclei.

References

1 J.E. Lynn, The Theory of Neutron Resonance Reactions, Clarendon Press, Oxford 1968, and references therein.

2 J.R. Huizenga and L.G. Movetto, Annual Rev. Nucl. Sci., 22, 427 (1972).

3 J.P. Felvinci, E. Melkonian, and W.W. Havens, Jr., Paper GB11 in Conference on Nuclear Cross Sections and Technology, Washington, 1975.

4 T. Ericson, Nucl. Phys., 6, 62 (1958).

5 A. Bohr and B.R. Mottelson, Nuclear Structure, Vol. I, p. 170. W.A. Benjamin, New York, 1969.

6 Neutron Cross Sections, Vol. I, Resonance Parameters, BNL-325, Third Edition.

7 M.E. Bunker and C.W. Reich, Rev. Mod. Phys., 43, 348 (1971).

8 L.M. Bollinger and G.E. Thomas, Phys. Rev. C6, 1322 (1972).

9 H.I. Liou et al., Phys. Rev., C5, 974 (1972).

10 J.D. Garrison, Private Communication, 1975.

11 J.D. Garrison, Phys. Rev. Lett., 29, 1185 (1972).

12 R.N. Alves, Nucl. Phys., AB1, 450 (1969) and CEA-R-3602, 1969.

13 M.R. Schmorak et al., Phys. Rev. Lett., 24, 1507 (1970).

14 F.K. McGowan et al., Phys. Rev., C10, 1146 (1974).

15 J.P. Felvinci and E. Melkonian, Paper HB5, Nuclear Cross Sections and Technology Conference, Washington, D.C. 1975.

ODD-EVEN FLUCTUATIONS IN NEUTRON STRENGTH FUNCTIONS

G. J. Kirouac
Knolls Atomic Power Laboratory*
Schenectady, N. Y. 12301

Systematic fluctions are reported for the s-wave neutron strength functions of adjacent mass target nuclei with odd and even neutron number. Within the 3S and 4S single-particle resonances, the fluctuations appear to be related to odd-even variations in the doorway state density which are correlated with the excitation energy. A simple model calculation successfully reproduces the strength function fluctuations in the first peak of the split 4S resonance ($143 \lesssim A \lesssim 160$). An examination of all available even-Z strength function data suggests a general trend; S-odd > S-even near single-particle resonances and S-even > S-odd between resonances. This result is discussed in terms of the optical model spreading width W and other fundamental nuclear properties.

(Neutron strength function; doorway states, optical model)

Introduction

In an earlier investigation of s-wave neutron strength functions of rare earth isotopes, $142 \lesssim A \lesssim 160$, it was observed that strength functions of even Z-odd N target nuclei are consistently larger than their even-even neighbors.[1] A preliminary report of an extended study of strength function fluctuations[2] has shown that odd-even fluctuations are essentially global in nature $40 < A < 240$ and appear to be related to the optical model spreading width W. In this paper the evidence for odd-even fluctuations is presented in detail and an attempt is made to relate them to fundamental nuclear properties. In the following Section II, the relationship between the strength functions and doorway states originally proposed by Block and Feshbach[3] is reviewed. In Section III, some simple model calculations are shown for the 4S resonance. Section IV, extends this examination of odd-even fluctuations into the mass region between the single particle resonances. Finally in Section V, these results are discussed and some tentative conclusions are offered.

Strength Functions and Doorway States

Block and Feshbach[3] have shown the relationship between two particle-one hole (2p-1h) doorway states and fluctuations in the smooth trend in the strength function vs. A predicted by the optical model. They computed the strength function from a "sum rule" relationship[5] between the energy averaged width and spacing of the compound states, $\overline{\Gamma}$ and D, and the corresponding average escape width $\overline{\Gamma^{\uparrow}}$ and spacing D_d of the (2p-1h) states

$$S_o = \frac{\overline{\Gamma}}{D} \simeq \frac{\overline{\Gamma^{\uparrow}}}{D_d} = \vartheta\, \overline{\Gamma^{\uparrow}} \qquad (1)$$

The average escape width is determined from the coupling matrix elements between the entrance channel wave function ψ_o^* and the 2p-1h states,

$$\overline{\Gamma^{\uparrow}} \simeq 2\pi \overline{|\langle \text{2p-1h} | V_r | \psi_o^{+} \rangle|^2}. \qquad (2)$$

However, it was assumed that the average escape width can be approximated by the product of the optical model strength function S-opt. and a residual matrix element $\bar{a}$. The final model equation takes the form,

$$S \simeq (a_o \vartheta_o + a_1 \vartheta_1 + a_2 \vartheta_2) \cdot \text{S-opt.} \qquad (3)$$

The a_L are 2π times the average square matrix elements of the L=0,1,2 terms of a multi-pole expansion of the residual interaction. The ϑ_L are the computed density of 2p-1h states classified according to multi-pole type. Block and Feshbach treat the three a_L values as parameters and use eqn. 3. to describe the strength functions of 26 even-even isotopes between A=40-130. These calculations indicate the number of available doorway states is most decisive for the strength function fluctuations.

Müller and Rohr[4] have also studied the strength functions of 20 odd and even mass nuclei in the 3S region. They used the same representation as Block and Feshbach, but for the residual matrix element $\bar{a}$, they proposed the semi-empirical ansatz,

$$\bar{a} = \frac{a^*}{A^3} \left[\sum_J (2J+1) \exp J(J+1)/2\sigma^2 \right]^{-1}. \qquad (4)$$

The target nucleus mass is A, σ is a spin cut-off parameter, J is the total angular momentum of the compound system and a^* is a free parameter used to fit the experimental data. The doorway state level density, ϑ, was obtained by counting the 3 quasi-particle states (3QP) in an energy window near the neutron binding energy. This calculation includes pairing correlations as well as shell structure. The agreement obtained provides justification for the empirical ansatz. The most important conclusions of this work was that the strength function fluctuations in the 3S resonance are primarily caused by the dependence of the doorway state density on the excitation energy of the A+1 system.

Calculations for the 4S Resonance

The evidence for odd-even fluctuations in the 4S resonance is shown in Fig. 1 for seven even Z-odd N targets and ten even-even targets in the range $142 \lesssim A \lesssim 158$. Although the uncertainties are in some cases large, all even-even isotopes except ^{144}Nd have strength function values[6] considerably lower than their even-odd neighbors. The difference approaches a factor of two for the first peak of the split 4S resonance.

Our calculation of s-wave strength functions in the 4S resonance uses a representation similar to that of Müller & Rohr. We assume $S_o = \vartheta\, \bar{a}$ S-opt. and compute $\bar{a}$ as in eqn. 4. with $\sigma = 5$. However, instead of using pairing theory to construct the 3QP states and the density ϑ, it is assumed that the doorway state density can be obtained from a statistical representation. Thus the simple Fermi-gas distribution is applied to the doorway state density,

*Operated for the U. S. Atomic Energy Commission by the General Electric Company, Contract No. W-31-109-Eng.-52.

$$\rho \simeq \exp 2\sqrt{\beta E_x}\,/12\,\sigma\sqrt{2}\;\beta^{1/4}\,E_x^{5/4} \quad . \qquad (5)$$

The important effect which we attempt to account for here is the strong dependence of the doorway state density on the excitation energy, E_x, the binding energy of the neutron in the A+1 system[6]. For S-opt. the calculations of Mughabghab[7] were used. The parameters β in eqn. 5 and a^* in eqn. 4 are obtained from the ratio and absolute magnitude of the strength functions for ^{151}Sm and ^{152}Sm. These two isotopes have relatively small strength function uncertainties. The value 7.16 MeV^{-1} is determined for β and the model equation $\rho = \bar{a}$ S-opt. is used to compute the strength function for all even-even and even-odd target isotopes in the first peak of the 4S resonance. This result is compared with experiment in Fig. 2. Considering the extreme simplicity of this model, the reproduction of the odd-even fluctuations is very encouraging.

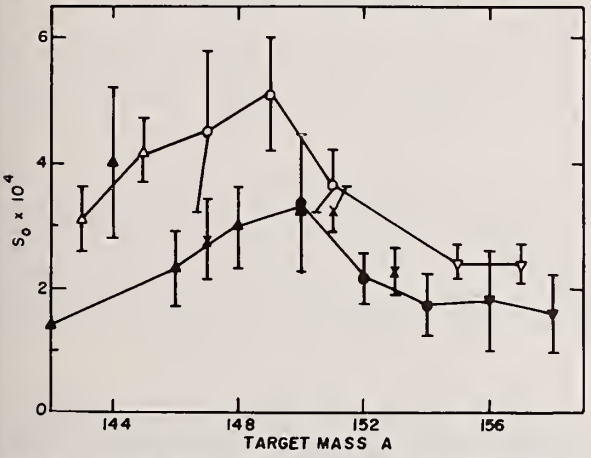

Fig. 1 s-wave neutron strength functions of even Z-odd N nuclei (open symbols) and even Z-even N nuclei (closed symbols) in the first peak of the 4S resonance. Three odd-Z isotopes (x) are also shown.

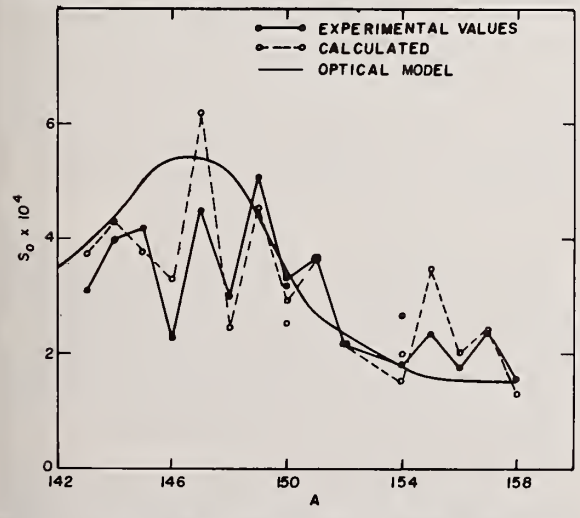

Fig. 2. Calculated fluctuations in s-wave neutron strength functions 143 A 158.

In order to further examine the validity of a statistical representation of doorway state density, the 3QP density computed by Müller and Rohr for the 20 isotopes in the 3S peak has been plotted vs. the excitation energy of the A+1 system in Fig. 3. The solid curve results from a least squares fit of eqn. 5 to the density computed for the even-even and even-odd targets. This fit yields a value for β of 7.0 $\pm$1.5 MeV^{-1} for the 3S resonance in agreement with our calculation of 7.2 MeV^{-1} for the 4S resonance. This apparent constancy of the doorway state density parameter β for the 3S and 4S resonances is noteworthy and can be contrasted with the usual level density parameter for compound nuclear states. The parameter which describes compound state density varies approximately linearly with A and changes by about a factor of 3 to 4 between the 3S and 4S neutron states.

An interesting observation seen in Fig. 3 is the fact that the 3QP density for odd Z-even N targets is about a factor of three higher than for the even Z-odd N targets in the 3S resonance.

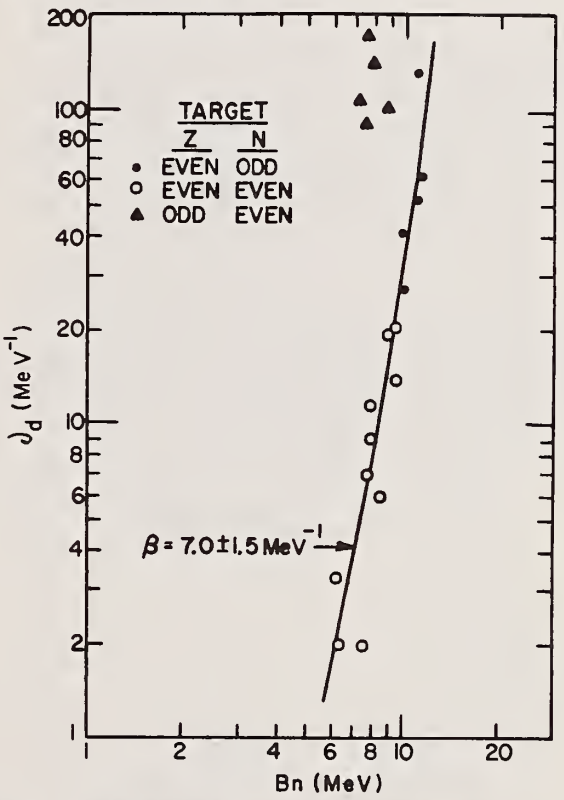

Fig. 3 Least squares fit of the computed doorway state density vs. neutron binding energy, eqn. 5.

Global Odd-Even Fluctuations

The fluctuations in neutron strength functions noted by Müller and Rohr in the 3S resonance also appear in the first peak of the 4S resonance. In order to extend this investigation into other mass regions, it is helpful to relate these fluctuations to the optical model. This can be done using the intermediate coupling picture of Lane, Thomas and Wigner[8] which relates the energy averaged compound nucleus fine structure to single-particle structure. The strength function now assumes a Lorentzian form vs. mass or energy.

$$S_o = \frac{2\,k_1 a}{\pi} \sum_p \frac{\gamma_p^2\, W}{(E_p - E)^2 + W^2} \qquad (6)$$

E_p is the eigenvalue of the pth, $\ell=0$ single-particle state and γ_p^2 is the natural width of this state. W is the spreading width of the single-particle state; essentially the imaginary part of the optical model potential. The neutron wavenumber at 1 eV is k_1 and a is the channel radius.

The range of the conventional optical potential varies smoothly and slowly, $R \sim r_o A^{1/3}$, and the single-particle eigenvalues and eigenfunctions do not change significantly between an even-even target and its even-odd neighbor. Thus rapid fluctuations in the neutron strength function can not be calculated in the usual optical model. Rather, as Block and Feshbach have shown, the fluctuations are caused by the facility of the entrance channel to couple to the doorway state configurations. Since the spreading width W represents this coupling in the optical model, rapid fluctuations in W should be expected.

In the context of this discussion, the general observation that S-odd > S-even in both the 3S and 4S resonances where $E_p \sim E$ and $S \sim 1/W$ (eqn. 6) suggests that the spreading width W for even-even targets is generally larger than for even-odd targets. Furthermore, since the strength function is proportional to W away from the single-particle resonances, ref. eqn. (6), this result implies a reversal of the odd-even fluctuations in the region between single-particle resonances. That is, in mass regions between the single-particle resonances, one might expect to find S-even > S-odd.

Data for the s-wave strength function of 25 even-Z isotopes in the $90 \leq A \leq 100$ and $110 \leq A \leq 120$ regions are shown in Fig. 4. The even-target strength functions are represented by closed symbols, the odd-targets by open symbols. Although some of the error bars are large, these results do indeed suggest odd-even fluctuation with S-even $\geq$ S-odd, just the reverse of the behaviour near single-particle resonances.

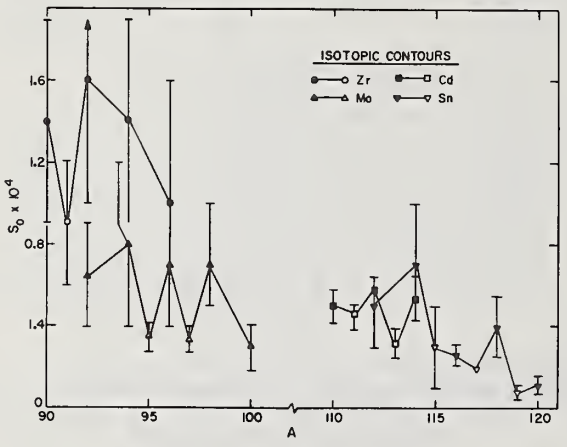

Fig. 4. Fluctuations in the strength function for $90 \leq A \leq 100$ and $110 \leq A \leq 120$.

An extension of the above examination to all available s-wave neutron strength function data for odd-even fluctuation has also been performed. Even-even and even-odd strength functions have been averaged separately for $40 \leq A \leq 230$. The average values were computed for 5 or 10 successive mass numbers (5 mass numbers in the resonance peaks to provide resolution). This averaging is expected to remove fluctuations which are not of an odd-even nature. This result is shown in Fig. 5. It appears that the averaged even Z-odd N strength functions are larger throughout the 3S and 4S peaks. The even-even strength functions seem to cross-over and dominate the even-odd strength functions away from the single-particle resonances. The small region $100 \leq A \leq 110$ does not follow the same trend. The shape resonances for the even-even targets appear to be lower and broader than those for the even-odd targets. This is consistent with greater dispersion of the single-particle strength of even-even isotopes due to an increased spreading width W. It should be emphasized that in this averaging calculation, significant fluctuations were also observed for individual neighboring even-isotopes and neighboring odd isotopes. However, a definite tendency for S-odd > S-even near single particle resonance and S-odd $\leq$ S-even between the resonances remains.

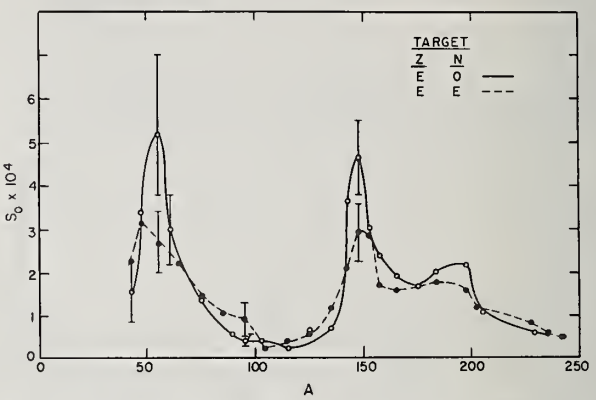

Fig. 5. Average values of even Z-odd N and even Z-even N strength functions for $40 \leq A \leq 240$.

Discussion and Conclusions

In this section, the evidence for odd-even fluctuations in neutron strength functions is summarized. An attempt is made to relate the fluctuations to fundamental nuclear properties.

Within the 3S and 4S resonances the existence of odd-even fluctuations seem conclusive. The evidence for fluctuations between single-particle resonances is highly suggestive but less convincing. Taken together, these two observations indicate a general tendency for W(even-N) > W(odd-N). From the ratio of strength functions of odd and even neutron targets in the 3S and 4S resonance, it may be estimated that W-even $\simeq$ 3/2 W-odd. Investigations by Tersawa[9] of the effect of pairing correlations on the imaginary part of the optical potential indicate that the pairing effects could increase W by as much as a factor of two.

In the neighborhood of the 3S and 4S resonances the simple model equation $S \simeq \nu \bar{a}$ S-opt. appears to work very well. Unfortunately, we know of no theoretical justification for the particular ansatz used for $\bar{a}$. Additionally, within the 3S and 4S resonances, the density of available 3QP first collision states seems decisive in determining the strength function. Also, the doorway state density is remarkably well correlated with the excitation energy of the A+1 system.

If we tentatively conclude that the doorway state density will be higher at the higher excitation energy for odd-target isotopes at all mass numbers, the doorway state model $S \simeq \nu \Gamma^{\uparrow}$ indicates that significant fluctuations must also be present in $\Gamma^{\uparrow}$ in the coupling matrix elements $|\langle 3QP|V_r|\psi_o^+\rangle|$. This is required in order to account for the S-even $\geq$ S-odd behaviour away from the single-particle resonances. Similarly, the simple model equation $S \simeq \nu \bar{a}$ S-opt. fails in these

regions if $\bar{a}$ has the form given in eqn. 4.

Alternative approaches to that of Block and Feshbach to strength function fluctuations have also been proposed. From perturbation theory, the optical model spreading width has the microscopic definition[10,11]

$$W = 2\pi \overline{|\langle q|V|\gamma_o^+\rangle|^2} \rho_q \qquad (7)$$

where $|q\rangle$ are the complicated final states and ρ_q the density of these states. If the states $|q\rangle$ can be associated with 3QP states and ρ_q replaced with ν_{3QP} then the above relationship provides another link between doorway states and the strength function and optical model.

Newstead[12] has recently demonstrated that the values of W empirically found to describe the strength function of seven isotopes near the 3S peak appear to be correlated with the 3QP density computed by Müller and Rohr.[4] The W values were observed to increase with increasing 3QP density. We find this relationship difficult to understand in the 3S peak since Müller and Rohr associate large values of S_o with high 3QP density and in general S_o is expected to decrease with increasing W near a resonance maximum.[13]

Near closed shell nuclei, the density of final states ρ_q is expected to be small and therefore reduced values of W are indicated by eqn. 7. In agreement with this relationship, Newstead[14] has shown that unusually low values of W are required in order to describe the s-wave strength functions in the minima near A=35 and 208 and the p-wave minima near A=55, 140 and 208.

It is unlikely that any of the simplified, non-microscopic models proposed to date can provide a reliable method for predicting fluctuations in S in all mass regions. However, the importance of doorway state structure to strength functions is becoming increasingly clear. The density of available doorway states seems to be most important, but we believe that the coupling matrix elements between the doorway states and the entrance channel deserve increased attention. If such calculations are performed, they will hopefully not be limited to even-even target nuclei. Also there is some evidence that the effect of pairing correlations on the ground and excited state wave functions may be important for strength function calculations.

Acknowledgements

In the course of this work continued encouragement has been received from N. C. Francis, C. R. Lubitz, J. T. Reynolds and C. J. Slavik and we gratefully acknowledge many helpful discussions.

References

1. G. J. Kirouac, H. M. Eiland, scheduled for Phys. Rev. C., March 1975.
2. G. J. Kirouac, Bull. Am. Phys. Soc. 19, No. 9, 1018, Oct. 1974.
3. B. Block, H. Feshbach, Ann. Phys. 23, 47 (1963).
4. K. N. Müller, G. Rohr, Nucl. Phys. A164, 97 (1971).
5. H. Feshbach, A. K. Kerman, R. H. Lemmer, Ann. Phys. 41, 230 (1967).
6. All strength function values quoted here are taken from our own work or from BNL-325, 3rd Ed., Vol. I, by S. F. Mughabghab and D. I. Garber.
7. S. F. Mughabghab, Proc. Conf. Neutron Cross Sections and Technology, Vol. 2, 386(1971) Knoxville, Tenn.
8. A. M. Lane, R. G. Thomas, E. P. Wigner, Phys. Rev. 98, 693 (1955).
9. T. Terasawa, Nucl. Phys. 39, 563 (1962).
10. G. E. Brown, C. T. DeDominicis, J. S. Langer, Ann. Phys. 6, 209 (1959).
11. C. Bloch, Nucl. Phys. 4, 503 (1957).
12. C. M. Newstead, Proc. Europhysics Study Conf., Plitvice Lakes, Yugoslavia Sept. 1972 and private communications 1974.
13. P. A. Moldauer, Nucl. Phys 47, 65 (1963).
14. C. M. Newstead, J. P. Delaroche, Proc. Int. Conf. on Nuclear Structure Study with Neutrons, Budapest, paper B7, 1972.

STATISTICAL ESTIMATION OF PHYSICAL QUANTITIES IN THERMAL- AND FAST-NEUTRON-INDUCED FISSION

Toru Yamamoto and Kazusuke Sugiyama
Department of Nuclear Engineeing
Tohoku University
Sendai, Japan

Making use of a model based on the statistical theory in which the scission-point distance is treated as an adjustable parameter, calculations were performed to obtain the mass yields of fission products, the kinetic energies of fission fragments and the numbers of prompt neutrons from neutron-induced fission of ^{232}Th, ^{231}Pa, ^{233}U, ^{235}U, ^{238}U, ^{237}Np, ^{239}Pu and ^{241}Pu for incident-neutron energies ranging from thermal to 14.7 MeV. Calculated results reproduced experimental values well. The proposed method could be used in the estimation of unknown physical quantities in fission.

(Fission; statistical theory; scission point; fission fragment; fission product; kinetic energy; prompt neutron; mass yield; fast-neutron-induced fission; actinide nuclide)

Introduction

For the design and operation of reactors, it is required to have accurate knowledge of various physical quantities in the neutron-induced fission of many actinide nuclides. For instance, the mass and the charge yields of fission products are particularly important quantities in many fields such as the physics design of the reactor core, the determination of the nuclear fuel burnup, safe guard techniques and others.[1] The kinetic energies of fission fragments and the number of prompt neutrons are also important. It is desired for the further development of nuclear reactors to obtain the accurate experimental data of such important physical quantities in neutron-induced fission of many actinide nuclides for wide incident-neutron energy from thermal to 14 MeV.

Despite this fact, experimental studies published so far have concentrated on the thermal-neutron-induced fission of fissile materials, and available experimental data on fast-neutron-induced fission is still lacking. These circumstances impart particular importance of the theoretical estimation of the unknown physical quantities relevant to fast-neutron-induced fission for the role they must play in the planning and the design of experimental studies and for the estimation of these quantities in practical applications.

In the IAEA Panel in Bologna, the studies by Sidebotham[2] and Crouch[3] for the methods of prediction of the mass yields of fission products and the studies by Musgrove et al.[3] and Crouch[4] for the charge yields of fission products are introduced. We discussed in previous report[5] the method to predict unknown physical quantities in nuclear fission making use of a model based on the statistical theory, and showed the calculated results for the mass yields of fission products and the average numbers of prompt neutrons from neutron-induced fission of ^{235}U for incident-neutron energies ranging from thermal to 14.7 MeV.

Present work is an attempt to calculate the mass yields of fission products, the kinetic energies of fission fragments and the numbers of prompt neutrons from neutron-induced fission of ^{232}Th, ^{231}Pa, ^{233}U, ^{235}U, ^{238}U, ^{237}Np, ^{239}Pu and ^{241}Pu for incident-neutron energies ranging from thermal to 14.7 MeV.

Method of Calculations

Statistical Description of Fission

The statistical description of fission has been presented in detail in the previous report.[5] We assume that the fissioning system at the moment of scission is described two coaxial droplets with quadrupole deformations and that the tips of the droplets are separated by a distance "d" as shown in Fig. 1, which we call a "scission-point distance". This scission-point distance will be treated varying with the mass number of the heavy fragments of fission as explained later. Further, it is assumed that once the scission point is passed, the only interaction remaining between two fragments is the Coulomb repulsion. This assumption implies that the mass and the charge distribution in the fission fragments are determined at the scission point. After the scission point, the fragments are accelerated in opposite directions by the large Coulomb repulsion. Hence, the total kinetic energy possessed by the fragments upon being fully accelerated can be obtained as the sum of the Coulomb repulsive energy and the translational energy at the scission point. The sum of the deformation energy and the internal excitation energy of each fragment at the scission point can be considered to be the total internal excitation energy before the emission of the first neutron.

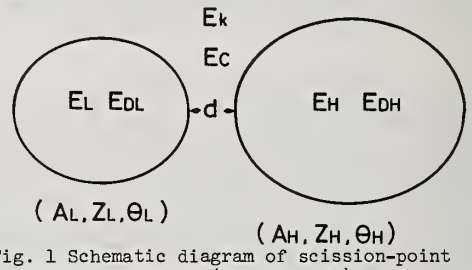

Fig. 1 Schematic diagram of scission-point configuration(From ref. 5)

Let the mass number, the proton number, the deformation parameter, the deformation energy and the internal excitation energy of each fragment at the scission point be denoted by A_i, Z_i, θ_i, E_{Di} and E_i respectively where i is written by L for a light and by H for a heavy fragment. Further, E_C and E_k are the Coulomb repulsive energy and the translational energy of the two fragments. Finally, let A_0, Z_0 and E_0 be the mass number, the proton number and the internal excitation energy of the fissioning nucleus produced by absorption of a neutron.

Using "the principle of detail balance", we are able to calculate the transition probability from the fissioning nucleus to the system of the two fragments at the scission point. It is written in the simple form:

$$T_f \equiv T_f(A_H, Z_H, \theta_H, \theta_L, E_H, E_k) = C\, \rho_L(E_L)\, \rho_H(E_H), \quad (1)$$

where C is a constant, and $\rho_L(E_L)$, $\rho_H(E_H)$ the densities of the light- and the heavy-fragment nucleus. From the conservation of energy,

$$E_T = E_P + E_L + E_H + E_k, \quad (2)$$

where E_T and E_P are the total energy release and the

potential energy:

$$E_T = M_o(A_o,Z_o)c^2 + E_o - M_L(A_L,Z_L)c^2 - M_H(A_H,Z_H)c^2, \quad (3)$$

$$E_P = E_{PL}(A_L,Z_L,\Theta_L) + E_{PH}(A_H,Z_H,\Theta_H) + E_C(A_L,Z_L,\Theta_L;\ A_H,Z_H,\Theta_H). \quad (4)$$

The fission-fragment-mass yield $y(A_H)$ is obtained by integration of Eq. (1):

$$y(A_H) = \int_0^{A_H} dZ_H \int_0^{\infty} d\Theta_H \int_0^{\infty} d\Theta_L \int_0^{E_T-E_P} dE_H \int_0^{E_T-E_P-E_H} dE_K\ T_f. \quad (5)$$

Disregarding the small contribution of the translational energy, the average total kinetic energy $\overline{E_K}$ is given by the average Coulomb repulsive energy:

$$\overline{E_K} = \frac{\int_0^{A_o} dA_H\ \overline{E_K(A_H)}\ y(A_H)}{\int_0^{A_o} dA_H\ y(A_H)}, \quad (6)$$

where

$$\overline{E_K(A_H)} = \frac{\int_0^{A_H} dZ_H \int_0^{\infty} d\Theta_H \int_0^{\infty} d\Theta_L\ E_C \int_0^{E_T-E_P} dE_H \int_0^{E_T-E_P-E_H} dE_K\ T_f}{y(A_H)}, \quad (7)$$

On the prompt decay of the fission fragments with neutrons and gamma-rays, we adopt a simple model. We assume in this model that the internal excitation energy of the fragment is spent in neutron emittion until it becomes smaller than the sum of binding energy and the average kinetic energy of emitted neutron, thereafter it is spent in gamma-ray emittions. The average kinetic energy of the neutrons is calculated as the average value of the Maxwell distribution 2T, assuming the neutron evaporation model. Here, T is the nuclear temperature of the residual nucleus having the maximum internal excitation energy. Let ν_L and ν_H represent the numbers of neutrons emitted from the light and the heavy fragment calculated in this model. The average number of prompt neutrons per fission is expressed by

$$\overline{\nu} = \frac{\int_0^{A_o} dA_H\ (\overline{\nu_H(A_H)} + \overline{\nu_L(A_L)})\ y(A_H)}{\int_0^{A_o} dA_H\ y(A_H)},$$

where

$$\overline{\nu_H(A_H)} = \frac{\int_0^{A_H} dZ_H \int_0^{\infty} d\Theta_H \int_0^{\infty} d\Theta_L \int_0^{E_T-E_P} dE_H\ \nu_H \int_0^{E_T-E_P-E_H} dE_K\ T_f}{y(A_H)}, \quad (9)$$

$$\overline{\nu_L(A)} = \frac{\int_0^{A_H} dZ_H \int_0^{\infty} d\Theta_H \int_0^{\infty} d\Theta_L \int_0^{E_T-E_P} dE_H \int_0^{E_T-E_P-E_H} dE_K\ \nu_L\ T_f}{y(A)}. \quad (10)$$

The mass yield Y(A) of fission products with a given mass number A is obtained by correcting the mass yiels of fission fragments for the prompt-neutron emittion from them:

$$Y(A) = \sum_{\nu=0}^{\infty} y(A+\nu)\ P_\nu(A+\nu). \quad (11)$$

where $P_\nu(A+\nu)$ is the probability that ν prompt neutrons will be emitted by a fission fragment of a mass number $A+\nu$. A treatment similar to that used in obtaining ν_L, ν_H is adopted for calculating $P_\nu(A+\nu)$.

The masses, the deformation energies and the neutron-binding energies of fission fragments are calculated using the mass formula by Myers and Swiatecki.[6] The Coulomb repulsive energy between two fragments at the time of scission point is calculated by Geilikman's expression.[7] The level densities and the nuclear temperatures of the fission fragments are calculated from the semi-empirical formula proposed by Gilbert and Cameron.[8]

Treatment of the Scission-Point Distance

This model is very simple to describe the complicated scission point configulation. Therefor, we tried to take into account the many factors which were disregarded for simplicity in this model by treating the scission-point distance as an adjustable parameter. This value is varied slightly with the mass number of the heavy fragments so that the calculated values of the mass yields of fission fragments $y(A_H)$, the average total kinetic energies $\overline{E_K}$ and the average number of prompt neutrons per fission $\overline{\nu}$ approach to the experimental values. For ^{232}Th, the experimental data of $y(A_H)$ and $\overline{E_K}$ by Sergachev et al.[9] for 1.38 MeV-neutron fission are used for this purpose, for ^{231}Pa, ^{238}U and ^{237}Np, by Bennett et al.[10] for pile-neutron fission, for ^{233}U, by Pleasonton[11] for thermal-neutron fission, for ^{235}U, by Schmitt et al.[12] for thermal-neutron fission, and for ^{239}Pu and ^{241}Pu, by Neiler et al.[13] for thermal-neutron fission. The experimental data of $\overline{\nu}$ are taken from BNL-325(1965). The incident neutron energies used in calculations are 1.38 MeV for ^{232}Th, 2 MeV for the pile-neutron fission and 0 MeV for the thermal-neutron fission.

By treating the scission-point distance as an adjustable parameter, the experimental data of $y(A_H)$ can be reproduced by the calculated values within the experimental errors, $\overline{E_K}$ within the experimental errors except for ^{233}U and ^{235}U for which the calculated values are 1.7 % smaller than the experimental data, and $\overline{\nu}$ within 4 % deviation. The values of the scission-point distance are about 3 fm for all nuclides and the variation of it amounts to 1 fm as shown in the previous report.[5] These values of the scission-point distance are used in calculating the mass yields of fission products Y(A), $\overline{E_K}$ and $\overline{\nu}$ for the neutron-induced fission for the neutron energies ranging from thermal to 14.7 MeV.

Calculated Results and Discussion

Mass Yields of Fission Products

We show the calculated values of the mass yields of fission products for ^{232}Th, ^{231}Pa, ^{233}U, ^{238}U, ^{237}Np, ^{239}Pu and ^{241}Pu by curves in Figs. 2, 3, and compare them with those recommended by Crouch[14] shown

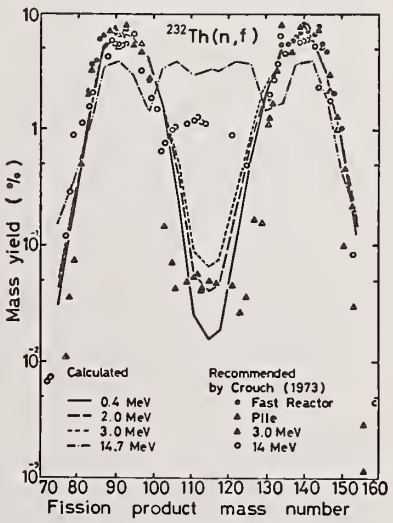

Fig. 2 Mass yields of fission products for ^{232}Th(n,f)

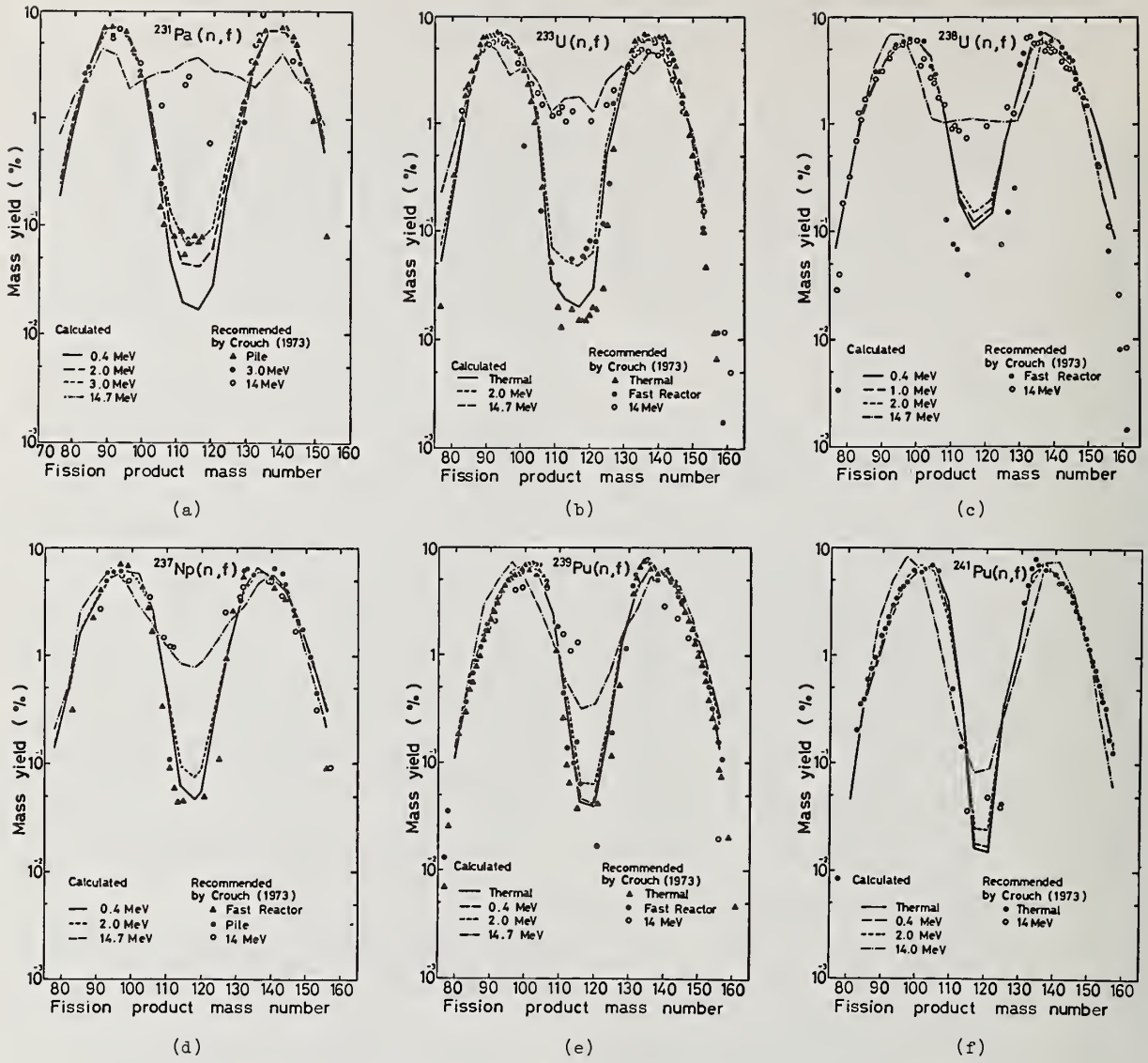

Fig. 3 Mass yields of fission products (a) for $^{231}Pa(n,f)$, (b) for $^{233}U(n,f)$, (c) for $^{238}U(n,f)$, (d) for $^{237}Np(n,f)$, (e) for $^{239}Pu(n,f)$, (f) for $^{241}Pu(n,f)$

by circles and triangles. The calculated values almost coincide with those recommended in the vicinity of the two asymmetry-fission peaks except for 14.7 MeV-neutron fission. Further, the calculated values in the vicinity of the valley of symmetry fission also nearly coincide with those recommended except for some nuclides. We noticed from the calculated results that the mass yields in the vicinity of the two asymmetry-fission peaks do not appreciably vary with the incident neutron energy which ranges from thermal to 3 MeV, and the rate of increasing of the yield in the valley of the symmetry fission with the incident-neutron energy decreases with the mass number of the fissioning nucleus.

Average Total Kinetic Energy

Fig. 4 presents the calculated values of $\overline{E_K}$ as a function of incident-neutron energy by closed circles. For ^{232}Th, the experimental data by Sergachev et al.[9] and for ^{235}U, by D'yachenko et al.[15] are shown by open triangles. The calculated results almost reproduce the variation of the average total kinetic energy with the incident-neutron energy. For the nuclides for which the experimental data cannot be found, we show the calculated values as an estimation.

Average Number of Prompt neutrons

Fig. 5 presents the values of $\overline{\nu}$ as a function of the incident-neutron energy by closed circles, and compares them with the experimental data taken from Howerton[16] shown by open triangles. The coincidence of the calculate values and the experimental values is almost good. For ^{237}Np and ^{231}Pa, the calculated values are shown as an estimation.

Conclusion

We have shown a method to estimate the unknown physical quantities in nuclear fission, and we believe that this method can be very useful for this purpose, even though the adopted model is a very simple one.

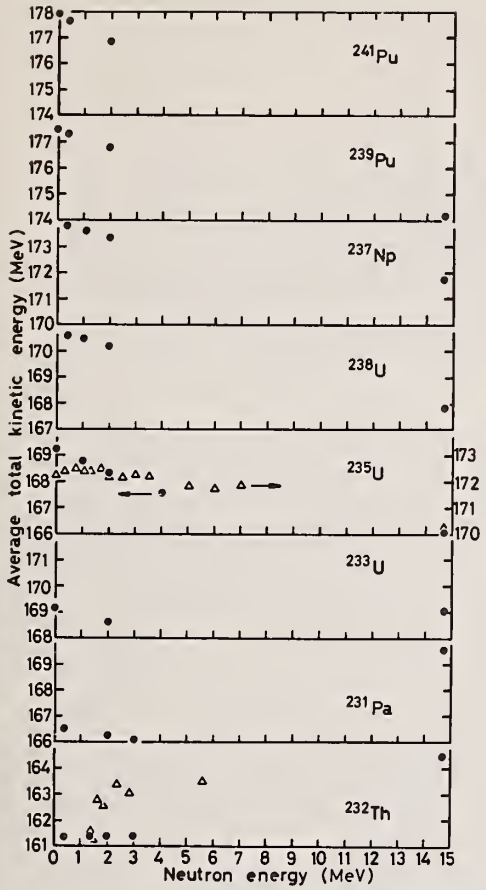

Fig. 4 Average total kinetic energy of fission fragments. Closed circles: Calculated values. Open triangles: Experimental data.[9,15]

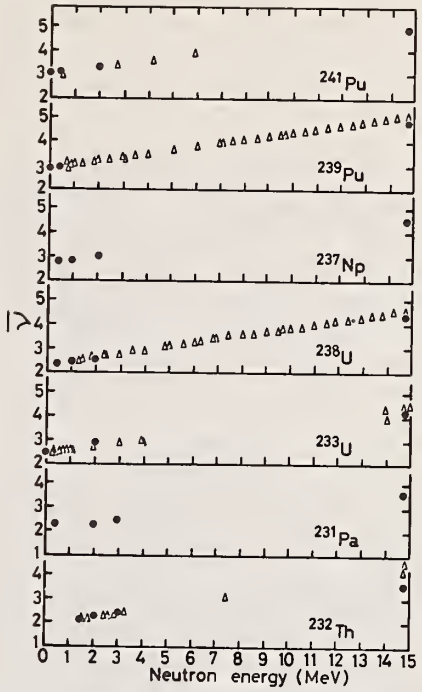

Fig. 5 Average number of prompt neutrons per fission. Closed circles: Calculated values. Open triangles: Experimental data.[16]

References

1 IAEA Panel on Fission Product Nuclear Data, Bologna, November 26-30, 1973.

2 Sidebotham, E.W., TRG Report 2143(R) (1972).

3 Masgrove, A.P.deL., Cook, J.L., Trimble, G.D., IAEA Panel on Fission Product Nuclear Data, Bologna,1973.

4 Crouch, E.A.C., AERE-R7680 (1974).

5 Yamamoto, T., Sugiyama, K., J. Nucl. Sci. Technol., 11(11), 461 (1974).

6 Myers,W.D., Swiatecki, W.J., Nucl. Phys., 81, 1 (1966), id. Ark. Fys., 36, 343 (1966).

7 Geilikman, B.T., Proc. 2nd Int. Conf. Peaceful Uses At. Energy, Geneva, 15, 273 (1958).

8 Gilbert, A., Cameron, A.G.W., Can. J. Phys., 43, 1446 (1965).

9 Sergachev, A.I., Vorob'eva, V.G., Kuz'minov, B.D., et al., Sov. J. Nucl. Phys., 7, 475 (1968).

10 Bennett, M.J., Stein, W.E., Phys. Rev., 156, 1277 (1967).

11 Pleasonton, F., ibid., 174, 1500 (1968).

12 Schmitt, H.W., Neiler, J.H., Walter, F.J., ibid., 141, 1146 (1966).

13 Neiler, J.N., Walter, F.J., Schmitt, H.W., ibid., 149, 894 (1967).

14 Crouch, E.A.C., AERE-R7209 (1973), id. AERE-R7394 (1973).

15 D'yachenko, P.P., Kuz'minov, B.D., Tarasko, M.Z., Sov. J. Nucl. Phys., 8, 165 (1969).

16 Howerton, R.J., Nucl. Sci. Eng., 46, 42 (1971).

THEORETICAL ESTIMATES OF (n,γ) CROSS SECTIONS FOR 6-15 MeV NEUTRONS

G. Longo and F. Saporetti

CNEN, Centro di Calcolo
Bologna, Italy

The knowledge of the correct values of (n,γ) cross sections for high energy neutrons is of great interest for studies into nuclear reaction mechanism as well as for reactor shielding purposes and in particular fusion-reactor design. The use of theoretical estimates is therefore required to fill the gaps in the available experimental data. For this purpose the semi-direct capture model has been refined a) by replacing the previous surface form factors of the interaction by volume form factors, b) by including quadrupole terms in addition to the dipole ones. Calculations, based on the refined model, agree satisfactorily with experimental data.

(Calculations; (n,γ) cross sections; semi-direct model; complex interaction; volume form)

Introduction

The various fusion reactor designs so far proposed have some common features, even if related to different thermonuclear plasma confinement systems. For example, in almost every case fast neutrons are emitted in some reaction occurring in the plasma. Therefore, a neutron blanket surrounding the plasma, where the neutrons are produced and captured, plays a prominent role in most reactor designs. In this framework the knowledge of the cross sections appears to be very important, as clearly revealed by the number of priority requests in WRENDA. In particular, the (n,γ) cross sections and the γ-ray spectra following the capture of fast neutrons up to 14 MeV by different nuclei, are of great interest for blanket design and shielding purposes.

In the past great efforts were devoted to measurements of fast neutron radiative capture cross sections and related γ-ray spectra. Until recently, the available data referred to many nuclei for neutron energies up to about 6 MeV and to about 40 nuclei for the isolated energy of 14 MeV. Only for four nuclei measurements were carried out up to about 20 MeV. In the last three years, the dependence of the radiative capture cross section on the incident neutron energy and the related γ-ray spectra, in a range covering a large part of the dipole giant resonance energy region, have been experimentally studied for three medium [1] and heavy [2] nuclei (^{89}Y, ^{140}Ce, ^{208}Pb) and for three [3] more light nuclei (^{28}Si, ^{32}S, ^{40}Ca).

As can be seen, the available experimental information is rather scarce over the energy range considered and there are very large gaps between 7 and 14 MeV. Moreover, it does not seem reasonable to assume that these gaps will be filled up in a short time, taking into account the experimental difficulties. The use of theoretical estimates is therefore required to fill the gaps in the observed data.

Theoretical Estimates

Until recently, the experimental data obtained by means of different techniques were contradictory and a comparison with the theoretical estimates was consequently very dubious. Essentially two techniques have been used to perform measurements of (n,γ) cross sections, the first based on the activation method and the second one on the integration of γ-ray spectra. The 14 MeV (n,γ) cross sections, deduced from integration of recorded γ-ray spectra, generally increase with the mass number up to about $A \approx 60$, then showing a very smooth mass dependence, with values around 1 mb. The activation cross section values differed markedly from the above results, specially for deformed nuclei, for which values higher by more than a factor of 10 were often obtained. At present, it seems established beyond any doubt [4] that a large number of the previous activation results were overestimated, because of neglected corrections for secondary neutrons produced in the sample, in target heads and in surrounding materials. Therefore it seems advisable to limit the comparison between theory and experiment to cross sections deduced from integration of γ-ray spectra or to those obtained by means of the improved activation technique, disregarding earlier activation measurements. The data for light nuclei are not considered here, because of complications arising from fragmentation of the giant dipole resonance into a fine structure. Also the data at the isolated energy of 14 MeV cannot be considered very significant for comparison sake and, therefore, the validity of the theory is here tested only on the three medium and heavy nuclei [1-2] for which (n,γ) cross sections have been measured in an energy range covering a large part of the giant dipole resonance.

The models usually used to analyse experimental data are the "compound nucleus", "direct" and "semi-direct" (or "collective") capture. As is well known, in the direct process [5] the incident neutron enters a shell-model orbit of the target nucleus and radiates a photon. In the semi-direct [6-7] process the capture is described by an interaction between the incoming neutron and the target nucleus, leading to an intermediate state, with the particle in a bound state and the nucleus excited to its giant dipole state. At low energies the compound-nucleus component is predominant. In the 4-8 MeV range, it can be expected that a superposition of all three mechanisms mentioned will be necessary to explain the observed data. As the incident neutron energy increases, however, the direct and semi-direct components become very likely predominant.

In consideration of the reasonable agreement between theory and experiment in the dipole giant resonance region, it was worthwhile to develop and refine the models in order to have a better reliability into the theoretical estimates. A first step was achieved [8] by introducing spin-orbit effects and interference between direct [5] and collective [7] capture. Even with these refinements, however, in many cases the agreement in magnitude between theory and experiment was reached by using questionable values for some of the input parameters. This indicated that some further improvement should be introduced into the substantially satisfactory semi-direct theory. In the last three years the main effort has been directed towards modifying the form of the coupling interaction between the nucleon and the nuclear E1 mode.

The different formulations [6-7] describing the fast nucleon radiative dipole capture process can be expressed in a common form, so that the direct-semidirect (n,γ) cross section for capture of an incident neutron into a final single particle bound state is written as

$$\sigma_{DSD}=\sigma_D\left|1+\text{const}\,\frac{R}{\varepsilon_\gamma-\hbar\omega_1+i\frac{\Gamma}{2}}\right|^2 ,$$

where

$$R=\frac{\int u(r)\,h(r)\psi(r)\,r^2\,dr}{\int u(r)\,r\,\psi(r)\,r^2\,dr}$$

and σ_D is the direct cross section; ε_γ the emitted γ-ray energy; $\hbar\omega_1$ and Γ the energy and width of the giant dipole state; $\psi(r)$ and $u(r)$ the initial and final radial wave functions and $h(r)$ is a function proportional to the particle-vibration coupling interaction for excitation of the giant dipole state. Cross section calculations have been performed with different $h(r)$ functions proposed. Too low values are seen to be obtained by using a surface-peaked real coupling. Values significantly higher (by a factor two or three) can be reached by using a real volume form of the coupling interaction.[9] Recently, a complex coupling interaction $h(r)=v_1\xi(r)+iw_1\eta(r)$ has been suggested [10] with its real part of volume form and an imaginary part of surface-peaked form. The inclusion of the imaginary interaction increases the calculated cross section and helps to remove the discrepancy between theory and experiment on the low energy side of the giant resonance. In fact, it was shown in [8] that a real coupling interaction in the collective term is responsible for constructive interference between direct and semi-direct capture on and above the giant resonance peak and for destructive interference below it. Of course, an opposite sign in the interference term is obtained from an imaginary interaction, thus displacing the cross section peak towards lower energies. The disturbing point with the formula of ref. [10] was that it contained different form factors, with different normalizations. In fact, formula [10] gives $\int\xi(r)r^3dr=1$, while $\int\eta(r)r^3dr>1$. This masked the fact that the effective strength of the imaginary term used in [10,1] was much greater than the strength of the real term and, therefore, the real term could often be neglected.[11] For this reason we prefer to derive the imaginary part of the interaction in the same way as was done in [9] for the real part, and to use a complex nucleon-nucleus coupling interaction with volume form for both the real and the imaginary parts, and furthermore with the same normalization. With reasonable real and imaginary strengths a satisfactory agreement between theory and experiment has been achieved in the cases considered. As an example, in Fig. 1 a comparison between experimental [1-2, 12-13] and theoretical cross sections for the $^{89}Y(n,\gamma)$, $^{140}Ce(n,\gamma)$ and $^{208}Pb(n,\gamma)$ reactions is shown. The continuous lines are obtained with a complex interaction and $v_1=w_1=130$ MeV, the other parameters being the same as used in [1,10]. With the strengths used, both parts of the interaction are obviously needed for obtaining a magnitude agreement between theory and experiment: the neglecting of either one of the two terms would give cross section values of about half the calculated ones. The energy displacement of calculated curves due to the interference term is shown by curves of the same magnitude obtained keeping $v_1^2+w_1^2=$ constant. The dot-dashed line is calculated for a pure real interaction ($v_1=184$ MeV ; $w_1=0$) , while the dashed one corresponds to a pure imaginary interaction ($v_1=0$; $w_1=184$ MeV), all the other parameters being unchanged.

As can be seen, the complex interaction increases the calculated curve at low energies on the left-hand side of the giant resonance peak. Keeping in mind a possible contribution to the cross sections by the statistical mechanism at those energies, the agreement obtained with reasonable strengths, such as $v_1=w_1=130$ MeV, can be considered as satisfactory. Another way of increasing the calculated cross sections on the low energy side of the giant resonance may be sought by including the quadrupole capture contribution. For neutron capture the direct quadrupole cross section is obviously negligible due to the low effective charge.[14] The situation is different with semi-direct capture.[11] In this case preliminary calculations show that quadrupole capture, though less important than E1 capture, should not be neglected. Of course, the remaining discrepancy can also be ascribed to the inadequacy of the theory, which in the present formulation involves many simplifications and has still to be improved. It is worthwhile noting that it is precisely in the 7-10 MeV energy region that the lack of experimental data is most felt.

A comparison between theoretical curves and γ-ray spectra from capture in ^{89}Y, ^{140}Ce and ^{208}Pb at some neutron energies between 6 and 15 MeV has also been performed. For this

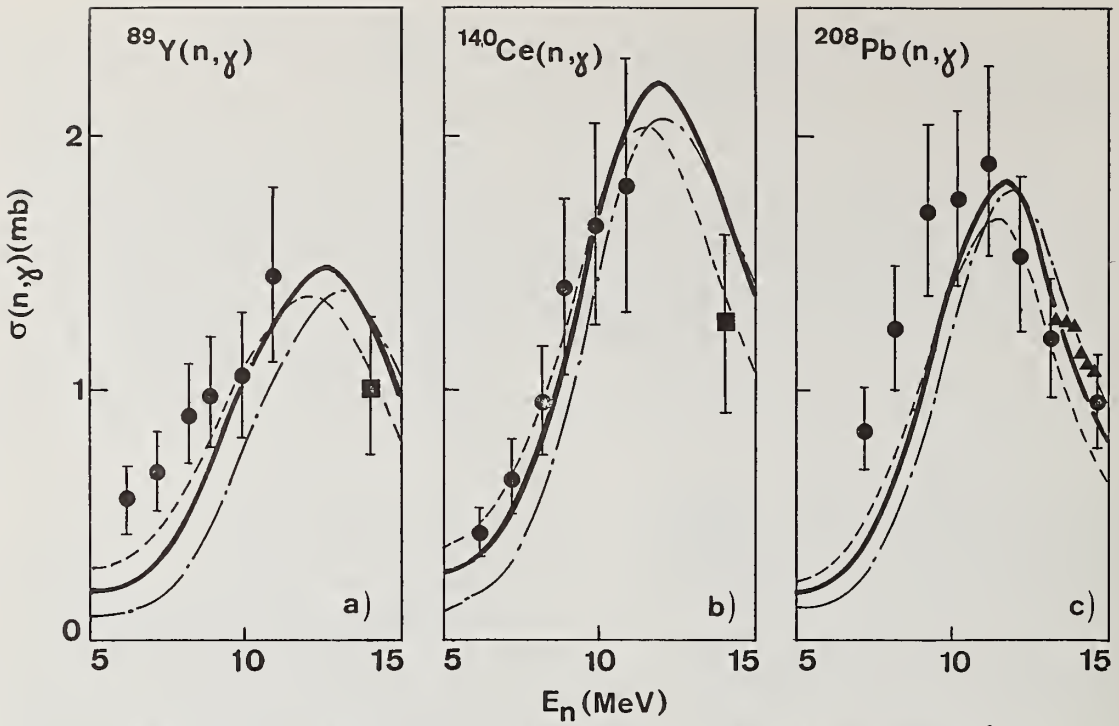

Fig.1. Cross sections for (n,γ) transitions: (a) to levels below 4.5 MeV in ^{90}Y, (b) to levels below 3.5 MeV in ^{141}Ce and (c) to all bound levels in ^{209}Pb. The experimental points are taken from refs.[1,2] (dots), ref.[12] (squares) and ref.[13] (triangles). The continuous curves are calculated by using a complex interaction with volume form for both real and imaginary parts (v_1=w_1=130 MeV). The dot-dashed and dashed curves represent the results of calculations with a pure real (v_1=184, w_1=0 MeV) and a pure imaginary (v_1=0, w_1=184 MeV) interaction respectively.

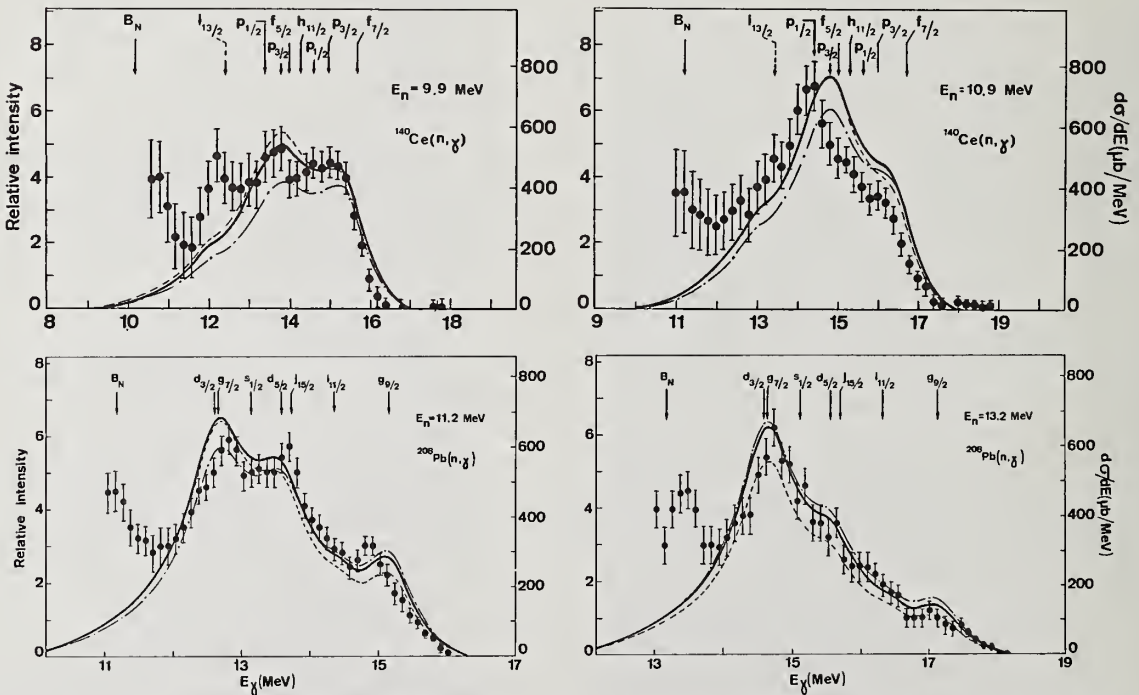

Fig.2. Comparison between experimental[1,2] and calculated spectra of high-energy photons emitted in (n,γ) reactions. The meaning of the continuous, dot-dashed and dashed curves is given in the caption of Fig.1.

purpose the cross sections for individual single-particle bound states are corrected for detector γ-ray efficiency and then spread over the energy interval corresponding to the response function of the spectrometer. The neutron single-particle structure here used is the same as in refs.[1-2]

Some results of calculations are shown on Fig.2 by continuous, dot-dashed and dashed curves, the meaning of which is the same as in Fig.1. Taking into account the magnitude agreement between theoretical and experimental cross-sections for the neutron energies considered, the calculated spectra are plotted in a scale (right side of fig.2) rendering nearly the same areas below the theoretical curves as below the upper portion of the experimental spectra given in relative intensity. The direct-semidirect models account satisfactorily for the essential features of the high energy part of the γ-ray spectra available from refs.[1-2], especially taking into account the insufficient knowledge of the single particle structure of ^{90}Y and ^{141}Ce.

Conclusions

In spite of the encouraging results achieved, further experimental data are needed in order to use theoretical estimates for reactor design purposes. In fact, the theoretical estimates account for the magnitude of the cross sections and their dependence on the incident energy as well as for the shape of γ-ray spectra, but the reliability of the estimated data is closely related to the calculation parameters - till now very uncertain. This specially refers to the crucial parameters v_1 and w_1. Only systematic analyses can lead to sufficient reliability of the calculated cross sections for use in reactor problems. It seems however that, when two or three experimental points are available in the 6-14 MeV range, the curves calculated by adjusting the v_1 and w_1 strengths to these points can give a useful indication of the cross section behaviour in the energy region considered.

Thanks are due to Dr. F. Fabbri for performing the required computations.

References

1 A. LINDHOLM, L. NILSSON, I. BERGQVIST and B. PÅLSSON, Proceedings of the "Second International Symposium on Neutron Capture Gamma Ray Spectroscopy and Related Topics", Petten, September 2-6, 1974.

2 I. BERGQVIST, D.M. DRAKE and D.K. McDANIELS, Nucl. Phys. A 191, 641 (1972).

3 L. NILSSON, A. LINDHOLM and I. BERGQVIST, Proceedings of the "Second International Symposium on Neutron Capture Gamma Ray Spectroscopy and Related Topics", Petten, September 2-6, 1974. I. BERGQVIST, D.M. DRAKE and D.K. McDANIELS, Nucl. Phys. A 231, 29 (1974).

4 J. KANTELE and M. VALKONEN, Phys. Letters 39 B, 625 (1972).
F. RIGAUD, M.G. DESTHUILLIERS, G.Y. PETIT, J.L. IRIGARAY, G. LONGO and F. SAPORETTI, Nucl. Sci. Eng. 55, 17 (1974).
J. VULETIN, P. KULIŠIĆ and N. CINDRO, Lettere al Nuovo Cimento, 10, 1 (1974).
K. PONNERT, G. MAGNUSSON and I. BERGQVIST, Physica Scripta, 10, 35 (1974).

5 A.M. LANE, Nucl. Phys. 11 625(1959); A.M. LANE and J.E. LYNN, Nucl. Phys. 11, 646 (1959).

6 G.E. BROWN, Nucl. Phys. 57, 339 (1964).
A.A. LUSHNIKOV and D.F. ZARETSKY, Nucl. Phys. 66, 35 (1965).

7 C.F. CLEMENT, A.M. LANE and J.R. ROOK, Nucl. Phys. 66, 273 (1965).

8 G. LONGO and F. SAPORETTI, Nuovo Cim. 56B, 264 (1968).

9 G. LONGO and F. SAPORETTI, Phys. Lett. 42B, 17 (1972) and Nucl. Phys. A 199, 530 (1973).

10 M. POTOKAR, Phys. Letters 46B, 346(1973).

11 G. LONGO and F. SAPORETTI, to be published.

12 F. RIGAUD, J. ROTURIER, J.L. IRIGARAY, G.Y. PETIT, G. LONGO and F. SAPORETTI, Nucl. Phys. A 154, 243 (1970) and A 176, 545(1971).

13 J. CSIKAI, G. PETŐ, M. BUCZKÓ, Z. MILIGY and N.A. EISSA, Nucl. Phys. A 95, 229 (1967).

14 G. LONGO and F. SAPORETTI, Nuovo Cim. 61 B, 167(1969).

REACTION MECHANISM IN THE HIGH ENERGY TAIL OF THE 14 MeV ^{56}Fe (n,n')-PROCESS

H.Jahn†, C.H.M.Broeders and I.Broeders
Institut für Neutronenphysik und Reaktortechnik
Kernforschungszentrum Karlsruhe

Measured cross-sections of 14 MeV-neutrons scattered inelastically on ^{56}Fe are analyzed to carry out investigations about the reaction mechanism. It is shown that a considerable part of direct inelastic scattering has to be added to the evaporation and pre-equilibrium processes in order to reproduce the data, especially the angular distribution, for energies of the scattered neutron above 7 MeV.

(Angular distribution; inelastic scattering; proton emission; scattered neutron)

Results of the Pre-equilibrium Model

Calculations of absolute spectral yields in pre-equilibrium decay processes can be performed using the most recent version of a model by Blann[1]. Blann makes the comment that a result which is within a factor two of the experimental result in absolute cross-section and which generally has the correct spectral shape and variation of yield with excitation energy is an encouraging result. Still for inelastic scattering of 62 and 39 MeV-protons on ^{209}Bi and ^{54}Fe Blann was able to obtain absolute cross-sections for proton-emission, the values of which are quite close to the measured cross-sections. Fig.1 shows that the calculated values may lie below, above or even closely along with the measured ones. This is especially true in that range of energy of the emitted proton, in which the pre-equilibrium process is assumed to be the dominating type of reaction mechanism.

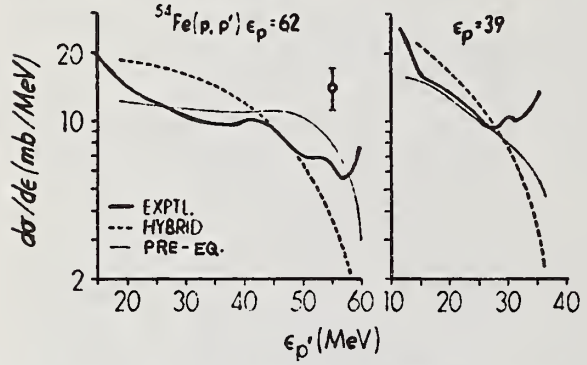

Fig.1 Inelastic scattering cross-section of protons on ^{54}Fe, comparison with experiment of Bertrand and Peelle[1].

As an alternative example we have carried out the corresponding Blann-type calculations for the case of inelastic scattering of 14,7 MeV neutrons on ^{56}Fe.

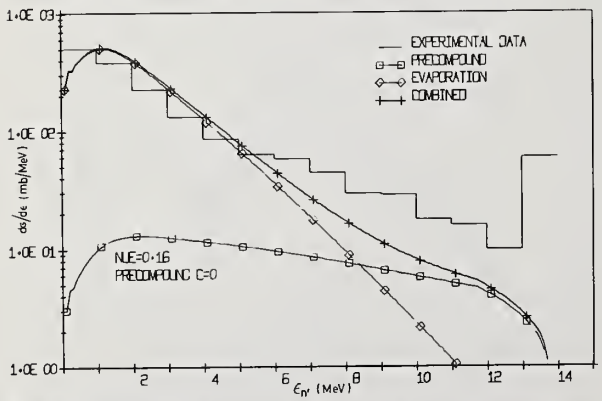

Fig.2 Inelastic scattering cross-section of neutrons on ^{56}Fe.

In contrast to Blann's previous results for 62 and 39-MeV protons we have obtained for the 14,7 MeV-neutron case a calculated neutron emission cross-section of which the value is only about 1/3 of the value of the cross-section above 7 MeV measured by Hansen et al.[2]. The calculated cross-section never reaches the measured one in the region above 7 MeV energy of the emitted particle in which now the pre-equilibrium process is assumed to be the dominating reaction mechanism as shown in Fig. 2.

Fig.2 nevertheless shows that the shape of the measured cross-section is about reproduced by the calculated values in the region above 7 MeV.

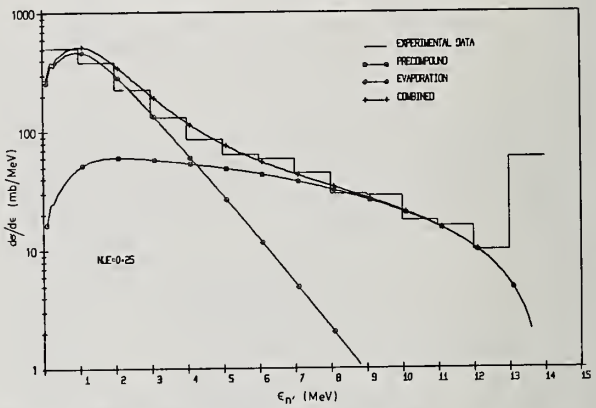

Fig.3 Comparison between the measured and calculated angular integrated cross-section where the fit is carried out without the direct part (ν=0,25 see equ. (2)).

Agreement of the absolute value of the calculated with the measured cross-section for the 14,7 MeV-neutron case within the framework of Blann's model as shown in Fig. 3 could only be obtained by assuming a mean free path of the emitted neutrons within the nucleus which is four times the mean free path following from the optial model[3]. But for this assumption it is hard to get a physical justification.

Semiclassical Analysis of Angular Distribution

Moreover, Hermsdorf et al.[4] recently have measured an angular distribution of the inelastically scattered 14,7 MeV-neutrons with a strongly forward directed anisotropy shown by Fig.4. This strongly forward directed anisotropy shown in Fig. 4 cannot be explained by pre-equilibrium processes, because pre-equilibrium processes only can be connected with an anisotropy of the angular distribution, which is symmetrical toward 90° according to Grimes, Anderson et al.[5] and Ericson and Strutinski[6].

† and Faculty of Physics, University of Karlsruhe

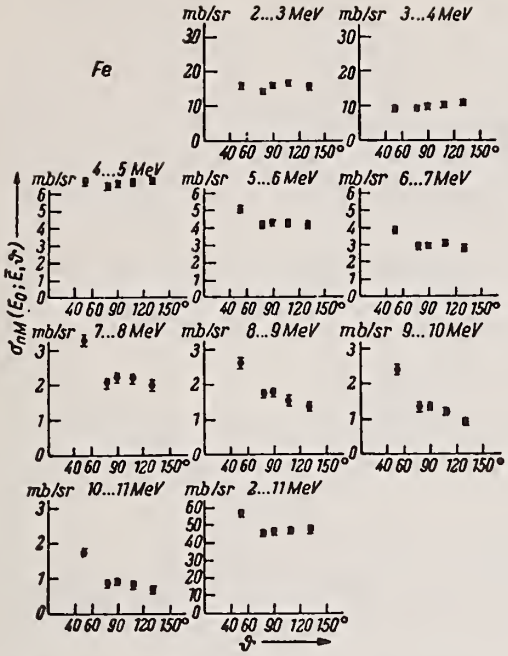

Fig.4 Angular distribution of 14,7 MeV neutron scattered inelastically on ^{56}Fe as measured by Hermsdorf et al.[4]

On the other hand we can show that the angular distribution values measured by Hermsdorf et al. are not too far away from a Const/$\sin^2\,\Theta/2$-distribution, which is predicted by the semiclassical treatment of direct nuclear reactions of Butler, Austern and Pearson[7]. Their prediction is valid for large scattering angles Θ for which the relation

$$\Theta \gg 2 \arcsin \frac{\ell}{2kR} \qquad (1)$$

is fulfilled, where ℓ is the quantum number of the transmitted angular momentum, $k = p/\hbar$ the wave number of the incident neutron with momentum $p = \sqrt{2m\varepsilon}$ and $R = (1{,}07A^{1/3} + 2{,}4)\ 10^{-13}$ cm $= 6{,}5 \cdot 10^{-13}$ cm the radius of the nuclear potential. For $\varepsilon = 14{,}7$ MeV incident energy of the neutron of mass m we obtain $kR \approx 5$, and ℓ is probably not greater than 2 as will be shown by the following explanations. The scattering angle dependent differential cross-section then is altogether:

$$\frac{d^2\sigma(\varepsilon,\varepsilon',\Theta)}{d\Omega\, d\varepsilon'} = \frac{1}{4\pi}\left(\frac{d\sigma(\varepsilon,\varepsilon')}{d\varepsilon'}\right)_{\text{Evap.}} + \frac{1}{4\pi}\left(\frac{d\sigma(\varepsilon,\varepsilon')}{d\varepsilon'}\right)_{\substack{\text{Blann}\\ \text{absolute}}} + \left(\frac{d\sigma(\varepsilon,\varepsilon',\Theta)}{d\Omega}\right)_{\text{direct}} \qquad (2)$$

with the **equilibrium part**

$$\frac{1}{4\pi}\left(\frac{d\sigma(\varepsilon,\varepsilon')}{d\varepsilon'}\right)_{\text{Evap.}} = A\,\sigma_r(\varepsilon')\,\varepsilon'\,e^{-\frac{\varepsilon'}{T}};\quad T = \sqrt{\frac{\varepsilon}{\nu A}}\ \text{MeV} \qquad (3)$$

where only the direct part

$$\left(\frac{d\sigma(\varepsilon,\varepsilon',\Theta)}{d\Omega}\right)_{\text{direct}} = \frac{\text{Const}}{\sin^2\,\Theta/2} \qquad (4)$$

is assumed to be angular dependent. In (3) $\sigma_r(\varepsilon')$ is the reaction cross-section of the optical model, and the constant A is taken from the fit of the combined part of the first two terms of (2) as shown in Fig.2.

Fig. 5 a - c shows how far the angular distribution values measured by Hermsdorf et al.[4] can be fitted already by the Const/$\sin^2\,\Theta/2$ - distribution used in (2) - (4) down to 8 MeV of the inelastically scattered neutron.

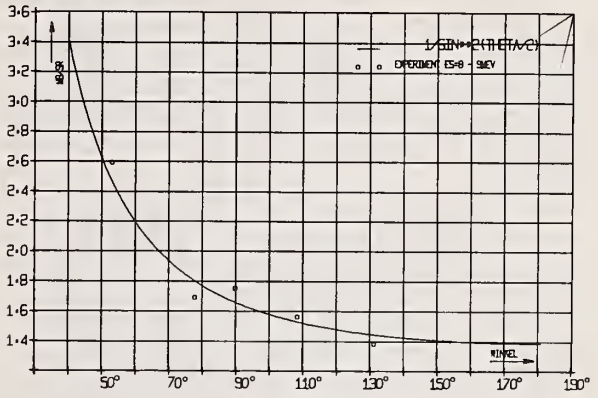

8 - 9 MeV

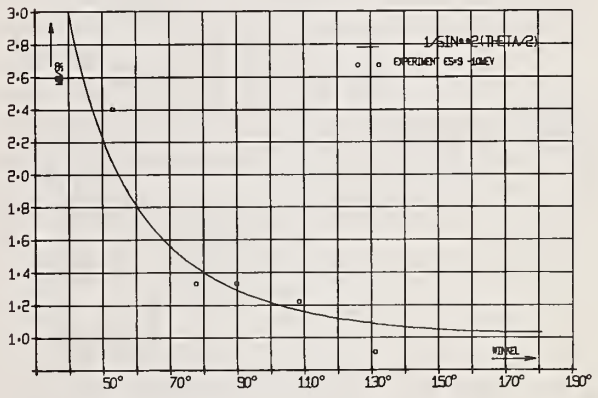

9 - 10 MeV

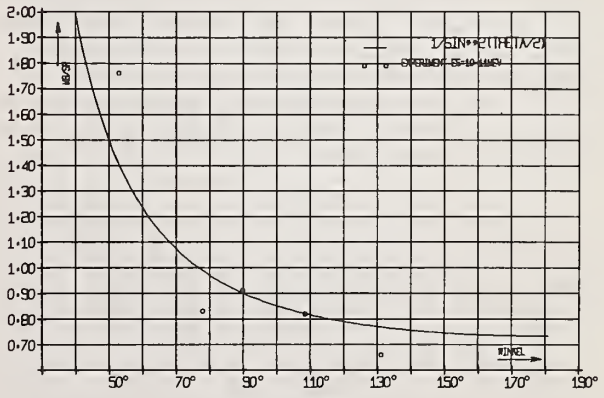

10 - 11 MeV

Fig.5 Semiclassical fit for angular distributions of 14,7 MeV neutrons scattered inelastically by ^{56}Fe.

Since the Const/$\sin^2\,\Theta/2$-distribution is the result of the semiclassical treatment of direct

reactions due to Butler, Austern and Pearson[7] as mentioned before, we anticipate that the anisotropy of the angular distribution measured by Hermsdorf et al.[4] is mainly caused by direct inelastic scattering of the 14,7 MeV neutron.

PWBA-Analysis of Angular Distribution

To confirm this anticipation and for the sake of extrapolation over the entire space of scattering angle we need an expression for the scattering-angle-dependent-differential cross-section of direct inelastic scattering, which is valid for any value of scattering angle and not only for large scattering angles as the semiclassical treatment. Furthermore it should show a shape which is typical for direct reactions.

At this point we should make it clear that we are using the term "direct inelastic scattering" in the usual sense of the theory of nuclear reactions as a direct quantum mechanical transition between an initial and a final state of the target nucleus plus an incident or outgoing neutron. From this we have to distinguish the use of the term "direct inelastic scattering" made by Blann[1] to denote the first step of the pre-equilibrium process with the smallest number of excitons. This clearly is the intermediate state of a reaction process as all the other pre-equilibrium and equilibrium states are, and reaction processes with an intermediate state are not direct processes in the usual sense.

In this sense and for the sake of simplicity and greatest physical transparency we choose for the purpose of first orientation the plane-wave-Born-approximation (PWBA) of the direct inelastic scattering process developed by Austern, Butler and McManus[8] which gives for the term of direct scattering (2) the expression:

$$\left(\frac{d\sigma(\varepsilon,\varepsilon',\Theta)}{d\Omega}\right)_{direct} = \text{const}\sqrt{\frac{\varepsilon'}{\varepsilon}}\,(2\ell'+1)\;x \qquad (5)$$

$$x \sum_{L} C_{\ell\ell'}\,(L,0;\,0,0)\,\{j_L(QR)\}^2$$

Where $Q = |k-k'|$ is the absolute value of the difference between the wave number vectors of the incident and scattered neutron, L is the quantum number of angular momentum transmitted between the neutron and the target nucleus by the scattering process by which a nucleon of angular momentum quantum number ℓ in the ground state of the target nucleus is lifted into the quantum number ℓ' of the excited state with $\ell + \ell' > L > |\ell - \ell'|$, $j_L(Q,R)$ is the corresponding spherical Bessel function and $C_{\ell\ell'}(L,0;\,0,0)$ is the Clebsch-Gordan-Coefficient.

Almost the same expression as (5) is valid for collective excitations of the target nucleus by a direct scattering process with the only difference that L then has the meaning of angular momentum quantum number of the corresponding collective state. Thus only this one L occurs in the expression corresponding to (5) instead of the summation over L.

Often also in the case of single nucleon excitation only one term in the summation over L in (5) is mostly used in the literature assuming that mainly one angular momentum L is transmitted. Thus the square of the spherical Bessel functions appears as the typical shape, which is closely related to the direct reactions. In case of ^{56}Fe the highest proton shell is 1 f 7/2 and the highest neutron shell is 2 p 3/2 in the ground state. The next unoccupied proton shell would be 2 p 3/2, the next unoccupied neutron shell would be 1 f 5/2. To lift a proton as well as a neutron into the next upper shell would mean $\Delta\ell = 2$ in both cases. On the other hand the quadrupole excitation 2^+ is dominating among the collective excited states of ^{56}Fe, while the 3^- octupole less often occurs. We therefore try to fit the angular distribution values measured by Hermsdorf et al.[4] with the term L = 2 alone with $\{j_2(QR)\}^2$ in the above expression (5). This is introduced into (2) and averaged over the energy regions of the scattered neutrons from 2-3 MeV till 10-11 MeV as has been done by Hermsdorf et al. for the measured values (see Fig.4). The obtained results are shown in Fig. 6 for the energy regions 7-8 MeV and 10-11 MeV of the scattered neutrons.

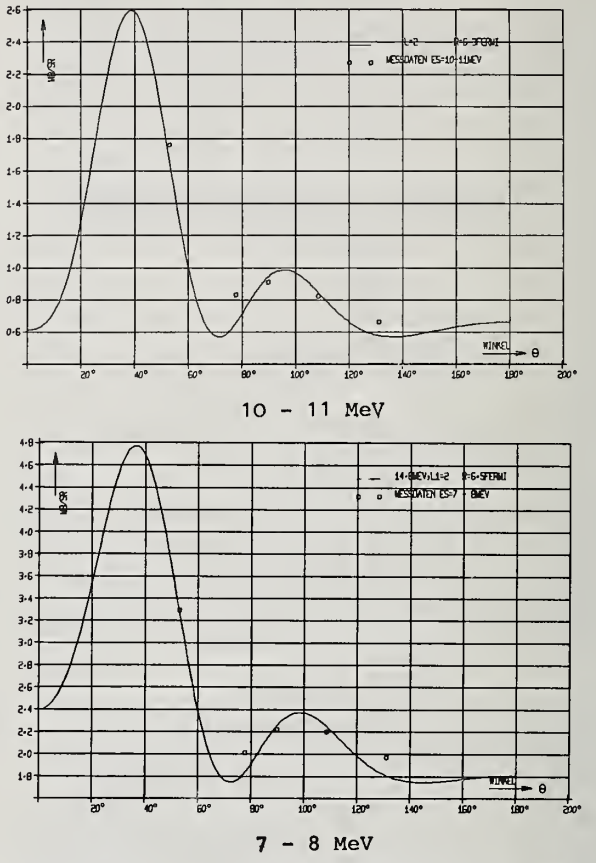

Fig.6 PWBA-fit of angular distributions of 14,7 MeV neutrons scattered inelastically by ^{56}Fe.

The diagrams of Fig.6 show that the measured values of the angular distribution of the inelastically scattered 14,7 MeV neutrons are fitted rather well by the $\{j_L(QR)\}^2$-behaviour of the square of the spherical Bessel function with index L = 2. The same is true for the other energy regions. This should be considered while taking into account that the errors of measurement amount to up to 10%. The still remaining deviations according to their trend correspond to quite those deviations which are to be expected and are found also otherwise between the PWBA- and the measured values. This means that the measured curves use to be more flat than the PWBA-curves while the positions of the maxima and minima are essentially maintained. Thus by means of the preceding and the following fits we have demonstrated that the angular distribution values measured by Hermsdorf et al.[4] show the typical shape of direct reactions which is closely related to the shape of the square of the spherical Bessel functions.

Comparison With Measured Angular Integrated Cross Sections

For this case of the $\{j_2(QR)\}^2$-fit with L = 2 as the only angular momentum transmitted by the reaction between the neutron and the target nucleus we have carried out the integration over the scattering angular space for every region of energy of the scattered neutron. The smoothed result of this integration is the combined curve of Fig.7. The result of this angular integration we then have compared with the scattering angular space integrated measured values of Hansen et al.[2]. Fig.7 shows this comparison while Fig.3 shows the former fit where only the evaporation and pre-equilibrium part but not the part of direct inelastic scattering was used in (2).

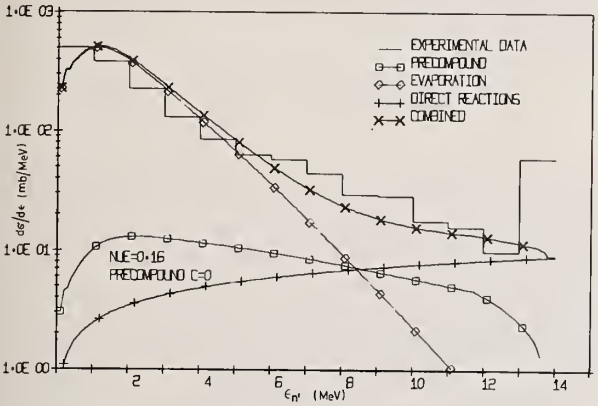

Fig.7 Comparison between measured and calculated angular integrated inelastic cross-sections, where the fit includes the direct part. (ν = 0,16 see equ. (2)).

Fig.7 and 3 show at first that taking into account the part of direct scattering gives a better possibility to fit the high energy end, while the former comparison without the part of direct scattering gives a better fit in the middle region of energies of the scattered neutron between 6 and 10 MeV. This can be explained in such a way that by taking into account the part of direct scattering yields a smaller participation of the processes with 3 and more excitons in the pre-equilibrium part in the middle energy region.

To sum up we can say that our investigations have shown that for a satisfactory description of inelastic scattering of 14,7 MeV neutrons on ^{56}Fe not only the pre-equilibrium processes in addition to the evaporation part have to be taken into account, but also the part of direct inelastic scattering is needed.

Literature

1 M.Blann, Nucl. Phys. A 213, 570 (1973)

2 L.F.Hansen, J.D.Andersen, P.S.Brown, R.J.Howerton, J.L.Kammerdiener, C.M.Logan, E.F.Plechaty and C.Wong, Nucl.Sc. and Eng.51, 278. (1973)

3 H.Borgwaldt, C.H.M.Broeders, I.Broeders, H.Jahn, M.Lalovic, D.Rusch, Reaktortagung, Nürnberg 1975

4 D.Hermsdorf, S.Sassonoff, D.Seeliger u. K.Seidel Kernenergie 17, 259 (1974)

5 S.M.Grimes, J.D.Anderson, J.W.McClure, B.A.Pohland, C.Wong,

C.Wong Phys.Rev. C, 3, 645 (1971)

6 T.Ericson and V.Strutinski, Nucl.Phys.8,284 (1958)

7 S.T.Butler, N.Austern and C.Pearson, Phys.Rev. 112, 1227 (1958)

8 N.Austern, S.T.Butler and McManus, Phys.Rev. 92, 350, (1953)

9 K.J. LeCouteur, Proc.Phys.Soc. A65, (1952), 718

CALCULATIONS OF (n,α) RATES FOR IRON-GROUP MATERIALS*

F. M. Mann and Z. E. Switkowski
California Institute of Technology
Pasadena, California 91125

The Hauser-Feshbach statistical model is used to calculate (α,n) and (n,α) cross sections for Fe-group elements to provide information on helium production within fusion reactors. A parametrization of the cross sections is discussed.

(Nuclear Reactions Fe group; calculated σ(E), (α,n), (n,α), Hauser-Feshbach)

Introduction

The copious production of high energy (~ 14 MeV) neutrons by the D + T fusion reaction requires a careful understanding of the subsequent interactions of these neutrons with the immediate reactor environment, particularly the first wall and divertors. The primary interactions will be elastic and inelastic scattering and nuclear reactions,[1] the manifestations of which are radiation damage phenomena such as void formation and embrittlement,[2-4] sputtering,[5,6] as well as build-up of radioactive by-products.[7]

One of the nuclear processes which significantly contributes to loss of structural integrity is the (n,α) reaction. The relative insolubility of helium gas in the metals making up the reactor[8] coupled with the well-known ability of He to occupy voids in the structure[9] may result in the production of high pressure gas bubbles leading to swelling and blistering.[3,10]

As the plasma vessel of the first generation fusion reactors seems likely to be fabricated from stainless steel, cross sections for (n,α) reactors on the various isotopes of Cr, Fe, and Ni are required. Furthermore, n-induced reactions on the secondary products of earlier reactions should also be included. In the absence of extensive experimental (n,α) rates for nuclei in the mass region $45 \leq A \leq 65$ and realizing that some target nuclei may be radioactive (e.g., the reaction sequence $^{58}Ni(n,\gamma)^{59}Ni(n,\alpha)$ is a well-known helium production source[11]) and hence are difficult to study with currently available techniques, theoretical calculations must be used to estimate helium production.

In this paper we describe one approach towards such a theoretical study. No attempt is made to include processes such as (n,n'α) or (n,^{3}He) whose contributions to inert gas production have been calculated to be small.[12] Cross sections for (n,α) reactions will be examined for a wide range of neutron energies extending up to ~ 14 MeV. Such calculations should be useful in order to correlate simulation studies performed with fission neutrons at lower energies.[13]

Theoretical Approach

The question of whether (n,α) reactions may be well described within a statistical model has been addressed by many authors.[12,14-18] Calculations using the Weisskopf-Ewing formalism[19] have not always successfully reproduced the data. Such discrepancies may often be attributed to poorly-known level density parameters, inconsistent data or a non-statistical reaction mechanism. Yet the requirements of stellar astrophysicists have resulted in extensive measurements, involving target nuclei within the Fe group, of charged particle induced reaction yields, most of which have been well described by Hauser-Feshbach statistical model calculations.[20-22] Encouraged by these results we have undertaken to compute the (n,α) reaction cross sections for the mass range $45 \leq A \leq 65$.

In the theory of average cross sections,[23] the angle integrated cross section, $\sigma_{\alpha\alpha'}$, for a reaction $\alpha \to \alpha'$ averaged over compound nucleus fluctuations, may be written

$$\sigma_{\alpha\alpha'} = \pi\lambda_\alpha^2 \sum_J \frac{(2J+1)}{(2I+1)(2i+1)} \frac{T^J_{\alpha'\ell's'}\ T^J_{\alpha\ell s}}{\sum T_{\alpha''\ell''s''}} \qquad (1)$$

where the notation is that of ref. 23. The calculation of the sum in the denominator of Eq. (1) requires knowledge of the energies, spins, and parities of all the final states in all the residual nuclei to which the compound nucleus can decay. Usually only the low-lying states are known and a level density formula must be employed for higher excitation energies. We have used the back-shifted Fermi gas formula of Dilg et al.[24] The transmission coefficients in Eq. (1) were numerically computed using the optical potentials of Becchetti and Greenlees[25] for protons and neutrons and McFadden and Satchler[26] for the alpha channels.

Results

We have calculated (α,n) cross sections for sixteen nuclei (viz. ^{27}Al, ^{45}Sc, ^{46}Ti, ^{50}Cr, ^{51}V, ^{54}Fe, $^{58,60,62}Ni$, ^{59}Co, $^{63,65}Cu$, and $^{64,66,68,70}Zn$) for which comprehensive data exist. Since the n-channels will account for the bulk of the reaction cross sections, these calculations test only whether the optical potential adequately describes the alpha-target interaction. There is little dependence on the details of the level densities for the residual nuclei. Figure 1 shows a comparison of the experimental data for $^{59}Co(\alpha,n)^{56}Fe$ with our calculations. Good fits were obtained for all the other systems considered with no parameter adjustments. Since the excitation energies at which the compound nuclei are formed by these (α,n) reactions are comparable with those in the inverse reaction with 14-MeV neutrons, (n,α) yields should be well described by such calculations. The possibility of non-statistical mechanisms such as direct or pre-equilibrium processes cannot be disregarded but these have been estimated[27] to constitute less than 20% of the cross sections for elements near the Fe group.

(n,α) calculations

The competition between the outgoing channels in calculations of (n,α) reactions depends sensitively upon the level density parameters. In Fig. 2(a) we show the calculations for $^{59}Co(n,\alpha)^{56}Mn$ where the solid curve is seen to overestimate the data at higher energies by a factor of ~ 2. Our calculations for the $^{56}Fe(n,p)^{56}Mn$ reaction also overpredicted the yield, leading to the suspicion that the level density for ^{56}Mn (ref. 24) was too high. Using parameters from Gilbert and Cameron[28] for this nucleus produced the dashed curve in Fig. 2(a) as well as the

*Supported in part by the National Science Foundation [GP-28027 and GP-43585] and The Ford Motor Company.

other curves in Figs. 2(b)-(e). The $^{56}Fe(n,p)$ yield was also correctly predicted.

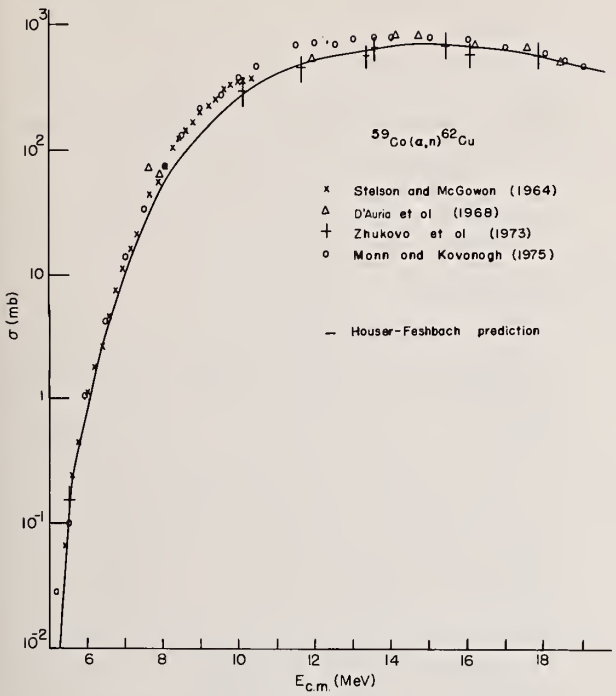

Fig. 1. Comparison of Hauser-Feshbach statistical model calculation with experimental data. References are P. H. Stelson and F. K. McGowan, Phys. Rev. 133B, 911 (1964), J. M. D'Auria et al., Phys. Rev. 168, 1224 (1968); O. A. Zhukova et al., Sov. J. Nucl. Phys. 16, 134 (1973); F. M. Mann and R. W. Kavanagh, private communication (1975). Sources of parameters for calculations are given in the text.

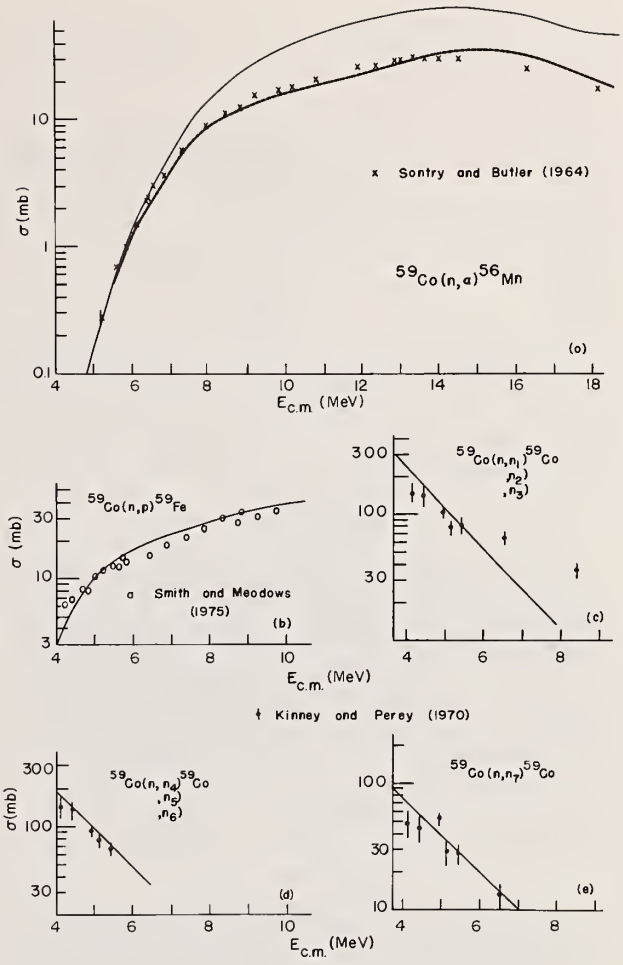

Fig. 2. Calculations of neutron-induced reactions with ^{59}Co. References to the data are: D. C. Santry and J. P. Butler, Can. J. Phys. 42, 1030 (1964); D. L. Smith and J. W. Meadows, Argonne Natl. Lab. report ANL/NDM-10 (1975), W. K. Kinney and F. G. Perey, ORNL-4549 (1970). The parameters used to produce the dashed curve in Fig. 2(a) also yielded fits shown in Figs. 2(b)-(e).

Our calculations for the (n,α) cross sections for ^{45}Sc, ^{55}Mn, ^{63}Cu have also required such parameter adjustments and it must be emphasized that theoretical calculations must be viewed with skepticism wherever reliable level parameters do not exist. In such cases other channels should be simultaneously fit.

Cross section parametrization

While the ability of a statistical model approach to account for (n,α) data is not new, its inclusion in n-transport codes etc. has not been wide-spread due to its unwieldy nature. We have considered a parametrization of the cross sections analogous to that used in stellar nucleosynthesis codes.[29] For low neutron energies, the (n,α) cross section is determined by the zero angular momentum alpha-particle penetration through the Coulomb barrier. This dependence is of the form $\exp(-2\pi\eta)$ where

$$\eta = \frac{Z_1 Z_2 e^2}{\hbar v_{rel}}$$

and Z_1 is equal to 2 for alphas, Z_2 is the atomic number of the residual nucleus and v_{rel} is the relative velocity in the α-channel. At higher energies the participation of other partial waves as well as increasing competition from other channels requires the introduction of a further energy dependent term in the exponent. We then write

$$\sigma(E) = \frac{1}{E} \exp(-2\pi\eta + a + bE)$$

where the energy refers to the alpha-particle channel and is related to the entrance channel center-of-mass energy, $E_{c.m.}$ by $E = E_{c.m.} + Q$ when Q is the reaction Q-value.

Fig. 3 illustrates the quality of fit achievable when the parameters a,b are least squares adjusted. Above the two particle emission threshold, another set of values for a,b is used. Extension to parametrization of (n,p) data is trivial and the fit for $^{56}Fe(n,p)$ is also shown.

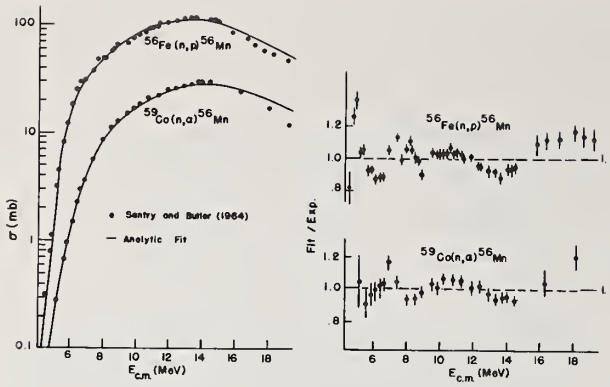

Fig. 3. Least squares fit of expression (2) to cross sections.

Conclusion

Until experimental data become available, statistical model calculations may be used to compute (n,α) rates although only a factor of two confidence may be achieved for those cases where no reliable level density parameters or measurements of other reaction channels exist. Application of the parametrization of Eq. (2) to a sufficiently large body of data may expose systematic trends in the parameters a,b to permit confident interpolation to cases of interest.

We appreciate the interest of Professor T. Tombrello in this work.

References

1. J. D. Anderson and H. F. Lutz, Lawrence Radiation Laboratory, report UCRL-14955 (1966).
2. C. Cawthorne and E. J. Fulton, Nature 216, 575 (1967).
3. D. I. Norris, Rad. Eff. 14, 1 (1972), ibid. 15, 1 (1972).
4. S. F. Pugh, J. Brit. Nucl. En. Soc. 10, 159 (1971).
5. M. S. Kaminsky, J. H. Peavey, and S. K. Das, Phys. Rev. Lett. 32, 599 (1974).
6. R. Behrisch, Nucl. Fus. 12, 695 (1972).
7. D. Steiner and A. P. Fraas, Nucl. Safety 13, 353 (1972).
8. S. Blow, J. Brit. Nucl. En. Soc. 11, 371 (1972).
9. S. T. Picraux and F. L. Vook, in Applications of Ion Beams to Metals, eds. S. T. Picraux, E. P. Eernisse, and F. L. Vook (Plenum Press, New York, 1974).
10. Proceedings of the Conference on Surface Effects in Controlled Thermonuclear Fusion Devices and Reactors, eds. H. Wiedersich, M. S. Kaminsky, and K. W. Zwilsky, J. Nucl. Mat. 53, 1 (1974).
11. G. L. Kulcinski in APS Summer Study — Physics Problems Relating to Energy Technologies: Radiation Effects on Materials, BNL, June (1974).
12. S. Pearlstein, J. Nucl. Energy 27, 81 (1973).
13. T. H. Blewitt in APS Summer Study — ref. 10.
14. F. Gabbard and B. D. Kern, Phys. Rev. 128, 1276 (1962).
15. E. Saetta-Menicella, F. Tonolini, and L. Tonolini-Severgnini, Nucl. Phys. 51, 449 (1964).
16. M. Seebeck and M. Bormann, Nucl. Phys. 68, 387 (1965).
17. C. Spira and J. M. Robson, Nucl. Phys. A127, 81 (1969).
18. S. M. Grimes, Bull. Am. Phys. Soc. 19, 988 (1974).
19. V. F. Weisskopf and D. H. Ewing, Phys. Rev. 57, 472 (1940).
20. A. J. Howard, H. B. Jensen, M. Rios, W. A. Fowler, and B. A. Zimmerman, Astrophys. J. 188, 131 (1974).
21. M. Rios, B. D. Anderson, and J. S. Schweitzer, Nucl. Phys., in press.
22. S. E. Woosley, J. A. Holmes, W. A. Fowler, and B. A. Zimmerman, private communication and to be published Rev. Mod. Phys. (1976).
23. H. Feshbach, The Compound Nucleus, Part B, ed. F. Ajzenberg-Selove (Academic Press, New York, 1960) p. 625.
24. W. Dilg, W. Schantl, H. Vonach, and M. Uhl, Nucl. Phys. A217, 269 (1973).
25. F. D. Becchetti and G. W. Greenlees, Phys. Rev. 182, 1190 (1969).
26. L. McFadden and G. R. Satchler, Nucl. Phys. 84, 177 (1966).
27. L. Milazzo-Colli and G. M. Broga-Marcazzon, Nucl. Phys. A210, 297 (1973).
28. A. Gilbert and A. G. W. Cameron, Can. J. Phys. 43, 1446 (1965).
29. W. A. Fowler, G. R. Caughlan, and B. A. Zimmerman, Ann. Rev. Astron. Astrophys. 5, 525 (1967).

PARAMETRIC FIT OF THE TOTAL CROSS SECTION OF ^{45}Sc*

B. A. Magurno and S. F. Mughabghab
Brookhaven National Laboratory
Upton, New York 11973

A parametric fit to the total cross section of Sc-45 based on the Breit-Wigner multilevel formalism was carried out. To reproduce the minimum in the total cross section at 2.0 keV and to get an acceptable fit for the low energy resonances, the spins of the bound level, the 3.24, and 4.27 keV resonances are 4,3,4 respectively. At higher energies the spins adopted for the resonances at 6.5, 7.9, 8.9, and 11.7 keV were 3,4,3,4. The parameters of the bound level are E_0 = -270 eV, Γ_n^o = 2.05 eV (J = 4) and Γ_γ = 0.38 eV.

(Bound level parameters; thermal cross sections; spin assignments)

Introduction

Because of the importance of Sc-45 in dosimetry applications and its use as a filter to produce a "monoenergetic" neutron beam at 2.0 keV an accurate knowledge of the neutron cross sections of Sc-45 is required. In this study we present the analysis and evaluation of the total cross section in the thermal and resonance regions. The total neutron cross section of Sc-45 was measured by Pattenden[1] in the energy range 0.0015 eV to 5.0 keV using a crystal spectrometer and slow and fast choppers. The data was parametrically fitted[1] in the low energy region with the aid of a negative energy resonance. However, above neutron energy region of about 300 eV, and around the famous minimum at 2.0 keV the calculated total cross section departed significantly from the measurements. Subsequent measurements carried out at the MTR showed[2,3] that the minimum at 2.0 keV is deeper than was previously measured.

The capture cross section of Sc-45 was measured by Romanov and Shapiro[4] in the energy range 1 eV to 40 keV. Alternative parameters of the bound level, and in particular a radiative width, were derived. In the resonance region, only one total cross section measurement[5] (3.0 - 35 keV) is available. The high resolution total cross section data of Cho et al[6] in the energy range 10 - 110 keV was not available during the evaluation.

Fitting Procedure

A multilevel Breit-Wigner total cross section was calculated using the code RESEND.[7] As a starting point, the resonance parameters recommended in BNL-325 (1973) were adopted. Since the spin and parity of the ground state of the target nucleus are $7/2^-$, s-wave neutron capture by Sc-45 forms compound states with spins and parities 3^- and 4^-. The spins of the resonances below 10 keV were not determined. In addition, thermal capture γ ray spectra measurements of Bolotin[8] and Delang et al[9] give some, but inconclusive, indication that the spin of the bound level is possibly 3. This is based on the observation of a primary transition to a low lying state at 142 keV with spin and parity 1^- and the lack of transitions to several low lying states with possible spin and parity of 5^+. It must be pointed out that at the start of the evaluation, thermal neutron polarization data which is important in shedding light on the coherent and incoherent cross sections and the spin of the bound level, were not available.

The total cross section in the energy range 3-10 keV was calculated and compared with the experimental data. The spin of the resonances at 3.24, 4.27, 6.59, 7.92, 8.90, 11.7 keV were found to be 3,4,3,4,3,4 respectively. With such a choice for the spins, several attempts were made to reproduce the minimum at 2.0 keV on the assumption that the spin of the bound level is 3. However, the best fit in the region of the minimum in the total cross section was achieved by adopting a spin 4 for the bound level. Table I presents the resonance parameters used in the present evaluation in the energy range up to 11.7 keV. The resonance parameters in the higher neutron energy 19.17 - 105.7 keV are the same as those quoted[10] in BNL-325 (1973). Figure 1, shows the calculated total cross section, represented by a solid smooth curve, in the energy range 10^{-5} eV to 3 keV. At low neutron energies, the solid curve passes through the data points of both Pattenden[1] and Wilson.[2] However, in the energy range 100 eV to ~ 1 keV, there is a significant discrepancy between the calculations and the data of Wilson.[2] Above the minimum, the calculations are in good agreement with the experimental data.[2] The calculated minimum of the total cross section at 1.9 keV is 85 mb. This is in good agreement with the experimental value $\sigma_t = 50^{+100}_{-50}$ mb within the stated error.

Figure 2 shows the calculated cross section in the energy range 1 - 10 keV and is compared with the low resolution data.[5] The calculated cross section shows another minimum of 189 mb at a neutron energy of 7.35 keV, which is not visible in the old measured cross section. A corroborative evidence for this minimum can be found in filtered beam experiments.[3]

Discussion

With the aid of resonance parameters determined from σ_t in the present evaluation, the partial cross sections can be calculated. Of particular interest is a comparison of the calculated cross sections at neutron energies of 0.0253 and 18.8 eV. Such a comparison is shown in Table II. The calculated thermal capture and scattering cross sections are found to be 26.9b and 23.7b respectively. These are in excellent agreement with the values recommended[10] in BNL-325 (1973).

Recent measurements carried out at neutron energy of 18.8 eV by Dilg[11] reported that σ_t = 22.03 ± 0.25b. This is in excellent agreement within the stated error with a calculated value of 21.7b. In addition, the coherent free scattering amplitudes (a+ and a-) associated with spins 4 and 3 can be calculated with the aid of the relation:

$$a_{\pm} = \left| R' + \sum_j \frac{\lambda\bar{}_j \Gamma_{nj}}{2(E-E_j) + i\Gamma_j} \right|$$

where the summation is carried out separately over j = 3 and j = 4 resonances. The nuclear scattering

*Research supported by U.S. Energy Research and Development Administration.

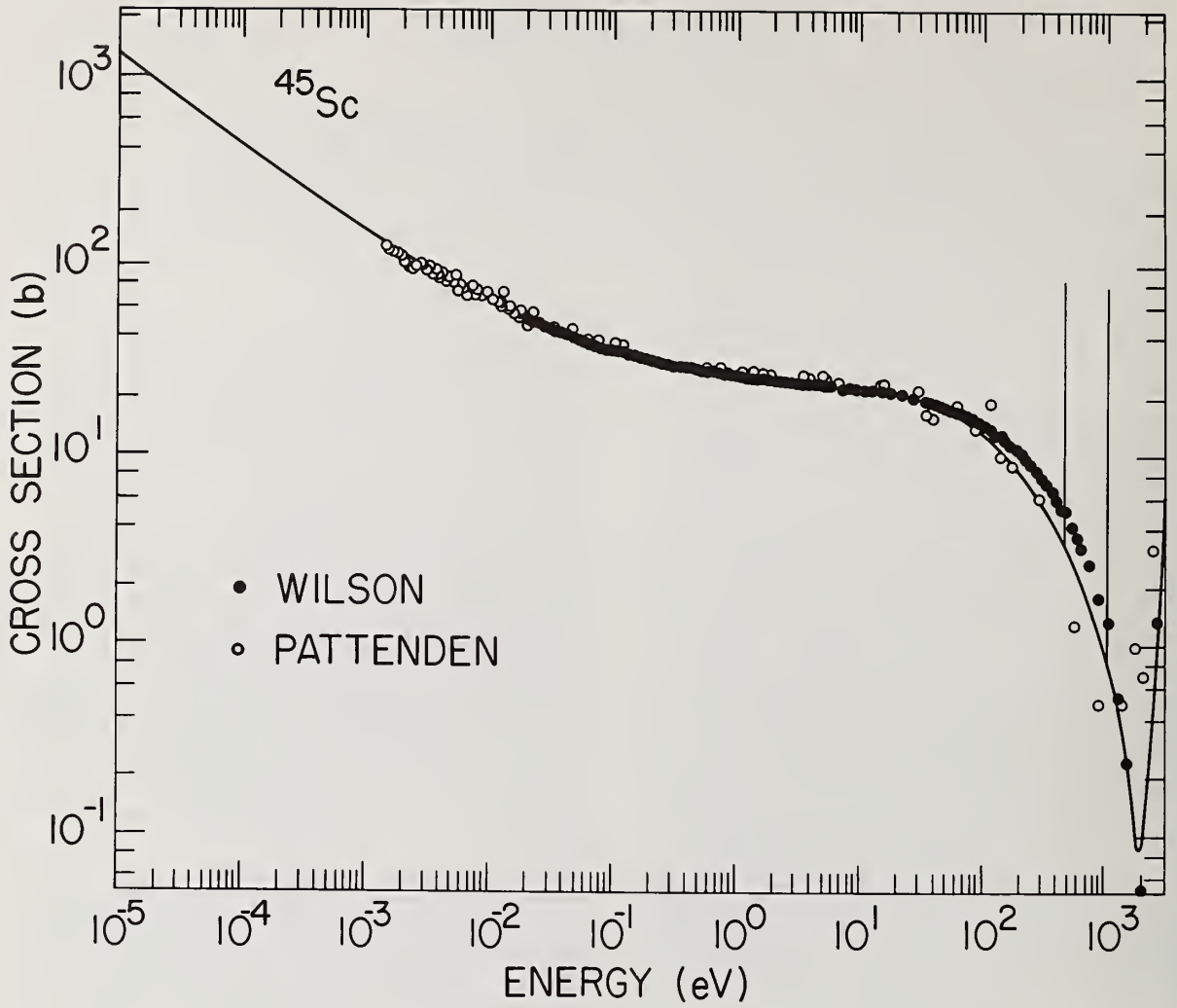

Figure 1

Total Cross Section of Sc-45 in Energy Range 10^{-5} eV to 3 keV

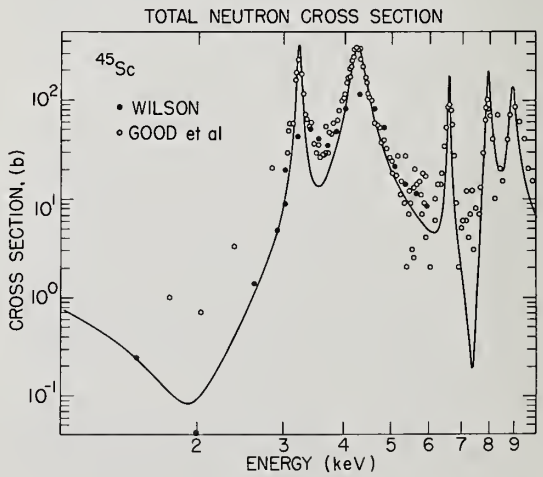

Figure 2

Total Cross Section of Sc-45 in Energy Range 1 keV to 10 keV

radius R′ is found to be 5.1 fm. The total coherent free scattering amplitued is then

$$a = g_+ a_+ + g_- a_-$$

where g_+ and g_- are the statistical weight factors associated with spins I + 1/2 and I - 1/2. In this evaluation we find

a+ = 18.2 fm
a- = 2.1 fm
a = 11.2 fm

From the latter value, we calculate a coherent bound scattering amplitude of 11.4 fm. This is in good agreement with a measured value of 11.8 ± 0.5 fm.

After the completion of the evaluation, a polarization measurement, in which the incoherent scattering amplitude was accurately determined, was reported by Roubeau et al[12]. The result is:

$$b_+ - b_- = 12.0 \pm 0.3 \text{ fm}$$

which strongly supports a spin assignment of 4 for the bound level in agreement with the present conclusions. However, the present evaluation gives

$$b_+ - b_- = 16.1 \text{ fm}$$

indicating that the calculated incoherent cross section is larger than measured by Roubeau et al.[12] Since the total scattering cross section is well established, this indicates that coherent scattering cross section should be larger than previously determined. A new measurement of the coherent scattering amplitude by Koester and Knopf[13] reporting a preliminary value b = 12.9 ± 0.7 fm supports this conclusion.

Table I

Resonance Parameters of
Low Energy Neutron Resonances

E_o (keV)	J	Γ_n (eV)	Γ_γ (eV)
- 0.270	4	Γ_n^0 = 2.05	0.379
3.24	3	70	0.3
4.27	4	300	0.35
6.59	3	73	(1.5)
7.92	4	160	(1.5)
8.90	3	260	(1.5)
11.7	4	140	(1.5)

Table II

Total, Scattering, and Capture Cross Sections
at 0.0253 eV and 18.8 eV

	0.0253 eV		18.8 eV	
E(eV)	BNL 325	present evaluation	Dilg	present evaluation
σ_t(b)	50.5±1.0	50.6	22.03±0.25	21.7
σ_γ(b)	26.5±1.0	26.9	(1.01)	0.9
σ_s(b)	24±2	23.7	21.0	20.8

References

1. N. J. Pattenden, Proc. Phys. Soc. (London) A68, 1955
2. W. L. Wilson, Master thesis University of Idaho 1966.
3. O. D. Simpson, J. R. Smith, and J. W Rogers, Neutron Standards and Flux Normalization
4. S. A. Romanov and F. L. Shapiro, J. Nucl. Phys. 1, 229 (1965)
5. P. D. Miller, J. H. Gibbons, W. M. Good, and J. H. Neiler, ORNL 2718, 22 (1959)
6. M. Cho, F. H. Fröhner, M. Kazerouni, K. N. Müller, and G. Rohr, Second International Conference on Nuclear Data for Reactors (Helsinki)(IAEA, Vienna, 1970) p619
7. O. Ozer, RESEND, BNL 17134, Brookhaven National Laboratory.
8. H. H. Bolotin, Physical Review 168, 1317 (1968)
9. W. Delang, P. Göttel, and H. Seyfarth, Contribution A56, Conference on Nuclear Structure Study with Neutron, (Budapest 1972) p.112
10. S. F. Mughabghab, and D. I. Garber, BNL 325, Neutron Cross Sections, Volume 1 (1973)
11. W. Dilg, Z. Naturforsch 29a, 1750 (1974)
12. P. Roubeau, A. Abragam, A. L. Bacchella, H. Alattli, A. Molinowski, P. Meriel, J. Piesvaux, and M. Pinot, Phys. Rev. Lett., 33, 102 (1974)
13. L. Koester and K. Knopf, NEANDC(E)161"U" p.118 (1974)

NEUTRON CAPTURE MECHANISM IN LIGHT AND CLOSED SHELL NUCLIDES[†]

B. J. Allen, J. W. Boldeman, M. J. Kenny, A. R. deL. Musgrove, Hla Pe
Australian Atomic Energy Commission, Lucas Heights, NSW, Australia
R. L. Macklin, Oak Ridge National Laboratory, Oak Ridge, Tenn. 37830

High resolution neutron capture cross section measurements have been made at the Oak Ridge Electron Linear Accelerator on Al, Si, ^{40}Ca, ^{52}Cr, ^{90}Zr and ^{138}Ba for the energy range above 2.5 keV. These data have been analysed at Lucas Heights where capture measurements with Ge(Li) and Moxon-Rae detectors have provided complementary information. While valence model calculations are important for these nuclides in explaining the shape of the γ-ray spectra and the observed correlation between reduced neutron and radiative widths, the valence component cannot adequately account for the observed radiative widths and a substantial single particle component, uncorrelated with neutron widths, is required.

(NUCLEAR REACTIONS: Al, Si, ^{40}Ca, ^{52}Cr, ^{90}Zr, ^{138}Ba(n,γ), E_n > 2.5 keV, measured σ(n,γ), ^{6}Li monitor, enriched targets, deduced resonance parameters, correlation coefficient, valence component.)

Introduction

High resolution neutron capture cross section measurements have been made at the Oak Ridge Electron Linear Accelerator (ORELA) with analysis and complementary γ-ray and cross section measurements at Lucas Heights. Emphasis has been placed on light and closed neutron shell nuclides where the neutron capture process is expected to be dominated by non-statistical effects. A detailed analysis of this data can therefore advance our understanding of the neutron capture mechanism.

In the original Lane and Lynn formalism[1], radiative capture was resolved into resonant internal, resonant channel capture with strength proportional to the reduced widths of initial and final states, and non-resonant channel or potential capture, with strength proportional only to the final state reduced width.

When channel capture is strong, large correlations between the neutron and partial radiative widths should occur and this is reported for capture in the magic nuclides discussed in this paper. A significant non-resonant cross section may also be present, which can be observed through interference with the resonant capture cross section. However, problems associated with the neutron sensitivity of the capture detectors preclude investigations of this effect.

The capture data are also of considerable interest for reactor and astrophysical applications, and average resonance parameters and capture cross sections are therefore tabulated in this paper.

Measurements

(a) Fluorocarbon scintillators[2] at the 40 m station of ORELA measure capture γ-ray yields and a thin ^{6}Li glass monitors the incident neutron flux. Capture events are weighted according to the γ-ray energy such that the average detector response is proportional to the total energy of the capture reaction.

Measurements have been made on enriched samples of the Ca, Cr, Zr and Ba isotopes and detailed results for ^{40}Ca, ^{90}Zr and ^{138}Ba will be found elsewhere[4,5]. While only the magic isotopes are discussed here, analysis of the near magic isotopes is proceeding so as to study the effect of shell closure on the neutron capture mechanism. Measurements on Al and Si have also been made both at ORELA and with Ge(Li) and Moxon-Rae detectors at the Lucas Heights pulsed Van de Graaff.

The ORELA data are converted to effective cross sections and resonances fitted by an iterative Monte Carlo program. In favourable cases it is possible to measure neutron widths (Γ_n) down to one quarter of the experimental resolution (i.e. ~3 eV at 9 keV) and in the case of ^{90}Zr resonance spins could be determined when $g\Gamma_n$ has been measured in the total cross section. In Figure 1, the 8.87 keV resonance in ^{90}Zr ($g\Gamma_n$ = 6 eV) is fitted for Γ_n = 3 and 6 eV when the experimental resolution is 13 eV. A better fit is obtained for g = 1 and Γ_n = 6 eV.

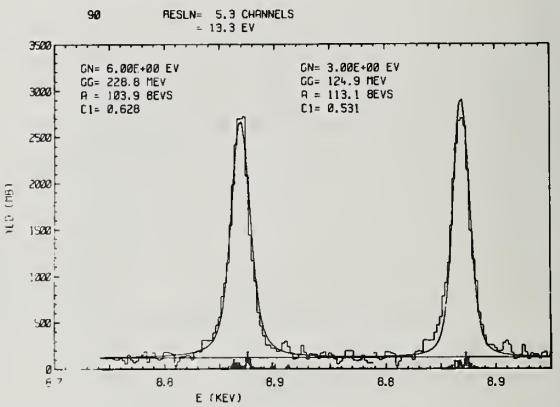

Figure 1

In the interpretation of the data, heavy reliance is placed on (ℓ,J) assignments from total cross section and threshold photonuclear experiments. A knowledge of Γ_n together with resonance parameter statistics, allows many additional ℓ-wave assignments.

A summary of average resonance parameters and cross sections is given in Tables 1 and 2. Results for Si, ^{40}Ca, ^{138}Ba supersede preliminary values reported elsewhere[6].

(b) Corrections to the ORELA data for the neutron sensitivity of the fluorocarbon scintillators are required. Usually the correction to the observed radiative width is small (~10^{-4} Γ_n eV), but when $\Gamma_n \gtrsim 1$ keV a substantial error can be introduced.

The capture yields of the 35 keV resonance in Al (Γ_n = 3.2 keV) and 55 and 188 keV resonances in Si (Γ_n = 1.5 keV and 56 keV respectively) are therefore expected to be quite sensitive to this effect. These

[†]Research sponsored in part by the USAEC under contract with Union Carbide Corporation

resonances were all found to be asymmetric (high energy tail), reflecting the s-wave scattering cross section and contribution of resonance scattered neutrons to the capture yield. Capture γ-ray and cross section measurements were therefore initiated at Lucas Heights in order to obtain independent estimates of the radiative widths.

Capture cross section measurements were made on three sample thicknesses of Al (0.02, 0.009, 0.0033 apb) relative to a Au standard. A value of $\Gamma_\gamma = 2.4 \pm 0.6$ was obtained which compares with published values of 1.9±0.3 with a NaI detector[7], and 2.3 eV with a liquid scintillator[7]. The high value of Singh et al.[8], (Γ_γ = 8.3 eV) extrapolated from the thermal capture cross section, is presumably influenced by a negative energy resonance.

The Al result is of particular importance because of the need to establish a standard transition for capture γ-ray measurements in the keV region. The 35 keV resonance is most suited for this purpose as it decays predominantly to the ground state[9] $\left(\Gamma_{\gamma_0} = (0.72 \pm 0.07)\Gamma_\gamma\right)$. Recommended values for this resonance are

$$\Gamma_\gamma = 2.1 \pm 0.2 \text{ eV}$$

$$\Gamma_{\gamma o} = 1.5 \pm 0.2 \text{ eV}$$

These values were used to normalise Ge(Li) measurements below 70 keV on a 0.09 apb sample of Si and a 0.137 apb sample of Al. Partial capture cross sections were obtained for the observed transitions in the 31.7, 38.8, 55 and 67.7 keV resonances in Si. Satisfactory agreement was obtained with the ORELA values, save for the radiative width of the 55 keV resonance which was found to have only ~20% of the ORELA value.

Estimates of the neutron sensitivity of the ORELA fluorocarbon scintillators can be made when the actual radiative widths are known, i.e. $(\Gamma_{\gamma obs} - \Gamma_\gamma) = k\Gamma_n$.

At 35, 55 and 188 keV, we find $k \sim 10 \times 10^{-4}$, 4×10^{-4}, 2×10^{-4} respectively. A detailed analysis of the energy dependence of the neutron sensitivity is in progress.

Neutron Capture at Closed Shells

Closed neutron shells occur in ^{40}Ca, ^{52}Cr, ^{90}Zr and ^{138}Ba and single particle effects are therefore expected to dominate over statistical processes.

For ^{40}Ca, ^{52}Cr and ^{138}Ba, single particle El transitions can occur from the $S^1/2$ shell at the neutron binding energy to low lying states with large $P^1/2$, $P^3/2$ components. For these isotopes the s-wave radiative widths are found to be ~6 times those of the p-wave values.

In ^{90}Zr, P→D and P→S transitions are possible and the p-wave radiative widths are almost twice those of the s-wave resonances.

Large correlation coefficients between the reduced neutron widths and radiative widths $\rho\left(\Gamma_n^\ell, \Gamma_\gamma(\ell)\right)$, are observed for s-wave resonances in ^{40}Ca, ^{52}Cr and ^{138}Ba, and for $P^3/2$ resonances in ^{90}Zr. We seek a quantitative explanation of these results through the valence model.

The radiative width ($\Gamma_{\gamma f}^V$) for valence neutron transitions to final state f has been calculated using the method of Lynn[10]. However, Lane and Mughabghab[11] have noted compensating errors in this method and have used the optical model approach to obtain estimaes of the valence widths. We have made calculations with both methods and find good agreement for Zr, but not so for Ca. However, the average valence width ($\bar{\Gamma}_\gamma^V$) is always less than the observed width ($\bar{\Gamma}_\gamma$) (see Table 1) and the residual component ($\bar{\Gamma}_\gamma - \bar{\Gamma}_\gamma^V$) remains large relative to the radiative widths of resonances in nearby nuclides.

A detailed examination of the ^{90}Zr results[5] provides an insight into the nature of these residual components.

In the $^{91}Zr(\gamma,n)$ reaction, Toohey and Jackson[12] found a residual, uncorrelated component for the ground state γ-ray width ($\Gamma_{\gamma o}$) (~62 meV), comparable to the calculated valence component (87 meV), which was attributed to statistical processes. However, this strength is ~14% of the total radiative width for $p^3/2$ resonances (440 meV) and far too large to be attributed as such.

On the assumption that the uncorrelated component ($\Gamma_{\gamma f}^u$) is comparable to the valence component ($\Gamma_{\gamma f}^V$) for all transitions to final states f, the average width due to statistical processes (Γ_γ^s) is found to be ~200 meV with a variance of ~120 meV.

We can therefore write the total radiative width (Γ_γ) as

$$\Gamma_\gamma = \sum_f \left[\Gamma_{\gamma f}^{V^{1/2}} + \Gamma_{\gamma f}^{u^{1/2}} \right]^2 + \Gamma_\gamma^s$$

and by sampling from a Porter-Thomas distribution of neutron widths, calculate the correlation coefficient

$$\rho(\Gamma_n^1, \Gamma_\gamma) = 0.62 \pm 0.12$$

This result is in good agreement with the experimental value of ρ = 0.58 for 37 $p^3/2$ resonances, and confirms the presence of an uncorrelated, non-statistical component in the radiative widths.

In ^{40}Ca it is possible to assign the residual strength to single particle transitions in the presence of a two particle-two hole core excitation.

The γ-ray spectra for 3 s-wave resonances below 100 keV exhibit similar spectral fractions[13] (~30%) to the $2p^3/2$ final states. Yet the valence component for these resonances is negligible because of their small neutron widths.

Theoretical calculations[14] of the splitting of the $p^3/2$ states in ^{41}Ca show strong mixing of the $P^3/2$ shell model state with $(1f^7/2)^2(1d^3/2)^{-2}$ deformed states. If the incoming neutron excites this component of the ^{40}Ca core, then single neutron (El) transitions can readily occur to the $p^3/2$ states because of the large overlap of initial and final state wave functions.

This interaction would not be well correlated with resonance neutron widths and could account for the residual strength of s-wave radiative widths in ^{41}Ca.

The role of core excitations in the closed shell nuclides remains uncertain, but it is clear that the valence model by itself cannot adequately account for the experimental data.

Acknowledgements

Discussions with A. M. Lane, J. R. Bird and R. R. Winters are acknowledged. One of us (BJA) is grateful for the cooperation shown him during an attachment to ORNL.

References

1. A. M. Lane and J. E. Lynn, Nucl. Phys. 17 (1960) 563.
2. R. L. Macklin and B. J. Allen, Nucl. Instr. & Methods 91 (1971) 565.
3. R. L. Macklin, N. W. Hill, B. J. Allen, Nucl. Instr. & Methods 96 (1971) 586.
4. A. R. deL. Musgrove, B. J. Allen, J. W. Boldeman, R. L. Macklin, papers on ^{40}Ca and ^{138}Ba in preparation.
5. J. W. Boldeman, B. J. Allen, A. R. deL. Musgrove, R. L. Macklin, submitted to Nucl. Phys.
6. B. J. Allen and R. L. Macklin, Proc. Int. Conf. Photonuclear Reactions & Applications, Asilomar, 1973.

   B. J. Allen, D. M. H. Chan, A. R. deL. Musgrove, R. L. Macklin, Soviet Nat. Conf. on Neutron Physics, Kiev, 1973.
7. G. Nystrom, B. Lundberg, I. Bergqvist, Physica Scripta 4 (1971) 95, and references therein.
8. U. N. Singh et al., Statistical Properties of Nuclei, Albany 1971, Plenum Press (1972) p. 81.
9. M. J. Kenny, P. W. Martin, C. E. Carlson, J. A. Biggerstaff, Aust. J. Phys. 27 (1974).
10. J. E. Lynn, Theory of Neutron Resonance Reactions, Clarendon Press 1968.
11. A. M. Lane and S. F. Mughabghab, Phys. Rev. C10 (1974) 412.
12. R. E. Toohey and H. E. Jackson, Phys. Rev. C9 (1974) 346.
13. D. M. H. Chan and J. R. Bird, Aust. J. Phys. 24 (1974) 671.
14. W. J. Gerace and A. M. Green, Nucl. Phys. A93 (1967) 110, and references therein.

TABLE 1 - AVERAGE RESONANCE PARAMETERS

Isotope	D (keV)	$10^4 S_0$	$10^4 S_1$	$10^4 S_2$	$\Gamma_\gamma(s)$ (eV)	$\Gamma_\gamma(p)$ (eV)	$\Gamma_\gamma(d)$ (eV)	No. of Resonances	$\rho(\Gamma_n^\ell, \Gamma_\gamma(\ell))$	Γ_γ^V (eV)
Al					(2.3)	2.8	(1.0)			
Si					1.5	3.0	1.4			0.80
^{40}Ca	37	2.9	~0.1	2.3	1.6	0.32	0.60	6 $s^1/_2$	0.4	0.35
^{52}Cr	49	2.5			1.5	0.4		4 $s^1/_2$	0.84	0.82
^{90}Zr	8.9	0.56	3.2		0.25	0.44		37 $p^3/_2$	0.58	0.12
^{138}Ba	7.5	0.9	~0.5		0.31	0.047		10 $s^1/_2$	0.67	0.03

TABLE 2 - AVERAGE CAPTURE CROSS SECTIONS (mb)

E_n (keV)		5-6	10-50	50-100	100-200	200-300	300-400	400-500						$\sigma_M(30)$
^{27}Al ±10%		150	2.9	2.54	2.05	1.02	0.60	1.20						3.9
^{28}Si ±10%			0.16	4.1	0.24	0.17	0.32	0.36						2.0
	2.5-5	5-10	10-20	20-30	30-40	40-50	50-60	60-70	70-80	80-90	90-100	100-150	150-200	
^{40}Ca ±15%	1.2	1.7	14.4	12.8	3.6	9.6	3.3	1.2	0.0	4.1	0.0	3.7	5.4	6.7
^{52}Cr ±25%	0.0	0.14	0.33	13.1	5.1	2.0	14.7	0.49	1.6	0.0	17.7	6.0	2.1	7.3
^{90}Zr ±15%	93.6	63.3	24.2	14.8	12.4	38.1	9.7	16.7	6.3	9.1	14.6	22.3		21.5
^{138}Ba ±20%	7.24	11.8	5.0	4.3	8.4	4.5	8.8	7.5	6.5	5.3				5.7

$\sigma_M(30)$ mb is the Maxwellian average cross section at kT = 30 keV

RADIATION SHIELDING INFORMATION CENTER DATA ACTIVITIES*

R. W. Roussin, B. F. Maskewitz, and D. K. Trubey
Radiation Shielding Information Center (RSIC)
Oak Ridge National Laboratory
Oak Ridge, Tennessee 37830

Activities developed at the Radiation Shielding Information Center (RSIC) play an important role in the utilization of nuclear cross sections in various radiation transport applications and help improve the general utility of the national ENDF/B effort. The activities involving processed and evaluated data libraries on behalf of RSIC's various sponsoring agencies are described.

(Information, cross sections, radiation, shielding, evaluation, processing, analysis)

Introduction

A significant proportion of the activities of the Radiation Shielding Information Center[1] (RSIC) involves data of various kinds but primarily neutron and gamma-ray cross-section data. The reason for this work is that the solution of most shielding (radiation transport) problems requires the use of large computer codes and their corresponding cross section libraries which together adequately treat the physics of neutron and gamma-ray interaction and production. As is discussed later, RSIC is involved in various aspects of this general problem by helping to provide evaluated neutron and gamma-ray cross-section data in standard formats, by packaging and distributing computer codes and associated cross-section libraries, by packaging and distributing specialized libraries of various types, and by assisting in the compilation of benchmark problem data for testing computation methods and cross section data.

The first section which follows outlines the role of RSIC in the cooperative effort to develop evaluated cross section data in the Evaluated Nuclear Data File (ENDF) format.[2] Here the emphasis is on providing neutron, gamma-ray production and gamma-ray interaction cross sections pertinent to radiation transport problems within various disciplines. All efforts are designed to augment and support the national ENDF/B effort. The next section describes activities associated with the acquisition, generation, and distribution of processed data libraries for direct use in treating various types of radiation transport problems. The final section deals with standards and benchmark data activities.

These activities are sponsored by the Reactor Research and Development (RRD) and the Controlled Thermonuclear Research (CTR) divisions of the Energy Research and Development Administration (ERDA), the Defense Nuclear Agency (DNA), and the Electric Power Research Institute (EPRI). They involve cooperation and collaboration with the National Neutron Cross Section Center (NNCSC) at Brookhaven National Laboratory, the Shielding Subcommittee of the Cross Section Evaluation Working Group (CSEWG), the CTR Subcommittee of the United States Nuclear Data Committee, and the ANS-6 Shielding Standards Committee of the American Nuclear Society.

*Research sponsored jointly by the Defense Nuclear Agency and the U.S. Energy Research and Development Administration under contract with the Union Carbide Corporation.

Evaluated Cross Section Data Activities at RSIC

Efforts dealing with evaluated cross sections began with various activities to help meet the needs of the shielding community through CSEWG. These were expanded to include a major effort for the Defense Nuclear Agency and have been extended to a similar program for the CTR neutronics community. All these efforts are designed to feed new evaluated data into the ENDF/B system.

Clearinghouse for CSEWG Shielding Evaluations

RSIC has always been concerned with cross sections and the problems associated with the proliferation of data in non-standard formats. Thus, the development of the ENDF program was supported by RSIC from inception. An RSIC staff member participated in the early planning stages, but more significant contributions were possible once the CSEWG Shielding Subcommittee was organized early in 1967. Since then, RSIC participation has been extensive, with emphasis on areas of vital interest to the shielding community.

RSIC continues to collaborate with NNCSC at Brookhaven National Laboratory and the CSEWG Shielding Subcommittee. The Center's role in this activity is to assist in the acquisition, checkout, and review of "shielding" cross sections in ENDF format which may ultimately be placed in the ENDF/B file. In this context, "shielding" cross sections are evaluations performed in the shielding, radiation effects or weapons communities which are likely to have an emphasis on gamma-ray production cross sections, gamma-ray interaction cross sections, and neutron cross sections in the energy range of interest for shielding with detailed energy and angular distribution resolution.

In preparation for the release of ENDF/B-IV, thirty-eight evaluations were received by RSIC and processed through checking codes, modified to conform to the ENDF format as necessary and forwarded to NNCSC, which prepared and distributed a packet for Phase I testing. These are listed in Table 1. Phase I testing discovers and eliminates clerical and format errors and results in a data set which seems reasonable. Phase II testing involves the use of the data to compare radiation transport calculations with integral experiments and results in knowledge about the adequacy of the data.

To further assist in the Phase I review process, an RSIC representative coordinated the review of structural materials being considered for inclusion in ENDF/B-IV.

In addition to the above activities, RSIC has coordinated the writing of a computer code[3] to translate, and subsequently has translated, earlier versions of the UKAEA library to ENDF/B format for NNCSC. A project currently underway involves working with the evaluators[4] to update the ENDF/B photon interaction cross section library and, for the first time, to provide photon

scattering form factors in the ENDF format for consideration as the official ENDF/B-IV version.

Through active participation in the activities of CSEWG and through cooperation with NNCSC, RSIC strives continually to improve the adequacy of the ENDF/B system as an evaluated library of general applicability.

TABLE 1. ENDF/B-IV "Shielding" Materials Checked by RSIC for CSEWG and NNCSC

Material Name	ENDF/B-IV MAT	In DNA Library
H-1	1269	X
H-2	1120	X
H-3	1169	X
He-4	1270	X
Li-6	1271	
Li-7	1272	
Be-9	1289	X
B-10	1273	
C-12	1274	X
N-14	1275	X
O-16	1276	X
F	1277	X
Na-23	1156	X
Mg	1280	X
Al-27	1193	X
Si	1194	X
Cl	1149	
K	1150	
Ca	1195	X
Ti	1286	
V	1196	
Cr	1191	
Mn-55	1197	
Fe	1192	X
Co-59	1199	
Ni	1190	
Cu	1295	X
Nb-93	1189	
Mo	1287	
Ta-181	1285	X
W-182	1128	X
W-183	1129	X
W-184	1130	X
W-186	1131	X
Au-197	1283	X
Pb	1288	X
U-235	1261	
U-238	1262	
Np-237	1263	
Pu-239	1264	
Pu-240	1265	
Pu-241	1266	

Defense Nuclear Agency Working Cross Section Library

RSIC maintains and distributes the DNA cross-section library.[5] This is a working library in ENDF format whose content can be modified and revised as often as the evaluator deems such changes to be necessary. The key to this approach is a selected evaluator, the person responsible for making the original evaluation for a particular element or elements. He is then responsible for authorizing changes in evaluations for those elements. The evaluated data are for those materials of interest to DNA, whose cross-section values are in a state of rapid change, and emphasis is placed on neutron energies up to 20 MeV and on secondary gamma-ray production. Evaluations of interest to DNA which are not in a state of rapid change are found in the ENDF/B library, which is available in the USA from NNCSC at Brookhaven National Laboratory.

The clearinghouse for the DNA program is RSIC. Initial versions of evaluations are received, processed through checking codes to eliminate obvious format errors, and modified as necessary in collaboration with the evaluator. Next, DNA Phase I data testing is performed whereby selected reviewers are provided with listings, output from checking codes, graphics, etc., and are asked to review the data and feed back their comments. These are relayed to the evaluator and, upon his instruction, appropriate changes are made. Changes are initiated only by the evaluator and each change is documented so that users can, at any time, refer to an identifiable data set when reporting results of their calculations.

Because the data are apt to be revised with some frequency, each evaluation is designated by a DNA MAT number and a MOD number. The DN MAT number is a unique identification number for an evaluation and is usually equal to the corresponding NNCSC-assigned ENDF MAT number plus three thousand for those evaluations which are submitted for inclusion in the ENDF/B library. The MOD number designates the number of times the DNA evaluation has been modified since its initial availability through RSIC.

Since the DNA library is in ENDF format and is available for consideration by CSEWG to become part of the ENDF/B library, the DNA program offers a good opportunity for improving the state of shielding cross sections. Materials from the DNA library which become part of ENDF/B-IV are indicated in Table 1.

The data, along with available documentation, are distributed upon request. The users are asked to feed back any comments they have, based on experience in using the data.

Controlled Thermonuclear Research Evaluated Cross Section Library

An evaluated library for the CTR neutronics community was recommended by the USNDC-CTR Subcommittee, and RSIC was chosen as the center for its establishment and distribution. The library is to be patterned after the DNA Working Cross Section Library so that new measurements can be incorporated, as they become available, into evaluated data files. The emphasis will be in the high energy region (8-15 MeV). As with the DNA project, the CTR library will be in ENDF format and will be available for inclusion into the official ENDF/B library.

Processed Cross Section Data Activities at RSIC

The RSIC Data Library Collection

Since inception, RSIC has been deeply involved with the acquisition, checkout, packaging, and distribution of a computer code library. Subsequently, a data library collection has been developed which includes not only cross-section libraries, but other nuclear data and also radiation transport results. The data sets are packaged in a manner analogous to the RSIC Computer Code Collection (CCC). Each data set, packaged as a unit, carries a Data Library Collection (DLC) number. As with the code packages, a particular data package does not remain static but is subject to revision, updating, and expansion as required. Such changes are announced in the RSIC Newsletter.

Data libraries were first announced as available from RSIC near the end of 1968. At that time it became evident that a collection of data libraries would be an extremely helpful companion to the RSIC Computer Code Collection.[6] The main objective is the interchange of

technology among installations engaged in radiation transport research, development, and application. A partial listing of the current contents of the Data Library Collection is given in Table 2.

The philosophy behind the packaging and distributing of these data libraries is to preserve and make available in a computer-readable form, data which may be useful to those utilizing or performing radiation transport calculations. Since this usually involves the use of large computer programs, several of these libraries are multigroup cross sections in the format utilized by many such programs.

Documentation is very important. The abstract format used for the DLC[7] sets is similar to that used to describe the code packages. Care was taken to make the format include all of the information necessary for adequately describing the contents and purpose of each data library. The main purpose of the abstracts is to give to a potential data library user several criteria for deciding whether or not he wishes to obtain the data.

Present activities with sponsors (on behalf of their contractors) has involved RSIC in projects where processed cross section libraries are generated directly for a particular user community. These activities on behalf of the DNA and CTR communities are summarized below.

TABLE 2. Partial Contents of RSIC Data Library Collection

Name	Comments (Contributor)*
DLC-2/ 100G	100 group, P_8, neutron cross sections by SUPERTOG from ENDF/B-III (ORNL).
DLC-3/ MEP	Analyzed cascade calculation results for n,p,π on several materials (ORNL).
DLC-7/ HPICE	Photon Interaction Library in ENDF format (LLL, NBS).
DLC-8/ BP	Input data for benchmark problems in ORNL-RSIC-25 (ORNL).
DLC-12/ POPLIB	Photon production library for POPOP4 (ORNL).
DLC-15/ STORM-ISRAEL	Storm-Israel photon interaction library-ENDF format (LASL).
DLC-16/ COBB	123 group neutron cross sections from ENDF/B-II for XSDRN (ORNL).
DLC-18/ NAB	100 group neutron cross sections used in analysis of ORNL-LMFBR sodium experiment (ORNL).
DLC-23/ CASK	22-18 group coupled cross sections for shipping cask analysis (ORNL).
DLC-24/ SINEX	100 group neutron reaction cross sections for ENDF/B-III library (ORNL).
DLC-27/ AMPX01	104-22 coupled cross sections by AMPX for concrete elements (ORNL).
DLC-28/ CTR	52-21 coupled cross sections used in ORNL CTR neutronics (ORNL).
DLC-29/ MACKLIB	100 group neutron kerma factors by MACK from ENDF/B-III (U. Wisc.)
DLC-30/ DECAYREM	Radioactive decay data, EXREM III format, many materials (ORNL).
DLC-31/ DPL	Defense Nuclear Agency processed cross section library - multigroup data ANISN format - point data SAM-CE format (ORNL, MAGI).
DLC-33/ MONTAGE	100 group neutron activation cross sections for CTR studies (LASL).

*Library contributors: ORNL, Oak Ridge National Laboratory, Oak Ridge, Tenn.; LLL, Lawrence Livermore Laboratory, Livermore, Ca.; NBS, National Bureau of Standards, Washington, D.C.; LASL, Los Alamos Scientific Laboratory, Los Alamos, N.M.; U. Wisc., Nuclear Engineering Department, U. Wisconsin, Madison, Wis.; MAGI, Mathematical Applications Group, Inc., Elmsford, N.Y.

Special DNA Processed Cross Section Libraries

A new class of data libraries was developed in cooperation with the DNA Radiation Transport Program. They are identified as Data Library Collection 31 (DLC-31) and include both multigroup and point cross section data. A coupled 37-neutron, 21-gamma-ray-group library in ANISN format was generated at ORNL[8] from recent ENDF/B and DNA evaluations for many materials using the AMPX[9] cross section processor. Documentation includes results of calculations of neutron sources in air and concrete. Other sets of data suitable for use in the SAM-CE[10] Monte Carlo code were generated at MAGI. They can be used to perform neutron, secondary gamma-ray, and primary gamma-ray transport calculations.

Special CTR Processed Cross Section Library

Using specifications developed through conversations and correspondence with various members of the CTR neutronics community, RSIC will direct the generation of a coupled 156-neutron and 23-gamma-ray multigroup cross section set as the beginning of a CTR Processed Data Library. Most of the materials were taken from the ENDF/B-IV and DNA evaluated libraries. Allowance is made for self-shielding and temperature dependence using the Bondarenko[11] scheme. The smooth weighting function used has Maxwellian weighting for the thermal group, a 1/E slowing down spectrum tied to a fission spectrum and joined at high energies to a D-T broadened 14 MeV spectrum. The library will be generated using a combination of the MINX[12] neutron processor and various modules of the AMPX code system with output in the AMPX interface format. In the generation process, a new module for the AMPX system will be programmed to perform the interpolation and iteration required to determine appropriate self-shielded and temperature-broadened cross-section values for a given problem. Special cross section handling codes will be packaged with the data to permit the user to allow for composition and temperature dependence for a specific problem and/or to collapse the data to reduce the group structure down to a number considered reasonable for a specific calculation. It is anticipated that the library will also be available in CCCC format.[13]

Standards Activities in RSIC

A continuing project, in cooperation with the American Nuclear Society, is to collect, edit, and publish reference data in the form of "benchmark

problems." The objective is to compile in convenient form a limited number of well-documented problems in radiation transport which will be useful in testing computational methods used in shielding analysis. The problem solutions, having been determined by several methods, should be representative of the state of the art. The problem descriptions are published[14] in looseleaf form so that revisions and additions can be easily made. Contributions to the benchmark collection are sought by the ANS Benchmark Problem Group. In conjunction with the benchmark work, data sets are packaged which allow the recalculation, with a particular calculational method, of already published results. An example is the data in DLC-8 which allows the calculation of ANS Shielding Benchmark Problem Number 3. This kind of calculation is useful for testing a new computer code or theoretical treatment.

Conclusions

It has always been RSIC policy to discuss with users their needs and recommend codes and data libraries. Insofar as possible, we assist those who are implementing codes and data at their installations. In cases where we lack experience to advise in particular problem areas, we call upon other experienced personnel locally and elsewhere to help them. This takes the form of offering advice on solving particular problems, as well as helping to diagnose problems in implementing calculational procedures.

As always, RSIC relies on members of the radiation transport and shielding community to share their ideas, codes, and data so that technology as a whole may be advanced.

In summary, RSIC strives to enhance the process of utilizing nuclear cross sections in various radiation transport applications and to improve the general utility of the national ENDF/B effort.

References

1. D. K. Trubey, "The Radiation Shielding Information Center - A Technical Information Service for Nuclear Engineers," Nuc. Eng. Des. 9, 392-395 (1969).

2. M. K. Drake, Editor, "Data Formats and Procedures for the ENDF Neutron Cross Section Library," BNL 50274 (T-601) ENDF-102, Vol. I (1961), and D. J. Dudziak, Compiler, "ENDF Formats and Procedures for Photon Production and Interaction Data," LA-4549 (ENDF-102, Rev., Vol. II).

3. R. Q. Wright, S. N. Cramer, and D. C. Irving, "UKE - A Computer Code for Translating Neutron Cross Section Data from the UKAEA Nuclear Data Format to the Evaluated Nuclear Data File Format," ORNL-TM-2880, ENDF-134 (March 1970).

4. J. H. Hubbell *et al*, "Tables of the Atomic Form Factor and Incoherent Scattering Function for $0.005 < \sin(\Theta/2)/\lambda \leq 10^9$ $\mathring{A}^{-1}$, and Photon Coherent and Incoherent Scattering Cross Sections for 0.1 keV $\leq E_\gamma \leq 100$ MeV, for $1 \leq Z \leq 100$," to be published in J. Phys. & Chem. Ref. Data (NBS, D. R. Tide, Ed.)

5. R. W. Roussin, "The Defense Nuclear Agency Working Cross Section Library: Description and Contents," ORNL-RSIC-34 (August 1972).

6. Betty F. Maskewitz, "Abstracts of the Computer Code Packages Assembled by the Radiation Shielding Information Center," ORNL-RSIC-13, Vols.I - III.

7. R. W. Roussin, "Abstracts of Data Library Packages Assembled by the Radiation Shielding Information Center," ORNL-RSIC-30 (1972).

8. D. E. Bartine *et al*, "Production and Testing of the DNA Few-Group Cross-Section Library," Trans. Am. Nucl. Soc., 19, 472 (1974).

9. N. M. Greene *et al*, "AMPX: A Modular Code System for Generating Coupled Multigroup Neutron-Gamma Libraries from ENDF/B," ORNL-TM-3706 (to be published).

10. M. O. Cohen *et al*, "SAM-CE: A Three Dimensional Monte Carlo Code for the Solution of the Forward Neutron and Forward and Adjoint Gamma-Ray Transport Equations - Revision 3," DNA 2830F-B (1973).

11. I. I. Bondarenko, Editor, "Group Constants for Nuclear Reactor Calculations," Consultants Bureau, New York (1964).

12. C. R. Weisbin *et al*, "MINX - A Multigroup Interpretation of Nuclear X-Sections," Trans. Am. Nucl. Soc. 16, 127 (1974).

13. B. M. Carmichael, Compiler, "Standard Interface Files and Procedures for Reactor Physics Codes, Version III," LA-5486-MS (1974).

14. A. E. Profio, Editor, "Shielding Benchmark Problems," ORNL-RSIC-25 (Sup. 1, 1970, Sup. 2, 1974).

EVALUATION OF THE RESONANCE PARAMETERS AND CAPTURE CROSS SECTION FOR CHROMIUM UP TO 600 keV

D. ABRAMSON, J.C. BLUET, P. FARDEAU

C.E.N. - CADARACHE

Experimental results are examined. An extensive comparison of recent sets of results allows a point-wise evaluation of the capture cross section versus energy. Moreover a set of resonance parameters has been chosen. The curve calculated with these parameters and a smoothly varying background agrees pretty well with the point-wise evaluation.

(Chromium, capture, neutron, cross section, evaluation, resonance)

Introduction

The importance of the knowledge of structural material cross sections for reactor design is quite obvious. As far as the chromium is concerned, and more specifically for the capture cross section in the energy range of separated resonances, the ENDF/B IV* file is identical to ENDF/B III which did not take into account the recent experiments made by the Karlsruhe team (BEER, FROHNER, SPENCER[1,2]) and by the Cadarache team (LE RIGOLEUR, ARNAUD[3,4]).

The purpose of the present work is the analysis of all the measurements. A special attention will be devoted to the results from Karlsruhe[1,2], Cadarache[3,4], and RPI[5], which are more complete and obtained with a good energy definition. Different aspects and detailed examples of the resulting evaluation are given.

Measurements description and analysis

The first measurements have been made with low energy resolution on natural chromium.

BELANOVA[6] (USSR) (1960) used several photoneutron sources with the shell transmission technique : Sb-Be giving 25 keV, Na-D_2O : 220 keV, Na-Be : 878 keV.

DIVEN et al[7] (Los Alamos) (1960) used a large liquid scintillator to detect the capture γ rays. Neutrons were produced in the range of 175 keV ± 25 to 1000 keV ± 90, with a pulsed Van de Graaff in order to reduce the background. The standardization was made from $(\sigma_{n,f} + \sigma_{n,\gamma})$ cross section.

GIBBONS, MACKLIN et al[8] (ORNL) (1960) used the same technique at 30 keV ± 7 and 65 keV ± 20. Data were normalized to the In cross section which was obtained from the shell transmission method.

STAVISKII and SHAPAR[9] (USSR) (1962) from 30 keV to 1 MeV (Energy spread ± 20 keV), detected the γ rays with a Ca-F2 crystal. They normalized data to DIVEN's results at 400 keV.

KAPCHIGASCHEV and POPOV[10] (USSR) (1960) measured ^{50}Cr, ^{52}Cr, ^{53}Cr, and natural chromium from 2.9 eV to 50 keV with the lead slowing down time spectrometer. They normalized data to the thermal capture cross sections of the same isotopes.

SPITZ et al[11] (South Africa) (1968) used a MOXON-RAE detector with fast time of flight technique from 8 to 120 keV, on a pulsed Van de Graaff and normalized data to In. Their energy resolution is better than the above-mentioned works but is not satisfactory.

The following measurements have been made with a good resolution. They showed a resonance structure in the capture cross section.

STIEGLITZ et al[5] (RPI) (1970) performed neutron capture measurements from 0.1 to 200 keV and transmission measurements from 0.1 to 300 keV on enriched samples of ^{50}Cr, ^{52}Cr, ^{53}Cr, and ^{54}Cr, with time of flight techniques on the RPI LINAC. The detector was a large liquid scintillator located on a 25,7 m flight path. The experimental resolution was about 0.6 ns m-1. The neutron detector was a $10B_4C$-NaI neutron detector located behind the capture detector on a 27,9 m flight path. The shape of the flux versus energy was determined with this ^{10}B detector. The absolute calibration was determined at 5.19 eV by the saturated resonance method using an Ag screen. The efficiency of the capture detector was calculated from the measured capture γ ray spectrum.

SPENCER at al[1,2] (Karlsruhe) (1972) made measurements from 6,5 to 198,9 keV on ^{50}Cr, ^{52}Cr, and ^{53}Cr using fast time of flight on the pulsed Van de Graaff ; the detector was also a large liquid scintillator located on a 2 m flight path. The resolution was 2 $ns.m^{-1}$. The measurements are relative to Au. The transmission measurements made at Karlsruhe from 10 to 250 keV used ^{10}B-NaI detectors, or proton recoil scintillators, or ^{6}Li glass scintillator with a flight path of 4,96 m and an energy resolution in the 0.2, 0.5 $ns.m^{-1}$ range.

LE RIGOLEUR et al[3,4] (Cadarache) (1973 and 1975) made measurements on natural chromium from 15 to 65, from 90 to 160 and from 216 to 540 keV using a pulsed Van de Graaff. The γ were detected with a MAIER-LEIBNITZ detector (using the total energy weighting technique). Absolute neutron flux was measured with a calibrated ^{10}BNaI detector or a Li^6 glass scintillator. The flight path was 85 cm and the experimental resolution was 1.8 ns/m.

These last three measurements show large enough energy overlappings to allow comparison.

.../....

* Evaluated Nuclear Data File of the neutron cross section library.
National Neutron Cross Section Center
Brookhaven.

There is a systematic disagreement between the resonance energies of SPENCER and those of STIEGLITZ. As the energy shift varies according to $E^{3/2}$, an error in the time scale can be suspected. The resonance energies of LE RIGOLEUR are generally nearly the same as those of STIEGLITZ. As an example the 22-58 keV range is shown in Fig. 1. The curves of STIEGLITZ and SPENCER for capture cross sections of the natural chromium are derived from the results they obtained with separated isotopes. The cross sections measured by LE RIGOLEUR are in good agreement with SPENCER's, but much lower than STIEGLITZ's sometimes by a factor of two. Although the resonance parameters given by STIEGLITZ and SPENCER are generally in good agreement. This might show that the difference comes from the background estimation. Actually, one of the most serious problems in capture cross section measurements is the determination of the background which is due to the sensitivity of the capture detector to scattered neutrons. This time dependant background is usually measured in replacing the sample by a carbon or a lead scatterer. So this technique is not always adequate, specially near the LINAC where the energy range of the incident-neutron spectrum is broader than the energy range of a pulsed Van de Gaaff. LE RIGOLEUR has made a detailed study of this background by experiments[4] and Monte Carlo calculations. He found cross section values similar to SPENCER's. In the 15-65 keV range, we took an average of data from SPENCER and LE RIGOLEUR.

In the 90-160 keV the capture cross sections obtained in these experiments agree well enough according to the experimental accuracy. But they are much higher than the values obtained in former experiments.

Resonance parameters

Resonance energies E_R, neutron widths Γ_n and the statistical factor g, are derived from transmission experiments by shape analysis technique. Capture measurements using area analysis gives :

$$g\Gamma_n\Gamma_\gamma / (\Gamma_n + \Gamma_\gamma)$$

Then the radiation width Γ_γ can be extracted. This process can be used conveniently for most of the "s" wave levels and for the broadest "p" levels. However, in general, the "p" wave resonances (or higher angular momentum resonances) appears only in the capture data. So for narrow resonances, the

$$g\Gamma_n\Gamma_\gamma / (\Gamma_n + \Gamma_\gamma)$$

quantity is only known.

There are also older transmission measurements for instance the Duke University ones[13, 14, 15]. The accuracy is low, but the measurements have been extended till 650 keV. The resonance parameters obtained by the RPI team and the KFK team, agree generally well according to the diversity of experimental techniques. For instance, Tables 1 list the reported and recommended values of the resonance parameters of ^{53}Cr up to about 60 keV.

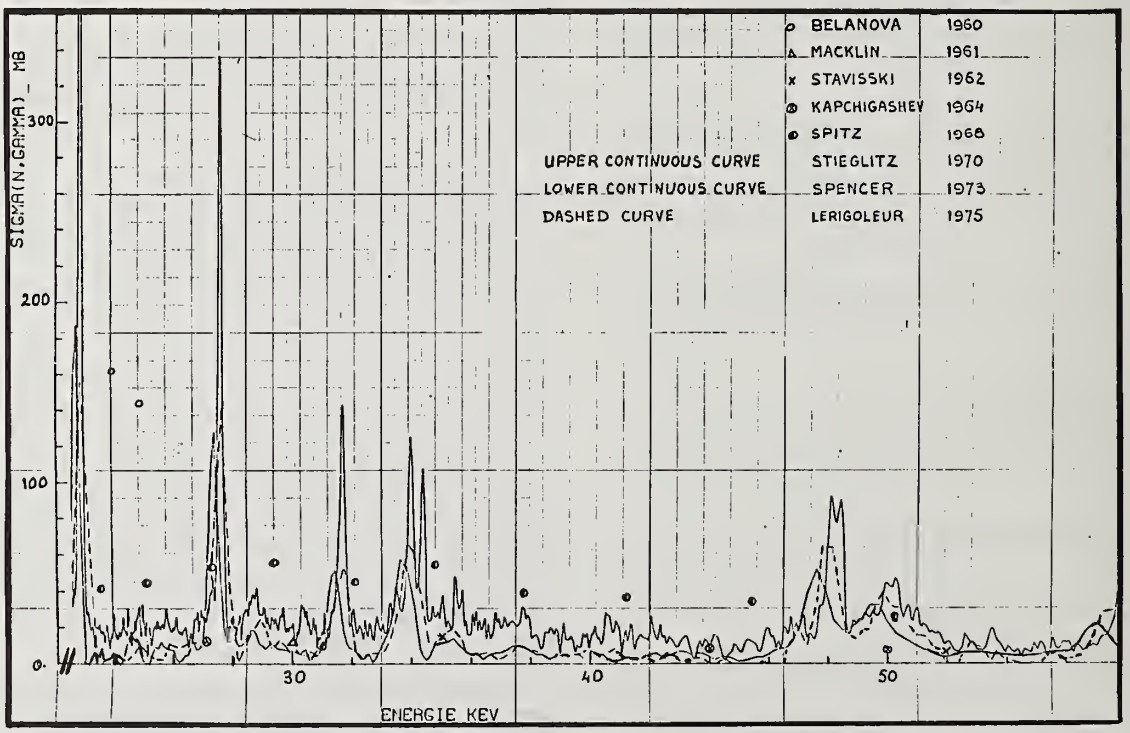

Fig. 1. $\sigma_{n,\gamma}$ for natural chromium from 22 to 58 keV - Experimental results.

^{53}Cr s wave resonance parameters

ORNL[17]		RPI[5]				KFK[2,18]				ENDF				This work			
E_R (KeV)	Γ_n (ev)	E_R (KeV)	J	Γ_n (ev)	Γ_γ (ev)	E_R (KeV)	J	Γ_n (ev)	Γ_γ (ev)	E_R (KeV)	J	Γ_n (ev)	Γ_γ (ev)	E_R (KeV)	J	Γ_n (ev)	Γ_γ (ev)
3,6	1,57																
4,2	445	4,185±0,015	1	1520± 80	3,23±0,45					4,185	1	1520	3,23	4,185	1	1520	3,23
5,4	212	5,67 ±0,025	2	220± 15	1,33±0,20					5,67	2	220	1,33	5,67	2	220	1,33
6,6	357	6,74 ±0,035	1	1200±100	5,28±0,8					6,74	1	1200	5,28	6,74	1	1200	5,28
8,0	10^{-3}	8,18 ±0,045	2	1030± 90	3,25±0,47	8,18	2		3,2±0,3	8,18	2	1030	3,25	8,18	2	1030	3,25
10,5	224																
19,3	132	19,75 ±0,06	2	107± 15	0,78±0,09	19,53	2	130± 20	0,8±0,1	19,75	2	107	0,78	19,7	2	120	0,8
25,3	237	25,95 ±0,08	2	235± 20	0,61±0,07	25,64	2	220± 30	0,7±0,1	25,95	2	235	0,61	25,9	2	225	0,65
26,4	350	27,24 ±0,09	1	760± 70	1,57±0,17	26,95	1	700±100	1,6±0,1	27,24	1	760	1,57	27,2	1	720	1,6
28,8	555	29,57 ±0,10	2	360± 35	1,21±0,14	29,23	2	330± 30	0,9±0,1	29,57	2	360	1,21	29,5	2	340	1,05
		66,1 ±0,4	2	5100±700	0,80±0,10	65,7	2	4500± 70	3,1±0,3	66,1	2	5100	0,8	66,1	2	4700	2

^{53}Cr p wave resonance parameters

RPI[5]		KFK[2,18]				ENDF				This work				
E_R (KeV)	$g\Gamma_n\Gamma_\gamma/\Gamma_t$ (ev)	E_R (KeV)	$g\Gamma_n\Gamma_\gamma/\Gamma_t$ (ev)	$g\Gamma_n$ (ev)	$g\Gamma_\gamma$ (ev)	E_R (KeV)	J	Γ_n (ev)	Γ_γ (ev)	E_R (KeV)	J	Γ_n (ev)	Γ_γ (ev)	$g\Gamma_n\Gamma_\gamma/\Gamma_t$ (ev)
12,1 ± 0,04	0,185 ± 0,031	12,12 ± 0,08	0,17 ± 0,04			12,1	2	0,584	0,6	12,1	2	0,56	0,6	0,18
12,9 ± 0,04	0,110 ± 0,020					12,9	2	0,249	0,6	12,9	3	0,16	0,6	0,11
14,6 ± 0,05	0,130 ± 0,025					14,6	2	0,318	0,6	14,6	1	0,84	0,6	0,13
20,2 ± 0,08	0,385 ± 0,070	20,15 ± 0,08	0,47 ± 0,05							20,2	3	2,7	0,6	0,43
		21,16 ± 0,08	0,09 ± 0,03											
22,4 ± 0,10	0,145 ± 0.026	22,35 ± 0,09	0,23 ± 0,04			22,4	2	0,378	0,6	22,4	2	0,62	0,6	0,19
		25,61 ± 0,12	0,028 ± 0,005											
28,8 ± 0,11	0,650 ± 0,120	28,70 ± 0,13	0,64 ± 0,05							28,8	3	2,7	1	0,64
31,5 ± 0,13	0,310 ± 0,060	31,46 ± 0,15	0,28 ± 0,03			31,5	2	2,862	0,6	31,5	2	2	0,6	0,29
32,0 ± 0,14	0,230 ± 0,045	31,94 ± 0,15	0,26 ± 0,03			32	2	0,952	0,6	32	2	1,2	0,6	0,25
34,9 ± 0,15	0,320 ± 0,065	34,9 ± 0,2	0,27 ± 0,03			34,9	2	3,491	0,6	34,9	3	0,8	0,6	0,3
37,7 ± 0,7	0,350 ± 0,070	37,6 ± 0,2	0,26 ± 0,03			37,7	2	8,4	0,6	37,7	2	2,4	0,6	0,3
42,4 ± 0,19	0,210 ± 0,040	42,2 ± 0,2	0,31 ± 0,04			42,4	2	0,764	0,6	42,4	3	0,58	0,6	0,26
43,2 ± 0,2	0,200 ± 0,038	43,0 ± 0,3	0,29 ± 0,05			43,2	2	6,86	0,6	43,2	2	1,1	0,6	0,24
47,1 ± 0,22	0,370 ± 0,070	46,70 ± 0,07	0,45 ± 0,05	≤ 20	≤ 0,46					47,1	3	23	0,48	0,42
49,8 ± 0,24		49,6 ± 0,3	0,27 ± 0,04							49,8	3	0,63	0,6	0,27
51,0 ± 0,26		50,70 ± 0,08	0,16 ± 0,05	≤ 30	≤ 0,16					51	1	80	0,43	0,16
53,5 ± 0,27	0,400 ± 0,075	53,2 ± 0,3	0,56 ± 0,08							53,5	3	6,4	0,6	0,48

Tables 1.

Results of our evaluation

The evaluated libraries use principally two types of data presentation ; pointwise sets of cross sections versus energy (UKNDL*), or sets of resonance parameters jointed to a varying background (ENDF/B). The first way is simple. It does not need a theoretical formalism and is convenient to energy group calculations. So we have produced a UKNDL format evaluation. (Data File number = 446). The energy points are identical with those of previous UKNDL chromium evaluation. The intervals between them are rather large and involve averaging calculations. According to the energy range we used the experimental results in different ways for instance :

* United Kingdom Nuclear Data Library-UKAEA.

I. In the low energy range below 0,2 keV, we took the results obtained by KAPCHIGASCHEV. In this range, the scattering and capture cross sections are following the 1/V law. But at higher energies, on account of large s wave scattering resonances, data are too low.

II. In the 0,7 keV - 8 keV range, we took STIEGLITZ's results.

III. In the 15-90 keV range, we took an average of the values from SPENCER and those from LE RIGOLEUR.

IV. In the 90-200 keV range, we took an average of the three experimental results, the SPENCER's data being shifted in energy.

V. In the 200-550 keV range, the only recent measurements have been performed by LE RIGOLEUR.

.../....

Cadarache Group N°	Energy range	Capture (mb)	
		UKNDL DFN = 45 Version D (Cadarache set).	UKNDL DFN=446 Version A (Present evaluation).
4	1.360meV 882.13keV	3.5	3.4
5	882.13keV 498.65	4.2	3.6
6	498.65 " 302.45 "	3.7	4.1
7	302.45 " 183.44 "	3.7	4.6
8	183.44 " 111.26 "	4.1	6.3
9	111.26 " 67.48 "	3.6	9.6
10	67.48 " 40.93 "	5.4	8.9
11	40.93 " 24.83 "	3.5	15.0
12	24.83 " 15.06 "	5.5	16.8
13	15.06 " 9.13 "	14.2	33.5
14	9.13 " 5.54 "	36.7	133.3
15	5.54 " 3.36 "	41.7	127.3
16	3.36 " 2.04 "	39.3	81.7
17	2.04 " 1.24 "	67.7	234.1
18	1.24 " 0.75 "	27.1	89.9
19	750 eV 454.71 eV	21.9	45.4
20	454.71 " 275.79 "	26.5	40.2
21	275.79 " 101.46 "	37.6	42.5
22	101.46 " 22.64 "	66.2	66.2

Table 2.

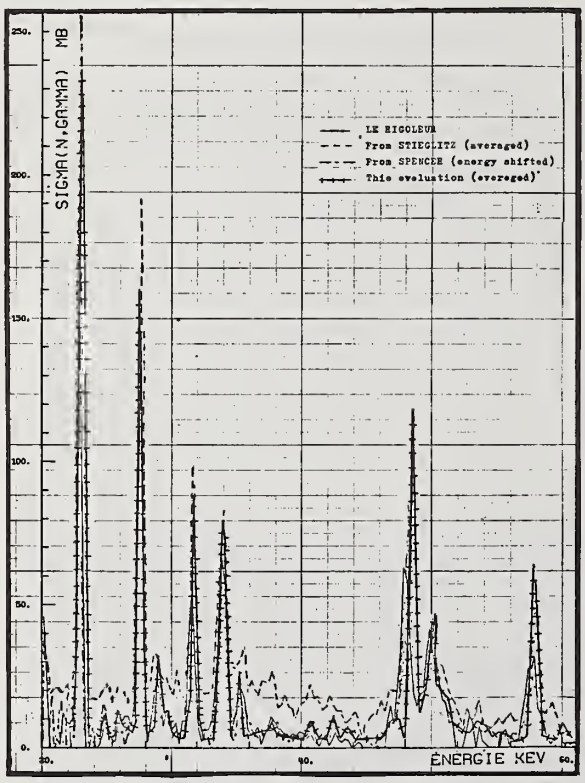

Fig. 2.

Table 2. gives a comparison between group cross section calculated from this evaluation and from the former UKNDL file used at Cadarache.

Group cross sections calculated from ENDF/B IV have intermediate values between the two UKNDL evaluations. It is obvious that most of the new values are higher than the former ones. From 1 to 100 keV the increase reaches 400 %.

We also worked with resonance parameters in order to present our evaluation in ENDF/B format. Indeed the ENDF/B IV evaluation reproduces up to 200 keV only STIEGLITZ's results. The resonance parameters are exactly STIEGLITZ's ones ; the background is not at all smooth. We try to give better resonance parameters ; we introduce them in a BREIT-WIGNER calculations and adding a smoothly varying background we find a curve of which Fig. 2. shows a part. An average with energy is used to allow an easier comparison with experimental curves.

Our work will be completed by the analysis of the other cross sections in order to achieve a coherent evaluation.

References

1. SPENCER R.R., BEER H. and FRÖHNER P.H. KFK 1517 (1972)
2. SPENCER R.R., BEER H. - KFK 2046 (1973)
3. LE RIGOLEUR C., ARNAUD A. - KFK 2046 (1973)
4. LE RIGOLEUR C., ARNAUD A. - This conference Washington 1975.
5. STIEGLITZ R.G., HUCHENBURY R.W. and BLUCK R.C. - Nucl. Phys. A 163, 592 (1971)
6. BELANOVA T.S. - Zh. Eksp. tea. Fiz. 34, 574 (1958)
7. DIVEN B.C. et al - Phys. Rev. 120, 556 (1960)
8. GIBBONS J.H. et al - Phys. Rev. 122, 182 (1960)
9. STAVISKII Y. and SCHAPAR A.V. - Atomnaya Energiya 10, 264 (1961) - Atomnaya energiya 12, 514 (1962)
10. KAPCHIGASCHEV S.V. and POPOV Y.P. - Atomnaya energiya 15, 120 (1965)
11. SPITZ L.M. - Nucl. Phys. A 121, 655 (1968)
12. COTE R.E. et al - Phys. Rev. 111, 288 (1958)
13. BILPUCH E.G. et al - Ann. Phys. 14, 387 (1961)
14. BOWMAN C.D. et al - Ann. Phys. 17, 310 (1962)
15. FARRELL J.A. et al - Ann. Phys. 37, 367 (1966)
16. JACKSON H.E. and STRAIT E.M. - Phys. Rev. C4 - 1314 (1971)
17. GOOD C.D. et al - Phys. Rev. 151, 912 (1966)
18. MULLER K.N. and ROMR G. - Nucl. Phys. A164 97 (1971).

REPRESENTATION OF THE NEUTRON CROSS SECTIONS IN THE UNRESOLVED RESONANCE REGION*

G. de Saussure and R. B. Perez
Oak Ridge National Laboratory
Oak Ridge, Tennessee 37830

We discuss some limitations of the statistical approach to the representation of cross sections in the unresolved region and suggest that the actual Doppler-broadened cross sections should be used instead.

(Neutrons, cross sections, unresolved, resonances, reactors, ENDF/B)

Introduction

The low-energy neutron cross sections of the heavy elements can be described with resonance parameters. Those parameters may be obtained by analyzing the total and partial cross sections, although in many cases, and particularly for the fissile nuclei, the analysis does not yield unique values for the resonance parameters.

Above the resolved resonance region, there is an unresolved region where the cross sections show considerable structure but where the resonance parameters cannot be obtained because the resonances overlap. The widths of the levels broadened by the Doppler effect and the instrumental resolution are comparable to the level spacing.

It is important to represent the cross sections in the unresolved region as accurately as possible, because of the large contribution of this energy region to the Doppler coefficient of reactivity of fast reactors.

It has become the custom to describe the cross sections in the unresolved region by specifying average values and distribution functions of the resonance parameters. Resonance self-protection factors can then be computed by appropriate statistical techniques.

In this paper we review some of the limitations of this statistical approach. We then show that with present neutron cross section technology it is possible to perform measurements that have sufficient energy resolution to permit the direct calculation of the Doppler-broadened cross sections needed for reactor calculations. This direct use of the actual cross sections would avoid some of the problems associated with the statistical approach, and hence it should be preferred.

The Statistical Approach and Its Limitations

The statistical treatment of the unresolved region has been described by Greebler and Hutchins,[1] Brissenden and Durston,[2] Dyos,[3] Levitt,[4] and others.[5] It is based on the statistical theory of nuclear reactions.[6] The cross sections are specified by the average values and distribution functions of the resonance parameters; the required statistical properties of the cross sections can then be obtained numerically, by the generation of ladders of pseudo resonances, and in some cases analytically.[7]

The development of this statistical approach was initiated at a time when very few good-resolution measurements above a few keV were available, and before intermediate structure in heavy nuclei had been observed.

Kelber and Kier,[8] and Dyos and Stevens[9] have investigated the statistical uncertainty inherent in the statistical approach: even if the average resonance parameters and the distribution functions could be known exactly, the computed reactor parameters would have a statistical uncertainty, since they are functions of a finite sample of resonances which may have properties differing from those of the average resonances. For example, Dyos and Stevens have shown that when the partial infinitely dilute resonance integral of ^{238}U between 4 and 5 keV is computed by the statistical approach, the probable statistical error is about 10%. Kelber and Kier have shown that the probable error in the statistical computation of the fissile component of the Doppler coefficient of reactivity is almost as large as the magnitude of this component!

In addition to this error inherent in the statistical approach, there are large uncertainties in the values of the average resonance parameters and some questions about the validity of the model from which the distribution functions of the resonance parameters are derived.

The average values of the resonance parameters in the unresolved region must be obtained by extrapolating values obtained in the resolved region and by analyzing the average cross sections and the fluctuations of the cross sections around their average values. However, the values of the resonance parameters in the resolved region often have very large uncertainties, particularly for the fissile isotopes where the multi-level analysis is not unique[10] and where a large percentage of the levels are missed.[11] Furthermore, for the fissile isotopes, only s-wave parameters may be obtained; even for the fertile isotopes some p-wave parameters (such as the radiation widths) cannot be determined reliably; hence the extrapolation of the resolved resonance parameters to higher energies and angular momenta must heavily rely on theoretical models.

The analysis of the average cross sections[12] and of the fluctuations[13] yields relations between the average resonance parameters, but these relations are usually not sufficient to determine uniquely all the average parameters.

In recent years intermediate structure has been observed in a number of heavy nuclei cross sections particularly important for reactor calculations,[14-17] such as the fission and capture cross sections of ^{235}U, ^{238}U, ^{239}Pu, and ^{240}Pu. This intermediate structure may be caused by doorway states in the entrance (neutron) channel[18] or by the coupling of the levels of the first and second wells of the fission potential barrier.[19]

The intermediate structure complicates considerably the statistical representation of the cross sections: First, the distribution laws of the resonance parameters are based on the statistical model of nuclear reactions which is inconsistent with intermediate structure, particularly where the strength function varies rapidly with energy. Second, the fluctuations of the cross sections are caused partly by changes in the average value of the resonance parameters, due to the doorway states, and partly by the fluctuations of the individual parameters around their average values. In general, there is no way to separate clearly these two causes of fluctuations.

A number of improvements in the statistical representation of cross sections have been suggested: "forced sampling" may be used in the construction of

ladders to ensure that the pseudoresonances reproduce low resolution experimental data.[2,3] This technique is limited to the construction of ladders and is not very practical when the fluctuations in the cross sections exceed the expected value, because they are due to intermediate structure.

In the ENDF/B-IV description of some cross sections, the "average" resonance parameters are made to vary rapidly with energy: The ^{235}U average parameters are redefined at five energies between 82 and 100 eV, hence "average parameters" apply only to about six levels! Such an approach must make an arbitrary division between fluctuations in the average parameters due to intermediate structure and fluctuations of the parameters around their average values. There is no guarantee that such a representation will yield the correct probability distribution of the cross sections, and hence the correct self-shielding factors.

An additional important objection to the statistical representation of cross sections is that this treatment is based on the assumption that the actual value of the cross section at a given energy is unimportant, the only relevant quantity being the probability distribution of the cross section. This assumption does not seem reasonable. Figure 1 shows the total cross section of iron,[20] and Fig. 2 shows two measurements of the capture cross section of ^{238}U;[21] in the core of a fast reactor which contains much iron, the neutron flux will "peak" at the position of the minimum in the iron cross section near 24 keV. It seems relevant to ask whether the iron cross section minimum "lines up" with a maximum or a minimum of the ^{238}U capture cross section. Clearly, the ENDF/B-IV statistical representation of the ^{238}U cross sections shown in Fig. 2 cannot provide an answer to such a question.

We have reviewed a few of the problems associated with the statistical approach to the unresolved region. We will now show how the results of measurements could be used directly (that is, without going through the step of generating statistical resonance parameters) to obtain those cross sections needed for reaction calculations.

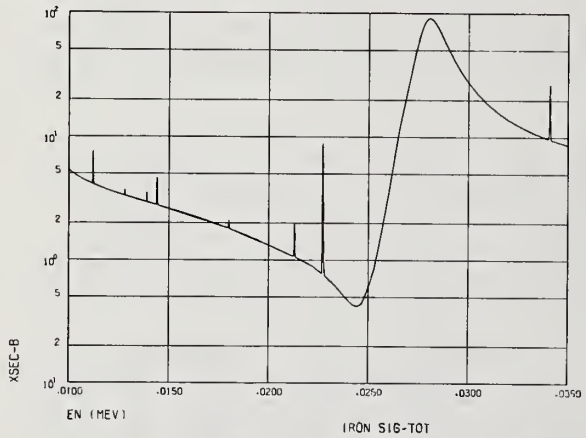

FIG. 1. Iron total cross section (10-35 keV).

Doppler Broadening and Resolution Broadening

Harris[22] and Fröhner[23] have given elegant proofs of the fact that if a Doppler broadened cross section is known for a temperature, T_1, the Doppler broadened cross section for any higher temperature, T_2, can be obtained by an appropriate convolution. If the broadening kernel is approximated by a Gaussian, the relation follows from a well-known property of the convolution of two Gaussians, and can be expressed as:

$$\sigma_\Delta(E,T_2) = \frac{E^{-1/2}}{\pi^{1/2}\Delta}\int E'^{-1/2}\,\sigma_\Delta(E',T_1)e^{-[(E-E')/\Delta]^2}dE' \quad (1)$$

and

$$\Delta^2 = \frac{4k(T_2 - T_1)}{A}E \quad , \qquad T_2 > T_1 \quad , \qquad (2)$$

where we use common notation.

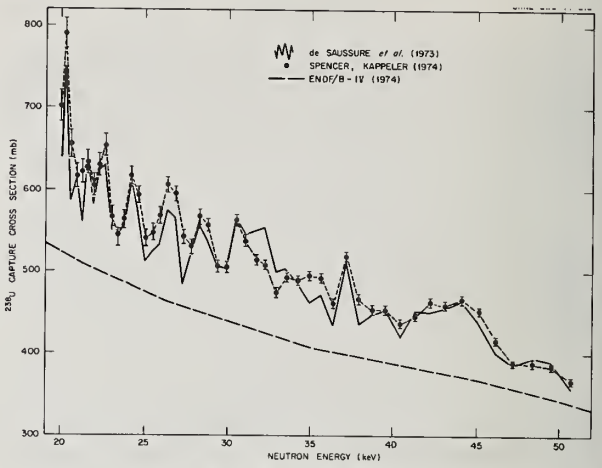

FIG. 2. ^{238}U capture cross section (20-50 keV).

Fröhner also noted that often the resolution broadening may be approximated by a Gaussian convolution of 1/e - width, W. In this case Eq. (1) still holds with:

$$\Delta^2 = \frac{4k(T_2-T_1)}{A}E - W^2 \quad , \qquad T_2 > T_1\left(1 + \frac{AW^2}{4kT_1E}\right) . \qquad (3)$$

In fact as long as $AW^2 \le 4kT_1E$ the effect of the resolution broadening can be "unfolded" with fair accuracy, as we will show later.

For most time-of-flight measurements W is given by:[24]

$$W^2 = \frac{2}{3}\left[\left(\frac{\ell}{L}\right)^2 E^2 + \left(\frac{\tau}{\mu L}\right)^2 E^3\right] \quad , \qquad (4)$$

where L is the length of the flight path, ℓ is the length uncertainty due to the thicknesses of the detector and of the neutron source, τ is the time uncertainty resulting from the finite duration of the source pulse and the resolution of the detector, and μ = 72.3 μs/m at 1 eV is the neutron flight time at the reference energy. If the source neutrons are slowed down by an hydrogeneous moderator, the moderation process introduces a broadening equivalent to that of a length uncertainty of approximately 2.4 cm.[25]

Figure 3 shows the room temperature Doppler width, Δ, for a typical heavy element (A = 240), as well as the resolution width, W, for three different instrumental conditions. The upper curves were computed for ℓ = 2.4 cm, τ = 5 nsec, and flight path L or 40 and 160 m respectively. The lowest curve is also for a 160 m flight path, for ℓ = 1.0 cm (no moderator) and τ = 5 nsec.

We see from Fig. 3 that in the energy region which contributes most to the Doppler effect, i.e., below 50 keV, the resolution width at a flight path of 160 m can be made smaller or comparable to the Doppler width at

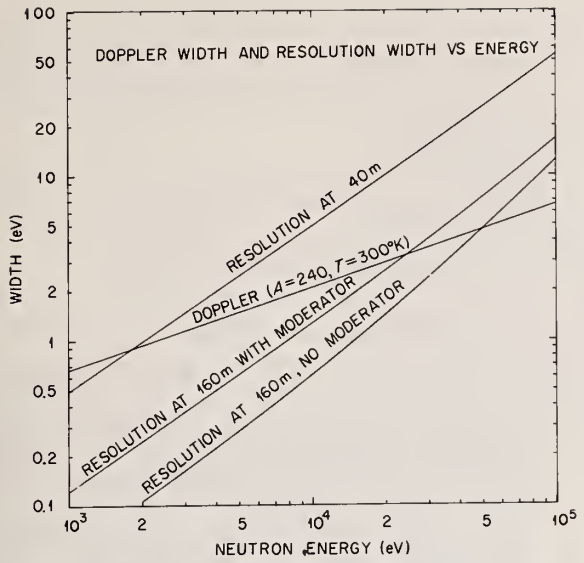

FIG. 3. Doppler width and resolution width vs energy.

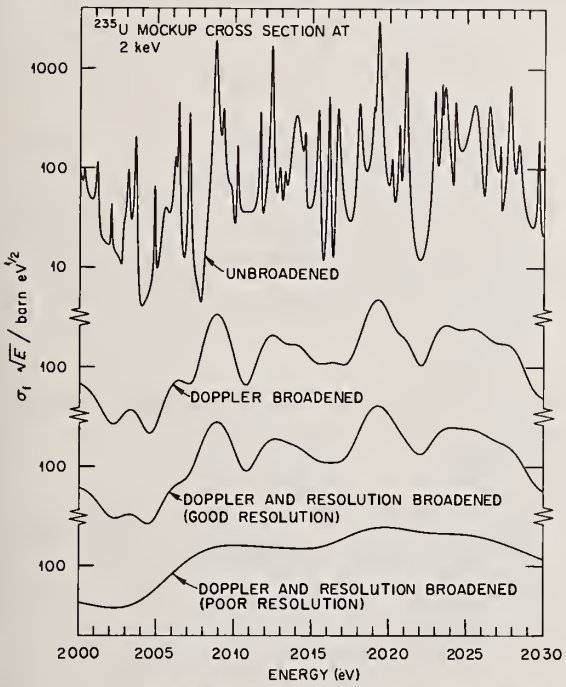

FIG. 4. ^{235}U mockup cross section at 2 keV.

300°K, altnough above 25 keV this requires measurements without moderator.

The direct use of cross sections measured with good resolution to compute Doppler-broadened cross sections for reactor calculations is illustrated in Figs. 4 and 5. The upper curve in Fig. 4 represents a mock-up of the fission cross section of ^{235}U between 2000 and 2030 eV. The resonance parameters at 2 keV are not known and the mock-up was obtained by selecting the same sequence of spacings and reduced widths that is found between 0 and 30 eV. This is reasonable since at 2 keV the cross section is still dominated by the s-wave contribution and since the s-wave average parameters would not be expected to change much over the small change in excitation energy. The second curve of Fig. 4 was obtained by Doppler broadening the upper curve to a temperature of 300°K; this is the cross section that might be required in a reactor calculation. The third curve of Fig. 4 shows the cross section as it would be obtained with the good resolution obtainable on an 80 m flight path at ORELA. The lowest curve shows the cross section as it would be obtained with the poorer resolution corresponding to a 20 m flight path at ORELA.

It is apparent from Fig. 4 that if only the "poor resolution measurement," shown in the lowest curve, is available, the Doppler broadened cross section cannot be reliably obtained by unfolding the resolution broadening; in this case the most reasonable approach is probably to generate ladders of pseudoresonances (such as that shown in the upper curve of Fig. 4) and Doppler broadening the ladders to obtain the probability distribution of the Doppler broadened cross section. On the other hand, if the "good resolution measurement" shown in the third curve of Fig. 4 is available, then an accurate estimate of the actual Doppler-broadened cross section may be obtained by unfolding the broadening due to the instrumental resolution. The resolution width, W, of the "good resolution measurement" of Fig. 4 is approximately equal to the Doppler width, Δ. In Fig. 5 we illustrate a possible technique to remove the effect of the resolution broadening.

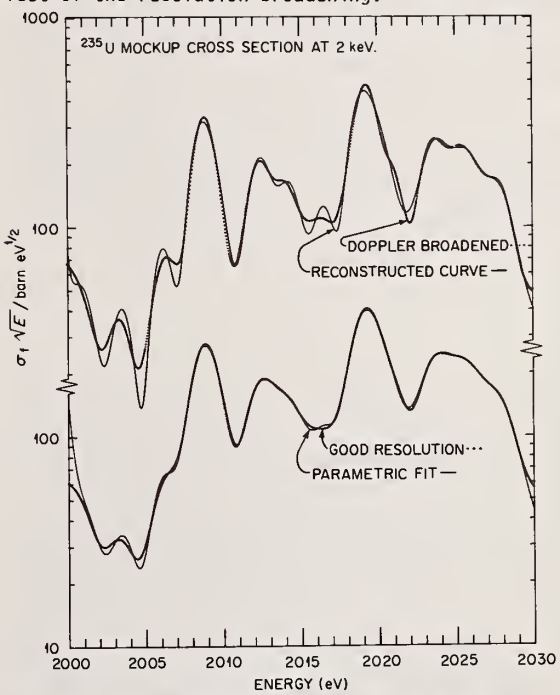

FIG. 5. ^{235}U mockup cross section at 2 keV.

In the lower part of Fig. 5 we show the "good resolution measurement" (third curve of Fig. 4) fitted by a linear combination of the form:

$$\sigma E^{1/2} = \sum_k \frac{1}{\nu_k} [G_k \psi(x_k, \beta_k^*) + H_k \phi(x_k, \beta_k^*)] \qquad (5)$$

and

$$x_k = \frac{E-\mu_k}{\nu_k} \qquad \beta_k^* = \frac{(\Delta^2 + W^2)^{1/2}}{\nu_k} \quad , \qquad (6)$$

where the ψ and ϕ are the usual Voigt profiles.[26] The values of μ_k, ν_k, G_k and H_k were obtained by a least squares fit. In the upper part of Fig. 5 we compare

the "unbroadened" cross section, obtained in setting W = 0 in Eqs. (5) and (6) to the "actual" Doppler broadened cross section (the second curve of Fig. 4).

The resolution unfolding illustrated in Fig. 5 is not exact but, with the limitation that $W \leq \Delta$, it provides a fairly accurate description of the actual Doppler-broadened cross section. Other, perhaps more powerful, methods exist to unfold resolution,[27] but the technique used here is convenient and also provides a parametric description of the Doppler broadened cross section.

Discussion and Conclusions

Until recently partial cross section measurements could be done only with the moderate resolution corresponding to flight paths of 20 to 50 m, because of the limited intensity of pulsed neutron sources. However, in recent years powerful neutron time-of-flight facilities have been developed which allow a great improvement in instrumental resolution.[28] For instance, the cross sections most important for the calculation of the Doppler coefficient of reactivity in fast reactors could be measured at ORELA with the resolution corresponding to the lowest curve in Fig. 3. Yet very few high resolution measurements have been reported, and none, to our knowledge, are used directly in reactor calculations.[29] The high resolution measurements are difficult and time consuming, and hence may not be performed unless requested by reactor designers.

The storage requirements for evaluated data consisting of actual Doppler broadened cross sections would be appreciable; if on the average n points per Doppler width are required to represent the Doppler broadened cross section, then the total number of points required to represent a cross section in the unresolved range is:

$$N = n \int_{E_1}^{E_2} \frac{dE}{\Delta(E)} = n\sqrt{\frac{A}{kT}} \left(E_2^{1/2} - E_1^{1/2}\right) \quad , \qquad (7)$$

where E_1 and E_2 are the limit of the unresolved range.

The Doppler broadened curve shown on Fig. 4 covers a range of 33 Doppler widths and can be represented to 3% accuracy by a linear interpolation with 35 points, indicating that for this type of cross section $n \approx 1$ or 2. For n = 1, Eq. (7) shows that approximately 2300 points would be required to represent a Doppler-broadened cross section up to 50 keV. This is a fairly large number of points, but the processing of a cross section represented by data points should be faster than the processing of average resonance parameters.

It appears to us that the expected increase in precision, particularly in the calculation of the Doppler coefficient of reactivity, makes it desirable to abandon the statistical approach to the unresolved region for the most important nuclides and to replace it as soon as possible by the use of the actual Doppler broadened cross sections obtained directly from high resolution measurements.

*Funded by ERDA under contract with Union Carbide Corporation.

1. P. Greebler and B. A. Hutchins, Proc. Seminar on Physics of Fast and Intermediate Reactors 3, 121, IAEA, Vienna (1962).
2. R. J. Brissenden and C. Durston, The Calculation of Neutron Spectra in the Doppler Region, Proc. Conf. Application of Computing Methods to Reactor Problems, p. 51, ANL-7050, Argonne National Lab. (1965).
3. M. W. Dyos, Nucl. Sci. and Eng. 34, 181 (1968).
4. L. B. Levitt, Nucl. Sci. and Eng. 49, 450 (1972).
5. Much of the early work on the subject is discussed in the six papers of the Proc. Invited Session on Resonance Cross Sections in the Unresolved Resonance Region, Meeting of ANS and CNA, CONF-680601, ANS-RPD-1, 1968.
6. "Statistical Theory of Spectra Fluctuation," Ed. C. E. Porter, Academic Press, New York, 1965. See also, C. E. Porter and R. G. Thomas, Phys. Rev. 104, 483 (1956).
7. R. N. Hwang, Nucl. Sci. and Eng. 36, 67 and 82 (1969).
8. C. N. Kelber and P. H. Kier, Nucl. Sci. and Eng. 24, 383 (1966) and 26, 67 (1966).
9. M. W. Dyos and C. A. Stevens, Nucl. Sci. and Eng. 25, 294 (1966).
10. M. S. Moore and C. W. Reich, Phys. Rev. 118, 718 (1960), D. W. Bergen and M. G. Silbert, Phys. Rev. 166, 1178 (1968), and G. de Saussure, R. B. Perez, and W. Kolar, Phys. Rev. C7, 2018 (1973).
11. D. R. Koenig and A. Michaudon, J. Nucl. Energy 25, 273 (1971), J. D. Garrison, Phys. Rev. Lett. 29, 1185 (1972), and E. Melkonian, J. P. Felvinci, and W. W. Havens, submitted to Phys. Rev. Lett. (1975).
12. A. M. Lane and J. E. Lynn, Proc. Phys. Soc. (London) A70, 557 (1957).
13. P. A. Egelstaff, J. Nucl. Energy 7, 35 (1958) and Proc. Phys. Soc. (London) 71, 910 (1958).
14. B. H. Patrick, M. G. Sowerby, and M. G. Schomberg, J. Nucl. Energy 24, 269 (1970).
15. R. B. Perez and G. de Saussure, "Intermediate Structure in the ^{238}U Neutron Capture Cross Section," this conference (BAPS II, 20, 161, 1975).
16. J. Blons, H. Derrien, and A. Michaudon, Proc. Second Intern. Conf. Nucl. Data for Reactors I, 513, IAEA Vienna (1970).
17. E. Migneco and J. P. Theobald, Nucl. Phys. A112, 603 (1968).
18. H. Feshbach and A. K. Kerman, Comments on Nuclear Particle Physics II, 4, 125 (1968).
19. H. Weigmann, Zeitschrift für Physik 214, 7 (1968).
20. Courtesy of F. G. Perey, 1975.
21. R. R. Spencer and F. Käppeler, Proc. Specialist Meeting on Resonance Parameters of Fertile Nuclei and ^{239}Pu, Saclay, May 20-22, 1974.
22. D. R. Harris, "Bettis Technical Review," WAPD-BT-30 41 (1964).
23. F. H. Fröhner, Nucl. Instr. and Methods 49, 89 (1967).
24. F. H. Fröhner and E. Haddad, Nucl. Phys. 71, 129 (1965).
25. J. Rainwater et al., Rev. Sci. Instr. 31, 481 (1960); A. Michaudon, Reactor Sci. and Tech. 17, 168 (1963).
26. W. Voigt, S. B. Bayer Akad Wiss, p. 603 (1912); A. W. Solbrig, Am. J. Phys. 29, 257 (1961).
27. For instance, J. W. Cooley, "Applications of the Fast Fourier Transform Method," Proc. IBM Scientific Computing Symp., Yorktown Heights, N. Y. (1966).
28. E. Rae, in Experimental Neutron Resonance Spectroscopy, Ed. J. A. Harvey, Academic Press, New York (1970) p. 66.
29. S. C. Cohen, p. 247 in ANL-7320 (1966).

HELIUM PRODUCTION IN REACTOR MATERIALS

E. P. Lippincott and W. N. McElroy
Hanford Engineering Development Laboratory
Richland, WA 99352
and
H. Farrar IV
Atomics International Division
Rockwell International Corporation
Canoga Park, CA 91304

Comparisons of integral helium production measurements with predictions based on ENDF/B Version IV cross sections have been made. It is concluded that an ENDF/B helium production cross section file should be established in order to ensure a complete and consistent cross section evaluation to meet accuracies required for LMFBR, CTR, and LWR applications.

(Helium; cross sections; benchmark; neutron)

Fast reactor irradiation of structural materials has established that helium produced by various nuclear reactions is an important determinant of material lifetime. For example, helium produced in stainless steel severely limits the ductility at certain elevated temperatures and helium atoms can serve as nuclei for void formation. The helium contribution to neutron damage will be even more significant in Controlled Thermonuclear Reactors (CTRs) because of the large number of high energy neutrons. Additionally, the measurement of helium content of a material for which the energy-dependent, helium-producing cross sections are known accurately provides an excellent means of fluence-spectra dosimetry for use in damage analysis for Liquid Metal Fast Breeder Reactors (LMFBRs), for CTRs, and for Light Water Reactors (LWRs).

Because of the inadequacy of evaluated energy-dependent cross sections of early versions of ENDF/B, a set of helium production curves for stainless steel and its constituents irradiated in LMFBR spectra was developed[1] jointly by AEC-sponsored programs at Hanford Engineering Development Laboratory (HEDL) and Atomics International (AI). Spectrum-averaged integral (n,α) cross sections were measured by irradiating alloys, compounds, and pure elements in a variety of spectra, and measuring the resulting helium concentrations by high sensitivity mass spectrometry. The exposures were made in EBR-II during high power dosimetry tests which provided the necessary flux-spectral data. Additional measurements of ^{10}B and ^{6}Li have been made in the Coupled Fast Reactivity Measurements Facility (CFRMF). Details of this work are given elsewhere.[1-4] These helium production curves are in use to predict helium generated in stainless steel and its major constituents in fission reactor spectra for the LMFBR program. They will not be adequate, however, for irradiations in fusion reactor spectra.

At the present time, there does not exist a complete set of energy-dependent cross sections that have been evaluated in a self-consistent manner. Such a set is now required to provide reliable estimates of helium production in elemental materials for fission and fusion reaction dosimetry and damage analysis applications. The current status of some important helium production cross sections is presented in Table I which compares evaluated and measured cross sections in a fission spectrum.

Preliminary values of EBR-II neutron spectrum averaged helium production cross sections measured at Atomics International using helium gas mass spectrometry are tabulated in Column 2 of Table I. These cross sections are derived from specimens of pure elements irradiated in EBR-II during the Run 50H dosimetry test at a Row 4 location having a mean neutron energy of $\sim$ 0.8 MeV. The cross sections measured in EBR-II can be related directly to fission spectrum cross sections because, at neutron energies sufficiently high for most (n,α) reactions to be significant, the EBR-II spectrum retains the fission spectrum shape. The measured helium production cross sections in Column 2 were therefore converted to fission spectrum averaged cross sections in Column 3, simply by multiplying them by the ENDF/B-IV calculated ratio of fission to EBR-II spectrum averaged cross section.[1] EBR-II irradiated specimens are presently on hand for most of the elements in Table I for which data are lacking.

The measured values in Columns 2 and 3 are the most recent values obtained in this work, but they still must be considered preliminary because several are based on only one or two measurements, whereas numerous additional irradiated specimens are presently awaiting analysis (not only from the Row 4 center location of EBR-II but also from other locations where the mean neutron energy is lower). In addition, the nitrogen impurity content of the structural material specimens must be determined, because nitrogen has a significant helium generation rate in EBR-II neutron spectra. At present, the helium contribution from nitrogen (and perhaps boron) is thought to be low or negligible on the basis of a few nitrogen measurements and on the fact that, in most cases, similar helium concentrations have been obtained from specimens taken from different lots of the same material.

Column 4 presents the results of an evaluation by Birss[5] based on available experimental data. In some cases the numbers quoted by Birss show inconsistency between elemental and isotopic measurements and Table I presents two values, the second derived from individual isotopic measurements and the isotopic composition.

Column 5 of Table I contains ENDF/B Version IV cross sections averaged over a Cranberg fission spectrum form defined by:

$$\phi(E) = \sqrt{E}\, e^{-E/1.29} \qquad (1)$$

where E is the neutron energy in MeV. The cross sections for ^{6}Li, ^{10}B, and ^{63}Cu helium production are from the dosimetry file[4], while the remaining elements are taken from the general purpose ENDF/B file. The latter generally include only the (n,α) cross section but when available other helium producing cross sections [usually $(n,n'\alpha)$] are included.

The last column of Table I shows the ratio of the AI measured values to those calculated using ENDF/B-IV cross sections. The ratios are generally greater than unity which can be attributed to one or more of the following:

a) In most cases the calculations failed to take into account such reactions as $(n,n'\alpha)$, $(n,2\alpha)$, etc. However, these reactions are expected to be negligible in fission reactors but not for CTRs.

b) The cross section evaluations used in the calculations are inadequate, especially in the region of the effective thresholds where cross sections

are difficult to measure. The effect of threshold inaccuracies is enhanced in fission spectra because of the rapid decrease in flux at higher energies, but this effect will be less important for CTR spectra.

c) The measured values could be biased by an error in the total neutron fluence or by errors in the factors used to convert spectrum-averaged to fission-averaged cross sections. These numbers have uncertainties of a few percent. However, since all the pure elements were irradiated together at one location, such errors would not affect relative helium production rates but would bias the whole set.

d) The measured values may include helium contributions from impurities such as nitrogen, boron, and phosphorus. Such contributions would be expected to vary radically between materials and perhaps between different lots of the same material.

On the other hand, the ratios in the last column of Table I are not far from unity for some of the elements, indicating that ENDF/B-IV (n,α) cross sections may be adequate in some cases for helium production estimates in fission reactor spectra. For example, the Version IV cross section for nickel, which is usually the principal helium contributor in irradiated stainless steel, has been brought into reasonable agreement with the integral measurements.

To make substantial additional improvements and, in particular, to be sure LMFBR, CTR, and LWR program needs are met, the following steps are considered necessary:

(1) All important (n,α) cross sections (including those in Table I) must be evaluated or re-evaluated for inclusion in the ENDF/B-V file. These evaluations must use nuclear models in a consistent manner for all elements when covering areas in which cross section data are poor or non-existent.

(2) The cross sections must be integrally tested in designated benchmark spectra to make up for the paucity of data for many isotopes. Thermal, resonance, fission, fusion, and a few accelerator-produced (tailored 1-8 MeV mean energy[6]), benchmark spectra have been identified for this data testing. Measurements in these designated spectra must be continued.

(3) The measurements at AI of the helium produced in numerous pure elements, compounds, and separated isotopes that were irradiated during three EBR-II dosimetry tests at locations adjacent to HEDL flux-spectral sets will serve as the primary source of fission spectrum values. The possible effects of nitrogen and other impurities, however, must be examined carefully before establishing benchmark-averaged elemental cross sections.

(4) The isotopic cross sections for some elements, including transmutation products, must be determined to allow accurate calculations of effects of very long reactor exposures.

(5) All the (n,α) cross sections, together with estimates for other helium production reactions must be accumulated in a single helium production cross section file for materials damage and dosimetry uses.

TABLE I

SPECTRUM AVERAGED HELIUM PRODUCTION CROSS SECTIONS

Element or Isotope	Helium Production Cross Section (mb)				
	Measured (this work)*		Evaluated (Birss[5])	Calculated (ENDF/B-IV)	Measured/ Calculated
	EBR-II Spectrum	Fission Spectrum	Fission Spectrum	Fission Spectrum	
^{6}Li	-	-	-	487.	-
^{7}Li	-	-	25.8	22.9	-
^{10}B	1240	-	-	515.	-
^{11}B	-	-	0.085	0.041	-
C	-	-	0.47	1.19	-
N	∿26	∿ 93	85.5	81.7	∿1.14
O	-	-	7.2	8.43	-
F	-	-	5.7	23.46	-
Na	-	-	0.55	0.648	-
Mg	-	-	2.9	2.86	-
Al	0.140	0.658	0.635	0.710	0.93
Si	-	-	0.13/0.99	2.95	-
Cl	-	-	4.7	12.4	-
K	-	-	5.8	20.4	-
Ca	-	-	6.5	-	-
Ti	0.055	0.26	0.060/0.508	0.145	1.8
V	≤0.073	≤0.31	0.012/0.04	0.022	≤14
Cr	∿0.030	∿0.14	0.17/0.2	0.107	∿1.3
Mn	-	-	0.13	0.115	-
Fe	0.074	0.36	0.205	0.294	1.21
Co	-	-	0.14/0.23	0.149	-
Ni	0.99	4.78	4.52	4.36	1.10
^{63}Cu	0.108	0.52	0.05	0.354	1.48
Cu	0.075	0.36	0.081	0.286	1.27
Zr	0.020	0.077	0.18	0.002	3.9
Nb	0.026	0.126	1.2	0.074	1.7
Mo	0.022	0.10	0.13/0.12	-	-
Ag	-	-	-	0.072	-
Cd	-	-	-	0.003	-
Ta	-	-	-	0.0006	-
Au	0.003	0.014	-	0.0005	30

* Recent preliminary data without corrections for impurity contributions (see text).

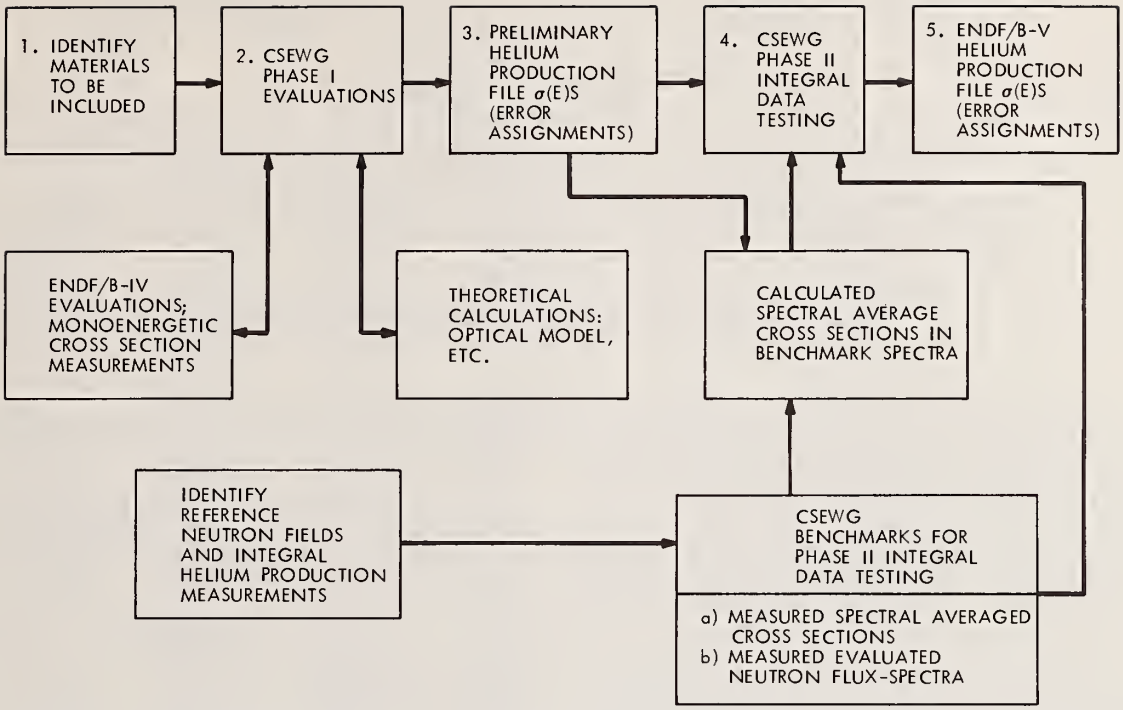

FIGURE 1. FLOW CHART FOR DEVELOPMENT OF ENDF/B-V HELIUM PRODUCTION FILE

HEDL is currently coordinating efforts for the development of such an ENDF/B-V helium production file for the LMFBR program, and this effort needs to be extended to include CTR and LWR program needs. The Cross Section Evaluation Working Group (CSEWG) has assigned its normalization and standards sub-committee the responsibility of developing such a file because of its previous work in developing the ENDF/B-IV evaluated dosimetry cross section file.[2-4]

Figure I presents a flow chart showing the different elements involved in the multi-laboratory development of this helium production file. The initial phase will be the identification of all (n,α) reactions of anticipated interest for fission and fusion reactor materials, and the identification of the benchmark spectra to be used for integral data testing of the file.

Acknowledgments

The authors wish to aknowledge contributions to this work by G. E. Shook and N. J. Graves at HEDL, C. A. Guderjahn and R. A. Britten at AI, and B. R. Leonard (Chairman, Normalization and Standards Sub-Committee of CSWEG) at Battelle Pacific Northwest Laboratories. This work was supported by the Energy Research and Development Administration (ERDA). Special thanks go to T. C. Reuther, P. B. Hemmig, and K. M. Zwilsky of ERDA for their interest and support of this work.

References

1. W. N. McElroy and H. Farrar IV, "Helium Production in Stainless Steel and Its Constituents as Related to LMFBR Development Programs," in Radiation-Induced Voids in Metals, pp 187-229, J. W. Corbett and L. C. Ianniello, eds. USAEC Symposium Series 26, (1972).
2. W. N. McElroy and L. S. Kellogg, "Fuels and Materials Fast-Reactor Dosimetry Data Development and Testing," Nucl. Technol, 25, 180 (1975).
3. H. Farrar IV, W. N. McElroy, and E. P. Lippincott, "Helium Production Cross Section of Boron for Fast Reactor Neutron Spectra," Nucl. Technol, 25, 305 (1975).
4. B. A. Magurno and O. Ozer, "ENDF/B File for Dosimetry Applications," Nucl. Technol, 25, 376 (1975).
5. I. R. Birss, "Review of Helium Production Cross Sections" presented at IAEA Working Group on Reactor Radiation Measurements Meeting, Seattle, Washington, October 30 - November 3, 1972.
6. N. D. Dudey and M. J. Fluss, Argonne National Laboratory contribution to the "LMFBR Reaction Rate and Dosimetry 4th Quarterly Progress Report," HEDL-TME 72-90, Hanford Engineering Development Laboratory, 1972.

FAST REACTOR FISSION YIELDS FOR ^{233}U, ^{235}U, ^{238}U, ^{239}Pu, AND RECOMMENDATIONS FOR THE DETERMINATION OF BURNUP ON FBR MIXED OXIDE FUELS

W. J. Maeck
Idaho Nuclear Engineering Laboratory
Allied Chemical Corporation
Idaho Falls, Idaho 83401

Absolute fast reactor fission yields are presented for over 40 stable and long-lived isotopes of Kr, Rb, Sr, Zr, Mo, Ru, Sb, Xe, Cs, Ba, La, Ce, Nd, and Sm for ^{233}U, ^{235}U, ^{238}U, and ^{239}Pu irradiated in EBR-II. A method for ordering fission yields as a function of neutron energy is given. Recommendations for the determination of burnup on mixed-oxide fuels irradiated in a fast reactor are given.

(Fast fission yields; ^{233}U, ^{235}U, ^{238}U, ^{239}Pu; burnup monitors; isotope dilution mass spectrometry; capture-to-fission; yields vs. energy)

I. Introduction

Early in 1973, the status of the nuclear data and analytical chemistry methodology requirements for the determination of burnup for fast reactor fuels was reviewed.[1] This review concluded that the preferred method for measuring burnup in FBR fuels was the fission product-residual heavy atom method because it is the only method applicable regardless of the levels of burnup, it is independent of the fuel composition, and it does not require specific knowledge of the fuel composition prior to irradiation.

In this method the irradiated fuel specimen is dissolved, and the concentration of the selected fission product monitor(s) and the heavy atoms in the solution are determined. The computational relationship is

$$\text{Burnup} = a/oF = 100 \frac{\frac{A}{Y}}{H + \frac{A}{Y}}$$

where

a/oF = atom percent fission

A = atoms of selected fission product monitor

Y = effective fission yield value of the fission product monitor

H = residual heavy atoms.

An error analysis[1] showed that the largest uncertainty in this method for the determination of burnup in FBR fuels was the uncertainty of the fission yield values for the various fissioning nuclides for neutron spectra characteristic of FBRs. These fast fission yield values were limited to ^{235}U and ^{239}Pu, which had been measured in a neutron spectra much harder than those expected for commercial FBRs. The uncertainties associated with applying such fission yield data to the determination of burnup in FBR cores was estimated to be as high as 5%. Also, no reliable fast reactor fission yield data were available for ^{238}U and ^{241}Pu which are significant source of fission in FBR fuels, nor for ^{233}U which is used in experimental FBR fuels.

This report summarizes the fast reactor fission yield data obtained to date in this laboratory for over 40 stable and long-lived nuclides on samples of highly enriched ^{233}U, ^{235}U, ^{238}U, and ^{239}Pu which were irradiated in EBR-II in a neutron spectra characteristic of mixed oxide fueled LMFBRs.

Detailed information pertaining to the experiment, the chemical separation techniques, mass spectrometric analyses, and data computations will be presented in a series of USAEC reports with report numbers ICP-1050-Serial I, II, III.... .

II. EXPERIMENTAL

Irradiation Package

The sample irradiation was conducted in row 8 of EBR-II to an integrated exposure of 3100 MWD. The irradiation package contained multiple capsules of ^{233}U, ^{235}U, ^{238}U, ^{237}Np, ^{239}Pu, ^{240}Pu, ^{241}Pu, ^{242}Pu, ^{241}Am, and ^{243}Am for fission yield measurements, various spectrum monitors to characterize the neutron spectrum and samples of ^{233}U, ^{235}U, ^{239}Pu, ^{240}Pu, ^{241}Pu, and ^{242}Pu for the measurement of the capture-to-fission ratio, α.

Fission Yield Capsules - Highly enriched isotopes as oxide powders were individually mixed with high purity (99.99+%) nickel powder, weld-sealed in nickel capsules machined from 99.99+% pure nickel rod, and loaded in a standard EBR-II B-7A subassembly for the irradiation. The geometry of the sample loading is shown in Figure 1. The amount of each oxide sample loaded was such that $\sim 10^{19}$ fissions would be obtained if the reactor was operating at 62.5 MW for 50 days.

Spectrum Monitor Capsules - To characterize the neutron spectrum, twelve spectrum monitor capsules, each containing nine monitors (Co, Sc, Fe, Ni, Ti, Cu, ^{237}Np, ^{238}U, ^{235}U) were included in the irradiation package as shown in Figure 1.

Capture-to-Fission Ratio Capsules - Three nickel capsules, each containing duplicate oxide samples of ^{233}U, ^{235}U, ^{238}U, ^{239}Pu, ^{240}Pu, ^{241}Pu, ^{242}Pu, and ^{237}Np, were irradiated in locations adjacent to spectrum monitor capsules (Figure 1).

Capsule Dissolution and Analysis

The ^{233}U, ^{235}U, and ^{238}U fast fission yield capsules were dissolved with 8M HNO_3 and the ^{239}Pu capsules with 8M HNO_3-0.1M HF. After the dissolution of the fissionable material started, measured quantities of $^{78-80}Kr$ and ^{129}Xe isotopic spikes were introduced into the dissolution flask. The Kr-Xe fission gases and spikes were trapped on Molecular Sieve at

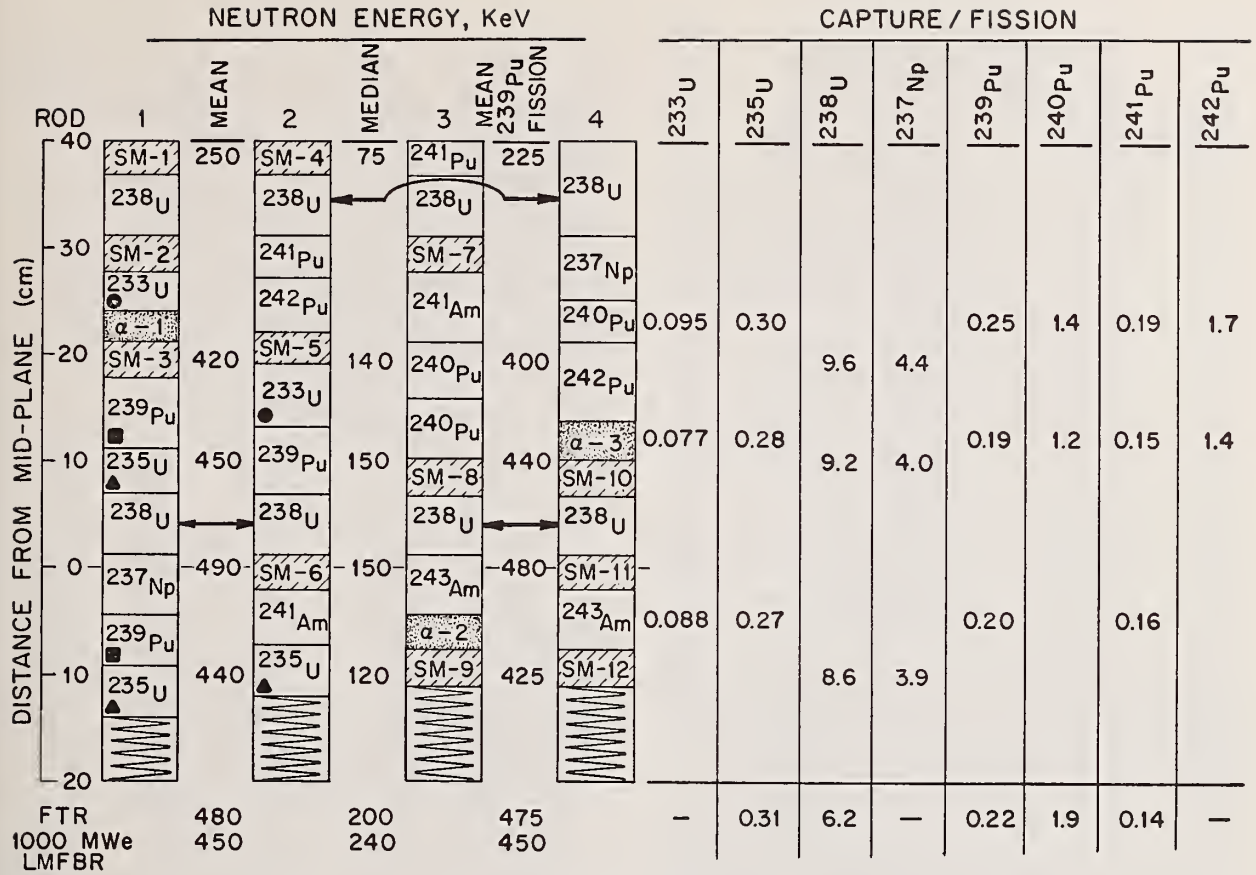

Figure 1. Irradiation Assembly - Neutron Energy Distribution and Capture-to-Fission Ratios

-178°. The gases were then desorbed and the Kr and Xe fractions were separated using gas chromatography and analyzed by mass spectrometry.

Following the dissolution, the sample solution was filtered and weighed. Weighed aliquots were used for all subsequent fission product analyses. The principal measurement technique was isotope dilution mass spectrometry. Usually, four spiked and four unspiked aliquots were analyzed for each element. A brief list of the isotope dilution spikes and separation techniques that were used is given in Table I. Highly purified reagents were used in the chemical separations.

III. RESULTS

Fission Yields

Determination of Number of Fissions - Because the burnup was low, less than 1%, the number of fissions (total fission product atoms in either the light or heavy mass peak) was determined by the summation technique. Generally, the heavy mass peak was used because a larger fraction of this peak can be measured with a higher degree of confidence. Only 5 to 10% of the heavy peak atom abundances and fission yields had to be estimated. The individual yields were calculated by dividing the measured atoms for each isotope by the sum of the measured and estimated atoms in the heavy peak.

Uranium-233 - Two capsules were dissolved. The location of the capsules in the irradiation package is shown in Figure 1. The fission yields and associated uncertainties are given in Table II. This is believed to be the first comprehensive measurement of fast-fission yields for ^{233}U.

Uranium-235 - Three capsules, identified in Figure 1, were dissolved separately and the fission product distribution for each was measured. The fission yields and associated errors are given in Table III.

TABLE I

ANALYTICAL SEPARATION PROCEDURES AND ISOTOPE DILUTION SPIKES

Element Separated	Added Spike	Separation Procedure
Rb	^{85}Rb	Ion exchange
Sr	^{87}Sr	Ion exchange on same sample aliquot used for Rb
Zr	^{90}Zr	Zr coprecipitated with Th $(IO_3)_4$ followed by ion exchange.
Mo	^{94}Mo	Solvent extraction
Ru	^{96}Ru	Distillation of RuO_4
Cs	^{133}Cs	Ion exchange on same sample aliquot used for Rb.
Ba	^{135}Ba	Ion exchange on same sample aliquot used for Rb.
La	^{138}La	Ion exchange
Ce	^{136}Ce	Solvent extraction of Ce(IV)
Nd-Sm	^{150}Nd-^{144}Sm	Sequential chromatographic ion exchange.

Uranium-238 - Because the fission cross section of ^{238}U is low compared to ^{235}U for this neutron spectrum and because the volume of the capsules was limited, eight capsules of ^{238}U were prepared to produce adequate amounts of fission products for analysis. As shown in Figure 1, four capsules were located in each of two axial planes, such that each group of four were exposed to a similar neutron spectrum. Three pairs of capsules (see Figure 1) were dissolved separately and analyzed. In general, the uncertainties associated with the fission yields given in Table IV for ^{238}U are larger than those for ^{233}U and ^{235}U because the number of fissions was significantly less, and the effect of natural contamination on the analysis of the lower quantities of fission products was greater.

Plutonium-239 - Four capsules of ^{239}Pu were irradiated. To date, the measurements have been completed for two capsules and the fission yield results are given in Table V. It is expected that these reported yields and their associated uncertainties will change slightly when the results from all four capsules are included. Hence, these data must be considered as preliminary.

Error Analysis - The standard deviation associated with each reported fission yield is given in Tables II - V and includes allowances for known sources of systematic errors. The standard deviation was calculated by first approximating the functions used to calculate the fission yields, by the linear terms of the Taylor series expansion, and then applying the usual method of calculating the standard deviation of a linear sum of random variables. The procedure consisted of four distinct steps. First, the propagated standard deviation of the measured number of atoms of each element was calculated. This computation included the systematic effect of uncertainty in the spike concentrations, the random mass spectrometer errors in the spike, natural, fission product, and mixed spike-fission product isotopic fractions, the Kr and Xe spike volume uncertainties, and the estimated systematic uncertainty in the mass spectrometer. Second, the standard deviation of the total number of atoms in the heavy peak was calculated using the above standard deviations for the measured atoms and estimated standard deviations for the interpolated, extrapolated and estimated atoms. Third, the standard deviation of each yield from each capsule was then calculated using the standard deviations of the total number of fissions, the atoms of the specific element, and the fraction of the specific isotope. Finally, the standard deviation of the average yield from all capsules was calculated considering the effects of the systematic and random errors.

TABLE II. FAST REACTOR FISSION YIELDS FOR ^{233}U

Mass Meas.	FY,%	Std. Dev.	Mass Meas.	FY,%	Std. Dev.
75-80	0.60[a]		116-124	0.23[a]	
81	0.37[b]	0.02	125 Sb	0.141[e]	0.015
82	0.58[b]	0.04	126	0.30[f]	0.04
83 Kr	0.995	0.008	127	0.63[f]	0.08
84 Kr	1.64	0.01	128	1.14[f]	0.08
85 Kr+Rb	2.12	0.02	129	1.78[f]	0.12
86 Kr	2.78	0.02	130	2.58[f]	0.18
87 Rb	3.84	0.03	131 Xe	3.73	0.02
88 Sr	5.12	0.03	132 Xe	5.04	0.03
89	5.79[c]	0.29	133 Cs	6.01	0.04
90 Sr+Zr	6.45	0.04	134 Xe	6.30	0.03
91 Zr	6.44	0.07	135 Cs	6.37	0.05
92 Zr	6.54	0.06	136 Xe	6.88	0.04
93 Zr	6.92	0.07	137 Cs+Ba	6.75	0.04
94 Zr	6.74	0.07	138 Ba	6.52	0.10
95 Mo	6.29	0.05	139 La	6.37	0.06
96 Zr	5.70	0.07	140 Ce	6.26	0.05
97 Mo	5.44	0.04	141	6.31[c]	0.19
98 Mo	5.14	0.03	142 Ce	6.36	0.05
99	4.76[c]	0.24	143 Nd	5.54	0.03
100 Mo	4.38	0.04	144 Ce+Nd	4.40	0.02
101 Ru	3.74[d]	0.20	145 Nd	3.20	0.02
102 Ru	2.83[d]	0.17	146 Nd	2.39	0.01
103	2.04[c,d]	0.16	147 Sm	1.68	0.01
104 Ru	1.24[d]	0.07	148 Nd	1.20	0.01
105	0.78[c,d]	0.05	149 Sm	0.707	0.006
106 Ru	0.33[d]	0.03	150 Nd	0.465	0.004
107	0.15[b]	0.01	151 Sm	0.309	0.003
108	0.08[b]	0.01	152 Sm	0.192	0.002
109-115	0.18[a]		153	0.113[c]	0.006
			154 Sm	0.033	0.001
			155-160	0.05[a]	
$\sum$	100.005		$\sum$	99.980	

Footnotes to this table are given at the end of Table V.

Neutron Spectrum Measurements

Based on the analysis of the various spectrum monitors and calculated reaction rates, the Physics Section located at the Test Reactor Facility characterized the neutron spectra using the fitting code SPECTRA[2]. From these data the mean neutron energy, median neutron energy, and mean fission energy for ^{233}U, ^{235}U, ^{238}U, ^{239}Pu, and ^{241}Pu in row 8 of the EBR-II lattice were calculated. The results of these calculations and comparison data for the expected neutron spectrum in FTR and in a conceptual 1000 MW_e LMFBR are given in Figure 1.

TABLE III. FAST REACTOR FISSION YIELDS FOR ^{235}U

Mass Meas.	FY,%	Std. Dev.	Mass Meas.	FY,%	Std. Dev.
75-80	0.24[a]		117-124	0.14[a]	
81	0.22[b]	0.05	125 Sb	0.038[e]	0.004
82	0.36[b]	0.09	126	0.071[f]	0.009
83 Kr	0.569	0.005	127	0.151[f]	0.019
84 Kr	1.03	0.01	128	0.372[f]	0.050
85 Kr+Rb	1.35	0.01	129	0.840[f]	0.107
86 Kr	1.96	0.02	130	1.71[f]	0.21
87 Rb	2.57	0.02	131 Xe	3.18	0.02
88 Sr	3.51	0.03	132 Xe	4.60	0.03
89	4.51[c]	0.23	133 Cs	6.82	0.05
90 Sr+Zr	5.52	0.04	134 Xe	7.67	0.05
91 Zr	5.70	0.05	135 Cs	6.52	0.05
92 Zr	5.79	0.05	136 Xe	6.16	0.04
93 Zr	6.18	0.06	137 Cs+Ba	6.21	0.05
94 Zr	6.23	0.06	138 Ba	6.66	0.06
95 Mo	6.42	0.06	139 Ba	6.76	0.07
96 Zr	6.13	0.06	140 Ce	6.19	0.05
97 Mo	5.99	0.05	141	5.85[c]	0.35
98 Mo	5.91	0.05	142 Ce	5.78	0.05
99	6.15[c]	0.31	143 Nd	5.80	0.05
100 Mo	6.39	0.06	144 Ce+Nd	5.27	0.04
101 Ru	5.24[d]	0.24	145 Nd	3.83	0.03
102 Ru	4.41[d]	0.20	146 Nd	2.94	0.02
103	3.25[c,d]	0.22	147 Sm	2.11	0.02
104 Ru	2.09[d]	0.10	148 Nd	1.68	0.02
105	1.32[c,d]	0.08	149 Sm	1.02	0.01
106 Ru	0.547[d]	0.025	150 Nd	0.672	0.008
107	0.17[b]	0.04	151 Sm	0.406	0.004
108	0.08[b]	0.02	152 Sm	0.265	0.005
109-116	0.16[a]		153	0.168[c]	0.009
			154 Sm	0.072	0.001
			155-160	0.07[a]	
$\sum$	99.996		$\sum$	100.025	

Footnotes to this table are given at the end of Table V.

TABLE IV. FAST REACTOR FISSION YIELDS FOR ^{238}U

Mass Meas.	Fy,%	Std. Dev.	Mass Meas.	FY,%	Std. Dev.
75-80	0.1[a]	0.03	118-124	0.214[a]	0.054
81	0.15[b]	0.04	125 Sb	0.039[e]	0.004
82	0.25[b]	0.06	126	0.055[g]	0.007
83 Kr	0.395	0.004	127	0.10[g]	0.01
84 Kr	0.816	0.008	128	0.41[g]	0.05
85 Kr+Rb	0.74	0.01	129	0.97[g]	0.13
86 Kr	1.28	0.01	130	1.84[g]	0.24
87 Rb	1.61	0.02	131 Xe	3.21	0.03
88 Sr	1.96	0.05	132 Xe	5.16	0.03
89	2.59[c]	0.14	133 Cs	6.70	0.06
90 Sr+Zr	3.21	0.05	134 Xe	7.95	0.05
91 Zr	4.44	0.27	135 Cs	6.92	0.06
92 Zr	4.95	0.29	136 Xe	7.07	0.05
93 Zr	5.26	0.31	137 Cs+Ba	5.99	0.05
94 Zr	5.03	0.30	138 Ba	5.73	0.17
95 Mo	4.94	0.08	139 La	5.94	0.14
96 Zr	6.05	0.36	140 Ce	5.92	0.12
97 Mo	5.47	0.06	141	5.31[c]	0.16
98 Mo	5.82	0.07	142 Ce	4.69	0.04
99	6.23[c]	0.32	143 Nd	4.56	0.04
100 Mo	6.63	0.08	144 Ce+Nd	4.48	0.04
101 Ru	6.14[d]	0.36	145 Nd	3.76	0.03
102 Ru	6.40[d]	0.38	146 Nd	3.40	0.04
103	5.70[c,d]	0.38	147 Sm	2.52	0.03
104 Ru	5.02[d]	0.30	148 Nd	2.08	0.03
105	3.75[c,d]	0.29	149 Sm	1.59	0.02
106 Ru	2.48[d]	0.16	150 Nd	1.25	0.02
107	1.25[b]	0.31	151 Sm	0.794	0.018
108	0.6[b]	0.15	152 Sm	0.521	0.005
109-117	0.75[a]	0.19	153	0.367[c]	0.019
			154 Sm	0.213	0.004
			155-160	0.27[a]	0.07
$\sum$	100.008		$\sum$	100.023	

Footnotes to this table are given at the end of Table V.

Capture-to-Fission Ratio Measurements

The capture-to-fission ratio, α, has been measured for eight heavy nuclides (^{233}U, ^{235}U, ^{238}U, ^{237}Np, ^{239}Pu, ^{240}Pu, ^{241}Pu, and ^{242}Pu) in row 8 of EBR-II. Of these, the ^{238}U and ^{237}Np were present in the spectrum monitor capsules and the others were individually sealed in stainless steel needles which were sealed in nickel capsules located adjacent to spectrum monitor capsules (Figure 1).

After irradiation, the stainless steel needles and their contents were sequentially dissolved in a mixture of HB_r-HI, and a mixture of HNO_3-HF. The number of fissions was determined from a ^{137}Cs analysis and corrected for fissions contributed by a neutron capture product based on the measured amount of capture product present and estimated cross section. The number of captures was determined from the change in the isotopic composition of the irradiated sample or by an analysis for the capture product. The measured α values are given in Figure 1. The estimated relative uncertainty for these values is ∿10%. For comparison, the calculated α values for these isotopes in the Fast Test Reactor lattice also are presented.

IV. VARIATION OF FISSION YIELDS WITH NEUTRON ENERGY

As previously stated, the most important parameter in the measurement of burnup is an accurate knowledge of the fission yield of the monitor nuclide. For thermal reactor fuels, the standard method is the isotope dilution mass spectrometric determination of ^{148}Nd and the residual heavy elements. This same method is being applied to fast reactor fuels with, however, a larger uncertainty in the ^{148}Nd fission yield value. In general, the fast reactor fission yields reported in the literature have wide variations and are not associated with a given neutron spectrum. Thus, any effect of neutron energy on fission yields is not accounted for. Studies in our laboratory show that this effect is significant, even for different positions in the same reactor.

Because of their importance as burnup monitors for fast reactor fuels, the fast reactor fission yields of the neodymium isotopes have been measured more than any other element. However, for ^{235}U fission, the variation in the reported yields range from 6 to 8% for masses 143 through 148 increasing to 16% for ^{150}Nd. This demonstrates that a major source of error in a burnup measurement of fast

TABLE V. FAST REACTOR FISSION YIELDS FOR ^{239}Pu

Mass Meas.	FY,%	Std. Dev.	Mass Meas.	FY,%	Std. Dev.
75-80	0.22[a]		119-124	0.29[a]	
81	0.16[b]	0.01	125 Sb	0.125[e]	0.012
82	0.23[b]	0.02	126	0.27[f]	0.03
83 Kr	0.309	0.002	127	0.52[f]	0.07
84 Kr	0.490	0.002	128	0.95[f]	0.08
85 Kr+Rb	0.595	0.006	129	1.61[f]	0.12
86 Kr	0.777	0.004	130	2.54[f]	0.18
87 Rb	1.03	0.01	131 Xe	3.84	0.06
88 Sr	1.31	0.02	132 Xe	5.27	0.09
89	1.67[c]	0.09	133 Cs	6.99	0.04
90 Sr+Zr	2.02	0.02	134 Xe	7.39	0.10
91 Zr	2.48	0.04	135 Cs	7.57	0.03
92 Zr	3.02	0.04	136 Xe	6.99	0.09
93 Zr	3.80	0.05	137 Cs+Ba	6.61	0.04
94 Zr	4.28	0.05	138 Ba	6.12	0.04
95 Mo	4.71	0.06	139 La	5.51	0.09
96 Zr	4.84	0.07	140 Ce	5.39	0.06
97 Mo	5.33	0.06	141	5.15[c]	0.16
98 Mo	5.66	0.07	142 Ce	4.89	0.04
99	6.09[c]	0.33	143 Nd	4.37	0.03
100 Mo	6.64	0.05	144 Ce+Nd	3.70	0.03
101 Ru	6.54[d]	0.11	145 Nd	3.01	0.02
102 Ru	6.64[d]	0.10	146 Nd	2.46	0.02
103	6.05[d]	0.92	147 Sm	1.99	0.02
104 Ru	6.53[d]	0.09	148 Nd	1.65	0.02
105	5.43[c,d]	0.39	149 Sm	1.23	0.02
106 Ru	4.32[d]	0.09	150 Nd	0.981	0.011
107	3.41[b]	0.43	151 Sm	0.776	0.011
108	2.40[b]	0.31	152 Sm	0.589	0.007
109	1.51[b]	0.19	153	0.444[c]	0.030
110-118	1.52[a]		154 Sm	0.264	0.003
			155-160	0.53[a]	
$\sum$	100.021		$\sum$	100.019	

a. Estimated yields.

b. Extrapolated yields.

c. Linear interpolation with adjacent measured yields.

d. Because of plateout of Ru in the dissolver flask, a direct measurement of the Ru conc. was not possible; however, isotopic data were obtained. These Ru yields were calculated by distributing the difference between the sum of the atoms in the heavy mass peak and the sum of the atoms in the light peak, which did not include the mass region of 101 through 106, according to the measured Ru isotopic composition.

e. Radiochemical measurements.

f. Interpolated values using mass 125 to 131 measured fast yeild values and ENDF/B-IV thermal values as a guide.

g. Interpolated value using mass 125 and 131 measured fast yield values and ENDF/B-IV fast yields as a guide.

reactor irradiated ^{235}U fuel is the uncertainty of the fission yield value for the burnup monitor. To date, these data have not been systematically evaluated with respect to the possibility of neutron energy dependency. In fact, the opposite has occurred, especially by the compilers of fast-reactor fission yield data where the tendency has been to average the literature values, sometimes using weighting factors dependent on the reported accuracy of the data.

In the process of evaluating our new ^{235}U fast fission yield data and comparing it to other data, the noted differences were considered to be too large to be attributed to measurement error and the evaluation of the relative isotopic data was undertaken because systematic errors in the number of fissions used to calculate the yields could be eliminated. During this evaluation, relative neodymium isotopic data became available for ^{235}U irradiated in the axial blanket of EBR-II and row 4 of EBR-II. A comparison of the relative isotopic data for these samples and the literature values are given in the top half of Table VI. The systematic changes are apparent when the data are ordered by neutron spectrum hardness. To amplify these changes, isotopic ratios were calculated and are given in the bottom half of Table VI. For the ratio of ^{150}Nd to ^{143}Nd, the change between thermal values and the very hard EBR-I spectrum is ~20%.

To quantify this correlation, an assessment of the spectrum hardness, that is a neutron energy index, was needed. Several types of index were considered, including mean neutron energy, median neutron energy, mean and median neutron energy for fission of a given heavy isotope, fraction of neutrons in a given energy range, and the ratio of cross sections values for two selected fissioning isotopes. Unfortunately, little spectral information was available for much of the literature-reported yield data. Of the possible indices considered, the effective fission cross section for ^{238}U relative to ^{235}U (σ_{f8}/σ_{f5}) was selected because more yield data could be associated with this index than any of the others, especially EBR-II data because the reactor has been mapped with these monitors. For some of the other data, measurement data existed or was obtained from the authors. Because ^{238}U has a threshold for fission near 1 MeV and the ^{235}U fission cross section is nearly constant from 0.01 to 10 MeV, the ratio of σ_{f8}/σ_{f8} is an indicator of the fraction of the flux with an energy greater than 1 MeV.

The isotopic ratio of ^{150}Nd to ^{143}Nd for those data which could be associated with the spectral index (σ_{f8}/σ_{f8}) are shown in Figure 2. That the neodymium isotopic composition of fissioned ^{235}U is correlated with neutron energy is clearly demonstrated. Of particular interest is the change in the neodymium ratio within the EBR-II reactor.

This initial study appears most promising and more advanced studies are in progress. It is anticipated that other fission yields can be correlated by a similar technique.

TABLE VI. RELATIVE Nd ISOTOPIC COMPOSITIONS AND ISOTOPIC RATIOS FOR ^{235}U FISSIONING

	$\sigma_{f_8}/\sigma_{f_5}$ Spectral Index, Reactor, and Reference						
SI $\sigma_{f_8}/\sigma_{f_8}$	Thermal[3] 0.0	EBR-II Axial Bl. 0.003	EBR-II Row-8 0.02	DFR[4] 0.035	EBR-II Row-4 0.06	OSIRIS[5] 0.089	EBR-I Core 0.12
Isotopes							
^{143}Nd	0.3926	0.3898	0.3891	0.3870	0.3840	0.3836	0.3826
^{145}Nd	0.2568	0.2589	0.2563	0.2544	0.2545	0.2546	0.2544
^{146}Nd	0.1963	0.1975	0.1969	0.1981	0.1985	0.1962	0.1973
^{148}Nd	0.1118	0.1110	0.1126	0.1133	0.1149	0.1167	0.1161
^{150}Nd	0.0425	0.0429	0.0450	0.0472	0.0481	0.0489	0.0496
Isotopic Ratios							
150/143	0.1083	0.1101	0.1157	0.1220	0.1253	0.1275	0.1296
150/145	0.1655	0.1657	0.1756	0.1855	0.1890	0.1920	0.1950
148/143	0.2847	0.2848	0.2894	0.2928	0.2992	0.3042	0.3034

V. CONCLUSIONS AND DISCUSSION

Based on the neutron spectrum measurement data and the measured α values given in Figure 1, the irradiation of the fast-fission yield capsules was conducted in a neutron environment which appears closely similar to that expected for the Fast Test Reactor and a conceptual mixed-oxide fueled 1000 MW_e LMFBR. The reported fast-fission yield data are, therefore, considered applicable to the determination of burnup for mixed uranium-plutonium fuels irradiated in similar neutorn spectra. Although these fast-fission yields are applicable to a variety of experimental fuels (oxides, advanced nitrides or carbides) irradiated in a representative mixed oxide lattice, the selected burnup monitor isotope(s) for the various fuel specimens may differ. The selection criteria for burnup monitors have been discussed in detail.[1] Of particular importance is the migration of the monitor element in the fuel during irradiation.

For thermally irradiated mixed-oxide fuel, ^{148}Nd has been used extensively for the determination of burnup. Because ^{148}Nd was assumed to be applicable to the determination of burnup for mixed-oxide LMFBR experimental fuels, the obtained fast-fission yield data for neodymium isotopes has been critically reviewed.

Listed in Table VII are the neodymium fast-fission yield data measured to date in this program, and data for one capsule of ^{235}U irradiated in rows 2 and 4 of EBR-II recently reported by R. P. Larsen.[7]

TABLE VII. FAST FISSION YIELDS OF NEODYMIUM ISOTOPES FROM ^{235}U AND ^{239}Pu

	Fission Yields, %			
	^{235}U		^{239}Pu	
Isotope	This work Row 8	ANL[7] Row-2-4	This work Row 8	
^{143}Nd	5.80±0.05	5.56±0.08	4.37±0.03	
^{144}Nd	5.27±0.04	5.04±0.08	3.70±0.03	
^{145}Nd	3.83±0.03	3.66±0.05	3.01±0.02	
^{146}Nd	2.94±0.02	2.84±0.04	2.46±0.02	
^{148}Nd	1.68±0.02	1.66±0.03	1.65±0.02	
^{150}Nd	0.672±0.008	0.683±0.010	0.981±0.011	

It is quite evident, that some of the ^{235}U neodymium fast-fission yields for these two experiments are different. This is clearly the result of the differences in the neutron energies in which the irradiations were made. For the ANL irradiation, made in a harder spectrum (in EBR-II rows 2 and 4) than that expected in commercial mixed-oxide LMFBRs, the yield of ^{150}Nd is higher and the yields of the lower mass neodymium isotopes are lower, relative to the yields measured for the irradiation made in row 8 of EBR-II. However, of particular importance, is that the change in the fast-fission yield of ^{148}Nd over this energy range is nil. Equally important, is that the preliminary measured fast-fission yield of ^{148}Nd for ^{239}Pu is not significantly different than that of ^{235}U. Thus, ^{148}Nd has been selected as the monitor for the determination of total fissions in experimental mixed-oxide fuels where the major sources of fission are from ^{235}U and ^{239}Pu and the neutron spectrum is characteristic of mixed-oxide fueled LMFBRs.

For advanced LMFBR experimental fuels, using mixed-carbides or mixed-nitrides, and irradiated in a neutron spectrum characteristic of mixed-oxide fueled LMFBRs, the selection of the preferred burnup monitor will require knowledge of fission product migration in the fuels during irradiation. This information will be obtained from postirradiation metallographic and chemical studies of advanced fuels to be conducted at the Los Alamos Scientific Laboratory and the final recommendations for a burnup monitor isotope(s) and associated yield(s) for experimental advanced fuels will be a cooperative effort between Allied Chemical and LASL. For LMFBRs entirely composed of advanced fuels, knowledge of the neutron spectrum as well as fission product migration will be required before the most appropriate burnup monitor can be specified.

VI. RECOMMENDATIONS

Based on the fast-fission yield data in Table VII and the discussion in Section V, the recommended monitor for the accurate determination of burnup in mixed-oxide fuels where the major sources of fission are ^{235}U and ^{239}Pu and the neutron spectrum is characteristic of a mixed-oxide fueled LMFBR is ^{148}Nd using a fast-fission yield of 1.66%. Use of this value in a burnup calculation for this type of fuel will introduce an uncertainty of less than 2% in the final burnup estimate.

This recommendation is based on the following:

1) that similar ^{235}U fast-fission yield values, 1.66±0.03 and 1.68±0.02 (see Table VII) were obtained by two different experimenters, on separate irradiation capsules, irradiated at different times in two different neutron spectra in EBR-II;

2) that the preliminary measured ^{239}Pu fast-fission yield for ^{148}Nd, 1.65±0.02 is not significantly different from the measured ^{148}Nd fast-fission yield of ^{235}U;

3) that little or no migration of neodymium in $(U\text{-}Pu)O_2$ mixed-oxide fuels has been observed; and

4) that well established chemical separation and mass spectrometric procedures for neodymium analysis exist.

At this time, neither a specific nuclide(s) monitor nor an associated fast-fission yield value(s) can be recommended for the determination of burnup in an LMFBR fuel where the major sources of fission are other than ^{235}U and ^{239}Pu and whose composition is other than reference $(U,Pu)O_2$.

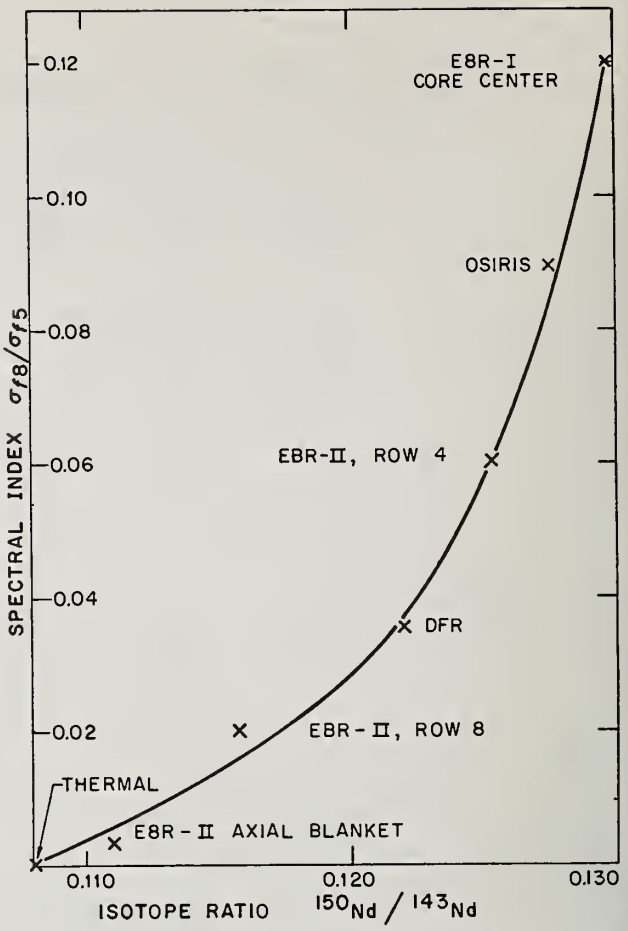

Figure 2. Change in Isotopic Ratio of $^{150}Nd/^{143}Nd$ with Neutron Energy

VII. ACKNOWLEDGEMENTS

The wide scope of this project required contributions from a number of scientists and technicians with specialized disciplines. Specifically, the author thanks D. E. Adams, W. A. Emel, F. A. Duce, R. L. Eggleston, A. L. Erikson, J. H. Keller, L. D. McIsaac, and R. L. Tromp who conducted the chemical separations and performed the many calculations; L. W. Buttars, J. E. Delmore, L. L. Dickerson, and R. A. Nielsen who performed the mass spectrometric analyses; Y. D. Harker for the spectrum evaluations, and F. W. Spraktes for the statistical evaluation of the data. In addition, the author thanks R. P. Larsen, Argonne National Laboratory, and J. E. Rein, Los Alamos Scientific Laboratory for their active participation in working group meetings devoted to extensive critical reviews of the experiment and resultant data.

REFERENCES

[1] W. J. Maeck, R. P. Larsen, J. E. Rein, Report TID-26209 (1973).

[2] J. A. Hallbid, USAEC Report SC-RR-70-251 (April 1970)

[3] Lisman, F. L., Abernathey, R. M., Maeck, W. J., Rein, J. E., Nucl. Sci. Eng. 42, 191 (1970).

[4] Sinclair, V. M., Davies, W., International Conference on Chemical Nuclear Data, BNES, Univ. of Kent, Canterbury, England (1971).

[5] Robin, M., Bouchard, J., Darrouzet, M., Frejaville, G., Lucas, M., Prost Marechal, F., International Conference on Chemical Nuclear Data, BNES, Univ. of Kent, Canterbury, England (1971).

[6] Maeck, W. J., Emel, W. A., Tromp, R. L., ICP-1058 (1974).

[7] Larsen, R. P., Argonne National Laboratory, private commmunication (1974).

EFFECTS OF NUCLEAR DATA UNCERTAINTIES UPON LMFBR FUEL CYCLE CHARACTERISTICS

R. D. McKnight and L. G. LeSage
Argonne National Laboratory
Argonne, Illinois 60439
and
J. M. Christenson
University of Cincinnati
Cincinnati, Ohio 45221

Fuel cycle sensitivity calculations have been performed to determine the effects which nuclear data uncertainties have upon the long term properties of a typical LMFBR. These effects are assessed by direct comparison of a series of fuel cycle calculations which evaluate the approach to equilibrium conditions. The effects of uniform cross section adjustments (for the fission and capture cross sections for ^{238}U, ^{239}Pu, ^{240}Pu, and ^{241}Pu) upon the fuel cycle characteristics, including breeding ratio, doubling time, power distribution, fissile loading, fissile mass discharge rates, control requirements and reactivity swing are presented for the initial burn cycle and the equilibrium cycle. ENDF/B-3 data are used for a data reference. Several of the cross section modifications produced significant uncertainties in LMFBR design parameters. The effects of these changes upon the fuel cycle characteristics propogate from cycle to cycle but, in general, do not increase with time. The most significant effects were produced by uncertainties in σ_f for ^{239}Pu and ^{241}Pu, and σ_c for ^{238}U. Uncertainties in these cross sections produce large changes in control requirements, breeding potential, and reactivity swing.

(Sensitivity study; cross section uncertainties; fuel cycle; equilibrium cycle; breeding ratio; reactivity swing)

Introduction

The economic analysis of a large fast breeder reactor is strongly dependent upon the fuel cycle characteristics. The parameters of primary interest are the breeding ratio and the fuel discharge rates. Detailed fuel cycle calculations are also required for neutronic, thermal, hydraulic and shielding designs. The reactor designer must know the reactivity swing due to burnup (in order to specify initial enrichment and control requirements) and the shift in the power distribution as fuel material is produced in the blanket regions (to specify coolant and shielding requirements). Each of these parameters is time-dependent and can change markedly over several burn cycles. The designer must know not only how these parameters vary over a burn cycle but also how they change from cycle to cycle in the approach-to-equilibrium conditions. The most significant composition changes during the reactor lifetime include: depletion of the fuel in the core regions, insertion or removal of control material, production of fissile material in the blanket regions, and buildup of fission products. The production and destruction rates for the fuel isotopes depend directly upon the fission and capture cross sections for these isotopes. Fuel cycle sensitivity calculations have been performed to determine the effects which the uncertainties in these data have upon the long term properties of a typical LMFBR.

Nuclear Data Uncertainties

Although the quantity and quality of cross section measurements have increased considerably within the last few years, most of the accuracy requirements of the important nuclear data set by fast reactor physicists have not yet been attained. Many cross section measurements are now performed to within 2% accuracy, yet, the disagreement among independent measurements is in many cases much greater. This can sometimes be traced to inconsistent normalizations, thereby eliminating discrepancies. However for most of the materials of interest there still exist large ranges where the only available measurements differ by ±5 to 20%.

There is also considerable disagreement among the estimates of current uncertainties in the principal cross sections. An estimate of the current uncertainties in the nuclear data for the principal isotopes in LMFBR design is of primary interest for these sensitivcalculations. A brief summary of the estimated uncertainties is given in Table I. A more complete

TABLE I. Estimated Cross Section Uncertainties

^{239}Pu σ_f	∿5-10%
σ_c	∿10-15%
^{238}U σ_c	∿10-15%
^{240}Pu σ_f	∿10-15%
σ_c	∿20%
^{241}Pu σ_f	∿10-15%
σ_c	∿20%

evaluation of nuclear data uncertainties may be found in Refs. 1 and 2 and in the literature cited therein.

Method of Calculation

The effects of uncertainties in the fission and capture cross sections for the principal U and Pu isotopes upon LMFBR fuel cycle parameters have been assessed by direct comparison of a series of reactor burnup calculations. The fuel cycle analyses were performed using the REBUS-2 [3] System (REactor BUrnup System). Reference fuel cycle characteristics were obtained using ENDF/B Version 3 data. The fuel cycle calculations were then repeated using modified cross sections.

1000 MWe LMFBR Fuel Cycle Model

The reactor model selected for these sensitivity calculations is representative of current designs of a 1000 MWe oxide-fueled fast breeder reactor. The 6000-liter core has two enrichment zones of equal volume, with 35% fuel (mixed oxide, 85% T.D.), 20% stainless steel, 44% sodium, and 1% control (natural boron carbide). The isotopic plutonium composition is 59% ^{239}Pu, 26% ^{240}Pu, 12% ^{241}Pu, and 3% ^{242}Pu, which is typical of plutonium recycled from light-water reactors. The volume fractions for the axial blanket are taken to be the same as for the core. The volume fractions for the radial blanket are 55 v/o fuel, 15 v/o stainless steel, and 30 v/o sodium. The fuel in the blanket

gions is depleted UO_2 at 90% T.D. The reflector contains 80 v/o stainless steel and 20 v/o sodium.

Since one objective of these sensitivity calculations was to analyze shifts in either radial or axial power distributions, the neutronics calculations involved two dimensional (RZ) diffusion theory for a cylindrical reactor model. Region- and composition-dependent cross section sets containing 9 broad groups were obtained from a homogeneous SDX[4] calculation which included resonance but not spatial self-shielding. To achieve reasonable average fuel burnup, the following refuelling method was used:

(1) The burn step was 300 full power days. This corresponds to 1 year with a load factor of 83%.

(2) The fuel management scheme was fractional batch-scatter reloading. The fuel was added and discharged in a random fashion.

(3) The core was refueled in batches, one-third of each enrichment zone at the end of each burn step.

(4) The radial blanket was refueled in the same fashion, but one-sixth at each time.

(5) The axial blanket was renewed in the same way as the adjacent core.

(6) The initial feed compositions were maintained for all refuelings (i.e., light-water reactor discharge plutonium).

With this refueling scheme, the reactor will operate in an initial transient cycle for the first six burnup intervals. The equilibrium cycle repeats thereafter every burn cycle.

Neutronics calculations (two-dimensional diffusion theory) were performed at the beginning (burn time = 0 days) and end (burn time = 300 days) of each burn cycle. At each time, a control search was made to maintain criticality. The fuel cycle calculations were obtained for 9 burn cycles (8 refuellings). After three burn cycles, the reactor is close to equilibrium conditions. The seventh burn cycle was reported as the equilibrium cycle. This was confirmed by comparisons with results calculated for later cycles.

Nuclear Data Adjustments

Fuel cycle calculations for the reference case were obtained using ENDF/B Version 3 data. These calculations were then repeated for the same 1000 MWe LMFBR reactor model using modified cross section data. Only uniform (over the entire energy range from 10 MeV to thermal) changes were made. The modifications included: σ_c^{49} (-10%), σ_f^{49} (+10%), σ_c^{28} (-10%), σ_c^{40} (-20%), σ_f^{40} (+20%), σ_c^{41} (-20%), σ_f^{41} (-20%). These cross section changes are comparable in magnitude to the estimated cross section uncertainties (compare with Table I), with exception of the ^{239}Pu and ^{241}Pu fission cross sections. All modifications were made such that the eigenvalue for the system would increase. This modification was then compensated for with a control search to critical. In light of previous cross section sensitivity calculations[2] for LMFBR design parameters, no modifications to the data for ^{242}Pu were considered. It should also be noted that results of any sensitivity calculations are dependent upon the method used to maintain the system at critical. For these calculations, the control volume fraction was adjusted. Other methods (e.g., adjusting the feed enrichments or the region boundaries) could have been employed. Regardless, the interpretation of any sensitivity study requires consideration of the effect which the adjustment-to-critical has upon the calculated parameters. One merit in the chosen method of maintaining a critical system is the fact that the breeding ratio is much less sensitive (by an order of magnitude) to adjustments in control loading than enrichment.

Results of Calculations

The results of the fuel cycle calculations are summarized in Table II. This table contains the reference values of the fuel cycle characteristics for the 1000 MWe LMFBR model and the parameters obtained with the modified cross section data for both the first cycle and the equilibrium cycle. Note that criticality was maintained throughout the approach-to-equilibrium by adjusting the amount of control material. The feed enrichments were maintained constant, as were the burn steps (300 full power days) and the total reactor power (2500 MWt). Therefore, the average fuel burnup is essentially fixed. Nevertheless, the effects of burnup will be reflected in the change in control requirements and the reactivity swing of a burn cycle. Note also that since the feed enrichment for all refuellings was maintained equal to the initial feed enrichment, the amount of control loaded in the initial cycle had to be increased to offset the high initial fissile loading for the beginning-of-life configuration. The reactivity swing over the first cycle is 6.0% δk. The components of this change in k are given in Table III. The major contribution to the change in eigenvalue which must be offset by removal of control material is the depletion of the core.

The results of the uniform cross section changes upon the fuel cycle characteristics are also included in Table II. The effects of these data modifications will now be considered individually.

^{239}Pu: $\sigma_c' = 0.9\ \sigma_c$

The 10% reduction of the ^{239}Pu capture cross section increases the cycle-averaged breeding ratio ~20% for the initial cycle and ~1.3% for the equilibrium cycle. The fissile mass discharged in the equilibrium cycle increases ~1% and the simple doubling time decreases ~6%. The control requirement increases ~4% at beginning-of-life and is ~7% larger for the equilibrium cycle. The effect of this cross section modification upon the power split is small (<1%).

^{239}Pu: $\sigma_f' = 1.1\ \sigma_f$

All the major fuel cycle characteristics are significantly affected by a 10% change in the ^{239}Pu fission cross section. The initial control requirements are increased almost 50%. Even more significantly, the change in the control requirements over the first cycle is increased ~150%. The reactivity swing over the first cycle is increased by 0.6% δk. These effects are decreased somewhat in the equilibrium cycle. The control requirement remained ~40% larger and the reactivity swing increased 0.5% δk. The breeding ratio is ~6% smaller over the first cycle and ~4% smaller over the equilibrium cycle. The doubling time increased ~34%. The change in the power split (as compared to the reference case) is large, particularly the ratio of the power between the core zones.

^{238}U: $\sigma_c' = 0.9\ \sigma_c$

The major effects of reducing the ^{238}U capture cross section are upon the control requirements, the reactivity swing per cycle and the breeding potential. The breeding ratio is decreased ~6%. The net fissile plutonium produced per year is decreased by 33% and

TABLE II. Effects of Uniform Cross Section Changes upon Fuel Cycle Characteristics for a 1000 MWe LMFBR

	Reference Case[a]		$^{239}Pu\ \sigma_c$ Decreased 10%		$^{239}Pu\ \sigma_f$ Increased 10%		$^{238}U\ \sigma_c$ Decreased 10%		$^{240}Pu\ \sigma_c$ Decreased 20%		$^{240}Pu\ \sigma_f$ Increased 20%		$^{241}Pu\ \sigma_c$ Decreased 20%		$^{241}Pu\ \sigma_f$ Increased 20%	
	Init. Cycle	Equil. Cycle	Init. Cycle	Equil. Cycle	Init. Cycle	Equil. Cycle	Init. Cycle	Equil. Cycle	Init. Cycle	Equil. Cycle	Init. Cycle	Equil. Cycle	Init. Cycle	Equil. Cycle	Init. Cycle	Equil. Cycle
Control Modifier[b]																
Beginning of Cycle	1.000	0.552	1.040	0.613	1.498	0.937	1.189	0.636	1.030	0.566	1.088	0.633	1.015	0.571	1.270	0.699
End of Cycle	0.415	0.129	0.470	0.201	0.042	0.420	0.498	0.142	0.426	0.131	0.482	0.201	0.434	0.149	0.546	0.199
Reactivity Swing, δk	0.060	0.045	0.058	0.044	0.066	0.050	0.071	0.054	0.062	0.047	0.059	0.045	0.059	0.045	0.070	0.052
Power Split																
Inner Core	0.421	0.390	0.420	0.388	0.406	0.374	0.417	0.383	0.420	0.389	0.417	0.387	0.420	0.390	0.413	0.384
Outer Core	0.527	0.460	0.527	0.460	0.542	0.470	0.529	0.464	0.528	0.460	0.531	0.464	0.527	0.460	0.535	0.467
Inner Axial Blanket	0.011	0.021	0.011	0.021	0.010	0.020	0.011	0.021	0.011	0.021	0.011	0.020	0.011	0.021	0.010	0.020
Outer Axial Blanket	0.009	0.017	0.009	0.017	0.009	0.017	0.009	0.017	0.009	0.017	0.009	0.016	0.009	0.016	0.009	0.016
Radial Blanket	0.030	0.104	0.030	0.104	0.031	0.109	0.031	0.105	0.030	0.104	0.030	0.103	0.030	0.104	0.030	0.104
Radial Blanket Ext.	0.003	0.009	0.003	0.009	0.003	0.010	0.003	0.010	0.003	0.009	0.003	0.009	0.003	0.009	0.003	0.009
Maximum Power Density, W/cm^3	571.3	486.5	572.2	486.3	572.9	493.9	567.0	489.9	570.7	487.0	574.9	490.6	571.9	487.0	573.0	492.9
Breeding Ratio[c,d]																
Inner Core	0.385	0.356	0.389	0.358	0.348	0.326	0.351	0.330	0.380	0.352	0.381	0.353	0.386	0.356	0.367	0.345
Outer Core	0.303	0.286	0.309	0.290	0.292	0.277	0.282	0.271	0.299	0.282	0.305	0.287	0.306	0.287	0.299	0.285
Inner Axial Blanket	0.093	0.093	0.095	0.094	0.087	0.088	0.089	0.089	0.094	0.093	0.093	0.093	0.094	0.093	0.091	0.091
Outer Axial Blanket	0.074	0.076	0.077	0.077	0.074	0.075	0.072	0.074	0.076	0.076	0.076	0.076	0.076	0.076	0.075	0.076
Radial Blanket	0.236	0.254	0.243	0.260	0.238	0.259	0.232	0.248	0.240	0.256	0.242	0.257	0.240	0.255	0.240	0.257
Radial Blanket Ext.	0.039	0.046	0.040	0.046	0.039	0.047	0.039	0.046	0.040	0.046	0.040	0.046	0.040	0.046	0.040	0.046
TOTAL	1.130	1.111	1.153	1.125	1.079	1.071	1.066	1.057	1.128	1.105	1.137	1.111	1.142	1.113	1.112	1.101
Average Burnup, MWD/MT																
Inner Core	35664	33296	35607	33166	34236	31878	35066	32551	35518	33146	35329	33040	35649	33277	34746	32594
Outer Core	44586	29223	44744	39321	45688	39962	44527	39366	44609	39230	44974	39564	44652	39276	44954	39644
Inner Axial Blanket	1802	3474	1794	3456	1667	3258	1816	3491	1795	3468	1755	3373	1799	3461	1696	3306
Outer Axial Blanket	1465	2717	1467	2725	1454	2748	1493	2796	1466	2729	1454	2688	1466	2715	1433	2683
Radial Blanket	1457	5095	1462	5167	1486	5369	1497	5127	1461	5126	1456	5093	1458	5097	1444	5094
Radial Blanket Ext.	253	874	254	884	254	926	273	938	253	880	252	870	253	874	250	873
Fissile Pu Discharged at End of Cycle, kg[e]																
Inner Core	319.7	301.1	321.1	304.8	314.9	290.4	312.5	285.8	318.5	298.9	319.7	301.4	320.1	301.9	317.5	298.1
Outer Core	439.5	358.0	441.2	361.7	433.4	345.4	433.1	343.8	437.9	354.6	439.6	358.3	439.9	359.0	437.0	353.6
Inner Axial Blanket	21.4	58.6	21.3	58.8	19.3	54.3	20.0	55.1	21.3	58.6	20.9	57.7	21.3	65.7	20.3	57.2
Outer Axial Blanket	19.5	51.8	19.5	52.0	18.5	49.6	18.4	49.0	19.5	51.8	19.3	51.5	19.5	46.1	19.0	51.2
Radial Blanket	46.4	172.2	46.6	174.7	44.7	164.7	43.4	160.2	46.4	172.7	46.2	172.3	46.4	172.7	45.6	171.9
Radial Blanket Ext.	8.4	44.0	8.4	44.4	8.2	42.9	8.1	42.3	8.4	44.1	8.4	43.9	8.4	44.0	8.3	43.9
TOTAL	854.9	986.2	858.1	996.4	839.0	947.3	835.4	936.2	852.1	980.7	854.1	985.1	855.6	989.4	847.7	975.9
Simple Doubling Time, yr.[f]	-	16.46	-	15.4	-	22.1	-	24.5	-	17.1	-	16.6	-	16.1	-	17.7
Compound Doubling Time, yr.[f]	-	11.41	-	10.7	-	15.3	-	17.0	-	11.8	-	11.5	-	11.2	-	12.2

[a] Reference values were obtained using ENDF/B Version 3 data.

[b] Relative to value of control modifier at beginning-of-life for reference system.

[c] Defined with respect to fissile Pu (i.e., ^{235}U is not considered fissile in breeding ratio definition).

[d] Time-averaged values, averaged over 300 day burn-cycle.

[e] Fissile Pu ≡ $^{239}Pu + {}^{241}Pu$.

[f] Obtained directly from mass inventories.

TABLE III. Components of Reactivity Swing Over the First Cycle

k = 1.000 at time = 0 days	
System Changes after 300 Full Power Days	δk[a]
Core Depletion	-0.053
Fission Product Buildup	-0.017
Blanket Plutonium Buildup	+0.010
Control Change	+0.060
k = 1.000 at time = 300 days	

[a] δk was obtained by eigenvalue difference (two-dimensional diffusion) calculations using atom densities from the reference fuel cycle calculations.

the doubling time is increased ∿50%. The control requirements are increased by ∿10-20%. The reactivity swing is increased from 6.0% δk to 7.1% δk over the equilibrium cycle. This uncertainty in fissile material production and concomitant uncertainty in the reactivity swing per cycle have significant impact on the specification of the initial enrichment and control requirements.

^{240}Pu: $\sigma_c' = 0.8\ \sigma_c$

Reducing the ^{240}Pu capture cross section produces only small changes in both the initial cycle and the equilibrium cycle. The changes over the first cycle are approximately equal to the effects calculated for the beginning-of-life conditions and do not change significantly over the reactor lifetime. The beginning-of-life control requirement increases ∿3%, the breeding ratio decreases ∿1%, and the power distributions are almost not affected. These changes are of the same magnitude during the equilibrium cycle. There is a 4% increase in the doubling time.

^{240}Pu: $\sigma_f' = 1.2\ \sigma_f$

A 20% increase in the ^{240}Pu fission cross section has almost no effect upon the breeding ratio, the power distribution, and the fissile material production and discharge rates for either beginning-of-life or equilibrium operation. The control requirement is ∿9%

larger initially. This amount of additional control is required throughout later cycles.

^{241}Pu: $\sigma_c' = 0.8\ \sigma_c$

Reducing the capture cross section of ^{241}Pu produces only small changes in the fuel cycle characteristics. The beginning-of-life breeding ratio is increased ∿0.6%. This effect is only ∿0.3% in the equilibrium cycle which has a smaller ^{241}Pu fraction. The power fractions are changed by <1% and approximately 1.5% more control is required throughout the reactor lifetime.

^{241}Pu: $\sigma_f' = 1.2\ \sigma_f$

Increasing the fission cross section of ^{241}Pu does produce significant changes in the fuel cycle characteristics. However, these effects decrease with time since the increased fission rate increases the depletion of the ^{241}Pu, thus diminishing the magnitude of the changes. The breeding ratio is ∿3% smaller at the start of the first cycle and ∿2% smaller at the end of that cycle. For the equilibrium cycle, the breeding ratio is ∿1% smaller. The control requirement is increased ∿27% for the beginning-of-life and ∿13% at the end of the first cycle. The reactivity swing increases from 6.0% δk to 7.0% δk over the first cycle. At the start of the equilibrium cycle ∿15% more control is required; ∿7% more is necessary at the end of that cycle. The difference in the reactivity swing is reduced to 0.7% δk. These uncertainties for the control requirements and the reactivity swing (δk/cycle) seriously impact the reactor design. The increased burnup of ^{241}Pu reduces the fissile mass discharge rate (∿2%) and increases the simple doubling time ∿8%.

Summary

Several of the cross section modifications considered in these fuel cycle calculations produce significant uncertainties in LMFBR design parameters. The effects of the cross section changes upon the fuel cycle characteristics propagate from cycle to cycle but, in general, do not increase with time. An increase (or decrease) in a reaction cross section produces a corresponding increase in removal (or production) of that material which offsets the effects of the cross section change. The modifications to the ^{239}Pu fission cross section and the ^{238}U capture cross section produce large changes in control requirements, breeding potential, and fissile mass discharge rates. Only the modification of the ^{239}Pu fission cross section had significant effects upon the power distribution and its time variation. As would be expected, the breeding ratio is most sensitive to the changes in the capture cross section of ^{238}U. The ^{238}U capture cross section changes also produce large uncertainties in the reactivity swing per burn cycle. Modification of the fission cross sections of ^{239}Pu and ^{241}Pu and the capture cross section of ^{238}U directly affect the rate of fissile material production and destruction over a burn cycle, and therefore directly affect the reactivity swing over the cycle. For each of these cross sections (σ_f^{49}, σ_f^{41}, and σ_c^{28}), the change in the reactivity swing per burn cycle produced by the uniform cross section modification was approximately 1%k. For the initial loading of the reference system, an increase of 1% k corresponds to a decrease of 1.6% in fissile inventory (i.e., ∿40 kg fissile plutonium) for an enrichment adjustment to critical. Such uncertainty in the reactivity swing between refuellings necessitates conservation in specifying the initial fissile loading (and therefore also in the control loading) which further reduces the breeding potential for the LMFBR.

References

1. E. M. Bohn, R. J. LaBanne, R. E. Maerker, B. A. Magurno, F. J. McCrosson, and R. E. Schenter, "Benchmark Experiments for Nuclear Data," Invited Paper for this Conference.

2. R. D. McKnight, L. G. LeSage, and J. M. Christenson, "Sensitivity Studies of the Effects of Nuclear Data Uncertainties for the Higher Plutonium Isotopes upon Fast Reactor Design," Conference on Advanced Reactors; Physics, Design and Economics, Atlanta, Ga. (1974).

3. Private Communication from A. P. Olson, Argonne National Laboratory, "A User's Manual for the Reactor Burnup System, REBUS-2," FRA-TM-62 (1974).

4. W. M. Stacey, Jr., et al., "A New Space-Dependent Fast-Neutron Multigroup Cross-Section Preparation Capability," Trans. Am. Nucl. Soc. 15, 292 (1972).

THE SENSITIVITY OF k_{eff} OF METALLIC ASSEMBLIES TO THE PARAMETRIC REPRESENTATION OF THE FISSION AND THE INELASTIC SCATTERING SPECTRA

H. Nissimov and J.J. Wagschal
The Hebrew University of Jerusalem
Jerusalem 91009, Israel

The fission spectrum and the inelastic scattering spectrum of ENDF/B-IV ^{239}Pu data were modified. The variations of k_{eff} and of the leakage spectrum induced by these modifications were calculated for a bare ^{239}Pu critical sphere, as a typical metallic assembly. In certain cases these modifications lead to substantial variations in k_{eff}. Guides for reasonable changes in the representation of the spectra were obtained. The variations in k_{eff} and in the leakage spectrum caused by these reasonable changes were found to be within their experimental errors.

(critical assemblies; fission spectrum; inelastic scattering; ^{239}Pu; ENDF/B-IV; sensitivity)

Introduction

Neutronics calculations necessitate, in addition to a detailed description of the energy dependence of the various neutron cross sections, a description of the secondary neutron energy spectrum. Except for small contributions from (n,2n) and (n,3n) reactions, the fission process is the mechanism that regenerates fast neutrons in critical assemblies. On the other hand, elastic and inelastic scattering determine the neutron slowing down. The critical masses (or the effective multiplication factor k_{eff})of metallic assemblies of simple geometry can be measured and calculated accurately, and hence serve to test neutron data files in the fast energy range. In metallic assemblies the inelastic scattering is the main mechanism of the neutron slowing down. Recognizing the main processes in fast critical assemblies, we proceed in this work to investigate the sensitivity of k_{eff} and of the neutron leakage spectrum from metallic critical assemblies to the representation of the fission spectrum and of the inelastic scattering.[1]

In the ENDF/B files the fission spectrum is represented by a simple Maxwellian

$$f(E\to E') = \frac{\sqrt{E'}}{I} e^{-E'/\theta(E)}$$

where E' is the secondary neutron energy, I is a normalization factor, and $\theta(E)$ is the effective nuclear temperature at incident energy E. The temperature $\theta(E)$ appears as a table of $\theta(E_j)$ values at given energies E_j, accompanied by an interpolation scheme (usually linear) for intermediate incident neutron energies.

The inelastic scattering process is represented by a series of inelastic excitation cross sections to the first n levels (up to 40), and by an inelastic excitation cross section to the continuum. The energy distribution of the secondary neutrons of the discrete level excitations is given by

$$f(E\to E') = \delta\left[E' - \frac{A^2+1}{(A+1)^2} E + \frac{A}{A+1}\theta\right]$$

where θ is the excitation energy of the level of the residual nucleus and A is the atomic weight ratio.

The energy spectrum of the secondary neutrons of the inelastic excitation to the continuum is given as an evaporation spectrum

$$f(E\to E') = \frac{E'}{I} e^{-E'/\theta(E)}$$

for energies $0 \leq E' \leq E - U$.

The effective nuclear temperature $\theta(E)$ is tabulated as function of incident energy and accompanied by an appropriate interpolation scheme for intermediate energies.

The fission effective nuclear temperatures and the inelastic scattering effective nuclear temperatures vary from one ENDF/B version to another. In the case of inelastic scattering the number of discrete levels and the threshold of the inelastic scattering to the continuum vary as well. In this work we first try to get some feeling for the range of possible nuclear temperatures from an analysis of the neutron yield of ^{238}U at high energies. The sensitivities of k_{eff} and of the neutron leakage spectrum to variations in the representation of the fission spectrum and in the description of the inelastic scattering process are then derived numerically for a simple bare ^{239}Pu sphere. These results will be discussed in the concluding sections.

Estimate of Effective Nuclear Temperature Uncertainties

The numerical values of the fission and inelastic scattering effective nuclear temperatures, θ_f and θ_{in} are usually deduced by fitting the theoretical Maxwellian and evaporation spectra (including (n,2n) and (n,3n) for high energies) to relevant experimental data. The values thus obtained are, of course, subject to some uncertainties.

Now, different ENDF/B versions quote different values of these temperatures, but do not give the uncertainties associated with them. In order to get some idea on the range in which the temperatures can be varied without destroying the fit, we have compared the theoretical expressions for given values of θ_f and θ_{in}, to some experimental data. Then, by changing these values we have been able to see to what extent the curves changed in shape, and did or did not remain within the range of the experimental points.

The comparison was carried out for ^{238}U for incident energies E = 3Mev and E = 14 Mev, where the experimental data was taken from the works of Salnikov et al.[2] and Batchelor et al.[3] The reference theoretical curves were calculated using the ENDF/B-III data.

For E = 14 Mev we find that the total secondary neutron energy spectrum is rather insensitive to the inelastic scattering nuclear temperature. A change of ± 50% of the value given by ENDF/B-III still gives a reasonable fit to the experimental data. On the other hand, a mere 10% change of the fission nuclear temperature leads to the same effect as the 50% change in θ_{in}. An envelope of the experimental points is

obtained with a slightly higher change in the fission temperature.

The case of E = 3 Mev, although less conclusive, indicates that a change of 10% in the inelastic nuclear temperature is the maximal permissible change. And also, a change of 5% in θ_f plays the same role as the 10% change in θ_f in the previous (E = 14 Mev) case.

We conclude that the freedom in changing the temperatures decreases with decreasing incident energy.

Method of Calculation

A bare ^{239}Pu sphere was used as a representative metallic assembly for our calculations. The ENDF/B-IV data for ^{239}Pu, material 1264, were processed into proper multi group sets. The processing code could handle all nuclear reactions according to the data file specifications, with the exception of the angular distribution of inelastically scattered neutrons to high discrete levels.

A series of data changes were made in order to test the sensitivity of k_{eff} and of the leakage spectrum to the representation of the fission spectrum and the inelastic scattering. These changes resulted in a variation of k_{eff}. Let us define

$$\delta k = \frac{k - k_{ref}}{k_{ref}}$$

where k_{ref} is the effective multiplication factor calculated with unchanged ENDF/B-IV data, and k is k_{eff} calculated with data subjected to a particular change. Similarly

$$\delta L = \frac{L - L_{ref}}{L_{ref}}$$

where L is a spectral index defined by the ratio of the leakage of neutrons of energies 1.3 Mev or less to the leakage of neutrons of higher energy.

The effective multiplication constant k_{eff} and the spectral index L, were calculated for a bare ^{239}Pu sphere of density 15.44 gm/cm^3 and radius 6.3 cm. All quoted results were obtained in S_8, 30 radial intervals, 20 group, transport corrected P_0 calculations. For this assembly both k_{ref} and L_{ref} are close to unity. Although k and L depend on the number of energy groups and their selection, and on the use of the transport approximation, δk and δL are not sensitive to these parameters. As a test δk and δL were calculated for a few cases with forty energy groups, or with five terms in the anisotropic elastic scattering source expansion, and remained constant for all practical purposes.

Results

Inelastic Scattering

The inelastic scattering of material 1159 (^{239}Pu of ENDF/B-III) is represented by cross sections for the inelastic excitation to 23 discrete levels up to .849 Mev, and by cross sections for inelastic scattering to the continuum. An evaporation spectrum is given for the inelastic scattering to the continuum. The effective nuclear temperature is given at five points with logarithmic interpolation for intermediate energies. Material 1264 (^{239}Pu of ENDF/B-IV) has 26 discrete levels going up to 5.975 Mev. Out of these 26 discrete levels the first 10 go up to .556 Mev, and the next 10 levels bring us to .849 Mev (the highest discrete level in the ENDF/B-III representation). The six new high discrete levels are also characterized by anisotropic scattering. The inelastic scattering to the continuum has a threshold corresponding to the eleventh discrete level, and the secondary neutron spectrum is given as evaporation with tabulated temperatures. These temperatures differ from those of ENDF/B-III. The interpolation between given points is linear. These changes in the data led to the series of calculations that are summarized in Table I.

TABLE I. The variation of k_{eff} and of L as function of the inelastic scattering representation

Inelastic scattering representation	$\delta k \times 10^3$	$\delta L \times 10^2$
A. ENDF/B-III secondary neutron spectrum	-.21	.05
B. Inelastic scattering to discrete levels higher than .556 Mev, treated as inelastic scattering to the continuum	-.44	1.02
C. The temperature θ_{in} (E) of the evaporation spectrum raised by 10%	.47	-1.10
D. Inelastic scattering to discrete levels higher than .556 Mev, treated as isotropic elastic scattering	.61	-1.37
E. Inelastic scattering to all discrete levels treated as isotropic elastic scattering	2.00	-4.54

In case A, the ENDF/B-III secondary neutron spectrum was simulated in the following way. The ENDF/B-IV effective nuclear temperatures of the inelastic scattering to the continuum, were replaced by the corresponding ENDF/B-III values, and the inelastic excitation of the six highest levels was also treated as inelastic scattering to the continuum. Both k_{eff} and L were hardly influenced by these changes. On the other hand taking the inelastic scattering to all discrete levels as elastic scattering, case E, decreases the slowing down, the leakage spectrum is harder, and k_{eff} changes by more than the experimental error in critical mass of a Jezebel type assembly.[4] Handling the inelastic excitation cross section to levels higher than .556 Mev either as isotropic elastic scattering or as inelastic scattering to the continuum, cases B and D in Table I, changes k_{eff} and the leakage spectrum only slightly. A 10% change of the effective nuclear temperature of the evaporation spectrum, case C in Table I, is accompanied by a change of only 1% in our spectral index and by a change of k_{eff} that amounts to one quarter experimental error in critical mass.

Fission Spectrum

As we have already mentioned, our reference calculation uses ENDF/B-IV ^{239}Pu data. There, the fission effective nuclear temperature, θ_f, is tabulated for a number of incident energies, and the values of θ_f for intermediate energies are obtained by linear interpolation. The first three points (up to 4 Mev) are colinear, and the additional straight lines for the higher energies are less steep, giving a θ_f value of only 1.5905 at 15 Mev, compared to 1.6225 on the line which passes through the first three points.

Case C in Table II shows that the replacement of the tabulated values of θ_f by the above mentioned straight line has practically no effect on k_{eff} and L. Remembering that 50% of the leakage neutrons are

TABLE II. The variation of k_{eff} and L as function of $\theta_f(E)$

Effective nuclear temperature $\theta_f(E)$	$\delta k \times 10^3$	$\delta L \times 10^2$
A. θ_f = 1.39 Mev over the whole energy range	-1.96	3.07
B. θ_f = 1.40 Mev over the whole energy range	-1.31	2.03
C. $\theta_f = 1.39 + \frac{1.6225-1.39}{15.} E(\text{Mev})$	.03	-.04
D. $\theta_f = 1.39 + \frac{1.01\times1.6225-1.39}{15.} E(\text{Mev})$	.17	-.25
E. $\theta_f = 1.40 + \frac{1.6225-1.40}{15.} E(\text{Mev})$	.60	-.90
F. ENDF/B-III material 1159 temperature	2.14	-3.15

below 1.3 Mev and that our straight line is identical to the ENDF/B-IV values up to 4 Mev this comes as no surprise. Representing $\theta_f(E)$ as a straight line, $\theta_1 = \theta_f(E=0)$ and $\theta_2 = \theta_f$ (E = 15 Mev) are the only two parameters that determine the fission effective nuclear temperature over the whole energy range. Therefore, any change in k_{eff} due to a change in θ_f can be expressed as a function of the relative changes of these two values:

$$\frac{\Delta k}{k} = \left(\frac{\partial k}{\partial \theta_1} \cdot \frac{\theta_1}{k}\right) \cdot \frac{\Delta \theta}{\theta_1} + \left(\frac{\partial k}{\partial \theta_2} \cdot \frac{\theta_2}{k}\right) \frac{\Delta \theta_2}{\theta_2}$$

We calculate the derivatives $\frac{\partial k}{\partial \theta_1}$ and $\frac{\partial k}{\partial \theta_2}$ by first changing θ_1 from 1.39 to 1.40 (case E, Table II), next by changing θ_2 by 1% (case D, Table II), and obtain

$$\frac{\Delta k}{k} = 0.0794746 \frac{\Delta \theta_1}{\theta_1} + 0.0141252 \frac{\Delta \theta_2}{\theta_2}$$

We can see that k_{eff} is much more sensitive to changes in θ_f for low incident energies than for the high ones. The k_{eff} in cases A and B were calculated twice, once using our regular procedure and once by utilizing $\frac{\Delta k}{k}$ that was obtained above, giving identical results.

The last case given in Table II, case F, is obtained when the ENDF/B-IV fission effective nuclear temperature is replaced by the ENDF/B-III values. These values are too high and were therefore replaced by the ENDF/B-IV evaluators. It is seen that this change leads to the largest deviation of k from its original value. Let us point out again here, that the experimental error in k_{eff} for the system treated in this paper is .0017 and therefore smaller than the deviations obtained in cases A and F.

Discussion

In the last two sections we presented the results obtained by changing the fission and inelastic scattering spectra of the ^{239}Pu ENDF/B-IV data. As was stated earlier in this work, the calculated effective multiplication factor k_{eff}, turns out to be within its experimental error for most of the performed changes. The experimental error of the fission effective nuclear temperature for thermal energies is estimated as 1-2%,[5] and indeed a modification of that order of θ_f changes k_{eff} by less than its experimental error. Similarly, a change of θ_{in} by 10% affects k_{eff} by less than its experimental error. The same goes for the leakage spectrum. It is seen that δL in all our results is less than the experimental error.[6]

TABLE III. Variations in k_{eff} and in L by going from ENDF/B-III to ENDF/B-IV

Test data	$\delta k \times 10^3$	$\delta k \times 10^2$
A. ENDF/B-III	5.98	-3.71
B. ENDF/B-IV; ENDF/B-III $\bar{\nu}$	-1.75	.10
C. ENDF/B-IV; ENDF/B-III fission spectrum	2.14	-3.15
D. ENDF/B-IV; ENDF/B-III inelastic spectrum	-.21	.05

Next, it was found that if we add the cross sections for the excitation of the high discrete levels either to the inelastic scattering to the continuum on to the elastic scattering, the criticality of the assembly is almost not affected. In other words the treatment of the inelastic scattering to high discrete levels as such is of no major importance in metallic assemblies.

On the other hand, it must be pointed out that the transformation from material 1159 (^{239}Pu, ENDF/B-III) to material 1264 (^{239}Pu, ENDF/B-IV) is accompanied by a change of almost four experimental errors in k_{eff} (case A Table III).

Now summing the results presented in cases B,C and D in Table III, it is clear that the difference between the ENDF/B-III and ENDF/B-IV data lies not only in the effective nuclear temperatures, but mainly in the cross sections.

References

1. M.K. Drake, Data Formats and Procedures for the Neutron Cross Section Library. BNL50274(T-601) ENDF102, vol. 1, p.10.2 (1970).
2. O.A. Salnikov et al.,Izv. Nauk. SSSR. SER FIZ(BAS) 32 (1968) 653 (BAS-p.600).
3. R. Batchelor et al. Nucl. Phys. 65 (1965) 236.
4. A. Pazy et al.,Nucl. Sci. and Ing. 55 (1974) 280.
5. E. Barnard et al., Nucl. Phys. 71 (1965) 228.
6. L. Stewart, Nucl. Sci. and Ing. 8 (1960) 595.

COMPARISON OF DOPPLER BROADENING METHODS

D. E. Cullen
Lawrence Livermore Laboratory
Livermore, California 94550
C. R. Weisbin, R. Q. Wright and J. E. White
Oak Ridge National Laboratory
Oak Ridge, Tennessee 37830

(Doppler broadening; line shape; comparison; calculation)

Introduction

The Doppler broadening equation is:[1]

- Energy

$$\sigma(E,T) = \frac{1}{2E}\sqrt{\frac{A}{\pi KT}}\int_0^\infty dE_r \sqrt{E_r}\,\sigma(E_r,0)\left\{e^{-\frac{A}{KT}(\sqrt{E}-\sqrt{E_r})^2} - e^{-\frac{A}{KT}(\sqrt{E}+\sqrt{E_r})^2}\right\} \quad (1)$$

- Speed

$$\sigma(v,T) = \frac{1}{v^2}\sqrt{\frac{M}{2\pi KT}}\int_0^\infty dv_r v_r^2\,\sigma(v_r,0)\left\{e^{-\frac{M}{2KT}(v-v_r)^2} - e^{-\frac{M}{2KT}(v+v_r)^2}\right\} . \quad (2)$$

By differentiating, this can be shown to be equivalent to solving the diffusion equation with spherical symmetry[1],

$$\frac{\partial^2}{\partial v^2}[v^2\sigma(v,T)] = \frac{2M}{K}\frac{\partial}{\partial T}[v^2\sigma(v,T)] \quad , \quad (3)$$

$$\frac{1}{v}\frac{\partial^2}{\partial v^2}[vR(v)] = v^2 R(v,T) = \frac{2M}{K}\frac{\partial}{\partial T}R(v,T) \quad , \quad (4)$$

with the initial condition:

$$R(v,0) = f(v) \text{ - Given} \quad (5)$$

This is completely analogous to solving the heat or age diffusion equation with the analogy:

(velocity, temperature) $\approx$ (space, time)

In particular, the following properties of the diffusion equation with spherical symmetry can be used to interpret the Doppler broadening equation.

- Derivative zero at the origin

$$\lim_{v\to 0} R(v,T) \to C \quad : \quad \lim_{v\to 0}\sigma(v,T) \to \frac{C}{v} \quad : \quad T > 0 \quad . \quad (6)$$

Therefore, the cross section will approach $\frac{1}{v}$ at low energies.

- Conservation

$$4\pi\int_0^\infty v^2 R(v,T)\,v^2 dv = \frac{\partial}{\partial T}\left[\frac{2M}{K}\,4\pi\int_0^\infty R(v,T)\,v^2 dv\right] = 0 \quad (7)$$

- Reaction rate integrated over phase space conserved

$$4\pi\int_0^\infty R(v,T)\,v^2 dv \text{ - independent of } T \quad . \quad (8)$$

- Cross section or "area under the curve" is not conserved

- "Smoothing"

  - Reaction rate is getting smoother
  - Asymptotic value - uniform throughout

$$\bar{R} = \lim_{a\to\infty}\left[\frac{4\pi\int_0^a R(v,0)\,v^2 dv}{4\pi\int_0^a v^2 dv}\right] \quad (9)$$

  - Cross section not necessarily smoother

$$\sigma(v,T) = \frac{1}{v}R(v,T) \quad (10)$$

Approximations to the Doppler Equation

For AE >> KT, three approximations may be introduced to simplify equation (1):

(1) the second exponential can be ignored
(2) contribution from $E_r\epsilon(-\infty,0)$ is negligible
(3) the following difference is approximated

$$(\sqrt{E} - \sqrt{E_r}) \equiv \frac{(E - E_r)}{(\sqrt{E} + \sqrt{E_r})} \quad (11)$$

In the Tempo[2] method it is assumed that

$$E_r \approx E \Rightarrow (\sqrt{E} - \sqrt{E_r}) \approx \frac{(E - E_r)}{2\sqrt{E}} \quad , \quad (12)$$

and in the Psi-Chi[3] method it is assumed that

$$E_r \approx E \approx E_0 \Rightarrow (\sqrt{E} - \sqrt{E_r}) \approx \frac{(E - E_r)}{2\sqrt{E_0}} \quad . \quad (13)$$

Upon defining a general Doppler width

$$\Delta(E_B) = \sqrt{\frac{4KTE_B}{A}} \quad (E_B - \text{Base Energy}) \quad , \quad (14)$$

the approximate Psi-Chi Doppler broadening equation becomes:

$$\sigma(E,T) = \frac{1}{\sqrt{E}}\frac{1}{\Delta}\int_{-\infty}^\infty dE_r\sqrt{|E_r|}\,\sigma(E_r,0)\,e^{-(E-E_r)^2/\Delta^2} \quad , \quad (15)$$

which is simply another diffusion equation. The variable conserved and "smoothed" depends upon the assumed form of the cross section.

In the Psi-Chi method for capture, the reaction rate is assumed to have a Breit-Wigner line shape

$$\sqrt{E_r}\sigma(E_r,0) \approx \frac{(\Gamma/2)^2}{(\Gamma/2)^2 + (E_r - E_0)^2} \quad , \quad (16)$$

while for elastic scattering, the cross section is assumed to have a Breit-Wigner line shape and $E_r \approx E$

$$\sigma(E_r,0) \approx \frac{(\Gamma/2)^2}{(\Gamma/2)^2 + (E_r - E_0)^2} \quad ; \quad \sqrt{\frac{|E_r|}{E}} \approx 1 \quad . \quad (17)$$

Therefore in these cases:

Conservation

- Capture - Reaction rate integrated over energy
- Elastic - Cross section integrated over energy (area under the curve)

- "Smooth"
  - Capture - Reaction rate
  - Elastic - Cross section

Applications

The three methods that will be compared are defined by the following equations and assumed forms for the cross sections.

SIGMA1 (exact)[4]

$$\sigma(v,T) = \frac{1}{v^2}\sqrt{\frac{M}{2\pi KT}}\int_0^\infty dv_r v_r^2 \sigma(v_r,0) \quad (18)$$

$$\left\{ e^{-\frac{M}{2KT}(v-v_r)^2} - e^{-\frac{M}{2KT}(v+v_r)^2} \right\}$$

Tabulated cross section - linear-linear interpolation

- Psi-Chi[3]

$$\sigma(E,T) = \frac{1}{\sqrt{E}}\frac{1}{\Delta}\int_{-\infty}^\infty dE_r \sqrt{|E_r|}\, \sigma(E_r,0)\, e^{-(E-E_r)^2/\Delta^2} \quad (19)$$

Breit-Wigner line shape

Tempo[2]

$$\sigma(E,T) = \frac{1}{\sqrt{E}}\frac{1}{\Delta}\int_0^\infty dE_r \sqrt{E_r}\, \sigma(E_r,0)\, e^{-(E-E_r)^2/\Delta^2} \quad (20)$$

Tabulated reaction rate - linear-linear interpolation

Low Energy Cross Sections

Low energy cross sections are almost always either constant or $1/v$.[5,6] For light isotopes this behavior is true into the keV region. Therefore the following results are valid even for CTR core applications.

The equations for the three methods can be analytically evaluated for constant or 1/v cross section. The effect of the three approximations introduced to obtain the approximate equations can be studied separately and in combination by defining two functions:

$$F(\pm X) = \frac{1}{X^2}\sqrt{\frac{1}{\pi}}\int_0^\infty Y^2\sigma(Y,0)\, e^{-(Y\mp X)^2}\, dY \quad , \quad (21)$$

and

$$G(\pm X) = \frac{1}{X^2}\sqrt{\frac{1}{\pi}}\int_0^\infty Y^2\sigma(Y,0)\, e^{-\frac{1}{4X^2}(Y^2\mp X^2)^2}\, dY \quad . \quad (22)$$

which only depend on the ratio $X^2 = \frac{AE}{KT}$. In terms of these two functions the various methods and approximations become:

- $F(X) - F(-X)$ (exact)
- $F(X)$ ignore second exponential
- $F(X) + F(-X)$ and extend integral to $-\infty$
- $F(X) - G(-X)$ introduce Doppler width
- $G(X)$ (Tempo) ignore second exponential
- $G(X) + G(-X)$ (Psi-Chi) extend integral to $-\infty$

Figures 1 and 2 illustrate the result of applying these equations to a 1/v and constant cross section, respectively.

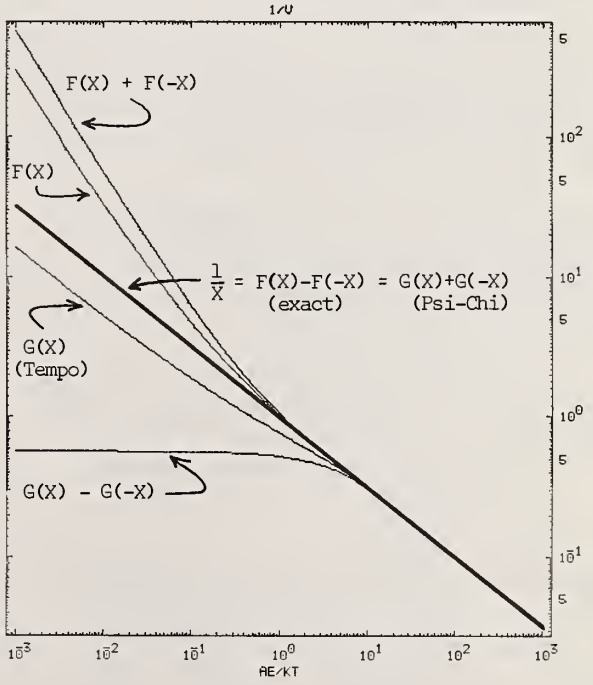

Fig. 1 $\frac{1}{v}$ cross section

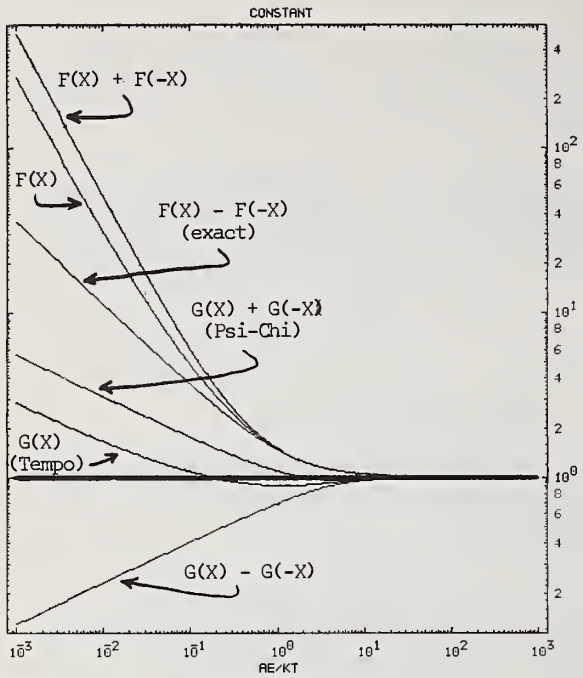

Fig. 2 Constant cross section

The results of the 1/v case illustrates that only the exact and Psi-Chi methods reproduce a 1/v cross section independent of temperature. In particular the Tempo result illustrates that the approximations introduced to obtain the method do not yield a properly normalized equation.

The constant cross section results indicate that in this case even the Psi-Chi method does not agree with the exact solution. The difference between the exact Doppler broadened and the 0 °K constant cross section is 50% at AE = KT (independent of T) (e.g. the hydrogen elastic cross section at E = KT is 30b, while the unbroadened cross section is 20b).

Figures 1 and 2 illustrate that of the three approximations introduced, use of the Doppler width is the most restrictive. This is evident since the family of G(X) curves diverges from the exact solution at higher energies than the F(X) curves.

Simple Breit-Wigner Line Shape

Solution of the Psi-Chi method for a simple Breit-Wigner line shape yields functions of only two variables.[3]

- $X = (2/\Gamma)(E-E_0)$ - half widths from peak

$$\xi_0 = \frac{\Gamma}{\Delta} = \Gamma\sqrt{\frac{A}{4KTE_0}} \quad , (23)$$

where the Psi and Chi functions are defined by:

$$\psi(X,\xi) = \frac{\xi_0}{2}\sqrt{\frac{1}{\pi}}\int_{-\infty}^{+\infty}\frac{dX'}{1+X'^2}\,e^{-[\xi_0(X-X')/2]^2} \quad (24)$$

$$\chi(X,\xi) = \frac{\xi_0}{2}\sqrt{\frac{1}{\pi}}\int_{-\infty}^{+\infty}\frac{X'dX'}{1+X'^2}\,e^{-[\xi_0(X-X')/2]^2} \quad . (25)$$

The exact solutions are a function of three variables

X and ξ_0

$Z_0 = (2/\Gamma)E_0$ - position of resonance, in half-widths, (26)

where the exact solutions are:[7]

$$\tilde{\psi}(X,\xi,Z_0) = \frac{\xi_0}{2}\sqrt{\frac{1}{\pi}}\int_{-Z_0}^{\infty}\frac{dX'}{1+X'^2} \quad (27)$$

$$\left\{e^{-Z_0\xi_0^2(\sqrt{X'}+Z_0-\sqrt{X+Z_0})^2} - e^{-Z_0\xi_0^2(\sqrt{X'}+Z_0+\sqrt{X+Z_0})^2}\right\}$$

$$\tilde{\chi}(X,\xi,Z_0) = \frac{\xi_0}{2}\sqrt{\frac{1}{\pi}}\int_{-Z_0}^{\infty}\frac{X'dX'}{1+X'^2}$$

$$\left\{e^{-Z_0\xi_0^2(\sqrt{X+Z_0}-\sqrt{X+Z_0})^2} - e^{-Z_0\xi_0^2(\sqrt{X+Z_0}+\sqrt{X+Z_0})^2}\right\} . \quad (28)$$

Figures 3 and 4 illustrate the exact $\tilde{\psi}(X,\xi,Z_0)$ function for large Z_0 (where it converges to $\psi(X,\xi)$) and at low Z_0 respectively. The low Z_0 results illustrate that compared to the $\psi(X,\xi)$ predictions the exact solution decreases considerably faster at lower Z_0.

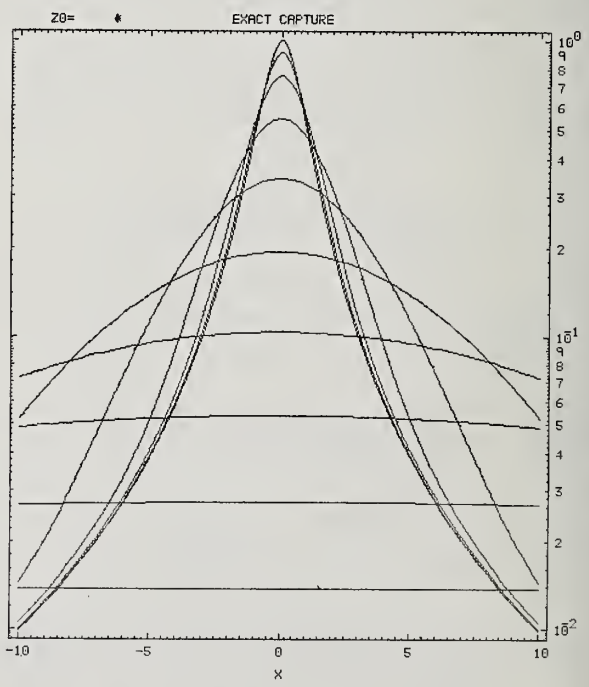

Fig. 3 High Z_0

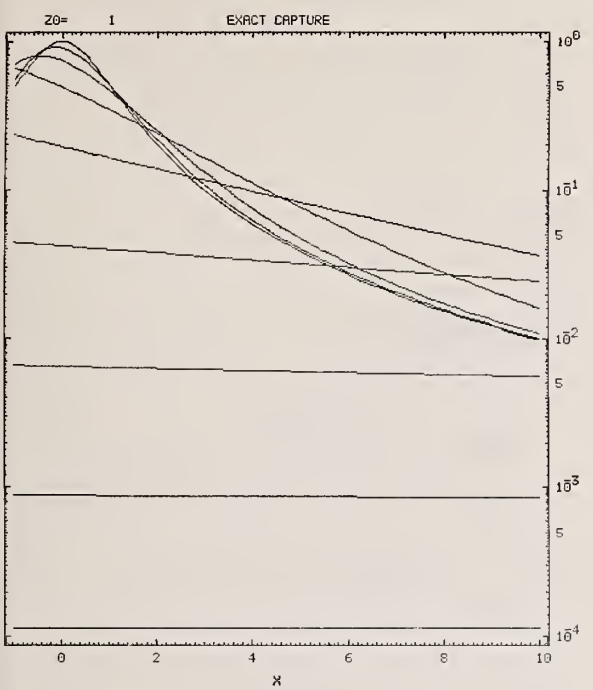

Fig. 4 Low Z_0

Figures 5 and 6 illustrate the exact $\tilde{\chi}(X,\xi,Z_0)$ function for large Z_0 (where it converges to $\chi(X,\xi)$) and at low Z_0 respectively. The low Z_0 results illustrate that compared to the $\chi(X,\xi)$ predictions the exact solution decreases slower at lower Z_0 due to the decreasing cross cancellation of the asymmetric scattering interference.

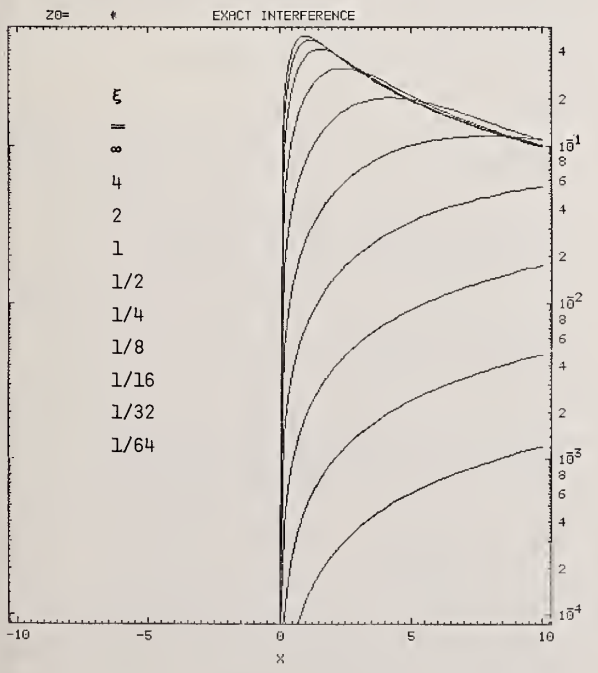

Fig. 5 High Z_0

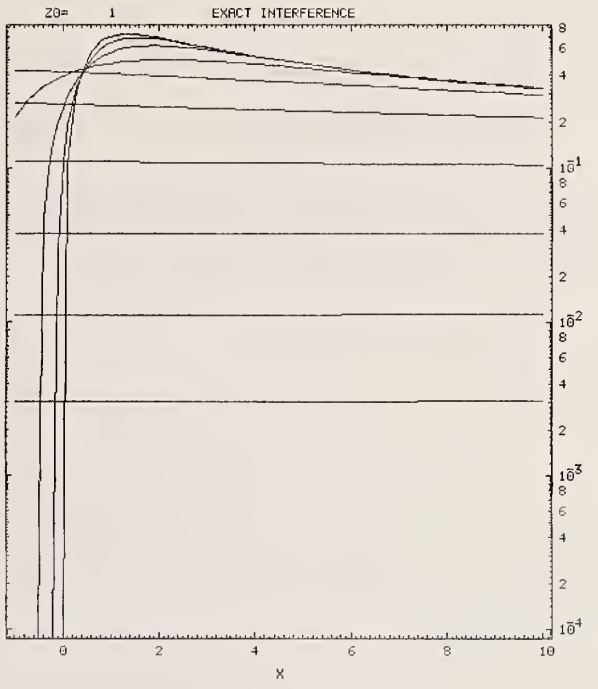

Fig. 6 Low Z_0

Both $\tilde{\psi}(X,\xi,Z_0)$ and $\tilde{\chi}(X,\xi,Z_0)$ show energy shifts toward the origin, as would be expected in a spherically symmetric diffusion problem.

U-235 and Pu-239 Self-Shielding

In the resonance region the ENDF/B-IV cross sections for U-235 and Pu-239 are represented by a combination of resonance parameters and a tabulated background cross section.[8]

The cross section obtained by the exact and Psi-Chi methods have been compared for U-235 and Pu-239 by examining the effect on the cross sections of transmission through slabs. Using broad energy groups defined by[9,10]

$$E_{G+1} = 2.15 * E_G \quad , \tag{29}$$

e.g. 10 - 21.5 - 46.4 - 100 (repeat in next decade). The uncollided flux, reaction rates and equivalent cross sections can be calculated analytically from the expressions:[9,10]

- Flux

$$\langle \phi(X) \rangle_G = \int_{E_G}^{E_{G+1}} e^{-\Sigma_T(E)X} \frac{dE}{E} \Big/ \int_{E_G}^{E_{G+1}} \frac{dE}{E} \tag{30}$$

- Reaction rates

$$\langle \dot{T}(X) \rangle_G = \int_{E_G}^{E_{G+1}} \Sigma_T(E)\, e^{-\Sigma_T(E)X} \frac{dE}{E} \Big/ \int_{E_G}^{E_{G+1}} \frac{dE}{E} \tag{31}$$

$$\langle f(X) \rangle_G = \int_{E_G}^{E_{G+1}} \Sigma_f(E)\, e^{-\Sigma_T(E)X} \frac{dE}{E} \Big/ \int_{E_G}^{E_{G+1}} \frac{dE}{E} \tag{32}$$

Cross sections

$$\langle \Sigma_T(X) \rangle_G = \langle T(X) \rangle_G / \langle \phi(X) \rangle_G \quad (33)$$

$$\langle \Sigma_f(X) \rangle_G = \langle f(X) \rangle_G / \langle \phi(X) \rangle_G \quad (34)$$

Figures 7 and 8 illustrate the results for the highest energy groups within the resolved resonance region of U-235 and Pu-239 respectively for slab thickness of 0 to 20 g/cm^2 (approximately 0 to 1 cm).

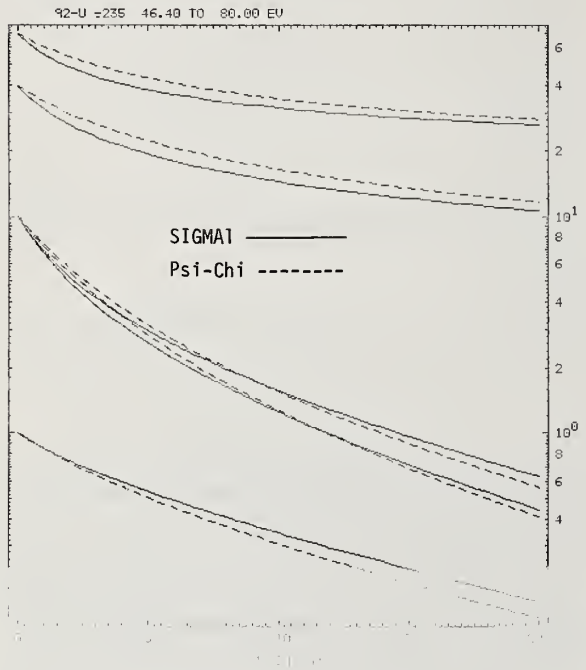

Fig. 7 U-235

These results indicate that although the unshielded (zero thickness) cross sections for these broad groups are essentially identical, the shielded flux, reaction rates and cross sections differ by up to 10%. The cross sections obtained by the exact method are consistently lower than the Psi-Chi results due to broadening of the tabulated background.

Both methods indicate that although both total and fission cross sections are both decreasing due to self-shielding, the fission cross section is decreasing faster. Therefore the shielded U-235 and Pu-239 is not worth as much in the sense that the number of secondary neutrons per collision is decreasing.

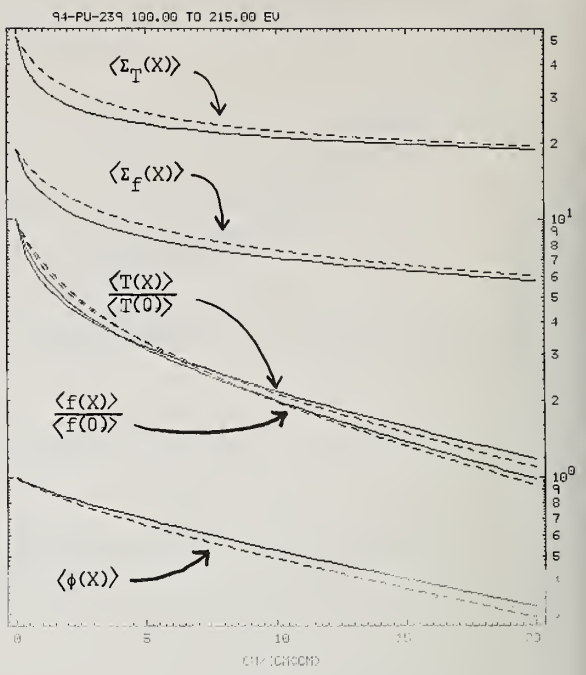

Fig. 8 Pu-239

Computer Costs

Although the actual expense associated with the three methods Psi-Chi, Tempo and SIGMA1 will vary from computer to computer both due to the type of computer and local charge algorithm, it is indicative to note that on the ORNL-IBM-360/91 the preparation of the U-235 and Pu-239 cross sections by the three methods were in the ratio:

PSI-CHI : TEMPO : SIGMA1 = 1 : 5 : 8

References

1. R. V. Megheblian and D. K. Holmes, Reactor Analysis, McGraw-Hill, New York, pp. 137-140 (1960).

2. K. Gregson and M. F. James, "Tempo - A General Doppler Broadening Program for Neutron Cross Sections", AEEW-M518, Winfrith (1965).

3. B. A. Hutchins, et al. "ENDRUN-II, A Computer Code to Generate a Generalized Multi-Group Data File From ENDF/B", GEAP-13704 (ENDF-145), General Electric, Sunnyvale (1971).

4. D. E. Cullen, "Program SIGMA1 (Version 74-1) - A Program to Exactly Doppler Broaden Tabulated Cross Sections in the ENDF/B Format", UCID-16426, Lawrence Livermore Laboratory (1974).

5. D. E. Cullen and P. J. Hlavac, "ENDF/B Cross Sections", BNL-17100, (ENDF-200), Brookhaven National Laboratory (1972).

6. D. E. Cullen, et al. "Graphical Experimental Data for Major Neutron-Induced Interactions", UCRL-50400, Vol. 7, Lawrence Livermore Laboratory (1974).

7. R. L. Murray, Nucl Sci. and Eng. 26, 362-365 (1966).

8. O. Ozer and D. Garber, "ENDF/B Summary Documentation", BNL-17541, (ENDF-201), Brookhaven National Laboratory (1973).

9. R. L. Bramblett and J. B. Czirr, Nucl. Sci. and Eng. 35, 350-359 (1969).

10. J. B. Czirr and R. L. Bramblett, Nucl. Sci. and Eng. 28, 62-71 (1967).

*Work was performed under the auspices of the U.S. Energy Research and Development Administration.

BURNUP CALCULATIONS FOR THE KWO REACTOR

Dietrich C. Lutz
Institut für Kernenergetik, Universität Stuttgart
Stuttgart
Federal Republic of Germany

An effort was made to reproduce the measured shape of the critical boron concentration for the KWO reactor (PWR) during the first cycle starting from basic nuclear data (ENDF/BII). The overall results are quite satisfactory but there are some local differences up to 80 ppm.

(Burnup calculation; KWO; burnup model; fission products; RSYST; critical boron concentration)

Introduction

In the commonly used burnup calculation models, cross section libraries and computational methods are well coordinated, due to a long time experience. Therefore it is very difficult to integrate improvements of cross sections, as published in the ENDF/B libraries, into these calculational models. For this reason we have assigned ourselves the task of carrying out calculations with basic data for the long time behavior of a power reactor, taking into account the disadvantages of costly computational methods. We have chosen for this research the KWO reactor[1,2], because it has a simple core geometry during the first cycle.

Methods

Generation of multigroup cross sections

A very important task for this research was the generation of multigroup cross sections - in our case 22 fast and 27 thermal groups (cutoff 1.855eV) - for all materials in the reactor core. For the heavy isotopes uranium to curium, the fission products Xe 135 and Sm 149, and for the moderator, the group cross sections have been produced in the fast energy range by the code GGC-4[3] using the ENDF/BII library. The program was modified[4] in such a way that in the resonance region cross sections for the pin instead of homogenized cell cross sections could be calculated. The effects of energetic and space dependent shielding have been taken into account by determining a resonance spectrum for the energy range from 1 to 60eV with RESAB-2[5]. RESAB-2 is a one-dimensional multigroup code based on collision probability theory with access to the ENDF/B-tape. The density of the uranium and plutonium isotopes in the pellet corresponded in this case to a burnup of 2MWd/kgU. The 27-group cross sections for the thermal region were produced with a 123-group B 1-spectrum using ENDF/BII from THERM 123[6]. This library contains thermal cross sections for fissionable isotopes and water at different temperatures generated with FLANGE II[7]. The cross sections of the structure materials were taken from the library THERM 49[8]. The data of the fission products are based on the UK library[9]. The related fission yields originated from ENDF/BII.
For the application of these 49-group sets for the whole burnup calculation we have assumed, that the spectral shifts during the reactor operation period did not influence these data essentially. The quality of this assumption has to be investigated further. In the epithermal range it is not fully valid[10,11], because the resonance spectra change with time due to the buildup of the plutonium isotopes. In the thermal region this effect is probably not important because the group boundaries are adjusted to the resonance structure.

The burnup model

From the many fission product isotopes, 88 have been taken into account in the burnup model. The criteria for selection have been:

availability of cross sections
half life $> 2d$
fission yield > 0.02 %.

For some isotopes we have assumed 1/v-cross sections rather than ommitting them. In the range of the actinides the isotopes NP237, PU238, AM241, AM242, AM243 and CM244 have been added to the commonly used fissionable isotopes. The isotopes included in the burnup model are listed in table 1.

Table 1: The isotopes included in the burnup model.

SE82	BR81	KR82	KR83	KR84	KR85	KR86
RB85	RB87	SR88	SR89	SR90	Y89	Y90
Y91	ZR91	ZR92	ZR93	ZR94	ZR95	ZR96
NB95	MO95	MO96	MO97	MO98	MO100	TC99
RU101	RU102	RU104	RU106	RH103	RH105	PD105
PD106	PD107	PD108	AG109	CD113	IN115	SB125
TE128	TE130	I127	I129	I131	I135	XE131
XE132	XE133	XE134	XE135	XE136	CS133	CS134
CS135	CS137	BA138	LA139	CE140	CE141	CE142
CE144	PR141	PR143	ND142	ND143	ND144	ND145
ND148	ND150	PM147	PM148	PM148	PM149	SM149
SM150	SM151	SM152	SM154	EU153	EU154	EU155
GD154	GD155	GD156	GD157			

U235	U236	U238	NP237	PU238	PU239	PU240
PU241	PU242	AM241	AM242	AM243	CM244	

Geometrical and physical model

The reactor has been described in r-z-geometry. For reactivity calculations during the first cycle this approximation seems to be justified. The control rods of the KWO reactor - nearly withdrawn during this operation period - have been taken into account by a homogeneous poison in the top reflector.
The flux spectra of the fuel assemblies have been determined for each batch by two one-dimensional 49-group calculations with the code ISOSTO[12] (ISOSTO is a very fast multigroup multizone transport program based on collision probability theorie). The first calculation was an ordinary pin cell calculation. The second one represented the assembly cell with a waterhole in the center surrounded by a layer of homogenized pin cells.
All measurements and temperatures are taken for the mean power density in the core.
After the cell calculations the cross sections have been homogenized and collapsed to 4 groups. For all isotopes with time dependent densities (the fissionable materials, the fission products and boron) microscopic data have been produced. All the other cross sections have been collected in a macroscopic set.
The 2-dimensional reactor calculation has been carried out with the program 2DB[13], which determines directly the critical boron concentration. Then a depletion calculation has been made for all enrichment zones with the code ABBRAND[14].
After each burnup time step the cell spectra have been recalculated thus the cross section changes of the fissionable isotopes and of the most important fission products are taken into account.
The whole calculation has been performed using the program system RSYST[15,16] (see fig.1). Only such a modular system of reactor and cross section codes with automatic data transfer allowes the completion of such an extensive work in a reasonable time.

Results

In fig. 2 the calculated critical boron concentration of the KWO reactor during the first cycle is presented together with the measured values. The theoretical shape as a whole agrees well with the measured one. There are some local descrepancies up to 80 ppm, which shall be discussed now.
The calculation overpredicts the reactivity in the second part of the cycle. The neglect of the axial distribution of the burnup in our approach probably causes this overprediction. Fuel depletion and poison buildup are placed into zones of lower importance compared to the 3D case by this approximation. Hellens[17] showed that this effect produces a reactivity overprediction of up to 0.5 %, which increases with the burnup.
At points of temperature and power increase in the middle of the cycle another problem arises. The measured reactivity jumps are not reproduced by our theory, although the water density changes have been considered in the spectral calculations. However, these jumps cannot be explained by the measured power and moderator temperature coefficients either. We presume a connection of this effect with the observed axially asymetric flux shape in the KWO, which has not been wholly explained up to now.
Regarding the deviations at the beginning of the cycle we suppose them to be caused by the inhomogeneous buildup of the plutonium isotopes in the pin.
Finally it should be mentioned that the critical boron concentration at the start of the cycle differs from the measured values by about 60 ppm. This corresponds to a reactivity error of 0,7 %.
We plan to repeat the calculations with ENDF/BIV cross section data. We also shall use an improved reactor model. Thus we hope to achieve better results.

Acknowledgements

I want to thank Professor Emendörfer for many helpful discussions.
I also acknowledge the work of Miss M.Mattes, who made available the basic data.
I am grateful to Dr.Rühle and his team for providing the facilities of RSYST.

References

1 Etzel,W.,H.Märkl: Physikalische Auslegung des Reaktorkerns des Kernkraftwerks Obrigheim. Atom und Strom 13, 47 (1962).
2 Bronner,G.,I.Dernedde,A.E.Grün,T.Katinger, W.D.Krebs: Experimentelle Verifikation der nuklearen Auslegungsrechnungen für Siemens-Druckwasserreaktoren: Gegenwärtiger Stand und Erfordernisse für die Zukunft. Reaktortagung DAtF 1973.
3 Adir,J.,K.D.Lathrop:Theory of Methods Used in the GGC-4Multigroup Cross Section Code. GA-9021 (1968).
4 Gulden,W.:Berechnung von Gruppenkonstanten im Bereich aufgelöster Resonanzen.IKE 4-15 (1970).
5 Rühle,R.,B.Riik: RESAB2, ein Programm zur Berechnung von Gruppenkonstanten im Resonanzbereich nach der Stoßwahrscheinlichkeitsmethode. IKE 3-3.6.12o9(1972).
6 Keinert,J.: THERM 123- eine Datenbibliothek für thermische Neutronenwirkungsquerschnitte. IKE6-61/1 und 2 (1973).
7 Honeck, H.C.,D.R.Finch: FLANGE II, A Code to Process Thermal Neutron Scattering Data from an ENDF/B Tape.
8 THERM 49, Wirkungsquerschnittsbibliothek des IKE, Stuttgart.
9 Cook,J.L.:Fission Product Cross Sections (AAEC, Australia).
Parker,K.: The Aldermaston Nuclear Data Library as at May 1963. AWRE O-70/63(1963).
10 Rühle,R.,D.Emendörfer,W.Gulden,D.Lutz: Group Constant Generation for the Resolved Resonance Region. ANS Topical Meeting, Kiamesha Lake (1972).Conf.72o91.
11 Mattes,M.,D.Emendörfer,J.Keinert,I.Brestrich,D.Lutz: Kerndaten für die Auslegung plutoniumhaltiger Brennelemente. IKE 6-80 (1974).
12 Riik,B.,R.Rühle: ISOSTO, ein Programm zur Lösung der Multigruppengleichungen durch Stoßwahrscheinlichkeiten.IKE3-3.4.1177 (1972).
13 Little Jr.,W.W.,R.W.Hardie: 2DB User's Manual BNWL-831 Rev.1.

14 Wohland,H.,R.Rühle: ABBRAND, ein Modul für Abbrandrechnungen in RSYST. IKE 4-10(1972).
15 Rühle,R.: RSYST, ein integriertes Modulsystem mit Datenbasis zur automatisierten Berechnung von Kernreaktoren.IKE 4-12 (1973).
16 Rühle,R.: RSYST, an Integrated Modular System for Reactor and Shielding Calculations. Conf.onMathmatical Models and Computational Techniques for Analysis of Nuclear Systems, Ann Arbor (1973).
17 Hellens, R.L.: The Physics of the PWR Reactors. ANS Topical Meeting, Kiamesha Lake (1972). Conf. 72o91.

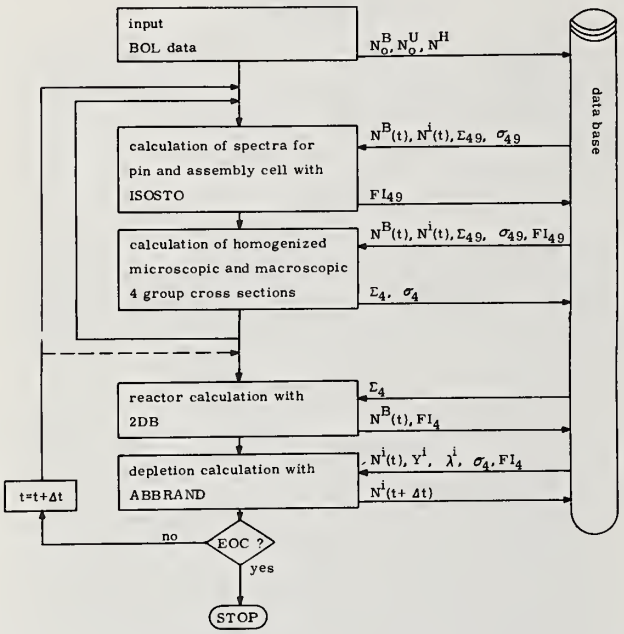

Fig. 1: Flow chart for burnup calculations using RSYST.

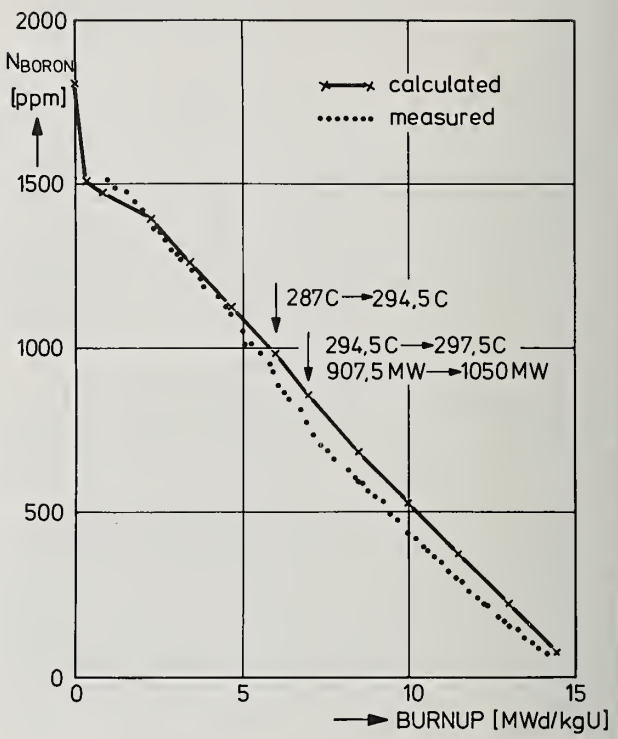

Fig. 2: Measured and calculated shape of the critical boron concentration for the KWO reactor.

FISSION PRODUCT NUCLEAR DATA OBTAINED BY USE OF AN ON-LINE MASS SPECTROMETER

P. L. Reeder, J. F. Wright and R. A. Anderl†
Battelle, Pacific Northwest Laboratories
Richland, Washington 99352

A Spectrometer for On-Line Analysis of Radionuclides (SOLAR) has been installed at a 1 MW TRIGA reactor at Washington State University. Fission product ions from a combination target/ion source located within the thermal column are brought out to a 60° magnetic sector mass spectrometer. Surface ionization provides copious beams of Rb^+ and Cs^+ ions and less intense beams of Br^- and I^- ions with negligible contamination by other elements. About 40 fission product nuclides can thus be chemically and physically separated in times of less than 1 second. Past results on independent and cumulative fission yields along with measurements of half-lives of some very neutron-rich nuclides will be presented. Current work on delayed-neutron emission probabilities and energy spectra of delayed neutrons from individual nuclides will be described.

(Mass spectrometry, fission products, half-lives, cumulative yields, independent yields, delayed-neutrons)

Introduction

The use of "on-line" mass spectrometry was pioneered by the French group under R. Bernas[1] and R. Klapisch.[2] This technique enables one to perform a rapid chemical and physical separation of selected fission product nuclides in times of less than 1 second. It is thus possible to perform yield measurements and a variety of nuclear spectroscopic studies on very short-lived nuclides.

The feature of on-line mass spectrometry which distinguishes it from other on-line isotope separation schemes is the incorporation of the target material within a surface ionization source. Radioactive nuclides produced in the target diffuse out of the target and are ionized on the hot surface of the oven. For a tantalum surface, the efficiency for ionization of Rb and Cs as positive ions is more than 1000 times greater than any neighboring elements. Thus chemical selectivity occurs within the ion source and copious beams of Rb^+ and Cs^+ ions can be obtained with negligible contamination by other elements. By changing the polarity of the accelerating voltage, usable beams of Br and I negative ions can be obtained with negligible contamination by neighboring elements.

In order to study fission products, an on-line mass spectrometer has been installed at the 1 MW TRIGA reactor at Washington State University. The facility is known as SOLAR (Spectrometer for On-Line Analysis of Radionuclides). It has been described in detail elsewhere.[3] The target/ion source is located within the graphite thermal column of the reactor. A 2.3 m-long flight tube is used to bring the ions out of the thermal column. The ions are bent 90° by an electrostatic mirror before entering the 60° analyzing magnet. In the original configuration two electron multipliers were located in the detector box with an electrostatic deflector to send the ion beam to one or the other detector. The detectors are sensitive to beta pulses from the radioactive atoms which build up on the first dynode. Being able to switch detectors was very convenient for yield and half-life measurements when low-backgrounds were needed.

Pulses from the electron multiplier detectors are recorded in 400-channel multiscalers. The counting rate of a single mass peak can be stored as a function of time by holding the acceleration voltage and magnetic field constant and advancing the multiscaler at the desired rate. Mass spectra can be obtained by sweeping the magnetic field or acceleration voltage synchronously with the channel advance of the multiscaler.

The entire SOLAR system is mounted on a rolling table which allows easy removal of the flight tube from the thermal column. This is done to prevent unnecessary irradiation of the target/ion source and to allow maintenance.

Half-Life Measurements

Although the sensitivity of the electron multipliers to beta decay on the first dynode is a nuisance in many experiments, it is possible to use this feature to measure half-lives of very short-lived nuclides. In our experiments we tuned the mass spectrometer for the desired mass and then switched the ion beam off by means of a voltage applied to horizontal deflection plates in the ion source. The beta decay curve at the desired mass was obtained in a series of repetitive cycles. Ions were collected on the first dynode of the detector for two half-lives, the ion beam was switched off at the ion source, and beta decay pulses were stored in the multiscaler as a function of time for at least 8 half-lives.

Decay curves have been obtained for $^{92-97}Rb$ and $^{142-145}Cs$. Each decay curve has contributions from daughter $(Z+1)^A$ and granddaughter $(Z+2)^A$ isobars in addition to the parent nuclide $(Z)^A$. These contributions come solely from growth and decay originating from parent deposited on the first dynode - i.e., ionization of daughter and granddaughter isobars in the ion source is negligible. Hence it is possible to calculate the daughter and granddaughter contributions exactly. For those nuclides with appreciable delayed neutron emission probabilities (P_n), additional components are present due to growth and decay of the delayed-neutron product $(Z+1)^{A-1}$ and its daughter $(Z+2)^{A-1}$. Because of the complex nature of these decay curves and the need to make corrections for multiple pulses, a computer program (INACRA) was written to calculate each of these contributions. The program INACRA was used with P_n values and half-lives taken from the literature to calculate the initial activity ratios of the granddaughter to daughter and the delayed neutron product to parent. These two ratios were held fixed by a least squares decay curve program (CLSQ)[4] which was used to fit initial activities for the parent, daughter, and constant background to the experimental decay curves. In addition to fitting initial activities, the CLSQ program also varied the half-life of the parent to give the best fit to the experimental decay curve.

The results of our measurements are given in Table I along with other recent measurements for comparison. The uncertainty shown for a single determination in our work is the statistical uncertainty from the CLSQ program. For cases where several determinations were made, the reported value is the weighted mean half-life.

There is excellent agreement between our half-lives and the values given by Roeckl, et al. The measurements by Roeckl, et al., were done by delayed-neutron counting which gives single component decay curves in most cases. Hence this method should be more accurate than methods based on counting beta

particles. We plan to repeat our half-life measurements with our highly efficient neutron counter described below.

The present work and that of Roeckl, et al.,shows some significantly different half-life values from those given on the 1972 Chart of the Nuclides particularly at masses 93, 95, and 145. In addition we have found that improved fits to our decay curves are obtained if the half-lives of ^{96}Sr and ^{97}Sr are changed from 4.0 sec and $\leq$.2 sec respectively given on the 1972 Chart to 1.22 sec and 0.65 sec respectively.

TABLE I. Half-lives (sec) of Rb and Cs Isotopes

Mass	1972 Chart*	SOLAR	Other
92	4.53	4.54 ±.02 (2)+	4.50± 04[b], 4.50±.03[c], 4.43±.05[d]
93	5.8	6.12 ±.08 (4)	6.39±.35[a], 5.80±.05[b] 5.86±.13[c], 5.89±.04[d] 5.8±.1[e]
94	2.69	2.83 ±.03 (4)	2.76±.08[a], 2.78±.05[b] 2.67±.04[d], 2.8±.1[e]
95	.36	.377±.004 (3)	.383±.006[a], .36±.02[d]
96	.207	.205±.004 (2)	.199±.004[a], .207±.003[f]
97	.17	.182±.007 (2)	.172±.005[a], .135±.010[g], .176±.005[f]
142	1.7	1.70±.02 (1)	1.68±.02[c]
143	1.7	1.79 ±.02 (1)	1.69±.13[g]
144	1.02	1.00 ±.04 (2)	1.05±.14[g]
145	.56	.65 ±.03 (2)	.61±.02[a], .56±.03[f]

*Knolls Atomic Power Laboratory - Chart of the Nuclides
+The number in parenthesis gives the number of determinations

[a] E. Roeckl, P. F. Dittner, R. Klapisch, C. Thibault, C. Rigaud, and R. Prieels, Nucl. Phys. A222, 621 (1974).

[b] B. Grapengiesser, E. Lund, and G. Rudstam, J. Inorg. Nucl. Chem. 36, 2409 (1974).

[c] G. Carlson, W. Schick, W. Talbert and F. Wohn, Nucl. Phys. A125, 267 (1969).

[d] I. Amarel, R. Bernas, R. Foucher, J. Jastrzebski, A. Johnson, and J. Teillac, Phys. Letters 24B, 402 (1967).

[e] S. Amiel, H. Feldstein, M. Oron, and E. Yellin, Phys. Rev. C5, 270 (1972).

[f] B. Tracy, J. Chaumont, R. Klapisch, J. Nitschke, A. Poskanzer, E. Roeckl, and C. Thibault, Phys Letters 34B, 277 (1971).

[g] I. Amarel, H. Gauvin, and A. Johnson, J. Inorg. Nucl. Chem. 31, 577 (1969).

Cumulative Yield Measurements

In a cumulative yield measurement by on-line mass spectrometry the neutron flux is turned on continuously and the mass spectrum is measured continuously also. The relative height of each mass peak is proportional to the relative cumulative yield provided corrections for diffusion and radioactive decay are applied.

The abundances and lifetimes for the diffusion components of the daughter which are needed for calculating these corrections are obtained from experimentally measured disappearance curves. The diffusion time of the parent is more difficult to determine experimentally since the parent is never observed directly. We have chosen to vary the Kr diffusion time in our calculations until the relative cumulative yield of ^{89}Rb agrees with the recommended value from Meek and Rider.[5] The best agreement was obtained with a Kr diffusion time of 20±5 sec. Our resulting cumulative yields for Rb are given in Table II along with Meek and Rider's recommended values[5] and Wolfsberg's calculated values.[6] Cumulative yields for Cs are given in Table III. These values are based on a Xe diffusion time of 10,000 sec which was determined by fitting the ratio of the relative cumulative yield of ^{140}Cs to ^{141}Cs to the ratio given by Meek and Rider.

TABLE II. Rb Cumulative Yield

Mass	SOLAR	Wolfsberg	Meek and Rider
89	0.92±0.02	0.84	0.88
90	0.83±0.02	1.05	1.16
91	1.00±0.02	1.00	1.00
92	0.91±0.02	0.85	0.89
93	0.70±0.01	0.65	0.68
94	0.35±0.01	0.38	0.29
95	0.15±0.01	0.15	0.08

TABLE III. Cs Cumulative Yield

Mass	SOLAR	Wolfsberg	Meek and Rider
140	1.00±0.01	1.00	1.00
141	0.73±0.01	0.78	0.82
142	0.42±0.01	0.56	0.53
143	0.25±0.01	0.29	0.23
144	0.08±0.01	0.10	0.06

The ion counting rates for Br and I isotopes were less than 4000 counts/sec at best and were subject to gradual decrease over a period of a few hours. Thus our data on the cumulative yield of Br and I isotopes are less precise than the Rb and Cs data. The cumulative yields at four temperatures were averaged and are shown in Table IV. We have only preliminary data on the I isotopes which indicates that the diffusion time of ^{131}I at 1600°C is 100 sec. Higher temperatures will be needed to get the I isotopes out fast enough to measure the very neutron-rich isotopes.

TABLE IV. Br Cumulative Yield

Mass	SOLAR	Wolfsberg	Meek and Rider
83	0.21±0.01	0.23	0.17
84	0.43±0.01	0.39	0.32
85	0.62±0.01	0.54	0.43
86	0.83±0.02	0.82	0.60
87	0.95±0.02	0.88	0.79
88	1.00±0.02	1.00	1.00
89	0.72±0.04	0.76	0.89
90	0.45±0.20	0.39	0.53

Independent Yield Measurements

The experiment to measure independent yields is designed in such a way as to minimize the cumulative yield contribution from beta decay. This is done in a pulsed-flux type of experiment. We use a Cd covered shutter surrounding the target/ion source to pulse the neutron flux. The mass spectrum is recorded during and immediately after a short (<1 sec) pulse of neutrons. Because of the rapid diffusion of Rb and Cs, a few seconds delay is sufficient for most of the independently formed Rb and Cs to diffuse out of the target. A background mass spectrum taken after this delay shows peaks due only to stable isotopes or

to daughter isotopes from parent beta decay. The cycle of flux-on spectrum, delay, and flux-off spectrum is repeated many times to get sufficient statistical accuracy. Mass spectra are stored cumulatively in two separate 400-channel multiscalers. The difference between the flux-on and flux-off mass spectra gives the relative independent yields after correction by diffusion and decay factors. The essential feature of this pulsed flux technique is that the cumulative yield contribution cancels out between the flux-on and flux-off spectra.

The relative independent yield of Rb was determined at two temperatures. These values were averaged and are presented in Table V along with other experimental values. Meek and Rider's experimental ratios of parent cumulative yield to daughter independent yield were used whenever possible, otherwise their recommended values were used in the calculation of the diffusion and decay correction factors.

TABLE V. Rb Independent Yield

Mass	SOLAR	Chaumont[a]	Radiochemical[b]
88	0.002±0.002		
89	0.012±0.001	0.07±0.02	0.06±0.01
90	0.10 ±0.01	0.25±0.03	0.25±0.05
91	0.50 ±0.01	0.79±0.03	0.71±0.10
92	0.88 ±0.01	1.10±0.03	1.01±0.20
93	1.00 ±0.01	1.00±0.01	1.00±0.15
94	0.56 ±0.01	0.51±0.01	
95	0.27 ±0.01	0.22±0.01	
96	0.060±0.003	0.044±0.002	
97	0.015±0.002	0.012±0.001	
98	0.001±0.002		

[a]J. Chaumont, Thesis, University of Paris, 1970.

[b]A. Wahl, private communication, 1969.

Two sets of independent yield data for Cs were obtained. The results were averaged and are shown in Table VI.

TABLE VI. Cs Independent Yield

Mass	SOLAR	Chaumont[a]	Forman[b]	Radiochemical[c]
139	0.18 ±0.02	0.49±0.05	0.49±0.11	0.36±0.06
140	0.54 ±0.02	0.64±0.04		0.75±0.10
141	1.00 ±0.02	1.00±0.04	1.00±0.22	1.00±0.15
142	0.77 ±0.02	0.74±0.03	0.57±0.18	
143	0.43 ±0.01	0.45±0.02	0.38±0.09	
144	0.081±0.01	0.09±0.03		
145	0.018±0.003		0.04±0.02	
146	0.006±0.002			

[a]J. Chaumont, Thesis, University of Paris, 1970.

[b]L. Forman, S. Balestrini, K. Wolfsberg, and T. Jeter, Int. Conf. on Properties of Nuclei far from the Region of Beta Stability, CERN 70-30, 589 (1970).

[c]A. Wahl, private communication, 1969.

A single experiment of Br independent yields has been done. The statistics were rather poor and the diffusion time was rather long so the results shown in Table VII are preliminary values only.

TABLE VII. Br Independent Yield

Mass	SOLAR[a]	Wolfsberg	Meek and Rider
85	.001±.040	.11	.03
86	.34 ±.16	.39	.21
87	1.10 ±.26	.69	.41
88	1.00 ±.21	1.00	1.00
89	.79 ±.21	.84	1.24

[a]Diffusion time = 61.2 sec.

Delayed Neutron Emission Probabilities

Our recent work has concentrated on a modification to the SOLAR facility to enable us to do delayed-neutron studies on chemically and mass separated nuclides. We have recently installed a 2.3 m long beam pipe extension which replaces the off-axis electron-multiplier detector. Only one mass peak passes through the slit in the detector box and travels down the flight-tube extension. This allows us to do neutron studies or other spectroscopic studies on a single nuclide in a shielded location free from neighboring masses.

The first experiments are being done now to measure the delayed-neutron emission probabilities of individual nuclides. The technique being used is to measure the neutron counting rate and ion counting rate simultaneously. Ions are counted by an electron multiplier in the middle of a cylindrical neutron counter. Ions are collected continuously to achieve equilibrium between the rate of deposit of ions on the first dynode and the rate of radioactivity decay. The neutron counter is a large block of polyethylene containing 42 counters each containing ^{3}He at 9 atmospheres pressure. The counter has been designed to give a flat response to neutrons from .01-4.0 MeV and has an efficiency of 25%.

The delayed neutron emission probability is given by the rate of delayed neutron emission divided by the rate of beta decay. In our experiments the neutron emission rate is simply the observed neutron counting rate divided by the neutron counter efficiency. The rate of beta decay is equal to the counting rate of the ion detector corrected for the beta sensitivity of the detector and divided by the ion counting efficiency. In this method it is very important that all the ions coming down the flight tube be focused onto the first dynode of the detector so we have spent considerable time in verifying how well the beam is focused.

Delayed-Neutron Energy Spectra

Neutron spectroscopy has been greatly improved with the recent development of a high resolution ^{3}He ionization chamber.[7] When combined with an on-line isotope separator, this detector has provided the first detailed energy spectra of delayed neutrons from individual precursors.[8] We have recently acquired a ^{3}He spectrometer and will use it with the SOLAR facility to continue and extend these energy-spectra measurements. We expect to be able to measure spectra for at least 20 delayed-neutron emitters including most of the prominent emitters formed in fission of ^{235}U with thermal neutrons.

References

†Present address, Aerojet Nuclear Company, Idaho Falls, Idaho 83401

1. R. Bernas, "On-Line Mass Spectrometry," in "Recent Developments in Mass Spectroscopy," ed. by K. Ogata and T. Hayakawa, University of Tokyo Press, 1970.
2. R. Klapisch, Ann. Rev. Nucl. Sci. 19, 33 (1969).
3. J. J. Stoffels, Nucl. Instr. Meth. 119 (2), 251 (1974).
4. J. B. Cumming, in "Applications of Computers to Nuclear and Radiochemistry," Ed. by G. D. O'Kelley (Office of Technical Services, Washington, D. C., 1963) NAS-NS 3107 (modified by B. Erdal).
5. M. Meek and B. Rider, "Compilation of Fission Product Yields," NEDO-12154-1, 1974.
6. K. Wolfsberg, "Estimated Values of Fractional Yields from Low Energy Fission and Compilation of Measured Fractional Yields," LA-5553-MS, 1974.
7. S. Shalev and J. Cuttler, Nucl. Sci., Eng. 51, 52 (1973).
8. S. Shalev and G. Rudstam, Nucl. Phys. A230, 153 (1974).

DIFFERENTIAL CROSS SECTIONS AND INTEGRAL DATA: THE ENDF/B-4 LIBRARY AND "CLEAN" CRITICALS

J.J. Wagschal, Atara Ya'ari and Y. Yeivin
The Hebrew University of Jerusalem Tel Aviv University
Jerusalem 91009 (Israel) Tel Aviv 61390 (Israel)

The ENDF/B-4 cross sections of the principal isotopes of U and Pu are adjusted by critical-mass data on 15 metallic assemblies. Only very minor cross-section modifications are needed in order for neutronic calculations to reproduce the integral data well within their experimental errors. The nature of the adjustments and the quality of the input integral data are discussed.

(Cross sections; evaluation; adjustment; integral data; sensitivities; uncertainties; critical assemblies)

Introduction

Present-day methods and techniques of neutron cross-section measurement are such that cross-section libraries exclusively based on the evaluation of *differential*, i.e. direct, measurements are still inadequate for reliable neutronic calculations. The reason for this inadequacy is that some *integral* quantities (e.g. reactivities), which are the object of the calculations, are very sensitive to the cross sections. In other words, variations much smaller than the uncertainties in the cross sections may result in significant variations of the calculated quantities. Thus, adequate libraries cannot *a priori* be expected from the evaluation of the differential data alone.

Yet the majority of evaluators charged with the preparation of cross-section libraries still hesitate to include valuable integral data in their evaluation procedures. All the same, they admit that in some cases at least their evaluated cross-sections are "tuned", meaning that the selection among different data sets pertaining to the same cross section was biased by the extent to which certain integral data were reproduced in calculations based on each of these sets.

But resorting to such a compromise just does not seem right in view of the availability of rather sophisticated and well tested procedures for the *systematic* adjustment of cross sections by means of integral data. Moreover, it is the designers of fast reactors, the principal users of cross-section libraries, who were among the first to develop and apply these adjustment procedures.

Experience in the use of integral (mainly critical-mass) data for cross-section adjustment has shown that in general only minor adjustments were necessary for an almost perfect "theoretical" reproduction of the experimental integral data. This implies that the better integral data should be used to determine the finer structure of the cross-section curves, while the differential data, owing to their limited accuracy, can only yield evaluations which, though essentially correct, are still characterized by rather large uncertainties.

Finally, in addition to adjusting evaluated cross sections by integral data for the solution of practical design problems, adjustment procedures are useful for checking any cross-section library. Such analyses not only indicate desirable modifications of the cross sections, but also serve to examine the consistency and reliability of the input integral data.

We have recently reported[1,2] on the adjustment procedure developed in Jerusalem, and on its application to the ENDF/B-3 library and critical-mass data on 15 metallic assemblies, taken mainly from the updated Los Alamos compilation[3]. In the present contribution we examine the principal isotopes of plutonium and uranium in the recently released ENDF/B-4 library by the same set of integral data. The method of analysis is elaborated in the above-mentioned publications. In describing our present results we employ the same notation and refer to Refs. 1 and 2 for details.

Input, Procedure, Results

The specifications of the critical assemblies, the reactivities of which comprise our integral data, are detailed in Ref. 1. The descriptions, as they appear in the original references, are quoted in the text, and the input for calculations, derived from these descriptions, is listed in Tables I, II and III of Ref. 1. For convenience we list here, in Table I, summary descriptions of these 15 assemblies.

TABLE I. Summary descriptions of critical assemblies
Plutonium alloy and oralloy masses are given in kg, and natural uranium reflector thicknesses in cm. In the mixed (Pu-Oy) systems the central core is always plutonium.

Assembly	Pu mass	Oy mass	Reflector thickness	Remarks
U 1		52.4		Godiva
UR 1		36.5	1.735	
2		26.6	4.42	
3		19.7	9.97	
4		17.8	18.01	Topsy
PUR 1	1.611	10.62	18.72	16% Pu-240
2	1.610	9.76	18.86	
3	1.615	9.52	18.90	
PU 1	2.53	26.8		
2	8.47	13.65		
PR 1	6.06		19.61	Popsy
2	6.28		11.64	
3	8.47		4.13	
P 1	17.02			Jezebel
2	19.46			20% Pu-240

The specifications of assembly PR2, however, have been recently re-examined by Paxton[4], following our observation that they were probably wrong[1]. The re-evaluated specifications of this assembly are listed in Table II.

All microscopic nuclear data were taken from the ENDF/B-4 library, of course, except for gallium, the source of which data was the UKNDL library (file 105, ENDF/B format material #8130). All partial cross sections and every detail of the spectra of secondary neutrons, as well as of the angular distributions in elastic scattering, as listed in the library files, were taken into account in calculating the reactivities and real and adjoint fluxes of the critical assemblies. On the other hand, in our adjustment procedure we have only considered sensitivities, i.e. derivatives of each assembly's reactivity, with respect to the fission, capture ($(n,\gamma)+(n,p)+(n,d)+...$), inelastic (discrete-

level plus continuous (n,n')+(n,2n)+(n,3n)), and elastic scattering cross sections and with respect to $\bar{\nu}$.

TABLE II. Specifications of assembly PR2
Densities are given in gm/cm³, dimensions in cm, and reactivity uncertainties in milli-k (10^{-3}).

		old	new
Pu core:	density	15.74	15.68
	radius	4.5679	4.5703*
Ni coating:	density		8.9
	thickness		0.0127
Nat.U reflector:	density	18.90	19.00
	radii	4.5679-16.2595	4.5834-5.1587
			5.1816-6.2865
			6.2992-16.2560
Uncertainty:	Δk	1.5 (assumed)	3.5 (1% core mass)

*Determined by extrapolated critical core-mass.

The fifteen reactivities were first calculated in a forty group - S_8 - transport corrected P_0 approximation. Then the following corrections were calculated in a four group approximation:

$$\Delta k(\text{tr.}) = k(\text{tr. corr. } P_0) - k(P_9)$$
$$\Delta k(S_8) = k(S_8) - k(S_{64}) \qquad (1)$$
$$\Delta k(I) = k(I) - k(2I)$$

The first two corrections are discussed in Ref. 1, and the third relates to doubling the number of radial divisions (I) in the forty-group calculations. The resulting transport and S_8 corrections are very similar to those calculated with the ENDF/B-3 cross sections (Ref. 1, Table V). The Δk(I) are rather small, amounting to 0.1-0.3 mk, but were still considered in the present analysis.

For all practical purposes these corrections are insensitive to the group approximation by which they are calculated, and are also additive. Thus, subtracting the three corrections from the forty-group reactivities, we obtain a very accurate value for the calculated reactivity of each assembly.

In Table III we list the reactivity uncertainties Δk corresponding to the experimental uncertainties (from Ref. 1, Table IV), the ENDF/B-3 reactivities (Ref. 1, Table V values minus the appropriate Δk(I) corrections), and the present ENDF/B-4 reactivity calculations.

Having derived the forty-group real and adjoint fluxes for each assembly, we next used a standard first order perturbation calculation to evaluate the derivatives $\partial k_i/\partial\sigma_j$, where i=1,2,...,15 and j refers to each of the 4(isotopes)×5(4 partial cross sections +$\bar{\nu}$)×40 (energy groups) microscopic group constants.

To the data we have so far collected we only need to add the uncertainties in our library cross sections, in order to be all set to apply the adjustment procedure. Available information on cross-section uncertainties, however, is rather vague and ambiguous. The rough estimates of the relative uncertainties, $\beta = \Delta\sigma/\sigma$, that we have found in the literature, and that we shall again employ in the present analysis, are listed in Ref. 1, Table VI.

But before reporting on the results of this analysis, we propose to summarize the adjustment procedure. To this end we employ the simpler notation of Ref. 2. Let $\hat{\sigma}_j$ be the set of group constants from the given cross-section library, $k_i(\hat{\sigma})$ the multiplication factors calculated by these cross sections, σ_j the (unknown) adjusted group constants, and $k_i(\sigma)$ the "adjusted" multiplication factors. Further, let ΔE_j be the energy-group width relating to σ_j.

TABLE III. Reactivities and reactivity uncertainties of critical assemblies
Reactivities and uncertainties (Δk) are given in mk (i.e. in units of 10^{-3}). The PR2 results refer to the re-evaluated specifications[4].

Assembly	Δk	ENDF/B-3	ENDF/B-4	Mod.(15)	Mod.(4)
U 1	0.8	5.04	6.11	0.16	0.08
UR 1	1.3	3.54	3.52	-0.33	-2.51
2	1.3	4.06	3.79	-1.01	-2.80
3	1.3	7.07	7.90	1.03	0.43
4	0.6	6.20	7.97	-0.02	-0.02
PUR 1	1.5	5.55	6.17	-0.27	0.35
2	1.5	7.37	5.81	-0.14	0.25
3	1.5	7.75	5.70	0.07	0.42
PU 1	1.5	6.41	3.36	0.76	-0.02
2	1.5	4.60	-0.25	-1.25	-1.56
PR 1	1.5	6.24	3.26	-0.34	0.98
2	3.5	10.76	5.69	3.07	4.00
3	1.0	5.94	1.04	0.03	-0.04
P 1	1.7	3.81	-0.26	0.28	0.01
2	2.3	-2.49	1.04	0.64	1.19

Let us now define the "normalized" individual adjustments

$$x_j = \frac{\sigma_j - \hat{\sigma}_j}{\beta_j\hat{\sigma}_j}\sqrt{\Delta E_j} \quad . \qquad (2)$$

This is a convenient definition, since we shall need a "natural" global measure for the adjustment, for which an obvious choice is

$$Q_\sigma = \tilde{x}x \simeq \sum\int\left[\frac{\sigma(E) - \hat{\sigma}(E)}{\beta(E)\hat{\sigma}(E)}\right]^2 dE \quad , \qquad (3)$$

where the approximate equality holds in the limit of sufficiently narrow energy groups.

Similarly, we define the normalized adjusted reactivities

$$y_i = \frac{k_i(\sigma) - 1}{\Delta k_i} \quad , \qquad (4)$$

and the (negatives of the) normalized original-library reactivities

$$c_i = -\frac{k_i(\hat{\sigma}) - 1}{\Delta k_i} \quad . \qquad (5)$$

These definitions furnish the obvious global measure for the quality of reproduction of the experimental reactivities, namely

$$Q_k = \tilde{y}y \quad \text{and} \quad Q_k(\hat{\sigma}) = \tilde{c}c. \qquad (6)$$

We further define the so-called sensitivity matrix, the elements of which are the "normalized" derivatives,

$$A_{ij} = \frac{\partial y_i}{\partial x_j} = \frac{\beta_j\hat{\sigma}_j}{\Delta k_i\sqrt{\Delta E_j}}\frac{\partial k_i}{\partial\sigma_j} \quad . \qquad (7)$$

Then, the assumption of linear dependence of the reactivities on the cross sections, common to all adjustment procedures, and *a posteriori* justified for relatively small adjustments, is expressed by the relation

$$Ax = y + c. \qquad (8)$$

Now the whole adjustment procedure boils down to a

conditional minimum problem, to find the vectors x and y which minimize the form

$$Q = \tilde{x}x + \Delta E_0 \tilde{y}y \ , \qquad (9)$$

subject to the constraint of Eq. (8). And the straightforward solution is

$$x = \Delta E_0 \tilde{A}(I + \Delta E_0 A\tilde{A})^{-1}c, \quad y = -(I + \Delta E_0 A\tilde{A})^{-1}c \ . \qquad (10)$$

The dimensional constant ΔE_0 is evidently necessary. It is considered as a free parameter, a measure of the weight assigned to the integral data relative to that of the given cross-section set.

In Ref. 2 an approach was suggested to determine an optimal value for ΔE_0. For the case considered there, the ENDF/B-3 cross sections and the present set of integral data, this optimal value was ΔE_0 = 490 keV. We have therefore started the present analysis with this value. In the course of work it turned out that there was no such pronounced optimum for ΔE_0 this time, and that any value in the range 100-1000 keV was just about as good. There was therefore no reason to modify our initial choice.

Our analysis consists of progressively adjusting the ENDF/B-4 cross-section set $\hat{\sigma}$ by the integral data on one, two, three assemblies, etc. The order of adding the integral data, one at a time, is such that at each step the added assembly is the one for which we obtain the best reproduction of all the integral data, i.e. the minimal value of Q_k. Thus, we find that whereas $Q_k(\hat{\sigma}) = Q_0 = 349$, adjusting the original $\hat{\sigma}$ set by assembly PUR 2 alone yields $Q_1 = 22.4$. On adding PU 1 to PUR 2 we get $Q_2 = 15.17$, and so on, until we finally obtain $Q_{15} = 3.26$. The results of this analysis are given in Table IV, which also lists the (increasing!) values of Q_σ at each step. The adjusted reactivities, corresponding to adjustment of the $\hat{\sigma}$ set by all fifteen assemblies and by the first four assemblies in the optimal sequence of Table IV, respectively, are listed in columns 5 and 6 of Table III.

TABLE IV. Measures of reactivity reproduction (Q_k) and cross-section adjustment (Q_σ) as ENDF/B-4 library is adjusted by increasing number of integral data in optimal order.

Assembly	Q_k	Q_σ
-	349	0
PUR 2	22.4	31.7
PU 1	15.17	35.9
UR 4	15.18	35.9
PR 3	11.72	47.8
PUR 3	10.05	66.9
P 2	9.30	79.9
PR 1	8.32	98.5
PUR 1	8.27	99.5
PR 2	8.57	109.2
P 1	8.98	109.7
UR 1	7.86	208
U 1	4.63	332
PU 2	3.80	395
UR 2	3.94	500
UR 3	3.26	560

The ENDF/B-4 cross-section adjustments generated by data on the four assemblies (PUR 2, PU 1, UR 4 and PR 3) are listed in Table V. No significant adjustments were obtained for the ^{240}Pu cross sections.

Discussion

Let us first consider the "unadjusted" reactivities and compare the values calculated with the ENDF/B-3 library with those calculated with ENDF/B-4, listed in columns 3 and 4 of Table III. Most

TABLE V. Recommended adjustments in ENDF/B-4 cross sections. Relative adjustments (p) are in %, and energy ranges (E) in MeV.

	^{235}U		^{238}U		^{239}Pu	
	p	E	p	E	p	E
σ_f	-2.5	0.0-0.2			-0.5	0.0-0.3
	-2.0	0.2-0.3				
	-1.5	0.3-0.4				
	-1.0	0.4-0.7				
	-0.5	0.7-1.2				
σ_c	+1.0	0.0-0.1	+2.0	0.0-0.1	+0.5	0.0-0.3
	+0.5	0.1-0.2	+1.0	0.1-0.3		
			+0.5	0.3-0.6		
σ_{in}	-0.5	0.3-0.5	+1.0	0.0-0.1	+0.5	0.0-0.7
	-1.0	0.5-1.0	+0.5	0.1-0.2	+1.0	0.7-3.0
	-0.5	1.0-3.0	-0.5	0.3-1.3	+0.5	3.0-4.5
			+0.5	1.5-3.0		
σ_{el}	-0.5	0.1-1.1	-1.0	0.0-0.5	+1.0	0.0-0.5
			-0.5	0.5-0.8	+0.5	0.5-1.5
$\bar{\nu}$	-0.2	0.0-0.1				
	-0.1	0.1-0.4				

obviously the later version reactivities generally fit the experimental data better, and the fit improves as one goes down the table. In other words, the more significant the plutonium content of an assembly, the better the relative fit of its ENDF/B-4 reactivity. In particular, the ENDF/B-4 reactivities of the two bare and the thin-reflector Pu assemblies fall within their respective experimental errors.

This, of course, is a clear indication that the cross sections of the Pu isotopes have been definitely improved in the course of their latest re-evaluation. They certainly seem to satisfy the requirements set by our present set of critical-mass data. And indeed Table V shows no important adjustments of the ^{239}Pu cross sections, and none at all for those of ^{240}Pu.

Now, although ^{240}Pu is only a minor component of our assemblies, still the analysis of the ENDF/B-3 library resulted in substantial adjustments of its cross sections when all assemblies were included. The obvious reason for this was the conspicuously low unadjusted reactivities of assemblies P 2 and PUR 1 (containing significant amounts of ^{240}Pu) relative to all other ENDF/B-3 reactivities. This is clearly not the case with the ENDF/B-4 reactivities, and the ^{240}Pu cross sections do not practically participate in the present analysis.

As for ^{239}Pu, it is worthy noting that its improved reproduction of the experimental data is entirely due to the modification of the cross sections proper. An analysis of the sensitivity of reactivity to $\bar{\nu}$ and to the fission and inelastic-scattering spectra[5] shows that for a pure ^{239}Pu critical sphere the effects of the modifications of these factors on transition from version 3 to version 4 of ENDF/B cancel to within 0.2 mk, while the total reactivity change is 6 mk.

In contrast to the substantial improvement in the plutonium cross sections, the new uranium cross sections remain practically unchanged. As a matter of fact, the slight actual modification of the ENDF/B-3 U data even tends to somewhat increase the deviations of the calculated reactivities from their experimental value of zero. Yet the cross-section adjustments needed to reduce these deviations to within the respective experimental errors, as listed in Table V, are very modest indeed. We therefore claim that the adjusted cross sections are just as consistent with the "raw"

differential data as the evaluated-unadjusted cross sections are. And further, we also suggest that adjustment is actually no more than just advanced "tuning."

Finally, referring to our progressive adjustment procedure, the results of which are given in Table IV, we note that with two assemblies only we already reach $Q_k \simeq 15$ (a rough indication for an overall fit), and that $Q_4 \simeq 12$, whereas in the case of ENDF/B-3 we had $Q_4 \simeq 30$. However, even on adjusting the ENDF/B-4 cross sections by data on four assemblies, there are still three calculated reactivities (of assemblies UR 1, UR 2 and PR 2) which are greater than the respective Δk's. The fact that after the similar adjustment of the ENDF/B-3 cross sections the very same reactivities, together with that of P 2 (a ^{240}Pu-case already mentioned), were also the ones that did not fall in line, seems significant, and may indicate that the critical specifications of these assemblies need further re-evaluation.

References

1. A. Pazy et al., The role of integral data in neutron cross-section evaluation. Nucl. Sci. and Eng. *55*, 280-295 (1974).
2. J.J. Wagschal et al., Cross-section sensitivities, adjustments and all that. ANS Topical Meeting on Advanced Reactors, Atlanta, Ga. (1974).
3. G.E. Hansen and H.C. Paxton, Re-evaluated critical specifications of some Los Alamos fast-neutron systems. Los Alamos Report LA-4208 (1969).
4. H.C. Paxton, Private communication (1974).
5. H. Nissimov and J.J. Wagschal, Sensitivity of k_{eff} of metallic assemblies to the parametric representation of fission and the inelastic-scattering spectra. This Conference.

NEUTRON ATTENUATION IN NORMAL AND ILMENITE CONCRETES

R.J. Adams and K.H. Lokan
Division of Physics
National Research Council of Canada
Ottawa, Ontario. K1A 0R6 Canada

ABSTRACT

Energy distributions of neutrons transmitted through slabs of normal (density = 147 lb/ft^3) and ilmenite loaded (240 lb/ft^3) concretes have been obtained using time of flight methods, for concrete thicknesses increasing in 3 inch steps from 0 to 18 inches. The incident spectrum was a photoneutron continuum from aluminium irradiated with 35 MeV bremsstrahlung, and was generally similar to a fission neutron spectrum.

The measured distributions are compared with the results of a Monte Carlo calculation, and agree well within the experimental errors. Results from the calculations are used to extrapolate to greater thicknesses and other ilmenite concrete densities.

(Neutron attenuation, ilmenite concrete, time of flight, Monte Carlo.)

Introduction

As part of a general study of the shielding properties of high density concretes a study of neutron attenuations in normal and ilmenite loaded concretes was undertaken in collaboration with the Houston Aggregate Co. of Montreal.

Experimental measurements were made using the photoneutron time of flight facility[2] at the N.R.C. for neutron energies between 0.5-20 for concrete thicknesses of 3, 6, 9, 12, 15 and 18 inches.

Monte Carlo calculations were made concurrently using the neutron transport code SHIELD[3] which permitted a direct comparison with the experimental data. The results were extended beyond the range of the experimental measurements to predict spectral distributions (in the forward direction) at depths up to 30 inches for normal and three grades of ilmenite concrete.

Experimental

The experimental arrangement for the attenuation measurements is shown in Fig. 1. A 35 MeV 10 nanosecond pulsed electron beam was directed onto a tantalum radiator to produce a well defined photon source. This then illuminated an aluminium target (approximately 15 cm in diameter) placed on the axis of the 31 m collimated flight tube. The photon flux was monitored through the 8.15 hr β^- activity induced in tantalum foils by the reaction $^{181}Ta(\gamma,n)^{180}Ta$. Transmission measurements were made in three inch steps, using 3 ft square test panels placed against the flight tube. Neutrons emerging from the rear face of the concrete barrier entered the evacuated flight tube and were detected at a distance of 31 metres with a fast proton recoil detector. The distribution of arrival times of neutrons, relative to the bremsstrahlung pulse was obtained, and after correcting for dead time and background, converted to the equivalent neutron energy distributions.

The overall resolution of the system was 0.60 ± 0.02 nanosecond/metre, with the uncertainty arising from the fact that neutrons which are scattered spend an unknown (but short) time in the concrete shield before emerging from the rear face. The observed spectral distributions, averaged over 200 keV are shown in Figures 2 and 3 for normal (147 lb/ft^3) and ilmenite loaded (240 lb/ft^3) concretes respectively. It should be noted that for clarity for Figures 2-7, each spectrum has been separated from its neighbours by a decade.

ATTENUATION MEASUREMENTS IN ILMENITE CONCRETES

Table 1. *Composition of concretes*

Density	Normal	Ilmenite		
		'A'	'B'	'C'
(lbs/ft^3)	147.0	180.3	241.8	267.7
Oxygen	0.499	0.4408	0.3305	0.2478
Aluminium	0.0456	0.000	0.0235	0.043
Calcium	0.108	0.0452	0.033	0.0254
Titanium	0.000	0.0935	0.204	0.1519
Iron	0.012	0.1799	0.3855	0.5409
Silicon	0.3358	0.235	0.0235	0.0342
Hydrogen	0.056	0.056	0.000	0.000

Monte Carlo Calculations

The transport code SHIELD was written for a Digital Equipment Corporation PDP-9 computer (16K, EAE and bulk storage) which is available in the laboratory. Although the program is some twenty five times slower than conventional codes extensive calculations with good statistics are possible at a nominal cost.

Based upon the compositions shown in Table I cross section data sets for the different concretes were constructed from ENDF/B library data for the elements iron[4], titanium[5], oxygen[6], calcium[7], aluminium[8] and

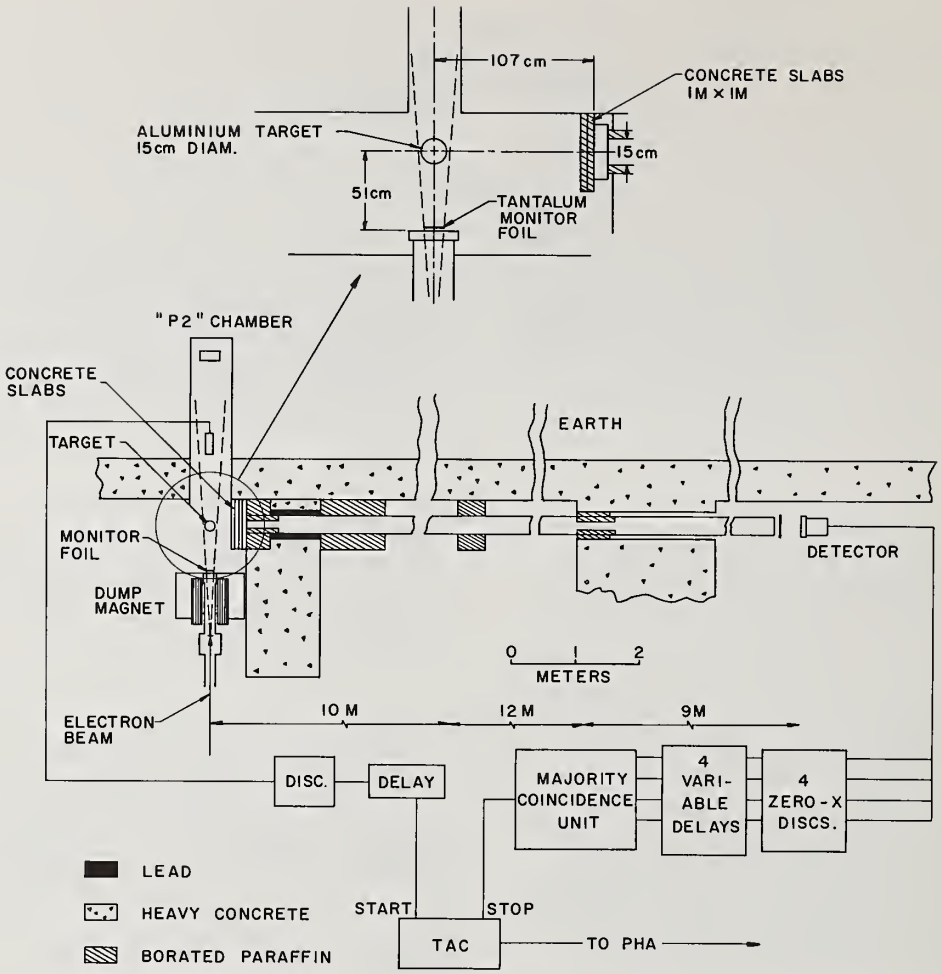

EXPERIMENTAL ARRANGEMENT

Figure 1

silicon[9], for elastic scattering, inelastic scattering through the first four excited states, and all significant absorption processes. Hydrogen was treated separately as an isotropic elastic scatterer[10]. The differential angular distributions for scattering processes were developed from the cross sections and the Legendre coefficients given in ENDF/B using methods developed for the Oak Ridge code 05R[11]. Inelastic scattering for higher excited states was treated as absorption.

The geometry used in the calculations consisted of a point source incident on a homogeneous infinite plane slab, and the measured aluminium photoneutron spectrum was used as the incident neutron energy distribution. Each calculation processed 14,000 neutrons over 256 energy steps subdivided into eight supergroups[11]. Absorption was not played for but each neutron was reduced in weight at each interaction by its transmission probability over the current trajectory. Collision histories were analysed at depts 0,3 ··· 30 inches for trajectories emerging from the back face at angles between 0 and 20^{o} from the normal[12]. The results are shown in Figures 4-7.

Discussion

Comparison of experimental and calculated spectra show clear qualitative agreement in the structure arising from specific absorption resonances, primarily oxygen. A typical comparison for 9" of normal concrete and 6" of ilmenite is shown in Figure 8. Quantitatively, however, two differences are apparent; there is a systematic difference of 10-15%, between the measured and computed spectra and at the greatest depths, the experiment shows a considerably larger number of low energy neutrons (<2 MeV) than calculated.

Although no estimates have been made of inaccuracies arising from errors in the nuclear cross sections, the reproducibility of the calculations has been assessed and an upper limit for the relative error of 5% has been determined. Any systematic difference would seem most likely to arise from the experimental uncertainties in removing the backgrounds, especially for the thickest shields.

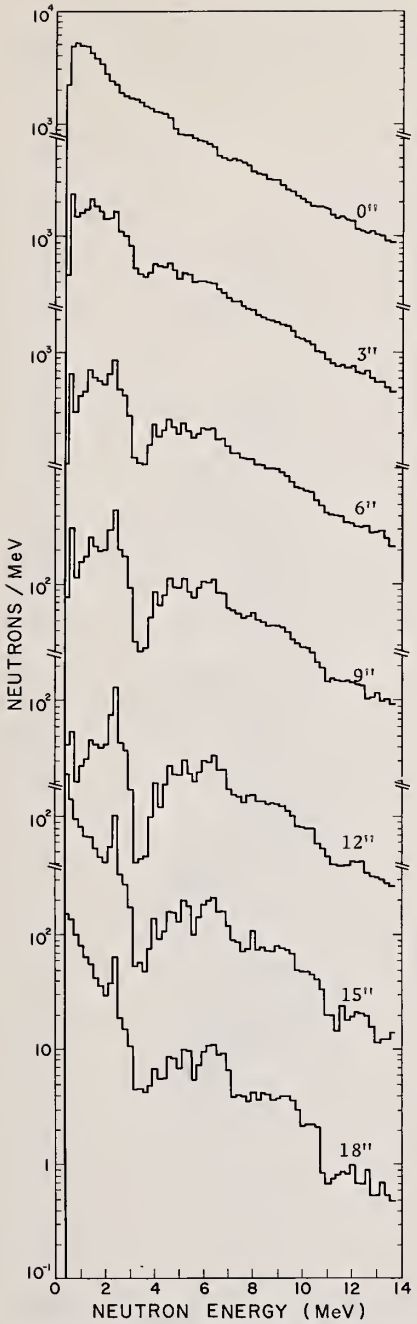

Figure 2. Transmission in Normal Concrete

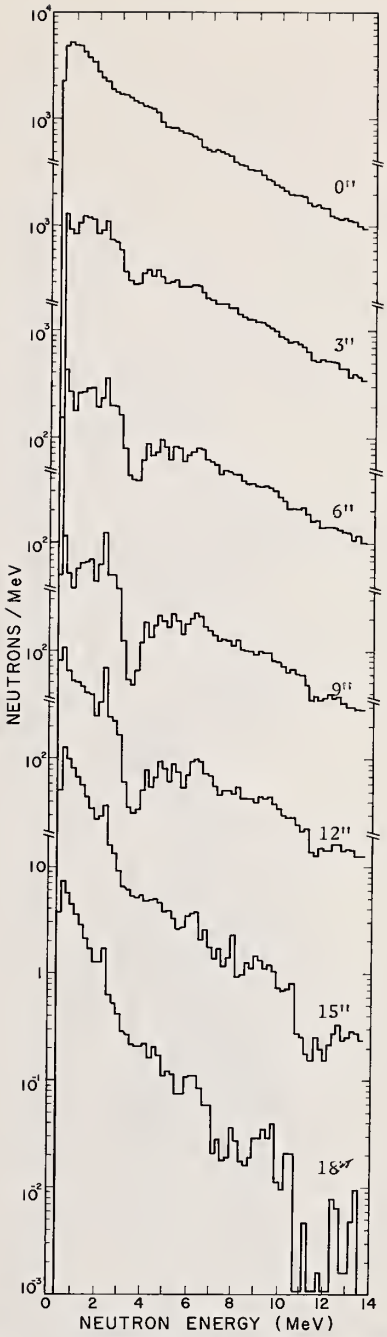

Figure 3. Transmission in 'B' Grade Ilmenite

It is noteworthy, that the Monte Carlo calculation shows a considerable number of second, and higher order interactions in the thick shields (leading to a neutron surplus) at energies below 2 MeV. A removal cross section estimate is shown for the two cases by the dashed lines in Figure 8. For thicker shields however, the experimental difficulties noted above, and the rapid change in detector efficiency below 2 MeV preclude a quantitative comparison between the calculation and experiment in this energy region.

The authors would like to thank N.K. Sherman, C.K. Ross, A. Nowak and D. Kleinbub of the Council laboratory staff for help with the experimental measurements.

References

1. K.H. Lokan and N.K. Sherman, R.W. Gellie *et al.* Health Physics 23, 193 (1972).

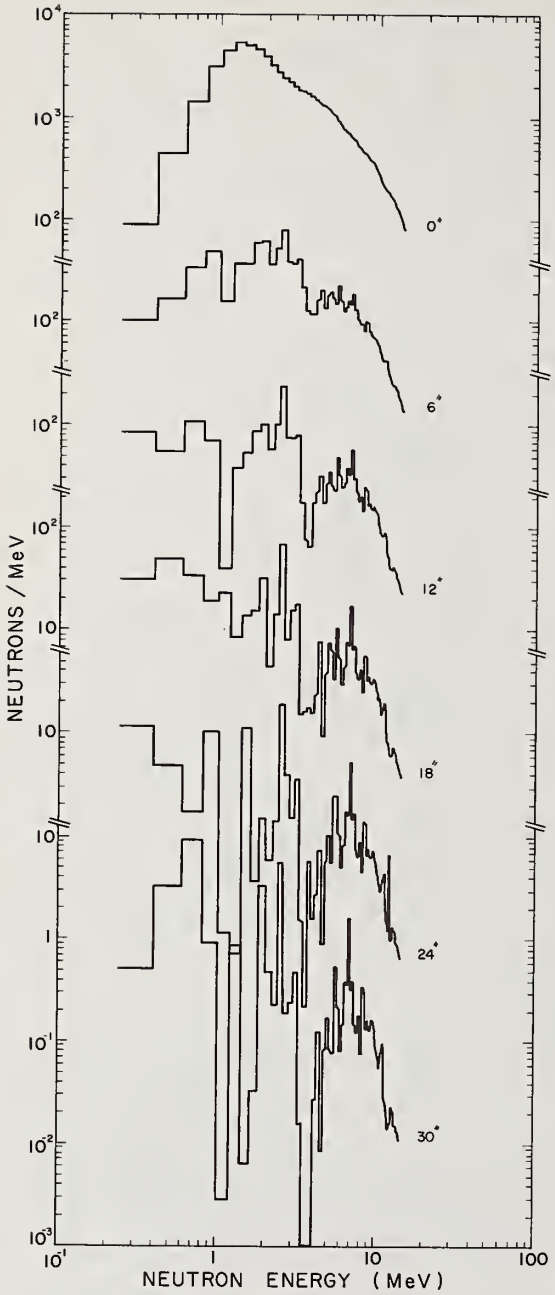

Figure 4. Transmission Spectra for Normal Concrete

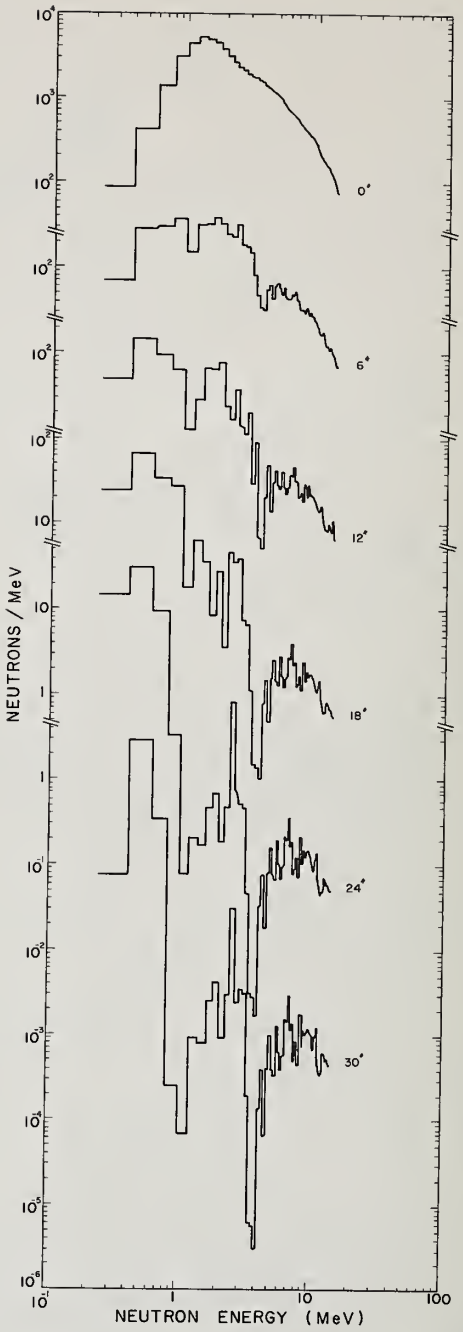

Figure 5. Transmission Spectra for Grade A Ilmenite

2. K.W. Geiger and K.H. Lokan, N.R.C. PXNR-2319 June (1972).

3. R.J. Adams, L.C. Henry and K.H. Lokan. Proc. 4th Int. Conference on Reactor Shielding 2, p. 434. Paris (9-13 Oct. 1972).

4. S.K. Penny and W.E. Kinney. ORNL 4617 ENDF 139 (1970).

5. E.M. Pennington and J.C. Gojntak. ANL 7387 (1970).

6. P.G. Young and D.G. Foster Jr. DNA 4134 (1972).

7. F. Penery and M.K. Drake. G.A.-7928 6, (1972).

8. M.K. Drake and R.D. Wright. G.A.-8628 (1971).

9. W.G. Foster Jr. and D.G. Young. LASL (1972).

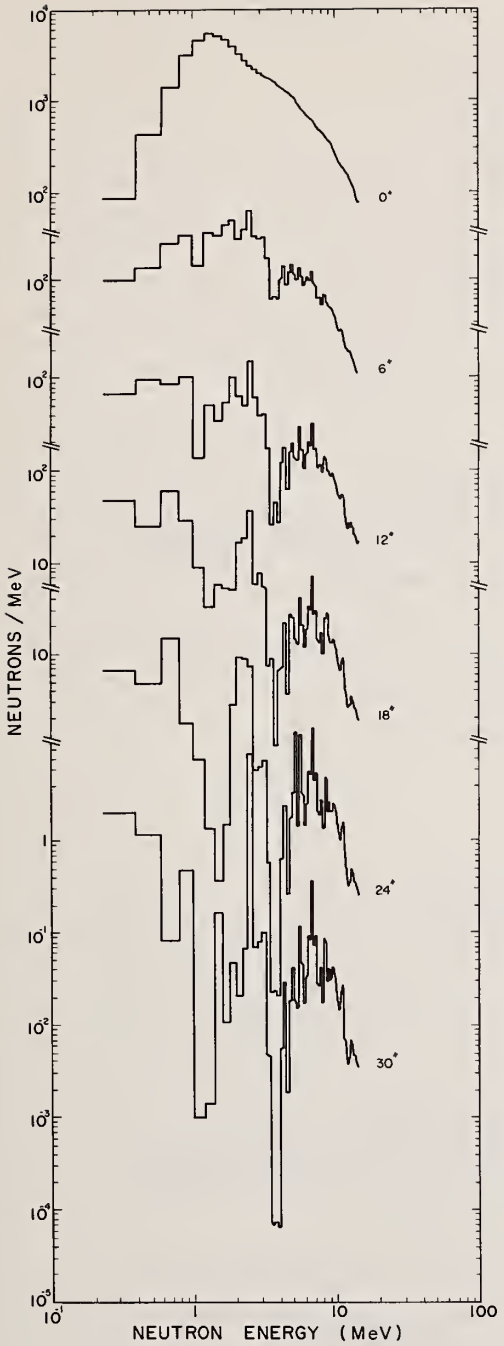

Figure 6. Transmission Spectra for Grade B Ilmenite

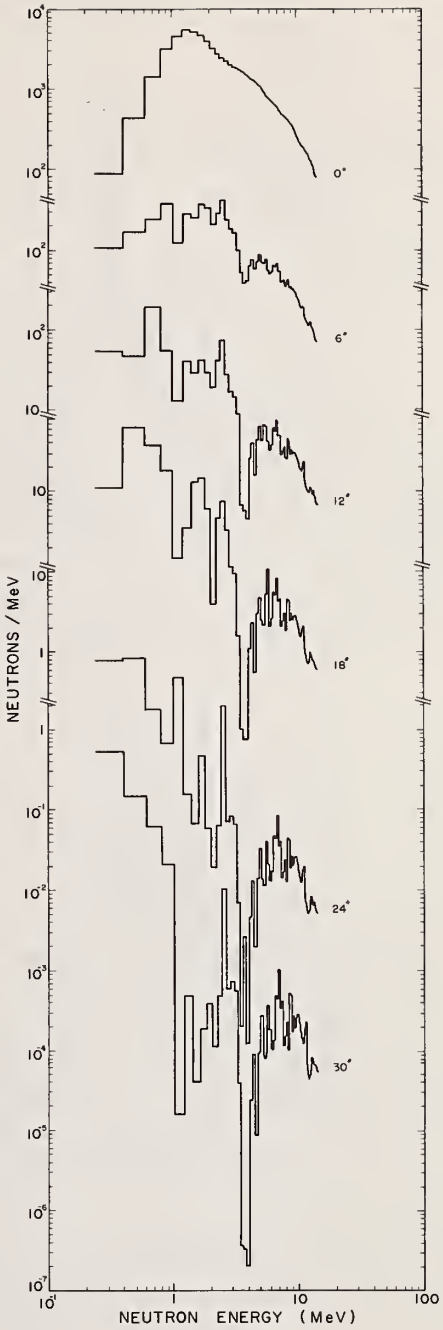

Figure 7. Transmission Spectra for Grade C Ilmenite

10. R.J. Labouve and P.G. Young. LA 4574 (1972).

11. D.C. Irving *et al.* ORNL-3622 UC-32 TID-4500. (1965).

12. A. Schneider "The Monte Carlo Method". Pergammon Press. Vol. 87, p. 158, 167 (1967).

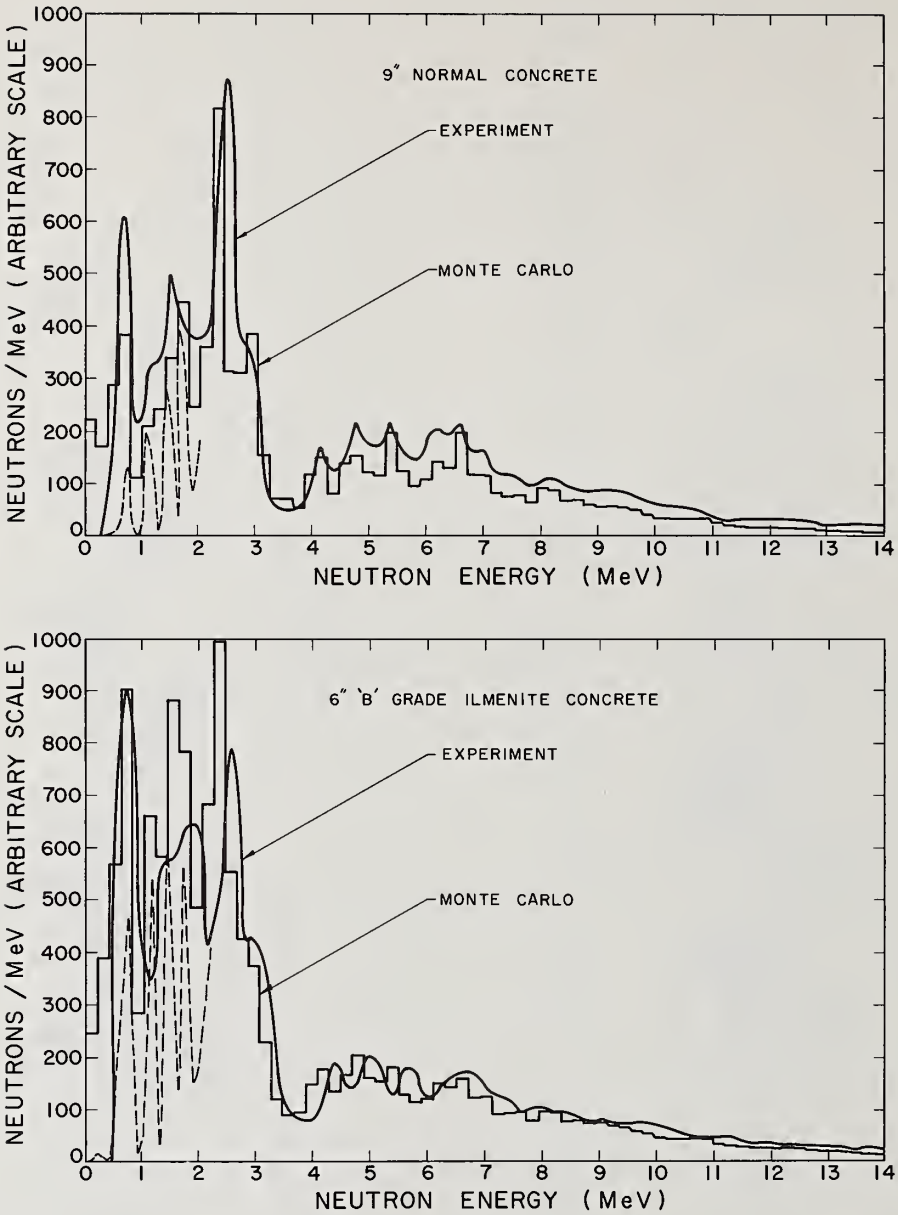

Figure 8. Experimental Data Compared to Monte Carlo Calculations for 9" Normal Concrete and 6" 'B' Grade Ilmenite.

ANALYSIS OF THE BNL ThO_2-^{233}U EXPONENTIAL EXPERIMENTS

D. Dabby
Westinghouse Nuclear Energy Systems
Pittsburgh, Pennsylvania 15230

The BNL ThO_2-3 w/o ^{233}U light-water-moderated exponential experiments[1,2] were analyzed to evaluate 1) cross section library sets for ^{233}U and ^{232}Th, and 2) correlations with measured ThO_2 resonance integral data. A total of six cross section library sets were evaluated, including ENDF/B-2 and ENDF/B-3[3] libraries for ^{232}Th, ENDF/B-2 library for ^{233}U, and ThO_2 resonance integral correlations based on data by Weitman[4] and Pettus[5], Hardy and Palowitch[6], and corrections to the latter data by Steen[7]. A modified version of the LEOPARD[8] code was used throughout this analysis. The principle results of this work are as follows: 1) The library set containing ENDF/B-2 data for ^{233}U and ENDF/B-3 data for ^{232}Th, together with ThO_2 resonance integral correlation based on Steen's corrections to the Hardy and Palowitch data, yields the best agreement with measurements, giving an average keff of 0.9975 with a standard deviation of 0.0067 for the 21 analyzed configurations. 2) With respect to this "best" set, the ENDF/B-2 ^{232}Th data is less reactive than the corresponding ENDF/B-3 data by ~0.1%Δk. 3) The ThO_2 resonance integral correlation based on data by Weitman and Pettus yields resonance integrals that are consistently higher than those produced by the correlation with Steen's values, even though the latter is normalized to an infinitely dilute resonance integral of 85.9 barns (0.5 ev cutoff), while the former is normalized to a corresponding value of 80 barns. Thus, with respect to the "best" set, the ThO_2 resonance integral correlation based on the Weitman and Pettus data is less reactive by ~0.7%Δk.

(Cross sections, ^{233}U, ^{232}Th, ThO_2 resonance integral)

I. Introduction

An extensive program of exponential experiments, utilizing $^{233}UO_2$-ThO_2 fuel elements in uniform arrays in light and heavy water, was carried out in 1966 at the Brookhaven National Laboratory. The main objective of these experiments was to provide a set of data which can be used to validate calculational models and integral neutron cross sections. The measured configurations analyzed here consisted of a set of 21 zirc-clad clean and borated experiments with a $^{233}U/(^{233}U + ^{232}Th)$ ratio of 3 w/o. The moderator-to-fuel volume ratios ranged from 1.0 to 9.3, while the soluble boron concentrations ranged from 0.0 to 4380 ppm, amply scanning the ranges of design interest. These experiments were analyzed to evaluate six cross section library sets. The methods, results, and conclusions of this evaluation are discussed in the following sections.

II. Cross Section Sets

A. Evaluated Sets

A total of six cross section library sets were evaluated here. Each set was made up of a common library for all elements except for ^{232}Th and ^{233}U, together with different combination of cross sections sets for these two elements, and of ThO_2 resonance integral correlations with measured data. The MILC[9] and ENDF/B-2 sets were evaluated for ^{233}U and ^{232}Th, while the ENDF/B-3 set was evaluated only for ^{232}Th. ThO_2 resonance integral correlations based on data by Weitman and Pettus (labeled RI1), Hardy and Palowitch (RI2), and Steen's corrections to the latter data (RI3), were evaluated in conjunction with the above evaluations for ^{233}U and ^{232}Th. Table I shows the contents of each of the evaluated cross section library sets.

TABLE 1

Contents of the Six Evaluated Cross Section Sets

Set No.	^{233}U	^{232}Th	ThO_2 R.I
1	MILC	MILC	RI1
2	ENDF/B-2	"	"
3	"	ENDF/B-2	"
4	"	"	RI2
5	"	ENDF/B-3	"
6	"	"	RI3

B. ^{233}U Data

Table 2 shows a comparison of ^{233}U nuclear data from MILC, ENDF/B-2 and ENDF/B-4[10]. Only the first two sets were evaluated here, since the latter set was not available in the appropriate processed form for use in the LEOPARD code. Note that the fission resonance integrals (I_f) given in Table 2 were corrected to the 0.625 ev thermal-energy-cutoff used in LEOPARD. The reactivity effects of the difference between the MILC and ENDF/B-2 data shown in Table 2 will be discussed within the context of the calculational results given in Section III.

TABLE 2

^{233}U Nuclear Data

Data Source	E>0.625 ev		E=0.0025 ev(2200 m/sec)	
	I_f(b)	α	η	α
MILC	829	.170	2.290	0.0933
ENDF/B-2	737	.187	2.293	0.0903
ENDF/B-4	738[11]	---	2.284	0.0866

C. ThO_2 Resonance Integral Data

The general form of the ThO_2 resonance integral correlation used in the LEOPARD code is

$$R.I.^{ThO_2} = aX + b + (cX+d)\ Teff^{\frac{1}{2}} \qquad (1)$$

where

$$X = \left[\frac{\Sigma_{so}}{N_o^{Th}}\ P_o + \frac{D_{eff}}{l_o N_o^{Th}}\right]^{\frac{1}{2}} \qquad (2)$$

and

Σ_{so} is the scatterning cross section of the fuel

N_o^{Th} is the ^{232}Th number density in the fuel

Po = 1-Pc where Pc is a tabulated function[12] of $\Sigma_{so}R_o$

l_o is the mean chord length in the fuel ($l_o = 2R_o$ for a fuel rod)

D_{eff} is the effective shielding factor of the lattice

T_{eff} is the effective fuel temperature

and a,b,c,d are fitted constants.

Steen has made extensive evaluations of the basic cross section data for ^{232}Th and for the ThO_2 resonance integrals evaluated here. He reports that the data used to obtain RI1 may have possible systematic errors that are significantly larger than those in the data used to obtain RI2 and RI3 (∿5% vs ∿3%). Furthermore, the former data were normalized to an infinite dilute resonance integral value of 80 barns, as opposed to the 85.9 barns to which the latter data (RI2, RI3) were normalized. The reactivity effects of these differences are discussed in Section III.

III. Results and Discussion

Table 3 presents the entire set of measured configurations as analyzed with each of the six cross section library sets being evaluated. Set 1 is clearly too reactive, mainly because of the high value of the fission resonance integral of ^{233}U (I_f - See Table 2). The standard deviation (s) of Set 1 is the highest of the eight sets, since the relative importance of an incorrect I_f is spectrum dependent, being most pronounced for the tight lattices. Set 2 underpredicts k_{eff} mainly because of the high value of RI1. Note that the reduction of I_f from 829 barns to 737 barns reduces k_{eff} by more than 3% in the tight lattice, but by only 2% in the loose ones. The inclusion of the ENDF/B-2 data for ^{232}Th further reduces the average k_{eff} (by $\sim$0.3%Δk), as shown in set 3 results. Set 4 shows the reactivity effects of RI2. As in the case of I_f, these effects are more pronounced for the tight lattices ($\sim$0.6%Δk) than for the loose ones ($\sim$0.1%Δk) Set 5 includes the ENDF/B-3 treatment for ^{232}Th, showing an increase of 0.1%Δk in average k_{eff} with respect to set 4. Set 6 yields the best results, showing an average k_{eff} of 0.9975 and a standard deviation of 0.0667. Only three configurations show k_{eff} values lower than 0.99. All three have negative bucklings and are in a V_{mod}/V_{fuel} range that is significantly higher than that typical of design configurations. Indeed, if we were to omit these configurations from our averages, we would obtain an average k_{eff} value of 0.9998 $\pm$.0037! Note that the ENDF/B-4 treatment for ^{233}U (not evaluated in this analysis) would result in slightly lower k_{eff} values than those obtained in set 6 because of its less reactive thermal parameters with respect to those in the ENDF/B-2 treatment.

IV. Conclusions

Based on the results of this analysis, we conclude that:

1. The ENDF/B-2 and ENDF/B-3 treatments for ^{233}U and ^{232}Th, respectively, together with a ThO_2 resonance integral correlation with Steen's corrections to the Hardy and Palowitch data, yield excellent agreement with the measured configurations.

2. The measured configurations analyzed here form a highly consistent set of experiments which should be used for future evaluations of ^{232}Th and ^{233}U cross sections data.

REFERENCES

1. Price, G. A., "Uranium-Water Lattice Compilation Part I, BNL Exponential Assemblies," BNL-50035 (T-449), December 1966.

2. Windsor, H. H., W. J. Tunny, and G. A. Price, "Exponential Experiments with Lattices of Uranium 233 Oxide and Thorium Oxide in Light and Heavy Water," Nucl. Sci. Eng.: 42, 150-161.

3. Drake, M. K., "Data Formats and Procedures for the ENDF Neutron Cross Section Library," BNL 50274 (T-601), October 1970.

4. Weitman, J., "The Effective Resonance Integral of ThO_2 Rods," AE-99, December 1962.

5. Pettus, W. G., "Geometric and Temperature Effects in Thorium Resonance Capture for the Consolidated Edison Thorium Reactor," BAE-144, June 1960.

6. Hardy, J., Jr. and B. L. Palowitch, "The Effective Resonance Integral and Doppler Coefficient of Thorium-Oxide Rods," Nuc. Sci. Eng.: 29, 111-121 (1967).

7. Steen, N. M., "Analysis of Resonance Integrals of ThO_2 Rods," Trans. Am. Nucl. Soc." 13, 713-714 (1970).

8. Barry, R. F., "LEOPARD - A Spectrum Dependent Non-Spatial Depletion Code for the IBM 7094," WCAP-3269-26 (Sept. 1963).

9. MILC Library, available from PHILCO Corporation, Willow Grove, Pa. (July 1, 1961).

10. Stehn, J. R., "Thermal Data for Fissile Nuclear in ENDF/B-IV, Trans. Am. Nucl. Soc., 18, 351 (June 1974).

11. Private Communication with M. Raymond and D. Garber.

12. Case, K. M., F. deHoffman and G. Placzec, "Introduction to the Theory of Neutron Diffusion," LASL (June 1953).

13. Steen, N. M., "An Evaluation of the Radiative Neutron Capture Cross Sections of Thorium-232 for the range 0.0 ev to 15 Mev," WAPD-TM-971 (Dec. 1970).

TABLE 3. Calculated K_{eff} for the BNL ThO_2-^{233}U Exponentials for the Six Evaluated Cross Section Library Sets

Pitch (In)	V_{mod}/V_{fuel}	BC(ppm)	$B^2_{exp}(m^{-2})$	Set 1	Set 2	Set 3	Set 4	Set 5	Set 6
		0	75.88	1.0278	.9911	.9819	.9879	.9929	.9991
.6269	.997	2330	42.1	1.0335	.9890	.9832	.9890	.9920	.9982
		4380	18.8	1.0420	.9901	.9872	.9931	.9946	1.0008
		0	86.06	1.0285	.9953	.9872	.9919	.9961	1.0008
.6767	1.384	1370	50.6	1.0343	.9963	.9908	.9958	.9981	1.0027
		4012	3.65	1.0406	.9917	.9911	.9958	.9961	1.0007
		0	89.34	1.0312	.9999	.9926	.9967	1.0003	1.0041
.7163	1.7134	830	60.4	1.0298	.9956	.9901	.9941	.9966	1.0004
		3308	-1.8	1.0356	.9905	.9906	.9947	.9946	.9980
		0	90.35	1.0318	1.0024	.9961	.9995	1.0023	1.0054
.7706	2.1943	822	50.5	1.0308	.9981	.9940	.9973	.9989	1.0020
		2330	-2.1	1.0308	.9910	.9910	.9943	.9942	.9972
		0	85.54	1.0301	1.0028	.9979	1.0005	1.0025	1.0047
.8542	3.0043	874	26.5	1.0262	.9950	.9929	.9955	.9961	.9982
		1370	1.99	1.0224	.9877	.9872	.9901	.9898	.9920
		0	69.80	1.0270	1.0017	.9983	1.0002	1.0017	1.0029
.9707	4.2722	469	22.6	1.0203	.9928	.9913	.9932	.9935	.9952
		869	-7.67	1.0115	.9920	.9920	.9940	.9838	.9854
1.172	6.8449	0	32.2	1.0157	.9926	.9911	.9923	.9926	.9936
		298	-10.8	1.0043	.9796	.9795	.9807	.9806	.9816
1.3346	9.2747	0	-1.22	1.0049	.9830	.9825	.9834	.9834	.9842
		Avg. K_{eff}		1.0266	.9932	.9899	.9933	.9943	.9975
		Std. Dev(s)		± .0103	± .0060	±.0051	±.0050	±.0060	±.0067

TABULAR CROSS SECTION FILE GENERATION AND UTILIZATION TECHNIQUES

D.E. Cullen, Lawrence Livermore Laboratory, Livermore, California 94550
O. Ozer, Electric Power Research Institute, Palo Alto, California
C.R. Weisbin, Oak Ridge National Laboratory, Oak Ridge, Tennessee 37830

Criteria of importance to the generation of linear cross section tabulations are presented. Algorithms for reducing or thinning such tables within a desired accuracy criterion and the implementation of paging techniques for efficient utilization of large data tables are reviewed.

(Cross sections, tables, pre-processing, relative error, linearization, thinning, paging.)

Introduction

For many applications it is necessary to reduce the ENDF/B data files into a tabular form with a linear functional variation specified between the data points. Such tabular data bases are presently in use at a number of national laboratories.

Tabular representation of the files greatly simplifies the requirements for computer programs utilizing such data. The straight forward task of displaying a cross section, which may require a rather expensive resonance calculation when the base ENDF/B file is used as the starting point, is reduced to a simple table look-up and interpolation problem for tabular files. Great reductions in computing time can be realized in various codes (such as the point Monte Carlo Code REP[1]) which have been designed to do repetitive cross section calculations at a large number of energies.

When generated at a temperature of 0^0K data tables can be easily Doppler broadened to any desired temperature using numerical kernel broadening techniques.[2] Numerical broadening has the advantage of not being restricted to the "resonance range" and not ignoring the contribution of the "smooth" background correction terms which in fact often exhibit considerable structure. These advantages become particularly significant in the case of high temperature or CTR applications and for light materials for which no explicit resonance parameters are given on the ENDF/B file.

The generation and use of such tabular files requires a number of special considerations: Tabular files are generated within a specified controlled accuracy criterion. (The accuracy is defined as the fractional deviation from the "true" value which would be obtained from the ENDF/B file.) Thus at any stage the upper bound on the processing error is known.

The accuracy criterion must be selected in a manner that will insure the adequacy of the tabular files in the widest range of applications yet result in the smallest number of points. Typically tables with 10000 to 40000 points per reaction type are generated when major isotopes are reconstructed at 0^0K with an accuracy of .1%. As the experimental resolution is improved and the unresolved resonance range is further reduced[3] files with 150000 to 200000 points should be expected.

Percent Accuracy	Number of points in the tabulation of the Total cross section		
	U-238	U-233	Fe
0.5	33644	2873	
1.0	12753	889	4215
2.0	9792	577	3834
5.0	6674	344	3100

Table I. Dependence of table size on accuracy

Such high accuracy files should be considered as a master data base and need to be generated only once. For many applications data with considerably lower accuracy may be sufficient. Thinning techniques are used to reduce the size of the tables depending on the required accuracy. Doppler broadened tables should be thinned even if the accuracy is the same because the smoothing effect of the Doppler process results in fewer points being required to represent a function within the same accuracy.

Finally special paging techniques for utilizing tabular data files a section (or page) at a time should be incorporated into codes operating on this data base since even with a virtual core capability it is often more efficient to have control over the amount of data brought in core at any one time.

Points to be considered during the generation, thinning and paging of tabular data files are discussed in the following sections.

Temperature ^{0}K	Number of points necessary to represent the U-238 total cross section within 1% (ENDF/B-IV Data)
0	12753
293	6819
1000	5050

Table II. Smoothing effect of the Doppler process.

Generation

The major consideration in generating tabular data files is the selection of a proper convergence or accuracy criterion. When reducing ENDF/B files into a linearized tabular form two problems are encountered:

a) Conversion of cross section data which is already in tabular form but may have a logarithmic or semilogarithmic functional dependence between the tabulated points into a linear tabulation (Linearization)

b) Processing of data given in parametric form (e.g. resonance range data) into tables with an energy grid selected in a manner to insure the fewest number of points for a desired accuracy.

Both of these problems can be considered as approximating a function f(E) defined for all E, by another $\overline{f}(E)$ such that:

$\overline{f}(E_i) \equiv f(E_i)$ at the tabulated points E_i, and the deviation of $\overline{f(E)}$ in areas between the tabulated points is less than a specified accuracy criterion.

For inherently positive functions such as a cross section the convergence between tabulated points should be determined on the basis of the fractional difference

i.e. $|f(E) - \overline{f(E)}| < \varepsilon f(E)$, as opposed to the absolute difference $|f(E) - \overline{f(E)}| < \varepsilon$.

Criteria based on the fractional difference are consistent with uncertainties in the experimental data and result in a more uniform distribution of data points in low as well as high cross section areas.

A numerical "interval halving" algorithm incorporated into the code RESEND[4] and compatible with the fractional difference criterion has been found well suited for the generation of tabular files in the resonance range as well as for the linearization of already tabular ENDF/B data files. This algorithm consists of the following steps:

a) A set of initial energy "node points" is selected. For tabular data, nodes are located at the edges of nonlinear interpolation ranges. For resonance data nodes are set at the peaks of resonances and mid-points between the peaks.

b) The exact cross section f(E) is calculated at the node points and $\overline{f(E)}$ is set equal to f(E).

c) The value of the approximate function $\overline{f(E)}$ at the mid-point between two nodes is obtained by linear interpolation and compared with the exact value f(E) at the same point. If the fractional difference at the mid-point is larger than the desired convergence criterion the mid-point is defined to be a new node and the process repeated in the halved interval. When a difference smaller than the convergence criterion is reached the interval is assumed to have converged and the process is repeated between the next set of nodes.

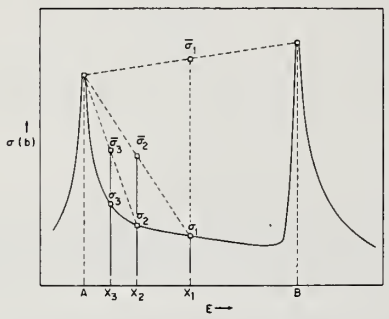

Figure 1. Generation of Energy Grid in Program RESEND.

When generating tabular cross section files from resonance parameter data, the convergence test should be applied to each of the individual reaction types separately and not be limited to the total cross section, since variations in reaction types with a low cross section (e.g. Interference dips in elastic scattering) tend to be washed out when contributions from other, larger reactions are added on.

For the process of linearization of data tables an algorithm based on the analytic determination of the location of the maximum in the absolute difference $|f(E) - \overline{f(E)}|$ has been developed and implemented in the code MINX.[5] However the interval halving technique is found to be preferable since it is dependent on the fractional error and is somewhat simpler and faster. An extension of the MINX algorithm to fractional errors has not been found to be practical.

Thinning

The thinning procedure is logically equivalent to the process of linearization since one starts with a function f(E) which is given as a table of values and a linear interpolation law between the tabulated values, and one tries to determine a function $\tilde{f}(E)$, such that:

a) $\tilde{f}(E)$ is also a table of values and linear interpolation laws.

b) The fractional difference between the "exact" f(E) and the approximation $\tilde{f}(E)$ is less than some desired allowable error ε for all energies.

i.e. $|f(E) - \overline{\tilde{f}(E)}| < \varepsilon f(E)$.

However an additional criterion is added:

c) The tabulated values of $\tilde{f}(E)$ must constitute the smallest possible sub set of the tabulated vales in f(E).

Thus all values in the tabulation of f(E) that can be approximated (to within ε) by linear interpolation between adjacent points must be eliminated.

The following multipoint algorithm has been developed for thinning data files.

a) The first and third point of a table are selected and a test is made to determine whether point number two can be approximated by linear interpolation between points 1 and 3.

b) If the test is successful the test interval is extended to include point 4 and again points 2 and 3 are tested to see whether they can be approximated by an interpolation between points 1 and 4.

c) Generalizing to N points, if the points 2, 3, . . . (N-1) can be approximated by interpolating between points 1 and N the algorithm proceeds to N + 1 points.

d) If any one (or more) of the points 2, 3, . . . (N-1) fail the interpolation test between points 1 and N the test interval has been extended too far. However since the previous test (with N-1 points) must have been successful for the algorithm to reach this far all the points between 1 and N-1 can be removed leaving only the end points 1 and N-1. The algorithm is repeated with points N-1, N and N + 1.

The multipoint algorithm is considerably different from the "three-point" thinning technique used in the earlier versions of the ENDF/B system routine CROP.[6]

The three point algorithm operates by discarding point 2 if it can be interpolated between the adjacent points 1 and 3 then proceeds to test point 3 by interpolating between points 1 and 4. If point 3 is rejected there remains no guarantee that point 2 which was rejected earlier can be obtained by interpolating between the remaining points 1 and 4. This method produces particularly erroneous results when thinning points located very closely on a slowly varying smooth curve. The multipoint thinning algorithm is not limited to linear tables but can be used with any interpolation law. A generalized version has been implemented in a revised subroutine CROP.

Paging

Two types of paging can be considered.

1. Physical Paging

If one recognizes that only a section of a large data table will be used in a computation for a reasonable length of time a program may be initially designed to keep only a portion of the table (a page) core resident at any one time. For applications requiring each portion of a table only once (e.g. group averaging, Doppler broadening) this physical paging may consist of simply allowing for the reading of a table a section at a time. Applications using different portions of a table repeatedly may require the use of scratch files or logic to randomly access different sections of a table.

2. Logical Paging

Programs written without a paging capability can easily be converted to a logical form of paging with only minor coding modifications.

Removing the name of an array to be paged from all COMMON and DIMENSION statements is equivalent to replacing that array by a function. One only needs to add a function by the same name to determine which section of the data table the desired point is located in, load that section if not already resident in core and return the desired value from the table. Such logical paging has been incorporated in code CHECKER and some versions of ETOG-3[7] programs with a paging capability are not only more versatile but may actually be more economical to use. The size of a page should be selected depending on the type of computer environment the program is to be used in.

a) In single user batch type of an environment I/O operation should be minimized by making the pages as large as possible within the available core. As the program is expanded, the page size can be reduced to allow it to fit in the same core.

b) In a multi-user time slice environment page size is determined by the amount of data that can be used within a single time slice. Ideally the size of a page in a time sharing environment should be such that the program can be finished and ready to read the next page at the end of its time slice.

3. Page Overlap

For applications requiring the use of two or more adjacent table entries simultaneously it is necessary to structure the paging logic in such a manner that the last few points of a page are repeated at the beginning of the next page. The purpose of this overlap is to avoid the repeated reading of pages that would result when the program attempts to use points located in two adjacent pages.

Conclusion

The methods described in this paper have been implemented into a number of computer programs. The programs given on Table III in combination supply all the software necessary for processing the ENDF/B data files into a linear tabulation at any desired temperature, or to a multigroup cross section form.

Program	Function	Characteristics
Scope[8]	Displays ENDF/B and/or experimental data (e.g. ENDF-2DD)	Thinning, Logical Paging
CHECKER[6]	Checks correctness of ENDF/B files	Logical Paging
RESEND[4]	Reconstructs pointwise ENDF/B data tables from Resonance parameter data	Physical Paging
LINEAR[9]	Linearizes point ENDF/B data	Linearizing, Thinning Physical Paging
SIGMA1[10]	Doppler broadens linearized tabular ENDF/B data	Thinning, Physical Paging
MINX[5]	System for the production of multi-group cross sections from ENDF/B data	Physical Paging

Table III. List of programs utilizing tabular data files

References

[1]W. Rothenstein, "Monte Carlo Code for the Calculation of Resonance Reaction Rates and Effective Resonance Integrals Based on ENDF/B Data (REPCDC)" BNL-13851 (1969).

[2]D.E. Cullen, C.R. Weisbin, R. Q. Wright, J.E.White, "Comparison of Doppler Broadening Methods", Proceedings of this conference.

[3]G. De Saussure, R.B. Perez, "Representation of Neutron Cross Sections in the Unresolved Resonance Region", Proceedings of this conference.

[4]O. Ozer, "RESEND: A Program to Pre-process ENDF/B Materials with Resonance Files into a Pointwise Form" BNL-17134, Brookhaven National Laboratory (1972).

[5]C.R. Weisbin, P.D. Soran, R.E. McFarlane, D.R. Harris, R.J. LaBauve, J.S. Hendricks, J.E. White. "MINX, a Multigroup Interpretation of Nuclear Cross Sections from ENDF/B" To be published as Los Alamos National Lab. report. Also ANS Trans. 16, 127 (1973).

[6]O. Ozer, Ed. "Description of ENDF/B Processing Codes and Retrieval Subroutines," BNL-50300, (REACT-TECH TID 4500) ENDF 110, Brookhaven National Laboratory (1971).

[7]M. Raymund, "ETOG-3 and ETOT-3, Advances in Processing ENDF/B-III Libraries" ANS Trans. 16, 323 (1973).

[8]D.E. Cullen, "Program SCOPE" BNL-16700 (1972).

[9]D.E. Cullen "Program LINEAR" To be published as UCID report.

[10]D.E. Cullen "Program SIGMA1" UCID 16426 University of California Lawrence Livermore Laboratory (1974).

NEUTRON ENERGY SPECTRUM CONTROLLED BLANKET FOR FAST BREEDER REACTOR

L. H. Tang
Physics Department, University of Detroit
Detroit, Mich. 48221

It is shown that the productivity of a blanket can be substantially improved by introducing a "moderation-jacket" around the inner blanket facing the fast core. The operational procedure and the expected significance of the jacket are investigated. For a flux level similar to that of EBR-II, it is shown that one can shorten the plutonium production time by 34.5% for 0.7% plutonium density buildup and 15.4% for 1.5% plutonium density buildup. The overall time saving is about 100 days per recycling from density buildup of 0.7% to 2.0%.

(Moderation-jacket in blanket; thermal boosts; high plutonium productivity)

Introduction

Although the efficiency of breeding in a blanket depends upon the magnitude of neutron flux leaked into the blanket from the fast core, some improvements within the blanket itself still can be done in order to increase the breeding efficiency. The plutonium buildup in the blanket is an exponential function of the irradiation time, the neutron flux level and the radioactive capture cross sections of the fertile materials. For a given fast core the neutron flux level in the blanket will essentially remain constant. A small changes in the neutron flux may be resulted from a variation of power output of the reactor. But for a power breeder reactor, it is expected to operate the reactor in a fairly constant power output. Thus the remaining factor which can be under our control will be the nuclear cross sections for the fertile materials.

For low and thermal neutron energies the capture cross sections for the ^{238}U have a 1/v characteristics and are much greater than that for the fast neutrons. In between the thermal and fast neutron energies there is a complicated resonance region. The cross sections in this region can change considerably with a small change in neutron energy. It is rather difficult to control the neutron energy to fit to a particular resonance. Therefore, for practical purposes, it is much easier to make use of the thermal region. The purpose of this report is to show the feasibility of operating a moderating-jacket within the blanket for controlling the neutron energy spectrum for higher capture cross sections for the fertile nucleus and less fission of plutonium in the blanket.

The Moderation-Jacket

The method to achieve the goal is to introduce a "moderation-jacket" around the inner blanket facing the fast core as shown in Fig.I. The jacket should be so designed that the moderating fluid can be turned on and off at any time. The moderating fluid can be D_2O or other neutron thermalizing fluid with various compositions and/or density. At the beginning, for a fresh and highly depleted uranium blanket, one operates the fast reactor with the moderating fluid on for a certain period of time. The length of this period depends upon the neutron flux level in the blanket. The fast neutron from the core are now thermalized, and the whole blanket is essentially exposed to the thermal neutrons for irradiation. Since ^{238}U has a fission threshold of about 0.825 Mev, essentially no fission will occur within the blanket for the first 56 hours of operation. From the nuclear reaction chain of ^{238}U, one sees that each ^{238}U after a non-fission capture of a neutron will eventually convert into a fissionable plutonium isotope. Because of the non-fission capture cross sections of ^{238}U for thermal neutrons are much larger than that for the fast neutrons, the plutonium buildup rate at this time will be much greater. This can be referred to as the "thermal boost" effect of the moderating jacket. However, the plutonium buildup will rapidly reach its maximum value and then start to decrease if the moderating fluid is still on after the maximum value. This is due to the fact that the ^{239}Pu has a very large thermal fission cross section. In order to further increase the plutonium buildup in the blanket, the moderating fluid should be cut off after the maximum value has been reached. Then the blanket is operated as in the conventional case and irradiated entirely by fast neutrons, and the plutonium buildup will increase again. Through this operational procedures, the breeding rate can be increased, and the recycling period can be reduced.

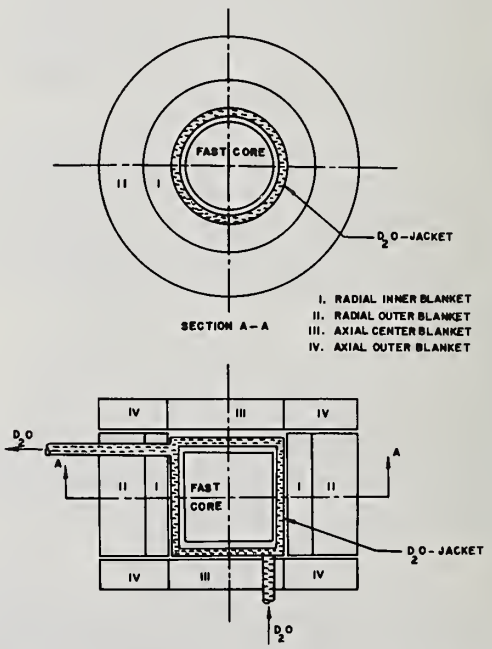

Fig. 1. Schematic drawing for the Moderating Jacket

The Principles of Operation and The Expected Results

1. Operation with Moderating Fluid Turn-on

For a fresh blanket, one operates a fast reactor with the moderating fluid turn-on. Then, the nuclear events in the blanket are mainly scattering and radioactive capture of the thermal neutrons by ^{238}U and non-fertile materials. The isotopic composition of the plutonium buildup will depend upon a particular reactor core and the previous irradiation history of the fertile materials. In general, more than 75% of the reaction chains go through the ^{239}Np and through the β-decays. The various plutonium isotopic concentrations in the blanket can be exactly calculated. However, in order to illustrate the principle of operation and to simplify the calculations, the total plutonium buildup including all the plutonium isotopes will be estimated. For irradiation time much longer than 56 hours, the total plutonium buildup can be expressed as

$$Pu(t) = U_o^{28}(1 - \exp(-\lambda_a t)), \text{ for } t \leqslant t_c = 56 \text{ hr.} \quad (1)$$

and

$$Pu(t) = U_o^{28}\left\{\frac{\exp(-\lambda_8 t)}{\beta - 1} + \left[1 - \frac{\beta}{\beta - 1}\exp(-\lambda_8 t_c)\right]\exp(-\lambda_9(t - t_c))\right\} \quad (2)$$

$$\text{for } t \geqslant t_c$$

where

$$\lambda_8 = \sigma_a(U^{28})\phi_{th}, \qquad \lambda_9 = \sigma_f(Pu^{29})\phi_{th},$$

$$\beta = \frac{\sigma_f(Pu^{29})}{\sigma_a(U^{28})},$$

and U_o^{28} is the initial ^{238}U density in the blanket and Pu(t) stands for the plutonium density buildup at time t. In equations (1) and (2) we have neglected the neutrons produced due to the thermal fission of plutonium.

As an example, the plutonium buildup will be calculated in the inner blanket for a flux level similar to EBR-II[1] as shown in Table I. From these data the plutonium buildup curves are calculated from equations (1) and (2) plotted as curve A in Fig. 2. The curve A shows that the plutonium yield increases much faster than that without the jacket and reaches its maximum after only about 50 days of operations. This is the "thermal boost" effect of the jacket. Then, it begins to decrease for continuous operations with the moderating fluid on. It is due to the large thermal fission cross sections of the ^{239}Pu. Therefore, in this case after 50 days of operation with the moderating fluid turn-on, one should turn it off for further irradiation. This enters the second phase of operation.

Table I. Neutron Fluxes for Five-energy Groups similar to EBR-II

Neutron Energy Group	Energy Interval, E_i, Mev	Neutron Fluxes, (E_i)	$\sigma(n,\gamma)^{2,3}$ ^{238}U, b
1	$E_i \geqslant 1.35$	2×10^{14}	0.04
2	$1.35 \geqslant E_i \geqslant 0.50$	3.7×10^{14}	0.10
3	$0.50 \geqslant E_i \geqslant 0.18$	5.4×10^{14}	0.15
4	$0.18 \geqslant E_i \geqslant 0.07$	4.2×10^{14}	0.26
5	$E_i \leqslant 0.07$	1.5×10^{14}	0.40

2. Operation With Moderating Fluid Turn-off

Once the moderating fluid has been cut off, the blanket is irradiated by fast flux only, and the plutonium density buildup can be calculated as

$$Pu(t) = U_o^{28}\{\xi_c \exp[-\lambda_a(1 + \mu_j)(t - t_p)] + (\eta_c - \xi_c)\exp(-\Gamma_f(t - t_c))\} \quad (3)$$

$$t \geqslant t_p = 50 \text{ days}$$

where

$$\lambda_a = \sum_{i=1}^{5} \sigma_a(U^{28}, E_i)\phi(E_i),$$

$$\lambda_f = \sum_{i=1}^{5} \sigma_f(U^{28}, E_i)\phi(E_i),$$

$$\Gamma_f = \sum_{i=1}^{5} \sigma_f(Pu^{29}, E_i)\phi(E_i), \qquad \mu_f = \frac{\lambda_f}{\lambda_a}$$

$$M_f = \frac{\Gamma_f}{\lambda_a}, \qquad \xi_c = \frac{\exp(-\lambda_8 t_c)}{M_f - \mu_f - 1},$$

$$\eta_c = \frac{\exp(-\lambda_8 t_c)}{\beta - 1} + \left[1 - \frac{\beta \exp(-\lambda_8 t_p)}{\beta - 1}\right]\exp(-\lambda_9(t_p - t_c))$$

Eq. (3) is plotted as curve B in Fig. 2.

One sees that the plutonium buildup increases again after the moderating fluid being turned off and will eventially reach its maximum again after 10^4 days of operation which is about 27.8 years. This maximum value exactly coincides with the maximum value for the conventional blanket as indicated by the curve C. This result is expected and can be considered as a check for the present theory. For the conventional blanket, the plutonium buildup can be expressed as

$$Pu(t) = U_o^{28}\left(\frac{1}{M_f - \mu_f - 1}\right)\left[\exp(-\lambda_a(1 + \mu_f t) - \exp(-\Gamma_f t)\right] \quad (4)$$

Equation (4) is plotted as curve C in Fig. 2.

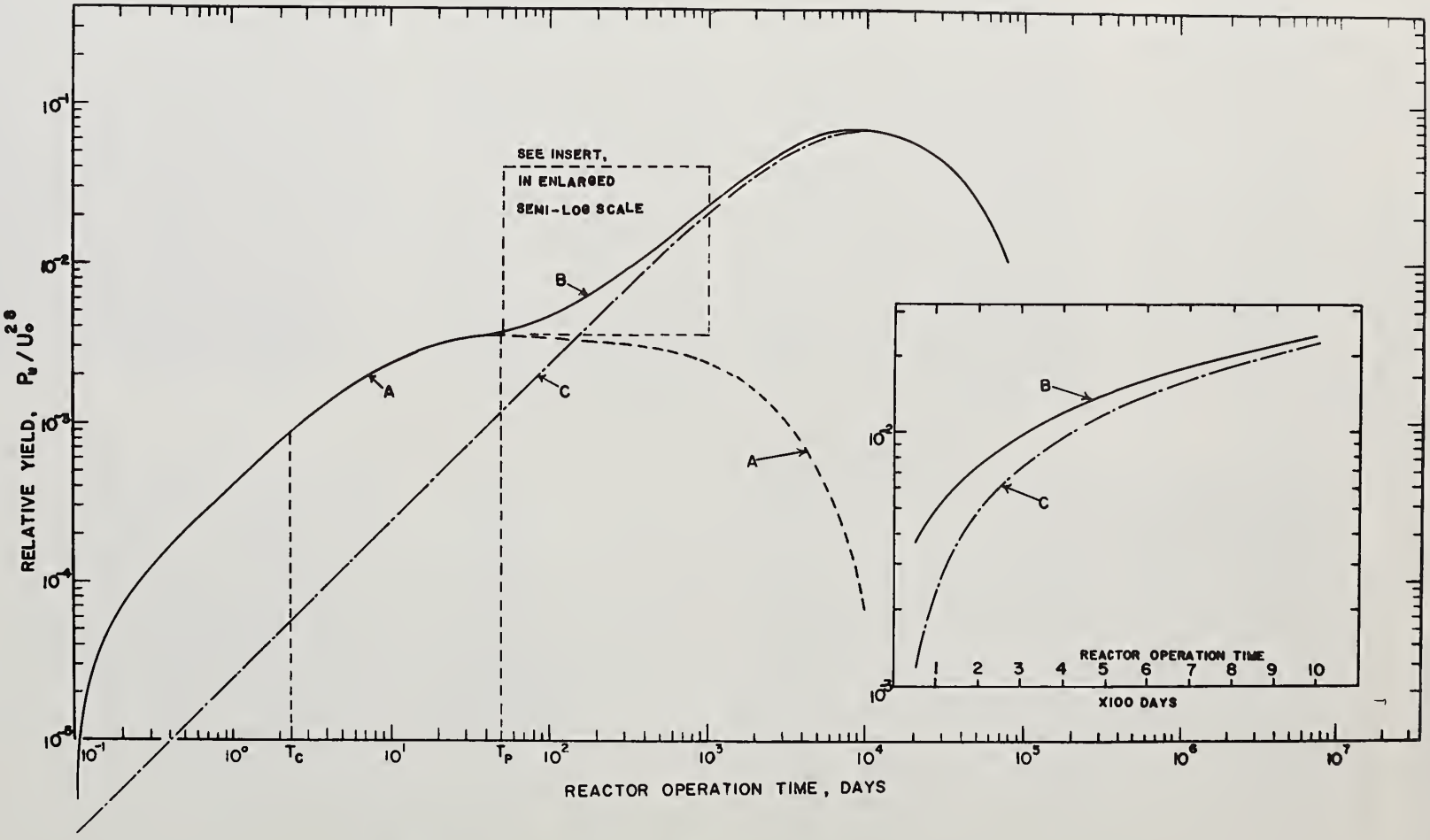

Fig. 2. Relative Plutonium yield in inner blanket vs reactor operation time.
A: With moderating jacket turned on.
B: With moderating jacket turned off at $t = T_p$.
C: conventional blanket

3. Results and Discussion

Comparing the curves A, B, and C in Fig.2, one realizes that the advantage of the proposed moderating jacket is to provide the so-called "thermal boosts" in the early stage of operation. The consequence of this effect is to shorten the plutonium recycling period by as much as, for our example here, 34.5% for low plutonium density buildup and 15.4% for high density buildup of 1.5%. For higher density buildup, from 0.35% to 2.0%, the moderating jacket operation can save 100 days per recycling. The efficiency of the jacket is higher for lower density buildup. The results are summarized in Table II and plotted in Fig. 3.

Table II. Irradiation Times for Blanket with Moderating Jacket and the Conventional Blanket

Plutonium Buildup in % of ^{238}U Density	Day/cycle, D_2O-jacket	Day/cycle, Conventional	Gain/cycle Days	Gain/cycle %
0.10	2.7	40	37.3	93.3
0.20	7.0	85	78.0	91.8
0.35	50.0	150	100.0	66.7
0.70	190.0	290	100.0	34.5
1.00	315.0	415	100.0	24.1
1.50	550.0	650	100.0	15.4
2.00	800.0	900	100.0	11.1

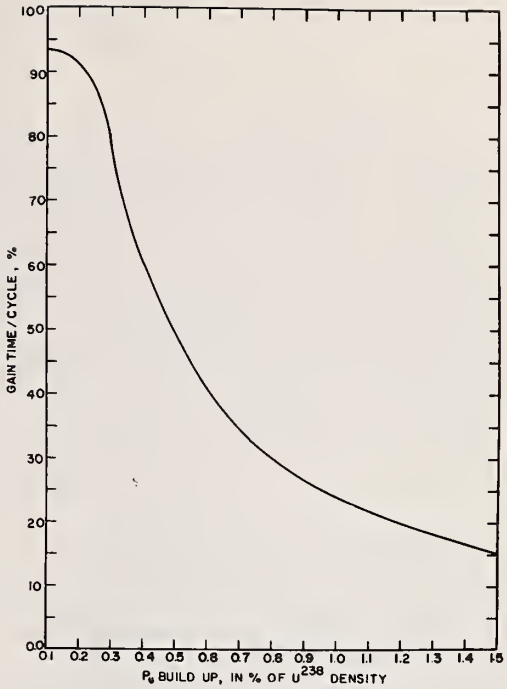

Fig. 3. Gain time/cycle with moderating jacket vs plutonium density buildup

References

1. L. J. Koch, et al "Experimental Breeder Reactor II", ANL-5719 (1957).

2. S. Yiftah and M. Sieger, "Nuclear Cross Section for Fast Reactors" IA-980, Israel Atomic Energy Commission.

3. L. J. Templin, "Reactor Physics Constants" ANL-5800 (1963).

USE OF MONTE CARLO METHOD IN THE ESTIMATION OF FAST NEUTRONS LEAKED THROUGH A CONCRETE-PARAFFIN SHIELDING

L. S. Chuang and K. C. Wong
Department of Physics, Science Centre,
The Chinese University of Hong Kong, Shatin, N. T.
Hong Kong

A neutron generator shielding house, in which a 14 MeV neutron generator* with a 4π yield of 1×10^{11} neutron per second is installed, was built with labyrinth geometry and made of ordinary concrete and paraffin block. Rough estimation for fast neutron flux in a location directly above the neutron generator target, but outside the shielding layers, is 7.7×10^{-3} n/cm^2-s which was resulted from the approximation that for 14 MeV neutron, the flux is reduced by a factor of 10 for each 15 inches of solid concrete, or for each 8.2 inches of paraffin wax, disregarding the effect of scattering from the surrounding shielding materials. In order to take the geometrical effect of the shielding into consideration, a computer program, FORTRAN IV, was devised for calculating the neutron flux at the same location, using the Monte Carlo technique in a simplified 1-dimensional diffusion of neutron through the shielding layers. The result of this calculation was about 10^{-1} n/cm^2-s; in good agreement with the result of measurement using a BF_3 counter.

(Application of nuclear cross section; 14 MeV neutron shielding; Monte Carlo method)

Description of the shielding house

A neutron generator, Kaman type-711A, with a 4π yield of maximum output 1×10^{11} neutron per second is installed in a pit on the Lower Ground Floor of the Science Centre of The Chinese University of Hong Kong. According to AEC regulation, 10 CFR 20, the normal allowable dose of fast neutron for 40 hour-week is 10 n/cm^2-s.[1] But as the neutron generator is installed in a teaching institution, with classrooms and uncontrolled area so near to the installation site, radiation shielding should be more considerate than just to meet the regulations.

The neutron generator shielding house is designed and built with labyrinth geometry, aiming at degrading the neutron energy as fast as possible by means of multiple scatterings of the escaping neutrons with the constituent nuclei of the shielding material. As in ordinary practice, shielding of fast neutrons by means of elastic, inelastic scatterings and absorption reaction of neutron with the constituent nuclei of the shielding materials, ordinary concrete, paraffin block, and iron plate were used in the shielding house. The scheme of construction of the whole shielding house is shown in figs. 1-3. The neutron generator room of area 47' x 28½' is situated on the Lower Ground Floor of The University Science Centre, with classrooms directly above and on the left. The space outside the room is an uncontrolled area. The neutron generator room is partitioned by a concrete wall into a control room and a source room. Lead plates are posted on the lower part of the wall to shield the capture gamma rays. The neutron generator system, excluding the control console which is placed in the control room, is entirely contained inside the source room, where no people is allowed to stay when the generator is in operation.

The shielding house, in which both the high voltage power supply and accelerator tube are installed, was built of a pit of size 30½' x 10' x 6'8" in the source room. Going down the staircase into the pit, there is a 2" thick iron door on the left of a 20" thick wall which leads to the first compartment where the high voltage power supply and the cooling unit are installed. The other compartment, where the accelerator tube is installed, is separated from the first one by two concrete walls, each of thickness 36" built with labyrinth geometry, and a 5" thick iron door with paraffin sandwiched inside. Trenches are provided for running of the power cables and the cooling lines. The top of the pit is covered with paraffin and concrete blocks of different thickness. The thickest part which is made of 24" thick of paraffin and 48" thick of concrete, is directly above the compartment for the accelerator tube. An exhaust gas pipe line, used to vent the SF_6 gas kept inside the power supply tank and the accelerator tube as an insulating medium, runs from the first compartment into the open air. The door to the source room and the other two doors in the pit are provided with interlocking system to ensure that the neutron generation cannot be started whenever any one of the doors is not tightly closed.

Rough estimation of fast neutron flux

The fast neutron flux at various locations around the shielding house was estimated using the formula.[2]

$$\Phi = \frac{N}{4\pi r^2} \times \frac{1}{F}$$

where Φ is the neutron flux in neutron/cm^2-sec;
N is the total neutron output of accelerator tube in neutron/sec, and equals to 10^{11} neutron/sec in the present case;
r is the distance of the source from the observed point;
F is the reducing factor (for 14 MeV neutron, neutron flux is reduced by a factor of 10 for each 15 inches of solid concrete,[3] or for each 8.2 inches of paraffin wax[4]).

*The neutron generator was provided by the International Atomic Energy Agency under its regular program of technical assistance.

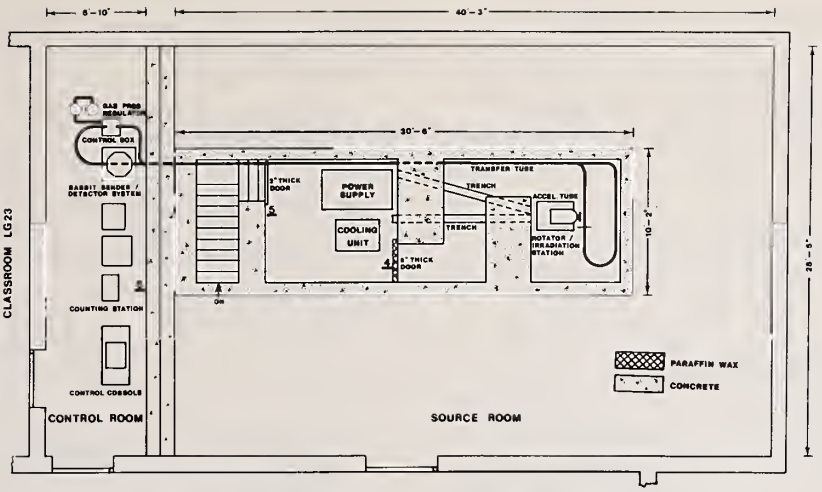

fig. 1 The Neutron Generator Room (Plan View)

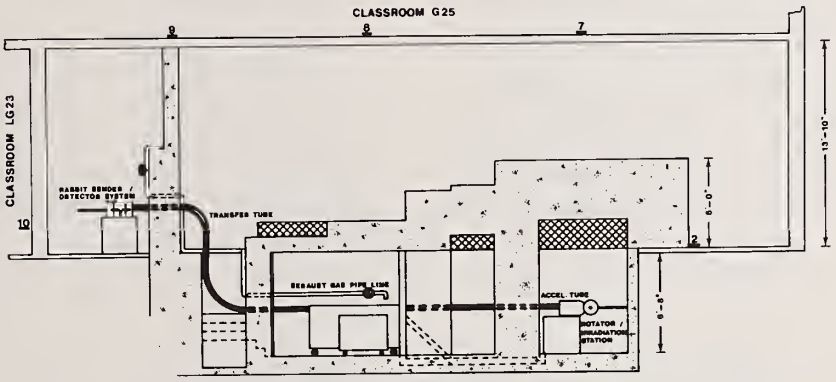

fig. 2 The Neutron Generator Room (Longitudinal Section)

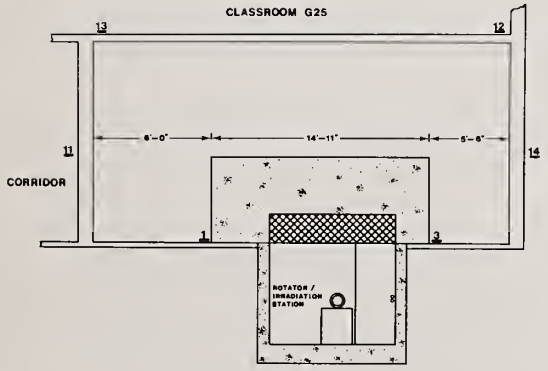

fig. 3 The Neutron Generator Room (Transverse Section)

At the locations marked 1 to 5 and 14 in figs. 1-3, are unoccupied area during operation of the generator, the calculation showed that the maximum flux is 8.8×10^{2} n/cm^{2}-s at location 3. While at locations marked 6 to 13 which are occupied areas, the fast neutron flux are well below the maximum permissible level of 10 n/cm^{2}-s for 40 hour-week. At location 7 which is in the classroom directly above the accelerator tube and the nearest uncontrolled area to the accelerator tube, the result of rough estimation showed that the fast neutron flux is 7.7×10^{-3} n/cm^{2}-s. In the calculation of the neutron flux here, the effect of scattering of neutrons due to the surrounding shielding material is neglected. The value of the neutron flux calculated for location 7 is too small as compared to the actual one. Therefore, account of the scattering effect of neutrons must be taken into consideration.

Monte Carlo calculation of diffusion of neutron through the shielding

In order to take the geometrical effect of the shielding in the calculation of neutron flux at location 7 into consideration, a computer program, FORTRAN IV, was devised. The method is a simplified one of Monte Carlo type, because it replaces the sophisticated 3-dimensional scattering by a 1-dimensional diffusion of neutron through the shielding.

The basic principle involved in this semi-analytical method, consists of a random generation of the neutron history in the shielding materials. The neutron history includes the scattering angle in CM frame and the scattering target (i.e. hydrogen or carbon in case of paraffin; silicon, oxygen, calcium or iron in case of concrete).

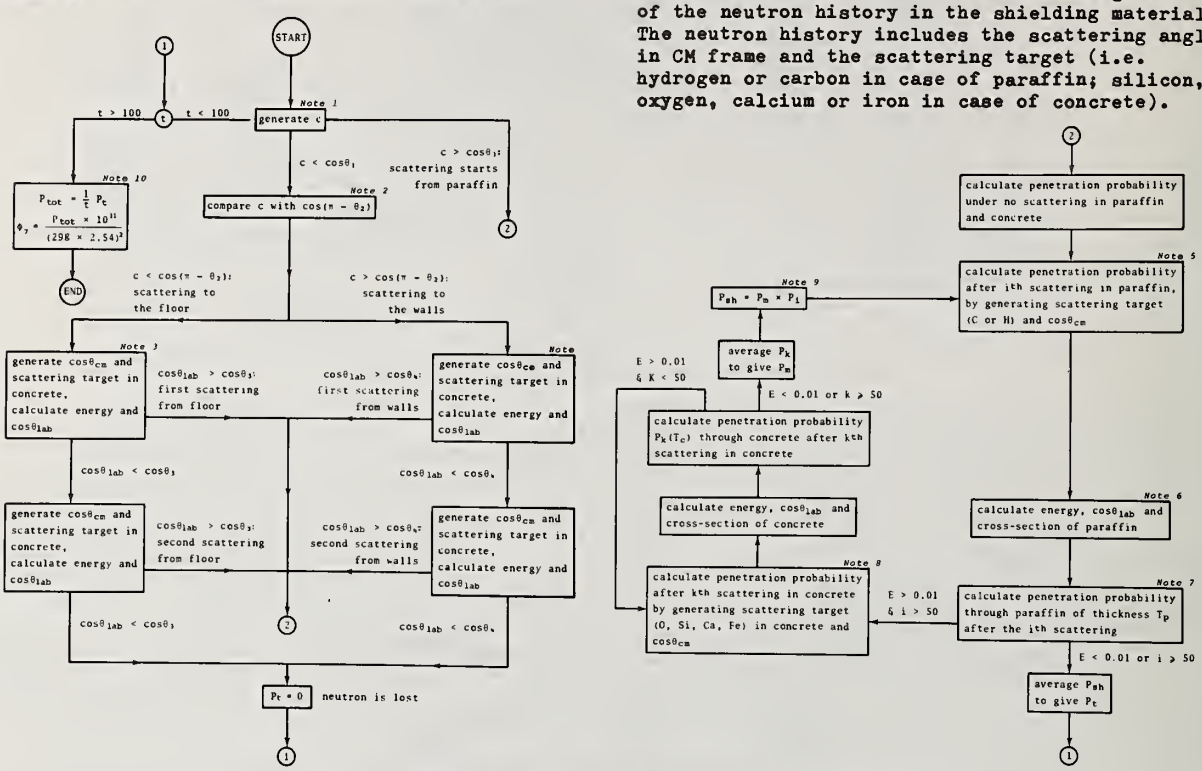

fig. 4 Illustrative Flow Chart to Show the Calculation of Neutron Flux by Monte Carlo Method (1-dimensional)

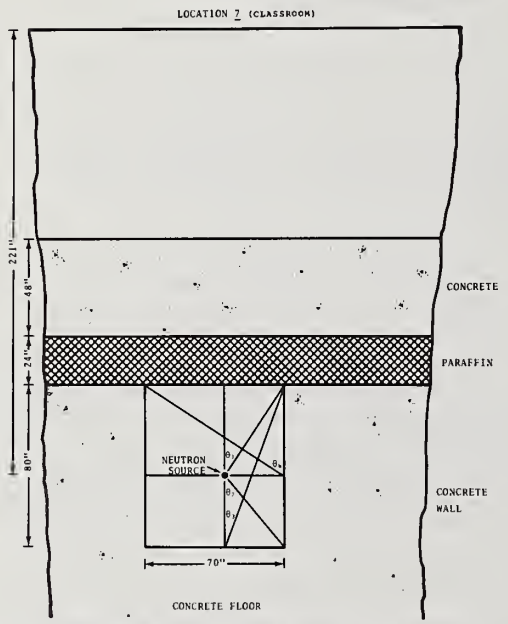

fig. 5 The Geometry of the Shielding House Considered in the Monte Carlo Calculation

From these, the energy of a neutron after scattering, the corresponding scattering angle in LAB frame, and the scattering cross-section are calculated. Using these parameters, the probability of penetration through a certain thickness of the shielding after a certain number of scattering can be calculated. Then the average probability of penetration with different number of scattering is used in the estimation of the flux at location 7. At the outset of the random generation of the neutron history, it has taken into consideration that the out-going neutron from the accelerator tube may enter directly into the paraffin-concrete shielding layer on the top or scatter into it from the surrounding concrete walls and floor of the rectangular compartment, fig. 5, inside which the accelerator tube is installed. In our calculation, totally 100 neutrons, each of them having its own set of history, were considered.

The illustrative flow chart, fig. 4, shows how the calculation of neutron flux is proceeded.

The following are the explanatory notes to the illustrative flow chart:

Note 1: c is generated by firstly generating a random number R, where it is calculated by $R(N+1) = R(N) \times 1953125 \text{ MOD } (2^{23})$

then $c = \cos\left(\frac{3.1416 \times R}{2^{23}-1}\right)$.

Thus the value of c is from -1 to +1, corresponding to cos 180° to cos 0°.
c is then compared with cos θ_1, (refer to fig. 5), and if c is between cos 0° and cos θ_1, the neutron is considered as entering into the paraffin shielding directly.

Note 2: If c is between cos θ_1 and cos$(\pi-\theta_2)$, (refer to fig. 5), then the neutron is considered as going to the side walls. While if c is between cos$(\pi-\theta_2)$ and cos 180°, the neutron is considered as going to the floor.

Note 3: When we consider the neutron scattering inside the concrete floor, by randomly generating the scattering angle in CM frame, θ_{CM}, and the scattering target in the concrete floor, then the scattering angle in LAB frame, θ_{lab}, and the energy after scattering are calculated. If cos θ_{lab} is greater than cos θ_3, the neutron is considered as going to the paraffin shielding following one scattering in the floor. The probability of such a process is exp(-2), for the neutron is considered as travelling one mean free path each before and after scattering in the concrete floor. Thus for this neutron a factor of exp(-2) is multiplied to the final probability of penetration through the paraffin-concrete shielding. On the other hand, if cos θ_{lab} is smaller than cos θ_3, the second scattering angle in CM frame, and the scattering target in concrete are generated. cos θ_{lab} is compared with cos θ_3 again, and if cos θ_{lab} is smaller than cos θ_3, the neutron is considered as lost, and the penetration probability of that neutron through the paraffin-concrete shielding is zero. However, if cos θ_{lab} is greater than cos θ_3, the neutron is considered as going to the paraffin shielding after two scatterings in the concrete floor. Thus for this neutron a factor of exp(-4) is multiplied to the final probability of penetration through the paraffin-concrete shielding.

Note 4: The neutron is regarded as scattering inside the side concrete wall. The process is similar to that considered in the concrete floor, except cos θ_{lab} is compared with cos θ_4, (refer to fig. 5), here.

Note 5: After considering the various possible process by which the neutron can enter into the paraffin-concrete shielding on the top, we start the calculation of the penetration probability of the neutron through the paraffin layer for a certain number of scattering inside the paraffin. The neutron energy must be greater than 0.01 MeV if it is to be considered for the next scattering process, and up to the maximum number of fifty times. At each scattering process, the scattering angle in CM frame and the scattering target in paraffin (i.e. hydrogen or carbon) are generated randomly. In paraffin, the fraction of hydrogen nuclei is 0.6743, and that of carbon nuclei is 0.3257. By generating a random number with value between 0 and 1, and compare this number with 0.6743, the scattering target in the scattering process is decided.

Note 6: The scattering angle in the LAB frame can be calculated as

$$\cos\theta_{lab} = \frac{(1 + A\cos\theta_{cm})}{(1 + A^2 + 2A\cos\theta_{cm})^{1/2}} = c_i$$

where A is the mass number of the scattering target, c_i, is equivalent to cos θ_{lab}, is stored as an array for the later use in the calculation of the penetration probability. i denotes the ith scattering process in paraffin.
The energy after ith scattering is

$$E_i = E_{i-1} \times \frac{(1 + A^2 + 2A\cos\theta_{cm})}{(1 + A)^2}$$

where E_{i-1} is the neutron energy just before the ith scattering. The initial neutron energy in the present case is 14.6 MeV if the neutron from the generator tube enters directly into the paraffin-concrete shielding, but is equal to the corresponding calculated value if it is scattered from the walls or floor into the paraffin-concrete shielding.
The scattering cross-section of the paraffin is calculated as $\sigma_{paraffin}(E) = 0.07935\,\sigma_H(E) + 0.03833\,\sigma_C(E)$. The values of the coefficients are n_H and n_C, in unit of 10^{-24}, with n denoting the number of nuclei per unit volume.
$\sigma_H(E)$ and $\sigma_C(E)$ are calculated from the empirical formula. $\sigma(E) = a_o + a_1E + a_2E^2 + a_3E^3 + a_4E^4 + a_5E^5$, where the coefficients a_o, a_1, a_2, a_3, a_4, and a_5 are determined by the least square polynomial fit of the total scattering cross-section at various energies.

Note 7: The probability $P_{i+1}(T)$ for a neutron to penetrate through the shielding of thickness T after the i+1 th scattering is calculated in the following manner:[5]

$$P_{i+1}(T) = \int_0^T P_i(q)\,\exp\left\{-\sigma_{i+1}(T-q)/c_{i+1}\right\}\frac{dq}{|c_i|}$$

for $c_{i+1} > 0$

$P_{i+1}(T) = 0$ for $c_{i+1} < 0$

The above integral has an analytic solution

$$P_i(T) = |c_i| \sum_{j=0}^{i} A_{ij}\,\exp\left\{-\sigma_j(T-u_j)/c_j\right\}$$

where u_j denotes 0 or T according to $c_j > 0$ or $c_j < 0$, respectively, and the constants A_{ij} can be calculated from the recurrence relation:

$A_{oo} = 1/c_o$

$$A_{i+1,j} = \sigma_i\,A_{ij}\,c_j/(\sigma_{i+1}\,c_j - \sigma_j\,c_{i+1})$$

$$A_{i+1,i+1} = -\sum_{j=0}^{i} A_{i+1,j}\,\exp\left\{-\sigma_j(u_{i+1}-u_j)/c_j\right\}$$

Note 8: Each time, when calculation of the penetration probability after a certain number of scattering in paraffin is finished, calculation of the penetration probability through the concrete layer is proceeded. The procedure in the concrete layer is similar to that of the paraffin layer. The maximum number of scattering considered in concrete is also 50 times, and the neutron energy must be greater than 0.01 MeV for it is to be considered for the next scattering

process. In the concrete, the scattering targets are oxygen, silicon, calcium and iron. The respective fraction of abundance of these scattering targets are 0.696, 0.256, 0.022 and 0.026. In generating the scattering target for a certain scattering process, the fractions of abundance are taken into account.
The scattering cross-section of the concrete is calculated as:

$$\sigma_{concrete}(E) = 0.04166\ \sigma_O(E) + 0.01512\ \sigma_{Si}(E) + 0.00138\ \sigma_{Ca}(E) + 0.00158\ \sigma_{Fe}(E)$$

Again, the coefficients are n_O, n_{Si}, n_{Ca}, n_{Fe} in units of 10^{-24} with n denoting the number of nuclei per unit volume.

Note 9: The average value of the penetration probability of the neutron through the concrete layer for different number of scattering inside the concrete is calculated by taking the mean value of the penetration probability of the neutron through the concrete layer after a certain number of scatterings inside the concrete. This value is multiplied with the value of penetration probability of the neutron through the paraffin layer after a certain number of scatterings in the paraffin to give the penetration probability through the paraffin-concrete shielding for the particular number of scatterings in the paraffin; this value is denoted by P_{sh}. When the maximum number of scatterings, 50, is reached or the neutron energy has degraded below 0.01 MeV, we calculate the average value of P_{sh} for different numbers of scatterings in paraffin to give, P_t, the average penetration probability of that particular neutron through the concrete-paraffin shielding after its birth from the neutron source. t ranges from 1 to 100, i.e. totally 100 neutrons are considered in our calculation.

Note 10: The final average penetration probability through the paraffin-concrete shielding for the neutron generated by the neutron source, P_{tot}, is obtained by taking the mean value of P_t; the neutron flux at location 7, ϕ_7, is

$$\phi_7 = \frac{P_{tot} \times 10^{11}}{(298 \times 2.54)^2} \text{ (neutron/cm}^2\text{-s)}$$

The denominator is the area subtended by twice of the angle θ_1 (refer to fig. 5), at a distance 221" directly above the neutron source; the area on which the incident neutrons are considered for leaking through the paraffin-concrete shielding layer.

The computer program consists of a main program, five subroutine segments, and two function segments. Totally there are 362 statements and computer core used is 6500 words. The computer time used is 600 mill-second for each initial input of the random number.

The calculated result was found to vary from 0.02 n/cm^2-s to 0.4 n/cm^2-s depending on the initial input of the random number. The average result for 12 different initial input of the random number was about 0.1 n/cm^2-s.

Conclusion and discussion

The result of the simplified Monte Carlo Calculation for the neutron flux at location 7, 0.1 n/cm^2-s, is in good agreement with the measured value using a BF_3 survey meter. The excellent agreement between the calculated and the measured result is considered as due to the simplicity of the geometry and the monochrome of the neutrons generated from the accelerator tube.

The discrepancy between the values by the rough estimation and by the simplified Monte Carlo Calculation, for the neutron flux at location 7, 7.7×10^{-3} n/cm^2-s and 1×10^{-1} n/cm^2-s, respectively, is certainly due to disregarding of the effect of scattering from the surrounding shielding materials in the rough estimation. Although the method of rough estimation is suggested by the manufacturer of the neutron generator, one should be more cautious about the estimation of the leaked neutrons in the uncontrolled area. In designing a neutron shielding house such as the present one, it is strongly advised to take into consideration at least a safety factor of 10 in addition to that allowed basing on the calculated flux using the method of rough estimation as suggested by the manufacturer.

References

1. Kaman Nuclear, A-711 Neutron Generator Instruction Manual, p.5-3.
2. Ibid.
3. Olive, G., Cameron, J. F., Clayton, C. G., AERE-R-3920, (June 1962).
4. Appleton, G., Health Physics Addendum, Safety Series No. 2, (1960), IAEA.
5. Hammersley, J. M., and Handscomb, D. C., Monte Carlo Methods, Methuen and Co. Ltd., London, (1960).

A COMPARISON OF AIR-OVER-GROUND TRANSPORT CALCULATIONS USING DIFFERENT CROSS SECTIONS

J. C. Saccenti
Ballistic Research Laboratories
Aberdeen Proving Grounds, Maryland 21005

W. A. Woolson
Science Applications, Inc.
La Jolla, California 92037

Time dependent neutron and secondary gamma-ray transport calculations for 14 MeV and fission sources were performed in air-over-ground geometry utilizing cross sections from the DNA working cross section library. These calculations were compared with earlier calculations which have been widely used in weapon effects studies. Several significant differences were found attributed to the different cross sections used in the calculations.

(Neutron; gamma ray; transport calculations; cross section sensitivity)

Detailed descriptions of the radiation environment from low altitude nuclear weapon detonations are required by the military to properly assess the vulnerability of equipment and systems, and the radiation exposure of personnel operating within tactical scenarios. Because of low altitude nature of the radiation source, the earth's surface plays a significant role in the radiation transport. Calculations of the radiation transport from weapon output descriptions have usually employed two-dimensional discrete ordinates techniques or the Monte Carlo method. The geometry model for both types of calculations is two-dimensional and consists of a flat air-ground interface (variations in the terrain are usually not considered) with air at some appropriate constant density above the interface and a standard ground composition below the interface. Each approach has it's advantages and disadvantages. Two-dimensional discrete ordinates air-over-ground radiation transport calculations are very time consuming (0.5 to 1.5 hours of CDC 7600 computer time) but have the advantage of providing a very detailed spatial discription of radiation environment. Energy and angular dependent fluence is computed at each mesh point in the problem. The Monte Carlo technique could hardly be used to compute fluxes as detailed as available with discrete ordinates methods but it can be run in far shorter computation times (5 to 20 minutes of CDC 7600 time) and can calculate the time dependence of the radiation transport.

Typically, vulnerability and exposure assessments only require a definition of the radiation environment near the air-ground interface. This type of problem with a relatively limited region of space in which the radiation flux is required is suitable for the Monte Carlo method. Our work involved producing an efficient Monte Carlo program to calculate time dependent neutron, secondary and prompt photon fluxes from time dependent sources in an air-over-ground geometry configuration. Part of the work involved comparing results of calculations performed with the new Monte Carlo code which utilized cross sections from the DNA Working Library[1] with calculations that have been used for vulnerability assessments in the past and which used different cross section data.

It was decided to modify the MORSE Monte Carlo code for problems specific to air-over-ground configurations. The MORSE code is available with several three-dimensional geometry modeling packages. The generality and flexibility in modeling physical systems with these geometry packages, however, causes a subsequent decrease in the efficiency of tracking particles compared with geometry packages constructed for specific, simple systems. The air-over-ground configuration is one of those simple systems where a specific geometry package would greatly improve the computational efficiency. This system consists of only two media – air and ground; and only one internal boundary – the interface between air and ground. Thus, a special geometry package was written for MORSE geared specifically for air-over-ground (A/G) calculations and designed to provide fast tracking times. The configuration employed is depicted in Fig. 1. A lower Z-boundary in the ground and an outer radius boundary

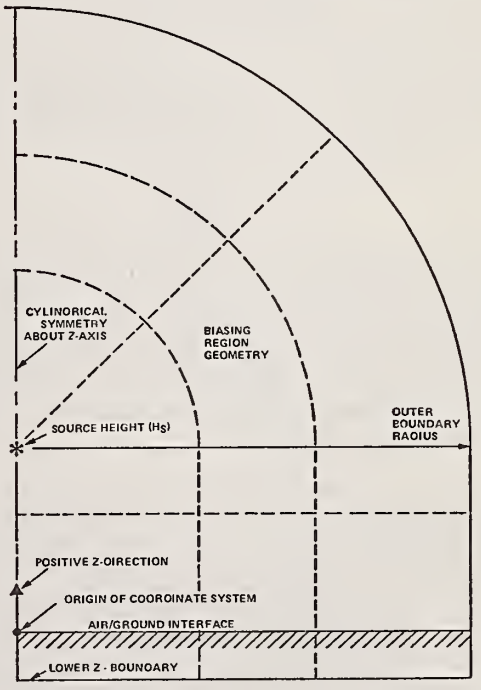

Fig. 1. Air over ground geometry configuration.

define the spatial extent of the problem. A boundary crossing at the air-ground interface occurs on sign change from the Z coordinate of the previous collision site to Z coordinate of the new site. Tracking to new collision sites, boundary crossings and escapes are determined without having to take a square root.

Biasing regions consist of spherical segments above the source height and cylindrical segments below the source height. The biasing regions are used to specify spatially dependent Russian Roulette, splitting, and path length stretching parameters for improving efficiency of the random walk and reducing the variance of the flux estimates. Source energy and emission direction biasing was incorporated into the code. For fission weapon type sources it is necessary to bias the sampled source energy spectrum to preferentially select higher energy neutrons which produce more inelastic photons, the main contributor to early time dose rates. Source directional biasing was used to preferentially commence more histories with directions that were more important to the calculation.

Two scoring techniques were used for flux estimation. A collision density estimator (CDE) was used to provide flux estimates throughout the entire air-ground configuration. The volumes employed for the CDE were similar to the region volumes employed for biasing, that is, spherical segments above the source and cylindrical segments below. CDE volumes were specified independently of the region volumes. We call the other estimator used in the calculations the expectation surface crossing estimator (ESCE). The ESCE was used to estimate the flux on a plane parallel to the ground. The surface detector regions consist of concentric annular areas centered about the vertical source symmetry axis. A score is made for every post collision ray generated during the random walk which, if extended, would intercept the scoring plane. A single score to eventually obtain $4\pi R^2$ weighted flux for the appropriate annular region is given by

$$\xi = \frac{4\pi R^2}{A} \frac{We^{-\rho}}{\cos\theta}$$

where A is the area of the annulus, W is the particle weight, ρ the optical thickness from the collision site along the post collision ray to the surface, θ is the angle between the ray and the surface normal, and R the distance from the source to the intersection point on the scoring plane. All the results reported here were calculated with an ESCE with the scoring surface one meter off the ground.

Two time dependent neutron and secondary photon transport calculations were performed with the modified MORSE code to compare results from computations using cross sections from the DNA Working Library with the calculations performed by Straker as reported in ORNL-4289.[3] The Straker calculations have been widely used by DoD organizations for data on air-over-ground radiation transport. Our comparison calculations utilized a 14 MeV source and the fission source distribution reported in ORNL-4289. The same 22 neutron and 18 photon energy group structure was used in our calculations.

The air was at density 1.11 mg/cc corresponding to an altitude of about 1 km. The ground was at density 1.7 g/cc of the same composition used by Straker.[3] The air and ground compositions and material identifications are given in Table 1. The nuclear cross section data for the computations were obtained from the DNA working cross section library.[1] This data was processed into multigroup cross sections by the AMPX code at the Oak Ridge National Laboratory.[4] A P3 expansion of the scattering distribution was used.

Table 1. Densities (atoms/b-cm) and DNA Material Number for Air and Ground Constituents

Element	Air (ρ = 1.11 mg/cc)	Ground (ρ = 1.7 g/cc)	DNA Material Numbers
H		9.7656-3	4148/MOD2
N	3.6614-5		4133/MOD4
O	9.7325-6	3.4790-2	4134/MOD2
Al		4.8828-3	4135/MOD3
Si		1.1597-2	4151/MOD2

Since Straker performed the calculations reported in ORNL-4289, more accurate cross section evaluations have been produced which include new experimental data and results from model calculations. In particular, the largest improvement has been in the development of more accurate photon production cross sections. Table 2 gives a comparison of the photon production probability at selected neutron energies for the air and ground compositions used in the calculations. The high energy photon production probability is lower for air and ground in the DNA data. For neutron energies from 6 to 2 MeV the production probabilities are higher for the DNA cross sections. Below 2 MeV the Straker photon production probability is much higher for ground than the DNA data. The DNA photon production probability for the thermal group is about a factor of two lower for both air and ground. The magnitudes and shifts in the photon production play a major role in the comparison of secondary photon doses and dose rates.

Table 2. Selected Photon Production Probabilities

Group	Neutron Energy Range (MeV)	Air		Ground	
		DNA XS	Straker XS	DNA XS	Straker XS
1	15.00 - 12.20	.2822	.6694	.4528	.5900
3	10.00 - 8.18	.3126	.4507	.3923	.4636
5	6.36 - 4.96	.0922	.0599	.1724	.1476
7	4.06 - 3.01	.0028	.0031	.0783	.0586
11	1.83 - 1.11	2.31×10^{-6}	.0	.00696	.0127
16	5.83×10^{-4} - 1.01×10^{-4}	1.65×10^{-4}	.0	2.95×10^{-4}	.0038
22	Thermal	.01058	.0213	.02164	.0431

Extensive comparisons with Straker's results for infinite air transport have already been reported.[5,6] The biggest discrepancy occurs in the photon dose from the 14 MeV neutron source; the dose from calculations using DNA cross sections is lower by about a factor of two. The neutron dose from the 14 MeV source is higher on the order of 25% using the DNA cross sections. For fission type sources the change in the secondary photon dose is about a 30% increase for infinite air transport using DNA cross sections.

A comparison of the tissue dose as a function of slant range for the 14 MeV source at 15 meter source height is presented in Fig. 2. The neutron dose calculated with the new cross sections is about 10% greater than the dose calculated by Straker. The photon dose, however, is reduced by almost a factor of 1.5. These trends are similar to those of the infinite air calculations but the magnitude of the differences are not as great.

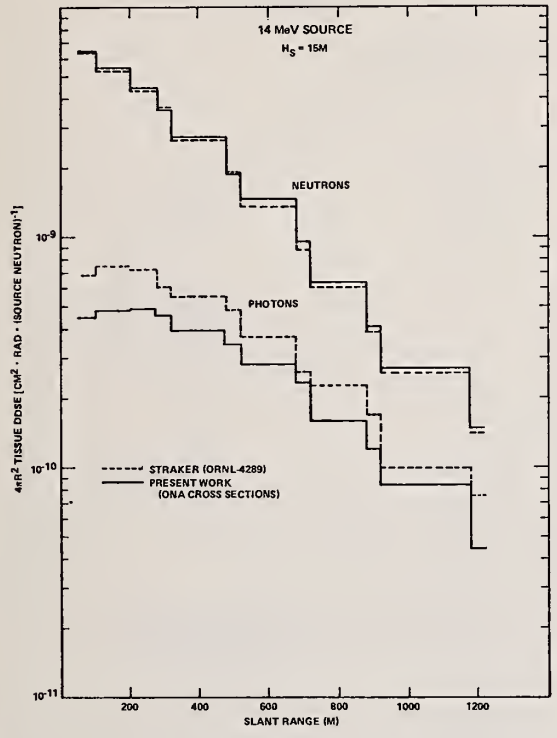

Fig. 2. Comparison of neutron and secondary photon doses from a 14 MeV source.

Some of the time dependent results for the 14 MeV source are presented in Figs. 3 through 5. A comparison of neutron dose rate at 800 m is shown in Fig. 3. Within the limits of the fractional standard deviations (10 - 15%) no noticeable differences in the time dependent behavior for neutrons could be detected.

The photon dose rates at 300 m and 900 m are presented in Figs. 4 and 5, respectively. In both cases, the early time dose rate computed by Straker is larger than the calculation with DNA cross sections. The difference is of the same magnitude which appears in the time independent results. At the relatively late times, the present calculations give higher results. The influence of the photon production cross sections can be clearly seen in these time dependent photon dose rates. At early times when the photons are produced by high energy neutrons, the dose rates computed by Straker are larger; as time increases and the average neutron energy decreases, the higher photon production in the DNA cross sections in 2 - 6 MeV range result in a higher dose rate than Straker's calculation.

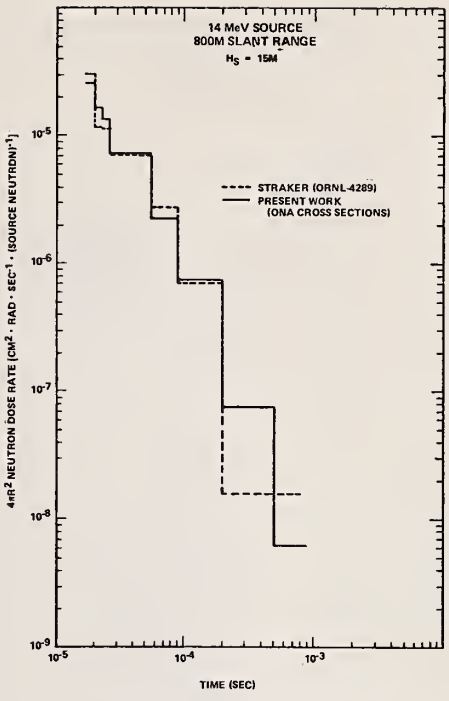

Fig. 3. Comparison of neutron dose rates at 800 m from a 14 MeV source.

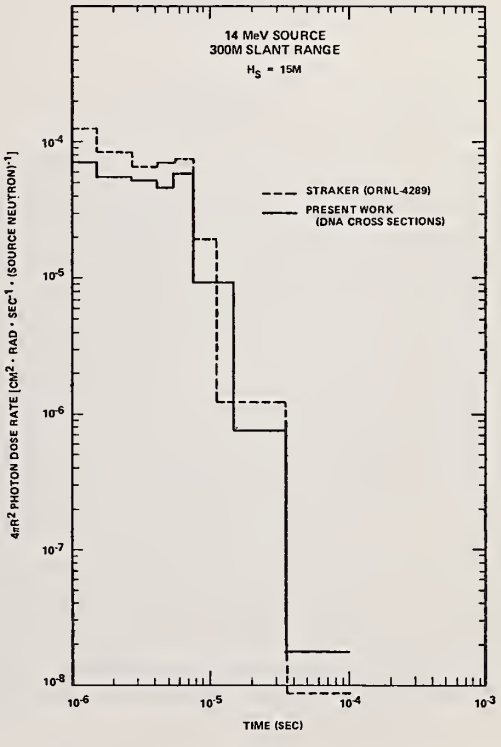

Fig. 4. Comparison of secondary photon dose rates at 300 m from a 14 MeV source.

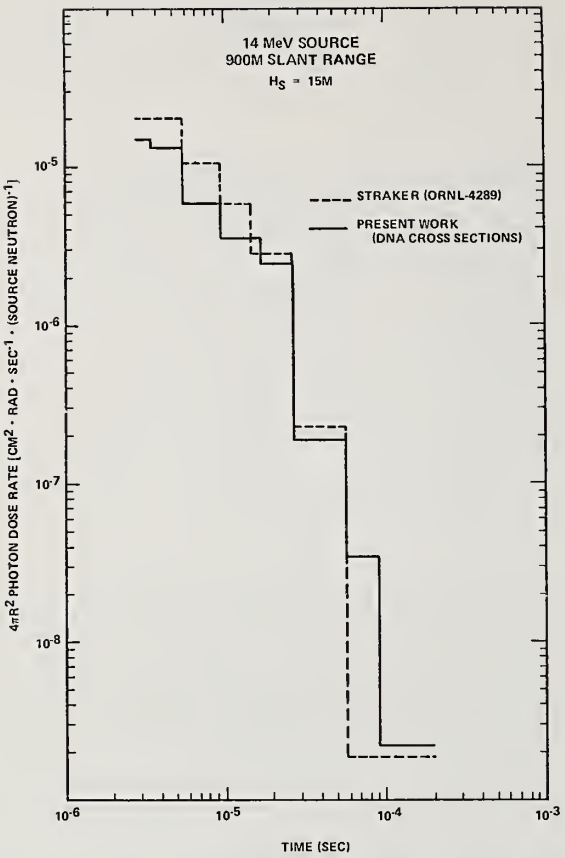

Fig. 5. Comparison of secondary photon dose rates at 900 m from a 14 MeV source.

A comparison of the neutron and secondary photon dose from the fission source is presented in Fig. 6. The time dependent calculations reported in ORNL-4289 had a neutron energy cutoff of 0.111 MeV and thus did not include capture photons. Therefore, the secondary photon doses computed by the discrete ordinates method which were reported in ORNL-4289 are compared with our Monte Carlo results. There is less than 10% difference between the neutron doses, although the Straker results are consistently higher. The secondary photon dose is lower by about a factor of 1.4 except at ranges less than 300 meters where the reduction is greater. This difference is attributed to the larger ground photon production probabilities used by Straker in the intermediate and thermal neutron energy range. The larger reduction at close-in ranges results from the more pronounced effect of the ground on secondary photon doses close to the source. A comparison of the secondary photon dose rate at 300 m with a later calculation by Straker[7] is shown in Fig. 7. The effect of the ground photon production can be clearly seen in the differences in the dose rate in the 0.01 to 1. millisecond regime.

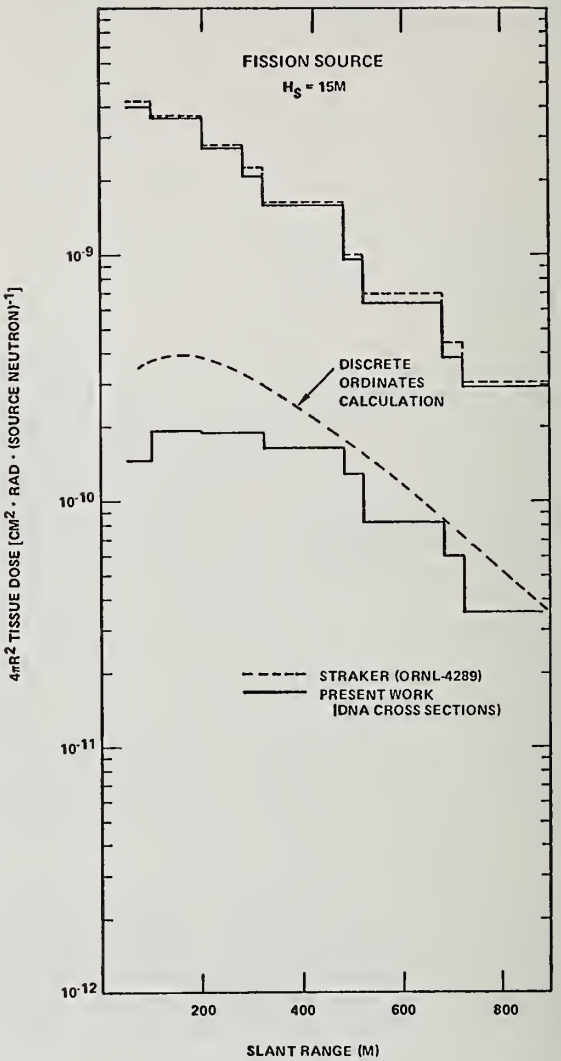

Fig. 6. Comparison of neutron and secondary photon doses from a fission source.

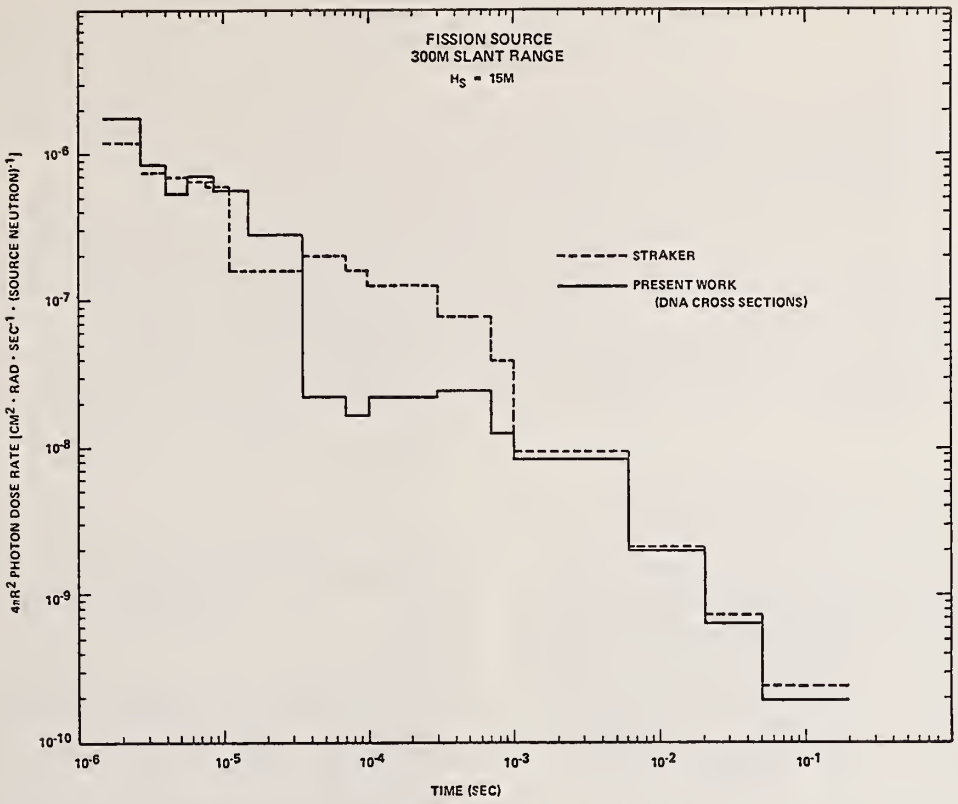

Fig. 7. Comparison of secondary photon dose rates at 300 m from a fission source. Straker's data from Ref. 7.

References

1. Defense Nuclear Agency Working Cross Section Library, Oak Ridge National Laboratory, ORNL-RSIC-34, Vol. 1

2. E. A. Straker, W. H. Scott, Jr, and N. R. Byrn, "The MORSE Code With Combinatorial Geometry," Defense Nuclear Agency, DNA 2860T (1972).

3. E. A. Straker, "Time-Dependent Neutron and Secondary Gamma-Ray Transport in an Air-Over-Ground Geometry, Volume II, Tabulated Data," Oak Ridge National Laboratory, ORNL-4289, Vol. II (1968).

4. Private communication with Dave Bartine, Oak Ridge National Laboratory.

5. W. W. Engle, Jr. and F. R Mynatt, "Time-Dependent Neutron and Secondary Gamma-Ray Transport in Infinite Homogeneous Air – Comparison of Two Cross-Section Sets," Oak Ridge National Laboratory, ORNL-TM-3932 (1972).

6. W. A. Woolson, L. Huszar, "Version III of the ATR Code," Science Applications, Inc., To be published.

7. E. A. Straker, "The Effect of the Ground on the Steady-State and Time-Dependent Transport of Neutrons and Secondary Gamma Rays in the Atmosphere," Nuclear Science and Engineering 46, (1971).

THE SENSITIVITY OF NEUTRON AIR TRANSPORT TO NITROGEN CROSS SECTION UNCERTAINTIES

A. Niiler, W.B. Beverly and N.E. Banks
USA Ballistics Research Laboratories
Aberdeen Proving Ground, MD 21005

The sensitivity of the transport of 14-MeV neutrons in sea level air to uncertainties in the ENDF/B-III values of the various Nitrogen cross sections has been calculated using the correlated sampling Monte Carlo neutron transport code SAMCEP. The source consisted of a 14.0- to 14.9-MeV band of isotropic neutrons and the fluences (0.5-15.0 MeV) were calculated at radii from 50 to 1500 metres. The maximum perturbations, assigned to the ENDF/B-III or base cross section set in the 6.0- to 14.5-MeV energy range were; (1) 2% to the total, (2) 10% to the total elastic, (3) 40% to the inelastic and absorption and (4) 20% to the first Legendre coefficient and 10% to the second Legendre coefficient of the elastic angular distributions. Transport calculations were carried out using various physically realistic sets of perturbed cross sections, bounded by evaluator-assigned uncertainties, as well as the base set. Results show that in some energy intervals at 1500 metres, the differential fluence level with a perturbed set differed by almost a factor of two from the differential fluence level with the base set.

(Neutrons, cross sections, air transport, sensitivity calculation, nitrogen)

Introduction

The purpose of this study was to investigate the effect of the uncertainties in the nitrogen cross section values upon the transport of neutrons from a 14-MeV point source in uniform, sea level air. The uncertainties in the radiation field caused by these nitrogen cross section uncertainties are very important in determining the effectiveness of nuclear weapons systems. Such cross section sensitivity studies are in general very useful in predicting gaps in the data which need to be filled with additional or more accurate experiments.

The correlated sampling Monte Carlo neutron transport code SAMCEP which was developed by Mathematical Applications Group, Inc.[1] under contract to Ballistic Research Laboratories, was used to perform the calculations. The strength of SAMCEP lies in its ability to efficiently calculate, in a complex geometry, to a high statistical accuracy, the differences in flux or flux associated quantities caused by changes in the basic cross section data. This is accomplished by using a common sampling of neutron collision space for calculating the fluence estimates for a set of problems each of which uses a unique set of neutron interaction probabilities. Constraints exist which require the use of equivalent geometries or identical nuclear interaction models in the problems in order to maintain correlation between the problem results. These constraints were all obeyed in the following studies.

The statistical improvement in the calculation of the fluence difference can be observed by the inspection of the equation relating the standard deviation of a fluence difference to the standard deviations of its two contributing fluences. The fluence difference, $\Delta\phi_{ij}$, has been calculated for some physical arrangement using the two different cross section sets i and j. The standard deviation S of this difference is given by

$$S^2_{\Delta\phi_{ij}} = S^2_{\phi_i} - 2C_{ij}S_{\phi_i}S_{\phi_j} + S^2_{\phi_j},$$

where C_{ij} is the correlation coefficient between the calculation of the two fluences. This coefficient is zero for independent calculations and is between 0.8 and 1.0 for a typical, realistic SAMCEP calculation.

A point, isotropic neutron source was located at the origin. Neutrons were emitted with equal probability between the source energy limits of 14.0 and 14.9 MeV. A uniform, homogeneous atmosphere, composed of twenty-one percent oxygen and seventy-nine percent nitrogen by weight, was used. The density of this atmosphere was 1.28×10^{-3} gm/cm^3. The ENDF/B III nitrogen and oxygen cross sections were used in calculating the base problem transport probabilities. The spherical symmetry of the calculational geometry permitted the use of origin-centered spherical shells as volume detectors. These shells were located with mean radii of 50, 100, 300, 500, 750, 1000, and 1500 metres. The inner shell had a thickness of five metres and the remaining shells had thicknesses of ten metres. The escape region of the problem was set at 2000 metres and neutrons whose paths exceeded this range were terminated. Importance sampling was used in order to ensure that an adequate number of particles would reach the deeper penetrations. Russian Roulette was played with those particles whose statistical importance (F-value) fell below a predetermined minimum and those surviving this crisis would have their F-values raised proportionately.

Cross Section Perturbations

Whenever a cross section is perturbed, a number of constraints must be obeyed in order to keep the set of cross sections to be used in the transport calculation consistent with reality. Firstly, the sum of all partial cross sections must equal the total cross section. This means that whatever amount is added to one partial must be subtracted from another partial if the total is unchanged. On the other hand, if the total is allowed to change, it may be possible to make a change to only one partial. Secondly, as all partials and the total have been measured to some degree of accuracy, a change which takes the value of a particular cross section outside the uncertainty limits set by the experiment would not be realistic. Thus the magnitude of any change to any particular component must be kept equal to or less than the experimental uncertainties. We have taken for these uncertainties the values quoted by the evaluators, Young and Foster[2]. Thirdly, the value of the elastic cross section at the 0^o angle in the laboratory is constrained by the Optical theorem to be greater than or equal to a quantity known as Wick's limit[3] which is proportional to the total cross section. Consequently, whenever

the elastic cross section is perturbed, the new 0^{o} value is checked against Wick's limit at that energy and only if it is greater than 95% of Wick's limit is it allowed as a valid perturbed cross section. With these constraints in mind, the cross sections used in the three air-transport problems in this paper will be described.

Problem 1

In this problem two new cross section sets were generated by perturbing the base ENDF/B III (RD-3) cross sections. The first set was generated by increasing the elastic scattering cross section by five percent over the energy range of 6.0 to 14.3 MeV (Nitrogen Perturbation No. 20 (NP-20)). The second new set was generated by decreasing the elastic cross section by three percent over the same energy span (NP-21). The compensating change in both perturbations was to the inelastic scattering cross section where the change was proportionately partitioned among all the levels which could be populated. The total cross section, the elastic angular distributions, as well as the secondary neutron energy distributions for both the inelastic total and inelastic levels remained unchanged in both of those cross section sets. In fact, secondary neutron energy distributions were not perturbed in any of the problems.

Problem 2

In this problem the primary change was to the elastic cross section from 6.3 to 14.3 MeV and was the full ten percent increase allowed by experimental uncertainties. In addition, the total cross section was allowed to increase by two percent over the same energy range which is twice the amount of the average quoted uncertainty. However, since several areas in the resonance region may be uncertain to as much as five percent, it was decided to use the two percent value throughout. The remaining compensating change was divided equally between the inelastic scattering and the absorption cross sections. The inelastic scattering and absorption partials were allowed to change by forty percent which was larger than the thirty-five percent uncertainty on these cross sections quoted by Young and Foster. The change to the inelastic total is proportionately partitioned among all the inelastic levels. This perturbation is labeled NP-29.

In addition to the above described changes, the shape of the elastic angular distributions were also changed two different ways in this problem. In NP-1202, the first and second Legendre coefficients were increased by twenty and ten percent respectively in the 6.3- to 14.3-MeV range. In NP-1203, both the first and second Legendre coefficients were decreased by ten percent. Larger decreases were prohibited by the Wick's limit condition.

Problem 3

The primary change in this problem set was the full ten percent increase in the elastic scattering cross section allowed by experimental uncertainties. The compensating change was divided equally between the inelastic and the absorption cross sections (NP-31). However, it should be noted that the amount of change necessary to the inelastic and absorption cross sections was more in this problem set than in the preceding set since none of the elastic scattering cross section change was compensated by a change in the total cross section. The unperturbed and perturbed cross sections of this problem are shown in Figure 1.

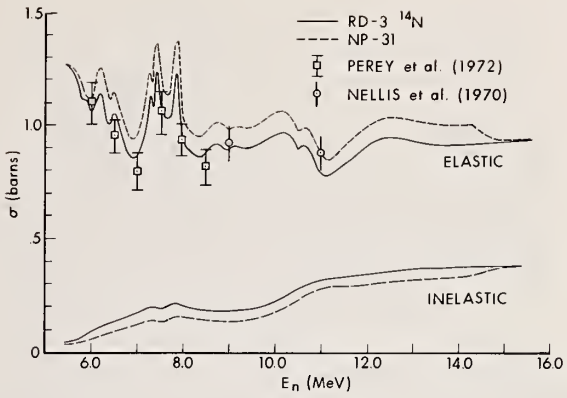

FIG. 1. Elastic and Inelastic Total Cross Sections in Problem 3.

The elastic angular distributions were also perturbed in this problem over the same energy interval and by the same amounts as in Problem 2. Representative samples of such angular distribution changes are shown in Figure 2 at 9.0 MeV along the best available data.

In summary, the perturbations to the various cross sections which are incorporated in Problems 2 and 3 are the maximum allowable changes on the basis of Young and Foster's evaluation.

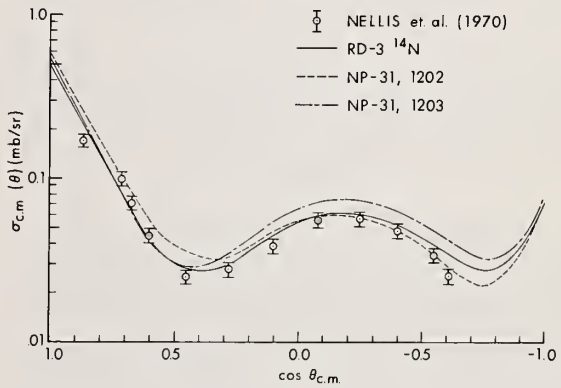

FIG. 2. Angular Distribution Perturbations at 9.0 MeV.

Results and Discussion

The results of the calculations will be presented in terms of neutron fluences in the two energy bands 12.0 - 15.0 MeV and 6.0 - 9.0 MeV at each of the seven spherical shell volume detectors. Due to space limitations, representative figures only will be shown.

Problem 1

The 12.0- to 15.0-MeV differential fast fluence results are displayed in Figure 3. This component of the fluence consists mainly of either the unscattered or the infrequently and forwardly elastically scattered neutrons and therefore the fluence differences between the problems are principally dependent upon the type of compensating change chosen from the other partial cross

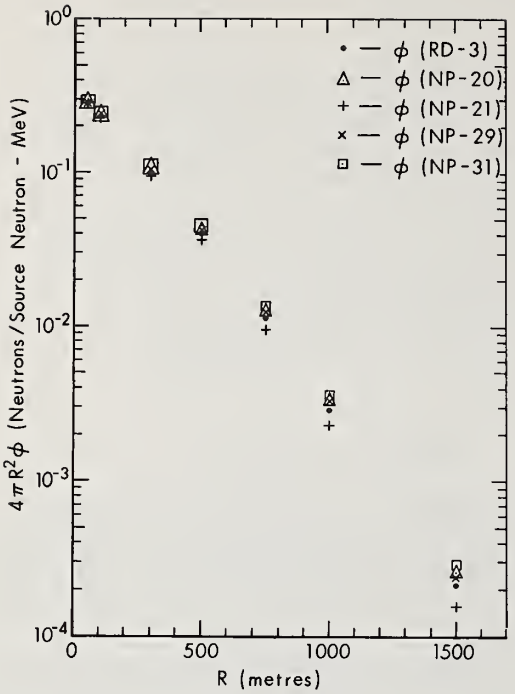

FIG. 3. Neutron Fluences (12.0 - 15.0 MeV) for the Three Problems.

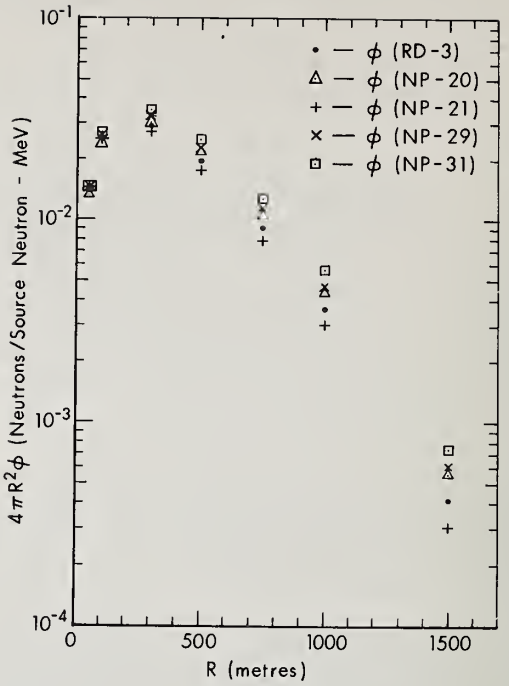

FIG. 4. Neutron Fluences (6.0 - 9.0 MeV) for the Three Problems.

sections. An increase in the elastic cross section at the expense of one of the other partial cross sections should produce an increase in the fluence at all ranges while a decrease in the elastic cross section should depress the fluence at all ranges. This was corroborated by the results of the calculations.

The 6.0- to 9.0-MeV differential fluence results are displayed in Figure 4. The analysis of the effect of the higher energy cross section perturbations on the fluence in this band is more complex than in the preceding energy band where the influx of neutrons came only from the source. The 6.0- to 9.0-MeV fluence, at the close-in ranges, will be very sensitive to the values of the inelastic cross section at the higher energies since a source particle can be moderated to this mid-range energy by a single inelastic scattering while it would require several elastic interactions to lose the same amount of energy. It would be expected that an increase in the elastic cross section that is compensated for by a decrease in the inelastic cross section would decrease the 6.0- to 9.0-MeV fluence level while the same elastic scattering perturbation that is compensated for by a decrease in the absorption probability would have less effect on this fluence.

Conversely, at deeper penetrations, this 6.0- to 9.0-MeV fluence will be sensitive to the probability of penetration of neutrons with higher energies to adjacent ranges since a large proportion of this fluence level will be contributed by the down-scattering of neutrons at nearby locations. An increase in this fluence at the larger ranges can be caused by increasing the elastic scattering component at the expense of either the inelastic or absorption cross sections. These effects are observed in Figure 4 where the fluence levels cross over at approximately 200 metres. It would be expected that fluences in the lower energy band of 0.5 to 1.5 MeV at close-in ranges would be even more sensitive to the higher energy inelastic cross section values than in the 6.0- to 9.0-MeV band. This was indeed found to be the case and the fluence cross-over point shifted out to about 500 metres. The 0.5- to 1.5-MeV energy band results are not displayed.

Problem 2

The thrust of the discussion of Problem 1 is also valid in this problem and the results of using NP-29 are also shown in Figures 3 and 4. It should be noted that expectations of much larger differences in these fluences, based on an intuitive extrapolation of the effect of the positive five percent elastic cross section perturbation in NP-20 to the positive ten percent elastic scattering perturbation in NP-29 should be modified by noting that two percent of the latter perturbation is added to the total cross section.

In this problem, the calculations were also performed for the case where the elastic angular distributions were perturbed. As can be seen from Figure 2, the NP-1202 changes the distribution to be more forward peaked while NP-1203 makes the distribution more backward peaked. The calculated fluences are similar for each of the sets RD-3, NP-1202/1203; NP-29, NP-1202/1203; and NP-31, NP-1202/1203. However, the results of the latter two sets are the only ones illustrated in Figure 5. As expected when the angular

distributions are more forward peaked, the fluence at all ranges is greater than when the angular distributions are more backward peaked. The effect is greatest in the source energy band of 12.0- to 15.0-MeV but is much less in the lower energy bands and in the total fluence band of 0.5- to 15.0-MeV.

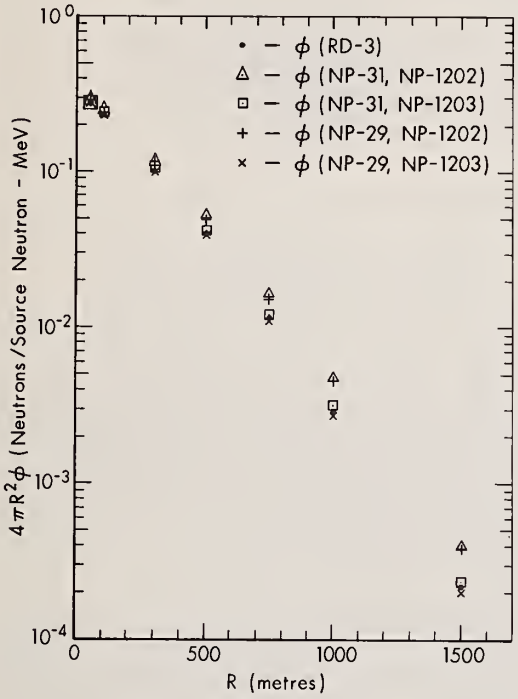

FIG. 5. Effects of Elastic Angular Distribution Perturbations in the 12.0 - 15.0 MeV Region for Problems 2 and 3.

Problem 3

From Figures 3 and 4 it can be seen that the fluences calculated by using base cross sections perturbed by NP-31 are appreciably larger than the fluences calculated using the base cross sections perturbed by NP-29. This difference can be easily understood by noting that the cross section set, constructed by perturbing the base set by NP-29, can also be constructed from the NP-31 perturbed base set by adding a second perturbation of one part inelastic scattering and one part absorption interaction along with a compensating two parts increase in the total cross section. A part is defined as one percent of the elastic scattering cross section in barns at the specified energies. Neutrons traveling through an NP-29 perturbed-base-set atmosphere will consequently have a larger probability of suffering an inelastic collision or an absorption than when traveling in a NP-31 perturbed-base-set atmosphere, while suffering no change in their elastic scattering probabilities. The effect of using NP-1202/1203 along with NP-31 has been discussed and is shown in Figure 5.

In concluding summary, it was found that significant differences in neutron differential fluences were calculated between the base set RD-3 cross sections and some of the perturbed sets. As expected, the largest difference occurred while using the NP-31 set at the deepest penetrations. From Figure 3 and 5 it can be seen that there is an eighty three percent difference between the base set and the NP-31, NP-1202 combination in the 12.0- to 15.0-MeV energy band at 1500 metres. Figure 4 shows a comparable seventy six percent difference between the base set and only NP-31 in the 6.0- to 9.0-MeV energy band at 1500 metres, although the addition of the angular distribution perturbation NP-1202 makes the difference smaller rather than larger in this energy band. In addition, by observing Figures 3 and 4, it can be seen that although there is a trend toward larger fluence differences with larger cross section perturbations, the size of perturbation dependence is neither linear nor is it dependent on only one single partial cross section. It is seen that with NP-20, where the elastic cross section was increased by five percent, the fluence change is about equivalent to the change brought about by NP-29 where the elastic was increased by ten percent but an accompanying total cross section decrease of two percent was also introduced.

References

1. S. Hui, et al., Ballistic Research Laboratories, Contract Report No. 62, December 1971, (AD#738185).

2. P.G. Young and D.G. Foster, Jr., Los Alamos Scientific Laboratory Report No. 4725, September 1972.

3. L. Stewart, Los Alamos Scientific Laboratory Report LA-3270, 1965.

MONTE CARLO STUDIES OF THE EFFECT OF CROSS SECTION CHARACTERISTICS ON FAST NEUTRON PENETRATION IN IRON

L.P. Ku and H. Goldstein
Columbia University
New York, New York 10027

Using Monte Carlo Method, we are able to study the mechanisms of neutron transport in natural iron and their relations to the cross section properties. Fission neutrons in 15 MeV to 10 keV range are discussed. It is concluded that the low energy spectrum exiting from a small bare sphere is particularly sensitive to inelastic cross sections near the threshold. For larger, and for reflected spheres, inelastic scattering plays a much less important role. At distances of practical significance ($\tilde{<}$ 1 meter) it is found that transport in the regions of cross section minima, while significant, does not provide dominant channels in determining the penetrating neutron spectra.

(Monte Carlo; Iron; Inelastic Scattering; Cross Section; Minima; Fission Neutrons)

Introduction

Neutron transport and slowing down processes can be represented as trajectories in phase space. Neutrons are born in a source region and observed at a detector region. The trajectories followed in phase space are stochastic in nature and can be simulated by the Monte Carlo method. For a particular source-detector and geometry configuration, the neutrons involved tend to follow preferred paths in phase space, determined at least in part by the cross section behavior of the given material. Just what these preferred trajectories or "channels" are cannot be determined in any simple fashion from deterministic transport calculations such as discrete ordinates methods. However, analysis of the detailed neutron histories used in Monte Carlo calculations could be expected to provide direct information on the characteristics of the favored trajectories and their relations to the cross section pecularities. Monte Carlo also has the advantage that the same set of histories can be used to study a variety of source-detector configurations. The method has been applied to the study of neutron transport in iron because previous investigations[1,2] suggested that deep minima in the cross sections play an important role in asymptotically far penetrations, but are not significant in small, bare systems. It was also desired to study the importance of inelastic scattering processes in a number of different configurations.

The Monte Carlo code SAM-CE[3] has been used to create neutron histories. Point cross sections for natural iron were obtained from the DNA MAT. 4180, Mod. 2 data set. As shown in Fig. 1 the total cross section shows marked fluctuations which increase in spread and regularity as we go down in energy. Interference minimum can go as low as 0.3 barns (e.g. at 138 keV) and the resonance peak can go as high as 90 barns (e.g. at 27 keV). The threshold for inelastic scattering is at 861 keV. In the 1 to 4 MeV region the average inelastic scattering cross section is about 30% of the total cross section. Continuum inelastic scattering occurs only above 4.6 MeV and (n,2n) reaction does not take place until 11.2 MeV.

All the analysis are based on the study of 10,000 histories generated in an iron medium so large that the only way a history can be terminated is either through scattering below the cut off energy or by absorption. No biasing was used in the Monte Carlo process.

Study of Fission Neutrons in Iron

The transport of fission neutrons from a point isotropic source is the main problem considered. The lower cut off energy was chosen as 10 keV, well below the energy of the lowest minimum at 24 keV. The energy spectrum of the current was sampled in 18 energy bins spanning the range from 15 MeV to 10 keV. In effect these bins act as energy-selective detectors of current. Table 1. lists the energy limits for the detectors covering the range below 0.5 MeV, the region of principal concern.

1. The Role of Inelastic Scattering

As shown in Figures 2 and 3, neutrons above the inelastic threshold rapidly disappear from the current spectrum with increasing distances from the source. This behavior clearly arises physically from the relatively short mean-free-path length in the MeV region (~ 4 cm on the average) combined with the high probability of rapid slowing down by inelastic scattering. The bulk of the energy spectrum, even at small distances from the source, is therefore below 1 MeV. The question arises as to how the iron cross section properties, particularly inelastic scattering, affects the shape of this keV region of the spectrum.

From Figures 2 and 3, again, it is clear that there are proportionately many fewer neutrons < 100 keV for small bare spheres than for the large reflected spheres. Obviously we are seeing the effects of the high leakage for the small bare geometries. The favored trajectories for those neutrons exiting in the lowest energy detectors for the 20 cm bare sphere must be those involving the shortest track length needed to reach the detector energy, else the probability of prior leakage is high. Of all source fission neutrons, 26% are born below the inelastic threshold with an average energy of about 580 keV. The only way this

Table 1. Detectors with Energy Limits Below 500 keV.

Detector No.	Energy Range (MeV)
11	0.500 - 0.400
12	0.400 - 0.280
13	0.280 - 0.200
14	0.200 - 0.120
15	0.120 - 0.060
16	0.060 - 0.027
17	0.027 - 0.020
18	0.020 - 0.010

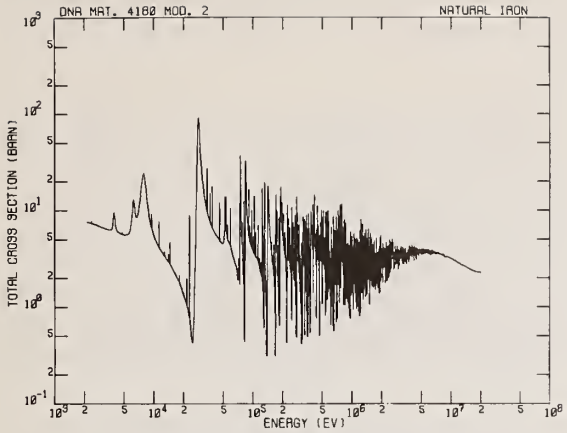

Fig. 1. Total Neutron Cross Section of Iron

type of source neutron can achieve a short track length is to be born relatively close to the detector energy limits, preferably in an energy region of high cross section. Thus the mean source energy of this fraction of neutrons reaching detector 17 (20 to 27 keV) in the smallest bare geometry is only 79.6 ± 14.5 keV, while it is 236 ± 24 keV for those which reach detector 14, and 462.5 ± 10.4 keV correspondingly for detector 12.

In order for a neutron born above the inelastic threshold to reach the low energy detectors in the small bare sphere it must slow down over a large lethargy interval and yet not leak out in the process. It is not surprising therefore that while 74% of the source neutrons are born above the threshold, they contribute only 62% of the exit current in detector 17 for the 20 cm radius bare sphere. Further, most neutrons born above the inelastic threshold suffer an inelastic collision sometime in their history irrespective of what detector they reach. But what distinguishes the fraction reaching low energies in small bare spheres is that their trajectories involve inelastic collisions with the maximum lethargy change. This is clearly shown in Table 2, which gives the statistics relating to those neutrons born above the inelastic threshold, contributing to various energy detectors for the 20 cm bare spheres which have scattered from the first exited level. The fraction scattering from the first level does not vary greatly with detector energy, but the initial and final energies of scattering do. For the lowest detector (10-20 keV) the average initial energy is only 23 keV above threshold. When the detector is in the 500 keV range the average initial energy is greater than 1.4 MeV. For detector 17 (20-27 keV) and a bare 20 cm sphere the average initial energy at scattering from the first level is about 85 keV above threshold for a bare 20 cm sphere. With a 100 cm bare sphere and the same detector this initial scattering energy has increased to about 400 keV above threshold, and to about 450 keV for the 100 cm reflected sphere. While inelastic scatterings from levels higher than the first contribute a much smaller fraction to the detector readings, the initial energies are then also close to the threshold for small bare systems and increase rapidly with larger systems or in reflected cases. Thus, the low energy exit spectra for small, leaky configurations are inordinately sensitive to the inelastic excitation cross sections close to threshold, especially in comparison to the situation for deep penetration.

It might be noted that the inelastic scattering rarely lands the neutron directly into the detector energy range. Rather, a number of further elastic collisions take place before the neutron crosses the detector. The number of such collisions depends on the character of the cross section immediately above the detector energy. Thus, for the 20 cm bare sphere, neutrons exiting in the region of the minimum (20-27 keV) are carried by inelastic scattering into the resonance region above the minimum and suffer about 28 elastic collisions before finally leaking. For detector 18 covering the 10-20 keV region below the minimum, the average final energy in the inelastic scattering is in the cross section dip, and it takes only about 10 further elastic collisions before exiting through the detector.

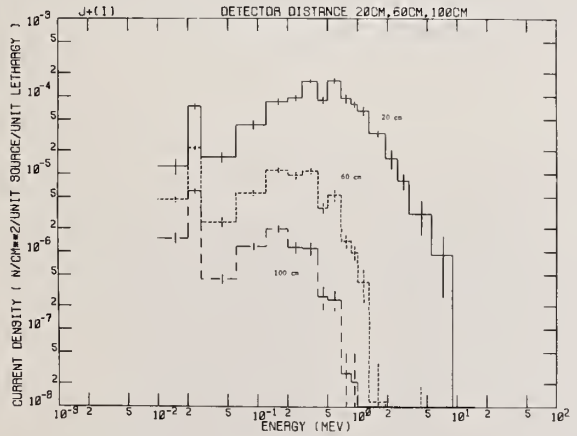

Fig. 2. Exit Current Spectrum of 20cm, 60cm, 100cm Padius Iron Sphere due to Fission Source in an Infinite Iron Medium.

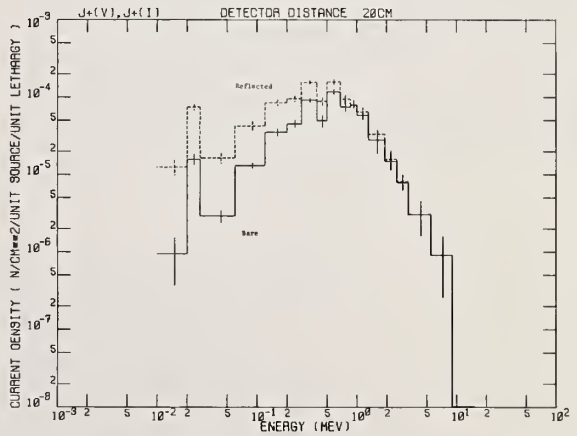

Fig. 3. Exit Current Spectrum of 20cm Bare and Reflected Iron Speres with Fission Source.

2. The Role of the Cross Section Minima in Deep Penetration

Previous evidence has suggested that the importance of the deep minima in the iron cross section for neutron transport depends sensitively on the problem being considered. Preeg et al.[1] found evidence that in slabs 1m or more thick the minima dominated the transport of fission source neutrons, at least in the higher portions of the spectrum. Ching et al.[2] on the other hand, investigating the leakage spectrum from a point isotropic 14 MeV source at the center of a bare 25 cm radius sphere could see no indication that the minima increase the penetrating flux. If anything, the minima are regions of high leakage and therefore tend to deplete the flux slowing down to lower energies. The present Monte Carlo studies enable one to investigate the possible transition between these two behaviors, at least for the portion of the spectrum below the inelastic threshold. (Too small a fraction of fission neutrons exit above this energy in large spheres for any conclusions to be drawn from the histories used here about the characteristics of their transport.)

To reveal the influence of the cross section minima on the neutron trajectories, the following method of analyzing the histories has been used. The lethargy range from 15 MeV down to the cut off is divided in some 86 subgroups chosen to be particularly narrow in the regions of the deep minima. From the histories of those neutrons which contribute to a given detector response at a given distance, the average point in space is calculated at which the neutrons leave each subgroup. (The standard error of this point is also calculated.) A plot of the location of this point versus the lethargy of the subgroup center is thus close to giving the trajectory in phase space of the center of the neutron cloud as it travels from source to detector. If any particular cross section minimum dominated, i.e. provided a favored trajectory for transport, then most of the spatial motion of this average point would be at the lethargy of the minimum and very little motion at any other lethargies.

To test this form of analysis an example was chosen in which dominance by one or more cross section minima was particularly to be expected. Neutrons from a point isotropic monoenergetic source at 150 keV were followed down to 85 keV. In this energy range there are two deep minima, one at 137.5 keV going down 0.3 barns and one at 128.6 keV with a minimum cross section of 0.6 barns. Elsewhere the cross section is mostly above 2 barns, being 5 barns at the source energy and peaking in two resonances at close to 20 barns. From previous experience it would be expected that even at detector distances of about 80 cm transport in the minima would be the dominant mechanism. Indeed, with a detector covering the lower part of the range (85-111 keV) the analysis described above for the "center" of the neutron cloud shows that 65-70 cm of the distance is travelled in the immediate vicinity of the minima.

No such pattern of dominance by the minima has been found for the fission source with any detector below 0.5 MeV and at distances that are of practical significance for shielding ($\lesssim$ 1.5 m). Thus, for detector 17 at a distance of 1.2 m transport in the prominent 24 keV minimum accounts for only 30 cm of the total distance. Since the lowest cross section in this minimum corresponds to a mean-free-path length of about 30 cm and the region of the minimum is wider than maximum lethargy change upon scattering, it is clear that no unusual or improbable neutron trajectories within the region of the minimum need be involved.

For detector bins at higher energies there is somewhat greater evidence for the importance of the minima. Thus for detector 14 (120-200 keV) at a distance of 1.2 m, something like 50-60 cm of the penetration is accomplished in the region of the minima around 138 keV and 300 keV. However, it is only at much larger distances that the cross section minima clearly dominate the transport process. For example, if detector 17 is stationed at 2 m from the source, transport in the 24 keV minimum alone accounts for 50 cm, with probably another 40 - 50 cm taking place near the 128 and 138 keV minima. In Figure 4, the location of the average point (and standard error) of neutrons just before entering the region of the 24 keV minimum is plotted against the distance of detector 17 (for an infinite medium). The distance these points are below the line at 45° indicates how much transport takes place in the 24 keV minimum. To within the statistical accuracy, Figure 4 shows that for detector distances of 80 cm or more, about 30% of the total travel occurs in this dip. For a detector distance of 3 m this corresponds to about 90 cm which is far in excess of the mean-free-path length in the dip. Thus it is only at these detector distances that the favored trajectories involve improbable long paths in the minima, magnifying the sensitivity of the penetrating flux to the values of the lowest cross section. For distances 80 cm or less (i.e. the more practical thicknesses) this prominent minimum plays no special role in determining the penetrating flux at this and lower energies.

Table 2. Effect of 1st Level Inelastic Scattering to a 20 cm Bare Sphere

Detector	F_1*	F_2+	Energy before scattering (MeV)	Energy after scattering (MeV)
11	0.642 ± 0.075	0.747 ± 0.070	1.435 ± 0.025	0.554 ± 0.024
12	0.615 ± 0.030	0.764 ± 0.039	1.328 ± 0.011	0.450 ± 0.011
13	0.675 ± 0.041	0.818 ± 0.042	1.188 ± 0.013	0.316 ± 0.012
14	0.662 ± 0.051	0.808 ± 0.064	1.103 ± 0.007	0.232 ± 0.005
15	0.687 ± 0.040	0.854 ± 0.054	1.011 ± 0.017	0.144 ± 0.016
16	0.647 ± 0.082	0.881 ± 0.113	0.974 ± 0.019	0.107 ± 0.019
17	0.621 ± 0.079	0.804 ± 0.065	0.948 ± 0.021	0.082 ± 0.019
18	0.727 ± 0.229	0.750 ± 0.335	0.884 ± 0.016	0.023 ± 0.013

*F_1 = Fraction of detector response due to neutrons born above the inelastic scattering threshold

+F_2 = Relative contribution from neutrons born above the inelastic threshold which have scattered from 1st excited level to the energy below the threshold

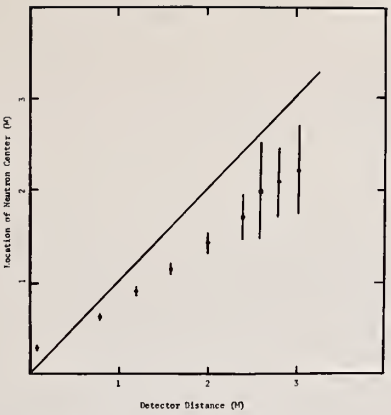

Fig. 4. Center of Neutron Cloud at 27 keV Resonance .VS. Distance of Detector 17.

Conclusions

The results of the Monte Carlo histories presented here, although only partial and still preliminary, are enough to lead to some specific conclusions for iron media about the roles of inelastic scattering and transport in the region of cross section minima. For small bare systems, the exit current spectrum below 100 keV is extremely sensitive to the details of the inelastic scattering in iron near the threshold. At greater distances, or with reflected systems, this region of the inelastic scattering is no longer singled out for emphasis. Thus, conclusions drawn from the measurements of leakage spectra with small bare assemblies, such as has been made at RPI[4] and LLL[5], may not at all be representative of the cross section sensitivities or transport mechanisms for deep penetrations of practical significance. On the other hand, the regions of cross section minima do not become dominant channels for transport except at distances far in excess of those encountered practically, or (possibly) for regions in the spectrum well above the threshold energy for inelastic scattering. But perhaps the most important conclusion to be drawn at this stage is that the analysis of Monte Carlo histories can indeed provide information on the details of transport mechanisms that is not available through forward or even adjoint deterministic transport calculations.

References

1 "Flux Sensitivity to Cross Section Data for Iron and Oxygen", W.E. Preeg, Doctoral Thesis, Columbia University (1970).

2 "Application of a Discrete-Energy, Discrete-Ordinates Technique to the Study of Neutron Transport in Iron", J. Ching, H. Goldstein, E.M. Oblow. ORNL-JM-4235 (1974).

3 "SAM-CE, A Three Dimensional Monte Carlo Code for the Solution of the Forward Neutron Transport and Adjoint Gamma Ray Transport Equations - Revision B" M.O. Cohen et al., DNA 2830-F-B/MR-7021, Rev. B (Aug. 1973).

4 "Experimental and Analytical Studies of Fast Neutron Transport in Iron", B.K. Malaviya et al., Nucl. Sci. & Eng., L7-329-348 (1972).

5 "Measurements and Calculations of the Neutron Spectra from Iron Bombarded with 14 MeV Neutrons", L.F. Hansen et al., Nucl. Sci. & Eng., 51, 278 (1973).

NEUTRON-COUPLED GAMMA-RAY CROSS-SECTION REQUIREMENTS FOR GAS-COOLED FAST BREEDER REACTORS*

M. Nagel and R. J. Cerbone
General Atomic Company
San Diego, California 92138

The generation, application, and testing of neutron-coupled gamma-ray cross sections required for Gas-Cooled Fast Breeder Reactor shield analysis are described.

(Neutron-coupled gamma-ray cross sections; gas-cooled fast breeder reactor)

Introduction

The Gas-Cooled Fast Breeder Reactor (GCFR) operates in the (Pu, U)O_2 fuel cycle in the core and axial blanket and in either the (Pu, U)O_2 or the Th-U^{233} fuel cycle in the radial blanket. The core, blanket, shielding, and primary system components (helium circulators, steam generators, etc.) are enclosed in a prestressed concrete reactor vessel (PCRV).

The primary purpose of the GCFR shielding is to protect the primary components and the PCRV from excessive exposure to radiation. Biological shielding is not a primary consideration because ample protection is provided by the concrete mass of the PCRV. Hence, the three major shielding functions are (1) to limit the rate of radiation-induced heat deposition in the PCRV concrete, (2) to limit fast-neutron-induced damage to vital structural components, including the PCRV liner and the reactor grid plate, and (3) to limit neutron-induced activation of the primary system components.

Neutron-induced secondary gamma-rays are the primary source of heat in the shielding and PCRV. In this paper, the methods used in calculating neutron-induced gamma-ray heating are described.

Calculational Methods

The calculation of gamma-ray heating effects in the GCFR shield involves the following steps:

1. Determine the relevant reactions for the shield materials, i.e., (n, γ) and (n, xγ).
2. Determine the energy-dependent gamma-ray source by folding in the reaction cross section, neutron flux, and gamma-ray yield per reaction.
3. Generate the gamma-ray transport cross sections.
4. Determine the energy deposition by folding in the energy absorption coefficient with the calculated gamma-ray flux.

This procedure involves a number of intermediate steps with manipulation of large amounts of data and separate neutron and gamma-ray transport calculations. A more direct and expedient method, requiring only one transport calculation, is the utilization of neutron-coupled gamma-ray transport cross sections. The transport code treats neutrons and gamma-rays as a single particle; the complete spatial-, energy-, and angular-dependent neutron and gamma-ray flux distributions are calculated simultaneously.

Neutron-coupled gamma-ray transport may be obtained by several methods. The most direct method, still under development, utilizes the AMPEX code,[1] which starts from ENDF/B data tapes and processes the data into one n-γ transfer matrix. AMPEX is a very large code that is not amenable to all computers. An alternative procedure used at General Atomic Company (GAC) is shown in the flow diagram in Fig. 1. This procedure involves the following steps:

1. The neutron transport cross sections are processed with the GGC-5 code.[2] This code prepares fast and thermal cross sections using sophisticated resonance treatments for the fast region and appropriate scattering kernels for the thermal regions.
2. The gamma-ray transport cross sections are generated with the DINT code,[3] which calculates the scattering transfer matrices using the Klein-Nishina formulation. Gamma-ray energy absorption coefficients are prepared in multigroup form by the DINT code.
3. The coupling of N multigroup neutron cross sections to the production of G multigroup gamma rays is achieved within the LAPHANO code.[4] This code retrieves photon production cross sections and multiplicities from the ENDF data files, applies suitable weighting functions over N specified neutron groups, and constructs a G x N photon production matrix.
4. The output from the three preceding codes is coupled via the RCOUPL code which prepares the cross sections for input to standard transport codes.

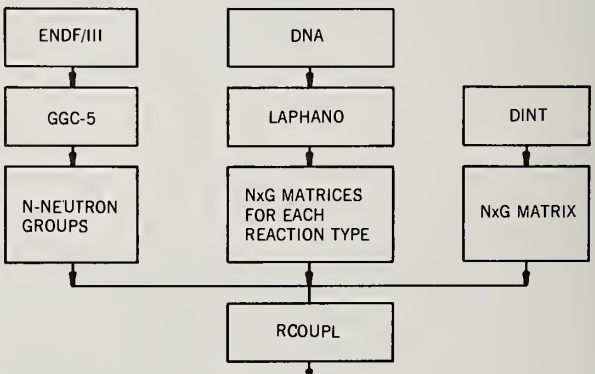

Fig. 1. Flow diagram for the generation of a neutron-coupled gamma-ray transport matrix

*This work was supported by the U.S. Energy Research and Development Administration under Contract AT(04-3)-167, Project Agreement 23.

Testing of Neutron-coupled Gamma-ray Cross Sections

Because the generation of neutron-coupled gamma-ray cross sections requires the processing of large amounts of data, care must be exercised in minimizing propagating errors. Experimental data were used where available to check the cross sections. Some difficulties were encountered with the LAPHANO code on using the option to combine reaction types. Therefore, each reaction had to be processed separately. These were later combined with the RCOUPL code.

For the GCFR shield materials iron and concrete, experiments were available to check the data. The neutron-coupled gamma-ray cross sections for iron were tested by calculating the ORNL Iron Benchmark.[5] The ANISN transport calculations were made using the incident neutron flux specified in the benchmark. A comparison between ORNL measured and GAC calculated gamma-ray spectra is shown in Fig. 2; above 1.5 MeV, agreement is better than 25%. For concrete, the Intelcom-Rad-Tech (IRT) measurements[6] were used as the basis for testing. Comparison between IRT measured and GAC calculated spectra through 80 cm of concrete is shown in Fig. 3; the overall agreement is reasonable.

Application of Neutron-coupled Gamma-ray Cross Sections to Gamma-ray Heating in the GCFR Shield

Using the methods described above, a 39-group cross-section set using 24 neutron and 15 gamma-ray groups was generated for the materials in a 300-MW(e) GCFR radial shield. Iron gamma-production data were used for chromium and nickel. The atom density specification for 4-B concrete* used in the PCRV are given in Table 1.

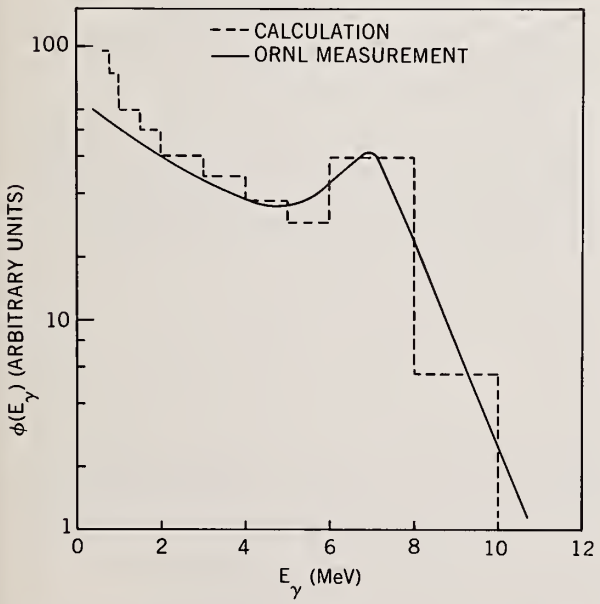

Fig. 2. Comparison of measured and calculated gamma-ray spectra through 56 cm of iron

*4-B concrete is the standard concrete used for the HTGR PCRV.

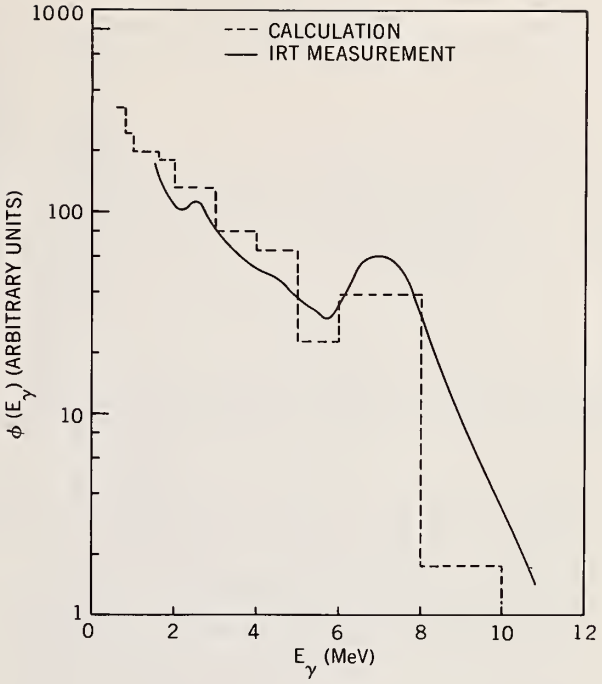

Fig. 3. Comparison of measured and calculated gamma-ray spectra through 80 cm of concrete

Table 1

Composition of 4-B Concrete

Element	Atom density (atom/barn-cm)
H	8.00×10^{-3}
O	4.44×10^{-3}
Al	4.87×10^{-3}
Si	1.59×10^{-2}
Ca	3.63×10^{-3}
Fe	3.10×10^{-4}

One-dimensional P_3, S_{16} transport calculations were then made using the ANISN code. The calculated gamma-ray heating rates are shown in Fig. 4. The right-hand ordinate is in absolute units corresponding to the operating level of the 300-MW(e) GCFR. The heating rate in the PCRV is approximately 0.1 mW/cm^3, which is well below the allowable level of 1 mW/cm^3.

A sensitivity study was then made to determine the primary contributors to energy deposition in 4-B concrete. The results are shown in Fig. 5. These results indicate that

1. Gamma-ray absorption is dominated by the high-energy gamma rays.
2. Oxygen and silicon are the dominating nuclei insofar as gamma-ray energy absorption in concrete is concerned.

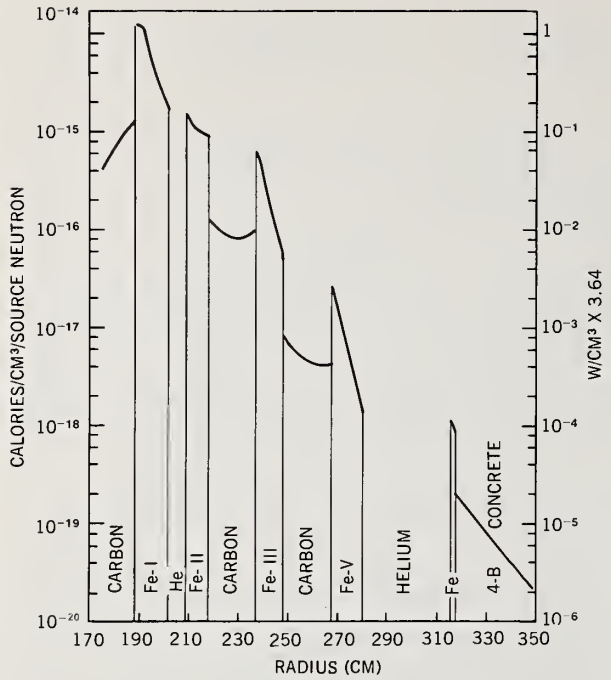

Fig. 4. Energy deposition profile in the GCFR shield (slab geometry) vs radial distance

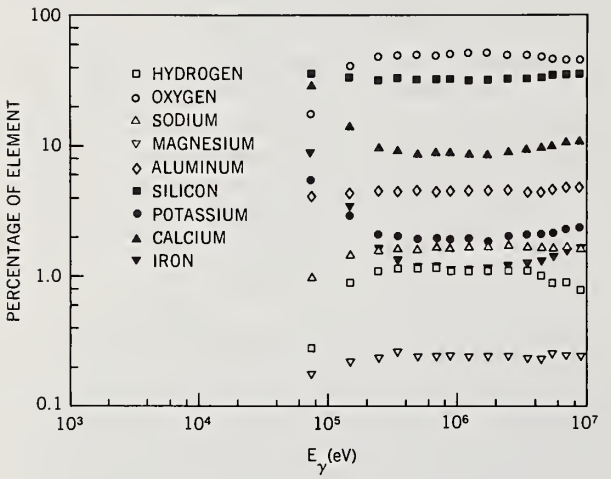

Fig. 5. Percentage of contribution of 4-B concrete (PCRV concrete) components to gamma-ray absorption as a function of gamma-ray energy

Summary and Conclusions

The methods for treating neutron-induced secondary gamma rays and their transport have been discussed. The advantages of utilizing the neutron-coupled gamma-ray transport cross sections were analyzed and applied to transport in iron and concrete, two of the major GCFR shield materials. These calculations were compared with available experiments with generally good agreement, thus lending confidence to the overall validity of the above methods.

Neutron-coupled gamma-ray cross sections were generated for the shield of the 300-MW(e) GCFR and a one-dimensional transport calculation was carried out to determine the gamma-ray heating profiles.

Acknowledgment

The authors would like to thank Dr. Larry Harris,Jr. for helpful discussions on the IRT data.

References

1. "AMPEX, Modular Code System for Generating Coupled Multigroup Neutron Gamma-ray Cross Section Libraries from ENDF/B," USAEC, Report ORNL-TM-3706, Oak Ridge National Laboratory, September 12, 1973.

2. Mathews, D. R., et al., "GGC-5, A Computer Program for Calculating Neutron Spectra and Group Constants," Gulf General Atomic, Report GA-8871, 1971.

3. Adams, K. G., et al., "DINT: A Computer Program which Prepares Multigroup Coherent-Incoherent Cross Sections for Photon Transport Calculations," Sandia Laboratory, New Mexico, SC-RR-720684, August 14, 1973.

4. Dudziak, D. J., et al., "LAPHANO: A P_0 Multigroup Photon-production Matrix and Source Code for ENDF," USAEC, Report LA-4750-MS, Los Alamos Scientific Laboratory, September 21, 1973.

5. Clifford, C. E., et al., "Fast Reactor Experimental Shielding Monthly Progress Report for May 1973," USAEC, Report ORNL-TM-4284, Oak Ridge National Laboratory, July 1973.

6. Harris, L., Jr., et al., "Time-dependent Fast-neutron and Secondary Gamma-ray Spectrum Measurements in Concrete," Defense Nuclear Agency, Report Gulf-RT-A12456 (DNA 2401-3), Gulf Radiation Technology Division, Gulf Energy & Environmental Systems Company, December 1972.

CROSS SECTION PREPARATION FOR THE CONTINUOUS-ENERGY MONTE CARLO CODE VIM*

R. E. Prael
Applied Physics Division
Argonne National Laboratory
Argonne, Illinois 60439

Improvements in the methods used to represent cross sections in the data library for the Monte Carlo code VIM are discussed. The degree to which observed difficulties have been eliminated and the reliability of the current VIM library based on ENDF/B Version 3 data are illustrated by comparison of broad-group cross section calculations made by VIM and by ETØE-2/MC^2-2.

(Monte Carlo, cross section, resonance, unresolved, probability, thinning, interpolation)

Introduction

The continuous-energy Monte Carlo code VIM is in active use at Argonne National Laboratory for the analysis of fast critical experiments.[1] Through the use of large point microscopic cross section sets, VIM is intended to provide an accurate representation of neutron physics as derived from ENDF/B data. Consequently, an intensive effort has been made to identify and resolve significant discrepancies which in the past have been observed in comparisons of broad-group cross section and reaction rate calculations made by VIM and by ETØE-2/MC^2-2.[2] In the discussion following, the difficulties observed and the solutions implemented will be examined. Examples will be presented which demonstrate the degree of consistency which has been obtained by the numerous refinements made to the VIM cross section library preparation system and to ETØE-2/MC^2-2. A detailed comparison of a V1M calculation with an ETØE-2/MC^2-2 calculation using the improved capabilities is presented in a companion paper.[3]

The V1M Cross Section Library Preparation System

The V1M cross section library system is based on five codes originally developed by Atomics International. The V1MB3 code produces a BCD library from ENDF/B Version 3, reformatting the data to the needs of the other codes and reconstructing ENDF/B File 3, 4, and 5 data into formats to be used in VIM. The UNIDØP-TH1N code (a descendent of UNICØRN)[4] constructs a Doppler-broadened cross section set from resonance parameters, merges it with File 3 data, and thins the output set to an interpolation error criterion. U3R produces unresolved resonance probability tables from ENDF/B unresolved resonance parameters;[5] recent extensive modifications have produced a descendent of U3R, called AURØX, which is being used for current processing of Version 4 data. The REDUCE code is used to contract the size of probability tables from a U3R or AURØX library to a desired size for VIM use. VIMTAP merges the output of VIMB3, UNIDØP-THIN, and REDUCE into a single isotopic cross section data file as used in the VIM Monte Carlo code.

All of the above codes have undergone considerable development at Argonne with respects to increased flexibility and efficiency. A major factor has been the implementation of dynamic storage allocation[6] to permit the generation of very large point data sets.

Resolved Resonance Methods

In comparison of VIM calculations with ETØE-2/MC^2-2 calculations, large local discrepancies in resolved resonance broad-group cross section output were detected. The source of the difficulties was traced to the following:

(1) insufficient point densities away from resonance peaks in the VIM and ETØE-2 libraries;

(2) failure to sum all resonance contributions at each grid point in UNIDØP and ETØE-2 (a feature optionally available with the MC^2-2 integral transport method for heavy resonance isotopes); and

(3) failure of the UNIDØP thinning method to prevent large relative distortion of absorption cross sections in the valleys between well-separated resonances.

To eliminate the first difficulty, a new algorithm to determine energy grid spacing relative to a single resonance was developed. The new algorith, based on the assumption of linear-linear cross section versus energy interpolation, replaces Otter's algorithm[4] which assumed log-linear interpolation. The new method, more consistent with actual VIM cross section usage, provides a greater relative point density in the wings of resonances than the original algorithm. Typically, 97 points per s-wave resonance and 47 or more points per p-wave resonance have been used. The code supplements the points generated around resonances with a 10-point per decade base energy grid. In the preparation of the final VIM Version 3 library, some inadequacy in grid point density between isolated resonances remained, as will be demonstated below.

An option to sum all resonance contributions at each energy point was incorporated in UNIDØP-THIN and has been employed in all cross section sets created for V1M at Argonne. Many large observed discrepancies, particularly in low energy scattering, have been eliminated by this step.

The original thinning procedure developed at Atomics International for use with UNIDØP was based only on accuracy of interpolating on total cross section. The method employs a "look ahead" procedure, extrapolating from an adjacent pair of points on the total cross section versus energy grid to find the last of a sequence of points, all of which lie within an input criterion of the extrapolation line. The first and last points of the sequence are retained and the intermediate points eliminated from the grid. The accuracy for interpolation on the thinned grid becomes a function of the cross section values over the region, but it may be shown that as the fractional error input criterion becomes small, the fractional interpolation error is bounded by approximately twice the input criterion.

The disadvantage encountered in the original application was the significant loss of accuracy in representing absorption cross sections away from resonance peaks. To obtain thinned resonance cross section of more uniform accuracy, the original algorithm is now applied twice, first to the total cross section and then to the absorption cross section, and points are thinned out of the grid only if both accuracy criteria are satisfied. In practice, a more restrictive criterion is applied to interpolation on total cross section, maintaining high accuracy in regions of greatest

significance, while a less restrictive criterion is applied to absorption cross sections to maintain a minimum level of accuracy in cross section representation over the full resonance range.

A number of VIM and ETØE-2/MC^2-2 comparison calculations have been run which illustrate the degree to which agreement has been reached. In these calculations, broad-group edits were produced for 27 groups with a lethargy width of 0.5 from 10 MeV to 13.71 eV. In Table I, broad-group cross sections for ^{238}U capture and ^{239}Pu capture and fission are shown. The problem solved consisted of an infinite homogeneous medium of ^{23}Na with an infinitely dilute admixture of heavy isotopes and a neutron source in the first ultra-fine-group at 10 MeV. The MC^2-2 integral transport option was used. The VIM results are shown with ±2 σ uncertainties. The ^{238}U data set now used by VIM has over 10,000 points in the resolved range; however, the comparison shown in Group 25 indicates some remaining difficulty in interpolation between isolated resonances. Comparable results have been attained with finite concentrations.[3]

TABLE I. Comparison of Infinite Dilution Broad-Group Resonance Cross Sections for Heavy Isotopes

Group	MC^2-2 Integral Transport	VIM/MC^2-2
	^{238}U σ_c	
17	1.419	1.007 ± 0.021
18	1.808	0.997 ± 0.018
19	2.918	0.988 ± 0.024
20	3.67	1.014 ± 0.030
21	3.61	0.981 ± 0.037
22	11.45	1.005 ± 0.030
23	23.6	1.000 ± 0.036
24	25.6	0.980 ± 0.038
25	1.386	1.047 ± 0.017
26	86.8	1.014 ± 0.046
27	126.4	1.042 ± 0.036
	^{239}Pu σ_c	
21	9.87	0.992 ± 0.014
22	14.23	0.998 ± 0.011
23	19.91	1.001 ± 0.019
24	29.5	0.997 ± 0.021
25	58.1	1.003 ± 0.022
26	10.49	0.989 ± 0.021
27	70.6	1.011 ± 0.017
	^{239}Pu σ_f	
21	10.54	0.985 ± 0.010
22	17.03	1.000 ± 0.008
23	19.49	0.997 ± 0.010
24	52.8	1.004 ± 0.013
25	40.0	0.998 ± 0.013
26	11.91	0.995 ± 0.017
27	87.0	1.006 ± 0.012

Results from the solution of a similar problem, an infinite medium of ^{12}C with infinitely dilute admixtures of structural materials, is shown in Table II. Given a near-perfect energy grid representation in both ETØE-2 and UNIDØP, the UNIDØP thinning procedure together with linear interpolation in VIM should produce slightly higher estimates by VIM for broad-group capture cross sections. Large discrepancies noted in Table II have been traced to energy grid insufficiencies remaining in UNIDØP or ETØE-2. The problem has been reduced for Version 4 data processing by UNIDØP by extending the grid around a resonance out to distance greater than 30,000 times the resonance total width; an alternative would be a denser background grid.

Unresolved Resonance Methods

In comparison of VIM broad-group cross section calculations for unresolved resonances with comparable ETØE-2/MC^2-2 calculations, discrepancies of the order of several percent were frequently observed. The source of these discrepancies was traced largely to numerical limitations in obtaining accurate infinite dilution average cross sections in U3R and to similar limitations in MC^2-2. A high-order quadrature scheme was added to U3R to obtain the dilute averages which are used to normalize the unresolved resonance probability tables; comparable improvements in numerical methods were developed for MC^2-2. Computation of infinite dilution average unresolved resonance cross sections at ENDF/B energy points now shows typical agreement of 0.02% or better.

A more subtle disagreement arises due to differences in interpolation schemes used in the two codes. In VIM, unresolved resonance cross sections at a particular energy during a particular neutron history are chosen by first selecting a probability table by random linear interpolation between table energies; subsequently, cross sections are obtained by random sampling from the selected table. In MC^2-2, unresolved resonance calcuations are made at ENDF/B energy points (which are the same as the energies at which VIM probability tables are specified). Log-log interpolation is then used to produce ultra-fine-group cross sections in the interval. VIM estimates ^{238}U broad-group capture cross sections up to about 1% higher than MC^2-2; capture and fission broad-group cross sections are up to 2% higher in limited regions of the ^{239}Pu unresolved range when estimated by VIM. Examples of this difference are shown in Ref. 3.

The degree to which agreement in unresolved resonance treatment between VIM and MC^2-2 has been achieved, apart from the question of interpolation scheme, was examined by modifying MC^2-2 to perform linear-linear interpolation in the unresolved region. A comparison of results from ^{238}U and ^{239}Pu broad-group unresolved resonance cross sections is shown in Table III; the data are again taken from solutions for slowing down in an infinite medium of ^{23}Na with an infinitely dilute admixture of heavy isotopes. Similar results have been obtained for finite concentrations of the heavy isotopes.

The most direct approach to resolving the interpolation scheme question would be to expand the number of unresolved resonance data points by interpolating unresolved parameters as specified by ENDF/B; the interpolation scheme dependence would thereby be minimized. Increasing the point density is preferable to implementing nonlinear interpolation schemes in VIM, both for running time considerations and for consistency with the probability table method of treating unresolved resonance cross sections.

Nonresonant Cross Section Methods

The conversion of ENDF/B File 3 data to a VIM library file involves the generation of an energy grid, including all essential points of the various reaction types, and the expansion of the reaction cross sections onto the common grid using the appropriate ENDF/B-specified interpolation scheme. The basic method of

TABLE II. Comparison of Infinite Dilution Broad-Group Resonance Cross Sections for Structural Materials and ^{23}Na

	Cr σ_c		Ni σ_c		Fe σ_c	
Group	MC^2-2	VIM/MC^2-2	MC^2-2	VIM/MC^2-2	MC^2-2	VIM/MC^2-2
6	0.00389	1.067 ± 0.004	0.00755	1.005 ± 0.001	0.00514	1.000 ± 0.001
7	0.00394	1.012 ± 0.008	0.00793	1.006 ± 0.003	0.00498	1.000 ± 0.001
8	0.00396	1.005 ± 0.020	0.00962	1.004 ± 0.005	0.00611	1.000 ± 0.001
9	0.00670	1.014 ± 0.028	0.01400	0.996 ± 0.005	0.00549	1.000 ± 0.001
10	0.00976	1.017 ± 0.022	0.01706	1.005 ± 0.006	0.00876	1.000 ± 0.001
11	0.01532	1.035 ± 0.036	0.0227	0.996 ± 0.033	0.00757	1.029 ± 0.089
12	0.0314	1.055 ± 0.040	0.0404	1.002 ± 0.051	0.0212	0.995 ± 0.055
13	0.0335	1.040 ± 0.061	0.0667	1.010 ± 0.023	0.00519	0.963 ± 0.148
14	0.0318	1.000 ± 0.007	0.1002	1.012 ± 0.038	0.00989	1.050 ± 0.078
15	0.0853	1.000 ± 0.004	0.0200	1.012 ± 0.029	0.0271	1.007 ± 0.010
16	0.0641	1.003 ± 0.002	0.0350	1.001 ± 0.014	0.00790	1.001 ± 0.008
17	0.0254	1.000 ± 0.001	0.0487	0.984 ± 0.060	0.00542	1.012 ± 0.015
18	0.2236	1.079 ± 0.076	0.0224	1.003 ± 0.007	0.01114	1.097 ± 0.030
19	0.01982	1.005 ± 0.025	0.0251	1.008 ± 0.001	0.451	1.080 ± 0.094

	^{23}Na σ_c		^{55}Mn σ_c		Cu σ_c	
Group	MC^2-2	VIM/MC^2-2	MC^2-2	VIM/MC^2-2	MC^2-2	VIM/MC^2-2
9	0.001709	1.116 ± 0.130	0.01437	1.001 ± 0.001	0.02702	1.000 ± 0.0001
10	0.000223	1.010 ± 0.001	0.02087	1.002 ± 0.002	0.0301	1.000 ± 0.0005
11	0.000292	1.055 ± 0.021	0.02988	0.999 ± 0.004	0.0374	1.000 ± 0.0005
12	0.000272	1.103 ± 0.165	0.0501	1.005 ± 0.007	0.0546	1.001 ± 0.007
13	0.000236	0.993 ± 0.001	0.0766	1.007 ± 0.013	0.0891	1.003 ± 0.016
14	0.000304	0.960 ± 0.001	0.0823	1.001 ± 0.001	0.1474	1.000 ± 0.013
15	0.001448	0.978 ± 0.062	0.0644	1.002 ± 0.009	0.2096	1.010 ± 0.028
16	0.01207	1.000 ± 0.010	0.01239	1.001 ± 0.005	0.2163	1.003 ± 0.021
17	0.1607	0.996 ± 0.008	0.340	1.002 ± 0.006	0.570	0.999 ± 0.032
18	0.01668	0.996 ± 0.003	0.1198	0.997 ± 0.004	0.1126	1.003 ± 0.016
19	0.00902	0.981 ± 0.001	2.057	1.025 ± 0.032	0.0447	1.002 ± 0.0002
20	0.00786	0.992 ± 0.001	0.219	1.000 ± 0.006	3.69	1.019 ± 0.066
21	0.00799	1.000 ± 0.001	1.442	1.008 ± 0.013	0.0438	0.997 ± 0.001
22	0.00838	1.000 ± 0.001	1.099	1.001 ± 0.005	0.504	0.982 ± 0.066

TABLE III. Comparison of Infinite Dilution Broad-Group Unresolved Resonance Cross Sections

VIM/MC^2-2 (Linear-Linear Interpolation)

Group	^{238}U σ_c	^{238}U σ_s	Group	^{239}Pu σ_c	^{239}Pu σ_f	^{239}Pu σ_s
11	1.0024 ± 0.0015	1.0008 ± 0.0010	12	0.9995 ± 0.0006	0.9998 ± 0.0002	1.0005 ± 0.0002
12	1.0007 ± 0.0021	1.0002 ± 0.0020	13	0.9991 ± 0.0034	0.9989 ± 0.0020	0.9996 ± 0.0013
13	1.0037 ± 0.0033	1.0037 ± 0.0032	14	0.9967 ± 0.0041	0.9985 ± 0.0026	0.9990 ± 0.0015
14	1.0011 ± 0.0034	0.9996 ± 0.0042	15	0.9993 ± 0.0037	1.0000 ± 0.0023	1.0000 ± 0.0017
15	0.9982 ± 0.0065	0.9995 ± 0.0067	16	1.0009 ± 0.0062	1.0004 ± 0.0042	1.0015 ± 0.0027
16	1.0079 ± 0.0096	1.0040 ± 0.0084	17	1.0025 ± 0.0104	1.0011 ± 0.0053	1.0025 ± 0.0043
			18	0.9958 ± 0.0120	1.0004 ± 0.0088	0.9980 ± 0.0043
			19	1.0087 ± 0.0093	1.0063 ± 0.0072	1.0023 ± 0.0040
			20	0.9976 ± 0.0140	0.9924 ± 0.0113	0.9969 ± 0.0090
			21	0.9836 ± 0.0143	0.9825 ± 0.0100	0.9936 ± 0.0101

grid generation is merely to form the union of the energy grids of all needed reaction types, supplement it with a uniform 20 points per decade mesh, and eliminate any duplicate or nearly duplicate points. Generally, the scheme has been shown to provide a sufficiently dense energy grid so that linear-linear cross section interpolation as performed in VIM provides a highly accurate representation of the original ENDF/B data. However, exceptions have been observed in cases of rapidly fluctuating elastic scattering cross sections such as the iron data in the range 320 keV to 59 keV which requires log-log interpolation.

At the present time, the VIMB3 code has been modified to expand the energy grid describing elastic scattering to sufficient density to ensure that linear-linear interpolation may be done with specified accuracy. Additional grid points are inserted at the location of maximum discrepancy until the interpolation discrepancy nowhere exceeds the input criterion. The expanded grid is then merged with the energy grids from other reaction types as before.

The effect of the improved procedure may be seen in Table IV; the results shown were obtained in the

TABLE IV. Comparison of Iron Broad-Group Scattering Cross Sections

Group	MC^2-2	VIM/MC^2-2[a]	VIM/MC^2-2[b]
7	2.978	0.994 ± 0.004	0.998 ± 0.003
8	3.286	1.009 ± 0.003	1.002 ± 0.004
9	2.943	1.022 ± 0.005	0.997 ± 0.004
10	4.616	1.045 ± 0.004	0.999 ± 0.004
11	4.528	1.001 ± 0.002	1.002 ± 0.002

[a] Previous iron cross section set for VIM.

[b] Current iron cross section set for VIM.

calculations described in Ref. 3. An additional 132 points were required — an increase of less than 3%.

Conclusions

The objective of supplying the VIM code with a faithful representation of ENDF/B Version 3 has, in general, been met. Excellent agreement with ETØE-2/MC^2-2 is being attained in calculations which can be performed by both codes when the more rigorous options of MC^2-2 are used. For those remaining small difficulties which have been noted above, the causes are understood and the remedies are currently being applied in the preparation of the new VIM library generated from ENDF/B Version 4 data.

References

1. E. M. Gelbard and R. E. Prael, "Monte Carlo Work at Argonne National Laboratory," *Proc. NEACRP Meeting of a Monte Carlo Study Group, July 1-3, 1974*, ANL-75-2 (NEA-CRP-L-118), Argonne National Laboratory (1975), p. 201.

2. H. Henryson, II and B. J. Toppel, "MC^2-2: A Code to Calculate Fast Neutron Spectra and Multigroup Cross Sections," ANL-8144, Argonne National Laboratory (to be issued).

3. R. E. Prael and H. Henryson, II, "A Comparison of VIM and MC^2-2 — Two Detailed Solutions of the Neutron Slowing Down Problem," *Proc. Conf. on Nuclear Cross Sections and Technology* (these proceedings).

4. J. M. Otter, "UNICØRN — A Program to Calculate Point Cross Sections from Resonance Parameters," NAA-SR-11980, Vol. VI, Atomics International (1966).

5. J. M. Otter, R. C. Lewis and L. B. Levitt, "U3R — A Code to Calculate Unresolved Resonance Cross Section Tables," AI-AEC-13024, Atomics International (1972).

6. L. C. Just, et al, "The System Aspects and Interface Data Sets of the Argonne Reactor Computation (ARC) System," ANL-7711, Argonne National Laboratory (1971).

*Work supported by the U. S. Energy Research and Development Administration.

A COMPARISON OF VIM AND MC^2-2 — TWO DETAILED SOLUTIONS OF THE NEUTRON SLOWING-DOWN PROBLEM*

R. E. Prael and H. Henryson, II
Applied Physics Division
Argonne National Laboratory
Argonne, Illinois 60439

A comparison of solutions by the Monte Carlo code VIM and by ETØE-2/MC^2-2 of a zero-dimensional slowing-down problem in the homogeneous ZPR-6 Assembly 7 core composition demonstrates the ability of either code to provide a reliable computational benchmark capability for such calculations.

(Cross section, multigroup, slowing-down, transport, Monte Carlo, resonance, reactor, eigenvalue, benchmark, stochastic)

Introduction

The generation of multigroup cross sections from point data represents one of the basic problems in reactor physics analysis. Since errors introduced into the processed data may lead to a significant uncertainty in the subsequent reactor calculations, there has been a great deal of interest in estimating the error introduced by specific methods and/or codes. In this study two distinct methods are compared for the solution of a zero-dimensional neutron slowing-down problem.[1-3] Both the continuous-energy Monte Carlo code VIM and the multigroup code MC^2-2 were designed to treat such a problem in a rigorous manner. As a consequence, a comparison of the two methods serves to evaluate both methods and codes and verify that they attain a sufficient accuracy in the representation and treatment of neutron interactions to provide a standard for future comparisons.

The problem selected for study was an infinite, homogeneous core composition representative of the benchmark ZPR-6 Assembly 7.[4] The ENDF/B-3 data were used. The atom densities defining the problem are shown in Table I. A uniform temperature of 300°K was

TABLE I. Atom Densities ($\times 10^{-21}$ atoms/cc)

Isotope	ENDF/B Mat No.	Atom Density
^{239}Pu	1159	0.88672
^{240}Pu	1105	0.11944
^{241}Pu	1106	0.0133
^{235}U	1157	0.01259
^{238}U	1158	5.78036
Mo	1111	0.2357
^{23}Na	1156	9.2904
^{16}O	1134	13.98
Fe	1180	12.97
Ni	1123	1.240
Cr	1121	2.709
^{55}Mn	1019	0.212

used. Broad-group edits were produced for 24 groups with a lethargy width of 0.5 from 10 MeV to 275.36 eV and 1.0 from 275.36 eV to 13.71 eV. Results available for direct comparison included broad-group edits for flux, fission spectrum, isotopic reaction rates, and isotopic microscopic cross sections.

Features of the VIM Calculation

As a continuous-energy Monte Carlo code, VIM provides a detailed energy and angular representation of neutron physics data obtained from ENDF/B libraries. Outside of the unresolved resonance region, isotopic microscopic cross sections are obtained by linear interpolation from dense cross section versus energy tables (Doppler broadened to 300°K in the resolved region). In an unresolved resonance region, cross sections are obtained by random sampling from probability tables corresponding to each ENDF/B specified unresolved resonance data point. Probability distributions are employed to represent anisotropy in the center of mass for both discrete level inelastic and elastic scattering. The full ENDF/B energy dependence of parameters for the determination of the energy distribution of secondary neutrons is utilized in VIM.

Of the 12 isotopes in the problem, 8 had new cross section sets prepared as described in Ref. 1: ^{238}U, ^{239}Pu, ^{240}Pu, Ni, Cr, Fe, ^{23}Na, and ^{55}Mn. A second iron cross section set was prepared, incorporating some small additional refinements, and used in a second VIM calculation.

The first VIM calculation, designated as VIM Run No. 1, consisted of 25,000 neutron histories. Absorption weighting was used to produce low variance estimates of reaction rates down to very low energies. A second VIM calculation, designated as VIM Run No. 2, consisted of 50,000 neutron histories followed with analog weighting. The iron cross section set used in the second run resulted in lower iron scattering cross sections, about 5% or less, from 320 keV to 59 keV. The results of both runs are presented below for quantities significantly affected by the change in iron scattering.

Eigenvalue estimation in VIM is made simultaneously with analog, collision, and track length estimators. Simple averaging of these estimators is used to reduce variance as is the method of combined estimators.[5] The detailed edits of isotopic reaction rates by energy group and group fluxes are obtained by track length estimation.

Features of the ETØE-2/MC^2-2 Calculation

The MC^2-2 code[6] solves the fundamental mode neutron slowing-down equations using multigroup, continuous slowing-down, and integral transport theory algorithms. The input data to MC^2-2 are prepared by the code ETØE-2 which reformats and preprocesses data from the ENDF/B tapes. The formats required by MC^2-2 were specified to permit efficient access to data by a processing code and thus are less general than the ENDF/B formats. The reformatting done by ETØE-2 does not, however, change the basic physics data. On the other hand, the processing of floor cross section data and light-element resonance data by ETØE-2 to ultra-fine-group cross sections ($\Delta u \approx 1/120$) does introduce approximations. In the initial comparisons of VIM and MC^2-2, many of the differences were traced to an inadequate treatment of the light-element resonances by ETØE-2. The numerical algoriths were refined as a consequence of this testing. The MC^2-2 code uses these data to calculate a flux and current spectrum which are used to collapse the data to broad-group cross sections

The rigor of the slowing-down calculation is user-specified. The comparison calculations reported in this study were performed using most of the more rigorous algorithms. In particular, isotope-dependent fission spectra, improved Goertzel-Greuling moderating parameters, detailed elastic matrix, and resonance calculations were used in the ultra-fine-group calculation and a hyperfine-group integral transport calculation was used below 4 keV to treat the resolved resonance region in detail. It has been found that one may relax the rigor of the calculation without much impact on such integral parameters as k_{eff}, whereas group cross section or flux comparisons require the most rigorous methods.

Results

Extremely close agreement in the eigenvalue computation was obtained. The ETØE-2/MC^2-2 value of 1.2121 is well within one standard deviation of both the VIM Run No. 1 value of 1.2128 (1 σ = 0.0014) and the VIM Run No. 2 value of 1.2129 (1 σ = 0.0030).

A comparison of group flux calculations is shown in Table II; the VIM results are shown with uncertainties of ±2 σ. The effect of the improvement in iron scattering cross sections used in VIM Run No. 2 may be noted in the data for Groups 8, 9, and 10. Although generally good agreement is obtained over the full energy range, the VIM spectrum appears slightly harder. A slightly more rapid attenuation is apparent in the VIM-computed flux below Group 16. It should be noted that the observed agreement in low-energy flux is attainable only with the MC^2-2 integral transport option.

TABLE II. Group Flux Comparison

Group No.	MC^2-2	VIM Run No. 1 MC^2-2	VIM Run No. 2 MC^2-2
1	0.4800	1.048 ± 0.106	0.977 ± 0.072
2	1.989	1.016 ± 0.060	1.048 ± 0.034
3	4.904	1.006 ± 0.034	1.010 ± 0.022
4	7.335	0.995 ± 0.026	0.993 ± 0.017
5	8.868	1.009 ± 0.022	1.002 ± 0.016
6	17.40	1.018 ± 0.015	0.997 ± 0.009
7	17.10	1.009 ± 0.011	1.005 ± 0.011
8	22.13	0.991 ± 0.010	1.002 ± 0.009
9	24.22	0.991 ± 0.008	1.005 ± 0.008
10	21.54	0.994 ± 0.008	1.000 ± 0.009
11	18.50	0.998 ± 0.008	0.999 ± 0.009
12	14.62	1.007 ± 0.007	1.005 ± 0.011
13	15.10	0.994 ± 0.008	1.006 ± 0.009
14	11.19	0.997 ± 0.008	0.999 ± 0.014
15	6.252	0.998 ± 0.006	1.006 ± 0.015
16	3.937	0.995 ± 0.007	0.992 ± 0.017
17	1.428	0.994 ± 0.010	0.999 ± 0.020
18	4.249	0.991 ± 0.009	1.000 ± 0.022
19	2.800	0.989 ± 0.010	1.011 ± 0.026
20	1.555	0.987 ± 0.014	0.989 ± 0.038
21	0.6586	0.977 ± 0.019	0.982 ± 0.048
22	0.4096	0.970 ± 0.034	0.963 ± 0.084
23	0.02851	0.951 ± 0.066	0.982 ± 0.258
24	0.000719	0.797 ± 0.260	1.248 (1 σ = ±0.678)

Individual isotopic capture rates are shown in Table III and fission rates in Table IV. The MC^2-2 rates shown were obtained without benefit of the integral transport option. The VIM results are again shown with ±2 σ uncertainties. The discrepancy in ^{238}U capture rate results primarily from the difference between the VIM and the MC^2-2 unresolved resonance treatment as will be discussed below. The very significant difference in iron capture is localized in Group 19 and undoubtedly results from the difference in the treatment of self-shielding of the 1150-eV p-wave resonance. In the VIM data library, approximately 40 points are used to represent this resonance, whereas in the ETØE-2 library, its strength is almost totally confined to one ultrafine group. Apart from the exceptions noted here, however, the agreement in reaction rates is generally good.

TABLE III. Isotopic Capture Rates

Isotope	MC^2-2	VIM Run No. 1 MC^2-2	VIM Run No. 2 MC^2-2
^{240}Pu	0.012385	0.9943 ± 0.0061	0.9998 ± 0.0126
^{241}Pu	0.0014452	0.9998 ± 0.0047	1.0047 ± 0.0103
^{235}U	0.0017975	0.9925 ± 0.0042	0.9992 ± 0.0101
^{238}U	0.3858	1.0052 ± 0.0038	1.0119 ± 0.0096
^{239}Pu	0.11419	0.9947 ± 0.0050	1.0029 ± 0.0122
Cr	0.011056	0.9853 ± 0.0132	0.9994 ± 0.0266
Ni	0.008198	1.0054 ± 0.0084	1.0072 ± 0.0114
Fe	0.03055	0.9704 ± 0.0142	0.9745 ± 0.0302
^{23}Na	0.004485	0.9921 ± 0.0104	1.0087 ± 0.0168
^{16}O	0.0019893	1.0354 ± 0.0574	1.0127 ± 0.0348
Mo	0.008655	0.9935 ± 0.0057	1.0040 ± 0.0148
^{55}Mn	0.003685	1.0062 ± 0.0126	1.0193 ± 0.0294

TABLE IV. Isotopic Fission Rates

Isotope	MC^2-2	VIM Run No. 1 MC^2-2	VIM Run No. 2 MC^2-2
^{240}Pu	0.007857	1.0000 ± 0.0094	1.0043 ± 0.0074
^{241}Pu	0.007516	0.9991 ± 0.0034	1.0020 ± 0.0078
^{235}U	0.005712	0.9946 ± 0.0031	0.9998 ± 0.0080
^{238}U	0.04288	1.0030 ± 0.0210	1.0077 ± 0.0141
^{239}Pu	0.3523	0.9972 ± 0.0033	1.0037 ± 0.0065

A detailed comparison of broad-group cross sections for ^{238}U capture and ^{239}Pu capture and fission below 40.9 keV are given in Table V. The very close agreement in the resolved range was obtained through use of the MC^2-2 integral transport option. The VIM results are shown with ±2 σ uncertainties.

Although broad-group cross section agreement as shown is typically of the order of 1% and frequently better, an important difference may be noted in the ^{238}U unresolved resonance range. The VIM code uses random linear-linear cross-section interpolation between probability tables generated for ENDF/B unresolved resonance energy points; MC^2-2 uses log-log interpolation between unresolved resonance calculations at specified energies. It has been determined that the difference in interpolation schemes alone will account for the greater part of the 0.5% to 1.0% increase in the VIM estimate of ^{238}U unresolved resonance capture over the corresponding MC^2-2 results.[3] Similar effects may be noted in ^{239}Pu fission, particularly in Group 18 where the difference in interpolation scheme produces a 2% greater VIM result.

In Table VI, a comparison of capture cross sections for structural materials over the energy range 820.9 keV to 748.5 eV is shown. The examples shown represent what are perhaps the most difficult cases in which to attain close agreement. The VIM data presented are shown with ±2 σ uncertainties and were taken from VIM Run No. 2 for Groups 6 to 15 and from VIM Run No. 1 for Groups 16 to 19. Although the agreement is frequently very good, a number of significant exceptions

TABLE V. Detailed Broad-Group Cross-Section Comparison

Group No.	^{238}U σ_c		^{239}Pu σ_c		^{239}Pu σ_f	
	MC^2-2	VIM/MC^2-2	MC^2-2	VIM/MC^2-2	MC^2-2	VIM/MC^2-2
12	0.4331	1.006 ± 0.002	0.5574	0.998 ± 0.001	1.7410	0.999 ± 0.0003
13	0.5290	1.011 ± 0.003	0.7706	1.001 ± 0.003	1.7679	1.000 ± 0.002
14	0.6408	1.006 ± 0.003	1.0587	1.001 ± 0.004	1.9175	1.000 ± 0.002
15	0.7622	1.008 ± 0.005	1.5853	1.006 ± 0.005	2.171	1.001 ± 0.003
16	0.8728	0.999 ± 0.008	2.156	1.004 ± 0.005	2.496	1.003 ± 0.004
17	1.1485	0.999 ± 0.018	3.387	1.006 ± 0.009	2.846	1.006 ± 0.006
18	1.0126	1.012 ± 0.013	3.496	1.011 ± 0.007	4.204	1.020 ± 0.005
19	1.3022	1.010 ± 0.018	4.283	1.006 ± 0.009	5.789	1.007 ± 0.006
20	1.3559	1.006 ± 0.025	6.332	1.001 ± 0.013	8.144	1.011 ± 0.009
21	1.3596	1.010 ± 0.033	7.349	1.016 ± 0.020	9.486	1.008 ± 0.012
22	1.9684	1.014 ± 0.027	12.645	1.006 ± 0.017	15.728	1.012 ± 0.012
23	1.9908	1.078 ± 0.088	14.849	0.979 ± 0.046	36.00	0.993 ± 0.033
24	8.467	0.989 ± 0.220	10.819	1.055 ± 0.216	13.79	0.978 ± 0.184

TABLE VI. Detailed Broad-Group Cross-Section Comparison

Group No.	Cr σ_γ		Ni σ_γ		Fe σ_γ	
	MC^2-2	VIM/MC^2-2	MC^2-2	VIM/MC^2-2	MC^2-2	VIM/MC^2-2
6	0.003873	1.072 ± 0.003	0.007570	1.006 ± 0.001	0.005150	1.0000 ± 0.0002
7	0.003939	0.998 ± 0.005	0.007989	1.008 ± 0.003	0.004997	1.0000 ± 0.0001
8	0.003909	0.973 ± 0.013	0.009657	1.004 ± 0.003	0.006100	1.0003 ± 0.0011
9	0.006492	0.993 ± 0.020	0.01425	1.000 ± 0.003	0.005498	1.0002 ± 0.0003
10	0.009700	1.011 ± 0.011	0.01701	1.003 ± 0.004	0.008763	0.9999 ± 0.0002
11	0.01503	0.991 ± 0.032	0.02375	0.997 ± 0.030	0.006547	1.035 ± 0.044
12	0.02932	1.009 ± 0.014	0.03816	1.006 ± 0.041	0.01691	1.014 ± 0.047
13	0.03423	1.042 ± 0.038	0.05977	0.995 ± 0.020	0.005640	0.987 ± 0.114
14	0.03149	1.001 ± 0.005	0.1039	0.998 ± 0.029	0.009607	0.984 ± 0.053
15	0.08302	0.999 ± 0.004	0.02020	1.029 ± 0.027	0.02631	0.999 ± 0.007
16	0.06855	1.002 ± 0.002	0.03647	1.002 ± 0.016	0.007592	1.004 ± 0.006
17	0.02341	1.001 ± 0.001	0.06266	1.129 ± 0.059	0.005840	1.013 ± 0.012
18	0.2108	0.897 ± 0.056	0.02242	1.004 ± 0.005	0.01086	1.071 ± 0.018
19	0.01974	1.005 ± 0.001	0.02494	1.007 ± 0.001	0.2546	0.930 ± 0.038

may be noted. Two major causes contribute to the differences:

(1) insufficient point densities in the VIM library in the extreme wings of narrow resonances may cause a bias toward higher capture in the valleys between isolated narrow resonances; and

(2) the much less detailed treatment of the peaks of very narrow capture resonances in ETØE-2 causes higher ETØE-2/MC^2-2 cross sections by underestimating self-shielding of the narrow resonances.

The latter effect is most noticeable in iron in Group 19, due to the 1150-eV resonance, and in chromium in Group 18, due to the 1626-eV resonance. The former difficulty probably accounts for the chromium discrepancy in Group 6 and in nickel in Group 18. A combination of these effects probably contributes to a lesser extent in other cases.

A comparison of other broad-group cross section data shows that agreement in total cross sections is generally within a few tenths of 1% and within 1% on capture throughout the resonance regions of the various isotopes. Other examples of the above difficulties with narrow capture resonances may be detected. The interpolation difficulty in the unresolved region described above appears to have little effect for ^{240}Pu, ^{241}Pu, or ^{235}U. Following the preparation of an improved iron data set for the VIM library, providing improved interpolation accuracy above the resonance region, no significant disagreement is observed with respect to nonresonant cross sections.

Conclusions

In recent years several studies have been reported which compare neutron cross section processing methods and codes. Such studies have generally concentrated on comparison of k_{eff} and reaction rate ratios and concluded that the methods and codes were in good agreement if k_{eff} differences were less than 0.5%. The current study was designed to determine whether there was agreement on a range of parameters between an essentially exact stochastic calculation and a detailed analytic calculation for a typical fast reactor core mixture. The extremely good agreement between the two methods permits one to conclude that either code provides a reliable computational benchmark capability for such an infinite medium calculation.

References

1. E. M. Gelbard and R. E. Prael, "Monte Carlo Work at Argonne National Laboratory," *Proc. NEACRP Meeting of a Monte Carlo Study Group, July 1-3, 1974*, ANL-75-2 (NEA-CRP-L-118), Argonne National Laboratory (1975), p. 201.

2. H. Henryson, II, B. J. Toppel, and C. G. Stenberg, "ETØE-2/MC^2-2/SDX Multigroup Neutron Cross Section Processing," *Seminar on Nuclear Data Processing Codes*, Ispra, Italy, December 5-7, 1973, EACRP-U-52.

3. R. E. Prael, "Cross-Section Preparation for the Continuous-Energy Monte Carlo Code VIM," *Proc. Conf. on Nuclear Cross Sections and Technology* (these proceedings).

4. *Cross Section Evaluation Working Group Benchmark Specifications*, BNL-19302 (ENDF-202), Brookhaven National Laboratory (November 1974).

5. M. Halpein, "Almost Linearly Optimum Combination of Unbiased Estimates," *Am. Stat. Assoc. J.*, 56, 36 (1961).

6. H. Henryson, II and B. J. Toppel, "MC^2-2: A Code to Calculate Fast Neutron Spectra and Multigroup Cross Sections," ANL-8144, Argonne National Laboratory (to be issued).

---

*Work supported by the U.S. Energy Research and Development Administration.

DECAY HEAT ANALYSIS FOR AN LMFBR FUEL ASSEMBLY USING ENDF/B-IV DATA*

G. W. Morrison C. R. Weisbin C. W. Kee

Oak Ridge National Laboratory
Oak Ridge, Tennessee 37830

Recently evaluated ENDF/B-IV fission product data have been used in decay heat calculations for typical LMFBR fuel assemblies exposed to 100,000 MWd/MT burnup. The decay heat and radioactivity of the fuel assemblies have been calculated as a function of time from discharge. Important contributors to the decay have been identified.

(Decay Heat; LMFBR; ENDF/B-IV Fission Product; CRBR; ORIGEN)

Introduction

Accurate calculation of nuclear transmutation and decay is required in a number of areas in the fast reactor fuel cycle. These include:

Sodium Void Calculations and Safety Requirements

Tyror[1] has estimated that the fission product capture rate in a fast reactor approaches 7% of the total captures in the fuel near the end of core life. This poisoning effect is energy dependent, and drastic changes in the spectrum (due for example to sodium voiding) leads to significant changes in the fission product capture rate and a positive reactivity coefficient. The uncertainties introduced in the analysis of a loss-of-coolant accident (LOCA) due to uncertainties in the basic data must also be assessed.

Waste Projections, Transportation, and Disposal

The projected accumulation of high level wastes cladding hulls, etc., at the repositories through the year 2000 have been estimated by Blomeke[2,3] to have some 18,500 (MCi) of radioactivity and a volume of 366,000 ft^3. Projected annual shipments of strategic nuclear materials, spent fuel, and wastes will number 112,000. The planning and design of methods and facilities that will be needed for handling and storage of the spent fuel and reprocessing wastes require accurate analysis for the composition, radioactivity, thermal power, and gamma and neutron release rates of the material. Claiborne[4] and Croff[5] have investigated the effect on the nuclear fuel cycle of recycling the actinide wastes. Croff indicates that including recycled actinides in the nuclear fuel cycle would require substantial changes in the nuclear fuel fabrication and shipping sectors. Concrete shield thicknesses in a fuel fabrication plant may have to be tripled because of the highly active neutron sources in the fuel.

The production of these heavy, radioactive isotopes involves a long series of neutron captures; accurate calculation requires knowledge of the spectrum and the energy dependence of the reaction cross sections of all competing reactions as well as branching ratios, half lives, and yields.

Nuclear Safeguards and Accountability

In a mature nuclear industry, large amounts of irradiated fuel from several reactors will be shipped to the reprocessing plant. In order to close the material balance and to deter diversion at the reprocessing stage, attention is being given to a number of proposals for nondestructive assay of the irradiated fuel. Direct measurement at the spent fuel pins or bundles requires accurate assessment of the background in which the measurement is to be made[6].

Fuel Cycle Optimization

As fuel is discharged from the reactor, it is desirable to begin reprocessing as soon as possible[7]. Short cooling times can, however, lead to "hostile" environments for chemical processing. Decay heat calculations are required to minimize "fissile holdup" while permitting safe fuel handling and transportation design.

In this paper, we focus our attention on the calculation of composition, radioactivity, and thermal power of irradiated CRBR fuel subassemblies using the recently available ENDF/B-IV data library. Extensive calculations[8-9] have been made previously of the properties of irradiated fuel from power reactors. However, these calculations did not include the comprehensive data library now available. Different nuclear data sets can produce significant differences in fast reactor static and dynamic parameters. Kee et al.,[10] have reported 20% differences in the decay heat one second after irradiation. Ilberg[11] reports 50% differences in the sodium void coefficient when using different product cross section sets. The results and experience obtained using the new ENDF/B-IV library for these problems are compared to similar studies made using the older ORIGEN library.

Data Base

Calculations of nuclear transmutation and decay require basic cross section and decay information for light element, fission-product, and actinide nuclides. An extensive fission-product data library in the ENDF/B-IV format has resulted from a two-year effort by the CSWEG Fission Product Task Force. The formulation and content of this library is discussed in more detail in another paper[12] of this conference.

Table I presents a comparison of the new fission-product library with the ORIGEN[13] fission-product library. The original fission-product cross-section formats in ORIGEN allowed only (n,γ) reactions, but the code can treat other reactions. Similar characteristics are provided in Table II for the ORIGEN light element (LMFBR) and heavy metal libraries. The paucity of data for nuclear transmutation of light and heavy nuclides for ENDF/B-IV is such that inclusion in the table was deemed unnecessary.

The LMFBR cross-sections in the ORIGEN libraries, until the present work, were based on a fixed reference spectrum[14]. We have processed the ENDF/B-IV fission products' capture cross section into 124 groups using the MINX[15] code. The ORIGEN program was then modified to derive group collapsed reaction rates "on-line" with a user specified reference spectrum[16].

*Research performed by Union Carbide Corporation under contract with the U. S. Energy Research and Development Administration.

Such capability permits more credible problem dependent analysis (e.g., foil and/or capsule measurements designed for dosimetry purposes.)

Table I.
Comparison of ORIGEN and ENDF/B Fission Product Data Library for the LMFBR

	ENDF/B-IV	ORIGEN
No. of nuclides	825	461
Radioactive	712	338
1st excited state	117	83
2nd excited state	7	-
Delayed neutron precursors	57	-
Alpha decay	6	0
Positron decay	17	11
Cross sections	181	423*

*1 group (n,γ) cross sections.

Table II.
ORIGEN Light Element and Heavy Metal Data Libraries for the LMFBR

	Light Elements	Heavy Metal
No. of nuclides	162	101
Naturally occurring	80	-
Radioactive	81	96
Nuclides with 1 group cross sections	142	53
Excited state	5	3
Alpha decay	1	58
Positron decay	14	2
Spontaneous fission	-	10

Methods and Data Testing

In a cooperative effort with HEDL under the auspices of the CSWEG Fission Product Task Force, the fission product decay heat following thermal neutron fission of ^{235}U was calculated[16] with the ORIGEN and RIBD[17] codes using the same ENDF/B-IV data base. This problem was picked because of its importance to the analysis of the loss-of-coolant accident (LOCA) in light water reactors, because the "zero flux", infinite irradiation benchmark case is "clean" in the sense that cross section and spectral complications are unimportant, and finally because it was thought that the myriad of new data, particularly those of importance at early times, could shed some light on the present credibility of summation calculation results at early times (> 100 seconds after shutdown).

Calculations using the ENDF/B-IV data were performed for several different irradiation times and flux levels. The total (β + γ) integral afterheat for a 60,000 day irradiation (∿ infinite) at a flux level of 10^6 n/cm^2-sec (low enough to neglect capture) is given in Table III along with ORIGEN calculations using earlier data,[18] the Perry et al.[19] evaluation, and the ANS-5 standard.[20] The calculations of ORIGEN and RIBD, using the ENDF/B-IV data base, agree to within the three figures printed on output. The largest difference between these calculations and the Perry et al., evaluation is 11% for times less than one second following discharge. At ten seconds, the difference is less than 4%. The calculated results will increase if transitions to second excited states are properly included.

Table III.
Fission Product Afterheat, (MeV/sec)/(fission/sec), for Thermal Neutron Fission of ^{235}U Following "Infinite" Operation at Constant Power

Time after Shutdown t (sec)	Total Afterheat (β + γ) ORIGEN (Earlier Data)	ANS-5	Perry et al.	ORIGEN/RIBD
1×10^0	10.0	12.50	13.52	11.72
1×10^1	9.05	10.00	10.05	9.44
1×10^2	6.82	6.62	6.54	6.35
1×10^3	4.00	3.70	3.941	3.93
1×10^4	2.01	1.93	2.001	1.93
1×10^5	1.05	0.95	1.012	.962
1×10^6	.583	0.534	0.561	.545

We conclude that for decay heat calculations of this type, ORIGEN and RIBD give essentially the same results (provided they start from the identical data base) even though the calculations use different numerical methods. The data represented by the ENDF/B-IV evaluated decay file represent a substantial improvement over previous libraries which are associated with codes of this type. Isotope generation and depletion calculations based upon such extensive libraries are feasible for determining beta and gamma energy release rates. The uncertainties associated with the proposed ANS-5[20] standard appear to be conservative.

Calculational Method - ORIGEN

The present calculations have been performed using the ORIGEN isotope generation and depletion code which uses the matrix exponential method to solve the linear differential equations for nuclear transmutation and decay which can be expressed as:

$$\dot{X} = AX(t) \tag{1}$$

where:

$$A = (B-I)\Lambda + (T-I)\Sigma\phi \tag{2}$$

and:

B = Decay transition matrix with b_{ij} = fraction of decays of nuclide j which produce nuclide i
I = Identity matrix
T = Transmutation matrix with t_{ij} = fraction of neutron captures with j to produce i
Λ and Σ = Diagonal matrices whose ith elements are λ_i and σ_i, respectively where
λ_i = decay constant (sec^{-1}) and
σ_i = capture cross sections (cm^2/atom)
$\dot{X}(t) = dX/dt$ (3)
ϕ = Scalar flux (n/cm^2-sec)

The solution is given by:

$$X(t) = X(0)\exp(-At) \tag{4}$$

A discussion of the numerical technique in ORIGEN is presented by Bell.[13]

Application to Fuel Storage Facility Problem

The fuel storage and test facility is designed to store irradiated fuel from the CRBR and FFTF as it becomes available. In order to properly design a fuel storage facility, a knowledge of the decay heat and radioactivity associated with the irradiated fuel is required input information. This study was undertaken to provide that information for equilibrium core

CRBR fuel assemblies irradiated to 100,000 MWD/MT burnup.

The design model of the CRBR core[21] employed in this work contains 198 fuel assemblies arranged in two zones with the outer zone of 2 rows of assemblies having a higher enrichment than the inner zone to improve power flattening. Both radial and axial reflectors surround the core. The core itself is 36" in height with the upper and lower axial reflector each of 14" in height.

A fuel assembly is a hexagonal structure of 316 stainless steel about 4 1/2" flat to flat containing 217 fuel rods of Uranium-Plutonium dioxide pellets. Each rod is 0.23" in diameter and has a cladding thickness of 15 mills. Each fuel assembly consists of three distinct regions, an upper axial blanket, a core region, and the lower axial blanket. The fuel assemblies were specified as three regions for the ORIGEN calculations and the results were blended by the code to obtain an effective fuel assembly.

The power history used for the calculations was based on the equilibrium fuel management plan for the CRBR which has a goal of 274 full power days of operation (.75 capacity factor) per fuel cycle. Each subassembly will remain in the core for three cycles.

Conclusions

The results of the ORIGEN decay heat calculations for the CRBR core fuel assemblies are given in Table IV and the total activities are given in Table V. Also shown are results calculated from previous ORIGEN data. From Table IV, it can be seen that fission products are the major contributors to decay heating in CRBR fuel. The largest changes due to the use of ENDF/B-IV data occurs at early times (i.e., the first 1000 seconds following shutdown). At longer times, there is approximately 9% difference between results obtained using the previous ORIGEN fission product library and results obtained by using ENDF/B-IV fission product data. In Table V, the total activities calculated from ENDF/B-IV data are approximately the same as the total activities calculated from the previous ORIGEN library.

A list of major contributors to fission-product decay heating is given in Table VI. It should be noted that for all times listed these 17 nuclides collectively contribute more than 90% of the total. Furthermore, nuclides from three mass chains (95, 106, and 144) contribute 56.7% at 30 days, 78.2% at 90 days, 85.2% at 180 days, and 76.8% at 720 days. Thus, only a small set of nuclides are crucial for decay heat calculations in a fuel storage facility.

Table IV
Thermal Power (kW) of a CRBR Core Fuel Assembly as a Function of Time from Discharge

Time (days)	Light Elements and Actinides	Fission Products	
		ENDF/B-IV Library	Previous ORIGEN Library
0	14.74	241.00	175.00
10	1.38	9.32	9.95
20	1.08	6.95	7.54
30	0.99	5.72	6.24
60	0.80	3.99	4.36
90	0.66	3.19	3.49
180	0.39	2.02	2.20
360	0.19	1.15	1.25
720	0.10	0.57	0.63

Table V
Activity (MCi) of a CRBR Fuel Core Assembly as a Function of Time from Discharge

Time (days)	Light Elements and Actinides	Fission Products	
		ENDF/B-IV Library	Previous ORIGEN Library
0	6.560	20.90	17.70
10	0.288	2.29	2.23
20	0.120	1.77	1.75
30	0.104	1.49	1.49
60	0.089	1.05	1.07
90	0.078	0.82	0.84
180	0.059	0.49	0.51
360	0.045	0.29	0.30
720	0.036	0.15	0.16

An extensive analysis of errors was not undertaken in this study. However, based on the calculated decay heats, the data parameters which most influenced the total fission-product decay heat at the times given in Table IV were identified as:

1. Yields for 95, 106, and 144 mass chains.
2. Decay constants for ^{95}Zr, ^{95}Nb, ^{106}Rh, and ^{144}Ce.
3. Q-values for ^{95}Zr, ^{95}Nb, ^{106}Rh, and ^{144}Pr.

Captures in the fission products lead to both destruction and production of the important nuclides. However, the most important fission-product cross-sections for this problem are the total capture cross-sections of Zr-95, Nb-95, Rh-106, and Ce-144; and the n-gamma cross-sections of Zr-95, Rh-105, and Ce-143.

Table VI
Percentage Contribution to Decay Heat of Significant* Fission-Product Isotopes Discharged CRBR Core Fuel

	Time since discharge from reactor (days)				
	30	60	90	180	720
Sr-89	2.9	2.8	2.8	1.1	0.0
Y-90	0.4	0.6	0.8	1.2	4.2
Y-91	4.3	4.3	3.8	2.1	0.0
Zr-95	11.1	11.6	3.8	6.4	0.1
Nb-95	13.1	16.1	10.5	11.7	0.2
Ru-103	8.7	7.4	5.5	1.8	0.0
Rh-106	18.0	24.5	28.9	38.6	49.5
Cs-134	0.9	1.2	1.5	2.2	4.6
Cs-137	0.3	0.3	0.4	0.6	2.1
Ba-137m	0.8	1.1	1.4	2.2	7.6
Ba-140	2.0	0.6	0.1	0.0	0.0
La-140	12.6	3.6	0.9	0.0	0.0
Ce-141	2.6	2.0	1.3	0.3	0.0
Ce-144	1.2	1.5	1.8	2.3	2.2
Pr-143	1.4	0.4	0.1	0.0	0.0
Pr-144	13.3	17.8	20.7	26.2	24.8
Pm-147	0.2	0.3	0.3	0.5	1.2
Others	7.2	4.0	3.4	2.7	3.6

*Greater than 1% contribution to total heat generation at any listed time.

References

1. J. G. Tyror, "The Importance of Fission Product Nuclear Data in the Physics Design Power Reactor Cores," AEEW-R-915, (November 1973).
2. J. O. Blomeke, C. W. Kee, and J. P. Nichols, "Projections of Radioactive Wastes to be Generated by the U.S. Nuclear Power Industry," ORNL-TM-3965, (February 1974).
3. J. O. Blomeke, C. W. Kee, and J. P. Nichols, "Projected Shipments of Special Nuclear Material and

Wastes by the Nuclear Power Industry," ORNL-TM-4631, (August 1974).

4. H. C. Claiborne, "Neutron Induced Transmutation of High-Level Radioactive Waste," ORNL-TM-3964, (December 1972).

5. A. Croff, "Seminar on Effects of Actinide Transmutation on Nuclear Fuel Cycle," Oak Ridge National Laboratory, (January 1975).

6. G. W. Morrison, C. R. Weisbin, and C. W. Kee, "Projected CRBRP Spent Fuel Characteristics and Their Impact Upon NDA Techniques," to be presented at ANS Annual Meeting, (June 1975).

7. D. B. Trauger, "On the Successful Commercialization of the LMFBR," Oak Ridge National Laboratory, (June 1974).

8. M. J. Bell, "Calculated Radiation Properties of Spent Plutonium Fuels," Nuclear Technology, 18, pp. 5-14, (April 1973).

9. H. O. Haug, "Calculations and Compilations of Composition, Radioactivity, Thermal Power, Gamma and Neutron Release Rates of Fission Products and Actinides of Spent Power Reactor Fuels and Their Reprocessing Wastes," KFK-1945, (April 1974).

10. C. W. Kee, C. R. Weisbin, R. E. Schenter, Trans. Am. Nucl. Soc. 19, 398 (1974).

11. D. Ilberg, D. Saphier, and S. Yiftah, "Sensitivity of Fast Reactor Static and Dynamic arameters to Different Fission-Product Cross-Section Data," Nucl. Tech. Vol. 24, pp. 111-122, (November 1974).

12. R. E. Schenter and F. Schmittroth, "Radioactive Decay Heat Analyses," Comference on Nuclear Cross Sections and Technology; Washington, D.C., (March 1975).

13. M. J. Bell, "ORIGEN - The ORNL Isotopes Generation and Depletion Code," ORNL-4628 (1973).

14. H. Kuster and M. Metzenroth, "The Influence on Some Important Group Constants on Integral Fast Reactor Quantities," ANL-7120 (1965).

15. C. R. Weisbin, P. D. Soran, R. E. MacFarlane, D. R. Harris, R. J. LaBauve, J. S. Hendricks, and J. E. White, "MINX, A Multigroup Interpretation of Nuclear Cross Sections from ENDF/B," Los Alamos Scientific Laboratory (to be published). See also Trans. Am. Nucl. Soc. 16, 127 (1973).

16. G. F. Flanagan, Oak Ridge National Laboratory, private communication (December 1974).

17. R. O. Gumprecht, "Mathematical Basis of Computer Code RIDB," DUN-4136, Douglas United Nuclear, Inc. (1968).

18. C. W. Kee, C. R. Weisbin, and R. E. Schenter, "Processing and Testing of ENDF/B-IV Fission Product and Transmutation Data," report to the Fission Product Task Force of the Cross Section Evaluation Working Group (June 1974).

19. A. M. Perry, F. C. Mainschein, and D. R. Vondy, "Fission-Product Afterheat - A Review of Experiments Pertinent to the Thermal-Neutron Fission of ^{235}U," ORNL-TM-4197 (October 1973).

20. American Nuclear Society, Proposed ANS Standard Decay Energy Release Rates Following Shutdown of Uranium-Fueled Thermal Reactors, Draft Standard ANS 5.1, approved by Subcommittee ANS-5 of the ANS Standards Committee, October 1971, revised October 1973.

21. James A. Lake, "LRA-73-251, Letter to M. W. Dyos on LMFBR Nuclear Analytical Model," (August 17, 1974).

A TWO DIMENSIONAL CROSS SECTION SENSITIVITY ANALYSIS OF IRON IN A CONCRETE SHIELD

T. E. Albert and G. L. Simmons
Science Applications, Inc.
Huntsville, Ala. 35805

A cross section sensitivity analysis of iron in a family of concrete shields is performed to illustrate the dependence of the cross section sensitivity to the spatial distribution of reinforcing steel. The results of this study demonstrate that one dimensional sensitivity methods can be inadequate for multidimensional problems.

(Sensitivity; cross section; two dimensional; shield)

Introduction

This paper was motivated by a discussion which occurred at the American Nuclear Society 1974 Annual Meeting in Philadelphia during the session on Shielding and Radiation Transport Applications. One of the papers discussed was a cross section sensitivity study of radiation transport in concrete.[1] Following that paper, the question was raised as to what effect representing the reinforcing rod and steel in a concrete shield as a homogeneous layer has on the results of the cross section sensitivity study. Two schools of thought emerged. One suggested that the sensitivity results had not been observed to be very sensitive to the exact distribution of the reinforcing steel. The other suggested that perhaps it would be more proper to ignore that steel which indeed was not a homogeneous layer. This paper will resolve that question, and in a larger sense address the spatial aspects of cross section sensitivity studies which may have previously been neglected.

This paper describes briefly the development of a two dimensional variation of the one dimensional cross section sensitivity code, SWANLAKE.[2] There are some important differences in the numerical solution of the sensitivity equation which require discussion. This will be followed by a discussion of a cross section sensitivity analysis of a family of concrete and iron shields to illustrate the dependence of the sensitivity of the iron cross section to the spatial distribution of the reinforcing steel.

At this point it may be appropriate to anticipate a possible misconception that may hinder the understanding of the conclusions drawn in this paper. It is not the point of this paper that the spatial distribution of reinforcing steel in a concrete shield has an influence on the shield effectiveness. That fact is well recognized. Rather, we are suggesting that the spatial distribution of reinforcing steel can have an influence on the sensitivity of the shield effectiveness to errors or uncertainities in a particular cross section. The reader is referred to reference 3 for a discussion of sensitivity theory.

2-D Cross Section Sensitivity

Cross section sensitivity analysis is an application of perturbation theory with the objective of determing the sensitivity of an integral quantity, such as dose, to cross section data used in the calculation. Following Bartine, Mynatt, and Oblow,[2] the sensitivity function $P_X(E)$ for a cross section, at energy E, may be expressed as:

$$P_X(E)=[R^{-1}]\left[\int_{\bar{r}} dr \int_{\bar{\Omega}} d\Omega\, \rho_X(\bar{r})\,[-\Phi^{\dagger}(\bar{r},\bar{\Omega},E)\sigma_X^t(E)\Phi(\bar{r},\bar{\Omega},E) + \int_{\bar{\Omega}'} d\Omega' \int_{E'} dE'\, \Phi^{\dagger}(\bar{r},\bar{\Omega}',E')\sigma_X^s(\bar{\Omega}\cdot\bar{\Omega}', E'\to E')\Phi(\bar{r},\bar{\Omega},E)]\right], \quad (1)$$

where R is the integral response,
$\rho_X(\bar{r})$ is the atomic density,
$\Phi^{\dagger}(\bar{r},\bar{\Omega},E)$ is the adjoint angular flux,
$\Phi(\bar{r},\bar{\Omega},E)$ is the forward angular flux,
σ_X^t is the total cross section for reaction type X and $\sigma_X^s(\bar{\Omega}\cdot\bar{\Omega}', E\to E')$ is the differential scattering cross section for reaction type X.

One approach to obtain a numerical solution of equation (1) is expand the angular fluxes in a Legendre series. For a problem that can be described with two spatial dimensions, the fluxes are expanded in a series of associated Legendre polynomials,

$$\Phi(\bar{r},\bar{\Omega},E) = \sum_{l=0}^{\infty}(2l+1)\sum_{m=0}^{l} R_l^m(\bar{\Omega})\,\Phi_l^m(\bar{r},E), \quad (2)$$

$$\Phi^{\dagger}(\bar{r},\bar{\Omega},E) = \sum_{l=0}^{\infty}(2l+1)\sum_{m=0}^{l} R_l^m(\bar{\Omega})\,\Phi_l^{\dagger m}(\bar{r},E). \quad (3)$$

The function $R_l^m(\Omega)$ is defined by,

$$R_l^m(\bar{\Omega}) = R_l^m(\mu,\varphi) = \left[\frac{(2-\delta_{mo})(l-m)!}{(l+m)!}\right]^{1/2} P_l^m(\mu)\cos m\varphi, \quad (4)$$

$\Phi_l^m(\bar{r},E)$ and $\Phi_l^{\dagger m}(\bar{r},E)$ are recognized respectively as the forward and adjoint flux moments. Substituting equations (2) and (3) into equation (1), and truncating with the Lth moment, the sensitivity function is expressed as

$$P_X(E)=[R^{-1}]\left[\int_{\bar{r}} dr\,\rho_X(\bar{r})\sum_{l=0}^{L}\sum_{m=0}^{l}[-(2l+1)\sigma_X^t(\bar{r},E)\cdot\Phi_l^{\dagger m}(\bar{r},E)\Phi_l^m(\bar{r},E) + \int_{E'} dE'\,\sigma_X^{sl}(E\to E')\Phi_l^{\dagger m}(\bar{r},E')\Phi_l^m(\bar{r},E)]\right], \quad (5)$$

where the σ_X^{sl} are the Legendre coefficients of the expansion of the differential scattering cross section.

An alternative method for calculating the term in equation (1) involving the total cross section is to approximate the integral over angle by a quadrature formula. In this case the sensitivity function would be expressed as

$$P_X(E) = [R^{-1}]\left[\int_{\bar{r}} dr\,\rho_X(\bar{r})\left[-\sigma_X^t(r,E)\sum_{k=1}^{N}\Phi^{\dagger}(\bar{r},\Omega_k,E)\Phi(\bar{r},\Omega_k,E)W_k + \sum_{l=0}^{L}\sum_{m=0}^{l}\int_{E'} dE'\,\sigma_X^{sl}(E\to E')\Phi_l^{\dagger m}(\bar{r},E')\Phi_l^m(\bar{r},E)\right]\right] \quad (6)$$

where W_k are the weights of the quadrature formula.

Although equation (6) is convenient for one dimensional problems, for many two dimensional problems the quadrature formula proves to be computationally unwieldy. For two dimensional cross section sensitivity studies, the truncated moments expansion of equation (5) proves to be more efficient.

One question that arises is how many moments are required for an accurate calculation of the sensitivity function. This is equivalent to the question of how many angles are required for the quadrature formula. The answer to both questions is that it depends on the particular problem which of course is not really an answer, but after all some aspects of radiation transport remain an art. A serious answer to this question is reserved for a future time, but it is appropriate that the question be raised here.

The formulation of equation (5) has been implemented in a computer code, SAIDOT, which accepts transport calculations from either DOT or ANISN. SAIDOT can, therefore, be used for both one or two dimensional sensitivity studies and proves to be a useful tool for comparing spatial effects on sensitivity. The convenient plotting routines from SWANLAKE have been transplanted into SAIDOT.

Problem Description and Results

In order to investigate the dependence of cross section sensitivities to the spatial distribution of reinforcing steel, a family of similar shields were studied. Figure 1 shows the geometry of the four shields. The shields are similar in that they all contain equal weight fractions of reinforcing steel but differ in the distribution of steel. Forward and adjoint transport calculations were performed for each of the shields using a fission neutron source on the upper surface and a tissue response on the lower surface.

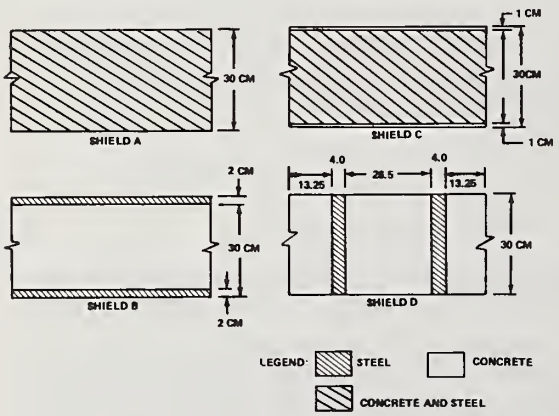

Figure 1: Four Shield Configurations with equal rebar volume fractions of 12%

The energy distribution of fission neutrons were given by

$$S(E) = 0.453 \exp(-E/0.965) \sinh(\sqrt{2.29E}) \quad (7)$$

where the energy, E, is in MeV.[4] This energy distribution was used for $.01 \le E \le 15$ MeV. For energies outside of this range, S(E) = 0. The response function was represented by the equation

$$R(E) = \exp(A + Bx + Cx^2 + Dx^3) \quad (8)$$

where x = lnE with E given in MeV. The coefficients A, B, C and D are as follows:

Neutron Energy (MeV)	A	B
2.5-08* To 1.07-07	-1.2514+01	
1.0-07 To 1.0-02	-1.2210+01	1.7165-01
0.01 To 0.1	-8.9302	7.8440-01
0.1 To 0.5	-8.6632	9.0037-01
0.5 To 1.0	-8.9359	5.0696-01
1.0 To 2.5	-8.9359	-5.5979-02
2.5 To 5.0	-9.2822	3.2193-01
5.0 To 7.0	-8.4741	-1.8018-01
7.0 To 10.0	-8.8247	
10.0 To 14.0	-1.1208+01	1.0352
14.0 To 20.0	-9.1202	2.4395-01

Neutron Energy (MeV)	C	D
2.5-08 To 1.07-07	0.0	0.0
1.0-07 To 1.0-02	2.6034-02	1.0273-03

Photon Energy (MeV)	A	B
0.03 - 0.5	-13.626	-0.57117
0.5 - 5.0	-13.133	0.72008
5.0 -15.0	-12.791	0.28309

Photon Energy (MeV)	C	D
0.03 - 0.5	-1.0954	-0.24897
0.5 - 5.0	-0.033603	
5.0 -15.0	-0.10873	

Cross section sensitivity calculations were performed using the SAIDOT code described previously. The results for the microscopic iron cross section from the DLC/31[5] multigroup cross section library are summarized in Table I. In addition to the total sensitivity, several components of sensitivity are tabulated. For the neutron cross section, the contribution to the total sensitivity is given for the total cross section, the scattering cross section and the gamma ray production cross section. For the gamma ray cross section, the contributions of the total and scattering cross sections are separated. The sensitivity function for the neutron cross section is plotted in Figures 2 through 5 respectively for the four shields.

* read as 2.5×10^{-8}

Table I
Summary of Results for Iron Cross Section Sensitivity

Shield Conf.	Neutron Collision	Scattering	Secondary Gamma ray	Total Neutron
A	-30.69	24.30	.268	-6.12
B	-31.03	25.20	.297	-5.54
C	-30.85	24.83	.290	-5.73
D	-27.65	23.02	.150	-4.48

Shield Configuration	Gamma ray Collision	Scattering	Total Gamma ray
A	-.292	.127	-.165
B	-.467	.220	-.248
C	-.383	.175	-.208
D	-.203	.081	-.122

Shield Configuration	Total Neutron and Gamma ray
A	-6.29
B	-5.78
C	-5.94
D	-4.61

Discussion of Results and Conclusions

There is a 5.5% variation in the total sensitivity of the three one dimensional shields A, B and C. The two dimensional shield, D, results in a 25% lower sensitivity to the iron cross section. Looking at the partial cross sections, most of this reduction can be attributed to the lower dependence on the gamma ray production cross section.

Shields A and D are perhaps the fairest comparison between a similar one and two dimensional shields. Comparing the sensitivity functions of the iron cross section given in Figures 2 and 5 as a function of neutron energy, it is observed that the 2-D shield sensitivity is about 30 - 60% lower than the 1-D shield for neutron energies greater than 1 MeV (Note that a solid line denotes a negative sensitivity). For energies between 100 keV and 1 MeV the 2-D shield sensitivity is about 20 percent lower than that of the 1-D shield. For energies less than 10 keV the 2-D shield is a factor of 2 to 4 less than the 1-D shield. The 2-D shield is a factor of 2 more sensitive to the 22 keV window in the iron cross section.

Our conclusions in this analysis is that the spatial distribution of reinforcing steel is not inconsequential. There appears to be more difference in the sensitivity between the 2-D shield and any of the other 1-D shields than between any of the 1-D shields. It would seem advisable to approach cross section sensitivity studies with the same geometric fidelity that is required for the transport analysis of a shield.

References:

1) D. E. Bartine et. al., "A Cross Section Sensitivity Study of Radiation Transport in Concrete," Trans. Am. Nuc. Soc., Vol 18, p381 (1974).
2) D. E. Bartine, F. R. Mynatt, E. M. Oblow, "SWANLAKE-A Computer Code Utilizing ANISN Radiation Transport Calculations for Cross Section Sensitivity Studies," ORNL-TM-3809, (1973).
3) D. E. Bartine, E. M. Oblow, F. R. Mynatt, "Radiation Transport Cross-Section Sensitivity Analysis-A General Approach Illustrated for a Thermonuclear Source in Air," ORNL-TM-4335 (1973).
4) G. L. Simmons, "Specifications for Power Reactor Shielding Benchwork Problems (Draft)," Memorandum to ANS 6.2 Standards Committee (1974).
5) R. W. Roussin, "DLC/31 Interim Documentation," Radiation Shielding Information Center (1974).

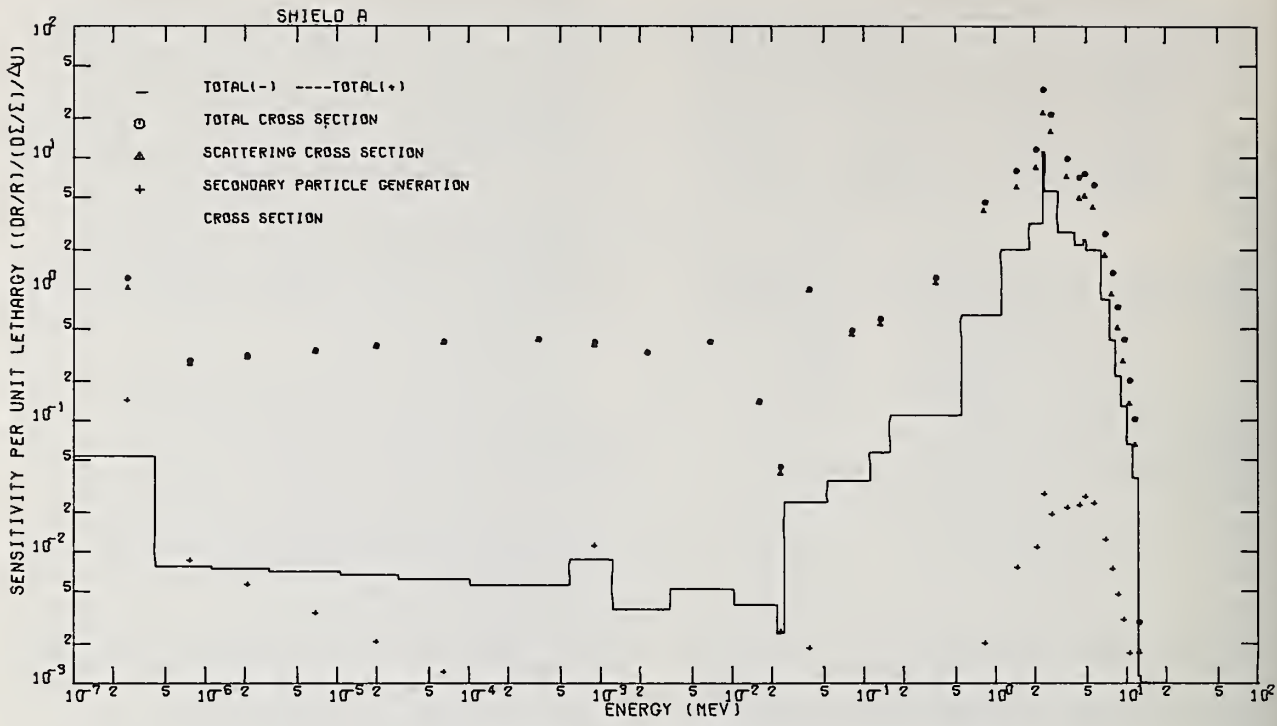

Figure 2. Sensitivity to iron neutron cross section for shield A

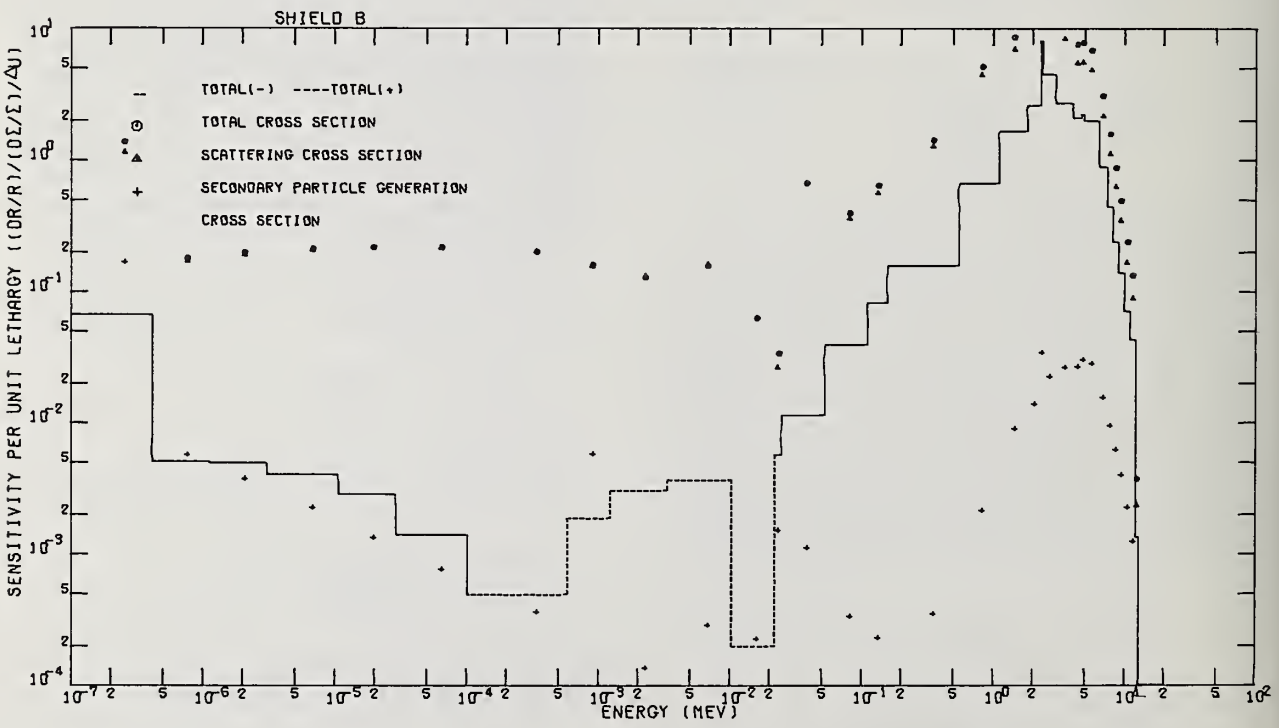

Figure 3. Sensitivity to iron neutron cross section for shield B

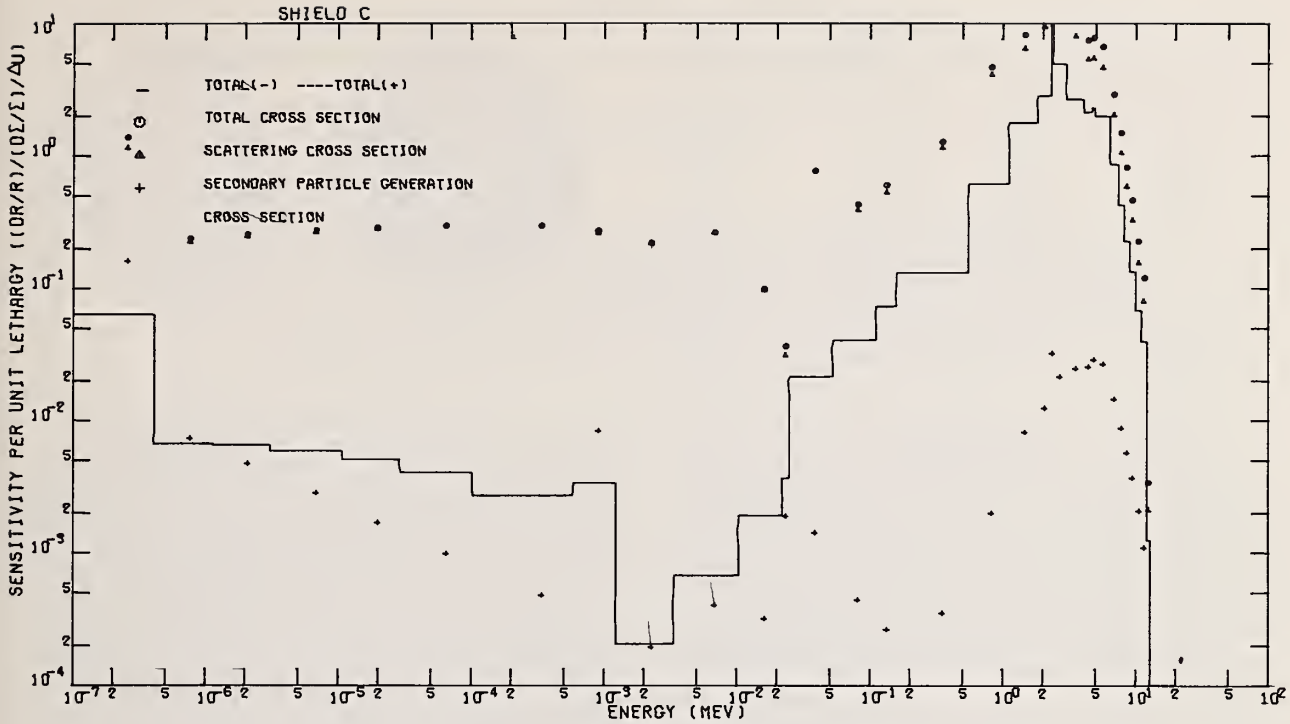

Figure 4. Sensitivity to iron neutron cross section for shield C

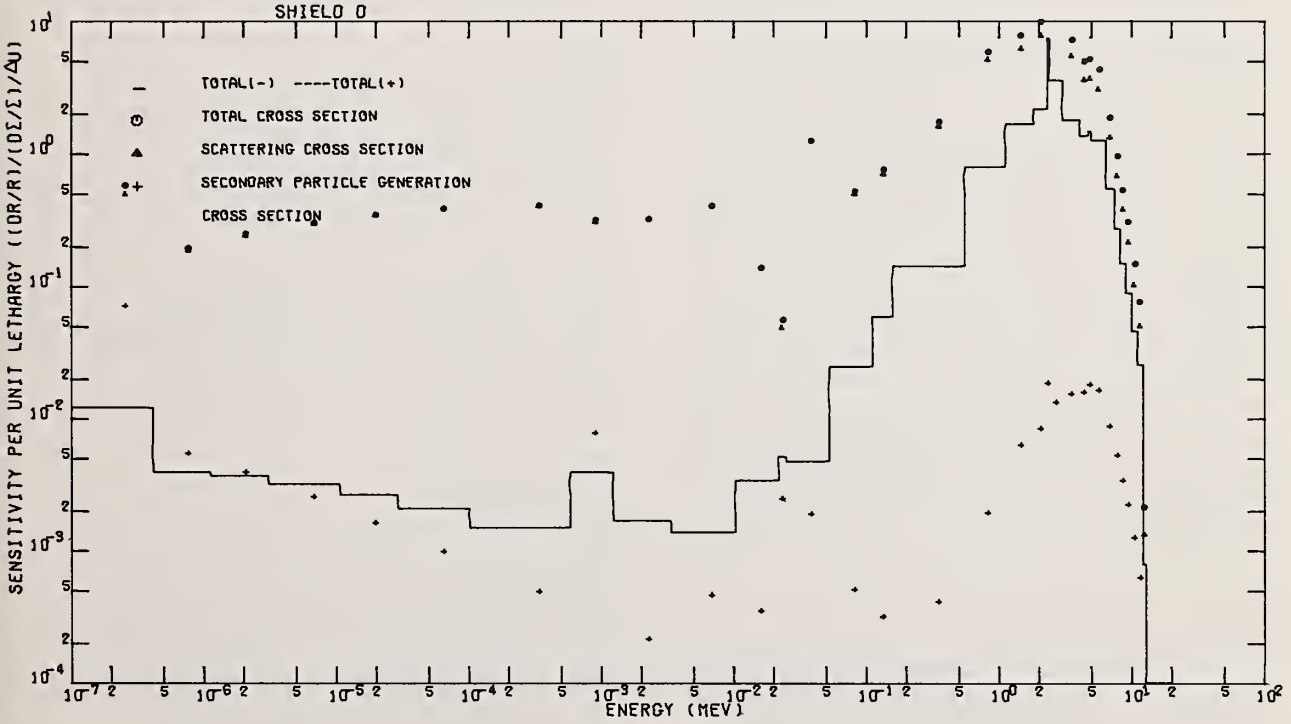

Figure 5. Sensitivity to iron neutron cross section for shield D

GCFR BENCHMARKS: EXPERIMENTS AND ANALYSIS

S.Seth, W.Heer, M.Jermann, C.McCombie, E.Ottewitte, R.Richmond and P.Wydler

Swiss Federal Institute for Reactor Research

CH-5303 Würenlingen

Measurements of reaction rate ratios and neutron spectra in GCFR benchmark lattices are described. An important feature of the lattices is that rod fuel elements are used. Several data sets have been tested against the experiments and deficiencies indicated.

(GCFR; benchmarks; integral measurements; data testing)

Introduction

The research effort on the PROTEUS zero-energy reactor is currently devoted to a benchmark study of the neutron physics properties of the Gas-Cooled Fast Reactor (GCFR) lattice. The test lattice was constructed in the central region of an existing thermal reactor. The converted fast-thermal coupled system basically consists of an outer thermal zone, an annular buffer zone to aid spectrum conversion and the central fast zone. The approach adopted is to measure one-group effective cross-section ratios, reaction rate profiles and neutron spectra in assemblies similar in geometry and composition to a typical GCFR lattice. It is important that unlike the great majority of critical experiments which use plate fuel elements, the present lattice is constructed of rod fuel elements. This gives the advantage that geometry dependent phenomena such as neutron streaming and heterogeneity are correctly represented.

The aim of this work is to check the performance of nuclear data sets and calculational methods used in GCFR design studies. The experiments in PROTEUS to date have dealt with a typical GCFR lattice (core 1), a GCFR lattice with enhanced steel fraction (core 2), a repeat of the basic lattice with an improved buffer zone (core 3), and simulated power reactor features (cores 3A, 3B and 3C) comprising a central UO_2 blanket zone, fully and partially inserted control absorber rods and a subassembly with a steel wall in the centre of the GCFR lattice. Future experiments will include the simulation of a steam entry accident, measurement of neutron streaming effects and studies of the blanket and shield. The present paper discusses the results of the first three cores.

Description of the Lattices

Typical GCFR Lattice

The fast zone of PROTEUS, containing the GCFR test lattice, is 50 cms in diameter and 140 cms high. The fuel consists of 6.7 mm diameter, 7 mm long pellets of PuO_2/UO_2 containing 15% plutonium with a Pu240 fraction of 17.6 %. The make up of a fuel element is indicated in Table I. The total fuel height is 88.9 cms (66.7 cms in core 1) and the axial blanket regions, above and below the fuel, are each 22.7 cms (34 cms in core 1) in height. The fuel rods are placed on a hexagonal array of 1 cm pitch (Fig.1). The averaged material volume fractions and nuclide concentrations in the lattice are given in Table III. The fast lattices of cores 1 and 3 were constructed to the above description. The neutron spectra for the normal and steel-enhanced cores are shown in Fig.3. The neutron balance summarized in Table III describes the neutron physics properties of the basic GCFR test lattice.

Steel-enhanced Lattice

The typical GCFR lattice was modified in core 2 by replacing one-third of the PuO_2/UO_2 fuel rods by stainless-steel rods. The same steel canning (Table I) was used to hold stainless-steel rods instead of the fuel-containing aluminium capsules. A section of the altered lattice is shown in Fig.2. The corresponding material and nuclear composition is included in Table II. This modification raised the steel volume fraction from 11% to 26%. A comparison of the normal and enhanced-steel cases is intended to provide a check on the integral data of steel.

Table I. Details of the Fuel Elements

Fuel Material	PuO_2/UO_2 Pellets
Pu/(Pu+U) (w%)	15.0
Pu240/Pu (w%)	17.6
Pu241/Pu (w%)	3.0
U235/U (w%)	0.43
Density (g/cm^3)	10.5
Pellet Diameter (cm)	0.670
Pellet Length (cm)	0.7
Capsule Can Material	Al
Wall Thickness (cm)	0.0085
Fuel Length in Capsule (cm)	5.5
Fuel Rod Can Material	18/8 Steel
Inner Diameter (cm)	0.74
Outer Diameter (cm)	0.82
Fuel Length in Rod (cm) (Core 1)	66.7
(Core 3)	88.9
Total Rod Length (cm)	142

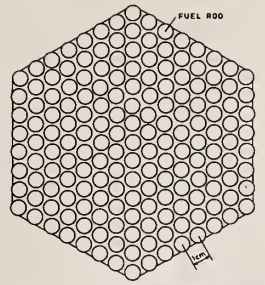

Fig. 1. Section of the PROTEUS GCFR Lattice

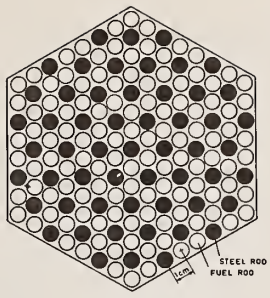

Fig. 2. Section of the Steel-Enhanced PROTEUS GCFR Lattice

PROTEUS Lattices as Benchmarks

In the case of core 1, which made use of a UO_2 buffer zone, the presence of zones outside the fast zone led to calculated deviations between the PROTEUS GCFR lattice and the reference single-zone GCFR of up to 5% for the individual central reaction rates of interest. These were primarily due to the radial penetration of excess high and low energy neutrons. A comparison with calculations of a number of measured radial reaction rate distributions through various zones of the core showed that the shapes of these distributions were predicted to an accuracy of ± 15%.[1] This implied that the radial penetration of unwanted neutrons could be calculated with similar accuracy so that the calculated reaction rate deviations between PROTEUS and the corresponding single-zone reactor would have a maximum uncertainty of ± 0.75 %. For all subsequent cores, therefore, the penetration of excess neutrons was reduced by replacing the uranium oxide buffer by a uranium metal buffer. This had the effect of reducing the deviations in reaction rates between PROTEUS and the reference single-zone reactor to less than ± 1.5 % so that the maximum uncertainty in their prediction is now estimated as ± 0.25 %. Table IV gives the necessary correction factors to adjust the reaction rate ratios measured in the centre of the PROTEUS fast zone to the reference single-zone reactor.

The limiting error estimated above is small in comparison to the experimental errors and to the target accuracies for fast reactor design studies (discussed below). The present measurements in PROTEUS are therefore considered to have the status of benchmark experiments.

Table II. Composition of Lattices

	Normal GCFR (Cores 1 and 3)	Steel-enhanced GCFR (Core 2)
Material	Volume Fraction (%)	
Fuel	40.4	26.9
Aluminium	2.8	2.0
Steel	11.3	25.6
Air	45.5	45.5
Nuclide	Average Concentration (atoms cm^{-3} $\times 10^{21}$)	
Pu239	1.116	0.7442
Pu240	0.2456	0.1637
Pu241	0.4108×10^{-1}	0.2739×10^{-1}
U 235	0.3478×10^{-1}	0.2319×10^{-1}
U 238	7.953	5.302
H	0.8669×10^{-1}	0.5779×10^{-1}
O	1.881×10^{1}	1.254×10^{1}
N	0.1735×10^{-1}	0.1715×10^{-1}
Al	1.660	1.179
Fe	6.549	1.541×10^{1}
Cr	1.739	4.086
Mo	0.1205	0.1440
Mn	0.2474	0.4779
Ni	1.005	2.180
Si	0.9686×10^{-1}	0.2021

Table III. Neutron Balance in the GCFR Lattice

Nuclide	Capture	Fission	Production
Pu239	0.083	0.378	1.121
Pu240	0.015	0.022	0.066
Pu241	0.002	0.018	0.056
U235	0.003	0.012	0.030
U238	0.356	0.081	0.227
Steel	0.026	-	-
Oxygen	0.004	-	-
Total	0.489	0.511	1.501

Experimental Methods

The quantities measured in the centre of the GCFR lattice are:

A. the relative values of the integral fission rates per atom in U235, U238 and Pu239 and the capture rate in U238; and .

B. the neutron energy spectrum.

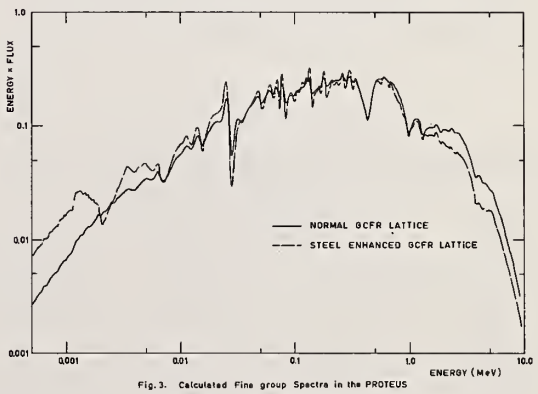

Fig. 3. Calculated Fine group Spectra in the PROTEUS Normal and Steel-Enhanced GCFR Lattices

Reaction Rate Measurements

The required accuracies for these measurements are related to the target accuracies for commercial fast reactor design calculations. These amount to ± 0.5 % in k-effective and ± 0.02 in breeding ratio[2]. The k-effective criterion is the most stringent and is equivalent to an error of ± 1.4 % in the prediction of the ratio of U238 capture to Pu239 fission, which is the most important quantity from the point of view of neutron physics. In order to ensure the accuracy of measurements, a check on the systematic errors was provided by measuring the same ratio by two methods.

Fission Rate Ratios. The first of the independent methods involves the irradiation of foils, each consisting primarily of one of the three fissile nuclides, inside fuel rods in the centre of the lattice. After irradiation the rate of emission from each foil of fission product gamma-rays with energies greater than 600 keV is measured using a two-channel NaI spectrometer. The fission-product activity ratios so obtained are related to the true fission rate ratios through simultaneous measurements in an off-centre-cavity with a back-to-back fission chamber containing thin deposits and foils of appropriate nuclides. The total error associated with this technique amounts to 1.4 %.

The other independent route for measuring fission ratios involves the use of solid state track recorders. Foils of polycarbonate resin (Macrofol KG) are irradiated adjacent to thin fissile deposits of U235, U238 and Pu239 within the fuel rods. Subsequently the tracks are enlarged by etching, stained and counted under the microscope of an automatic image analyser. The number of observed tracks, corrected for track-overlap, is proportional to the fission rate in the adjacent deposit. The total error on a given ratio using the track recorders is estimated to be about 2% for σ_{f5}/σ_{f9} and 2.5 % for σ_{f8}/σ_{f9}.

Capture-to-fission Ratio. The capture in U238 is determined by measuring the intensity of Np239 radiations emitted by depleted uranium foils subsequent to irradiation within the lattice fuel. Two methods of measurement are used in order to give a check on the experimental errors: 1. measurement by means of NaI counters, of the rate of coincident emission of the 106 keV gamma-ray and the 104 keV x-ray produced in the decay of Np239; 2. measurement by a germanium diode of the rate of emission of the 278 keV gamma-ray. The total estimated error on the ratio is 1.6 %. Work is in progress to reduce this error further in order to meet the target accuracy mentioned above.

Table IV. Comparison of the Central Reaction Rate Ratios for PROTEUS and Single-Zone Reactor Lattices

Ratio	PROTEUS GCFR Lattice / Single-Zone GCFR		
	Core 1	Core 2	Core 3
$\frac{\sigma_c\ U238}{\sigma_f\ Pu239}$	0.9732	0.9727	0.9920
$\frac{\sigma_f\ U238}{\sigma_f\ Pu239}$	1.0290	1.0204	0.9757
$\frac{\sigma_f\ U235}{\sigma_f\ Pu239}$	1.003	0.9824	1.0035

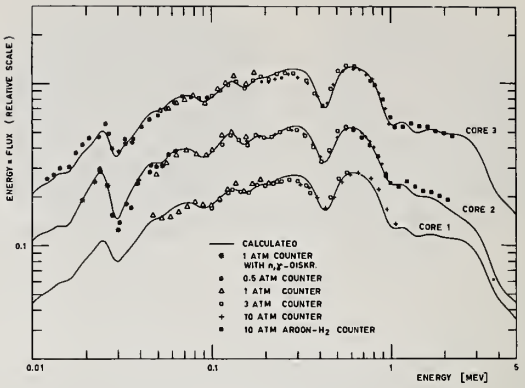

Fig.4. Measured and Calculated Neutron Spectra

Spectrum Measurements

The neutron spectrum was measured by means of the proton-recoil technique in which a hydrogen-filled proportional counter is placed in a cavity in the lattice and the measured proton-recoil spectrum is subsequently unfolded to obtain the corresponding neutron spectrum. Three spherical counters with filling pressures of 1,3 and 10 atm were used in core 1 to cover the energy range from 50 keV to 1.1 MeV. For cores 2 and 3 the energy range was substantially extended. At the upper end, the use of a 10 atm argon-hydrogen counter enabled the measurement of neutron energies up to 2 MeV. At the lower end, the range was extended to 10 keV (20 keV for core 2) using pulse shape discrimination to reduce the background gamma-ray contribution. The systematic error in the spectrum measurements varies from 5% to 10% depending on the measured energy range, while random errors are of the order of 2-3 % on individual points.

Calculational Method

Calculations carried out in parallel with the experimental program to check theoretical predictions of the central reaction rates and neutron spectrum were based on cross sections derived from the British FGL4 set[4]. This is a 2176-group set obtained primarily from the UK Nuclear Data Library[5] and from GENEX tabulations of resonance cross sections[6]. The set was used together with a cylindrical version of the code MURAL[4] to calculate spectra

Table V. Comparison of Experimental and Calculated (C/E) Values of Reaction Rate Ratios

A. Typical GCFR Lattice

Ratio	Experimental Value	FGL4	FGL5	ENOF/B-3 GGC5	ENOF/B-3 SPENG	ASEA ATOM	KFKINR	CADARACHE III	ABBN	JAERI
$\frac{\sigma_c\ U238}{\sigma_f\ Pu239}$	0.1341 ±0.0021	0.989	0.976	1.057	1.082	1.042	1.030	0.975	1.050	1.082
$\frac{\sigma_f\ U238}{\sigma_f\ Pu239}$	0.03118 ±0.00040	0.963	1.078	0.955	0.969	0.981	1.005	1.023	1.111	0.970
$\frac{\sigma_f\ U235}{\sigma_f\ Pu239}$	1.0137 ±0.0136	1.019	0.977	1.018	1.030	0.993	1.009	1.004	1.105	1.010

B. Steel- enhanced Lattice

$\frac{\sigma_c\ U238}{\sigma_f\ Pu239}$	0.1450 ±0.0025	0.965	0.978	1.038
$\frac{\sigma_f\ U238}{\sigma_f\ Pu239}$	0.02297 ±0.00033	0.930	1.045	0.981
$\frac{\sigma_f\ U235}{\sigma_f\ Pu239}$	1.069 ±0.017	1.007	0.963	0.990

in the multiregion cells of the fast and buffer zones using collision probability methods and to prepare 28-group cross sections. In the driver zones of the reactor, where thermal neutrons predominate, a separate 38-group cross section library with 33 fast (also related to FGL4) and 5 thermal groups was used in the calculation of cell fluxes, resonance screening and subsequent condensation to the same 28 groups used for the fast and buffer zones.

The radial dependence of the neutron spectrum and reaction rate was calculated by means of the 1-dimensional transport theory code EDSN (based on the WDSN[7] routine) using the S4 approximation. The axial leakage was taken into account by carrying out EDSN slab calculations for each zone of the system and using the derived axial bucklings in the radial calculation.

For the calculation of the steel-enhanced core 2, the only basic difference arises in the theoretical treatment of the mixed lattice cells, namely of fuel and steel. The geometrical effect of one steel rod being surrounded, on an average, by two fuel rods is accounted for by altering a MURAL subroutine to give collision probabilities for a system of two coupled cells[8].

Discussion of Results

We consider first the performance of the FGL4 data-set used in the initial calculations. Table V contains the summary of all central reaction measurements and calculations together with the calculation-to-experiment (C/E) ratios. The quoted experimental values have been adjusted to the reference single-zone GCFR using the corrections shown in Table IV and are averages of the core 1 and core 3 values which were in good agreement.

A comparison between the experimental neutron spectrum at the centre and the cell-averaged fine group spectrum calculated with MURAL is shown in Fig.4. The theoretical spectrum has been smoothed to correspond to the experimental energy resolution. Prominent features in the spectrum are the 29 keV and 433 keV resonances due to iron and oxygen respectively.

In the case of the typical GCFR lattice, the C/E values for σ_cU238/σ_fPu239 and σ_fU235/σ_fPu239 are similar to those reported for a series of measurements on ZEBRA cores containing Pu-fuelled, zero-leakage test regions[3]. The error in σ_fU238/σ_fPu239 is however much less than that observed (10-15%) for the ZEBRA cores. This suggests a better performance of the FGL4 set for the lower U238 fractional content and harder spectrum of a GCFR lattice. The discrepancy in the calculated σ_fU238/σ_fPu239 is accentuated in core 2 with increased steel fraction. The spectrum of Fig.4 also shows that the neutron flux above 1 MeV is underpredicted in this case. Thus the evidence from the normal and enriched steel cases put together implies an error in the inelastic scattering data for stainless-steel.

One possible mechanism which could explain the deficiencies in the integral data of U238 and steel is the increased anisotropy of elastic and inelastic scattering evidenced in a coupled-channel analysis of scattering data. This has been observed for both the Fe vibrational and U238 rotational nuclei. The effect of including this anisotropy in the reactor cross sections would be to harden the neutron spectrum.

Following the initial checks on the FGL4 data-set, the PROTEUS GCFR lattice data of core 1 were used to check the performance of several other nuclear data sets in collaboration with a number of organisations in other countries. A description of the nuclear data, calculation methods and results of this exercise has been given earlier[9]. Since that time the results of repeat measurements in core 3 have provided an improved experimental basis for this work and the availability of calculations based on additional data-sets (including one similar to FGL5) and for the steel-enhanced core 2 has extended its scope. A summary of the comparisons and the conclu-

sions is given below.

Table V and Fig.5 compare the C/E values obtained for the reaction rate ratios using various data sets. The error bars in the figure correspond to the uncertainty of measured values. As can be seen a majority of the data sets fail to meet the target accuracy of ±1.4% in predicting the important ratio $\sigma_c U238/\sigma_f Pu239$.

The worst predictions (ENOF/B-3, SPENG and JAERI) correspond to an error of -3% in k-eff and +0.08 in breeding ratio. A detailed comparison of fluxes in different groups show that the neutron spectrum was, in general, adequately predicted over the measured energy range. Further, the deviations of the calculated spectrum in individual energy regions was largely self-cancelling in the prediction of $\sigma_c U238/\sigma_f Pu239$ (0.2% for the spectrum calculated using the FGL4 data-set). The observed discrepancies are therefore produced primarily by errors in the cross-section data for U238 capture and Pu239 fission and it is in this area that improvements are required.

A separate observation is related to the observed difference in the ENOF/B-3 results processed respectively by the GGC5 and SPENG codes. The differences in the spectra given by the two methods are not sufficient to produce any significant change in the calculated values of $\sigma_c U238/\sigma_f Pu239$. The difference of 2.4% is, in fact, produced almost entirely by the difference (of 2.3%) in the calculated values of $\sigma_f Pu239$. Similar discrepancies between cross sections produced by different processing codes have been reported by Weisbin et al.[10]

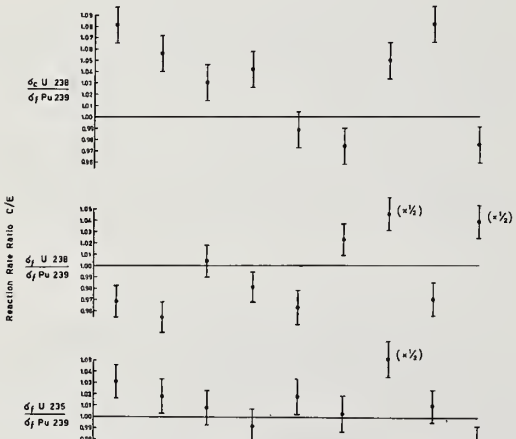

Fig.5. Comparison of Calculated to Experimental GCFR Reaction Rate Ratios for Various Participants

Conclusions

The present paper has described the measurement of reaction rate ratios and neutron spectra in a set of GCFR benchmark lattices. The results of these experiments were initially used to test the theoretical predictions based on the British FGL4 data library and subsequently to check the performance of a wide range of other data sets, commonly in use in other countries. Analysis points particularly to the general need for improved capture and fission data to give a better prediction of the ratio of U238 capture to Pu239 fission.

References

1. R. Richmond et al., "Measurements of Neutron Spectrum and Reaction Rates in a Gas-Cooled Fast Reactor Lattice," EIR Report 239 (1973)
2. B. Greebler and B.A. Hutchins, "Significance of Integral Parameters in the Design and Performance of Fast Breeder Reactors," Proc.Nat.Topical Mtg., New Developments in Reactor Physics, Conf.-720901 p.928 (1972)
3. A.M. Broomfield, et al., "Measurements of k-Infinity, Reaction Rates and Spectra in ZEBRA Pu Lattices," Proc. BNES Int.Conf., Physics of Fast Reactor Operation and Design, Paper 1.1 (1969)
4. J.L. Rowlands and J.O. MacDougall, "The Use of Integral Measurements to Adjust Cross Sections and Predict Reactor Properties," loc.cit., Ref.2, Paper 1.16
5. D.S. Norton, "The UKAEA Nuclear Data Library," AEEW-M824 (1968)
6. R.J. Brissenden and C. Durston, "A Users Guide to GENEX, SOR and Related Computer Codes," AEEW-R622 (1968)
7. J.R. Askew and R.J. Brissenden, "Some Improvements in the Discrete Ordinate Method of B.G. Carlson for Solving the Neutron Transport Equation," AEEW-R161 (1963)
8. P. Köhler, private communication
9. R. Richmond et al., "Testing of Nuclear Data-Sets Using PROTEUS GCFR Lattice Data," Proc. ANS Topical Mtg. Advanced Reactors: Physics Design and Economics (1974)
10. C. Weisbin et al., "Fast Reactor Processing Codes - Is There a Dollar's Worth of Difference Between Them ?," loc.cit.,Ref.9

NBS-114A (REV. 7-73)

U.S. DEPT. OF COMM. BIBLIOGRAPHIC DATA SHEET	1. PUBLICATION OR REPORT NO. NBS SP-425, Vol. I	2. Gov't Accession No.	3. Recipient's Accession No.

4. TITLE AND SUBTITLE

Proceedings of the Conference on Nuclear Cross Sections and Technology, March 3-7, 1975

5. Publication Date October 1975

6. Performing Organization Code

7. Editors: R. A. Schrack and C. D. Bowman

8. Performing Organ. Report No.

9. PERFORMING ORGANIZATION NAME AND ADDRESS

NATIONAL BUREAU OF STANDARDS
DEPARTMENT OF COMMERCE
WASHINGTON, D.C. 20234

10. Project/Task/Work Unit No.

11. Contract/Grant No.

12. Sponsoring Organization Name and Complete Address *(Street, City, State, ZIP)*

Energy Research Development Administration

13. Type of Report & Period Covered Final

14. Sponsoring Agency Code

15. SUPPLEMENTARY NOTES

Library of Congress Catalog Card Number: 75-619216

16. ABSTRACT *(A 200-word or less factual summary of most significant information. If document includes a significant bibliography or literature survey, mention it here.)*

These proceedings are the compilation of 217 papers presented at the Conference on Nuclear Cross Sections and Technology held in Washington, D.C. on March 3-7, 1975. The Conference summarized the present status of nuclear cross sections and technology and discussed future cross section needs. Special emphasis is placed on reactor technology and biomedical applications of nuclear science and the measurement of standard cross sections.

17. KEY WORDS *(six to twelve entries; alphabetical order; capitalize only the first letter of the first key word unless a proper name; separated by semicolons)*

Biomedical; Conference; cross section; nuclear; standards; technology.

18. AVAILABILITY

[X] Unlimited

[ ] For Official Distribution. Do Not Release to NTIS

[X] Order From Sup. of Doc., U.S. Government Printing Office Washington, D.C. 20402, SD Cat. No. C13.10:425/vol. I

[ ] Order From National Technical Information Service (NTIS) Springfield, Virginia 22151

19. SECURITY CLASS (THIS REPORT) UNCLASSIFIED X

21. NO. OF PAGES Vol. I 487

20. SECURITY CLASS (THIS PAGE) UNCLASSIFIED X

22. Price

☆ U.S. GOVERNMENT PRINTING OFFICE : 1975 O—591—092

USCOMM-DC 29042-P74